Advances in Natural and Technological Hazards Research

Yasuhiro Yamada · Kiichiro Kawamura
Ken Ikehara · Yujiro Ogawa
Roger Urgeles · David Mosher
Jason Chaytor · Michael Strasser *Editors*

Submarine Mass Movements and Their Consequences

Springer

Submarine Mass Movements and Their Consequences

Advances in Natural and Technological Hazards Research

Volume 31

For further volumes:
http://www.springer.com/series/6362

Yasuhiro Yamada • Kiichiro Kawamura
Ken Ikehara • Yujiro Ogawa • Roger Urgeles
David Mosher • Jason Chaytor
Michael Strasser
Editors

Submarine Mass Movements and Their Consequences

5th International Symposium

Springer

Editors
Yasuhiro Yamada
Department of Earth Resources Engineering
Kyoto University
Katsura, Nishikyo
615-8540 Kyoto
Japan
yamada@earth.kumst.kyoto-u.ac.jp

Ken Ikehara
Geological Survey of Japan
1-1-1 Higashi, Tsukuba
305-8567 Ibaraki
Japan
k-ikehara@aist.go.jp

Roger Urgeles
Institut de Ciències del Mar (CSIC)
Passeig Marítim de la Barceloneta, 37-49
08003 Barcelona
Spain
urgeles@icm.csic.es

Jason Chaytor
Oceanographic Institution
United States Geological Survey
Woods Hole Science Center
Woods Hole Road 384
02543 Woods Hole
Massachusetts
USA
jchaytor@usgs.gov

Kiichiro Kawamura
Fukada Geological Institute
2-13-12 Honkomagome, Bunkyo
113-0021 Tokyo
Japan
kichiro@fgi.or.jp

Yujiro Ogawa
University of Tsukuba
Yokodai 1-127-2-C-740
Tsukubamirai 300-2358
Japan
fyogawa45@yahoo.co.jp

David Mosher
Bedford Institute of Oceanography
Geological Survey of Canada
Natural Resources Canada
Challenge Dr. 1
Dartmouth, NS B2Y 4A2
Canada
dmosher@nrcan.gc.ca

Michael Strasser
Geological Institute
ETH Zurich
Sonneggstrasse 5
8092 Zurich
Switzerland
strasser@erdw.ethz.ch

ISBN 978-94-007-2161-6 e-ISBN 978-94-007-2162-3
DOI 10.1007/978-94-007-2162-3
Springer Dordrecht Heidelberg London New York

Library of Congress Control Number: 2011939086

Inoue Foundation for Science

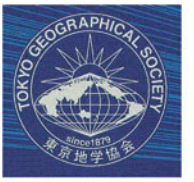

Contents

Contributors

David Airey University of Sydney, Sydney, NSW, Australia

Patrick Albéric Institut des Sciences de la Terre d'Orléans, UMR 6113 CNRS, Université d'Orléans, Université François Rabelais de Tours, Observatoire des Sciences de l'Univers en région Centre, 1A rue de la Férollerie 45071, Orléans cedex 2, France

Tiago Alves 3D Seismic Lab, School of Earth and Ocean Sciences, Cardiff University, Main Building, Park Place CF10 3YE, Cardiff, UK

Andrea Anasetti Leibniz Institute of Marine Sciences (IFM-GEOMAR), Wischhofstr. 1-3 24148, Kiel, Germany, aanasetti@ifm-geomar.de

Ryo Anma Graduate School of Life and Environmental Sciences, University of Tsukuba, 1-1-1 Tennodai Tsukuba, Ibaraki, 305-8572, Japan

Juichiro Ashi Atmosphere and Ocean Research Institute, The University of Tokyo, 5-1-5 Kashiwanoha Kashiwa, Chiba, 277-8564, Japan, ashi@aori.u-tokyo.ac.jp

Toshitaka Baba Earthquake and Tsunami Research Project for Disaster Prevention, Japan Agency for Marine-Earth Science and Technology, 2-15 Natsushima-cho Yokosuka 237-0061, Japan, babat@jamstec.go.jp

Nicole Baeten Department of Geology, University of Tromsø, Tromsø, Norway

Christophe Basile Laboratoire de Géodynamique des Chaînes Alpines, UMR-CNRS 5025, Observatoire des Sciences de l'Univers de Grenoble, Université Joseph Fourier, Maison des Géosciences, 1381 rue de la Piscine 38400, St. Martin d'Hères, France

Jan H. Behrmann SFB574, IFM-GEOMAR Leibniz Institute for Marine Sciences, University of Kiel, Wischhofstr. 1-3 Kiel, Germany, jbehrmann@ifm-geomar.de

Valerie Bellec Geological Survey of Norway (NGU), 6315 Sluppen 7491, Trondheim, Norway

International Centre for GeoHazards (ICG), 3930 Ullevål Stadion N-0806, Oslo, Norway

Sara Benetti School of Environmental Sciences, University of Ulster, Cromore Road Coleraine BT52 1SA, Northern Ireland, UK

Jörg Bialas Leibniz Institute of Marine Sciences (IFM-GEOMAR), Wischhofstr. 1-3 24148, Kiel, Germany

Reidulv Bøe Geological Survey of Norway (NGU), 6315 Sluppen7491, Trondheim, Norway; International Centre for GeoHazards (ICG), 3930 Ullevål Stadion N-0806, Oslo, Norway

Gualtiero Böhm Istituto Nazionale di Oceanografia e di Geofisica Sperimentale - OGS, Borgo Grotta Gigante 42/C34010 Sgonico (TS), Italy

Pierre Boivin Laboratoire Magma et Volcans, UMR 6524 CNRS, M163 IRD, PRES Clermont, Université Blaise Pascale, 5 rue Kessler 63038, Clermont-Ferrand Cedex, France

Alessandro Bosman CNR, Istituto di Geologia Ambientale e Geoingegneria, Via Salaria km 29.300, Monterotondo Stazione (Roma) Roma 00016, Italy

Georges Boudon Institut de Physique du Globe de Paris, 1 rue Jussieu 75238, Paris Cedex 05, France

Ron Boyd University of Newcastle, Newcastle, NSW, Australia ConocoPhillips, Houston, TX, USA

Jo Brendryen Department of Earth Science, University of Bergen, Bergen, Norway

Warner Brückmann Leibniz Institute of Marine Sciences (IFM-GEOMAR), Wischhofstr. 1-3 24148, Kiel, Germany

Stefan Bünz Department of Geology, University of Tromsø, N-9037, Tromsø, Norway

Angelo Camerlenghi Departament d'Estratigrafia, P. i Geosciènces Marines, ICREA, Istitució Catalana de Recerca I Estudis Advançats, c/o Universitat de Barcelona, C/Martí i Franques, s/n E-080028, Barcelona, Spain, acamerlenghi@ub.edu

D. Calvin Campbell Geological Survey of Canada (Atlantic), Bedford Institute of Oceanography, 1006, Darmouth, NS, Canada, B2Y 4A2

Miquel Canals GRC Geociències Marines, Universitat de Barcelona, Barcelona E-08028, Spain

Joe Cartwright 3D Seismic Lab, School of Earth and Ocean Sciences, Cardiff University, Main Building, Park Place CF10 3YE, Cardiff, UK

Daniele Casalbore CNR, Istituto di Geologia Ambientale e Geoingegneria, Via Salaria km 29.300, Monterotondo Stazione (Roma) Roma 00016, Italy, daniele.casalbore@unibo.it

Aurélie Casedevant UMR EPOC, University Bordeaux 1, Avenue des Facultés 33405, Talence, France

Antonio Cattaneo Géosciences Marine, IFREMER, BP70 F-29280, Plouzané Cédex, France

Genevieve Cauchon-Voyer Département de géologie et génie géologique, Université Laval, Québec, Québec, Canada, G1K 7P4, genevieve.cauchon-voyer.1@ulaval.ca

Duane Champion Volcano Science Center, U.S. Geological Survey, MS-910, 345 Middlefield Road, Menlo Park, CA, 94025, USA

Shyam Chand Geological Survey of Norway (NGU), Postboks 6315 Sluppen 7491, Trondheim, Norway; International Centre for GeoHazards (ICG), 3930 Ullevål Stadion N-0806, Oslo, Norway

C. Borden Chapman Geological Survey of Canada, Natural Resources Canada, Bedford Institute of Oceanography, 1 Challenger Dr. Dartmouth, NS B2Y 4A2, Canada,

Emmanuel Chapron Institut des Sciences de la Terre d'Orléans, UMR 6113 CNRS, Université d'Orléans, Université François Rabelais de Tours, Observatoire des Sciences de l'Univers en région Centre, 1A rue de la Férollerie 45071, Orléans cedex 2, France, emmanuel.chapron@univ-orleans.fr

Jason D. Chaytor U.S. Geological Survey, Woods Hole Coastal and Marine Science Center, 384 Woods Hole Road, Woods Hole, MA, 02543, USA, jchaytor@usgs.gov

Ken Chi C-CORE, Captain Robert A. Bartlett Building, Morrissey Road St. John's, NL, A1B X5, Canada; Faculty of Engineering and Applied Science, Memorial University of Newfoundland, St. John's, NL, A1B 3X5, Canada, kfchi@mun.ca

Francesco Latino Chiocci Dip. Scienze della Terra, Sapienza. University of Roma, P.le Aldo Moro 5, Roma 00185, Italy

CNR, Istituto di Geologia Ambientale e Geoingegneria, Via Salaria km 29.300, Monterotondo Stazione (Roma) Roma 00016, Italy

Shun Chiyonobu RITE, Kizugawa 619-0292, Japan

Samantha Clarke University of Sydney, Sydney, NSW, Australia, samantha.clarke@sydney.edu.au

Chris I. Clayton School of Civil Engineering and the Environment, University of Southampton, Highfield, Southampton, SO17 1BJ, UK

Giulia Codegone Dipartimento di Scienze della Terra, Università degli Studi di Torino, via Valperga Caluso, 35 I-10125, Torino, Italy

Sian Cosham RPS Energy Ltd, Goldsworth House, Denton Way Woking, Surrey, GU21 3LG, UK

Alexandre Dano UMR GéoAzur, UNS-UPMC-CNRS-IRD, Port de la Darse 06235, Villefranche/Mer, France

Christine Deplus Institut de Physique du Globe de Paris, 1 rue Jussieu 75238, Paris Cedex 05, France

Marc Desmet Institut des Sciences de la Terre d'Orléans, UMR 6113 CNRS, Université d'Orléans, Université François Rabelais de Tours, Observatoire des Sciences de l'Univers en région Centre, 1A rue de la Férollerie 45071, Orléans cedex 2, France

Julie A. Dickinson RPS Energy Ltd, Goldsworth House, Denton WayWoking, Surrey, GU21 3LG, UK, dickinsonju@rpsgroup.com

Brandon Dugan Department of Earth Science, Rice University, 6100 Main Street MS-126, Houston, TX, 77005, USA, dugan@rice.edu

Raymond S. Eilertsen Geological Survey of Norway (NGU), Tromsø, Norway

Neville Exon Earth and Marine Sciences, Australian National University, Canberra, ACT, Australia

Andrea Festa Dipartimento di Scienze della Terra, Università degli Studi di Torino, via Valperga Caluso, 35 I-10125, Torino, Italy

Stephen S. Flint School of Environmental Sciences, University of Liverpool, Liverpool L69 3GP, UK

Michael Formolo The University of Tulsa, 800 South Tucker Drive Tulsa, OK, 74104, USA

Carl Fredrik Forsberg NGI – Norwegian Geotechnical Institute, ICG – International Centre for Geohazards c/o NGI, Ullevål, 0806 3930, Oslo, Norway

Matthias Forwick Department of Geology, University of Tromsø, Tromsø N-9037, Norway, Matthias.Forwick@uit.no

Anne Le Friant Institut de Physique du Globe de Paris, 1 rue Jussieu 75238, Paris Cedex 05, France

Davide Gamboa 3D Seismic Lab, School of Earth and Ocean Sciences, Cardiff University, Main Building, Park Place CF10 3YE, Cardiff, UK, GamboaDA1@cf.ac.uk

James Gardner CCOM, University of New Hampshire, Durham, NH, USA

Verginie Gaullier CEFREM – UMR 5110, Université de Perpignan Via Domitia, 52 Avenue Paul Alduy 66860, Perpignan Cedex, France

Jacob Geersen Leibniz Institute of Marine Sciences (IFM-GEOMAR), Wischhofstr. 1-3 24148, Kiel, Germany

Aggeliki Georgiopoulou UCD School of Geological Sciences, University College Dublin, Belfield, Dublin 4, Ireland, aggie.georg@ucd.ie

Sylfest Glimsdal Norwegian Geotechnical Institute (NGI) & ICG, Oslo, Norway

Clemencia Gómez Agencia Nacional de Hidrocarburos, Av. El Dorado, Edif. Cámara Colombiana Infraestructura, Bogota, Colombia, clemencia.gomez@anh.gov.co

Kazuhisa Goto Planetary Exploration Research Center, Chiba Institute of Technology, 2-17-1 Tsudanuma Narashino 275-0016, Chiba, Japan; Disaster Control Research Center, Graduate School of Engineering, Tohoku University, Aoba 6-6-11-1104, Aramaki, Aoba-ku, Sendai 980-8579, Japan

Matthias Gruen Leibniz Institute of Marine Sciences (IFM-GEOMAR), Wischhofstr. 1-3, 24148 Kiel, Germany

Haflidi Haflidason Department of Earth Science, University of Bergen, P.O. Box 7800, 5020 Bergen, Norway

Yasuaki Hanamura JX Nippon Oil and Gas Exploration Corporation, 2-6-3, Otemachi Chiyoda-ku, Tokyo 100-8163, Japan, haflidi.haflidason@geo.uib.no

Till J.J. Hanebuth Center for Marine Environmental Sciences (MARUM), Faculty of Geosciences, University of Bremen, Leobener Str, Klagenfurter Str 28359, Bremen, Germany

Louise Hansen Geological Survey of Norway (NGU)/ICG, 6315 Sluppen 7491, Trondheim, Norway

Carl B. Harbitz Norwegian Geotechnical Institute (NGI) & ICG, Oslo, Norway

Rieka Harders SFB 574 and IFM-GEOMAR, Wischhofstrasse 1-3 Kiel 24148, Germany, rharders@ifm-geomar.de

Yoshitaka Hashimoto Department of Applied Science, Kochi University, Kochi 780-8520, Japan

Virginie Hassoun UMR GéoAzur, UNS-UPMC-CNRS-IRD, Port de la Darse 06235, Villefranche/Mer, France

Peter D.W. Haughton UCD School of Geological Sciences, University College Dublin, Belfield Dublin 4, Ireland

Bipul Hawlader Faculty of Engineering and Applied Science, Memorial University of Newfoundland, St. John's, NL A1B 3X5, Canada

Susann Henkel Alfred Wegener Institute for Polar and Marine Research (AWI), Am Handelshafen 1227570, Bremerhaven, Germany, susann.henkel@awi.de

Rüdiger Henrich MARUM and Faculty of Geosciences, University of Bremen, Bremen, Germany

Pierre Henry CEREGE - College de France, Aix en Provence, France

Berit Oline Hjelstuen Department of Earth Science, University of Bergen, Bergen, Norway

David M. Hodgson Stratigraphy Group, School of Environmental Sciences, University of Liverpool, Liverpool L15 3GP, UK, hodgson@liv.ac.uk

Megumi Hojo Department of Earth and Planetary Science, The University of Tokyo, Tokyo 113-0033, Japan

Thomas Hubble University of Sydney, Sydney, NSW, Australia, Thomas.Hubble@sydney.edu.au

Deborah Hutchinson United States Geological Survey, 384 Woods Hole Road Quissett Campus Woods Hole, MA, 02543-1598, USA

Tadahiro Hyakudome Marine Technology Center, Japan Agency for Marine-Earth Science and Technology, 2-15 Natsushima-cho Yokosuka 237-0061, Japan

Hiroshi Ikeda Fukada Geological Institute, 2-13-12 Honkomagome, Bunkyo, Tokyo 113-0021, Japan

Ken Ikehara Geological Survey of Japan, AIST, Tsukuba Central 7, 1-1-1, Higashi Tsukuba, Ibaraki 305-8567, Japan, k-ikehara@aist.go.jp

Fumihiko Imamura Disaster Control Research Center, Graduate School of Engineering, Tohoku University, Aoba 6-6-11-1104, Aramaki, Aoba-ku, Sendai 980-8579, Japan

IODP Expedition 333 Scientists Alves T (UnivCardiff, UK); Bauersachs T (UnivKiel, Germany); Chiyonobu S (RITE-Kyoto, Jp); Daigle H (Rice Univ, USA); Ekinci K (Univ Missouri, USA); Gao S (Univ Nanjing, China); Garcon M (CEREGE, France); Kawamura K (Fukada Geol Inst, Jp), Kitamura Y (JAMSTEC, Jp); Laberg JS (Univ Tromsø, Norway);Lee G (Pukyong Univ, Korea); Lee Y (Korea Inst Geosci); Lu Y (Univ Alabama, USA); Marcaillou B (Univ Antilles & Guayne, France); Matsubayashi O (AIST Tsukuba, Jp); Nagahashi Y (FukushimaUniv, Jp); Novak B (W. Washington Univ, USA); Saito Y (Doshisha Univ, Jp); Satoguchi Y (Lake Biwa Museum, Jp);Screaton E (Univ. Florida, USA); Scudder R (BostonUniv, USA); Yamaguchi A (Univ. Tokyo, Jp)

Dieter Issler Norwegian Geotechnical Institute (NGI) & ICG, Oslo, Norway

Michael Ivanov UNESCO Centre for Marine Geology and Geophysics, Moscow State University, Moscow 119899, Russia

Hilde B. Johannessen Department of Geology, University of Tromsø, Tromsø N-9037, Norway

Runar Johansen Department of Geology, University of Tromsø, N-9037 Tromsø, Norway

Toshiya Kanamatsu Institute for Research on Earth Evolution, Japan Agency for Marine-Earth Science and Technology (JAMSTEC), 2-15 Natsushima-cho, 237-0061 Yokosuka, Japan, toshiyak@jamstec.go.jp

Yoshiyuki Kaneda Earthquake and Tsunami Research Project for Disaster Prevention, Japan Agency for Marine-Earth Science and Technology, 2-15 Natsushima-cho, Yokosuka 237-0061, Japan

Kazuhiko Kashiwase Earthquake and Tsunami Research Project for Disaster Prevention, Japan Agency for Marine-Earth Science and Technology, 2-15 Natsushima-cho Yokosuka 237-0061, Japan

Sabine Kasten Alfred Wegener Institute for Polar and Marine Research (AWI), Am Handelshafen 1227570, Bremerhaven, Germany

Kiichiro Kawamura Fukada Geological Institute, 2-13-12 Honkomagome Bunkyo, Tokyo 113-0021, Japan, kichiro@fgi.or.jp

John Keene University of Sydney, Sydney, NSW, Australia

Masataka Kinoshita IFREE, JAMSTEC, 2-15 Natsushima Yokosuka, Kanagawa, 273-0061, Japan

Yujin Kitamura Japan Agency for Marine-Earth Science and Technology, Institute for Research on Earth Evolution, 2-15 Natsushima-cho Yokosuka, Kanagawa, 237-0061, Japan, ykitamura@jamstec.go.jp

Satoru Kojima Department of Civil Engineering, Gifu University, Gifu 501-1193, Japan, skojima@gifu-u.ac.jp

Jean-Christophe Komorowski Institut de Physique du Globe de Paris, 1 rue Jussieu 75238, Paris Cedex 05, France

Achim Kopf Marine Geotechnics, MARUM – Center for Marine Environmental Sciences and Faculty of Geosciences, University of Bremen, Leobener Str 28359, Bremen, Germany, akopf@uni-bremen.de

Sebastian Krastel Leibniz Institute of Marine Sciences (IFM-GEOMAR), Wischhofstr. 1-3 24148, Kiel, Germany, skrastel@ifm-geomar.de

Stefan Kreiter MARUM – Research Center for Marine Environmental Science and Faculty of Geosciences, University of Bremen, Leobener Str 28359, Bremen, Germany

Tore J. Kvalstad NGI – Norwegian Geotechnical Institute, ICG – International Centre for Geohazards c/o NGI, Ullevål, 0806 PO Box 3930, Oslo, Norway

Jean-Sebastien L'Heureux Geological Survey of Norway (NGU)/ICG, PO Box 6315, Sluppen 7491, Trondheim, Norway; ICG – International Centre for Geohazards c/o NGI, Ullevål, 0806 PO Box 3930, Oslo, Norway, jean.lheureux@ngu.no

Jan Sverre Laberg Department of Geology, University of Tromsø, Tromsø N-9037, Norway, jan.laberg@uit.no

Patrick Lajeunesse Centre d'études nordiques & Département de Géographie, Université Laval, Québec, QC, G1V0A6, Canada

Matthias Lange Marine Geotechnics, MARUM – Center for Marine Environmental Sciences and Faculty of Geosciences, University of Bremen, Leobener Str 28359, Bremen, Germany, matlange@uni-bremen.de

Galderic Lastras GRC Geociències Marines, Universitat de Barcelona, Barcelona E-08028, Spain

Elodie Lebas Institut de Physique du Globe de Paris, 1 rue Jussieu 75238, Paris Cedex 05, France

Nina Lebedeva-Ivanova Woods Hole Oceanographic Institution, 266 Woods Hole Rd. MS# 22 Woods Hole, MA, 02543, USA

Isabelle Lecomte NORSAR & ICG, Kjeller, Norway

Grégoire Ledoux Centre d'études nordiques & Département de Géographie, Université Laval, Québec, QC, G1V0A6, Canada

Serge Leroueil Département de génie civil, Université Laval, Québec, Canada, G1K 7P4

Gang Li Department of Coastal Ocean Science, Nanjing University, Nanjing 210093, China, gangli1@hotmail.com

Katja Lindhorst Leibniz Institute of Marine Sciences (IFM-GEOMAR), Wischhofstr. 1-3 24148, Kiel, Germany, klindhorst@ifm-geomar.de

Camino Liquete Rural, Water and Ecosystem Resources Unit, European Commission – Joint Research Centre, Institute for Environment and Sustainability, Via E. Fermi 2749 TP 46021027, Ispra, Italy; Dept. Estratigrafia, Paleontologia i Geociències Marines, Facultat de Geologia, Universitat de Barcelona, c/ Martí i Franquès s/n 08028, Barcelona, Catalonia, Spain

Jacques Locat Laboratoire d'études sur les risques naturels, Département de géologie et de génie géologique, Université Laval, Québec, QC, Canada, G1K 7P4

Lies Loncke CEFREM – UMR 5110, Université de Perpignan Via Domitia, 52 Avenue Paul Alduy 66860, Perpignan Cedex, France

Oddvar Longva Geological Survey of Norway (NGU), PO Box 6315, Sluppen 7491, Trondheim, Norway; International Centre for GeoHazards (ICG), P.O. Box 3930 Ullevål Stadion N-0806, Oslo, Norway

Benoît Loubrieu Géosciences Marines, IFREMER, BP7029280, Plouzané, France

Renata G. Lucchi Istituto Nazionale di Oceanografia e di Geofisica Sperimentale - OGS, Borgo Grotta Gigante 42/C34010 Sgonico (TS), Italy; Departament d'Estratigrafia Paleontologia i Geociències Marines, Facultat de Geologia, Universitat de Barcelona, C/ Martí i Franquès, s/n E-08028, Barcelona, Spain, rglucchi@inogs.it

Claudio Corrado Lucente Servizio Tecnico dei Bacini Conca e Marecchia, Regione Emilia-Romagna, via Rosaspina, 7, I-47923, Rimini, Italy

Hideaki Machiyama Submarine Resources Research Project, JAMSTEC, 3173-25 Showa-machi, Kanazawa-ku, Yokohama, 236-0001, Japan

Gianni Madrussani Istituto Nazionale di Oceanografia e di Geofisica Sperimentale - OGS, Borgo Grotta Gigante 42/C34010, Sgonico (TS), Italy

Agnès Maillard LMTG, Université UPS (SVT-OMP), 14 Avenue Edouard Belin 31400, Toulouse, France

Paul Mann Institute for Geophysics, University of Texas at Austin, J. J. Pickle Research Campus, Bldg. 196 Austin, TX, 78758, USA, paulm@ig.utexas.edu

Doug G. Masson National Oceanography Centre, European Way, Southampton, SO14 3ZH, UK

Hiroyuki Matsumoto Earthquake and Tsunami Research Project for Disaster Prevention, Japan Agency for Marine-Earth Science and Technology, 2-15 Natsushima-cho Yokosuka 237-0061, Japan, hmatsumoto@jamstec.go.jp

Toshifumi Matsuoka Department of Earth Resources Engineering, Kyoto University, Katsura, Nishikyo Kyoto 615-8540, Japan

Stephen McCarron Department of Geography, National University of Ireland, Maynooth, Co Kildare, Ireland

Sandra Meissl SFB574, IFM-GEOMAR Leibniz Institute for Marine Sciences, University of Kiel, Wischhofstr. 1-3 24148, Kiel, Germany

Willem C.van derMerwe School of Environmental Sciences, University of Liverpool, Liverpool L69 3GP, UK

Mathias Meyer Leibniz Institute of Marine Sciences (IFM-GEOMAR), Wischhofstr. 1-3 24148, Kiel, Germany, mmeyer@ifm-geomar.de

Aaron Micallef GRC Geociències Marines, Universitat de Barcelona, Barcelona, E-08028, Spain; University of Malta, Msida MSD 2080, Malta, micallefaaron@ub.edu; micallefaaron@gmail.com

Sébastien Migeon UMR GéoAzur, UNS-UPMC-CNRS-IRD, Port de la Darse, 06235, Villefranche/Mer, France, migeon@geoazur.obs-vlfr.fr

Toshiro Misu Shizuoka Prefecture, 9-6, OhtemachiAoi-ku, Shizuoka, 420-6801, Japan

Keitaro Miyazawa Disaster Control Research Center, Graduate School of Engineering, Tohoku University, Aoba 6-6-11-1104, Aramaki, Aoba-ku Sendai 980-8579, Japan, miyazawa@tsunami2.civil.tohoku.ac.jp

Ben De Mol Dept. Estratigrafia, Paleontologia i Geociències Marines, Facultat de Geologia, Universitat de Barcelona, c/ Martí i Franquès s/n 08028, Barcelona, Catalonia, Spain; Parc Científic de Barcelona, c/ Adolf Florensa 8 08028, Barcelona, Catalonia, Spain

Gregory F. Moore University of Hawaii, Honolulu, USA

Eugene Morgan Geohazards Engineering Research, Tufts University, Medford, USA

Sumito Morita Research Institute for Geo-resources and Environments, Geological Survey of Japan, National Institute of Advanced Industrial Science and Technology, 1-1-1, Higashi Tsukuba, Ibaraki, 305-8567, Japan, morita-s@aist.go.jp

Tobias Mörz MARUM – Research Center for Marine Environmental Science and Faculty of Geosciences, University of Bremen, Leobener Str28359, Bremen, Germany

David Mosher Natural Resources Canada, Geological Survey of Canada – Atlantic, Bedford Institute of Oceanography, 1 Challenger Dr Dartmouth, NS, B2Y 4A2, Canada, dmosher@nrcan.gc.ca

Joshu J. Mountjoy National Institute of Water and Atmospheric Research, Private Bag 14901, Wellington, New Zealand, j.mountjoy@niwa.co.nz

Breandan Murphy RPS Energy Ltd, Goldsworth House, Denton Way, Woking, Surrey, GU21 3LG, UK

Emiliano Mutti Localita' Nociveglia, 24 - 43041, Bedonia (Parma), Italy

Farrokh Nadim International Centre for Geohazards (ICG), Norwegian Geotechnical Institute (NGI), P.O. Box 3930 Ullevaal Stadion, NO-0806 Oslo, Norway, farrokh.nadim@ngi.no

Takeshi Nakajima Research Institute for Geo-resources and Environments, Geological Survey of Japan, National Institute of Advanced Industrial Science and Technology, 1-1-1, Higashi Tsukuba, Ibaraki, 305-8567, Japan

Hajime Naruse Faculty of Science, Department of Earth Sciences, Chiba University, 1-33 Yayoicho, Inage-ku Chiba 263-8522, Japan, naruse@faculty.chiba-u.jp

Kei Ogata Department of Artic Geology, UNIS (University Centre in Svalbard), Pb. 1569171, Longyearbyen, Norway, kei.ogata@gmail.com; kei.ogata@unis.no

Yujiro Ogawa University of Tsukuba, Yokodai 1-127-2-C-740, Tsukubamirai 300-2358, Japan, fyogawa45@yahoo.co.jp

Yusuke Oshima Department of Earth Resources Engineering, Kyoto University, Katsura, Nishikyo, Kyoto 615-8540, Japan

Makoto Otsubo Research Center for Deep Geological Environments, National Institute of Advanced Industrial Science and Technology, Tsukuba Central 7, 1-1, Higashi 1-Chome, Tsukuba-shi, Ibaraki-ken, 305-8567, Japan, otsubo-m@aist.go.jp

Daniel Otto MARUM – Research Center for Marine Environmental Science and Faculty of Geosciences, University of Bremen, Leobener Str 28359, Bremen, Germany

Gary Parker Ven Te Chow Hydrosystems Lab, Department of Civil Engineering, College of Engineering, University of Illinois at Urbana-Champaign, Urbana, IL, 61802, USA

Martin Patriat Géosciences Marines, IFREMER, BP70 29280, Plouzané, France

France Pattier Géosciences Marines, IFREMER, BP7029280, Plouzané, France CEFREM – UMR 5110, Université de Perpignan Via Domitia, 52 Avenue Paul Alduy, 66860, Perpignan Cedex, France, france.pattier@etudiant.univ-perp.fr

Maria T. Pedrosa Departament d'Estratigrafia Paleontologia i Geociències Marines, Facultat de Geologia, Universitat de Barcelona, C/ Martí i Franquès, s/ nE-08028, Barcelona, Spain

Gian Andrea Pini Dipartimento di Scienze della Terra e Geologico-Ambientali, Università di Bologna, via Zamboni, 67, 40127, Bologna, Italy, gianandrea.pini@ unibo.it

David J.W. Piper Geological Survey of Canada (Atlantic), Bedford Institute of Oceanography, 1006, Darmouth, NS, Canada, B2Y 4A2

Pere Puig Institut de Ciències del Mar (CSIC), Pg. Marítim de la Barceloneta, 37-49 08003, Barcelona, Catalonia, Spain

César R. Ranero ICREA at CSIC, Barcelona Center for Subsurface Imaging, Instituto de Ciencias del Mar, Pg. Marítim de la Barceloneta 37-49 Barcelona 08003, Spain

Michele Rebesco Istituto Nazionale di Oceanografia e di Geofisica Sperimentale - OGS, Borgo Grotta Gigante 42/C34010Sgonico (TS), Italy, mrebesco@ogs.trieste.it

Thomas Reichel Statoil ASA, Vækerø, Norway

Anna Reusch MARUM – Research Center for Marine Environmental Science and Faculty of Geosciences, University of Bremen, Leobener Str 28359, Bremen, Germany

Natascha Riedinger University of California, 900 University Avenue Riverside, CA, 92521, USA

Leif Rise Geological Survey of Norway (NGU), Postboks 6315 Sluppen 7491, Trondheim, Norway; International Centre for GeoHazards (ICG), P.O. Box 3930 Ullevål Stadion N-0806, Oslo, Norway, leif.rise@ngu.no

Walter R. Roest Géosciences Marines, IFREMER, BP7029280, Plouzané, France

Giuliana Rossi Istituto Nazionale di Oceanografia e di Geofisica Sperimentale - OGS, Borgo Grotta Gigante 42/C34010 Sgonico (TS), Italy

Etienne Ruellan UMR GéoAzur, UNS-UPMC-CNRS-IRD, Port de la Darse 06235, Villefranche/Mer, France

Arito Sakaguchi IFREE1, Japan Agency for Marine Science and Technology, 2-15 Natsushima-cho Yokosuka, Kanagawa, 237-0061, Japan; Institute for Research on Earth Evolution (IFREE), Japan Agency for Marine-Earth Science and Technology (JAMSTEC), Yokohama, 236-0001, Japan

Mamoru Sano Nippon Marine Enterprises, Ltd, Nissei Yokosuka Center Building (8th Floor), 14-1, Ogawa-cho Yokosuka 238-0004, Japan

Hiroyoshi Sano Department of Earth and Planetary Sciences, Kyushu University, Fukuoka 812-8581, Japan

Shinji Sassa Port and Airport Research Institute, 3-1-1 Nagase Yokosuka 239-0826, Japan, sassa@ipc.pari.go.jp

Kenji Satake Earthquake Research Institute, The University of Tokyo, 1-1-1 Yayoi Bunkyo-ku, Tokyo 113-0032, Japan, satake@eri.u-tokyo.ac.jp

Chiara Sauli Istituto Nazionale di Oceanografia e di Geofisica Sperimentale - OGS, Borgo Grotta Gigante 42/C34010 Sgonico (TS), Italy

Derek E. Sawyer ExxonMobil Exploration, 222 Benmar DrHouston, TX, USA

Tilmann Schwenk Center for Marine Environmental Sciences (MARUM), Faculty of Geosciences, University of Bremen, Leobener Str, Klagenfurter Str 28359, Bremen, Germany

Hideo Sekiguchi Osaka City University, Osaka, Japan

Patrick M. Shannon UCD School of Geological Sciences, University College Dublin, Belfield Dublin 4, Ireland

Tadahiro Shibata IFREE, JAMSTEC, Yokohama 236-0001, Japan

John Shimeld Geological Survey of Canada, Natural Resources Canada, Bedford Institute of Oceanography, 1 Challenger Dr. Dartmouth, NS, Canada, B2Y 4A2

Shipboard Party SS12/2008 Ron Boyd, Jock Keene, Neville Exon, Asrar Talukder, Tom Hubble, Kev Ruming, Jim Gardner, Janice Felzenberg, David Mitchell, Samantha Clarke, Michael Kinsela, Peter Dunn, Hiski Kippo, Tony Veness, Bernadette Heaney

Masaaki Shirai Tokyo Metropolitan University, 1-1 Minami-osawa Hachioji, Tokyo, 192-0397, Japan

Anaëlle Simonneau Institut des Sciences de la Terre d'Orléans, UMR 6113 CNRS, Université d'Orléans, Université François Rabelais de Tours, Observatoire des Sciences de l'Univers en région Centre, 1A rue de la Férollerie 45071, Orléans cedex 2, France

Inger-Lise Solberg Geological Survey of Norway (NGU) & International Centre for Geohazards (ICG), Trondheim, Norway

R. Stephen J. Sparks Department of Earth Sciences, University of Bristol, Bristol BS8 1TH, UK

Guillaume St-Onge Canada Research Chair in Marine Geology, ISMER and GEOTOP, Université du Québec à Rimouski, Rimouski, Québec, Canada, G5L 3A1

Alois Steiner Marine Geotechnics, MARUM – Center for Marine Environmental Sciences and Faculty of Geosciences, University of Bremen, Leobener Str 28359, Bremen, Germany, asteiner@uni-bremen.de

Michael Strasser Geological Institute, ETH Zurich, Sonneggstrasse 5, 8092, Zürich, Switzerland; MARUM – Centre for Marine Environmental Sciences, University of Bremen, Bremen, Germany, strasser@erdw.ethz.ch

Nabil Sultan Géosciences Marine, IFREMER, BP70 F-29280, Plouzané Cédex, France

Peter J. Talling National Oceanography Centre, European Way, Southampton, SO14 3ZH, UK

Akio Tanaka Department of Applied Science, Kochi University, Kochi 780-8520, Japan

David R. Tappin British Geological Survey, Kingsley, Dunham Centre, Keyworth, Nottingham NG12 5GG, UK

Uri S. ten Brink U.S. Geological Survey, USGS Woods Hole Coastal and Marine Science Center, Woods Hole, MA 02543, USA

Moe K. Thu CDEX-JAMSTEC, Yokohama, Japan

Roberto Tinterri Dipartimento di Scienze della Terra, Università degli Studi di Parma, Viale G.P. Usberti 157/A, Campus 43100, Parma, Italy

Juan Tomasini Administración Nacional de Combustibles Alcohol y Pórtland (ANCAP), Paysandú s/n esq. Avenida del Libertador Montevideo 11100, Uruguay

Fabio Trincardi ISMAR (CNR), v. Gobetti 101 40129, Bologna, Italy

Jess Trofimovs National Oceanography Centre, European Way, Southampton, SO14 3ZH, UK

Dominique Turmel Laboratoire d'études sur les risques naturels, Département de géologie et de génie géologique, Université Laval, Québec, QC, Canada, G1K 7P4, dominique.turmel.1@ulaval.ca

David C. Twichell U.S. Geological Survey, USGS Woods Hole Coastal and Marine Science Center, Woods Hole, MA, 02543, USA

Kohtaro Ujiie Department of Geosciences, University of Tsukuba, 1-1-1 Tenno Tsukuba 305–8577, Japan

Roger Urgeles Consejo Superior de Investigaciones Científicas (CSIC), Institut de Ciències del Mar, Passeig Marítim de la Barceloneta 37–49, 08003, Barcelona, Spain, urgeles@icm.csic.es

Morelia Urlaub National Oceanography Centre, European Way, Southampton, SO14 3ZH, UK, m.urlaub@noc.soton.ac.uk

Maarten Vanneste NGI – Norwegian Geotechnical Institute, ICG – International Centre for Geohazards c/o NGI, Ullevål, 0806 PO Box 3930, Oslo, Norway, maarten.vanneste@ngi.no

Mark E. Vardy School of Ocean and Earth Science, University of Southampton, Southampton, UK

Carlos A. Vargas Departamento de Geociencias, Universidad Nacional de Colombia, Ed. Manuel Ancizar Bogotá, Colombia, cavargasj@unal.edu.co

Bruno Vendeville FRE 3298 CNRS, Université de Lille 1, Bâtiment SN5 59655, Villeneuve d'Ascq Cedex, France

Barry Voight Geosciences, Penn State University, University Park, PA, 16802, USA, voight@ems.psu.edu

David Völker SFB574, IFM-GEOMAR Leibniz Institute for Marine Sciences, University of Kiel, Wischhofstr. 1-3 Kiel, Germany, dvoelker@ifm-geomar.de

Tore O. Vorren Department of Geology, University of Tromsø, Tromsø N-9037, Norway, Tore.Vorren@uit.no

Karen Ware RPS Energy Ltd, Goldsworth House, Denton Way Woking, Surrey, GU21 3LG, UK

Philip Watts Applied Fluids Engineering, Inc, 6216 E. Pacific Coast Highway, #237 Long Beach, CA, 90803, USA, phil.watts@appliedfluids.com

Willhelm R. Weinrebe SFB574, IFM-GEOMAR Leibniz Institute for Marine Sciences, University of Kiel, Wischhofstr. 1-3 Kiel, Germany

Gauvain Wiemer MARUM – Research Center for Marine Environmental Science and Faculty of Geosciences, University of Bremen, Leobener Str, 28359, Bremen, Germany, gauvainwiemer@yahoo.de

Daniel Winkelmann Leibniz Institute of Marine Sciences (IFM-GEOMAR), Wischhofstr. 1-3 24148, Kiel, Germany

Russell B. Wynn National Oceanography Centre, Southampton, UK

Tomomasa Yamada Department of Applied Science, Kochi University, Kochi 780-8520, Japan

Yasuhiro Yamada Department of Earth Resources Engineering, Kyoto University, Katsura, Kyoto 615-8540, Japan, yamada@earth.kumst.kyoto-u.ac.jp

Yuzuru Yamamoto Japan Agency for Marine-Earth Science and Technology, Institute for Research on Earth Evolution, 3173-25 Showa-machi Kanazawa-ku, Yokohama, Kanagawa, 236-0001, Japan, yuzuru-y@jamstec.go.jp

Yoshihiko Yamashita Department of Earth Resources Engineering, Kyoto University, Katsura, Kyoto 615-8540, Japan

Shunji Yokoyama Department of Applied Science, Kochi University, Kochi 780-8520, Japan

Norihiro Yoshimura Shikoku-Try Corporation, Kochi 780-0082, Japan

Phyllis Yu University of Sydney, Sydney, NSW, Australia

Arash Zakeri C-CORE, Captain Robert A. Bartlett Building, Morrissey RoadSt. John's, NL, A1B X5, Canada

Antonis Zervos School of Civil Engineering and the Environment, University of Southampton, Highfield, Southampton, SO17 1BJ, UK

Chapter 1
Submarine Mass Movements and Their Consequences

Yasuhiro Yamada, Kiichiro Kawamura, Ken Ikehara, Yujiro Ogawa, Roger Urgeles, David Mosher, Jason Chaytor, and Michael Strasser

1.1 Introduction

Submarine mass movements represent major offshore geohazards due to their destructive and tsunami-generation potential. This potential poses a threat to human life as well as to coastal, near shore and offshore engineering structures. Recent examples of catastrophic submarine landslide events that affected human populations (including tsunamis) are numerous; e.g., Nice airport in 1979 (Dan et al. 2007), Finneidfjord in 1996 (e.g., L'Heureux et al., this volume, Steiner et al., this volume), Papua-New Guinea in 1998 (Tappin et al. 2001), Stromboli in 2002 (Chiocci et al. 2008), and the 2006 and 2009 failures in the submarine cable network around Taiwan (Hsu et al. 2008). The Great East Japan Earthquake of March 2011 also generated submarine landslides that may have amplified effects of the devastating tsunami as shown in Fryer et al. (2004). Given that 30% of the World's population lives within 60 km of the coast, the hazard posed by submarine landslides is

Y. Yamada (✉)
Department of Earth Resources Engineering, Kyoto University,
Katsura, Kyoto 615-8540, Japan
e-mail: yamada@earth.kumst.kyoto-u.ac.jp

K. Kawamura
Fukada Geological Institute, 2-13-12 Honkomagome, Bunkyo, Tokyo 113-0021, Japan
e-mail: kichiro@fgi.or.jp

K. Ikehara
Geological Survey of Japan, AIST, Tsukuba Central 7, 1-1-1, Higashi, Tsukuba,
Ibaraki 305-8567, Japan
e-mail: k-ikehara@aist.go.jp

Y. Ogawa
University of Tsukuba, Yokodai 1-127-2-C-740, Tsukubamirai 300-2358, Japan
e-mail: fyogawa45@yahoo.co.jp

Y. Yamada et al. (eds.), *Submarine Mass Movements and Their Consequences*,
Advances in Natural and Technological Hazards Research 31,
DOI 10.1007/978-94-007-2162-3_1, © Springer Science+Business Media B.V. 2012

expected to grow as global sea level rises. In addition, the deposits resulting from such processes provide-various types of constraints to offshore development (Shipp et al. 2004), and have significant implications for non-renewable energy resource exploration and production (Weimer and Shipp 2004; Beaubouef and Abreu 2010).

There is therefore a need to better understand underwater landslides, their consequences and resulting deposits. Great advances in underwater mapping, sampling and monitoring technologies, laboratory analogue and numerical modeling capabilities developed over the past two decades enhance progress in this area. Multibeam sonar, 3D seismic reflection, and remote and autonomous underwater vehicle technologies provide hitherto unparalleled imagery of the geology beneath the oceans, permitting investigation of submarine landslide deposits in great detail. Increased and new access to drilling, coring, in situ measurements and monitoring devices allows ground-truthing of geophysical data, provides access to samples for geotechnical laboratory experiments and unprecedented in situ information on strength and effective stress conditions of underwater slopes susceptible to fail. Great advances in numerical simulation of submarine landslide kinematics and tsunami propagation (Grilli and Watts 2005; Haugen et al. 2005), have also lead to increased understanding and predictability of submarine landslide consequences.

The international community has been leading these advances through various projects, for which the International Geosciences Program (IGCP) Projects 511 (2005–2009) and 585 (2010–2014) have had a catalyst role. The objective of these IGCP projects, funded by United Nations Educational Scientific and Cultural Organization (UNESCO) and International Union of Geosciences (IUGS), is to bring a world-wide perspective to submarine mass movements and their consequences. The projects have hosted five international symposia, Nice (France) in 2003, Oslo (Norway) in 2005, Santorini (Greece) in 2007, Austin (USA) in 2009 and Kyoto

R. Urgeles
Institut de Ciències del Mar (CSIC), Passeig Marítim de la Barceloneta,
37-49, 08003 Barcelona, Catalonia, Spain
e-mail: urgeles@icm.csic.es

D. Mosher
Natural Resources Canada, Geological Survey of Canada – Atlantic, Bedford Institute
of Oceanography, 1 Challenger Dr, Dartmouth, NS B2Y 4A2, Canada
e-mail: dmosher@nrcan.gc.ca

J. Chaytor
U.S. Geological Survey, Woods Hole Coastal and Marine Science Center,
384 Woods Hole Road, Woods Hole, MA 02543, USA
e-mail: jchaytor@usgs.gov

M. Strasser
Geological Institute, ETH Zurich, Sonneggstrasse 5, 8092, Zürich, Switzerland

MARUM – Centre for Marine Environmental Sciences, University of Bremen,
Bremen, Germany
e-mail: strasser@erdw.ethz.ch

(Japan) in 2011. The previous symposia produced three books (Locat and Meinnert 2003; Lykousis et al. 2007; Mosher et al. 2010) and a special issue in the Norwegian Journal of Geology (Solheim 2006). The latest symposium in Kyoto is represented by this volume, a collection of 65 papers that are categorized by (1) Physical properties of sediments and slope stability assessment, (2) Seafloor geomorphology for trigger mechanisms and landslide dynamics, (3) Role of fluid flow in slope instability, (4) Mechanics of mass-wasting in subduction margins, (5) Post-failure dynamics, (6) Landslide generated tsunamis, (7) Witnessing and quasi-witnessing of slope failures, (8) Architecture of Mass Transport Deposits/complexes, (9) Relevance of natural climate change in triggering slope failures. The aim of this introductory paper is to present a summary of the book contents and the state of the art of our understanding of submarine mass movements and their consequences.

1.2 Part I: Physical Properties of Sediments and Slope Stability Assessment

Stability evaluation of submarine slopes under various types of loading conditions is a challenging issue in many offshore geohazard studies. Submarine slope stability evaluation helps us understand pre-conditions and triggers under which submarine slopes fail (Urgeles et al. 2006, Vanneste et al., this volume, Hubble et al., this volume). It also informs us of the security of a certain region and action to undertake at the seafloor to mitigate the issue. Measurement of high-quality physical and mechanical properties of marine sediments, both in-situ (Cauchon-Voyer et al., this volume, Steiner et al., this volume) and in the laboratory (Wiemer et al., this volume) is of utmost importance not only for the performance evaluation of submarine slopes but also to understand the small-scale physical processes involved in shear failure of marine sediments (e.g., the effect of grain size/sediment composition in cyclic strength behavior, Wiemer et al., this volume). Geotechnical data also provide us with new insights on several other processes occurring in the submarine domain such as knickpoint migration in submarine channels (Turmel et al., this volume). For adequate geohazard evaluation, we also need to take into account the recurrence of slope instability in a certain region (Haflidason et al. 2005, Clarke et al., this volume), which will provide us with a probabilistic approach to slope failure (Nadim et al. 2005). In this regard, understanding the timing of slope failure is a critical step that it not often completed (Camerlenghi et al. 2010). Finding non-steady state conditions in pore water geochemistry and geochemical simulation (Henkel et al., this volume) may provide new elements to determine the age of mass wasting events. Finally, for the safe development of offshore and coastal activities, it is necessary to establish new risk assessment procedures that take into account both the geotechnical information and geological evidence (such as dating of previous slide events) so that a rational estimate of the annual probability of submarine slope instability can be made (Nadim et al. 2005, Nadim, this volume).

1.3 Part II: Seafloor Geomorphology for Trigger Mechanisms and Landslide Dynamics

Study of seafloor geomorphology has advanced during the last two decades largely thanks to improved multibeam bathymetry and side-scan sonar technologies, either used from hull-mounted systems on surface vessels or AUV/ROV operated systems. Collaboration with industry has enhanced the use of 3D seismic technology for academic purposes, leading to the development of seismic geomorphology in the last decade. 3D seismic data does not only provide detailed surface information, but also the basal and internal structure is imaged in detail (Gee et al. 2006; Sawyer et al. 2009). Submarine geomorphology in combination with other geophysical and groundtruthing data, provide the most direct evidence for slope failure of the seafloor. Evidence that may provide ambiguous interpretation (Lee et al. 2002; Urgeles et al. 2011, Meyer et al., this volume, Urgeles et al., this volume). The detailed images offered by seafloor and subseafloor imaging systems give new insights into the triggering (Chapron et al., this volume), dynamics (Chaytor et al., this volume), and runout potential of submarine landslides. Volumetric estimates from detailed geomorphic data also provide constraints (Chaytor et al., this volume, Lindhorst et al., this volume) for a number of inputs to simulation of landslide dynamics and landslide-generated tsunamis.

Submarine geomorphology in combination with other tools such as seismic imaging can be used to understand how submarine slope failure controls the evolution and/or acts to modify the morphology of passive (Mosher et al., this volume) and subduction continental margins (Mountjoy and Micallef, this volume) and how their major elements, submarine canyons, form and evolve by submarine slope failure, again both in active (Micallef et al., this volume) and passive/glaciated (Sultan et al. 2007, Dickinson et al., this volume, Rise et al., this volume) continental margins. Submarine geomorphology may also provide some insights on the recurrence or timing of submarine slope failure, particularly when used with high resolution deep-towed survey techniques (Laberg et al., this volume).

1.4 Part III: Role of Fluid Flow in Slope Instability

Submarine slopes may be pre-conditioned for failure by geological and hydrological processes resulting in elevated pore pressure, reducing stability of slopes and facilitating landslide initiation also by relatively "weak" triggers (e.g., Sultan et al. 2004a, b; Lee et al. 2007; Stigall and Dugan 2010). Margin stratigraphy and permeability architecture have been recently recognized to induce flow focusing, development of fluid overpressure and preconditioning low-angle slopes for failure (Dugan et al., this volume). Despite pore fluids are the dominant factor in preconditioning slopes for failure, earthquake triggering appears to be key to initiating failures, even along passive margins (Dugan et al., this volume). Coupled fluid flow, overpressure and slope stability models applied in low-sedimentation passive margins also suggest

that factors other than overpressure must be fundamental for initiating slope failure in such settings (Urlaub et al., this volume).

In subduction margins fluid migration along faults are hypothesized to have contributed to low slope stability conditions (Anasetti et al., Kawamura et al., this volume), as inferred from seismic and seafloor video images offshore Costa Rica and in the Nankai Trough, Japan, respectively. Morita et al. (this volume) shows dewatering structures related to thick slumps imaged in 3-D seismic data and points out that high methane flux is also a possible cause for slope instability. The influence of gas flux, along with sensitive clay layers and groundwater flow is also discussed by L'Heureux et al. (this volume) for the 1996 landslide in Finneidfjord, Norway. Further supporting arguments for a relationship between high overpressure, fluid flow and submarine landslides is presented by Pattier et al. (this volume) who studied the Demerara plateau (Guiana-Surinam transform margin) and describe pockmarks which are systematically associated with mass-transport deposits.

1.5 Part IV: Mechanics of Mass-Wasting in Subduction Margins

There are a number of submarine mass movements at subduction margins and the mechanics of the movements, defined by preconditions and triggers, include factors specific to this tectonic setting (e.g., McAdoo et al. 2004; von Huene et al. 2004; Strasser et al. 2011). As a simplified mechanical example, sandbox experiments have been used to model accretionary wedges and associated slope failures (e.g., Yamada et al. 2010). Results from these analogue models show that topographic relieve in the basement causes differences in magnitude and periodic occurrence of slope failures (Yamada et al., this volume). Yamamoto et al. (this volume) examine middle Miocene sediments in Japan and analogue models and report two types of slope failures corresponding to successive stages of failure development. Detailed bathymetric mapping also shows that subduction of the oceanic plate, and long-term tectonics results in different styles of slope failure, as shown along the Middle America Trench (Harders et al., this volume). There are also other factors that affect the size, style and possible preconditioning factors and triggering mechanisms of submarine slope failures in subduction margins. Amongst those are incision by submarine canyons, focused basal sediment accretion and uplift of the marine forearc (Volker et al., this volume) and also the presence of oceanic asperities being brought by the subducting plate below the overlying plate during the subduction process (Vargas et al., this volume).

1.6 Part V: Post-failure Dynamics

Three main stages, comprising the pre-failure, failure and post-failure stage are typically distinguished to characterize mass movements (Leroueil et al. 1996). Whereas at the failure stage, soil or rock mechanics principles are needed in order

to explain landslide initiation (see Part I), the post failure dynamics sometimes may rely rather on fluid mechanics principles (Locat 2001). Understanding this post-failure dynamics has an important applied perspective as this may help determine the number of structures that may be put at risk along the path of a submarine slope failure, or control the design parameters for submarine pipelines that need to resist the impact of sediment gravity flows. Flume experiments (Zakeri et al. 2008) and centrifuge models (Chi and Zakeri, this volume) have been used to derive power function equations and model parameters that can be used to this end. Sassa and Sekiguchi (this volume) present an analytical framework that simulates the dynamics of subaqueous liquefied sediment flows leading to redeposition on the basis of two-phase physics. They show the crucial role of solidification, in reproducing concurrent processes of flow stratification, deceleration, and redeposition. For large-scale slope failures developing large run-out Voigt et al. (this volume) indicate that undrained loading of marine sediments and shear friction heat may help to develop the high excess-pore pressures necessary for the failures to develop the large run-outs that were previously cited as enigmatic. Process-based physical understanding of sediment mass-transport dynamics can also be established from detailed investigation of the geometric and internal-fabric architecture of landslide deposits by means of 3D-seismic data analysis (Laberg et al., this volume), very-high resolution bathymetric AUV data (Migeon et al., this volume) and physical property analysis on drill cores (Behrmann et al., this volume).

1.7 Part VI: Landslide Generated Tsunamis

Amongst the most devastating natural disasters is undoubtedly tsunamis. Tsunamis are generally explained by rapid displacement at the seafloor, often caused by uplift/subsidence during displacement along an earthquake fault (e.g., Satake and Atwater 2007). Historic events show that submarine mass movements have also caused significant tsunamis (e.g., Tappin et al. 2001; Tinti et al. 2005; Fine et al. 2005; Dan et al. 2007), as this has also been recorded in tsunami deposits (Bondevik et al. 2005). The nuclear crisis after the recent Great East Japan Earthquake and tsunami show that large earthquakes, mass failure, and volcanic events should be considered as potential threats to nuclear power plants (Watts, this volume), and points that a probabilistic framework for tsunami hazard assessment should include all possible tsunami sources and reach comfortably to 50,000 year events and beyond. Watts and Tappin (this volume) also place a cautionary note on tsunami models and highlight the benefit of using Boussinesq wave models. Satake (this volume) reviews current numerical approaches to model tsunamis generated by submarine landslides, and classify these into landslide as fluid motion, rigid-body motion, and initial or kinematic water surface profiles. Two examples of tsunamis caused by submarine slumping and volcanic collapse are also described in detail. Baba et al. (this volume) investigated a tsunami in Suruga Bay, Japan after a 6.5 magnitude earthquake and

conclude that slope failures probably also contributed to the tsunami generation. Miyazawa et al. (this volume) reevaluated the tsunami source model of the 1771 Meiwa tsunami (up to 30 m height) at the southern Ryukyu Islands, Japan and point out that such unusual run-up heights require submarine landslides. L'Heureux et al. (this volume) modeled sediment dynamics and tsunami resulting from the 1978 Rissa landslide in Norway, and show that rafted blocks most likely triggered the flood wave of 6.8 m height.

1.8 Part VII: Witnessing and Quasi-Witnessing of Slope Failures

A major issue affecting the study of submarine slope failure is the difficulty to directly observe the process, particularly in deep-sea environments, resulting in inferences being made mostly from geomorphological or sedimentological evidence (see Parts II and VIII). There are only a few cases in which we have directly experienced submarine slope failure, and yet in these cases we only have a partial view of the process derived from cable breaks (Piper et al. 1999; Dan et al. 2007; Hsu et al. 2008) or availability of survey data before and after such events (Chiocci et al. 2008; Casalbore et al. 2011). Repeated multibeam surveys represent a fundamental tool to study instability phenomena, because they may depict even small-scale landslides and allow a quantitative estimate of the erosion-deposition made by submarine landslides that, otherwise, cannot be detected. By understanding the amount of material released in individual landslides, the distribution of landslides within a given geographic region, their recurrence time and the mechanisms responsible for the generation of the landslides, we may be better able to determine that potential hazard of these events (Casalbore et al., this volume). In subduction continental margins, the occurrence of frequent earthquakes means that there is a relatively high chance to observe slope failure phenomena and sediment remobilization. The high recurrence rate makes it possible to maintain marine observatories that are able to record the turbidity currents induced by submarine landslides and find which ground shaking conditions are able to trigger such events (Ikehara et al., this volume). Detailed AUV/ROV observations in these areas also indicate that slope instability is triggered by earthquake shaking (Matsumoto et al., this volume, Ashi et al., this volume). Bathymetric changes due to the crustal movement during coseismic events are clearly reported in the Nankai subduction zone (Suruga trough; Matsumoto et al., this volume and SE off Kii peninsula; Ashi et al., this volume). In addition to submarine landslides, a dilute suspension layer and a bottom turbid layer were commonly observed during various ROV surveys carried out in response to a series of earthquakes that occurred in 2004 on the Kii Peninsula, Nankai prism (Ashi et al., this volume). Such phenomena have probably occurred due to the Great East Japan Earthquake of March 11, 2011. Their magnitude and influence on the subsequent tsunami still awaits detailed investigation.

1.9 Part VIII: Architecture of Mass Transport Deposits/Complexes

Mass Transport Deposits (MTDs) provide constraints to understanding physical processes involved in failure development (see Part V) but also have significant implications in sequence stratigraphy (Beaubouef and Abreu 2010) and non-renewable energy resource exploration and production (Posamentier and Kolla 2003; Weimer and Shipp 2004; Gamboa et al. 2010). MTDs can be investigated at different scales, ranging from margin-wide tectono- or sequence-stratigraphic considerations to small-scale microfabric analysis of MTDs inferring paleo-stress conditions, transport direction, depositional mode and resulting porosity and permeability structure. The concepts can be applied to fossil MTD-containing stratigraphic successions (e.g., successions now cropping out in the Apennines, Pini et al., this volume, Ogata et al., this volume; Hokkaido, Naruse et al., this volume; central Japan, Kojima and Sano, this volume; and the exhumed Karoo Basin, South Africa, Hodgson et al., this volume). Fossil outcrops present detailed insights into different types of kinematic translation and emplacement processes and allow contrasting this with the palaeogeographic and sequence/tectono stratigraphic context in which they occurred. The deposits of deeply buried MTDs can be accessed thanks to scientific ocean drilling programs such as IODP, revealing internal architectures and deformation fabrics, age control and ground-truthing of seismic data (Yamamoto et al., this volume, Kitamura et al., this volume, and Strasser et al., this volume). However, because of the limited view provided by sedimentary cores, it is not always easy to identify MTDs. Methods have been developed that allow identification of distal mass movement deposits in the sedimentary cores by means of paleomagnetic and rock-magnetic analysis (Kanamatsu et al., this volume) as well as geochemical element analysis (Geogiopoulou et al., this volume). In addition, these methods allow inferring the timing and sources of giant submarine landslides. 3D seismic offers a broader and comprehensive view of MTDs (e.g., the Espírito Santo Basin, SE Brazil, Gamboa et al., this volume), including the occurrence of rafted blocks within the MTDs and the relationship between those and salt-related structures.

1.10 Part IX: Relevance of Natural Climate Change in Triggering Slope Failures

Climate variations induce indirect stress changes in seafloor and subseafloor sediments, particularly in high-latitude regions, that can result in massive catastrophic slope failure events (Solheim et al. 2005, Forwick and Vorren, this volume, Li et al., this volume, Lucchi et al., this volume, Rebesco et al., this volume). Climatic control on offshore geohazards is exerted in various ways: (1) an increase in bottom water temperature or lowering of sea level induces gas-hydrates dissociation, generation of free gas and pore pressure build up, therefore reducing the strength of marine

sediments (Lee 2008). A relationship between rising bottom temperatures, gas hydrate dissociation and large-scale failure of the continental slope has been suspected in the geological record (Jung and Vogt 2004). Numerical models indicate that bottom water temperature increase during the last deglaciation resulted in retrogressive failure of continental margins bearing gas-hydrates (Sultan et al. 2004a, b). (2) Equally important climate variations control glacial advances and retreats, which (a) cause significant stress changes in the sedimentary column and redistribution of interstitial fluids, (b) induce a particular margin stratigraphic architecture with contrasting sediment types of distinct physical properties (Rebesco et al., this volume, Lucchi et al., this volume) and permeability (Bryn et al. 2005), (c) cause large variations in sedimentation rates (Bryn et al. 2005) and (d) are at the origin of isostatic adjustments that may reactivate seismogenic faults (Fjeldskaar et al. 2000, Forwick and Vorren, this volume). Therefore, climate is a first order control on timing and location of high-latitude submarine slope failure and offshore geohazards.

1.11 Future Perspectives

Scientific and engineering research on 'Submarine Mass Movements and Their Consequences' has advanced significantly in the past decade as it can be easily grasped by inspection of the different books in this series, but there are still a number of areas in which further progresses are required.

Observations: Our knowledge on submarine mass movements is still limited and we need to expand it to understand the diversity of processes involved in this natural phenomenon by a number of observations on past and present events. Precise observations and descriptions form the foundation of our research.

Measurements: Quantification of submarine mass movements requires precise measurements of every aspect of these events. Accurate measurements of physical and mechanical properties of ocean floor sediments are vital for slope stability evaluation and this requires the use of undisturbed coring technology for shallow soft sediments as demonstrated by (Sakaguchi et al. 2011). In-situ measurements of fluid flow in the upper sedimentary cover are also necessary not only for understanding precondition and triggering mechanisms, but also for understanding the early phases of failure development and monitoring of potentially hazardous regions. The ODP and IODP have installed a series of observatory systems within boreholes, but these are designed for deeper reservoirs/faults zones. Substantial modifications and engineering development is underway (Moran et al. 2006) for the required measurements and monitoring in shallow sediments.

Modeling: In order to adequately understand the various phenomena related to submarine slope failure and to develop predictive capabilities, we need to construct models that allow explaining the observations and measured properties. Numerical and analogue modeling approaches significantly improve our understanding of all stages of submarine slope failure, including the mechanics of failure, the dynamics

of failed sediments and the generation and propagation of resulting tsunamis. The dynamic effects of seismic loading and seismic waveform on triggering submarine slope failures also need to be examined. Numerical and analogue modeling techniques may contribute to understand this problem. Care should be taken that models honor observations, measurement datasets and tested with benchmark problems. We need to be aware of the various assumptions and simplifications that are built in these models and understand that we can just partly explain the phenomenon of submarine slope failure. Progress in modeling, measuring and observation techniques will gradually reduce the gap between data and models.

References

Beaubouef RT, Abreu V (2010) MTCs of the Brazos-Trinity slope system; thoughts on the sequence stratigraphy of MTCs and their possible roles in shaping hydrocarbon traps. In: Mosher DC, Shipp RC, Moscardelli L, Chaytor JD, Baxter CDP, Lee HJ, Urgeles R (eds) Submarine mass movements and their consequences, advances in natural and technological hazards research, vol 28. Springer, Dordrecht, pp 475–490

Bondevik S, Mangerud J, Dawson S, Dawson A, Lohne Ø (2005) Evidence for three North Sea tsunamis at the Shetland Islands between 8000 and 1500 years ago. Quat Sci Rev 24: 1757–1775

Bryn P, Berg K, Forsberg CF, Solheim A, Kvalstad TJ (2005) Explaining the Storegga slide. Mar Petrol Geol 22:11–19

Camerlenghi A, Urgeles R, Fantoni L (2010) A database on submarine landslides of the Mediterranean Sea. In: Mosher DC, Shipp RC, Moscardelli L, Chaytor JD, Baxter CDP, Lee HJ, Urgeles R (eds) Submarine mass movements and their consequences, advances in natural and technological hazards research, vol 28. Springer, Dordrecht, pp 491–501

Casalbore D, Chiocci FL, Scarascia MG, Tommasi P, Sposato A (2011) Flash-flood hyperpycnal flows generating shallow-water landslides at Fiumara mouths in Western Messina Strait (Italy), Mar Geophys Res 32(1–2):257–271. doi: 10.1007/s11001-011-9128-y

Chiocci FL, Romagnoli C, Bosman A (2008) Morphologic resilience and depositional processes due to the rapid evolution of the submerged Sciara del Fuoco (Stromboli Island) after the December 2002 submarine slide and tsunami. Geomorphology 100:356–365

Dan G, Sultan N, Savoye B (2007) The 1979 Nice harbour catastrophe revisited: trigger mechanism inferred from geotechnical measurements and numerical modelling. Mar Geol 245:40–64

Fine IV, Rabinovich AB, Bornhold BD, Thomson RE, Kulikov EA (2005) The Grand Banks landslide-generated tsunami of November 18, 1929: preliminary analysis and numerical modelling. Mar Geol 215:45–57

Fjeldskaar W, Lindholm C, Dehls JF, Fjeldskaar I (2000) Postglacial uplift, neotectonics and seismicity in Fennoscandia. Quat Sci Rev 19:1413–1422

Fryer GJ, Watts P, Pratson LF (2004) Source of the great tsunami of 1 April 1946: a landslide in the upper Aleutian forearc. Mar Geol 203:201–218

Gamboa D, Alves T, Cartwright J, Terrinha P (2010) MTD distribution on a 'passive' continental margin: the Espírito Santo Basin (SE Brazil) during the Palaeogene. Mar Petrol Geol 27: 1311–1324

Gee MJR, Gawthorpe RL, Friedmann SJ (2006) Triggering and evolution of a giant submarine landslide, offshore angola, revealed by 3D seismic stratigraphy and geomorphology. J Sediment Res 76:9–19

Grilli ST, Watts P (2005) Tsunami generation by submarine mass failure part I: modeling, experimental validation, and sensitivity analysis. J Waterw Port Coast Ocean Eng 131:283–297

Haflidason H, Lien R, Sejrup HP, Forsberg CF, Bryn P (2005) The dating and morphometry of the Storegga slide. Mar Petrol Geol 22:123–136

Haugen KB, Løvholt F, Harbitz CB (2005) Fundamental mechanisms for tsunami generation by submarine mass flows in idealised geometries. Mar Petrol Geol 22:209–217

Hsu S-K, Kuo J, Lo C-L, Tsai C-H, Doo W-B, Ku C-Y, Sibuet J-C (2008) Turbidity currents, submarine landslides and the 2006 Pingtung earthquake off SW Taiwan. Terr Atmos Ocean Sci 19(6):767–772. doi:10.3319/TAO.2008.19.6.767(PT)

Jung W-Y, Vogt PR (2004) Effects of bottom water warming and sea level rise on Holocene hydrate dissociation and mass wasting along the Norwegian-Barents Continental Margin. J Geophys Res 109:B06104. doi:10.1029/2003JB002738

Lee HJ (2008) Timing of occurrence of large submarine landslides on the Atlantic Ocean margin. Mar Geol. doi:10.1016/j.margeo.2008.09.009

Lee HJ, Syvitsky JPM, Parker G, Orange D, Locat J, Hutton JHW, Imran J (2002) Distinguishing sediment waves from slope failure deposits: field examples, including the "Humboldt Slide" and modelling results. Mar Geol 192:79–104

Lee HJ, Locat J, Desgagnés P, Parsons JD, McAdoo BD, Orange DL, Puig P, Wong FL, Dartnell P, Boulanger E (2007) Submarine mass movements on continental margins. In: Nittrouer AC, Austin JA, Field ME, Kravitz JH, Syvitski PM, Wiberg PL (eds) Continental margin sedimentation: from sediment transport to sequence stratigraphy. Blackwell Publishing Ltd., Oxford, pp 213–273

Leroueil S, Vaunat J, Picarelli L, Locat J, Lee H, Faure R (1996) Geotechnical characterization of slope movements. In: Proceedings of the international symposium on landslides, Trondheim, 1, 53–74

Locat J (2001) Instabilities along ocean margins: a geomorphological and geotechnical perspective. Mar Petrol Geol 18:503–512

Locat J, Meinnert J (eds) (2003) Submarine mass movements and their consequences: 1st International symposium: advances in natural and technological hazard research. Kluwer Academic/Springer, Dordrecht, 540 pp

Lykousis V, Sakellariou D, Locat J (eds) (2007) Submarine mass movements and their consequences: advances in natural and technological hazard research, vol 27. Springer, Dordrecht, 424 pp

McAdoo BG, Capone MK, Minder J (2004) Seafloor geomorphology of convergent margins: implications for Cascadia seismic hazard. Tectonics 23:TC6008. doi:10.1029/2003TC001570

Moran K, Farrington S, Massion E, Paull C, Stephen R, Trehu A, Ussler W (2006) SCIMPI: a new seafloor observatory system, OCEANS 2006. IEEE 1–6. doi:10.1109/OCEANS.2006.307103

Mosher DC, Shipp RC, Moscardelli L, Chaytor JD, Baxter CDP, Lee HJ, Urgeles R (2010) Submarine mass movements and their consequences: advances in natural and technological hazard research, vol 28. Springer, Dordrecht, 786 pp

Nadim F, Kvalstad TJ, Guttormsen T (2005) Quantification of risks associated with seabed instability at Ormen Lange. Mar Petrol Geol 22:311–318

Piper DJ, Cochonat P, Morrison ML (1999) The sequence of events around the epicentre of the 1929 Grand Banks earthquake: initiation of debris flows and turbidity current inferred from sidescan sonar. Sedimentology 46:79–97

Posamentier HW, Kolla V (2003) Seismic geomorphology and stratigraphy of depositional elements in deep-water settings. J Sediment Res 73:367–388

Sakaguchi A, Kimura G, Strasser M, Screaton EJ, Curewitz D, Murayama M (2011) Episodic seafloor mud brecciation due to great subduction zone earthquakes. Geology 39:923–926. doi:10.1130/G32172.1

Satake K, Atwater BF (2007) Long-term perspectives on giant earthquakes and tsunamis at subduction zones. Annu Rev Earth Planet Sci 35:349–374

Sawyer DE, Flemings PB, Dugan B, Germaine JT (2009) Retrogressive failures recorded in mass transport deposits in the Ursa Basin, Northern Gulf of Mexico. J Geophys Res 114:B10102. doi:10.1029/2008JB006159

Shipp RC, Nott JA, Newlin JA (2004) Physical characteristics and impact of mass transport complexes on deepwater jetted conductors and suction anchor piles. In: Offshore technology conference, paper number 16751-MS, DOI: 10.4043/16751-MS

Solheim A, Berg K, Forsberg CF, Byrn P (2005) The Storegga slide complex: repetitive large scale sliding with similar cause and development. Mar Petrol Geol 22:97–107

Solheim A (ed) (2006) Submarine mass movements and their consequences. In: Proceeding of 2nd international conference, Oslo, 2005. Nor J Geol 86:151–372

Stigall J, Dugan B (2010) Overpressure and earthquake initiated slope failure in the Ursa region, northern Gulf of Mexico. J Geophys Res 115:B04101

Strasser M, Moore GF, Kimura G, Kopf AJ, Underwood MB, Guo J, Screaton EJ (2011) Slumping and mass transport deposition in the Nankai fore arc: evidence from IODP drilling and 3-D reflection seismic data. Geochem Geophys Geosyst 12:Q0AD13

Sultan N, Cochonat P, Foucher J-P, Mienert J (2004a) Effect of gas hydrates melting on seafloor slope instability. Mar Geol 213:379–401

Sultan N, Cochonat P, Canals M, Cattaneo A, Dennielou B, Haflidason H, Laberg JS, Long D, Mienert J, Urgeles R, Vorren T, Wilson C (2004b) Triggering mechanisms of slope instability processes and sediment failures on continental margins: a geotechnical approach. Mar Geol 213:291–321

Sultan N, Gaudin M, Berne S, Canals M, Urgeles R, Lafuerza S (2007) Analysis of slope failures in submarine canyon heads: an example from the Gulf of Lions. J Geophys Res 112: F01009. doi:10.1029/2005JF000408

Tappin DR, Watts P, McMurtry GM, Lafoy Y, Matsumoto T (2001) The Sissano, Papua New Guinea tsunami of July 1998 – offshore evidence on the source mechanism. Mar Geol 175:1–23

Tinti S, Manucci A, Pagoni A, Armigliato A, Zniboni F (2005) The 30 December 2002 landslide-induced tsunamis in Stromboli: sequence of the events reconstructed from the eyewitness accounts. Nat Hazards Earth Sys Sci 5:763–775

Urgeles R, Leynaud D, Lastras G, Canals M, Mienert J (2006) Back-analysis and failure mechanisms of a large submarine slide on the Ebro continental slope, NW Mediterranean. Mar Geol 226:185–206

Urgeles R, Cattaneo A, Puig P, Liquete C, De Mol B, Sultan N, Trincardi F, Amblàs D (2011) A review of undulated sediment features on Mediterranean prodeltas: distinguishing sediment transport structures from sediment deformation. Mar Geophys Res. doi:10.1007/s11001-011-9125-1

von Huene R, Ranero CR, Watts P (2004) Tsunamigenic slope failure along the Middle America Trench in two tectonic settings. Mar Geol 203:303–317

Weimer P, Shipp C (2004) Mass transport complex: musing on past uses and suggestions for future directions. In: Offshore technology conference, paper number 16752-MS, Houston. DOI: 10.4043/16752-MS

Yamada Y, Yamashita Y, Yamamoto Y (2010) Submarine landslides at subduction margins: insights from physical models. Tectonophys 484:156–167. doi:10.1016/j.tecto.2009.09.007

Zakeri A, Høeg K, Nadim F (2008) Submarine debris flow impact on pipelines – part I: experimental investigation. Coast Eng 55:1209–1218

Part I
Physical Properties of Sediments and Slope Stability Assessment

Chapter 2
Risk Assessment for Earthquake-Induced Submarine Slides

Farrokh Nadim

Abstract Stability evaluation of submarine slopes under earthquake loading is an important and challenging issue in many offshore geohazards studies. Generally, three scenarios of earthquake-induced slope failure should be evaluated and analyzed: (1) Failure occurs during the earthquake. In this scenario, the excess pore pressures generated by the cyclic stresses degrade the shear strength so much that the slope is not able to carry the static shear stresses, (2) Post-earthquake failure due to increase in excess pore pressure at critical locations caused by seepage from deeper layers; and (3) Post-earthquake failure due to creep. Soils that have strong strain-softening characteristics and high sensitivity are most susceptible to failure during earthquake shaking. The scenario of excess pore pressure migration from deeper layers into critical areas, leading to slope instability, is quite important and could occur over a time span of years or even decades in deep marine clay deposits. However, post-earthquake creep-type failure is believed to be the most common mechanism for clay slopes. In a risk assessment framework, the uncertainties in all the parameters and models used in the stability assessment must be addressed and the consequences of slope failure must be evaluated. It is often difficult to separate the uncertainties due to lack of knowledge (epistemic uncertainties) from the natural variability of the physical parameters such as soil shear strength and earthquake characteristics. The risk assessment procedure outlined in the paper integrates the results of geotechnical evaluations with other evidence, like dating of the previous slide events, to provide a more rational estimate of the annual probability of earthquake-induced submarine slope instability.

Keywords Submarine landslide • Earthquake • Risk assessment • Seismic slope stability

F. Nadim (✉)
International Centre for Geohazards (ICG), Norwegian Geotechnical Institute (NGI),
P.O. Box 3930, Ullevaal Stadion, NO-0806, Oslo, Norway
e-mail: farrokh.nadim@ngi.no

Y. Yamada et al. (eds.), *Submarine Mass Movements and Their Consequences*,
Advances in Natural and Technological Hazards Research 31,
DOI 10.1007/978-94-007-2162-3_2,

2.1 Introduction

Exploitation of offshore resources, development of communication and transport corridors, fishing habitat protection, and the protection of coastal communities, have contributed to a growing interest in the quantification of the risk posed by offshore geohazards. The offshore petroleum industry is developing oil and gas fields in greater and greater water depths where the assessment of the offshore geohazards, in particular seafloor mass movements and their consequences, is a necessity. For example for the Storegga slide area in the Møre and Vøring basin areas offshore Norway, the following features were identified as important issues for slope instability assessment (Solheim et al. 2005): slide scars and slide sediments, diapirism, gas hydrates and free gas, seabed grooves, gas leakage and slide areas, fracture zones and earthquakes.

Submarine slides can be caused by natural on-going processes or by human activities. During one single event enormous sediment volumes can be transported on very gentle slopes over distances exceeding hundreds of kilometers Nadim and Locat (2005). Earthquakes are known to have triggered major submarine mass movements all over the world (NGI 1997; Hance 2003). In areas with minor sedimentation at present, earthquakes are the most important release factor for natural submarine slides. Hance (2003) developed a database of submarine slide events on the basis of published literature. Information on the triggering mechanism(s) leading to slope failure was available for 366 of the 534 events in the database. Most slides were reported to have multiple triggers, and in over 40% of the cases (225 of the 534 events) slope failure was attributed to earthquake and faulting mechanisms, Fig. 2.1.

2.2 Stability of Submarine Slopes Under Earthquake Loading

Stability evaluation of submarine slopes under earthquake loading is one of the most challenging issues in offshore geohazard studies. To illustrate some of the important factors in the assessment of seismic response of a submarine clay slope, Nadim et al. (1996, 2007) considered a simple, one-dimensional (infinitely long) slope under seismic loading. When only gravity loads are acting, a generic soil element is subjected to a stress in the direction normal to the slope, represented by the effective normal stress (σ'_n), and a stress in the plane of the slope, parallel to the dip, represented by the consolidation shear stress (τ_c) as shown at the bottom of Fig. 2.2. For simplicity, the earthquake motion is assumed to consist of shear waves propagating perpendicular to the slope. This consideration is analogous to the assumption of vertically propagating "horizontal" shear waves for level ground conditions. The seismic motion results in additional cyclic shear stress acting on the plane of the slope in a direction oriented at some angle to that of the consolidation shear stress. Although the seismic shear stress changes direction instantaneously, most analyses choose the critical direction to be parallel to the dip of the slope (i.e., the direction of shear shaking and initial shear stress coincide) as shown in Fig. 2.2.

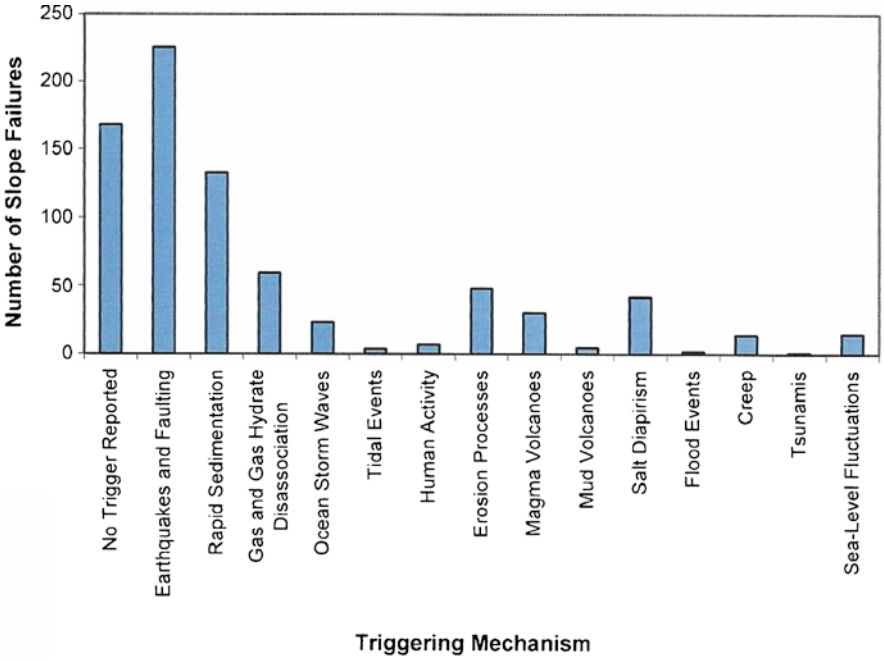

Fig. 2.1 Distribution of triggering mechanisms for submarine slides (Hance 2003)

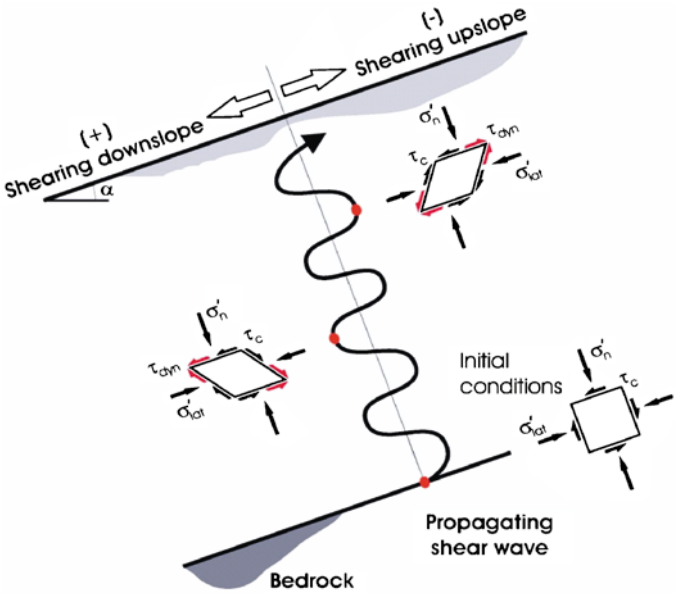

Fig. 2.2 Infinite slope under one-dimensional seismic excitation

Three scenarios for triggering of a submarine slide by earthquake shaking are possible (Biscontin et al. 2004):

Scenario 1 – Failure occurs during the earthquake. For this scenario to be viable, the soil would need to have strong strain-softening characteristics and high sensitivity. The strains and pore pressure generated by the cyclic stresses degrade the shear strength so much that the slope is not able to carry the static shear stresses. It should be noted that even if the earthquake does not cause a complete failure of the slope, it might still induce large down-displacements (slumping). The earthquake-induced permanent displacement may be from a few centimeters to several meters.

Scenario 2 – Post-earthquake failure due to increase in excess pore pressure caused by upward seepage from deeper layers. This scenario requires a layer near the sea floor (5–10 m depth) with much lower permeability and lower consolidation coefficient (at least two orders of magnitude lower) than the rest of the soil deposit. This scenario could occur over a time span of decades or even centuries in deep marine clay deposits.

Scenario 3 – Post-earthquake failure due to creep and/or significant reduction of static shear strength. This scenario requires that large cyclic and/or accumulated shear strains are experienced during the earthquake shaking. The effective stress paths for a typical soil element on a potential slip surface for these scenarios are depicted on Fig. 2.3.

2.3 Factors Influencing Soil Strength Under Seismic Loading

2.3.1 Rapid Loss of Shear Strength and Liquefaction Phenomenon

Soils that have strong strain-softening characteristics and high sensitivity are most susceptible to complete failure during earthquake shaking. Generally, liquefaction-susceptible sediments, such as loose sand and silt, are most vulnerable to earthquakes. The phenomenon of liquefaction is related to rapid build-up of the pore water pressure. During the shaking, the loose sand/silt tends to compact. The water in the pores cannot escape quickly enough to accommodate instantaneously the compaction. Therefore the stresses are thrown on the water, increasing the pore water pressure, and generating upward fluid flow towards the seabed. This leads to a reduction in the effective stress. The upward flow gradient may, in the upper meters of soil, reach the critical value, reducing the effective stress to zero, and fluidization of the soil. This phenomenon is called liquefaction.

2.3.2 Special Considerations for Clay Slopes Under Earthquake Loading

As mentioned earlier, most of the deepwater sites consist of clay or clayey sediments. The great majority of clays will not liquefy during earthquakes (Seed et al. 1983)

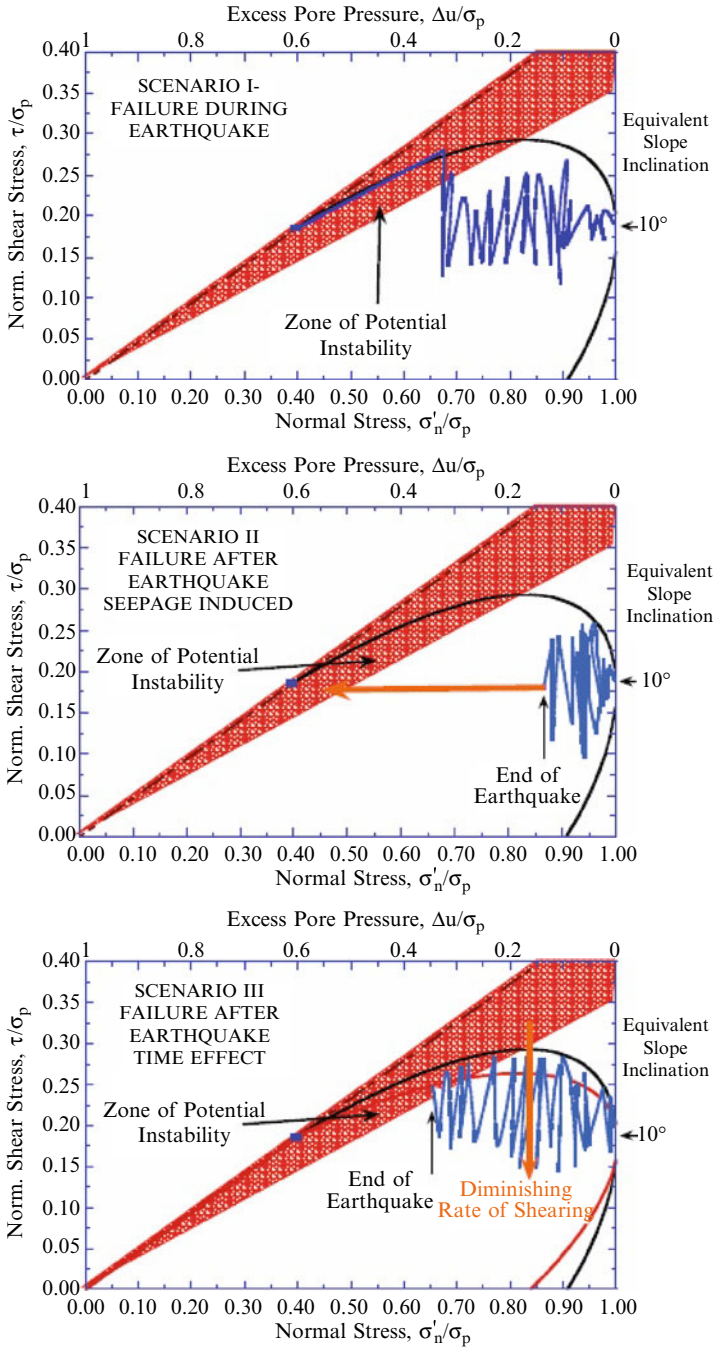

Fig. 2.3 Stress paths for soil elements on the slip plane for different earthquake-induced slope failure scenarios

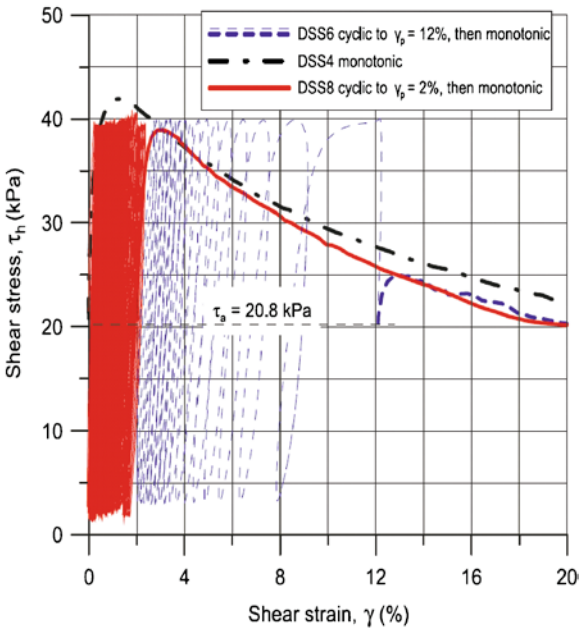

Fig. 2.4 Stress–strain behaviour in monotonic, cyclic, and post-cyclic monotonic DSS tests with $\tau_a = \tau_c = 20.8$ kPa $= 0.16\sigma'_{vc}$. τ_h is the horizontal shear stress (Andersen 2009)

and clay slopes are thus less susceptible to developing into a slide due to an earthquake than sand and silt slopes, although they could experience significant permanent down-slope deformations and slumping. However, clays with high sensitivity may undergo severe loss of strength. An accurate estimation of the soil strength during and after the earthquake is crucial in the assessment of slope stability. Unfortunately, shear strength is not a unique property of soil. It is affected by a number of factors, each with different effects and variable influence. Rate effects and existing permanent shear stresses in the soil tend to **increase**, while cyclic loading tends to **degrade** the undrained shear strength of clayey soils.

The main factors influencing the undrained shear strength of clays under earthquake loading are discussed below and some of them are exemplified by special laboratory tests reported by Andersen (2009). The tests were run on high-quality block samples of a Norwegian quick clay with a sensitivity of more than 75.

2.3.3 Effect of High-Frequency Cyclic Loading on Static Shear Strength

A series of tests were performed by Andersen (2009) to assess the effect of high-frequency cyclic loading on the static shear strength of a slope. Examples of cyclic tests consolidated with $\tau_c/\sigma'_{vc} = 0.16$, corresponding to a slope of about 10°, are presented in Fig. 2.4. The figure shows one reference monotonic test and two cyclic

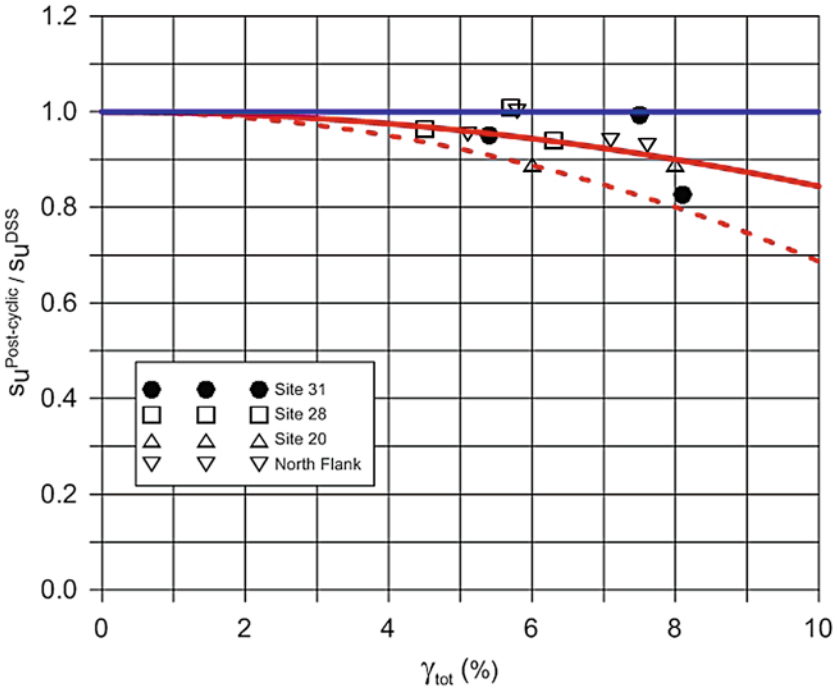

Fig. 2.5 Effects of permanent strains accumulated during cyclic loading on post-cyclic undrained shear strength – results of special cyclic DSS-tests on marine clay from Ormen Lange (Nadim et al. 2005a)

tests that were run with monotonic loading to failure after cycling. The monotonic tests were run strain-controlled with a rate of shear strain of 4.5%/h. The reason why the cyclic stress–strain curves go beyond the monotonic stress–strain curve is that the cyclic tests are run stress-controlled and that the rate of strain is significantly higher in the cyclic tests when they develop large strains than the rate of strain in the monotonic tests. The cyclic loading was stopped when a permanent shear strain of $\gamma_p = 2\%$ was reached in the first cyclic test (DSS8) and when $\gamma_p = 12\%$ was reached in the other cyclic test (DSS6). The results in Fig. 2.4 show that the monotonic peak shear strength is reduced by the cyclic loading and that the post-cyclic monotonic stress–strain curves rapidly join the virgin monotonic stress–strain curve. Differences in the monotonic curves are believed to be due to soil variability. The series of tests consolidated under other shear stresses show better agreement. It thus appears that the post-cyclic static shear strength is governed by the virgin monotonic stress–strain curve and the permanent shear strain that is developed during cyclic loading. Similar results have been found on Drammen clay (Andersen 1988), but the behavior is even more evident for the quick clay due to the more pronounced strain-softening.

Figure 2.5 shows similar results from special cyclic DSS-tests run for the assessment of seismic stability of slopes at the Ormen Lange gas field in the North Sea

(Nadim et al. 2005a). The three curves on this plot show the range for the post-earthquake static undrained strength (normalized with respect to the pre-earthquake shear strength) as function of the total shear strain (sum of permanent and cyclic shear strains) experienced by a soil element during earthquake loading.

Tests with symmetrical cyclic loading ($\tau_a = 0$) show a somewhat different picture, where the post-cyclic monotonic stress–strain curve does not reach the monotonic stress–strain curve. This more severe effect of symmetrical cyclic loading in observed in most marine clays (Andersen 1988).

2.3.4 Effect of Cyclic Loading on Undrained Creep

A slope subjected to an earthquake will experience both cyclic and permanent shear strains and displacements. However, the failure mode is not likely to be large cyclic shear strains and displacements because of the relatively significant average shear stress in a slope. The cyclic loading will instead cause large permanent shear strains and displacements, as pointed out by Newmark (1965) and illustrated in the tests in Fig. 2.4. Nor is the failure likely to occur during the peak earthquake load. The duration of the peak load is not long enough to mobilise the soil mass and the factor of safety for the slope drops below one only for a few seconds or fraction of a second. The critical mechanism is therefore likely to be development of large permanent shear strains during the earthquake, leading to a significant reduction in the post-earthquake shear strength (Scenario 3 depicted on Fig. 2.3). The critical period may be some time after the earthquake, before the excess pore pressure generated by the cyclic loading has dissipated. During this period, the clay will creep under undrained conditions and a delayed failure may occur. This can be simulated in the DSS tests and is illustrated by the tests reported by Andersen (2009).

Based on the studies summarized in this paper, the seismic stability of a submarine clay slope may be assessed by first running a dynamic analysis to determine the permanent shear strain due to the design earthquake. The post-cyclic shear strength may then be determined as the shear stress on the monotonic stress–strain curve at a shear strain equal to the calculated permanent shear strain. This shear strength should be reduced by 15–25% to account for (i) the post-cyclic stress–strain curve reaching the virgin curve at a somewhat larger strain than the permanent strain developed during the earthquake and (ii) the time to failure being significantly longer than in the standard time to failure for monotonic laboratory tests (1–2 h).

2.4 Risk Assessment for Submarine Slides

According to the ISSMGE Glossary of Risk Assessment Terms (listed on TC304 web page: http://jyching.twbbs.org/issmge/home_2010.htm), "*hazard*" is the probability that a particular danger (threat) occurs within a given period of time, and "*risk*" is the

measure of the probability and severity of an adverse effect to life, health, property, or the environment. Quantitatively risk is the product of the hazard times the potential worth of loss and can be expressed as (e.g., Lacasse and Nadim 2007):

$$R = H \times C = H \times V \times E \tag{2.1}$$

where R is risk, H is hazard, C is consequence, V is the vulnerability of element(s) at risk, and E is the cost of total loss of element(s) at risk.

Nadim and Locat (2005) emphasized that the specific hazard and risk approaches adopted for submarine slides and other geohazards depend on the elements at risk and consequences of sliding, but general guidelines could be established from the experience acquired so far. Nadim and Locat (2005) proceeded to suggest a staged approach for offshore geohazards evaluation.

2.4.1 Probabilistic Slope Stability Assessment

In the assessment of the risk associated with submarine landslide, the main challenge for geo-scientists is to estimate the annual probability of instability of the slopes that pose a threat to the sea floor installations, i.e. the "hazard" term in Eq. 2.1. A regional perspective of the geological precedent situation is always useful for estimating the probability of underwater slope failure. Nadim et al. (2003) indicated that steep slopes of the Sigsbee escarpment in the Gulf of Mexico were ancient features that developed some 60,000 years ago, and that geological evidence suggests there have not been catastrophic failures since then. The uncertainties that must be taken into account in estimating slope failure probability include (in addition to human uncertainty and human error resulting from lack of skills or understanding) (1) parameter uncertainty, which can be dealt with by appropriate sampling and testing, sensitivity analyses of the slope model, and back-analysis, (2) model uncertainty, directly related to the quality of the investigations and their interpretation, and to the analytical methods used and the assumption made in the method and (3) behavioral uncertainty, in predicting changes in slide movement rates as a result of strain effects and other load changes.

Nadim et al. (2005b) and Lacasse and Nadim (2007) described the principles of probabilistic slope stability analysis using the first order reliability method (FORM, Hasofer and Lind 1974). To perform the probabilistic analyses with FORM, one needs a precise mathematical description for failure. This is achieved by defining a performance function $G(\boldsymbol{X})$, such that $G(\boldsymbol{X}) \geq 0$ means satisfactory performance and $G(\boldsymbol{X}) < 0$ means "failure". $\boldsymbol{X}$ is a vector of basic random variables including resistance parameters, load effects, geometry parameters and modeling uncertainty. For example, a viable performance function for slope stability assessment is:

$$G(X) = FS - 1 \tag{2.2}$$

where FS is the factor of safety for the slope.

2.4.2 Estimation of Annual Probability of Slope Failure

In some situations the annual probability for a slope instability may be estimated from the geological evidence, e.g., observed slide frequency, geological history, geophysical investigations, and radiocarbon dating of sediments; while in other situations analytical simulations, like the FORM approach mentioned above, are more suitable. Ideally, both approaches should be employed.

If the trigger for inducing a slide is identified, then the annual probability of slope instability can be established by evaluating the conditional probability of failure for different return periods of the trigger. The conditional probabilities are then integrated over all return periods to obtain the unconditional failure probability. Calculation can be simplified by using the approximation suggested by Cornell (1996) or a similar approach as described in Sect. 2.5 of the paper.

When the triggering mechanism is not obvious, the probabilistic slope stability calculations provide an estimate of failure probability for static conditions. In this situation, it is not straightforward to relate the calculated "timeless" failure probability to a failure frequency. Nadim et al. (2003) and Lacasse and Nadim (2007) developed several ideas for quantifying the annual probability of slope instability:

- Bayesian approach with Bernoulli sequence
- Statistical model for failure frequency
- Interpretation of the static failure probability as the instantaneous hazard function
- Interpretation of computed static failure probability in Bayesian framework

The first two approaches are purely statistical and do not involve any geotechnical calculations. Their input is the frequency of slide events (or lack thereof), which may be based on observations or inferred from geological evidence, for example dating of slide sediments. The third approaches combines the calculated probability of static slope failure with the slide frequency estimated from the geological evidence. The third approach is described by Nadim et al. (2003) and Lacasse and Nadim (2007). The last approach is briefly described below because it forms the basis for the new calculation procedure suggested in the last section.

2.4.3 Interpretation of Computed Static Failure Probability in a Bayesian Framework

The interpretation of the probability of static slope failure computed with FORM or other methods like Monte Carlo simulation, is not straightforward. The fact that the slope is standing today implies that the current factor of safety, although unknown, is greater than one. The question of annual probability of failure becomes the question of the likelihood that the current factor of safety will fall below one during next year. The current factor of safety is unknown, but its distribution can be computed (distribution from FORM analysis, but truncated to reflect the fact that the slope is

stable today). This interpretation is basically a Bayesian updating procedure where the a-priori information is that FS ≥ 1. The updated (or posterior) distribution of the factor of safety is:

$$P[FS < z \mid FS \geq 1] = \frac{F_{FS}(z) - F_{FS}(1)}{1 - F_{FS}(1)} \tag{2.3}$$

The slope will fail during the next year only if its current value of safety factor is such that, with the given rate of deterioration, it will fall below unity during 1 year. This very simple calculation can be performed in several slightly different ways. Using this approach for the same submarine slope mentioned in the previous section, Nadim et al. (2003) obtained annual failure probabilities in the range between 10^{-7} and 10^{-9} (depending on the assumptions made). It is clear that additional research is needed to formalize the interpretation of the annual failure probability on the basis of the "timeless" failure probability obtained by FORM, Monte Carlo simulation or other methods.

2.5 Recommended Calculation Procedure

The procedure outlined in this section has been developed through a number joint-industry research projects, and offshore geohazards studies in the North Sea, the Caspian Sea, the Black Sea, offshore Indonesia, and the Gulf of Mexico. The procedure attempts to account for uncertainties in all steps of the assessment and utilize the available information to come up with a rational estimate of the annual probability of earthquake-induced slope failure. The different steps of the analyses are as follows:

1. Identify the critical slopes and establish the geometry and mechanical soil properties for the slope in a probabilistic format.
2. Using Monte Carlo simulation, or FORM, or any other established technique, establish the cumulative distribution function (CDF) of the static, undrained safety factor for the slope.
3. Using Eq. 2.3, update the CDF for static safety factor.
4. Do a probabilistic seismic hazard assessment for the site of interest and identify representative acceleration time histories for return periods of interest
5. Establish a dynamic response model for the slope and perform earthquake response analyses for at least two return periods. Use a Monte Carlo simulation procedure to account for the uncertainties in the soil properties and input earthquake motion characteristics. The main output parameter of interest from the simulations is the maximum earthquake-induced shear strain along the potential failure surface.
6. Through a special testing program or literature survey establish the range of reduction in the post-earthquake undrained shear strength as function of maximum earthquake-induced shear strain (e.g., the curves in Fig. 2.5).
7. Using the results of Steps 5 and 6, establish the distribution function for the shear strength reduction factor.

8. Using results of Steps 3 and 7, establish the CDF for post-earthquake static safety factor. The conditional probability of failure (given that the earthquake with the specified return period has happened) is the value of this CDF at FS equal to 1.
9. The annual failure probability is the sum (integral) of all conditional failure probabilities given a specific return period, divided by that return period. The analyses above must be done for at least two return periods. These return periods should ideally be above and below the return period that contributes most to the annual failure probability (some iteration might be necessary as this is not known beforehand). Once the analyses for the two return periods are done, establish a simple model with load and resistance that matches the computed failure probabilities at the return periods of interest. The most usual load parameter is the input annual peak ground acceleration (PGA), which typically has an exponential or a Pareto distribution. If PGA is used as the representative load parameter, then the slope resistance must also be specified as an acceleration parameter. A log-normal distribution for resistance is commonly assumed.
10. Using the simplified analogue in Step 9, estimate the probability that the resistance of the slope is less that the applied load (e.g., the annual PGA). This value is the estimate of the annual probability of earthquake-induced slope failure.

2.6 Discussion and Conclusion

The offshore petroleum industry is developing oil and gas fields in deep and ultra-deep water sites where the assessment of the risk associated with offshore geohazards is a necessity. One of the most challenging problems faced by geo-scientists in the risk assessment exercise is the assessment of the annual probability of earthquake-induced failure for submarine slopes. There are large uncertainties in the input parameters required for the analyses and these uncertainties must be dealt with in a quantitative manner. A procedure for calculating the annual probability of earthquake-induced failure for a submarine clay slope was outlined in the paper.

The main challenges for improved hazard and risk assessment are not only related to the probabilistic or risk analysis aspects of the offshore geohazards, but also to reducing the uncertainties in the geo-aspects of the problem.

Acknowledgments The author would like to express his thanks to his colleagues whose contributions to the subject matter of this paper received only a passing mention. He also thanks the reviewers Prof. Juan M. Pestana and Prof. Marui Hideaki for critiquing and improving this manuscript.

References

Andersen KH (1988) Properties of soft clay under static and cyclic loading, invited lecture. In: International conference on engineering problems of regional soils, proceeding, Beijing, edited by Chinese institution of soil mechanics and foundation engineering, 7–26

Andersen KH (2009) Bearing capacity under cyclic loading – offshore, along the coast, and on land. Can Geotech J 46:513–535

Biscontin G, Pestana JM, Nadim F (2004) Seismic triggering of submarine slides in soft cohesive soil deposits. Mar Geol 203(3 & 4):341–354

Cornell CA (1996) Calculating building seismic performance reliability: a basis for multi-level design norms. In: 11th world conference on earthquake engineering, Acapulco, 1996

Hance JJ (2003) Development of a database and assessment of seafloor slope stability based on published literature. MS thesis, University of Texas, Austin

Hasofer AM, Lind NC (1974) An exact and invariant first order reliability format. J Eng Mech Div ASCE 100(EM1):111–121

Lacasse S, Nadim F (2007) Probabilistic geotechnical analyses for offshore facilities. Georisk 1(1):21–42

Nadim F, Locat J (2005) Risk assessment for submarine slides. In: International conference on landslide risk management, Vancouver, 31 May – 2 June 2005

Nadim F, Kalsnes B, Eide A (1996) Analysis of submarine slope stability under seismic action. In: Proceeding of 7th ISL, 561–565

Nadim F, Krunic D, Jeanjean P (2003) Probabilistic slope stability analyses of the Sigsbee Escarpment. OTC paper 15203, offshore technology conference, Houston, 2003

Nadim F, Kvalstad TJ, Guttormsen TR (2005a) Quantification of risks associated with seabed instability at Ormen Lange. Mar Petrol Geol 22:311–318

Nadim F, Einstein H, Roberds W (2005b) Probabilistic stability analysis for individual slopes in soil and rock – state of the art paper 3. In: International conference on landslide risk management, Vancouver, 31 May – 2 June 2005

Nadim F, Biscontin G, Kaynia AM (2007) Seismic triggering of submarine slides. In: Offshore technology conference ′07, OTC paper 18911, Houston, 2007

Newmark MN (1965) Effects of earthquakes on dams and embankments. Geotechnique 15(2):139–160

Norwegian Geotechnical Institute (1997) Earthquake hazard and submarine slide – a literature survey, NGI report 963014–1

Seed HB, Idriss IM, Arango I (1983) Evaluation of liquefaction potential using field performance data. J Geotech Eng ASCE 109(3):458–482

Solheim A, Bryn P, Sejrup HP, Mienert J, Berg K (2005) Ormen Lange – an integrated study for safe development of a deep-water gas field within the Storegga Slide Complex, NE Atlantic continental margin: executive summary. Mar Petrol Geol 22:1–9

Chapter 3
Shallow Landslides and Their Dynamics in Coastal and Deepwater Environments, Norway

Maarten Vanneste, Jean-Sebastien L'Heureux, Nicole Baeten, Jo Brendryen, Mark E. Vardy, Alois Steiner, Carl Fredrik Forsberg, Tore J. Kvalstad, Jan Sverre Laberg, Shyam Chand, Oddvar Longva, Leif Rise, Haflidi Haflidason, Berit O. Hjelstuen, Matthias Forwick, Eugene Morgan, Isabelle Lecomte, Achim Kopf, Tore O. Vorren, and Thomas Reichel

Abstract In this manuscript, we present the first results of integrated slope stability studies to investigate smaller-scale mass movement processes in different physiographic settings of Norway. These include coastal areas (Sørfjord, Finneidfjord), and pristine open ocean settings in intermediate (Vesterålen) and deep waters (Lofoten)

M. Vanneste (✉) • C.F. Forsberg • T.J. Kvalstad
NGI (Norwegian Geotechnical Institute) & International Centre for Geohazards (ICG), Oslo, Norway
e-mail: maarten.vanneste@ngi.no

J.-S. L'Heureux • S. Chand • O. Longva • L. Rise
Geological Survey of Norway (NGU) & ICG, Trondheim, Norway
e-mail: jean.lheureux@ngu.no; leif.rise@ngu.no

N. Baeten • J.S. Laberg • M. Forwick • T.O. Vorren
Department of Geology, University of Tromsø, Tromsø, Norway
e-mail: jan.laberg@uit.no; Matthias.Forwick@uit.no

J. Brendryen • H. Haflidason • B.O. Hjelstuen
Department of Earth Science, University of Bergen, Bergen, Norway

M.E. Vardy
School of Ocean and Earth Science, University of Southampton, Southampton, UK

A. Steiner • A. Kopf
Marine Geotechnics, MARUM – Center for Marine Environmental Sciences and Faculty of Geosciences, University of Bremen, Leobener Str 28359, Bremen, Germany
e-mail: asteiner@uni-bremen.de

E. Morgan
Geohazards Engineering Research, Tufts University, Medford, USA

I. Lecomte
NORSAR & ICG, Kjeller, Norway

T. Reichel
Statoil ASA, Vækerø, Norway

Y. Yamada et al. (eds.), *Submarine Mass Movements and Their Consequences*, Advances in Natural and Technological Hazards Research 31,
DOI 10.1007/978-94-007-2162-3_3, © Springer Science+Business Media B.V. 2012

on the Norwegian margin. Triggers, pre-conditioning factors and sedimentary processes associated with these landslides are currently not well constrained.

The landslides occur either in clusters or isolated, and have variable geomorphologic expressions and run-out. These smaller landslides appear to be comparatively recent phenomena. However, failures likely happened repeatedly and recurrence may affect coastal communities or jeopardize offshore installations. New data indicate that the landslides developed within thin, gently-dipping sediment units that served as slip planes. Some soil samples from these units may show strain-softening behaviour, higher plasticity and higher sensitivity compared to other units. The slide-prone layers in Sørfjord can furthermore be related to specific depositional processes. Shallow gas – although clearly present in Sørfjord – is not considered a key factor.

Keywords Submarine mass movements • Offshore geohazards • Landslide dynamics • Shear strength • Very-high-resolution seismic reflection profiling

3.1 Introduction

Submarine landsliding, shallow gas and excess pore pressures – are prime concerns for the offshore industry. Systematic, high-resolution bathymetric mapping of the Norwegian margin highlights its complexity and variability, in terms of geomorphology and sedimentology (e.g., www.mareano.no). The data reveal the widespread occurrence of mass movement features across the entire margin, from coastal areas to deepwater settings. Whereas the larger landslides are well documented (e.g., Laberg and Vorren 2000; Bryn et al. 2005), little is known about smaller features. Recent research illustrated the negative impact of e.g., debris flows on seabed infrastructure (Zakeri 2008). Hence, the origin and development of smaller features need to be addressed.

In two R&D projects (LOslope, CDog), we investigate a selection of smaller landslides in different physiographic environments off Norway (Fig. 3.1). An integrated approach, using novel and state-of-the-art techniques combining geological, geotechnical and geophysical data, aims at addressing the following topics: (1) Identify and parameterize the slip planes; (2) Understand pre-conditioning processes affecting stability conditions and; (3) Assess the present-day stability and geohazards.

This paper presents an overview and topics covered within the two projects. Further details on the different areas are presented in accompanying papers (Baeten et al. 2011; L'Heureux et al. 2012; Rise et al. 2012; Steiner et al. 2012).

3.2 Geological Setting

The sedimentary and erosional processes that influence and have influenced the Norwegian continental margin are largely controlled by its distinct Quaternary glacial history and changes in oceanographic patterns (Vorren et al. 1998;

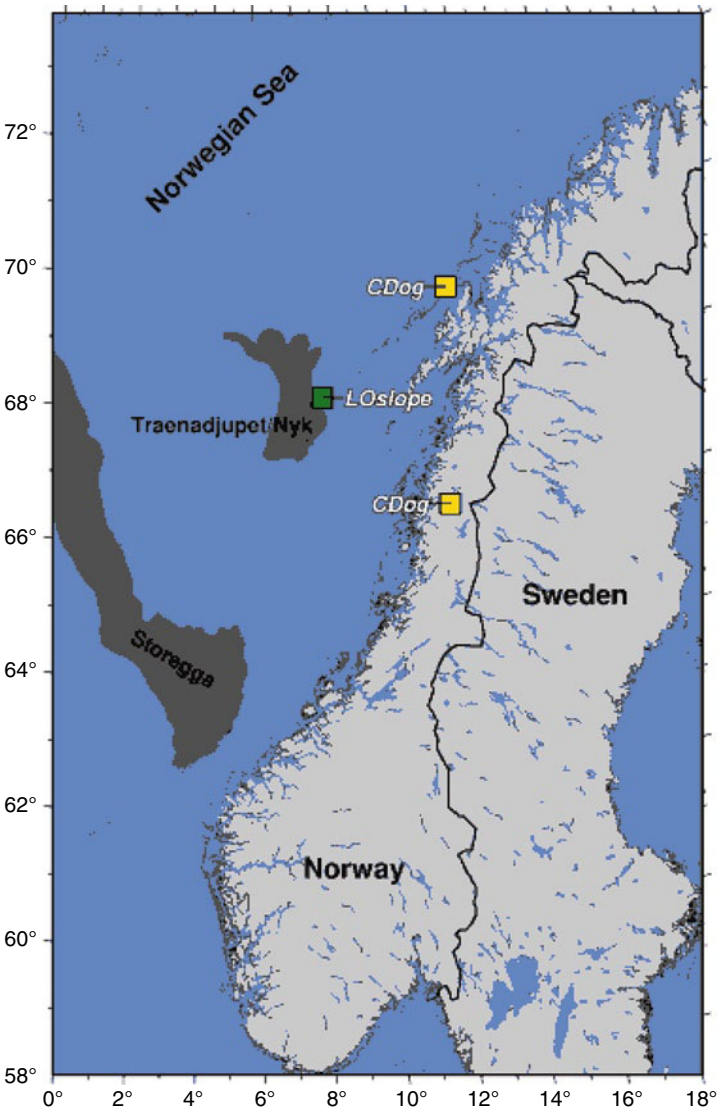

Fig. 3.1 Location of the three study areas on the Norwegian margin (*CDog* = Coastal and Deepwater Offshore Geohazards, *LOslope* = Lofoten slope stability)

Hjelstuen et al. 2004; Solheim et al. 2005). Glacial-interglacial fluctuations created unstable slope conditions that developed into massive sediment failures (e.g., Storegga), perhaps triggered by earthquakes following isostatic rebound (e.g., Bryn et al. 2005).

Along the Lofoten-Vesterålen margin (northern Norway) no massive glacial sediment inflows took place, due to its physical separation from the mainland by the Lofoten-Vesterålen mountains (Fig. 3.1). Elongated contourite drifts containing

sandy muds with ice-rafted debris dominate the late Cenozoic succession off Lofoten (Laberg et al. 2005). Laminated muds, likely related to melt-water plumes, also occur. A thin veneer of Holocene mud drapes the seabed. Sedimentation rates are high during glacials compared to the Holocene (Laberg and Vorren 2004). Off Vesterålen, well-developed canyon systems contribute to mass transfer from the shelf to the deep ocean (Haflidason et al. 2007; Laberg et al. 2007). In between the canyons, the seabed is relatively undisturbed (Rise et al. 2009, 2012).

Coastal areas of formerly-glaciated margins have typically experienced isostatic uplift following deglaciation (Corner 2006). The resulting relative sea level drop exposed marine clays to non-marine conditions. In places, leaching gave rise to very sensitive clays (i.e. quick clays), which can liquefy when disturbed (Rosenquist 1953). In Sørfjorden (south of the Finneidfjord village), quick clay landslide debris were occasionally deposited into the fjord during the Holocene, forming thin, laminated, soft clay beds that are distinct from the normal homogeneous post-glacial sediments (L'Heureux et al. 2012). Mass movements may use these beds as slip planes, e.g., for the 1996 failure (L'Heureux et al. 2012). Human activity (blasting) is the likely trigger for three historical retrogressive failures (1978, 1996, 2006). A model of the Sørfjorden landslide development is presented in the accompanying paper by L'Heureux et al. (2012).

3.3 Data and Methods

Within this project, we combine a variety of data and methods, crucial for integrated slope stability investigations. These include: (1) Swath bathymetry data (geomorphology, sedimentary processes, run-out) (Fig. 3.2); (2) Side-scan sonar or backscatter data (geomorphology, sedimentary processes) (Fig. 3.5); (3) High- to very-high-resolution 2D seismic and very-high-resolution 3D chirp seismic (VHR3D) Vardy et al. (in preparation) (seismic characterization, mapping of slip plane) (Fig. 3.3); (4) Sediment sampled by shallow gravity and Calypso piston cores (geological analysis including X-ray imaging, X-ray fluorescence (XRF) data, lithology, water content, multi-sensor core logging results, fall-cone shear strength, AMS ^{14}C dating) (Fig. 3.4); (5) High-quality soil samples for advanced geotechnical laboratory tests (anisotropically consolidated undrained triaxial shear tests (CAUc), constant rate of strain oedometer tests, and direct simple shear tests (DSS)) (Figs. 3.4 and 3.5); (6) *In-situ* cone penetration tests (CPT) using a free-fall piezocone penetrometer (high-resolution geotechnical soil characterization, pore pressure development and dissipation) (Fig. 3.3) and (7) Long-term double-sensor *in-situ* pore pressure measurements (Sørfjorden), (pore pressure development).

The results of all data analysed will subsequently be fed into slope stability assessment and further seismic characterization, e.g., through inversion of physical properties.

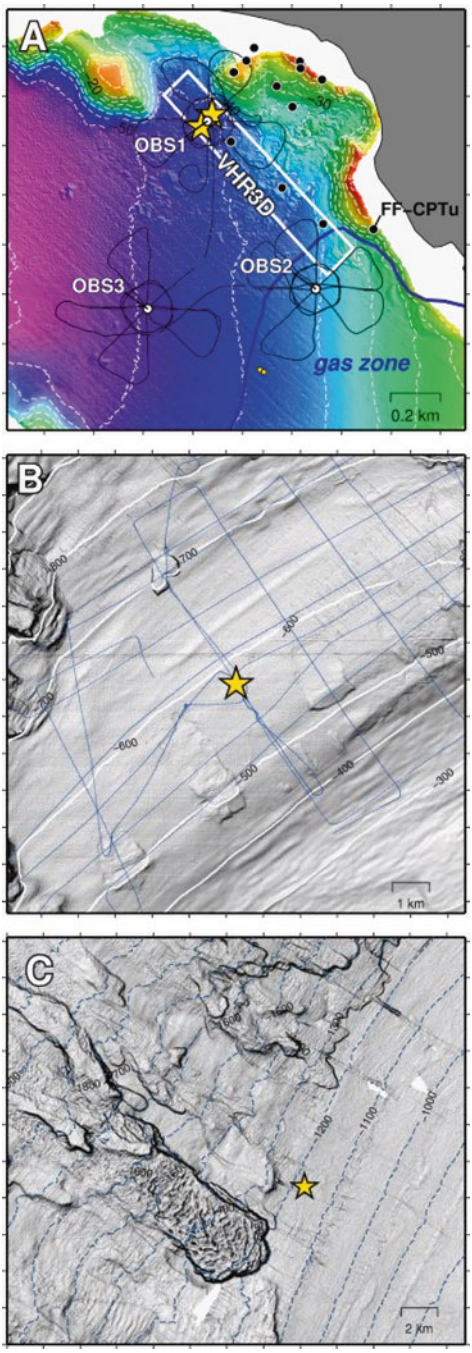

Fig. 3.2 Overview maps of the three target areas, i.e. Sørfjorden (Finneidfjord) shaded relief bathymetry (**a**), off Vesterålen (**b**, dip magnitude) and Lofoten (**c**, dip magnitude). *Gold stars* mark Calypso core locations

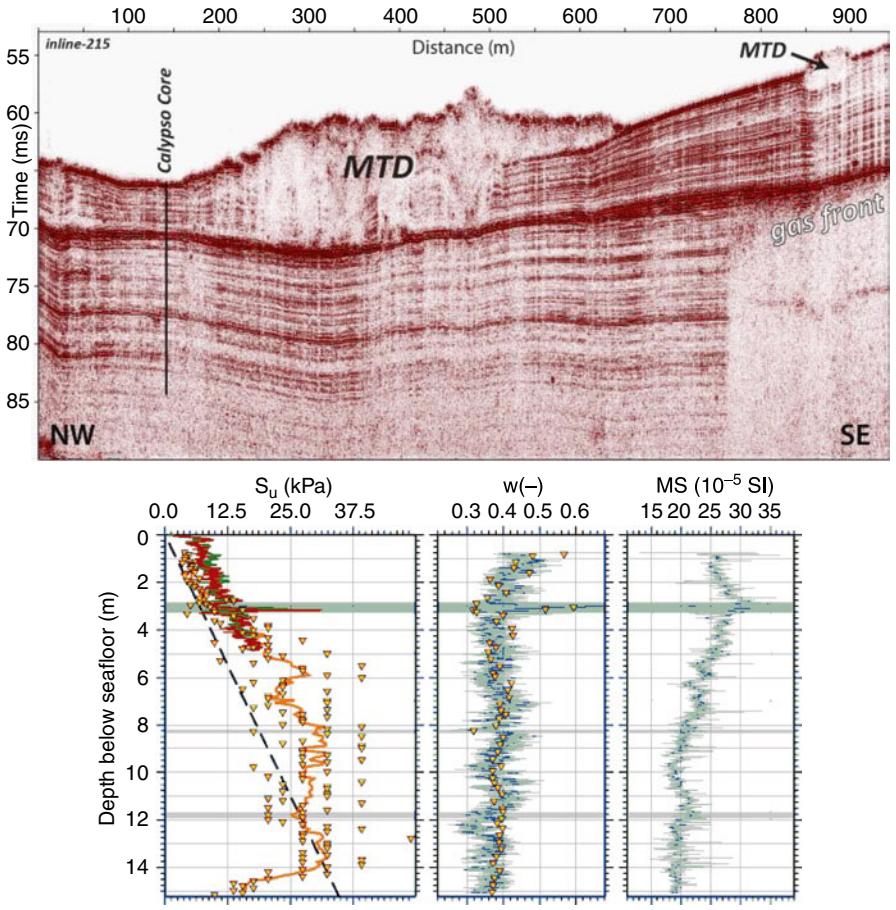

Fig. 3.3 (*top*) VHR3D central inline across MTD, after Kirchhoff migration. Note the composite reflection as well as the gas front. (*bottom*) Shear strength results from fall cone (*triangles*, note: only single readings performed, causing poorer resolution), moving average (*orange curve*), and from two nearby FF-CPTu (*green, dark red*), with reference for normally-consolidated clays (*dashed black line*); as well as water content (w from log and measurements) and magnetic susceptibility log (MS). Shaded intervals are suspected "weak" layers, in particular the top one

3.4 Results – From Geomorphology to Soil Properties and Stability

3.4.1 Coastal Environment – Sørfjorden (Finneidfjord)

Mass movements in Sørfjorden (Fig. 3.2a) typically occur on the foreshore slope, where dip angles vary between 13° and 21°. Remobilized masses are partially evacuated from the failure area. Landslide debris and out-runner blocks accumulated on the gently dipping (<3°) basin floor.

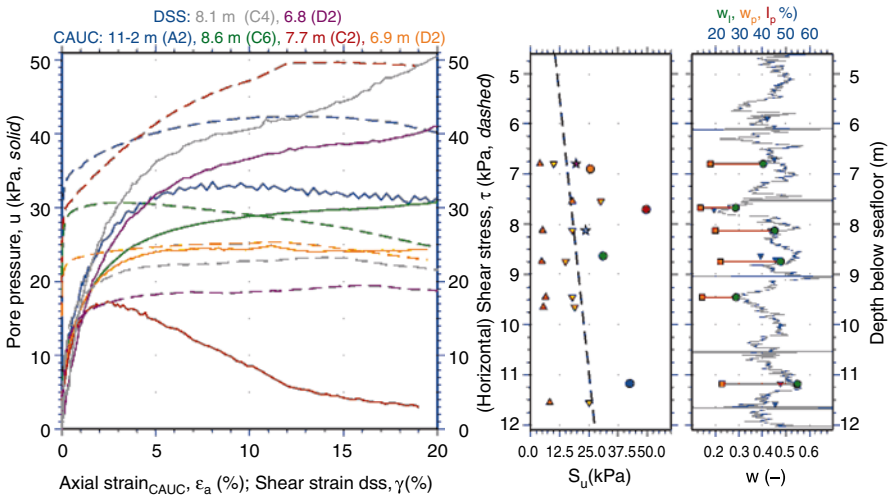

Fig. 3.4 (*Left*) Shear stress (*dashed*) and pore pressure development (*solid*) vs. strain from CAUc and DSS, core GS10-165-5, Vesterålen; (*Right*) Shear strength vs. depth, same colours as in figure left; *stars* DSS, *circles* CAUc, *triangles* fall-cone, undisturbed (*gold*) or remoulded (*orange*); *dashed curve*: reference for normally-consolidated clays. Water content (w) and Atterberg limits (liquid limit (w_l), plastic limit (w_p), plasticity index (I_p)) vs. depth

VHR3D data were collected in an area 940 m by 175 m large. Vertical resolution is ~10 cm, and horizontal sampling is 12.5 cm. The 3D cube extends across the main mass transport deposit (MTD) and into the zone with shallow gas (Figs. 3.2a and 3.3). Also smaller MTDs occur (Fig. 3.3). The main MTD has some internal architecture, likely due to compression during movement or the presence of slide blocks embedded in the debris. The base of the main MTD corresponds to a regionally continuous, high-amplitude reflection. It is along this horizon that the slope failed, confirming earlier observations (Longva et al. 2003). The new data illustrate that this horizon is essentially a composite reflection away from the failure zone, and that only the lower part remains unaltered at the base of the MTD (Fig. 3.3). The upper portions are heavily deformed in the proximal areas and absent altogether in the distal part.

A 14.5-m long core was taken adjacent to the MTD (Figs. 3.2a and 3.3). The lowest 1 m of the core was disturbed during sampling (Fig. 3.3). The core consists mainly of homogeneous, brownish, bioturbated, silty clays of Holocene age. Two intervals have slightly different characteristics. They are 10 and 25 cm thick and occur at 8.3 and 11.7 mbsf, respectively. However, the most peculiar interval, at 3 mbsf, shows distinct variations of magnetic susceptibility and water content (Fig. 3.3). It is a 20 cm thick turbidite sand that fines upwards and is sandwiched between two 10 and 15 cm thick clay layers. The colour suggests higher organic carbon content in the turbidite. The composite reflection observed on the seismic corresponds to this laminated clay layer with sand seam, and is the main slip plane of the 1996 landslide. These thin layers are interpreted as deposits related to quick-clay landslides in the

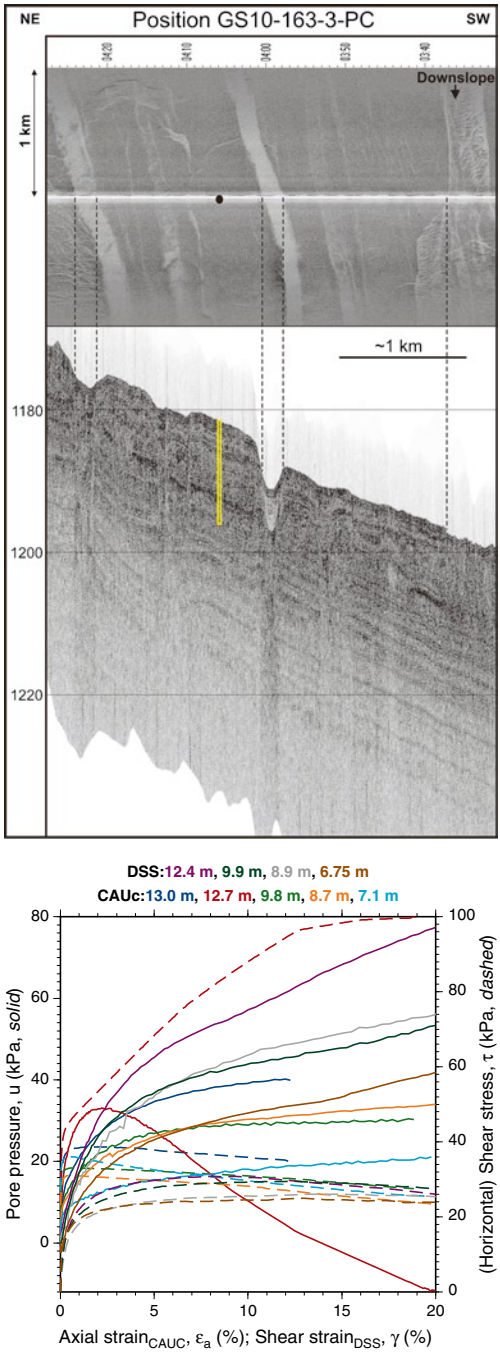

Fig. 3.5 (*Top*) Side-scan sonar and sub-bottom profiler data, Lofoten; (*bottom*) stress and pore pressure development vs. strain from CAUc and DSS tests between 6 and 13 mbsf

fjord catchment. The clay-sand-clay sequence is a single event (L'Heureux et al. 2012). Laboratory and *in-situ* geotechnical tests illustrate that undrained shear strength in these clays (both undisturbed and remoulded) is lower compared to the typical, siltier sediments (Fig. 3.3), and hence, they are geotechnically weaker. Advanced geotechnical tests are not yet available.

Infinite slope equilibrium analysis yields factor of safety (FoS) close to 1. Hence, this could explain the subtle evidence for creep on the bathymetry data. A number of pre-conditioning factors played a significant role in Finneidfjord: (1) regional occurrence of this composite reflection, and thus likely this particular sediment unit; (2) high Holocene fjord-marine sedimentation rates; (3) steep flanks; and (4) likely excess pore pressure development. The latter is inferred from periods of heavy rainfall shortly before the landslide, which may well have affected the phreatic zone underneath the coastlines. Piezometers installed at shallow sub-surface depths (3.1 and 5.3 m) in the undisturbed area adjacent to the slide scar and within the gas-charged zone indicate lateral variations in pore pressure as well. For further details on the Sørfjorden-Finneidfjord data, we refer to L'Heureux et al. (2012) and Steiner et al. (2012).

3.4.2 Intermediate Water Depths – Vesterålen Margin

Mass movements on the gently dipping (3°) upper slope off Vesterålen occur as isolated features just beyond the 500 m isobath (Fig. 3.2b). The landslides have no direct connection, neither with the canyon systems further downslope, nor with the glacial termini further upslope (Laberg et al. 2007). One important observation is the limited mobility (Fig. 3.2b). The mobilized mass only moved over a short distance before deposition. The landslides occur in an area essentially devoid of topographic relief (Fig. 3.2b). However, just upslope from the landslide areas, a change in seafloor dip occurs, and geomorphology upslope is irregular, likely as a result of erosion under the influence of the Norwegian Atlantic Current or iceberg scouring and furrowing.

Both local and regional seabed fractures occur (Rise et al. 2012). These could be indicative of ongoing displacement or instability, and may therefore be the locus of future failures. Seismic data illustrate that the slip plane for some of the landslides may be within one and the same seismo-stratigraphic boundary, at about 10 mbsf. Others may have slipped along somewhat deeper surfaces.

The 12-m long core was taken from the undisturbed area in between two landslides (Fig. 3.2b). X-ray imagery was used for lithofacies characterization, and to select specific targets for geotechnical tests. Sediments are glacimarine (silty to sandy) clays, with variable amounts of clasts, interpreted as ice-rafted debris (IRD). X-ray imagery reveals alternating sediment facies throughout the core, ranging from finely laminated sections with very little IRD to massive, IRD-rich units. Density/water content vary throughout the core (Fig. 3.4). The laminated sediments are interpreted to be rapidly deposited from suspended meltwater plumes that formed in front of active or disintegrating glaciers. The IRD-rich units are considered the result of normal glacimarine sedimentation.

Laboratory tests indicated that the clays are generally normally-consolidated with intermediate plasticity (Fig. 3.4). DSS and CAUc shear strength tests on samples consolidated to the in situ stress state reveal two particular results (Fig. 3.4). The sample from 7.7 mbsf (C2) shows decreasing pore pressure with axial strain. It has high density/low water content, low plasticity index (14%) and low sensitivity (1.7). The sample from 8.6 mbsf (C6) has higher plasticity (26%) and higher sensitivity (3). C6 is the only sample with strain-softening behaviour – i.e. loss of shear resistance with strain after peak strength is reached – and makes this unit a potential candidate as a slip plane. Infinite slope equilibrium analysis yields a FoS well above 1. Therefore, external triggers and/or additional pre-conditioning factors are needed to explain failure in this area.

Further details on stratigraphy and geomorphology are presented in Rise et al. (2012).

3.4.3 Deepwater Setting – Lofoten Margin

Swath bathymetry data reveal a complex mass wasting zone off the Lofoten slope, in water depths beyond 800–1,000 m, with mean dip less than 4° (Fig. 3.2c). Some failures are similar to the larger landslides on the Norwegian margin. Others comprise a stair-case pattern of escarpments, with headwalls and secondary escarpments several tens of metres high. Such patterns are likely indicative of retrogressive failure development (Baeten et al. 2011). Contrary to the Vesterålen margin, the remobilized masses are nearly completely evacuated, resulting in much longer run-out distances and deposition beyond the surveyed area.

High-resolution side-scan sonar images reveal other intriguing features and specific patterns in seabed geomorphology and character that cannot be discerned from the bathymetry data (Fig. 3.5). An along-slope fabric of smaller escarpments delineates instable sediment slabs. Their spatial dimensions are variable, but can be several hundreds of metres wide and 10–15 m thick. They are sharply delineated by shear margins or small escarpments. Interestingly, different stages of development are documented for these subtle instabilities, from shallow graben structures to seabed cracks (Baeten et al. 2011). These small features move along a slip plane a few metres beneath the seafloor. The bathymetry data also show several gullies that terminate within the landslide complex (Fig. 3.2c).

A 13.5 m long core was collected from one of the failing sediment slabs (Figs. 3.2c and 3.5). Sediments are predominantly normally-consolidated clays (in places silty and/or sandy), with variable clast content and laminations. Geotechnical analyses focussing on different lithofacies identified from X-ray scans were performed. Deformation structures are present within a few intervals. One event occurs at about 12.5 mbsf, and corresponds to a clay interval with a sensitivity of 8 (compared to the mean sensitivity of 3). Plasticity is in general higher than on the Vesterålen margin. The CAUc and DSS tests indicate that strain-softening may occur in different units. Integration of all geological and geotechnical data will shed further light on potential

slip planes in this area. Infinite slope equilibrium analysis using the preliminary shear strength data yields a FoS well above 1 for the Lofoten slope as well.

For more details on the geomorphology, lithology and stratigraphy, we refer to Baeten et al. (2011).

3.5 Discussion and Conclusions

The data acquired in the different settings clearly indicate that the occurrence of landslides is very common. Nevertheless, the differences in geomorphology, seismic character, and geological-geotechnical properties imply that local and regional conditions control slope stability to a large extent.

Despite their different dimensions, the landslides in the different physiographic settings involve displacement along specific horizons, indicative of weak layers. These are often fine laminated muds with distinct provenance or depositional mode, unlike the remainder of the sediments. Geotechnical results reveal a contractive behaviour under shear, hence pore pressure increase, during shearing, in these units, which may facilitate retrogressive failure. This was also the case for the Storegga landslide (Kvalstad et al. 2005). The geological and geotechnical data from Finneidfjord and Vesterålen make it possible to link these weaker layers to specific depositional processes, which can be identified on high- to very-high-resolution seismic data.

One critical observation from the integrated data sets is the evidence of incipient mass movements in two of the studies areas. The slopes in Finneidfjord fail regularly, with at least one landslide documented between 2003 and 2009 through repeated bathymetry mapping. There is also geophysical evidence of creep in the area between the 1996 landslide and the shallow gas front. The presence of the sediment slabs with different displacements and seabed fractures on the Lofoten slope is a possible indication of ongoing slip.

Similar smaller-scale landslides are documented in other coastal and fjord settings, e.g., in Canada (Locat et al. 2003), Svalbard (Forwick and Vorren 2012) and Nice (Dan et al. 2007). Coastal and fjord margins have typically steeper slopes. Therefore, they are gravitationally less stable, and may either set off spontaneously or only require small triggers (e.g., human activity). Much larger energy (e.g., seismicity) is needed for initiating mass movements on the continental margins, or perhaps additional (ephemeral) pre-conditioning mechanisms.

Interestingly, and despite the fact that the presence of shallow gas is considered as one of the major offshore geohazards, there is little indication that mass movements occurred in the immediate vicinity of the prominent gas front in Finneidfjord. This could be related to local, smaller slope angles. Nevertheless, this calls for further investigations on the actual role of free gas in submarine mass movements.

Acknowledgments We thank the SEABED project of the Norwegian Deepwater Programme (www.ndwp.org) (CDog) and the Norwegian Research Council (LOslope) for financial support.

Additional data were acquired during the UNESCO programme "Training Through Research" and within MAREANO (www.mareano.no). Figures were made with GMT (http://gmt.soest.hawaii.edu/). This is publication no. 353 of the International Centre for Geohazards (ICG). We also thank the reviewers Dr. Björn Lindberg and Prof. Dr. Christian Berndt for their constructive comments to improve this manuscript.

References

Baeten N, Laberg JS, Forwick M, Vorren TO, Ivanov M, Vanneste M, Forsberg CF, Kvalstad TJ (2011) Small-scale mass wasting on the continental slope offshore Lofoten, Northern Norway. EGU2011. EGU, Vienna

Bryn P, Berg K, Forsberg CF, Solheim A, Kvalstad TJ (2005) Explaining the Storegga slide. Mar Petrol Geol 22(1–2):11–19

Corner G (2006) A transgressive-regressive model of fjord-valley fill: stratigraphy, facies and depositional controls. In: Dalrymple RW, Leckie DA, Tillman RW (eds) Incised valleys in time and space. Society of Sedimentary Geology (SEPM), Tulsa, pp 161–178

Dan G, Sultan N, Savoye B (2007) The 1979 Nice harbour catastrophe revisited: trigger mechanism inferred from geotechnical measurements and numerical modelling. Mar Geol 245(1–4): 40–64

Forwick M, Vorren TO (2012) Submarine mass wasting in Isfjorden, Spitsbergen. In: Yamada Y et al (eds) Submarine mass movements and their consequences, vol. 31, Advances in natural and technological hazards research. Springer, Dordrecht, pp 711–722

Haflidason H, De Alvario MM, Nygård A, Sejrup HP, Laberg JS (2007) Holocene sedimentary processes in the Andøya Canyon system, north Norway. Mar Geol 246:86–104

Hjelstuen BO, Sejrup HP, Haflidason H, Berg K, Bryn P (2004) Neogene and Quaternary depositional environments on the Norwegian continental margin, 62°N-68°N. Mar Geol 213(1–4): 257–276

Kvalstad TJ, Andresen L, Forsberg CF, Berg K, Bryn P, Wangen M (2005) The Storegga slide: evaluation of triggering sources and slide mechanics. Mar Petrol Geol 22(1–2):245–256

L'Heureux J-S, Steiner A, Longva O, Chand S, Vanneste M, Kopf A, Haflidason H, Kvalstad TJ, Forsberg CF, Vardy ME (2012) Identification of weak layers and their role for the stability of slopes at Finneidfjord, northern Norway. In: Yamada Y et al (eds) Submarine mass movements and their consequences, vol. 31, Advances in natural and technological hazards research. Springer, Dordrecht, pp 321–330

Laberg JS, Vorren TO (2000) The Trænadjupet slide, offshore Norway – morphology, evacuation and triggering mechanisms. Mar Geol 171(1–4):95–114

Laberg JS, Vorren TO (2004) Weichselian and Holocene growth of the northern high-latitude Lofoten Contourite Drift on the continental slope of Norway. Sediment Geol 164(1–2):1–17

Laberg JS, Stoker MS, Dahlgren KIT, de Haas H, Haflidason H, Hjelstuen BO, Nielsen T, Shannon PM, Vorren TO, van Weering TCE, Ceramicola S (2005) Cenozoic alongslope processes and sedimentation on the NW European Atlantic margin. Mar Petrol Geol 22(9–10):1069–1088

Laberg JS, Guidard S, Mienert J, Vorren TO, Haflidason H, Nygard A (2007) Morphology and morphogenesis of a high-latitude canyon; the Andoya Canyon, Norwegian Sea. Mar Geol 246(2–4):68–85

Locat J, Martin F, Locat P, Leroueil S, Levesque C, Konrad J-M, Urgeles R, Canals M, Duchesne MJ (2003) Submarine mass movements in the upper Saguenay Fjord (Québec, Canada), triggered by the 1663 earthquake. In: Locat J, Mienert J (eds) Submarine mass movements and their consequences, vol 19, Advances in natural and technological hazards research. Kluwer Academic, Dordrecht, pp 509–520

Longva O, Janbu N, Blikra LH, Bøe R (2003) The 1996 Finneidfjord slide: seafloor failure and slide dynamics. In: Locat J, Mienert J (eds) Submarine mass movements and their consequences,

vol 19, Advances in natural and technological hazards research. Kluwer Academic, Dordrecht, pp 521–530

Rise L, BellecV, Bøe R, Thorsnes T (2009) The Lofoten-Vesterålen continental margin, North Norway: Canyons and mass-movement activity. In: 1st international conference on seafloor mapping for geohazard assessment, Ischia, 2009

Rise L, Chand S, Haflidason H, L'Heureux J-S, Hjelstuen BO, Bellec V, Longva O, Brendryen J, Vanneste M, Bøe R (2012) Investigation of landslides at the upper continental slope off Vesterålen, North Norway. In: Yamada Y et al (eds) Submarine mass movements and their consequences, vol. 31, Advances in natural and technological hazards research, Springer, Dordrecht, pp 167–176

Rosenquist IT (1953) Considerations on the sensitivity of Norwegian quick clays. Geotechnique 3:195–200

Solheim A, Berg K, Forsberg CF, Bryn P (2005) The Storegga slide complex: repetitive large scale sliding with similar cause and development. Mar Petrol Geol 22(1–2):97–107

Steiner A, L'Heureux J-S, Longva O, Lange M, Haflidason H, Vanneste M, Kopf A (2012) In-situ free-fall piezocone penetrometer for characterizing soft and sensitive clays at Finneidfjord (northern Norway). In: Yamada Y et al (eds) Submarine mass movements and their consequences, vol. 31, Advances in natural and technological hazards research. Springer, Dordrecht, pp 99–109

Vardy ME, L'Heureux J-S, Vanneste M, Chand S, Longva O, Haflidason H, Forsberg CF, Brendryen J, Steiner A, Kreiter S (in preparation) Integrated geophysical and geotechnical investigation of a shallow, retrogressive, near-shore landslide, Finneidfjord, Norway. Near Surface Geophysics, Speciall Issue on Marine Engineering Geophysics

Vorren TO, Laberg JS, Blaume F, Dowdeswell JA, Kenyon NH, Mienert J, Rumohr J, Werner F (1998) The Norwegian-Greenland sea continental margins: morphology and late Quaternary sedimentary processes and environment. Quaternary Sci Rev 17(1–3):273–302

Zakeri A (2008) Submarine debris flow impact on pipelines. University of Oslo, Oslo

Chapter 4
Physical Properties and Age of Continental Slope Sediments Dredged from the Eastern Australian Continental Margin – Implications for Timing of Slope Failure

Thomas Hubble, Phyllis Yu, David Airey, Samantha Clarke, Ron Boyd, John Keene, Neville Exon, James Gardner, and Shipboard Party SS12/2008

Abstract A large number of submarine landslides were identified on the continental slope of the southeastern Australian margin during voyages aboard the RV Southern Surveyor in 2008. Preliminary sedimentological, geotechnical and biostratigraphic data are reported for dredge samples of Neogene compacted, calcareous sandy-muds recovered from submarine scarps located on the mid-continental slope. The scarps are interpreted to represent submarine landslide failure surfaces. Slope stability modeling using classical soil mechanics techniques and measured sediment shear-strengths indicate that the slopes should be stable; however, the ubiquity of evidence for mid-slope landslides on this margin indicates that their occurrence is a relatively commonplace event and that submarine-landsliding can probably be considered a normal characteristic of the margin. This presents an apparent contradiction that is probably resolved by one or both of the following: an as yet unidentified mechanism acts to reduce the shear resistance of these sediments to

T. Hubble (✉) • P. Yu • D. Airey • S. Clarke • J. Keene
University of Sydney, Sydney, NSW, Australia
e-mail: tom.hubble@sydney.edu.au; samantha.clarke@sydney.edu.au

R. Boyd
University of Newcastle, Newcastle, NSW, Australia

ConocoPhillips, Houston, TX, USA

N. Exon
Earth and Marine Sciences, Australian National University, Canberra, ACT, Australia

J. Gardner
CCOM, University of New Hampshire, Durham, NH, USA

Shipboard Party SS12/2008
Ron Boyd, Jock Keene, Neville Exon, Asrar Talukder, Tom Hubble, Kev Ruming, Jim Gardner, Janice Felzenberg, David Mitchell, Samantha Clarke, Michael Kinsela, Peter Dunn, Hiski Kippo, Tony Veness, Bernadette Heaney

Y. Yamada et al. (eds.), *Submarine Mass Movements and Their Consequences*,
Advances in Natural and Technological Hazards Research 31,
DOI 10.1007/978-94-007-2162-3_4, © Springer Science+Business Media B.V. 2012

values low enough to enable slope failure; or geologically frequent seismic shaking events large enough to mobilise slides. It is hypothesised that the expansion of the Antarctic Icesheet in Mid-Miocene time and the consequent large-scale production of cold, equator-ward migrating, bottom water has caused significant erosion and removal of material from the mid and lower slope of the Australian continental margin in the Tasman Sea since the Mid-Miocene. It is also hypothesised that erosion due to equator-ward moving bottom water effectively and progressively removed material from the toe of the continental slope sediment wedge. This rendered the slope sediments that were deposited throughout the Tertiary more susceptible to mass failure than would have otherwise been the case.

Keywords Submarine landslides • Mass failure • Multibeam • Seafloor geomorphology • Passive margin

4.1 Introduction

There have been few studies on submarine mass failures on the continental margins of Australia. Jenkins and Keene (1992) were the first to report evidence of submarine landslides on the southeastern Australian continental margin which have been studied in more detail recently with the advent of high-resolution multibeam sonar devices that provide the detailed bathymetric information required to positively identify and accurately describe these features (Glenn et al. 2008; Boyd et al. 2009).

Preliminary investigations have made use of the information collected by the RV Southern Surveyor (Glenn et al. 2008; Boyd et al. 2010) and established that some if not most of the large-scale submarine landslides identified on the SE Australian continental margin are relatively young in the geological sense (Boyd et al. 2010; Clarke et al. 2012) and have occurred in both unconsolidated and compacted, calcareous, sandy-silts. This paper reports sedimentologic, physical properties and biostratigraphic data for mid-slope materials collected during a detailed examination of the SE Australian margin aboard RV Southern Surveyor SS2008/12. We demonstrate that the mid-slope sediments recovered were deposited in a hemi-pelagic, passive-margin setting during the Neogene rather than the inferred origin of Late-Cretaceous/Early-Tertiary rift-basin fill as initially suggested by Boyd et al. (2009). The geomechanical character of the mid-slope failures is established using static slope stability modeling methods.

4.2 Study Area

The study area is located along the SE Australian continental margin, approximately 30–70 km offshore the coasts of southern Queensland and northern New South Wales, between Point Cartwright in the north and Clarence Head in the south; in water depths of between approximately 1,000 m and 3,000 m (Figs. 4.1 and 4.2).

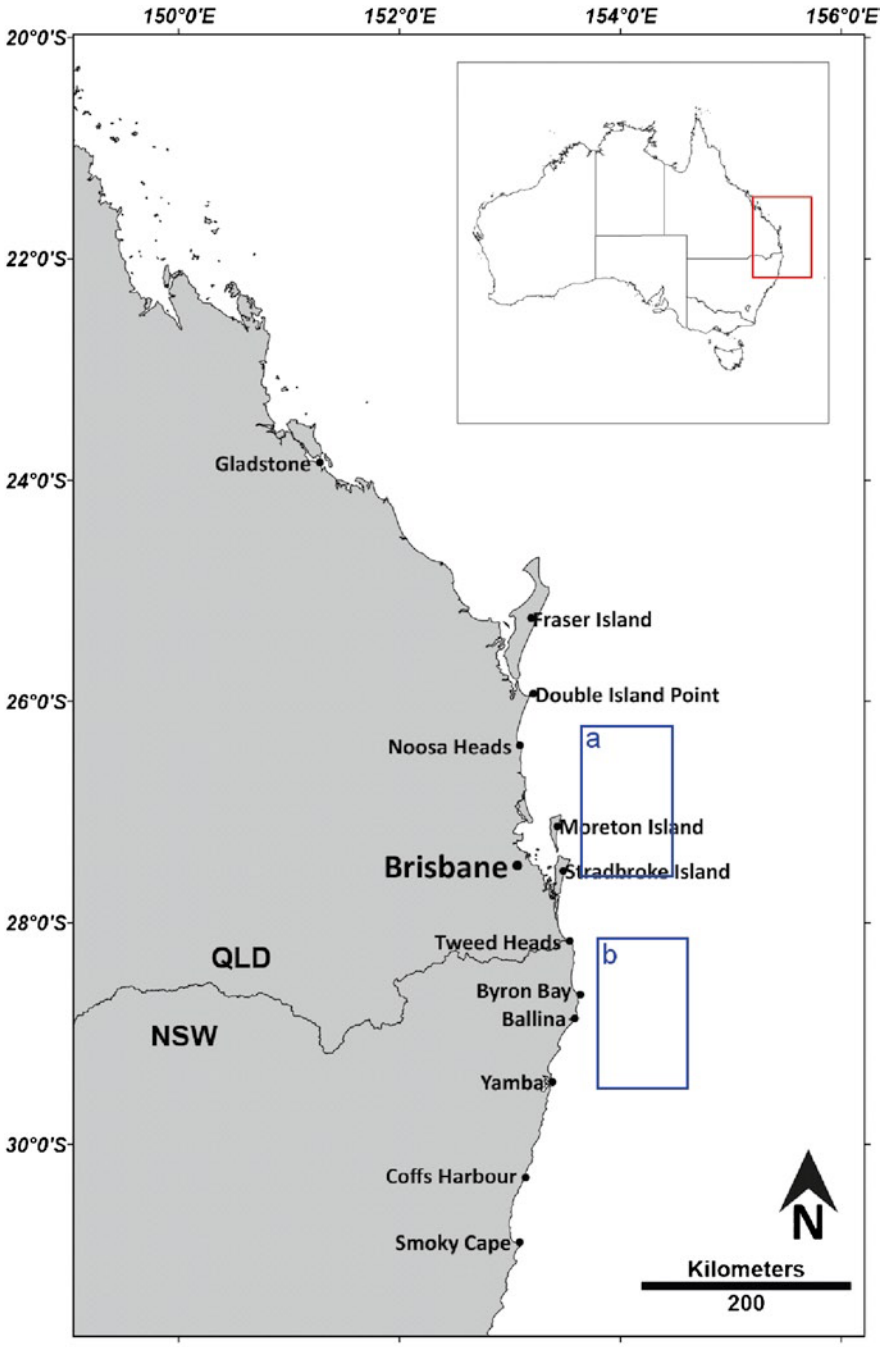

Fig. 4.1 Location map of the southern Queensland to northern New South Wales coastline. *Blue* insets (**a**) and (**b**) mark the location of the bathymetric maps presented in Fig. 4.2

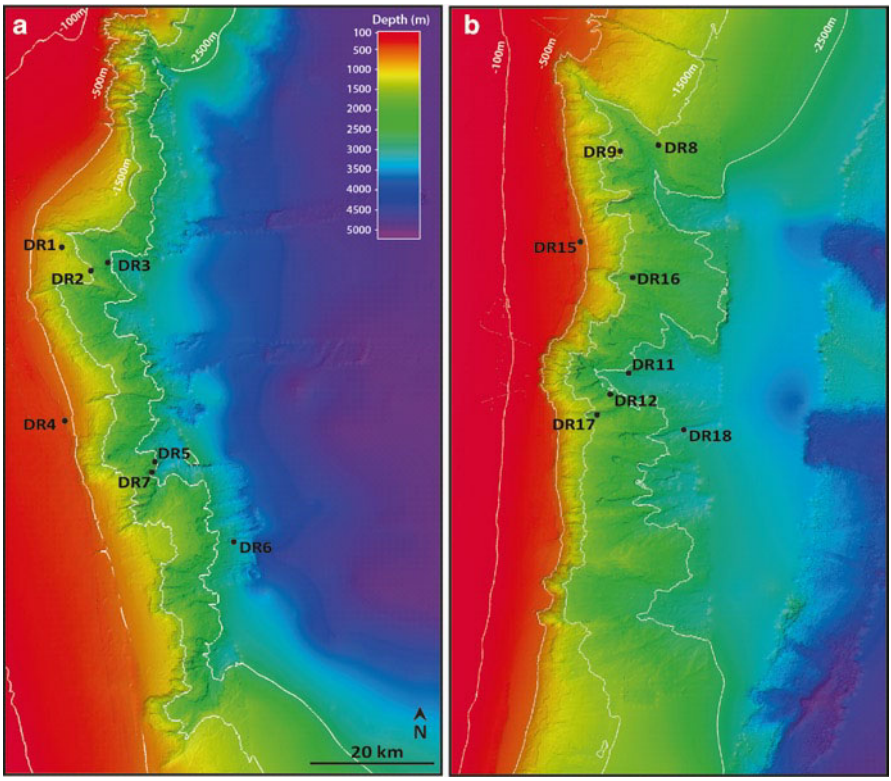

Fig. 4.2 Bathymetric maps of the (**a**) northern and (**b**) southern sections of the study area. Also shown are locations of the box-dredge sites (Boyd et al. 2009). See Fig. 4.1 for the regional location of the images

High-resolution multibeam data of the local and regional bathymetry were collected using a Simrad EM300 multibeam echosounder (Boyd et al. 2010). Fledermaus v7.1.2 was used to process and merge the raw bathymetric data to produce a single complete regional dataset for the entire study area (Boyd et al. 2010).

The continental slope of the SE Australian continental margin is, on average 50 km wide, with the shelf break developed at approximately 150 m water depth and the abyssal plain at about 4,500 m. Average slope angles range from 2.8° to 8.5° (Boyd et al. 2010). The mid-slope region of the study area is generally dominated by the failure scars of slab slides, some of which present amphitheatre-shaped crests, as well as box and linear canyons. These mass-failure features range from common, small landslides with volumes of less than 0.5 km^3 to rarer, large landslides that displace up to 20 km^3 of sediment (Boyd et al. 2010; Fig. 4.3).

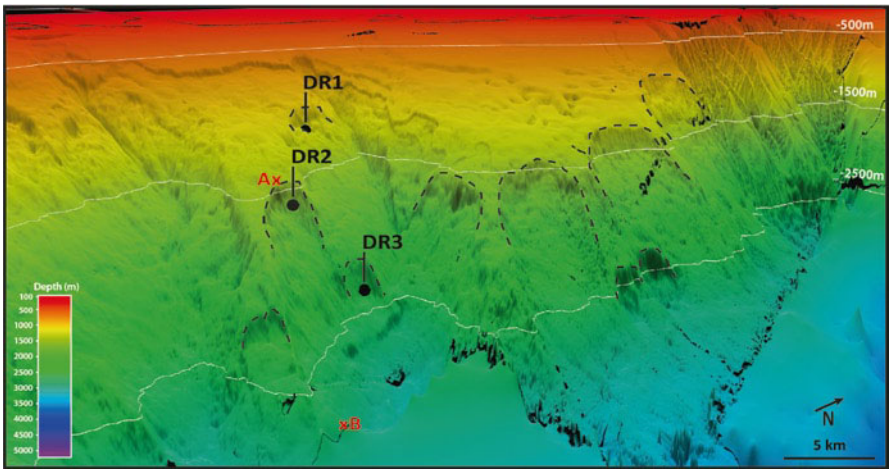

Fig. 4.3 Digital elevation model (DEM) of a section of the mid-slope within the study area. Also shown are the locations of the dredge sites DR1, DR2, and DR3. Note the abundance of slump/slide scars presenting arcuate crests (*crest outlines denoted by black dashed lines*). The section A–B represents the cross-section used in the slope stability model presented in Fig. 4.5

4.3 Results

4.3.1 Dredged Materials – Sedimentology and Geomechanical Properties

Compacted but unlithified sediments were collected from nine mid-slope locations (Fig. 4.2). Physical and geotechnical parameters were determined for representative samples. The testing regime included grainsize analysis (Mastersizer), direct-shear tests, and oedometer tests which provided grainsize data, apparent cohesion, friction angle, dry and wet bulk density, and void ratio. A typical hand-specimen example (DR-9) of these sediments is shown in Fig. 4.4. The material presents no evidence of cementation and meets the standard engineering geology criteria for stiff clay S4 (ISRM 1981) with a maximum uniaxial compressive strength less than 0.5 MPa. It presents as a yellowish-brown sandy-mud containing prominent terrestrial plant fossils (including twigs and leaves not dissimilar to material shed by modern-day eucalypts) as well as abundant plantkontic pelagic foraminifera. It was this mixing of pelagic marine fauna with obviously terrestrial flora which prompted the reasonable but erroneous initial identification (Boyd et al. 2009) of this material as marginal-marine, rift-basin fill. On first inspection it seemed reasonable to infer that they were probably deposited during the early stages of the late-Cretaceous to early-Tertiary events (Gaina et al. 1998) that formed the Tasman Sea Basin and SE

Fig. 4.4 Typical example of compacted mid-slope, silty-sand sediment, which presents obvious fossil leaf and twig impressions. The matrix of the material also presents abundant foraminifera

Australia's passive continental margin between 90 and 52 Ma ago. The subsequent biostratigraphic age determination is entirely incompatible with this interpretation (see below).

The sediments in these samples consist of mixtures of carbonates and silicates and despite their unlithified nature are compacted, relatively-malleable, sandy-silts. Grainsize distribution and physical properties results are presented in Table 4.1. Note that the values determined in shear-box tests that are given for apparent cohesion (average ~26 kPa) and friction angle (average ~29°) are applicable for peak strength conditions rather than residual strength. The void ratio values (average ~1.5) are higher than would be expected from typical consolidated sandy silt; this gives rise to relatively low dry and saturated bulk weight values (averages ~9 kNm^{-3} dry, ~15.7 kNm^{-3} saturated) and is most likely due to the substantial foraminiferal content of the samples. Visual inspection of the material with a high-powered binocular microscope indicates that the tests tend to be undamaged by compaction and consequently present hollow, sediment-fill-free interiors.

4.3.2 Palaeontology/Dating

Four samples were dated on the basis of their contained foraminifera. These samples were prepared by initial disaggregation (as described above) and then wet-sieving. The coarsest fractions (63–150 μm, 150 μm–1 mm, >1 mm) were sent for biostratigraphic analysis (Chaproniere 2010) and the results are presented in Table 4.2. The biostratigraphically determined ages range from latest Oligocene to Miocene-Pliocene boundary with sediment sample age increasing with increasing

Table 4.1 Summary of the physical and geomechanical properties of the dredge samples

	Grainsize distribution			Sediment classification				Geomechanical properties			
Sample	d(0.1) (min) (μm)	d(0.5) (med) (μm)	d(0.9) (max) (μm)	% clay (0–2.0 μm)	% fine and medium silt (2.0–20 μm)	% coarse silt and fine sand 20–200 μm)	% coarse sand (200–2,000 μm)	Apparent cohesion (c') (kPa)	Friction angle (Φ) (°)	Bulk density (γ) (kNm^{-3})	Void ratio
DR1-A	4.473	18.050	65.136	1.11	52.58	44.79	1.52	–	–	–	–
DR1-B	4.819	18.897	61.486	0.88	51.28	47.44	0.39	–	–	–	–
DR2-A	2.688	17.011	–	4.86	47.87	42.81	–	–	28.8	10.0	1.50
DR3-A	4.555	18.290	–	1.25	51.64	46.12	0.99	17.1	22.4	11.8	1.07
DR6-B	4.155	13.023	42.238	1.20	66.62	31.91	0.28	–	–	–	–
DR6-C	4.518	15.640	54.159	1.09	58.72	39.27	0.93	–	–	–	–
DR6-D	4.528	14.882	46.866	0.69	61.39	37.66	0.25	28.8	31.4	7.1	–
DR6-F	4.846	13.942	44.412	1.13	65.75	32.98	0.14	–	–	–	–
DR6-G	3.739	12.089	47.668	1.94	67.84	29.50	0.71	–	–	–	–
DR6-H	–	11.949	57.601	–	45.81	36.34	1.03	–	–	–	–
DR8	3.827	11.635	38.418	1.47	70.92	27.61	0.00	22.5	30.7	9.3	1.67
DR8-Ab	2.965	10.124	59.890	3.71	66.03	30.21	0.05	–	–	–	–
DR8-Ac	3.696	13.482	46.778	1.92	63.18	34.72	0.17	–	–	–	–
DR9-B	3.733	11.465	44.311	1.90	70.51	27.43	0.15	20.4	29.6	8.9	1.70
DR11-B	3.288	19.375	–	3.36	47.45	48.35	0.84	–	–	–	–
DR16-B	3.877	13.890	57.050	1.51	61.61	36.00	0.88	–	–	–	–
DR17	4.426	15.404	58.610	1.09	59.13	39.47	0.31	40.8	29.4	10.3	1.47

Physical properties include grainsize distribution (μm) and clay/silt/sand content (%), while geomechanical properties include apparent cohesion (kPa), friction angle (°), bulk density (kNm^{-3}) and void ratio

Table 4.2 Summary of the biostratigraphical analysis results collected from four dredge samples

Sample	Coordinates (lat/long)	Water depth (m)	Biostratigraphy	Comments
DR1-A	26°40.01'S/ 153°47.08'E	1,000	SN11; N.17 to N.18 Pliocene-Miocene boundary	Presence of *Globorotalia conomiozea, Gr. panda, Gr. lenguaensis, Globoquadrina dehiscens* without *Gr. sphericomiozea*
DR1-B			SN11; N.17 to N.18 Pliocene-Miocene boundary	Presence of *Globorotalia conomiozea, Gr. panda, Gr. lenguaensis, Globoquadrina dehiscens* without *Gr. sphericomiozea*
DR9-B	28°24.50'S/ 153°59.55'E	1,500–1,300 m	SN10 to SN11; N.17 to N.18 with SN13; N.21 Pliocene–Miocene boundary; late Pliocene	Presence of *Gr. miotumida* and *Gr. lenguaensis* with *Gq. dehiscens*; *Gr. inflata* and *Pulleniatina obliquiloculata* without *Gr. truncatulinoides*
DR16-B	28°37.29'S/ 154°01.02'E	2,020–1,970	SN1; N4B Early Miocene	Presence of *Gq. dehiscens* and *Catapsydrax dissimilis* with *Ga.?labiacrassata* without *Ga woodi*

This analysis was performed by George Chaproniere of the Australian National University

depth of dredging. This apparent age/depth correlation is consistent with each dredge sample's probable position in the margin's stratigraphic section with deeper-water dredge samples having been sampled from positions lower in the stratigraphic column. Given the geologic setting, and the geologic history of the study area (see Gaina et al. 1998) it follows that the compacted mid-slope sandy-muds described here were deposited directly onto the continental margin (hemipelagic deposits). Some samples contain a surprisingly large amount of terrestrial plant material and all include some terrigenous silt of undetermined source origin.

In one sense these age determinations are the most significant piece of information determined for the sediment samples recovered from the study area as they provide an indication of the maximum potential age of initiation of mass-failure on the margin. In the first instance, as there are slope failures described here which are developed in latest Oligocene and Neogene age materials then it follows that these slope failures can be no older than early Neogene; failures developed in the latest Miocene to early Pliocene materials provide another useful date; while the latest Pleistocene age determined for nearby upper slope failures (~3 km^3) described

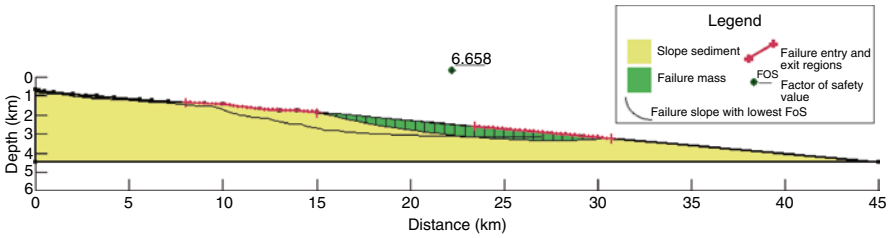

Fig. 4.5 Bishop's method, minimum circle calculation determined by GEOSLOPE W/ for average parameters (Table 4.1) for the section AB as shown in Fig. 4.3. The calculated Factor of Safety value of ~6.7 was determined using an apparent cohesion of 26 kPa, friction angle of 29° and a dry bulk unit density of 9.6 kNm^{-3}, and indicates that the slope is inherently very stable

by Clarke et al. (this volume) indicate that this the margin has also shed material relatively recently.

4.3.3 Geomechanical Modeling

Static geomechanical modeling of several mid-slope failures identified in the study area was undertaken using the program GEOSLOPE/W. This paper will focus on one particular failure (containing DR-2) located in the north of the study area (Fig. 4.2) which is representative of the several mass failures examined to date (Yu 2010). A two-dimensional, pre-failure slope profile was reconstructed by projection of the geometry of the adjacent, unfailed slope surface across the scar area. The failure was based on Bishop's variation of the Swedish slip-circle method (Lambe and Whitman 1979) and used the physical properties data reported above (cohesion 25 kPa, friction angle 30° and saturated weight of 15 kNm^{-3}). This calculation generates a dimensionless parameter known as the Factor of Safety (FoS) that is defined as the ratio of the restoring forces to the disturbing forces (stable slope, FoS > 1; unstable slope, FoS < 1; critically stable slope, FoS = 1). The software was set up to search for the minimally stable slip-circle and the results for this site are given in Fig. 4.5. The GEOSLOPE generated a FoS of 6.8 for the northern slide mass. This value was typical of the other sites studied (Yu 2010) and indicates that the mid-slope sediments are inherently very stable at the slope angles (~8°) present in this region. Back-analysis of the failure was undertaken to determine the sediment shear-strength that would reduce the FoS to a value below one and characteristic of failure. For this slope to fail in a static mode the shear strength must be reduced to one eighth of the values determined in testing (0 kPa and a friction angle of ~8°) which are considered to be unrealistically low values that are well below the measured residual strengths of the sediment. A very crude investigation of seismic loading on the slope indicates that lateral and vertical accelerations (ah = 0.3 g, av = −0.3 g) at the upper limit of those used to investigate the stability of earth dams during earthquakes (Ozkan 1998) would also destabilise the slopes.

4.4 Discussion and a Hypothesis

The presence of at least ten, similar-sized mid-slope landslide scars in the area immediately adjacent to the modelled failure and the striking abundance of these features along the 300 km section of the margin examined for this study (Boyd et al. 2009) as well as at other sites offshore SE Australia (Boyd et al. 2010) demonstrates that mass-failure of the mid-slope sediments is a ubiquitous phenomenon on this passive margin. Furthermore, these observations suggest that failure of the continental slope may be a relatively frequent event (at least in the geological sense of perhaps one event per several hundred thousand years) or that there have been short periods during the Neogene when mid-slope failure has been a relatively common event. The factor of safety calculations indicating the inherent stability of these slopes despite the obvious, numerous and widespread instances of slope-failure present a striking interpretational paradox, at least from the perspective of classical geomechanics.

An enormous, olistostromic block (~25 km long, 0.5 s two-way-travel time thick ~500 m thick) located above a distorted seismic reflector of probable middle to late Neogene age offshore the northern limit of the study area was reported by Hill (1992). Its presence and age provides an indication of the timing of the onset of failure of slide blocks from the SE Australian margin. To date, we are aware of only one such block. That said, the large number of landslide scars reported here and elsewhere (Glenn et al. 2008; Boyd et al. 2009, 2010) suggest that many other similar blocks should be present within the Neogene units of the Tasman Sea Basin's abyssal plain sediments. It is therefore suggested that one or more of the following processes are acting to destabilise the slope: (1) a dramatic reduction of the shear strength of the mid-slope sediments to extremely low values possibly induced by creep or a build-up of pore-pressure ; (2) a long-term modification of the slope-geometry i.e. sedimentation on the head of the slope and/or erosion of the toe of the slope; and (3) infrequent large earthquakes triggering sediment liquefaction or a relatively rapid increase of pore-fluid pressure. In contrast, the invocation of an unknown, extremely weak and un-sampled layer is not favoured due to the ubiquity of mass-failures.

The apparent mid-Neogene timing of the onset of failure is pene-contemporaneous with, and indicates a potential causal link with, the global reorganisation of deep-water oceanic currents that arose from the expansion of the Antarctic Icesheet during the Mid-Miocene (Potter and Szatmari 2009). This event and process is well-recognised to have eroded deep oceanic sediments throughout the Australian region (Exon et al. 2004) and has been suggested by Hubble et al. (2010) to be responsible for the enigmatic, but widespread absence of sediment cover from the New South Wales portion of the middle continental slope (water depths 1,500 m–3,500 m) where fresh Devonian granites outcrop (Hubble et al. 1992). Currently, deep oceanic water probably derived from the Antarctic is known to flow northwards into the Tasman Basin (McCartney and Donahue 2007). Mata et al. (2006) have identified a large mass of northerly moving bottom water in the western Tasman Sea (located below 2,500 m

and extending to the seafloor) which "hugs the continental slope" (Mata et al. 2000) and develops peak velocities of 40 cm s^{-1} adjacent to the toe of the continental slope at a water depth of 3,500 m just to the south of the study area (offshore Coffs Harbour at 32°S 154°E; Mata et al. 1998). It is strongly suspected that this process is much more intense during glacial maxima.

It is hypothesized that a flow of cold, equator-ward migrating, bottom water has caused significant erosion and removal of sediment from the mid and lower slope of the Australian continental margin in the Tasman Sea; possibly from as early as the Oligocene and that this flow probably intensified after the expansion of the Antarctic Ice-Sheet in the Mid-Miocene. It is further hypothesised that erosion due to these currents has progressively removed material from the toe of the continental slope sediment wedge rendering the slope sediments that were deposited throughout the Tertiary more prone to mass failure than would have otherwise been the case. This situation has also increased the susceptibility of the slope's sediments to the destabilising effects of the larger but relatively rare earthquakes of Magnitude >6.5 that occur on the east coast of Australia (see Clark 2010).

A great deal more investigation of the continental margin of southeastern Australia is required to demonstrate the validity of the suspected geologic processes leading to the slope failure documented in this study. Such studies will need to undertake further sampling, bathymetric and seismic surveying of the lower slope and adjacent abyssal plain and examine long-term deep-water current meter records as well as complete further detailed geomechanical testing and modeling work.

Acknowledgments We would like to acknowledge the P&O crew and scientific crews of the RV Southern Surveyor voyage (12/2008). Funding for this voyage was provided by ARC Australia and ConocoPhillips Pty Ltd. Assistance with dating was provided by Tony Allen, CSIRO, Sydney. This paper benefitted from reviews by Dr. Greg Skilbeck (University of Technology, Sydney) and Dr. Jason D. Chaytor (U.S. Geological Survey).

References

Boyd R, Keene J, Ruming K, Exon N, Shipboard Party (2009) SS12/2008 Voyage summary: marine geology and geohazard survey of the SE Australian margin off Northern NSW and Southern Queensland. CSIRO

Boyd R, Keene J, Hubble T, Gardner J, Glenn K, Ruming K, Exon N (2010) Southeast Australia: a Cenozoic continental margin dominated by mass transport. In: Mosher DC, Moscardelli L, Shipp RC, Chaytor JD, Baxter CDP, Lee HJ, Urgeles R (eds) Submarine mass movements and their consequences, vol 28, Advances in natural and technological hazards research. Springer, Dordrecht, pp 1–8

Chaproniere GC (2010) Foraminiferal biostratigraphy of samples from the CSIRO cruise SS 12/2008. Sydney: p 5

Clark DJ (2010) Large earthquake recurrence in New South Wales: implications for earthquake hazard. Paper presented at the Australian geomechanics society (Sydney chapter) symposium, seismic engineering – design for management of geohazards, darling harbour Sydney, 13th Oct 2010

Clarke S, Hubble T, Airey D, Yu P, Boyd R, Keene J, Exon N, Gardner J (2012) Submarine landslides on the upper East Australian continental margin – preliminary findings. In: Yamada Y et al (eds) Submarine mass movements and their consequences, vol. 31, Advances in natural and technological hazards research. Springer, Dordrecht, pp 55–66

Exon N, Brinkhuis H, Robert CM, Kennett JP, Hill PJ, Macphail MK (2004) Tectono-sedimentary history of uppermost Cretaceous through Oligocene sequences from the Tasmanian region, a temperate Antarctic margin. In: Exon N, Kennett JP, Malone M (eds) The Cenozoic Southern Ocean: tectonics, sedimentation and climate change between Australia and Antarctica, vol 151, Geophysical monograph. AGU, Washington, DC, pp 319–344

Gaina CM, Muller RD, Royer J-Y, Stock J, Hardebeck J, Symonds P (1998) The tectonic history of the Tasman Sea: a puzzle with 13 pieces. J Geophys Res 103:12413–12433

Glenn K, Post A, Keene J, Boyd R, Fountain L, Potter A, Osuchowski M, Dando N, Party S (2008) NSW continental slope survey – post cruise report vol geoscience Australia, record 2008/14, 160 pp

Hill PJ (1992) Capricorn and northern Tasman Basins: structure and depositional systems. Explor Geophys 23:153–162

Hubble TCT, Packham GH, Hendry DAF, McDougall I (1992) Granitic and monzonitic rocks dredged from the southeast Australian continental margin. Aust J Earth Sci 39:619–630

Hubble T, Yu P, Airey D, Clarke S, Boyd R, Exon N, Gardner V (2010) Physical properties and age of mid-slope sediments dredged from the Eastern Australian continental margin and the implications for continental margin erosion processes. In: Abstract OS13E-1297, Fall Meeting American Geophysical Union (AGU), San Francisco, 2010

International Society for Rock Mechanics (ISRM) (1981) Rock characterisation, testing and monitoring; ISRM suggested method. Pergammon Press, Oxford

Jenkins CJ, Keene JB (1992) Submarine slope failures on the southeast Australian continental slope. Deep Sea Res 39:121–136

Lambe TW, Whitman RV (1979) Soil mechanics. Wiley, New York, p 553

MacCartney MS, Donahue KA (2007) A deep cyclonic gyre in the Australian-Antarctic Basin. Prog Oceanogr 75:675–750

Mata MM, Wijffels S, Tomczak M, Church JA (1998) Direct measurements of the transport of the East Australian Current: a data report from the WOCE Pacific current meter array 3, CSIRO marine research and Flinders institute of marine and atmospheric sciences, Hobart, 1998

Mata MM, Tomczak M, Wijffels S, Church JA (2000) East Australian current volume transports at 30°S: estimates from the World Ocean Circulation Experiment hydrographic sections PR11/P6 and the PCM3 current meter array. J Geophys Res 105(C12):28509–28526. doi:10.1029/1999jc000121

Mata MM, Wijffels S, Tomczak M, Church JA (2006) Statistical description of the east Australian current low-frequency variability from the WOCE PCM3 array. Mar Freshw Res 57:273–290

Ozkan MY (1998) A review of considerations on seismic safety of embankments and earth and rock-fill dams. Soil Dyn Earthq Eng 17:439–458

Potter PE, Szatmari P (2009) Global Miocene tectonics and the modern world. Earth Sci Rev 96:279–295

Yu P (2010) Submarine mass failure on the Australian east coast: causes, controls and consequences. Unpublished honours thesis, School of geosciences, The University of Sydney

Chapter 5
Submarine Landslides on the Upper Southeast Australian Passive Continental Margin – Preliminary Findings

Samantha Clarke, Thomas Hubble, David Airey, Phyllis Yu, Ron Boyd, John Keene, Neville Exon, James Gardner, and Shipboard Party SS12/2008

Abstract The southeast Australian passive continental margin is narrow, steep and sediment-deficient, and characterized by relatively low rates of modern sedimentation. Upper slope (<1,200 m) sediments comprise mixtures of calcareous and terrigenous sand and mud. Three of twelve sediment cores recovered from geologically-recent, submarine landslides located offshore New South Wales/Queensland (NSW/QLD) are interpreted to have sampled failure surfaces at depths of between 85 and 220 cm below the present-day seabed. Differences in sediment physical properties are recorded above and below the three slide-plane boundaries. Sediment taken directly above the inferred submarine landslide failure surfaces and presumed to be post-landslide, returned radiocarbon ages of 15.8, 20.7 and 20.1 ka. The last two ages correspond to adjacent slide features, which are inferred to be consistent with their being triggered by a single event such as an earthquake. Slope stability models based on classical soil mechanics and measured sediment shear-strengths indicate that the upper slope sediments should be stable. However, multibeam sonar data reveal that many upper slope landslides occur across the margin and that submarine landsliding

S. Clarke (✉) • T. Hubble • D. Airey • P. Yu • J. Keene
University of Sydney, Sydney, NSW, Australia
e-mail: samantha.clarke@sydney.edu.au; Thomas.Hubble@sydney.edu.au

R. Boyd
University of Newcastle, Newcastle, NSW, Australia

ConocoPhillips, Houston, TX, USA

N. Exon
Earth and Marine Sciences, Australian National University, Canberra, ACT, Australia

J. Gardner
CCOM, University of New Hampshire, Durham, NH, USA

Shipboard Party SS12/2008
Ron Boyd, Jock Keene, Neville Exon, Asrar Talukder, Tom Hubble, Kev Ruming, Jim Gardner, Janice Felzenberg, David Mitchell, Samantha Clarke, Michael Kinsela, Peter Dunn, Hiski Kippo, Tony Veness, Bernadette Heaney

Y. Yamada et al. (eds.), *Submarine Mass Movements and Their Consequences*,
Advances in Natural and Technological Hazards Research 31,
DOI 10.1007/978-94-007-2162-3_5,

is a common process. We infer from these results that: (a) an unidentified mechanism regularly acts to reduce the shear resistance of these sediments to the very low values required to enable slope failure, and/or (b) the margin experiences seismic events that act to destabilise the slope sediments.

Keywords Mass-failure • Multibeam • Seafloor geomorphology • Continental slope

5.1 Introduction

The geological record contains many examples of submarine landslides. They have been often associated with locations presenting inclined seafloor slopes, areas where sedimentation rates are high, sediments are fine-grained, or seafloor rocks are weakened by fractures. Despite extensive literature on the nature and causes of submarine landslides, their dynamics and triggering processes are not well understood (Locat and Lee 2002; Bardet et al. 2003). One of the principal reasons for this is the limited data on the physical and mechanical properties of sediments from the slide plane, as these materials have not traditionally been collected in historical studies.

In Australia, there are only a few studies that have investigated submarine landslides on the Australian continental slopes (e.g., Jenkins and Keene 1992; Glenn et al. 2008; Boyd et al. 2010; Hubble et al. 2012). While evidence for submarine landslides on the SE Australian margin was first reported by Jenkins and Keene (1992), it was not until high resolution, multibeam bathymetric data became available (Glenn et al. 2008; Boyd et al. 2010) that the true distribution of these slides could be established.

Preliminary investigations from our survey on the RV Southern Surveyor (SS12/2008) indicate that many large submarine landslides occur on the SE Australian coastal margin between Byron Bay and Tweed Heads (Fig. 5.1). Radiocarbon ages from the sediment indicate that they are also geologically young (<20 ka) (Boyd 2009; Boyd et al. 2010).

5.1.1 Study Area

The study area is located along the SE Australian continental margin off northern New South Wales and southern Queensland (Fig. 5.1). Mapping of the seabed and sampling occurred approximately 30–70 km seaward of the present coastline between Point Cartwright in the north to Clarence Head in the south, in water depths of 150–4,500 m.

Three submarine landslides identified by Boyd et al. (2010) on the upper continental slope are described in this work. They are known as the Coolangatta 1 slide (headwall depth 500 m; centre of mass water depth 600 m), the Cudgen slide (headwall depth 550 m; centre of mass water depth 600 m), and the Byron slide (headwall depth 500 m; centre of mass water depth 800 m) (Figs. 5.1 and 5.2). A total of eight gravity cores were recovered from these landslides.

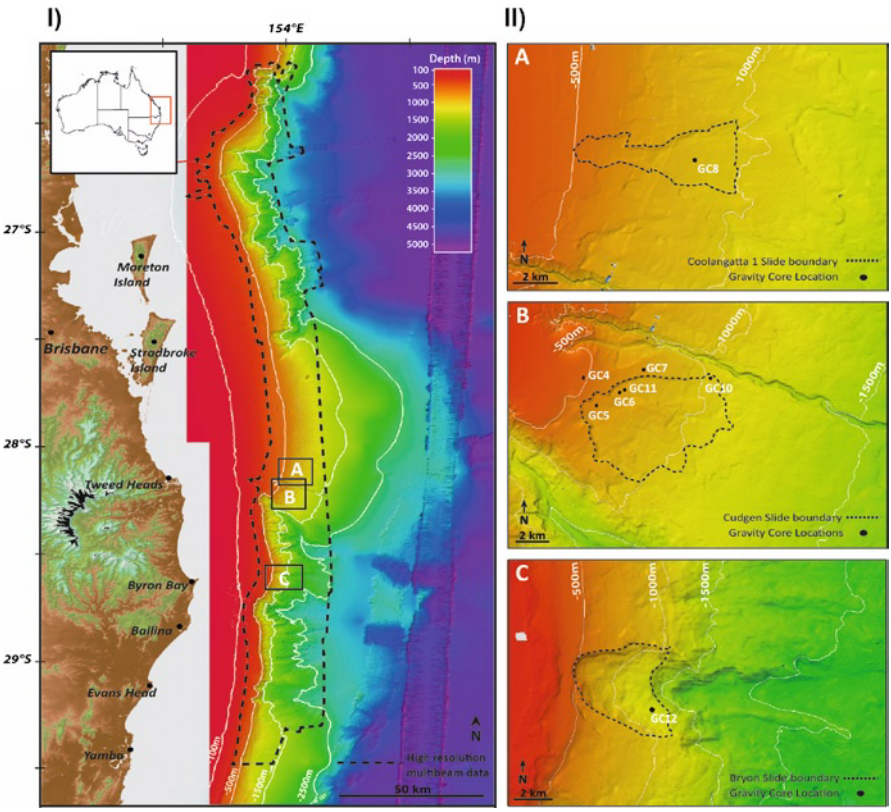

Fig. 5.1 (**I**) Location map of showing the location and bathymetry of the study area (dashed line). Insets mark the three slides (north to south): (**a**) Coolangatta 1 Slide, (**b**) Cudgen Slide, (**c**) Byron Slide. (**II**) The three slide sites showing the locations of eight gravity cores (GC) collected on the RV Southern Surveyor (SS2008/12) voyage

5.2 Data and Methods

5.2.1 Bathymetry and Slide Geometry

High-spatial resolution bathymetric data were acquired during the RV Southern Surveyor voyage (SS12/2008) using a Simrad EM300 multibeam echosounder. Sub-bottom profile data (Topaz) were also acquired in water depths less than 1,000 m (Boyd et al. 2010). The raw multibeam data was processed and merged to produce a single complete dataset for the entire study area (for details see Boyd et al. 2010; Fig. 5.1). This dataset was then displayed using Fledermaus v7.1.2 software.

Several distinct large sediment slides varying in volume from <0.5 to 20 km^3 are identified on the upper slope (<1,200 m) of the SE Australian margin (Boyd et al. 2010).

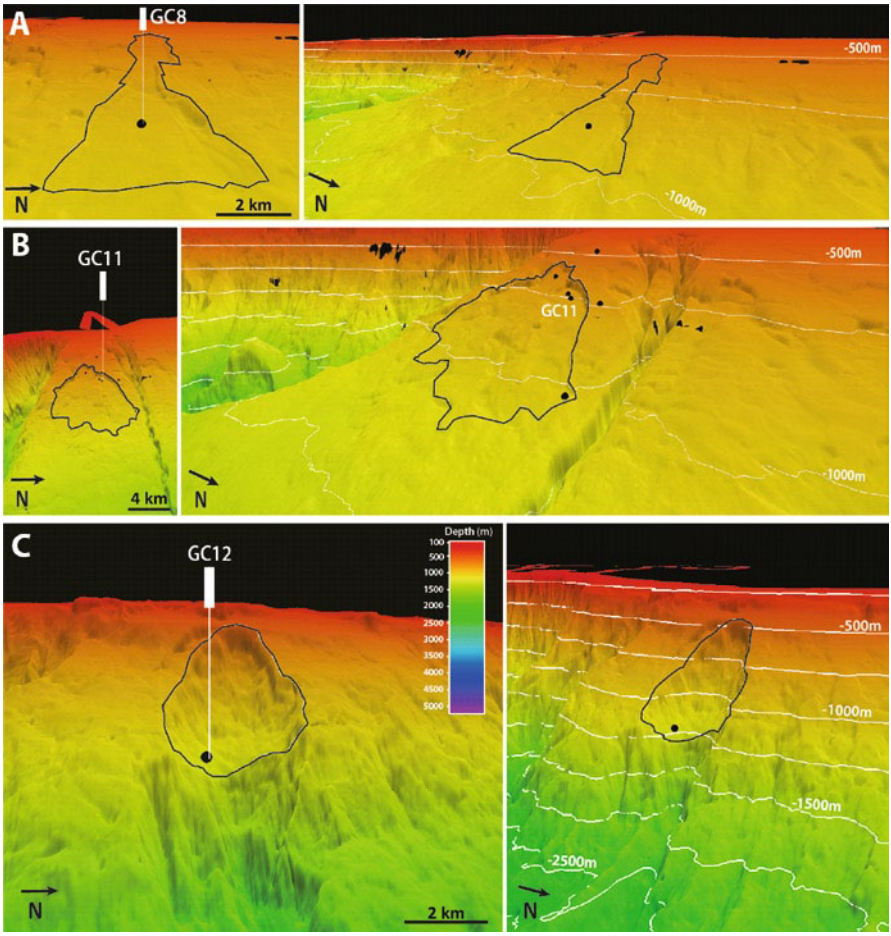

Fig. 5.2 Digital elevation model (DEM) of the slope geometry for the three slide sites (outlines denoted by *black line*): (**a**) Coolangatta 1 Slide, (**b**) Cudgen Slide, (**c**) Byron Slide. Also shown are locations of the three gravity cores (GC8, GC11, GC12) in this study

The three slides (Fig. 2) which are the focus of the present study, typically comprise a distinct U-shaped trough in cross-section (3–6 km wide and 20–250 m deep) backed by an amphitheatre shaped crestal zone. In each case, this slide morphology is similar to the classical circular failure profile described by Varnes (1978), but they are elongated in longitudinal profile.

5.2.2 Sediment Properties

The three gravity cores used in this study (GC8, GC11 and GC12) were visually logged and sub-sampled for: grainsize and mean grainsize distribution (analysis using

GRADISTAT 4.0, Blott and Pye 2001), carbonate and organic carbon content (loss on ignition method, following Heiri et al. 2001), dry bulk unit density, unit weight, void ratio, specific gravity, and water content.

The mechanical behaviour of the sediment was also investigated using geomechanical tests to determine the collapse potential of the sediment, and the influence of composition and stress level on this behaviour. Monotonic triaxial tests were performed on ~126 cm-long core sections taken from adjacent gravity cores from the same feature in order to generate input parameters (i.e., cohesion and friction angle) required for geomechanical modeling. These tests included one-dimensional consolidation in triaxial apparatus at a range of stress paths, followed by undrained shearing to failure.

5.3 Results and Interpretation

5.3.1 Sediment Properties

Two distinct sediment units occur in cores GC8, GC11 and GC12 (Fig. 5.3): a younger, sediment drape overlies an older, sediment unit. These two units are separated by a distinct physical boundary located below the present-day seabed at 87 cm in GC12, 90 cm in GC8 and 220 cm in GC11. The boundary features are all clearly distinguishable and while they all easily identified by a colour change it was the distinct, down-core increase in stiffness identified during the initial logging of the core that indicated their potential genetic significance (Fig. 5.3II). In all three cases these boundaries are interpreted to represent the basal surfaces of submarine landslides. This interpretation is based on distinct down-core changes in bulk density (increase from 851 to 1,062 kg m^{-3} in GC12), unit weight (increase from 15.0 to 16.4 kN m^{-3} in GC12) and moisture content (decrease from 80% to 57% in GC12) across the inferred slide-plane boundary (Fig. 5.4). The bulk density determined for the sediment sampled below the identified boundary in GC12 is consistent with a burial and compaction by column of material at least 200 m thick, if comprised of similar sediments that are present above the boundary. In contrast, the sediment sampled just above the boundary feature presents a density consistent with its present-day depth (i.e. approximately 1 m) below the sea floor. The down-core changes in unit weight and water content are also consistent with 200 m of burial. The depth reconstructed at the GC12 site by replacing the material apparently missing from the U-shaped trough, i.e. by maintaining the continuity and shape of the adjacent slope and projecting it above the GC12 site, is approximately 250 m.

While there is an obvious change in colour, stiffness, density and water content across the boundary identified in GC8, GC11, and GC12, there is no significant difference in the texture and composition of the sediment between the two units, with grainsize, carbonate and organic carbon content remaining relatively invariant (Fig. 5.4). Sediment in both units comprises poorly sorted, medium to coarse sandy silts, with low clay and high silt and sand contents. Carbonate and organic carbon content also remain uniform across the boundary.

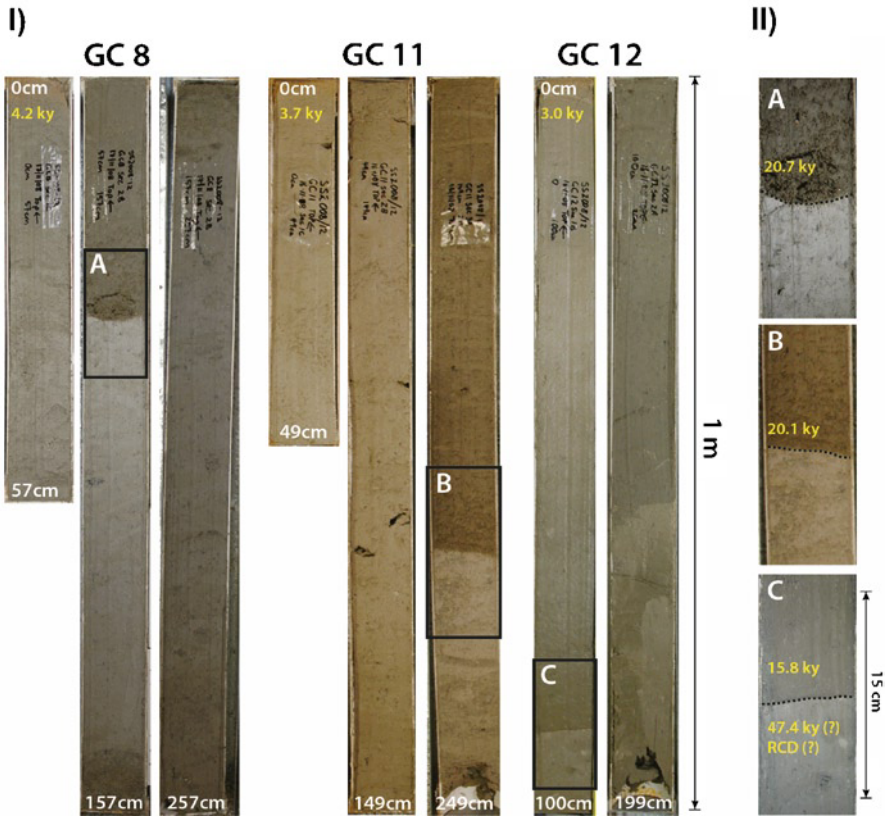

Fig. 5.3 (**I**) Images of the three gravity cores (GC) analysed in this study that present boundary features: GC8, GC11 and GC12. See Figs. 5.1 and 5.2 for the locations of the gravity cores. (**II**) Close up of the boundary feature in each core. The inferred slide plane is indicated with a dashed *black line*. Bulk radiocarbon ages for each core are also shown in *yellow* (ky 1,000 years before present, RCD radiocarbon dead)

5.3.2 ^{14}C Radiocarbon Ages

Bulk radiocarbon ages were used to establish minimum age constraints on the timing of the submarine landslide slide plane material recovered within three gravity cores (GC8, GC11 and GC12). Radiocarbon ages were determined at the Radiocarbon Laboratory, University of Waikato, New Zealand. Conventional ^{14}C years BP were converted into calibrated calendar ages using OxCal V3.10 using marine calibration curve Marine09 (Bronk Ramsey 2005; Marine data from Reimer et al. 2009) following Stuiver and Henry (1977) and are reported here with 2σ errors.

Seven radiocarbon ages were determined from bulk sediments collected from the three gravity cores (Table 5.1). The ages indicate that a significant time gap exists

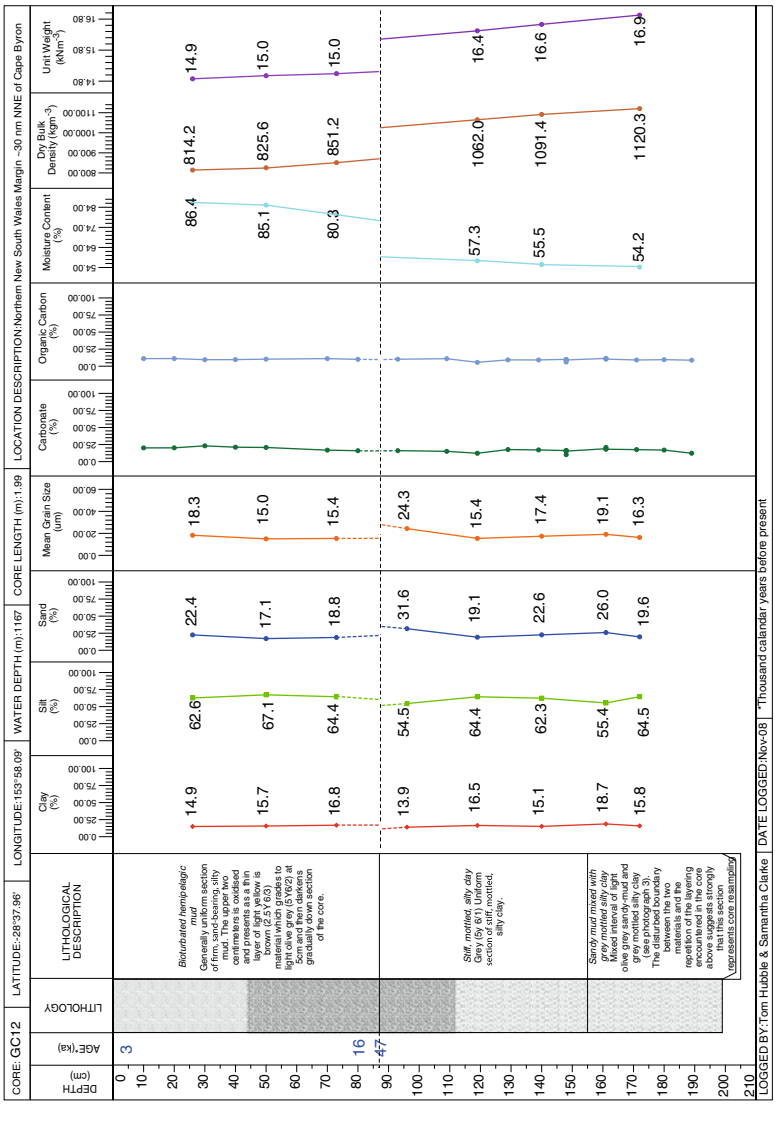

Fig. 5.4 Core log for GC12 showing physical properties with depth below seabed. Bulk radiocarbon dates are also shown. The presumed slide plane is indicated with a dashed *black line* at 87 cm depth below seabed. GC8 and GC11 show similar trends

Table 5.1 ^{14}C dating results of bulk sedimentary organic carbon samples

Lab code	Core	Depth (cm)	Conventional ^{14}C age (BP)	^{14}C error[a]	Median calibrated age (2σ) (BP)	2σ calibrated age range (95.4% probability) (BP)
SS2008-12/ GC8/1C-6/D	GC8	6	4,157	±45	4,229.5	4,079.5–4,379.5
SS2008-12/ GC8/2B-85/D	GC8	85	17,732	±95	20,699.5	20,249.5–21,149.5
SS2008-12/ GC11/1C-3	GC11	3	3,763	±44	3,699.5	3,569.5–3,829.5
SS2008-12/ GC11/3A-206	GC11	206	17,417	±91	20,149.5	19,849.5–20,449.5
SS2008-12/ GC12/1B-5	GC12	5	3,207	±51	3,024.5	2,859.5–3,189.5
SS2008-12/ GC12/1B-81	GC12	81	13,463	±77	15,799.5	15,149.5–16,449.5
SS2008-12/ GC12/1B-88	GC12	88	44,288	±1,205	47,399.5	45,149.5–49,649.5

All samples were taken from above the inferred slide plane boundary except for sample SS2008-12/GC12/1B-88

[a]Quoted errors are 1 standard deviation

across the boundary within the cores, which confirms our interpretations of two distinct sediment units. Sediment sampled directly above one slide plane (Byron Slide, GC12) dates at 15.8 ka, while sediment directly below the slide plane dates at 47.4 ka or radiocarbon dead (see Fig. 5.3II).

Importantly, radiocarbon ages from sediment just above the inferred slide surfaces in cores GC8 and GC11 returned pene-contemporaneous dates of 20.7 and 20.1 ka, respectively (Cudgen and Coolangatta I slides respectively). This material is inferred to be the basal layer of post-landslide sediment. These two slides are adjacent features separated by 13 km; their similar ages are consistent with their being simultaneous events.

Although bulk radiocarbon ages measured from marine carbonates can provide basic constraints on a core's chronology, this sampling method is not ideal for obtaining precise age information. Bulk samples can introduce uncertainties in interpretation because they can be derived from different sources of different age (Harris et al. 1996). Specifically, bulk sediment samples generally contain older re-worked material which results in the calculated age of sedimentation being older than the true age. In addition, because bulk carbonate contains both planktonic and benthic foraminifera, the 400 year reservoir correction cannot be applied to these samples.

5.4 Modeling

Geomechanical modeling of the landslides was undertaken using the slope stability program GEO-SLOPE/W (2007) to examine the influence of several parameters on the stability of the slope profiles (cohesion, friction angle, and slope geometry).

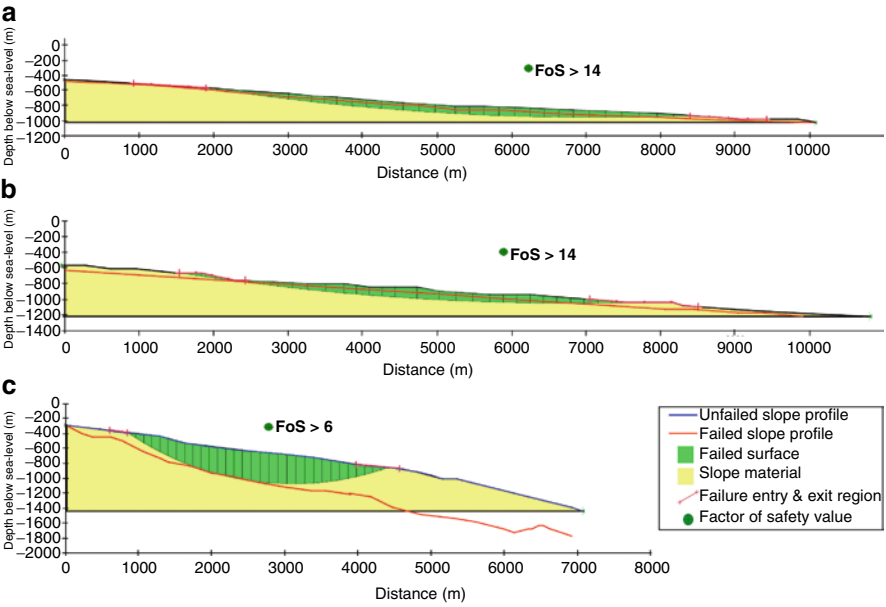

Fig. 5.5 Affect to the Factory of Safety (FoS) values for the slides under static conditions using measured strength values for the materials (c = 0 kPa, Φ = 40°) as input parameters: (**a**) Coolangatta1 Slide (**b**) Cudgen Slide (**c**) Byron slide

The profiles of adjacent unfailed sections of the landslide region were used to indicate the pre-failure geometry of the upper slope (see McAdoo et al. 2000). For each slope stability calculation, a dimensionless parameter, the Factor of Safety (FoS), is determined. It is defined as the ratio of the restoring forces to the disturbing forces (stable slope, FoS > 1; unstable slope, FoS < 1; critically stable slope, FoS = 1).

Static modeling of the slopes associated with each of the three landslides indicate that they are all inherently very stable (Fig. 5.5). This apparently inherent stability is inconsistent with the wide presence of slope failures in the study area. We infer from these data that that the landslides are the result of external triggers, either short term or long term, which reduce the shear strength of the sediments, and/or change the geometry of the slope such that the margin is frequently destabilised.

Back analysis modeling further indicates a dramatic reduction of sediment shear strength is required for slope failure to occur. Values well below the measured strength for the materials (c = 0kPa, Φ = 40°) are required. The average range of values used for modeling are summarised in Table 5.2. Table 5.3 summaries the resultant FoS values for each scenario. For failure to occur, the friction angle value must drop to values less than 8°, with cohesions of zero.

Modeling the response of submarine slopes to seismic shaking using pseudo-static methods, which include a factor for seismic accelerations in classical limit-equilibrium calculations, is useful but of limited value here (Seed and Martin 1966). Selecting an appropriate value for the seismic coefficient acting on the failure mass can be especially difficult (Seed and Martin 1966). A very crude investigation of seismic

Table 5.2 Numerical input parameters used for modeling the slides with GEO-SLOPE/W

Parameter	Unit	Input value range
Unit weight (γ)	kN/m³	15–17
Apparent cohesion (c')	kPa	0–22
Friction angle (Φ)	°	0–40

The friction angle (Φ) represents the friction component of the soil strength and the apparent cohesion (c') represents the cohesive component of the soil strength

Table 5.3 Back analysis GeoSlope outputs: a summary of the factors of safety (FoS) for the Byron slide arising from reducing c and Φ is shown in Table 5.2

Site	Scenario description	Cohesion (kPa)	Friction angle (°)	FoS (lowest)
Byron slide	Residual cohesion, decreasing friction angle	0	40	6.19
			30	4.26
			15	1.98
			7.5	<u>0.97</u>
			3.75	<u>0.48</u>
	Peak friction angle, decreasing cohesion	11	40	8.8
		5.5		7.8
		2.75		7.28
		1.375		6.98

Critical FoS are underlined. The Coolangatta1 and Cudgen slides follow the same trends

loading on the slopes indicate that lateral and vertical accelerations of 0.3 g (ah = 0.3 g, av = −0.3 g), the upper limit of those used to investigate the stability of earth dams during earthquakes (Seed and Martin 1966; Ozkan 1998), would be sufficient to destabilise the slopes of the seafloor in the present study.

Focusing only on the magnitude of the critical acceleration required to destabilise the slopes does not consider a number of other potential mechanisms that could contribute to the wide occurrence of slides on the SE Australian margin. For example, our preliminary analysis treats the landslide mass as a rigid block on a plane and does not consider the substantial effects of soil liquefaction, which is likely given the saturated loose to medium cohesion of the sediments comprising the landslides (cf., Ozkan 1998).

5.5 Conclusions

Regional mapping of the SE Australian continental margin reveals several large-volume submarine slides in water depths of 400–1,200 m. Gravity cores recovered from three of these landslides reveal that each slide contains a distinct, bulk-density contrast defined boundary between 85 and 220 cm below the seabed. We consider that the distinct density contrasts across the boundaries between the upper and lower units of GC8, GC11 and GC12 are highly significant. The inference that these

boundaries represent failure surfaces of submarine landslides is reasonable and consistent with all the available data. Also important, two adjacent but separated landslides have pene-contemporaneous ages of 20.7 and 20.1 ka directly above the slide plane. These ages are consistent with a common external trigger. The experimental results imply that the sediment forming the margin is reasonably strong and inherently stable. Classical limit-equilibrium modeling indicates that submarine landslides should not be a common occurrence on the margin.

The wide occurrence of upper slope slides across the SE Australian margin indicates that submarine sliding should be considered to be a common characteristic of this passive continental margin. This indicates that one or more of the potential triggering mechanisms can operate in passive margin settings to destabilise the slope. The processes suspected to be most likely include: (1) dramatic reduction of the shear strength of the upper-slope sediments to extremely low values, possibly induced by creep or a build-up of pore-pressure; (2) long-term modification of the slope-geometry i.e., sedimentation on the head of the slope and/or erosion of the toe of the slope; and/or (3) seismic events large enough to trigger sediment liquefaction or a sudden increase of pore-fluid pressure.

Acknowledgments We would like to acknowledge the P&O crew and scientific crews of the RV Southern Surveyor voyage (12/2008). Funding for this voyage was provided by ARC Australia and ConocoPhillips Pty Ltd. Funding for the radiocarbon age determinations was provided by Professor Ron Boyd and Newcastle University, Australia. This paper benefitted from reviews by Dr. Andrew D. Heap and Dr. Julie Dickinson.

References

Bardet JP, Synolakis CE, Davies HL, Imamura F, Okal EA (2003) Landslide tsunamis: recent findings and research directions. Pure Appl Geophys 160:1793–1809

Blott SJ, Pye K (2001) Gradistat: a grain size distribution and statistics package for the analysis of unconsolidated sediments. Earth Surf Proc Landf 26:1237–1248. doi:10.1002/esp. 261

Boyd R (2009) SS12/2008 Voyage summary: marine geology and geohazard survey of the SE Australian margin off Northern NSW and Southern Queensland. CSIRO Division of Marine and Atmospheric Research Hobart

Boyd R, Keene J, Hubble T, Gardner J, Glenn K, Ruming K, Exon N (2010) Southeast Australia: a Cenozoic continental margin dominated by mass transport. In: Mosher DC, Moscardelli L et al (eds) Submarine mass movements and their consequences, vol 28, Advances in natural and technological hazards research. Springer, Dordrecht, pp 1–8

Bronk Ramsey C (2005) Improving the resolution of radiocarbon dating by statistical analysis. In: Levy TE, Higham T (eds) The bible and radiocarbon dating: archaeology, Text and Science. Equinox, London, pp 57–64

Glenn K, Post A, Keene J, Boyd R, Fountain L, Potter A, Osuchowski M, Dando N, Party S (2008) NSW continental slope survey – post cruise report vol Geoscience Australia, Record 2008/14, 160 pp

Harris PT, O'Brien PE, Sedwick P, Truswell EM (1996) Late Quaternary history of sedimentation on the Mac. Robertson Shelf, East Antarctica: problems with ^{14}C-dating of marine sediment cores. Papers and proceedings. Royal Soc Tas 130:47–53

Heiri O, Lotter AF, Lemcke G (2001) Loss on ignition as a method for estimating organic and carbonate content in sediments: reproducibility and comparability of results. J Paleolimnol 25(1):101–110

Hubble T, Yu P, Airey D, Clarke S, et al (2012) Physical properties and age of continental slope sediments dredged from the Eastern Australian continental margin – implications for timing of slope failure. In: Yamada Y et al (eds) Submarine mass movements and their consequences, vol. 31, Advances in natural and technological hazards research. Springer, Dordrecht, pp 43–54

Jenkins CJ, Keene JB (1992) Submarine slope failures on the southeast Australian continental slope. Deep Sea Res 39:121–136

Locat J, Lee HJ (2002) Submarine landslides: advances and challenges. Can Geotech J 39: 193–212

McAdoo BG, Pratson LF, Orange DL (2000) Submarine landslide geomorphology, US continental slope. Mar Geol 169:103–136. doi:10.1016/s0025-3227(00)00050-5

Ozkan MY (1998) A review of considerations on seismic safety of embankments and earth and rock-fill dams. Soil Dyn Earthq Eng 17:439–458

Reimer PJ, Baillie MGL, Bard E, Bayliss A, Beck JW, Weyhenmeyer CE (2009) Intcal09 and Marine09 radiocarbon age calibration curves, 0–50,000 years cal BP. Radiocarbon 51: 1111–1150

Seed HB, Martin GR (1966) The seismic coefficient in earth dam design. J Geotech Eng ASCE 92:25–58

Stuiver MP, Henry A (1977) Discussion: Reporting of ^{14}C data. Radiocarbon 19:355–363

Varnes DJ (1978) Slope movements and types and processes. Landslides: analysis and control, special report, vol 176. Transportation Research Board, National Academy of Sciences, Washington, DC

Chapter 6
Development and Potential Triggering Mechanisms for a Large Holocene Landslide in the Lower St. Lawrence Estuary

Genevieve Cauchon-Voyer, Jacques Locat, Guillaume St-Onge, Serge Leroueil, and Patrick Lajeunesse

Abstract The Betsiamites 7,250 cal BP submarine landslide mobilized a volume of 1.3 km^3 in the St. Lawrence Estuary, Eastern Canada. The failure was initiated in shallow water between 10 and 140 mbsl and most likely developed in a unit stratified clayey silt deposits following a very strong earthquake. Most of the failed mass appears dislocated and evacuated the failure source area. This paper concludes that gas hydrates dissociation could not have influenced slope stability on the shelves of the Lower St. Lawrence Estuary in the Early Holocene and that despite the high sedimentation rates prior to the failure this condition did not act independently as a significant trigger for the Betsiamites failure.

Keywords Submarine mass movements • Holocene failures • Morphology

6.1 Introduction

In Eastern Canada, submarine landslides have recently received more attention (e.g., Duchesne et al. 2003; Lajeunesse et al. 2007; Campbell et al. 2008; Cauchon-Voyer et al. 2008; Gagné 2008) and their consequences have been

G. Cauchon-Voyer (✉) • J. Locat
Département de géologie et génie géologique, Université Laval, Québec, Québec, Canada G1K 7P4
e-mail: genevieve.cauchon-voyer.1@ulaval.ca

G. St-Onge
Canada Research Chair in Marine Geology, ISMER and GEOTOP, Université du Québec à Rimouski, Rimouski, Québec, Canada G5L 3A1

S. Leroueil
Département de génie civil, Université Laval, Québec, Canada G1K 7P4

P. Lajeunesse
Centre d'études nordiques and Département de géographie, Université Laval, Québec, Canada G1K 7P4

Y. Yamada et al. (eds.), *Submarine Mass Movements and Their Consequences*, Advances in Natural and Technological Hazards Research 31,
DOI 10.1007/978-94-007-2162-3_6,

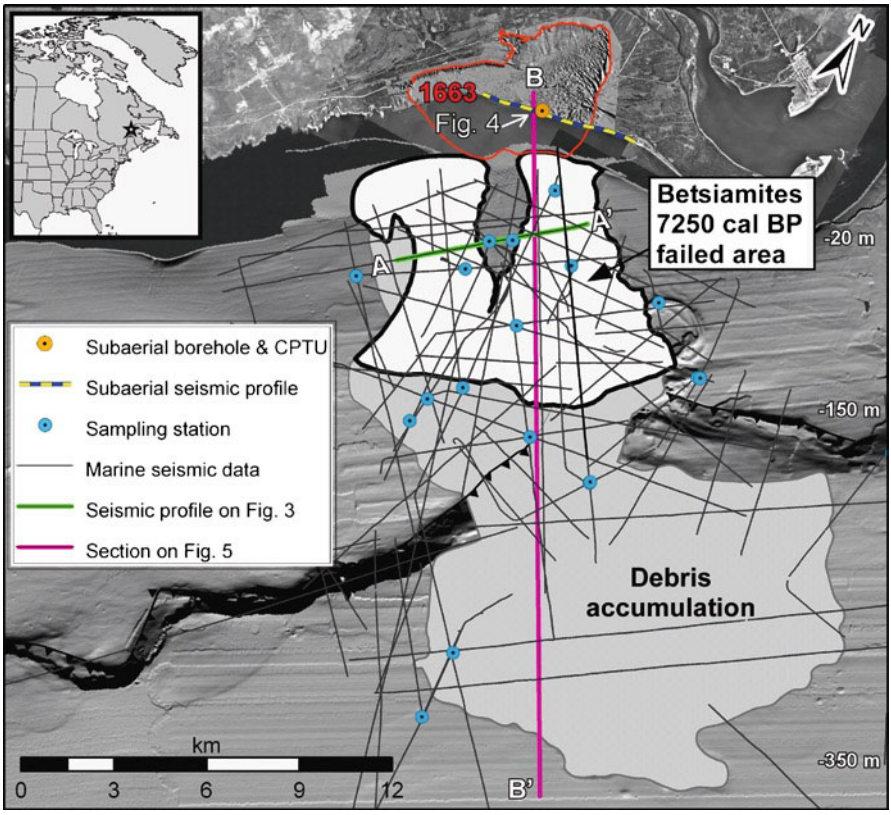

Fig. 6.1 Study site and extent of the Betsiamites landslide scar

summarized (Mosher 2008). The Lower St. Lawrence Estuary is characterized by two ~10 km wide sub-horizontal 2° slope shelves breaking at water depth between 150 and 200 m (Fig. 6.1) where many mass movement scars are observed. The deepest section of the Estuary, the Laurentian Channel at water depth of about between 350 and 375 m, is a long sub-horizontal NE-SW topographic depression.

The North Coast of the St. Lawrence Estuary exhibits areas with subaerial and submarine landslide scars with the largest located on the seafloor off the Betsiamites river delta (Fig. 6.1). This delta was constructed in a time of falling relative sea-level as a result of the melting of the Laurentide Ice Sheet and glacio-isostatic rebound during the Late Wisconsinan, which transported great amounts of sediments from the continent into the Estuary. The Betsiamites landslide complex is the result of at least three distinct landslide events, i.e. the submarine and subaerial Colombier failure in 1663, which extend is indicated on Fig. 6.2, a large failure in 7,250 cal BP and a failure in 9,250 cal BP (Cauchon-Voyer et al. 2011). Morphological analysis of the scar of the 7,250 cal BP landslide event, thereafter

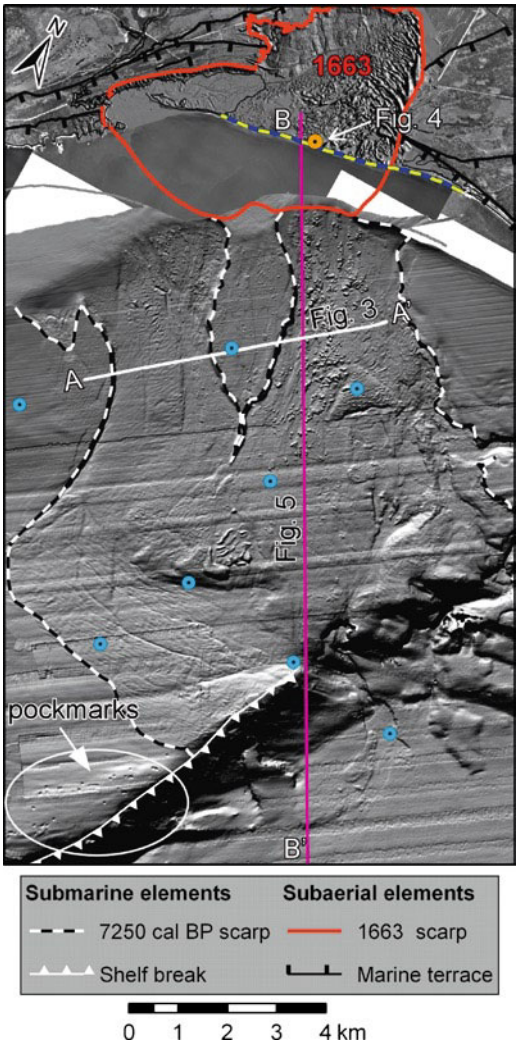

Fig. 6.2 Geomorphology of the Betsiamites scar, see Fig. 6.1 for legend of data source

named Betsiamites slide event, allows establishing that it occurred only in the submarine portion (Cauchon-Voyer et al. 2011) when relative sea-level was about similar to present level (Bernatchez 2003).

6.1.1 Objectives

The 7,250 cal BP Betsiamites submarine slide is the largest scar yet identified on the seafloor of the St. Lawrence Estuary. The main objective of this paper is to describe this massive submarine landslide and discuss its development and potential trigger mechanism.

6.2 Data and Methods

Bathymetric data were acquired using a SIMRAD EM1000 multibeam echosounder. The seismic reflection profiles presented in this study were obtained with an EG&G chirp system (2–12 kHz). Technical details and results on the submarine bathymetric and geophysical data can be found in Cauchon-Voyer et al. (2008). Forty-six sediments samples were recovered in the submarine segment of the delta and the locations of some sampling stations are indicated in Figs. 6.1 and 6.2. In addition, a cone penetration test with pore water pressure measurement (CPTU), providing tip resistance (q_T) and pore pressure measured immediately behind the tip (u_{base}) profiles, which can be compared to hydrostatic condition (u_{hydro}), and a 58 m long borehole (site 46,010) were performed onshore along the current beach (Figs. 6.1 and 6.2). Detailed description of the CPTU and core data analysis and results can be found in (Cauchon-Voyer et al. 2011).

6.3 Morphology of the Betsiamites Slide Complex

The Betsiamites failure developed over an area of 54 km^2 at water depth from −10 mbsl to −140 mbsl (Fig. 6.2) and mobilized about 1.3 km^3 of sediments, leading to an average landslide thickness of 24 m. This scar is made up of two main topographic depressions, the West depression and the East depression, separated by an intact butte with steep flanks (15–20°) and flat top (Figs. 6.2 and 6.3). In the West and East depressions of the scar, the escarpment height ranges from 12 to 20 m above the seafloor. The floor of the landslide scar is overlain by up to 20 m of landslide debris deposits (Fig. 6.3).

Based on core data and seismic profiling, the upper 3–10 m of these landslide debris deposits are associated with subaerial landslide debris resulting from the 1663 Colombier landslide event (Cauchon-Voyer et al. 2011). The intact butte within the central part of the scar extends over 5 km^2 with a maximum length and width of 4.5 and 1.6 km respectively. The average slope of the top of this butte is 1°, which corresponds more or less to the slope of the seafloor prior to failure. In the Laurentian Channel, at water depths between 350 and 375 m, there is a large debris lobe covering an area of 115 km^2 with a maximum diameter of 15 km (Fig. 6.2). With an average thickness of 9 m, the lobe has an estimated volume of 1 km^3.

6.4 Lithostratigraphy and Failure Surface

The lithostratigraphy and the material involved in the 7,250 cal BP Betsiamites slide are mostly assessed on the basis of geophysical surveys (Fig. 6.3) as most of the sediment cores recovered offshore consist of 1,663 landslide debris or post-glacial hemipelagic sediments deposited after the Betsiamites slide. The main challenge for

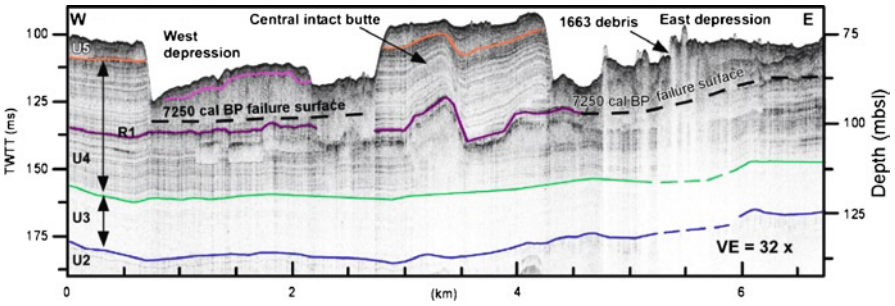

Fig. 6.3 Seismic profile across the Betsiamites landslide scar, along line A–A′, on Fig. 6.2 (Modified from Cauchon-Voyer et al. 2008)

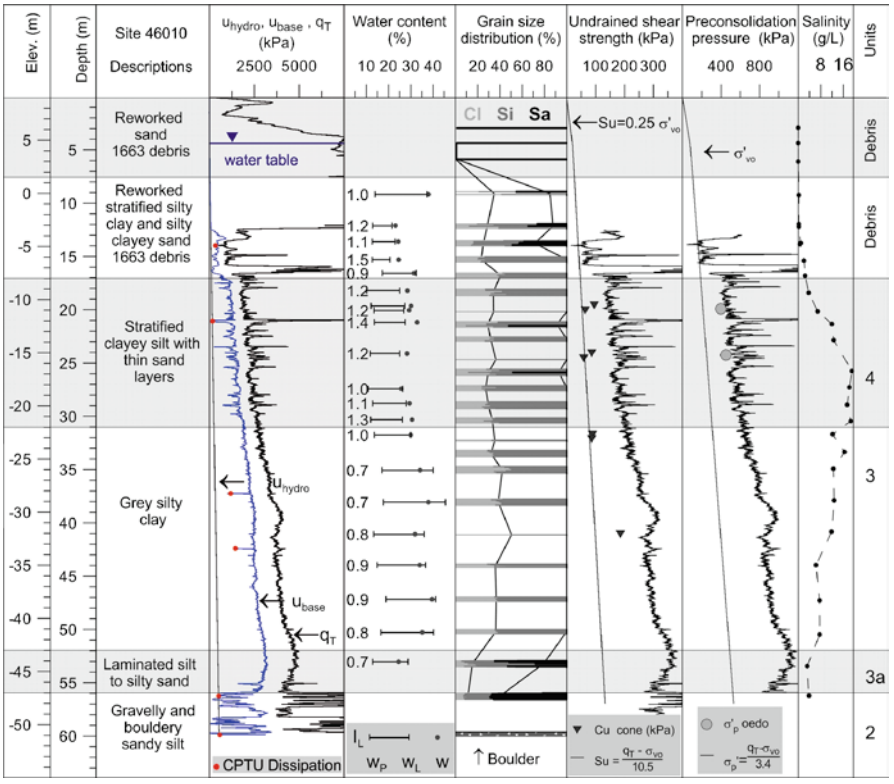

Fig. 6.4 Geotechnical profile carried out onshore along the shoreline (Modified from Cauchon-Voyer et al. 2011). This borehole is located outside the 7,250 cal BP scar but inside 1,663 failure scar. The 7,250 cal BP failure developed within unit 4. Shear strength and preconsolidation pressure profiles are estimated from CPTU results

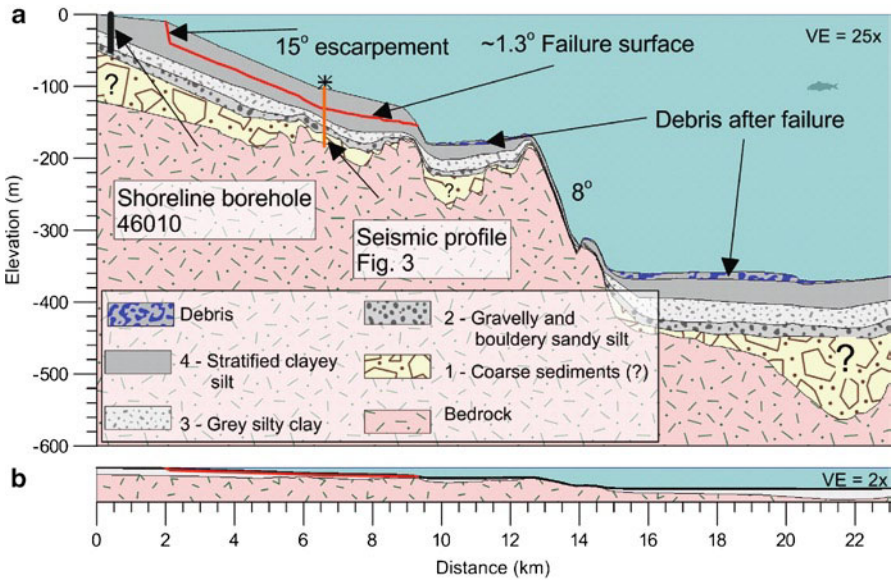

Fig. 6.5 (**a**) Morphostratigraphic reconstitution of the Betsiamites landslide showing the topography prior to failure and the accumulation of debris after failure. See location on Fig. 6.1, profile B–B′. (**b**) Same profile at VE = 2×

offshore work on older landslides is to obtain geological validation and properly evaluate the in situ geotechnical properties. To counter this limitation in this coastal area, a subaerial CPTU and borehole (Fig. 6.4) were carried out along the coastline. six main geotechnical units are identified at this site. The upper two are debris from the 1,663 events. Unit 4 contains many ~5 cm-thick silty layers interbedded in clayey layers. Unit 3 is a homogenous grey silty clay, unit 3a is a thin layer of a laminated silt and unit 2 is a gravelly and bouldery silt.

The seismic profiling shows that the bedrock has an irregular topography and creates a sediment basin at the toe of the failure scar on the shelf (Fig. 6.5). Prior to failure, the sediment layers deposited conformably on the underlying bedrock and allowed for little accumulation of sediments at the toe of the scar (Fig. 6.5). Seismic interpretations (Fig. 6.3) associated with core data (Fig. 6.4) shows that the Betsiamites failure developed in a unit of more than 25 m of stratified clayey silt deposit (Fig. 6.5), labeled 4 (Figs. 6.4 and 6.5) and U4 on the seismic profiles (Fig. 6.3). On average, unit 4 consist of 30% of clay ($d < 2$ μm), 67% of silt ($2 < d < 63$ μm) and 2% of sand (+63 μm).

The failure surface identified from the seismic profiles has a slope angle of about 1.3°. Local and regional chronostratigraphic and paleogeographic work (Bernatchez 2003; St-Onge et al. 2003, 2008; Cauchon-Voyer et al. 2011) shows that the sequence of glaciomarine sediments (units 2–3–4) shown on Fig. 6.3 was deposited approximately in about 4,000 years between 11 and 7 cal ka in a time of significant sea-level fall. These very high sedimentation rates, averaging 15 mm/year, occurred prior to the 7,250 cal BP Betsiamites failure.

6.5 Movement Development

The failure developed along a surface with a low angle of about 1°. According to the geometry of the slope, the failure was likely initiated at the bottom of the mass and propagated upslope (Fig. 6.5).

Most of the failed mass appears to have moved outside the source area. In fact, when comparing the volume of the 54 km^2 scar on the shelf (1.3 km^3) and the volume of the sediment lobe (1 km^3) in the Laurentian Channel, only 20% of the debris remained in the source area and on the shelf. When the landslide mass reached the shelf break, it flowed down to the Laurentian Channel and appears on the seismic profile completely remolded. The height potential, more than 200 m, of the shelf break likely helped the sediments to remold, facilitating the mobility of the mass to create the debris fan. In fact, the material did not accumulate on the 8° slope which would have obstructed the movement and reduced the overall flow of the mass.

6.6 Triggering Mechanisms

The Betsiamites failure developed over more than 8 km in deposits with slope angle of about 1° (Fig. 6.5). To create such a large failure in these conditions, diverse factors could have contributed to the development of the failure, its propagation and the evacuation of the failed mass. The effects of gas and excess pore water pressure resulting from high sedimentation rate or an earthquake are investigated in order to define their potential influence on the development of the Betsiamites failure. As the Betsiamites River had a configuration similar to what it is at present (Fig. 6.1) at the time of the failure (Bernatchez 2003) and the water depth of the scar area range between −10 and −140 m, we assume that significant erosive currents did not form to influence the stability of the area. As the failure developed 7,520 cal BP, is it difficult to assess if groundwater flow influenced the initiation.

Areas with greater amount of pockmarks in the vicinity of the Betsiamites landslides (Fig. 6.2) have been identified (Cauchon-Voyer et al. 2008). The pockmarks in the St. Lawrence estuary have recently been studied and these studies suggest that they formed through the recent and still active release of gas from a reservoir within the Paleozoic sedimentary succession (Pinet et al. 2008, 2009; Lavoie et al. 2010) and thus are not biogenic gas resulting from synchronous sedimentation of organic matter. Such observations led to the questioning that gas could have been a possible trigger for submarine landslides in the St. Lawrence Estuary (Campbell et al. 2008; Cauchon-Voyer et al. 2008; Pinet et al. 2008). Gas can have an effect on seafloor stability if gas hydrates dissociate (Sultan et al. 2004) or if free gas influences the permeability and/or the structure of the sediments (Best et al. 2003). Along the North shelf (water <150 mbsl) of the Estuary where there are many failure scars, we can discard that gas hydrates dissociation acted as a trigger mechanism because the conditions for hydrate formation (mainly pressure and temperature), and thus dissociation, were likely never met following the last deglaciation (Pinet et al. 2008).

Another hypothesis for the origin of this failure would be that the very high sedimentation rates estimated prior to the failure could have generated high pore water pressure. For an average thickness (h) of 24 m of sediments having a buoyant unit weight (γ') of 9.7 N/m^3 deposited on an angle of 1.3°, a simple infinite slope stability analysis indicates that the pore pressure required to bring the slope to failure (FS = 1), if no other mechanisms are involved, correspond to 0.98 of the weight of the sediment layer. This value corresponds to 230 kPa of overpressure, which is extremely high and hence would require that only 2% of dissipation and consolidation have occurred. Such high overpressures are obtained at much greater depth (more than 250 m with rate up to 35 mm/year) with more advanced modeling (Hustoft et al. 2009). This simple demonstration indicates that pore water pressure resulting only from high sedimentation rates likely had the time to dissipate and hence did not play an important role in the development of the Betsiamites failure.

Pore pressures generated by rapid sedimentation might not cause failure on their own but could still contribute to failure through another mechanism, e.g., an earthquake. Earthquakes are known to generate slope failure by degrading the shear strength and increasing the pore pressure within a slope. Such mechanisms likely played an important role in the initial triggering of a failure on such a low slope (1°) for the Betsiamites failure. In fact, shaking could cause significant strength reduction in one or several layers within the stratified unit (labeled U4 on Fig. 6.3). In the case of the Betsiamites failures, more study are required to investigate the cyclic behavior of the sediments involved, but similar demonstration of the influence of stratification on cyclic strength of stratified sand-silt samples were demonstrated (e.g., Konrad and Dubeau 2003; Dan et al. 2009). A related mechanism has been proposed by Kokusho (1999) which suggested that following the earthquake, the water expulsed from the liquefied layer could become trapped between less permeable layers above, which may generate a water film over which the soil mass could start sliding. This mechanism could support the morphological observations within the landslide scar as the deposits were easily transported outside the scar. In fact, to account for the large scar observed on a low slope angle with less than 10 m of debris of the shelf (20%), a significant sliding mechanism must have been involved (Fig. 6.3).

6.7 Concluding Remarks and Future Work

The 7,250 cal BP Betsiamites slide (1.3 km^3 over 54 km^2) is one of the largest landslides in the St. Lawrence Estuary. The failure surface developed in a thick stratified sequence clayey silt. This paper concludes that gas hydrates dissociation could not have influenced slope stability on the shelves of the St. Lawrence Estuary in the Early Holocene. The stability of the slope prior to failure does not appear to have been influenced by excess pore pressures resulting independently from high sedimentation rates as dissipation in the deposits could occur efficiently. The most likely trigger for such a large failure would be excess pore pressures resulting from an earthquake. With a volume of more than 1.3 km^3, it would be important to direct further analysis to determine if this event triggered a tsunami.

Acknowledgments The authors wish to thank the Ministère des Transports du Québec (MTQ), NSERC and FQRNT for their financial support. We thank the MTQ for the permission to use their topographic and LIDAR surveys, borehole, and piezocone soundings data of the Colombier – Betsiamites area. We recognize the contribution of all scientists and crew members on board the Coriolis II, F.G. Creed, and Guillemot vessels. The Canadian Hydrographic Service and GSC-Quebec are also acknowledged for their contribution to bathymetric data acquisition. We thank Homa Lee and Jean-Sébastien L'Heureux for their constructive comments.

References

Bernatchez P (2003) Évolution littorale holocène et actuelle des complexes deltaiques de Betsiamites et de Manicouagan-Outardes: synthèse, processus, causes et perspectives. Université Laval, Québec

Best A, Clayton C, Longva O, Szuman M (2003) The role of free gas in the activation of submarine slides in Finneidfjord. In: Locat J, Mienert J (eds) Submarine mass movements and their consequences 1st international symposium, 2003. Kluwer Academic, Dordrecht, pp 419–498

Campbell C, Duchesne MJ, Bolduc A (2008) Geomorphological and geophysical evidence of Holocene instability on the Southern slope of the Lower St. Lawrence Estuary, Québec. Paper presented at the 4e conférence canadienne sur les géorisques: des causes à la gestion – 4th Canadian conference on geohazards: from causes to management, Québec

Cauchon-Voyer G, Locat J, St-Onge G (2008) Late-Quaternary morpho-sedimentology and submarine mass movements of the Betsiamites area, Lower St. Lawrence Estuary, Quebec, Canada. Mar Geol 251(3–4):233–252

Cauchon-Voyer G, Locat J, Leroueil S, St-Onge G, Demers D (2011) Large-scale subaerial and submarine Holocene and recent mass movements in the Betsiamites area, Quebec, Canada. Eng Geol. doi:10.1016/j.enggeo.2011.04.011

Dan G, Sultan N, Savoye B, Deverchere J, Yelles K (2009) Quantifying the role of sandy–silty sediments in generating slope failures during earthquakes: example from the Algerian margin. Int J Earth Sci 98(4):769–789

Duchesne MJ, Long BF, Urgeles R, Locat J (2003) New evidence of slope instability in the Outardes Bay delta area, Quebec, Canada. Geo-Mar Lett 22(4):233–242. doi:10.1007/s00367-003-0121-6

Gagné H (2008) Géomorphologie et géologie marine du Quaternaire du secteur Trois-Pistoles-Forestville, estuaire du Saint-Laurent (Québec). Université Laval, Québec

Hustoft S, Dugan B, Mienert J (2009) Effects of rapid sedimentation on developing the Nyegga pockmark field: constraints from hydrological modeling and 3-D seismic data, offshore mid-Norway. Geochem Geophys Geosys 10(6):Q06012

Kokusho T (1999) Formation of water film in liquefied sand and its effect on lateral spread. J Geotech Geoenviron Eng ASCE 125(10):817–826

Konrad JM, Dubeau S (2003) Cyclic strength of stratified soil samples. In: Locat J, Mienert J (eds) Submarine mass movements and their consequences 1st international symposium. Kluwer Academic, Dordrecht, pp 47–57

Lajeunesse P, St-Onge G, Locat J, Labbé G (2007) Multibeam bathymetry and morphostratigraphy of submarine gravity flows and slopes failures in the St. Lawrence Gulf and Lower Estuary (Québec, Canada). Paper presented at the submarine mass movements and their consequences

Lavoie D, Pinet N, Duchesne M, Bolduc A, Larocque R (2010) Methane-derived authigenic carbonates from active hydrocarbon seeps of the St. Lawrence Estuary, Canada. Mar Petrol Geol 27(6):1262–1272

Mosher DC (2008) Submarine mass movements: geohazards with far-reaching implications. Paper presented at the 4e conférence canadienne sur les géorisques: des causes à la gestion – 4th Canadian conference on geohazards : from causes to management, Presse de l'Université Laval, Québec

Pinet N, Duchesne M, Lavoie D, Bolduc A, Long B (2008) Surface and subsurface signatures of gas seepage in the St. Lawrence Estuary (Canada): significance to hydrocarbon exploration. Mar Petrol Geol 25(3):271–288. doi:10.1016/j.marpetgeo.2007.07.01

Pinet N, Duchesne M, Lavoie D (2009) Linking a linear pockmark train with a buried Palaeozoic structure: a case study from the St. Lawrence Estuary. Geo-Mar Lett 30(5):517–522. doi:10.1007/s00367-009-0179-x

St-Onge G, Stoner JS, Hillaire-Marcel C (2003) Holocene paleomagnetic records from the St. Lawrence Estuary, eastern Canada: centennial- to millennial-scale geomagnetic modulation of cosmogenic isotopes. Earth Planet Sci Lett 209(1–2):113–130. doi:10.1016/s0012-821x(03)00079-7

St-Onge G, Lajeunesse P, Duchesne M, Gagné H (2008) Identification and dating of a key Late Pleistocene stratigraphic unit in the St. Lawrence Estuary and Gulf (Eastern Canada). Quaternary Sci Rev 27(25–26):2390–2400

Sultan N, Cochonat P, Foucher J, Mienert J (2004) Effect of gas hydrates melting on seafloor slope instability. Mar Geol 213(1–4):379–401

Chapter 7
Spatially Fixed Initial Break Point and Fault-Rock Development in a Landslide Area

Arito Sakaguchi, Shunji Yokoyama, Yoshitaka Hashimoto, Tomomasa Yamada, Akio Tanaka, Kohtaro Ujiie, and Norihiro Yoshimura

Abstract The relationship between slip behavior and fault-rock properties has been investigated from several perspectives, including rock mechanics, landsliding, and earthquake faulting. This includes mainly studies on land, but recently also from submarine settings, since increasing availably of new offshore technologies allow marine fault/slip zone drilling and monitoring. Here we present a detail study for a subaerial landslide in SW Japan, the conceptual and methodological approach of which may provide important means towards better understanding various friction behaviors including ocean margin slope creeping and submarine landslides.

Thousand of landslides occur in the Japanese mountains during precipitation events, and monitoring systems have been installed for disaster management and mitigation. Slopes in many of these areas undergo repeated continuous stable creep and episodic acceleration without catastrophic failure. We monitored the dynamic processes of pore-fluid-induced episodic landslides during two typhoons associated with heavy rain in the 300 m × 800 m Utsugi landslide area in the Jurassic Chichibu complex. A basal fault defining the landslide body has a maximum depth of approximately 30 m and is exposed at the surface at the top and bottom ends.

A. Sakaguchi (✉)
IFREE1, Japan Agency for Marine Science and Technology, 2-15 Natsushima-cho
Yokosuka, Kanagawa, 237-0061, Japan

Institute for Research on Earth Evolution (IFREE), Japan Agency for Marine-Earth
Science and Technology (JAMSTEC), Yokohama, 236-0001, Japan
e-mail: arito@jamstec.go.jp

K. Ujiie
Department of Geosciences, University of Tsukuba, 1-1-1 Tenno, Tsukuba 305-8577, Japan

S. Yokoyama • Y. Hashimoto • T. Yamada • A. Tanaka
Department of Applied Science, Kochi University, Kochi 780-8520, Japan

N. Yoshimura
Shikoku-Try Corporation, Kochi 780-0082, Japan

Y. Yamada et al. (eds.), *Submarine Mass Movements and Their Consequences*,
Advances in Natural and Technological Hazards Research 31,
DOI 10.1007/978-94-007-2162-3_7,

Borehole pipes that penetrate the basal fault have been installed at 13 sites for monitoring tilt and groundwater levels. We used five of these sites for dynamic monitoring. In two cases, slip initiation occurred in the area where the groundwater level rose quickly during the rainfall. We analyzed the fault rocks at this site in a drill core obtained during the dry season and in another drill core obtained immediately after a slip event. The fracture zone at the slip depth is overlaid with low permeable gouge, inferred to have developed by shear grind. In the post-slip event core, the fracture zone has much higher water content than that in the dry season core. The gouge layer and fracture zone may thus act as an impervious cap rock and a conduit for fluid, respectively. The fault rock and fluid flow system likely developed over a long period, and thus can explain the repeated initiation of slip at the same location.

Keywords Landslide • Initial break point • Fluid pressure • Slip propagation • Monitoring • Fault rock

7.1 Introduction

Slip heterogeneity in a rock-friction context has been observed at many scales, ranging from that of compressive laboratory experiments to seismogenic fault scale. For example, acceleration of local deformation and nucleation of rupture have been observed in laboratory rock-friction tests (Ohnaka and Shen 2003; Lei 2003), and Suemine (1983) reported on progressive rupture propagation in a landslide area, whereas Aki (1979) and Lay and Kanamori (1981) have described heterogeneous coseismic slip along a fault during large earthquakes. As for submarine landslides, Stegmann et al. (2011) used data from in situ pore pressure measurement deployments offshore Nice, Western Mediterranean Sea, to document that onland precipitation and melt water fluxes induced pore pressure transients which effectively reduced submarine slope stability in a area where creeping and progressive failure planes are assumed (Sultan et al. 2010). However, the geological causes of slip heterogeneity and fluid pressure are still uncertain because it is difficult to compare dynamic processes and fault-rock properties in the same natural fault.

Landslides are common in the mountains of Japan, and monitoring systems have been installed for disaster management in most areas that experience frequent landslides. The landslide area studied here displays very slow creep, which accelerates during rainfall events, but without catastrophic breakdown or sediment flow (Figs. 7.1 and 7.2). These episodic slip events may depend on rainfall-related changes in pore fluid pressure. In this study, we monitored the occurrence of slip and groundwater conditions during heavy typhoon rains to understand the detailed slip behavior, and we investigated fault zone properties in drill cores obtained before and after a slip event. Combination between slip monitoring and fault rock analysis studies in the landslide on land will play a role to understand various rock friction behaviors including submarine landslide.

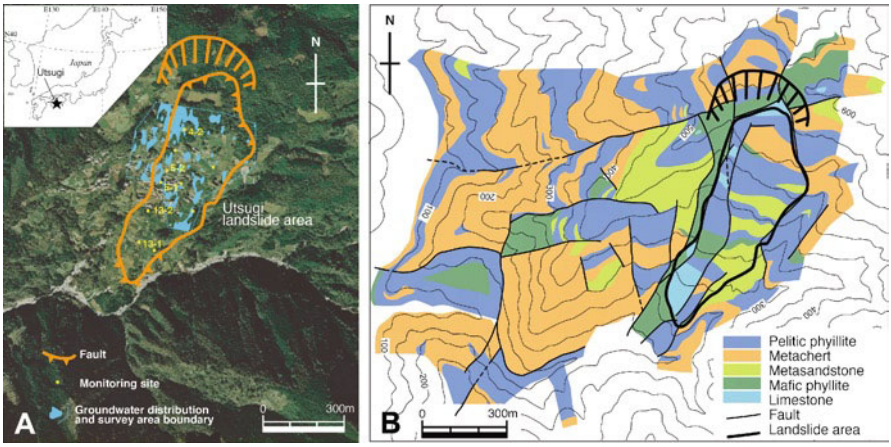

Fig. 7.1 Normal fault circumscribing the Utsugi landslide area at Kochi, southwest Japan; *blue* hatching shows the groundwater distribution inferred by a ground temperature survey (**a**). The landslide body is composed of *black* schist, without large chert blocks (**b**). The aerial photograph map is from Japanese ministry of Land, Infrastructure, Transport and Tourism

7.2 Setting

The Utsugi landslide area covers a 300 m × 800 m area in the Jurassic Chichibu accretionary complex of southwestern Japan (Fig. 7.1a). The rocks are low-grade metamorphic chert, sandy schist, limestone and meta-basalt blocks within a black schist matrix (Fig. 7.1b). The landslide body develops on a flattened ridge top, where rigid chert blocks are absent (Fig. 7.1b). A basal fault up to approximately 30 m in depth is exposed at the surface at the top and bottom ends of the landslide body (Fig. 7.1c).

The distribution of groundwater in the landslide area has been observed during a ground-temperature survey and in borehole pressure gauges by Kochi Prefecture (unpublished data). During the temperature survey, the ground temperature was measured at 1 m depth in summer and in winter, when there are large thermal differences between the air and groundwater temperatures. In general, in groundwater concentration areas, the ground temperature is unaffected by air temperature changes because the specific heat of water is higher than that of the ground. The ground-temperature survey revealed that groundwater is concentrated in the western part of the landslide area (Fig. 7.1a) (Kochi Prefecture unpublished data).

Monthly monitoring by Kochi Prefecture (unpublished data) has revealed that recent slip behavior (Fig. 7.2) can be characterized by two contrasted slip modes which are very slow creep (<15 mm/year) in the dry season, and accelerated slip events associated with heavy rain (5–10 mm per event). The two slip modes occur repeatedly through time, and the cumulative displacement, dominantly caused by the accelerated slip after rain, increases downslope (Fig. 7.2). It is empirically known that slip acceleration in this area occurs only when more than 150 mm of rain falls, and monthly monitoring is too infrequent to observe rupture propagation

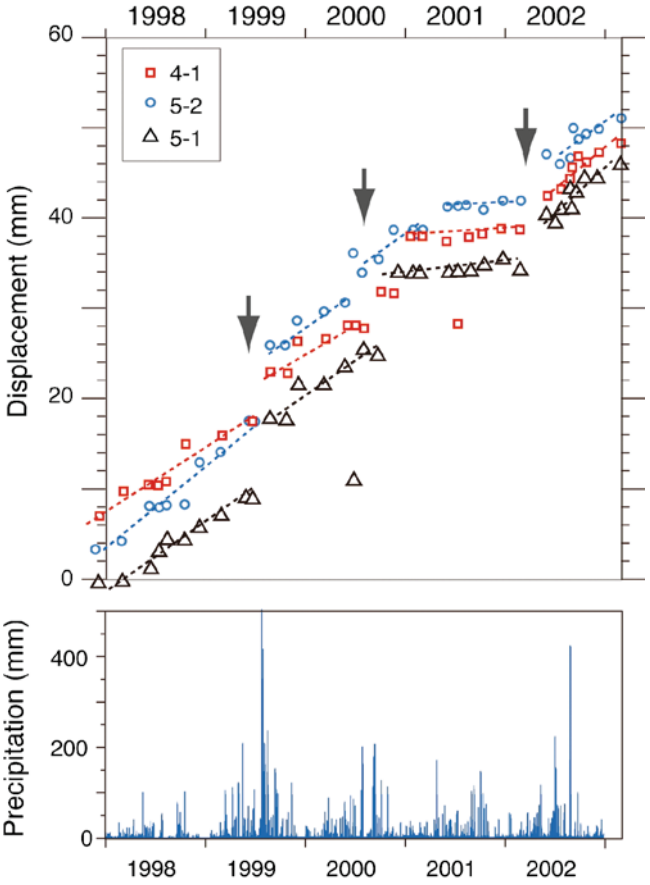

Fig. 7.2 Cumulative displacement of the landslide body during long-term monitoring at three monitoring sites showing periods of stable creep between episodic accelerated slip events (*Top*). Slip events were concurrent with heavy rainfalls, especially summer typhoons (*Bottom*)

during these events. Therefore, for this study, we measured slip at 6- to 8-h intervals in the first 24 h of heavy rainfall events and once a day during the heavy precipitation events of 2003 and 2004.

7.3 Methods

7.3.1 Tilt and Groundwater Level Measurement

Borehole monitoring pipes installed at different times for tilt and groundwater level measurements penetrate the basal fault at 11 sites (labeled sites in Fig. 7.1a), with the bottom of each pipe fixed in the basement rock. Groundwater level changes

during the drilling of these boreholes indicated that the aquifer is around the fault depth. We measured the tilt at 5 of the monitoring 11 sites by using wire-line tiltmeters to measure tilt at 50 cm intervals from the bottom of each pipe to the surface. The error on the tilt measurement is less than 0.000278°, which is equivalent to a slip displacement of less than 0.024 mm. Measurements were performed twice, and the average of the two measurements was used as the tilt value. The older borehole pipes have become strongly deformed in the fault zone by cumulating displacement. The magnitude of the latest deformation, which is much smaller than the cumulative deformation, can thus be estimated by the difference between the two deformation amounts.

7.3.2 Core Analysis

We also analyzed the physical properties and deformation textures of the fault rock in two cores obtained at a site near the initial break point of a slip event. We estimated the water distribution around the fault zone in these cores by using X-ray computed tomography (CT; Hitachi Medical Corporation Radix-Pratico; X-ray tube voltage, 120 kV; current, 100 mA; scan time, 4.0 s; slice interval, 1.0–2.0 mm) (Anderson et al. 1988; Byrne et al. 1993; Soh et al. 1993; Ujiie et al. 2004). X-ray linear absorption coefficients are converted by the CT scanner to CT numbers. In rocks with similar compositions, the CT number reflects sediment density differences due to water content differences. We therefore compared the CT numbers between these two mineralogically and chemically similar cores, one collected before and one after a slip event. The relationship between water content and CT number was determined by using the classic wet/dry mass fraction method that obtained from volume and weight of indexing samples.

7.3.3 Detailed Monitoring During Slipa

Detailed groundwater level monitoring was performed during two typhoons accompanied by heavy rains lasting up to 80 h, one in August 2003 and the other in July 2004. During the second typhoon, 857 mm of rain was recorded, that is 33% of the total mean annual rainfall in this area (2,600 mm). The groundwater level increased after only 7–10 h from the beginning of the rainfall (Fig. 7.3), and it tended to increase more quickly in the lower portion of the landslide area (Fig. 7.3). The groundwater level around sites 5-1 and 5-2 in the west central part of the landslide area increased slightly more than that in the surrounding area 16–22 h after the beginning of the rainfall (Fig. 7.3b).

Detailed slip monitoring by borehole tilt meters was carried out at five sites in the western part of the study area (Fig. 7.3a; sites 4-2, 5-2, 5-1, 13-2, and 13-1). In general, the borehole pipes deformed in the downdip direction, but upward tilting of

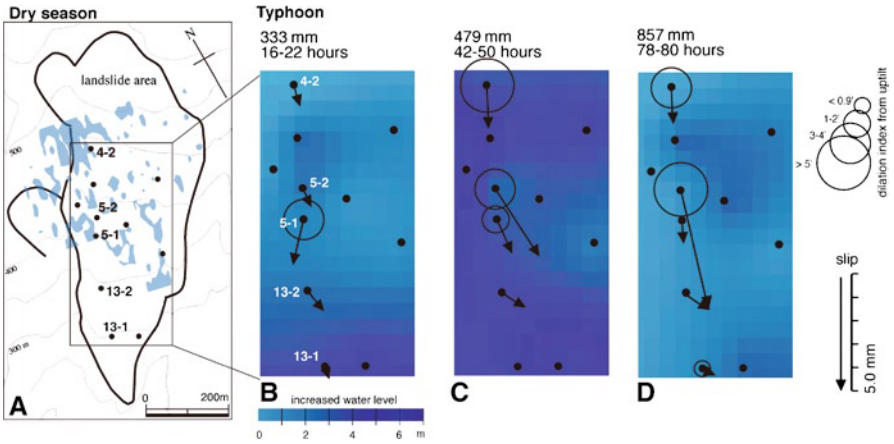

Fig. 7.3 Results of detailed groundwater monitoring in the Utsugi landslide area during the July 2004 typhoon. Groundwater distribution during the dry season (**a**). Dilation and slip after a typhoon in July 2004 (**b**, **c**, and **d**). The *blue shading* indicates changes in the groundwater level from the beginning of the rainfall. The circles at the monitoring sites with old borehole-monitoring pipes show the amount of dilation of the fault zone, inferred from uptilting of the pipe (see text). The *arrows* indicate the direction and magnitude of landslide displacement at each of the five studied sites

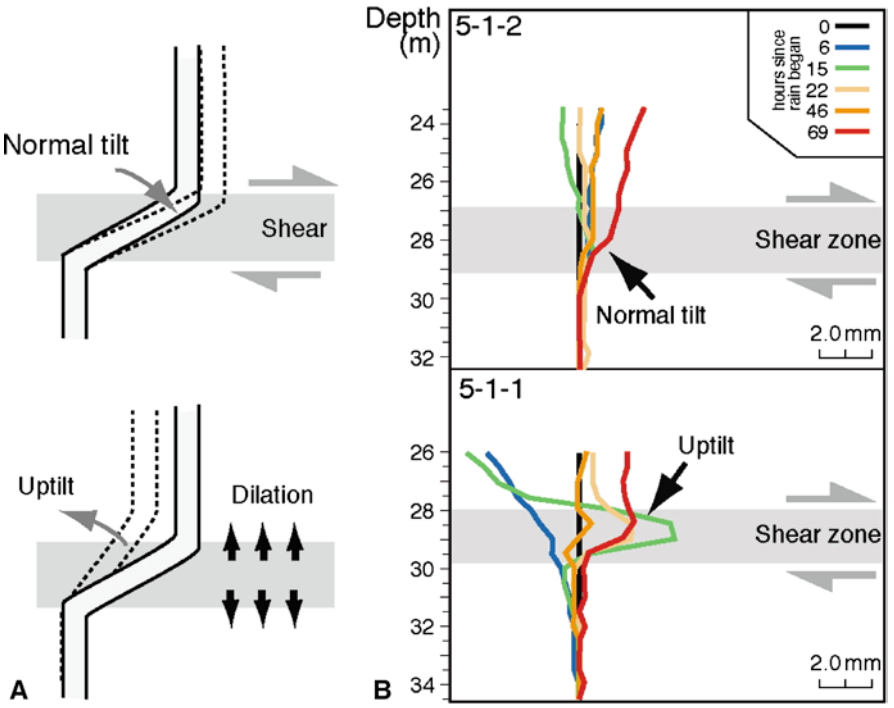

Fig. 7.4 The borehole pipes bend within the fault zone in the downslope direction (**a**), but transient uptilting occurs prior to large slips at old borehole pipe sites. The large bending of the old borehole may act as a buffer for fault dilation, as shown schematically in (**b**). Only the site 5-1 has new borehole pipe (5-1-2)

the borehole pipes preceded the downward deformation in the fault zone at some sites (Fig. 7.4a). This uptilting, which occurred at the depth where the borehole pipe had a crank-shaped bend as a result of the cumulative slip, can be explained by dilation in the fault zone (Fig. 7.4b). When an increase in the pore-fluid pressure dilates the fault zone, the bent portion of the old borehole pipe acts as a dilation buffer because of the difference in rigidity between the gouge clay of the fault zone and the metal pipe. As a result, the bent portion is uptilted (Fig. 7.4b). The 15-year-old borehole pipe at site 5-1 (5-1-1; top of Fig. 7.4a) showed much more uptilt than the 5-month-old pipe (5-1-2; bottom of Fig. 7.4a). The relatively large amount of bending and thus the large dilation buffer of the old borehole pipe can account for the increased uptilting in that pipe. The amount of uptilting may indicate relative dilation of the fault zone.

7.4 Results

7.4.1 Dilation and Slip

Slip and dilation initiated at 28.0–29.5 m depth 6–7 h after the beginning of a rainfall event. It is likely that localized shear developed after dilation of the fault zone. The distribution of slip and the dilation process during the typhoon of July 2004 are summarized in Fig. 7.3. By 17 h after the beginning of the rainfall, considerable dilation had occurred at site 5-1 and slip had initiated (Fig. 7.3b). The slip and dilation had propagated to other sites by 42–50 h after the beginning of the rainfall (Fig. 7.3c). The largest slip, 5.1 mm, was observed 78–80 h after the beginning of the rainfall at site 5-2 (Fig. 7.3d). A similar slip pattern with the initial break point was also observed at site 5-1 during the typhoon of July 2003.

7.4.2 Core Analysis

Cores were obtained from the fault zone before and after a given slip event. The first core was obtained during the dry winter season under ordinary groundwater conditions, and the second core immediately after a typhoon, while the groundwater level was high. At site 5-1, the initial break point was at 28–29.5 m, the same depth as the slip zone. The fault rock consisted of two layers of breccia, a lower black schist and an upper brecciated green schist, sandwiching a 50-cm-thick gouge layer (Fig. 7.5). The gouge layer consisted of brecciated blocks within a fine matrix of chlorite with a few zeolite and mica crystals. Both the breccias and the gouge layer have fractal grain-size distributions with fractal dimensions of 1.91–2.61. Such a self-similarity is a remarkable feature of cataclasis (Turcotte 1986), and fractal dimensions in this value range are consistent with the experimentally determined value range for cataclastic rocks (Sammis et al. 1986; Marone and

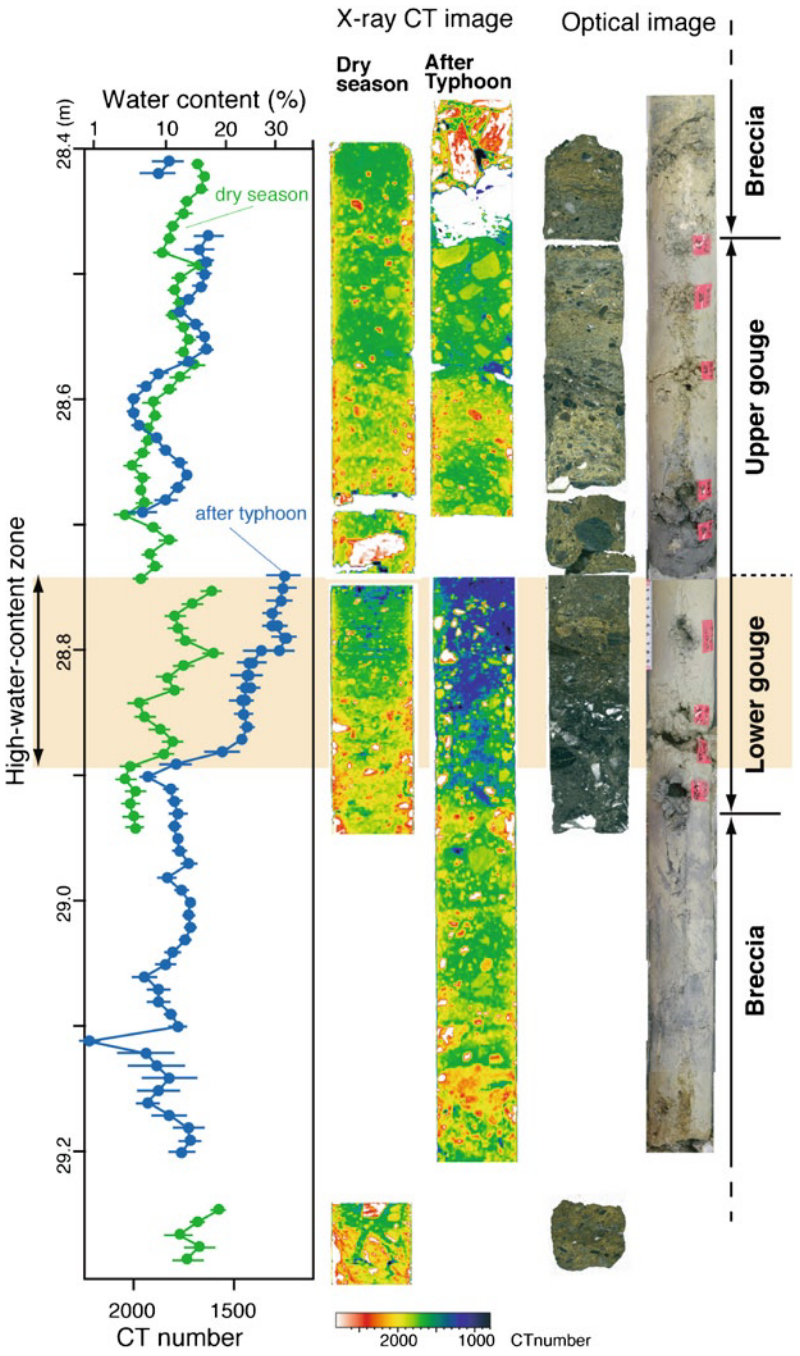

Fig. 7.5 Analysis results of the cores collected at site 5–1, where the initial slip break point occurred. The fault zone was sampled twice, once during the winter dry season and again immediately after a slip event. In the *left* panel, the X-ray CT number-derived water contents are compared between the dry season core (*green*) and the event core (*blue*)

Scholz 1989), indicating that the gouge layer originated from slip grinding. Details of the microstructure and fractal analysis will be described in another paper (in preparation).

We compared the water content before the slip event with that after the slip event. In the post-event core, a 14-cm-thick fracture zone in the lower part of the gouge layer, corresponding to the slip depth, had a high water content of 20–30% (Fig. 7.5), whereas elsewhere in the core, the water content was just 10–20%, that is similar to that in the core obtained in winter. In the X-CT image, some dark portions indicating opened cracks are found within the lower gouge zone (Fig. 7.5). In a sediment permeability experiment carried out by Oyo Corporation following ISO-17892-11 and JIS-A1218, the permeability of upper gouge layer was estimated to be $5.66–5.74 \times 10–16/m^2$. This low permeability suggests that the fracture zone may have acted as a conduit for pore fluid, making possible the quick dilation after rainfall, and that the upper part of the gouge layer may have acted as a cap rock, sealing in the pore fluid.

7.5 Summary

Short-term monitoring of groundwater levels and tilt related to rainfall events in the western part of the Utsugi landslide area revealed that a characteristic hydrologic behavior preceded a landslide. The groundwater level increased by 7–10 h after the beginning of a rainfall event, which is a very short delay for rainwater penetrating low-permeability sediments to 30 m depth by diffuse flow. Moreover, the delay was shorter in the lower part of the landslide area. This quick groundwater response to rainfall suggests the existence of a hydrologic conduit beneath the surface, and that the hydraulic head in the lower slope may be high. The ground temperature data showed that this western part was water-rich even in the dry season. Landsliding initiated near site 5-1, accompanied by fault zone dilation, and then propagated to surrounding sites. The landsliding may have been induced by an increase in pore fluid pressure in the fault zone. The behavior of the landslide may be related to the hydrologic structure. Core analyses revealed that the water content increased in only the lower part of the gouge zones after a slip event, which implies that this lower gouge zone is a fluid conduit. The grain size distribution of the fault gouge in the slip zone indicates that the gouge was formed by fault slip. These findings suggest that the fault rock and the fluid conduit developed by landslide activity occurring over a long period. Because the fault and hydrologic structures may develop over a long period, slip behavior, such as the site of slip initiation, does not change over the short term. We propose that similar behavior may also have important repercussions in understanding creeping and progressive slip plane development in shallow submarine settings, as it has been reported by Sultan et al. (2010) and Stegmann et al. (2011) for the Var Delta ofshore Nice (Western Mediterranean Sea), where also a tsunamigenic slope failure has occurred in 1979.

Acknowledgments This research was supported in part by a grant from the Japan Society for the Promotion of Science, no. 15340173. We used the landslide disaster monitoring system in the Utsugi area of Kochi Prefecture. X-ray CT analyses were performed at the Center for Advanced Marine Core Research, Kochi University. We are grateful to the students at Kochi University who helped with the monitoring. Thanks are also due to Dr. Hiroshi Kameya of Oyo Corporation, as well as to reviewers K. Kawabata, O. Fabbri and associate editor M. Strasser for helpful suggestions.

References

Aki K (1979) Characterization of barriers on an earthquake fault. J Geophys Res 84:6140–6148

Anderson SH, Gantzer CJ, Boone JM, Tully RJ (1988) Rapid nondestructive bulk density and soil-water content determination by computed tomography. Soil Sci Soc Am J 52:35–40

Byrne T, Maltman A, Stephenson E, Soh W, Knipe R (1993) Deformation structures and fluid flow in the toe region of the Nankai accretionary prism. Proc ODP Sci Results 131:83–101

Lay T, Kanamori H (1981) An asperity model of great earthquake sequences. In: Simpson D, Richards P (eds) Earthquake prediction: an international review, Maurice Ewing series. AGU, Washington, DC, pp 579–592

Lei X (2003) How do asperities fracture? An experimental study of unbroken asperities. Earth Planet Sci Lett 213:347–359

Marone C, Scholz CH (1989) Particle-size distribution and microstructures within simulated fault gouge. J Struct Geol 11:799–814

Ohnaka M, Shen L (2003) Scaling of the shear rupture process from nucleation to dynamic propagation: implication of geometric irregularity of the rupturing surfaces. J Geophys Res 104:817–844

Sammis C, Osborne R, Anderson JL, Banerdt M, White P (1986) Self-similar cataclasis in the formation of fault gouge. Pageoph 124:53–78

Soh W, Byrne T, Taira A, Kono A (1993) Computed tomography (CT) scan image analysis of Site 808 cores: structural and physical property implications. Proc ODP Sci Result 131:135–140

Stegmann S, Sultan N, Kopf A, Apprioual R, Pelleau P (2011) Hydrogeology and its effect on slope stability slong the coastal aquifer of Nice, Franc. Mar Geol 280:168–181

Suemine A (1983) Observational study on landslide mechanism in the area of crystalline schist (Part 1) an example of propagation of Rankine state. Bull Disaster Prev Inst Kyoto Univ 33:105–127

Sultan N, Savoye B, Jouet G, Leynaud D, Cochonat P, Henry P, Stegmann S, Kopf A (2010) Invesitgation of a possible submarine landslide at the Var delta frong (Nice-slope – SE France). Can Geotech J 47:486–496

Turcotte DL (1986) A fractal model for crustal deformation. Tectonophysics 132:261–269

Ujiie K, Maltman AJ, Sanchez-Gomez M (2004) Origin of deformation bands in argillaceous sediments at the toe of the Nankai accretionary prism, southwest Japan. J Struct Geol 26:221–231

Chapter 8
Pore Water Geochemistry as a Tool for Identifying and Dating Recent Mass-Transport Deposits

Susann Henkel, Tilmann Schwenk, Till J.J. Hanebuth, Michael Strasser, Natascha Riedinger, Michael Formolo, Juan Tomasini, Sebastian Krastel, and Sabine Kasten

Abstract Several previous studies have shown that submarine mass-movements can profoundly impact the shape of pore water profiles. Therefore, pore water geochemistry and diffusion models were proposed as tools for identifying and dating recent (max. several thousands of years old) mass-transport deposits (MTDs). In particular, sulfate (SO_4^{2-}) profiles evidentially indicate transient pore water conditions generated by submarine landslides. After mass-movements that

S. Henkel (✉) • S. Kasten
Institute of Geology and Mineralogy, University of Cologne, Zülpicher Str. 49a,
50674 Cologne, Germany
e-mail: susann.henkel@uni-koeln.de

T. Schwenk
Center for Marine Environmental Sciences (MARUM), Faculty of Geosciences,
University of Bremen, Klagenfurter Str, 28359 Bremen, Germany

T.J.J. Hanebuth
Center for Marine Environmental Sciences (MARUM), Faculty of Geosciences,
University of Bremen, Leobener Str, 28359 Bremen, Germany

M. Strasser
Geological Institute, ETH Zurich, Sonneggstrasse 5, 8092, Zürich, Switzerland

MARUM – Centre for Marine Environmental Sciences, University of Bremen, Bremen, Germany

N. Riedinger
University of California, 900 University Avenue, Riverside, CA 92521, USA

M. Formolo
The University of Tulsa, 800 South Tucker Drive, Tulsa, OK 74104, USA

J. Tomasini
Administración Nacional de Combustibles Alcohol y Pórtland (ANCAP),
Paysandú s/n esq. Avenida del Libertador, Montevideo 11100, Uruguay

S. Krastel
Leibniz Institute of Marine Sciences (IFM-GEOMAR), Wischhofstr. 1-3,
24148 Kiel, Germany

Y. Yamada et al. (eds.), *Submarine Mass Movements and Their Consequences*,
Advances in Natural and Technological Hazards Research 31,
DOI 10.1007/978-94-007-2162-3_8,

result in the deposition of sediment packages with distinct pore water signatures, the SO_4^{2-} profiles can be kink-shaped and evolve into the concave and linear shape with time due to molecular diffusion. Here we present data from the RV METEOR cruise M78/3 along the continental margin off Uruguay and Argentina. SO_4^{2-} profiles of 15 gravity cores are compared with the respective acoustic facies recorded by a sediment echosounder system. Our results show that in this very dynamic depositional setting, non-steady state profiles occur often, but are not exclusively associated with mass-movements. Three sites that show acoustic indications for recent MTDs are presented in detail. Where recent MTDs are identified, a geochemical transport/reaction model is used to estimate the time that has elapsed since the perturbation of the pore water system and, thus, the timing of the MTD emplacement. We conclude that geochemical analyses are a powerful complementary tool in the identification of recent MTDs and provide a simple and accurate way of dating such deposits.

Keywords Mass-movement • Pore water profiles • Non-steady state • Seismo-acoustic facies • Geochemical modeling

8.1 Introduction

Seismo-acoustic approaches provide the means to estimate dimensions of MTDs, but for absolute dating and identifying small-scale internal structures they need to be complemented by sediment data. However, based on visual core descriptions, MTDs are often hard to distinguish from homogeneous hemipelagic sediments, as both might lack clear stratification. Pore water profiles can be used to close this gap as was demonstrated first by De Lange (1983), who identified a "fresh-to-brackish sediment 'slab', with preservation of structural and pore water composition" underlying marine sediments in the Norwegian Sea.

With respect to pore water, sediments are classified into steady state and non-steady state systems (Schulz 2006). Simplified, steady state systems are in equilibrium and show a linear SO_4^{2-} decrease with depth towards the sulfate-methane transition zone (SMTZ) where the process of anaerobic oxidation of methane (AOM; e.g., Barnes and Goldberg 1976) occurs. Zabel and Schulz (2001) and Hensen et al. (2003) presented non-steady state SO_4^{2-} profiles from the Zaire deep-sea fan and the continental margin off Uruguay and suggested that kink, concave-up, and s-type SO_4^{2-} profiles can be explained by submarine landslides that carry their initial pore water signals downslope. The base of an MTD can, according to the authors, be indicated by a kink of the pore water profile, which evolves into a concave and finally a linear shape due to molecular diffusion. The re-equilibration of the SO_4^{2-} pore water profile was modeled to estimate the timing of the mass-movement.

With this review paper, we expand on the previous approaches and give a regional compilation showing the pervasiveness of non-steady state SO_4^{2-} profiles at the continental margin off Uruguay and Argentina and their relation to MTDs as indicated

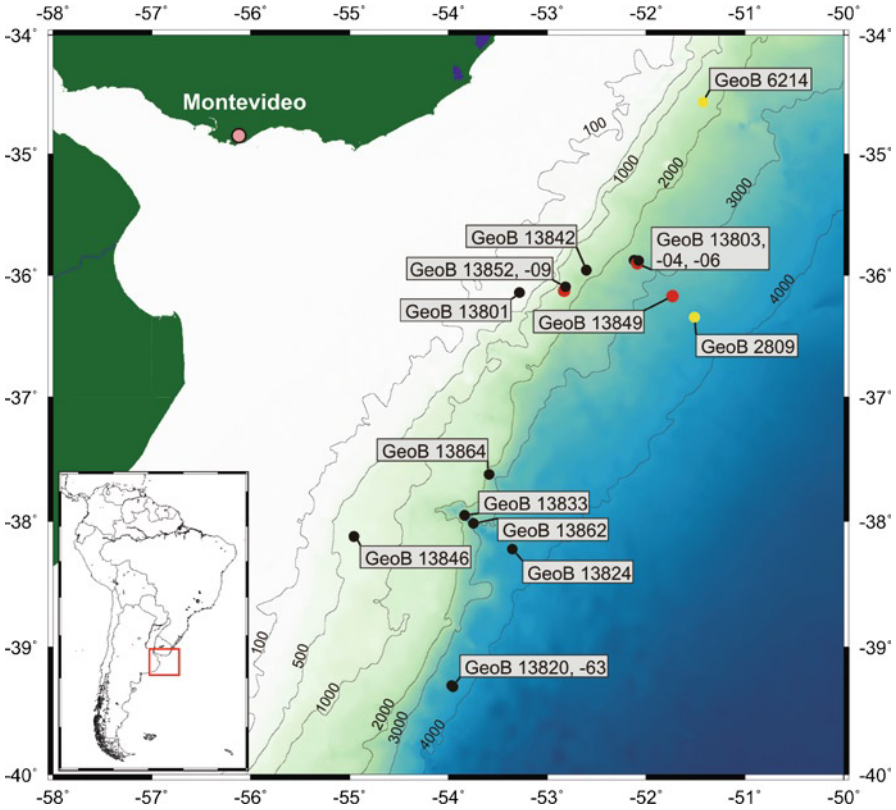

Fig. 8.1 Study area off Uruguay and Argentina and core locations. The sites marked in *red* are discussed in this study. The *yellow dots* mark the sites that are discussed in detail by Hensen et al. (2003)

by sediment echosounder data. The integration of geochemical, sedimentological, and geophysical data allows a better understanding of the dynamic interactions of pore water, sediments, and physical processes and offers a unique approach to date recent MTDs.

8.2 Study Area

The study area (Fig. 8.1) is characterized by dynamic oceanographic conditions including the Brazil-Malvinas Confluence near 38°S and the interaction of Antarctic water masses with the North Atlantic Deep Water at different depths (Piola and Matano 2001). The sedimentary processes along the margin were described in detail by Krastel et al. (2011). Mass movements occur within canyons and on the lower slope (Krastel et al. 2011).

8.3 Material and Methods

Sediment echosounder data were obtained with the Atlas Hydrographic PARASOUND system, which gives a dm-scale vertical resolution and a horizontal resolution of 7% of the water depth. Gravity cores were retrieved from various water depths (Table 8.1). Methane (CH_4) and pore water samples were gained as described in Henkel et al. (2011).

We performed transport/reaction modeling using the software CoTReM (Adler et al. 2001) and following the method of Hensen et al. (2003). We consider AOM (Eq. 8.1) as the most important process for SO_4^{2-} reduction at depth.

$$CH_4 + SO_4^{2-} \rightarrow HCO_3^- + HS^- + H_2O \tag{8.1}$$

Borowski et al. (1996) proposed that the upward flux of CH_4 can be quantitatively estimated from the downward flux of SO_4^{2-}. Measured CH_4 data were not used for the simulation because of the known inaccuracy related to degassing during core retrieval (e.g., Dickens et al. 1997). Except for bioirrigation and sedimentation rate (SR) that are considered in the model as advective terms, we simulated exclusively diffusive transport of pore water species. The reaction-specific change in concentration at a specific sediment depth ($\Delta C_{s,d}$) was calculated as follows:

$$\Delta C_{s,d} = R_{s,d} \times dt_{num} \times SC_{s,d} \tag{8.2}$$

Where $R_{s,d}$ is the reaction rate, dt_{num} is the time step used in the model run, and $SC_{s,d}$ is a stoichiometric factor (see Hensen et al. 2003). Details to $R_{s,d}$ are given in Sect. 8.4.

8.4 Results and Discussion

Identification of submarine landslides by SO_4^{2-} profiles is restricted to MTDs that are only a few meters thick. A thicker MTD that is not completely penetrated by the gravity corer may show a linear SO_4^{2-} profile in the cored interval. In such a case, the change in gradient (the kink) occurs below the cored depth and the MTD could thus not be identified on the basis of the SO_4^{2-} profile. Fifteen of the investigated cores penetrated the SMTZ and therefore provided the required information for an appropriate description of the SO_4^{2-} profile (Table 8.1, Fig. 8.1). The SO_4^{2-} profiles are classified into the types linear, concave-up, and kink shape (Table 8.1). The acoustic facies with special emphasis on reflection configuration and amplitude are included as well in Table 8.1. Nine of the investigated cores reveal non-linear profiles. Three of these nine cores (GeoB 13801, –03, –42) are not related to MTDs as indicated by PARASOUND data (Table 8.1). We therefore consider that the non-linearity of these SO_4^{2-} profiles can be attributed to alternative processes, such as CH_4 gas ebullition (Haeckel et al. 2007) or a sudden increase in the upward flux of CH_4 (Kasten et al. 2003) possibly due to gas hydrate dissociation.

Table 8.1 M78/3 core locations complemented by the shape of SO_4^{2-} profile and the acoustic facies

GeoB #	Latitude	Longitude	Depth [mbsf]	SO_4^{2-} profile	Acoustic facies
13801–2	36° 08.49′ S	53° 17.16′ W	243	Concave-up	Parallel layered; low to high amplitudes
13803–2	35° 52.65′ S	52° 07.19′ W	2,462	Concave-up	Parallel layered; medium to high amplitudes
13804–1	35° 54.30′ S	52° 05.42′ W	2,593	Kink	Chaotic, hummocky
13806–1	35° 52.82′ S	52° 04.61′ W	2,586	Concave-up	Transparent sheet-like layer; parallel layered sediment below
13809–1	36° 07.67′ S	52° 49.90′ W	1,400	Linear	Transparent sheet-like layer; parallel layered sediment below
13820–1	39° 18.06′ S	53° 58.03′ W	3,613	Linear	Parallel layered; low to high amplitudes
13824–1	38° 13.14′ S	53° 21.29′ W	3,821	Linear	Parallel layered; low to high amplitudes
13833–2	37° 57.45′ S	53° 50.21′ W	3,404	Concave-up	No data
13842–1	35° 57.57′ S	52° 36.30′ W	1,555	Kink	Parallel-subparallel layered; low to high amplitudes
13846–2	38° 07.19′ S	54° 57.46′ W	637	Linear	Parallel layered; low to high amplitudes
13849–1	36° 10.41′ S	51° 43.96′ W	3,278	Concave-up	Lens-shaped transparent unit; parallel layered below
13852–1	36° 05.70′ S	52° 48.98′ W	1,320	Concave-up	Transparent sheet-like layer; parallel layered below
13862–1	38° 01.11′ S	53° 44.70′ W	3,588	Kink	No data
13863–1	39° 18.70′ S	53° 57.16′ W	3,687	Linear	Parallel layered; low to high amplitudes
13864–2	37° 37.47′ S	53° 35.33′ W	2,757	Linear	Parallel layered; medium to high amplitudes

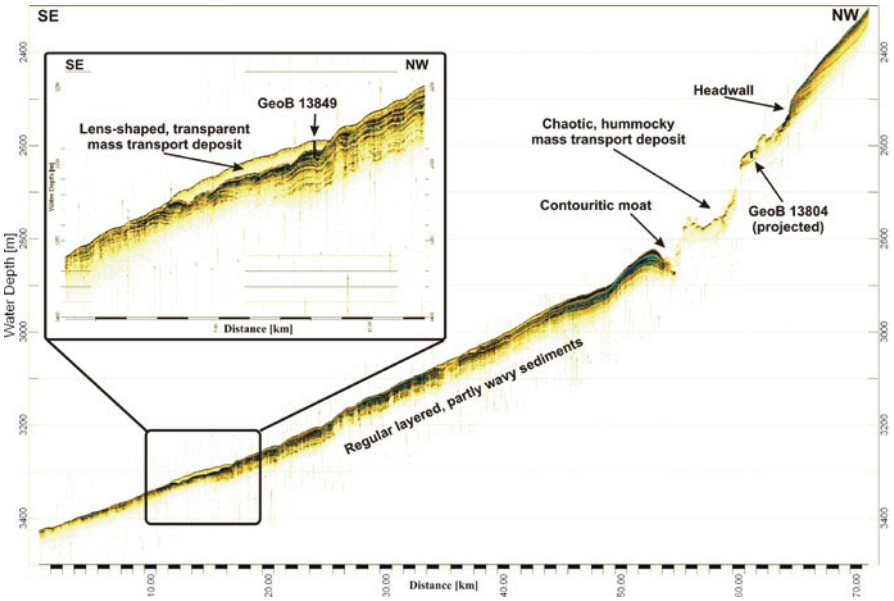

Fig. 8.2 PARASOUND profile obtained during RV METEOR cruise M78/3 crossing the continental slope in SE-NW direction. The profile shows the position of core GeoB 13804 (projected) at a hummocky surface interpreted as mass-transport deposit. Site GeoB 13849 is shown in the close-up at the rim of a lens-shaped transparent unit overlying parallel layered sediments. At the core location, the transparent unit interpreted as a gravity flow deposit is ~6 m thick

At several sites (GeoB 13806, –09, –49, –52), acoustically transparent deposits overlay parallel layered sediments (Table 8.1, Figs. 8.2 and 8.3). In general, such transparent units represent either homogeneous or extremely heterogeneous sediments with loss of internal bedding (Kuehl et al. 2005). Transparent acoustic facies often represent MTDs, which may also show a hummocky surface and an erosional base (Hampton et al. 1996).

Three sites (GeoB 13804, –49, and –09) will be discussed, that represent the three different categories of SO_4^{2-} profiles and which have all been recovered from sites that show acoustic indication of potential MTDs (Fig. 8.4). Core GeoB 13804 was retrieved from an acoustically chaotic facies with a hummocky surface. Core GeoB 13849 was recovered from a lens-shaped transparent unit (Fig. 8.2) and core GeoB 13809 was taken from an acoustically-transparent, sheet-like deposit downslope of a prominent scar (Krastel et al. 2011). This 5–6 m thick sedimentary body is characterized by parallel upper and lower boundaries and shows no termination within the surveyed area (Fig. 8.3). The interpretation of this feature from PARASOUND data is therefore not unambiguous. It may result either from downslope sediment-transport processes or from sheeted-contouritic deposition of homogeneous material (see discussion below).

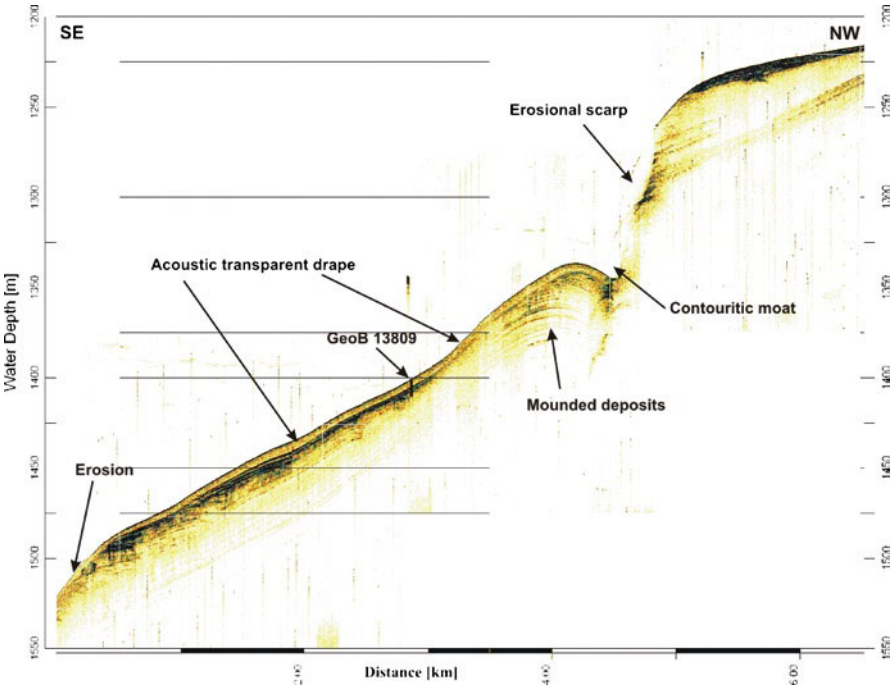

Fig. 8.3 PARASOUND profile obtained during RV METEOR cruise M78/3 crossing the continental slope in SE-NW direction. Station GeoB 13809 is located to the SE of a contouritic moat. The profile at the core location shows parallel layered sediments and a strong reflector in 5–6 depth that has an erosive character and is overlain by a sheet-like transparent unit

8.4.1 Pore Water Profiles at Potential MTD Sites

The SO_4^{2-} profile at site GeoB 13804 has a kink shape with a gradient change at ~2.8 m (Fig. 8.4). A sedimentological boundary between gray and very dark gray mud occurs at 2.43 m, thus ~0.35 m above the gradient change of the SO_4^{2-} profile (Fig. 8.4). Above this sedimentological contact, which is also reflected by a significant downcore increase in undrained shear strength (Henkel et al. 2011), the core shows a stack of undisturbed sand/silt layers (Fig. 8.4). Bioturbation structures are present between 0 and 2.79 m depth. Bioirrigation and vertical gas or fluid migration in the whole ~2.8 m thick package can be excluded (Henkel et al. 2011). Therefore, we conclude that the kink shaped SO_4^{2-} profile is the result of the combination of bioirrigation to a paleo-depth of 0.35 m and a ~2.4 m thick slide mass. In accordance with the studies of Zabel and Schulz (2001) and Hensen et al. (2003) at other locations, the most recent mass-transport event at site GeoB 13804 must have happened in the form of a coherent slide mass carrying its initial SO_4^{2-} profile downward, because the internal structure of this package was not destroyed. It is known from previous expeditions that sites with nearly constant SO_4^{2-} concentrations over the length of a

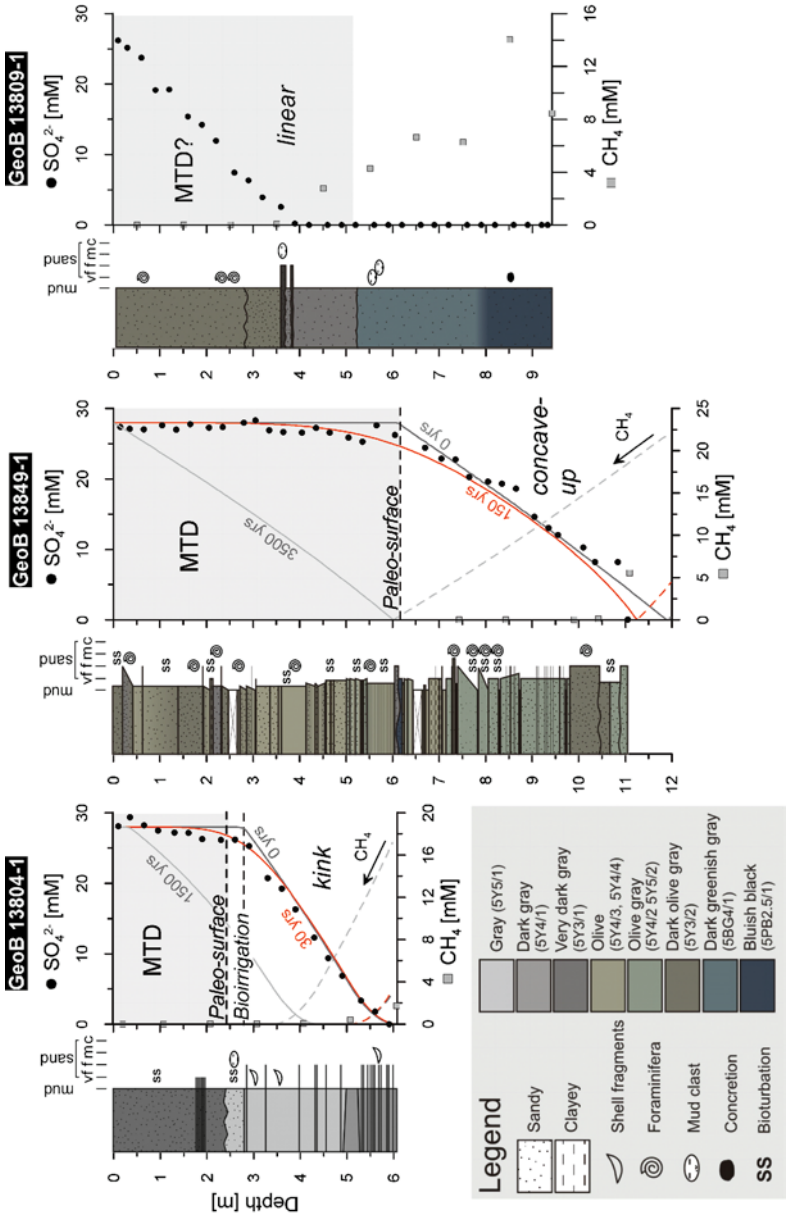

Fig. 8.4 Lithology, SO_4^{2-}, and CH_4 profiles of gravity cores. The non-steady state SO_4^{2-} profiles at sites GeoB 13804 and GeoB 13849 are related to recent MTDs (*gray shaded*). The *gray* lines labeled with "0 years" in the graphs of GeoB 13804 and −49 show the starting conditions for the models that were set up to estimate the timing of the mass-transport deposition. Data of site GeoB 13804 including the geochemical simulation are described in detail in Henkel et al. (2011). The values in *brackets* (legend) represent the Munsell color code

Table 8.2 Parameterization for transport and reaction modeling for sites GeoB 13804 and –49

Basic parameters GeoB 13804/–49		Boundary conditions GeoB 13804/–49	
Model length [m]	8/15	Sedimentation rate [cm kyear^{-1}]	80–180[a]/5[b]
Cell discretisation [cm]	5	Upper boundary SO_4^{2-} [mmol l^{-1}]	28[c]
Time step [year]	0.05	Upper boundary CH_4 [mmol l^{-1}]	0[c]
Porosity φ	0.6/0.7[d]	Lower boundary SO_4^{2-} [mmol l^{-1}]	0
Temperature [°C]	3.5	Lower boundary CH_4 [mmol l^{-1}]	40/35
Diffusion coefficients[e]	D_0	D_{sed}	
SO_4^{2-} [cm^2 year^{-1}]	179.5	88.79	
CH_4 [cm^2 year^{-1}]	293.6	145.2	

[a]Exceptionally high sedimentation rate derives from unsupported ^{210}Pb. For details see Henkel et al. (2011)
[b]According to Ewing et al. (1971) and Hensen et al. (2003)
[c]Bottom water concentrations
[d]Average porosity as measured on board
[e]Diffusion coefficient in free solution (D_0) calculated for a temperature of 3.5°C and corrected for tortuosity (θ) after Boudreau (1997); $D_{sed} = D_0/\theta^2$, while $\theta^2 = 1 - \ln(\varphi^2)$

gravity core (as it is expected for the source area of the slide) occur in the study area (Bleil et al. 1994).

Site GeoB 13849 is characterized by a concave-up shaped SO_4^{2-} profile (Fig. 8.4). Based on PARASOUND data, the thickness of the surficial MTD unit is estimated to be ~6 m (Fig. 8.2), which fits well to the SO_4^{2-} profile showing a change in gradient at the same depth. The lithology displays a sharp contact between bluish black fine sand interbedded with olive muddy fine sand below and dark gray muddy fine sand above 6.10 m. Based on the geochemical and PARASOUND data this boundary is interpreted as the base of the MTD.

The visual description of core GeoB 13809 reveals a sharp, irregular contact at 5.12 m. Since this boundary correlates to the base of the acoustically transparent layer imaged in PARASOUND data, it possibly represents the base of an MTD (Fig. 8.4). Core GeoB 13809 displays a linear SO_4^{2-} profile. The inferred mass-movement thus took place several hundreds to thousands of years ago, so that the SO_4^{2-} profile could diffusively re-equilibrate into a linear shape.

8.4.2 Geochemical Transport/Reaction Modeling

The diffusive re-equilibration of the SO_4^{2-} profile over time was simulated for sites GeoB 13804 and –49 (parameterization in Table 8.2). A maximum reaction rate $R_{s,d}$ of 0.1 mol dm^{-3} year^{-1} was defined to produce a broad SMTZ with overlapping CH_4 and SO_4^{2-} profiles at site GeoB 13804 (Fig. 8.4). That rate was used as long as the reactants were available in sufficient amounts (0th order kinetics). For lower concentrations of the reactants and for site GeoB 13849, where the SMTZ is restricted to a distinct depth, the AOM reaction rate was determined based on second order kinetics. The starting conditions for the model runs are shown as gray

lines in Fig. 8.4: Each sediment package (the MTD and the sediment below) still hosts its initial pore water characteristic. For site GeoB 13804, the model results reveal that the proposed mass-movement took place less than 30 years ago (Fig. 8.4, Henkel et al. 2011). The event could therefore have been associated with a weak (5.2 m_b) earthquake in 1988 (Henkel et al. 2011). The epicenter was ~70 km away from the core location (Assumpção 1998; Benavídez Sosa 1998).

According to the best fit between measured SO_4^{2-} concentrations and the simulation (red line in Fig. 8.4), the MTD at site GeoB 13849 occurred approximately 150 years ago. The age of the MTD roughly corresponds to an earthquake in 1848 (intensity in Montevideo IV-V based on the Mercalli scale) with an epicenter ~200 km west of the study site (Benavídez Sosa 1998). Complete re-equilibration of the SO_4^{2-} profile is reached after ~3,500 years (Fig. 8.4).

8.5 Conclusions

This study demonstrates that integrating geophysical, sedimentological, and pore water data provides a scientifically valid approach to constrain the ages of recent MTDs. Pore water geochemical analyses are cost-efficient, easily accessible compared to other methods, and can provide information regarding paleosurfaces or erosive contacts that are not apparent from visual core inspection. Applying a comprehensive, multi-disciplinary approach as presented in this study over a larger region could provide a historical record of the frequencies of mass-transport events. Such a record may be compared to documented earthquakes and in this way shed light on the dynamic and complex links between various geological processes.

Acknowledgments GL Arnold and J Sawicka are acknowledged for analyzing SO_4^{2-}. R Violante and V Bender are acknowledged for the visual description of the cores. The PARASOUND figures were created using the free software SENT developed by H Keil, University of Bremen. The manuscript benefited from the very constructive reviews of C Hensen and B Dugan. This study was funded by the Deutsche Forschungsgemeinschaft (DFG) in the frame of the International Graduate College "Proxies in Earth History" (EUROPROX) and the Research Center/Cluster of Excellence "The Ocean in the Earth System" (MARUM). We appreciate further financial support from the Helmholtz Association (AWI Bremerhaven). All data are available via the database Pangaea (http://www.pangaea.de).

References

Adler M, Hensen C, Wenzhöfer F, Pfeifer K, Schulz HD (2001) Modeling of calcite dissolution by oxic respiration in supralysoclinal deep-sea sediments. Mar Geol 177:167–189

Assumpção M (1998) Seismicity and stresses in the Brazilian passive margin. Bull Seismol Soc Am 88:160–169

Barnes RO, Goldberg ED (1976) Methane production and consumption in anoxic marine sediments. Geology 4:297–300

Benavídez Sosa A (1998) Sismicidad y sismotectónica en Uruguay. Física de la Tierra 10:167–186

Bleil U and cruise participants (1994) Report and preliminary results of Meteor Cruise M29/2, Montevideo – Rio de Janeiro, 15.07.1994 – 08.08.1994. Berichte aus dem Fachbereich Geowissenschaften der Universität Bremen 59

Borowski WS, Paull CK, Ussler W (1996) Marine pore-water sulfate profiles indicate in situ methane flux from underlying gas hydrate. Geology 24:655–658

Boudreau BP (1997) Diagenetic models and their implementation: modeling transport and reactions in aquatic sediments. Springer, Berlin/Heidelberg/New York

De Lange GJ (1983) Geochemical evidence of a massive slide in the southern Norwegian Sea. Nature 305:420–422

Dickens GR, Paull CK, Wallace PJ (1997) Direct measurement of in situ methane quantities in a large gas-hydrate reservoir. Nature 385:426–428

Ewing M, Eittreim SL, Ewing JI, Le Pichon X (1971) Sediment transport and distribution in the Argentine basin. 3. Nepheloid layer and processes of sedimentation. Phys Chem Earth 8:49–77

Haeckel M, Boudreau BP, Wallmann K (2007) Bubble-induced porewater mixing: a 3-D model for deep porewater irrigation. Geochim Cosmochim Acta 71:5135–5154

Hampton MA, Lee HJ, Locat J (1996) Submarine landslides. Rev Geophys 34:33–59

Henkel S, Strasser M, Schwenk T, Hanebuth TJJ, Hüsener J, Arnold GL, Winkelmann D, Formolo M, Tomasini J, Krastel S, Kasten S (2011) An interdisciplinary investigation of a recent submarine mass transport deposit at the continental margin off Uruguay. Geochem Geophys Geosyst 12:Q08009. doi:10.1029/2011GC003669

Hensen C, Zabel M, Pfeifer K, Schwenk T, Kasten S, Riedinger N, Schulz HD, Boetius A (2003) Control of sulfate pore-water profiles by sedimentary events and the significance of anaerobic oxidation of methane for the burial of sulfur in marine sediments. Geochim Cosmochim Acta 67:2631–2647

Kasten S, Zabel M, Heuer V, Hensen C (2003) Processes and signals of nonsteady-state diagenesis in deep-sea sediments and their pore waters. In: Wefer G et al (eds) The south Atlantic in the late Quaternary: reconstruction of mass budget and current systems. Springer, Berlin/Heidelberg/New York, pp 431–459

Krastel S, Wefer G, Hanebuth TJJ, Antobreh AA, Freudenthal T, Preu B, Schwenk T, Strasser M, Violante R, Winkelmann D, M78/3 shipboard scientific crew (2011) Sediment dynamics and geohazards off Uruguay and the de la Plata River region (Northern-Argentina and Uruguay). Geo-Mar Lett 31:271–283

Kuehl SA, Allison MA, Goodbred SL, Kudrass HR (2005) The Ganges-Brahmaputra delta. In: Giosan L, Bhattacharya JP (eds) River deltas—concepts, models, and examples, SEPM Special Publication No. 83, pp 413–434

Piola AR, Matano RP (2001) Brazil and Falklands (Malvinas) currents. In: John HS et al (eds) Encyclopedia of ocean sciences. Academic, Oxford, pp 422–430

Schulz HD (2006) Quantification of early diagenesis: dissolved constituents in pore water and signals in the solid phase. In: Schulz HD, Zabel M (eds) Marine geochemistry. Springer, Berlin, pp 73–124

Zabel M, Schulz HD (2001) Importance of submarine landslides for non-steady state conditions in pore water systems – lower Zaire (Congo) deep-sea fan. Mar Geol 176:87–99

Chapter 9
An In-Situ Free-Fall Piezocone Penetrometer for Characterizing Soft and Sensitive Clays at Finneidfjord (Northern Norway)

Alois Steiner, Jean-Sebastien L'Heureux, Achim Kopf, Maarten Vanneste, Oddvar Longva, Matthias Lange, and Haflidi Haflidason

Abstract The identification and characterization of weak layers, potentially acting as detachment planes, are key elements in submarine landslide research. In this study, the MARUM Free-Fall Piezocone Penetrometer (FF-CPTU) was used to characterize soft and sensitive clays at Finneidfjord, a site with historical landslide events. The FF-CPTU measurements are compared with standard, industry Cone Penetration Testing (pushed CPTU) data in order to verify and validate the penetration rate effect by using an empirical closed-form solution to convert dynamic properties to quasi-static ones. The quasi-static properties and sedimentological/laboratory results across the weak layers show significantly lower values for the CPTU parameters (q_t and f_s) and undrained shear-strength (s_u), build-up of excess pore-water pressure (Δu) as well as a normally-consolidated behavior in comparison with the surrounding sediment. These findings allow us to develop a 2D model of

A. Steiner (✉) • A. Kopf • M. Lange
Marine Geotechnics, MARUM – Center for Marine Environmental Sciences and Faculty of Geosciences, University of Bremen, Leobener Str, 28359 Bremen, Germany
e-mail: asteiner@uni-bremen.de; akopf@uni-bremen.de; matlange@uni-bremen.de

J.-S. L'Heureux • O. Longva
NGU – Geological Survey of Norway, Sluppen, 7491, PO Box 6315, Trondheim, Norway

ICG – International Centre for Geohazards c/o NGI, Ullevål, 0806, PO Box 3930, Oslo, Norway
e-mail: jean.lheureux@ngu.no; oddvar.longva@ngu.no

M. Vanneste
NGI – Norwegian Geotechnical Institute, ICG – International Centre for Geohazards c/o NGI, Ullevål, 0806, PO Box 3930, Oslo, Norway
e-mail: maarten.vanneste@ngi.no

H. Haflidason
Department of Earth Science, University of Bergen, PO Box 7800, 5020 Bergen, Norway
e-mail: haflidi.haflidason@geo.uib.no

Y. Yamada et al. (eds.), *Submarine Mass Movements and Their Consequences*, Advances in Natural and Technological Hazards Research 31,
DOI 10.1007/978-94-007-2162-3_9, © Springer Science+Business Media B.V. 2012

the sub-surface in which the weak horizon is mapped, and to demonstrate that the light-weight FF-CPTU instrument is a powerful, versatile device for the geotechnical evaluation of submarine mass movements and their consequences.

Keywords Free-fall cone penetration testing • Soft and sensitive clay • Weak layer • Submarine landslide

9.1 Introduction

The presence of weak layers, in this study defined as soft and sensitive clay strata, in conjunction with pre-conditional factors (e.g., rapid sediment accumulation and under-consolidation, gas charging, excess pore-water pressure) has recently been recognized as an important factor for the initiation of slope instabilities and submarine landslides (e.g., Haflidason et al. 2003; Longva et al. 2003). Hence, state-of-the-art in-situ measurements across such layers are important in order to improve our knowledge of the initiation of submarine landslides and for geohazard assessments.

CPTU is an efficient and widely used in-situ measurement technique for geotechnical site investigations, both onshore and offshore (Lunne et al. 1997; Osler et al. 2005). It measures three parameters in a semi-continuous way upon penetration, these being cone resistance, sleeve friction and pore-water pressure (pp) (with possibility for dissipation tests). The combination of these parameters yields vital information on lithology, soil stratification and geotechnical engineering properties. An autonomous, light-weight, modular, FF-CPTU instrument was recently designed at MARUM (Center for Marine Environmental Sciences and Faculty of Geosciences), University of Bremen. This instrument is a straightforward, cost- and time-effective technique to measure de-/accelerations, tilt/temperature and CPTU parameters (q_c, f_s and u_2) (Stegmann et al. 2006).

In this paper, a set of FF-CPTU measurements collected off the village of Finneidfjord, Northern Norway (Fig. 9.1), is compared with pushed CPTU and laboratory data. The aim is (i) to explain the procedure and handling of the FF-CPTU results with respect to the dynamic, non-linear penetration velocity (Dayal and Allen 1975) in contrast to the fixed penetration velocity (0.02 m/s) used in pushed CPTU tests (Lunne et al. 1997), and (ii) to use the data set to identify and geotechnically characterize the slide-prone layers at Finneidfjord.

9.2 Setting

On 20th June, 1996 a combined submarine/subaerial, retrogressive landslide mobilized approximately 1×10^6 m^3 of sediment and claimed four human lives (Longva et al. 2003). Ground investigations conducted prior and subsequent to the

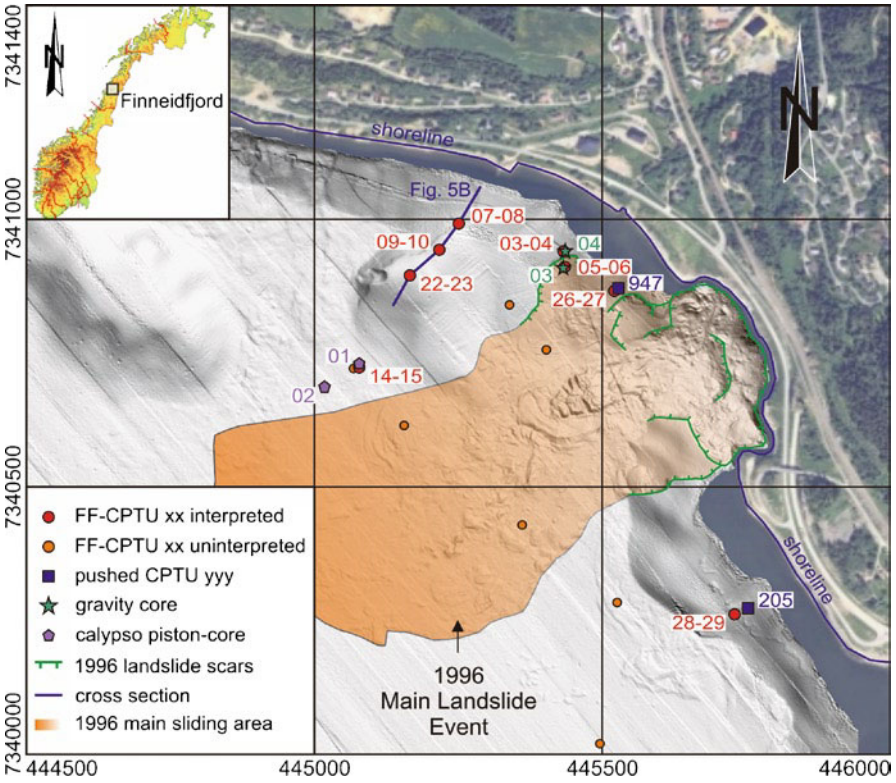

Fig. 9.1 Morphological analysis according to swath bathymetry data off Finneidfjord presenting the 1996 landslide deposits and landslide scars. The locations of the FF-CPTU measurements, pushed CPTU tests and calypso piston/gravity cores are illustrated

landslide illustrate that the sediments comprised Holocene silty clay to sandy silt and a pocket of soft, sensitive clay below the shore- and foreshore regions. At the shoreline, the basement lies between 15 and 20 m below ground level (mbgl) (Janbu 1996; Longva et al. 2003). A schematic illustration of the near-shore setting is presented in L'Heureux et al. (2012)).

9.3 Material and Methods

This study comprises 38 measurements using a FF-CPTU instrument. This instrument relies on a 15 cm^2 Geomil subtraction piezocone measuring the cone resistance (q_c), sleeve friction (f_s), penetration pp measured behind the tip (u_2), and tilt/temperature. The probe is extended by metal rods (maximum length up to 7.5 m) and hosts a pressure housing at the top containing microprocessor, tiltmeter and accelerometer (Stegmann et al. 2006). The penetration depth calculation is based on the first and

second integration of the de-/acceleration taking into account a maximum error of ≤2%. In our study, the terminal depth varied between 2.0 and 5.3 m below seabed (mbsb) with the vertical resolution of measurements being <0.01 m. The accuracy of the piezocone sensors ranges between 2 and 5 kPa.

Two pushed CPTU tests (205 and 947; Fig. 9.1), performed in 1995 by the Norwegian Road Authorities, were used to compare and validate the FF-CPTU records. A penetration depth of 10–20 mbsb was achieved with a conventional vertical resolution of 0.02 m. The 10 cm^2 Memocone MK II probe sensors had an accuracy varying between 2 and 20 kPa.

We use also results from 2 short gravity and 2 longer calypso piston-cores collected in 2009 and 2010. Detailed sedimentological description and various geotechnical analyses (e.g., water content, peak- and remolded undrained shear-strength using fall-cone tests) were performed on the gravity cores. On the calypso piston-cores sedimentological and geotechnical analyses were undertaken including gamma density and magnetic susceptibility measurements using a GEOTEK Multi-Sensor Core Logger (MSCL).

9.4 Results

9.4.1 Comparison of FF-CPTU and Pushed CPTU Tests

Conventional CPTU equipment is pushed in the soil with a quasi-static penetration velocity of 0.02 m/s (Lunne et al. 1997). This is a major difference compared to FF-CPTU's. Due to their non-linear penetration velocity, the dynamics of the probe accentuate the natural sediment parameters (penetration rate effect). To correct this effect, a penetration rate factor (PRF) represented by an empirical closed-form solution (Eq. 9.1) and developed for clay and sand was introduced (Dayal and Allen 1975). This solution is based on a logarithmic function subject to the ratio of the dynamic (v_{dyn}) and quasi-static penetration velocity (v_{q-s} = 0.02 m/s), and the soil viscosity coefficients (K_{qt} and K_{fs}) associated for cone resistance and sleeve friction (Eq. 9.1).

$$PRF = 1 + K_{qt/fs} \cdot \log_{10}\left(\frac{V_{dyn}}{V_{q-s}}\right) \tag{9.1}$$

The soil viscosity coefficients are determined by back-calculations (Eqs. 9.1–9.2 and 9.3) using comparison of FF-CPTU and pushed CPTU tests (Fig. 9.2), and validated by Dayal and Allen 1975. The value for the cone resistance (K_{qt}) varies between 0.1 and 0.2. The sleeve friction coefficient (K_{fs}) is expected to be between 0.3 and 0.7. The hereafter presented data are based upon K_{qt} = 0.13 and K_{fs} = 0.45.

Figure 9.2 illustrates the comparison of the FF-CPTU data with pushed CPTU results at two locations. The first comparison includes the FF-CPTU 26 and 27

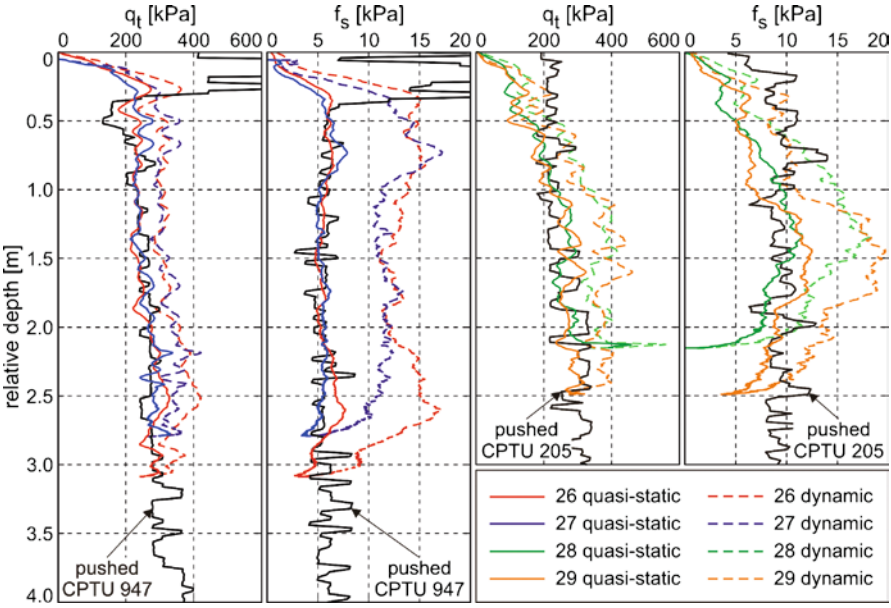

Fig. 9.2 Comparison of the dynamic and quasi-static FF-CPTU corrected cone resistance and sleeve friction with the pushed CPTU data. Note that the upper 0.5 m of the pushed CPTU 947 shows inconsistent results (most likely related to internal effects of the equipment) (Note: cone resistance corrected for pp effects (q_t), sleeve friction (f_s))

and pushed CPTU 947, whereas FF-CPTU 28 and 29 and pushed CPTU 205 are compared at the second location (Fig. 9.1 for location).

The quasi-static properties ($q_{t,q-s}$, $f_{s,q-s}$) are obtained by dividing the dynamic parameters ($q_{t,dyn}$, $f_{s,dyn}$) by the PRF (Eqs. 9.2 and 9.3). PRF, $q_{t,q-s}$ and $f_{s,q-s}$ are calculated for each recorded point.

$$q_{t,q-s} = \frac{q_{t,dyn}}{PRF} \quad \text{and} \quad f_{s,q-s} = \frac{f_{s,dyn}}{PRF} \qquad (9.2 \text{ and } 9.3)$$

The effect of penetration rate on the pp (u_2) measurements were also observed and depend on penetration velocity, permeability and consolidation state of the sediments (e.g., Kim and Tumay 2004; Silva et al. 2006). Consequently, the presented solutions are not proper to evaluate the quasi-static pp.

9.4.2 Laboratory Analyses

The lithology in gravity cores 04 and 03 (Fig. 9.1) is dominated by silty clay to clayey silt. It also includes a suspected weak layer with laminated sand (Fig. 9.3).

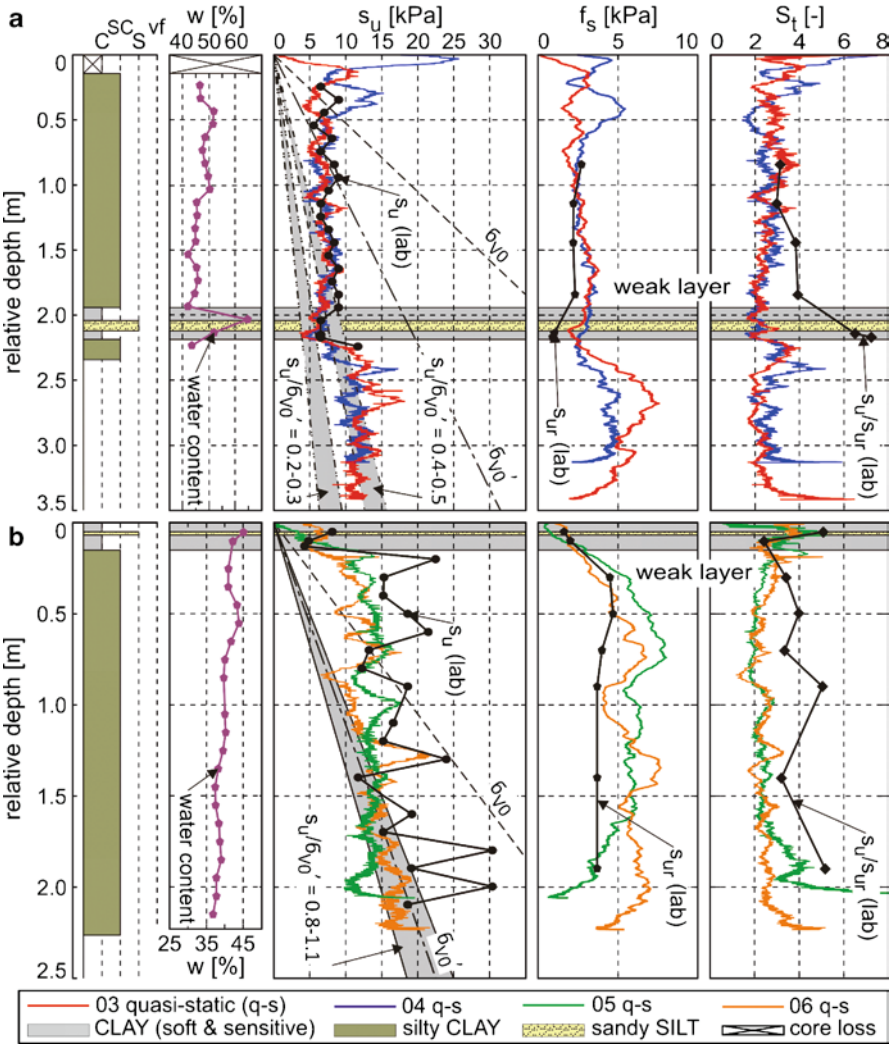

Fig. 9.3 (**a**) Comparison of FF-CPTU measurements (in-situ undrained shear-strength, sleeve friction and in-situ sensitivity) with core log, water content and fall-cone tests for locations FF-CPTU 03 and 04 and (**b**) for locations FF-CPTU 05 and 06 (Note: undrained shear-strength (s_u), water content (w), sensitivity (S_t))

In core 04, this particular layer is found between 1.90 and 2.15 mbsf, whereas in core 03, this layer is found in the uppermost 0.15 m (L'Heureux et al. 2012).

Calypso piston-cores 02 and 01 (Fig. 9.1 for location) are mainly homogeneous, clayey silt. A weak and laminated clay layer was detected at 2.8–3.2 mbsb. The clays have low magnetic susceptibility and gamma density, whereas the sandy interval within the clay bed shows positive peaks (Fig. 9.4).

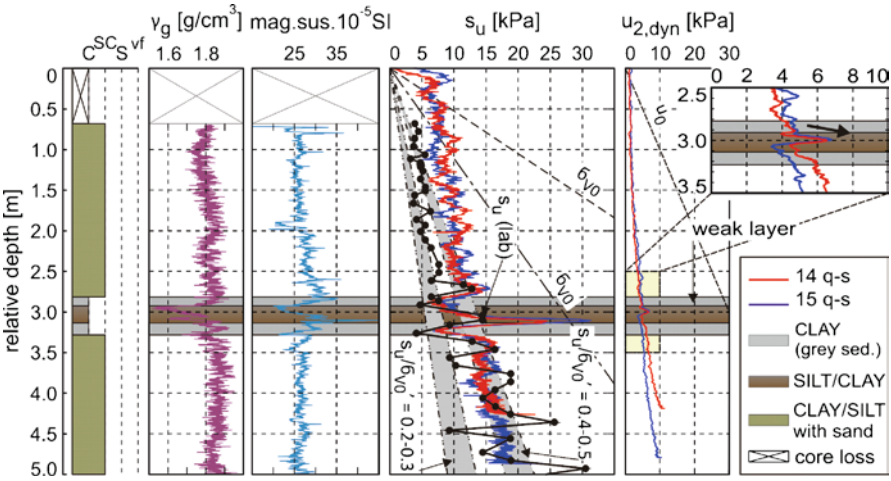

Fig. 9.4 Comparison of in-situ undrained shear-strength, dynamic pp with core log, MSCL data and fall-cone tests for the location FF-CPTU 14 and 15 (Note: gamma density (γ_g), magnetic susceptibility (mag.sus.), dynamic pp ($u_{2,dyn}$))

The undrained shear-strength ratio (s_u/σ_{vo}') generally exceeds 0.3 for the massive clayey silt, which is characteristic for normally- to slightly over-consolidated sediments. For the weak layers, the undrained shear-strength ratio is lower ($0.2 < s_u/\sigma_{vo}' < 0.3$) and representative of normally-consolidated sediment (Figs. 9.3 and 9.4).

9.4.3 Comparison of In-Situ and Laboratory Results

The evaluation of the in-situ undrained shear-strength is based on the empirical relationship: $s_u = (q_t - \sigma_{vo})/N_{kt}$, where q_t is the corrected cone resistance, σ_{vo} is the in-situ vertical stress and N_{kt} is the empirical cone factor. For the Finneidfjord sediments, the cone factor typically falls in the range from 10 to 18 (used 14) (Lunne 2010). The ratio of in-situ undrained shear-strength to sleeve friction (s_u/f_s) provides a qualitative indication for the sensitivity (Lunne et al. 1997), but is highly influenced by the penetrometer used (Lunne 2010).

Comparison of in-situ and laboratory undrained shear-strength values shows a good correlation for sites FF-CPTU 03–06 (Fig. 9.3). The correlation for FF-CPTU 05 and 06 towards the terminal depth is less evident and most likely related to coring effects (e.g., under-sampling) and sediment disturbance (Fig. 9.3b). Both FF-CPTU tests exhibit an over-consolidation characteristic with undrained shear-strength ratio higher than 0.4. The weak layer is classified as normally-consolidated ($0.2 < s_u/\sigma_{vo}' < 0.3$). Moreover, the sleeve friction compares well with the remolded undrained shear-strength (s_{ur}) for the upper 1.5 mbsb (FF-CPTU 03 and 04) and the upper 1.0 mbsb (FF-CPTU 05 and 06), whereas the sensitivity varies between 2 and 6 (Fig. 9.3).

When comparing the FF-CPTU 14 and 15 data with the calypso piston-core results, we observe a similar trend in the undrained shear-strength data (Fig. 9.4). However, estimates of undrained shear-strength tend to be larger when based upon the FF-CPTU results (i.e. 50–70%). A good correlation of the FF-CPTU data is encountered at depths beyond 2.5 mbsb.

The FF-CPTU measurements reveal significant drops in the undrained shear-strength, associated with a decrease in sleeve friction in the weak layers. The undrained shear-strength is at least 1.8–2.2 times lower compared to the surrounding sediments. A similar behavior is observed for the sleeve friction (from 3.5 to < 2.0 kPa). The soft and sensitive clay shows an increase in the sensitivity (laboratory) from approximately 4.0 to 7.5. The FF-CPTU measurements further illustrate a pp build-up. In addition to this build-up, a decrease immediately below the soft and sensitive clay occurs (Fig. 9.4). This decrease in pp underneath the weak layer may reflect dilatancy in the potentially gas-rich sediments (L'Heureux et al. 2012).

9.5 Discussion and Conclusion

Several studies illustrated that strength properties of sediments are highly influenced by the deformation/strain rate (Casagrande and Shannon 1949; Lucius 1971). This so-called penetration rate effect was first described for penetrometers by Dayal and Allen (1975). This effect accommodates for the fact that a dynamic impact serves to accentuate the geotechnical characteristics compared to pushed CPTU systems (Stoll et al. 2007). Dynamic data sets from FF-CPTU tests have non-linear insertion velocity and thus need to be corrected for the penetration rate effect in order to properly compare the results with pushed CPTU data. Several studies show good agreement with pushed deployments (see Sect. 9.4.1 above; and Stoll et al. 2007; Stegmann 2007). Hence, we chose the PRF to be ≤1.5 for cone resistance and ≤2.3 for sleeve friction, as is common for soft, marine clay at impact velocities <5.0 m/s (Dayal and Allen 1975). The good agreement between our dynamic CPTU measurements and the earlier pushed CPTU data attest that the approach is valid (Eqs. 9.1–9.2 and 9.3).

The soil's sensitivity, i.e. the ratio of undisturbed peak- and remolded shear-strength, is an important parameter for characterizing intrinsic weakness of sediments (e.g., Leroueil 2001). From CPT tests, Robertson and Campanella (1983) and Lunne et al. (1997) have depicted that sleeve friction is a qualitative reference for remolded undrained shear-strength measured in the laboratory, in particular for fine-grained deposits. The comparison of the FF-CPTU data to laboratory measurements on adjacent cores show, in general, similar trends (Fig. 9.3). Some deviation between the two data sets can be explained by (i) the presence of interbedded, thin layers or pockets of soft- or stiff material (thickness <0.2 m) within the surrounding glacial deposits, and (ii) the fact that the test setup (conical cone) is not suitable to obtain full remolding of the sediment. Further discrepancies in the undrained shear-strength are probably related due to the effects of over-sampling in the upper portions of the

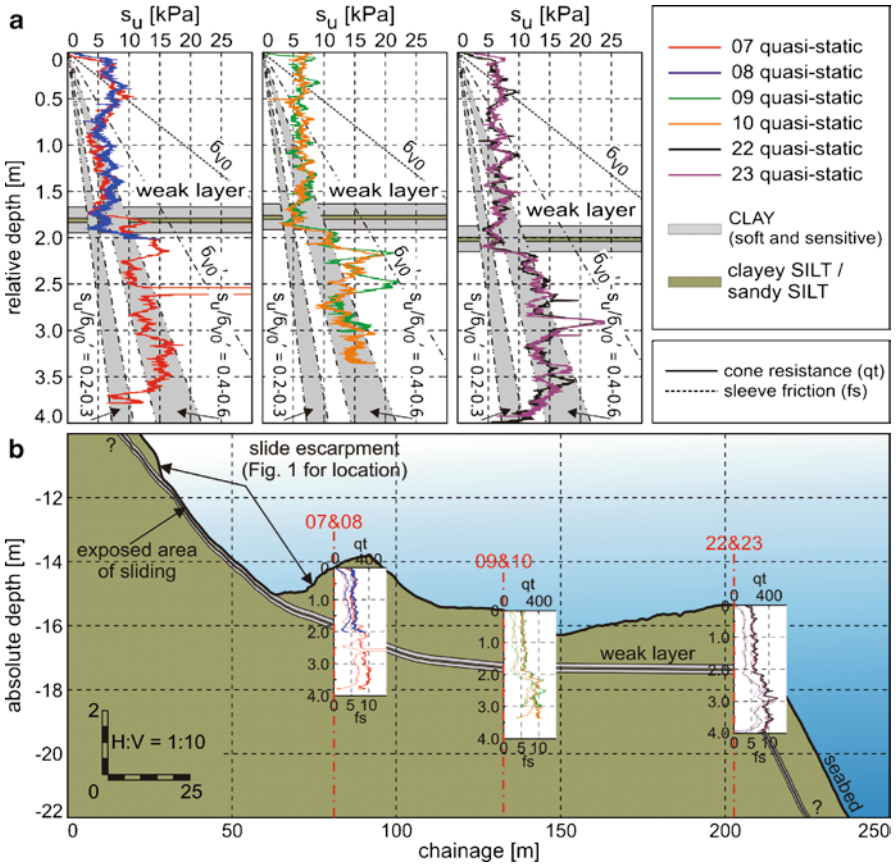

Fig. 9.5 (**a**) Analysis of the in-situ undrained shear-strength. (**b**) Geological and geotechnical ground model including cone resistance and sleeve friction profiles

calypso piston-cores and under-sampling in the gravity cores (Chap. 9.4.3; Skinner and McCave 2003). The over-sampling can be seen in the lower undrained shear-strength compared to the FF-CPTU 14 and 15 results assuming a vertical disturbance according to the dilatational effects during deployment for the calypso piston-core (Fig. 9.4). In addition, a slight compaction due to frictional forces between the core barrel and sediment inside results in higher undrained shear-strength compared to the FF-CPTU 03–06 results (Fig. 9.3).

From a geological standpoint, the FF-CPTU data provide important hints for potential slope destabilization as well as the actual location of the failure plane. Cone resistance and sleeve friction values are consistently lower by a factor of 1.5 to 2.0 in those units compared to the surrounding sediments (Figs. 9.3a, 9.4 and 9.5). These weak layers are composed of normally-consolidated, soft and sensitive clay with undrained shear-strength ratio (s_u/σ_{vo}') between 0.2 and 0.3. They are surrounded by massive, post-glacial, normally- to over-consolidated silts ($s_u/\sigma_{vo}' > 0.3$).

Consequently, these horizons are believed to represent the potential failure planes in future mass wasting events. This is of particular importance, considering that the factor of safety (from infinite slope equilibrium) lies close to 1, hinting at potentially unsafe conditions. Layers with similar characteristics were also found to affect the stability of submarine slopes along the Var delta, France (Dan et al. 2007) and in the fjord of Trondheim, Norway (L'Heureux et al. 2010). L'Heureux et al. (2012) interpreted the slide mechanism in Finneidfjord to be translational within the weak layer based on the use of integrated data sets (i.e. including the FF-CPTU data). In addition, the FF-CPTU data presented here show a contractive behavior for the mechanically weaker beds (Fig. 9.4). Hence, the failure mechanism could probably involve progressive softening of the sensitive, weak layers as also described for the Storegga slide (e.g., Kvalstad et al. 2005).

In summary, 38 FF-CPTU deployments were successfully carried out within a 3 days survey in Finneidfjord. The large amount of in-situ data collected shows the capability of the instrument to characterize complex, shallow depositional environments in a time and cost-effective way. Furthermore, the mechanically weak layers were not only identified, but characterized to be laminated with a thin seam of sand from the high-resolution FF-CPTU record (Fig. 9.5a). Therefore, this geotechnical device is well suited for exploring the shallow sub-surface of slide-prone areas in shallow water environments (Fig. 9.5b) and can be used for slope stability assessments and geohazard identification when combined with multibeam bathymetry data and high-resolution seismic (2D, 3D).

Acknowledgments We thank the SEABED project with the Norwegian Deepwater Program (www.ndwp.org) for financial support. We also thank Arild Sleipnes and the Norwegian road authorities for access to the push CPTU data as well as John Anders Dahl for the field assistance. This is publication no. 355 of the International Centre for Geohazards (ICG). The manuscript benefited from the criticism and suggestions from reviewers and editor Drs. T. Lunne, C. Baxter and J. Chaytor.

References

Casagrande A, Shannon WL (1949) Strength of soils under dynamic load. T ASCE 114:755–772

Dan G, Sultan N, Savoye B (2007) The 1979 Nice harbour catastrophe revisited: trigger mechanism inferred from geotechnical measurements and numerical modeling. Mar Geol 245:40–64

Dayal U, Allen JH (1975) The effect of penetration rate on the strength of remolded clay and sand samples. Can Geotech J 12:336–348

Haflidason H, Sejrup HP, Berstad IM, Nygard A, Richter T, Bryn P, Lien R, Berg K (2003) A weak layer feature on the northern Storegga slide escarpment. In: Mienert J, Weaver PPE (eds) European margin sediment dynamics. Springer, Berlin, pp 37–43

Janbu N (1996) Raset I Finneidfjord – 20 juni 1996. Report number 1, revision 1, unpublished experts report prepared for the County Sheriff of Nordland

Kim D-K, Tumay MT (2004) Miniature piezocone test results in cohesive soils. EJGE 9(D)

Kvalstad TJ, Andresen L, Forsberg CF, Berg K, Bryn P, Wangen M (2005) The Storegga slide: evaluation of triggering sources and slide mechanics. Mar Petrol Geol 22:245–256

L'Heureux J-S, Hansen L, Longva O, Emdal A, Grande L (2010) A multidisciplinary study of submarine landslides at the Nidelva fjord delta, Central Norway – implications for geohazards assessments. Nor J Geol 90:1–20

L'Heureux JS, Longva O, Steiner A, Hansen L, Vardy ME, Vanneste M, Brendryen J, Haflidason H, Kvalstad TJ, Forsberg CF, Chand S, Kopf A (2012) Identification of weak layers and their role for the stability of slopes at Finneidfjord, northern Norway. In: Yamada Y et al (eds) Submarine mass movements and their consequences, vol. 31, Advances in natural and technological hazards research. Springer, Dordrecht, pp 321–330

Leroueil S (2001) Natural slopes and cuts: movement and failure mechanisms. Geotechnique 51(3):197–243

Longva O, Janbu N, Blikra LH, Bøe R (2003) The 1996 Finneidfjord slide; seafloor failure and slide dynamics. In: Locat J, Mienert J (eds) Submarine mass movements and their consequences. Springer, Dordrecht, pp 531–538

Lucius J (1971) Study of the influence of speed of deformation on the strength of soil. Deut Agratech 21:526–528

Lunne T (2010) The CPT in offshore soil investigations - a historic perspective. In: Mitchell et al (eds) 2nd International symposium on cone penetration testing (CPT' 10). Huntington Beach, California

Lunne T, Robertson PK, Powell JJM (1997) Cone penetration testing in geotechnical practice. Spon Press, London

Osler JC, Furlong A, Christian H (2005) A sediment probe for the rapid assessment of seabed characteristics. In: Caiti A, Chapman NR, Hermand J-P, Jesus SM (eds) Acoustic inversion methods and experiments for assessment of the shallow water environment. Springer, New York, pp 171–182

Robertson PK, Campanella RG (1983) Interpretation of cone penetration tests. Part II: clay. Can Geotech J 20(4):734–745

Silva MF, White DJ, Bolton MD (2006) An analytical study of the effect of penetration rate on piezocone tests in clay. Int J Numer Anal Methods 30:501–527

Skinner LC, McCave IN (2003) Analysis and modelling of gravity- and piston coring based on soil mechanics. Mar Geol 199(1–2):181–204

Stegmann S (2007) Design of a free-fall penetrometer for geotechnical characterisation of saturated sediments and its geological application. PhD thesis, University Bremen, 181 pp

Stegmann S, Villinger H, Kopf A (2006) Design of a modular, marine free-fall cone penetrometer. Sea Technol 47(2):27–33

Stoll D, Yue-Feng S, Bitte I (2007) Seafloor properties from penetrometer tests. IEEE J Ocean Eng 32(1):57–63

Chapter 10
Static and Cyclic Shear Strength of Cohesive and Non-cohesive Sediments

Gauvain Wiemer, Anna Reusch, Michael Strasser, Stefan Kreiter, Daniel Otto, Tobias Mörz, and Achim Kopf

Abstract Submarine slope failures are common along tectonically and seismically active margins and may have devastating impact on onshore and offshore infrastructure as well as coastal communities. Soils show a variable response to periodic loading compared to static loading – making static and cyclic loading experiments compulsory for submarine slope stability and mass-movement initiation studies. Results from (i) a generic study investigating the shear strength of water-saturated sediments upon drained static vs. undrained cyclic loading, and from (ii) a comparison to natural samples are presented. A direct shear apparatus and the MARUM Dynamic Triaxial Testing Device have been used to compare undrained, cyclic to drained, static shear strengths of reconstituted samples with different clay to quartz (sandy silt) ratios. With this experimental set-up we aim to identify the failure potential of cohesive to granular material under cyclic and static loading condition. Results indicate that the cyclic shear strengths of material mixtures with less than 20% clay mineral content are significantly lower than their static shear strengths. Mixtures with a clay mineral content exceeding 20% show converging cyclic, undrained and static, drained shear strengths. Ongoing studies build on the knowledge gained from the generic endmember tests and integrate natural samples from the Nankai Trough accretionary wedge (Japan).

Keywords Slope failure • Shear strength • Cyclic vs. static loading • Nankai Trough

G. Wiemer (✉) • A. Reusch • S. Kreiter • D. Otto • T. Mörz • A. Kopf
MARUM – Research Center for Marine Environmental Science and Faculty of Geosciences, University of Bremen, Leobener Str, 28359 Bremen, Germany
e-mail: gauvai nwiemer@yahoo.de

M. Strasser
Geological Institute, ETH Zurich, Sonneggstrasse 5, 8092, Zürich, Switzerland

MARUM – Centre for Marine Environmental Sciences, University of Bremen, Bremen, Germany
e-mail: strasser@erdw.ethz.ch

Y. Yamada et al. (eds.), *Submarine Mass Movements and Their Consequences*, Advances in Natural and Technological Hazards Research 31,
DOI 10.1007/978-94-007-2162-3_10, © Springer Science+Business Media B.V. 2012

10.1 Introduction

Submarine landslides may occur along the shelves and slopes throughout the world's oceans and transport sediments and/or rock blocks from upslope, high potential energy positions, to downslope by converting potential to kinematic energy. A part of the energy may be transmitted to the ocean surface causing tsunamis (Feeley 2007). The costs and efforts that evolve from the damage caused by submarine mass movements make the understanding of such geo hazard crucial (Locat and Lee 2002). Scientists and geo-engineers have been investigating submarine mass movements for several decades aiming for reliable prediction and mitigation of both the initiation and the consequences. Among the numerous short-term triggers for initiation (see review by Hampton et al. 1996), earthquake shaking is a prominent one.

Given that most sediments show a different response to seismic loading than to static loading, the comparison of cyclic and static loading experiments are required for submarine slope stability and mass-movement initiation studies. Seismic activity can lead to alternating stress conditions, which usually result in a decrease in strength (see Sultan et al. 2004). Numerous cyclic triaxial tests show that granular soils often fail in conjunction with liquefaction (e.g., Singh 1995; Ishihara and Tsukamoto 2004). Liquefaction occurs when the effective stress acting upon the soil skeleton decrease due to excess pore pressure increase. Especially granular, non-cohesive sediment is prone to liquefy under low cyclic shear stress.

Failure of clayey soils may either be caused by cyclic softening, i.e. by progressive failure under cyclic loading or static shear under static loading. The presence of weak mineral phases, such as clays, causes low static shear strength and might lead to gravitational slope destabilization due to gravitational forces (Ferentinos et al. 1981; Brown et al. 2003; Huhn et al. 2006).

However, non-ambiguous allocation of sediment failure either to static loading of weak mineral phases or to granular sediment deposits that may liquefy during cyclic loading is difficult. Here we aim at addressing this challenge by comparing the shear strength of artificial sample materials with different ratios of clay mineral content upon static and cyclic loading conditions. The artificial samples are similar to different types of hemipelagic sediments occurring along continental margins. In an applied case study, we then expose natural slope-sediment samples from the Nankai Trough accretionary wedge (Japan) to cyclic loading. Earthquake shaking is common along this subduction margin (e.g., Ando 1975) so that knowledge concerning the sediment's strength to cyclic stress is indispensable.

10.2 Methods

10.2.1 Research Approach

A soil's response upon loading depends highly on the amount and type of clay minerals present (Bray and Sancio 2006). Brown et al. (2003) show within a series of ring shear tests that the static shear strength, expressed by the coefficient of residual

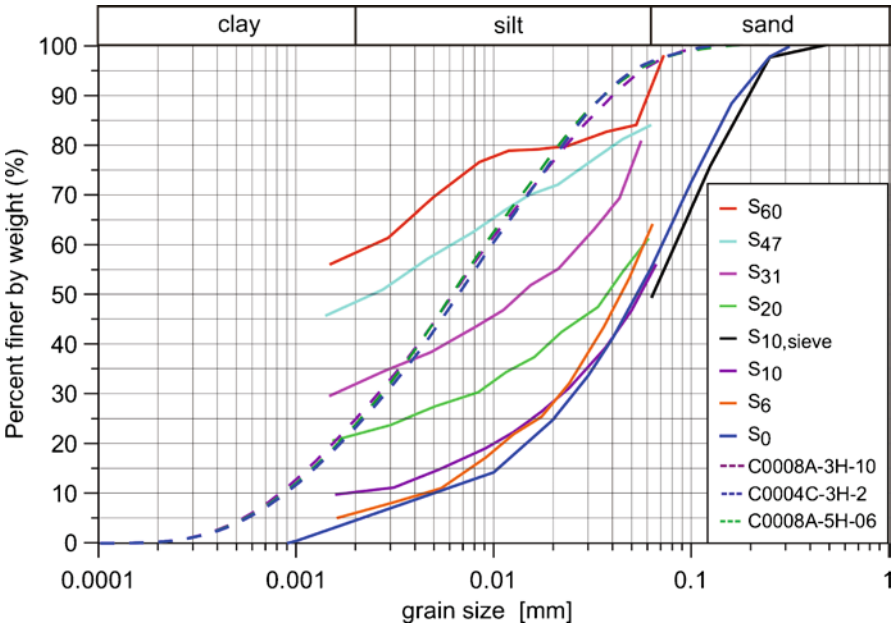

Fig. 10.1 Cumulative grain size distribution curves for all artificial samples (*continuous lines*) determined after Bouyousos-Casagrande method and natural samples (*dotted lines*) determined by laser diffraction. Indices of reconstituted sample materials indicate the clay mineral content

friction μ_r of granular, non-cohesive material (quartz) decreases from about 0.6–0.1 when mixed in ratios from 0% to 100% with cohesive, weak mineral phases (e.g., smectite, illite). On the other hand, the cyclic shear strength of silt-clay mixtures with a plasticity index exceeding 5–10 increases with increasing plasticity index (Prakash and Puri 1999).

Based on these observations we conceive a threshold value of clay mineral content of sediments at which the static shear strength might assimilate with the cyclic shear strength. In a first order approximation we compare undrained, cyclic and drained, static shear strength of reconstituted sandy silt – clay mixtures in a bandwidth of 0–60% clay mineral content. With this approach we assume that sediment excess pore pressure can be dissipated during gravitational (static) loading, whereas stress conditions during seismic (cyclic) loading change too fast to make dissipation of excess pore pressure possible. The findings of the generic study are then applied to natural slope sediment samples from the Nankai Trough.

10.2.2 Sample Description

For the generic study, all samples were reconstituted from two endmember materials in different ratios. An industrial sandy silt (99% quartz), served as granular, non-cohesive endmember (Fig. 10.1 – S_0, Table 10.1). Natural illite and montmorillonite

Table 10.1 Table shows the water content (wc), the bulk density, the mean grain size (D_{50}), grading (G_0) and the coefficient of uniformity (U) for all artificial and natural samples

Sample material	wc (%)	ρ bulk (g/cm³)	B-value≥	D_{50} (mm)	G_0	U	LL (%)	PL (%)	PI (%)	Wc/LL
S_{60}	44.3	1.68	0.95	n.d.	n.d.	n.d.	59.6	18.8	40.8	0.7
S_{47}	33.4	1.89	0.95	0.0025	16.43	n.d.	40.0	14.9	25.1	0.8
S_{31}	25.6	2.02	0.95	0.014	7.91	n.d.	29.0	12.5	16.4	0.9
S_{20}	18.0	2.12	0.81	0.040	7.30	86	20.8	10.5	10.3	0.9
S_{10}	18.7	2.19	0.95	0.065	2.30	35	n.d.	n.d.	n.d.	n.d.
S_6	18.2	2.15	0.95	0.045	2.36	16	n.d.	n.d.	n.d.	n.d.
S_0	18.8	2.12	0.95	0.065	2.35	14	n.d.	n.d.	n.d.	n.d.
S_{01}	18.8	2.12	0.95	0.065	2.35	14	n.d.	n.d.	n.d.	n.d.
S_{02}	18.8	2.12	0.95	0.065	2.35	14	n.d.	n.d.	n.d.	n.d.
C0008A-3H-10	56.4	1.82	0.77	0.0067	3.06	12	n.d.	n.d.	n.d.	n.d.
C0004C-3H-02	60.9	1.67	0.85	0.0061	2.92	11	n.d.	n.d.	n.d.	n.d.
C0008A-5H-06	60.4	1.68	0.6	0.0061	2.79	11	n.d.	n.d.	n.d.	n.d.

n.d. stands for 'no data'. The data within the grey field is based on extrapolated results. The Atterberg limits could only be assigned for sample material with 20% or more clay mineral content

LL water content at the Liquid Limit, *PL* water content at the Plastic Limit, PI=LL-PL: Plasticity Index. [C0008A-3H-10 (100.0–110.0 cm, 25.47 mbsf); C0004C-3H-02 (15.0–25.0 cm, 17.49 mbsf); C0008A-5H-06 (73.5–83.5 cm, 40.82 mbsf]

were mixed in a 50/50 ratio and served as cohesive endmember. Seven different mixtures with clay mineral contents ranging from 0% to 60% have been saturated with sea water and tested. Figure 10.1 shows the grain size distribution for all reconstituted material mixtures and the natural samples of the Nankai Trough. Note that sieve analysis was conducted only on the S_{10} sample material. The clay mineral content of the clayey endmember that results from XRD analysis equals the amount of clay size particles (<2 μm) within an error of ±5%. All silt-size particles of the clayey endmember are therefore regarded as non-cohesive.

Table 10.1 lists the index properties water content (wc), bulk density (ρ), B-value, medium grain size (D_{50}), grading (G_0) and the coefficient of uniformity (U) of the artificial and natural samples. Atterberg limits are listed for artificial samples with clay mineral contents of 20% or more.

The three natural samples from the Nankai Trough originate from undisturbed whole round core samples recovered from the hemipelagic slope apron in the mid-slope at the IODP Sites C0004 and C0008, from depths down to 41 mbsf. See Kinoshita et al. 2009, or also Strasser et al. 2012 for more information about the Nankai Trough study area, site locations and detailed description of related data and results. Sample materials consist mainly of clayey silt with little fine sand fractions. The grain size distribution curves of the natural samples are nearly congruent. In terms of clay size fraction (<2 μm) and grading the natural samples are comparable to the sample material S_{20}.

10.2.3 Testing Procedure

The direct shear apparatus GIESA RS2 that complies with DIN 18137 part 3 (1990) was used to measure the static peak shear strength of each reconstituted sample.

The direct shear box consists of two stacked rings that hold a sample of 2.5 cm height and 40 cm^2 surface. The contact between the two rings is at approximately the mid-height of the sample. The sample is placed between two porous plates to allow free drainage and then loaded vertically with constant stress until consolidation is finished. The lower ring is then pulled laterally with a rate of 0.002 mm/min (PI > 40), 0.008 mm/min (25 < PI < 40) or 0.04 mm/min (PI < 25) for a path of at least 8.5 mm until residual shear strength is reached. Static shear strength of each sample material was tested at normal stresses of 150, 300 and 450 kPa.

The cyclic shear strength was tested using the MARUM Dynamic Triaxial Testing Device (DTTD). The capacity of the DTTD is to induce cyclic stresses upon a specimen over a computer control unit that allows the user to apply up to 15 kN dynamic load at frequencies of up to 50 Hz and displacements of ±0.5 mm (see details in Kreiter et al. 2010).

Cylindrical specimens with a basal area of 10 cm^2 and a minimum height of 68.11 mm were prepared. The vacuum saturation method (i.e. applying low-pressure of – 1.0 bar to the samples with subsequent flooding with de-aired water) was applied to improve saturation for artificial samples. Saturations of 95% were

reached for six of seven samples (B-value in Table 10.1). Lower saturation ratios of 60–85% were reached for natural samples. Undrained, symmetric, cyclic loading was carried out at a loading frequency of 1.0 Hz at (i) 100 kPa initial effective confining pressure and maximum 150 cycles for artificial samples and (ii) in-situ confining pressure, without restriction of the numbers of cycles to failure for natural Nankai samples.

10.2.4 Data Acquisition and Analysis

The results of the direct shear tests were used to deduce the parameters of the Mohr-Coulomb constitutive law:

$$\tau_f = \sigma'_n \tan(\varphi') + c' \tag{10.1}$$

where φ′, is the effective angle of internal friction, c' the effective cohesion, σ'_n the effective normal stress and τ_f the shear stress, both at failure. The static shear strength at 100 kPa (the confining pressure for the cyclic triaxial tests) was calculated using the appropriate Mohr-Coulomb parameters for all the materials.

In cyclic loading experiments, the cyclic stress ratio (CSR) and the cyclic resistance ratio (CRR) are often used to quantify the cyclic load and the resistance of the sediment to that specific cyclic load (Kramer 1996). The CSR is defined as:

$$CSR = q / 2\sigma'_{3c} \tag{10.2}$$

$$\text{with } q = \sigma_{1,cyc} - \sigma'_{3c} \tag{10.3}$$

where, q is the cyclic deviator stress, $\sigma'_{1,cyc}$ is the maximum total cyclic vertical stress and σ'_{3c} is the confining pressure at the beginning of the cyclic loading. The CRR is the CSR at failure for a given number of cycles. The CRR is a measure for the capacity of a sediment layer to resist failure (Sultan et al. 2004). The ratio between CRR and CSR is the factor of cyclic safety.

The maximum shear stress and the mean normal stress under cyclic loading are defined, respectively, as:

$$\tau_{cyc} = q / 2 \quad \text{and} \tag{10.4}$$

$$\sigma'_{n,cyc} = (\sigma_{1,cyc} + 2\sigma'_{3c}) / 3 \tag{10.5}$$

Hence, the CSR can also be understood as the ratio between cyclic shear stress and the confining pressure.

The recorded parameters during cyclic loading experiments include the axial strain ε, vertical load σ_1, cell pressure $\sigma_2 = \sigma_3$ and pore pressure u. The axial strain is

defined as the vertical displacement of the piston. In order to improve the data handling and to reduce the noise the mean of 10 values of the data (sampled at 1,000 Hz) was used, resulting in 100 data points per second.

Samples were considered as failed when either:

1. Pore pressure reached 90% of the effective confining pressure within 150 cycles, i.e. when liquefaction is initiated (Kramer 1996), or when
2. Stiffness, the ratio of 2q and the double amplitude axial cyclic strain ($2\varepsilon_{cyc}$), drops below 5 GPa in case that the required pore pressure for liquefaction initiation has not been reached within 150 cycles (generic study).
3. The double amplitude axial strain exceeds 5% (after Ishihara and Tsukamoto 2004) (case study)

10.3 Results and Discussion

10.3.1 Exemplary Cyclic Test Results

Figure 10.2 shows an exemplary cyclic test record of artificial sample S_{20} and natural sample C0004C-3H-02. The stiffness of the artificial sample drops below 5 GPa after 64 cycles at a CSR of 0.26. Normalized pore pressure reaches a maximum of only 0.88. The natural sample C0004C-3H-02 reaches 5% double amplitude axial strain after 9 significant cycles at a CSR of 0.49.

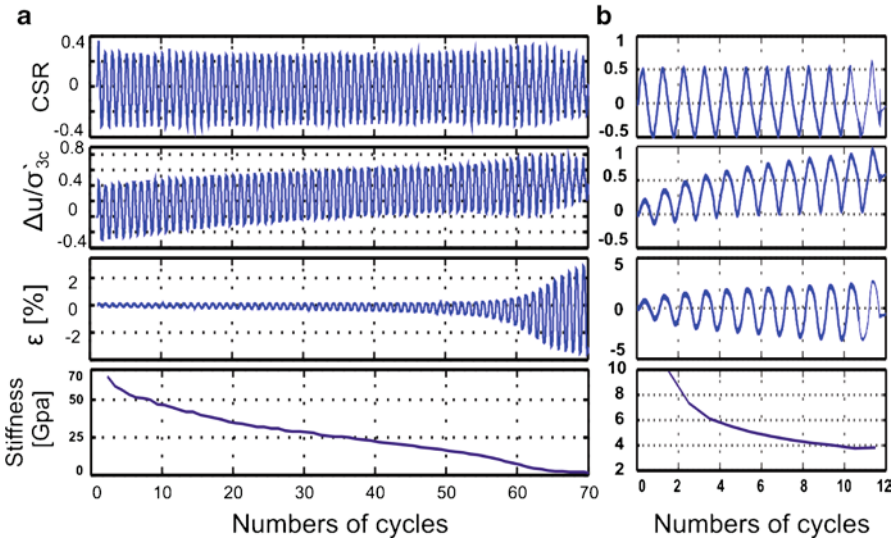

Fig. 10.2 Plot (**a**) and (**b**) show the evolution of excess pore pressure, axial strain and stiffness degradation induced by symmetric, cyclic loading, expressed in CSR with the number of loading cycles. (**a**) sample material S20 and (**b**) natural sample C0004C-3 H-02

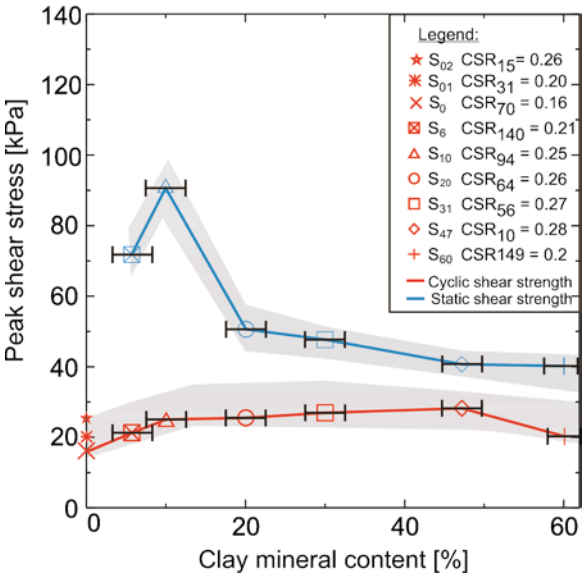

Fig. 10.3 Evolution of maximum shear stress (q/2) at failure under undrained cyclic loading [*red graph*] and the peak, drained shear strength (τ_f) [*blue graph*] under static conditions in dependence of the clay mineral content. The standard error of the XRD analysis (±5% clay mineral content) is plotted. The legend lists the sample names (S_0 to S_{60}). The indices represent the clay mineral content. The CSR and the number of cycles to failure (indices of CSR) are listed for each specimen

10.3.2 Generic Study

Figure 10.3 shows the peak, static, drained shear strength and the cyclic, undrained shear strength as derived from direct shear and DTTD tests, respectively, versus the clay mineral content of the individual artificial test samples.

Sample materials with clay mineral contents ranging between 0% and 20% show significantly higher resistivity to static shear stresses than to cyclic shear stresses. The drained, static and undrained, cyclic shear strength converge with increasing clay mineral content. Material with more than 20% clay mineral content show similar drained, static and undrained, cyclic shear strengths.

The only constraint of the cyclic test procedure is to induce failure within 150 loading cycles; at whichever cyclic shear stress. The exact number of cycles to failure must be regarded to make a prediction of a potentially lower or higher cyclic shear stress bringing the specimen to failure. Three tests have been conducted on the granular endmember (S_0, S_{01} and S_{02}). These tests show exemplarily the effect of varying cyclic shear stress on the number of cycles to failure. The grey corridors in the background of Fig. 10.3 are based on these three tests and are speculative for all other mixtures. It is meant to illustrate a conceivable bandwidth of cyclic shear stresses leading to failure within 150 cycles. This bandwidth of cyclic shear stress induces a bandwidth of static shear strength due to changing normal stress conditions. The lower boundary of the grey band results from cyclic test experiments in which failure did not occur within 150 cycles.

If the static shear strength from a direct shear box is slightly overestimated due to the constraint of a horizontal shear plane, the finding of converging drained, static and undrained, cyclic shear strength with increasing clay mineral content is supported.

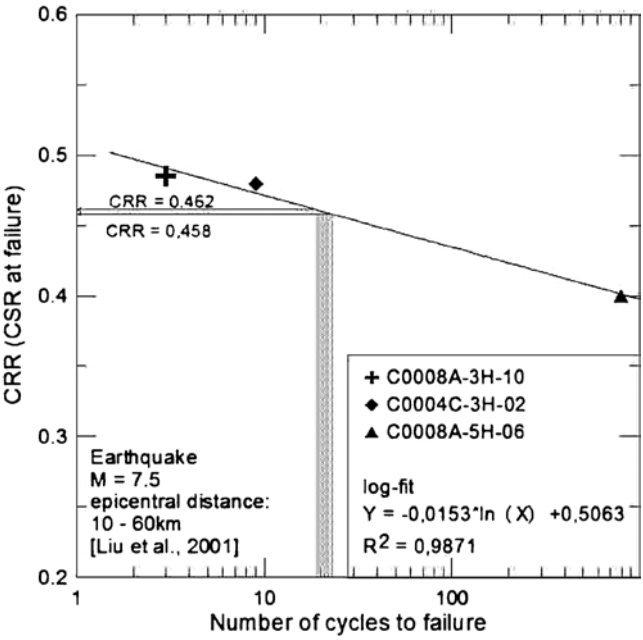

Fig. 10.4 Potential failure diagram: cyclic resistance ratio as a function of the numbers of cycles to failure of natural samples from slope sediments overlying the Nankai Trough accretionary prism. The *grey band* illustrates the example of an earthquake of magnitude 7.5 at 10–60 km epicentral distance with 19–23 significant cycles according to the empirical regression equations given by Liu et al. (2001)

10.3.3 Case Study

Grain size distribution of the natural Nankai samples show a low clay content, even though their sand content is significantly lower than the sand content of the artificial samples (see Fig. 10.1). The grain size distribution of the natural samples is comparable to artificial samples with low clay content. Therefore we tentatively follow the conclusion from the generic study that material with low clay content is less stable under cyclic loading than under static loading, and suggest that cyclic loading tests are an important factor for assessing slope stability in the Nankai Trough setting.

Figure 10.4 shows the variation of CRR as a function of the cycles to failure. To evaluate the sediment failure potential of the slope sediments covering the Nankai Trough accretionary wedge, we fitted a logarithmic trend line to the data points. Initial results from natural Nankai slope sediment samples show 5% double-amplitude strain at a CSR of 0.485 after 3 loading cycles (C0008A-3H-10), CSR of 0.48 after 9 loading cycles (C0004C-3H-02) and CSR of 0.4 after 795 loading cycles (C0008A-5H-06), respectively. It has to be noted that the sample C0008A-5H-06 experienced multiple undrained dynamic loading steps until failure, as the original applied load was too low to trigger failure. A multistage test with increasing cyclic stress and no drainage of the pore fluid pressure was performed until failure.

To conceptually show the potential of evaluating seismic slope stability using this data set, we examine critical stability conditions for a hypothetical earthquake of magnitude 7.5 in 10–60 km epicentral distance. According to empirical regression equations given by Liu et al. (2001), such an earthquake may have 19–23 significant cycles. For such a scenario, our data indicate material failure at a CSR of 0.462 for 19 significant loading cycles and CSR of 0.458 for 23 significant loading cycles. If ground shaking intensity exceeds CSR-equivalent values of 0.46 within 20 significant loading cycles, our data indicate sediment failure of the tested slope sediment samples of the Nankai Trough accretionary wedge.

Such results can then be evaluated to quantitatively assess critical ground motion scenarios on the slope stability conditions in the study area. An additional step could be to evaluate an average stress caused by the earthquake and compare this value to the CRR to estimate a factor of safety.

However, this result is only based upon three cyclic triaxial tests of representative material and more experiments are required to verify the failure criteria and account for the natural variability of the sediments.

10.4 Conclusion

The comparison of the undrained, cyclic shear strength with the drained, static shear strength of sediment with varying clay mineral content reveals a similar likelihood of slope sediment failure under static and cyclic conditions at clay mineral contents exceeding 20%. This enforces that slope destabilization may occur if weak mineral phases are present. There is no imperative need for an external, short-term stimulus to trigger soil failure.

By analyzing the clay mineral content of natural slope sediments from earthquake prone areas it is possible to assess the importance of cyclic shear strength investigation.

Initial results from natural slope sediment samples of the Nankai Trough define a preliminary empirical relationship, which – when further improved with additional tests to account for natural variability of samples – may contribute to a comprehensive submarine slope stability analysis of the Nankai Trough accretionary prism.

Acknowledgement This research used samples and data provided by the Integrated Ocean Drilling Program (IODP). This study was funded through DFG-Research Center/Cluster of Excellence "The Ocean in the Earth System". Reviewer Dr. G. Biscontin and Dr. K. Lesny are kindly acknowledged. Mathias Lange is thanked for outstanding technical assistance with the DTTD and Direct Shear devices. Alois Steiner is thanked for constructive ideas and discussions.

References

Ando M (1975) Source mechanisms and tectonic significance of historical earthquakes along the Nankai Trough, Japan. Tectonophysics 27(2):119–140. doi:10.1016/0040-1951(75)90102-X

Bray JD, Sancio RB (2006) Assessment of the liquefaction susceptibility of fine-grained soils. J Geotech Geoenviron 132(9):1165–1177

Brown KM, Kopf A, Underwood MB, Weinberger JL (2003) Compositional and fluid pressure controls on the state of stress on the Nankai subduction thrust: a weak plate boundary. Earth Planet Sci Lett 214(3–4):589–603

DIN Deutsche Institut für Normung e. V (1990) DIN 18137-Bestimmung der Scherfestigkeit. Beuth, Berlin

Feeley K (2007) Triggering mechanisms of submarine landslides. Research report department of civil and environmental engineering northeastern university, Boston 02115, 2007

Ferentinos G, Brooks M, Collins M (1981) Gravity induced deformation on the north flank and floor of the Sporadhes basin of the North Aegean Sea Trough. Mar Geol 44:289–302

Hampton MA, Lee HJ, Locat J (1996) Submarine landslides. Rev Geophys 34(1):33–59

Huhn K, Kock I, Kopf A (2006) Comparative numerical and analogue shear box experiments and their implications for the mechanics along the failure plane of landslides. Nor J Geol 86(3):209–220

Ishihara K, Tsukamoto Y (2004) Cyclic strength of imperfectly saturated sands and analysis of liquefaction. Proc Jpn Acad Ser B 80:372–391

Kinoshita M, Tobin H, Ashi J, Kimura G, Lallemant S, Screaton EJ, Curewitz D, Masago H, Moe KT the Expedition 314/315/316 Scientists (2009) Proceeding IODP, 314/315/316, Washington, DC (Integrated Ocean Drilling Program Management International, Inc.). doi:10.2204/iodp.proc.314315316.2009

Kramer SL (1996) Geotechnical earthquake engineering. Prentice Hall, Upper Saddle River

Kreiter S, Moerz T, Strasser M, Lange M, Schunn W, Schlue BF, Otto D, Kopf A (2010) Advanced dynamic soil testing – introducing the new marum dynamic triaxial testing device. In: Mosher DC, Shipp C, Moscardelli L, Chaytor JD, Baxter CDP, Lee HJ, Urgeles R (eds) Submarine mass movements and their consequences. Springer, Dordrecht/Heidelberg/London/New York, pp 31–42

Liu AH, Stewart JP, Abrahamson NA, Moriwaki Y (2001) Equivalent number of uniform stress cycles for soil liquefaction analysis. J Geotech Geoenviron Eng 127:1017–1026. doi:10.1061/(ASCE) 1090-0241(2001) 127:12(1017)

Locat J, Lee HJ (2002) Submarine landslides: advances and challenges. Can Geotech J 39(1):193–212

Prakash S, Puri VK (1999) Liquefaction of silts and silt-clay mixtures. J Geotech Geoenviron Eng 125(8):706–710

Singh S (1995) Liquefaction characteristics of silts. Geotech Geol Eng 14:1–19

Strasser M, Henry P, Kanamatsu T, Thu MK, Moore GF, and the IODP expedition 333 scientists (2012) Scientific drilling of mass-transport deposits in the Nankai accretionary wedge: first results from IODP expedition 333. In: Yamada Y et al (eds) Submarine mass movements and their consequences, vol. 31, Advances in natural and technological hazards research. Springer, Dordrecht, pp 674–682. doi 10.1007/978-94-007-2162-3_60

Sultan N, Cochonat P, Canals M, Cattaneo A, Dennielou B, Haflidason H, Laberg JS, Long D, Mienert J, Trincardi F, Urgeles R, Vorren TO, Wilson C (2004) Triggering mechanisms of slope instability processes and sediment failures on continental margins: a geotechnical approach. Mar Geol 213:291–321

Chapter 11
Upstream Migration of Knickpoints: Geotechnical Considerations

Dominique Turmel, Jacques Locat, and Gary Parker

Abstract Multiple knickpoints have been observed in recent years on the lakefloor of Wabush Lake, Labrador, Canada. Two or more sequential high-resolution geophysical surveys have revealed that these knickpoints tend to migrate updip, i.e. upstream relative to the turbidity currents that overflow them. In order to understand the different processes accountable for the migration of these knickpoints, laboratory studies have been performed to reproduce the sedimentological setting and hydrodynamics of Wabush Lake. Knickpoints are topographic depressions, characterized by a steep slope and a flatter profile downslope and upslope. In the present case they are initiated by morphodynamic interaction between an erodible bed and an overriding turbidity current. A set of 22 experiments have been performed in a facility able to run continuous turbidity currents. Knickpoints created in laboratory are up to 1 cm deep and migrate upstream at variable speed. Experimentation results show that migration of the knickpoints is controlled by two factors: erosion by the turbidity current and a landsliding process in the knickpoint head scarp. Knickpoint migration has also been observed when no turbidity current was present. These results show that this phenomenon is governed by not only hydraulics, as previously described in the literature, but must also be studied from a geotechnical point of view.

Keywords Knickpoints • Landslides • Turbidity currents • Physical modeling

D. Turmel (✉) • J. Locat
Laboratoire d'études sur les risques naturels, Département de géologie et de génie géologique, Université Laval, Québec, QC, Canada G1K 7P4
e-mail: dominique.turmel.1@ulaval.ca

G. Parker
Ven Te Chow Hydrosystems Lab, Department of Civil Engineering, College of Engineering, University of Illinois at Urbana-Champaign, Urbana, IL 61802, USA

Y. Yamada et al. (eds.), *Submarine Mass Movements and Their Consequences*, Advances in Natural and Technological Hazards Research 31,
DOI 10.1007/978-94-007-2162-3_11,

11.1 Introduction

Wabush Lake, located in Labrador, Canada, is a lake where very high sedimentation rates are seen. Wabush Lake, as detailed in Turmel et al. (2010), has a length of approximately 15 km in an N-S orientation and is 3.5 km wide (Fig. 11.1). A trench up to 90 meters deep runs through most of the Lake in an N-S orientation. On both sides of the trench, benches are present. Using multiple bathymetric surveys as well as seismic surveys, the evolu tion of Wabush Lake morphology has been monitored between 1999 and 2008 (Turmel et al. 2010) providing a unique occasion of monitoring multiple channel evolution. Knickpoints are shown to be at the head of most of these channels, and were found to migrate upstream between each survey. Knickpoints can be defined as bed depressions with a steep gradient on the upstream side and a gentle slope on the downstream side (Toniolo and Cantelli 2007). It is speculated that

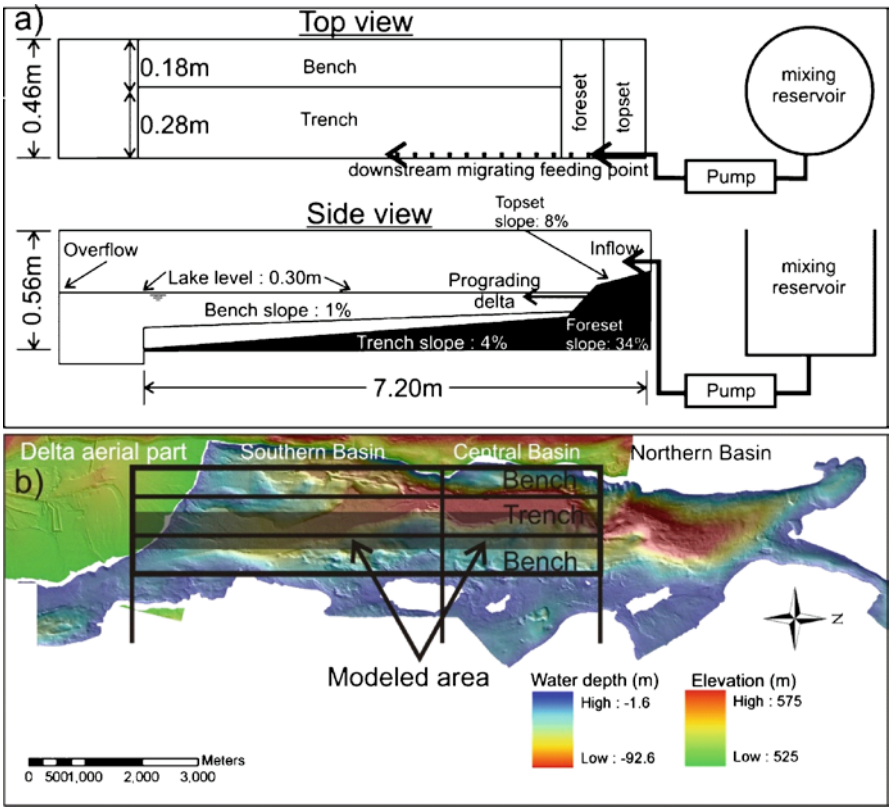

Fig. 11.1 (**a**) shows the laboratory settings, from the *side* and from the *top*. The setting used is a simplification of Wabush Lake morphology; (**b**) shows Wabush Lake bathymetry and the part of the lake modeled in laboratory. The modeled area has been shaded (Modified from Fernandez et al. 2011)

knickpoints are found in areas where turbidity current characteristics are modified by submerged hydraulic jumps (Normark et al. 1979; Mitchell 2006; Toniolo and Cantelli 2007). Fildani et al. (2006), for example, have identified a series of scour holes on the Monterey East Channel as upstream-migrating features created by a morphodynamic interaction between an erodible bed and an overriding turbidity current punctuated by hydraulic jumps (cyclic steps; see also Kostic et al. (2010)). Since turbidity current-bed morphodynamic interaction is not easily followed in the field, physical experiments are necessary in order to understand the different process responsible for the creation and migration of knickpoints. Toniolo and Cantelli (2007) conclude that upstream migration of knickpoints is due to net erosion rather than geotechnical instability, such as landsliding process. Here Wabush Lake has been used as prototype in order to design and perform physical experiments specifically designed to reproduce evolution of that lake. Evidence of landsliding process has been found in these experiments, whether the turbidity currents were present or not. The experimental method will first be described, and then some results where landsliding processes were present will be presented and discussed.

11.2 Experimental Setup and Method

Experimental work was conducted at the Ven Te Chow Hydrosystems Laboratory, University of Illinois at Urbana-Champaign, in a flume designed to approximate half the width of the trench and one-fourth of the width of the east bench found in Wabush Lake (Fig. 11.1). The flume is a transparent tank 7.2 m long, 0.46 m wide and 0.55 m deep. Geometric scaling (Ω) was distorted by a factor of 5: $\Omega = X_r / Y_r = 5$, with a horizontal scale factor (X_r) of 1,250 and a vertical scale factor (Y_r) of 250. Using this distortion factor to approximate Wabush Lake geometry, trench slope has been set to 4 percent and bench slope has been set to 1% (Fig. 11.1a). The geometric scaling used in this experiment is described in more details in Fernandez et al. (2011).

The key factor in the creation of the knickpoints studied here is the presence of a turbidity current overriding an erodible bed (e.g., Mitchell 2006; Toniolo and Cantelli 2007). Turbidity currents in Wabush Lake are sustained continuously due to the constant disposal of tailings from a mine. The turbidity currents themselves have been scaled from the Lake to the model using similitude in the densimetric Froude number, which is defined as $F_D = U / \sqrt{RgCh}$, where U is the mean velocity of the turbidity current, R the submerged specific gravity of the sediment (~1.67 for quartz), g the gravitational acceleration, C the volumetric concentration of suspended sediment and h the height of the turbidity current. Froude similarity requires that F_D must be the same for both the Lake turbidity current and the laboratory model turbidity current. Considering the difference in the submerged specific gravity of the sediment used in the model (quartz ~1.67) and that found in Wabush Lake (~2.05), the excess in density ($R*C$) was made equal between Lake and model. The sediment, *i.e.* silica flour, used in the laboratory tests were also scaled to the prototype, according to fall velocity. More information about turbidity current scaling can be found in Fernandez et al. (2011).

The material used in laboratory is quartz sand and has an estimated friction angle of 33° (Bolton 1986). At very low stress (less than 1 kPa), sand can have cohesion of up to 125 Pa (Krantz 1991; Schellart 2000; Lohrmann et al. 2003).

At the beginning of the experiment, the flume was first pre-filled with sediment-free fresh water. Water and sediment were then mixed in a 0.2 m^3 mixing tank, at concentrations between 2.5% and 10% by volume. The mixture was released in the flume by means of a peristaltic pump, at various flow rates. The flow rate and the sediment concentration were held constant for a particular experiment. Delta construction was achieved by running several experiments; the sediment was not removed from the flume between each experiment.

Because of an increase in water turbidity with time, pictures from the top were limited at the beginning of each experiment while those from the side of the tank were taken for most of the time. Pictures were taken at 3–10 s intervals. These side pictures allowed measurements at millimetric resolution of the morphological features. The contrast and brightness of the pictures presented in this paper were adjusted for a better image clarity.

11.3 Results

Subaqueous knickpoints were observed in a majority of the experiments. Only a selection of three data sets of laboratory results is presented in this paper. The first set represents a sequence where photographs were taken from the top of the flume (Fig. 11.2). The second set consists of a sequence where photographs were taken from the side of the flume (Fig. 11.3). The last set shows, from the side of the flume, the evolution of knickpoints in the absence of turbidity currents (Fig. 11.4). The first two sequences were taken during the same experiment, where sediment concentration was 2.5% and flow rate was 200 ml/min. The third set of data was taken after an experiment during which sediment concentration was also 2.5%, but with a higher flow rate at 700 ml/min.

The first set of data (Fig. 11.2) presented shows the evolution of the delta foreset for a period of 48 s. All frames are separated by 3 s, and represent an approximately 10 cm × 10 cm section of the delta foreset. The turbidity current direction, visible as a blur under the black arrow in Frame 1, is visible on all frames and is always in the same direction, from the lower right of the frames toward the upper left of the frame. The elevation of the foreset is higher in the lower right corner of the frames than in the upper left of the frames.

The first frame (Frame 1) of Fig. 11.2 shows the debris of a previous landslide (not shown) in the knickpoint. Six seconds later (Frame 3), the debris has been totally evacuated from the scar. Tension cracks are visible 3 s later under the turbidity current (Frame 4). Along these tension cracks, a landslide appears 3 s later (Frame 5), and retrogression is also present: new tension cracks are seen to be present behind the ones in Frame 4. The debris of these landslides are totally evacuated 6 s later (Frame 7). This leaves a 1.5 cm wide by 1.5 cm long landslide when compared to the original

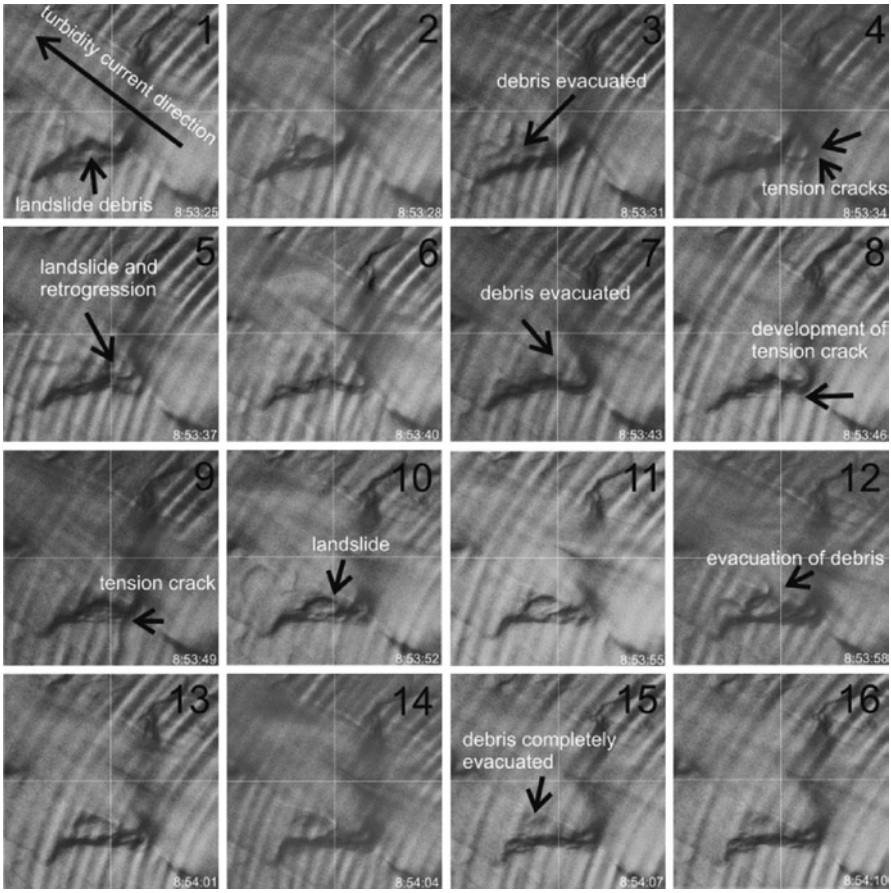

Fig. 11.2 Pictures (16) taken at 3 s intervals show the evolution of a knickpoint subjected to two landsliding events (Frames 5 and 10). See text for explanation. The *curved lines* present on all pictures are waves at the water surface

profile (Frame 3). A tension crack then develops 3 s later (Frame 8) on the sides of the landslide scar. Three to six seconds later (Frame 9 and 10), a landslide develops, and the resulting debris is completely evacuated by the time of frame 15.

The second set of data (Fig. 11.3) shows, from the side of the flume, a landslide event which occurred later in the same experiment. This figure shows 8 frames, separated by 3 s, of a 5 cm × 5 cm section of the delta foreset. The white dashed line in all the frames represents the delta profile before the landslides and the black line in the first frame represents the final profile after 24 s. Before the landslides, it is possible to observe that the mean slope angle between the toe of the surface of rupture of the landslide and its crown is near 49°, with a maximum of 75° in its lower section. Sand cohesion present at very low shear stress or grain interlocking effects (Sture et al. 1998) may explain the very high slopes reached in these experiments.

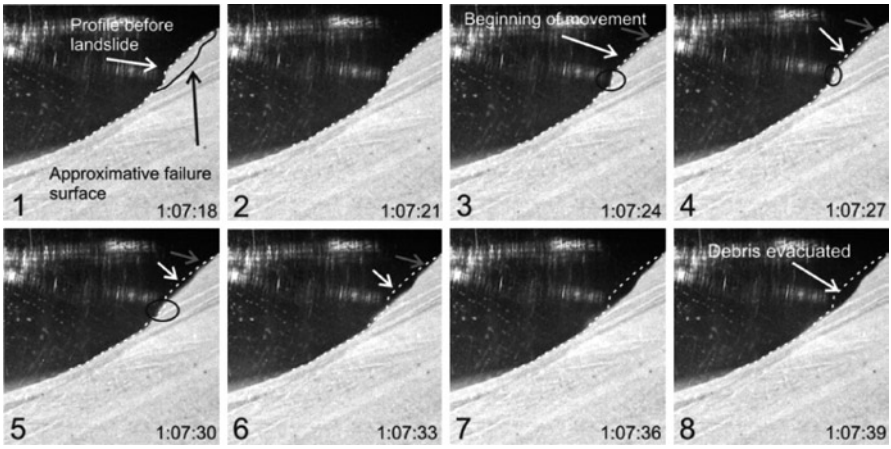

Fig. 11.3 A series of eight pictures taken at an interval of 3 s shows the evolution of a knickpoint subjected to a landslide. Each frame is 5 cm long by 5 cm wide. The *white dotted line* shows the initial profile and the black line in the first frame shows the final profile. See text for details

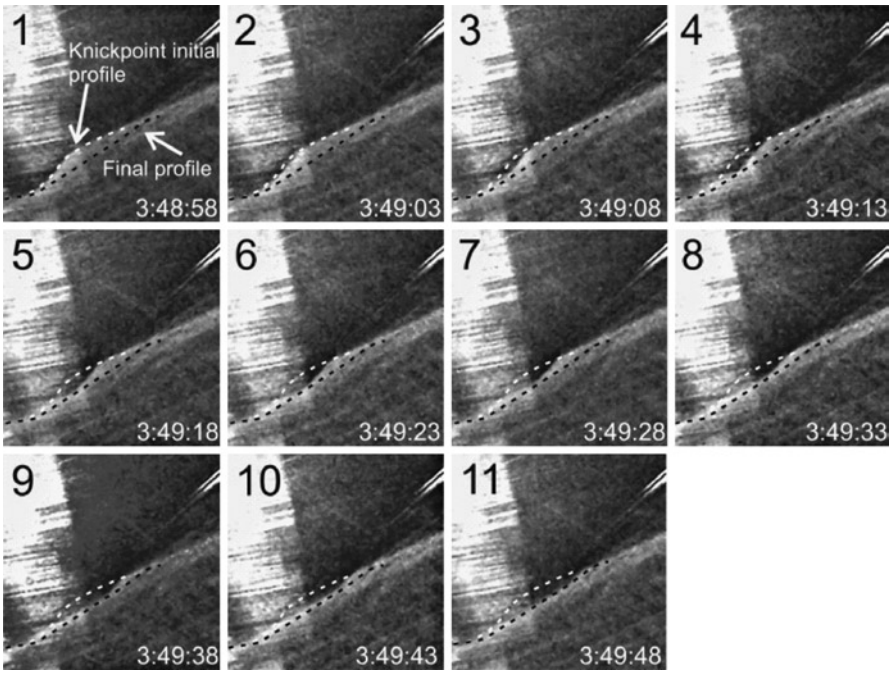

Fig. 11.4 These 11 pictures shows the evolution of a knickpoint when no turbidity currents are present into the flume. Taken at 5 s interval, these pictures are 3 cm wide by 3 cm long. *White line* shows the initial profile and the *black line* shows the final profile

The landsliding process starts at frame 3, where the sediment surface lowers compared to the initial profile in the upper part of the slope (white arrows in the figure). In the same frame, the deformed sediments cross the original profile at the lower boundary of the landslide (section marked with a circle). A more prominent deformation is visible in frames 4 and 5, where more downslope movement appeared as compared to the initial profile (as indicated by white arrows). Debris are still visible in the circled areas but the debris volume is less than the material previously evacuated. Most of the movement between frame 3 and 5 appeared in the lower section of the slope, with minor movement in the upper section of the slope (grey arrows). Frame 6 shows that 9 s after the beginning of the movement (Frame 3), the most profound rupture has almost been evacuated of all debris. The rupture is about 0.5 cm deep. The upper failure is now more visible. Six seconds later, all debris has been evacuated from the scar. After the landslide, the angle of the lower main scarp is 53°, and that of the higher main scarp is 45°.

The last set of data (Fig. 11.4) shows the evolution of a 3 cm × 3 cm section of the delta foreset for a period of 50 s, with the help of 11 frames taken at 5 s intervals. Sediment and water input was terminated at the time when these pictures were taken, so no hyperpycnal flow was present in the flume. In all frames, the white line shows the original profile and the black line shows the profile after 50 s. The initial knickpoint slope is 51° and the original upslope and downslope slopes are 24.1° and 24.5° respectively. The evolution between the different frames shows that even when no turbidity currents are present, the knickpoint is migrating upslope toward the delta shoreline. The slope and height of the knickpoint are decreasing between the different frames, indicating a behavior which differs from that seen when turbidity currents are present. The resulting slope is 31°.

11.4 Discussion

The first experimental set described (Fig. 11.2) shows the evolution of a knickpoint still subject to an overriding turbidity current, as viewed from the top of the flume. During the 48-s period presented, at least two phases of landsliding events are visible, enabling knickpoint to migrate upslope over 2 cm. The two landslides have different character; which could be due to their position within the knickpoint. The first landslide occurs under the turbidity current, in the center of the knickpoint. This landslide is longer than wider. The other landslide occurs on the banks of the knickpoint, but not under the turbidity currents. It apparently occurs as a result of the first slide. This landslide is wider than larger. Figure 11.2 also shows that knickpoints may be wider than the turbidity current, in part due to landslides occurring on the edges of the channel formed by the migrating knickpoint.

Based on Fig. 11.3, landslides are observed when knickpoint faces become very steep. Mean slopes over 45° and local slopes over 75° are seen during the experiments. Such steep slopes are the result of local erosion by turbidity currents. A general limit equilibrium stability analysis of this slope in drained conditions

shows a factor of safety less than 1 for a friction coefficient less than 42° and no cohesion. With a friction coefficient of 33°, expected for this kind of material, cohesion of approximately 5 Pa is necessary to obtain a factor of safety of 1. Contrary to the conclusions of Toniolo and Cantelli (2007) it is here possible to conclude that the upstream migration of knickpoints can be ascribed to geotechnical instability, in addition to morphodynamic interaction with an overriding turbidity current.

Observations of knickpoint migration for the case when no turbidity currents are present (Fig. 11.4) indicates that factors other than erosion by turbidity currents are needed to explain such migration. The knickpoint migration in the case where no turbidity currents are present, however, shows a different morphology from that subject to an overriding turbidity current. In this former scenario, the knickpoint totally disappears during the migration, leading to a flatter profile rather than keeping approximately the same shape up to the shoreline. This process seems very similar to breaching failures described by Van den Berg et al. (2002) which results in a gradual retrogradation of a steep subaqueous slope (Torrey 1995), as a result of shear-dilatancy effect (Breusers 1974; Meijer and van Os 1976). Such failures are common in dredging activities (e.g., Van Den Berg et al. 2002; Mastbergen and Van Den Berg 2003; Raaijmakers 2005; Eke et al. 2009) when those activities create steep slopes in lightly overdensified sandy material. Then, migration of knickpoints is possible, even if no turbidity currents are over the slope and that the knickpoint slope is higher than the internal friction angle, but turbidity currents are still necessary to maintain the shape of the knickpoint. Erosion process by turbidity currents then seems faster than breaching process.

11.5 Conclusion

Multiple knickpoints were observed in laboratory experiments designed to simulate the dynamics of those observed in Wabush Lake.

The experiments show that landslide events are associated with these knickpoints. Landslide events appear either under the turbidity currents creating the knickpoint or on the edges of the channel created by the migrating knickpoints. The morphology of the knickpoints prior to these landslides shows a very steep face. General limit equilibrium slope stability analysis of one of these landslide shows that the slope is unstable ($FS < 1$) for internal friction angles below 42°. No data is available concerning the friction coefficient of the material used in laboratory, but in the case of quartz, it is expected to be between 30° and 35°. The presence of very steep slopes in the experiments may be explained by the cohesion in sand subjected to very low shear stress (e.g., Lohrmann et al. 2003) or due to grain interlocking effects (Sture et al. 1998). Knickpoint migration is also observed when no turbidity currents are present in the flume. This migration could be explained by a process similar to breaching failures seen in dredging activities.

Acknowledgments The authors are grateful to A. Waratuke, E. Eke and E. Viparelli for their help with the experiments. We thank the Fonds de recherche sur la nature et la technologie du Québec (FQRNT) for a student grant to Dominique Turmel. We also thank Rio Tinto and the National Science and Engineering Research Council of Canada for their financial support. The authors would also like to acknowledge both reviewers, Hajime Naruse and Norihiro Izumi, for their constructive remarks.

References

Bolton MD (1986) The strength and dilatancy of sands. Geotechnique 36(1):65–78

Breusers H (1974) Suction of sand. Bull Eng Geol Environ 10(1):65–66. doi:10.1007/BF02634636

Eke E, Parker G, Ruiyu W (2009) Breaching as a mechanism for generating sustained turbidity currents. In: 33rd internation association of hydraulic engineering & research congress: water engineering for a sustainable environment, Vancouver, IAHR

Fernandez Rl, Cauchon-Voyer G, Locat J, Dai H-H, Garcia Mh, Parker G (2011) Co-evolving delta faces under the condition of a moving sediment source. J Hydraul Res 49(1):42–54. doi:10.1080/00221686.2010.538577

Fildani A, Normark Wr, Kostic S, Parker G (2006) Channel formation by flow stripping: large-scale scour features along the Monterey East Channel and their relation to sediment waves. Sedimentology 53(6):1265–1287. doi:10.1111/j.1365-3091.2006.00812.x

Kostic S, Sequeiros O, Spinewine B, Parker G (2010) Cyclic steps: a phenomenon of supercritical shallow flow from the high mountains to the bottom of the ocean. J Hydro-Environ Res 3(4):167–172. doi:10.1016/j.jher.2009.10.002

Krantz Rw (1991) Measurements of friction coefficients and cohesion for faulting and fault reactivation in laboratory models using sand and sand mixtures. Tectonophysics 188(1–2):203–207

Lohrmann J, Kukowski N, Adam J, Oncken O (2003) The impact of analogue material properties on the geometry, kinematics, and dynamics of convergent sand wedges. J Struct Geol 25(10):1691–1711. doi:10.1016/S0191-8141(03)00005-1

Mastbergen D, Van Den Berg J (2003) Breaching in fine sands and the generation of sustained turbidity currents in submarine canyons. Sedimentology 50(4):625–637

Meijer K, Van Os A (1976) Pore pressures near moving underwater slope. J Geotech Eng Div 102(4):361–372

Mitchell N (2006) Morphologies of knickpoints in submarine canyons. Bull Geol Soc Am 118(5–6):589–605. doi:10.1130/B25772.1

Normark W, Piper D, Hess G (1979) Distributary channel, sand lobes, and mesotopography of Navy submarine fan, California Borderland, with applications to ancient fan sediments. Sedimentology 26:749–774

Raaijmakers T (2005) Submarine slope development of dredged trenches and channels. Delft University of Technology, Delft

Schellart W (2000) Shear test results for cohesion and friction coefficients for different granular materials: scaling implications for their usage in analogue modelling. Tectonophysics 324(1–2):1–16. doi:10.1016/S0040-1951(00)00111-6

Sture S, Costes N, Batiste S, Lankton M, Alshibli K, Jeremic B, Swanson R, Frank M (1998) Mechanics of granular materials at low effective stresses. J Aerosp Eng 11(3):67–72. doi:10.1061/(ASCE)0893-1321(1998) 11:3(67)

Toniolo H, Cantelli A (2007) Experiments on upstream-migrating submarine knickpoints. J Sediment Res 77:772–783. doi:10.2110/jsr.2007.067

Torrey V (1995) Retrogressive failures in sand deposits of the Mississippi River. In: Thorne CR, Abt SR, Barends FBJ, Maynord ST, Pilarczyk KW (eds) River, coastal, and shoreline protection: erosion control using riprap and armourstone. Wiley, Chichester, pp 361–377

Turmel D, Locat J, Cauchon-Voyer G, Lavoie C, Simpkin P, Parker G, Lauzière P (2010) Morphodynamic and slope instability observations at Wabush Lake, Labrador. In: Submarine mass movements and their consequences, vol 28, Advances in natural and technological hazards research. Springer, Dordrecht, pp 435–446, doi:10.1007/978-90-481-3071-9

Van Den Berg J, Van Gelder A, Mastbergen D (2002) The importance of breaching as a mechanism of subaqueous slope failure in fine sand. Sedimentology 49(1):81–95. doi:10.1111/j.1525-139X.2006.00168.x-i1

Part II
Seafloor Geomorphology for Trigger Mechanisms and Landslide Dynamics

Chapter 12
A Reevaluation of the Munson-Nygren-Retriever Submarine Landslide Complex, Georges Bank Lower Slope, Western North Atlantic

Jason D. Chaytor, David C. Twichell, and Uri S. ten Brink

Abstract The Munson-Nygren-Retriever (MNR) landslide complex is a series of distinct submarine landslides located between Nygren and Powell canyons on the Georges Bank lower slope. These landslides were first imaged in 1978 using widely-spaced seismic reflection profiles and were further investigated using continuous coverage GLORIA sidescan imagery collected over the landslide complex in 1987. Recent acquisition of high-resolution multibeam bathymetry across these landslides has provided an unprecedented view of their complex morphology and allows for a more detailed investigation of their evacuation and deposit morphologies and sizes, modes of failure, and relationship to the adjacent sections of the margin, including the identification of an additional landslide within the MNR complex, referred to here as the Pickett slide. The evacuation zone of these landslides covers an area of approximately 1,780 km^2. The headwalls of these landslides are at a depth of approximately 1,800 m, with evacuation extending for approximately 60 km downslope to the top of the continental rise. High-relief debris deposits, in the form of blocks and ridges, are present down the length of the majority of the evacuation zones and within the deposition area at the base of the slope. On the continental rise, the deposits from each of the most recent failures of the MNR complex landslides merge with debris from earlier continental slope failures, canyon and along-slope derived deposits, and prominent upper-rise failures.

Keywords Canyons • Multibeam bathymetry • Debris deposits • Seismic reflection

J.D. Chaytor (✉) • D.C. Twichell • U.S. ten Brink
U.S. Geological Survey, USGS Woods Hole Coastal and Marine Science Center,
Woods Hole, MA 02543, USA
e-mail: jchaytor@usgs.gov

Y. Yamada et al. (eds.), *Submarine Mass Movements and Their Consequences*,
Advances in Natural and Technological Hazards Research 31,
DOI 10.1007/978-94-007-2162-3_12, © Springer (outside the USA) 2011

12.1 Introduction

The lower continental slope and upper rise off Georges Bank, east of Massachusetts, USA (Fig. 12.1), is known for some time to be the location of several large submarine landslides (e.g., Scanlon 1984), but the spatial and temporal distribution of

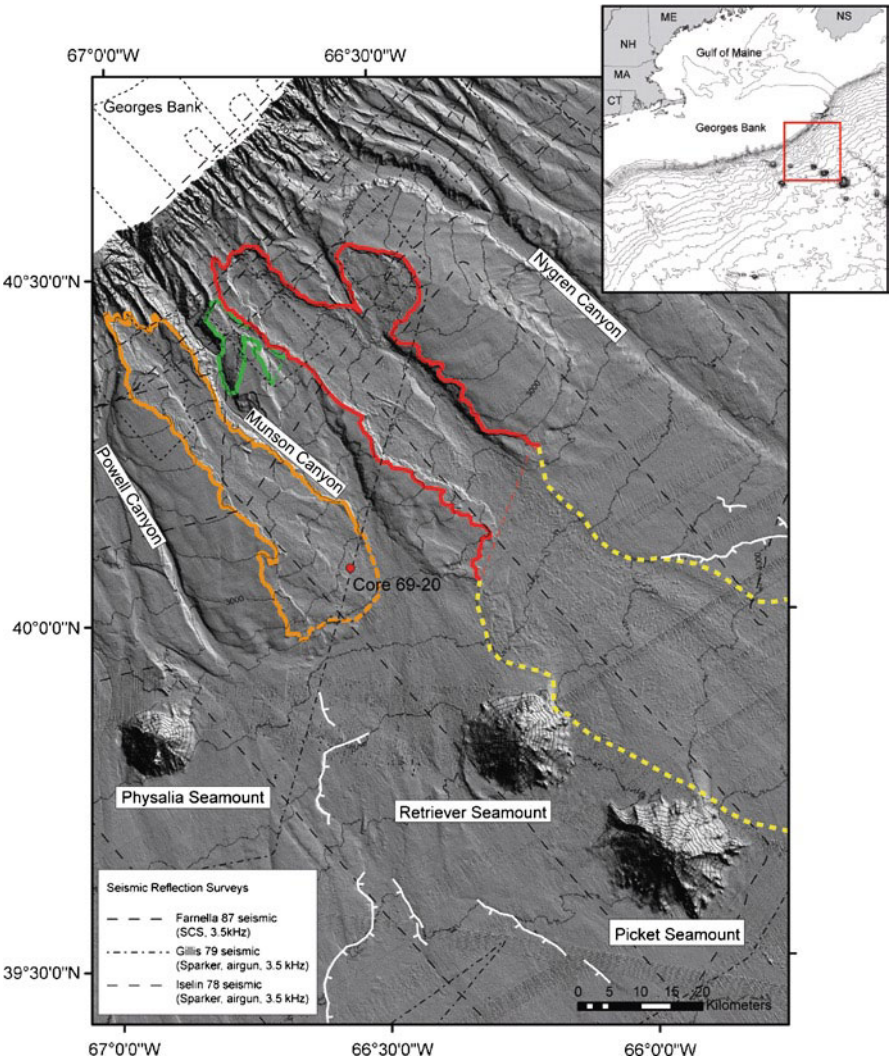

Fig. 12.1 Shaded-relief bathymetry of the MNR complex area with the Munson-Nygren (*red*), Retriever (*orange*) and Picket (*green*) submarine landslide scars (evacuation zones) *highlighted*. The debris deposit of the Munson-Nygren slide is outlined by the yellow dashed line. Upper rise landslide scars are marked in *white*. Seismic reflection profiles that cover the area are also shown. *Inset* shows the location of the study area

slope failure has proven elusive. O'Leary (1986a) using seismic reflection profiles provided the first detailed examination of the lower slope off Georges Bank specifically for the characterization of the Munson-Nygren landslide. Using additional data collected as part of the 1987 GLORIA surveys along the US east coast, O'Leary (1993) observed that the Retriever slide was a distinct feature adjacent to, but not part of the Munson-Nygren slide and resolved three time periods of landslide activity.

The continental slope and upper rise along Georges Bank consists of a layered succession of Cretaceous through Cenozoic sediments overlying a basement of Triassic breakup and Jurassic reef units (Poag 1982). The scars for each of the landslides in the MNR complex incise the Layered Rise Unit (LRU) of O'Leary (1986b, 1988) or upper continental rise sedimentary wedge of Danforth and Schwab (1990), which onlaps Upper Cretaceous-Paleocene age lower slope units (Poag 1982). O'Leary (1988) identified three subunits of the LRU based on seismic data: (1) an upper layered subunit consisting of Pleistocene to Pliocene silty-clay; (2) a middle transparent subunit of Pliocene to early Oligocene pelite; and (3) a lower parallel-layered subunit of Eocene stratified mudstones. Danforth and Schwab (1990) identified four seismostratigraphic units within the LRU and concluded that the age of the base of the section is mid- to late Miocene (Merlin reflector). Local variability within the LRU is present along the margin due to interfingering of locally derived slope and shelf material deposited by debris flows and turbidites. It is likely that sections of the LRU are time-correlative, if not downslope extensions of, similar Tertiary sedimentary units along the upper slope above the MNR complex.

In this paper, we use newly acquired multibeam bathymetry data and previously collected subbottom reflection data to reevaluate the surficial morphological features and relative ages of the landslides (slides) within the MNR complex. A more detailed understanding of these characteristics of the slides is required in order to investigate their potential pre-conditioning factors, triggering mechanisms, and failure processes.

12.1.1 Data

A new multibeam bathymetry compilation was the primary source of information used in the reevaluation of the MNR complex (Fig. 12.1). This new compilation merged multibeam data from the 2005 University of New Hampshire (UNH) USNS Henson 4–1 survey undertaken as part of the U.S. extended continental shelf program (Gardner et al. 2006) and a 2009 U.S. Geological Survey (USGS) cruise on the NOAA Ship Ronald H. Brown. The UNH data were acquired with a Kongsberg EM121 and extend from water depths of ~1,800 to over 4,000 m, while the USGS data were acquired with a SeaBeam 2112 and cover the upper slope from water depths of ~400 to 1,800 m. The merged data were gridded at resolutions of 100 m, and where data density was sufficiently high, 30 m.

Single-channel (airgun and sparker) and 3.5 kHz seismic reflection profiles collected from the late 1970s to the mid 1980s were reexamined in light of the new bathymetry dataset. These included data from the 1979 R/V James Gillis (Bailey and Aaron 1982a), 1978 R/V Columbus Iselin (Bailey and Aaron 1982b), and 1987 R/V Farnella (GLORIA) surveys (EEZ-SCAN 87 1991).

Only one core is known to have been collected from within the MNR complex and only a limited number of cores have been collected in adjacent areas. Core 69–20 was collected at the seaward end of the Retriever slide scar (Fig. 12.1; Zimmerman 1972), and contained a Holocene/Pleistocene sedimentary section similar to that found along the Scotian slope to the north (Mosher et al. 2004). Core 69–20 was composed of olive-gray/green clay with a relatively high carbonate content overlying alternating layers of moderate reddish-brown clay and silt with isolated pebbles (low carbonate content). No landslide facies similar to those described by Tripsanas et al. (2008) or turbidite layers were described in the core.

12.2 Results and Interpretations

12.2.1 Munson-Nygren Slide

The Munson-Nygren submarine slide is one of the most northern and largest (in terms of area and volume) surficial submarine mass failures identified along the US Atlantic continental margin. The morphology of the evacuation zone of Munson-Nygren slide bears the characteristics of a retrogressive landslide, but is complicated by its interaction with an unnamed canyon and a large secondary landslide on the northern flank of the main scar (flank slide; Fig. 12.2). Because of a lack of cores and high-resolution seismic reflection data, the mode of failure for the Munson-Nygren slide is unknown, but may be similar to that of the Logan Canyon debris-flow corridor on the Scotian slope (Mosher et al. 2004).

The downslope length of the main evacuation zone is approximately 60 km, with a maximum width of approximately 12 km, excluding the width of the adjacent canyon and a secondary landslide. These values are significantly different from those of O'Leary (1986a), who measured a length of at least 35 km and a width of 20 km. The headwall is characterized by a series of concave, stepped scarps that cut slope gullies, the shallowest at a depth of 1,790 m (present only along the western side of the evacuation), the main headwall scarp at approximately 1,880 m, and the lower scarp at approximately 2,230 m (Figs. 12.2 and 12.3). The main headwall scarp has a maximum height of 280 m, while the maximum heights of the lower and shallow scarps are only 100 and 50 m, respectively. Seismic reflection profiles (e.g., Fig. 12.3) show the presence of chaotic reflections above the main headwall, leading O'Leary (1986a) to suggest sediment loading by debris from an earlier failure upslope of the Munson-Nygren slide served as the trigger for failure. Sidewall heights exceed 200 m along much of the length of the main evacuation zone and in places are prominently stepped,

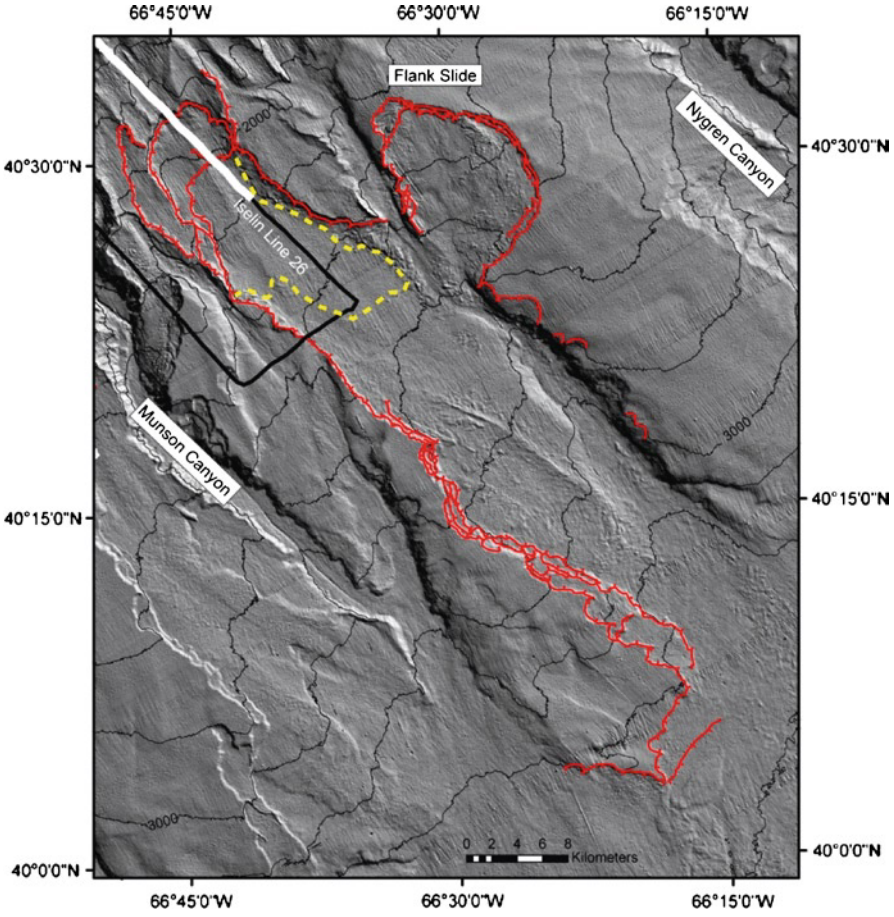

Fig. 12.2 The Munson-Nygren slide scar (evacuation zone). Prominent headwalls and sidewalls marked by red *hatched lines*. The *yellow dashed line* marks the upslope limit of blocky debris deposits. The location of the seismic profile in Fig. 12.3 is highlighted by the *white line*

revealing the architecture of the upper rise stratigraphy. The gradient of the failure surface, as measured down the main axis of the evacuation zone is 1.3°. A roughly circular flank slide breaches the northeastern sidewall of the Munson-Nygren evacuation zone, which occurred coeval with, or subsequent to, the failure of main Munson-Nygren slide. A number of small curved scarps are observed along the margin of the channel downslope of the flank slide, likely revealing the location of incipient landslides. Using the method outlined in Chaytor et al. (2009), the area and volume of the evacuation zone of the Munson-Nygren slide, including the flank landslide were calculated to be 973 and 152 km^3, respectively. These and subsequent area and volume values are only estimates, given the presence of debris within the evacuations and at times, poorly defined downslope lengths.

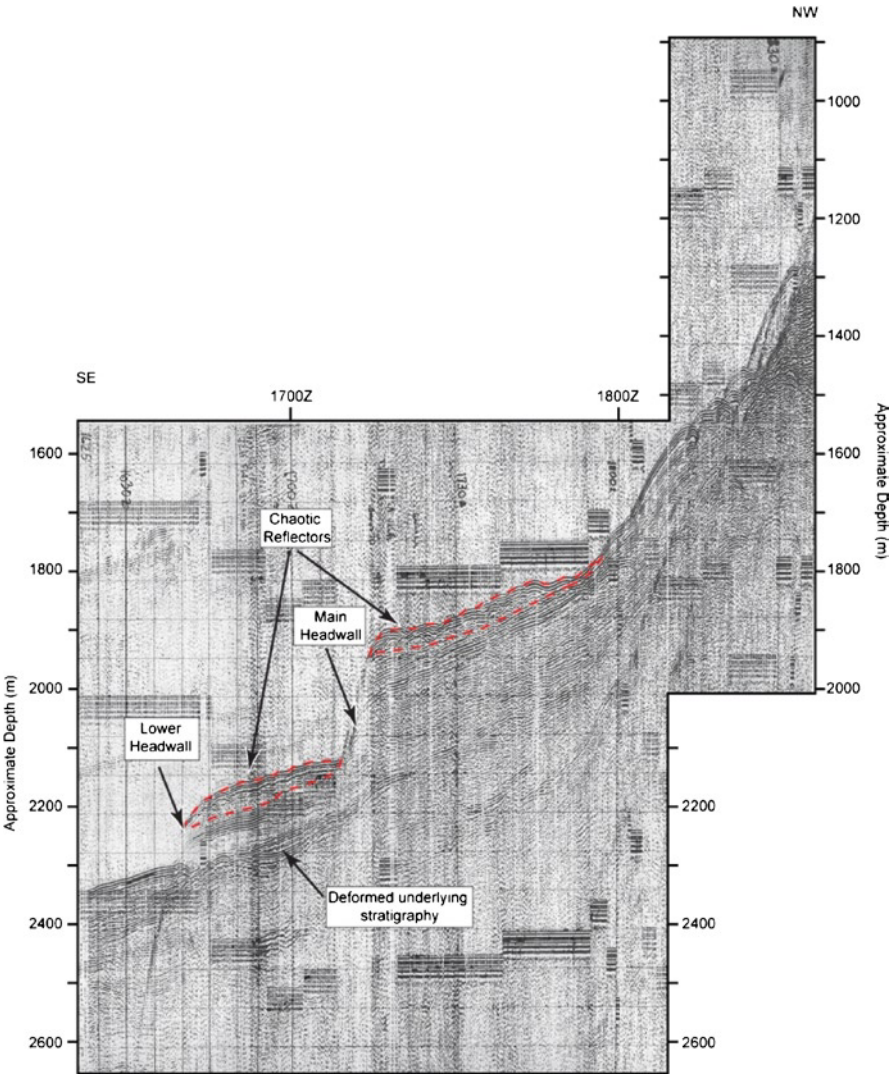

Fig. 12.3 A portion of Iselin air-gun line 26. Note the main and lower headwall scarps and the presence of chaotic (debris?) deposits above the headwall scarps (outlined by *dashed red line*) and deformed stratigraphy underlying the main scarp

Seismic reflection profiles show that the seafloor within the evacuation zone is covered by debris deposits of varying thicknesses (Fig. 12.3). Blocky surficial debris deposits from the Munson-Nygren slide are present within the evacuation zone of the landslide and further downslope (Figs. 12.1 and 12.2). In the upper part of the evacuation zone, blocky debris is only present at the base of sidewall scarps, but blocky and hummocky deposits become more widespread throughout the evacuation zone beginning adjacent to the flank landslide. Debris from the flank slide

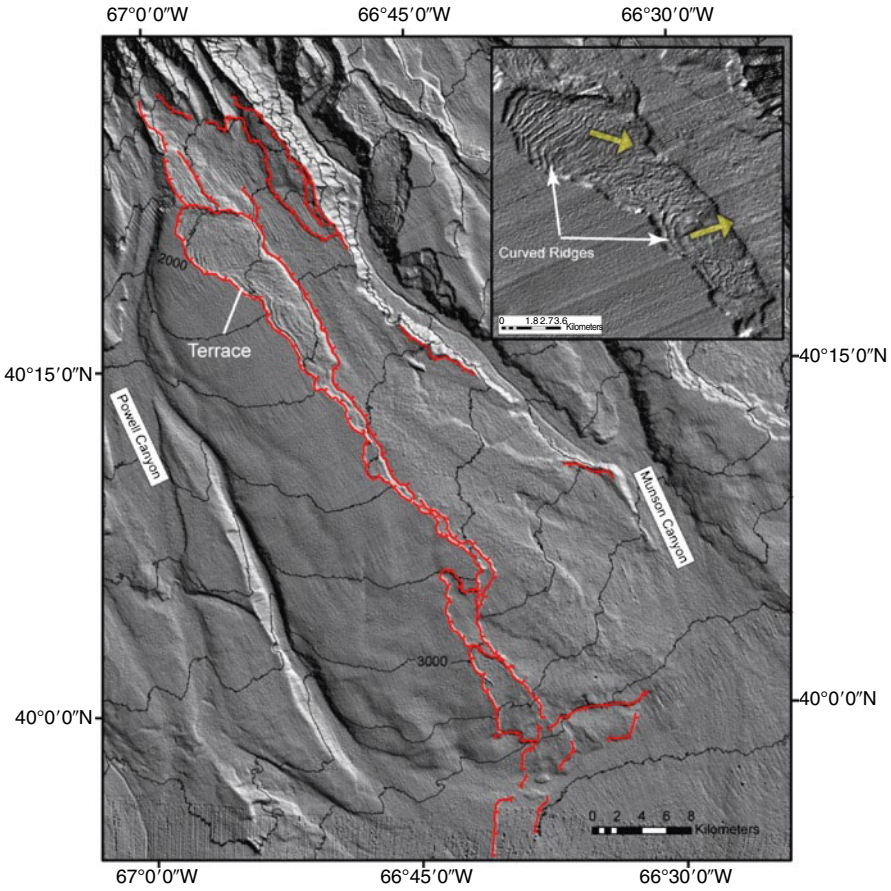

Fig. 12.4 Shaded-relief bathymetry of the Retriever landslide scar (evacuation zone). The headwall and sidewalls are marked by the *red lines*. The *inset* shows the curved debris ridges/troughs on the terrace, with the *yellow arrows* indicating the direction of flow of the ridges

forms a prominent lobe at the base of the evacuation zone, infilling and blocking the channel. Beyond this, debris deposits extend at least 50 km downslope from the base of the evacuation zone, infilling slope and rise channels and partially burying the base of Picket Seamount. At present, it is not clear whether these deposits are the result of a single or multiple landslide events.

12.2.2 Retriever Slide

The Retriever slide is located immediately adjacent to the western edge of Munson Canyon (Fig. 12.4). The evacuation zone of the Retriever slide has similar downslope and across slope dimensions as the Munson-Nygren slide, a downslope length of

approximately 62 km and an average width of approximately 12 km. Along the deepest section of the evacuation where the eastern margin merges with Munson Canyon, the width is 16 km. The area of the Retriever slide evacuation zone (728 km^2) is similar to that of the Munson-Nygren slide (973 km^2), but the 30 km^3 volume is an order of magnitude smaller, reflecting different evacuation depths. The gradient of the seafloor, as measured down the main axis of the evacuation zone is 1.4°, essentially the same as that measured for the Munson-Nygren slide.

Unlike the Munson-Nygren slide to its north, the Retriever slide does not have a clearly defined headwall, but rather has a discontinuous, low-relief scarp that forms the shallowest part of the evacuation zone (minimum headwall depth of approximately 1,780 m). This upper scarp of the Retriever slide cuts numerous gullies and ridges along the lower slope, attaining a maximum height of not more than 150 m. From the bathymetry, it is not evident if the discontinuous morphology of the headwall is original or if it has undergone post failure modification (e.g., renewed canyon incision). Except for the upper 15 km of the slide, significant sidewalls are only present along the western margin of the evacuation zone, with only a low-relief lip present along its eastern side where it flanks Munson Canyon. Sidewall scarp heights exceed 100 m along most of the evacuation zone, and as with the Munson-Nygren slide, display a stepped morphology. Below 2,600 m, a number of subdued scarps are present along the eastern margin and main axis of the evacuation zone. While these scarps may be temporally related to the most recent phase of failure, it is possible that they are relict landslide or canyon features partially covered by more recent debris deposits. Seismic reflection data show that failure deposits are present down the length of the evacuation zone, but blocky surficial deposits like those associated with the Munson-Nygren slide are largely absent on the bathymetry.

One of the most prominent feature of the Retriever slide is an elevated, approximately 15 km long terrace on the western flank of the evacuation zone that contains debris ridges up to 20 m high (Fig. 12.4). In plan view, the shape of these ridges and troughs generally conforms to the shape of the adjacent sidewall scarps. Micallef et al. (2007) described a similar ridge and trough morphology within the Storegga Slide, attributing it to a spreading mechanism.

12.2.3 Picket Slide

Between the Munson-Nygren and Retriever source scars lies the Picket slide (Fig. 12.5a). While this feature was initially considered to be part of the Munson-Nygren slide (O'Leary 1986a), it has well defined head and sidewalls that are adjacent to, but separate from the Munson-Nygren and the Retriever landslides. It is the smallest of the three distinct landslides, with a source evacuation area of 76 km^2 and a volume of 3 km^3. The concave headwall of the Picket slide is at a depth of approximately 1,880 m, and has a maximum height of 100 m. The gradient of the seafloor within the excavation zone is approximately 1.7°. About 6 km downslope of the headwall, the bulk of the evacuation zone bends to the southwest towards Munson Canyon, while a narrow arm of the evacuation zone continues downslope to the

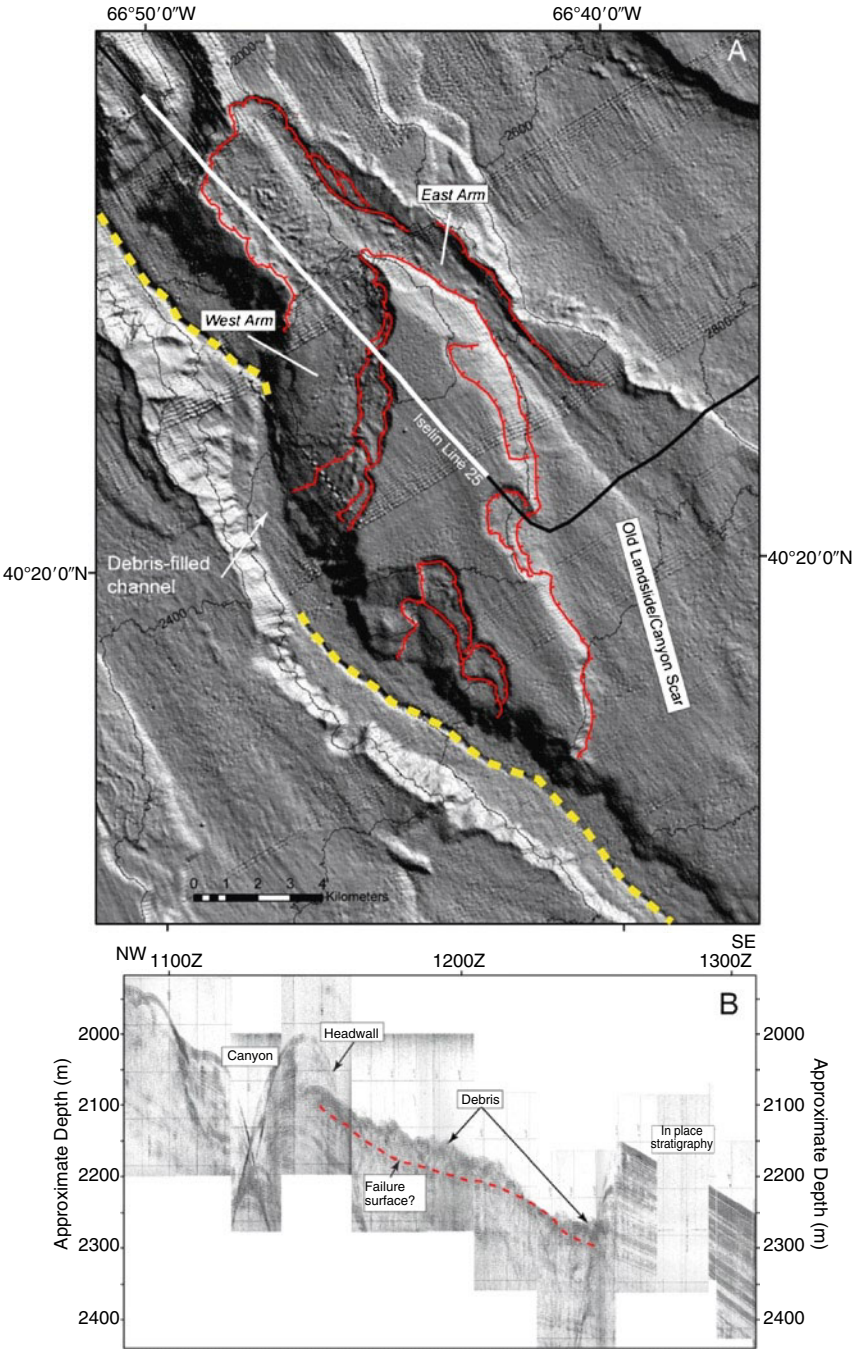

Fig. 12.5 (**a**) Shaded-relief bathymetry of the Picket slide. The location of the seismic profile in (**b**) is highlighted by the white line. Note that the thalweg of Munson Canyon (*dashed yellow line*) is cut and infilled by debris from the Picket slide; (**b**) A portion of Iselin air-gun line 25. Blocky debris is as much as 50 m thick. The likely failure surface is marked by the *red dashed line*

southeast (Fig. 12.5a) where it intersects a section of what appears to be an older landslide scar or buried canyon. Sidewalls along the western arm are distinctly scalloped and stepped and their heights exceed 100 m in places. The morphology of the Picket slide suggests failure occurred as a single event, with only minor secondary sidewall collapses.

Landslide deposits were funneled down both arms of the evacuation zone, but the majority of the material appears to have been focused down the southwest arm (Fig. 12.5a, b). Blocky debris deposits are present from about 2.5 km downslope of the headwall to the top of the southeastern area of the evacuation and to the toe of the debris lobe that is located in the axis of Munson Canyon. Deposits from the Picket slide completely fill the thalweg of Munson Canyon immediately below the landslide (Fig. 12.5a). The downslope extent of landslide deposits funneled down the southeastern arm is currently unknown.

12.3 Age of Slope Failure

Beyond a detailed examination of the landslide morphology, the primary interest in the reevaluation of the MNR landslide complex is the determination of the age of the failures as a means of investigating pre-conditioning factors and triggering mechanisms along the Georges Bank section of the US Atlantic margin. From the seismic reflection data, it appears that the youngest regionally correlatable units (LRU and younger) have been cut by these landslides. Because of the lack of cores collected within the evacuation and deposit zones, the absolute ages and sequencing of the landslides within the MNR complex are unknown and little is known about the characteristics of the sediments involved in the failures. That said, a first approximation of the relative age of these failures is provided by the morphology of the debris deposits and cross-cutting relationships of the landslide scars and canyons.

Blocky landslide deposits are relatively rare along the U.S. Atlantic continental margin, which is likely due to a combination of landslide age (i.e., insufficient time to be buried by younger sediments) and the mechanisms of failure (i.e., disintegration of the failed mass). The presence of blocky debris associated with the Munson-Nygren, Picket, and the terrace part of the Retriever slides suggests that these landslides may have occurred relatively recently, within the late Pleistocene-Holocene period. Furthermore, a recent age for the Picket slide is supported by the infilling of the thalweg channel of Munson Canyon directly in front of the downslope end of the western arm. Similarly, the axis of canyon below the flank slide of the Munson-Nygren slide appears to be filled with blocky debris, indicating deposition post-dates the last canyon cutting episode. Finally, debris deposits from the Munson-Nygren slide can be seen overlying and possibly cutting scars of broad continental rise landslides (Fig. 12.1) which have thick layers of recent sediment accumulated across and below them. Discontinuous landslide scars are also present on the continental rise SW of Retriever Seamount (Fig. 12.1), but the source of these draping sediments cannot be definitively identified. Additional high-resolution subbottom

profiles and coring are needed to determine the presence and thickness of recent sediment drape layers overlying each of the debris deposits.

Reevaluation of the MNR complex using the new multibeam dataset reveals that the sequence of failure of individual landslides is likely substantially more complex than previously thought (O'Leary 1986a; Twichell et al. 2009). While the reevaluation presented here supports the contention of O'Leary (1986a) that the Retriever slide (with the possible exception of the failure of the upper terrace) is the oldest of the landslides in the complex, it differs from the more detailed headwall-depth based sequencing scenario of Twichell et al. (2009) by the identification of the Picket slide as a separate slide that is the youngest of the three and a younger age for the flank slide in the Munson-Nygren complex (headwall 4A of Twichell et al.).

Acknowledgments We thank the U.S. Nuclear Regulatory Commission project N6480 for funding the 2009 multibeam data collection and analysis. The authors would like to express their appreciation to the officers and crew of the NOAA Ship Ronald H. Brown. David Mosher, Kathy Scanlon, and Emily Himmelstoss provided excellent reviews which improved many aspects of the manuscript. Any use of trade, product, or firm names is for descriptive purposes only and does not imply endorsement by the U.S. Government.

References

Bailey NG, Aaron JM (1982a) High-resolution seismic-reflection profiles collected aboard R/V James M. Gilliss, Cruise GS-7903-3, over the Atlantic continental slope and rise off New England: USGS open-file report 82–718, 2 p

Bailey NG, Aaron JM (1982b) High-resolution seismic-reflection profiles from the R/V Columbus Iselin, Cruise CI 7-78-2, over the continental shelf and slope in the Georges Bank area: USGS open-file report 82–607, 2 p

Chaytor JD, ten Brink US, Solow AR, Andrews BD (2009) Size distribution of submarine landslides along the U.S. Atlantic margin. Mar Geol 264:16–27

Danforth WW, Schwab WC (1990) High-resolution seismic stratigraphy of the upper continental shelf seaward of Georges Bank. USGS map, MF-2111

EEZ-SCAN 87 (1991) Atlas of the U.S. Exclusive Economic Zone, Atlantic continental margin. USGS miscellaneous investigations series I-2054, 174 pp

Gardner JV, Mayer LA, Armstrong AA (2006) Mapping supports potential submission to U.N. Law of the Sea. EOS Trans Am Geophys Union 87:157–159

Micallef A, Masson DG, Berndt C, Stow DAV (2007) Morphology and mechanics of submarine spreading: a case study for the Storegga Slide. J Geophys Res 112. doi:10.1029/2006JF000739

Mosher DC, Piper DJW, Campbell DC, Jenner KA (2004) Near-surface geology and sediment-failure geohazards of the central Scotian Slope. AAPG Bull 88:703–723

O'Leary DW (1986a) The Munson-Nygren slide: a major lower-slope slide off Georges Bank. Mar Geol 72:101–114

O'Leary DW (1986b) Seismic structure and stratigraphy of the New England Continental Slope and the evidence for slope instability. USGS open-file report, 86–118, 182 pp

O'Leary DW (1988) Shallow Stratigraphy of the New England Continental Margin. USGS bulletin, 1767, 40 pp

O'Leary DW (1993) Submarine mass movements, a formative process of passive continental margins: the Munson-Nygren complex and the southeast New England landslide complex. In: Schwab WC, Lee HJ, Twichell DC (eds) Submarine landslides: selected studies in the U.S. exclusive economic zone. USGS Bulletin 2002:23–39

Poag CW (1982) Stratigraphic reference section for Georges Bank basin – depositional model for New England passive margin. AAPG Bull 66:1021–1041
Scanlon KM (1984) The continental slope off New England: a long-range sidescan-sonar perspective. Geo-Mar Lett 4:1–4
Tripsanas EK, Piper DJW, Jenner KA, Bryant WR (2008) Submarine mass-transport facies: new perspectives on flow processes from cores on the eastern North American margin. Sedimentology 55:97–136
Twichell DC, Chaytor JD, ten Brink US, Buczkowski B (2009) Morphology of late Quaternary landslides along the U.S. Atlantic continental margin. Mar Geol 264:4–15
Zimmerman HB (1972) Sediments of the New England continental rise. GSA Bull 83:3709–3724

Chapter 13
Submarine Landslides in Arctic Sedimentation: Canada Basin

David C. Mosher, John Shimeld, Deborah Hutchinson, Nina Lebedeva-Ivanova, and C. Borden Chapman

Abstract Canada Basin of the Arctic Ocean is the least studied ocean basin in the World. Marine seismic field programs were conducted over the past 6 years using Canadian and American icebreakers. These expeditions acquired more than 14,000 line-km of multibeam bathymetric and multi-channel seismic reflection data over abyssal plain, continental rise and slope regions of Canada Basin; areas where little or no seismic reflection data existed previously. Canada Basin is a turbidite-filled basin with flat-lying reflections correlateable over 100s of km. For the upper half of the sedimentary succession, evidence of sedimentary processes other than turbidity current deposition is rare. The Canadian Archipelago and Beaufort Sea margins host stacked mass transport deposits from which many of these turbidites appear to derive. The stratigraphic succession of the MacKenzie River fan is dominated by mass transport deposits; one such complex is in excess of 132,000 km^2 in area and underlies much of the southern abyssal plain. The modern seafloor is also scarred with escarpments and mass failure deposits; evidence that submarine landsliding is an ongoing process. In its latest phase of development, Canada Basin is geomorphologically confined with stable oceanographic structure, resulting in restricted depositional/reworking processes. The sedimentary record, therefore, underscores the significance

D.C. Mosher (✉) • J. Shimeld • C.B. Chapman
Geological Survey of Canada, Natural Resources Canada, Bedford Institute of Oceanography, 1 Challenger Dr., Dartmouth, NS, Canada B2Y 4A2
e-mail: dmosher@nrcan.gc.ca

D. Hutchinson
United States Geological Survey, 384 Woods Hole Road Quissett Campus, Woods Hole, MA 02543-1598, USA

N. Lebedeva-Ivanova
Woods Hole Oceanographic Institution, 266 Woods Hole Rd. MS# 22, Woods Hole, MA 02543, USA

Y. Yamada et al. (eds.), *Submarine Mass Movements and Their Consequences*, Advances in Natural and Technological Hazards Research 31,
DOI 10.1007/978-94-007-2162-3_13, © Springer Science+Business Media B.V. 2012

of mass-transport processes in providing sediments to oceanic abyssal plains as few other basins are able to do.

Keywords Submarine landslide • Mass-failure • Mass-transport deposit • Tsunami • Geohazard • Seismic reflection

13.1 Introduction

The geology of Canada Basin of the Arctic Ocean is the least studied basin in the World. Prior to the year 2006, less than 3,000 line-km of seismic reflection data existed in the basin. Between 2006 and 2011, six marine seismic reflection expeditions were undertaken from ice breakers, acquiring in excess of 14,000 line-km of seismic reflection and multibeam bathymetric data over abyssal plain, continental rise and slope regions of Canada Basin. The success of these missions was achieved through novel technical modifications to equipment to permit towing in heavy ice conditions (see Hutchinson et al. 2009; Mosher et al. 2009, 2011a) and through international collaboration, enabling utilization of two ice breakers during data acquisition in heavy ice. These expeditions coincided with years of record low Arctic pack ice extent and percentage of multi-year ice, aiding access to survey areas that would previously have been impossible to reach. The objective of this paper is to study mass transport deposits along the margins of Canada Basin and demonstrate the dominant effect of this process on sediment delivery to the basin.

13.1.1 Regional Geology

Canada Basin forms the largest part of the Amerasian Basin of the Arctic Ocean superbasin (Gramberg et al. 1999). The physiography of the Arctic Ocean seafloor is described by Jakobsson et al. (2003, 2008) based on the International Bathymetric Chart of the Arctic Ocean (IBCAO) (Fig. 13.1). Using their descriptive classification scheme, this study includes the Canada Abyssal Plain and the MacKenzie and Canada-Greenland rises and adjacent slopes. The area is bound by the Alpha-Mendeleev Ridge in the north and Northwind Ridge to the west. It measures 1,500 km north to south and 650 km west to east, totaling about 1,000,000 km^2 in area. For simplicity, this study will refer to the entire area as Canada Basin.

Tectonic formation of Canada Basin is still in debate (see review by Lawver and Scotese 1990) in large part because of the paucity of data and because aeromagnetic and gravity anomaly patterns are weak and overprinted by the Alpha-Mendeleev Ridge volcanic province (e.g., Taylor et al. 1981; Kenyon and Forsberg 2008). In any of the models, seafloor spreading is largely assumed to have ended in the mid Cretaceous between 120 and 125 Ma, although some authors would have basin

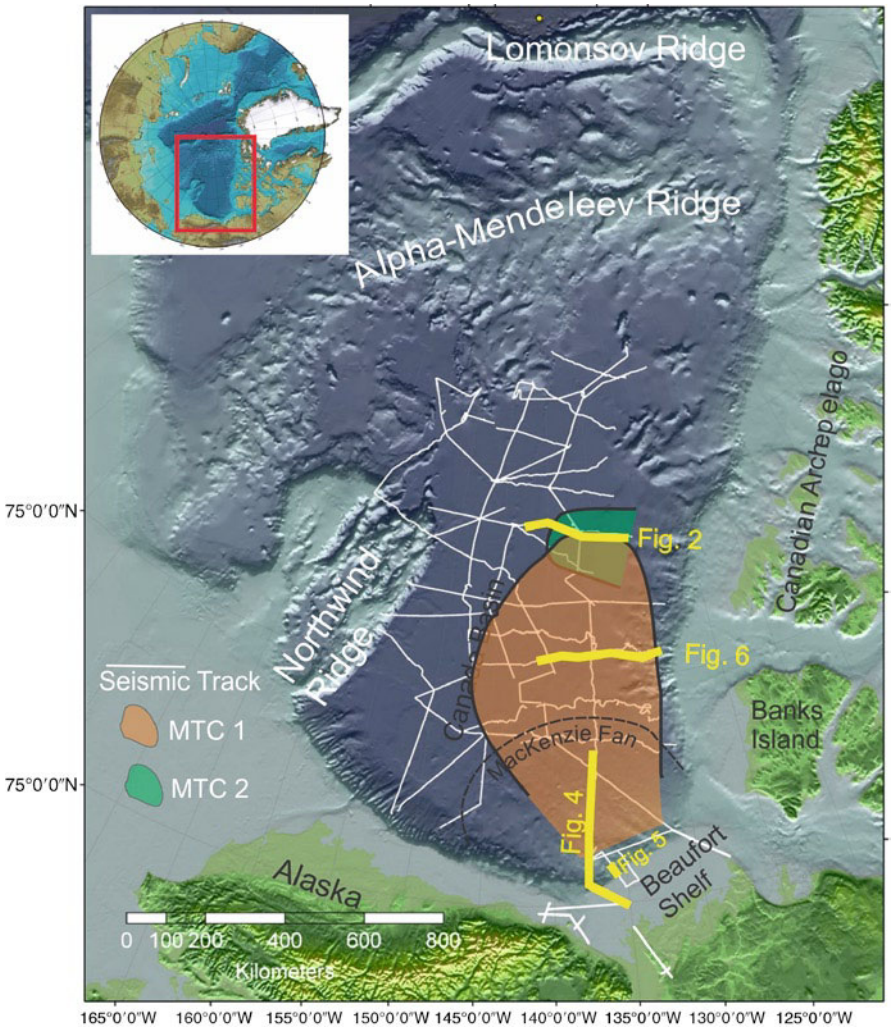

Fig. 13.1 Study area centered on Canada Basin. MTC are mass transport complexes. The outer limit of the McKenzie River fan is shown by *dashed line*, as interpreted from this bathymetric image. Bathymetric data are from the IBCAO compilation (Jakobsson et al. 2008)

formation terminate at 80 Ma. There is little evidence of syndepositional deformation, suggesting the basin largely formed prior to sediment infill (Mosher et al. 2011b).

Prior to this study, little was known of the sedimentary section in Canada Basin. Limited ice drift station seismic data, particularly refraction data, gave glimpses of the reflection character and minimum thicknesses for short segments of the sedimentary section (e.g., Campbell and Clark 1977). These stations also acquired short piston cores, providing information on sedimentary processes for the youngest

portion of the section. Seismic reflection data were acquired on the southern margins of Canada Basin in the late 1970s (e.g., Grantz and May 1983) and the 1980s with the Canadian Lithoprobe program. Using these data, Jackson and Oakey (1990) produced a sediment thickness chart of the Arctic Ocean, including Canada Basin, but contours are broad and based on little measured data. In the early 1990s single channel seismic reflection profiles were acquired on the western edge and southern portion of Canada Basin off of Northwind Ridge (Grantz et al. 2004). Other than these few data sets, the vast majority of Canada Basin remained unexplored.

13.1.2 Methods

Approximately 14,000 line-km of seismic reflection data were acquired from the *CCGS Louis S. St-Laurent* between 2007 and 2010. Full details of the equipment and procedures employed for this program are provided in Mosher et al. (2009, 2011a) and logistical challenges in acquiring data in ice covered seas are described by Hutchinson et al. (2009). Standard seismic reflection practices were used with an 1,150 in^3 (18.8 l) G-gun array and a 16 channel digital hydrophone streamer with a hydrophone spacing of 6.25 m. The source array was towed vertically off the stern of the vessel at 11.5 m depth in order to shelter it from ice. The hydrophone streamer was towed from the rear of the source array tow sled, also to keep it deep beneath the sea ice. Offset between the source and streamer was small and the length of the streamer was short for operating in such deep water, but necessary to protect the equipment from damage. Data bandwidth is limited from about 5 to 65 Hz because of the significant tow depth of the source and receiver. This frequency band indicates vertical seismic resolution is limited to about 8 m (assuming a velocity of 2,000 m/s and Rayleigh criteria of one fourth wavelength for seismic resolution). The reflection program was complimented with 120 expendable sonobuoys to provide wide angle seismic reflection and refraction information for velocity analysis.

Approximately 18,000 line-km of multibeam sonar bathymetric data were acquired from the *USCGC Healy* using a hull-mounted SeaBeam 12 kHz system for the first 3 years of operation and a Kongsberg EM122 system in 2010. Chirp subbottom profiler data were acquired concurrently, centered about a frequency of 3.5 kHz. Additional multibeam data on the Beaufort Slope are EM300 data and were acquired in the ArcticNet program by the University of New Brunswick's Ocean Mapping Group from the *CCGS Amundsen*.

13.2 Results

Aside from correlating the seafloor and acoustic basement horizons, two additional reflection events were correlated to the extent possible within the seismic data set. The deeper event is the R30 and the shallower is the R10. These data provide the

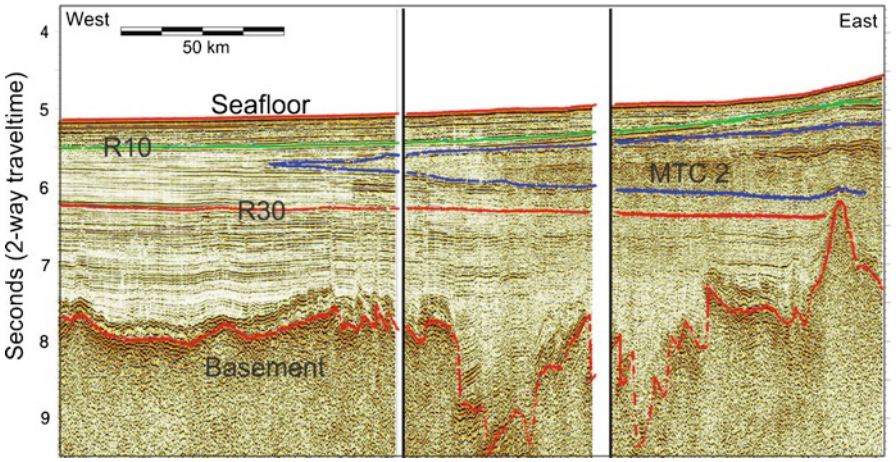

Fig. 13.2 Seismic profile down-dip along the Canadian Archipelago margin showing the regional seismic stratigraphy and the stratigraphic context of a large MTC (MTC 2) emanating from this margin. See Fig. 13.1 for line location

broad seismic stratigraphic framework for the recent-most (Neogene?) sedimentary sequence within Canada Basin. In the context of this study, tops and bottoms of major mass transport deposits were also correlated.

13.2.1 Canadian Archipelago Slope and Rise

The margin along the Canadian Archipelago is part of the Canada-Greenland rise as categorized by Jakobsson et al. (2003). The IBCAO bathymetric chart shows a large scale complexity to the margin, with lobe-shaped topography offshore of the various straits and inlets. In general, the slope has a 0.5–0.8° dip. There is not a well-defined base of slope, but it appears as though the slope transitions to the abyssal plain by 3,600 m water depth.

Seismic surveying the slope proved difficult as heaviest ice conditions in the Arctic prevail along this margin. Four profiles from the abyssal plain up to the mid-slope were acquired in the southeastern portion of Canada Basin, off Banks Island and McClure Strait and several of the northern transects reach to the continental rise. These data show largely flat-lying parallel reflections extending from the margin to underlie the modern abyssal plain (Fig. 13.2). In general, the section thins from east to west. Against the margin and shallower in the section, profiles are dominated by thin (10 ms) to thick (900 ms) lense- and wedge-shaped units of incoherent reflections, separated by coherent reflections. The thickest of these incoherent units, interpreted to be a mass transport deposit or a mass transport complex, correlates through several slope seismic lines and underlies the abyssal plain (Fig. 13.2). It lies between the

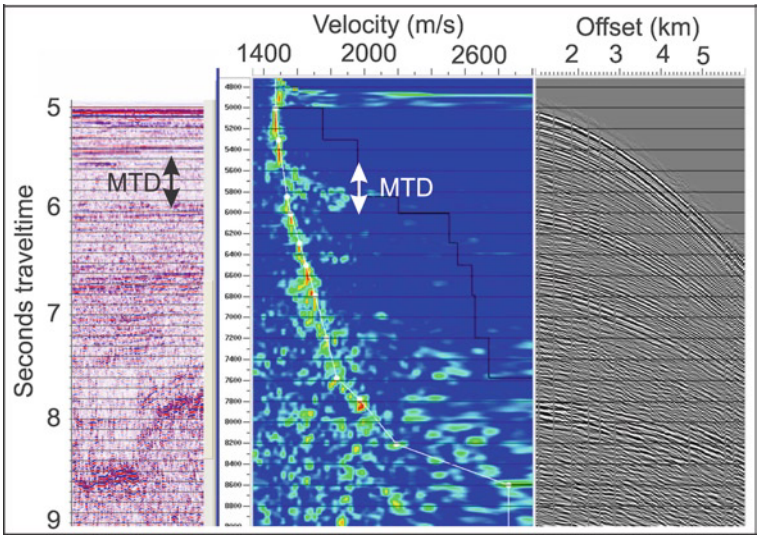

Fig. 13.3 Semblance velocity analyses of sonobuoy data highlight the mass transport deposit because of scattering of acoustic energy

R30 and R10 reflection events and appears on three profiles extending from the Canadian Archipelago. It is 880 ms (~920 m) thick at its upslope end, as far as the data extend eastward, and encompasses a minimum of 15,000 km^2 area. This unit is also distinguished on sonobuoy data. The scattering of acoustic energy due to its incoherency characteristics causes a shallow anomaly in semblance analysis plots (Fig. 13.3).

13.2.2 MacKenzie-Beaufort Slope and Rise

The southern margin of Canada basin comprises the Beaufort slope and rise including the MacKenzie River fan. Although the base of sediments is not imaged beneath the upper slope and shelf regions in our data, it is in excess of 12 s (2-way traveltime) (>15 km) thick Kumar et al. (2009). The sedimentary succession thins northward and in particular distally from the main MacKenzie River discharge area. The shelf edge lies in just over 100 m water depth. Modern slope angles are generally less than 1°. The fan merges with the abyssal plain in about 3,600 m water depth.

Seismic stratigraphy in this region is complex. Specific to the MacKenzie slope and rise, the modern slope morphology is relatively smooth, cut by the MacKenzie Trough, and dips gently northward. The fan creates a cone-shaped morphologic expression on the seafloor recognized on the IBCAO chart that encompasses about 200,000 km^2 in area (Fig. 13.1). The shelf edge in the MacKenzie delta region is

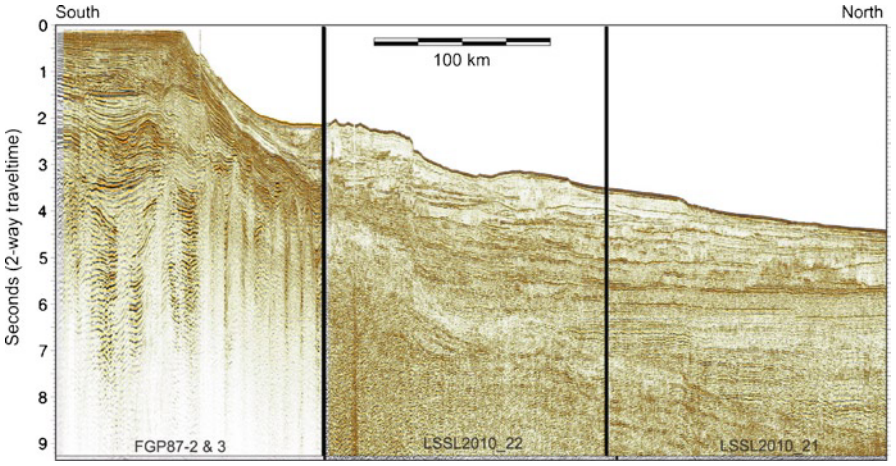

Fig. 13.4 Seismic profile across the Beaufort Shelf (Lithoprobe lines FGP87-2&3) and MacKenzie River fan (LSSL 2010 lines 21 and 22). See Fig. 13.1 for location

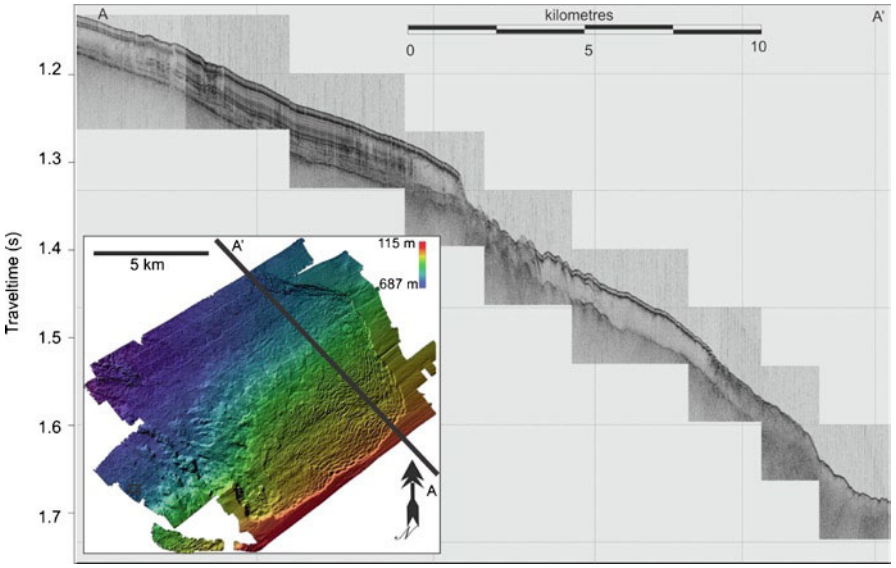

Fig. 13.5 Chirp profile with accompanying multibeam image showing evidence of submarine mass failure on the modern seafloor. See Fig. 13.1 for location

characterized by truncated progradational clinoform reflections (Fig. 13.4). The top 2 s (twtt) or about 2 km in the stratigraphy of the slope are contorted reflections with a general appearance of bodies of incoherent reflections. This characteristic is interpreted to be reflective of stacked mass transport complexes (MTC) (Fig. 13.4). Figure 13.5 shows that mass-failure occurs even on the modern

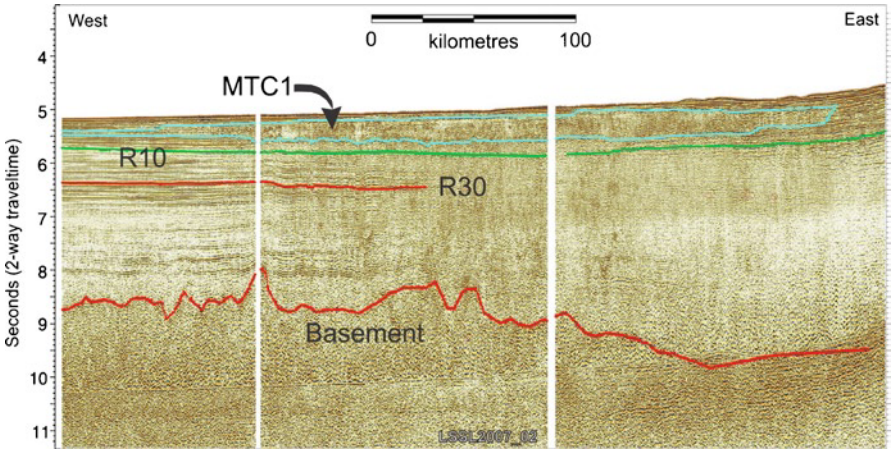

Fig. 13.6 A strike profile offshore of the MacKenzie River fan showing the large MTC (MTC 1) above the R10 horizon. See Fig. 13.1 for location. Note parallel reflections to the west of the image

seafloor of this slope, with a head scarp over 100 m in height. A buried MTC lies above the R10 event and emanates from the MacKenzie River fan (Fig. 13.6). This unit underlies much of the southern abyssal plain and maps to a minimum area of 132,000 km^2 (Fig. 13.1). It is at least 700 ms thick (~700 m) at the southern extent of the data.

Further offshore, this sequence of incoherent reflections evolves into a sequence of numerous, strongly reflective, parallel reflections. The entire sequence thins from south to north. The R10 to seafloor interval appears to be emanating from the MacKenzie River fan as the interval thins in a radial pattern from this point. This unit overlies unconformably and pinches out against the Alaska Beaufort and Canadian Archipelago slopes. It sharply truncates against basement highs to the north and west, with little evidence of onlap or of reworking around bathymetric highs.

13.3 Discussion and Conclusions

Sediment mass failure is recognized as one of the fundamental processes in margin evolution (Mienert and Weaver 2002; Mosher et al. 2010; Shipp et al. 2011). Mass transport deposits are recognized on most continental margins, and some deposits are recognized as truly massive in scale (Nisbet and Piper 1998; Haflidason et al. 2002). The Canadian Archipelago continental margin bordering the eastern edge of Canada Basin appears to be no different than most passive margins, with portions of the stratigraphic succession consisting of mass transport deposits. The largest deposit mapped on our data set in this region is estimated to be about

15,000 km^3 in volume, on par with giant submarine landslides mapped on many continental margins.

Sediment mass failure is also a characteristic of deep sea fans (e.g., Piper et al. 1997; Loncke et al. 2002; Newton et al. 2004) and the MacKenzie River fan appears to reflect this fact. The stratigraphic succession of this fan appears to be stacked mass transport deposits and few seismic horizons correlate over any lateral distance. Even the modern seafloor is scarred with escarpments and mass transport deposits (Fig. 13.5); evidence of submarine landsliding. The largest mass transport deposit mapped on our data appears to emanate from the fan and is about 132,000 km^2 in area; larger than the Storegga Slide which is the largest known surficial submarine landslide complex (Haflidason et al. 2002). This MTD underlies much of the southern abyssal plain. A deposit of this size may be a complex of many failures and not a single event, as is characteristic of deep water fans and deltas (Piper et al. 1997; Newton et al. 2004).

Submarine landslide trigger mechanisms in the Arctic are unknown, but globally, most are initiated by ground motions due to earthquakes, usually in concert with some pre-conditioning factors (see Mosher et al. 2010). In the Beaufort Sea region, seismicity potential is considered moderate (Adams and Atkinson 2003); possibly higher during deglacial phases due to isostatic rebound (see Mosher 2009). The two largest recorded events in the Beaufort region were a M6.5 earthquake in 1920 and a M5 event in 1975 (Hyndman et al. 2005). Mosher (2009) considers the risk of submarine landsliding as significant because of this seismic potential in combination with slope angles, thick sediment accumulation and rapid sedimentation rates on the MacKenzie River fan. In addition, earthquake ground acceleration amplification, variable permafrost thicknesses, and the presence of significant in situ gas and possible gas hydrate (Paull et al. 2007) must be taken into consideration in assessing the probability of submarine landsliding in the region of the delta. The potential of tsunami generation due to one of these failures is unknown, but Mosher (2009) discusses this possibility with respect to the landslide shown in Fig. 13.5.

The seismic facies of the majority of the sedimentary section within Canada Basin, with high frequency laterally coherent reflections is characteristic of turbidity current deposits. Given the pattern of sediment thinning and the proximal to distal relationship of mass transport deposits and turbidites, it is suggested that the majority of the Neogene sediments infilling Canada Basin commenced as mass failure along the Canadian Archipelago and Beaufort margins and evolved into turbidity currents (cf. Mohrig and Marr 2003; Piper and Normark 2009). The strong lateral continuity of reflections within the basin suggests these turbidity currents were unconfined and spread laterally over 100s of km without interruption. They ultimately abut against or onlap bathymetric highs such as Northwind Ridge on the western edge of Canada Basin or far to the north on Alpha-Mendeleev Ridge. There is no evidence of subsequent reworking by geostrophic or other bottom flowing currents, making Canada Basin a natural laboratory for understanding the role of sediment mass failure and basin fill processes.

Acknowledgments The authors would like to express their appreciation to the officers and crew of the Canadian icebreaker Louis S. St-Laurent and the US Icebreaker Healy, as well as to the Canadian and US Extended Continental Shelf mapping programs. There are too many colleagues involved in data acquisition and analysis to name, but to all of them, we thank you. D. Long and M. Jakobsson conducted the external review for publication. P. Hart, J. Chaytor, D. C. Campbell and J. Shaw conducted internal reviews. The authors would like to express our appreciation to all of these reviewers.

References

Adams J, Atkinson G (2003) Development of seismic hazard maps for the proposed 2005 edition of the National Building Code of Canada. Can J Civil Eng 30:255–271

Campbell JS, Clark DL (1977) Pleistocene turbidites of the Canada Abyssal Plain of the Arctic Ocean. J Sediment Petrol 47:657–670

Gramberg IS, Verba VV, Verba ML, Kos'ko MK (1999) Sedimentary cover thickness map – sedimentary basins of the Arctic. Polarforschung 69:243–249

Grantz A, May SD (1983) Rifting history and structural development of the continental margin north of Alaska. In: Watkings JS, Drake C (eds) Studies in continental margin geology, vol 34, American Association of Petroleum Geologist Memoir. American Association of Petroleum Geologist, Tulsa, pp 77–100

Grantz A, Hart PE, May SD (2004) Seismic reflection and refraction data acquired in Canada Basin, Northwind Ridge, and Northwind Basin, Arctic Ocean in 1988, 1992, and 1993, US Geological Survey open-file report 2004-1243. U.S. Department of the Interior, U.S. Geological Survey, Menlo Park

Haflidason H, Lien R, Sejrup HP, Forsberg CF, Bryn P (2002) The dating and morphometry of the Storegga Slide. Mar Petrol Geol 22:123–136

Hutchinson DR, Jackson HR, Shimeld JW, Chapman CB, Childs JR, Funck T, Rowland R (2009) Acquiring marine data in the Canada Basin, Arctic Ocean. EOS Trans Am Geophys Union 90:197–204

Hyndman RD, Cassidy JF, Adams J, Rogers GC, Mazzotti S (2005) Earthquakes and seismic hazard in the Yukon-Beaufort-Mackenzie. Can Soc Explor Geophys Recorder 30:32–66

Jackson HR, Oakey GN (1990) Sedimentary thickness map of the Arctic Ocean. In: Grantz A, Johnson L, Sweeney JF (eds) The Arctic Ocean Region, the Geology of North America, L Plate 5. Geological Society of America, Boulder

Jakobsson M, Grantz A, Kristoffersen Y, MacNab R (2003) Physiographic provinces of the Arctic Ocean seafloor. Geol Soc Am Bull 115:1443–1455

Jakobsson M, Macnab R, Mayer L, Anderson R, Edwards M, Hatzky J, Schenke H-W, Johnson P (2008) An improved bathymetric portrayal of the Arctic Ocean: Implications for ocean modeling and geological, geophysical and oceanographic analyses. Geophys Res Lett 35:L07602–L07635. doi:10.1029/2008GL033520

Kenyon SC, Forsberg R (2008) New gravity field for the Arctic. EOS Trans 89(32):289–290

Kumar N, Helwig J, Dinkelman MG (2009) Preliminary evaluation of a potential major petroleum province from BeaufortSPAN seismic data: Canadian Arctic passive margin, Banks Island segment. Can Soc Expl Geophys Recorder 34:26–33

Lawver LA, Scotese CR (1990) A review of tectonic models for the evolution of the Canada Basin. In: Grantz A, Johnson L, Sweeney JF (eds) The Arctic Ocean Region, Geology of North America, L: 93–618. Geological Society of America, Boulder

Loncke L, Gaullier V, Bellaiche G, Mascle J (2002) Recent depositional patterns of the Nile deep-sea fan from echo-character mapping. Am Assoc Petrol Geol B 86:1165–1186

Mienert J, Weaver P (eds) (2002) European margin sediment dynamics. Springer, Berlin, 446 pp

Mohrig D, Marr JG (2003) Constraining the efficiency of turbidity current generation from submarine debris flows and slides using laboratory experiments. Mar Petrol Geol 20:883–899

Mosher DC (2009) Submarine landslides and consequent tsunamis in Canada. Geosci Canada 26:179–190

Mosher DC, Shimeld JW, Hutchinson DR (2009) 2009 Canada Basin seismic reflection and refraction survey, western Arctic Ocean: CCGS Louis S. St-Laurent expedition report, Geological Society of Canada open file 6343, 266 p

Mosher DC, Moscardelli L, Shipp C, Chaytor J, Baxter C, Lee H, Urgeles R (2010) Submarine mass movements and their consequences. In: Mosher DC, Shipp C, Moscardelli L, Chaytor J, Baxter C, Lee H, Urgeles R (eds) Submarine mass movements and their consequences IV, vol 28, Advances in Natural and Technological Hazards Research. Springer, Dordrecht, pp 1–10. doi:10.1007/978-90-481-3071-9

Mosher DC, Shimeld JW, Chapman CB (2011a) 2010 Canada Basin seismic reflection and refraction survey, western Arctic Ocean. CCGS Louis S. St-Laurent expedition report, Geological Survey of Canada open file 6720, 252 p

Mosher DC, Shimeld J, Jackson R, Hutchinson D, Chapman CB, Chian D, Childs J, Mayer L, Edwards B, Verhoef J (2011b) Sedimentation in Canada Basin. Geological Survey of Canada open file 6759, poster, 1 sheet

Newton CS, Shipp RC, Mosher DC (2004) Importance of mass transport complexes in the Quaternary development of the Nile Fan, Egypt. In: Offshore technology conference, paper 16742, May, 2004, Houston

Nisbet EG, Piper DJW (1998) Giant submarine landslides. Nature 392:329–330

Paull CK, Ussler W, Dallimore DR, Blasco SM, Lorenson TD, Melling H, Mediloi BE, Nixon FM, McLaughlin FA (2007) Origin of pingo-like features on the Beaufort Sea shelf and their possible relationship to decomposing methane gas hydrates. Geophys Res Let 34: L01603, doi:10.1029/2006GL027977, 5 p

Piper DJW, Normark WR (2009) Processes that initiate turbidity currents and their influence on turbidites: a marine geology perspective. J Sediment Res 79:347–362. doi:10.2110/jsr.2009.046

Piper DJW, Pirmez C, Manley PL, Long D, Flood RD, Normark WR, Showers W (1997) Mass-transport deposits of the Amazon Fan. In: Flood RD, Piper DJW, Klaus A, Peterson LC (eds) Proceeding ODP, Science Results, 155. College Station (Ocean Drilling Program), pp 109–146. doi:10.2973/odp.proc.sr.155.212.1997

Shipp C, Weimer P, Posamentier H (eds) (2011) Mass-transport deposits in deepwater settings, vol 96, SEPM special publication. Society for Sedimentary Geology, Tulsa, OK, 520 p

Taylor PT, Kovacs LC, Vogt PR, Johnson GK (1981) Detailed aeromagnetic investigation of the Arctic Basin. J Geophys Res 86:6323–6333

Chapter 14
Extensive Erosion of the Deep Seafloor – Implications for the Behavior of Flows Resulting from Continental Slope Instability

Jan Sverre Laberg, Hilde B. Johannessen, Matthias Forwick, Michael Ivanov, and Tore O. Vorren

Abstract Deep-towed, high- to ultra high-resolution side-scan sonar data from the deep sea realm offshore Norway reveal flute marks in a variety of morphological forms showing that apparently undisturbed areas of smooth sea floor have been exposed to extensive erosion and sediment bypass. The presence of flute marks at the lower continental slope (~2,700 m water depth) and in the slope – abyssal plain transitional area (~3,200 m water depth) shows that large and unconfined turbidity currents eroded and increased their loads in these settings that have been regarded as areas of deposition. This indicates that episodes of mass wasting originating from the adjacent continental slope included both large turbidity currents in addition to debris flows. Alternatively, the flows occurred during separate events and episodes of sediment failure were more frequent than previously inferred. In any case, large and unconfined turbidity currents may form important parts of submarine mass wasting that are difficult to identify without high-resolution data from the deep-sea realm.

Keywords Norwegian sea • Slope instability • Flute marks • Turbidity currents

14.1 Introduction

Detailed studies including swath bathymetry, side-scan sonar and seismic data, as well as sediment cores (e.g., Pratson et al. 2007) have documented that the relief of the continental slope results from a complex interplay of smaller and larger events.

J.S. Laberg (✉) • H.B. Johannessen • M. Forwick • T.O. Vorren
Department of Geology, University of Tromsø, Tromsø N-9037, Norway
e-mail: jan.laberg@uit.no

M. Ivanov
UNESCO Centre for Marine Geology and Geophysics, Moscow State University, Moscow 119899, Russia

Y. Yamada et al. (eds.), *Submarine Mass Movements and Their Consequences*, Advances in Natural and Technological Hazards Research 31,
DOI 10.1007/978-94-007-2162-3_14, © Springer Science+Business Media B.V. 2012

These are controlled by external factors, such as sea-level variations, climate and ice sheet fluctuations, seismicity, as well as internal factors like basin physiography, sediment properties, rate of deposition, as well as pore pressure, fluid composition and migration.

Decoding the properties and successions of events responsible for the formation of this seascape remains challenging. The majority of studies (e.g., Haflidason et al. 2004, 2005; Canals et al. 2004) have focused on the area of sediment evacuation on the continental slope. This approach includes detailed studies of the processes responsible for the formation of the slope relief and dating of post-slide sediments for a minimum age of the events. But from the slope morphology it is often difficult to separate features formed during a single or multiple events. In addition, data sets (multi-beam, side-scan sonar) for detailed morphological analyses are seldom providing a complete cover of the features of interest.

The other approach has focused on the deep-sea area of slide deposits and includes studies of their morphology, geometry, sedimentology and age. Offshore Norway, debris-flow deposits and turbidites have been associated with mass wasting in the Storegga and Trænadjupet Slides (e.g., Haflidason et al. 2005; Laberg et al. 2006). However, little is known about sedimentary processes related to the Andøya Slide and adjacent canyons (Fig. 14.1). In consequence, a proper evaluation of the recurrence interval of these features is still pending. Worldwide, only a few deep-sea basins have been targeted for scientific drilling for the purpose of studying the nature and frequency of gravity flows resulting from slope failures (e.g., Weaver 2003).

In this study, we utilize newly acquired deep-towed, high- to ultra high-resolution side-scan sonar data (MAK system, operating at 30 and 100 kHz, swath range up to 2 km, towing speed of 1.5–2 knots) from the deep sea (>2,500 m) realm offshore Norway. Based on detailed morphological analyses in two areas, we elucidate the nature and properties of the most recent mass wasting processes that have affected these areas.

14.2 Areas of Erosion by Gravity Currents

The first study area (Area 1) is located on the distal continental slope at about 2,700 m water depth (Fig. 14.1). Here, three debris lobes several km wide, about 25 m thick and acoustically transparent with a slightly irregular relief are inferred to represent deposits from submarine landslides originating from the nearby continental slope (Fig. 14.2). These deposits were by Dowdeswell et al. (1996), Vorren et al. (1998), Laberg et al. (2000) and Taylor et al. (2002) inferred to be part of the distal Andøya Slide. Our data show that the seafloor between the debris flows is irregular due to closed seafloor depressions. These occur randomly and with a variety of forms up to 1 km across, 500 m wide and some meters deep. A buried reflection, some meters below the sea floor shows the same characteristic. However, no debris flow deposits were identified at this depth (Fig. 14.2). The areal extent of the zone of depressions is presently not known but it can be followed alongslope for several tens of kilometers.

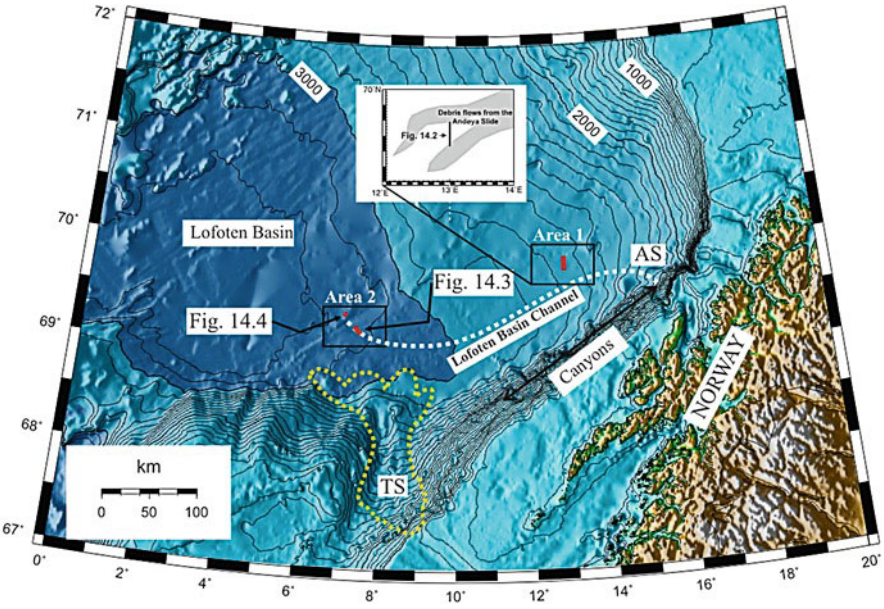

Fig. 14.1 Bathymetric map of the continental margin offshore northern Norway and the abyssal Lofoten Basin. *Inset* shows the distal parts of the two southern debris-flow deposits originating from the Andøya Slide (AS) (study area 1). The *yellow stippled line* outlines the area affected by the Trænadjupet Slide (TS) (the area of sediment evacuation is upslope from ~2,400 m water depth and the corresponding debris flows can be followed to 3,000–3,100 m water depth). The continental slope separating the two slide areas is dominated by canyons. The approximate location of the Lofoten Basin Channel and study area 2 near its termination is also indicated. The bathymetry is based on Jakobsson et al. (2008). The location of Figs. 14.2–14.4 is indicated

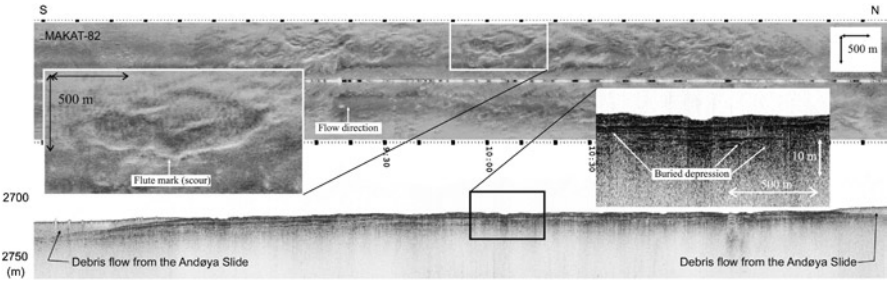

Fig. 14.2 Part of side-scan sonar record MAKAT-82 (30 kHz) and co-registered sub-bottom profile (7.5 kHz) from the distal continental slope revealing the irregular bathymetry between the debris flows from the Andøya Slide. The depressions are inferred to be flute (or scour) marks. See Fig. 14.1 for location

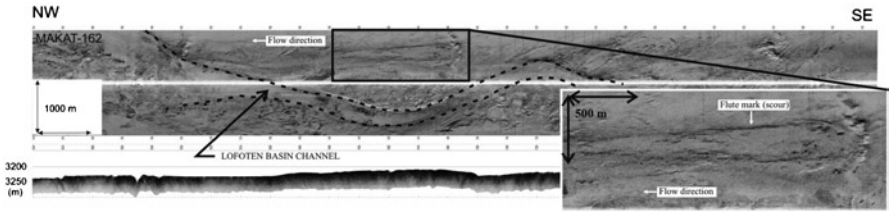

Fig. 14.3 MAKAT-162 side-scan sonar record (30 kHz) and co-registered sub-bottom profile (7.5 kHz) along part of the distal Lofoten Basin Channel (outlined by *stippled line*) showing a large flute mark northwest of the channel. For location see Fig. 14.1

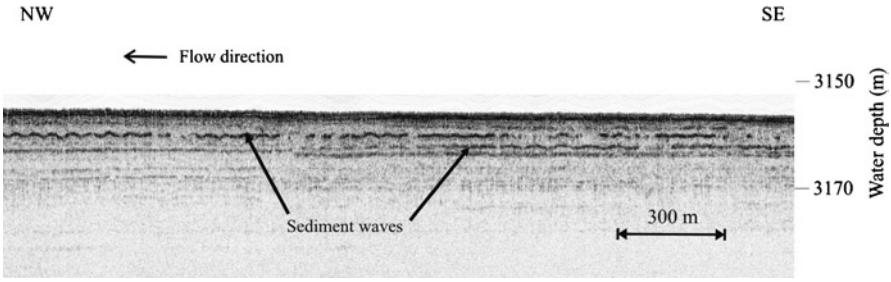

Fig. 14.4 Sub-bottom profile (7.5 kHz) from the Lofoten Basin displaying stacked turbidite and/or debris flow units separated by thin intervals of hemipelagic and/or turbiditic mud. Levels comprising *sediment waves* are indicated. See Fig. 14.1 for location

Study area 2 is located near the termination of the Lofoten Basin Channel at about 3,200 m water depth (Fig. 14.1). Laterally extensive sheets of normally graded sand interbedded with thinner mud layers characterize the abyssal plain beyond (i.e. west of) the termination (see below). However, on the channel flanks, previously unrecognized sea floor depressions occur in several shapes. The largest depression is more than 2 km long, up to 250 m wide, some meters deep. It becomes less distinct in the down-flow direction (Fig. 14.3).

14.3 Areas of Deposition from Gravity Currents

The deepest part of the Lofoten Basin is the area beyond the mouth of the Lofoten Basin Channel (Fig. 14.1). Several 2–5 m thick units extending over tens of kilometers were identified on high-resolution (deep-towed) sub-bottom profiler records (Fig. 14.4). They are separated by continuous to slightly discontinuous medium to high amplitude reflections, indicating marked differences in physical and/or lithological properties. Some reflections are partly wavy with wave heights and lengths

of up to a few meters and several tens of meters, respectively. The repetition in the seismic facies (Fig. 14.4) suggests that the uppermost part of the Lofoten Basin is composed of a series of stacked, coarse-grained turbidite units separated by thin intervals of hemipelagic and/or turbiditic mud (Laberg et al. 2005). The wavy signature is interpreted to reflect sediment waves suggesting that some of the units were deposited from large-volume, high-concentration turbidity currents following Wynn and Stow (2002).

14.4 Discussion

Sea-floor depressions imply erosion. Although not symmetric parabolic erosional marks inferred to be flute marks by Allen (1971, 1982) or the giant flute marks from the Eastern valley of the Laurentian Fan, which are much deeper than the one reported in the present study (Shor et al. 1990), we suggest that the depressions described in our study most likely are flute (or scour) marks. The complex morphology of some of the large flute marks could be due to amalgamation (or clustering; Allen (1982)) of several smaller features while the morphological simpler forms are single marks. We assume that the morphological variations across an area of several tens of kilometers are caused by significant variations in the properties of the eroded sediments, as well as velocity (basal shear stress) and duration of the eroding current(s).

The presence of flute marks shows that erosion of the sea floor by unconfined turbidity currents can be highly selective and thus difficult to estimate as reported by Wetzel and Aigner (1986). The erosion occurred most likely from eddies in the head region of the current (Middleton 1993). Experimental studies have shown that instantaneous velocities associated with large eddies could exceed the maximum mean downstream velocity by up to 50% (Kneller and Buckee 2000). The flutes demonstrate that some turbidity currents have been able to erode and increase their load with time. If erosion was exceeding deposition some of these flows may have been ignitive and increasing in size (Parker 1982) and may thus have been able to flow until they reached the deepest part of the basin.

So far, large flute marks have mainly been identified on modern (Normark and Piper 1991; Masson et al. 1995) and ancient (Winn and Dott 1979) submarine fans, and in channel-lobe transitional zones (Kenyon et al. 1995; Palanques et al. 1995; Huvenne et al. 2009). They are not commonly described from channel flanks and areas of slide deposits as shown here. In the studied part of the abyssal Lofoten Basin, dominated by smaller channels formed by confined turbidity currents (Ó Cofaigh et al. 2006), the flute marks indicate erosion from much larger and unconfined events. Their source area(s) have not been identified yet, but erosion by and deposition from turbidity currents have been reported from the distal Trænadjupet Slide ~50 km south-east of our study area (Laberg et al. 2006). Our results indicate that the turbidity currents associated with the Trænadjupet Slide or older slides in the adjacent area had much longer run-out distances than previously assumed and that they most probably terminated in the deepest part of the basin, west of the study area (Fig. 14.4).

This is in conformity with Haflidason et al. (2007), showing that sandy turbidies from the Trænadjupet Slide also is found west of study Area 2.

Similarly, the occurrence of flute marks in the area of the distal Andøya Slide indicates passage of spatially extensive and unconfined turbidity currents possibly associated with the slide event, although recent studies by Rise et al. (2009) have shown that the source area for this event probably is less extensive than originally anticipated (see references above). This may indicate that episodes of mass wasting at the adjacent continental slope may have resulted in large turbidity currents in addition to previously identified debris flows. Alternatively, the flows occurred during separate events. This would, in consequence, indicate that sediment failure occurred more frequently than previously assumed. Thus, estimates of the recurrence intervals of sediment failures in this area including the Trænadjupet and Andøya Slides only are probably too low.

The age of the flute marks remains yet unknown. However, if the features identified in study area 2 can be associated with the Trænadjupet Slide they have a minimum age of ~4,500 calendar years (~4,060 ^{14}C years BP; Laberg et al. 2002). The flutes from area 1 may have formed some time after the last glacial maximum if associated with the Andøya Slide. Alternatively, the flutes may be older and have formed during multiple events as indicated by occasional clustering (Fig. 14.2). In this case, the flute-forming events may tentatively be correlated to the buried turbidite unit comprising sediment waves in the deepest part of the Lofoten Basin (Fig. 14.4), that probably were deposited from large-volume, high-concentration turbidity currents.

Substantial erosion of the deep-sea floor offshore Norway was not realized until high – ultra-high resolution side-scan data became available. This is, at least partly, because flute marks are more easily identified from their acoustic contrast rather than their relief. Thus, seemingly undisturbed areas of smooth sea floor could instead be areas of erosion and sediment bypass. Data with this level of resolution is rarely available from the deep-water realm. Thus, it should not be excluded that the frequency of gravity flows may be larger than previously realized also elsewhere. A proper evaluation of recurrence intervals of submarine landslides and related events is of vital importance both for evaluation of the tsunamogenic potential and a sustainable exploration and exploitation of offshore resources and related infrastructure. The findings reported here indicate that, in order to obtain correct recurrence intervals, detailed studies of the deep-sea realm should be included.

14.5 Conclusions

Flute marks at the lower continental slope and in the slope – abyssal plain transitional area indicates that large and unconfined turbidity currents eroded and increased their loads in these settings. This led us to suggest that episodes of mass wasting originating from the adjacent continental slope included both large turbidity currents in addition to debris flows. Alternatively, the flows occurred during separate events and episodes of sediment failure were more frequent than

previously inferred. In any case, large and unconfined turbidity currents may form important parts of submarine mass wasting that are difficult to identify without high-resolution data from the deep-sea realm.

Acknowledgement This work is a contribution to the *Democen* project (http://www.ig.uit.no/Democen/) and the UNESCO program *Training Trough Research*. We acknowledge the Research Council of Norway and Statoil for financial support, the Captain and crew of the Russian research vessel *Professor Logachev* who provided essential support for the acquisition of the data and the reviewers L. Rise and P. Knutz. The bathymetry for Fig. 14.1 was displayed using the Generic Mapping Tools (GMT) software (Wessel and Smith 1998). Thanks always to Neil H. Kenyon for his support, enthusiasm and many valuable discussions on the issues presented in this paper.

References

Allen JRL (1971) Transverse erosional marks of mud and rock: their physical basis and geological significance. Sediment Geol 5:167–384

Allen JRL (1982) Sedimentary structures: their character and physical basis, vol 1 & 2. Elsevier, New York, 593 pp and 663 pp

Canals M, Lastras G, Urgeles R et al (2004) Slope failure dynamics and impacts from seafloor and shallow sub-seafloor geophysical data: case studies from the COSTA project. Mar Geol 213:9–72

Dowdeswell JA, Kenyon NH, Elverhøi A et al (1996) Large-scale sedimentation on the glacier-influenced Polar North Atlantic margins: long-range side-scan sonar evidence. Geophys Res Lett 23:3535–3538

Haflidason H, Sejrup HP, Nygård A, Mienert J, Bryn P, Lien R, Forsberg CF, Berg K, Masson D (2004) The Storegga Slide: architecture, geometry and slide development. Mar Geol 213:201–234

Haflidason H, Lien R, Sejrup HP, Forsberg CF, Bryn P (2005) The dating and morphometry of the Storegga Slide. Mar Petrol Geol 22:123–136

Haflidason H, de Alvaro MM, Nygård A, Sejrup HP, Laberg JS (2007) Holocene sedimentary processes in the Andøya canyon system, north Norway. Mar Geol 246:86–104

Huvenne VAI, McPhail SD, Wynn RB, Furlong M, Stevenson P (2009) Mapping giant scours in the deep ocean. EOS 90(32):274–275

Jakobsson M, Macnab R, Mayer L, Anderson R, Edwards M, Hatzky J, Schenke HW, Johnson P (2008) An improved bathymetric portrayal of the Arctic Ocean: implications for ocean modeling and geological, geophysical and oceanographic analyses. Geophys Res Lett 35 L07602 doi:10.1029/2008GL033520

Kenyon NH, Millington J, Droz L, Ivanov MK, Kenyon NH, Millington J, Droz L, Ivanov MK (1995) Scour holes in a channel-lobe transition zone on the Rhône Cone. In: Pickering KT, Hiscott RN, Kenyon NH, Ricci Lucchi F, Smith RDA (eds) Atlas of deep water environments-architectural style in turbidite systems. Chapmann & Hall, London, pp 212–215

Kneller B, Buckee C (2000) The structure and fluid mechanics of turbidity currents: a review of some recent studies and their geological implications. Sedimentology 47(Suppl 1):62–94

Laberg JS, Vorren TO, Dowdeswell JA, Kenyon NH, Taylor J (2000) The Andøya Slide and the Andøya Canyon, north-eastern Norwegian-Greenland Sea. Mar Geol 162:259–275

Laberg JS, Vorren TO, Mienert J, Bryn P, Lien R (2002) The Trænadjupet Slide: a large slope failure affecting the continental margin of Norway 4000 years ago. Geo-Mar Lett 22: 19–24

Laberg JS, Vorren TO, Kenyon NH, Ivanov M, Andersen ES (2005) A modern canyon-fed sandy turbidite system of the Norwegian continental margin. Norw J Geol 85:267–277

Laberg JS, Vorren TO, Kenyon NH, Ivanov M (2006) Frequency and triggering mechanisms of submarine landslides of the North Norwegian continental margin. Norw J Geol 86:155–161

Masson DG, Kenyon NH, Gardner JV, Field ME, Masson DG, Kenyon NH, Gardner JV, Field ME (1995) Monterey Fan: channel and overbank morphology. In: Pickering KT, Hiscott RN, Kenyon NH, Ricci Lucchi F, Smith RDA (eds) Atlas of deep water environments: architectural style in turbidite systems. Chapmann & Hall, London, pp 74–79

Middleton GV (1993) Sediment deposition from turbidity currents. Annu Rev E Plan Sci 21:89–114

Normark WR, Piper DJW (1991) Initiation processes and flow evolution of turbidity currents: implications for the depositional record. SEPM Spec Publ 46:207–230

Ó Cofaigh C, Dowdeswell JA, Kenyon NH (2006) Geophysical investigations of a high-latitude submarine channel system and associated channel-mouth lobe in the Lofoten Basin, Polar North Atlantic. Mar Geol 226:41–50

Palanques A, Kenyon NH, Alonso B, Limonov A (1995) Erosional and depositional patterns in the Valencia Channel mouth: an example of a modern channel-lobe transition zone. Mar Geophys Res 17:503–517

Parker G (1982) Conditions for the ignition of catastrophically erosive turbidity currents. Mar Geol 46:307–327

Pratson LF, Nittrouer CA, Wiberg PL et al (2007) Seascape evolution on clastic continental shelves and slopes. In: Nittrouer CA, Austin JA, Field ME, Kravitz JH, Syvitski JPM, Wiberg PL (eds) Continental margin sedimentation: from sediment transport to sequence stratigraphy, vol 37, Special Publication for International Association of Sedimentologists. Blackwell Publication, Malden/Oxford, pp 339–380

Rise L, Bellec V, Bøe R, Thorsnes T (2009) The Lofoten – Vesterålen continental margin, North Norway: Canyons and Mass-movement activity. In: International conference on seafloor mapping for Geohazard assessment, 11–13 May 2009, Ischia. Rendiconti Online, Societa Geologica Italiana, Ext Abs 7:79–82

Shor AN, Piper DJW, Hughes Clarke JE, Mayer LA (1990) Giant flute-like scour and other erosional features formed by the 1929 Grand Banks turbidity current. Sedimentology 37:631–645

Taylor J, Dowdeswell JA, Siegert MJ (2002) Late Weichselian depositional processes, fluxes, and sediment volumes on the margins of the Norwegian Sea (62–75°N). Mar Geol 188:61–77

Vorren TO, Laberg JS, Blaume F et al (1998) The Norwegian-Greenland Sea continental margins: morphology and late Quaternary sedimentary processes and environment. Quat Sci Rev 17:273–302

Weaver PPE (2003) Northwest African continental margin: history of sediment accumulation, landslide deposits, and hiatuses as revealed by drilling the Madeira Abyssal Plain. Paleoceanography 18. doi:10.1029/2002PA000758

Wessel P, Smith WHF (1998) Improved version of the generic mapping tools released. EOS 79:579

Wetzel A, Aigner T (1986) Stratigraphic completeness. Tiered trace fossils provide a measuring stick. Geology 14:234–237

Winn RD Jr, Dott RH Jr (1979) Deep-water fan-channel conglomerates of Late Cretaceous age, southern Chile. Sedimentology 26:203–228

Wynn RB, Stow DAV (2002) Classification and characterisation of deep-water sediment waves. Mar Geol 192:7–22

Chapter 15
Investigations of Slides at the Upper Continental Slope Off Vesterålen, North Norway

Leif Rise, Shyam Chand, Haflidi Haflidason, Jean Sebastian L'Heureux, Berit Oline Hjelstuen, Valerie Bellec, Oddvar Longva, Jo Brendryen, Maarten Vanneste, and Reidulv Bøe

Abstract Multibeam bathymetry, high-resolution seismic profiles and sediment cores were collected from the upper continental slope outside Andøya, the northernmost island in Vesterålen, northern Norway (69°N). Eight small slides are identified at water depths between 500 and 800 m. These are linked to a larger slide related to the development of the Andøya Canyon by high resolution seismic. Slope angles adjacent to the headwalls of the small slides are 3–4° while slide deposits have accumulated where slope angles are 2–3°. The slides occurred in parallel-stratified glacial marine sediments, and three seismic horizons are interpreted. One of these horizons coincides with failure planes in four of the slides. A 12 m long core terminates above this level, but penetrates another horizon representing a slip plane in two of the slides. The core comprises silty clay with varying content of ice rafted debris. The upper slope shallower than 450 m appears stable although it may be up to 8° steep. Tension cracks up to 2 m deep on the lower slopes may suggest that deformation is active near the canyon systems.

Keywords Submarine slides • Failure planes • Continental slope • Multibeam bathymetry • High resolution seismic lines • Calypso core

L. Rise (✉) • S. Chand • J.S. L'Heureux • V. Bellec • O. Longva • R. Bøe
Geological Survey of Norway (NGU), Postboks 6315, Sluppen,
7491 Trondheim, Norway

International Centre for GeoHazards (ICG), P.O. Box 3930,
Ullevål Stadion, N-0806 Oslo, Norway
e-mail: leif.rise@ngu.no

H. Haflidason • B.O. Hjelstuen • J. Brendryen
Department of Earth Science, University of Bergen, Bergen, Norway

M. Vanneste
Norwegian Geotechnical Institute (NGI), Oslo, Norway

International Centre for GeoHazards (ICG), P.O. Box 3930,
Ullevål Stadion, N-0806 Oslo, Norway

Y. Yamada et al. (eds.), *Submarine Mass Movements and Their Consequences*,
Advances in Natural and Technological Hazards Research 31,
DOI 10.1007/978-94-007-2162-3_15,

15.1 Introduction

Several large slides have occurred on the continental margin off northern Norway and the southwestern Barents Sea (67–72°N) (Vorren et al. 2003). The Lofoten-Vesterålen continental margin is characterized by several deep canyons systems (Fig. 15.1), and numerous instabilities have occurred on steep slopes. This region receives increased attention as it may be one of the next areas opened for hydrocarbon exploration in Norway. The study area is located on the upper slope between the Andøya Canyon to the north and a 1,000 m deep canyon to the south (Laberg et al. 2007; Bellec et al. 2010) (Fig. 15.1). Although this area appears relatively smooth and undisturbed compared to surrounding slopes, detailed morphology reveals eight well defined small slide scars (Fig. 15.2). Five of these slides are studied in more detail together with a larger slide related to the development of a branch of the Andøya Canyon (Fig. 15.2).

The main objective of this paper is to describe the morphology of the slides and relate the acoustic stratigraphy to failure planes. This is the first study of seabed stability in this poorly investigated area.

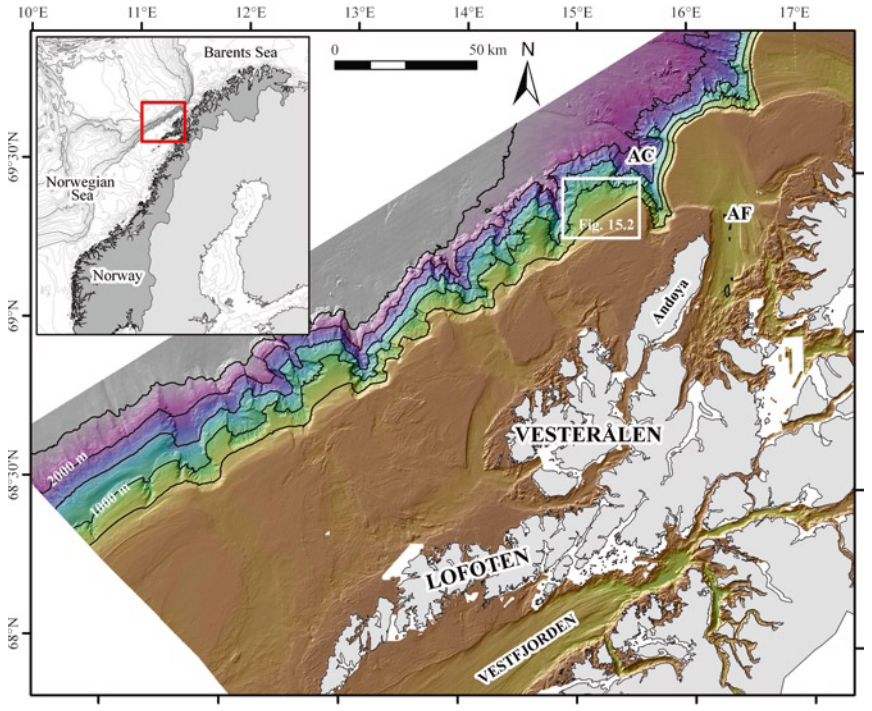

Fig. 15.1 The Lofoten – Vesterålen continental margin. The Andøya Canyon (*AC*) is the second northernmost of c. 15 deep canyons intersecting the continental slope. The study area (Fig. 15.2) is shown. *AF* Andfjorden

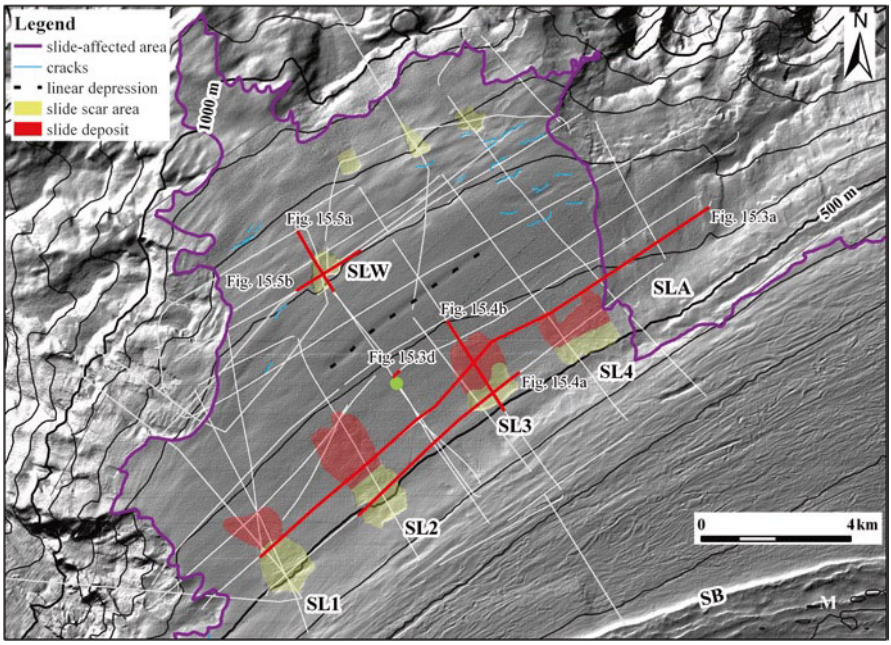

Fig. 15.2 Shaded relief bathymetric image of the study area (100 m contour interval). The grid of Topas profiles is shown together with the location of the 12 m long piston core (*green circle*). Note that the canyon slopes and the lower slope between the canyons are affected by mass movements (*violet line*). *Slide SLA* is within this area, related to a branch of the Andøya Canyon (*AC*). In addition to the five slides *SL1–4* and *SLW*, three other slide scars are detected, as well as seabed cracks and a long linear depression. Note the moraine ridges (*M*) and shelf break (*SB*) at the southeastern corner of the image, and the iceberg scoured furrows on the uppermost slope. The locations of Figs. 15.3–15.5 are shown

15.2 Database

Multibeam bathymetry was acquired by the MAREANO seafloor mapping programme (www.mareano.no) using Simrad echosounder systems EM710 and EM1002. Bathymetric grids have cell size of 5 m in water depth shallower than c. 1,000 and 25 m grid cell size beyond. High-resolution reflection data were collected by a hull-mounted Parametric Sub-bottom Profiler System (Topas) onboard R/V G.O. Sars in July 2010. Topas profiles acquired by MAREANO have also been available, and a total of ~280 line-kilometers have been interpreted in the 175 km^2 large study area (Fig. 15.2). To ground truth the seismic stratigraphy a 12 m long calypso piston core was collected. Multi Sensor Core Logging (MSCL) and X-ray imagery were performed, and various geological (e.g., dating, grain size distributions, XRF) and geotechnical (e.g., triaxial tests, direct simple shear tests, oedometer) analyses are under processing (Vanneste et al. 2012).

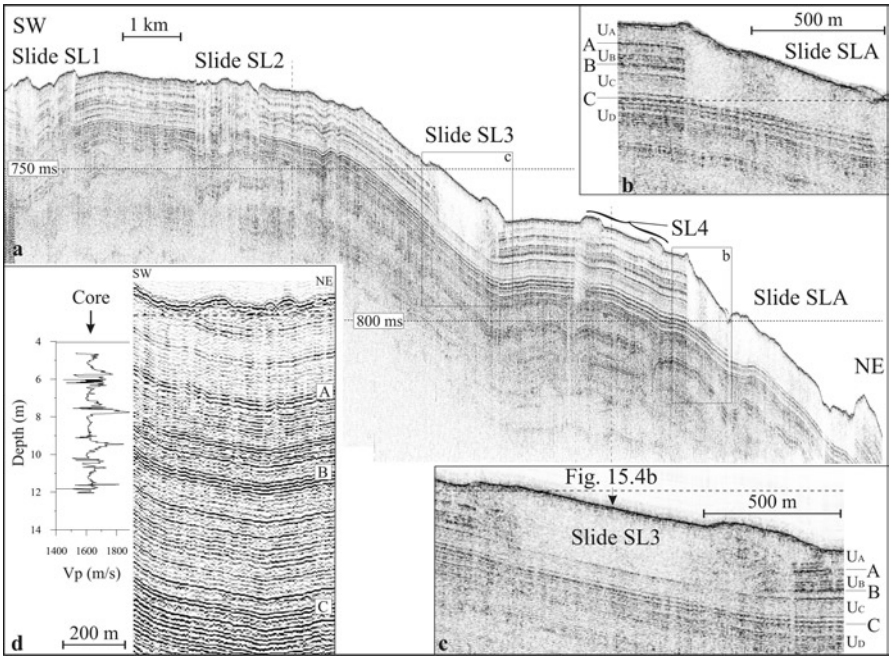

Fig. 15.3 (**a**) Topas line along the slope crossing slides *SL1–3*, two depositional lobes of slide *SL4*, ending in slide *SLA*. (**b**) Enlarged image showing that horizon *C* served as the main glide plane for slide *SLA*. (**c**) Enlarged image showing a failure plane directly below horizon *B* in the depositional area of slide *SL3*. (**d**) Reflection pattern of a line ending c. 200 m north of the core location shown together with the velocity log from the core (1,660 m/s used for correlation)

15.3 Landforms and Geological Setting

The continental shelf of the Lofoten–Vesterålen margin narrows northwards to c. 25 km west of Andøya (Fig. 15.1). It is characterized by shallow banks separated by cross-shelf troughs which were eroded by ice streams originating in the high mountain areas to the east (Ottesen et al. 2005). The Quaternary succession on the shelf is commonly less than 25 m thick, and comprises mainly till lying discordantly above sub-cropping Cretaceous strata. The shallow banks are commonly covered by a layer of gravel, cobbles and boulders indicating winnowing by waves during a lower sea level after the ice sheet retreated. The Lofoten-Vesterålen margin was sheltered from the Scandinavian inland ice, as high mountains formed a barrier and large ice streams followed the deep Andfjorden and Vestfjorden troughs (Fig. 15.1). Thus, only small amounts of material were transported to the shelf edge and distributed as glacigenic debris flows down the continental slope (Rise et al. 2009).

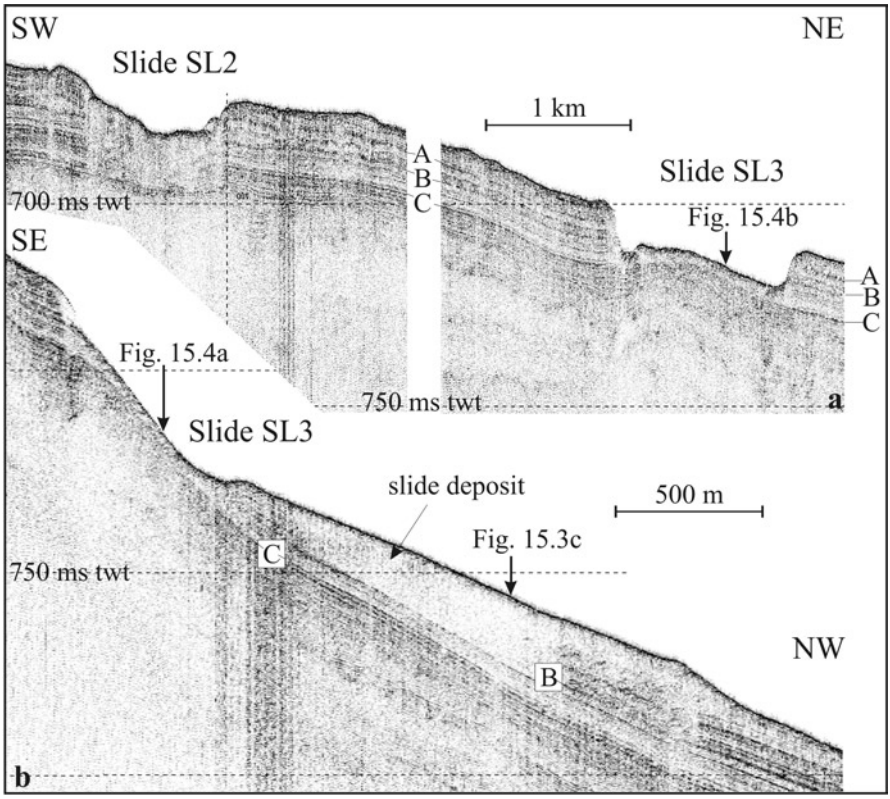

Fig. 15.4 (**a**) Topas line along the slope crossing the upper slide scars of slides *SL2* and *SL3*. Horizon *C* appears to be the failure plane in slide *SL3*. (**b**) Seismic line perpendicular to the contours showing the slide scar and deposits of slide *SL3*. The *arrows* show the intersection of other *lines* presented

Multibeam data reveal detailed morphology of about 15 canyons, several of them being eroded 500–1,100 m below their adjacent shoulders (Bellec et al. 2010) (Fig. 15.1). The average slope angle from the shelf edge to the base of the slope is 4–10°. Canyon slopes are commonly much steeper and may exceed 20°. The canyons have probably developed over several million years. Numerous large and smaller slide scars occur on the canyon slopes and flanks. This shows that slides and other gravity flows have been, and still are, important processes in the evolution of the canyons. The areas between the canyons are also affected by erosion and mass movements, particularly in the lower region (Rise et al. 2009). Some fairly smooth areas with slopes of 1–4° occur between the canyons at water depth less than ca. 1,000 m (Fig. 15.2). Parallel-laminated acoustic facies indicates predominantly hemipelagic deposition (Bellec et al. 2010).

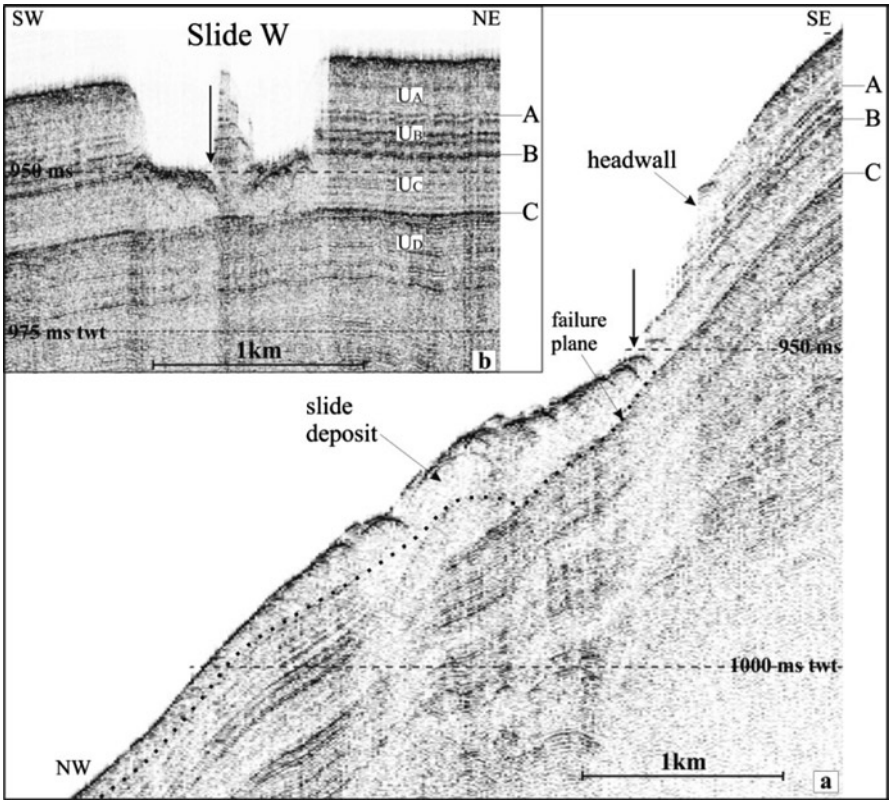

Fig. 15.5 (**a**) Topas line perpendicular to the contours showing the slide scar and deposits of slide *SLW*. (**b**) The *line along the slope* indicates that horizon *C* represents the main glide plane. The *arrows* show the *intersection of the lines*

15.4 Results

15.4.1 Morphological Features

Beyond the shelf edge at ca. 150 m water depth the iceberg-grooved seafloor dips gently (1–2°) northwestwards. The seafloor is smoother along a steeper slope segment (3–8°) at depths between 350 and 550 m. However, four small slides occur in water depths of ca. 500 m (SL1–4, Fig. 15.2). Their escarpments are up to ca. 10 m high with slope angles of 5–10°. The dip of the undisturbed seafloor adjacent to these headwalls is on average 3–4°. The slide masses have travelled only 1–2 km, revealed by positive topography in the depositional areas where the slopes are 2–3°. Another slide at ca. 700 m depth (SLW) has 10–15° steep escarpments that are up to 15 m high. It is not possible to identify the deposits of this slide which probably were dispersed as a thin layer. Three unnamed small slides at ca. 800 m water depth lie close to the lower slope area (>900 m).

The upper part of the canyon walls and their adjacent shoulders on either side of the study area are also sculpted by slide scars of various dimensions. Slide SLA is the largest slide, and is part of the slide area extending upslope of a branch of the Andøya Canyon (Figs. 15.1 and 15.2). Also this slide has its upper escarpment along the same steeper slope segment as slides SL1–4.

Between slide SLW and slides SL1–4, where the water depth is 600–700 m, the slope angle is commonly less than 1°. A very subtle depression can be seen as an approximately 300 m wide and 6 km long linear feature (Fig. 15.2). Several very short and partly curved linear depressions are also detected (1–2 m deep and 20–30 m wide), most of them northeast of the lineament (Fig. 15.2).

15.4.2 Seismic Stratigraphy, Slides and Failure Planes

The upper 20–30 m of the seabed are mainly characterized by continuous, parallel to sub-parallel reflections (Figs. 15.3–15.5). Three horizons (A (youngest) -C) are interpreted, subdividing the sedimentary succession into units U_A–U_D. Horizons B and C are both strong, continuous reflections across the entire area. They likely represent failure planes for the slides, but their seismic character varies within the area. U_A and U_C are more transparent than U_B and U_D – the latter ones are characterized by narrowly spaced and often higher amplitude reflections than the former ones (see Figs. 15.3b and 15.5b).

Slide SL2 has eroded the sediments below horizon C (Fig. 15.4a), indicating a failure plane at the base of the stratified unit U_D. The seismic lines crossing slide scar SL1 have poorer resolution, but this slide also eroded into stratified sediments of unit U_D (Fig. 15.3a).

Slide SL3 most likely slipped along horizon C in the upper part of the slide scar (Fig. 15.4). In the lower slide scar area, the mass movement took place above a distinct reflection directly below horizon B (Figs. 15.3c and 15.4b). The seismic lines crossing slide SL4 give a less clear image, however, horizon C most likely represents the main glide plane. Also in this slide, much of the slide deposits accumulated above horizon B.

Also slide SLA has horizon C as its main failure plane (Fig. 15.3b). In the north-eastern part, the mass flow locally followed horizon B, and towards the deep parts of this slide area also surfaces below horizon C acted as failure planes. Also slide SLW utilized horizon C as a glide plane in the deepest part of the slide scar (Fig. 15.5).

15.4.3 X-Ray Images, Core Logging and Soil Mechanical Testing

X-ray images show that most of the core contains varying contents of coarse sand to gravel sized ice rafted debris (IRD) dispersed in a silty-clayey matrix of grey-bluish or more brownish colour. Five intervals, up to 0.7 m thick, contain only few IRD-clasts. These layers show weak laminations and coincide with low values in the MSCL

records of sound velocity, density and magnetic susceptibility. Between the laminated intervals, IRD-content is highest at peak values in the MSCL records. The rhythmically changing depositional environment is illustrated by the sonic log (Fig. 15.3d). One of the fine-grained laminated intervals (8.1–8.8 m depth in the core) exhibits contractive behaviour during triaxial undrained shear test.

15.5 Discussion

Units U_A–U_C become slightly thicker with increasing water depths. They exhibit only small thickness variations along the slope, and a glacimarine depositional environment dominated at water depths larger than ca. 450 m. IRD-free laminated intervals may represent periods of rapid deposition due to high flux of suspended particles. Although the seafloor slopes are 5–8° directly upslope of the headwalls of slides SL1–4, no mass movements are observed at water depths shallower than 450 m. Above this depth sediment units thin upslope, probably due to stronger ocean currents causing bypass of the finest sediment particles. Both factors may have led to greater slope stability.

Horizon C, defining the top of the stratified unit U_D, appears to be a weak layer as it represents a failure plane in both slide SLA and slide SLW (Figs. 15.3 and 15.5). It is not straightforward to pinpoint the failure plane for slide SL3. In the lower part of this slide scar horizon B (or the distinct reflection directly underneath) appears to be a slip plane (Fig. 15.4b). If this surface was the initial slip plane in the upper slide scar some erosion of unit U_C must have occurred during sliding. We find it most likely that horizon C represents the failure plane in the upper part of the slide scar, and that slide deposits were not totally evacuated. Much of the distal mass flow, however, followed horizon B, indicating that both horizons were involved in the slide development.

MSCL-data show an average sound velocity of c. 1,660 m/s. The core does not penetrate horizon C at ca. 19–20 ms two way time thickness (ms twt) (16–17 m). If we apply a constant velocity of 1,660 m/s for correlation of the core and the seismic (Fig. 15.3d), horizon B at 11–12 ms twt corresponds to a depth of 9.2–10.0 m below the seafloor. A laminated fine-grained layer with very few IRD-clasts at 9.8–10.2 m in the core may therefore represent a weak layer which developed into a failure plane. It must be noted that the velocity profile for the upper 4.5 m of the core is missing and that the along-slope line with the best resolution ends 200 m from the core location (Fig. 15.3d). Triaxial undrained shear testing of a similar, fine-grained layer at 8.1–8.8 m in the core shows a contractive behaviour. This indicates build-up of excess pore pressure during lateral (shear) movement. Studies in the Storegga Slide area have shown that failure planes were developed in clay-rich stratified sediments with contractive and strain softening behaviour (Bryn et al. 2005).

The ages of the slides are not known yet, but although features appear ‘fresh’ the mass movements may have occurred more than 10,000 years ago. The detailed

bathymetry indicates some post-slide deposition in one of the slide scars, but it is not possible from seismic data to resolve post-slide sediments above the slide deposits.

The 6 km long subtle linear seafloor feature (Fig. 15.2) mirrors a small depression ca. 30 m below the seafloor which probably formed during a period of strong contour-parallel currents. Prevailing hemipelagic sedimentation has preserved the feature, and there is no indication of stress-related deformation in the laminated sediments. However, the short and curved features seen in Fig. 15.2 could be attributed to extension due to loss of lateral support caused by sliding on the nearby steeper slopes. Such deformation mechanism might still be active. Alternatively, the features are old and were formed by initial movements that not developed into slides.

15.6 Summary and Conclusions

- Five small slides and one larger slide were studied at water depths of 500–700 m on the upper slope of the Vesterålen margin (Fig. 15.2). The slides have occurred in parallel-stratified hemipelagic sediments where slope angles are 3–4°, while the slide deposits have accumulated where slope angles are 2–3°.
- Horizon C appears to have been the major failure plane (Figs. 15.3–15.5) in four of the slides. A layer close to horizon B has also acted as a failure plane.
- A 12 m long core shows fine-grained, laminated layers separating coarser grained diamictic intervals with IRD, and a ca. 0.4 m thick layer at ca. 10 m depth may represent the failure plane close to horizon B. Triaxial undrained shear testing of a different fine-grained, laminated layer show a contractive and strain softening behavior. Failure plane C was not penetrated by the core.
- The uppermost slope shallower than 450 m and the central part of the slope with slope angle lower than 2° are stable without slides.

Acknowledgements We thank the SEABED-Project within the Norwegian Deepwater Programme (www.ndwp.org) for financial support, and the MAREANO programme (www.mareano.no) for providing the multibeam bathymetric data. The reviewers, Drs. Dave Long and Dag Ottesen, are thanked for constructive comments. This is ICG publication no. 356.

References

Bellec V, Thorsnes T, Rise L, Bøe R, Dolan M, Hansen OH (2010) Dyphavet utenfor Lofoten-Vesterålen-Troms – Havbunnen – landskap, geologi og prosesser. In: Buhl-Mortensen L, Hodnesdal H, Thorsnes T (eds) Til bunns i Barentshavet og havområdene utenfor Lofoten – ny kunnskap fra MAREANO for økosystembasert forvaltning. Norges geologiske undersøkelse, Trondheim, pp 63–67

Bryn P, Berg K, Forsberg CF, Solheim A, Kvalstad TJ (2005) Explaining the Storegga Slide. Mar Petrol Geol 22:11–19

Laberg JS, Guidard S, Mienert J, Vorren TO, Haflidason H, Dowdeswell JA, Nygård A (2007) Morphology and morphogenesis of a high-latitude canyon; the Andøya Canyon, Norwegian Sea. Mar Geol 246:68–85

Ottesen D, Dowdeswell JA, Rise L (2005) Submarine landforms and the reconstruction of fast-flowing ice streams within a large Quaternary ice sheet: the 2500 km-long Norwegian-Svalbard margin (57° to 80°N). Geol Soc Am Bull 117(7/8):1033–1050

Rise L, Bellec V, Bøe R, Thorsnes T (2009) The Lofoten – Vesterålen continental margin, North Norway: Canyons and Mass-movement activity. In: Chiocci FL, Ridente D, Casalbore D and Bosman A (eds) International conference on seafloor mapping for Geohazard assessment, Ischia, 11–13 May 2009

Vanneste M, L'Heureux, JS, Baeten, N, Brendryen, J, Vardy ME, Steiner A, Forsberg CF, Kvalstad TJ, Laberg JS, Chand S, Longva O, Rise L, Haflidason H, Hjelstuen BO, Forwick M, Morgan E, Lecomte I, Kopf A, Vorren TO, Reichel T (2012) Shallow landslides and their dynamics in coastal and deepwater environments, Norway. In: Yamada Y et al (eds) Submarine mass movements and their consequences, vol. 31, Advances in natural and technological hazards research. Springer, Dordrecht, pp 29–41

Vorren TO, Sejrup HP, Dowdeswell JA (2003) The Norwegian margin. In: Weaver P, Mienert J (eds) European margin sediment dynamics: side-scan sonar and seismic images. Springer, New York

Chapter 16
Dakar Slide Offshore Senegal, NW-Africa: Interaction of Stacked Giant Mass Wasting Events and Canyon Evolution

Mathias Meyer, Jacob Geersen, Sebastian Krastel, Tilmann Schwenk, and Daniel Winkelmann

Abstract Acoustic data reveal giant submarine slides offshore Senegal. The most prominent slide, named Dakar Slide, shows a headwall with a length of at least 100 km in water depths of 2,000–3,100 m. The slide is situated between two canyons, the Dakar Canyon in the north and the Diola Canyon in the south. Seismic data indicate a complex interaction of mass wasting and canyon evolution during the formation of this part of the continental margin. The northern sidewall of the Dakar Slide crosses the distal part of the Dakar Canyon, which was repeatedly destroyed and filled by slide deposits. The area above the headwall does not show major mass-wasting events though the slope gradient there is significantly steeper. The Dakar Slide is underlain by multiple giant mass transport deposits reaching back to Oligocene times.

Keywords Submarine landslide • Mass failure • Canyon • Seismic reflection

16.1 Introduction

The evolution of the NW-African continental margin is characterized by large but infrequent submarine slides and big canyon systems (Wynn et al. 2000; Krastel et al. 2006). It is still not well understood why only specific sections of the margin repeatedly fail while others remain stable over long periods of time (Krastel et al. 2012).

M. Meyer (✉) • J. Geersen • S. Krastel • D. Winkelmann
Leibniz Institute of Marine Sciences (IFM-GEOMAR), Wischhofstr. 1-3 24148, Kiel, Germany
e-mail: mmeyer@ifm-geomar.de

T. Schwenk
Marum and Faculty of Geosciences, Bremen University, Bremen, Germany

Y. Yamada et al. (eds.), *Submarine Mass Movements and Their Consequences*, Advances in Natural and Technological Hazards Research 31,
DOI 10.1007/978-94-007-2162-3_16,

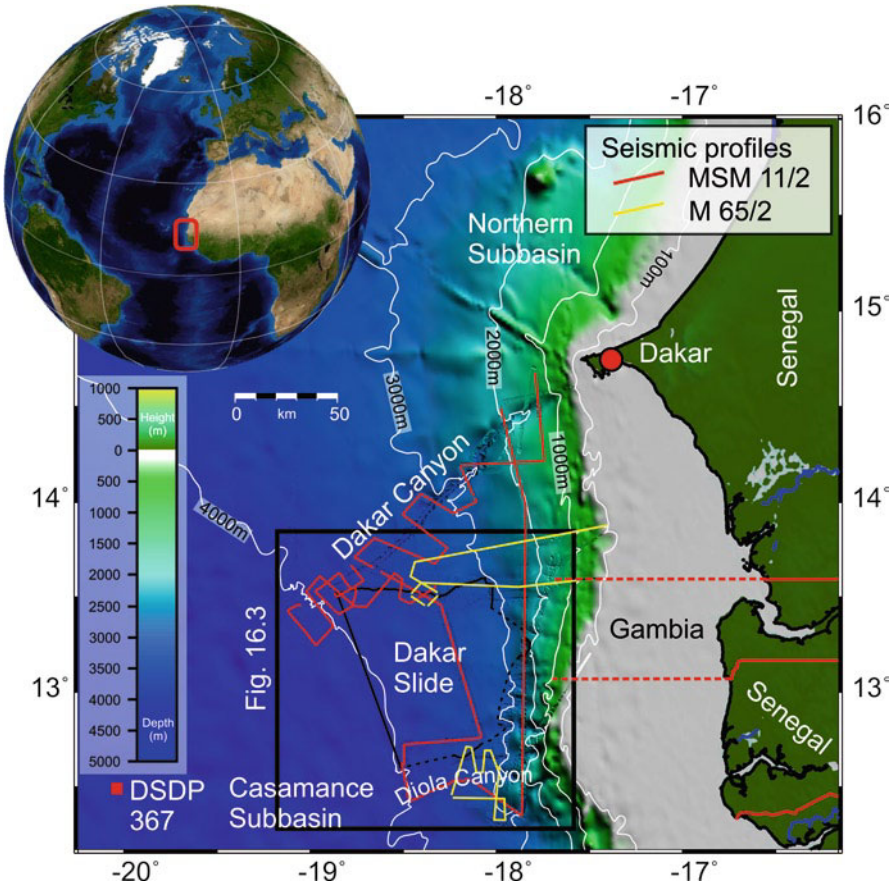

Fig. 16.1 Location of the study area offshore Senegal. The Dakar Slide is located between the Dakar and Diola Canyon. *Solid lines* around the Dakar Slide indicate the location of head and sidewalls; *dashed lines* mark their inferred continuation

Offshore the coast of Senegal and Gambia, a large submarine landslide, the Dakar Slide, is confined by two major canyon systems (Fig. 16.1). Both canyons, the Dakar Canyon in the north and the Diola Canyon in the south, were destroyed at some point by mass wasting in this area.

The main aim of this study is to analyze the Neogene and Quaternary sedimentary history of the continental margin off Senegal with special focus on the interactions between canyon evolution and slope failures.

16.1.1 Structural Setting

The Senegal Basin is classified as an Atlantic type passive margin or marginal sag basin of Middle Jurassic to Holocene age (Brownfield and Charpentier 2003;

Hansen et al. 2008). The study area is located in the southernmost part of the Senegal Basin, in the Casamance Sub-basin, offshore Senegal and Gambia (Fig. 16.1). The shelf break is found in water depths of 80–120 m. Slope inclinations range from 1° to 4°. The continental rise lies in a water depth of 4,000–4,500 m and displays slope gradients of <1°.

Hemipelagic particle flux from coastal upwelling and dust supply are the dominant sediment sources along the NW-African continental margin today (Henrich et al. 2010). Very little fluvial sediment reaches the margin. Local upwelling gives rise to high accumulation rates along the upper slope (Martinez et al. 1999). This leads to average modern sedimentation rates of ca. 4 cm/ka for the last 220 ka offshore Senegal (Pierau 2008). Well log data from DSDP site 367 (Fig. 16.1, The Shipboard Scientific Party and Bukry 1978) and ODP site 659 (approximately 600 km north of the working area off Mauritania in 3,080 m water depth, Ruddiman et al. 1988) show accumulation rates of 3 cm/ka for the entire Pleistocene and Pliocene. During the Miocene sedimentation rates decrease from ~1 cm/ka for Late Miocene to ~0.5 cm/ka during Early Miocene times.

16.1.2 Data

High resolution seismic and hydro-acoustic data were acquired during RV Meteor Cruise M65/2 in 2005 and RV M.S. Merian Cruise MSM11/2 in 2009 (Fig. 16.1). Seismic data were acquired using a 1.7 l GI-Gun with a vertical resolution of ~5 m. The data were recorded using a 450 m-long 72-channel analogue streamer during Cruise M65/2 and a 200 m-long 128-channel digital streamer during Cruise MSM11/2. Bathymetric data were acquired by a Kongsberg EM1120 multibeam echo-sounder (MSM11/2) and a Hydrosweep DS2 system (M65/2), respectively. A grid size of 100 m was chosen.

16.2 Results

16.2.1 Seismic Units and Stratigraphy

Seismic Profile SHK09-011 (Fig. 16.2, see Fig. 16.3 for location) includes all important units and is used to describe the general seismic stratigraphy of the working area. Due to the lack of a detailed stratigraphy from the nearby DSDP site 367 (see Fig. 16.1 for location), results from ODP site 659 were used to further constrain the stratigraphy. Despite their distance to the working area, both sites show a strong resemblance in thickness and seismic character to seismic units identified in the working area. Seismic units A, B, C (from young to old; Figs. 16.2 and 16.4) can be matched to seismic units 1, 2, 3 described by Ruddiman et al. (1988) for ODP site 659. Unit A displays parallel strong reflectors up to Middle Pliocene age. Unit B is characterized by mostly low amplitude reflectors reaching back to Middle

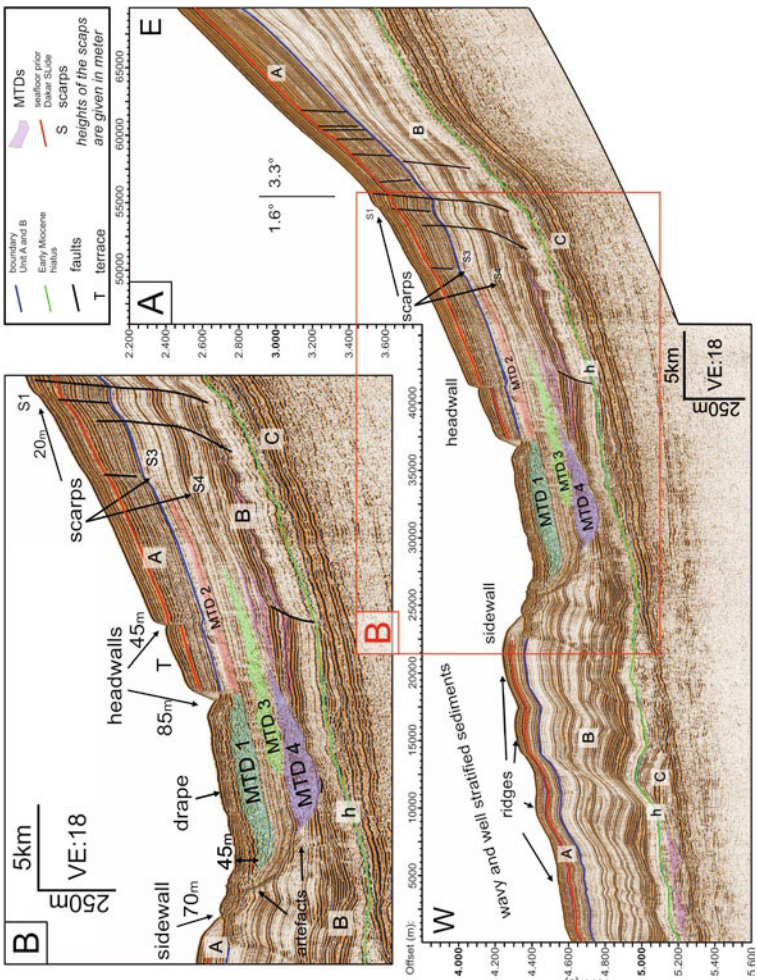

Fig. 16.2 (**a**) Seismic profile SHK09-011 showing headwall and sidewall of the Dakar Slide. *MTD 1* corresponds to the Dakar Slide and shares the same basal reflector as *MTD2*. *MTD2* is located downslope of slide scar *S3*. *MTD3* is located downslope of slide scar *S4*. *MTD4* represents the oldest large-scale slide. Horizon h marks an Early Miocene hiatus (Von Rad and Wissmann 1982). *S1* marks a 20 m high scarp. (**b**) Zoom showing the 70 m high sidewall and the two-stepped 85 and 45 m high headwall. T: 2 km wide terrace. For location of the profiles see Fig. 16.3

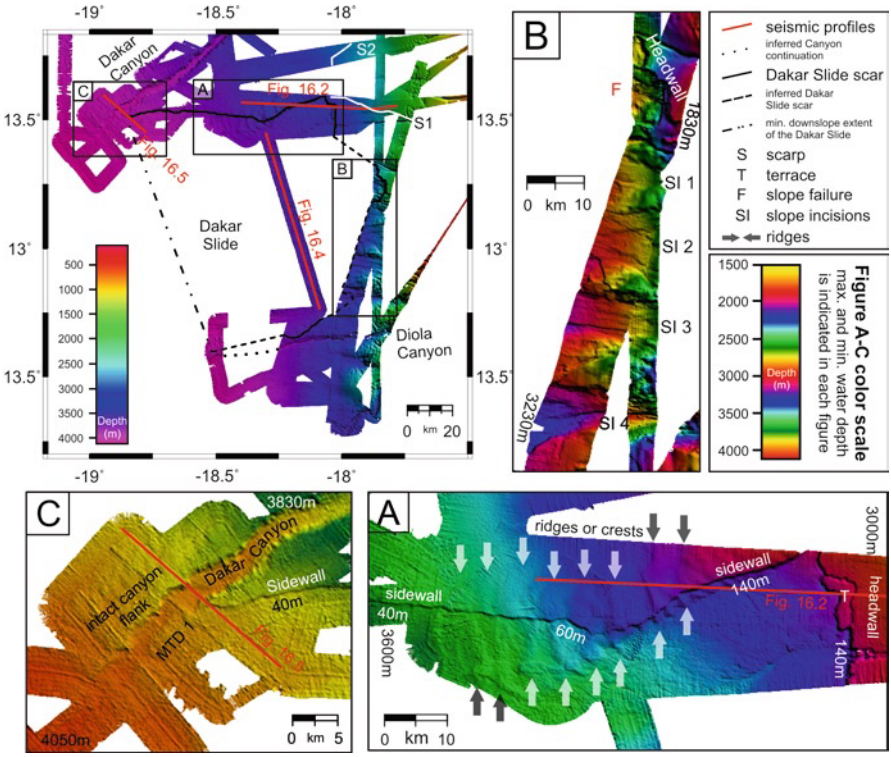

Fig. 16.3 Combined bathymetric map from Hydrosweep (M65/2) and EM1120 (MSM11/2) data of the Dakar Slide and its surrounding slope. Numbers along the scarps indicate the height. For location see Fig. 16.1

Miocene times. Horizon h (green line in Figs. 16.2, 16.4 and 16.5) marks the boundary between Unit B and C. Tracing this horizon through our dataset and along seismic lines published by Hansen et al. (2008), we correlate it to a hiatus described at DSDP site 367 (Lancelot 1978; Hansen et al. 2008). This 5 Ma spanning hiatus (18–23 Ma) (Ruddiman et al. 1988) incorporates most of the Early Miocene. Unit C comprises strong sub-parallel reflectors with good to moderate continuity of Early Miocene to Late Oligocene age. The upper part of this unit shows discontinuous to nearly chaotic reflections (Fig. 16.2b).

16.2.2 Dakar Slide

The Dakar Slide (MTD1) is located between 12°40′N and 13°35′N offshore central Senegal and Gambia (Fig. 16.1). To the northwest the slide is confined by the bordering Dakar Canyon and to the south by the Diola Canyon. The headwall is located

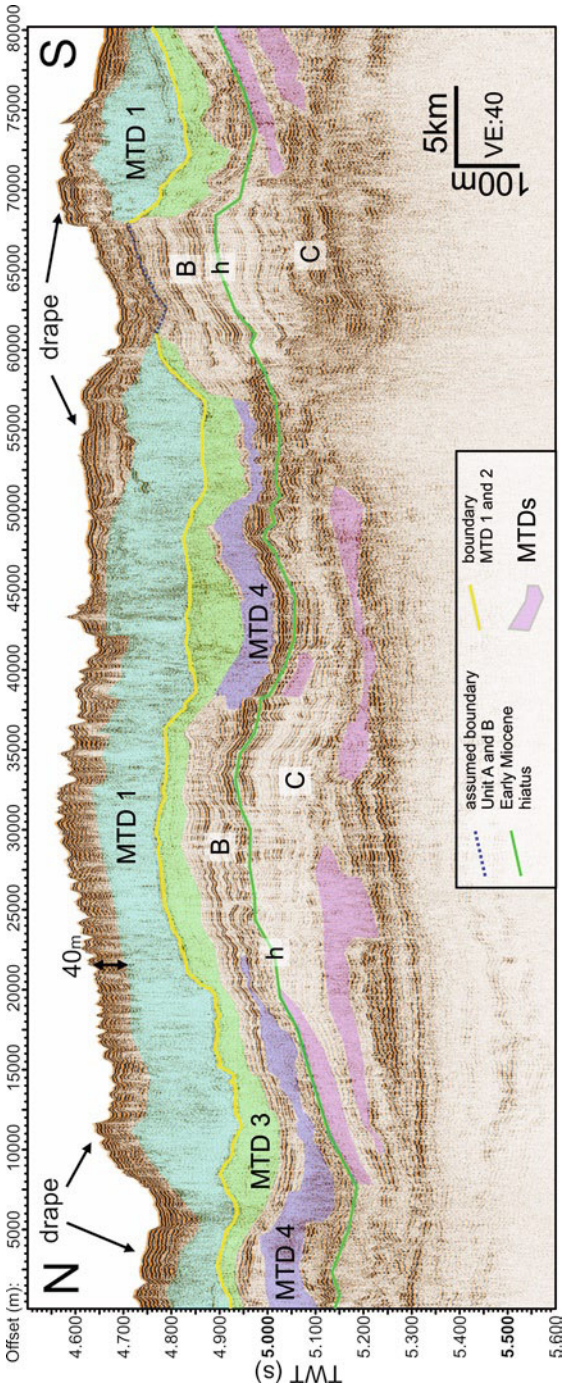

Fig. 16.4 Seismic profile GeoB03-056, cutting the Dakar Slide deposits in N–S direction. The *yellow horizon* separates *MTD 1* and *3* with a very small sediment package in between. For location of the profile see Fig. 16.3

in water depths between 2,000 and 3,100 m in an area with an average slope inclination of 1.5–3.6°. The slide scarps are up to 140 m high and show a stepped pattern in the most northern part of the headwall (T in Fig. 16.3a). Although our data does not cover the entire headwall area, bathymetric data upslope of the inferred position of the headwall reveals the existence of four slope incisions, each cutting 300 m deep (Fig. 16.3b, SI 1–4). All four incisions show scarps on both flanks. Combined with an up to 200 m-high scarp further north (labeled F on Fig. 16.3b) they most likely represent the continuation of the headwall. The length of the reconstructed headwall is ~100 km. A pronounced sidewall runs for 90 km from the northern edge of the headwall down to the Dakar Canyon. The minimum size of the failed area (though not fully mapped) is 8,000 km². Seismic data shows that the deposits of the Dakar Slide (MTD 1) are 120–150 m thick (Figs. 16.2 and 16.4). Therefore, the Dakar Slide contains a minimum volume of 1,000 km³ not taking into account the unmapped distal deposits. This volume makes the Dakar Slide to one of the largest slides at passive margins worldwide.

16.2.3 Older MTDs

Several older MTDs are imaged on seismic data (labeled MTD 2–4 on Figs. 16.2 and 16.4). MTD 3 shows a similar areal extent as MTD 1, but in some parts up to 50 m-thick undisturbed hemipelagic deposits are found between them (Fig. 16.2b). Hence, we interpret them as separate events. MTD 4 also shows a comparable extend as MTD 3. MTDs 3 and 4 are separated by multiple reflectors throughout the dataset. MTD 2 is a much thinner deposit that has the same basal reflector as MTD 1 (Fig. 16.2b).

16.2.4 Dakar Canyon

The Dakar Canyon is a relatively straight, deeply incised (up 1,000 m) canyon running from Dakar Cape in a SE direction (Figs. 16.1 and 16.3). At 3,900 m water depth, the southeastern canyon flank was destroyed by the Dakar Slide (Fig. 16.3c) and filled with MTDs (Fig. 16.5). At around 4,100 m water depth, the entire canyon disappears under hummocky slide topography. Profile GeoB05-073 (Fig. 16.5) images the architecture of the destroyed distal Dakar Canyon and can be horizontally subdivided into three parts: a northwestern levee where sediments are continuous and undisturbed, the partially destroyed canyon, and a southern part with disturbed sediments. The 440 m-deep, V-shaped canyon is almost filled leaving a 30 m-deep, U-shaped depression on the sea-floor. The basal fill shows some stratification, suggesting an interlayering of turbidites and background sediments. A significant part of the canyon is filled by MTD1 (corresponding to the Dakar Slide). A 50 m-thick undisturbed drape is found on top of MTD1.

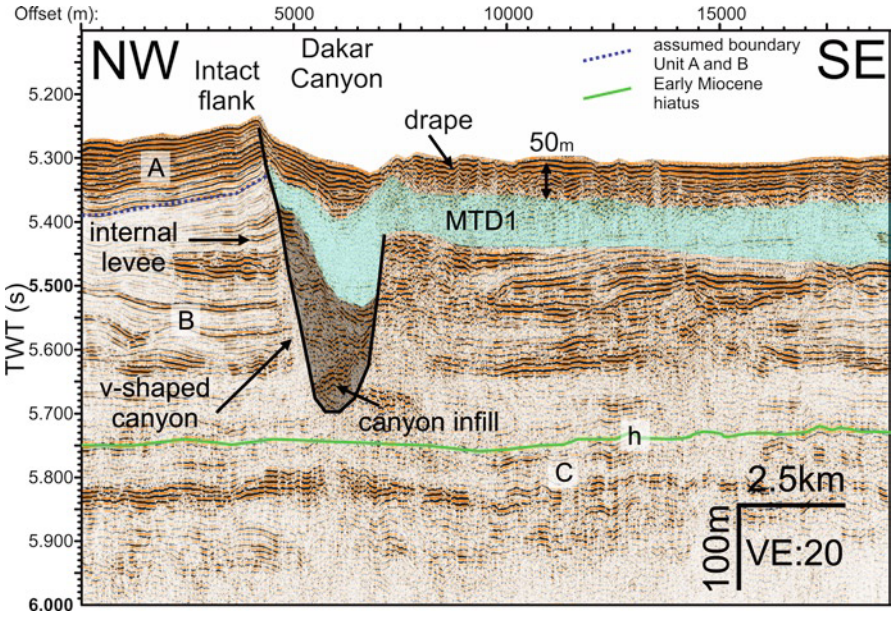

Fig. 16.5 Seismic profile showing the Dakar Canyon partially destroyed by the Dakar Slide (*MTD1*). The northwestern canyon flank is intact. For location of the profile see Fig. 16.3

16.2.5 Sedimentary Ridges

N-S striking smooth ridges rising up to 50 m above the surrounding seafloor overprint the eastern part of the northern sidewall (each marked by a pair of arrows in Fig. 16.3a). These ridges are parallel to the slope and show a downslope decrease in spacing (Figs. 16.2a and 16.3a). They cover an area of approximately 600 km² (area marked by arrows in Fig. 16.3a). The northern sidewall cuts rectangular into these ridges along their whole downslope extent. Seismic profile SHK09-011 (Fig. 16.2) crosses these ridges and shows wavy, well stratified, strong reflectors extending down to 600 ms two-way travel time subsurface depth (between offset 0–25,500 m). The ridges seem to be truncated by MTD 1 and MTD 4.

16.3 Discussion

16.3.1 Dakar Slide: Age and Type of Failure

The Dakar Slide shows several features pointing to a retrogressive failure. The northern headwall is divided into two steps by an up to 2 km wide terrace (Fig. 16.3a).

Furthermore, Scarp F (Fig. 16.3b) interpreted as part of the headwall, lies in 1,000 m shallower water depth compared to other sections of the headwall.

Several pronounced slope incisions are found upslope of Dakar Slide (Fig. 16.3b). Seismic data show that these incisions pre-date the Dakar Slide. Large amounts of sediments were possibly transported through these incisions from the upper slope and shelf directly to the area, which later failed as the Dakar Slide. Quickly accumulated sediments in this area are most likely an important preconditioning factor for slope failure.

We also speculate about a possible connection between the Dakar Slide and the wavy sediment features underlying the northern sidewall. The wavy features may have formed as sediment waves or they represent ductile sediment deformation along faults. Both processes would have significant impact for slope stability but data coverage is too sparse to distinguish between these processes. Throughout all seismic profiles (Fig. 16.1), the hummocky topography of the Dakar Slide is covered by 50–70 m of undisturbed sedimentary drape. Known sedimentation rates vary between 3 and 4 cm/ka for the Quaternary (Ruddiman et al. 1988; Pierau et al. 2010) resulting in a minimum age of 1.2 Ma for the Dakar Slide.

16.3.2 History of Mass Wasting Off Southern Senegal

Several additional MTDs and scarps point to a long history of mass wasting. Chaotic to transparent bodies in Unit C (Figs. 16.2 and 16.4) point to mass wasting since Late Oligocene times. MTD 4 represents the oldest major event imaged by the seismic data (Figs. 16.2 and 16.4) and is imbedded into sediments of Middle Miocene age. MTD 3 is connected to scarp S4 (Fig. 16.2b), which cuts horizons of Late Miocene to Early Pliocene age. MTD 2 is a relatively thin MTD (20 m) located downslope of scarp S3 (Fig. 16.2b). Its position in the upper part of Seismic Unit B suggests an Early to Middle Pliocene age. MTD1 corresponds to the Dakar Slide.

It is interesting to note, that only a very thin interval exists between MTDs 1 and 3 in the central area of the Dakar Slide (Fig. 16.4) despite the significantly different ages of both slides. This fact points to strong erosion and incorporation of sediment into the Dakar Slide. A similar observation can be made for MTDs 1 and 2, which share the same glide plane despite their different ages. We interpret this reflector as a lithological weak layer which was utilized by both slide events.

The data also show indications for relatively recent slope failures. Two small scarps (S1 and S2) are found on the seafloor (Figs. 16.2 and 16.3a). They might be connected, but incomplete data coverage does not allow safe correlation between the two scarps. Seismic data show multiple faults in the vicinity of S1, which occur in an area characterized by a change in slope gradient from 3.3° to 1.6° (Fig. 16.2a, Offset 55,000 m). The location of the scarps is most likely controlled by these faults. The failed material related to S1 and S2 is much smaller than the previously discussed

MTDs. Seismic data, however, show that the whole area downslope of the scarps, down to the Dakar Canyon, misses a sediment package of 20–25 m thickness but we cannot identify any slide deposits; therefore, we assume that the missing sediments were deposited in the Dakar Canyon and subsequently transported further down in the canyon.

It is interesting to note, that most of the faults terminate ~50 m beneath the seafloor (marked by the red line on Fig. 16.2). This depth resembles the post-Dakar Slide sediment accumulation. Therefore, the red reflector in Fig. 16.2 represents the approximate seafloor during the failure of the Dakar Slide. As the faults do not reach in the post-slide sediments, the underlying tectonic process ceased at the time of the Dakar Slide failure. This observation implies a possible connection between tectonic processes on the slope and the Dakar Slide initiation.

In summary, the area off Senegal is characterized by a long and on-going history of slope failures, reaching back to Middle Miocene times. The frequency of slope failures, however, appears to be very low (less than one major failure per two million years).

16.3.3 Interaction Between Slope Failures and Canyons

The area affected by the Dakar Slide is bounded by two major canyons, while no major canyons are found in between. This observation suggests that the canyons stabilize the slopes in their direct vicinity. Turbidity currents in the canyons transport significant amounts of sediments into the deep basins (Pierau et al. 2010). Potentially unstable sediments are transported through the canyons and do not accumulate in vicinity to the canyons. In addition, the canyons cut deep into the sedimentary successions thereby opening a drainage path for fluids. Hence, high pore pressure will not develop close to the canyons. The role of pore pressure remains speculative for the area but high amounts of organic material may favour the development of gas and overpressure in specific sedimentary layers (Antobreh and Krastel 2007).

Accumulation rates between the two major bounding canyons might be further increased by sediment transport through the incisions identified upslope of the Dakar Canyon (Fig. 16.3b).

When failure occurred between the two canyons the interaction became more direct. The width of the downslope moving mass increases with increasing distance from the headwall, until reaching the canyons. The canyons were destroyed and filled by slide deposits but the slide debris did not cross the canyon. Thus, the canyons represent a natural boundary that restricted the propagation of the slide. The destruction of the Dakar Canyon by the Dakar Slide as well as the older events buried beneath it indicates a minimum age of at least 1 Ma for the canyon. Furthermore, we observe levees at 150 mbsf (Fig. 16.5) suggesting a minimum age for the Dakar Canyon of Middle Pliocene times.

16.4 Conclusion

The Dakar Slide is one of the mega slides found along the NW-African continental margin. An area of at least 8,000 km² failed ~1.2 Ma ago, thereby involving a minimum 1,000 km³ of sediments. This makes the Dakar Slide to one of the largest slides at passive margins worldwide.

The continental slope off southern Senegal was repeatedly affected by large-scale submarine sliding since Oligocene times with clear indications for recent failures. The recurrence rate of large slides, however, is very low (>2 Ma).

The slide is bounded by two major canyons, which seem to control the location of the slide. The canyons stabilize the surrounding slope by channeling sediment into the deep basin and opening pathways for pore pressure migration. In between the canyons, no such process exists and a thick, potentially unstable sedimentary succession might accumulate. Sediment accumulation between the bounding canyons is further increased by sediment transport through incisions upslope of the failed area. Once these sediments failed, the surrounding canyons are a natural barrier for the downslope moving mass.

Acknowledgments We thank all scientists and crew who supported data collection. The authors are thankful to Aggeliki Georgiopoulou and Jan Sverre Laberg for their reviews and constructive comments. Financial support was provided by the DFG.

References

Antobreh A, Krastel S (2007) Mauritania Slide Complex: morphology, seismic characterisation and processes of formation. Int J Earth Sci 96:451–472

Brownfield ME, Charpentier RR (2003) Assessment of the undiscovered oil and gas of the Senegal Province, Mauritania, Senegal, the Gambia, and Guinea-Bissau, Northwest Africa. U.S. Department of the Interior, U.S. Geological Survey, Denver

Hansen DM, Redfern J, Federici F et al (2008) Miocene igneous activity in the Northern Subbasin, offshore Senegal, NW Africa. Mar Petrol Geol 25:1–15

Henrich R, Cherubini Y, Meggers H (2010) Climate and sea level induced turbidite activity in a canyon system offshore the hyperarid Western Sahara (Mauritania): the Timiris Canyon. Mar Geol 275:178–198

Krastel S, Wynn RB, Hanebuth TJJ et al (2006) Mapping of seabed morphology and shallow sediment structure of the Mauritania continental margin, Northwest Africa: some implications for geohazard potential. Nor Geol Tidsskr 86(3):163–176

Krastel S, Wynn RB, Georgiopoulou A et al (2012) Large-scale mass wasting on the Northwest African Continental Margin: some general implications for mass wasting on passive continental margins. In: Yamada Y et al (eds) Submarine mass movements and their consequences, vol. 31, Advances in natural and technological hazards research. Springer, Dordrecht, pp 189–199

Lancelot Y (1978) The evolution of the Central Northeastern Atlantic – summary of results of DSDP Leg 41. DSDP Vol XLI 41:1121–1134

Martinez P, Bertrand P, Shimmield GB et al (1999) Upwelling intensity and ocean productivity changes off Cape Blanc (northwest Africa) during the last 70,000 years: geochemical and micropalaeontological evidence. Mar Geol 158:57–74

Pierau R (2008) Climate and sea level controlled sedimentation processes in two submarine canyons off NW-Africa. PhD thesis, Bremen University, p 90

Pierau R, Hanebuth TJJ, Krastel S et al (2010) Late Quaternary climatic events and sea-level changes recorded by turbidite activity, Dakar Canyon, NW Africa. Quat Res 73:385–392

Ruddiman W, Sarnthein M, Baldauf J (1988) Proceedings of the Ocean Drilling Program, initial reports. Proceeding ODP 108:16

The Shipboard Scientific Party, Bukry D (1978) Site reports of DSDP Leg 41 – Site 367: Cape Verde Basin. DSDP 41:163–232

Von Rad U, Wissmann G (1982) Cretaceous-Cenozoic history of the West Saharan continental margin (NW Africa): development, destruction and gravitationl sedimentation. In: von Rad U et al (eds) Geology of the Northwest African continental margin. Springer, Berlin/Heidelberg/ New York, pp 106–131

Wynn RB, Masson DG, Stow DA et al (2000) The Northwest African slope apron: a modern analogue for deep-water systems with complex seafloor topography. Mar Pet Geol 17:253–265

Chapter 17
Large-Scale Mass Wasting on the Northwest African Continental Margin: Some General Implications for Mass Wasting on Passive Continental Margins

Sebastian Krastel, Russell B. Wynn, Aggeliki Georgiopoulou, Jacob Geersen, Rüdiger Henrich, Mathias Meyer, and Tilmann Schwenk

Abstract The continental margin off Northwest Africa is shaped by a complex interplay of sediment transport processes, directed both downslope and alongslope. During several recent cruises, sediment transport processes between 12°N and 29°N off Senegal, Mauritania, and Western Sahara were investigated by means of geophysical and sedimentological methods. Sediment transport on the Northwest African continental margin operates with different rates and styles: some sections of the margin show a large concentration of upper slope canyons but no indication for significant mass wasting, whereas other sections are characterized by large-scale mass wasting with no canyons or gullies. Four mega-slides, each affecting over 20,000 km^2 of seafloor, have been identified along the continental slope off Northwest Africa. All slides are complex in morphology and show a stepped headwall pattern typical for retrogressive failure. Several buried mass transport deposits are seismically imaged beneath all near-surface slides indicating a long history of mass wasting for some sections of the margin. Two of the mega-slides show headwalls at atypically large water depths, deeper than 3,000 m.

Keywords Submarine landslides • Canyons • Geohazards • Acoustic imaging

S. Krastel (✉) • J. Geersen • M. Meyer
Leibniz Institute of Marine Sciences (IFM-GEOMAR), Kiel, Germany
e-mail: skrastel@ifm-geomar.de; mmeyer@ifm-geomar.de

R.B. Wynn
National Oceanography Centre, Southampton, UK

A. Georgiopoulou
School of Geological Sciences, University College Dublin,
Belfield, Dublin 4, Ireland
e-mail: aggie.georg@ucd.ie

R. Henrich • T. Schwenk
MARUM and Faculty of Geosciences, University of Bremen, Bremen, Germany

Y. Yamada et al. (eds.), *Submarine Mass Movements and Their Consequences*,
Advances in Natural and Technological Hazards Research 31,
DOI 10.1007/978-94-007-2162-3_17, © Springer Science+Business Media B.V. 2012

17.1 Introduction

The passive continental margin off Northwest Africa (south of 26°N) is characterized by low sediment supply by rivers, even during glacial times, but high primary productivity caused by oceanic upwelling results in relatively high sedimentation rates exceeding 10 cm/ka in places (Martinez et al. 1999; Weaver et al. 2000). In addition, the margin is characterized by significant dust import from the Sahara desert (Sarnthein and Koopmann 1980). The margin shows several large-scale landslides and numerous canyon/channel systems (Weaver et al. 2000). Acoustic imaging off Northwest Africa began more than 30 years ago; the first maps showing the distribution of seafloor features were published by Jacobi (1976) and Jacobi and Hayes (1992). Updates of these maps were presented by Wynn et al. (2000), Weaver et al. (2000), and Krastel et al. (2006).

This study presents a new map covering the African margin from Senegal to the Canary Islands (Fig. 17.1). New geophysical and sedimentological data allowed the area off Senegal to be included in these maps for the first time; several other seafloor features (e.g.,off Cap Blanc, headwall area of the Sahara Slide, see Fig. 17.1) are characterized in more detail. We combine the work of previous studies with these new data in order to discuss sediment transport processes and potential geohazards off Northwest Africa, and finish by drawing some general conclusions for mass wasting at passive margins.

17.2 Results and Interpretations

The new map (Fig. 17.1) covers an area from 12°N to 29°N, showing numerous seafloor features mainly generated by turbidity currents and landslides. Most of the features are interpreted from acoustic data collected during a variety of research cruises during the last 10 years. Where new data do not exist, features were adopted from a map covering the entire Northwest African margin published by Wynn et al. (2000). The new map shows four major landslides and numerous canyon/channel systems. Slide margins are marked “inferred” if data coverage is too sparse for a robust reconstruction.

17.2.1 Sahara Slide

The Sahara slide is a mega-slide with a run-out distance of 900 km and an estimated volume of 600 km^3 (Embley 1976; Masson et al. 1993; Gee et al. 1999; Georgiopoulou et al. 2010). The Sahara slide is a complex landslide, comprising elements of translational sliding as well as debris flow. The headwall area is located at ~1,900 m water depth. Bathymetric data show two major headwalls, each about 100 m high (Fig. 17.2).

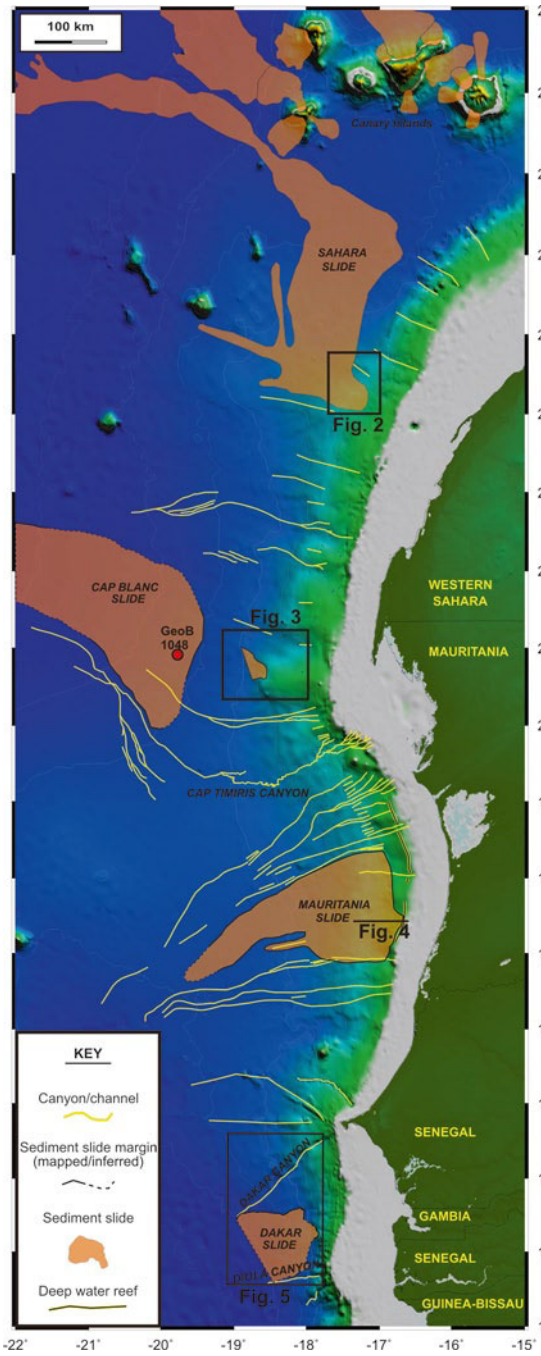

Fig. 17.1 Map showing the distribution of sea-floor features on the Northwest African continental margin. Volcanic landslides around the Canary Islands are shown but not discussed in this manuscript (Some features adopted from Wynn et al. 2000)

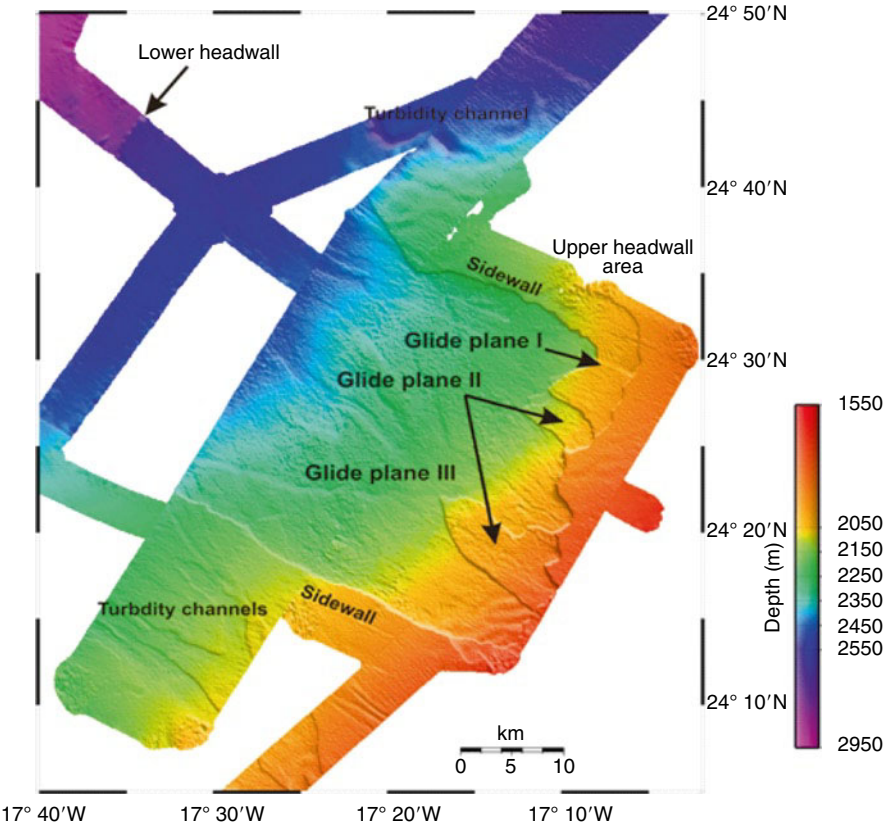

Fig. 17.2 Bathymetric map showing the headwall area of the Sahara Slide. See Fig. 17.1 for location of image

Detailed images of the upper headwall (Fig. 17.2) reveal a complex morphology typical for a retrogressive slab-type failure, with multiple headwall incisions and at least three levels of glide planes (Fig. 17.2). The evolution of the Sahara slide on its way downslope is summarized by Georgiopoulou et al. (2010). The initial failure rapidly disintegrated and transformed into a debris flow. While passing close to the Canary Islands, the debris flow incorporated volcaniclastic sand from the substrate, forming a two-phase flow structure: a pelagic debris flow phase that was carried on top of a basal volcaniclastic debris flow phase. Gee et al. (1999) suggested that the volcaniclastic debris flow phase acted as a low friction layer, thereby explaining the unusually long run-out distance of the Sahara slide. The age of the main slide event is estimated to be ~60 ka, occurring during rapid sea-level rise after a significant lowstand (Gee et al. 1999). However, Georgiopoulou et al. (2009) also presented evidence for late Holocene reactivation of the headwall. Multiple buried events beneath the present-day headwall suggest large-scale mass wasting in the area of the Sahara slide since at least Miocene times (Georgiopoulou et al. 2007).

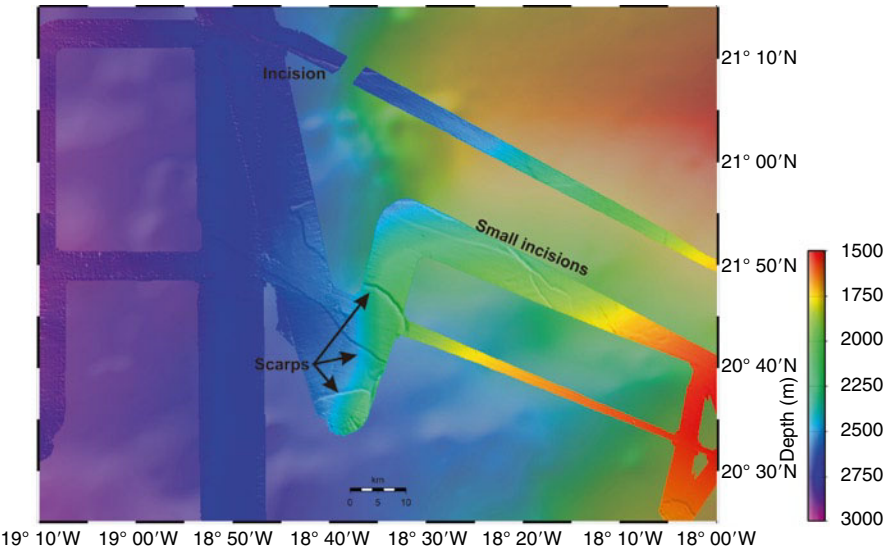

Fig. 17.3 Bathymetric map off Cap Blanc showing a relatively small headwall scarp. The large Cap Blanc Slide originates further downslope. See Fig. 17.1 for location of image

17.2.2 Cap Blanc Slide

A very large mass transport deposit off Cap Blanc (called Cap Blanc slide, Fig. 17.1) is bounded by a 25 m-high headwall at ~3,575 m water depth, on a slope angle of ~0.4° (Krastel et al. 2006). The margins of the Cap Blanc slide are only visible at specific locations (solid lines on Fig. 17.1) but, taking all data into account, a slide area exceeding 40,000 km^2 and a slide width of ~175 km can be reconstructed. Acoustic data show a drape of several meters on top of slide deposits. The boundary between undisturbed and slide sediments occurs at a depth of 686 cm in core GeoB1048, recovered from within the slide area (see Fig. 17.1 for location of core). Undisturbed sediments immediately on top of the highly deformed slide deposits are dated at 165 ka by correlating the $CaCO_3$ curve from the pelagic sequence with that from an oxygen isotope-dated core outside of the slide scar (Krastel et al. 2006). 165 ka is the minimum age of the slide corresponding to a sea-level lowstand.

Jacobi and Hayes (1992) also mapped a series of slides off Cap Blanc originating further upslope, at ~2,000 m water depth. This observation is only partly confirmed by new data. Bathymetric data show numerous small incisions and canyons as well as some local <50 m-high scarps at ~2,000 m water depth (Fig. 17.3). The volume of the evacuated area surrounded by the scarps shown on Fig. 17.3 is difficult to reconstruct due to incomplete bathymetric coverage but the lateral extent of the evacuated area is less than 400 km^2 and the thickness of the missing sedimentary succession is

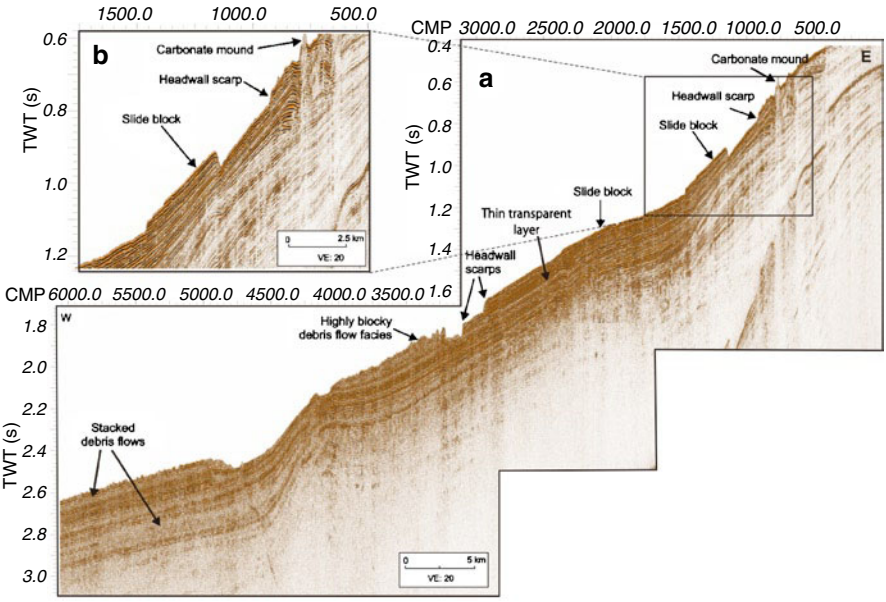

Fig. 17.4 (**a**) Seismic profile crossing the headwall area and the main depositional area of the Mauritania Slide Complex. (**b**) Enlargement of the headwall area (Modified after Antobreh and Krastel 2007). See Fig. 17.1 for location of profile

at most 50 m. Hence 20 km^3 is the maximum volume and therefore significantly smaller compared to the large-scale slides at this margin, which all have volumes exceeding 100 km^3.

17.2.3 Mauritania Slide Complex

The Mauritania Slide Complex was first discovered by Seibold and Hinz (1974) and subsequently mapped and described by Jacobi (1976). This slide was investigated in detail by acoustic methods and sediment coring (Antobreh and Krastel 2007; Henrich et al. 2008; Förster et al. 2010). The slide has affected an area of ~30,000 km^2 (Fig. 17.1); the estimated volume of the deposits is 400–600 km^3. The headwall scarps commonly occur as a series of steps ranging between 25 and 100 m high, between 600 and 2,000 m water depths (Fig. 17.4). A chain of deep-water reef mounds is found immediately upslope of the headwall scarps (Colman et al. 2005). The area beneath the headwall scarps is characterized by blocky debris, while thick tongue-shaped debris flows with relatively smooth surfaces dominate the lower (depositional) area (Fig. 17.4). The uppermost debris unit is dated at 10.5–10.9 ka (Henrich et al. 2008), which occurred at the end of Last Glacial Maximum

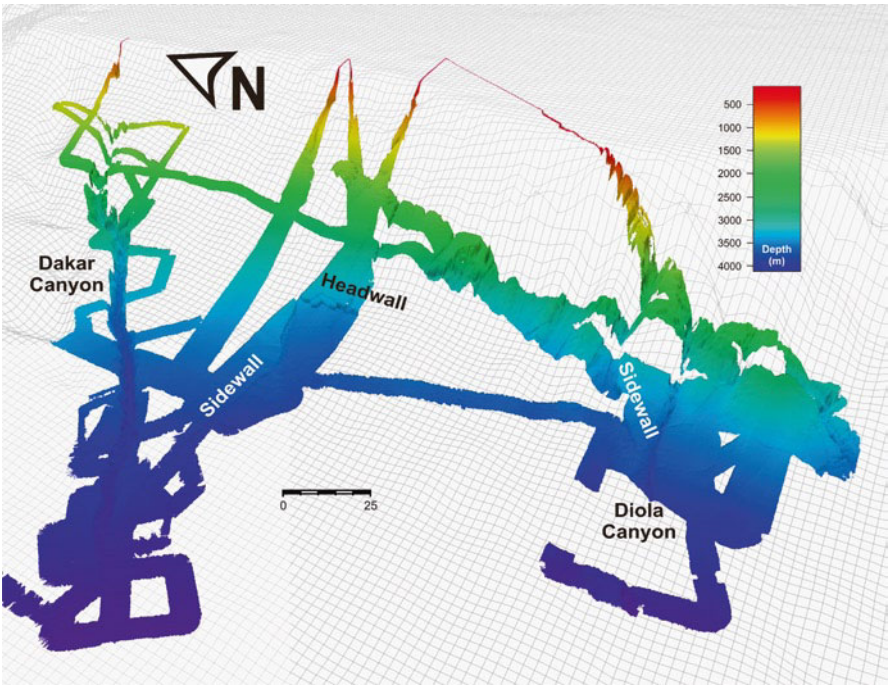

Fig. 17.5 3D-perspective view of the Dakar slide. See Fig. 17.1 for location of image

sea-level rise. Förster et al. (2010) suggest an additional slide, dated at <24 ka, occurred during the glacial lowstand. Seismic data show several buried slide units, indicating a long history of instability on this part of the margin.

17.2.4 Dakar Slide

Dakar slide, located off southern Senegal, is described in detail by Meyer et al. (2012) so only a brief description is given here. The headwall occurs at a water depth of 3,100–3,400 m; no indications for mass wasting are found on the upper or middle continental slope (Fig. 17.1). Slope gradients in the headwall area are as low as 1°. Dakar slide is bounded by two major canyons: Dakar Canyon to the north and Diola Canyon to the south (Fig. 17.5). The full extent of Dakar Slide is not yet mapped, but a clearly visible sidewall runs from the northern edge of the headwall for about 90 km to the Dakar Canyon, which seems to be locally destroyed by the slide (Fig. 17.5). The age of Dakar slide is currently unknown, but a 50 m thick hemipelagic drape suggests a minimum age of 1 Ma. Multiple large-scale mass wasting deposits, reaching back to Miocene times, are found beneath the youngest deposits (Meyer et al. 2012).

17.3 Discussion

17.3.1 Mass Wasting Off Northwest Africa: Where and Why?

Extensive areas of the NW African continental margin are dominated by large-scale mass wasting, although some sections show a concentration of upper slope canyons with no indication for widespread failures (Fig. 17.1). Similar distributions of canyons and slides are found at other passive margins, e.g., along the U.S. Atlantic continental margin (Twichell et al. 2009). It remains unclear why only specific sections of the margin off NW Africa show repeated failure. Jacobi (1976) suggested that earthquakes associated with fracture zones might play a role, but comprehensive analyses of the earthquake history are not available for this region. High sediment accumulation rates caused by upwelling definitely play a key role as a pre-conditioning factor. Rapid sediment build-up leads to sediment instabilities arising primarily from underconsolidation of deposited sediments and widespread lithological weak layers (Antobreh and Krastel 2007). In this context it is interesting to analyze the role of upper slope canyons and gullies. Canyons off NW Africa represent an important pathway for downslope sediment transport (Hanebuth and Henrich 2009; Henrich et al. 2010; Pierau et al. 2010); however, large submarine slides are preferably found in regions with no major canyons. There is no evidence that canyons are destroyed by slides, i.e. no prominent canyons are found upslope of slide headwalls or buried beneath slide sediments. Some slides are actually bounded by major canyons (Fig. 17.1). Hence we believe that canyons represent an effective pathway for regular downslope sediment transport by turbidity currents, evacuating sediments away from the slope, while the areas without canyons become increasingly burdened by deposition of thick sedimentary successions (Masson et al. 2010). Infrequent triggers, especially the lack of regular earthquakes, result in long periods of undisturbed sediment accumulation; these thick sedimentary packages occasionally fail as large slides.

Two of the slides off NW Africa originate at water depths >3,000 m on slope angles around 1° or less. These water depths are unusually large compared to other slides along Atlantic margins, which typically originate in water depths of 800–2,500 m (Hühnerbach et al. 2004; Twichell et al. 2009). For the Cap Blanc region, the continental rise shows high sedimentation rates because filaments of cold upwelling water can locally extend for hundreds of kilometres offshore (van Camp et al. 1991). We assume that such a depocenter controls the location of Cap Blanc slide, whereas the location of Dakar slide is probably controlled by canyon systems bounding the slide and turbidity channels above the central slide (Meyer et al. 2012).

All sections of the NW African margin that are affected by mass wasting show a long history of mass wasting. Sediments deposited above buried scarps are potentially unstable. For the Sahara slide, Georgiopoulou et al. (2007) suggest that differential compaction across bounding escarpments generates compaction hinges, leading to oversteepening and excess pore pressure. A similar process is suggested

by Alves and Cartwright (2010) for a slide area offshore Brazil. They show that differential compaction along landslide strata can control depositional systems well after generation of the initial slide event. In addition, landslide scars form depressions where rapid deposition of contourites may occur. It is well known, that excess pore pressure may develop within contourite units that are sandwiched between impermeable horizons (Laberg and Camerlenghi 2008), thus further promoting differential compaction. The causes of initial failure in the sections affected by mass wasting offshore NW Africa remain unclear, but successive failures seem to be controlled by differential compaction across previous landslide scarps, thereby explaining the long history of mass wasting for some sections of the margin.

17.3.2 Timing of Landslides and Geohazard Potential

It is important to assess the geohazard potential related to submarine mass wasting off NW Africa, especially as the area offshore Mauritania is a current focus for hydrocarbon exploration and production (Colman et al. 2005). No age information are available for the Dakar slide but all other slides occurred during periods of low or rising sea level. Direct linkage between sea level and slide occurrence in this region is not well understood, but indirect effects include spatial variations in primary productivity and hence the maximum sedimentation rate (Georgiopoulou et al. 2010). The probability of future large-scale slope failures during the current highstand is generally considered to be low. However, our new data indicate a relatively recent (<2 ka) large-scale reactivation of the Sahara slide headwall (Georgiopoulou et al. 2009), which needs to be considered for future risk assessments.

Despite the relatively low probability of voluminous mass wasting off NW Africa in the near future, we also discuss the tsunami potential of such slides. Volume and initial acceleration are considered as the most important parameters influencing tsunamigenesis, but other factors (e.g., flow dynamics, water depth, velocity, length, thickness) may also be important (Harbitz et al. 2006). Both Dakar and Cap Blanc slides occur in deep water on gentle slope; it is very unlikely that they reached high velocities and triggered a tsunami. Georgiopoulou et al. (2010) concluded that the Sahara slide was a slow-moving slide, as the absence of a related turbidite indicates that the slide was not moving sufficiently quickly to generate shear mixing between the slide and the overlying water. In addition, the relatively large water depth of 1,900 m in the headwall area is also not in favour for generating a tsunami. The water depth of 600–1,500 m in the headwall region of the Mauritania slide is more typical for landslide-generated tsunamis. The initial acceleration of the Mauritania slide is unknown but a turbidite containing shelf sands, deposited immediately above the slide deposits, might indicate mobilization of shelf sands by a tsunami (Krastel et al. 2006; Henrich et al. 2008).

17.4 Conclusions

The NW African continental margin is characterized by large-scale but infrequent mass wasting. Mass wasting off NW Africa is a geohazard but the probability for major events in the near future is low. New acoustic data allow us to draw several conclusions for mass wasting off NW Africa, which might be relevant for other passive margin settings: (i) Open slope areas without major incisions allow rapid and undisturbed sediment accumulation beneath zones of high primary productivity, which in turn leads to sediment instabilities arising primarily from underconsolidation of deposited sediments and widespread lithological weak layers. In contrast, canyons and gullies act as effective pathways for regular downslope sediment transport by turbidity currents, preventing extensive slope failure. (ii) Vertical stacking of mass wasting events suggests that sediments deposited above buried scarps are potentially unstable. (iii) The large size of the slides off NW Africa is caused by high sedimentation rates but infrequent triggers, with all major slides in the last 200 ka occurring during sea-level lowstands or periods of sea-level rise. (iv) Mega-slide headwalls at water depths >3,000 m on the Northwest African continental margin expand the known depth range of large-scale North Atlantic slides.

Acknowledgments We thank all scientists and crew who supported data collection during numerous cruises. The authors are thankful to Anders Solheim, Asrar Talukder, and Jason D. Chaytor for their reviews and constructive comments. Financial support was provided by the Deutsche Forschungsgemeinschaft. AG acknowledges funding from a Griffith Geoscience Research Award of the Department of Communications, Energy and Natural Resources under the National Geoscience Programme 2007–2013.

References

Alves TM, Cartwright JA (2010) The effect of mass-transport deposits on the younger slope morphology, offshore Brazil. Mar Petrol Geol 27:2027–2036

Antobreh AA, Krastel S (2007) Mauritania Slide Complex: morphology, seismic characterisation and processes of formation. Int J Earth Sci 96:451–472

Colman JG, Gordon DM, Lane AP et al (2005) Carbonate mounds off Mauritania, north-west Africa: status of deep-water corals and implications for management of fishing and oil exploration activities. In: Freiwald A, Roberts JM (eds) Cold-water corals and ecosystems. Springer Berlin, Heidelber New York, pp 417–441

Embley RW (1976) New evidence for occurrence of debris flow deposits in the deep sea. Geology 4:371–374

Förster A, Ellis R, Henrich R et al (2010) Geotechnical characterization and strain analyses of sediment in the Mauritania Slide Complex, NW-Africa. Mar Petrol Geol 27:1175–1189

Gee MJR, Masson DG, Watts AB, Allen PA (1999) The Saharan debris flow: an insight into the mechanics of long runout submarine debris flows. Sedimentology 46:317–335

Georgiopoulou A, Krastel S, Masson DG, Wynn RB (2007) Repeated instability of the NW African Margin related to buried landslide scarps. In: Lykousis V et al (eds) Submarine mass movements and their consequences, vol 27, Advances in natural and technological hazards research. Springer, Dordrecht, The Netherlands, pp 29–36

Georgiopoulou A, Wynn RB, Masson DG, Frenz M (2009) Linked turbidite-debrite resulting from recent Sahara Slide headwall reactivation. Mar Petrol Geol 26:2021–2031

Georgiopoulou A, Masson DG, Wynn RB, Krastel S (2010) The Sahara Slide: initiation and processes from headwall to deposit of a giant submarine slide. Geochem Geophys Geosyst 11(7). doi:10.1029/2010GC003066

Hanebuth TJJ, Henrich R (2009) Recurrent decadal-scale dust events over Holocene western Africa and their control on canyon turbidite activity (Mauritania). Quat Sci Rev 28:261–270

Harbitz CB, Løvholt F, Pedersen G, Masson DG (2006) Mechanisms of tsunami generation by submarine landslides: a short review. Norw J Geol 86:255–264

Henrich R, Hanebuth TTJ, Krastel S et al (2008) Architecture and sediment dynamics of the Mauritania Slide Complex. Mar Petrol Geol 25:17–33

Henrich R, Cherubini Y, Meggers H (2010) Climate and sea level induced turbiditic activity in a canyon system offshore the hyperarid Western Sahara: the Timiris Canyon. Mar Geol 275:178–198

Hühnerbach V, Masson DG, Project Partners (2004) An analysis of submarine landslide dynamics and processes in the North Atlantic. Mar Geol 213:343–362

Jacobi RD (1976) Sediment slides on the northwestern continental margin of Africa. Mar Geol 22:157–173

Jacobi RD, Hayes DE (1992) Northwest African continental rise: effects of near-bottom processes inferred from high-resolution seismic data. In: Poag CW, de Graciansky PC (eds) Geologic evolution of Atlantic continental rises. Reinhold, New York, pp 293–325

Krastel S, Wynn RB, Hanebuth TJJ et al (2006) Mapping of seabed morphology and shallow sediment structure of the Mauritania continental margin, Northwest Africa: some implications for geohazard potential. Norw J Geol 86:163–176

Laberg JS, Camerlenghi A (2008) The significance of contourites for submarine slope stability. In: Rebesco M, Camerlenghi A (eds) Contourites, vol 60, Developments in sedimentology. Elsevier, Amsterdam, pp 537–556

Martinez P, Bertrand P, Shimmield GB et al (1999) Upwelling intensity and ocean productivity changes off Cape Blanc (northwest Africa) during the last 70,000 years: geochemical and micropalaeontological evidence. Mar Geol 158:57–74

Masson DG, Huggett QJ, Brunsden D (1993) The surface texture of the Saharan Debris flow deposit and some speculations on submarine debris flow processes. Sedimentology 40:583–598

Masson DG, Wynn RB, Talling PJ (2010) Large landslides on passive continental margins: processes, hypotheses and outstanding questions. In: Mosher DC et al (eds) Submarine mass movements and their consequences, vol 28, Advances in natural and technological hazards research. Springer, Dordrecht, Heidelberg London New York, pp 153–165

Meyer M, Geersen J, Krastel S et al (2012) Dakar Slide offshore Senegal, NW-Africa: interaction of stacked giant mass-wasting events and canyon evolution. In: Yamada Y et al (eds) Submarine mass movements and their consequences, vol. 31, Advances in natural and technological hazards research. Springer, Dordrecht, pp 177–188

Pierau R, Hanebuth TJJ, Krastel S, Henrich R (2010) Late Quaternary climatic events and sea level changes recorded by turbidite activity, Dakar Canyon. NW-Afr Quat Res 73:385–392

Sarnthein M, Koopmann B (1980) Late Quaternary deep-sea record on northwest African dust supply and wind circulation. Palaeoecol Afr 12:239–253

Seibold E, Hinz K (1974) Continental slope construction and destruction, West Africa. In: Burk CA, Drake CL (eds) The geology of continental margins. Springer, New York, pp 179–196

Twichell DC, Chaytor JD, ten Brink US, Buczkowski B (2009) Morphology of late Quaternary submarine landslides along the U.S. Atlantic continental margin. Mar Geol 264:4–15

Van Camp L, Nykjaer L, Mittelstaedt E, Schlittenhardt P (1991) Upwelling and boundary circulation off Northwest Africa as depicted by infrared and visible satellite observations. Prog Ocean 26:357–402

Weaver PPE, Wynn RB, Kenyon NH, Evans J (2000) Continental margin sedimentation with special reference to the Northeast Atlantic margin. Sedimentology 47:239–256

Wynn RB, Masson DG, Stow DAV, Weaver PPE (2000) The Northwest African slope apron: a modern analogue for deep-water systems with complex seafloor topography. Mar Petrol Geol 17:253–265

Chapter 18
Deep-Seated Bedrock Landslides and Submarine Canyon Evolution in an Active Tectonic Margin: Cook Strait, New Zealand

Aaron Micallef, Joshu J. Mountjoy, Miquel Canals, and Galderic Lastras

Abstract The Cook Strait sector of the Hikurangi subduction margin, off south-east central New Zealand, is dominated by a multi-branched canyon system where landslides are widespread. The objective of this study is to determine the character, origin, and influence of these landslides on the evolution of the canyon system. Multibeam bathymetry covering seven submarine canyons is utilised to characterise landslides' spatial distribution, morphological attributes and area-frequency characteristics. We demonstrate that mass movements within the Cook Strait canyons consist of spatially dense, predominantly retrogressive, small, deep-seated, translational bedrock landslides occurring in Late Cenozoic sequences. These landslides affect up to a quarter of the canyoned area. Concentration of landslides in the shallow canyon reaches (down to 800 m) is attributed to the influence of oceanographic processes originating on the continental shelf such as tide-generated currents, dense shelf water cascading and internal waves. Canyon incision and wall undercutting, locally favoured by underlying lithological control, are proposed as major landslide drivers in Cook Strait. Ground motion during regional earthquakes is considered a secondary cause. Retrogressive landslides are responsible for canyon widening and wall retreat,

A. Micallef (✉) • M. Canals • G. Lastras
GRC Geociències Marines, Facultat de Geologia, Universitat de Barcelona, Barcelona E-08028, Spain

University of Malta, Msida MSD 2080, Malta
e-mail: micallefaaron@ub.edu

J.J. Mountjoy
National Institute of Water and Atmospheric Research, Private Bag 14901, Wellington, New Zealand
e-mail: j.mountjoy@niwa.co.nz

Y. Yamada et al. (eds.), *Submarine Mass Movements and Their Consequences*, Advances in Natural and Technological Hazards Research 31,
DOI 10.1007/978-94-007-2162-3_18,

cross-sectional asymmetry, preconditioning for additional failure, destabilisation of adjacent slopes and delivery of sediment into canyon floors.

Keywords Bedrock landslide • Submarine canyon • Morphometric analysis • Cook Strait

18.1 Introduction

The Hikurangi margin is a transpressional subduction arc located off New Zealand's North Island. The Cook Strait (CS) sector is located in the southern Hikurangi margin and is traversed by a series of active thrust and strike-slip faults (Barnes and Audru 1999). The CS sector also hosts the largest canyon system in the whole margin, where landslide scars are widespread (Fig. 18.1). High-resolution multibeam bathymetric data from the CS sector offer an excellent opportunity to investigate the regional impact of landslides on canyon morphology and evolution in an active margin. This is important because active tectonic margins comprise about a third of global continental margins, and the influence of active tectonics provides a distinctive context for canyon evolution that has not been fully explored. Landsliding is receiving increasing consideration as a key factor in canyon formation (e.g., Sultan et al. 2007), although studies relating bedrock landslides to canyons evolution are few and the

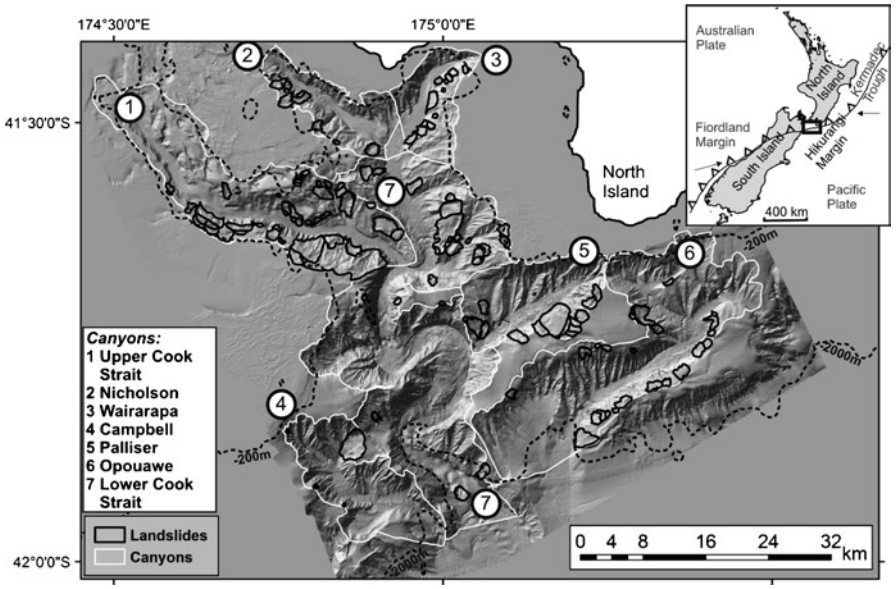

Fig. 18.1 Location (inset) and shaded relief map of Cook Strait submarine canyon system in the southern Hikurangi margin. The mapped landslides are outlined in *solid black*. *Dotted black lines* denote bathymetric contours

nature and frequency of the these processes are poorly constrained. The objective of this study is therefore to determine the character and origin of bedrock landsliding, and its influence on the long-term evolution of the CS submarine canyon system.

18.2 Data Sets and Methodology

This study is based on 8,400 km^2 of multibeam bathymetry collected by RV *Tangaroa* between 2002 and 2005 using a hull-mounted Simrad EM300 multibeam system operating at a 30 kHz frequency and a POS/MV system with differential GPS. The navigational accuracy is ±5 m and vertical accuracy in 1,000 m water depth is ±2 m. The data were gridded to a 10 m × 10 m bin size.

Landslides within the CS canyon system have been identified and mapped on the basis of morphology. Standard morphometric attributes were extracted from the bathymetric data set using Geographic Information System (GIS) software. A geomorphometric map and an automated topographic classification (using the standard deviation of slope gradient) were also generated using techniques described in Micallef et al. (2007). These were carried out to delineate the boundaries of landslides and segment the seabed according to roughness. Our method of landslide extraction is limited by the difficulty of mapping old, shallow-seated landslides and overlapping failures accurately.

Once the landslide boundaries were determined, measurements of specific morphometric attributes of each individual landslide were made. These included: (i) Bathymetric depth: The depth of the centroid of each landslide; (ii) Headwall length: The terminations of a headwall are defined by the zone where material has moved perpendicularly to the escarpment; (iii) Headwall height: Difference in elevation between top and foot of headwall; (iv) Landslide direction: Predominant direction of material mobilisation; (v) Area: Total area of the headwall, slide scar and deposit; (vi) Volume: A smooth surface was interpolated from the polygon that defines the boundary of each landslide scar and then subtracted from the original bathymetry. The method and associated assumptions are detailed in Chaytor et al. (2009).

For headwall height, several measurements were made from adjacent cross-sections in order to calculate a mean value. Where features were not prominent, the steepest section of the features was considered.

18.3 Results

18.3.1 Submarine Canyon Morphology

Seven canyons dissect the continental slope of the CS sector, from the continental shelf down to the Hikurangi Channel at a depth of ~2,500 m (Fig. 18.1). Nicholson, Wairarapa, Upper Cook Strait and the shallower part of the Lower Cook Strait

Canyons are incised in Late Cenozoic sedimentary sequences of consolidated and gently dipping mudstone, siltstone or sandstone (Mountjoy et al. 2009). The northern walls of Nicholson and Wairarapa canyons comprise Torlesse Greywacke Mesozoic basement, which consists of well-indurated and slightly metamorphosed mudstones and silty sandstones (Barnes and Audru 1999). Palliser, Opouawe, Campbell and the deeper part of Lower Cook Strait Canyons are incised in Neogene turbidite sequences (Uruski 2010). The morphological characteristics of each canyon are presented in Table 18.1. The cross-sectional shape of the canyons is generally V-shaped, with a gently sloping canyon floor that can be up to 2.5 km wide. The walls can locally reach slope gradients in excess of 30°; they are eroded by linear and dendritic gullies (Micallef and Mountjoy 2011) and landslides.

18.3.2 Landslides

18.3.2.1 Morphological Characteristics

There are at least 141 landslides on the walls of the CS canyons. They are characterised by well-defined arcuate headwalls, sub-parallel sidewalls and a near-planar, smooth failure surface (Figs. 18.1 and 18.2a). The direction of landslide movement is predominantly perpendicular or quasi-perpendicular to that of the canyon thalweg (Fig. 18.3d). Several canyon walls display up to three levels of landslide retrogression (Fig. 18.2a). Numerous landslide scars are perched above high and steep overhangs (Fig. 18.2a); a few landslides are located upslope of gully systems (Fig. 18.2b).

The morphometric characteristics of the mapped landslides are listed in Table 18.1. The landslides' dimensions range across 3 orders of magnitude (0.03–29.56 km^2 for area and 0.0005–0.88 km^3 for volume). The landslides are predominantly small-scale, as implied by a log-normal area-frequency distribution (Fig. 18.3c), with a median slide area and volume of 0.82 and 0.013 km^3, respectively. The median headwall height, at 74 m, is relatively high for such small landslides. A very good correlation is obtained when plotting landslide area with volume ($R^2 = 0.9$) (Fig. 18.3a). The amount of work carried out by landslides, which is an expression of the amount of material moved by a geomorphic event (Wolman and Miller 1960), has been estimated by multiplying the area of the landslide and frequency for each bin of the area-frequency distribution (Fig. 18.3c). The plot shows that the majority of the work is carried out by the smaller landslides.

18.3.2.2 Distribution

The landslides are located across the entire depth range covered by the canyons, although 75% of landslides occur in the shallow canyon reaches (200–800 m) (Fig. 18.3b). The majority of the landslides originate in Late Cenozoic sequences.

Table 18.1 Canyon and landslide morphological information

	Cm	UCS	LCS	Nc	Op	Pr	Wp	All landslides
Canyon morphology								
Length (km)	27.7	45.0	70.0	19.5	39.5	20.9	14.7	–
Maximum width (km)	12.0	12.7	14.8	8.9	13.7	11.9	10.7	–
Head depth (m)	310	150	110	110	390	90	45	–
Maximum incision depth (m)	650	575	750	500	750	650	500	–
Depth from canyon head to mouth (m)	2,070	900	1,800	590	1,730	1,450	630	–
Thalweg mean slope gradient (°)	4.27	1.35	1.39	1.73	2.50	3.97	2.30	–
General orientation	NW–SE	NW–SE	N–S	NW–SE	NE–SW	NE–SW	NE–SW	–
Area (km^2)	182	385	683	112	465	166	99	–
Landslide morphology								
Landslides (*n*)	5	45	27	8	28	16	12	141
Total landslide area (km^2)	9.76	88.75	78.31	11.00	30.94	32.32	9.28	260.35
Median slide area (km^2)	0.13	0.72	0.91	1.52	0.76	1.65	0.65	0.82
Landslides:canyon area (km^{-2})	0.03	0.12	0.04	0.07	0.06	0.10	0.12	0.07
Mean landslide area:canyon area (%)	5.36	23.05	11.47	9.81	6.65	19.48	9.33	12.44
Total landslide volume (km^3)	0.66	1.71	1.28	0.21	0.45	0.77	0.13	5.22
Median landslide volume (km^3)	0.001	0.011	0.014	0.022	0.081	0.042	0.010	0.013
Median headwall length (m)	344	1,156	1,489	1,472	1,217	1,363	852	1,199
Median headwall height (m)	62	73	78	67	63	108	67	74

Cm Campbell, *UCS* Upper Cook Strait, *LCS* Lower Cook Strait, *Nc* Nicholson, *Op* Opouawe, *Pr* Palliser, *Wp* Wairarapa

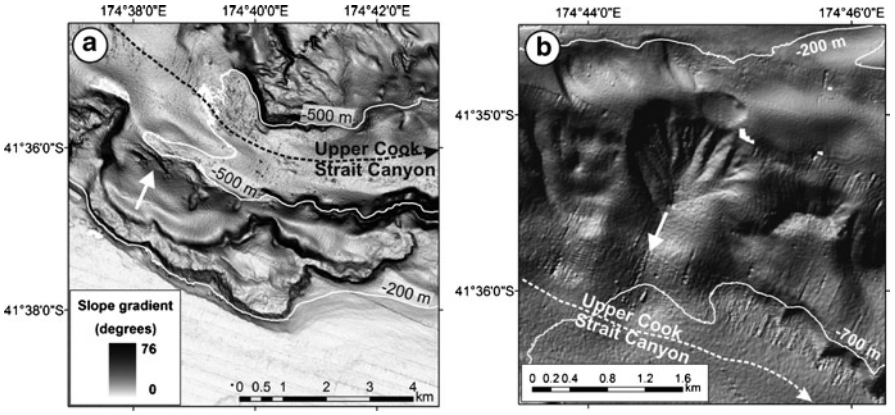

Fig. 18.2 (**a**) Slope gradient map of the south-western wall of Upper Cook Strait Canyon showing perched, coalescing landslide scars with well-defined arcuate headwalls and a smooth failure surface. (**b**) Shaded relief map, illuminated from the NW, showing a landslide scar located on the north-eastern wall of Upper Cook Strait Canyon that has been incised by a gully system. Loss of support at the head of the gully system has caused a small landslide to occur. *White arrows* indicate direction of movement of landslide material. Canyon axes are marked by *dotted lines*

Landslide deposits are either located at the base of the failure scar or they are absent from both slide scar and canyon thalweg. Landslide deposits are only occasionally visible on the canyon floor in the form of blocks (e.g., Palliser Canyon). The highest landslide area:canyon area fractions are observed in the canyons with the shallowest heads (Table 18.1). Landslides cluster along the lower to middle canyon wall sections and they tend to preferentially occur on one side of each canyon (Fig. 18.4). The slope gradients of canyon walls where landslides occur are gentler than those without landslides, which give rise to canyon wall asymmetry in cross-section (Fig. 18.4).

18.4 Discussion and Conclusions

18.4.1 Nature of Landslides

Seismic reflection profiles presented in Mountjoy et al. (2009) demonstrate that landsliding within the CS submarine canyons is stratigraphically-controlled. The failure planes tend to follow stratification, with weak layers within the bedded marine sequences facilitating slope failure. The stratigraphic control is also revealed in the estimated mean headwall height, which is comparable for all canyons but Palliser (Table 18.1). By combining the information in these profiles with our observations of slide scar morphology and distribution, we interpret the landslides within the CS canyons as deep-seated, translational, bedrock landslides occurring in Late

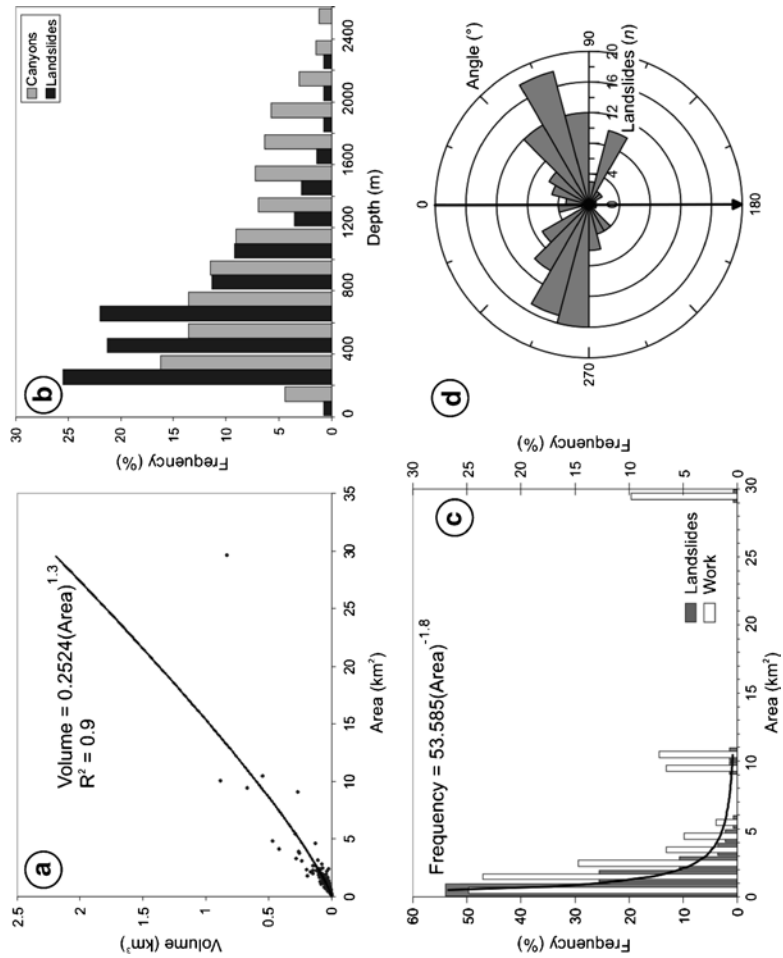

Fig. 18.3 (**a**) Plot of mapped landslide area vs. volume; (**b**) Histogram of water depth of the seabed within canyons, compared with a histogram of the water depth of the centroid of each mapped landslide; (**c**) Histogram and inverse power trend line for the area-frequency of the mapped landslides, and histogram of work carried out by the landslides; (**d**) Rose diagram of landslide movement vectors in respect to canyon thalweg direction (*black arrow*)

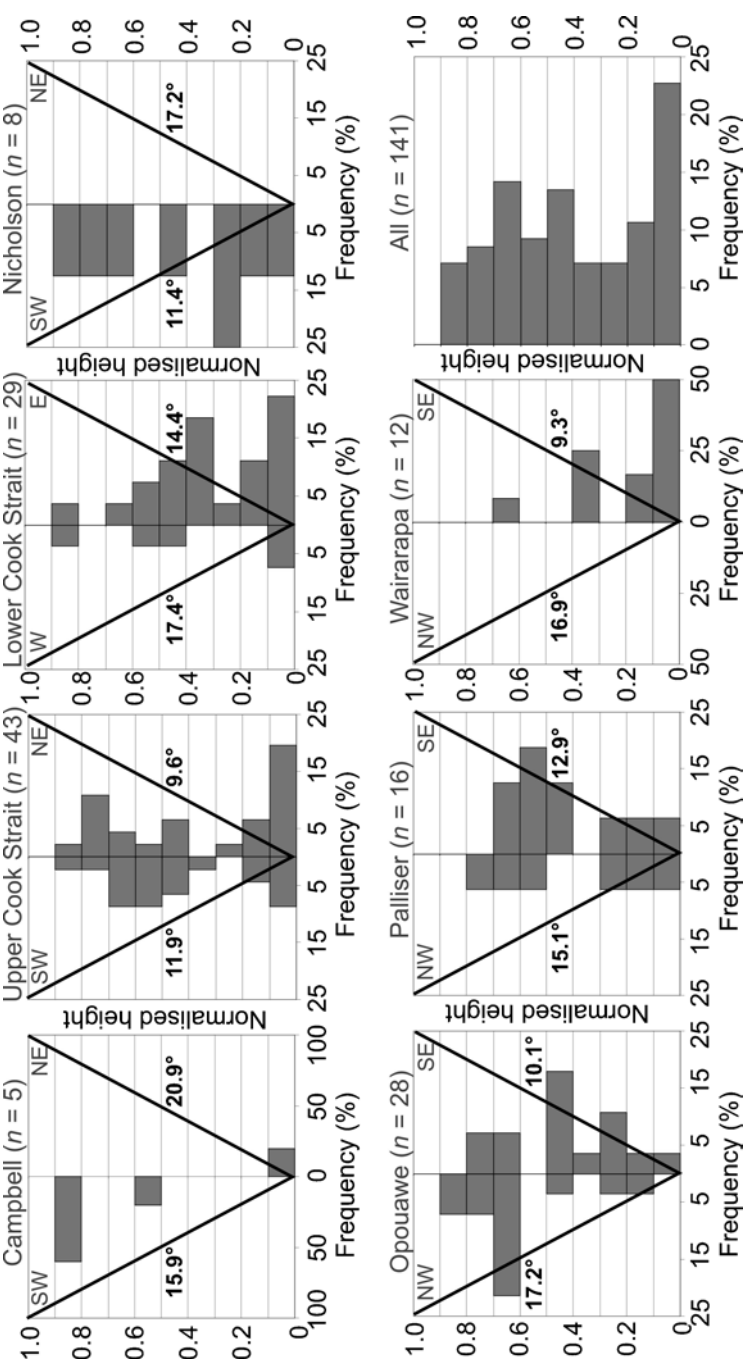

Fig. 18.4 Histograms of normalised landslide height above canyon floor for all canyon walls. Also shown is the mean slope gradient estimated for each canyon wall

Cenozoic to Pleistocene sequences. Furthermore, the power law relationship between landslide area and volume is characterised by an exponent of 1.3 (Fig. 18.3a), which is similar to that obtained by ten Brink et al. (2006) for slides in layered limestones, and higher than that obtained by Issler et al. (2005) for clay-rich debris flows. This exponent indicates deeper excavation of material by the larger slope failures in the CS canyons. This contrasts with landslides in the Atlantic Ocean, where volume increases almost linearly with area, indicating a relatively constant evacuation depth (e.g., Chaytor et al. 2009; Issler et al. 2005).

18.4.2 Causes of Landslides

We propose two main causes of canyon landslides:

a. **Canyon incision and wall undercutting.** Landslide scars are generally concentrated in the lower half of the canyon walls. The direction of the majority of slides is quasi-perpendicular to the canyon thalweg (Fig. 18.3d). The presence of perched slides attests to periods of thalweg excavation. Retrogression is observed at a number of places in the form of small landslides stepping upslope from larger landslides on the canyon wall. Canyon incision and wall undercutting are therefore proposed as the first order driver of landslides in the CS canyons. The larger landslides occur where scouring of the canyon floor undermines and steepens the base of the canyon wall, whereas the upper, smaller slides occur due to loss of support; this is comparable to the origin of terrestrial bedrock landslides in the physical model of Densmore et al. (1997). In spite of the numerous canyon wall failures, we notice a general absence of landslide deposits within the canyon axes. This supports the hypothesis that canyons were active at the same time as the canyon walls were failing or shortly after, and that material was removed from the canyon bed. Proof that this activity may be recent can be found in cores from Nicholson and Upper Cook Strait Canyons, which show repeated sandy turbidites and a lack of any large accumulation of hemipelagic sequences on the canyon floor (Mountjoy et al. 2009). Few landslides are located in Campbell Canyon (Table 18.1); this observation emphasises the importance of canyon downcutting because Campbell Canyon is an abandoned, infilled tributary of the Lower Cook Strait Canyon (Mountjoy et al. 2009). Repeated mass movements across the canyon walls may also account for the width of the canyon floor, which cannot be explained by canyon incision alone. Canyon cross-sectional asymmetry (Fig. 18.4), on the other hand, may be explained by flows within the canyon thalweg impinging on the north-facing canyon walls due to gravity, giving rise to landslide clustering across these slopes. Cross-sectional asymmetry in Palliser and Opouwae canyons, on the other hand, may be due to the presence of tectonic ridges, the forelimbs of which can be up to two times steeper than the backlimbs.
b. **Earthquakes.** Some landslides are located in the upper half of canyon walls with no connection to canyon thalwegs (Fig. 18.4). Landslide scar distribution occasionally correlates with active faults, which act as significant earthquake sources

(e.g., Christchurch February 2011 M6.3 earthquake). Ground motion during regional earthquakes and its influence on steep, undercut canyon walls is proposed as a second major cause of landslides. The role of earthquakes in causing slope failure is believed to be important in the CS canyons because of a high concentration of active faults and the modelled frequent occurrence of strong earthquake-generated ground motion (Stirling et al. 2002). We suggest that failures occur as either co-seismic events, due to deformation of slopes during ground shaking, or through generation of excess pore pressures in high permeability horizons due to cycling loading (Mountjoy et al. 2009).

Uplift and over-steepening of canyon walls due to active anticlinal folding may constitute an additional cause of landslides, but this would only account for landslide occurrence in Palliser and Opouawe canyons.

18.4.3 Spatial Distribution of Landslides

Bedrock landslides can be found in all the canyons. The concentration of landslides in the shallow, shelf-incised canyon reaches (Fig. 18.3b) implies that there is a dominating influence on the depth zonation of failures. One possible reason for this zonation is that canyon incision is driven by an oceanographic process originating in the shelf area. We assume that such a process would influence the shallower canyons the most (Nicholson, Wairarapa, Upper Cook Strait, shallower Lower Cook Strait Canyons), and it could explain why landslides cluster in the lower half of these canyons' walls (Fig. 18.4). A possible candidate for such an oceanographic process is tide-generated currents and related sediment input. Tides may play a role in generating a strong, recurring and directionally stable flow that can transport sediment and deepen the canyon. The signal of such a flow has been identified at depths down to 1,000 m (Law et al. 2010). Other potential candidates include cascading dense water (Micallef and Mountjoy 2011) and internal waves, although these oceanographic processes still need to be documented in CS. At present, large scale ocean currents and fluvial sediment discharge are not considered influential in the study area (Chiswell 2000; Hicks and Shankar 2003), although the latter should have been more significant during glacial lowstands. In comparison to the shallower canyons, the deeper canyons (deeper Lower Cook Strait, Campbell, Palliser and Opouawe Canyons) exhibit a lower number of landslides and a concentration of landslides in the upper half of the canyon walls (Fig. 18.4); this may indicate that canyon downcutting may be a less important driver of landslides in this region, and that earthquakes may be more significant.

A second possible reason for landslide zonation is lithological control, reflecting the contrast between the deep, Late Cenozoic sedimentary basins located on the shelf, and the slope cover and Neogene turbidite sequences underlying the continental slope (Mountjoy et al. 2009; Uruski 1992). Landslide zonation may also be attributed to their retrogressive nature, with shallower landslides tending to be more numerous than deeper failures.

18.4.4 Role of Landslides in Canyon Evolution

Bedrock landslides are numerous in the CS canyon system and they have an important influence in canyon evolution, predominantly in the form of wall erosion, lateral extension and dendritic network evolution. They have the potential to rapidly remove material from the continental slope and can affect up to a quarter of the canyon. Landslides represent a major cross-canyon source of material and an important process introducing material into canyon floors. As a result, landslide deposits may play an important role in the re-hierarchisation of canyon branches by blocking a canyon branch and favouring up-canyon infill. Area-frequency analyses show that the majority of the material is removed by small landslides (Fig. 18.3c); this contrasts with terrestrial environments, where most of the work tends to be carried out by moderately-sized landslides (Guthrie and Evans 2007). Axis-normal slope failures along canyon walls occur once the canyon floor has been excavated and the walls have been undercut, suggesting that bedrock landslides may become more important as the canyon matures; otherwise failure is initially restricted to the canyon head (Pratson and Coakley 1996). Bedrock mass failures can also affect adjacent slopes by removal of support, potentially leading to further destabilisation and retrogression. Landslides may also have an important role in gully initiation and development by generating the steep topography required for gully formation (Fig. 18.2b). The median slope gradients of both the headwalls and scars of the landslides are higher than the threshold of 5.5° associated with gully initiation in the CS sector (Micallef and Mountjoy 2011) (Table 18.1). Gully formation can, in turn, also trigger landslides due to loss of support (Fig. 18.2b).

Acknowledgments This research was supported by Marie Curie Intra-European Fellowship PIEF-GA-2009-252702, Royal Society of New Zealand ISAT Fund, NIWA capability funding, FRST CEOC contracts, the HERMIONE EC project (grant agreement n° 226354) and the GRACCIE-CONSOLIDER (ref. CSD2007-00067) Spanish project. We are indebted to NIWA Ocean Geology technicians and the crew of RV *Tangaroa* for collecting the bathymetry data. AM, MC and GL belong to CRG on Marine Geosciences, supported by grant 2009 SGR 1305 of Generalitat de Catalunya.

References

Barnes PM, Audru JC (1999) Quaternary faulting in the offshore Flaxbourne and Wairarapa Basins, southern Cook Strait, New Zealand. NZ J Geol Geophys 42:349–367

Chaytor JD, Ten Brink US, Solow AR et al (2009) Size distribution of submarine landslides along the U.S. Atlantic margin. Mar Geol 264:16–27

Chiswell SM (2000) The Wairarapa Coastal current. NZ J Mar Fresh 34:303–315

Densmore AL, Anderson RS, McAdoo BG et al (1997) Hillslope evolution by bedrock landslides. Science 275:369–372

Guthrie RH, Evans SG (2007) Work, persistence, and formative events: the geomorphic impact of landslides. Geomorphology 88:266–275

Hicks DM, Shankar U (2003) Sediment from New Zealand rivers. NIWA, Wellington

Issler D, De Blasio FV, Elverhøi A et al (2005) Scaling behaviour of clay-rich submarine debris flows. Mar Petrol Geol 22:187–194

Law CS, Nodder SD, Mountjoy JJ et al (2010) Geological, hydrodynamic and biogeochemical variability of a New Zealand deep-water methane cold seep during an integrated 3-year time-series study. Mar Geol 272:189–208

Micallef A, Berndt C, Masson DG et al (2007) A technique for the morphological characterization of submarine landscapes as exemplified by debris flows of the Storegga Slide. J Geophys Res 112:F02001

Micallef A, Mountjoy JJ (2011) A topographic signature of a hydrodynamic origin for submarine gullies. Geology 39:115–118

Mountjoy JJ, Barnes PM, Pettinga JR (2009) Morphostructure and evolution of submarine canyons across an active margin: Cook Strait sector of the Kikurangi Margin, New Zealand. Mar Geol 260:45–68

Pratson LF, Coakley BJ (1996) A model for the headward erosion of submarine canyons induced by downslope-eroding sediment flows. Geol Soc Am Bull 108:225–234

Stirling MW, McVerry GH, Berryman KR (2002) A new seismic hazard model for New Zealand. B Seismol Soc Am 92:1878–1903

Sultan N, Gaudin M, Berne S et al (2007) Analysis of slope failure in submarine canyon heads: an example from the Gulf of Lions. J Geophys Res 112:F01009

ten Brink US, Geist EL, Andrews BD (2006) Size distribution of submarine landslides and its implication to tsunami hazard in Puerto Rico. Geophys Res Lett 33:L11307–L11311

Uruski CI (1992) Sedimentary basins and structure of Cook Strait, 92/3. Institute of Geological and Nuclear Science, Lower Hutt

Uruski CI (2010) New Zealand's deepwater frontier. Mar Petrol Geol 27:2005–2026

Wolman MG, Miller JP (1960) Magnitude and frequency of forces in geomorphic processes. J Geol 68:54–74

Chapter 19
Polyphase Emplacement of a 30 km^3 Blocky Debris Avalanche and Its Role in Slope-Gully Development

Joshu J. Mountjoy and Aaron Micallef

Abstract Failure of the upper slope of the Hikurangi subduction margin resulted in emplacement of ~30 km^3 of debris across ~250 km^2 area of a mid-slope basin. The landslide deposit is well preserved in slope morphology. In this study we use morphometric analysis of Simrad EM300 multibeam data and stratigraphic analysis of multichannel seismic reflection data to assess a possible role for deep-seated bedrock failure in the erosional development of the upper continental slope. We interpret the blocky debris avalanche deposit as resulting from retrogressive polyphase failure. Late stage events are inferred to have impacted earlier debris and caused localised secondary remobilization failure. Morphometric analysis of upper-slope gully development indicates that gully systems become less mature to the north. Among several possible explanations for this pattern of gully development we infer a causal link between large-scale mass failure retrogression and the initiation of slope gully erosion systems.

Keywords Subduction margin • Slope gullies • Seafloor development • Morphometric • Multibeam bathymetry • Seismic reflection • Debris avalanche • Bathymetry • Kuroshio Current

J.J. Mountjoy (✉)
National Institute of Water and Atmospheric Research, Private Bag 14901, Wellington, New Zealand
e-mail: j.mountjoy@niwa.co.nz

A. Micallef
University of Malta, Msida MSD 2080, Malta

GRC Geociències Marines, Universitat de Barcelona, Barcelona E-08028, Spain
e-mail: micallefaaron@gmail.com

Y. Yamada et al. (eds.), *Submarine Mass Movements and Their Consequences*, Advances in Natural and Technological Hazards Research 31,
DOI 10.1007/978-94-007-2162-3_19, © Springer Science+Business Media B.V. 2012

19.1 Introduction

Submarine landslides move large volumes of material on continental margins and have a significant impact on margin development (e.g., Pratson 2001). The combination of high resolution (e.g., 30 kHz) multibeam bathymetry and seismic reflection data enable the construction of three-dimensional models of landslide debris emplacement across many different scales and over large areas (e.g., Lamarche et al. 2008). In addition, high resolution multibeam bathymetry reveal the fine-scale erosional slope processes such as branching slope gully systems, which appear to be ubiquitous features of continental slopes and canyon walls (e.g., Lastras et al. 2009; Micallef and Mountjoy 2011). Base level control, which is a key driver of terrestrial fluvial systems (Howard et al. 1994), has received little attention in seafloor erosion studies but may have a role in continental slope evolution, including canyon and gully formation. Landslides are one mechanism that can affect the relative base level of a slope system.

In this study, we develop a conceptual model of polyphase landslide and slope gully development on the Hikurangi margin of New Zealand (Fig. 19.1a). The objective of the study is to understand the spatial pattern of gully development and consider whether this can be related to large-scale mass failure as a local base level control.

19.2 Tectonic and Sedimentary Setting

The Poverty Re-entrant is a continental-slope-scale, morpho-tectonic feature of the northern Hikurangi subduction margin (Fig. 19.1a) that is interpreted to result from the impact of seamounts on the incoming Pacific Plate ~1 million years ago (Lewis and Pettinga 1993; Collot et al. 1996; Pedley et al. 2010). The post-impact structural and sedimentary re-configuration includes canyon development, large-scale mass failure, and slope-gully development (Orpin 2004; Walsh et al. 2007; Mountjoy et al. 2009; Pedley et al. 2010). Significant Quaternary-age shelf edge sediment loading is recorded by thick shelf-basin sequences and shelf edge clinoforms (Pedley et al. 2010; Mountjoy and Barnes 2011). Miocene to Cretaceous age rocks underlie Quaternary sequences and are exposed in the gullies and canyon heads in the Poverty Re-entrant headwall (Field et al. 1997; Mountjoy and Barnes 2011).

Two major landslide complexes are recognised in the upper re-entrant. The Tuaheni Landslide Complex (TLC) covers ~145 km^2 of the northern re-entrant between 200 and 1,000 m water depth (Fig. 19.1b), and has been interpreted as a terrestrial-style submarine earthflow (Mountjoy et al. 2009). The TLC is eroding the Quaternary sedimentary sequences of the low stand wedge above Tuaheni Ridge. The Poverty Debris Avalanche (PDA) has a large (~250 km^2) blocky debris deposit that covers most of the floor of the Paritu basin at 1,100–1,500 m water depth and slopes gently (~1°) to the S–SE (Fig. 19.1b) (Pedley et al. 2010). This study focuses on this landslide complex.

The upper slope spans a depth range of ~1,000 m in the north to 1,300 m in the south, and is eroded by numerous slope gully systems. Gullies have a well defined

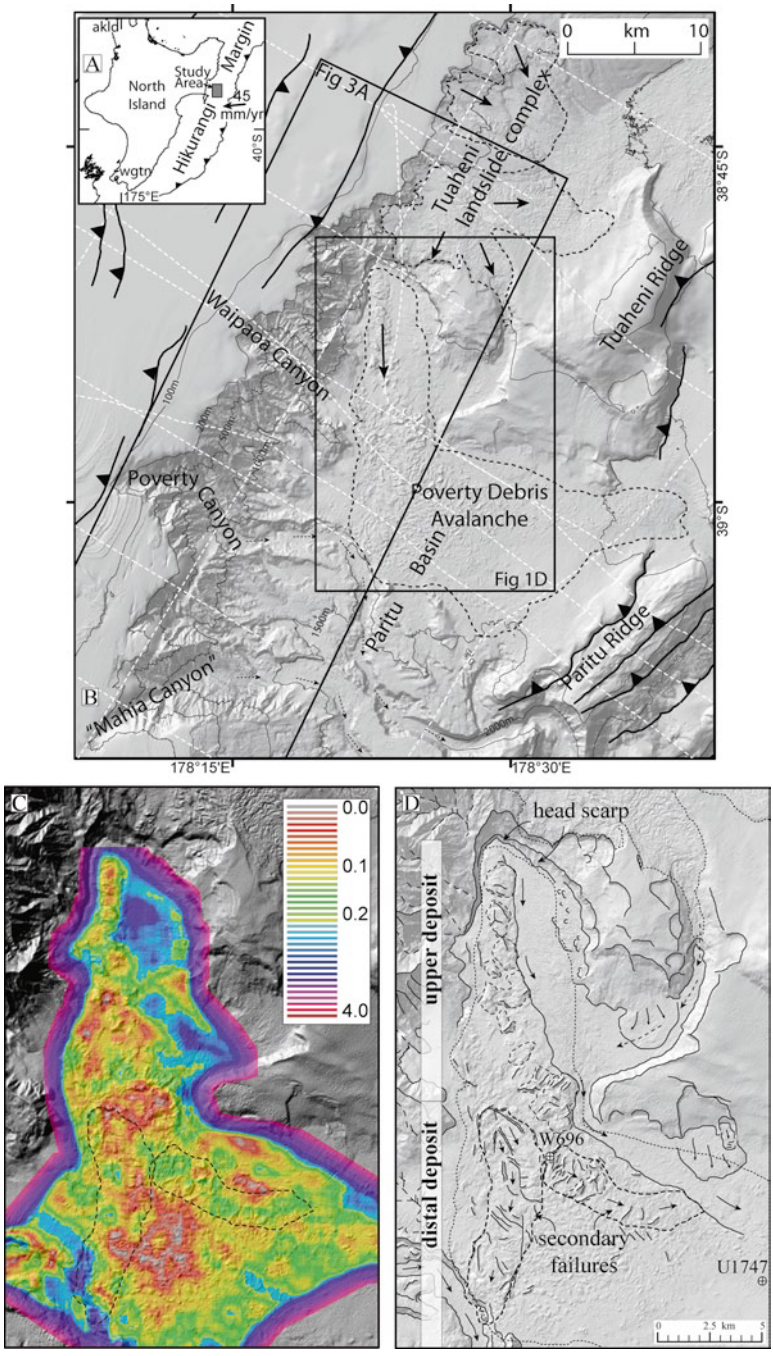

Fig. 19.1 PDA setting. (**a**) Location of the study area and motion vectors of the Pacific Plate after Beavan et al. (2002). (**b**) Upper Poverty Re-entrant showing debris bodies (*dashed line*), active faults from Mountjoy and Barnes (2011), and MCS profiles (*dashed white lines*). (**c**) Eigenvalue analysis of the landslide deposit (1,000 × 1,000 m window) showing secondary failures (*black dashed lines*). (**d**) Interpreted geomorphic map of the PDA

dendritic/pinnate pattern with main-stem channel and bifurcating channels, and exhibit a high visual similarity to terrestrial upland stream catchments. While some of the gully systems are connected to canyons, the majority exit to the Paritu basin.

19.3 Data and Methods

Continental slope multibeam sonar data were collected using a Simrad EM300 during surveys in 2001 and 2008, and are gridded at 25 m (Mountjoy et al. 2009; Pedley et al. 2010). Shelf/upper slope data include Simrad EM 3000 and Atlas Hydrosweep MD-2/30 (Royal New Zealand Navy) data, and are gridded at 10 m. These high resolution data are augmented with a regional 100 m bathymetric grid built from a combination of 12 kHz SIMRAD EM12Dual multibeam (Collot et al. 1996) and single beam echo sounder bathymetric data held in the NIWA database.

Bathymetric data are interpreted using traditional geomorphic mapping techniques as well as quantitative roughness analysis. Eigenvalue analysis of landslide surface roughness can be used to provide an objective measure of spatial variation in roughness scales across landslide deposits; the technique is explained in more detail in (McKean and Roering 2004; Mountjoy et al. 2009). Low eigenvalues signify areas of fine-scale rough seafloor causing eigenvector scattering, while higher values signify larger scale blocky debris causing eigenvector clustering (Fig. 19.1c).

The thalwegs of slope gullies and the boundaries of their catchments were defined using standard terrestrial hydrological algorithms in ArcGIS. Thalweg profiles were extracted for 11 catchments, for the "background" slope, and for the Tuaheni landslide area to the north. Metrics that were extracted for the catchments include: skewness of slope gradient histograms, drainage density (channel length per unit catchment area), basin length, mean slope of the catchment area, and relative density (frequency of channel segments divided by drainage density squared).

Two multichannel seismic reflection (MCS) datasets are presented in this study (coverage shown in Fig. 19.1b): (i) sixfold, 24-channel seismic profiles acquired with a GI-gun source in 45/105 mode, and (ii) up to 960-channel high fold 2D MCS data recorded to 12 s TWT (Barker et al. 2009; Pedley et al. 2010; Mountjoy and Barnes 2011).

Post-stack time-migrated seismic sections were imported into GeoGraphix SeisVision® for interpretation. For volume calculations interpolated horizons (in TWT) were exported from SeisVision to ArcGIS and converted to depth using an assumed material velocity of 1,800 m/s.

19.4 Stratigraphic and Morphological Analyses

The Paritu Debris Avalanche (PDA) deposit has an irregular and blocky surface roughness with marked lateral variation (Fig. 19.1b–d). Individual blocks within the deposit vary from ~1,000 m across in the upper part, to ≤100 m in the lower part.

The roughness characteristics and geometry distinguish an upper and lower zone in the deposit (Fig. 19.1d).

In seismic reflection (MCS) data landslide deposits are recognized by discontinuous weak reflectivity with respect to the generally coherent reflectivity of sediments emplaced by other processes (e.g., Lamarche et al. 2008). MCS profiles resolve the internal structure of the PDA deposit, its thickness and lateral variability, and they image several previous mass-failure deposits at depth within the Paritu Trough (Fig. 19.2). Semi-continuous coherent reflectivity occurs within the debris deposit (Fig. 19.2a1, b1). The PDA deposit volume is estimated at 33 ± 5 km^3.

The landslide source area was reconstructed based on a projection of scar area morphology and stratigraphic horizons, and the basal surface of the PDA debris (Fig. 19.2b, c). The volume for the source area is estimated to be 40 ± 6 km^3.

The sculptured, terrestrial catchment-like morphology of the gully systems on the upper slope of the Poverty Re-entrant lends itself to stream network analyses (Fig. 19.3a). Gully profiles (Fig. 19.3b, c) exhibit a degree of clustering of the blue and purple colored profiles, particularly in the cross margin plot (Fig. 19.3c). The projected base of the low stand wedge sediments (Fig. 19.3c) indicates that gullies are forming in the older underlying sequences. Profiles to the north of the gullies (light blue) are affected by the TLC; these gullies have been formed in the low stand wedge sediments.

Catchment metrics (Fig. 19.3d–g) are plotted against the distance along the length of the re-entrant headwall (Fig. 19.3a). There is a strong relationship between catchment size and headwall distance along slope, indicating a clear decrease in catchment size to the north (Fig. 19.3d). Drainage density, relative density and basin length all show moderately strong trends with distance along slope (Fig. 19.3f, g). In contrast, catchment slope characteristics (skewness and mean slope) show little or no trend (Fig. 19.3e, g). Note, however, that the negatively skewed catchments all occur on the northern portion of the headwall (from 18 to 35 km).

19.5 PDA Emplacement and Upper Slope Gully Development

Geomorphic expression, particularly surface roughness of the PDA deposit, (Fig. 19.1) and the presence of coherent internal reflectivity within the debris, as imaged in MCS profiles (Fig. 19.2), allow us to characterise at least two, and potentially up to four, phases of mass failures that gave rise to the PDA deposit.

In the distal deposit we recognise two areas that we interpret as being affected by secondary failure and deformation (Figs. 19.3c and 19.1d). These post-emplacement failures are highlighted by the eigenvalue analysis and include: (i) headscarp development, (ii) lateral scarps interpreted as lateral shears, and (iii) regularly spaced ridges perpendicular to the direction of movement, which are interpreted as compressional folds that do not cross the lateral scarps. One explanation for triggering these secondary failures is failure in the upper deposit impacting an existing debris mass in the Paritu Basin (i.e. the distal deposit).

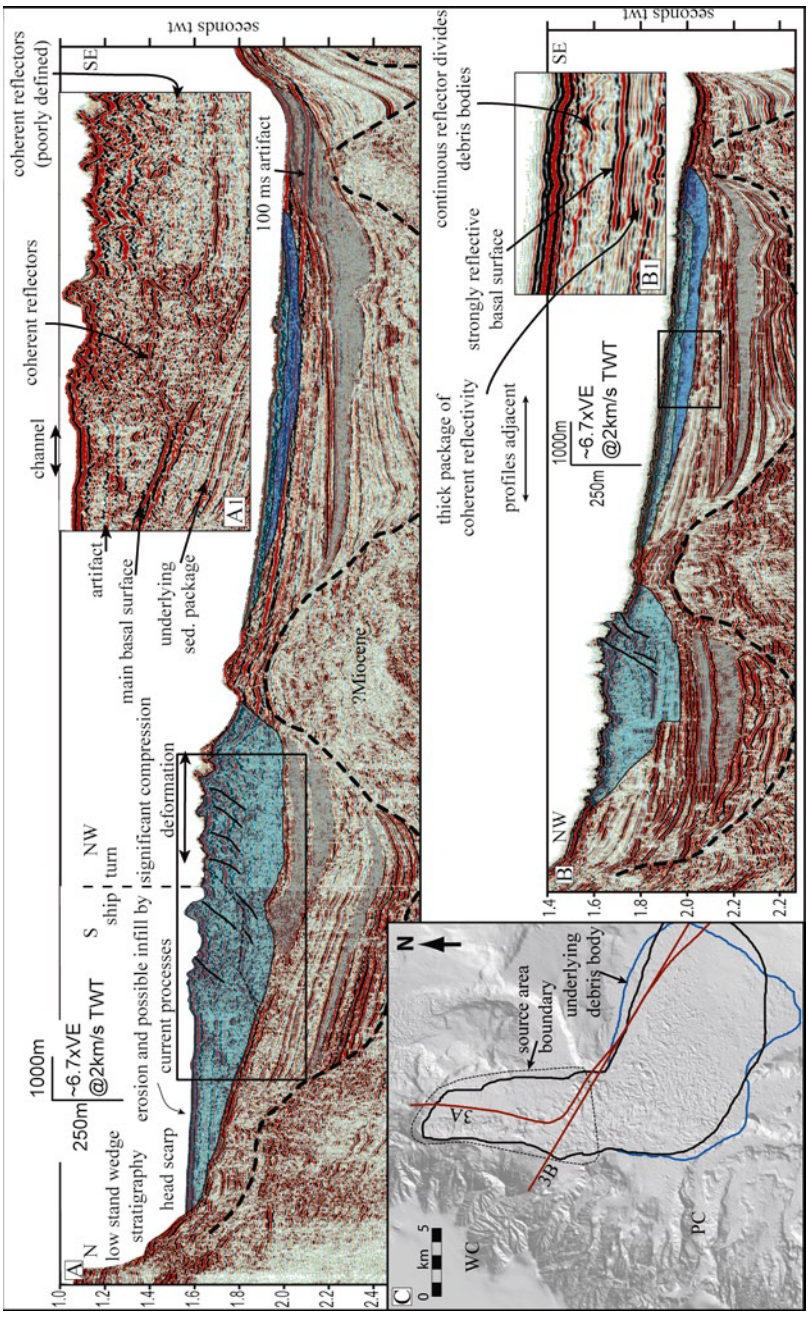

Fig. 19.2 (**a** & **b**) Deposit stratigraphy in MCS data showing surface debris bodies (*blue*) and buried debris bodies (*grey*). Enlargements (**a1** and **b1**) show internal reflectivity within the deposits. (**c**) Location of profiles, debris extent and interpreted source area

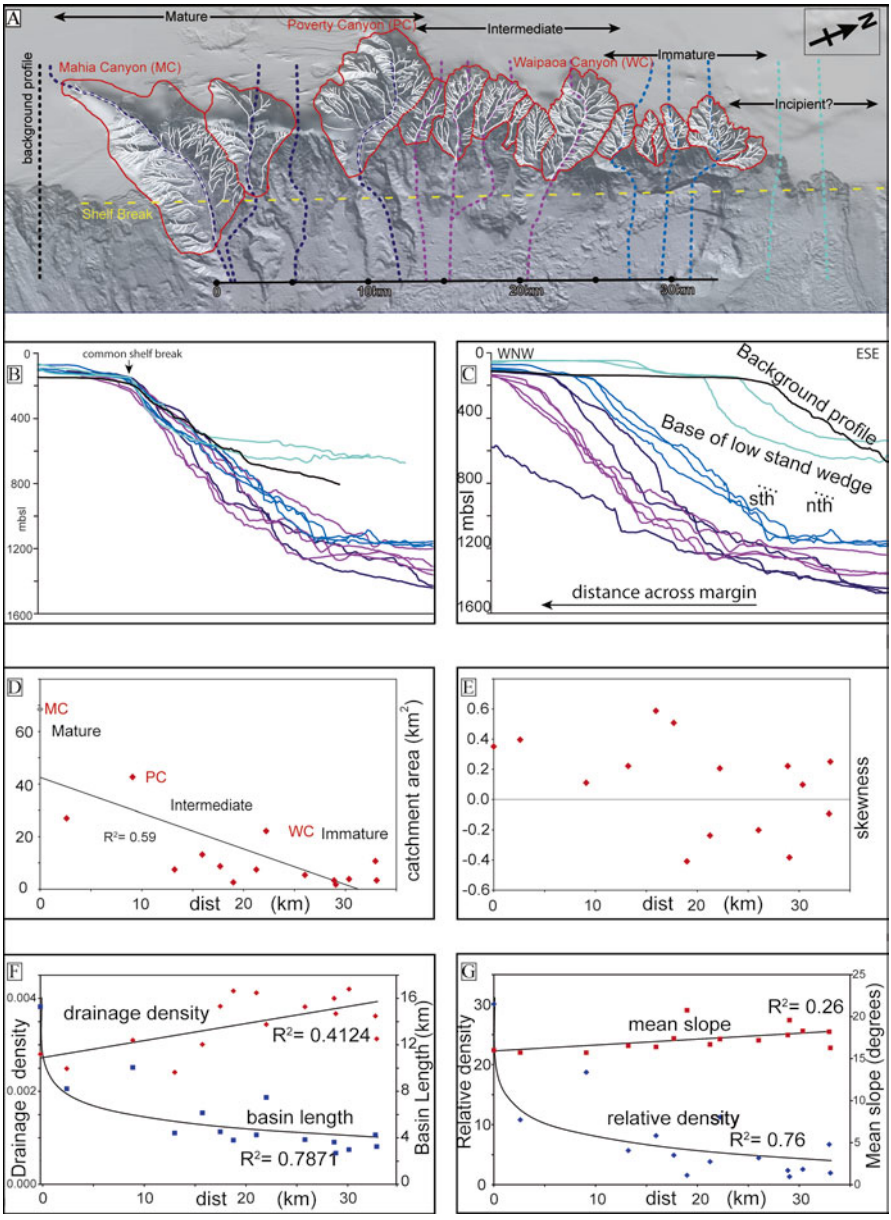

Fig. 19.3 Morphometrics of the upper slope gully systems. (**a**) Catchment, gully networks and profile locations. (**b**) Long profiles with local shelf break (gully head) aligned to a common point. (**c**) Long profiles plotted as distance across margin to illustrate the relative position on the upper slope. The indicated base of the lowstand wedge has been from interpretations of Mountjoy et al. (2009) in the north and Mountjoy (2009) in the south. Plots of catchment metrics plotted against headwall distance along the slope: (**d**) Catchment area; (**e**) Skewness of slope gradient histograms; (**f**) Drainage density and basin length; (**g**) Relative density and mean slope of catchment area

The total volume of the deposit and interpreted scar agree within error margins. We propose a retrogressive failure to the north involving ≥2 events. The timing of the PDA is constrained to being prior to 3,472 year BP based on dated tephra in core W696 (Fig. 19.1d) reported by Orpin (2004). Given that the landslide is polyphase, however, this age constraint does not necessarily apply to the entire landslide complex.

The change of gully metrics with distance along slope in Fig. 19.3e–g, and clustered gully profiles in Fig. 19.3b, c, indicate systematic differences between gully catchments. We infer a decrease in catchment age from south to north and define mature, intermediate, and immature catchment systems, with incipient gully development to the north. The pattern of variation from south to north is also apparent in morphology, where at the southern end large canyon head gully systems are well incised into the shelf and catchments become less incised to the north. Several possible explanations exist for why there is a progressive decrease in catchment age with distance in the development of the upper slope gullies:

1. Canyons started at the southern end of the upper Poverty Re-entrant, and encroached through Paritu basin, undercutting the base of the upper slope and facilitating gully development. Canyons were then infilled with sediment, including landslide debris. In this case, bottom-up erosion would be the primary gully formation mechanism.
2. Development of gullies is driven by sediment input. The spatial age variation could be a function of tectonically controlled sediment supply. In this scenario top-down processes dominate gully development.
3. Erosion in the northern part of the upper Poverty Re-entrant is limited by the presence of Tuaheni Ridge, allowing sediment accumulation and limiting gully development. Gullies cannot form until the sediment is removed (e.g., by mass failure – phase 1 of PDA). This provides the necessary steep slopes for gully erosion, and both top-down and bottom-up erosion will facilitate gully formation.

Slope gully systems generally have a lower boundary sediment removal mechanism acting as an active local base level control – such as a canyon system (e.g., Lastras et al. 2009). However, in the Poverty Re-entrant, over half of the gully systems exit to a depositional basin. Mass failure at the slope base may play a role in slope development by destabilizing the lower slope and enabling bottom-up erosion processes to dominate. Without good age control, however, it is difficult to develop a robust understanding of the temporal aspects of seafloor slope evolution and these models remain inferential and in need of further investigation and corroboration.

19.6 Summary

A polyphase model for emplacement of the ~30 km^3 PDA is established based on seafloor geomorphic mapping, quantitative roughness analysis, and seismic interpretation. For slope gully systems, quantitative morphometric analyses indicate a

possible model of poly-generational slope erosion, decreasing in age from south to north. The proposed explanation for the upper slope evolution is that a relationship exists between seafloor mass-failure and gully evolution.

Despite the rapid advance in our understanding of seafloor landscape development, we still lack many of the landscape age-dating techniques available to terrestrial geomorphologists. We therefore expect to see an exponential growth in the use of marine geomorphometric techniques to compare different parts of the seafloor and understand evolutionary sequencing.

Acknowledgments We appreciate the data collection effort of Keith Lewis for both Multibeam and MCS. Jarg Pettinga and Phil Barnes are thanked for their input into JJM's PhD project. Enlightening discussions and a review of an early draft by JP Walsh is appreciated. Reviews by Alan Orpin and Calvin Campbell significantly improved the manuscript. JJM was funded by MSI CEOC program, NIWA capability funding. AM was funded by Marie Curie Intra-European Fellowship PIEF-GA-2009-252702 and belongs to CRG on Marine Geosciènces (grant 2009 SGR 1305 by Generalitat de Catalunya). Both benefited from an RSNZ International Mobility Fund.

References

Barker DHN, Sutherland R, Henrys S et al (2009) Geometry of the Hikurangi subduction thrust and upper plate, North Island, New Zealand. Geochem Geophys Geosyst 10. doi:10.1029/2008GC002153

Beavan J, Tregoning P, Bevis M et al (2002) Motion and rigidity of the Pacific Plate and implications for plate boundary deformation. J Geophys Res Solid Earth 107(B10):2261

Collot J-Y, Delteil J, Lewis KB et al (1996) From oblique subduction to intra-continental transpression; structures of the southern Kermadec-Hikurangi margin from multibeam bathymetry, side-scan sonar and seismic reflection. Mar Geophys Res 18(2–4):357–381

Field BD, Uruski CI et al (1997) Cretaceous – Cenozoic geology and petroleum systems of the East Coast region, New Zealand. Institute of Geological and Nuclear Sciences Monograph, 19, GNS, 301 pp

Howard AD, Dietrich WE, Seidl MA (1994) Modeling fluvial erosion on regional to continental scales. J Geophys Res Solid Earth 99(B7):13971–13986

Lamarche G, Joanne C, Collot J (2008) Successive, large mass-transport deposits in the south Kermadec fore-arc basin, New Zealand: the Matakaoa Submarine Instability Complex. Geochem Geophys Geosyst 9(4). doi:10.1029/2007GC001843

Lastras G, Arzola RG, Masson DG et al (2009) Geomorphology and sedimentary features in the Central Portuguese submarine canyons, Western Iberian margin. Geomorphology 103(3): 310–329

Lewis KB, Pettinga JR (1993) The emerging, imbricate frontal wedge of the Hikurangi margin. In: Ballance PF (ed) South Pacific sedimentary basin, vol 2, Sedimentary basins of the world. Elsevier, Amsterdam, pp 225–250

McKean J, Roering J (2004) Objective landslide detection and surface morphology mapping using high-resolution airborne laser altimetry. Geomorphology 57(3–4):331–351

Micallef A, Mountjoy JJ (2011) A topographic signature of a hydrodynamic origin for submarine gullies. Geology 39(2):115–118

Mountjoy JJ (2009) Development of submarine canyon systems on active margins: Hikurangi Margin, New Zealand. PhD thesis, University of Canterbury, Riccarton

Mountjoy JJ, Barnes PM (2011) Active upper-plate thrust faulting in regions of low plate-interface coupling, repeated slow slip events, and coastal uplift: example from the Hikurangi Margin, New Zealand. Geochem Geophys Geosyst 12(Q01005). doi:10.1029/2010GC003326

Mountjoy JJ, McKean J, Barnes PM et al (2009) Terrestrial-style slow-moving earthflow kinematics in a submarine landslide complex. Mar Geol 267:114–127

Orpin AR (2004) Holocene sediment deposition on the Poverty-slope margin by the muddy Waipaoa River, East Coast New Zealand. Mar Geol 209(1–4):69–90

Pedley KL, Barnes PM, Pettinga JR et al (2010) Seafloor structural geomorphic evolution of the accretionary frontal wedge in response to seamount subduction, Poverty Indentation, New Zealand. Mar Geol 270(1–4):119–138

Pratson LF (2001) A perspective on what is known and not known about seafloor instability in the context of continental margin evolution. Mar Petrol Geol 18(4):499–501

Walsh JP, Alexander CR, Gerber T et al (2007) The demise of a submarine canyon? Evidence for highstand infilling on the Waipaoa River continental margin, New Zealand. Geophys Res Lett 34(L20606). doi:10.1029/2007GL031142

Chapter 20
Slope Failure and Canyon Development Along the Northern South China Sea Margin

Julie A. Dickinson, Karen Ware, Sian Cosham, and Breandan Murphy

Abstract The continental margin of the northern South China Sea is a NE-SW trending passive continental margin. Mapping of the continental slope from short offset processed 3D seismic across the offshore Pearl River Mouth Basin shows the margin to be characterised by a canyoned morphology from 600 to 1,500 m water depth. Shallower than these depths the slope is undisturbed while at greater depths there is a return to a smooth base of slope morphology with broad runout channels reflecting mass transport deposition fed from the canyons. The canyons are typically ~1 km wide and up to 20 km long, steep sided and asymmetric with a higher slope angle along their eastern margins. Comparatively, the western margins show increased evidence of slumping and slope failure. The intercanyon ridges exhibit arcuate slump features. Mapping of the base Pleistocene shows this slumping has resulted in removal of Quaternary sediment along the intercanyon ridges. Mass transport deposits are also identified along the lower slope. The erosion of these canyons is considered to be related to the internal waves generated from the strong Kuroshio Current crossing the shallow bathymetry of the Luzon Strait into the South China Sea resulting in internal waves interacting with the slope below 600 m. Understanding the dynamics of canyon systems such as these is essential for determining risk to deep sea exploration infrastructure.

Keyword Internal waves

J.A. Dickinson (✉) • K. Ware • S. Cosham • B. Murphy
RPS Energy Ltd, Goldsworth House, Denton Way, Woking, Surrey GU21 3LG, UK
e-mail: dickinsonju@rpsgroup.com

Y. Yamada et al. (eds.), *Submarine Mass Movements and Their Consequences*,
Advances in Natural and Technological Hazards Research 31,
DOI 10.1007/978-94-007-2162-3_20,

20.1 Introduction

The exploration of deep water canyon systems for hydrocarbons presents short and long term concern for drilling and stability of seabed infrastructure. There is a general perception that canyons are by their nature unstable and therefore represent a risk to seabed infrastructure. However, understanding the broader geological evolution and modern sedimentary regime facilitates management of this risk.

The influence of down-slope gravity flows on canyon development has been well established (e.g., Shepard 1981). Less understood is the interaction of internal waves acting on the slope. Numerous canyons have been recognised along the northern slopes of the South China Sea margin including the Kaoping, Formosa and Penghu canyons southwest of Taiwan (e.g., Liu et al. 1993; Yu and Chang 2002; Zhu et al. 2010). This study describes the morphology of modern canyons on the northern South China Sea margin to the west of Dongsha Rise. This is an area where internal waves are focused and slope failure is common. Here we present an explanation for the setting of the canyons, which suggests a relationship between internal waves and mass movements.

20.2 Regional Setting

The northern South China Sea is characterised by a passive margin that extends from Hainan Island to Taiwan (Fig. 20.1). The margin formed as a result of rifting through the Paleogene and has been subsiding since the late Oligocene (Teng and Lin 2004). A number of Tertiary sedimentary basins occur along the margin including the Pearl River Mouth Basin, which extends offshore from Guandong Province of China. The deposition of syn-rift sediments within the basins is associated with the initial opening of the South China Sea in the Eocene and Oligocene (Ru and Pigott 1986). Subsequent post-rift subsidence started in the early Miocene filling the basin with deposits of nearshore through to abyssal environments (Xie et al. 2006). The development of migrating submarine canyons from 12.5 Ma characterises the upper section of the post-rift sequence (Zhu et al. 2010). Progradation of slope sediments coincided with the onset of uplift in the Dongsha region where Pliocene and Quaternary faults are concentrated west of the Dongsha Islands (Lüdmann et al. 2001; Wu et al. 2003). The reactivation of older underlying faults is considered to be responsible for the variation in sediment thickness and stratigraphic patterns along the shelf and slope break (Xie et al. 2006).

The modern oceanographic setting of the northern South China Sea is dominated by ocean currents that enter through the Luzon Strait (Fig. 20.1; Xue et al. 2004). Surface circulation in the region is driven by seasonal monsoons, which are cyclonic in winter and anti-cyclonic in summer (Hu et al. 2000). Acting counter to this circulation in the winter is the northeastward South China Sea Warm Current that forms a strong, narrow band in the deep water off Guangdong Province up to 800 m water depth (Hu et al. 2000). Intrusion of the Kuroshio Current (a warm western boundary current from the Pacific) through the Luzon Strait is thought to influence and moderate the intermediate and deep water cyclonic circulation (Xue et al. 2004).

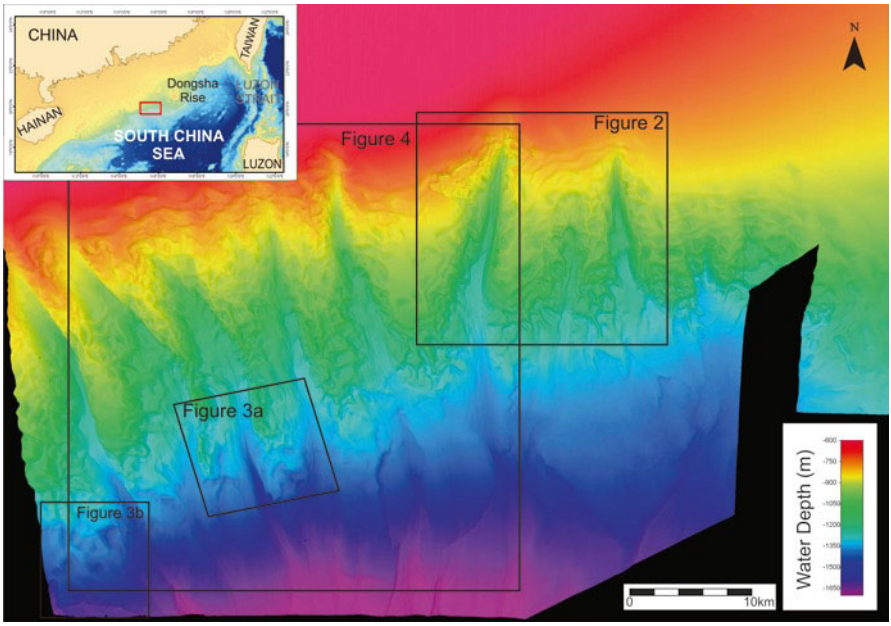

Fig. 20.1 3D image of canyons on northern South China Sea slope with inset showing location of study area (*red block*). Vertical Exaggeration 10×

20.3 Data and Methods

The study of canyon development on the northern South China Sea margin is based on 3D seismic data acquired by China Oilfield Services Ltd in 2006 and 2007. The full volume of seismic data has been processed using the Fugro Seismic Imaging (FSI) short-offset method, which is designed to preserve data integrity. The data were depth converted under the direction of Husky Energy, however both the time and depth volumes have been made available. Bathymetric data is derived from the seismic seabed pick and was loaded into Fledermaus and ArcGIS packages to enable morphological analysis of drainage patterns to be determined and modeled across the area. This data set has been displayed as depth maps.

20.4 Results

20.4.1 Canyon Morphology

The continental shelf off the mouth of the Pearl River, although not clearly defined, is particularly wide at ~240 km (Fig. 20.1). The continental slope extends from the shelf break to 1,500 m. From a depth of 1,500 to 3,400 m is the continental rise

(Wu et al. 1999). The upper slope is characterised by a smooth profile with gradients of 1–3°. Active faults are observed at the seafloor orientated generally NW-SE and WSW-ENE. The orientation of these faults is equivalent to older faults in the underlying Neogene-Pleistocene sequence.

The topography of the mid slope is represented by a series of submarine canyons (Fig. 20.1). Seven regularly spaced, sub-parallel and sub-linear canyons extend from ~650 m water depth at their head to ~1,600 m water depth where they tend to broaden into a wide runout zone on the lower slope. Below 1,600 m the bathymetry of the continental rise has a generally smooth, low gradient of 1–3°, disrupted by the distal channels of the canyons above. The canyons run perpendicular to the slope and broadly trend NNW-SSE with deflections along their course to a N-S orientation and back to an easterly orientation at their base. Typically the canyons are confined to one channel but some branch upslope with tributary channels evident. The canyons are narrower and more deeply incised in their upper reaches, extending to ~800–900 m across and maximum depth of ~210 m. Downslope, the canyons broaden to a wider valley with an average width of 1,500 m downslope. The axes of the canyons are concave upward. The canyon walls commonly slope at 10–15° up to a maximum of 48° and are generally steeper with higher relief on the eastern side producing an asymmetric profile (Fig. 20.2). The intercanyon ridges can be smooth and undulating, which is more common on the upper slopes, or exhibit sharp pinnacle-like forms on the lower slope.

20.4.2 Slope Failure Features

The upper margin of the canyoned slope is characterised by a "crumpled" morphology that is typically evident at the head of the canyons (Fig. 20.2). These crumple zones are narrow bands hundreds of meters across with wavy, ribbon-like morphology and extend laterally for up to 8 km, although distances in the order of 3–5 km are more typical. Gradients of up to 15° can be attained along the front of these slumps, which step down the slope to create a terraced morphology.

The intercanyon ridges are marked by arcuate slump scars and associated deposits. The scars are typically up to 1 km across and up to 80 m deep, with concave walls commonly <10° that can range up to 20° with an absolute maximum of 42°. On seismic profiles suspected slope failure deposits commonly show internal bedding planes coincident with adjacent strata (Fig. 20.3). The basal surfaces of these failures are concave upward along a rotational plane with no evidence of failure along bedding planes.

Less common are slope failures that are observed away from the canyons in the planar-bedded soft clay deposits of the upper and lower slope (Fig. 20.3). These slump scars are small features up to 30 m deep, with relatively flat bases and linear walls. Their deposits are located immediately downslope spreading out in a radial pattern over an area of a few square kilometers. The internal reflection pattern shows disruption of internal bedding.

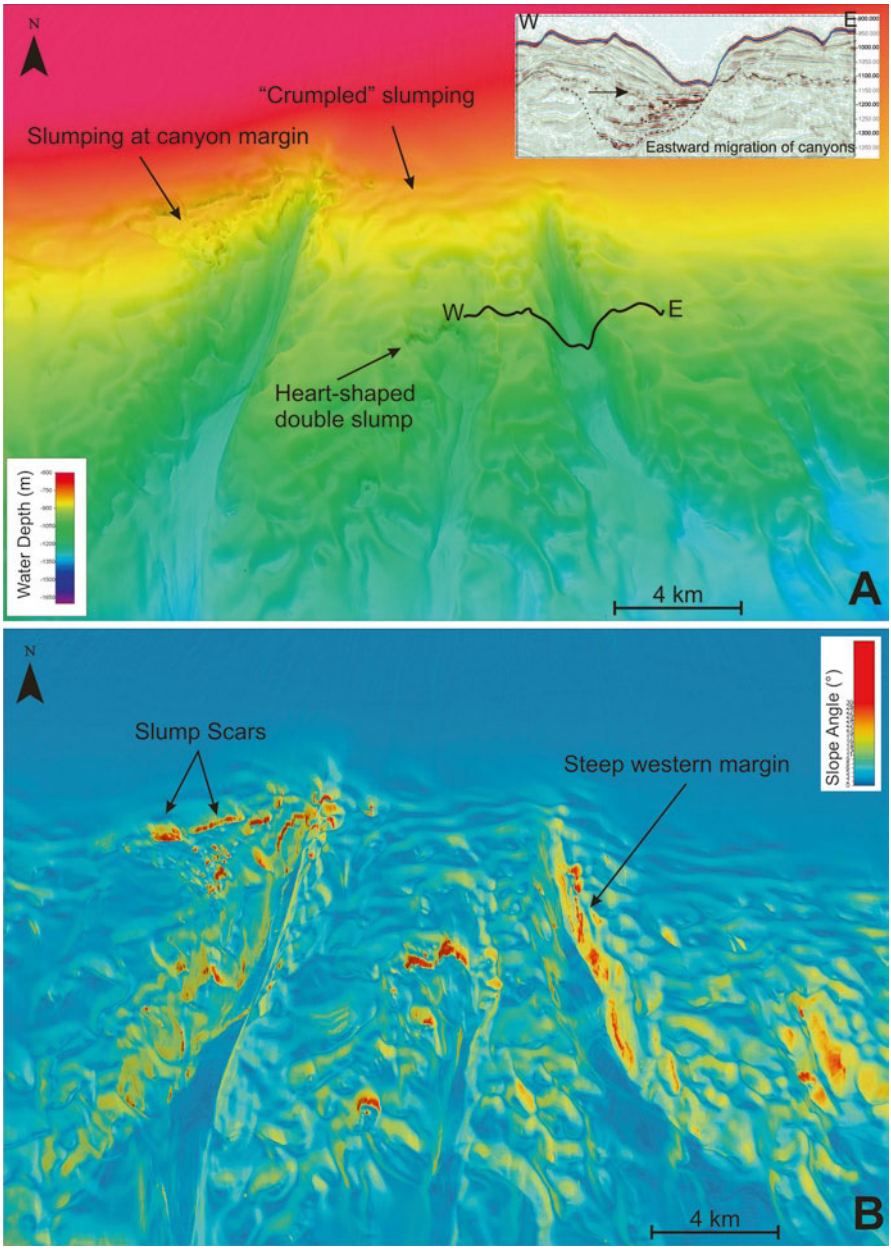

Fig. 20.2 (**a**) View looking upslope showing detail of canyon morphology. Seismic section displays the asymmetric profile of the canyons with steeper eastern margin and eastward migration of canyon systems over time. (**b**) Seabed dip map of view above. Note the high angles of slump scars and along canyon margins

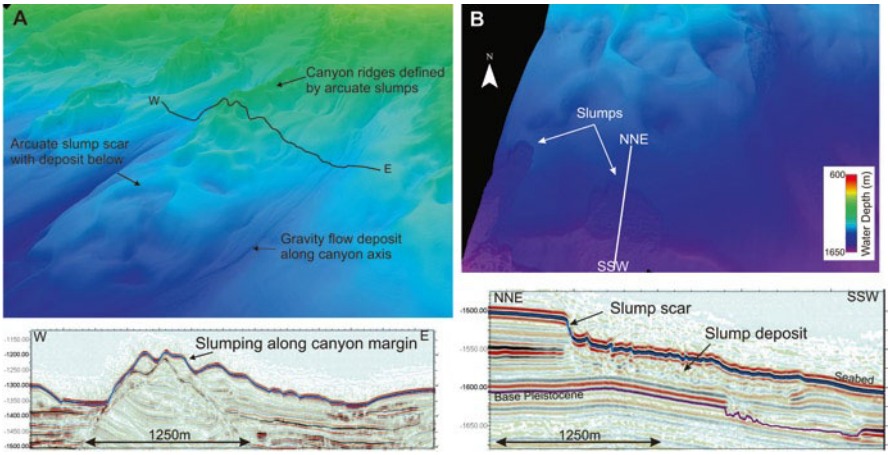

Fig. 20.3 (**a**) Oblique view to the slope to highlight the arcuate slump morphology and pinnacle like ridge formed. Internal structure of slumps shows bedding intact. Gravity flow deposits are found to fill the lower canyon sections. (**b**) Recent slumps on the lower slope with chaotic internal reflection signature evident in seismic

Mass gravity flows are evident along the canyon axes filling the lower canyon floor (Fig. 20.3). They are expressed as thin (~10–30 m) tongues of sediment hundreds of meters across and up to 5 km long. The base Pleistocene has been mapped across the study area (Fig. 20.4). Above the canyon system the thickness of this unit generally increases towards the canyon edge. Where the canyons are present there is more variability in the thickness of the Pleistocene and past the slope break the interpretation of the Pleistocene becomes more complex. Nevertheless, the Pleistocene appears to be thicker to the north and along the canyon margins away from the canyon axis, where slumping has resulted in a localised increase in sediment accumulation. The Pleistocene thins along the axis of the canyons but becomes thicker in the lower section of the canyon valleys.

20.5 Discussion

20.5.1 Canyon Origin

Slope-confined and shelf-indenting canyons are thought to represent different stages of canyon evolution (Farre et al. 1983; Pratson et al. 1994). Slope-confined canyons, such as these observed on the northern South China Sea margin, are a result of failure on the continental slope that can subsequently erode headward. The canyon itself is carved by turbidity currents, debris flows, mass movements and oceanographic currents. A variety of factors can trigger the onset of slope failure including sediment

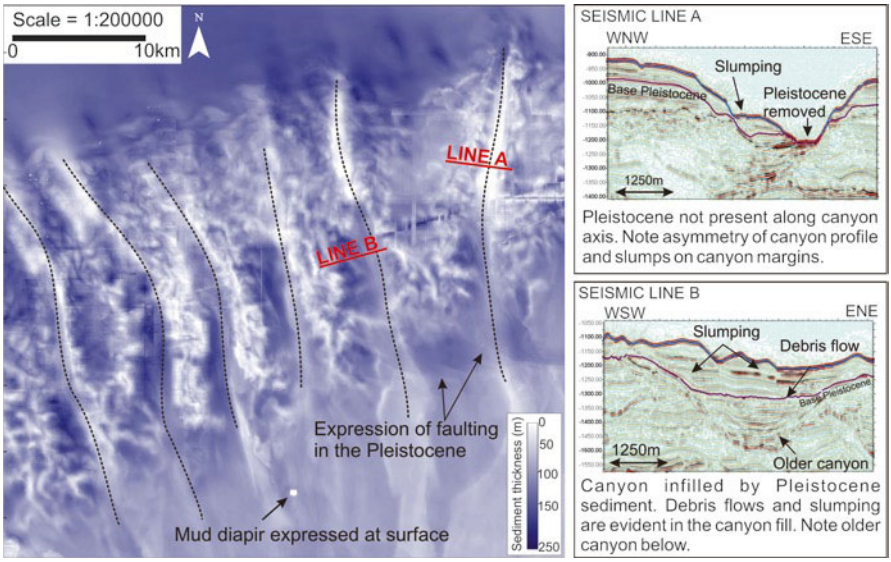

Fig. 20.4 Map of thickness from seabed to base Pleistocene. Axis of canyons is marked by *black dotted line*. Upper canyons show removal of Pleistocene sediment (*Line A*) while lower section exhibit infilling (*Line B*)

loading on the shelf, tectonic events, gas hydrate disassociation and currents within canyons (Shepard 1981; Mitchell 2008). The canyon morphology and position on the slope can also be controlled by such factors as faulting and pore-fluid flow (e.g., Song et al. 2000).

The intact nature of the Quaternary sequence on the slope above the canyon system with no evidence for canyon linkages to the shelf suggests that the modern canyons described above are a result of processes directly relating to their mid slope depths. Furthermore, the outer shelf is sediment starved and dominated by relict sand (Wang et al. 1986) with sediment from the Pearl River accumulating within its estuary and the inner shelf. A longshore drift to the SW transports much of the silty clay westwards (Wang et al. 1986). Therefore shelf processes are not considered to be a factor here.

Canyons have been a feature of the margin since the Miocene and across the study area a buried system of northeastward migrating canyons is evident (Zhu et al. 2010). These canyons appear to have laterally migrated by successive cut and fill events, where erosional surfaces overlain by thalweg deposits are likely due to turbidity currents and their resulting deposits. The laterally inclined packages and northeastern migration of these ancient canyons suggest strong bottom currents influenced sediment dynamics at the time. This was taken as evidence for the development of strong bottom currents in the South China Sea (Zhu et al. 2010).

Canyons along the margin have been attributed a structural control to their origin (e.g., Song et al. 2000). Faults are a common feature including active faults expressed

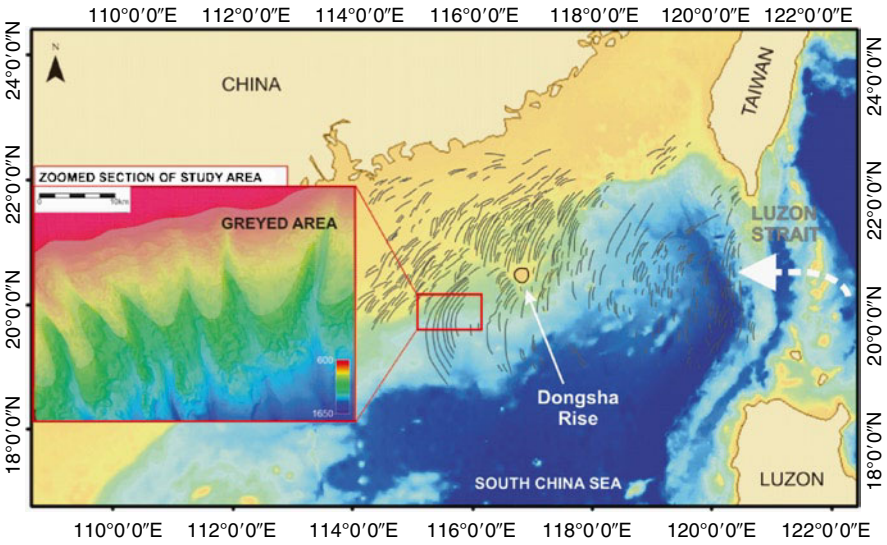

Fig. 20.5 Distribution of internal waves (*grey lines*) in the study area (after Alpers et al. 2006). *White dotted arrow* shows intrusion of the Kuroshio Current across the Luzon Strait. Inset: Zoomed view of study area, "*greyed area*" shows zone where internal waves generated between 600 and 1,000 m water depth would break along the slope west of Dongsha Rise

at the seafloor. Two fault sets are observed, one striking NE-SW and the other NW-SE. There is no clear evidence that the orientation or motion of the faults is controlling the asymmetry of the canyons. However, two episodes of Neogene uplift centered on the Dongsha Rise have been recognised (Lüdmann and Wong 1999; Wu et al. 2003). These events at ~5 Ma and ~1.89–1.4 Ma led to subaerial exposure of the Dongsha Rise and substantial erosion of the Pio-Pleistocene strata (Wu et al. 2003). The tectonic activity also likely resulted in reshaping the margin and influenced the movement of bottom water currents.

The Dongsha Rise is a focus for nonlinear internal waves (or solitons) that travel westwards across the South China Sea and break on the northern continental margin (Alpers et al. 2006). The internal waves are thought to be generated by the shallow bathymetry of the Luzon Strait when strong currents from the Kuroshio Current intrude into the South China Sea (Hsu and Liu 2000; Duda et al. 2004;). Regardless, it is well established that these internal waves interact with the shelf east and west of the Dongsha Islands at water depths of less than ~120 m (Fig. 20.5). Less understood is the generation of mode-two and depression internal waves generated at the shelf break with water depths of 600 to 1,000 m (Hsu and Liu 2000). However, the interaction of these internal waves with the slope at these depths is a possible cause of the canyons asymmetric profiles. We suggest that the westward traveling internal waves break along the western margin of the canyon progressively causing slumping and retrogressive failure. Progressive erosion of the western margin fills the canyon with slump debris shifting the thalweg to the east.

20.5.2 Implications for Geohazard Risk

The installation of petroleum infrastructure such as pipelines and production manifolds are exposed to numerous processes that impact the slope, including internal waves (e.g., Bole et al. 1994) that could result in failure of the structure. Risk assessment is based on the lifetime of the development (50 or 100 year periods of activity). To establish the level of risk of future slope failures, gravity flows and potential for sediment erosion and transportation within the canyon system requires an understanding of what processes are still acting today.

This study suggests that internal waves are partly responsible for slope failure and corresponding canyon morphology along the slope west of Dongsha Rise. It is however not clear if these currents are still actively influencing the slope dynamics or if the slope has reached a point of stability and the morphology is a relict of past activity. It is also not clear what impact changing sea level has had on the frequency and intensity of internal waves across the margin. A greater understanding of these processes is required to improve risk management.

Acknowledgements We would like to thank Husky Energy Ltd for permission to use the dataset. Colleagues within RPS Energy are thanked for many discussions regarding the outcomes of this work. Critical reviews by Dei Huws and Jock Keene and careful editorial work by Jason Chaytor have improved this manuscript.

References

Alpers W, He M, Zeng K, Guo L, Li X (2006) The distribution of internal waves in the China Seas studied by multi-sensor satellite images. In: Proceedings 2005 Dragon symposium "Mid-term Results", Santorini, ESA SP-611, Jan 2006

Bole JB, Ebbesmeyer CC, Romea RD (1994) Soliton currents in the South China Sea: measurements and theoretical modelling. Paper OTC 7417, presented at the offshore technology conference, Houston, 2–5 May 1994, pp 367–376

Duda TF, Lynch JF, Irish JD, Beardsley RC, Ramp SR, Chiu C, Tang TY, Tang Y (2004) Internal tide and nonlinear internal wave behaviour at the continental slope in the northern South China Sea. IEEE J Ocean Eng 29:1105–1130

Farre JA, McGregor BA, Ryan WBF, Robb JM (1983) Breaching the shelfbreak: passage from youthful to mature phase in submarine canyon evolution. SEPM Spec Publ 33:25–39

Hsu MK, Liu AK (2000) Nonlinear internal waves in the South China Sea. Can J Remote Sens 26:72–81

Hu J, Kawamura H, Hong H, Qi Y (2000) A review of the currents of the South China Sea: seasonal circulation. South China Sea warm currents and Kuroshio intrusion. J Oceanogr 56:607–624

Liu CS, Lundberg N, Reed DL, Huang YL (1993) Morphological and seismic characteristics of the Kaoping Submarine Canyon. Mar Geol 111:93–108

Lüdmann T, Wong HK (1999) Neotectonic regime on the passive continental margin of the northern South China Sea. Tectonophysics 311:113–138

Lüdmann T, Wong HK, Wang P (2001) Plio-Quaternary sedimentation processes and neotectonics of the northern continental margin of the South China Sea. Mar Geol 172:331–358

Mitchell NC (2008) Summary of progress in geomorphologic modelling of continental slope canyons. Geol Soc Lond Spec Publ 296:183–194

Pratson LF, Ryan WBF, Mountain GS, Twichell GS (1994) Submarine canyon initiation by downslope-eroding sediment flows: evidence in late Cenozoic strata on the New Jersey continental slope. GSA Bull 106:395–412

Ru K, Pigott JD (1986) Episodic rifting and subsidence in the South China Sea. AAPG Bull 70:1136–1155

Shepard FP (1981) Submarine canyons: multiple causes and long-term persistence. AAPG Bull 65:1062–1077

Song GS, Ma CP, Yu HS (2000) Fault-controlled genesis of the Chilung Sea Valley (northern Taiwan) revealed by topographic lineaments. Mar Geol 169:305–325

Teng LS, Lin AT (2004) Cenozoic tectonics of the China continental margin: insights from Taiwan. Geol Soc Lond Spec Publ 226:313–332

Wang Y, Ren RM, Zhu D (1986) Sediment supply to the continental shelf by the major rivers of China. J Geol Soc 143:935–944

Wu S, Wong HK, Ludmann T (1999) Gravity-driven sedimentation on the northwestern continental slope in the South China Sea: results from high-resolution seismic data and piston cores. Chin J Oceanol Limnol 17:155–169

Wu S, Liu Z, Wang W, Guo J, Ludmann T, Wong HK (2003) Late Cenozoic tectonic deformation in the Dongsha islands and adjacent sea area. Chin J Oceanol Limnol 21(4):377–388

Xie X, Muller RD, Ren J, Jiang T, Zhang C (2006) Stratigraphic architecture and evolution of the continental slope system in offshore Hainan, northern South China Sea. Mar Geol 247: 129–144

Xue H, Chai F, Pettigrew N, Xu D, Shi M, Xu J (2004) Kuroshio intrusion and the circulation in the South China Sea. J Geophys Res 109:C02017. doi:10.1029/2002JC001724

Yu H, Chang J (2002) Penghu submarine canyon off southwestern Taiwan: morphology and origin. TAO 13:547–562

Zhu M, Graham S, Pang X, McHargue T (2010) Characteristics of migrating submarine canyons from the middle Miocene to present: implication for paleoceanographic circulation, northern South China Sea. Mar Petrol Geol 27:307–319

Chapter 21
Distinguishing Sediment Bedforms from Sediment Deformation in Prodeltas of the Mediterranean Sea

Roger Urgeles, Antonio Cattaneo, Pere Puig, Camino Liquete, Ben De Mol, Nabil Sultan, and Fabio Trincardi

Abstract Most Mediterranean prodeltas show undulated sediments on the foresets of their Holocene wedges. These features have been described all along the Mediterranean and interpreted as either soft sediment deformation or, more recently, as sediment bedforms. We present a detailed analysis of these features using ultrahigh-resolution seismic and bathymetric data, as well as geotechnical information and hydrodynamic time series and hydrographic transects. We show that the characteristics of the sediment undulations (morphology and configuration of the reflections

R. Urgeles (✉) • P. Puig
Institut de Ciències del Mar (CSIC), Passeig Marítim de la Barceloneta, 37-49, 08003 Barcelona, Catalonia, Spain
e-mail: urgeles@icm.csic.es

A. Cattaneo • N. Sultan
Géosciences Marines, IFREMER, BP70, F-29280 Plouzané Cédex, France

C. Liquete
Rural, Water and Ecosystem Resources Unit, European Commission – Joint Research Centre, Institute for Environment and Sustainability, Via E. Fermi 2749, TP 460, 21027 Ispra, Italy

Dept. Estratigrafia, Paleontologia i Geociències Marines, Facultat de Geologia, Universitat de Barcelona, c/ Martí i Franquès s/n, 08028 Barcelona, Catalonia, Spain

B. De Mol
Dept. Estratigrafia, Paleontologia i Geociències Marines, Facultat de Geologia, Universitat de Barcelona, c/ Martí i Franquès s/n, 08028 Barcelona, Catalonia, Spain

Parc Científic de Barcelona, c/ Adolf Florensa 8, 08028 Barcelona, Catalonia, Spain

F. Trincardi
ISMAR (CNR), v. Gobetti 101, 40129 Bologna, Italy

Y. Yamada et al. (eds.), *Submarine Mass Movements and Their Consequences*, Advances in Natural and Technological Hazards Research 31,
DOI 10.1007/978-94-007-2162-3_21, © Springer Science+Business Media B.V. 2012

down section and between adjacent undulations) are incompatible with a genesis by sediment deformation.

Keywords Undulated sediments • Prodeltas • Slope failure • Sediment bedforms

21.1 Introduction

Profuse evidence of undulated sediment features exists on Mediterranean prodeltas. Early studies of these features proposed interpretations involving sediment deformation and slope failure phenomena (e.g., Checa et al. 1988; Chiocci et al. 1996; Correggiari et al. 2001; Fig. 21.1). With popularization of chirp profiling and swath mapping systems, seafloor geometries compatible with submarine slope deformation alone were questioned (e.g., Cattaneo et al. 2004; Urgeles et al. 2007; Fernandez-Salas et al. 2007). An intense debate started on whether these features were in fact created by sediment transport processes (i.e. we were imaging sediment waves), or by deformation. The debate was not restricted to the Mediterranean Sea, a few specific case studies in shallow water settings (e.g., Bornhold and Prior 1990; Mosher

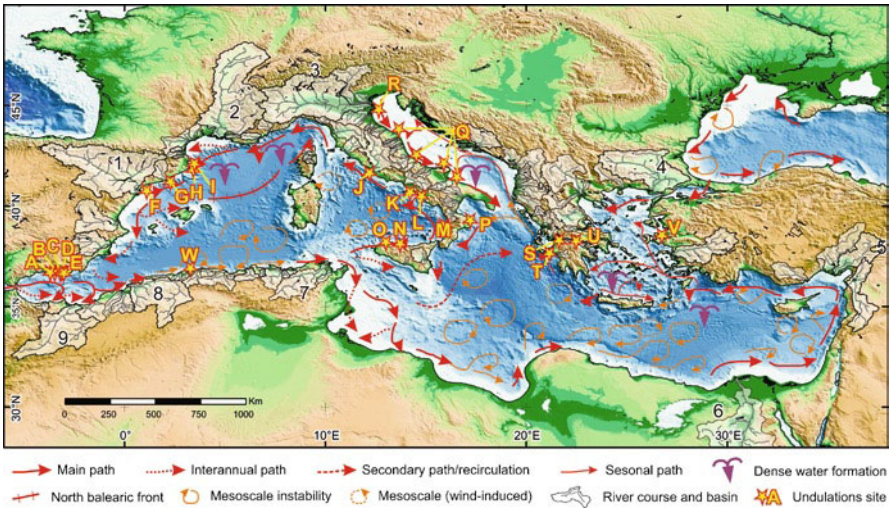

Fig. 21.1 Distribution of sediment undulations on Mediterranean prodeltas (*yellow stars*) in the frame of surface oceanographic circulation patterns (Millot and Taupier-Letage 2005) and major river basins, including the Ebro (*1*), Rhone (*2*), Po (*3*), Evros (*4*), Ceyhan (*5*), Nile (*6*), Medjerda (*7*), Chelif (*8*) and Moulouya (*9*). *A*, Verde and Seco; *B*, Guadalfeo; *C*, Gualchos; *D*, Albuñol; *E*, Adra; *F*, Ebro; *G*, Llobregat; *H*, Ter; *I*, Fuvià-Muga; *J*, Tiber; *K*, Sarno; *L*, Bonea; *M*, Calabrian shelf; *N*, northern Sicilian shelf; *O*, Gulf of Castellammare; *P*, Corigliano basin; *Q*, Adriatic shelf; *R*, Po; *S*, northern Kyparissiakos Gulf; *T*, Patraikos Gulf; *U*, western Gulf of Corinth; *V*, Gediz; *W*, Algerian littoral prism

and Thompson 2002) and deep-water settings (e.g., Normark et al. 1980; Gardner et al. 1999; Lee et al. 2002) of various areas of the world ocean also attracted quite vivid debate.

In the case of Mediterranean prodeltas, with one of the most heavily populated coastlines of the world, the identification of the sediment undulations as depositional or deformation features has important implications for offshore and coastal management. The aim of this paper is to provide the latest view on the origin of undulated seafloor features in the prodeltas of the Mediterranean Sea, where these types of structures have many characteristics that are not found in deeper water settings.

21.1.1 Regional Setting

The Mediterranean region is seismically active, and is currently undergoing rather rapid deformation (Jiménez-Munt et al. 2006). In a very simplified way, the Mediterranean region records, from west to east, a passage from a simple deformation at the oceanic plate boundaries of the Atlantic, characterized by narrow seismic belts, to a broad belt of seismicity and deformation that characterizes a continental collision setting (England and Jackson 1989). The Mediterranean Sea has a relatively mild climate on the average, but substantial storms are possible, usually in winter with a maximum measured significant wave height of 10 m (Cavaleri 2005). Tidal currents in the Mediterranean Sea are important only close to some passages, as well as in all coastal pond outlets, where they can reach a few m s^{-1} (Millot and Taupier-Letage 2005). Due to the Coriolis Effect all waters at basin scale (at all depths) are forced to circulate in a counterclockwise sense following the isobaths corresponding to their density level (Millot and Taupier-Letage 2005). The current freshwater surface discharge to the Mediterranean Sea is estimated to be 400–450 km^3 $year^{-1}$, about one half of what it was at the beginning of the twentieth century (Ludwig et al. 2009). Average suspended sediment yield is 352 t km^{-2} $year^{-1}$, which is approximately twice the 150–200 t km^{-2} $year^{-1}$ world average (Milliman and Syvitski 1992). Quaternary climate change had a profound effect on Mediterranean river watersheds, which resulted in a sedimentary flux 3–3.5 times greater than the present one, during the maximum of glaciation (Bossuet et al. 1996). The position of relative sea-level during the maximum lowstand is at least 115 m lower than present in the Mediterranean Sea (Jouet et al. 2006). On Mediterranean continental shelves, sediment supply decreased abruptly at 15 kyr BP, because of the rapid landward shift of fluvial outlets during the deglacial sea-level rise (e.g., Jouet et al. 2006). Sea-level rise for the Post Younger Dryas period in the Mediterranean shows a constant global sea-level rise with values between 1 and 1.5 cm/year (Berné et al. 2007). Archaeological observations along the Mediterranean coast indicate that sea level remained below its present level until about 3 ka BP (Lambeck et al. 2004).

21.1.2 Methods

Evidence discussed in this manuscript was typically obtained from a variety of shallow water multibeam echosounder data, 3.5 kHz profiles, sediment samples from a geotechnical borehole (see also Sultan et al. 2008), deployment of two boundary-layer tripods (equipped with two RCM-9 current meters and thermistors) and hydrographic sections (see Puig et al. 2007 for details).

21.2 Results

21.2.1 Morphology of Undulated Prodeltas

Most sediment undulations in Mediterranean prodeltas develop in water depths ranging between 20 and 100 m, mainly beyond the clinoform rollover point, on the steepest part of Holocene prodeltas. They are found on slopes between 0.2° and 3° and affect areas of different size (3.7 km^2 in the Ebro prodelta, 25 km^2 in the Llobregat prodelta, 25.7 km^2 on the Guadalfeo, 100 km^2 in the Tiber prodelta and about 800 km^2 on the central Adriatic shelf). Where multibeam data is available, the undulation crests are often parallel to the bathymetric contours and have slightly sinuous to rectilinear shape in platform view (Cattaneo et al. 2004; Fernandez-Salas et al. 2007; Urgeles et al. 2007; Fig. 21.2). The undulations often show an intricate pattern of bifurcating and truncated ridges and can be traced for distances ranging between a few tens of meters to 2 km, but most commonly range in between 200 to 400 m.

The amplitude of the undulations range from as high as 5 m to a few cm. They also range from about 1,000 m wavelength to about 20 m (Fig. 21.2). Generally no trend is observed in wave amplitude or wave length with water depth and increasing distance from shore. The shallower undulations show relatively short upslope limbs and long downslope limbs (near 0 asymmetry) while in deeper waters the undulations are more symmetric. The undulations that develop on the prodeltas of the Mediterranean Sea generally have L/H (wavelength/height) ratios in the range of 50–400.

21.2.2 Seismostratigraphy of Prodelta Undulations

On chirp profiles, sediment undulations of Mediterranean prodeltas hold the following characteristics: (1) They are rooted at the Maximum Flooding Surface (MFS) or a secondary flooding surface and develop on the Late-Holocene High-stand Systems Tract (HST) (Fig. 21.3); (2) the shallowest parts of the prodeltas appear largely void of reflectors and more chaotic character (see Correggiari et al. 2001; Cattaneo et al. 2004; Urgeles et al. 2007; Lykousis et al. 2009). This facies is distinctive of shallow

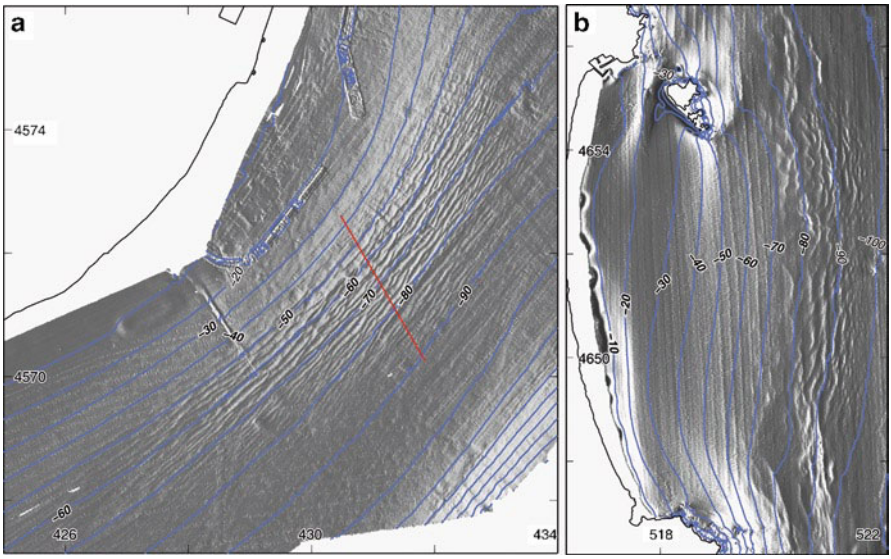

Fig. 21.2 Shaded relief multibeam maps displaying undulated sediment features on prodelta settings. Contours are plotted at 10 m intervals. (**a**) Llobregat prodelta, (**b**) Ter prodelta. Maps are displayed in UTM km (zone 31). *Red line* shows profile of Fig. 21.3

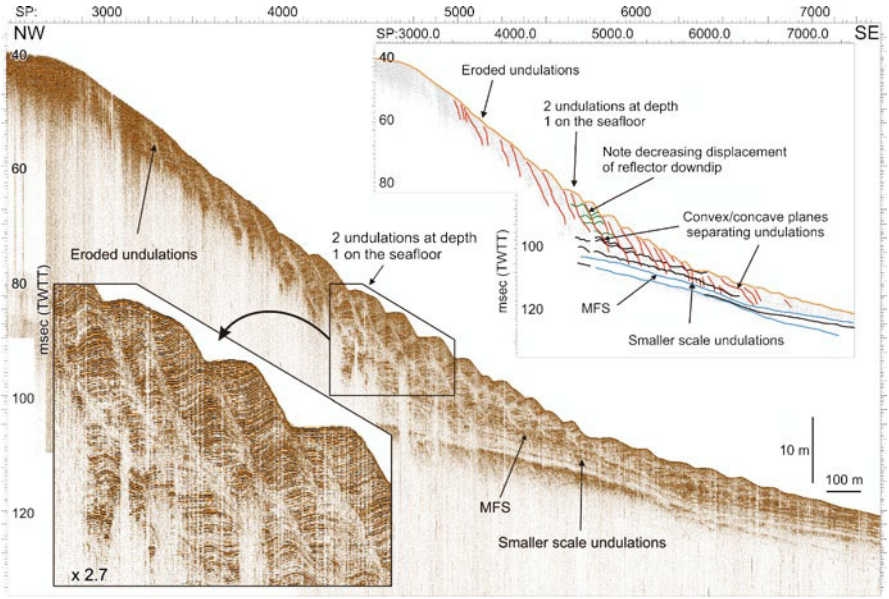

Fig. 21.3 5 kHz seismic section showing overall aspect of sediment undulations and internal structure on the Llobregat prodelta foresets. For location see Fig. 21.2. Inset shows line drawing with main characteristic elements of the sediment undulations

gas enriched sediments, masking the underlying reflectors (Sultan et al. 2008); (3) the sediment undulations are mostly characterized by a wavy stratified pattern of strong to faint prograding reflectors on the prodelta front, in which both wavelength and amplitude of the undulations generally decrease with increasing stratigraphic depth (Fig. 21.3). The prodeltaic Holocene mud wedges that are affected by the undulations have thicknesses that do not exceed 50 ms TWTT and extend offshore for a few kilometers (generally <10 km).

Analysis of high resolution seismic reflection profiles shows that single undulations at the seafloor may correspond to multiple undulations at depth below the seafloor or, in some cases, fewer undulations at depth (Fig. 21.3). Also areas that do not presently show undulations at the seafloor, may show evidence of seafloor undulations down section, with the undulations being truncated at the seafloor (eroded undulations in Fig. 21.3). The crest and trough angle of climb of most sediment undulations are not homogeneous down section (Fig. 21.3). Variations are also not consistent, i.e. the angle may increase or decrease or change in trend down section, i.e. displaying alternations between convex and concave shapes (Fig. 21.3).

21.2.3 Physical Properties of Prodelta Undulations

The largest sediment undulation fields in the Adriatic and Llobregat prodeltas are predominantly muddy (respective average clay, silt and sand contents of 65%, 35% and 5% in the Adriatic and 15%, 46% and 39% in the Llobregat). In more energetic environments the undulations may be formed in coarser material, with sand being the predominant grain size fraction (Fernández-Salas et al. 2007). Samples for deep geotechnical investigation have only been obtained in the Adriatic Sea (Sultan et al. 2008). Undrained shear strength of undulated sediments in the Adriatic Sea shows a sharp increase of about 12 kPa near the boundary between the upper to the lower undulation. Cyclic triaxial tests indicated that silty and sandy sediments such as those occurring near the MFS (Fig. 21.4) were the most sensitive to earthquake loading. Pre-consolidation pressures measured with an incremental loading oedometer indicated normal to slightly underconsolidated sediments.

21.2.4 Sediment Transport Processes on Undulated Prodeltas

Puig et al. (2007) addressed the relationships between active sediment dynamics and the formation/maintenance of the undulated seafloor features in the western Adriatic using boundary-layer tripods and a mooring in 50 m water depth equipped with current meters and thermistors, in addition to two hydrographic sections conducted at the time of instrument deployment, maintenance and retrieval (see Puig et al. 2007). Temperature and salinity data showed a wide and well-developed

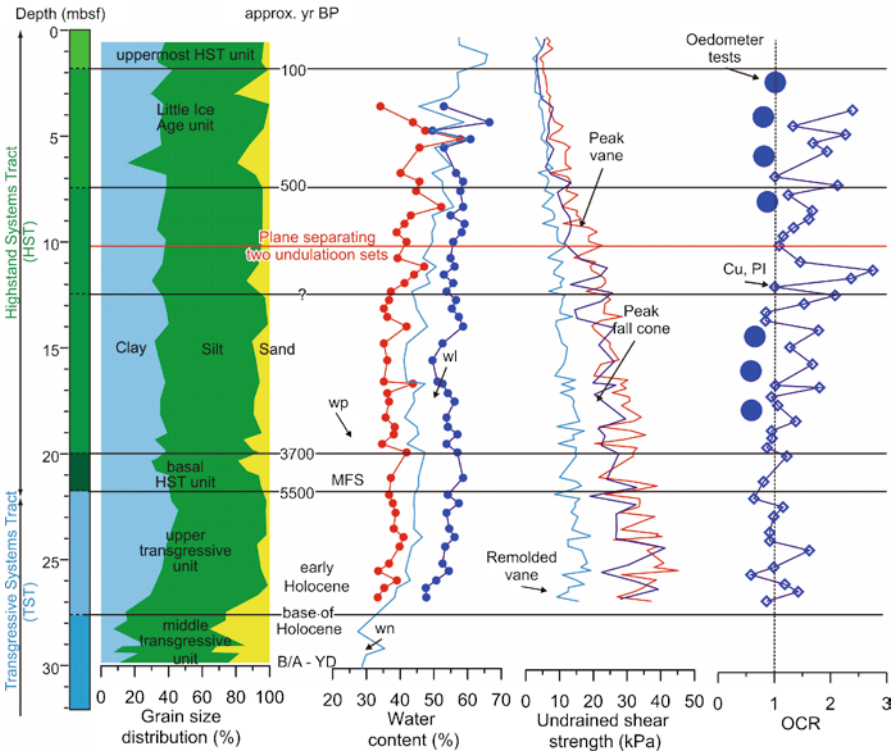

Fig. 21.4 Summary of chrono-stratigraphic and geotechnical characteristics of undulations from the Adriatic Sea north of Punta Penna (*wp* plastic limit, *wl* liquid limit, *wn* natural water content, *Cu,PI* consolidation state derived from undrained shear strength and plasticity, *OCR*, OverConsolidation Ratio)

thermocline with the maximum gradient between 40 and 80 m water depth, coinciding with the region affected by the undulated seafloor (Fig. 21.5). Suspended Sediment Concentration (SSC) distribution indicated the presence of a surface nepheloid layer, being constrained by coastal colder and less saline waters, and the development of a bottom nepheloid layer that detaches where the thermocline intersects the seabed (Fig. 21.5a).

During the investigation period, several sediment-resuspension events were recorded during which current and wave shear stresses reached similar values. After the passage of a storm, activity of near-inertial internal waves (~17 h) was also recorded by the moored current meters and temperature sensors (Fig. 21.5b). In periods of strong near-inertial fluctuations, increases of the water SSC clearly coincided with the offshore direction of the cross-shelf velocity component and with strong temperature and salinity fluctuations showing excursions through the water column of tens of meters (Fig. 21.5b).

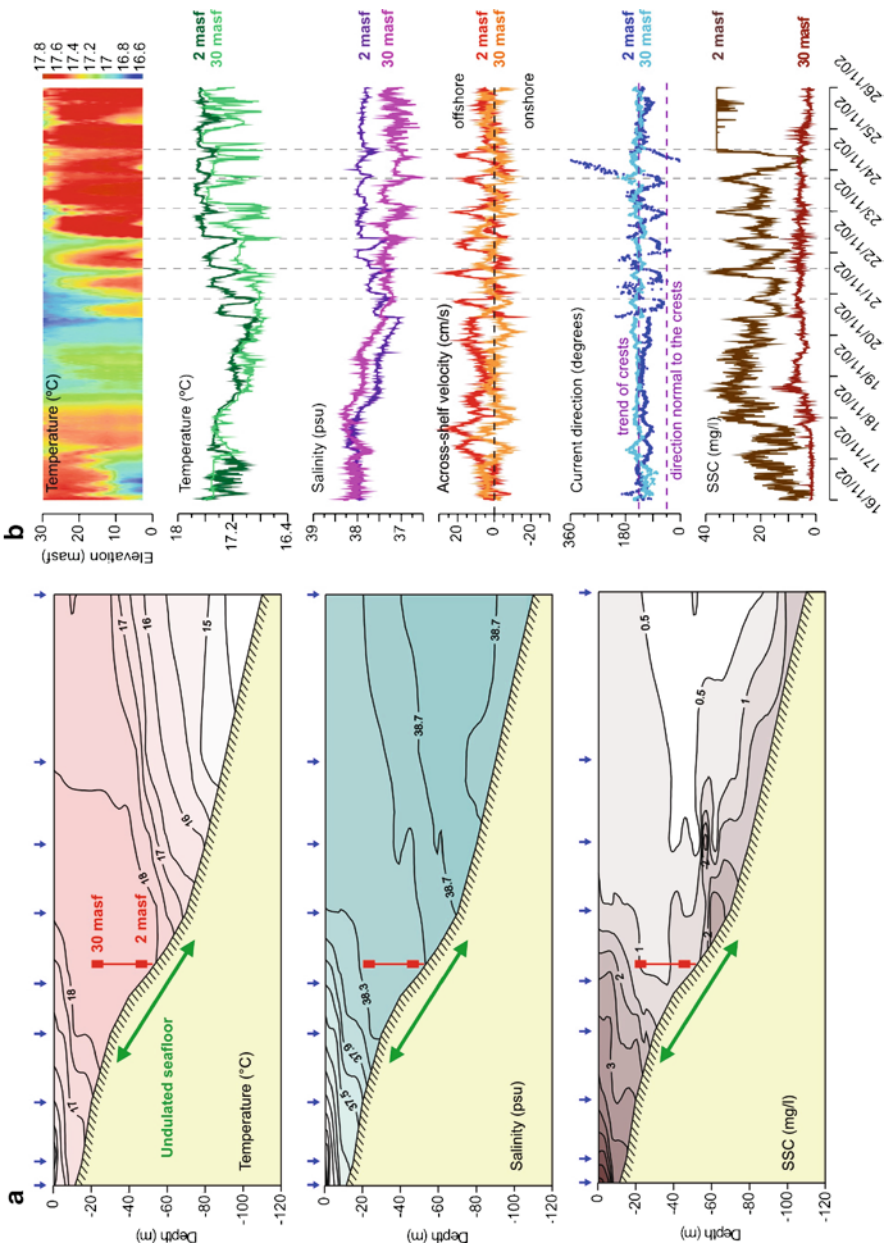
a
Depth (m)
Temperature (°C)
Undulated seafloor
30 masf
2 masf
Salinity (psu)
SSC (mg/l)
b
Elevation (masf)
Temperature (°C)
Salinity (psu)
Across-shelf velocity (cm/s)
offshore
onshore
Current direction (degrees)
trend of crests
direction normal to the crests
SSC (mg/l)
16/11/02
17/11/02
18/11/02
19/11/02
20/11/02
21/11/02
22/11/02
23/11/02
24/11/02
25/11/02
26/11/02

Fig. 21.5 (**a**) Across-shelf hydrographic sections on the Adriatic prodeltaic wedge north of Punta Penna showing the distribution of temperature, salinity and SSC in November 2002. Image displays a surface nepheloid layer constrained by coastal colder and less saline waters, and the development of a bottom nepheloid layer that detaches where the thermocline intersects with the seabed. Location of the instrumented mooring and the region affected by an undulated seafloor are also shown. (**b**) Detail of the instrumented mooring time series for a period of strong near-inertial signal. Temperature from 20 to 50 m water depth varied with the same periodicity (~17 h) as the fluctuations of the near-bottom turbidity and velocity components, indicating a strong displacement of the thermocline and the presence of active sediment transport by near-inertial internal waves. Increases of the SSC coincide with the offshore direction of the cross-shelf velocity component, with current orientations normal to the crests of the seafloor undulations

21.3 Discussion and Conclusion

Influence of gravity-induced sediment instabilities is preferentially invoked in many prodeltas displaying undulated seafloor (e.g., Agate et al. 2009; Chiocci et al. 1996; Correggiari et al. 2001; Díaz and Ercilla 1993; Fig. 21.1), however the lack of a major headwall suggests that in all these areas failure would be at a very incipient stage, if at all. If it is assumed that the sediment undulations are formed by slow gravitational deformation, the lack of compressional features at the toe of the prodelta wedge implies a low angle detachment level. Mud-diapir-like structures have been identified at certain locations of the toe of the Adriatic prodelta wedge (Correggiari et al. 2001), and it could be argued that they result from sediment compression at the toe of the mud-wedge. However, mud reliefs could also result from fluid expulsion and successive differential deposition guided by the dominant countour-parallel bottom current. In addition, mud reliefs are not found in several other areas of the Adriatic prodeltaic wedge and nowhere else in the fields of undulations of the Mediterranean Sea.

The lack of hyperbolaes on the synform part of the folds would also imply that there is no rupture of the reflectors and therefore that deformation is ductile rather than brittle. Indeed, because the dipping of strata is relatively constant within each undulation (Chiocci et al. 1996; Correggiari et al. 2001; Cattaneo et al. 2004; Urgeles et al. 2007; Lykousis et al. 2009; Fig. 21.3), this implies that there is no synchronous deformation during deposition that could induce growth features (i.e. if the undulations result from sediment deformation, there must be one single phase of deformation). In other words, deformation cannot be gradual.

Genesis due to a punctual event, such as an earthquake or major storm, needs to be relatively recent, as the undulations affect the whole or the upper Holocene mud wedge in most instances (Fig. 21.3). Comparing the seismic stratigraphy between adjacent undulations shows that on the upper part of the undulations the displacement is larger than on the lower part (Fig. 21.3), which is kinematically not possible if these are deformation features. Also the fact that the plane separating the different undulations shows no consistent trend with depth (i.e. normally there should be a progressive reduction in angle) appears mechanically incompatible with gravity deformation (Fig. 21.3).

An additional exercise to rule out the genesis of the undulations by sediment deformation is to assume that the difference in elevation from trough to crest on the landward side of the undulations corresponds to the vertical component of the deformation. That elevation may reach values of ~0.5 m. From seismic data it can be seen that the slope angle of the plane that separates the different undulations (supposed shear plane) is up to 20°, while the angle of the supposed detachment level at the base of the undulations is less than 1°. Supposing that failure occurs along these two planes in a circular fashion, than the 0.5 m in vertical displacement must translate to ~1.5 m horizontal displacement. Because there are various undulations in each sediment undulation field (Chiocci et al. 1996; Correggiari et al. 2001; Cattaneo et al. 2004; Urgeles et al. 2007; Lykousis et al. 2009; Fig. 21.3), this implies that the total horizontal displacement may amount to more than 10 m. Such a large displacement

is unlikely to take place without brittle deformation. Thus, the fact that reflectors are not broken is inconsistent with an origin of the undulations by one single phase of sediment gravitational deformation.

Finally, assessment of the sediment liquefaction potential (Sultan et al. 2008) showed that, at least in the Adriatic case, formation of the undulations by deformation is only possible at a very early stage in the sedimentation of the Holocene mud wedge and that latter undulation evolution or preservation is not related to sediment deformation. Cattaneo et al. (2004) proposed a hybrid genetic mechanism by which the sediment undulations were initiated by seafloor liquefaction, which generated a roughness facilitating the latter growth of the undulations by processes in the bottom boundary layer. As explained earlier, however, most of the undulations root at the MFS, and such an interpretation would imply that sediment liquefaction occurred shortly after that event took place. Therefore, it is difficult to explain the synchronous onset of the many undulation fields in the Mediterranean Sea by a generalized liquefaction event. Although this roughness might be an important factor in the initial development of the sediment undulations of the Adriatic, the actual mechanism that generates this roughness, if present at all, does not need to be sediment deformation. On the other hand, the work by Puig et al. (2007) has shown that basin-wide oceanographic processes such as internal waves can play a role in resuspending and transporting sediment in prodeltaic undulated areas (Fig. 21.5). Near-inertial internal waves induced by local wind pulses tend to propagate across the water column through isopycnals and concentrate their energy at the shelf regions where the seasonal thermocline intersects the seabed, which turns out to be the depth range characterized by having an undulated seafloor (Puig et al. 2007). Similarly, work by Lee et al. (2002) has also shown that similar features may be formed by hyperpycnal flows.

Acknowledgments The data on the Iberian prodeltas was acquired in the frame of the Spanish projects PRODELTA (REN2002-02323). We thank captain and crew of R/V L'Atalante (campagne PRISME 2007) and funding from French ANR projects ISIS and DANACOR. Data for some areas of the continental shelf (Ter prodelta) were acquired by "Secretaría General del Mar" of the "Ministerio de Medio Ambiente, y Medio Rural y Marino" and provided free of charge. Borehole geotechnical data was acquired in the frame EC funded project PROMESS-1 (EVR1-CT-2002-40024). Hydrodynamic transects and instrumented moorings were funded by the Office of Naval Research, NICOP Grant N00014-02-1-0252. The "Generalitat de Catalunya" is acknowledged for support through an excellence research group grant (2009-SGR-146). J. Déverchère (UBO-IUEM, Brest) and K. Yelles (CRAAG, Algiers) are thanked for discussions about the Algerian shelf. Reviews by Homa Lee and Michele Rebesco greatly improved the submitted version of the manuscript.

References

Agate M, Di Grigoli G, Lo Iacono C et al (2009) Decoding the instabilities features along the continental margin of sicily (Central Mediterranean Sea). Rend Online Soc Geol It 7:99–101

Berné S, Jouet G, Bassetti MA et al (2007) Late Glacial to Preboreal sea-level rise recorded by the Rhône deltaic system (NW Mediterranean). Mar Geol 245:65–88

Bornhold BD, Prior DB (1990) Morphology and sedimentary processes on the subacqueous Noeick river delta, British Columbia, Canada. In: Colella A, Prior DB (eds) Coarse-grained

deltas, Special Publication 10, International Association of Sedimentologists. Blackwell Scientific, Oxford/London, pp 169–184
Bossuet G, Ruffaldi P, Magny M et al (1996) Dynamique et approche quantitative des remplissages fini- et postwürmiens du bassin lacustre de Cerin (Jura, France). Bull Soc Géol France 167:483–494
Cattaneo A, Correggiari A, Marsset T et al (2004) Seafloor undulation pattern on the Adriatic shelf and comparison to deep-water sediment waves. Mar Geol 213:121–148
Cavaleri L (2005) The wind and wave atlas of the Mediterranean Sea – the calibration phase. Adv Geosci 2:255–257
Checa A, Díaz JI, Farrán M, Maldonado A (1988) Sistemas deltaicos holocenos de los ríos Llobregat, Besós y Foix: modelos evolutivos transgresivos. Acta Geol Hispànica 23:241–255
Chiocci FL, Esu F, Tommasi P, Chiappa V (1996) Stability of the submarine slope of the Tiber River delta. In: Senneset K (ed) Landslides. Balkema, Brookfield, pp 521–526
Correggiari A, Trincardi F, Langone L, Roveri M (2001) Styles of failure in Late Holocene highstand prodelta wedges on the Adriatic shelf. J Sediment Res 71:218–236
Díaz JI, Ercilla G (1993) Holocene depositional history of the Fluviá-Muga prodelta, northwestern Mediterranean Sea. Mar Geol 111:83–92
England P, Jackson J (1989) Active deformation of the continents. Annu Rev Earth Planet Sci 17:197–226
Fernández-Salas LM, Lobo FJ, Sanz JL et al (2007) Morphometric analysis and genetic implications of pro-deltaic sea-floor undulations in the northern Alboran Sea margin, western Mediterranean Basin. Mar Geol 243:31–56
Gardner JV, Prior DB, Field ME (1999) Humboldt slide – a large shear-dominated retrogressive slope failure. Mar Geol 154:323–338
Jiménez-Munt I, Sabadini R, Gardi A, Bianco G (2006) Active deformation in the Mediterranean from Gibraltar to Anatolia inferred from numerical modeling and geodetic and seismological data. J Geophys Res 108. doi:10.1029/2001JB001544
Jouet G, Berné S, Rabineau M et al (2006) Shoreface migrations at the shelf edge and sea-level changes around the Last Glacial Maximum (Gulf of Lions, NW Mediterranean Sea). Mar Geol 234:21–42
Lambeck K, Antonioli F, Purcell A, Silenzi S (2004) Sea level change along the Italian coast from the past 10,000 yr. Quat Sci Rev 23:1567–1598
Lee HJ, Syvitsky JPM, Parker G et al (2002) Distinguishing sediment waves from slope failure deposits: field examples, including the "Humboldt Slide" and modelling results. Mar Geol 192:79–104
Ludwig W, Dumont E, Meybeck M, Heussner S (2009) River discharges of water and nutrients to the Mediterranean and Black Sea: major drivers for ecosystem changes during past and future decades? Prog Oceanogr 80:199–217
Lykousis V, Roussakis G, Sakellariou D (2009) Slope failures and stability analysis of shallow water prodeltas in the active margins of Western Greece, northeastern Mediterranean Sea. Int J Earth Sci 98:807–822
Milliman JD, Syvitski JPM (1992) Geomorphic/tectonic control of sediment discharge to the ocean: the importance of small mountainous rivers. J Geol 100:525–544
Millot C, Taupier-Letage I (2005) Circulation in the Mediterranean Sea. Environ Chem 5:29–66
Mosher DC, Thomson RE (2002) The Foreslope Hills: large-scale, fine-grained sediment waves in the Strait of Georgia, British Columbia. Mar Geol 192:275–295
Normark WR, Hess GR, Stow DAV, Bow AJ (1980) Sediment waves on the Monterrey fan levee: a preliminary physical interpretation. Mar Geol 42:201–232
Puig P, Ogston AS, Guillén J et al (2007) Sediment transport processes from the topset to the foreset of a crenulated clinoform (Adriatic Sea). Cont Shelf Res 27:452–474
Sultan N, Cattaneo A, Urgeles R et al (2008) A geomechanical approach for the genesis of sediment undulations on the Adriatic shelf. Geochem Geophys Geosyst 9:Q04–R03. doi:10.1029/2007GC001822
Urgeles R, De Mol B, Liquete C et al (2007) Sediment undulations on the Llobregat prodelta: signs of early slope instability or bottom current activity? J Geophys Res 112:B05102

Chapter 22
Hydroacoustic Analysis of Mass Wasting Deposits in Lake Ohrid (FYR Macedonia/Albania)

Katja Lindhorst, Matthias Gruen, Sebastian Krastel, and Tilmann Schwenk

Abstract Lake Ohrid is a tectonically formed basin on the Balkan Peninsula. The Udenisht slide complex (USC), in the southwestern part of the lake, is by far the largest mass failure event within the basin. The slide deposits cover an area of ~27 km², are up to 50 m thick, and sum up to a volume of ~0.11 km³. The USC extends for up to 10 km into the central basin. First age estimations suggest that the USC is less than 1,500 years old. The volume of the USC is well within the range of landslide volumes capable to trigger tsunamis. However, since the slide event was retrogressive with at least two sub-events and sudden failures of major blocks are not supported by available data, no major tsunami was triggered by the USC. In contrast, subsurface and morphological indications for lake floor instabilities north of the USC suggest rotational slumping processes occurring in this area with higher possibility for tsunami generation in the future.

Keywords Lake Ohrid • Sublacustrine landslides • Lake floor morphology • Hydro-acoustic methods • Tsunamigenic potential

22.1 Introduction

Studies of mass movements in lakes are important especially in seismically active regions as their temporal record can be used for unraveling the paleoseismicity of a certain area (Chapron et al. 2004; Strasser et al. 2006; Moernaut et al. 2007).

K. Lindhorst (✉) • M. Gruen • S. Krastel
Leibniz Institute of Marine Sciences (IFM-GEOMAR), Wischhofstr. 1-3,
24148 Kiel, Germany
e-mail: klindhorst@ifm-geomar.de

T. Schwenk
Department of Geosciences, University of Bremen, Bremen, Germany

Y. Yamada et al. (eds.), *Submarine Mass Movements and Their Consequences*,
Advances in Natural and Technological Hazards Research 31,
DOI 10.1007/978-94-007-2162-3_22, © Springer Science+Business Media B.V. 2012

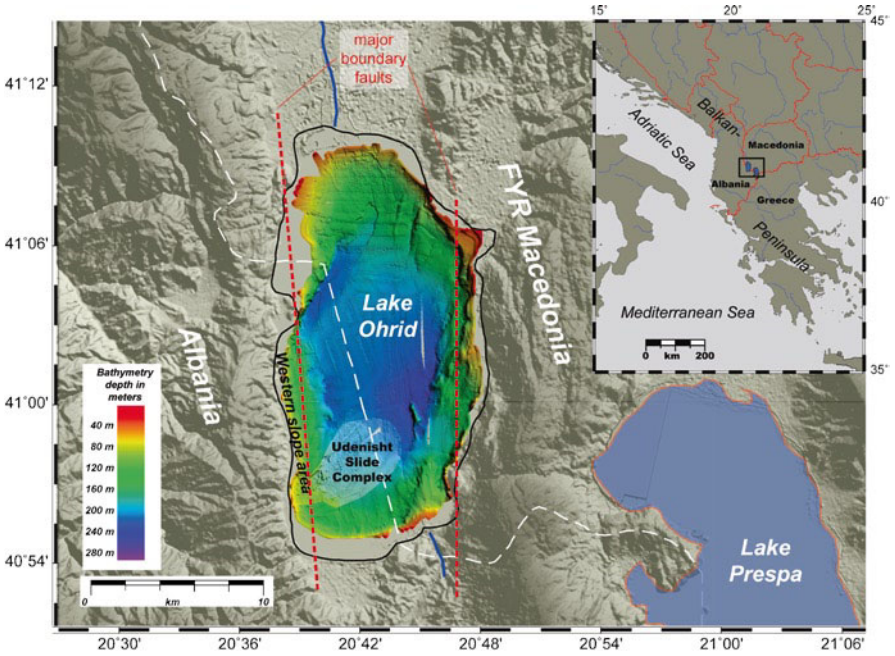

Fig. 22.1 Overview map of the topography (*grey*) and bathymetry (*colored*) of Lake Ohrid and the surrounding area. *White dashed line* marks the boundary between Albania and FYR Macedonia. Main boundary faults are shown as *red dashed lines*. The USC is found in the southwestern part of the lake. Inlet shows the general location of Lake Ohrid on the Balkan Peninsula

Furthermore, lakes offer the opportunity to investigate slope failure events in great detail due to the restricted area (Strasser et al. 2007).

Lake Ohrid is most likely one of the oldest lakes in Europe (3–5 Ma) located on the border between FYR of Macedonia and Albania (Albrecht and Wilke 2008). The lake is surrounded by high mountain chains on the eastern and western sides; the lake level is at an altitude of 693 m above sea level (Fig. 22.1). Lake Ohrid extends 30 km (N-S) by 15 km (E-W) covering an area of ~360 km². Maximum water depth is 293 m.

The region around Lake Ohrid is seismically active with several medium to large earthquakes that have occurred within the last 2,000 years (Wagner et al. 2008). One prominent example is the 518 AD event that nearly entirely destroyed the city of Ohrid (Hoffmann et al. 2010).

Landslide deposits are widespread in Lake Ohrid. In this article we present a detailed morphological description of the Udenisht Slide Complex (USC) area through the analysis of bathymetric data. In addition, we use high resolution seismic profiles to delineate the internal structure of the slide itself and the sediments deposited before the failure. We further provide a first age estimation and discuss possible causes and trigger mechanisms of the USC. Moreover, we examine the tsunamigenic potential of the western slope area of Lake Ohrid.

22.2 Seismic Stratigraphy and Slide Bodies

Interpretation of seismic lines (sediment echo-sounder and multichannel seismic data collected during several surveys between 2004 and 2009) provide new insights into the internal structure of the southwestern part of Lake Ohrid. The seismic stratigraphic analysis of the southwestern part of the lake is based on variations in seismic facies; the seismic sections have been divided into three units (A–C; oldest to youngest, respectively) overlying the acoustic basement (Fig. 22.2). In general,

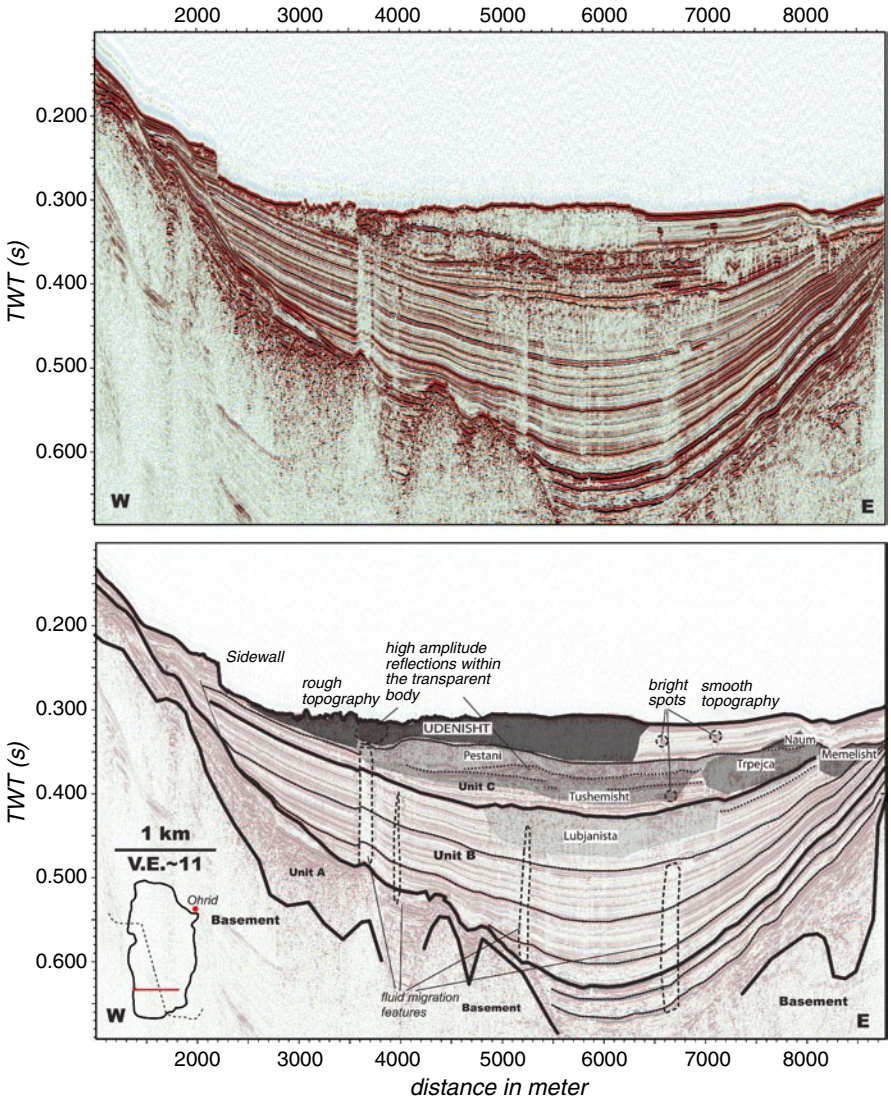

Fig. 22.2 W-E seismic section crossing the USC (*top*) and interpretation (*bottom*)

all units thicken toward the central part of the basin. Seismic reflections onlap the western margin but are sub-parallel and tilted on the eastern side (Fig. 22.2).

Unit A consists of high amplitude reflections of partially deformed sediments filling sub-basins of the basement. Alternating high and low amplitude reflections, including several prominent horizons, can be observed within the overlying Unit B. The unit is characterized by thick (~150 m) undisturbed sediments without clear evidence of reworking processes aside from a transparent body, the Lubjanista slide, recognized within the central part of the profile (Fig. 22.2). The youngest Unit C hosts several additional transparent bodies interpreted as slide deposits (Pestani, Tushemisht, Naum, Trpejca, and Memelisht). The most recent slide, the USC is imaged over a length of 4 km. In addition, several fluid migration features and bright spots are imaged mainly in the deepest part of the basin (Fig. 22.2).

22.3 Udenisht Slide Complex

22.3.1 Morphological Pattern

Bathymetric data were collected in 2009 using an ELAC Seabeam 1180 system operating at a frequency of 180 kHz allowing a detailed morphological description of the USC (Fig. 22.3). We divided the area affected by the mass movement event into a failure surface and a displaced mass deposit area (Fig. 22.3).

Although the Udenisht head scarp was not detected in the bathymetry, the uppermost part is clearly defined by steep slope angles of up to 10° confined by sidewalls up to 25 m height and several isolated blocks (~40–60 m × 10 m; Fig. 22.3). The sliding area widens further downslope and the northern sidewall changes its direction northwards at water depths of ~150–220 m (Fig. 22.3). The slide deposit area starts at water depths of ~150 m and is accompanied by a decrease in slope angle to <4° (Fig. 22.3). The largest part of the slide deposits with a run-out distance of 10 km is hardly distinguishable from the overall smooth morphology in this area (Fig. 22.3). Slope angles decrease to values less than 1.5°. Two distinct morphological steps occur at ~100 m and ~180 m water depth (Fig. 22.3) indicating the presence of fault lineaments cross cutting the slide area in N-S direction. A continuation of the lower fault structure is imaged on the northern side of the slide area as a morphological step in the bathymetric data.

Channel structures were recognized further north and may also be related to faulting (Fig. 22.2). Two additional slides are imaged north of the USC in water depths around 180 m (Fig. 22.2). They have short run out lengths and resemble typical slump features.

22.3.2 Internal Structure

Sediment echo-sounder penetration depth within the upslope area of the USC is limited due to the steep slope and a strong lake floor reflector prevents deeper penetration.

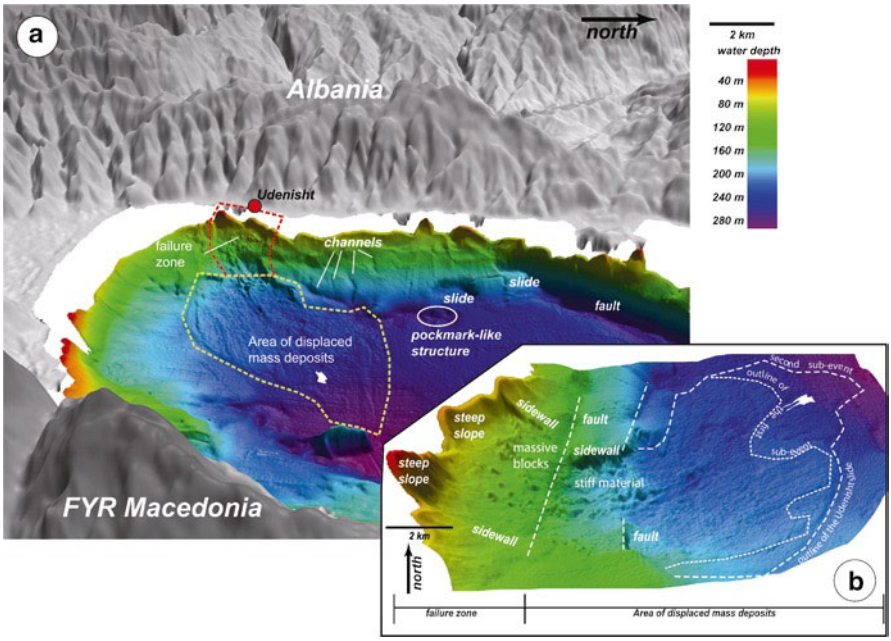

Fig. 22.3 (**a**) Westward 3D perspective view of the southern area of Lake Ohrid. *Dashed red line* indicates the failure zone of the USC, while the main slide deposits are surrounded by the *orange dashed line*. Two additional smaller-scale slides, sediment evacuation channels, pockmark-like structures and one prominent normal fault are marked north of the USC. (**b**) Detailed 3D image of the USC area with the most prominent morphological features described in the text

The lake floor reflector shows a sudden increase in water depth across the failure surface (Fig. 22.4). Further downslope, areas of massive blocks occur with a subsequent increase in slope angle. The lower series of blocks have trapped some slide deposits upslope, while undisturbed sedimentary successions inclined towards the central basin are imaged further downslope (Fig. 22.4). An up to 50 thick transparent body representing the main slide deposits is visible from 250 m water depth on (corresponding to 300 ms Two-Way Travel Time, TWT).

The main transparent body can be divided laterally into three sections differentiated by their internal structures, thicknesses, and surface morphology (Fig. 22.4). The first section (I) is defined by overall higher amplitudes, with some sub-parallel layered reflections and one prominent horizon representing the base of the slide. The second section (II) is thickest (up to 50 m) and shows a chaotic to transparent seismic facies. Due to the high reflectivity of the lake floor reflector, the base of the slide is not well imaged. A sudden decrease in thickness of the transparent body in combination with a morphological step marks the transition to the third section (III), which is characterized by patchy, discontinuous lake floor reflectors indicating a high roughness. Downslope of section III, undisturbed parallel to sub-parallel horizons are imaged in the central basin.

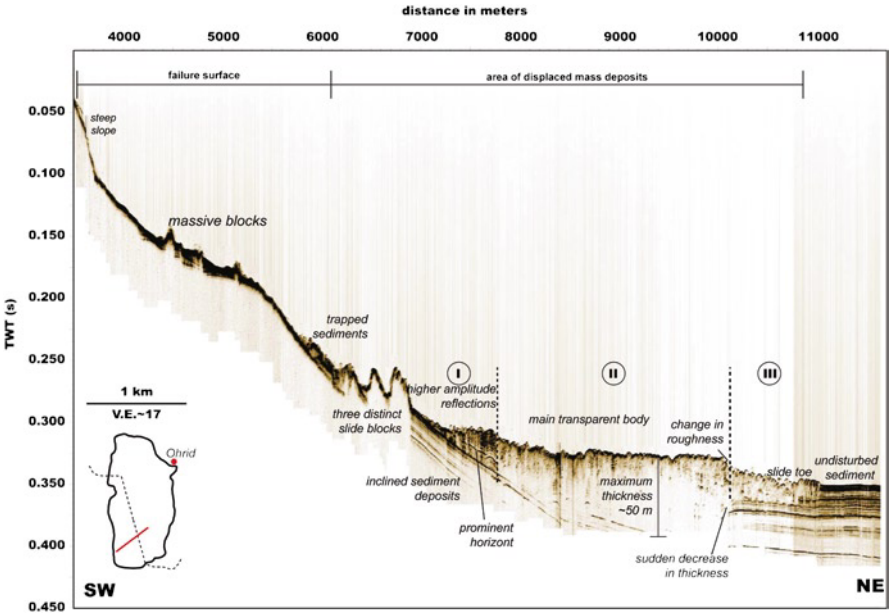

Fig. 22.4 Sediment echo-sounder profile crossing the slide area from SW to NE

The sediment echo-sounder and multichannel seismic data allowed estimating the extent and the volume of the USC. The failure surface covers an area of about 8 km² in contrast to the much larger area of deposition of 24 km². The total volume of the slide material is estimated to 0.11 km³. A change in thickness can be observed within the depositional area suggesting that the USC was probably not a single event but a sequence of at least two events with sufficient energy to transport material far into the central basin (Fig. 22.4).

22.4 Discussion

22.4.1 Age Estimations of Landslides

Age determination of the USC is difficult because no cores are currently available within the slide area. We can only estimate the age of the USC by analyzing the thickness of post slide sediments covering the acoustically transparent slide body. No undisturbed drape is detectable on the sediment echo-sounder profiles (Fig. 22.4). We operated the sediment echo-sounder at a frequency of 10 kHz, resulting in a theoretical vertical resolution of ~10 cm. Rough surface morphologies reduce the theoretical vertical resolution by lateral smearing effects, but a drape exceeding

30 cm would be detectable on the sediment echo-sounder data; hence we consider 30 cm as the maximal thickness of post-slide sediments. A drape less than 30 cm implies that the slide is a relatively recent event. Cores taken from the northeastern part of the lake show a sedimentation rate of 0.2 mm/a for the Holocene (Wagner et al. 2009). Holocene sedimentation rates should be relative homogenous across the lake. Taking 0.2 mm/a as sedimentation rate for the USC area results in a maximum age of 1,500 years for the youngest event of the USC. This number is obviously quite ambiguous due to the uncertainties of thickness of the drape and variations in accumulation rate. However, the slide must have occurred in the late Holocene.

The other six transparent units older than the USC indicate that the southwestern part of Lake Ohrid has a long history of mass wasting. No measured age data are available for the deeper reflectors but Lindhorst et al. (2010) developed a preliminarily age model based on sedimentation rates and seismic data. According to this age model, the slides within Unit C must be older than 130 kyr and the deepest slide in Unit B (Lubjanista) has an age greater than 510 kyr. No major mass movements older than 600 kyr are imaged on the seismic data.

22.4.2 Pre-conditioning Factors and Triggering Mechanisms

As Lake Ohrid is located in a seismically active region it is most likely that the USC was triggered by an earthquake. Nevertheless, some pre-conditioning factors must prevail before an earthquake triggers a sediment failure. The slopes in the USC area are very steep (up to 10°), which is one important pre-conditioning factor. Pockmarks and bright spots point to the importance of fluids in the USC area (Fig. 22.2); as a result high pore pressure may develop in distinct layers, which are sandwiched between fine-grained impermeable layers. Such over pressured layers are another important pre-conditioning factor for slope failure (Masson et al. 2010). Numerous fluid migration features at the western margin of Lake Ohrid imply that overpressured layers maybe widespread, which would make the western margin prone for future slope failures.

Our data suggest that the USC behaved as a retrogressive slide with at least two separated mass transport events. Within the slide area, two faults are clearly associated with activity along the western major boundary fault complex (Fig. 22.2). Even minor activity along these faults can induce slope failures in an area characterized by thick sedimentary successions deposited on high slope angles. Material removal at a water depth of ~180 m (location of the lower fault, Fig. 22.3) would result in loss of support for sediments further upslope. In connection with small earthquakes along local active faults, a second slope failure (~100 m water depth, location of the second fault, Fig. 22.3) may have occurred. It is not possible to infer the time interval between the two failures based on the acoustic data.

22.4.3 Tsunamigenic Potential of Slides in Lake Ohrid

The high resolution seismic stratigraphic analysis of Lake Ohrid shows that the western margin of Lake Ohrid has a long history of mass wasting. The current setting with indications for over pressured horizons and steep slope angles suggest that western margin of Lake Ohrid is prone to future slope failures. It is therefore pertinent to discuss whether the USC could have triggered a tsunami and further to evaluate the geohazard potential of the entire western margin. Studies of submarine landslides that caused tsunamis with local run-up heights of more than 15 m reveal that the most important factor is a high vertical displacement of an intact block in shallow water close to the coast at high initial accelerations (Okal and Synolakis 2003; Watts et al. 2003; Grilli and Watts 2005).

There is absence of onshore evidence or historical reports of waves that may have hit the coast within the last 1,500 years. According to Murty (2003) the volume of the USC is sufficient to trigger a tsunami. Yet, the largest uncertainties are related to the submergence depth and the initial acceleration of the USC. If we assume that an intact block with the volume of the USC failed in water depths of about 100 m, tsunami generation is likely. Our bathymetric data, however, shows that the USC has a long run-out distance, which points to quick disintegration and massive internal deformation. Therefore we exclude the movement of a rigid block with a high vertical displacement. In addition, slope failure occurred in two phases, thereby reducing the volume of individual events of the USC. Due to these observations, it is very unlikely that the USC triggered a major tsunami. In contrast, the two slump-features observed further to the north show less internal deformation indicating a smaller degree of disintegration. If similar events would occur at shallow water depth in the future, they have a higher tsunami potential though their initial acceleration is unknown.

In light of the results presented in this study, the western margin of Lake Ohrid is potentially unstable. The region is susceptible to seismic activity along active faults; hence it is most likely that mass failures will occur in the future, which might be tsunamigenic.

22.5 Conclusions

The USC is a young (<1,500 years) event that occurred in the southwestern part of Lake Ohrid. Older slides suggest a long history of sliding in this part of the lake. Ruptures along active faults crossing the USC area most likely acted as final trigger. The long run-out distance points to quick disintegration with intense sediment deformation. It is unlikely that such a flow triggered a significant tsunami, especially as it occurred in at least two phases in a retrogressive pattern. Slumps north of the USC show less disintegration and might have triggered tsunamis. Migrating fluids resulting in over pressured layers in combination with steep slope angles and ongoing seismicity make future slope failures likely. As such failures might occur

in a similar pattern as the slumps north of the USC, we cannot fully exclude that tsunamis will be initiated in the future.

Acknowledgments We would like to thank our Macedonian colleagues from the Hydrobiological Institute Ohrid for their logistic support. Thanks to W. Weinrebe and N. Lindhorst for their technical support. We are grateful to S. Hall and C. Berndt for valuable comments on earlier versions of the manuscript. We are grateful to comments of the reviewers P. Mazzanti and N. Waldmann that further improved the paper. This research was supported by DFG grant Kr2222/7.

References

Albrecht C, Wilke T (2008) Ancient Lake Ohrid: biodiversity and evolution. Hydrobiologia 615:103–140

Chapron E, Van Rensbergen P, De Batist M et al (2004) Fluid-escape features as a precursor of a large sublacustrine sediment slide in Lake Le Bourget, NW Alps, France. Terra Nova 16:305–311

Grilli S, Watts P (2005) Tsunami generation by submarine mass failure. I: modeling, experimental validation, and sensitivity analyses. J Waterw Port Coast Ocean Eng 131:283–297

Hoffmann N, Reicherter K, Fernández-Steeger T, Grützner C (2010) Evolution of ancient Lake Ohrid: a tectonic perspective. Biogeosciences 7:4641–4664

Lindhorst K, Vogel H, Krastel S et al (2010) Stratigraphic analysis of lake level fluctuations in Lake Ohrid: an integration of high resolution hydro-acoustic data and sediment cores. Biogeosciences 7:3531–3548

Masson DG, Wynn RB, Talling PJ (2010) Large landslides on passive continental margins: processes, hypotheses and outstanding questions. In: Mosher DC et al (eds) Submarine mass movements and their consequences, vol 28, Advances in natural and technological hazards research. Springer, Dordrecht, pp 153–165

Moernaut J, De Batist M, Charlet F et al (2007) Giant earthquakes in South-Central Chile revealed by Holocene mass-wasting events in Lake Puyehue. Sediment Geol 195:239–256

Murty T (2003) Tsunami wave height dependence on landslide volume. Pure Appl Geophys 160:2147–2153

Okal E, Synolakis C (2003) A theoretical comparison of tsunamis from dislocations and landslides. Pure Appl Geophys 160:2177–2188

Strasser M, Anselmetti F, Fah D et al (2006) Magnitudes and source areas of large prehistoric northern Alpine earthquakes revealed by slope failures in lakes. Geology 34:1005–1008

Strasser M, Stegmann S, Bussmann F et al (2007) Quantifying subaqueous slope stability during seismic shaking: Lake Lucerne as model for ocean margins. Mar Geol 240:77–97

Wagner B, Reicherter K, Daut G et al (2008) The potential of Lake Ohrid for long-term palaeoenvironmental reconstructions. Palaeogeogr Palaeoclim Palaeoecol 259:341–356

Wagner B, Lotter A, Nowaczyk N et al (2009) A 40,000-year record of environmental change from ancient Lake Ohrid (Albania and Macedonia). J Paleolimnol 41:407–430

Watts P, Grilli S, Kirby J et al (2003) Landslide tsunami case studies using a Boussinesq model and a fully nonlinear tsunami generation model. Nat Hazards Earth Sys Sci 3:391–402

Chapter 23
New Evidence of Holocene Mass Wasting Events in Recent Volcanic Lakes from the French Massif Central (Lakes Pavin, Montcineyre and Chauvet) and Implications for Natural Hazards

Emmanuel Chapron, Grégoire Ledoux, Anaëlle Simonneau, Patrick Albéric, Guillaume St-Onge, Patrick Lajeunesse, Pierre Boivin, and Marc Desmet

Abstract High-resolution seismic profiling (12 kHz) surveys combined with sediment cores, radiocarbon dating, tephrochronology and multibeam bathymetry (when available) allow documentation of a range of Holocene mass wasting events in nearby contrasting lakes of volcanic origin in the French Massif Central (45°N, 2°E): two deep maar lakes (Pavin and Chauvet) and a shallow lake (Montcineyre) dammed by the growth of a volcano. In these lacustrine environments dominated by authigenic sedimentation, recent slide scars, acoustically transparent to chaotic lens-shaped bodies, slump deposits or reworked regional tephra layers suggest that subaqueous mass wasting processes may have been favoured by gas content in the sediments and lake level changes. While these events may have had a limited impact in both lakes Chauvet and Montcineyre, they apparently favoured the development of lacustrine meromicticity in maar Lake Pavin along with possible subaerial debris flows resulting from crater outburst events.

E. Chapron (✉) • A. Simonneau • P. Albéric • M. Desmet
Institut des Sciences de la Terre d'Orléans, UMR 6113 CNRS, Université d'Orléans, Université François Rabelais de Tours, Observatoire des Sciences de l'Univers en région Centre, 1A rue de la Férollerie, 45071 Orléans cedex 2, France
e-mail: emmanuel.chapron@univ-orleans.fr

G. Ledoux • P. Lajeunesse
Centre d'études nordiques & Département de Géographie, Université Laval, Québec, QC G1V0A6, Canada

G. St-Onge
Canada Research Chair in Marine Geology, Institut des sciences de la mer de Rimouski (ISMER), Université du Québec à Rimouski, Rimouski, QC G5L 3A1, Canada

P. Boivin
Laboratoire Magma et Volcans, UMR 6524 CNRS, M163 IRD, PRES Clermont, Université Blaise Pascale, 5 rue Kessler, 63038 Clermont-Ferrand Cedex, France

Y. Yamada et al. (eds.), *Submarine Mass Movements and Their Consequences*, Advances in Natural and Technological Hazards Research 31,
DOI 10.1007/978-94-007-2162-3_23, © Springer Science+Business Media B.V. 2012

Keywords Subaquatic landslide • Limnic eruption • Volcanic lake • Subbottom profiling • Sediment cores • Geohazard

23.1 Introduction

On August 15, 1984 in Lake Monoun and August 21, 1986 in Lake Nyos, two catastrophic limnic eruptions with sudden outgassing of CO_2 from meromictic crater lake deep waters, occurred in Cameroun and killed 37 and 1,700 people, respectively (Sigurdsson et al. 1987). These two events demonstrated that meromictic maar lakes are prone to specific geological hazards. The possible triggering factors and the evolution of processes during limnic eruptions are still controversial, but their association with violent waves and subaquatic landslides suggest that these rare events can be recorded in the deep basin infills of maar lakes (Chapron et al. 2010a). Lake Pavin is the only meromictic maar lake in France and is surrounded by several contrasting small lakes of volcanic origin (Fig. 23.1). The investigation of the basin infill of these three lakes may thus help reconstructing environmental changes and evaluating specific natural hazards associated with meromictic maar lakes.

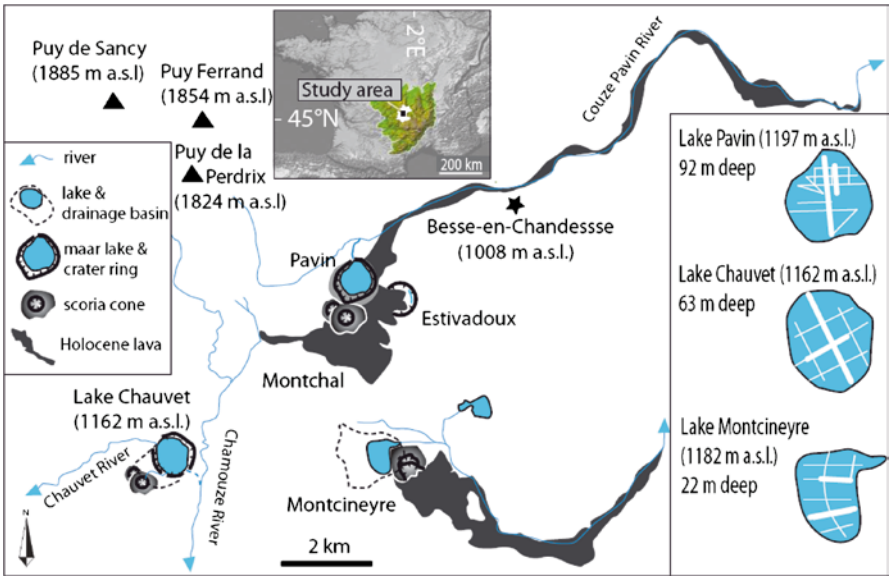

Fig. 23.1 Geomorphologic setting and location of investigated volcanic lakes in the French Massif Central, also showing the seismic grids surveyed in each lake and illustrated seismic sections (*thick lines*). Ice extent (*white area in small upper panel*) during the last glacial period in the Puy de Sancy area is also indicated (After Etlicher and Göer de Herve 1988)

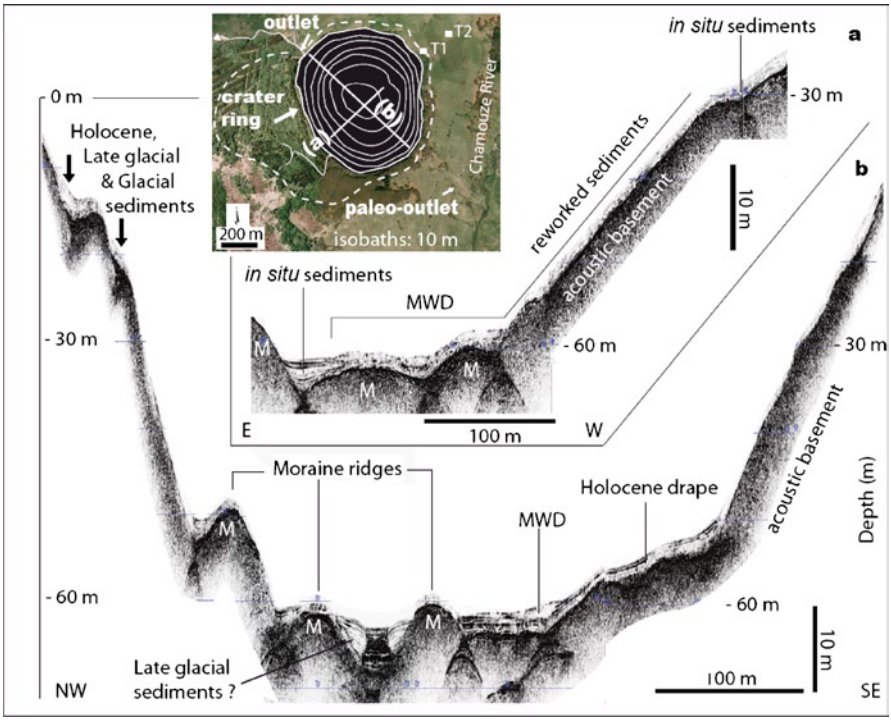

Fig. 23.2 Lake Chauvet geomorphology (*upper panel*) and seismic sections illustrating the occurrence of Glacial Moraines(*M*), Late Glacial and Holocene deposits. Holocene mass wasting deposits (*MWD*) are visible on two sections in the deep basin and described by Juvigné (1992) from piston cores in shallower environments (*black arrows*)

23.1.1 Geological Setting

The southern flanks of the Sancy stratovolcano constructed between 1 and 0.25 Ma (Boivin et al. 2009) today culminate at 1,885 m above sea level (asl) and were shaped by mountain glaciers extending down to ca. 650 m asl during the last glacial period (Etlicher and Göer de Herve 1988). Moraines locally outcrop near the Lake Chauvet outlet and were also documented by Juvigné (1992) in trenches T1 and T2 around this circular lake (Fig. 23.2). In the early Holocene, four small nearby volcanoes (Fig. 23.1) successively developed within a short period, as documented by previous tephrostratigraphic studies on outcrops and on tephra layers in peat deposits (Gewelt and Juvigné 1988; Bourdier 1980): first Montcineyre (ca. 6027 ± 660 year BP, i.e. 6812 ± 680 cal BP); then Estivadoux (ca. 6760 ± 130 year BP; 7635 ± 115 cal BP); Montchal (ca. 6670 ± 160 year BP; 7555 ± 130 cal BP) and finally Pavin (ca. 6000 ± 110 year BP; 6864 ± 140 cal BP). Lava flows associated with Montcineyre and Montchal scoria cones were essentially developed in fluvial valleys of glacial

origin, while Estivadoux and Pavin phreatomagmatic eruptions formed deep craters (Fig. 23.1). The regional seismicity of the study area is presently moderate (Boivin et al. 2009).

Lakes Chauvet, Montcineyre and Pavin have very small drainage basins compared to their areas (Fig. 23.1) and are thus dominated by organic rich authigenic Holocene sedimentation. The first bathymetric maps acquired by Delebecque (1898) revealed that these lakes have different maximum depths, but are all characterized by steep slopes and conical shapes. Juvigné (1992) and Chapron et al. (2010a) documented mass wasting deposits (MWDs) within Holocene fine-grained sediments in maar lakes Chauvet and Pavin, respectively.

23.1.2 Methods

The lakes were mapped in 2009 using a 12 kHz Knudsen subbottom profiler and conventional GPS positioning from an inflatable boat. In lakes Chauvet and Montcineyre, these grids allowed generating bathymetric and isopach maps using the ArcGIS and Surfer V9 software. In Lake Pavin, a detailed bathymetric map was previously established with a multibeam echosounder (Chapron et al. 2010a) and this dataset has been merged together with a detailed (5 m resolution) digital elevation model of the Pavin crater ring using ENVI and MA Publisher software.

New gravity cores were retrieved in Lake Pavin at 20 m (PAV09C5) and 92 m (PAV09B1) water depths in 2009 and at 17.5 m (PAV10E) in 2010 using a UWITEC hammer action corer. Gravity cores were also retrieved in Lake Montcineyre at 9 m (MO 10 G) and 18.5 m (MO 10B) water depths in 2010. Sediment cores were split in two halves and analysed in detail: sediment magnetic susceptibility (MS) and diffuse spectral reflectance were measured using a Bartington MS2E1 point sensor and a Minolta 2600D hand-held spectrophotometer, respectively. The lithology of each core was established through detailed visual descriptions and digital radiographs using a Siemens Axiom Iconos R200. Two new AMS radiocarbon ages obtained from plant macro remains sampled in cores PAV09C5 and PAV09B1 were dated at the Poznan Radiocarbon Laboratory, Poland. Data from Lake Pavin is correlated with previously available sediment data and 14 radiocarbon ages from piston core PAV08 (Chapron et al. 2010a; Chapron et al. 2010b) and used for the present study.

23.2 Results

23.2.1 High Resolution Seismic Reflection Mapping

In Lake Chauvet, seismic profiling revealed an irregular acoustic basement morphology, with local ridges of variable sizes and diffractions in the deep basin and along the northern slopes (Fig. 23.2). In between these ridges and in the deep basin,

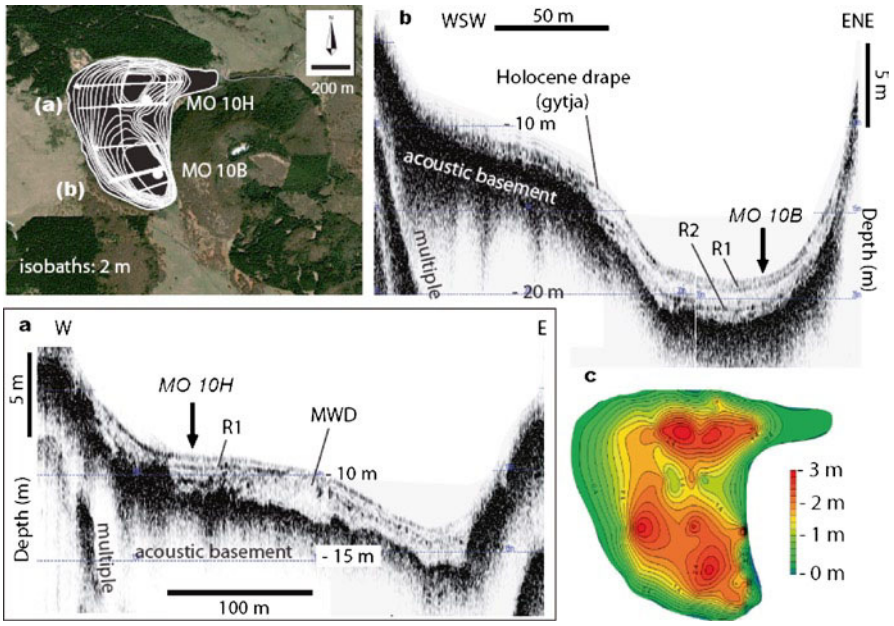

Fig. 23.3 Lake Montcineyre geomorphology map (*left upper panel*), seismic sections (**a** and **b**) illustrating the basin fill geometry in each sub-basin together with gravity core locations. A sediment isopach map (**c**) is also shown

up to 5 m of fine-grained sediments are identified. Locally, a chaotic to transparent lens-shaped body is also identified near the lake floor.

In Lake Montcineyre, the acoustic basement is characterized by two sub-basins (maximum depth: 22 m) and its morphology becomes more irregular above 15 m water depths (Fig. 23.3). Up to 3 m of fine-grained sediments are identified in the deepest parts of the sub-basins. The basin infill is made of a transparent acoustic facies developing a draping geometry that thins out laterally above 10 m water depths (Fig. 23.3d). Above 10 m water depth, acoustic penetration is low, probably due to local gas pockets. Two basin-wide higher amplitude and continuous reflections are identified: one at ca. 0.5 m below the water-sediment interface (R1) and the other (R2) just above the acoustic basement. R2 is only observed in the deepest part of the sub-basins and may reflect regional tephra layers. Locally, an up to 2.5 m thick and 100 m wide transparent to chaotic lens-shaped body caped by R1 is identified in the northern sub-basin.

In Lake Pavin, the acoustic basement shows a subaquatic plateau with a hummocky morphology along the northern part of the basin (Fig. 23.4). In the deep flat basin, the penetration of the acoustic signal is very limited due to the presence of gas in the sediments (Chapron et al. 2010a). Up to 5 m of fine-grained sediments are visible above the plateau, but the steep basin slopes are almost free of sediment cover. Three main acoustic facies are identified on the plateau with the 12 kHz subbottom profiler: (i) a littoral facies (between 26 m water depths and the shore line) that thins quickly upslope and

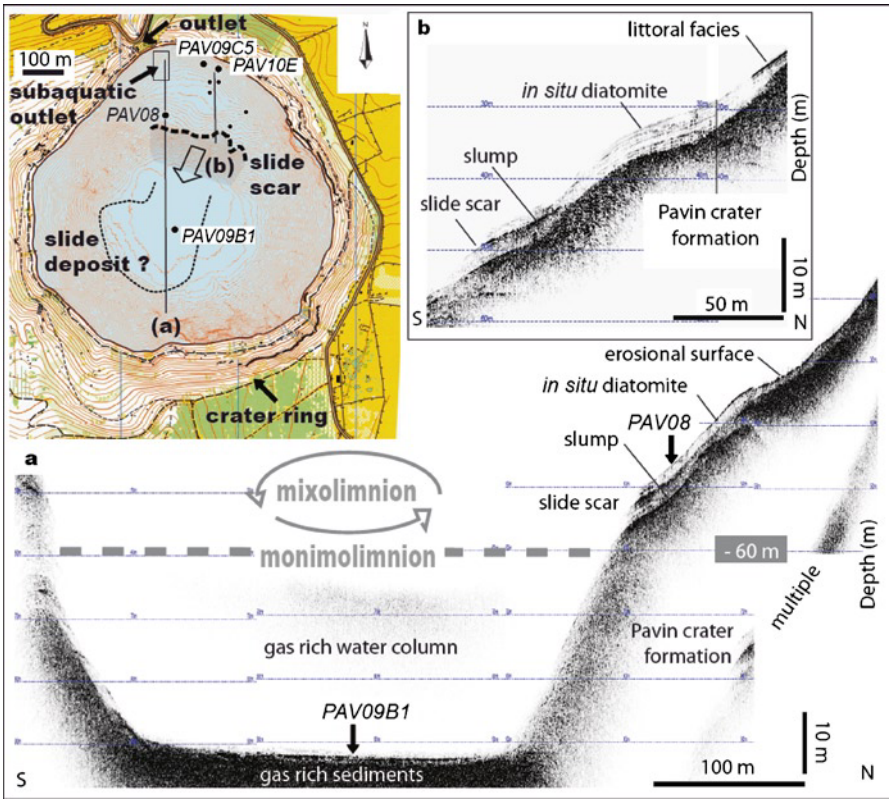

Fig. 23.4 Lake Pavin geomorphology (*upper panel*) and seismic sections (**a** and **b**) illustrating contrasting deposits in the deep basin, on a sub aquatic plateau and along the littoral. Also shown are the locations of the studied sediment cores and the occurrence of a monimolimnion rich in gas in the deep waters of the lake

develops a transparent facies and a high-amplitude reflection at the water-sediment interface; (ii) an up to 5 m thick acoustically well-stratified facies composed of continuous and high-frequency low-amplitude reflections draping the underlying morphologies and (iii) an up to 3 m thick and 100 m wide chaotic to transparent lens-shaped body deposited above the acoustic basement hummocks. At the southern edge of the plateau, the sediment depocentre ends abruptly and an up to 4 m high slide scar (well-identified in the bathymetry) returns diffractions on seismic profiles.

23.2.2 Basin Fills Lithologies and Chronologies

Lake Chauvet basin fill lithologies were previously documented by Juvigné (1992) with two piston cores retrieved in the north-western part of the basin at 13 and 20 m

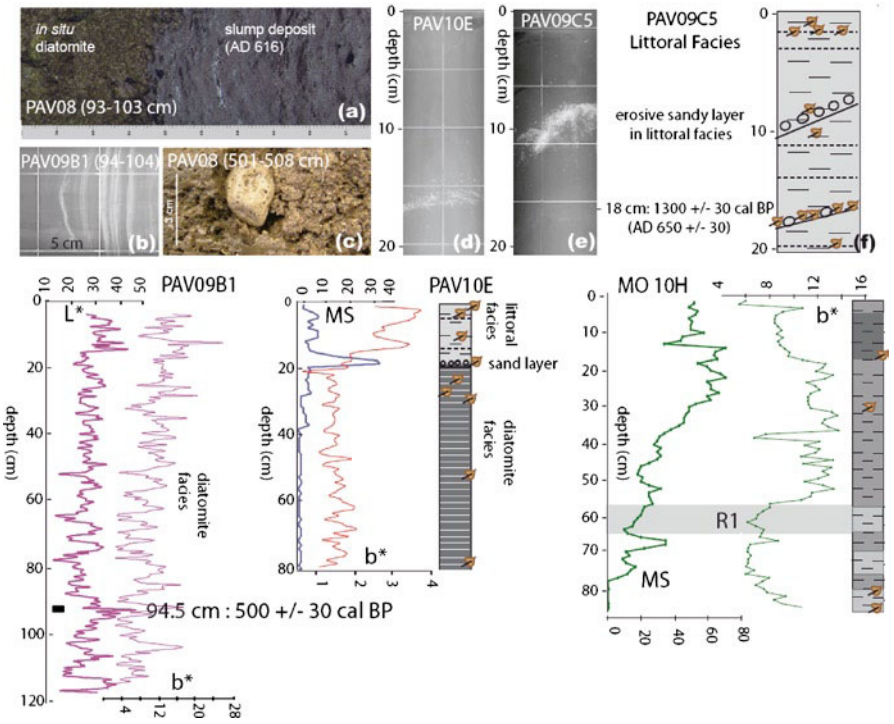

Fig. 23.5 Multiproxy characterization of sedimentary facies from cores retrieved in lakes Pavin and Montcineyre. Core photographs (**a** and **c**), radiographs (**b**, **d**, **e**), lithological log (**f**), sediment lightness (L^*) magnetic susceptibility (MS) and diatomite content (b^*) allows distinction of background sedimentation from sedimentary events

water depths (Fig. 23.2, black arrows), respectively. They consist (from top to base) in (i) dark mud rich in diatoms and organic macro remains where the Pavin, Montcineyre and Taphanel regional Holocene tephra layers are not systematically in chronological order ; (ii) light grey clays, slightly organic, bearing the Godivelle T4 (ca. 12,250 cal BP) and T5 (ca. 12,730 cal BP) regional Late Glacial tephra layers (in chronological order); and (iii) a mixture of silts and trachyandesite stones of variable size similar to the moraine deposits identified in trenches T1 and T2 near the lake. These lithologies are in good agreement with the seismic data. Glacial deposits can be correlated to the ridges of the acoustic basement. The basal basin infill can be related to Late Glacial sediments essentially observed in between moraine ridges, and the upper draped deposits can be linked to Holocene organic-rich sediments (Fig. 23.2). The reworked tephra layers are suggesting that subaqueous MWDs identified on seismic sections occurred after the most recent regional volcanic event (i.e. the Pavin eruption, ca. 7,000 years ago). Since these MWDs are identified near the lake floor, they are probably much younger in age.

Lake Montcineyre recent sedimentation is only documented by cores MO 10H and MO 10B (Figs. 23.3 and 23.5), which consist of light- to dark-brownish mud

rich in organic terrestrial leaves. Several sub units are identified based on sediments' MS and diffuse spectral reflectance (Fig. 23.5), especially with the b* parameter, which is considered as a good proxy for diatom content in bioturbated or anoxic sediments (Debret et al. 2006). In core MO 10 H, fluctuations in b* and in MS may thus reflect recent environmental changes. Between 55 and 65 cm, abrupt changes in b* and MS can be correlated to horizon R1 on seismic sections. Similarly, R1 occurs between 50 and 60 cm in core MO 10B. A rough estimation of the age of horizon R1 can be based on the most likely age of the formation of this lake (ca. 7495 ± 565 cal BP), on the depth of R1 and on the thicknesses of the basin infill at coring site MO 10H. This estimate suggests a mean sedimentation rate of ca. 0.3 mm/a and an age of around 1,900 cal BP (ca. AD 50) for R1. Taking into consideration dating uncertainties (±565 years), this MWD in Lake Montcineyre could be contemporaneous to a slump deposit dated to AD 610 ± 30 (1340 ± 30 cal BP) on the plateau of Lake Pavin (Chapron et al. 2010a). On going radiocarbon dating on samples from core MO 10 H will be used to test this assumption.

In Lake Pavin, three main sedimentary environments identified on seismic profiles can be ground-truthed by sediment cores and their chronologies are either constrained by radiocarbon dating, pollen and diatom assemblages or by biochemical varve counting from a freeze-core (Stebich et al. 2004; Schettler et al. 2007; Chapron et al. 2010a). The acoustic basement has been sampled (Fig. 23.5c) by piston core PAV08 and related to the formation of the Pavin crater (Chapron et al. 2010a). The lacustrine sedimentation developing a stratified facies on seismic profiles is characterized by the *in situ* diatomite facies, made of biochemical varves in the basin (core PAV09B1, Fig. 23.5b) and on the plateau (PAV08, PAV10E, Fig. 23.5a, d). This facies is characterized by a dark brown to greenish colour, very low MS values but finely fluctuating values of sediment lightness (L*) and b* throughout PAV09B1 and below 20 cm core depth in PAV10E (Fig. 23.5). The varve chronology developed on thin sections in the deep basin (Schettler et al. 2007) is in agreement with the age of leaf debris sampled at 94.5 cm in core PAV09B1 (500 ± 30 years cal BP). This further supports that a plurimetric MWD covered by a large turbidite deposit documented in the deep basin by piston coring between 650 and 220 cm below the lake floor (Schwab et al. 2009) dates around AD 1200 (Chapron et al. 2010a) and is related to the slide scar identified at the edge of the plateau (Fig. 23.4). Littoral facies identified on seismic profiles down to 26 m water depths have been sampled in core PAV09C5 and in the upper 20 cm of core PAV10E. In this environment, the sediment is generally composed of light brown to greenish homogenous fine-grained mud rich in diatoms (high values in b*) and with frequent thin layers made of leaves and leaf debris (Fig. 23.5f). Two erosive horizons are also identified on PAV09C5 (Fig. 23.5e): a 1 cm thick sand layer at 10 cm core depth, and a stricking 1 cm thick layer at 18 cm, very rich in leaves and also containing few pebbles and some fine sands. This organic and erosive layer is dated to 1300 ± 30 cal BP (AD 650 ± 30). On core PAV10E, a 2 cm thick sandy layer (identified visually, on radiographs and from MS data) matches the transition from a littoral facies to a diatomite facies. This abrupt change in sedimentation from a deeper to a shallower

environment occurring below 17.5 m water depth indicates a rapid lake level drop of ca. 6.5 m at that time (taking into consideration that first human infrastructure around 1855 at the outlet induced a lake level rise of ca. 2 m).

23.3 Discussion and Conclusions

This study highlights a range of Late Holocene MWDs in three small lakes of volcanic origin dominated by authigenic sedimentation. The largest events are found in meromictic Lake Pavin and well-dated at ca. AD 610 and AD 1200. Radiocarbon ages from gravity cores in the two other lakes are still needed to establish if MWDs are contemporaneous and regional. This will be essential to identify a triggering factor for these MWDs and to carry out risk assessment in this young volcanic province.

MWDs in Lake Pavin were previously related to high gas content in authigenic sediments and possibly to abrupt lake level changes associated with crater outburst events (Chapron et al. 2010a). The erosive layer at 18 cm in core PAV09C5 identified at 20 m water depth in the littoral environment is contemporaneous with the slump deposit on the plateau. This confirms that this slump in ca. AD 610 was large enough to be associated with violent waves in Lake Pavin. Such exceptional waves can favour erosion at the outlet and a rupture of the Pavin crater ring resulting in: (i) abrupt lake level drop and (ii) the spill over of a debris flow downstream in the Couze Pavin valley. Such violent waves may also result from a limnic eruption. Another striking erosive layer at 10 cm in core PAV09C5 is rich in littoral sands and probably resulted from violent waves or abrupt lake level drop. This second erosive event may be associated with the second MWD identified on Lake Pavin. Abrupt lake level drop of ca. 6.5 m identified in core PAV10E by a sand layer at the transition from a diatomite to a littoral facies may either result from the first or the second MWD identified in Lake Pavin. This abrupt lake level drop can be related to a rupture of the crater ring (outburst event) and imply a sudden discharge of ca. 2.8 million m^3 (2.8 billion litres) down stream Lake Pavin in the Couze Pavin River (Fig. 23.1). Such outburst event would trigger a large debris flow in the Couze Pavin River and could also favour a limnic eruption (abrupt release of gas due to pressure drop). Radiocarbon dating just above erosive layers in the littoral facies is in progress and will be used to determine the impact of MWDs in Lake Pavin. Finally, the identification of a significant reservoir age in radiocarbon dates from bulk sediment in core PAV08 above the AD 610 slump suggest that MWDs in Lake Pavin may have supplied significant amount of gas in the deep waters and favoured the onset of its meromicticity (Chapron et al. 2010b).

Acknowledgments The authors would like to acknowledge the MEEDDAT for funding, JL Bourdier (ISTO) for scientific discussions, D. Jézéquel (IPGP Université Diderot, Paris) and master students from Université d'Orléans (2009 and 2010) for their contributions to coring operations and Dr. J. Sitbon and A. Barroca (RES radiology, Orléans) for digital radiographies. The digital elevation model of the Pavin crater was kindly provided by the city of Besse-St-Anataise. The constructive reviews of Stéphanie Girardclos and David Piper improved this paper.

References

Boivin P, Besson JC, Briot D, Camus G, de Göer de Herve A, Gougaud A et al (2009) Volcanologie de la Chaîne des Puys, 4eme édition, Edition du Parc Régional des Volcans d'Auvergne, Aydat, France, 196 p, map 120×90 cm 1/25000

Bourdier JL (1980) Contribution à l'étude volcanoligique de deux secteurs d'intéret géothermique dans le Mont Dore: le groupe holocène du Pavin et le Massif du Sancy. unpublished Ph.D thesis, Université de Clermont-Ferrand II, 180 p

Chapron E, Albéric P, Jézéquel D, Wersteeg W, Bourdier J-L, Sitbon J (2010a) Multidisciplinary characterisation of sedimentary processes in a recent maar lake (Lake Pavin, French Massif Central) and implication for natural hazards. Nat Hazards Earth Syst Sci 10:1–13

Chapron E, Albéric P, Jézéquel D, Ledoux G, Massault M (2010b) Les archives sédimentaires de l'histoire du lac Pavin (Massif Central, France). In: Proceedings of the international meeting – Lake Pavin and other Meromictic Lakes, Revue des Sciences naturelles d'Auvergne 74:57–65

Debret M, Desmet M, Balsam W, Copard Y, Francus P, Laj C (2006) Spectrophotometer analysis of Holocene sediments from an anoxic fjord: Saanich Inlet, British Columbia, Canada. Mar Geol 229:15–28

Delebecque A (1898) Les lacs français. Chamerot & Renouard, Paris, 436 p

Etlicher B, Göer de Herve A (1988) La déglaciation wurmienne dans le Massif Central Français: le point des travaux récents. Bulletin de l'Association française pour l'étude du quaternaire 25:103–110

Gewelt M, Juvigné E (1988) Téphrochronologie du Tardiglaciaire et de l'Holocène dans le Cantal, le Cézallier et les Monts Dore (Massif Central, France): résultats nouveaux et synthèse. Bulletin de l'Association française pour l'étude du quaternaire 25:25–34

Juvigné E (1992) Approche de l'âge de deux cratères volcaniques lacustres d'Auvergne (France). C R Acad Sci Paris 314:401–404

Schettler G, Schwab MJ, Stebich M (2007) A 700-year record of climate change based on geochemical and palynological data from varved sediments (Lac Pavin, France). Chem Geol 240:11–35

Schwab M, Schettler G, Bruchmann C, Acksel D, Negendank JF, Brauer A (2009) Stratigraphy, chronology and paleoenvironment information of the sediment record from Lac Pavin, Massif Central (France), International Meeting-Lake Pavin and Other Meromictic Lakes, Besse, France, Abstract p 30, 14–16 May 2009

Sigurdsson H, Devine JD, Tchua FM, Presser FM, Pringle MK, Evans WC (1987) Origin of the lethal gas burst from Lake Monoun, Cameroun. J Volcanol Geotherm Res 31:1–16

Stebich M, Bruchmann C, Kulbe T, Negendank JFW (2004) Vegetation history, human impact and climate change during the last 700 years recorded in annually laminated sediments of Lac Pavin, France. Rev Paleobot Palynol 133:115–133

Part III
Role of Fluid Flow in Slope Instability

Chapter 24
A Review of Overpressure, Flow Focusing, and Slope Failure

Brandon Dugan

Abstract Submarine slope failures with low-angle failure planes are commonly observed in the sedimentary record. These failures can be large (1,000s km^2) or small (1 km^2), and can have long runouts (100s km) or short runouts (<1 km). While the size and runout are well documented, the initiation and evolution of these failures are insufficiently understood. I review the role that fluid overpressure and flow focusing play in preconditioning low-angle slopes for failure by describing the stability of slopes in terms of overpressure, and reviewing the coupling of sedimentation, overpressure and fluid flow. I illustrate these processes with simple, one- and two-dimensional examples. I then review three regions that have slope failures that have been attributed to overpressure: the Ursa region in the Gulf of Mexico; the Storegga slide offshore Norway; and the Cascadia margin offshore Canada. Each study confirms that elevated pore pressure was critical to failure, but only under very specific conditions were overpressures the sole cause of failure. All three environments invoked earthquake shaking as the ultimate trigger for failure; however the earthquake magnitude ranged from small-to-large depending on the environment and the pressure conditions. These studies thus show that pore fluids are a dominant factor for preconditioning slopes for failure; however earthquake triggering appears to be key to the initiation of failures, even along passive margins. Future research is needed to understand the dynamics of weak slopes during earthquakes and the linkages between preconditioning, triggers, and failure morphology.

Keywords Overpressure • Fluid flow • Slope failure • Geohazard

B. Dugan (✉)
Department of Earth Science, Rice University, 6100 Main Street,
MS-126, Houston, TX 77005, USA
e-mail: dugan@rice.edu

Y. Yamada et al. (eds.), *Submarine Mass Movements and Their Consequences*,
Advances in Natural and Technological Hazards Research 31,
DOI 10.1007/978-94-007-2162-3_24, © Springer Science+Business Media B.V. 2012

24.1 Introduction

Submarine slope failures occur along continental margins around the world. They commonly exist in active margins where tectonic compression occurs and steep slopes may exist. Also, they occur along passive margins where sedimentation and subsidence are important stress controls but seafloor slopes are low. Overpressure (pressure in excess of hydrostatic) is often cited as a contributing factor to slope failure, and contributes to the post-failure evolution of a failure (e.g., Dugan and Flemings 2002; Sawyer et al. 2009; Stigall and Dugan 2010; Urgeles et al. 2007).

In this paper, I review the role of overpressure in preconditioning a submarine slope for failure. First, I present a simple, one-dimensional model for slope failure (infinite slope analysis) in terms of sediment and slope properties and overpressure. I then explore the origin of overpressure due to sediment loading and flow focusing. For simplicity, I explore overpressure and stability for undrained loading in one and two dimensions to emphasize the importance of geometry and flow focusing (e.g., Flemings et al. 2002). Then I summarize the how permeability facilitates partial drainage leading to increased stability (e.g., Gibson 1958; Dugan and Flemings 2000). Last I present case studies of two large slope failures (Ursa region, Gulf of Mexico; Storegga slide, offshore Norway) and one small slope failure (Cascadia margin, offshore Canada) where overpressure has been invoked as a significant factor for failure. These examples highlight that overpressure preconditions a slope to fail, but is rarely the trigger.

Studies on the triggers of submarine slides are less well constrained; however, seismic acceleration due to earthquakes is often cited as a primary trigger (e.g., Biscontin and Pestana 2006; Kvalstad et al. 2005a, b; Strasser et al. 2006; Strozyk et al. 2010). These studies define potential earthquake-related triggering mechanisms consistent with interpreted preconditioning (e.g., overpressure, weak layers), but also illustrate that more research is required to understand solid-fluid coupling and transmission of seismic energy through soft sediments during earthquakes. Such scientific advancements will help us better understand the importance of earthquakes in slope failure and the progression from overpressure genesis to earthquake loading to slope failure and runout.

24.2 Shallow Slope Failure

Slope failure in shallow sedimentary systems is a well-documented phenomenon, occurring when the failure-resisting strength of the slope is exceeded by the failure-inducing stresses (see review by Hampton et al. 1996). In one dimension, an approximation for slope stability is the infinite slope factor of safety (FS) (e.g., Lambe and Whitman 1969; Loseth 1998):

$$FS = \frac{c + \left[(S_v - \rho_w g z) \cos^2 \theta - P^* \right]}{(S_v - \rho_w g z) \sin \theta \cos \theta} \tan \phi_f \tag{24.1}$$

where c is cohesion, S_v is total overburden stress, ρ_w is density of water, g is acceleration due to gravity, z is depth, θ is seafloor slope, P^* is overpressure, and φ_f is internal angle of friction. This approximation assumes that the failure plane is parallel to the seafloor, neglects edge effects, and assumes the failure is much thinner than it is long. All of these conditions are valid first-order approximations for many submarine slope failures. This approach is also less computationally complex than two-dimensional safety analyses, like the method of slices (Bishop 1955).

In shallow, normally consolidated materials, c is approximately 0 (Lambe and Whitman 1969), and Eq. 24.1 can be simplified as:

$$FS = \frac{\tan \phi_f}{\sin \theta \cos \theta} \left(\cos^2 \theta - \lambda^* \right) \tag{24.2}$$

where λ^* is the normalized overpressure [$\lambda^* = P^*/(S_v - \rho_w g\, z)$]. Equation 24.2 demonstrates that for a constant slope and friction angle, overpressure is a primary control on FS, therefore its characterization is fundamental for understanding failure.

24.3 Shallow Overpressure Genesis

Overpressure in basin sediments has been observed (in)directly for a range of depths and environments. Athy (1930) related anomalously high porosity deep in sedimentary basins to overpressure. Other models expanded this to relate porosity to vertical effective stress and overpressure (e.g., Rubey and Hubbert 1959; Hart et al. 1995). Often, models invoke pressure build-up due to sedimentation that outpaces pressure dissipation. Poro-elastic models explain the pressure response from loading (e.g., Green and Wang 1986), whereas coupled sedimentation-fluid flow models (e.g., Gibson 1958; Dugan and Flemings 2000) explain the pressure response from loading and dissipation.

24.3.1 One-Dimensional Burial

The overpressure generated within water-saturated sediment during undrained burial is (Flemings et al. 2002):

$$dP^* = B\rho_b g dz - \rho_w g dz \tag{24.3}$$

where ρ_b is bulk density, dz are increments of burial, and B is the pore pressure build-up coefficient (Green and Wang 1986):

$$B = \frac{\beta}{\beta - \beta_f \phi} \tag{24.4}$$

β is the bulk sediment compressibility, β_f is water compressibility, and ϕ is porosity.

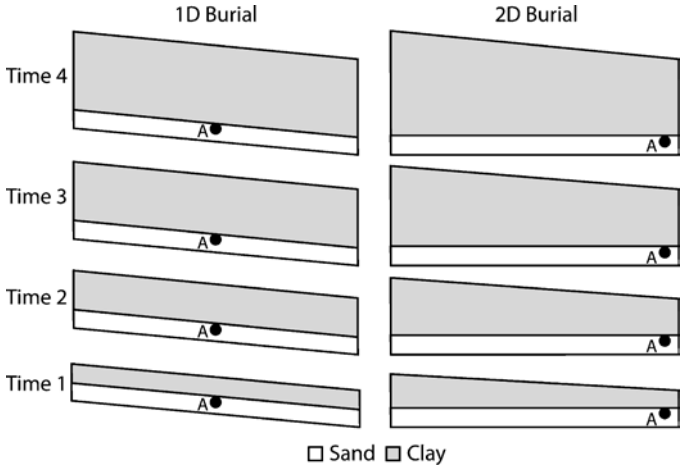

Fig. 24.1 Schematic of 1D burial geometry and 2D burial geometry of a sand layer through time. *Point A* in both scenarios is located at the same depth below seafloor. Both models have the same final seafloor slope (3°) and all sediments have a constant internal angle of friction (25°). In 1D burial the seafloor slope is constant with time. In 2D burial the seafloor slope increases with time because of differential sedimentation

To illustrate overpressure evolution, I consider a thin sand layer with hydrostatic pressure that is buried 3 m below the seafloor. Then, this layer is buried in an undrained manner to 50 meters below sea floor (mbsf) (Fig. 24.1). For typical bulk sediment compressibility and fluid compressibility, shallow sediments have $B \sim 1$. To solve for overpressure during burial, I assume a bulk density (ρ_b) of 2,000 kg/m^3 and a water density (ρ_w) of 1,000 kg/m^3. Increments of burial (dz) are 1 m.

One-dimensional, undrained burial for a compressible sediment and low compressibility fluid (i.e., B = 1) produces overpressure that increases parallel to the hydrostatic effective stress (σ_{vh}') (Fig. 24.2). Hydrostatic effective stress is the total overburden stress less the hydrostatic water pressure. As the overpressure increases at the same rate as the hydrostatic effective stress, the normalized overpressure increases asymptotically toward $\lambda^* = 1$ (Fig. 24.2). For constant sediment strength properties (average internal angle of friction = 25°) and a constant seafloor slope (3°), this increase in normalized overpressure results in lowered FS (Eq. 24.2) during burial, until FS < 1 and the slope fails (Fig. 24.2).

24.3.2 Two-Dimensional Burial

Undrained burial of a thin sand layer by a triangular wedge illustrates the impact of flow focusing on overpressure and slope stability. Similar to the 1D example, fluid is unable to drain, thus pore pressure increases to support the applied load. Fluid, however, can flow and equilibrate within the permeable sand body, which drives

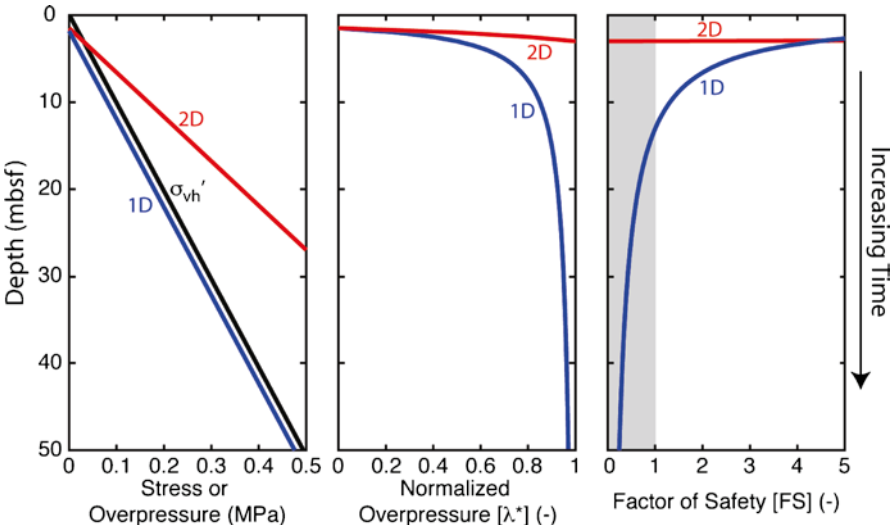

Fig. 24.2 Undrained model results at point A (located in Fig. 24.1) showing the hydrostatic effective stress (σ_{vh}'), overpressure, normalized overpressure, and factor of safety for burial of a sand layer from 3 to 50 m below sea floor (mbsf) by 1D and 2D burial (Fig. 24.1). Factor of safety less than 1 (*grey-shaded*) indicates failure after ~13 mbsf for 1D burial and near 3 mbsf for 2D burial due to flow focusing

flow laterally in the sand body from areas of thick overburden to regions of thin overburden. For undrained conditions, the sand unit will equilibrate to a constant overpressure (e.g., Flemings et al. 2002; Yardley and Swarbrick 2000). During undrained burial, the overpressure in the sealing clay will be identical to that for 1D burial, controlled by the overburden. However, overpressure in the sand will equilibrate to a constant value controlled by the geometry and density of the load applied over the sand body and the geometry of the sand body (Flemings et al. 2002). For a simple wedge-shaped load on a rectangular sand body (Fig. 24.2), the overpressure at any location within the sand is:

$$dP^* = B\rho_b g dz_{ave} - \rho_w g dz \tag{24.5}$$

where dz_{ave} is the average thickness at the center of the wedge-shaped load, and dz is the thickness at the point of interest.

In this scenario, overpressure at point A (Fig. 24.1) increases more rapidly during 2D burial than it does in 1D burial (Fig. 24.2). This is the result of the burial geometry and pressure equilibration increasing pressure where overburden is thin, and decreasing it where overburden is thick (flow focusing effect). The net result is a faster increase in λ^* and a corresponding faster decrease in FS (Fig. 24.2). For this undrained 2D system, failure occurs immediately after burial begins. This condition illustrates that flow focusing is important for thin failures, and for driving failures where sedimentation rates are low.

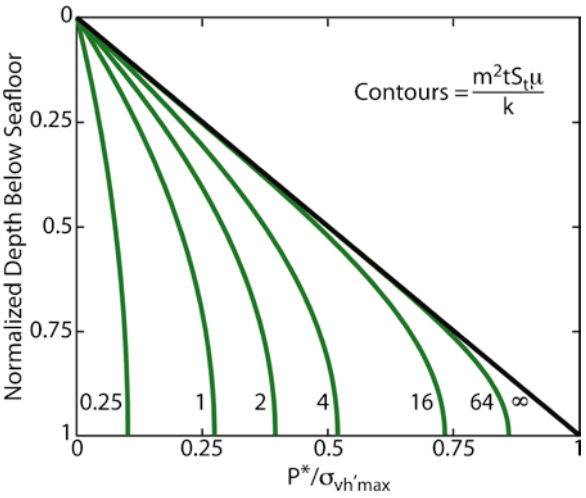

Fig. 24.3 3 One-dimensional solutions to Eq. 24.6 demonstrating the decrease in overpressure during sedimentation as permeability is increased. Each contour line value represents a different ratio of sedimentation rate [m] to permeability [k]. For a constant sedimentation rate and increasing permeability (decreasing contour value), the overpressure at any depth is decreased from the undrained burial reference (contour = ∞). As the overpressure decreases, the flow focusing effect also decreases and stability of the slope increases

24.3.3 Impact of Permeability

Permeability of the clay-sized particles will influence overpressure genesis during burial (e.g., Gibson 1958):

$$\frac{\partial P}{\partial t} = \frac{k}{S_t \mu} \nabla^2 P^* + B \frac{\partial S_v}{\partial t} \tag{24.6}$$

P is total fluid pressure, t is time, k is permeability, S_t is storativity, μ is dynamic viscosity, and S_v is overburden stress. In the undrained loading scenario, permeability is zero and Eq. 24.6 can be simplified to Eqs. 24.3 and 24.5 for 1D or 2D burial. When permeability is finite, the control of the rate of pressure generation is the competition between the loading rate (dS_v/dt), and the rate at which overpressure is dissipated ($k\nabla^2 P^*$). The loading rate is controlled by bulk density and sedimentation rate. The permeability is controlled by the lithology and porosity. For a constant sedimentation rate (or loading rate), increasing permeability results in lower overpressure (Fig. 24.3). As the overpressure field is dissipated, the impacts of flow focusing (Fig. 24.2) are decreased, because the net overpressure in the system is lower. Thus, elevated permeability increases stability of the slope. Therefore it is important to know the permeability architecture to accurately understand the pressure and stability evolution of a slope.

24.4 Field Examples

Sedimentation-induced overpressure has been proposed as a driving factor in many slope failures; however, direct observations of the conditions at failure do not exist. Thus, many studies have forward-modeled basin conditions to evaluate the role of overpressure in slope failure. Two examples of regional failures attributed to high overpressures are the Ursa basin of the northern Gulf of Mexico and the Storegga Slide offshore Norway. In a more qualitative assessment, pressures associated with gas hydrate occurrence and free gas accumulation have been estimated for smaller failures offshore Cascadia.

24.4.1 Ursa Basin, Gulf of Mexico

Detailed drilling, coring, and laboratory experiments on shallow sediments in the Ursa basin of the northern Gulf of Mexico have documented overpressure starting near the seafloor at Sites U1324 and U1322. Dugan and Germaine (2008) used consolidation experiments to document permeability behavior and normalized overpressure (λ^*) near 0.5 by 25 mbsf. Through analysis of penetrometer data, Flemings et al. (2008) documented λ^* approaching 0.7 in sediments from 50 to 600 mbsf.

Forward basin models of the Ursa basin, based on measured properties, recreated the observed overpressures and constrained the evolution of the overpressures and their importance for slope failures, which have been well documented as recurring in this region (e.g., Sawyer et al. 2007; Urgeles et al. 2007). Stigall and Dugan (2010) successfully matched the modern overpressure, while showing the importance of depositional geometry and sedimentation rate in controlling overpressure and slope failure in the Ursa region. Coupled sedimentation-fluid flow-slope stability models simulated one slope failure (basal surface 61 ka) on the eastern end the Ursa transect (detailed seismic, age, and failure data in Sawyer et al. 2007 and Stigall and Dugan 2010), solely due to overpressure and flow focusing. Sawyer et al. (2009) showed that once initiated, this low angle (<2.5°) failure would fail retrogressively and have a long run-out due to its high initial overpressure. For the failure whose basal surface is 27 ka, Stigall and Dugan (2010) showed modest overpressure and flow focusing decreased FS, but did not create FS<1. For the overpressure at the time of failure ($\lambda^* \sim 0.7$), acceleration due to a magnitude 5 or smaller earthquake would have been sufficient to drive failure in the Ursa basin. Thus, analysis of the Ursa basin showed that periods of very rapid, asymmetric loading and flow focusing can generate failures; however failure during times with moderate flow focusing may be preconditioned by the overpressure, but a trigger mechanism is required to initiate failure. The difference in initial overpressure and triggering mechanisms for two mass transport deposits (MTDs) at Ursa led to different run-out lengths and deformation features.

24.4.2 Storegga Slide, Offshore Norway

The Storegga Slide offshore Norway is another well-documented, large (3,500 km^3) slope failure on a low angle seafloor (background slope ~1°). Originally gas hydrate was invoked as the driver for failure, however detailed geotechnical characterization, age dating, pressure analysis, and numerical modeling have led to the conclusion that the retrogressive Storegga slide was controlled by overpressure, flow focusing, and an earthquake trigger. Kvalstad et al. (2005a) present a detailed numerical investigation of the large Storegga slide to conclude that normalized overpressure of 0.3–0.6 and flow focusing were controlled by high sedimentation rates in the region during glacial periods. Higher overpressures were not reasonable and did not match modern pressure. With $\lambda^* < 0.6$, it was interpreted that local earthquake loading initiated small failure on locally steeper slopes. Kvalstad et al. (2005b) concluded that a significantly large earthquake with a low probability of occurrence was the only feasible source of the required loading. These earthquake-triggered failures then evolved through a retrogressive model that took advantage of strain weakening and sensitive clays (Kvalstad et al. 2005a; Sawyer et al. 2009). The key to long run-out of the Storegga Slide was low strength controlled by the overpressure at the time of failure. Therefore the initiation of the Storegga slide required modest overpressure that preconditioned the slope for failure followed by a large earthquake (Kvalstad et al. 2005a, b). These high pressures were also essential to the retrogressive evolution and run-out of this enormous slide on a 1° slope.

24.4.3 Cascadia Margin, Offshore Canada

The occurrence of slide scars and the presence of natural gas hydrate on the Cascadia margin offshore Canada yield insights to slope failure, hydrate presence, and failure initiation. Lopez et al. (2010) characterize the geometry of this failure, which is approximately 2,000 m in width and has a scar wall up to 300 m high. The central region of the failure is coincident with the base of gas-hydrate stability interpreted from seismic data. While data on in situ geotechnical properties and fluid pressures are limited, Lopez et al. (2010) document a complex failure surface which they propose results from integrated effects that preconditioned the slope and triggered the failure. They hypothesize that high fluid pressures could be focused through permeable faults which locally weakens the region as a preconditioning factor. The origin of the faults is controlled by the stress regime and local uplift. These conditions concentrated gas hydrate accumulations, which may localize or focus flow. Ultimately, however, the pressures are insufficient for failure, and earthquakes are proposed as the trigger for failure. The earthquakes could have initiated failure through local acceleration, as in the Ursa region and Storegga, or could have created dynamic pore pressure responses or locally over-steepened faults. Continued modeling and geotechnical studies of this region will help constrain the pressure history as it impacts faulting, gas hydrate accumulation, and slope failure.

24.5 Discussion and Future Directions

Overpressure generation appears to be instrumental in preconditioning slope sediments for failure. When depositional conditions are optimized (e.g., differential loading, very rapid sedimentation rates), failures can be initiated on very low slope (<3°) seafloors. As more data are collected on pressure and geotechnical properties, however, it is apparent that many slopes are preconditioned for failure due to low internal strength from high overpressure, but an additional trigger is needed to drive the slope into local failure. The end result can be relatively small failures or enormous failures that reshape margins and redistribute sediment over 100s of km. In many scenarios, even passive margin settings, small earthquakes are viable triggers for these weakened slopes. As overpressure decreases and materials strengthen, larger earthquakes, that have a smaller chance for recurrence, are required to initiate failure. Once failed, materials strain-weaken and produce retrogressive failures.

The mechanism of overpressure generation from sedimentation and flow focusing along permeable units is integral to weakening materials on many slopes that experience failure. The physics of this problem are well defined, and recent data provide valuable tests on the flow-focusing model. The exact mechanics of earthquake-triggered failure on these overpressured, low-angle slopes requires more detailed investigation. Earthquakes can initiate failure due to lateral acceleration of the weakened slope, by creating dynamic overpressure within the sediments, or by steepening slopes. The seismic acceleration of soft, high-porosity clay lacks constraint, while dynamic pressure response lacks sufficient data. Future research into these areas will help unravel the dynamics at the time of failure, and may also shed light on the different internal structures of slides.

Acknowledgments I thank the Submarine Mass Movements and Their Consequences Symposium organizers for encouraging this review. A. Camerlenghi and C. Shipp are thanked for constructive and valuable comments to this paper.

References

Athy LF (1930) Density, porosity, and compaction of sedimentary rocks. Am Assoc Petrol Geol Bull 14:1–24

Biscontin G, Pestana JM (2006) Factors affecting seismic response of submarine slopes. Nat Haz Earth Sci 6:97–107

Bishop AW (1955) The use of the slip circle in the stability analysis of earth slopes. Geotechnique 5:7–17

Dugan B, Flemings PB (2000) Overpressure and fluid flow in the New Jersey continental slope: implications for slope failure and cold seeps. Science 289:288–291

Dugan B, Flemings PB (2002) Fluid flow and stability of the US continental slope offshore New Jersey from the Pleistocene to the present. Geofluids 2:137–146

Dugan B, Germaine JT (2008) Near-seafloor overpressure in the deepwater Mississippi Canyon, northern Gulf of Mexico. Geophys Res Lett 35:L02304. doi:10.1029/2007GL032275

Flemings PB, Stump BB, Finkbeiner T, Zoback M (2002) Flow focusing in overpressured sandstones: theory, observations, and applications. Am J Sci 302:827–855

Flemings PB, Long H, Dugan B, Germaine JT, John C, Behrmann JH, Sawyer D, IODP Expedition 308 Scientists (2008) Erratum to "Pore pressure penetrometers document high overpressure near the seafloor where multiple submarine landslides have occurred on the continental slope, offshore Louisiana, Gulf of Mexico" (vol 269, pg 309, 2008). Earth Planet Sci Lett 274 (1–2):269–283. doi: 10.1016/j.epsl.2008.06.027

Gibson RE (1958) The progress of consolidation in a clay layer increasing in thickness with time. Geotechnique 8:171–182

Green DH, Wang HF (1986) Fluid pressure response to undrained compression in saturated sedimentary rock. Geophysics 51:948–956

Hampton MA, Lee HJ, Locat J (1996) Submarine landslides. Rev Geophys 34:33–59

Hart BS, Flemings PB, Deshpande A (1995) Porosity and pressure: role of compaction disequilibrium in the development of geopressures in a Gulf Coast Pleistocene basin. Geology 23:45–48

Kvalstad TJ, Andresen L, Forsberg CF, Berg K, Bryn P, Wangen M (2005a) The Storegga slide: evaluation of triggering sources and slide mechanics. Mar Petrol Geol 22:245–256. doi:10.1016/j.marpetgeo.2004.10.019

Kvalstad TJ, Nadim F, Kaynia AM, Mokkelbost KH, Bryn P (2005b) Soil conditions and slope stability in the Ormen Lange area. Mar Petrol Geol 22:299–310. doi:10.1016/j.marpetgeo.2004.10.021

Lambe TW, Whitman RV (1969) Soil mechanics. Wiley, New York, 553 pp

Lopez C, Spence G, Hyndman R, Kelley D (2010) Frontal ridge slope failure at the northern Cascadia margin: margin-normal fault and gas hydrate control. Geology 38(11):967–970. doi:10.1130/G31136.1

Loseth TM (1998) Submarine massflow sedimentation: computer modelling and basin-fill stratigraphy. Springer, New York, 156 pp

Rubey WW, Hubbert MK (1959) Overthrust belt in geosynclinal area of western Wyoming in light of fluid-pressure hypothesis, part 2: role of fluid pressure in mechanics of overthrust faulting. GSA Bull 70:167–205

Sawyer DE, Flemings PB, Shipp C, Winker C (2007) Seismic geomorphology, lithology, and evolution of the late Pleistocene Mars-Ursa turbidite region, Mississippi Canyon area, northern Gulf of Mexico. Am Assoc Petrol Geol Bull 91(2):215–234. doi:10.1306/08290605190

Sawyer DE, Flemings PB, Dugan B, Germaine JT (2009) Retrogressive failures recorded in mass transport deposits in the Ursa Basin, northern Gulf of Mexico. J Geophys Res 114:B10102. doi:10.1029/2008JB006159

Stigall J, Dugan B (2010) Overpressure and earthquake initiated slope failure in the Ursa region, northern Gulf of Mexico. J Geophys Res 115:B04101. doi:10.1029/2009JB006848

Strasser M, Anselmetti FS, Fah D, Giardini D, Schnellmann M (2006) Magnitudes and source areas of large prehistoric northern Alpine earthquakes revealed by slope failures in lakes. Geology 34(12):1005–1008. doi:10.1130/G22784A.1

Strozyk F, Strasser M, Forster A, Kopf A, Huhn K (2010) Slope failure repetition in active environments: constraints from submarine landslides in the Hellenic fore arc, eastern Mediterranean. J Geophys Res 115:B08103. doi:10.1029/2009JB006841

Urgeles R, Locat J, Dugan B (2007) Recursive failure of the Gulf of Mexico continental slope: timing and causes. In: Lykousis V, Sakellariou D, Locat J (eds) Advances in natural and technological hazards research 27: submarine mass movements and their consequences. Springer, Heidelberg, pp 207–219

Yardley GS, Swarbrick RE (2000) Lateral transfer: a source of additional overpressure? Mar Petrol Geol 17(4):523–537

Chapter 25
How Do ~2° Slopes Fail in Areas of Slow Sedimentation? A Sensitivity Study on the Influence of Accumulation Rate and Permeability on Submarine Slope Stability

Morelia Urlaub, Antonis Zervos, Peter J. Talling, Doug G. Masson, and Chris I. Clayton

Abstract Overpressure generation due to rapid sediment deposition can result in low effective stresses within the sediment column. It has been proposed that these large overpressures are the main preconditioning factor for causing large-scale submarine slope failure on passive continental margins, such as those in the Gulf of Mexico and offshore Norway. The rate of overpressure generation depends on the sedimentation rate, sediment compressibility and permeability. The Gulf of Mexico and the Norwegian continental slope have experienced comparatively high sediment input, but large-scale slope failure also occurs in locations with very low sedimentation rates such as the Northwest African continental margin. Here we show results from 2D numerical modelling of a 2° continental slope subjected to deposition rates of 0.15 m/ka. These results do not indicate any evidence for significant overpressure or slope instability. We conclude that factors other than overpressure must be fundamental for initiating slope failure, at least in locations with low sedimentation rates.

Keywords Overpressure • Continental margin • Submarine landslide • Slope stability modelling

M. Urlaub (✉) • P.J. Talling • D.G. Masson
National Oceanography Centre, European Way, Southampton SO14 3ZH, UK
e-mail: m.urlaub@noc.soton.ac.uk

A. Zervos • C.I. Clayton
School of Civil Engineering and the Environment, University of Southampton, Highfield, Southampton SO17 1BJ, UK

Y. Yamada et al. (eds.), *Submarine Mass Movements and Their Consequences*, Advances in Natural and Technological Hazards Research 31,
DOI 10.1007/978-94-007-2162-3_25, © Springer Science+Business Media B.V. 2012

25.1 Introduction

Submarine landslides that occur on the open slopes of passive continental margins represent the largest submarine mass flows on our planet. Perhaps the most remarkable feature of huge continental slope failures is that they occur in locations worldwide on gradients of just ~2°. Such low gradient slopes are almost always stable on land. We are yet to monitor one of these huge underwater landslides in action, and the reason(s) for such large-scale failure on such low gradients are contentious.

IODP Leg 308 drilling in the Gulf of Mexico recently confirmed that high excess pore pressures can be generated in areas of rapid sediment accumulation (Flemings et al. 2008). Low permeability prevents sufficiently rapid dewatering and excess pore pressures are produced that are up to 70% of the lithostatic weight. Numerical models using these IODP results suggest that a combination of rapid (up to 30 m/ka) sediment deposition caused by Mississippi River discharge and lateral fluid flow can generate slope failures (Flemings et al. 2008; Stigall and Dugan 2010). Similarly high sedimentation rates are likely to occur offshore from many major rivers and thereby cause large-scale slope failures. Sediment deposition at the margins of ice streams can also be very rapid and lead to excess pore pressures. Sedimentation rates of up to 36 m/ka occurred near the Storegga Slide headwall at the end of the last glaciation (Leynaud et al. 2007), although eventual failure of the Storegga Slide occurred ~7 ka after this peak sedimentation.

It might therefore be proposed that rapid sediment accumulation generating high excess pore fluid pressures are a major reason for large-scale continental slope failure on low (~2°) gradients. However, large-scale slope failures also occur on continental margins with much slower sediment accumulation rates, such as off the coast of Northwest Africa south of 26°N (Wynn et al. 2000). Deposition rates in this area do not exceed 0.15 m/ka, measured over the last 3.6 Ma (Ruddiman et al. 1988). Landslides in this area have a similar bedding-parallel slab-like morphology to failures like those in the Gulf of Mexico and the Storegga Slide (Haflidason et al. 2005; Twichell et al. 2009; Krastel et al. 2012), suggesting a common failure mechanism. Failure of the NW African slope has been attributed to overpressure (e.g., Antobreh and Krastel 2007) but a detailed analysis of how such overpressure might build up was not undertaken. Some key information and relationships of the three considered continental margins is given in Fig. 25.1.

25.1.1 Aims

Here we undertake a sensitivity analysis of how sediment accumulation rate and permeability influence the stability of low-angle continental slopes, starting with a one-dimensional column followed by a two-dimensional slope profile. The models are meant to be generic and broadly representative of a NW African type of continental

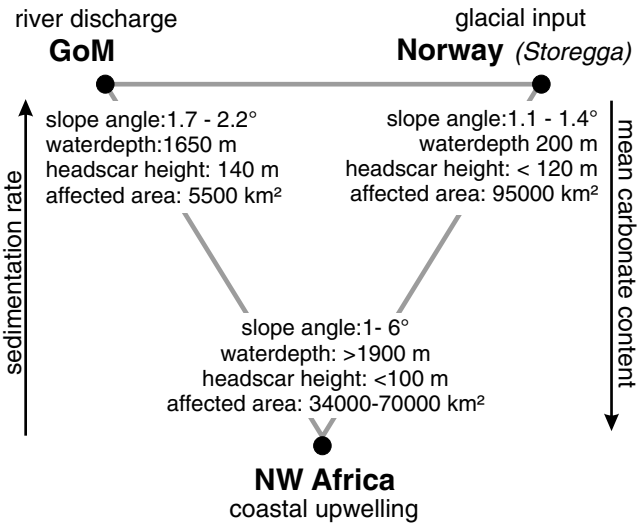

Fig. 25.1 Characteristics of continental margins and slides (mean values) discussed here (*GoM* Gulf of Mexico)

margin. The model is not intending to mimic all the detailed aspects of this location. Our aims are to identify the situations in which particularly high excess pore fluid pressures might be generated, and whether slow sedimentation rates can produce high excess pore pressures that bring a slope close to failure, for reasonable values of sediment permeability. If we are unable to initiate slope failure through build up of high excess pore fluid pressures in this way, then slope failure in low sedimentation rate settings is more likely due to other factors such as internal sediment structures.

25.1.2 Proto-Type Field Location – NW African Margin South of 26°N

The NW African continental margin is relatively uniform over long distances and is disrupted only by widely-spaced canyons. Pelagic and hemipelagic background sedimentation is dominant and originates from a continuous upwelling cell that produces large quantities of biologic material and is located at the upper slope (Sarnthein et al. 1982). Sediment cores recover fine-grained carbonate rich marls and oozes consisting mainly of planktonic shell fragments and terrigenous dust (e.g., Henrich et al. 2008). Sediment accumulation decreases offshore, with rates of up to 0.15 m/ka at the upper slope, and 0.01 m/ka at the mid and lower slope (Ruddiman et al. 1988; Henrich et al. 2008).

25.2 Methodology

25.2.1 Gibson's (1958) Approach to One-Dimensional Consolidation

Gibson's (1958) theory of 1D consolidation under constant deposition is a simple approach to estimate overpressure within a continuously growing clay layer. Key variables are sedimentation rate, time, Darcy's permeability k [m/s], stiffness E [kPa] and the unit weight of the pore fluid γ_w [kPa]. We solve Gibson's theory for sedimentation rate/permeability pairs that result in an overpressure ratio $u^*=0.7$ in a generic, very soft marine clay. u^* [] is the excess pore water pressure at the base of the sediment column normalised to effective stress due to overburden (submerged weight of the overlying sediment). γ_w is 10.24 kN/m³ and a stiffness E of 480 kPa is assumed, which represents the lower limit for very soft clay suggested by USACE EM 1110-1-1904.

25.2.2 Finite Element Modelling of Two-Dimensional Slopes

A 2D plane strain nonlinear elastoplastic coupled pore pressure-deformation model was developed using the finite element (FE) software package ABAQUS.

We use the Modified Cam Clay model (Roscoe and Burland 1968) with isotropic nonlinear elasticity and constant Poisson ratio ν. The slope of the critical state line M [] is a constant and is calculated from the friction angle φ_{crit}' [°] by

$$M = \frac{\sin\varphi_{crit}' \cdot 6 \cdot \sqrt{1-b+b^2}}{3+\sin\varphi_{crit}' \cdot 2b - \sin\varphi_{crit}'} \tag{25.1}$$

where $b=0.5$ for plane strain conditions (Potts and Zdravkovic 2001). Strain hardening is exponential. Void ratio changes due to effective stress changes are controlled by the logarithmic bulk modulus (or compression index) λ []. The sediment is cohesionless and its coefficient of earth pressure K_0 [] equals 1-sin φ_{crit}'. Table 25.1 lists the constants that define the constitutive model consistent with a calcareous marine clay as typically found off NW Africa.

A simplified continental margin geometry is adopted based on the morphology of the NW African margin and is shown in Fig. 25.2. The entire continental margin is modelled as one layer without abrupt material changes and only vertical (not lateral) density and permeability gradients. The model domain is partitioned into region 1, which comprises the upper 500 m of the seafloor and region 2, which covers the deeper part. The mesh consists of 76,050 rectangular plane strain elements and 238,347 nodes. Elements have a size of 10 × 10 m at the seafloor, whilst a coarser mesh size (100 × 100 m) was adopted at 500 m below the seafloor as changes in mechanical properties are less pronounced at these deeper levels (Hamilton 1976;

Table 25.1 Spatially and temporarily constant input parameters used in the Modified Cam Clay constitutive model

Notation		Value	Reference
κ	Swelling index	0.027	Valent et al. (1982), Demars (1982)
ν	Poisson's ratio	0.3	Karig and Hou (1992)
λ	Compression index	0.28	Valent et al. (1982), Demars (1982)
φ_{crit}' [°]	Friction angle	28	Valent et al. (1982)
M	Slope of critical state line	0.87	Eq. 25.1, b = 0.5
γ_w [kN/m³]	Specific weight of fluid	10.24	
g [m/s²]	Gravity	9.81	

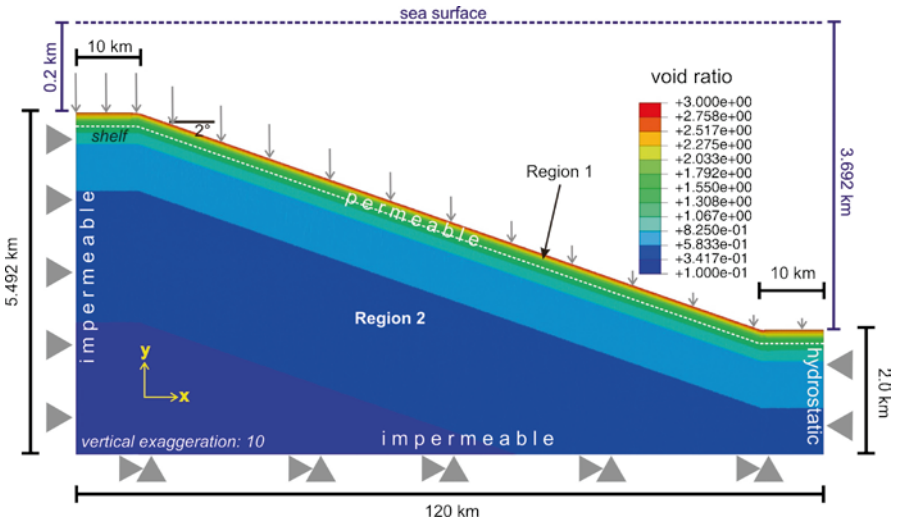

Fig. 25.2 2D slope model geometry (not to scale) with boundary and loading conditions. Pore pressure at the right boundary is hydrostatic so that flow into or out of the model is allowed. As deposited sediment is simulated as a surface load at the seafloor, the flow normal to the surface is governed by the pore pressure gradient and the vertical permeability. The seafloor is free to move in any direction whereas the side boundaries are fixed in the x direction and the bottom is fixed in both directions. The water column is represented as a hydrostatic pressure load on the seafloor, such that there is zero effective stress at the seafloor. Sedimentation decreases exponentially from the shelf edge towards the abyssal plain (*grey vertical arrows*). Colours represent the initial void ratio on which permeability and density depend linearly

Karig and Hou 1992). Element sizes further increase towards the model's bottom as well as towards lateral boundaries at both sides.

Boundary conditions are given in Fig. 25.2. Sedimentation is simulated by progressively adding a vertical surface load that decreases from the shelf edge towards the abyssal plain. At the shelf the rate is uniform. The exponential rate of decrease ($e^{-0.032x}$, where x [km] is the distance from the shelf edge) is based upon thinning rates of seismic sequences in Antobreh and Krastel (2007). A unit weight, $\gamma = 12$ kN/m³,

was assumed for the newly deposited fully saturated sediment corresponding to a dry density of 670 kg/m^3. The peak sedimentation rate at the shelf edge is 0.15 m/ka.

25.2.2.1 Initial Conditions

Seafloor sediments are considered normally consolidated and have an initial void ratio of 3.0 (75% volume porosity). Sediment porosity φ and void ratio e are related by $\varphi = e/(1+e)$. In the interval 0–500 m below the seafloor (region 1) φ is defined by

$$\varphi = 0.75 \cdot 0.987z + 0.83z^2 \tag{25.2}$$

where z [km] is the depth below the seafloor after Hamilton (1976) for calcareous sediments. In region 2 porosity decreases linearly from 40% at 500 m below the seafloor, to 10% at 5,000 m below the seafloor (Velde 1996).

Permeability depends linearly on void ratio and is anisotropic, as measured for pelagic clay (Kawamura and Ogawa 2004). The horizontal sediment permeability k_x at the seafloor before burial (where $e = 3.0$), is 10^{-8} m/s based on oedometer measurements of calcareous sediments compiled by Demars (1982). Yang and Aplin (2010) found vertical permeability k_y as low as 10^{-13} m/s for mudstones with 40% porosity, which we use as the lower limit for vertical permeability variations. Below 500 m (region 2) k is isotropic and constant ($k = 10^{-13}$ m/s). In our models we keep the permeability at the seafloor constant and varied k at 500 m as well as the anisotropy coefficient in order to explore model sensitivity. k_y can be up to one order of magnitude smaller than k_x.

Sediment at the seafloor has a dry density of 670 kg/m³ ($\gamma = 12$ kN/m^3) that increases linearly to 1,400 kg/m³ at 500 m depth ($\gamma = 20$ kN/m³). Sediment more than 500 m below the seafloor has constant density of 2,400 kg/m³ ($\gamma = 26$ kN/m³).

25.2.2.2 Key Assumptions

The continental margin is simulated as one layer (no abrupt property changes) to investigate whether failure could occur without the need for weak layers or glide planes. This effectively assumes spatially uniform deposition of the same material in space and time. Geotechnical properties have not been measured on deep sediments off NW Africa. Those properties used in this model are thus based on a literature review for calcareous pelagic and hemipelagic sediments measured elsewhere (Hamilton 1976; Velde 1996; Yang and Aplin 2010, and references in Table 25.1). The FE model is comparatively simple; it does not include geometric nonlinearity and the deposited sediment is simulated by a surface load. The latter is important because it means that the added sediment is not a source of fluid, and possible failure within the additional sediment thickness cannot be modelled. However, this model serves to explore the general relationships between sediment accumulation rates

and permeability in a continental slope with a geometry broadly similar to that of the NW African margin, Gulf of Mexico or Norwegian margin.

25.3 Results

25.3.1 One-Dimensional Consolidation

High sedimentation rates for prolonged periods of time, and low permeability and stiffness, tend to result in high overpressure. Our 1D modelling indicates that a significant overpressure ratio of $u^*=0.7$ does indeed build up in settings with rapid sediment accumulation, such as the Gulf of Mexico (after sedimentation periods of about 50 ka) and the Norwegian continental slope after 10 ka (Fig. 25.3; Leynaud et al. 2007; Flemings et al. 2008). When sedimentation is ~500 times slower (0.15 m/ka) as in the case of the NW African margin, the permeability must be lower than 10^{-12} m/s and continuous sedimentation must go on for long periods (>1.5 Ma) to generate significant overpressure ratio. Such low values of permeability have been measured perpendicular to bedding for mudstones with clay content >50% and porosities <30% (Yang and Aplin 2010). However, the average clay content of sediment at the NW African margin is about 25% and the porosity at 300 m depth below seafloor is 50%

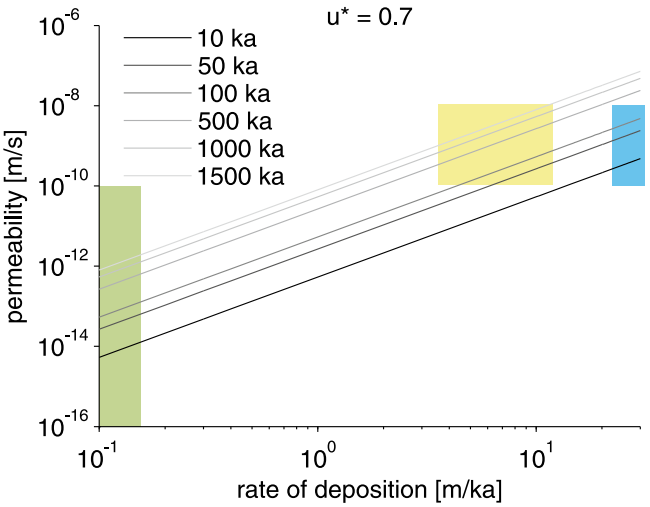

Fig. 25.3 Log-log plot of combinations of permeability and sedimentation rate that result in an overpressure ratio $u^*=0.7$ at the base of a consolidating layer for time periods of 10 ka–1.5 Ma after Gibson (1958). All parameters are assumed constant. The bottom boundary is impermeable. Shaded backgrounds highlight typical sedimentation rate ranges off NW Africa (*green*) as well as sedimentation rate and permeability ranges in the Gulf of Mexico (*yellow*) and off Norway (*blue*). A stiffness of 480 kPa is used for all calculations

(Ruddiman et al. 1988). The occurrence of permeabilities $<10^{-12}$ m/s in a sediment as found off NW Africa is thus unlikely, but cannot be fully excluded as clay mineral accumulation may peak locally. Due to sparse data coverage, especially at greater depths, this is not well constrained and requires further investigation. With a higher but more realistic permeability of 10^{-9} m/s (Demars 1982), the overpressure ratio is negligible and the slope is not close to failure.

25.3.2 Two-Dimensional Consolidation

Several numerical experiments with different vertical permeability gradients and anisotropy ratios were run for 1 Ma. Slope stability is evaluated by analysing vertical effective stresses, σ_v', overpressure ratios, u^*, and Factors of Safety (FoS, ratio of the critical state friction angle to the mobilised friction angle). In summary, all models are stable. All simulations show an expected increase in vertical effective stress and pore pressure due to the overburden. Fluid flow patterns vary within the different models and lateral flow is observed in the models with permeability anisotropy but does not generate significant overpressure ratios at the lower slope. Where permeability is isotropic, fluid flow is purely vertical.

To give an example, Fig. 25.4 shows the model with lowest permeability (k_x decreasing from 10^{-8} to 10^{-12} m/s at 500 m depth, $k_x/k_y = 10$) and a sedimentation rate of 0.15 m/ka at the shelf. The σ_v' contour lines are not parallel to the slope; with higher values at the shelf and lower values towards the foot of the slope (Fig. 25.4a). This is due to asymmetric loading. σ_v' does not show any abnormal pattern and is nowhere near zero.

The maximum overpressure ratio u^* is 0.074 near the shelf edge and at a sub-seafloor depth of about 1,500 m (Fig. 25.4b). However, in the top 500 m u^* is significantly lower. Fluid flow has a small component towards the foot of slope but is predominantly vertical (as shown by black vectors in Fig. 25.4b).

The FoS is as low as 1.3 below the shelf edge, and from $x > 60$ km (Fig. 25.4c) at sub-sea floor depths of about 2,000 m and greater than 300 m, respectively. Undulations of the contour lines near both side boundaries are due to coarse meshing in that area. The FoS contour lines along the slope converge towards the lower slope indicating that the lower slope is less stable than the upper slope, especially at shallow depths. Nevertheless, FoS is >1 everywhere in the model and so no failure mechanism could be identified.

25.4 Discussion

Previous 1D and 2D slope modelling suggests that rapid (peaking at ~30 m/ka) and prolonged (several ka) sediment deposition from river discharges or ice streams can generate sufficiently high over-consolidation ratios ($u^* > 0.7$) to make a continental

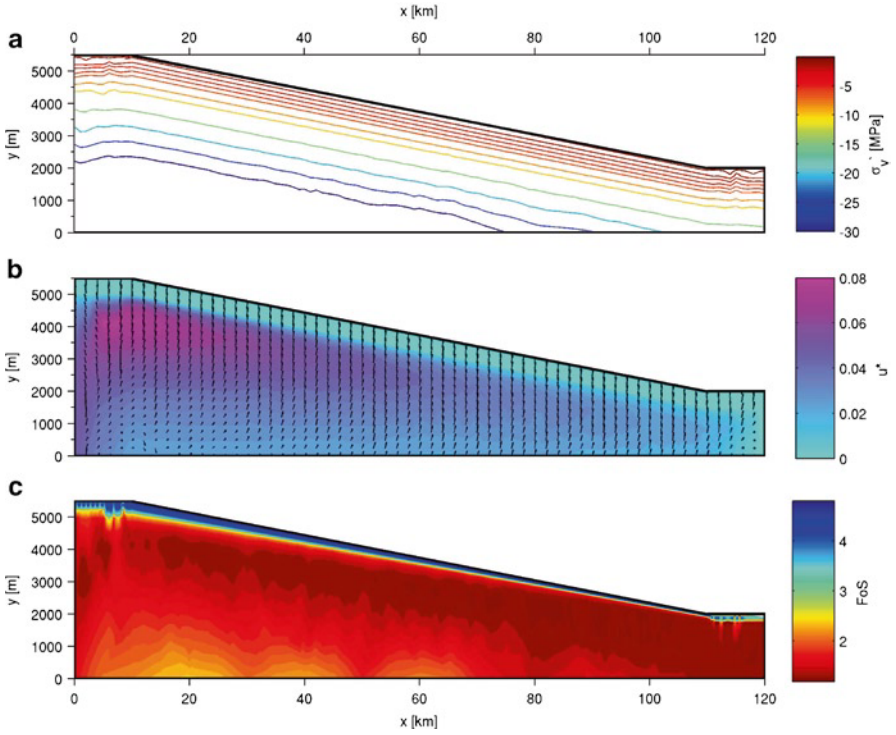

Fig. 25.4 2D FE solution for vertical effective stress σ_v' (**a**) overpressure ratio u^* with flow velocity vectors normalised to their absolute magnitude (**b**) and factor of safety calculated at each node (**c**) after continuous loading with 0.15 m/ka for 1 Ma. Vertical exaggeration is 5

slope unstable (Leynaud et al. 2007; Flemings et al. 2008). However, our modelling suggests that such large pressurisation ratios are not generated in locations such as the NW African margin where sedimentation rates are much lower (0.01–0.15 m/ka), for reasonable values of initial permeability and changes of permeability with depth.

Our work therefore suggests that large-scale failures of slope made of homogeneous low-permeability sediment are in at least some cases not generated by rapid sediment loading alone (perhaps with lateral fluid flow to the toe of slope). It appears that layers of anomalously low permeability that prevent fluid migration, or high permeability layers that allow more rapid lateral fluid flow would be needed. Alternatively, weak layers must be present, all of which are not included in our modelling.

If weak layers are needed for low angle slope failure in areas of slow sedimentation, what are those weak layers? It has been suggested that dissociation of gas hydrates could produce weak layers in a number of ways including rapid removal of cement to leave sediment under-consolidated, formation of voids (gas bubbles) and fractures, and freshening of pore fluids leading to quick clay behaviour (e.g., Bull et al. 2009). All three margins considered here show evidence for gas hydrate

occurrence (Sager et al. 1999; Bouriak et al. 2000; Davies and Clarke 2010). However, slide headscars in the Gulf of Mexico and off NW Africa are located at water depths well below the gas hydrate stability zone (Wynn et al. 2000; Twichell et al. 2009). Shifts of the upper end of the gas hydrate stability zone therefore are unlikely to affect sediments near the headscars. We therefore conclude that gas hydrates as a trigger can be excluded. It appears that some other mechanism is capable of producing weak layers in locations offshore NW Africa, and potentially also in other locations where sedimentation rates are greater.

Acknowledgments Sebastian Krastel kindly provided reflection seismic lines offshore NW Africa. Brandon Dugan, Peter Flemings and Derek Sawyer are thanked for their encouragement to address these problems. We also thank the reviewers C. Berndt and A. Kopf for their constructive reviews.

References

Antobreh AA, Krastel S (2007) Mauritania slide complex: morphology, seismic characterisation and process of formation. Int J Earth Sci 96:451–472

Bouriak S, Vanneste M, Saoutkine A (2000) Inferred gas hydrates and clay diapirs near the Storegga slide on the southern edge of the Voring plateau, offshore Norway. Mar Geol 163: 125–148

Bull S, Cartwright J, Huuse M (2009) A subsurface evacuation model for submarine slope failure. Basin Res 21:433–443

Davies RJ, Clarke AL (2010) Methane recycling between hydrate and critically pressured stratigraphic traps, offshore Mauritania. Geology 38:963–966

Demars KR (1982) Unique engineering properties and compression behavior of deep-sea calcareous sediments. In: Demars KR, Chaney RC (eds) Geotechnical properties, behavior and performance of calcareous soils. ASTM, Philadelphia

Flemings PB, Long H, Dugan B, Germaine JT, John CM, Behrmann JH, Sawyer DE et al (2008) Erratum to "pore pressure penetrometers document high overpressure near the seafloor where multiple sub- marine landslides have occurred on the continental slope, offshore Louisiana, Gulf of Mexico". Earth Planet Sci Lett 274:269–283

Gibson RE (1958) The progress of consolidation in a clay layer increasing in thickness with time. Geotech 8(2):171–182

Haflidason H, Lien R, Sejrup HP, Forsberg CF, Bryn P (2005) The dating and morphometry of the Storegga slide. Mar Petrol Geol 22:123–136

Hamilton EL (1976) Variations of density and porosity with depth in deep-sea sediments. J Sediment Petrol 46(2):280–300

Henrich R, Hanebuth TJJ, Krastel S, Neubert N, Wynn RB (2008) Architecture and sediment dynamics of the Mauritania slide complex. Mar Petrol Geol 25(1):17–33

Karig DE, Hou G (1992) High-stress consolidation experiments and their geological implications. J Geophys Res 97(B1):289–300

Kawamura K, Ogawa Y (2004) Progressive change of pelagic clay microstructure during burial process: examples from piston cores and ODP cores. Mar Geol 207:131–144

Krastel S, Wynn RB, Geersen J, Henrich R, Georgiopoulou A, Meyer M, Schwenk T (2012) Large scale mass wasting at the NW-African continental margin: some general implications for mass wasting at passive continental margins. In: Yamada Y et al (eds) Submarine mass movements and their consequences, vol. 31, Advances in natural and technological hazards research. Springer, Dordrecht, pp 189–199

Leynaud D, Sultan N, Mienert J (2007) The role of sedimentation rate and permeability in the slope stability of the formerly glaciated Norwegian continental margin: the Storegga slide model. Landslides 4:297–309

Potts DM, Zdravkovic L (2001) Finite element analysis in geotechnical engineering: theory. Thomas Telford, London

Roscoe KH, Burland JB (1968) On the generalised stress-strain behaviour of 'wet' clay. In: Engineering plasticity. Cambridge University Press, Cambridge, pp 535–609

Ruddiman WF, Sarnthein M et al (1988) In: Proceedings of the ODP 108, ODP initial reports, College station

Sager WW, Lee CS, Macdonald IR, Schroeder WW (1999) High- frequency near-bottom acoustic reflection signatures of hydrocarbon seeps on the northern Gulf of Mexico continental slope. Geo-Mar Lett 18:267–276

Sarnthein M, Thiede J, Pflaumann U, Erlenkeuser U, Fütterer D (1982) Atmospheric and oceanic circulation patterns off Northwest Africa during the past 25 million years. In: von Rad U (ed) Geology of the Northwest African continental margin. Springer, Berlin, pp 545–604

Stigall J, Dugan B (2010) Overpressure and earthquake initiated slope failure in the Ursa region, northern Gulf of Mexico. J Geophys Res 115(B4):B04101

Twichell DC, Chaytor JD, ten Brink US, Buczkowski B (2009) Morphology of late quaternary submarine landslides along the U.S. Atlantic continental margin. Mar Geol 264:4–15

Valent PJ, Altschaeffl AG, Lee HJ (1982) Geotechnical properties of two calcareous oozes. In: Demars KR, Chaney RC (eds) Geotechnical properties, behavior and performance of calcareous soils. ASTM, Philadelphia

Velde B (1996) Compaction trends of clay-rich deep sea sediments. Mar Geol 133:193–201

Wynn RB, Masson DG, Stow DAV, Weaver PPE (2000) The northwest African slope apron: a modern analogue for deep-water systems with complex seafloor topography. Mar Petrol Geol 17:253–265

Yang Y, Aplin AC (2010) A permeability-porosity relationship for mudstones. Mar Petrol Geol 27:1692–1697

Chapter 26
The BGR Slide Off Costa Rica: Preconditioning Factors, Trigger, and Slide Dynamics

Andrea Anasetti, Daniel Winkelmann, Sebastian Krastel, Jörg Bialas, and Warner Brückmann

Abstract The Pacific Margin of Costa Rica is an area of intense tectonic deformation and repeated slope instability. Several processes are assumed to affect the long-term stability of the slope. Convergence-related seamount subduction and erosion are the primary reasons for large-scale failures at the lower slope. A second type of smaller slope failures occurs on the upper slope coincident with the landward termination of the regional Bottom Simulating Reflector (BSR). The coincidence of the BSR boundary and the position of slide headwalls might suggest a close genetic relationship. In this paper we present a detailed analysis of the so called "BGR Slide", a small-type submarine landslide located on the upper slope offshore the Golfo de Nicoya. The 60 m-high headwall is embedded in an area characterized by small canyon structures on the continental slope in water depths where the regional BSR reaches the sea floor. The slide with a volume of ~0.3 km³ affected an area of ~8 km². Our acoustic data set suggest faults and migrating fluids playing key roles as preconditioning factors for slope failure, while there is no clear indication for the occurrence of gas hydrates in the headwall region. Furthermore, we assume that an external trigger, e.g., an earthquake, finally initialized the sediment mobilization.

Keywords Submarine landslide • Costa Rica • Pacific Ocean • Hydrate dissociation • Faults • Slope stability

A. Anasetti (✉) • D. Winkelmann • S. Krastel • J. Bialas • W. Brückmann
Leibniz Institute of Marine Sciences (IFM-GEOMAR), Wischhofstr. 1-3,
24148 Kiel, Germany
e-mail: aanasetti@ifm-geomar.de

Y. Yamada et al. (eds.), *Submarine Mass Movements and Their Consequences*,
Advances in Natural and Technological Hazards Research 31,
DOI 10.1007/978-94-007-2162-3_26,

26.1 Introduction

The subduction of the Cocos Plate beneath the Central American Plate in a direction close to orthogonal to the Pacific margin of Costa Rica at an azimuth of 27° represents an tectonically highly active setting (Fig. 26.1). The subduction along the Middle America Trench has a relative convergence rate of about 8 cm/a (DeMets et al. 1994). Located on the Cocos Plate, volcanic seamounts are subducted with the oceanic plate in the so-called seamount segment (Fig. 26.1), affecting the morphology of the overriding continental margin (Ranero and von Huene 2000; von Huene et al. 2000). Many authors (von Huene et al. 2004; Hühnerbach et al. 2005) consider the seamount subduction as responsible trigger mechanism for several large-scale landslides located along this part of the continental slope (Fig. 26.1). Seamount underthrusting initially causes deformation of the slope toe colliding with the leading

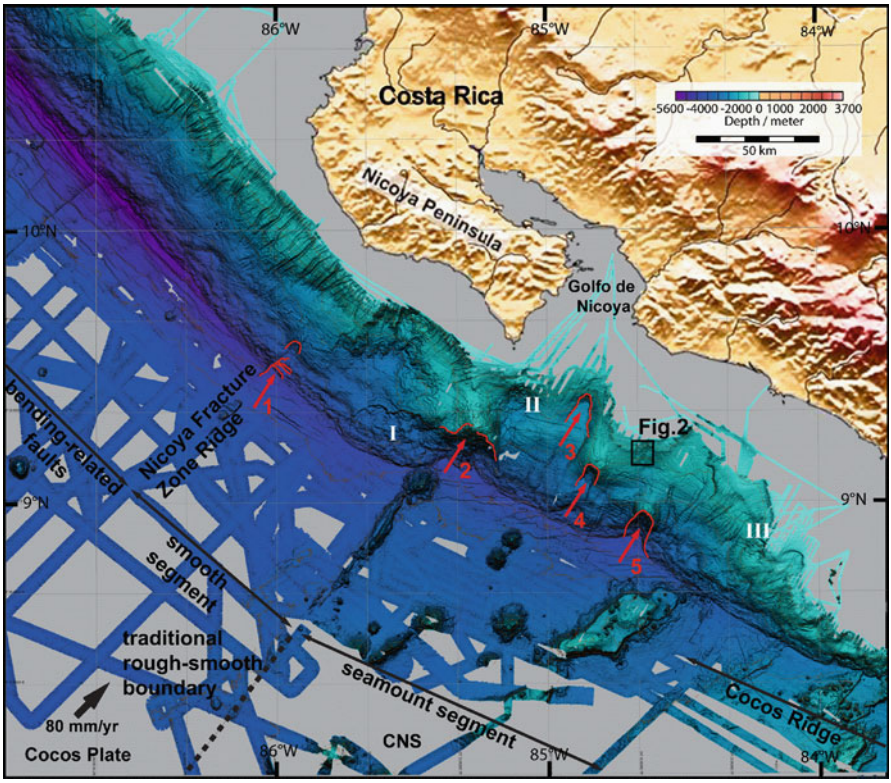

Fig. 26.1 Shaded bathymetry of the continental margin offshore Costa Rica. Small *red arrows* indicate scars probably caused by seamount and ridge subduction: *1*, Fracture Zone Ridge Scar; *2*, Rio Bongo Scar; *3*, Tarcoles Scar; *4*, Jaco Scar; *5*, Parita Scar.Roman numbers indicate landslides: I, Nicoya Landslide; II Capo Blanco Landslide; III, Quepos Landslide. The location of Fig. 26.2 is shown in the *black box* (Modified from Sahling et al. 2008)

edge of the seamount, followed by uplift of the upper plate as the seamount subduction continues. Finally, landsliding occurs at its trailing wake. Some smaller slides occur on the upper slope at water depths that coincide with the upper boundary of the HSZ (Hydrate Stability Zone) (Brückmann et al. 2009). The role of gas hydrates for slope stability is still heavily discussed (Paul et al. 2000; Sultan et al. 2004; Grozic 2010). Hydrate in the pore space glues the sediment together, thereby acting as stabilizing cement. Dissociation of gas hydrate (e.g., induced by rising temperatures and/or descending pressure), challenges slope stability (e.g., Mienert et al. 2005). Destruction of the glue between sediment particles and liquefaction of the remaining sediment formerly bound by hydrate results in loss of structural support and increasing pore pressure. These effects could lead to slope failure.

The BGR Slide is one of the smaller submarine landslides along the margin off Costa Rica located at the upper slope offshore the Golfo de Nicoya (Fig. 26.1). The headwall of the BGR Slide lies in water depths where the regional BSR (Bottom Simulating Reflector) reaches the seafloor suggesting genetic relationship of slope failure to hydrate dissociation (Brückmann et al. 2009). Therefore, we surveyed this slide in great detail to gain a data set that enables us to test this hypothesis. Here, we present an integrated acoustic data set to investigate the structure of this slide with emphasis on the relationship to gas hydrate occurrence, fluid migration, and the structural geological setting. Furthermore, we address future slope stability along the upper slope.

26.2 Data Set

The data set used in this study was acquired during RV Sonne cruise SO206 in June 2010 and previous cruises off Costa Rica. Bathymetric mapping was carried out with an EM120 Kongsberg multibeam echo sounder system. Sediment echo sounder data were collected with an Atlas Hydrographic Parasound subbottom profiler. Multichannel seismic data were collected with a 100 m-long 64-channel Geometrics GeoEel streamer. The source used for this survey was a 1.7l GI-Gun, with a main frequency around 150 Hz.

26.3 Morphological Description of the BGR Slide

The BGR Slide lies at 84°40′W 9°13′N along the upper slope of the Costa Rica margin, at water depths between 500 and 1,100 m (Fig. 26.2). The area around the slide is characterized by well-defined morphological features. Deep and steep submarine channels, major faults, headwalls, and others small slope failures are identified on the acoustic data set. Figure 26.2b shows a slope map with the principal features of the BGR Slide and the surrounding area. The BGR Slide headwall has an arcuate shape. The headwall is located between 500 and 600 m water depth,

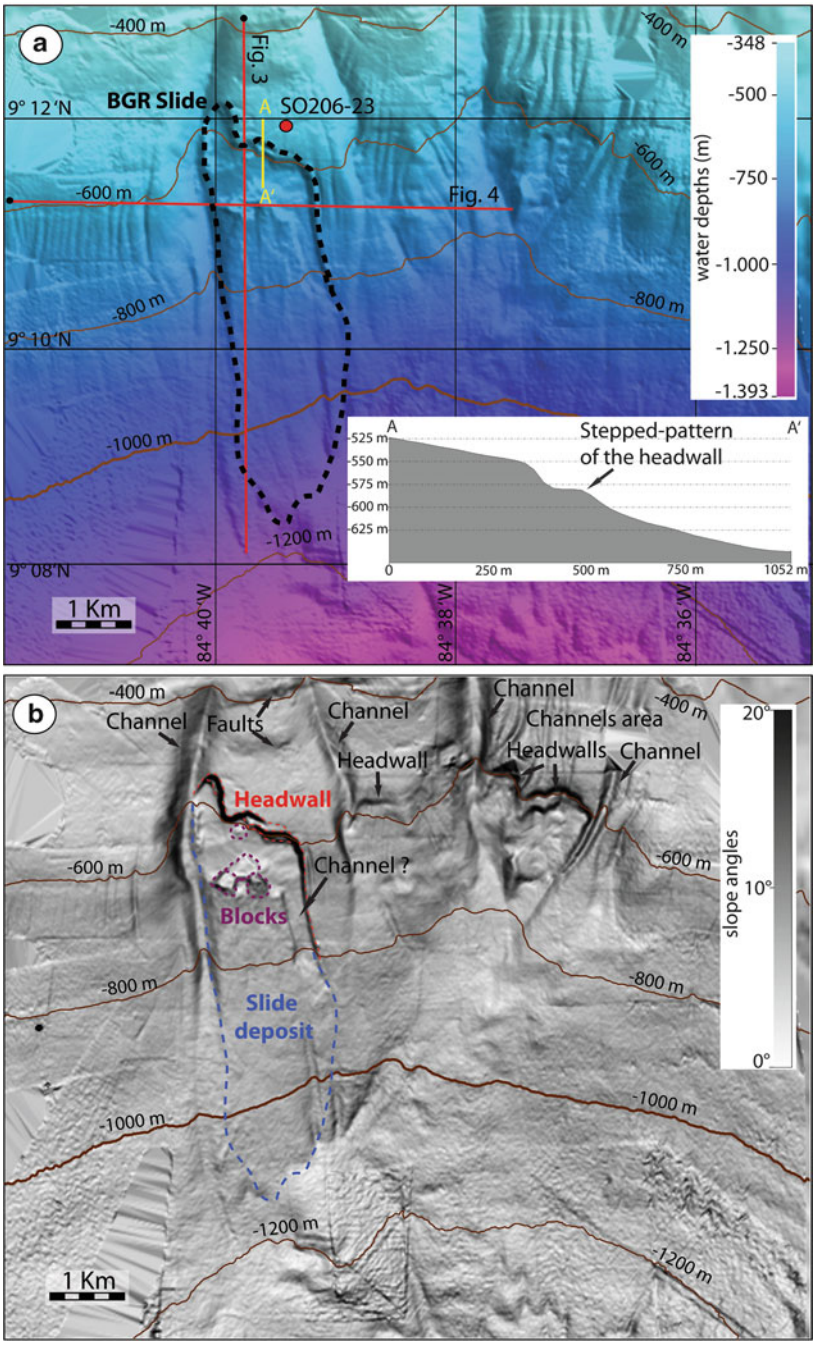

Fig. 26.2 (**a**) Shaded bathymetry of the upper slope of the Costa Rica continental margin showing the BGR Slide in detail. Locations of Figs. 26.3 and 26.4 are shown as *red lines*. The *yellow line* A-A' shows the location of the profile in the *bottom right* of the picture. The *red dot* shows the location of the reference core SO206-23 (**b**) Slope map of the BGR Slide and surrounding area

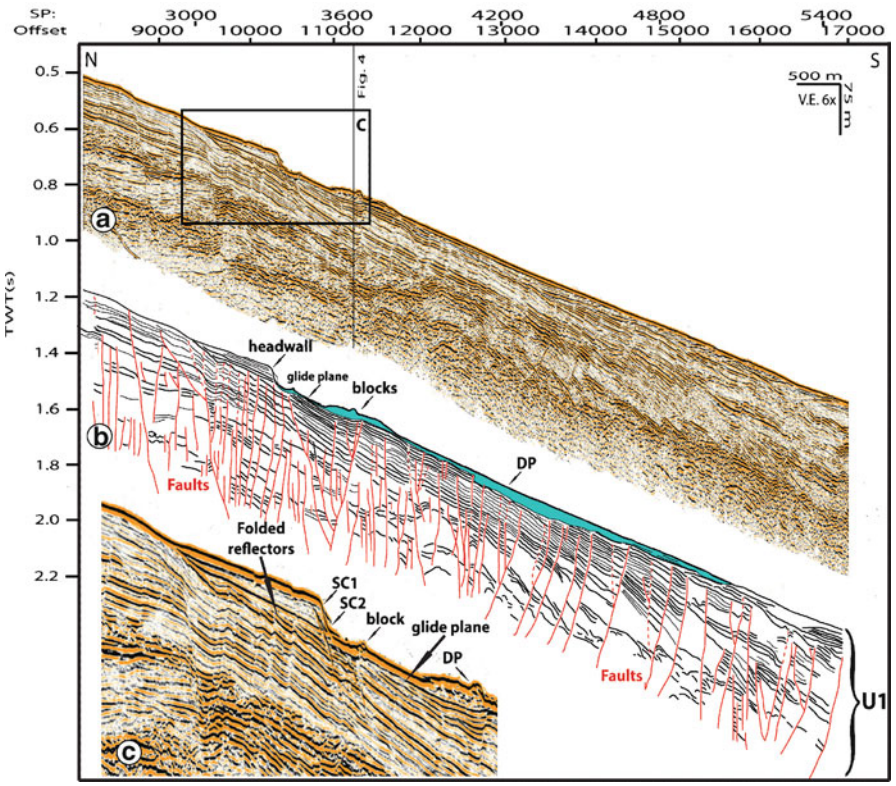

Fig. 26.3 (**a**) North-South reflection seismic profile crossing the headwall and the deposit of the BSR Slide. For location see Fig. 26.2a (**b**) Interpretation of the seismic section: slide deposits (*DP*) marked in *blue* (**c**) close-up of the headwall area of the BGR Slide showing the presence of two distinct *headwalls* (*SC1–SC2*). Note the alignment of the headwalls with underlying faults

averaging 2 km in width and up to 60 m in height. The headwall is characterized in some areas by a particular stepped pattern morphology (Fig. 26.2a).

To determine the surface covered by slide deposits, we traced the seaward limit of a corresponding debrite deposit (Fig. 26.2b) using PARASOUND profiles, where the edge of the deposit is well visualized. The run-out of the BGR Slide, measured from the headwall to the maximum reached depth by the slide measures 6.2 km. The slide deposits form a flat-topped fan elongated in N-S direction (Fig. 26.2b). Three blocks of up to 30 m height, covering an area of 0.3 km², are observed in the upper part of the slide deposits. Another block of ~10 m height is located beneath the headwall (Figs. 26.2b and 26.3c). Except for these blocks, the slide deposit is characterized by a smooth morphology with average downslope inclination of ~3°. The western edge of the slide is located along a submarine canyon at water depths between 400 and 950 m (Fig. 26.2). The canyon is straight and characterized by a V-shaped cross-profile in the slope area above the slide. Here, the canyon's thalweg reaches a depth of 80 m. Downslope the BGR headwall, the eastern flank of the

canyon in the area up to a water depth of 700 m may have been affected by the slide event. Along the eastern edge of the BGR Slide another channel structure is displayed at water depth between 700 and 800 m. From the acoustic data, it is difficult to evaluate whether this feature is a post slide event or if it was formed before. The BGR slide deposit is confined to the area between these two canyons.

26.4 Seismic Characterization

Seismic and sediment echo sounder data are used to define the extent and thickness of the slide deposits. The main focus of the seismic investigation is drawn on the geological structures of the continental slope in order to analyze the precondition factors and the possible trigger mechanism of the slide. Based on the seismic data, we distinguish three different units: (1) the background sediments (Unit U1, Figs. 26.3 and 26.4), (2) headwalls area indicating the source of the BGR Slide (SC1-2; Fig. 26.3), and (3) deposits of the BGR Slide (DP; Figs. 26.3 and 26.4).

26.4.1 Background Sediment (U1)

The background Unit U1 is characterized by a parallel to sub-parallel stratified reflection pattern showing numerous reflectors offsets of varying scales (Fig. 26.3a, b). The reflectors show vertical and lateral variations in seismic amplitude facies. The reflectors up to 0.25–0.3 s TWT subsurface depth are folded, tilted, and deformed by fault propagation movements, but they show lateral continuity (Fig. 26.3b). Only in a few cases these reflectors are laterally interrupted by small offsets, associated with deep-seated faults, especially upslope the headwall. The deeper reflectors >0.3 s TWT subsurface depth are heavily faulted. We interpret two major trends by combining bathymetry and seismic data. A first pattern can be traced approximately WNW-ESE. The second pattern strikes approximately E–W direction (Figs. 26.3 and 26.4). The faults are mostly characterized by normal movements and their offsets tend to increase towards the deeper sediments of U1.

26.4.2 The Headwall Area

The headwall area of the BGR Slide is a deep truncation of U1, showing high slope gradients of head- and sidewalls up to 20–25°. Furthermore, Fig. 26.3c displays how the headwall is characterized, by a stepped morphology from two sub-parallel surfaces (SC1 and SC2). SC1 is the major headwall, up to 60 m high and characterized by an inclination of ~20°; SC2 is a smaller headwall, 30-m-high, downslope of SC1, with an inclination of 25°. SC1 and SC2 are both parallel to the major fault system

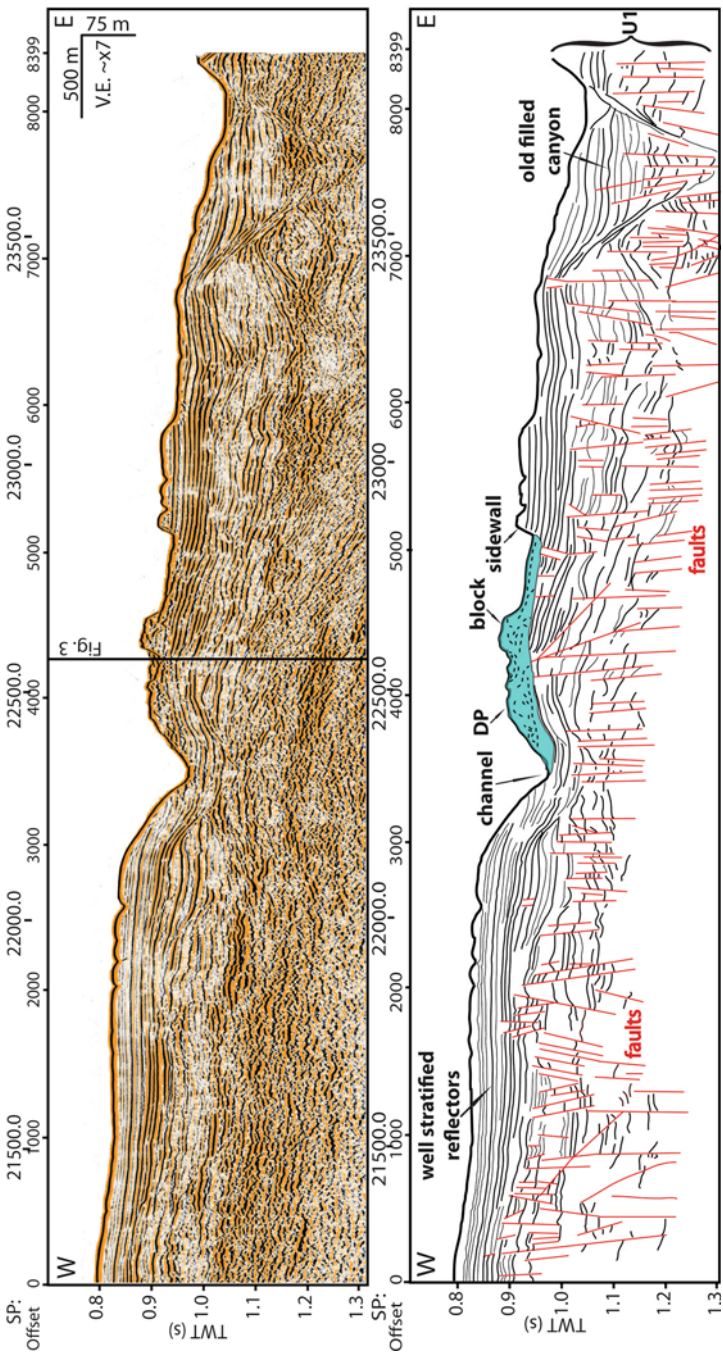

Fig. 26.4 (**a**) West-East seismic profile crossing the DP, the sidewall of the BGR Slide, and the channel structure located on the edge of the slide. For location see Fig. 26.2 (**b**) interpretation of seismic section

below the headwall (Fig. 26.3b). The sidewalls cut the well stratified reflectors of U1 and are characterized by an inclination of 17° and up to 40 m height. Furthermore, an active submarine channel is located along the western edge of the BGR Slide, over-printing the western sidewall.

26.4.3 Slide Deposits (DP)

The deposits of the BGR Slide (DP) are identified as a confined body of chaotic to nearly transparent seismic reflection pattern, indicating different grades of deformation and disintegration of eroded U1 sediments during transport (Figs. 26.3 and 26.4). The DP are of varying thickness with a maximum of ~90 m at SP 4500 (Fig. 26.4), in the area where the blocks (see Figs. 26.3b and 26.4b) are located. We interpreted the topmost intact reflector below the DP as the glide plane of the slide. No detectable hemipelagic drape is visible on the acoustic data. The single, small block in front of the headwall (see Figs. 26.2b and 26.3b) is located on top of the glide plane. The blocks further downslope are seismically characterized by a chaotic to transparent pattern. Between SP 3800 and SP 4100 (Fig. 26.3) downslope of these blocks, the DP thickness decreases to 10–20 m and the slide material in this area covers and fills small surficial depressions generated by folded reflectors of U1. Further downslope the thickness of DP increases up to 70 m (Fig. 26.3b). Here, the DP is characterized by a chaotic to slightly stratified seismic pattern. In the PARASOUND data, the distal edge of the DP shows an onlap on the stratified U1 reflectors.

Calculated volumes of the DP and the eroded material from the headwall area show values of ~0.3 and ~0.4 km³, respectively. The small volume difference might be caused by uncertainty from measurements and small calculation errors, but could also be related to post-slide sediment transport. The active submarine canyon located along the western edge of the slide (Fig. 26.4a) could have remobilized parts of the DP further down the slope.

26.5 Discussion

26.5.1 Slide Evolution

Based on our observations, we created a conceptual model of slope failure development. We assume that an external trigger mechanism, e.g., an earthquake, initialized sediment mobilization on a weak zone. Consequently, downslope movement of a sediment package along an inclined slide plane occurred. This initial failure was followed by a second phase of slope destabilization retreating upslope towards the north/northeast direction. The presence of SC2 downslope of SC1 (Fig. 26.3c) as well as the morphological shape of the headwall (Fig. 26.2) supports this model.

It is difficult to assess whether the whole DP failed quasi simultaneously or with intervening time periods. As we are not able to identify individual slide bodies in the seismic data, the DP may originate either from a quasi-simultaneous or several events of sediment failures in a short-time period with upslope retrogression. The absolute timing of the failure is not known yet but considering the high sedimentation rates of the Costa Rica continental margin, we would expect a detectable post-slide sediment drape covering the glide plane and the DP if the BGR Slide is not Holocene in age. Hence, we consider that the BGR Slide is a young slope failure event.

26.5.2 Role of Gas Hydrate Occurrence, Fluid Flow Migration, and Tectonics for Slope Failure

The headwall of the BGR Slide is located at water depths between 500 and 600 m (Fig. 26.2) corresponding with the upper limit of the HSZ. A BSR is clearly imaged at a water depth greater than the BGR Slide (Brückmann et al. 2009). Gas hydrates are widespread at this part of the margin (Sahling et al. 2008), but our newly acquired seismic data, however, do not image a BSR in the area of the BGR Slide. Imaging of gas hydrates with high resolution seismic data is not always successful, and there are plenty of examples where gas hydrates were recovered but no BSR was found (Holbrook et al. 1996). However, hydrates were recovered from the deeper parts of the slope, and a reference core (SO206-23, see Fig. 26.2 for location) taken above the headwall of the BGR Slide showed high amounts of methane in its lower segment. Based on this data, we consider gas (possibly from dissociating hydrates) as one potential pre-conditioning factor contributing to slope failure development by generation of excess pore pressure. But other possible factors, especially the tectonic setting, need to be considered as well.

Multichannel seismic profiles (Figs. 26.3 and 26.4) show a large number of active faults along the continental margin, and the head and sidewalls of the BGR Slide are parallel or sub-parallel to major faults (Fig. 26.3b, c) Hence, a relationship between the faults and the location of the headwalls is most likely. Based on these observations, we consider the general tectonic setting, especially the occurrence of faults reaching close to the sea floor as a main preconditioning factor for the BGR slide. While migrating fluids and the possible generation of pore overpressure may play a key role, we do not have evidence that gas hydrates are directly involved in this process. However, we assume that an additional final trigger was required, which most likely was one of the frequently occurring, subduction-related earthquakes that are typical for active margins.

26.5.3 Current Stability of the Area

The possible genetic link to the fault systems and the young age of the deposits let us speculate that the BGR Slide is the current snapshot of a retrogressive system of

slope failure events. Several headwalls and slide deposits as well as submarine channels and faults are located at the same water depths east of the BGR Slide (Fig. 26.2). The occurrence of these features indicates that this part of the continental slope is a highly active sedimentary system and in a fast and dynamic morphological evolution. Seismic data recorded along an adjacent undisturbed part of the slope next to the BGR Slide showed a major fault that reaches the surface approximately at the same water depth as the BGR headwall. Furthermore, other faults reach the surface in the area located upslope of the BGR headwall (Figs. 26.2b and 26.3b). Considering the nature of the BGR Slide, the assumed pre-conditioning factors, the trigger scenario and the associated geological characteristics of the slope, we expect that similar slope failure events most likely occur in the future. The continental slope adjacent to the BGR Slide and the undisturbed slope sediments upslope are therefore considered to be instable in the long-term.

26.6 Conclusions

The upper slope of the active margin offshore Nicoya, Costa Rica, shows a type of slope failures that differs from the large seamount related landslides on the lower slope. These upper slope failures are generally smaller in scale and are characterized by upslope retrogression. The BGR Slide is one of these small submarine slope failures covering an area of ~8 km², in a water depth (500–600 m) corresponding to the upper limit of the gas hydrate stability zone. We consider the tectonic setting, especially faults reaching the sea floor, as main pre-conditioning factor for this slope failure. Fluid flow along faults probably contributed to the slope failure, while a direct relationship to dissociating gas hydrates or migrating gas at the base of the gas hydrate stability zone is not supported by our data. The retrogressive system of the BGR slide and adjacent areas may generate further slide events in the future.

Acknowledgment The authors want to thank the captain and crew of RV Sonne during research cruise SO 206. We also thank Frank Strozyk and Kathrin Huhn for constructive comments, which improved the manuscript. Funding was provided by the DFG.

References

Brückmann W, Rhein M, Rehder G et al (eds) (2009) SUBFLUX Cruise No 66 August 12–December 22 2005. METEOR-Berichte 09-2. Universität Hamburg, 158 pp. ISSN 0 9 3 6 – 8 9 5 7

DeMets C, Gordon RG, Argus DF et al (1994) Effect of recent revisions to the geomagnetic reversal time scale on estimates of current plate motions. Geophys Res Lett 21:2191–2194

Grozic JLH (2010) Interplay between gas hydrates and submarine slope failure. In: Mosher DC, Baxter CDP, Urgeles R et al (eds) Submarine mass movements and their consequences. Springer, Dordrecht

Holbrook WS, Hoskins H, Wood WT et al (1996) Methane hydrate and free gas on the Blake Ridge from vertical seismic profiling. Science 273(5283):1840–1843

Hühnerbach V, Masson DG, Bohrmann G et al (2005) Deformation and submarine landsliding caused by seamount subduction beneath the Costa Rica continental margin – new insights from high-resolution sidescan sonar data. In: Hodgons DM, Flint SS (eds) Submarine slope systems: processes and products. Geological Society Special Publications 244, London, pp 195–205

Mienert J, Vanneste M, Bünz S et al (2005) Ocean warming and gas hydrate stability on the mid-Norwegian margin at the Storegga slide. Mar Petrol Geol 22(1–2):233–244

Paul CK, Ussler W III, Dillon WP (2000) Potential role of gas hydrate decomposition in generation submarine slope failures. In: Max M (ed) Natural gas hydrate in marine and permafrost environments. Kluwer, Dordrecht, pp 149–156

Ranero CR, von Huene R (2000) Subduction erosion along the Middle America convergent margin. Nature 404:748–752

Sahling H, Masson DG, Ranero CR et al (2008) Fluid seepage at the continental margin offshore Costa Rica and southern Nicaragua. Geochem Geophys Geosyst 9:Q05S05. doi:10.1029/2008GC001978

Sultan N, Cochonat P, Foucher JP et al (2004) Effect of gas hydrates melting on seafloor slope instability. Mar Geol 213:379–401

von Huene R, Ranero CR, Weinrebe W (2000) Quaternary convergent margin tectonics of Costa Rica, segmentation of the Cocos Plate, and Central American volcanism. Tectonics 19:314–334

von Huene R, Ranero CR, Watts P (2004) Tsunamigenic slope failure along the Middle American Trench in two tectonic settings. Mar Geol 203:303–317

Chapter 27
Detailed Observation of Topography and Geologic Architecture of a Submarine Landslide Scar in a Toe of an Accretionary Prism

Kiichiro Kawamura, Arito Sakaguchi, Michael Strasser, Ryo Anma, and Hiroshi Ikeda

Abstract This paper deals with detailed geologic and topographic features of three recent submarine landslides on a convergent margin. We surveyed the submarine landslide scars on the toe of the Nankai accretionary prism, SW Japan, using the remotely operative vehicle (ROV) *KAIKO7000II* (7K). The water depth is 3,200–3,800 m. The total volumes of moved masses are 3.3, 30.6 and 11.3 km^3. During the dive surveys, the 7K observed debris blocks fractured by two directions of joints. These result from retrogressive small collapses at the landslide scar. Seeps associated with bacterial mats were observed at the top of the scar. We interpret these seeps to be related to the formation of the slide.

Keywords ROV *KAIKO7000II* (7K) • Bacterial mats • Prism toe • Nankai prism • Uniaxial compressive strength

K. Kawamura (✉) • H. Ikeda
Fukada Geological Institute, 2-13-12 Honkomagome, Bunkyo, Tokyo 113-0021, Japan
e-mail: kichiro@fgi.or.jp

A. Sakaguchi
IFREE1, Japan Agency for Marine Science and Technology, 2-15 Natsushima-cho Yokosuka, Kanagawa, 237-0061, Japan

Institute for Research on Earth Evolution (IFREE), Japan Agency for Marine-Earth Science and Technology (JAMSTEC), Yokohama, 236-0001, Japan
e-mail: arito@jamstec.go.jp

M. Strasser
Geological Institute, ETH Zurich, Sonneggstrasse 5, 8092, Zürich, Switzerland

MARUM – Centre for Marine Environmental Sciences, University of Bremen, Bremen, Germany
e-mail: mstrasser@marum.de

R. Anma
Graduate School of Life and Environmental Sciences, University of Tsukuba, 1-1-1 Tennodai, Tsukuba, Ibaraki 305-8572, Japan

Y. Yamada et al. (eds.), *Submarine Mass Movements and Their Consequences*, Advances in Natural and Technological Hazards Research 31,
DOI 10.1007/978-94-007-2162-3_27,

27.1 Introduction

Submarine landslides are significant threat not only in terms of tsunami hazard, but also with respect to damage of submarine cables and coastal constructions (e.g., Locat and Lee 2002). In 1929, and Magnitude (M) 7.0 earthquake hit Grand Banks, Newfoundland, and seven deep-sea cables were cut by turbidity currents derived from submarine landslides (Heezen and Ewing 1952). Recently, turbidity currents have cut repeatedly a deep-sea cable system offshore Taiwan (Hsu et al. 2008). On 26th December 2006, submarine landslides and turbidity currents were triggered by M8.0 earthquake in southwest Taiwan. Those currents cut at least six cables. On 14th August 2009, deep-sea cables were cut, probably also by turbidity currents in the same area. On 16th Oct. 1979, the harbor built during extension of Nice airport suddenly collapsed by submarine landslides and subsequent tsunami of 2–3 m in height hit to the residential area and also airport (Dan et al. 2007; Maliverno et al. 1988). Baba et al. (2010) demonstrated that a submarine landslide induced by an earthquake in a convergent margin has broken a deep-sea water pipe. To predict next tsunamigenic submarine landslides, and to protect marine constructions, we need to understand processes and mechanisms of submarine landslide formation. However, we still do not fully understand locality, frequency, magnitude, and trigger of submarine landslides so far (Locat and Lee 2002; Lee 2009).

In this study, we describe submarine landslide scars in a convergent margin of the Nankai trough, in southwest Japan (Fig. 27.1). In general, there are many earthquakes and maybe also many submarine landslides in convergent margins, but we do not understand in detail the submarine landslides in there. The Nankai trough has been studied by seismic survey, sediment coring and submersible observation (e.g., Kawamura et al. 2009). These data allow us to reconstruct geometric features of submarine landslides (e.g., volume loss, travel distance of moved mass).

27.2 Topographic Features and Seismic Profiles in Dive Survey Area

The Nankai prism is located in the Nankai trough, which is a convergent margin between the Philippine Sea plate and Amur plates (Miyazaki and Heki 2001). The Philippine Sea plate subducts beneath southwest Japan with a convergent rate of 4–5 cm/year (Seno et al. 1993; in a case of the Eurasia plate) to 6–8 cm/year (Miyazaki and Heki (2001); in a case of the Amur plate). Trench-fill sediments in the Nankai trough are accreted into the prism. It forms a thrust-anticline system of turbidite sequences. The frontal thrust-anticline can be seen as an asymmetrical ridge in bathymetric maps. The ridge consists of a steep oceanward (northward) slope (slope angle >40°) and a gentle landward (southward) slope (slope angle <30°) (Fig. 27.1). The ridge is composed of an anticline fold of turbidite layers in the hanging wall of the frontal thrust and forms steep oceanward-facing slopes along which submarine landslides are developed (Kawamura et al. 2009).

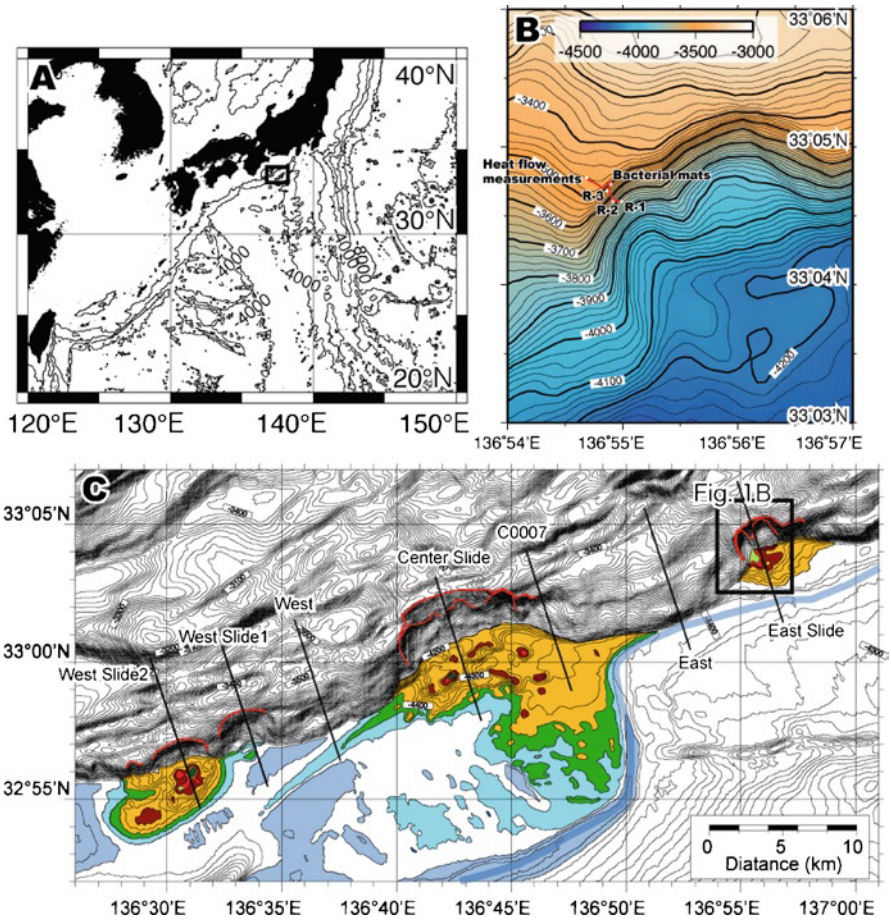

Fig. 27.1 Bathymetric maps of study area in the Nankai accretonary prism, southwest Japan (**a**) *Solid square* shows study area. Contours are 2,000 m intervals (**b**) Detailed map of the East Slide scar. Dive route of 7K#459 is shown by *red line*. R−1, −2 and −3 show rock-sampling points. Bacterial mats are observed on top of the submarine landslide scar. Contour intervals are 20 m (**c**) Bathymetric map and its interpretation in the toe of the Nankai prism. Three major submarine landslides occur on the lower slope of the trench-facing slope in the hanging wall of the frontal thrust. *Red arcuate-shaped lines* show heads of landslide scars. *Colored areas* show moved masses of submarine landslides, which are derived from the scars. The moved masses are deposited on the Nankai trough floor. Large moved mass in *center* of this figure deflects an axial channel (*blue line*) in the Nankai trough floor. *Solid lines* (West, Center Slide, C0007, East and East Slide) correspond to topographic profiles shown in Fig. 27.2. Contour lines are 20 m intervals

There are three major submarine landslides (west, center, and east slides in Fig. 27.1) at the toe of the prism in this study area. The landslide deposits run out 3, 15 and 4 km in length and 4, 10 and 4 km in width, respectively, on the trough floor (Fig. 27.1). There are many blocks of about 0.1 km in diameter and 0.2–0.3 km in height within these deposits (Fig. 27.1). The distal part of the landslide deposits

might be eroded along a deep-sea channel of the Nankai trough. In particular, the channel is deflected to the south by the center landslide deposits as shown by Kawamura et al. (2010) (Fig. 27.1). The total volumes of moved masses calculated from shapes of the landslide deposits are roughly 3.3, 30.6 and 11.3 km^3.

Based on the results of 3D seismic survey, subducted seamounts were observed north of the submarine landslides (Moore et al. 2009). These seamounts are several hundreds meters in height and several km in diameter. When the seamount subducts beneath the prism, the prism toe recedes and becomes high slope angle (e.g., Dominguez et al. 2000). The prism body uplifts and subsequently subsides after the seamount subduction/collision. Such an uplift and a subsidence induce large submarine landslides in Costa Rica (von Huene et al. 2004). Following this reasoning, the submarine landslides at the Nankai Trough prism toe might also be induced by slope instability, which occurred in response to the seamount subduction/collision as shown in Kawamura et al. (2011).

27.3 Dive Survey Results

We have surveyed using the ROV *KAIKO 7000II* (hereafter 7K) the scar of the submarine landslide (east slide in Fig. 27.1) on the hanging wall of the toe of the prism. The average slope angle of the east slide is about 37° in the upper part, and 20° in the lower part (Fig. 27.2).

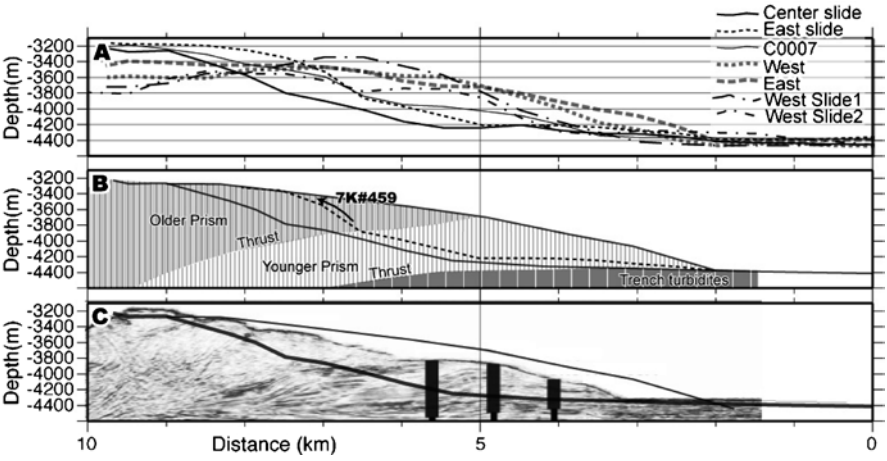

Fig. 27.2 (**a**) Stacked topographic profiles and presumable volume loss by submarine landslides. Locations of each topographic profile are indicated by *solid lines* in Fig. 27.1 (**b**) Geologic cross section of the submarine landslides. Presumable slip planes of center slide and east slide are shown by *gray* and *dotted lines*, respectively. The presumable volume loss areas of both slides are indicated by areas surrounded by *gray* and *dotted lines*. *Arrow* shows dive route of 7K#459. Geologic structures are interpreted on the basis of seismic image of Fig. 27.1c (**c**) Topographic profiles superposed on high-resolution, time-migrated three-dimensional seismic profile through IODP Sites C0006 and C0007 drilled during IODP Expedition 316 (Younger prism and older prism as indicated in *B*, are seen in the seismic image as shown in Kimura et al. (2007))

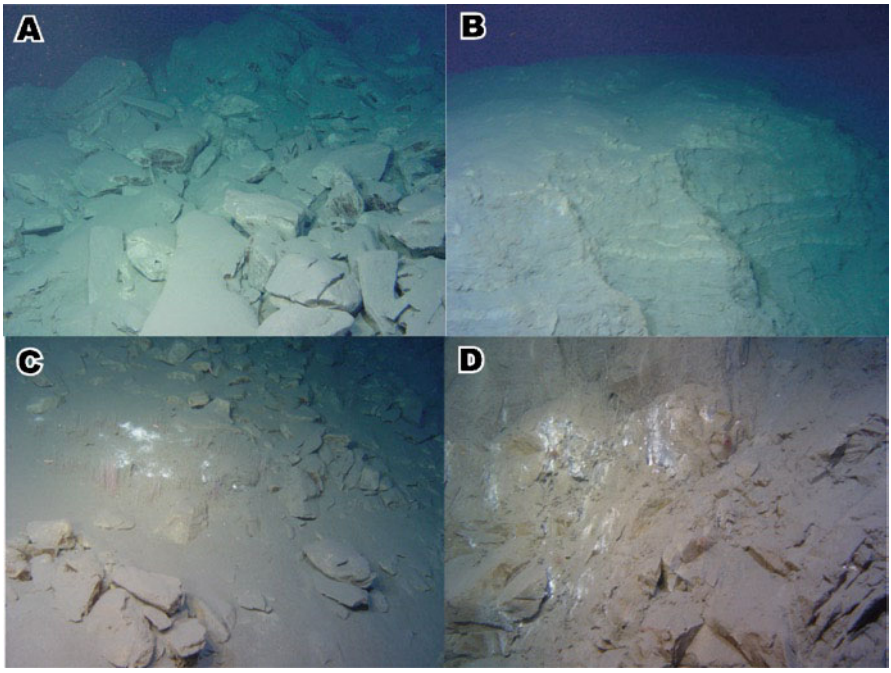

Fig. 27.3 Dive photographs of 7K#459 at upper part of submarine landslide scar, the Nankai accretionary prism (**a**) Debris blocks transported by subsequent collapses at the site around R-1 in 3,700 m water depth. Each block is about 1–3 m in diameter (**b**) A scar of subsequent collapses in 3,650 m water depth. Turbidite layers of horizontal and/or gentle south dip are seen on the scar. Each layer is about several tens of centimeters in thickness (**c**) Bacterial mats on debris floor in 3,500 m water depth. *White spots* of about 10–50 cm in diameter are bacterial mats (**d**) Bacterial mats on a scar near site Fig. 27.3c in 3,500 m water depth

The 7K was landed on a sea floor characterized by debris deposits. Some of the debris blocks (1–3 m in diameter) are distributed in fan-shaped fashion as a talus deposit (Fig. 27.3a). Those debris were eroded from the cliffs located a few hundreds meters upslope of the depositional area. Along the cliffs, the geologic architecture of the accretionary prism can be observed along out-crops lacking any cover sediments (Fig. 27.3b). These indicate that the debris blocks were deposited by subsequent small-scale collapses after the main submarine landslide. We observed three sets of cliffs and associated debris deposits during the dive survey. Therefore, we interpret that the submarine landslide scar is retrogressively shaped by these subsequent small collapses. Those debris blocks are formed failures along two conjugated sets of joints, as indicated by the observed directions of joint sets in the out-crop of the accretionary prism (strike of joint are approximately oriented N-S and E-W).

On the top of the scar, scattered seeps and bacterial mats of several tens of centimeters in diameter are observed. Most of them are distributed on the debris floors (Fig. 27.3c), but some of them occur on the sandy strata in the cliffs (Fig. 27.3d). We think that the seeps are not derived from shallow level (e.g., gas hydrate), but

Table 27.1 Sample data

Sample	Latitude	Longitude	WD	Rock type	UCS
R-1	33°04.50′N	136°54.96E	3,850 m	Siltstone	0.42 MPa
R-2	33°04.58′N	136°54.86E	3,700 m	Sandy siltstone	3.07 MPa
R-2	33°04.58′N	136°54.86E	3,700 m	Siltstone	1.06 MPa
R-3	33°04.64′N	136°54.90E	3,680 m	Silty claystone	1.66 MPa
R-3	33°04.64′N	136°54.90E	3,680 m	Sandy siltstone	2.10 MPa
R-3	33°04.64′N	136°54.90E	3,680 m	Siltstone	3.51 MPa

WD water depth, *UCS* uniaxial compressive strength

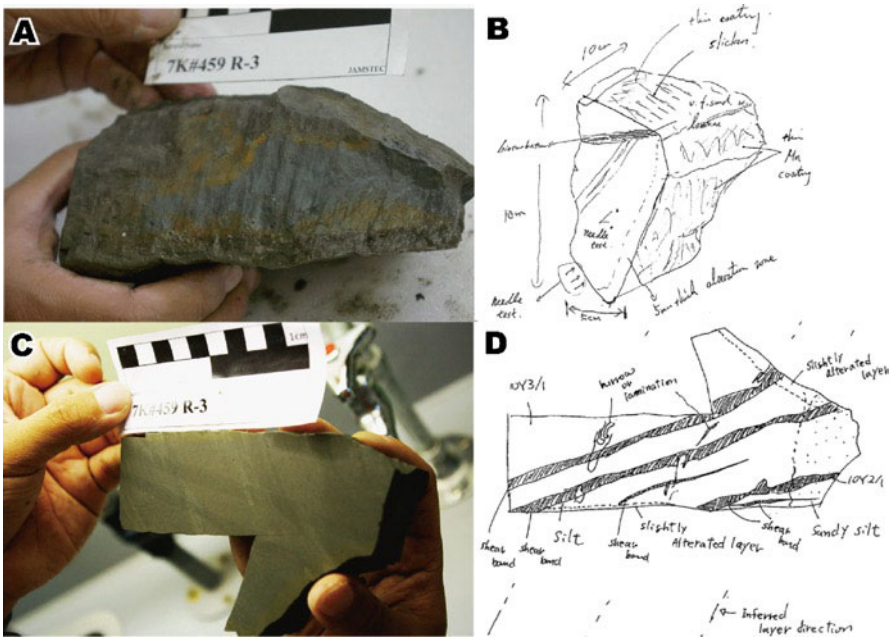

Fig. 27.4 Rock samples collected during 7K#459 (**a**) 7K#459 R-3, a siltstone with a slickenside oblique (~30°) to the bedding plane (**b**) A sketch of a cutting surface in *A* (**c**) 7K#459 R-3 a bedded siltstone with deformation bands (**d**) A sketch of *C*. The deformation bands are oblique (~40°) to the bedding plane. Two fractures are observed oblique (~60°) to the bedding plane

from deeper level of the prism along the active fault (e.g., Kawamura et al. 2009), because there are thrust sheets in the prism without any gas hydrate signals (e.g., BSR) (see Fig. 27.2c). These seeps may be one of the significant triggers for the submarine landslide.

We collected rock samples from the scar during the dive (Table 27.1). Uniaxial compressive strengths were measured using a penetrometer as shown by Kawamura et al. (2009). Those strengths are 1–2 MPa stronger than those at the prism toe in the Tenryu Canyon (Kawamura et al. 2009) which is located ~100 km east of our study area. This might suggest that the toe of the prism was receded to the inner part (North side). The dive result is summarized as shown in Fig. 27.4.

27.4 Concluding Remarks

We surveyed a submarine landslide scar on the toe of the Nankai accretionary prism, SW Japan, using the ROV *KAIKO7000II*. The 7K revealed talus deposits including prism blocks of a few meters in diameter. This suggests that the submarine landslide scar was collapsing retrogressively. The prism blocks are formed by joint sets of the prism rocks that play an important role in formation of debris in submarine landslides. Seeps are observed in place along the same horizon on the top of the scar (Fig. 27.5). These may indicate active faults blanching from the frontal thrust. The fault movement of these faults might be a trigger of the slide. We revealed geologically the submarine landslide in detail as follows;

1. There are blocks of prism rocks on an upper scar of a submarine landslide on the Nanka prism toe, This results probably from repeated small collapses of prism rocks after the main sliding.
2. We found small methane seeps on the upper scar. This may be associated with one of the major triggers in submarine landslides on the Nankai prism toe.

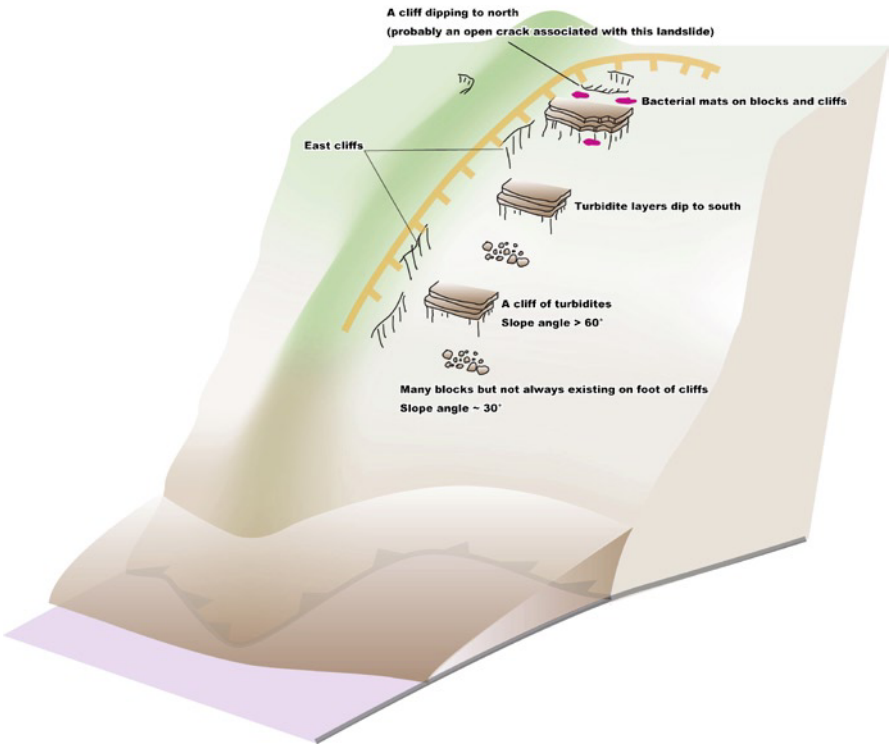

Fig. 27.5 Schematic model of geologic and topographic features on the submarine landslide scar as observed during dive survey of 7K#459

3. Uniaxial compression strengths of rock samples collected from the Nankai prism toe are 1.0–3.5 MPa. These values correspond to those of rock samples collected from an eastern prism toe in Tenryu Canyon.

Acknowledgements We greatly acknowledge to the *KAIKO* team and *KAIREI* crew for help during this research cruise. A part of the study was supported by Grant-in-Aid (KAKENHI) for Scientific Research on Innovative Areas (Super Deep KAIKO Drilling "KANAME" Project) from MEXT.

References

Baba T, Kashiwase N, Matsumoto H, Kaneda Y (2010) Bathymetric survey in the source region of the earthquake occurred in Suruga Bay on 11 Aug 2009. In: JpGU meeting, May 27, Makuhari, MIS003-P01

Dan G, Sultan N, Savoye B (2007) The 1979 Nice harbour catastrophe revisited: trigger mechanism inferred from geotechnical measurements and numerical modeling. Mar Geol 245:40–64

Dominguez S, Malavieille J, Lallemand SE (2000) Deformation of accretionary wedges in response to seamount subduction: insights from sandbox experiments. Tectonics 19:182–196. doi:10.1029/1999TC900055

Heezen BC, Ewing M (1952) Turbidity currents and submarine slumps, and the 1929 Grand-Banks earthquake. Am J Sci 250:849–873

Hsu S-K, Kuo J, Lo C-L, Tsai C-H, Doo W-B, Ku C-Y, Sibuet J-C (2008) Turbidity currents, submarine landslides and the 2006 Pingtung earthquake off SW Taiwan. Terrestr Atmos Ocean Sci 19(6):767–772. doi:10.3319/TAO.2008.19.6.767(PT)

Kawamura K et al (2009) Structural architecture and active deformation of the Nankai Accretionary Prism, Japan: submersible survey results from the Tenryu Submarine Canyon. Geol Soc Am Bull 121:11–12, 1629–1646; doi:10.1130/B26219.1

Kawamura K et al (2010) Redistribution of sediments by submarine landslides on the eastern Nankai accretionary prism. In: Mosher DC et al (eds) Submarine mass movements and their consequences IV, vol 28, Advances in natural and technological hazards research. Springer, Dordrecht, pp 313–322. doi:10.1007/978-90-481-3071-9

Kawamura K et al (2011) Rapid exhumation of subducted sediments from the seismogenic zone along an out-of-sequence thrust in an active accretionary prism, Nankai Trough (Japan. In: Ogawa Y, Anma R, Dilek Y et al (eds) Accretionary prisms and convergent margin tectonics in the Northwest Pacific Basin: submersible studies and recent advances (Part of series of modern approaches in solid earth sciences). Springer, Dordrecht and recent advances (Part ofseries of modern approaches in solid earth sciences), vol 8. Springer, Dordrecht, pp. 215–228. doi: 10.1007/978-90-481-8885-7

Kimura G, Screaton EJ, Curewitz D (2007) NanTroSEIZE Stage 1: NanTROSEIZE shallow megasplay and frontal thrusts. IODP Sci Prospectus 316. doi:10.2204/iodp.sp. 316.2007

Lee HJ (2009) Timing of occurrence of large submarine landslides on the Atlantic Ocean margin. Mar Geol 264:53–64. doi:10.1016/j.margeo.2008.09.009

Locat J, Lee H (2002) Submarine landslides: advances and challenges. Can Geotech J 39:193–212

Maliverno A, Ryan WBF, Auffret G, Pautot G (1988) Sonar images of the path of recent failure events on the continental margin off Nice, France. Geol Soc Am Spec Paper 229:59–75

Miyazaki S, Heki K (2001) Crustal velocity field of southwest Japan: subduction and arc-arc collision. J Geophys Res 106:4305–4326

Moore GF et al (2009) Structural and seismic stratigraphic framework of the NanTroSEIZE Stage 1 transect. In: Kinoshita M, Tobin H, Ashi J, Kimura G, Lallement S, Screaton EJ,

Curewitz D, Masago H, Moe KT and the Expedition 314/315/316 Scientists. Proceedings of the IODP, 314/315/316, Washington, DC (IODP-MI, Inc.). doi: 10.2204/iodp.proc.314315316.102.2009

Seno T, Stein S, Gripp AE (1993) A model for the motion of the Philippine Sea plate consistent with NUVEL-1 and geological data. J Geophys Res 98:17941–17948

von Huene R, Ranero CR, Watts P (2004) Tsunamigenic slope failure along the Middle America Trench in two tectonic settings. Mar Geol 203:303–317

Chapter 28
Possible Ground Instability Factor Implied by Slumping and Dewatering Structures in High-Methane-Flux Continental Slope

Sumito Morita, Takeshi Nakajima, and Yasuaki Hanamura

Abstract A three-dimensional seismic survey off Shimokita Peninsula, NE Japan revealed a number of typical deformations due to slumping and the related dewatering in the Pliocene and younger sedimentary sequences. The slumping was generated primarily by layer-parallel slip on a very gentle continental slope. The slump units often exhibit an imbrication structure formed by repeated thrusting in the bottom layers. The dewatering structure is observed as widespread parallel dikes of which distribution is strongly dependent on the imbrication of the slump units. By tracing seismic layers, slip planes of the slumps proved to be generally characterized as low-amplitude layers having some thickness, and some of the slip planes exhibit flattened features under the slump units of the imbrication structure accompanied by parallel dikes. This implies that excess fluid in the slip plane was drained through the parallel dikes during slumping and that the excess fluid in the slip plane caused the lubrication to enhance the slumping. In the survey area, high methane flux has been reported, and natural gas-related structures, e.g., gas chimneys, have also been observed. These features are considered to be typical of such a high-methane-flux continental slope, and the high methane flux should be an important ground instability factor to cause the slumping and the dewatering phenomena.

Keywords Ground instability • Methane flux • Slump • Dewatering • Slip plane • 3D seismic survey

S. Morita (✉) • T. Nakajima
Research Institute for Geo-resources and Environments, Geological Survey of Japan,
National Institute of Advanced Industrial Science and Technology,
1-1-1, Higashi, Tsukuba, Ibaraki 305-8567, Japan
e-mail: morita-s@aist.go.jp

Y. Hanamura
JX Nippon Oil and Gas Exploration Corporation, 2-6-3, Otemachi,
Chiyoda-ku, Tokyo 100-8163, Japan

Y. Yamada et al. (eds.), *Submarine Mass Movements and Their Consequences*,
Advances in Natural and Technological Hazards Research 31,
DOI 10.1007/978-94-007-2162-3_28, © Springer Science+Business Media B.V. 2012

28.1 Introduction

The origin of submarine ground instability has not yet been fully clarified. However, the behavior of the pore fluid may change the pore pressure and cause ground instability leading to formation of submarine landslides (e.g., Masson et al. 2006). Verifying the processes of submarine landslides and the related fluid migration is very important from the viewpoints of geoscience and geohazard mitigation.

In our previous study, a number of slump deposits and the associated dewatering structures were recognized by observing high-resolution 3D seismic data in the Pacific off Shimokita Peninsula, Northeastern Japan (Morita et al. 2011). We discussed that excess fluid remaining in specific layers that correspond to the slip planes of the slumps had been drained with the formation of the slumps. In the present study, we traced the slip planes and found some specific characteristics which support the idea of the dewatering system. In the present paper, we first review the features of the slump deposits and the related dewatering structures based on the previous study (Morita et al. 2011), and newly discuss possible ground instability factors involved in slumping, taking into account some characteristics of the slip planes.

28.1.1 Geological Background

The study area is located in a gentle continental slope off Shimokita Peninsula in Northeastern Japan (Fig. 28.1). Geologically, the main Cenozoic formations lie unconformably over an erosion surface of the folded Mesozoic-Eocene basement (e.g., von Huene et al. 1980). There are some minor unconformities within the Cenozoic sequence. This area is a part of the long and narrow series of connected sedimentary basins named Yufutsu-oki and Sanriku-oki Basins, which extends from north to south for more than 300 km (Osawa et al. 2002; Tanahashi et al. 2005: Fig. 28.1) and which is expected to contain hydrocarbons on an order similar to the Yufutsu oil/gas field. In particular, a shallow sulfate-methane interface (SMI) of 3.5–12 mbsf (Kotani et al. 2007) indicates a high methane flux over a widespread area. An oil production test in the Eocene formation was successful (JNOC 2000).

28.1.2 3D Seismic Data

The seismic data used in the present study was obtained during the period from March to May in 2008 through the Ministry of Economy, Trade and Industry Japan (METI) fundamental seismic survey 2008, *Sanriku-oki 3D*, which was performed by the 3D seismic vessel, *Shigen*. The rectangular survey area declines slightly toward the west and covers an area of 806.3 km^2. The dimensions of the survey area

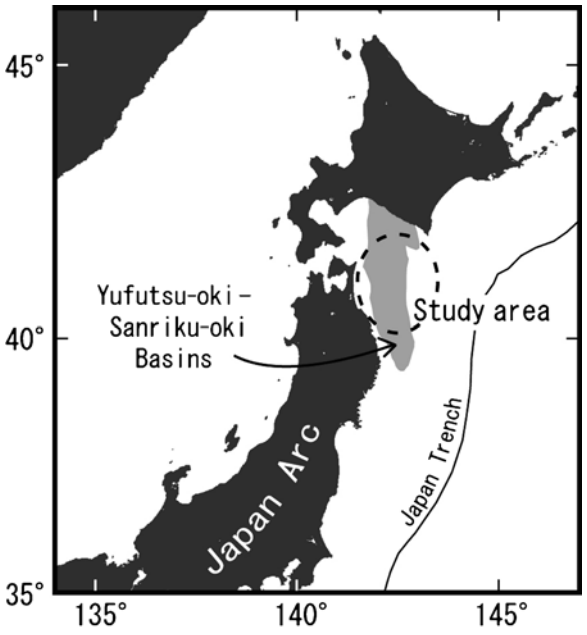

Fig. 28.1 Location of study area. A number of slump sediments were observed in 3D seismic survey area in Yufutsu-oki – Sanriku-oki Basins

are 40 km In-line (N-S) and 20 km X-line (W-E). The data was processed by pre-stack time migration (PSTM) seismic processing. The bin size is 12.5 m (In-line) × 25.0 m (X-line). The stacking number is 47, and the resampling rate is 4 ms. The data processing was carried out by Japan Oil, Gas and Metals National Corporation (JOGMEC).

28.2 Characteristics of Slump and Dewatering Structures

28.2.1 Slump Units

The slump deposits described in Morita et al. (2011) were abundant in the Pliocene and Quaternary formations. Most of the slumpings appear to be layer parallel slip, where unconsolidated surface sedimentary layers suffered gravitational sliding on a gentle slope (Fig. 28.2). Within the range of the survey area, the sizes of the larger slumps exceed 25 km in width and 25 km in length in the slip direction. But, those slumps are assumed to be much larger because the survey area cannot cover the whole bodies of the slumps. The maximum thickness is more than 200 ms in two-way travel time (approximately 160 m). These slumpings occurred on very gentle slopes of less than 1°.

There are a number of slump units characterized by imbrication structure, which exhibits repeated layers formed by thrusting (Fig. 28.2). The imbrication structure

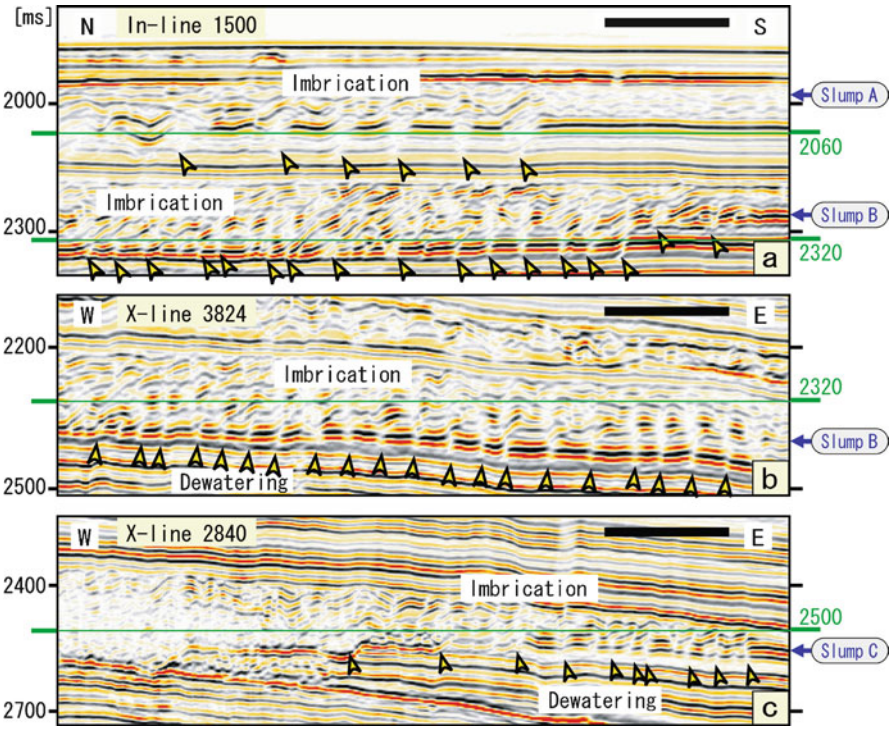

Fig. 28.2 Various features of slumps and the related dewatering structures on 3D seismic cross section. The slumps often show imbrication structure. Parallel dikes, the dewatering structures, indicated by open triangles occur highly depending on the imbrication structure. Each scale bar is 1 km. Time slice images at the depth of green lines are shown on Fig. 28.4 (Modified from Morita et al. 2011)

is mainly observed in slump layers that maintain their structural outline, exhibits multiple thrusts, as in the case of an imbricate thrust zone in a juvenile accretionary prism. The thrusts dip all the way to the upper slope (landward). The imbrication structure exhibits repeated thrusting and peeling off of the basal layers due to horizontal compression, which is likely caused by counteraction along the backstop on the displacement front, where the thrusts may act to compensate the large displacement on the slip plane (Fig. 28.3). This deformation system is similar to systems in previous reports (e.g., Frey-Martinez et al. 2006; Gafeira et al. 2007). The scale of imbrication varies in slump layers, and the thrust generally repeats at intervals of approximately 100–400 m (Fig. 28.2).

28.2.2 Parallel Dikes of the Dewatering Structure

Typical dewatering structures that form equally spaced parallel dikes, which are associated primarily with imbrication type slumps, have been observed (Morita

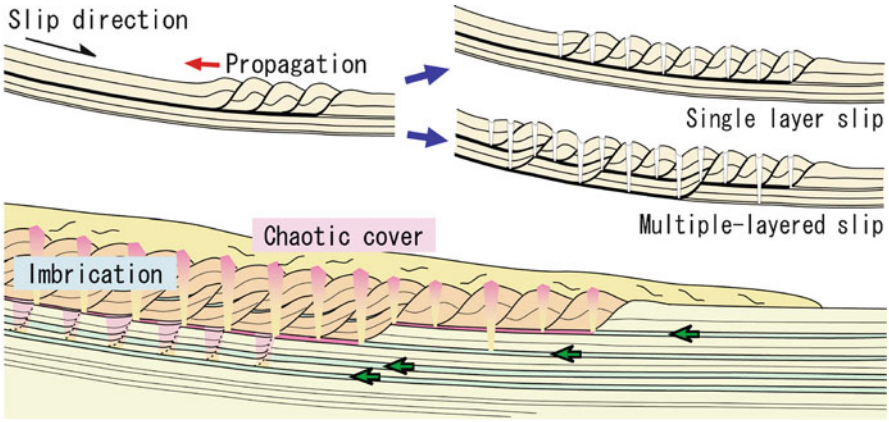

Fig. 28.3 Schematics of the formation of imbrication structure in the slump and the related dewatering structures. Dewatering dikes typically occur at the foot of ramps in the imbricated thrusts. Green layers (*green arrows*) in the *bottom* figure correspond to the slip planes of slumping

et al. 2011: Fig. 28.2). These structures develop from the base of the slump to the upper portion of the unit in each dike. Most of the dikes stand at the feet of the ramp of the repeating thrusts and cut the slanting thrust blocks linking the imbrication vertically (Fig. 28.2). Thus, the dikes of the dewatering structure strongly depend on the imbrication structure of the slumps, so that the structure forms a vertical planar fabric, where the dikes are distributed almost parallel on time slice sections, maintaining equal space intervals according to the thrust-related lineation within the slumps (Fig. 28.4). Consequently, the parallel dikes strike almost perpendicular to the slip direction of slumping, and some dikes in the radial spread of distal slumping exhibit a concentric distribution according to the distribution of the imbrication (Fig. 28.4).

The rearrangement of fluidized clastic sediments is likely to have occurred in the dikes as fluid paths, resulting from the upward drainage of fluid caused by the fluidization at the lower level. The feet of the ramp of the imbrication thrusts appear to have acted as weak points, causing vertical fluid intrusion. In this manner, the parallel dikes are considered to have formed strongly depending on the imbrication structure in the slump units, where the structure acted to drain the excess fluid that was retained in the base of the slump, which corresponds to the slip plane (Fig. 28.3).

The parallel dikes are observed approximately 100 ms below the seafloor (about 80 mbsf) in the shallowest level. The dikes do not cut layers above their slump units, which indicates that these intrusions occurred soon after each slumping. The vertical intrusions in the shallow unconsolidated layers must have occurred as very rapid phenomena. The conformation of the parallel uniform dikes in a very wide area suggests that the dikes formed at approximately the same time as the formation of the imbrication, i.e., at the same time as the slumpings. In the time slice images, the lineation of the parallel dikes, which is somewhat wiggly rather than smooth, indicates that the dikes have passed through unconsolidated surface sedimentary layers rather than through firm beds (Fig. 28.4).

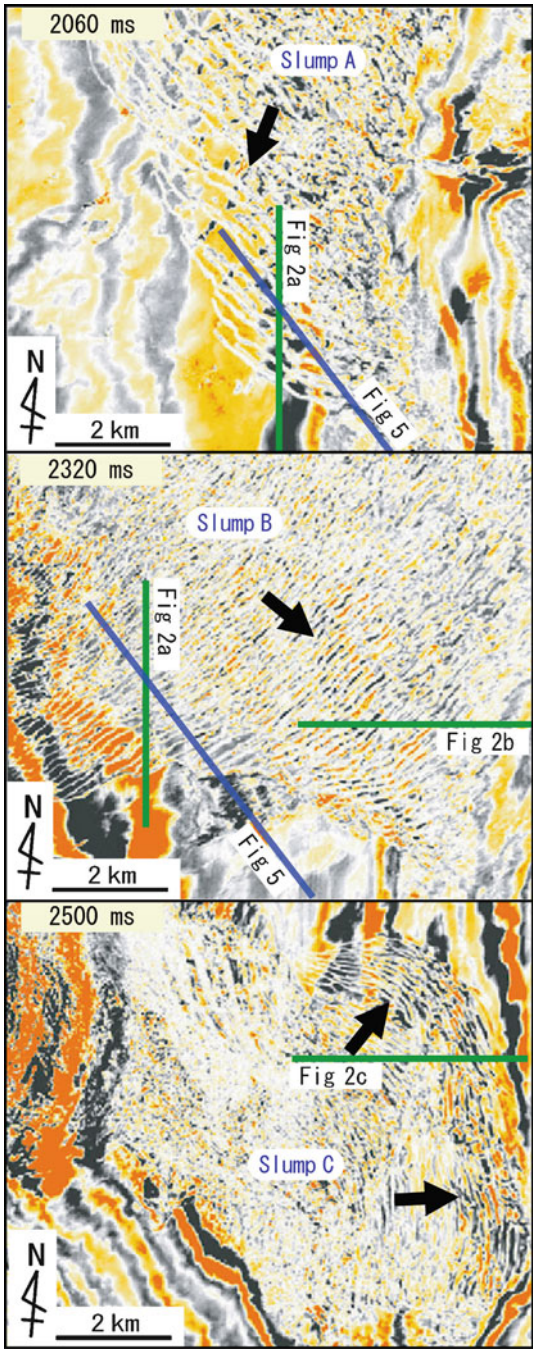

Fig. 28.4 Time slice images of the slumps and the dewatering structures. Parallel dikes of the blanked lineation strike perpendicular to slumping directions (*arrows*). Green and blue lines are locations of the cross sections on Figs. 28.2 and 28.5, respectively (Modified from Morita et al. 2011)

28.3 Slip Planes of Slumping

The present paper tried to examine the slip planes of the slumpings. Within the 3D survey area, the seismic horizons corresponding to the slip planes can be traced from the basal plane of a slump unit, even to the area where the slumping has not reached. This reveals that the horizons of the slip planes are typically characterized by low-amplitude layers having some thickness (Fig. 28.2). The layers corresponding to the slip planes are generally less than 30 ms thick, although quantifying the actual thickness of the slip layers is not easy because of the limit of the seismic resolution. In addition, at present, there is no lithological information with respect to the slip plane layers.

Lateral changes of slip planes are shown in Fig. 28.5. For example, a layer corresponding to a slip plane of a slump unit (red arrow) is similarly characterized by a low amplitude of some thickness. However, the thickness decreases in the part of the slump. Here, a low-amplitude (light gray) layer of approximately 20 ms in

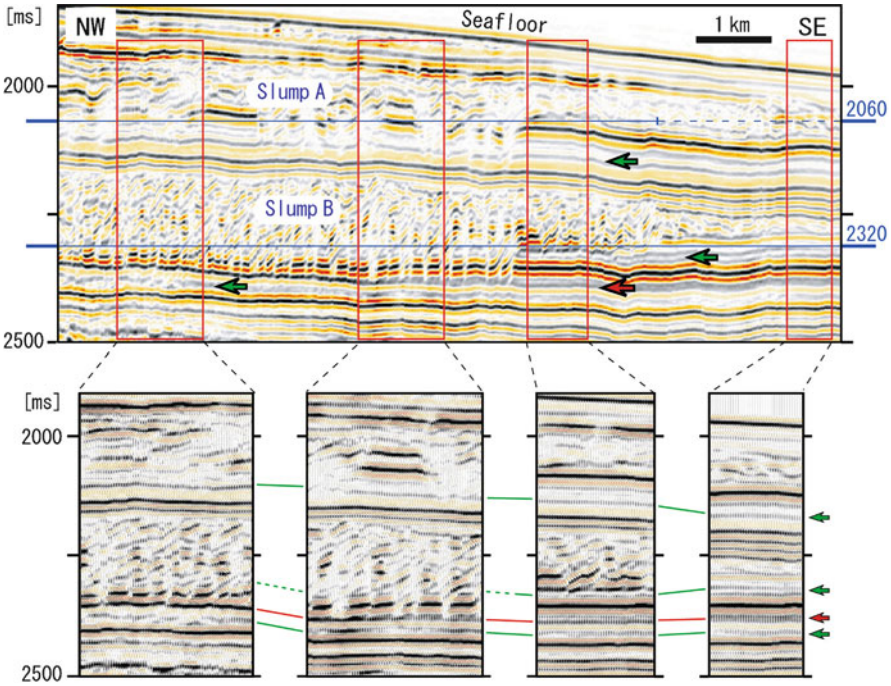

Fig. 28.5 A seismic profile crossing the slump units A and B (*top*) and some partial close-ups of the profile (*bottom*), showing that the dewatering occurs on the slip planes. Layers corresponding to the slip planes of slumping are similarly characterized by low amplitude of some thickness (*arrows*). However, the profile of Slump B, which is cut in slip direction, shows the slip plane layers increase amplitude and decrease thickness in the part of the slump (especially in the layer of *red arrow*). Time slice images at the depth of blue lines are shown on Fig. 28.4

thickness in normal coherent strata changes into clear positive-amplitude (black) layer of approximately 13 ms in thickness in the base of the slump unit (Fig. 28.5). In the survey area, similar changes are observed in some layers, corresponding to slip planes.

Generally, regional variation in thickness of sedimentary layers may occur, and physical properties in the layers, which affect seismic reflection, may change over time. However, even taking into account these possible changes, the difference in thickness in the layer of the slip plane between the case of normal strata and the base of the slump unit is significant. This feature gives us the impression which supports the idea of Morita et al. (2011) that the excess fluid in the specific layers of the slip plane were drained upward through the paths of the parallel dike, accompanying the deformation caused by the slumping.

28.4 Discussion: Possible Ground Instability Factor

For ground instability factors related to underwater slumping, it is necessary to create a slip plane derived by some phenomenon, such as pore pressure change, as well as landslides on land (e.g., Masson et al. 2006). In the survey area, the variation of permeability in an alternated formation is considered to become the determining factor of the layer-parallel slip plane. It is strongly related to the creation of a pressure compartment. When the fluid is supplied from the greater depth, the creation of high pore pressure and the decrease in friction just below a non-permeable layer are to be expected. If the shear stress generated by the load of the upper formation becomes greater than the frictional stress in the anticipated layer, then gravitational sliding will occur. The analogue experiments performed by Kokusho (2000) and Anegawa and Miyata (2001) support this idea. They proved that excess fluid creates water film or water chamber just below non-permeable layer, which can induce horizontal sliding and vertical dewatering eventually.

In our survey area, most of the slumps and the dewatering structures are considered to have formed by this mechanism. The dewatering structure indicates that there was retained excess fluid in the slip plane, and the slumpings should have occurred on the fluid-saturated layers. The excess fluid may have created a film of pressure compartment, which caused the lubrication to enhance the slumping. In Fig. 28.5, as compared with the flattened portion of the layer in the base of the slump unit, the low-amplitude portion in the normal strata may imply lower density of the sediments, i.e., worse grain contact in the sediments if the lithology is horizontally continuous. This might be affected by overpressure, although the lithology is not clear at present.

As mentioned earlier, the survey area has a high methane flux, so that regular advection of hydrocarbon gas-related fluid is assumed. External gas derived from greater depth influences pore pressure and may create a specific pressure compartment that leads to underground sediment mobilization (e.g., Løseth et al. 2003). Additional acoustic reflection anomalies are observed around this survey area, for

example, gas chimneys observed by Taira et al. (2005). Taking into account the geological background of this area, these reflection anomalies are considered to be related to the gas phase in the strata, and most of the series of intrusive structure observed in the area is likely associated with the natural gas. In particular, in this area of high methane flux, the advection of gas-related fluid from the lower level is assumed, so that the slumpings generated by the ground instability and the occurrence of the dewatering structure should be typical phenomena in such regions. High methane flux is an important factor in creating the ground instability in such very horizontal area.

28.5 Conclusions

The detailed geologic structure of the Sanriku-oki Basin off Shimokita Peninsula, NE Japan, observed in 3D seismic data reveals that (1) there are a number of slump units and related dewatering structures in the Pliocene and younger formations, (2) the slump units often show imbrication structure formed by repeated thrusting in the bottom layers, (3) the formation of the dewatering structure strongly depends on the imbrication structure of the slumps, which reveals the existence of vertical parallel clastic dikes, (4) the parallel dikes intruding into the slump units drain excess fluid in the slip plane when slumping occurs, and (5) the formations of the slip planes, the slump units, and the dewatering structures are all related to natural gas bearing fluid, and high methane flux should be an important factor in the ground instability in this area.

Acknowledgments The authors would like to express their appreciation to JOGMEC for permitting use of the seismic data, METI fundamental seismic survey 2008, *Sanriku-oki 3D*. We would also like to thank the reviewers, Drs. Yuzuru Yamamoto and Toshiya Kanamatsu, and the editor, Dr. Kiichiro Kawamura, who were involved in this paper.

References

Anegawa T, Miyata Y (2001) Fluid migration through unconsolidated system -fluid injection structures in alternated sandstone and mudstone layers of the Nichinan Group, Miyazaki Prefecture, Japan. J Geol Soc Jpn 107:270–280

Frey-Martinez J, Cartwright J, James D (2006) Frontally confined versus frontally emergent submarine landslides: a 3D seismic characterization. Mar Petrol Geol 23:585–604

Gafeira J, Bulat J, Evans D (2007) The southern flank of the Storegga slide: imaging and geomorphological analyses using 3D seismic. In: Lykousis V et al (eds) Submarine mass movements and their consequences, III. Springer, Dordrecht, pp 57–65

JNOC (2000) Report of MITI fundamental research well, "Sanrikuoki" 1988. Japan National Oil Company, Tokyo

Kokusho T (2000) Mechanism for water film generation and lateral flow in liquefied sand layer. Soils Found 40:99–111

Kotani R, Matsumoto R, Ishida Y, Hiruta A, Machiyama H (2007) Unusual BSRs and methane activity off Shimokita Peninsula in the western North pacific. J Sediment Soc Japan 64:117–120

Løseth H, Wensaas L, Arntsen B, Hovland M (2003) Gas and fluid injection triggering shallow mud mobilization in the Hordaland Group, North Sea. In: Rensbergen V et al (eds) Subsurface sediment mobilization, Geological society special publications 216. The Geological Society, London, pp 139–157

Masson D, Harbitz C, Wynn R, Pederson G, Løvholt F (2006) Submarine landslides: processes, triggers and hazard protection. Philos Trans R Soc 364:2009–2039

Morita S, Nakajima T, Hanamura Y (2011) Submarine slump sediments and related dewatering structures: observations of 3D seismic data obtained for the continental slope off Shimokita Peninsula, NE Japan. J Geol Soc Japan 117:95–98

Osawa M, Nakanishi S, Tanahashi M, Oda H (2002) Structure, tectonic evolution and gas exploration potential of offshore Sanriku and Hidaka provinces, Pacific Ocean, off northern Honshu and Hokkaido, JAPAN. J Jpn Assoc Petrol Technol 67:38–51

Taira A, Curewitz D, et al. (2005) Shimokita area site survey: northern Japan trench seismic survey, Northern Honshu, Japan. CDEX Technical Report, 2, CDEX JAMSTEC, Yokohama, pp 155

Tanahashi M, Osawa M, Nakanishi S, Oda H, Sato S, Hatanaka M, Suzuki Y, Nakajima T, Tokuhashi S (2005) Fuel resource geology map, “Off Sanriku”. Digital geoscience map series, Geological Survey of Japan, AIST, FR-1

von Huene R, Langseth M, Nasu N, Okada H, Scientific Party (1980) Summary, Japan Trench transect. Init Rep DSDP 57:473–488

Chapter 29
Identification of Weak Layers and Their Role for the Stability of Slopes at Finneidfjord, Northern Norway

Jean-Sebastien L'Heureux, Oddvar Longva, Alois Steiner, Louise Hansen, Mark E. Vardy, Maarten Vanneste, Haflidi Haflidason, Jo Brendryen, Tore J. Kvalstad, Carl Fredrik Forsberg, Shyam Chand, and Achim Kopf

Abstract The 1996 Finneidfjord landslide, which took four human lives in northern Norway, initiated along a weak layer in the fjord-marine sediments before developing retrogressively across the shoreline. The integration of results from sediment cores, free-fall cone penetrometer tests and high-resolution 3D seismic data indicates that the slide-prone layer is a regional bed likely sourced from clay-slide activity in the catchment of the fjord. The sediments in this regional layer are softer and more sensitive than the typical bioturbated, fjord-marine deposits, which explains their role in slope instability. In addition, biogenic gas in the stratified event bed may further affect its geotechnical properties. Similar, fine-grained, stratified beds with comparable origin and properties occur in other Norwegian fjords. They are presumably also present along coastlines of other previously glaciated margins, where they could contribute to mass movements.

J.-S. L'Heureux (✉) • O. Longva • L. Hansen • S. Chand
Geological Survey of Norway (NGU)/ICG, Postboks 6315, Sluppen,
7491 Trondheim, Norway
e-mail: jean.lheureux@ngu.no

A. Steiner • A. Kopf
Marine Geotechnics, MARUM – Center for Marine Environmental Sciences
and Faculty of Geosciences, University of Bremen, Leobener Str,
28359 Bremen, Germany
e-mail: asteiner@uni-bremen.de

M.E. Vardy
School of Ocean and Earth Science, University of Southampton, Southampton, UK

M. Vanneste • T.J. Kvalstad • C.F. Forsberg
NGI – Norwegian Geotechnical Institute, ICG – International Centre
for Geohazards c/o NGI, Ullevål, 0806, PO Box 3930, Oslo, Norway
e-mail: maarten.vanneste@ngi.no

H. Haflidason • J. Brendryen
Department of Earth Science, University of Bergen, Bergen, Norway

Y. Yamada et al. (eds.), *Submarine Mass Movements and Their Consequences*,
Advances in Natural and Technological Hazards Research 31,
DOI 10.1007/978-94-007-2162-3_29, © Springer Science+Business Media B.V. 2012

Keywords Weak layer • Event bed • Sensitive clay • Geotechnical properties • Slope stability • Fjord

29.1 Introduction

Submarine landslides at all scales are often controlled by mechanically weak layers in the marine deposits. There has been an increased focus in the past decade on mapping and characterizing such weak layers in order to understand their contribution to mass wasting processes and to correctly perform geohazard assessments (e.g., Lastras et al. 2004; Kvalstad et al. 2005; L'Heureux et al. 2010).

In this paper, special attention is given to weak layers found off the village of Finneidfjord, Northern Norway, where a catastrophic near-shore landslide occurred in 1996. The landslide mobilized 1×10^6 m^3 of sediment and, due to its retrogressive behavior, encroached 100–150 m inland. The results were the destruction of the E6 highway and three houses. The landslide claimed four human lives. Swath bathymetry and high-resolution seismic data show that initial detachment occurred along a specific layer in the Holocene sedimentary succession offshore (Longva et al. 2003). Geotechnical investigations conducted prior and subsequent to the landslide revealed that large volumes of highly sensitive clays (quick clays), below the shore, were mobilized in the later stages of the landslide (Gregersen 1999; Longva et al. 2003). In this study, we combine sedimentological, geotechnical and geophysical data in order to unravel the origin and the role of the weak layers for the stability of subaqueous slopes at Finneidfjord.

29.2 Regional Setting

Following the last glacial period, the area around Sørfjorden was subject to intense glacio-isostatic rebound and a rapid fall of relative sea-level (the marine limit is at 124 m above sea level; m.a.s.l.). This resulted in the emergence of glacio-marine and marine deposits, followed by a high rate of river erosion. Today, the lowlands in the study area are almost entirely covered by marine deposits (clay and silt), overlain locally by fluvial or littoral deposits. During their emergence in the Holocene, the marine deposits became exposed to groundwater flow and leaching of salts which resulted in the development of quick clays (Rosenquist 1953). Numerous quick clay landslides have occurred along the Røssåga River until the present day (Fig. 29.1a).

Olsen et al. (1996) showed that the shoreline south of Finneidfjord, and in the vicinity of the 1996 landslide, is covered by beach deposits (sand and gravel). These coarser sediments overly a thick sequence of clayey silts resting on bed-rock. Pockets

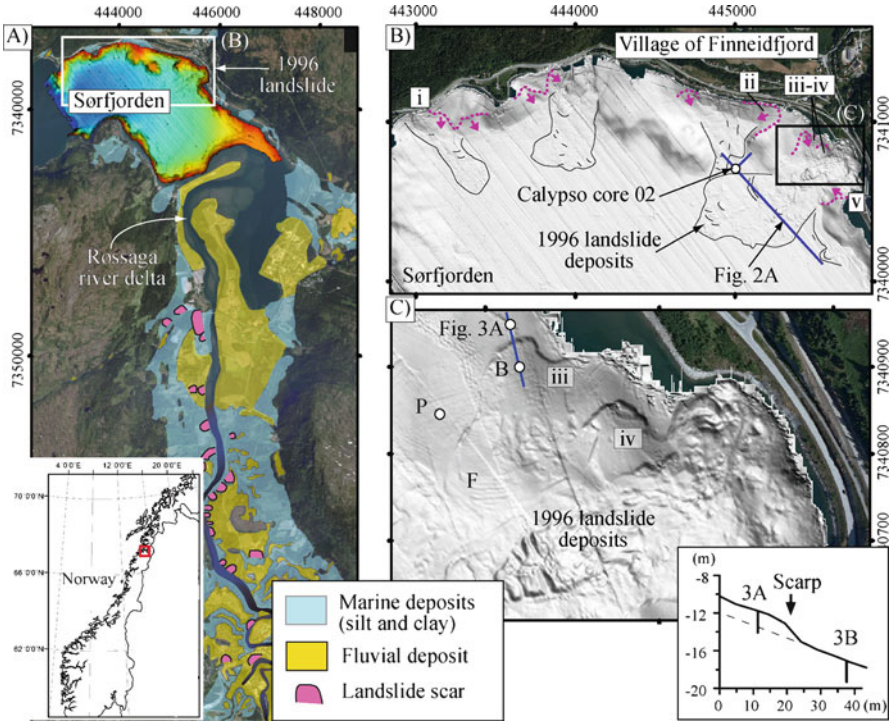

Fig. 29.1 (**a**) Location of the study area with historical landslide scars in the marine deposits along the Røssåga River valley (After Olsen et al. 1996) (**b**) Morphological interpretation of swath bathymetry data off Finneidfjord showing landslide deposits (*black lines*) and the location of landslide scars i–v (*pink lines*) (**c**) Zoom at the initial sliding area for the 1996 landslide as described by Longva et al. (2003). See text for details

of very sensitive clay (i.e. quick clay) are also found at several locations along the shoreline and offshore (Gregersen 1999).

29.3 Data and Methods

Bathymetric data from Sørfjorden were collected in 2003 and again in 2009 using a 250 kHz interferometric sonar system (GeoAcoustics) mounted onboard R/V Seisma. The bathymetric grids have 1 m by 1 m cell size. During the same surveys, a dense network of parametric sub-bottom profiler (TOPAS) was acquired. Also in 2009, 12 gravity cores up to 2.5 m long were retrieved. X-ray imagery, detailed sedimentological description and various geotechnical analyses were performed on the cores.

A very-high-resolution 3D seismic volume (940 m by 175 m) over part of the 1996 landslide area was acquired in 2010. The 3D chirp system provides decimetre-scale

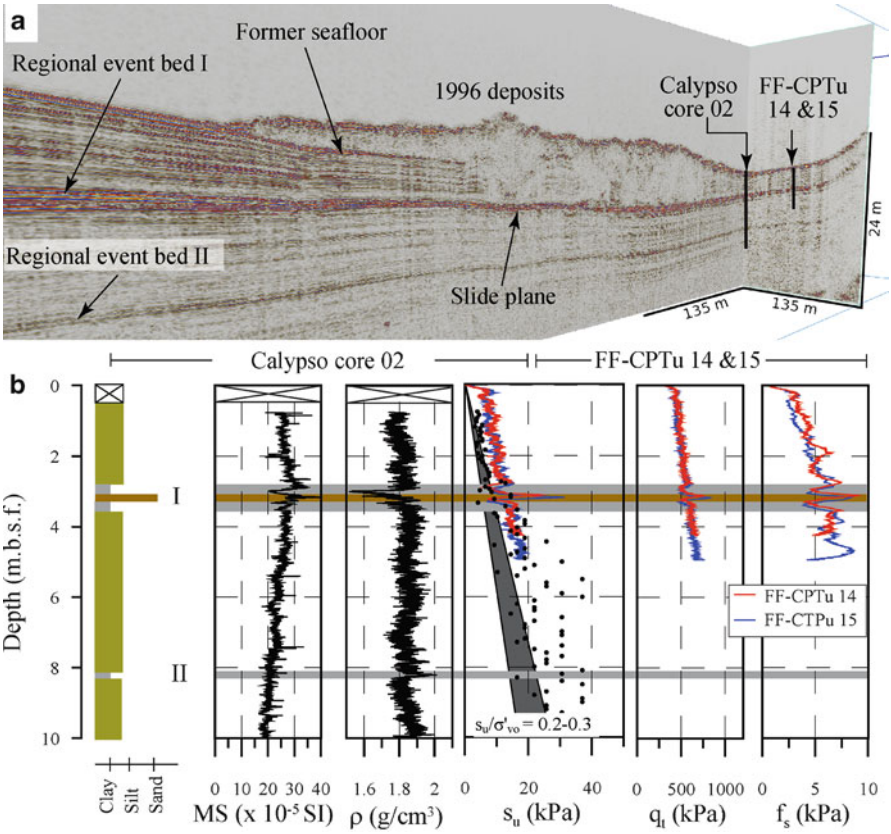

Fig. 29.2 (**a**) Fence diagram from the 3D seismic cube showing the 1996 landslide deposits (see Fig. 29.1b for location) (**b**) Sedimentological and geotechnical details of calypso core 02 (full name GS-10-163-02) and results of in-situ FF-CPTu tests 14 & 15. GS-10-163-02 is shifted 0.73 m vertically to match with FF-CPTu data. (*MS*: magnetic susceptibility, ρ: gamma density log, s_u: undrained shear strength, q_t: total corrected cone resistance, f_s: sleeve friction)

horizontal and centimetre-scale vertical resolution sub-surface images (Vardy et al. 2008)). Within the 3D survey area, two long Calypso cores were collected in 2010 with R/V G.O. SARS (Fig. 29.2b). Multi-sensor core logging (MSCL), XRF core scanning, sedimentological description and geotechnical analyses are being performed on the Calypso cores.

In-situ geotechnical tests were conducted in 2010 using MARUM's free-fall piezocone penetrometer (FF-CPTu) from R/V Seisma. We performed 38 tests to obtain information about soil type and sediment physical properties in various parts of the landslide as well as adjacent areas. For more information about the FF-CPTu data, we refer to Steiner et al. (2012).

29.4 Results

29.4.1 Landslide Morphology

Evidence for mass wasting processes is clearly observed at several locations along the Sørfjorden shoreline (Fig. 29.1b). Two distinct end-members exist in terms of seafloor geomorphology: smooth and rough. Smooth seafloor corresponds to evacuated landslide scars devoid of landslide debris (e.g., slides i to v; Fig. 29.1). The slope gradient within the evacuated landslide scars is usually similar to the surrounding, intact slopes and varies between 13° and 21°. In general, the height of the escarpments is of 2–3 m.

In contrast, rough seafloor morphology corresponds to mass wasting deposits up to a few meters thick (Figs. 29.1 and 29.2). The debris deposits occur mainly in the central part of the fjord (Fig. 29.1), and consist of blocks and slabs of compressed sediment (see F; Fig. 29.1c). The blocks moved along a high-amplitude seismic reflection (e.g., Longva et al. 2003) (Fig. 29.2a). Bathymetry data also indicate that several landslides where exposed for a retrogressive process extending beyond the shoreline.

29.4.2 Sediment Core Analysis

The calypso core 02 (GS-10-163-2) was collected outside the 1996 landslide deposits (Fig. 29.1b). The sediment is dominated by a homogenous, brownish, bioturbated, clayey silt with some shell fragments. Physical properties only show subtle variation in gamma density and magnetic susceptibility (Fig. 29.2). At 2.8 m depth, a 0.45 m thick and distinct stratified bed is present. It consist of a sharply based, 15 cm thick, grey clay overlain by 20 cm of coarse sand fining upwards, with another 10 cm of clay on top. Similar, but thinner, beds occur in gravity cores 03 and 04 (Fig. 29.3). These cores were collected within and immediately upslope of the ~2 m high headwall created by the initial landslide of 1996 (slide iii; Fig. 29.1c).

In core 04, this particular unit is found at 1.9 mbsf, whereas in core 03, only part of the event bed is found in the uppermost 15 cm of the core (Fig. 29.3b). X-ray analysis of cores 03 and 04 reveal vesicular spots indicative of gas bubbles in the brownish clayey silt immediately below the clay layer. Gas vesicles were also observed within the stratified bed in core 04 (Fig. 29.3a). The beds are marked on the logs of magnetic susceptibility, gamma density and on the results from the FF-CPTu tests. The clays give low peaks in both magnetic susceptibility and gamma density, whereas the inverse is observed for the sandy layer (Figs. 29.2 and 29.3). From the FF-CPTu tests, a significant drop in cone resistance accompanied by a decrease in sleeve friction is observed for the stratified clay bed. Total organic carbon (TOC) is slightly lower in the clays compared to the "normal brownish sediments". TOC peaks within the sandy layer (Fig. 29.3).

The depth at which the stratified beds occur matches the level of the failure plane for slide iii (Fig. 29.1c). The failure plane was previously interpreted to correspond

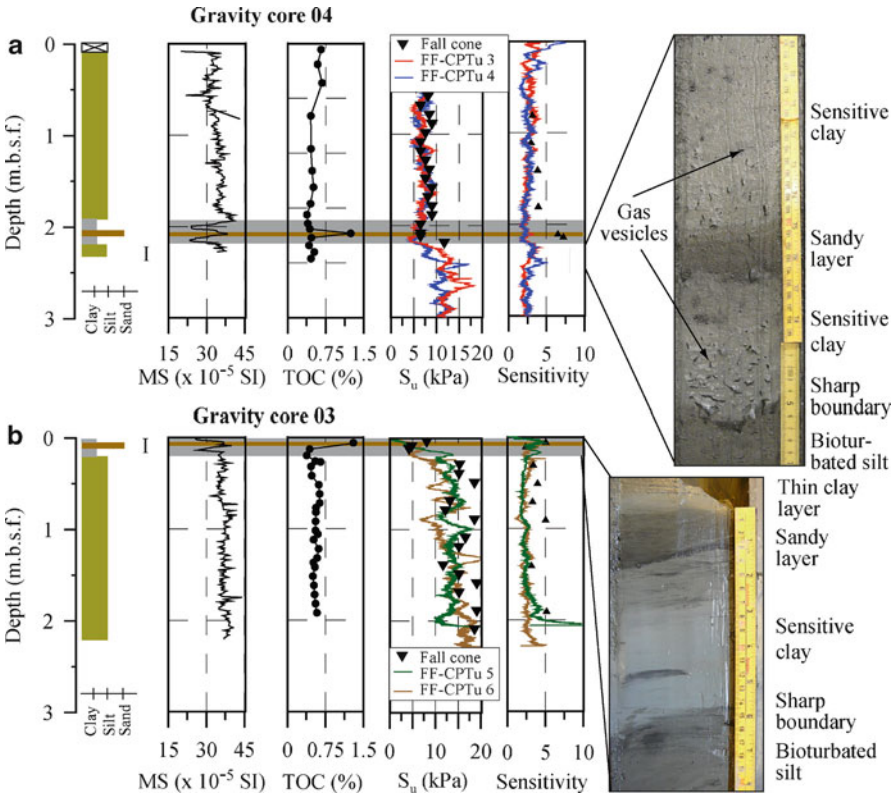

Fig. 29.3 Stratigraphy and geotechnical profiles for (**a**) gravity core 04 and FF-CPTu 03 & 04 collected upslope of the ~2 m high back-wall of slide iii; and (**b**) gravity core 03 and FF-CPTu 05 & 06 collected within the evacuated scar of slide iii (see Fig. 29.1c for location). Photographs from the clay-rich event bed matching the slide plane are also shown. (*TOC* total organic carbon)

to a band of high-amplitude reflections on TOPAS data (Longva et al. 2003). The bed found here confirms this (Fig. 29.2). Importantly, this layer can be mapped throughout the entire fjord basin and this suggests that it corresponds to a regional sedimentological event.

29.4.3 Geotechnical Properties

Water contents average around 35% and vary marginally for the brownish bioturbated sediment for all three cores. In contrast, the water content varies significantly in the event beds, varying within a range of 45–65%. Undrained shear strength (s_u), determined from fall cone tests, are typically lower for the event bed with values of 4–8 kPa and undrained shear strength ratios (s_u/σ'_{v0}) in between 0.2 and 0.3. Strength ratios for the brownish silt generally exceed 0.3 (Fig. 29.2b). Shear strengths from in-situ

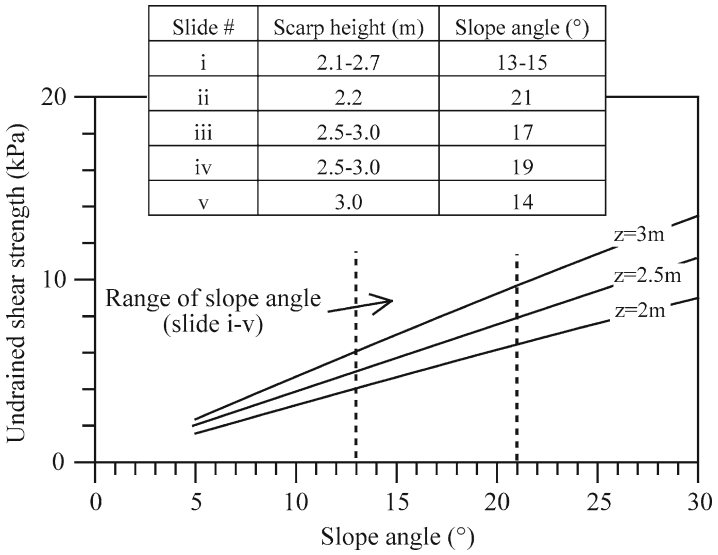

Fig. 29.4 Combination of slope angle and undrained shear strength needed for the failure of sediment slabs. As a comparison, the values of scarp height (z) and slope angle for 5 translational slides in Sørfjorden are given (Location in Fig. 29.1)

FF-CPTu tests compare well with fall cone results (Figs. 29.2b and 29.3). In all analyzed in-situ tests, the cone resistance and the sleeve friction is 1.5–2.0 times lower in the weak layers than in the surrounding sediments (see also Steiner et al. 2012). Results from both laboratory data and FF-CPTu tests also show that the sensitivity of the event bed is greater than for the "normal" sediment with values up to 7.5 (Fig. 29.3).

29.4.4 Back-Calculation of Strength from Slope Morphologies

Many of the translational slope failures in the fjord have a relatively thin moving mass (around 2–3 m) compared to the height of the slope (up to 30 m). In several cases, the triggering mechanism for slope failures is related to nearby human activities, e.g., blasting and rapid loading. Such situations are suitable for infinite slope stability analyses using undrained conditions, which can be evaluated using:

$$\mathrm{FoS} = s_u / \gamma' \cdot z \cdot \sin\alpha \cdot \cos\alpha \tag{29.1}$$

where FoS is the factor of safety, s_u the undrained shear strength at depth z, γ' the submerged unit weight, z the depth to the failure plane and α the slope angle. Using Eq. 29.1, one can find combinations of s_u and z which would produce failure (i.e. FoS = 1). For slope angles of 13–21° and slab thicknesses of 2–3 m, the required s_u values needed to produce failure are in the range 4–8 kPa (Fig. 29.4). These results

are comparable to the measured shear strength data for the stratified event bed in the cores and calculated from in-situ FF-CPTu tests. This testifies to a low natural stability of the slopes prior to failure.

29.5 Discussion and Conclusions

The integrated data set illustrates that landslides in Sørfjorden tend to initiate along a regional, weak bed in the stratigraphy identified in the fjord basin (Fig. 29.5). This weaker unit contains alterations of clays and sands and show properties and internal stratification comparable to those described in a fjord system further south (i.e. Trondheimsfjorden; L'Heureux et al. 2010; Hansen et al. 2011). Applying this study as an analogue, the stratified event beds at Finneidfjord were likely deposited as turbidity currents/flows generated in the fjord following landslides in the emerging marine clays in the catchment (Fig. 29.1). Such flows may have been followed by delta slope failure and/or flooding in the nearby river. Similar types of event are also documented from Canadian fjords (e.g., St-Onge et al. 2004).

Following landslide activity in the catchment area of the fjord, the sudden and extensive supply of sediment caused an abrupt burial of benthic ecosystems, anoxic conditions in the buried sediments and most likely the production of biogenic gas (e.g., Leduc et al. 2002). This would explain the occurrence of gas vesicles within and immediately below the event bed in the cores (Fig. 29.2). Biogenic gas is known

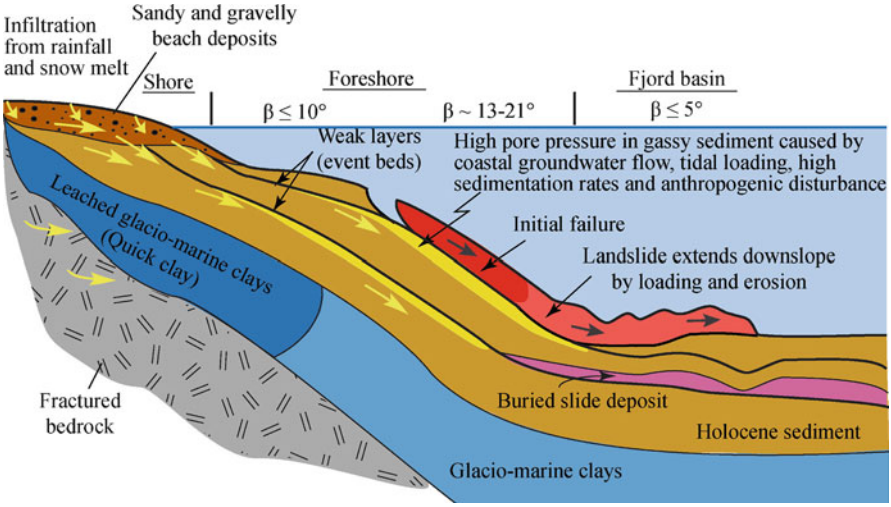

Fig. 29.5 Schematic illustration of the near-shore setting at Finneidfjord and showing different factors affecting the stability of slopes. The model shows how the low-permeability weak layers affect the general land-fjord groundwater flow and how they further control the stability of slopes along the steep foreshore slopes

to significantly alter the sediment's geotechnical properties, primarily by increasing the compressibility and reducing the undrained shear strength (Sills and Wheeler 1992; Seifert et al. 2008).

The integrated data set suggest that initial failure occurs by translational sliding (basal shear) located in the thin event beds (Fig. 29.5). A slab of sediments starts moving down-slope along these beds, as they are softer and more sensitive than the surrounding sediments. The regional extent and low-permeability of the beds may also allow for the formation of artesian groundwater pressure at different stratigraphic levels (Fig. 29.5). This causes lowering of effective stresses in the surrounding deposit and undermines slope stability. An excess pore pressure (8 kPa in average) exists at 3 mbsf (see "P" in Fig. 29.1c for piezometer location). Unfavorable groundwater conditions (e.g., periods of heavy rainfall) as a pre-conditional factor in place at the time of external triggering of the initial landslide (from human activity) may lead to a landslide that develops retrogressively from the fjord to the shore. In the case where quick clay pockets are present below the shoreline deposits and on land, these slides can extend far inland with dramatic consequences such as in the case of the 1996 landslide (Longva et al. 2003).

A prerequisite for the occurrence of the weak event beds, such as those found in this study, is the presence of prehistoric clay-slide activity in the catchment and a low to moderately dipping fjord margin on which the event beds are able to accumulate (Hansen et al. 2011). As sensitive, glacio-marine sediments and clay-slides are common in uplifted fjord valleys of Canada and Scandinavia, and to a lesser extent in Alaska, beds with a similar origin as to those found in this study could play an important role for the stability of other near-shore areas (e.g., Saguenay fjord; Perret et al. 1995). Detecting these slide-prone beds is, therefore, of great importance for geohazards assessment. Such slide-prone beds have successfully been detected in Sørfjorden using high-resolution seismic data in combination with in-situ geotechnical testing because of their characteristic acoustic and geotechnical signature.

Acknowledgments We thank the SEABED project with the Norwegian Deepwater Programme (www.ndwp.org) for financial support. Jacques Locat and Chris Baxter are acknowledged for their constructive reviews. This is contribution no. 354 of the International Centre for Geohazards.

References

Gregersen O (1999) Kvikkleireskredet i Finneidfjord 20 juni 1996. NGI Rep 980005–1. NGI, Oslo

Hansen L, L'Heureux J-S, Longva O (2011) Turbiditic, clay-rich event beds in fjord-marine deposits caused by landslides in emerging clay deposits – paleoenvironmental interpretation and role for submarine mass-wasting. Sedimentology 58: 890–915 doi:10.1111/j.1365-3091.2010.01188.x

Kvalstad TJ, Andresen L, Forsberg CF, Berg K, Bryn P, Wangen M (2005) The Storegga slide: evaluation of triggering sources and slide mechanics. Mar Petrol Geol 22:245–256

L'Heureux J-S, Hansen L, Longva O, Emdal A, Grande L (2010) A multidisciplinary study of submarine landslides at the Nidelva fjord delta, Central Norway – implications for geohazards assessments. Nor J Geol 90:1–20

Lastras G, Canals M, Urgeles R, Hughes-Clarke JE, Acosta J (2004) Shallow slides and pockmark swarms in the Eivissa Channel, western Mediterranean Sea. Sedimentology 51:1–14

Leduc J, Bilodeau G, De Vernal A, Mucci A (2002) Distribution of benthic foraminiferal populations in surface sediments of the Saguenay Fjord, before and after the 1996 flood. Palaeogeogr Palaeoclimatol Palaeoecol 180:207–223

Longva O, Janbu N, Blikra LH, Boe R (2003) The 1996 Finneidfjord slide: seafloor failure and slide dynamics. In: Locat J, Mienert J (eds) Submarine mass movements and their consequences, 531–538. Kluwer Academic, Dordrecht

Olsen L, Sveian H, Blikra LH (1996) KORGEN 1927 II. Quaternary map – M: 1:50 000, with description. Geological Survey of Norway

Perret D, Locat J, Leroueil S (1995) Strength development with burial in fine-grained sediments from the Saguenay Fjord, Quebec. Can Geotech J 32:247–262

Rosenquist IT (1953) Considerations on the sensitivity of Norwegian quick-clays. Geotechnique 3:195–200

Seifert A, Stegmann S, Lange M, Wever T, Mörz T, Kopf A (2008) *In situ* pore pressure evolution during FF-CPT measurements in soft sediments of the western Baltic Sea. Geo-Mar Lett. doi:org/10.1007/s00367-008-0102-x

Sills GC, Wheeler SJ (1992) The significance of gas for offshore operations. Cont Shelf Res 10:1239–1250

Steiner A, L'Heureux JS, Kopf A, Vanneste M, Longva O, Lange M, Haflidason H (2012) An in-situ free-fall piezocone penetrometer for characterizing soft and sensitive clays at Finneidfjord, northern Norway. In: Yamada Y et al (eds) Submarine mass movements and their consequences, vol. 31, Advances in natural and technological hazards research. Springer, Dordrecht, pp 99–109

St-Onge G, Mulder T, Piper DJ W, Hilaire-Marcel C, Stoner JS (2004) Earthquake and flood-induced turbidites in the Saguenay Fjord (Québec): a Holocene paleoseismicity record. Quaternary Science Reviews 23:283–294

Vardy ME, Dix JK, Henstock TJ, Bull JM, Gutowski M (2008) Decimeter-resolution 3D seismic volume in shallow water: A case study in small-object detection. Geophysics 73(2):33–40

Chapter 30
Mass Movements in a Transform Margin Setting: The Example of the Eastern Demerara Rise

France Pattier, Lies Loncke, Verginie Gaullier, Bruno Vendeville, Agnès Maillard, Christophe Basile, Martin Patriat, Walter R. Roest, and Benoît Loubrieu

Abstract The eastern Demerara Rise located offshore French Guiana was surveyed in 2003 (GUYAPLAC cruise, part of the French EXTRAPLAC program) using multibeam bathymetry and imagery, 6-channel seismic data and 3–5 kHz echosounding. Analysis of seismic data shows that the flank of the Demerara Rise endures repetitive sliding of its Paleogene to Neogene sedimentary cover towards the ocean. Fluid escapes seem to be closely associated with the activity of those slides and deep faults

F. Pattier (✉)
Géosciences Marines, IFREMER, BP70, 29280 Plouzané, France

CEFREM – UMR 5110, Université de Perpignan Via Domitia,
52 Avenue Paul Alduy, 66860 Perpignan Cedex, France
e-mail: france.pattier@etudiant.univ-perp.fr

L. Loncke • V. Gaullier
CEFREM – UMR 5110, Université de Perpignan Via Domitia,
52 Avenue Paul Alduy, 66860 Perpignan Cedex, France

B. Vendeville
FRE 3298 CNRS, Université de Lille 1, Bâtiment SN5,
59655 Villeneuve d'Ascq Cedex, France

A. Maillard
LMTG, Université UPS (SVT-OMP), 14 Avenue Edouard Belin,
31400 Toulouse, France

C. Basile
Laboratoire de Géodynamique des Chaînes Alpines, UMR-CNRS 5025,
Observatoire des Sciences de l'Univers de Grenoble, Université Joseph Fourier,
Maison des Géosciences, 1381 rue de la Piscine,
38400 St. Martin d'Hères, France

M. Patriat • W.R. Roest • B. Loubrieu
Géosciences Marines, IFREMER, BP70, 29280 Plouzané, France

Y. Yamada et al. (eds.), *Submarine Mass Movements and Their Consequences*,
Advances in Natural and Technological Hazards Research 31,
DOI 10.1007/978-94-007-2162-3_30,

seems to impact the location of the main headscarp. We suspect fluid overpressures and the specific architecture of transform boundaries ("free border") to be key parameters in the development of wide MTD's retrogressively eroding the eastern Demerara Rise.

Keywords Transform margin • MTD's • Demerara Rise • Fluid escapes

30.1 Introduction

Transform margins represent 30% of continental passive margins. Sediment mass movements in those geological settings has been poorly studied up to now even though these margins display many architectural elements that amplify the potential for mass failure. Such elements include:

– a steep (~20°) ocean-continent boundary inherited from the vertical transform fault along which opening occurred. Therefore the continental slope is subjected to erosional processes, the sediments being frequently mobilized by gravity instabilities at different scales (De Caprona 1992; Mosher et al. 2005; O'Regan and Moran 2007; Loncke et al. 2009).
– Syn or post-transform layers can outcrop along the ocean-continent transition and the post-transform unconformity is generally tilted landward or seaward depending on the marginal ridge development. This may favors the development of stratigraphic décollement layers

The objective of this work is to demonstrate the prominent role of mass transport processes along transform margins in the delivery of sediments to the deep ocean. The transform margin along Demerara Rise is used to typify this environment. In addition, controlling factors in mass failure that may be specific to this margin are presented.

30.2 Geological Setting

The study area is located on the French Guiana margin, in the western Equatorial Atlantic Ocean (Fig. 30.1a). There, the Demerara Rise prolonging the continental shelf. This rise is 380 km long and 220 km wide and delimited by a steep continental slope representing the continent to ocean transition.

This margin formed during two successive stages: (1) In the Early Jurassic, the opening of the central Atlantic created the western edge of the Demerara Rise as a divergent margin (Klitgord and Schouten 1986; Gouyet 1988; Unternehr et al. 1988); (2) at the end of the Early Cretaceous, during opening of the Equatorial Atlantic, the northern and eastern border of the Demerara Rise separated from the Guinea Rise in a strike-slip regime along a main transform zone (Gouyet 1988; Unternehr et al. 1988; Greenroyd et al. 2008) (Fig. 30.1a).

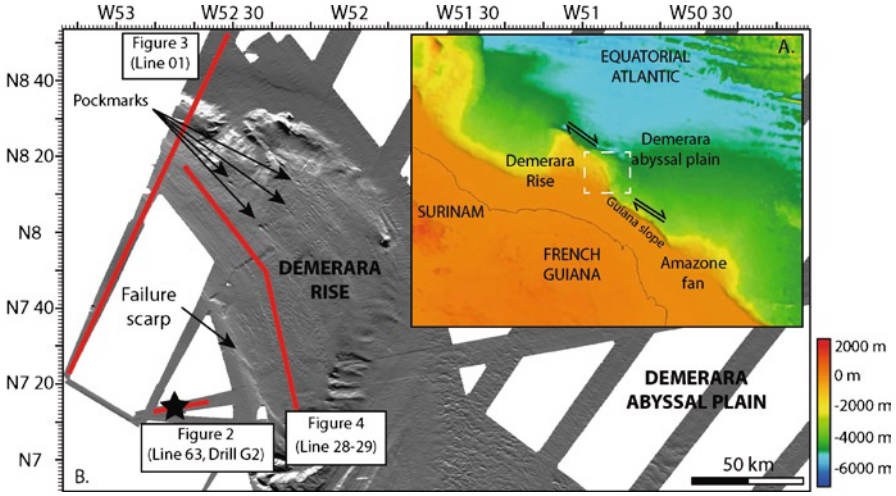

Fig. 30.1 (**a**) Location of the study area (*white dotted box*) in the western equatorial Atlantic ocean (**b**) Location of seismic lines profiles shown in Figs. 30.2, 30.3 and 30.5 and the G2 drill hole position

Along Demerara Rise, the transform segments are NW-trending and the divergent segments are NE-trending (Fig. 30.1a). Transform activity ceased in the upper Albian and organic rich sediments deposited between the Turonian to Cenomanian (Gouyet 1988; Mosher et al. 2005) followed by deposition of a carbonaceous to clay rich sedimentary cover (Mosher et al. 2005). Sedimentation rates are low during the Cenozoic (in average less than 1 cm/ky) (Danelian et al. 2005). The eastern Demerara Rise seems to have been tilted seaward during the Paleogene and no clear marginal ridge could be observed (Maillard et al. 2010; Loncke et al. 2010). In the western Demerara Rise, giant slumps affect Oligocene to recent sediments (O'Regan and Moran 2007; Ingram et al. 2011).

30.3 Dataset

The French Guiana margin and the adjacent Demerara abyssal plain were surveyed in 2003 during the GUYAPLAC cruise onboard the R/V l'Atalante, as a part of the EXTRAPLAC French Program (Ifremer-IFP–SHOM-IPEV). The dataset comprises: (1) EM12-Simrad multibeam bathymetry and backscatter imagery, (2) 3.5 kHz echograms, (3) 6-channel seismic profiles. Bathymetric data were processed using CARAIBES software developed by IFREMER using a 100 m resolution grid. The combination of bathymetric and 3.5 kHz analyses allowed identification and characterization of the main recent sedimentary processes shaping the study area (Loncke et al. 2009; Gaullier et al. 2010).

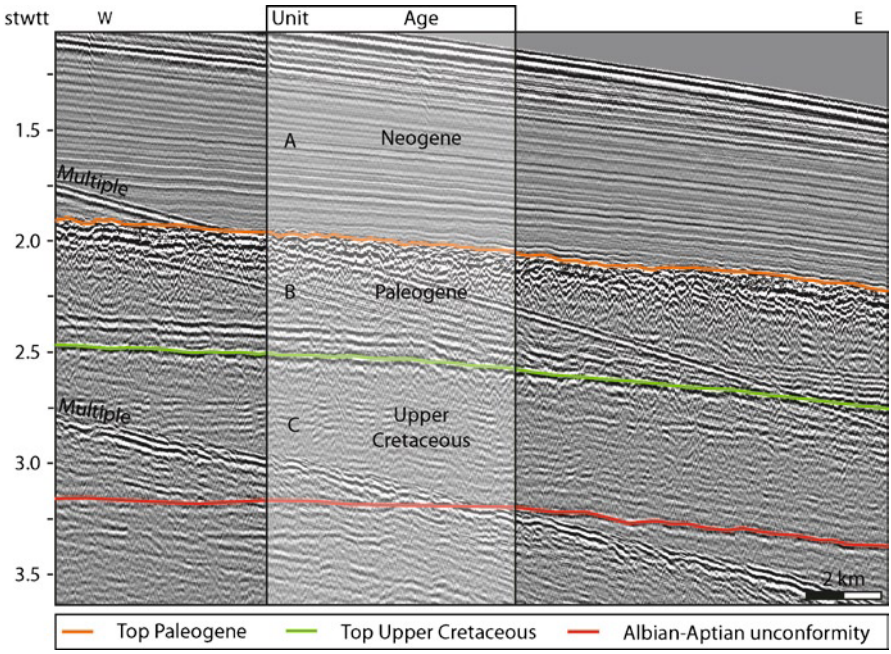

Fig. 30.2 Seismic units on seismic line Guyaplac 63 (Vertical Exaggeration: 4). The stratigraphy is correlated to drill hole G2 (Gouyet 1988). The *seismic line* is located in Fig. 30.1b

In this paper, we present mainly the GUYAPLAC seismic data calibrated by a correlation to the G2 industrial drill site presented by Gouyet (1988) (Fig. 30.2).

30.4 Results

30.4.1 Seismic Stratigraphy

The sedimentary cover along eastern Demerara Rise is deposited above the post-transform Albian-Aptian unconformity (in red on Fig. 30.2) that caps deformed upper-cretaceous and older rocks. The seismic stratigraphy of this sedimentary cover is divided into three main units:

– Unit C is poorly reflective, especially in its lower part where the transparent seismic facies corresponds to the Cenomanian-Turonian Black-shales. This unit is upper Cretaceous in age.
– Unit B is characterized by diffractions in the upper part, transparent seismic facies in the middle part, and a reflective lower part. This unit is Paleogene in age, with the base of Eocene located at the boundary between the transparent and reflective facies, and the base of Paleocene at the base of the reflective lower part.

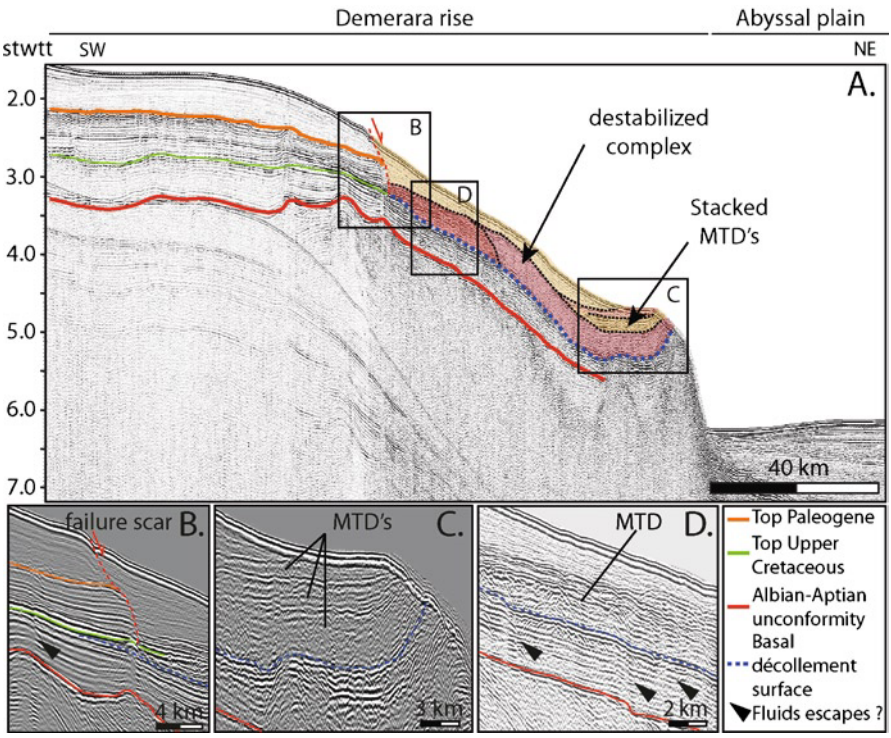

Fig. 30.3 Demerara Rise on seismic line Guyaplac 01 (see location Fig. 30.1) (Vertical Exaggeration: 5). The basal décollement surface is indicated by a *dotted blue line*

– The uppermost unit A shows reflections that are laterally continuous high amplitude reflections. This unit is Neogene in age, and its base fits with the base of Miocene.

30.4.2 Seismic Analysis

A regional seismic line across the eastern Demerara Rise shows that the Albian-Aptian unconformity and the Cenozoic sedimentary cover are dipping seaward (Fig. 30.3). Where the plateau is tilted seaward, the post-transform sedimentary cover is clearly affected by numerous mass transport deposits (MTD's) (Fig. 30.3a). Those initiate far inboard on the Demerara rise along a failure scarp that is clearly visible on bathymetry (Fig. 30.1b). There, a near vertical normal fault affects recent sediments (Fig. 30.3b). This fault seems to connect to a deeper fault slightly offsetting the Albian unconformity (Fig. 30.3a, b). Going downslope, the slide complex evolves into stacked disorganized bodies where seismic reflectors are sparse. At least four different successive events are identified (Fig. 30.3c). The oldest one is sealed by

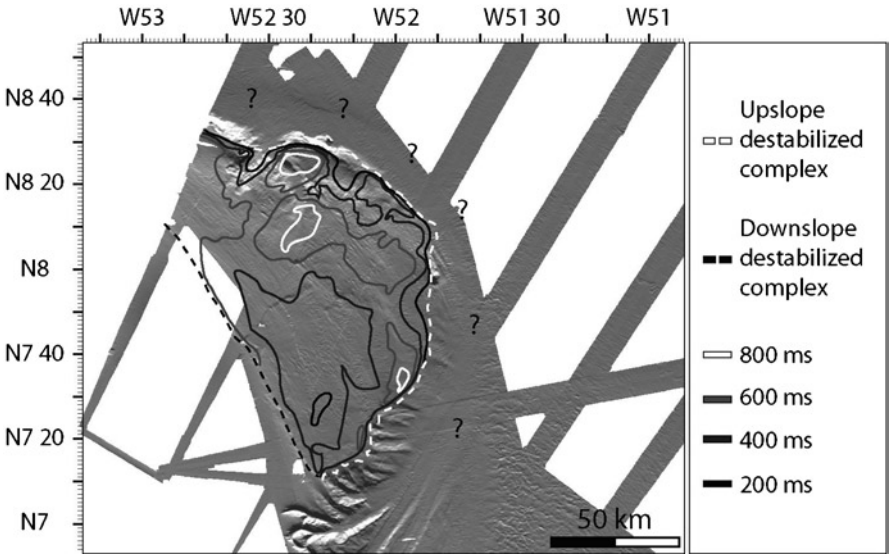

Fig. 30.4 Isopach contour map (in ms) of the destabilized complex. The distal termination of the oldest slides is questionable (*?* on figure) since no age calibration exist in the Demerara abyssal plain

non-remobilized Paleogene sediments (Fig. 30.3b). The youngest one is late Neogene to recent. The basal décollement layer (in dotted blue in Fig. 30.3a.) seems to follow the main stratigraphic horizons. No clear compressional deformations have been observed in the distal tip of sided masses (Fig. 30.3c). The termination of those MTD's is sharp approaching the Demerara steep border (Figs. 30.3a and 30.4).

The total thickness of this destabilized complex was mapped (Fig. 30.4) in order to better quantify the cumulative importance of those events. This slide complex, about 10.521 km² in area shows variable thicknesses. The MTD's thickness is 800–900 ms towards the NE border of the plateau. Towards the east, thicknesses decrease (200 ms). Maximum thicknesses are observed along the Demerara NE border. Some MTD's likely extend onto the abyssal plain (Fig. 30.4). The lack of drill data prevents any accurate correlations of MTD's recognized in the abyssal plain with Demerara Rise MTD's.

Bellow the MTD's, Cretaceous to Paleogene sediments appear highly faulted by sub-vertical faults or crossed by vertical pipes. These pipes may have been may generated by fluid escapes (Figs. 30.3d and 30.5). The faults occur in two different directions seismic lines with similar wavelength (2 km). Therefore, we interpreted those as polygonal faults (Fig. 30.5). This evidence past or even recent dewatering processes (some polygonal faults reach the seafloor upslope the failure scarp). This polygonal fault interval mainly affects unit B (Paleogne) but faults frequently propagate more or less in units A and C. Under the destabilized complex, they even affect Cretaceous sediments and root on the Albian-Aptian unconformity (Fig. 30.5).

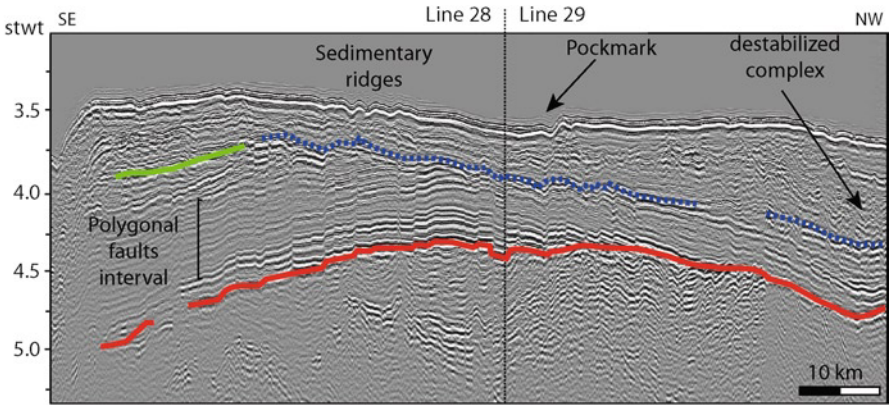

Fig. 30.5 Polygonal faults on seismic line Guyaplac 28–29 (see location Fig. 30.1) (Vertical Exaggeration: 5)

On surface data (bathymetry and imagery) numerous giant pock-marks (Figs. 30.1 and 30.5), reaching 1–2 km in diameter, affect the Demerara Rise seafloor. These pock-marks appear on the surface of MTD's but are difficult to image to depth on seismic data.

We suspect that this faults interval may allow fluid transfer between pre-Albian deformed sediments and Neogene sediments and MTD's (see vertical pipes) and plays a role in the triggering of the observed mass movements.

30.5 Discussion – Controlling Factors

The eastern Demerara Rise endured significant and repetitive mass movements during the Cenozoic. These mass failures initiate far inboard on the Demerara Rise where slope gradients are low, suggesting a structural control and/or retrogressive evolution of slides from the steep continental slope to the inner rise through time. The basal décollement layer seems to follow stratigraphy and outcrops along the continental slope. The MTD's dislocate polygonal fault intervals and are systematically associated with fluid escape structures on the seafloor (giant pockmarks).

These observations suggest that: (i) fluid overpressures could play a role in initiating some of those slides in weakening some stratigraphic horizons, (ii) the structure of the margin is a key parameter in allowing massive sliding of the Cenozoic sedimentary cover towards the ocean by localizing failure scars (above deep faults) and creating a "free border" towards the ocean.

Recent experimental models applied to natural slides in New-Zealand have shown that the combination of a free border (post-albian sediments outcrop on the slope) and fluid overpressures can be extremely favorable for triggering massive retrogressive slides (Lacoste et al. 2011).

During the ODP leg 207, Mosher et al. (2005) described erosion events in late Miocene along the western Demerara Rise. O'Regan and Moran (2007) even estimated that 220 m sediment was removed during this slide. It has been shown also that Cretaceous deposits are overpressured (O'Regan and Moran 2007). The mass movement and erosion defined by O'Regan and Moran (2007), could be an equivalent of the described destabilized complex on the eastern Demerara Rise.

Alternatively, some authors (Ingram and Wise 2006; Ingram et al. 2011) proposed that the western Demerara slide could relate to massive hydrate dissociation. The ice-house to green-house transition (Eocene-Oligocene transition; Seranne et al. 1999) could be an excellent candidate for causing such events. Those hypothesis are still to investigate more in details and probably need additional dating and numerical/experimental modellings.

Finally, the lack of present seismicity supports the hypothesis of over-pressure or climatic initiation but we can not exclude that a Cenozoic seismic event could have occurred, as proposed on the western Demerara Rise (Ingram et al. 2011).

30.6 Conclusions

The western Demerara Rise is a rather poorly sedimented passive transform margin where important slides were not expected. Our analysis show at the contrary, that slides are massive (10.521 km^2) and repetitive through time. We suspect that fluid overpressures combined with outcrop of potential décollement layers (free border effect) are key parameters in the development of wide mass movements retrogressively eroding the Demerara Rise. Climatic and other structural controls can however not be excluded in controlling the development of those destabilized complexes. Further analysis is necessary to better investigate those possibilities.

Acknowledgments The authors would like to thank Extraplac for giving access to this data set and the French Research Program "Action Marges" for supporting this project. We also deeply thank David Mosher and Francky Saint Ange for their very useful reviews and comments.

References

Danelian T, Le Callonnec L, Erbacher J, Mosher DC, Malone MJ, Berti D, Bice KL, Bostock H, Brumsack H-J, Forster A, Heidersdorf F, Henderiks J, Janecek TJ, Junium C, MacLeod K, Meyers PA, Mutterlose JH, Nishi H, Norris RD, Ogg JG, O'Regan MA, Rea B, Sexton P, Sturt-Fredricks H, Suganuma Y, Thurow JW, Wilson PA, Wise SW, Glatz C (2005) Résultats préliminaires sur la sédimentation pélagique de l'Atlantique tropical au Crétacé et au Tertiaire (plateau de Demerara, Leg ODP 207). C R Geosci 337(6):609–616

De Caprona G (1992) The continental margin of western Côte d'Ivoire: structural framework inherited from intra-continental shearing. Geologiska Institutionen, Göteborg, 150 p, Publ A 69. ISBN 91-7032-685-1

Gaullier V, Loncke L, Droz L, Basile C, Maillard A, Patriat M, Roest WR, Loubrieu B, Folens L, Carol F (2010) Slope instability on the French Guiana transform margin from swath-bathymetry

and 3.5 kHz echograms. In: Mosher D et al (eds) Submarine mass movements and their consequences, Advances in natural and technological hazards research, vol 28. Springer, Dordrecht, pp 561–571

Gouyet S (1988) Evolution tectono-sédimentaire des marges guyanaise et Nord-Brésilienne au cours de l'ouverture de l'Atlantique Sud. PhD thesis, University of Pau et des Pays de l'Adour, pp 974

Greenroyd CJ, Peirce C, Rodger M, Watts AB, Hobbs RW (2008) Do fracture zones define continental margin segmentation ? – Evidence from the French Guiana margin. Earth Planet Sci Lett 272(3–4):553–566

Ingram WC, Wise SW Jr (2006) Anatomy of oligocene-miocene debris flows and slumps from Demerara Rise: implications for margin destruction. American Association of Petroleum Geologists 2006 annual Convention, Houston, 11–14 Apr 2006 (Abstract)

Ingram WC, Mosher DC, Wise SW Jr (2011) Biostratigraphy of an upper Miocene mass-transport deposit on Demerara Rise, northern South American margin. In: Shipp C, Weimer P, Posamentier H (eds) Mass-transport deposits in deepwater settings. SEPM Special Publication 96, SEPM, Tulsa, pp 475–498

Klitgord KD, Schouten H (1986) Plate kinematics of the central Atlantic. In: Vogt PR, Tuckolke BE (eds) The western north Atlantic region, The geology of North America, vol. M. Geological Society of America, Boulder, pp 351–377

Lacoste A, Vendeville B, Loncke L (2011) Influence of combined incision and fluid overpressure on slope stability: experimental modelling and natural applications. J Struct Geol 33(4):731

Loncke L, Droz L, Gaullier V, Basile C, Patriat M, Roest W (2009) Slope instabilities from echo-character mapping along the French Guiana transform margin. Mar Petrol Geol 26(5):711–723

Loncke L, Gaullier V, Basile C, Maillard A, Patriat M, Roest W, Vendeville B (2010) Deep to surface processes of the French Guiana transform margin, eastern Demerara Plateau, II North Atlantic conjugate margins conference, Lisbon, 29 Sept–1 Oct 2010

Maillard A, Patriat M, Basile C, Loncke L, Gaullier V, Folens L, Vendeville B (2010) Syn- and post-rift evolution of the Demerara plateau, French Guiana transform margin. EGU general assembly, Vienna, 02–07 May 2010, Geophysical Research Abstracts, vol 12, EGU2010-10979, 2010

Mosher DC, Erbacher J, Zuelsdorff L, Meyer H (2005) Stratigraphy of the Demerara Rise, Suriname, South America: a rifted margin, shallow stratigraphic source rock analogue. American association of petroleum geologists annual meeting, Calgary, 19–22 June

O'Regan M, Moran K (2007) Compressibility, permeability and stress history of sediments from Demerara rise. In: Mosher, DC, Erbacher J, Malone MJ (eds) Proceedings of the ocean drilling program, Scientific Results, vol 207, College Station

Séranne M (1999) Early Oligocene stratigraphic turnover on west Africa continental margin: a signature of the Tertiary greenhouse to icehouse transition? Terra Nova 11:135–140

Unternehr P, Curie D, Olivet JL, Goslin J, Beuzart P (1988) South Atlantic fits and intraplate boundaries in Africa and South America. Tectonophysics 155:169–179

Part IV
Mechanics of Mass-Wasting in Subduction Margins

Chapter 31
Slope Failures in Analogue Models of Accretionary Wedges

Yasuhiro Yamada, Yusuke Oshima, and Toshifumi Matsuoka

Abstract Sandbox models commonly produce slope failures and mass-transport on the top free surface, which can be an analogue for submarine slides. We have been conducting shortening experiments to model accretionary wedges at subduction margins under several basement configurations of the subducting plate. Slope failures periodically occur when thrust faults reach the top surface of the models. These failures are triggered by steepening of slopes related to the displacement along the underlying thrusts. Internal stress field and physical property of materials may have little impact on the pattern and geometry of failures. Experiments with a topographic relief (e.g., horst) in the basement produce irregular distribution in time of thrusting. Long-lived thrusts, generally initiate at the foot of topographic highs, tend to form longer slopes with thick piles of failed sediments in the footwall. These suggest that anomalous amount of failed sediments in accretionary wedge regions can be used to assume topographic relief in the basement that affected the geometry of detachment. When subducted, such detachment geometries may not be easy to recognize with geophysical technique.

Keywords Analogue model experiments • Submarine landslide • Slope-failure • Subduction margin • Accretionary wedges • Geohazard • Seismic reflection

31.1 Introduction

Slope failures are commonly observed along subduction margins. Recent high-resolution geophysical techniques recognized a number of large-scale submarine slides and smaller size of submarine slope failures along subduction margins around

Y. Yamada (✉) • Y. Oshima • T. Matsuoka
Department of Earth Resources Engineering, Kyoto University, Katsura, Nishikyo, Kyoto 615-8540, Japan
e-mail: yamada@earth.kumst.kyoto-u.ac.jp

Y. Yamada et al. (eds.), *Submarine Mass Movements and Their Consequences*, Advances in Natural and Technological Hazards Research 31,
DOI 10.1007/978-94-007-2162-3_31,

the Japanese island arc system; the Japan Trench, the Izu-Mariana Trench, and the Nankai Trough (Cadet et al. 1987; Kobayashi et al. 1987; Lallemand et al. 1989; Ogawa et al. 1997). The sizes of these submarine mass movements tend to be smaller than those in the passive continental margins (e.g., over 5,000 km^3 of the Storegga slide near Norway; Kenyon 1987). This may be a consequence of characteristics of subduction margins, such as frequent seismicity, the steepening of ocean-floor slopes due to active folding, and elevated pore pressures during dewatering enhanced by tectonic deformation (Yamada et al. 2010).

Along the Nankai Trough, off SW Japan, a number of submarine mass movements have been identified in the region of a large and relatively steep accretionary prism complex. Investigations by deep-tow sonar and manned-dives discovered a number of present submarine slides in the vicinity of active thrusts (Henry et al. 2002; Kawamura et al. 2008). Most of these landslides are observed along the steeper trench-side of elongate hills. Yamamoto et al. (2007, 2009) examined outcrops of the Pleistocene and late Miocene submarine slide and concluded that earthquake vibrations may have triggered the slides.

The primary kinematics of accretionary prism formation has been explained by off-scraping of sediments on the subducting oceanic plate by a sub-horizontal compressional stress environment, and this has been investigated by analogue models (e.g., Colletta et al. 1991; Huiqi et al. 1992; Willet 1992; Lallemand et al. 1992; Mulugeta and Koyi 1992; Gutscher et al. 1996; Nieuwland et al. 2000; Koyi and Vendeville 2003; Yamada et al. 2006). Analogue experiments require to follow the scaling laws (Hubbert 1937) and to approximate the rheology of rocks. Rock under deformation behaves approximately as elasto/frictional-plastic body, with strain-hardening preceding failure (at peak strength), followed by strain-softening until a dynamically constant shear load is reached (Jager and Cook 1976). Granular materials such as sand behave in a similar way (Lohrmann et al. 2003), and can be used in experiments to model rocks (sandbox models).

Slope failures in analogue models have been investigated in details by Yamada et al. (2010), performing shortening of dry sands above three rigid basement blocks delimited by two thrust faults. Shortening produced a long continuous slope on the model surface on which a number of slope failures were identified. These slope failures can be classified into two types: frequent minor failures at the lower part of the slope, and less-frequent major failures at the top of the slope. The major failures sometimes occur where several minor failures were observed. This suggests that minor failures produce instability in the slope and this topographic instability may trigger the subsequent major failures. The experiments also show lateral migration of the failures and this may also be explained by local instability of the slope generated by the earlier failures. The results can be applied to submarine mass movements because the pore space has been saturated by single fluid, i.e. air in models and water in nature (Yamada et al. 2010).

The analogue models of Yamada et al. (2010) used pre-defined planar thrusts in the basement thus the deformation of the sand layer is a type of a forced fold. This kinematics of deformation is different from that of natural accretionary prisms formed under horizontal shortening environment. Purpose of this paper is to examine

geometry and kinematic processes of the slope failures in the analogue models of simplified accretionary prisms under horizontal shortening. The effects of basement configurations on the geometry of slope failures are also addressed.

31.2 Methods

We performed a series of simplified shortening experiments above a horizontal planar basal plate. The experimental rig has a moving-wall that shortens the experimental material at a rate of 10 mm/min and a transparent sidewall to observe the deformation (Fig. 31.1). The initial dimensions of the sand body in the experiments were 100 cm in length, 30 cm in width, and 6 cm in thickness. The sand was sprinkled from 30 cm above the model surface to avoid preexisting weak planes and not pre-compacted before deformation.

Two configurations were examined in this study simulating a flat basement (flat model, Fig. 31.1a) and the presence of an horst above the basement (horst model, Fig. 31.1b). The horst is a rigid block of 30 mm wide (at the top) and 30 mm high (Fig. 31.1c). This horst block is fixed to the flat basement at 50 cm from the initial position of the moving wall.

Time-lapse digital pictures of the experiments, acquired and saved automatically every 15 s using a PC-based controller, were analyzed using the Digital Image

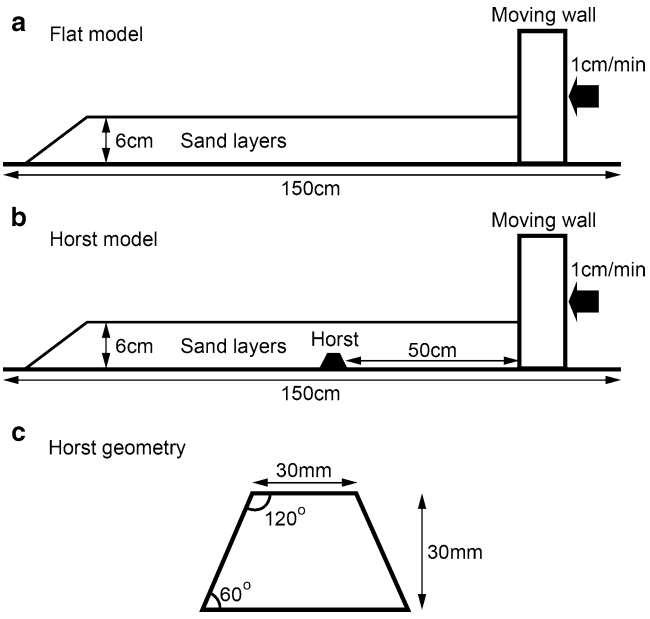

Fig. 31.1 Deformation rig used in this study. The flat model uses the planar base plate (**a**) and the horst model uses a rigid horst block on the base (**b**, **c**)

Correlation (DIC) technique. This technique is also known as Particle Image Velocimetry (PIV) that is commonly used for dynamic flow analysis (e.g., Hryciw et al. 1996), and has been applied to strain monitoring in experimental structural geology (White et al. 2001; Adam et al. 2005; Wolf et al. 2003; Yamada et al. 2006, 2010). The method divides the pictures into sub-units and calculates the displacement field of each unit by correlating the pattern of brightness in the time series of pictures. DIC analysis can cover various types of structural deformation, from folding to the stick-slip behavior of faults (Adam et al. 2005), thus the technique is useful in the quantitative analysis of deformation in analog experiments. In this paper, we used the commercial software StrainMaster developed by LaVision.

31.3 Results

31.3.1 Flat Model

The shortening applied to the flat model produced a series of thrusts and uplifting of the material typical of accretionary wedges (Fig. 31.2). At the deformation front, the thrust faults initiate as a pair, a fore-thrust and a back-thrust, to form a V-shaped pop-up structure. The fore-thrust then continues the displacement until new thrusts generate at the deformation front. The activity of the back-thrust, however, terminates after a minor displacement and a new back-thrust initiate immediately underneath the previous back-thrust forming a piggy-back sequence. The model surface produces a gentle slope that keeps an angle of ca. 7° throughout the experiment, as suggested by the critical taper theory based on the balance of forces affecting on the accretionary wedge (Davis et al. 1983; Dahlen and Suppe 1984; Dahlen 1984).

Slope failures are commonly observed at the slopes in front of the frontal thrust (Fig. 31.2). This slope is generated by periodic failure events triggered by steepening of the slope due to displacement of the thrust, thus the height of the slope increases as the development of the underlying thrust. The failed sediments deposited in the footwall of the thrust, thus the lower part of the slope consists of this failed sediments. The failure events on this slope discontinue when a new thrust generates.

31.3.2 Horst Model

Shortening applied to the horst model initially generates several thrust systems similar to the flat model, then a pair of thrusts (a fore-thrust and a back-thrust) generate in front of the horst after 13 cm of shortening (Fig. 31.3). The fore-thrust continues the activity until the end of this experiment without generating further thrust formation.

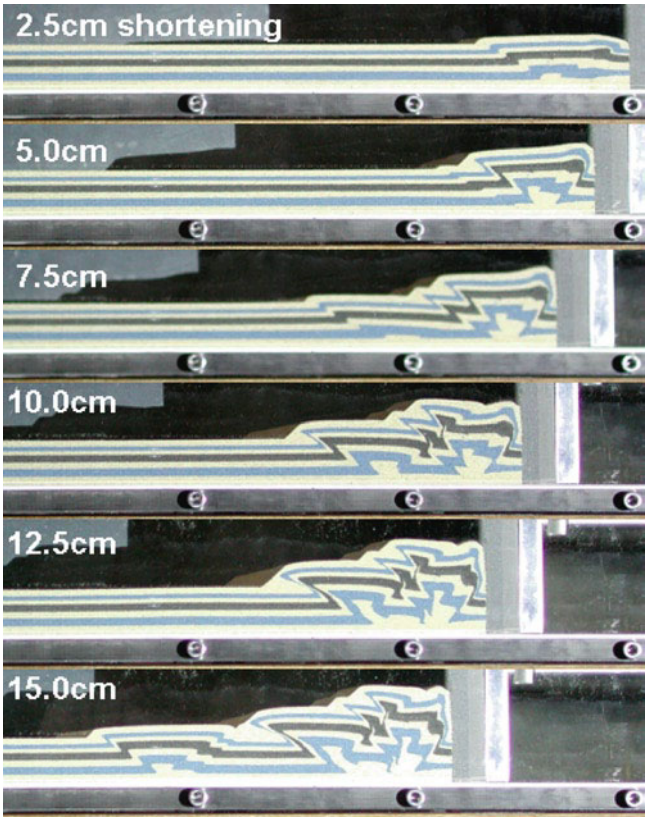

Fig. 31.2 Results of the flat model characterized by typical accretionary wedge formation and slope failures only above active thrusts

The geometry of this thrust is planar in the earlier stages (ca. 13 · 17 cm of shortening), then shows a convex-upward curvature. The back-thrust ceases its activity after a few cm of displacement then a new back-thrust generates immediately underneath the previous back-thrust. The geometry of the back-thrust is generally planar. As a result, the accretionary wedge extremely uplifted between the horst structure and the moving wall (Fig. 31.3).

The slope failures are also commonly observed at the frontal thrust in the horst model (Fig. 31.3). Several faults that were observed in the earlier stages in the experiment produced slope failure events but these are relatively minor. The fore-thrust formed after 13 cm of shortening has a long history of activity, thus the slope also continuously develops throughout the experiment with periodic failure events on the slope. The failed sediments deposit at the foot of the slope then are overlaid by the thrust hangingwall and preserved showing wedge geometry on the cross-section.

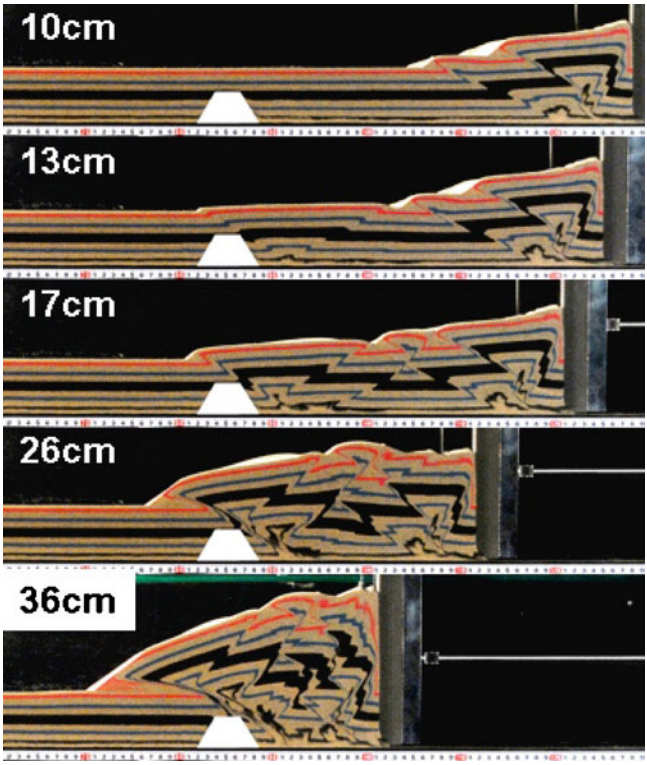

Fig. 31.3 Results of the horst model characterized by a long-lived thrust causing continuous slope failures

31.4 Discussions

31.4.1 Geometry of Failed Deposits

The failed sediments generally show wedge geometry in the footwall of the thrust (Fig. 31.4). On the cross-section, the area of the failed sediments is generally greater than that of estimated area in the hanging wall from where these materials were failed (Fig. 31.4). This volume increase is commonly observed (cf. Yamamoto et al. 2012), since the failed sediments increase the inter-granular porosity during sliding and is released from confining pressure. The internal structure of the failed sediments is not clear but can be partly assumed from the cross-section (i.e. Fig. 31.5). The series of minor bands sub-parallel to the thrust surface suggests that the sediments experienced simple shearing by thrusting, in agreement with Yamada et al. (2010).

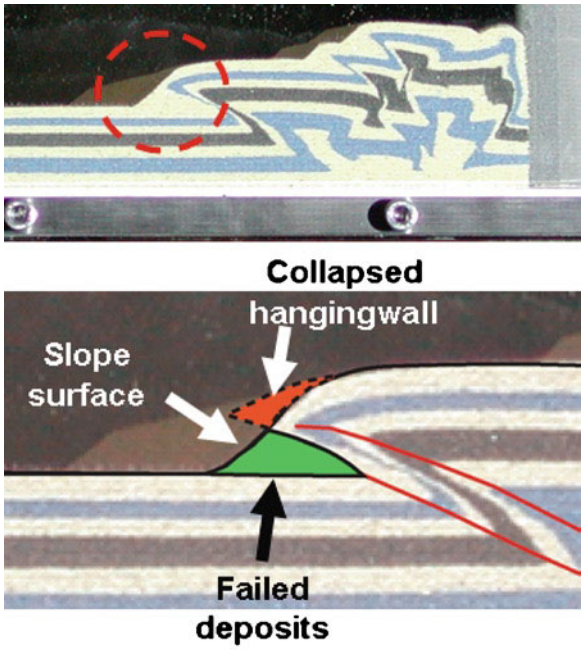

Fig. 31.4 Slope failures at the frontal thrust in the flat model

31.4.2 Activity of Slope Failures

In the both models, the failure events are only observed at the slopes corresponding to the frontal thrust. When the frontal thrust ceases its activity and a new frontal thrust is generated, the failure events also move from the slope above the abandoned thrusts towards the new, active one. Slope failure characterizes, therefore, the slope above the outer thrust faults, which accommodates the majority of deformation. This phenomenon may be explained by rotation of the younger thrust hanging-wall, which also correspond to the hinterland-ward rotation of the entire imbricate stack of thrusts. This causes the decrease of the slope angle above the stacked older thrusts.

31.4.3 Slope Failures by Anomalous Basement Topography

In the horst model, the fore-thrust generated in front of the horst structure showed an extremely long period of activity accompanied by a number of periodic slope failures (Fig. 31.3). In the later stages of experiment (e.g., 26 cm of shortening), this thrust shows a convex geometry and the space filled by the failed deposits shows an elongated wedge-shape. This geometry of the failed deposits is a characteristic of

the horst model. Since deeply buried beneath the thrust hangingwall, the failed deposits may have better chance to be preserved against possible surface erosion in real accretionary wedges. The extremely uplifted accretionary wedge between the horst structure and the backstop may cause large scale landslides. This is because the steepened slope at the deformation front can be wider than that in the flat model. Such large scale submarine slides are similar to those induced by seamount subduction (e.g., Dominguez et al. 2000). Lewis et al. (1998) and Collet et al. (2001) described continuous development of submarine debris avalanche on the northern Hikurangi margin, NZ, that may have been caused by seamount subduction. The avalanche includes mega-size debris occurred at oversteepened margin front. These suggest that the topographic anomaly of the detachment surface has a strong impact not only on the number but on the size of submarine landslides in accretionary wedges.

31.4.4 Effects of Model Kinematics

The analogue models of Yamada et al. (2010) used pre-defined planar thrusts in the basement and produced a forced fold in their sand layers, thus the materials were not entirely shortened. This is the primary difference between the models in Yamada et al. (2010) and natural accretionary prisms that formed under horizontal shortening throughout. Such horizontal shortening commonly generates ca 10% of reduction in volume in the loosely packed sand layers before the onset of faulting and folding, as Yamada and McClay (2004) demonstrated. This horizontal compaction may change the physical properties of dry sand layers, in particular an increase in cohesion and internal friction (Krantz 1991). These are fundamental parameters to define failure behavior and deformation geometry. The slope failures in both Yamada et al. (2010) and this study, however, showed a similar periodic pattern of development and similar resultant geometry. This suggests that the increases in cohesion and internal friction due to the horizontal compaction may not be strong control on the slope failures in sand layers.

The shortening kinematics also affects the stress field in the material. Cosgrove and Ameen (2000) examined fracture patterns in various folds and showed that the direction of maximum compressional stress axis ($\sigma 1$) is vertical (i.e. extensional) in the uplifted-part of forced folds and it rotates to be sub-parallel to the basement fault in the tightly folded part. In contrast, horizontal shortening generally produces stresses of lateral compression and the $\sigma 1$ direction commonly rotates perpendicular to the thrust surface immediately above the thrust surface, as visualized by Yamada et al. (2006) and Miyakawa et al. (2010) in their granular numerical models. Despite such stress differences, the slope failures in the models of Yamada et al. (2010) and this study show a similar pattern and geometry. This suggests that the internal stress field has little impact on the surface process and the slope failures may be more sensitive to the local triggering factors. The area of slope failures in accretionary wedges is generally located at the frontal thrust and the models of both Yamada et al. (2010) and this study generated a convex geometry of the thrust. As explained

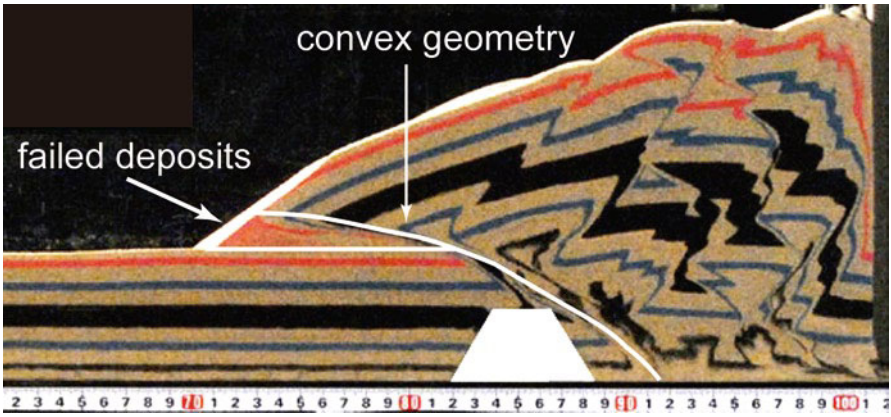

Fig. 31.5 Convex geometry of the thrust and the elongated failed deposits buried underneath the thrust hangingwall, in the horst model

by Yamada et al. (2010) in detail, a thrust of a convex geometry produces extension in the hangingwall and this local extensional setting may have stronger effect on slope instability.

31.5 Conclusions

Slope failures are commonly observed in analogue models of accretionary wedges at subduction margins. The failures are periodically developed on the slope formed above the active frontal thrust. When a new thrust is generated and the previous thrust ceases its activity, the activity of the slope failure also switches to the new slope. The failed sediments are deposited in the thrust footwall and consequently buried and shared by the thrust hangingwall. By comparing the results with other models conducted under different shortening kinematics, internal stress field and physical property of materials may have little impact on the pattern and geometry of failures. Where a topographic relief (e.g., horst) exists in the detachment surface, a long-lived thrust tends to generate and a long slope develops with thick piles of failed sediments in the footwall. Thus anomalous geometry of failed sediments in accretionary wedge regions can be used to assume topographic relief in the basement. This study can be another example to show benefits of analogue model experiment that have been applied to various geologic phenomena.

Acknowledgments The authors appreciate the reviewers Drs. Yuzuru Yamamoto and Gian Andrea Pini for constructive criticism and improving this manuscript. Editorial assistance by Dr. Michael Strasser is also acknowledged. This work was partly supported by Grant-in-Aid for Scientific Research (KAKENHI: 213101115) and by Grant-in-Aid for Scientific Research on Innovative Areas (21107002).

References

Adam J et al (2005) Shear localisation and strain distribution during tectonic faulting – new insights from granular-flow experiments and high-resolution optical image correlation techniques. J Struct Geol 27:283–301

Cadet J-P et al (1987) The Japan Trench and its juncture with the Kuril Trench: cruise results of the Kaiko project, Leg 3. Ear Planet Sci Lett 83:267–284

Colletta B et al (1991) Computerized X-ray tomography analysis of sandbox models: examples of thin-skinned thrust systems. Geology 19:1063–1067

Collot JY et al (2001) The giant Ruatoria Avalanche on the northern Hikurangi margin, New Zealand: result of an oblique seamount subduction. J Geophy Res 106:19271–19297

Cosgrove JW, Ameen MS (2000) A comparison of the geometry, spatial organization and fracture patterns associated with forced folds and buckle folds. In: Cosgrove JW, Ameen MS (eds) Forced folding and fractures. Geological society special publication 169. Geological Society of London, London, pp 7–21

Dahlen FA (1984) Non cohesive critical Coulomb wedges: an exact solution. J Geophy Res 89:10125–10133

Dahlen FA, Suppe J (1984) Mechanics of fold and thrust belts and accretionary wedges: cohesive Coulomb theory. J Geophy Res 89:10087–10101

Davis D, Suppe J, Dahlen FA (1983) Mechanics of fold-and-thrust belts and accretionary wedges: cohesive Coulomb theory. J Geophy Res 88:1153–1172

Dominguez S, Malavieille J, Lallemand SE (2000) Deformation of accretionary wedges in response to seamount subduction: insights from sandbox experiments. Tectonics 19:182–196

Gutscher MA et al (1996) Cyclical behavior of thrust wedges: insight from high basal friction sandbox experiments. Geology 24:135–138

Henry P et al (2002) Surface expression of fluid venting at the toe of the Nankai wedge and implications for flow paths. Mar Geol 3107:1–25

Hryciw RD et al (1996) Video tracking for experimental validation of discrete element simulation of large discontinuous deformations. Comp Geotech 21:235–253

Hubbert MK (1937) Theory of scaled models as applied to the study of geological structures. Geol Soc Am Bull 48:1459–1520

Huiqi L, McClay KR, Powell D (1992) Physical models of thrust wedges. In: McClay KR (ed) Thrust tectonics. Chapman & Hall, London, pp 71–81

Jager JC, Cook NGW (1976) Fundamentals of rock mechanics. Wiley, New York, 585 pp

Kawamura K et al (2008) Structural architecture and active deformation of the Nankai Accretionary Prism, Japan: submersible survey results from the Tenryu Submarine Canyon. Geol Soc Am Bull 121:1629–1646

Kenyon NH (1987) Mass-wasting features on the continental slope of Northwest Europe. Mar Geol 74:57–77

Kobayashi K et al (1987) Normal faulting of the Daiichi-Kashima Seamount in the Japan Trench revealed by the Kaiko I cruise, Leg 3. Earth Planet Sci Lett 83:257–266

Koyi HA, Vendeville BC (2003) The effect of decollement dip on geometry and kinematics of model accretionary wedges. J Struct Geol 25:1445–1450

Krantz RW (1991) Faulting and fault reactivation in laboratory models using sand and sand mixtures. Tectonophy 188:203–207

Lallemand S, Culotta R, von Huene R (1989) Subduction of the Daiichi Kashima Seamount in the Japan Trench. Tectonophy 160:231–247

Lallemand SE, Malavieille J, Calassou S (1992) Effects of oceanic ridge subduction on accretionary wedges: experimental modelling and marine observations. Tectonics 11:1301–1313

Lewis KB, Collot JY, Lallem SE (1998) The dammed Hikurangi Trough: a channel-fed trench blocked by subducting seamounts and their wake avalanches (New Zealand–France GeodyNZ Project). Basin Res 10:441–468

Lohrmann J et al (2003) The impact of analogue material properties on the geometry, kinematics, and dynamics of convergent sand wedges. J Struct Geol 25:1691–1711

Miyakawa A, Yamada Y, Matsuoka T (2010) Effect of increased friction along a plate boundary fault on the formation of an out-of-sequence thrust and a break in surface slope within an accretionary wedge, based on numerical simulations. Tectonophy 484:89–99

Mulugeta G, Koyi HA (1992) Episodic accretion and strain partitioning in a model sand wedge. Tectonophy 202:319–333

Nieuwland DA, Leutscher JH, Gast J (2000) Wedge equilibrium in fold-and-thrust belts. Prediction of out-of-sequence thrusting, based on sandbox experiments and natural examples. Geologie en Mijnbouw 79:81–91

Ogawa Y et al (1997) Tension cracks on the oceanward slopes of the northern Japan and Mariana Trenches. Mar Geol 141:111–123

White DJ, Take WA, Bolton MD (2001) Measuring soil deformation in geotechnical models using digital images and PIV analysis. In: 10th international conference on computer methods and advances in geomechanics, Tucson

Willett SD (1992) Dynamic and kinematic growth and change of a Coulomb wedge. In: McClay KR (ed) Thrust tectonics. Chapman & Hall, London, pp 19–31

Wolf H, Krig D, Triantafyllidis T (2003) Experimental investigation of shear band patterns in granular material. J Struct Geol 25:1229–1240

Yamada Y, McClay KR (2004) 3-D analog modeling of inversion thrust structures. In: McClay KR (ed) Thrust tectonics and hydrocarbon systems. American Association of Petroleum Geologists Memoirs 82. American Association of Petroleum Geologists, Tulsa, pp 276–301

Yamada Y, Baba K, Matsuoka T (2006) Analogue and numerical modelling of accretionary prisms with a decollement in sediments. In: Buiter S, Scherurs G (eds) Numerical and analogue modelling of crustal-scale processes. Geological society special publication 253. Geological Society, London, pp 169–183

Yamada Y, Yamashita Y, Yamamoto Y (2010) Submarine landslides at subduction margins: insights from physical models. Tectonophysics 484:156–167

Yamamoto Y et al (2007) Large-scale chaotically mixed sedimentary body within the late Pliocene to Pleistocene Chikura Group, Central Japan. Island Arc 16:505–507

Yamamoto Y et al (2009) Formation of chaotic rock-units during primary accretion processes: examples from the Miura–Boso accretionary complex, Central Japan. Island Arc 18:496–512

Yamamoto Y et al (2012) Systematic development of submarine slope failures at subduction margins: fossil record of accretion-related slope failure in the Miocene Hota accretionary complex, Central Japan. In: Yamada Y et al (eds) Submarine mass movements and their consequences, vol. 31, Advances in natural and technological hazards research. Springer, Dordrecht, pp 355–364

Chapter 32
Systematic Development of Submarine Slope Failures at Subduction Margins: Fossil Record of Accretion-Related Slope Failure in the Miocene Hota Accretionary Complex, Central Japan

Yuzuru Yamamoto, Yasuhiro Yamada, Yoshihiko Yamashita, Shun Chiyonobu, Tadahiro Shibata, and Megumi Hojo

Abstract A comparative study of fossil sliding masses and the results of analog experiments indicates the systematic accumulation of submarine sliding masses at subduction margins. An analysis of sliding masses in the Middle Miocene Hota accretionary complex, Central Japan, combined with the results of analog experiments that simulated an accretionary wedge, revealed two types of slope failures at the toe of the accretionary wedge or at the head of an out-of-sequence thrust: relatively small but frequently developed failures on the lower parts of the slope (Type I failures), and relatively large but less frequent failures that affect the entire slope (Type II failures). The Type I slides are precursors of the larger Type II failures. These successive failure processes are recorded in the Hota accretionary complex as the following depositional sequence: three thin conglomerate layers containing small clasts (type I failure deposits) are overlain by a thick slope-failure deposit containing larger clasts (type II). In such an environment, carbonate-cemented and brecciated sandstones, which contain web structures, generally form at depth and behave as competent layers during failure. Clasts of such sandstones are indicative of large slope failures and are found only in type II failure deposits. Type II failures affect

Y. Yamamoto (✉) • T. Shibata
IFREE, JAMSTEC, Yokohama 236-0001, Japan
e-mail: yuzuru-y@jamstec.go.jp

Y. Yamada • Y. Yamashita
Department of Earth Resources Engineering, Kyoto University,
Katsura, Kyoto 615-8540, Japan

S. Chiyonobu
RITE, Kizugawa 619-0292, Japan

M. Hojo
Department of Earth and Planetary Science, The University of Tokyo,
Tokyo 113-0033, Japan

Y. Yamada et al. (eds.), *Submarine Mass Movements and Their Consequences*,
Advances in Natural and Technological Hazards Research 31,
DOI 10.1007/978-94-007-2162-3_32, © Springer Science+Business Media B.V. 2012

the sediment to a depth of ~2–10 m, whereas type I failures are surficial (<1 m depth), as inferred from the results of analog experiments and field observations. This systematic pattern of slope failure is important in terms of understanding the formation mechanism of submarine slope failures and in predicting such failures.

Keywords Submarine slope failure • Hota accretionary complex • sandbox experiments

32.1 Introduction

Submarine landslides are a significant mass-wasting process at subduction margins (e.g., Kobayashi et al. 1987; Lallemand et al. 1989; Underwood and Moore 1995; Lucente and Pini 2007; Yamamoto et al. 2007, 2009). Such landslides originate from gravitational instability associated mainly with uplift of the hanging wall of subduction-related thrusts. Submarine landslides have the potential to destroy infrastructure, including telecommunication cables (e.g., Heezen and Ewing 1952) and oil–gas platforms (e.g., Bea et al. 1983), and they may generate large tsunamis (e.g., Bondevik et al. 2005; Talling et al. 2007); consequently, such failure events represent a risk to human life.

Recent studies have examined the mechanism and formation process of submarine landslides from many perspectives, citing the influence of fluid pressure (e.g., Fleming et al. 2008; Sawyer et al. 2009; Dugan and Germaine 2008), gas expansion (Morita et al. 2011), and earthquake-induced liquefaction (e.g., Yamamoto et al. 2007, 2009). However, no previous study has analyzed the style and pattern of submarine-landslide formation, which would be important for disaster prevention and for predicting the occurrence of such events. The lack of research in this area may reflect the difficulties involved in making high-resolution, time-lapse observations of submarine landslides on the deep ocean floor.

To address this shortcoming, in the present study we integrated the fossil record of submarine landslides exposed in the Miocene Hota accretionary complex, central Japan, with the results of analog modeling that focused on the scale of slope failures. This study follows on from Yamada et al. (2010), who identified systematic patterns of slope failure based on the results of sandbox experiments, revealing multiple small-scale slope failures are precursors of large-scale failure.

32.2 Geological Setting

The unique tectonic setting of Central Japan comprises two plate subduction systems: the Philippine Sea Plate is being subducted beneath the North America/Eurasia Plate, and the Pacific Plate is being subducted beneath both of these former plates

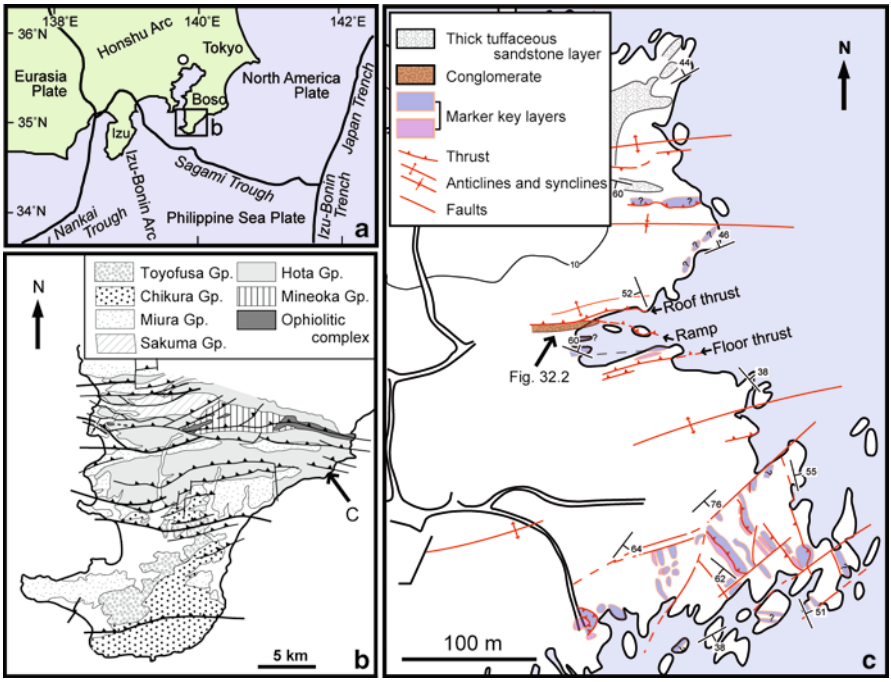

Fig. 32.1 Index (**a**) and geological (**b**) maps of the Miocene Hota accretionary complex, Central Japan. (**c**) Map showing slope failure deposits exposed in the footwall of an accretion-related thrust

(Fig. 32.1a). The Izu–Bonin island arc, on the Philippine Sea Plate, began colliding with Honshu arc in the Middle Miocene, resulting in the northward bending and rapid uplifting of the geological architecture on the Honshu. (e.g., Koyama and Kitazato 1989; Amano 1991; Yamamoto and Kawakami 2005). Young, non-metamorphosed sedimentary sequences of these subduction systems (e.g., accretionary prism, forearc basin, and trench-slope basin) have been rapidly uplifted and exposed on the Miura and Boso peninsulas of Central Japan (Fig. 32.1c).

Two accretionary complexes – the Late Miocene to Early Pliocene Miura–Boso accretionary prism and the Early to Middle Miocene Hota accretionary complex – have exposed in the southern parts of the Miura and Boso peninsulas. The former developed in the southernmost part of the peninsulas and comprises alternating beds of hemipelagic siltstone and volcaniclastic sandstone/conglomerate derived from the Izu–Bonin island arc, representing an off-scraped accretionary prism that was buried to depths of less than 1 km (Yamamoto et al. 2005; Yamamoto 2006).

The Hota accretionary complex, which developed immediately north of the Miura–Boso accretionary prism, consists mainly of alternating beds of hemipelagic siltstone and acidic tuff/tuffaceous sandstone. The stratigraphy of the Hota accretionary complex is equivalent to that of the southern Hota Group on the Boso Peninsula, which comprises sandstone/conglomerate of the Maejima Formation and mudstone

of the Aokiyama Formation (Saito 1992). The Hota accretionary complex extends to the Miura Peninsula, where it occurs as the Hayama Group.

32.3 Fossil Submarine-Slope Failure Deposits

A slope failure mass, comprising four conglomerate layers, occurs in the footwall of a major thrust in the Hota accretionary complex (Figs. 32.1c and 32.2). The conglomerates are clast-supported and dip at ~50° to the north, similar to the dip of the surrounding coherent sequence. The clasts show no preferred orientation and no systematic variations in size (e.g., grading), and the conglomerate layers contain no sedimentary/tectonic foliation. The thickness of the conglomerate layers tends to increase upward: the three lower layers are 0.035–0.17 m thick, whereas the uppermost layer is ~3 m thick (Fig. 32.2). The thickness of the interbedded siltstone layers is relatively constant throughout the sequence (25–28 cm). The conglomerate layers do not contain exotic rock fragments such as chert, basalt, or limestone. The siltstone

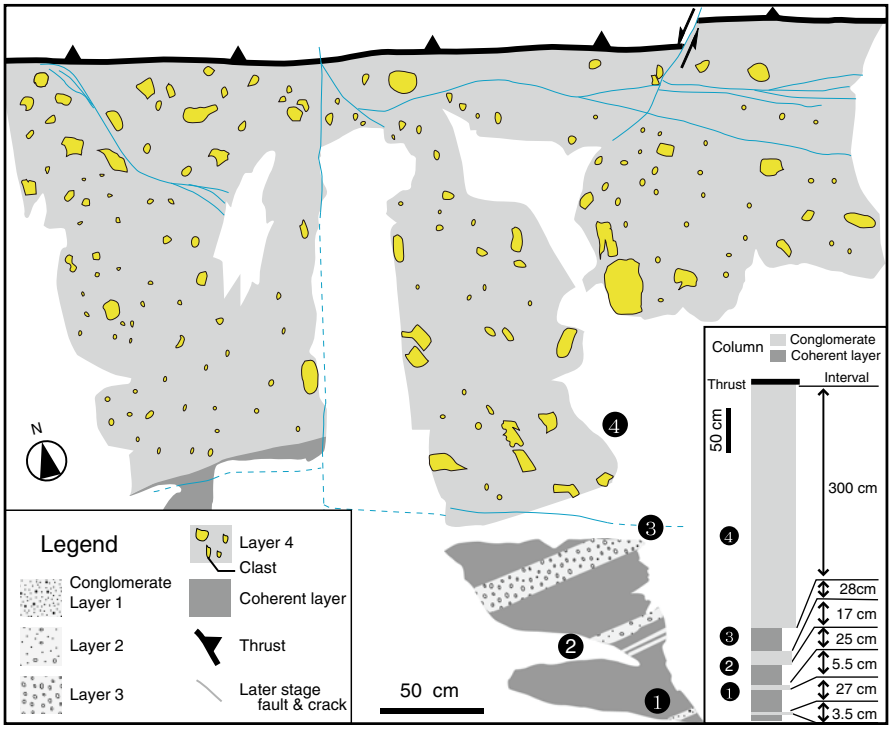

Fig. 32.2 Sketch showing the occurrence of fossil submarine slope failures. The outcrop, which occurs in the footwall of an accretion-related thrust, shows four independent failure deposits (conglomerate layers *1–4*) that tend to thicken upward

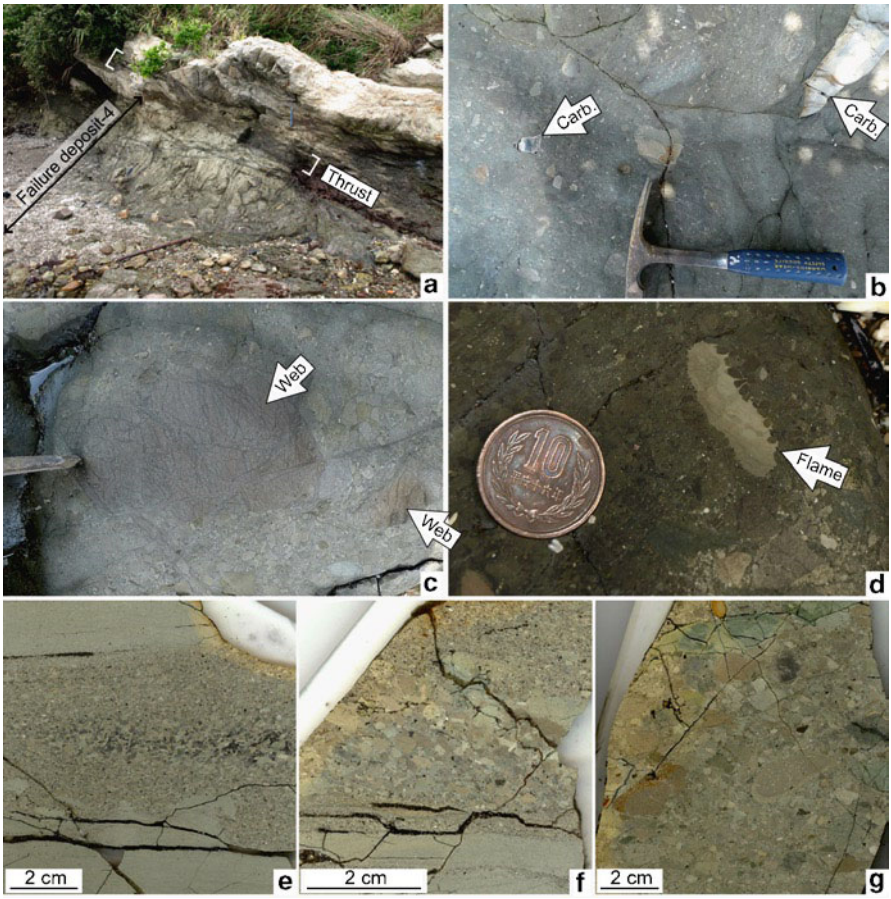

Fig. 32.3 Photographs of fossil submarine slope failures. (**a**) The thickest and uppermost conglomerate is cut by an accretion-related thrust. (**b**–**d**) Close-up photographs of clasts in the uppermost conglomerate layer (failure deposit-4). *White arrows* labeled "*carb*", "*web*", and "*flame*" indicate carbonate-cemented/brecciated sandstone clasts, web structure developed in sandstone clasts, and flame structure, respectively. (**e**–**g**) Polished sections of failure deposits −1 (**e**), −2 (**f**) and −3 (**g**) The clast sizes in each layer tend to increase toward the *upper* layers

clasts in the conglomerates and siltstone in the surrounding coherent layers contain no nannofossils, which is consistent with the depositional environment of the Hota Group (i.e., at water depths below the calcite compensation depth).

The clasts in the uppermost (thickest) conglomerate layer are angular to subangular, and consist of siltstone, tuffaceous siltstone, sandstone, and acidic tuff (Fig. 32.3b–d). This layer alone contains calcite or dolomite veins, carbonate-cemented and brecciated sandstone clasts, and sandstone clasts containing web structure (Fig. 32.3b, c). Some clasts of siltstone and acidic tuff contain loading-induced flame structures, whereby grains that were disaggregated from the clasts were

intruded upwards to fill inter-clast voids (Fig. 32.3d). The three lower conglomerates layers consist of angular to sub-angular clasts of siltstone and tuffaceous siltstone. The upward increase in layer thicknesses is matched by an increase in clast size (Fig. 32.3e–g).

The upper part of the uppermost conglomerate layer is cut by a subduction–accretion-related thrust fault. Sets of branching and merging thrusts define a complicated duplex structure (Figs. 32.1c and 32.2). The thrust comprises a shear zone (several tens of centimeters wide) that possesses a block-in-matrix texture and S–C structure. The shear zone cuts the siltstone clasts along sharp boundaries.

32.4 Analog Models of Type I and II Slope Failures

Analog modeling is a useful technique with which to investigate geological processes. Models that use dry granular materials (e.g., sand) show deformation behaviors similar to those of rock; consequently, such models have been applied to subsurface geological structures in recent decades (e.g., Cobbold and Castro 1999; Koyi and Mancktelow 2001; Lohrmann et al. 2003), and to submarine slides, clarifying several fundamental mechanisms related to such failures (e.g., Yamada et al. 2010).

In the present study, we used an experimental rig with three rigid basement blocks to produce faults in the experimental material (dry sand; Fig. 32.4). As the basement blocks are shortened, the block boundaries produce two thrust faults that displace the sand layers. Where the thrusts propagate to the surface, slopes are produced and slope failure occurs. The initial dimensions of the sand layers were 100 cm in length, 30 cm in width, and 6 cm in height. The experimental configurations were the same as those reported by Yamada et al. (2010). The scaling ratio between nature and the model is 10^{-3}–10^{-4}; thus, 1 cm in the model corresponds to 10–100 m in nature.

Similarly to Yamada et al. (2010), the experiments produced two types of slope failure: small-scale Type I failures that are relatively frequent and occur in the lower half of the slope, and large-scale Type II failures that occur at the top of the slope.

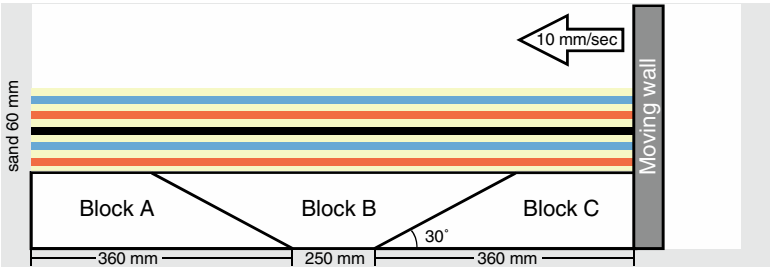

Fig. 32.4 Schematic diagram of the experimental rig

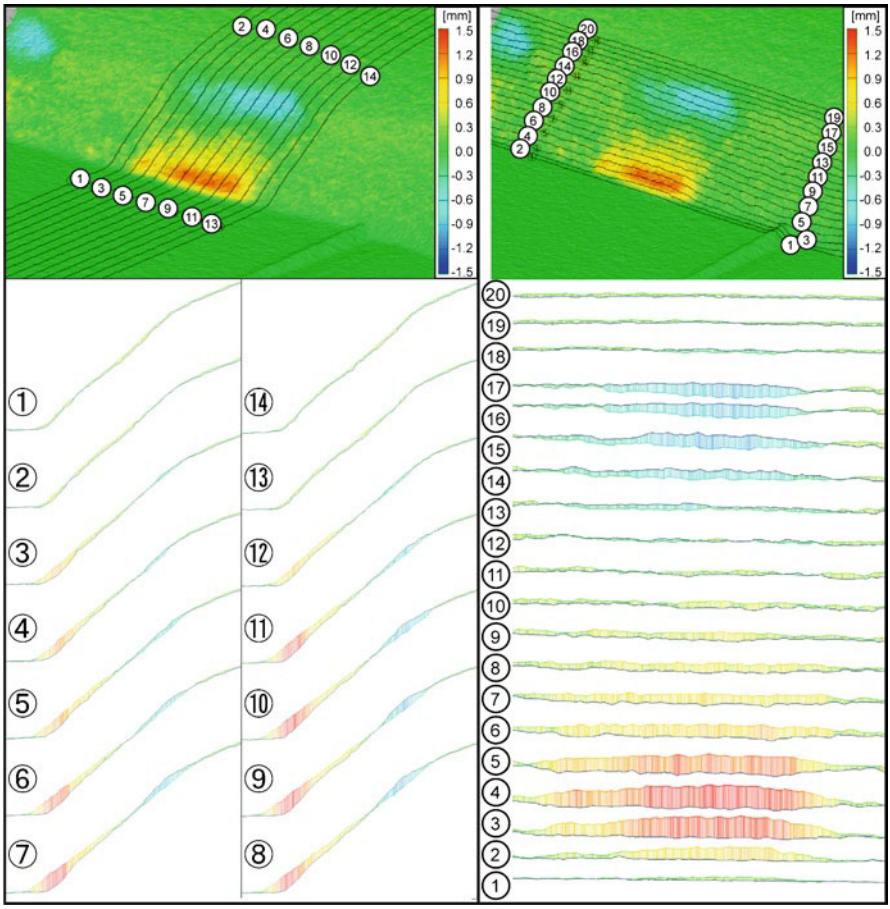

Fig. 32.5 Changes in topography resulting from slope failure in an analog model, shown in sections oriented parallel to the dip of the slope (**a**) and to the strike of the slope (**b**) This failure event was recorded when the total uplift of the central block increased from 18.8 to 19.1 mm. The spacing between sections is 2.0 mm for the along-dip sections and 1.0 mm for the along-strike sections. The *black lines* correspond to the topography before the failure event. *Cool* and *warm colors* indicate areas of subsidence and uplift, respectively, produced by the failure event

Given that this study focused on the detailed geometry of slope failures, we used a commercial surface-measurement system (ATOS, developed by GOM mbH) that analyzes stereoscopic images from a pair of CCD cameras to detect and calculate the model topography with a maximum accuracy of ~0.1 mm. The surface topography of the model was measured at time intervals of 2 s of shortening and the deviations were calculated between successive topographies.

Type I failures upon the lower half of the slope were identified by digital image correlation (DIC) technique (see Yamada et al. 2010 for details), but topographic deviations produced by this type of failures were not clearly detected by ATOS

(Fig. 32.5). This is because Type I failures are too thin to produce topographic anomalies that can be distinguished from background variations in the topography of the slope. Given the scaling ratio of the experiment, the Type I slope failures occur to a depth of less than 1 m when the result is applied to nature.

Topographic deviations produced by Type II failures were detected by ATOS. A typical example is shown in Fig. 32.5, which was produced from two sets of topographic data acquired for uplift amounts of the central block of 18.8 and 19.1 mm. The along-dip sections numbered 7–10 in the figure, from the central region of the failure, clearly show the topographic deviations produced by failure. The failure occurred at the top of the slope and the failed sediments were deposited at the foot of the slope. Topographic deviations are also evident in the along-strike sections numbered 2–17 in Fig. 32.5.

The measurements show that a maximum deviation at the top of the slope was −1.4 mm (area of cool colors in Fig. 32.5), and +1.3 mm at the foot of the slope (warm colors). The volume of failed sediment, as calculated from the topographic deviations, is 105.6 mm^3 at the top of the slope and 118.2 mm^3 at the foot of the slope. The increase in volume at the foot of the slope may be due to fragmentation of the failed sediments during sliding (i.e., an increase in porosity). The surface area of failed sediment deposited at the foot of the slope is larger than that of the failure area. According to the scaling law, the thickness of the failure is 2–10 m and the volume of the failed deposits is 10^2–10^5 m^3. To accurately measure the amount of topographic deviations, we correlated the effect of hangingwall uplift due to displacement upon the thrust.

32.5 Discussion

A fossil submarine slide mass occurs in the Middle Miocene Hota accretionary complex, in the footwall of an accretion-related thrust fault. The slide mass formed on the seafloor and has subducted beneath the thrust. The thrust system generated an intense shear zone within the top half of the uppermost conglomerate and formed a complicated duplex structure during exhumation. The geometry of the accretion-related thrust fault controlled the distribution of the slope failure deposit, similarly to the physical models reported by Yamada et al. (2010).

Given the lack of exotic clasts in the conglomerate layers, and the fact that the clasts are angular to sub-angular, they were probably derived locally. The occurrence of flame structure (Fig. 32.3d) indicates that the clasts formed soon after sedimentation. Only the uppermost (thickest) slope failure deposit contains relatively lithified sandstone clasts that commonly show carbonate cementation/brecciation and contain web structures (Fig. 32.3b, c). Because carbonate-cemented sandstones generally develop in the hanging walls of thrusts in accretionary prisms (e.g., Kobayashi 2002; Yamamoto et al. 2005) and behave as competent layers, the transportation of these rocks to the footwall of the thrust may require a relatively large slope failure that collapsed rocks in the hanging wall of the thrust and on the trench slope. Given

that the formation of web structure requires the rocks to be buried (e.g., Byrne 1984), the slope failure in the present case must have extended down to basement rocks (i.e., the upper part of the accretionary prism). This scenario suggests that the uppermost conglomerate layer formed as a result of a Type II slope failure. In contrast, the lower three conglomerate layers, which are relatively thin and contain smaller clasts without carbonate-cemented rocks or web structures, may have formed by smaller-scale slope failures in the footwall, equivalent to Type I failures. Given that the interbedded siltstone layers are of constant thickness throughout the succession (Fig. 32.2), these slope failures occurred at relatively constant intervals, if we ignore the erosion associated with the failure.

The surface topography measured in our sandbox experiments indicates that collapse of the slope associated with type II failure extends to depths of ~2–10 m, whereas type I failures extend to depths of <1 m (Fig. 32.5). This result indicates that type I failures occur at the surface, whereas type II failures potentially result in collapse of the upper part of the accretionary prism (i.e., collapse of the hangingwall anticline of the thrust). These modeling results are consistent with the occurrence and nature of the uppermost (thickest) slope failure deposit examined in the present study, which contains sandstone clasts with web structures and carbonate cementation.

In conclusion, a detailed study of fossil slope failures and the results of analog modeling revealed a systematic pattern of submarine slope failure at a subduction, with small-scale type I failures occurring as precursors of large-scale type II failures. The recognition of this pattern is important in terms of understanding the mechanism of slope failure and in predicting hazardous submarine slope failures.

Acknowledgments This study was supported by a JSPS Research Grant (No. 21740363) awarded to the first author. Jun Kameda and Yujiro Ogawa are appreciated for their detailed and constructive reviews, which improved the manuscript. We sincerely thank Ryo Murakami and his family for their kind hospitality during fieldwork.

References

Amano K (1991) Multiple collision tectonics of the South Fossa Magna in central Japan. Mod Geol 15:315–329

Bea RG, Sircar P, Niedoroda AW (1983) Wave-induced slides in South Pass Block 70, Mississippi Delta. J Geotech Eng 109:619–644

Bondevik S, Løvholt F, Harbitz CB et al (2005) The Storegga slide tsunami – comparing field observations with numerical simulations. Mar Petrol Geol 22:195–208

Byrne T (1984) Early deformation in melange terranes of the Ghost Rocks Formation, Kodiak Islands, Alaska. Spec Pap Geol Soc Am 198:21–51

Cobbold PR, Castro L (1999) Fluid pressure and effective stress in sandbox models. Tectonophysics 301:1–19

Dugan B, Germaine JT (2008) Near-seafloor overpressure in the deepwater Mississippi Canyon, northern Gulf of Mexico. Geophys Res Lett 35:L02304. doi:10.1029/2007GL032275

Flemings PB, Long H, Dugan B et al (2008) Pore pressure penetrometers document high overpressure near the seafloor where multiple submarine landslides have occurred on the continental slope, offshore Louisiana, Gulf of Mexico. Earth Planet Sci Lett 269:309–324. doi:310.1016/j.epsl.2008.1006.1027

Heezen BC, Ewing M (1952) Turbidity currents and submarine slumps and the 1929 Grand Banks earthquake. Am J Sci 250:849–873

Kobayashi K, Cadet JP, Aubouin J et al (1987) Normal faulting of the Daiichi-Kashima seamount in the Japan trench revealed by the Kaiko I Cruise, Leg 3. Earth Planet Sci Lett 83:257–266

Kobayashi K (2002) Tectonic significance of the cold seepage zones in the eastern Nankai accretionary wedge - an outcome of the 15 years' KAIKO projects. Mar Geol 187:3–30

Koyama M, Kitazato H (1989) Paleomagnetic evidence for Pleistocene clockwise rotation in the Oiso Hills: a possible record of interaction between the Philippine Sea plate and Northeast Japan. In: Hillhouse JW (ed) Deep structure and past kinematics of accreted terranes. Geophys Monogr 50, American Geophysical Union, Washington, DC, pp 249–265

Koyi HA, Mancktelow NS (2001) Tectonic modeling: a volume in honor of Hans Ramberg, Mem Geol Soc Am 193. Geological Society of America, Boulder

Lallemand S, Culotta R, von Huene R (1989) Subduction of the Daiichi Kashima seamount in the Japan trench. Tectonophysics 160:231–247

Lohrmann J, Kukowski N, Adam J, Onchen O (2003) The control of sand wedges by material properties: sensitivity analyses and application to convergent margin mechanics. J Struct Geol 25:1691–1711

Lucente CC, Pini GA (2007) Basin-widemass-wasting complexes as markers of the Oligo–Miocene foredeep-accretionary wedge evolution in the Northern Apennines, Italy. Basin Res 20:49–71

Morita S, Nakajima T, Hanamura Y (2011) Submarine slump sediments and their related dewatering structures: Observations of 3D seismic data in continental slope off Shimokita Peninsula, NE Japan. J Geol Soc Japan 117:95-98

Saito S (1992) Stratigraphy of Cenozoic strata in the southern terminus area of Boso Peninsula, Central Japan. Contributions from the Institute of Geology and Paleontology, Tohoku University 93:1-37

Sawyer DE, Flemings PB, Dugan B, Germaine JT (2009) Retrogressive failures recorded in mass transport deposits in the Ursa Basin, Northern Gulf of Mexico. J Geophys Res 114:B10102. doi:10.1029/2008JB006159

Talling PJ, Wynn RB, Masson DG et al (2007) Onset of submarine debris flow deposition far from original giant landslide. Nature 450:541–544

Underwood MB, Moore GF (1995) Trenches and trench-slope basins. In: Busby CJ et al (eds) Tectonics of sedimentary basins. Blackwell Science, Cambridge, MA, pp 179–219

Yamada Y, Yamashita Y, Yamamoto Y (2010) Submarine landslides at subduction margins: insights from physical models. Tectonophysics 484:156–167

Yamamoto Y (2006) Systematic variation of shear-induced physical properties and fabrics in the Miura–Boso accretionary prism: the earliest processes during off scraping. Earth Planet Sci Lett 244:270–284. doi:10.1016/j.epsl.2006.01.049

Yamamoto Y, Kawakami S (2005) Rapid tectonics of the late Miocene Boso accretionary prism related to the Izu-Bonin arc collision. Island Arc 14:178–198

Yamamoto Y, Mukoyoshi H, Ogawa Y (2005) Structural characteristics of shallowly buried accretionary prism: rapidly uplifted Neogene accreted sediments on the Miura–Boso Peninsula, central Japan. Tectonics 24: TC5008. doi: 10.1029/2005TC001823

Yamamoto Y, Ogawa Y, Uchino T, Muraoka S, Chiba T (2007) Large-scale chaotically mixed sedimentary body within the Late Pliocene to Pleistocene Chikura Group, Central Japan. Island Arc 16:505–507

Yamamoto Y, Nidaira M, Ohta Y, Ogawa Y (2009) Formation of chaotic rock-units during primary accretion processes: examples from the Miura–Boso accretionary complex, Central Japan. Island Arc 18: 496-512

Chapter 33
Morphologic Expression of Accretionary Processes and Recent Submarine Landslides Along the Southwestern Pacific Margin of Colombia

Carlos A. Vargas, Paul Mann, and Clemencia Gómez

Abstract We analyzed 9,750 km^2 of high-resolution, bathymetric data recorded by a multi-beam echo-sounder along the southwestern Pacific margin of Colombia (1°25′N–2°00′N and 78°44′W–80°14′W). This margin has experienced several great subduction zone earthquakes during the twentieth century (1906, Mw = 8.8; 1942, Mw = 7.8; 1958, Mw = 7.7, 1979, Mw = 8.2). The most prominent morphological features imaged by the survey include the Tumaco high, the Emerald canyon and the Mira canyon, limited on its western edge by the Manglares high. Our results suggest that the Mira canyon was likely formed by a 50-km-long, earthquake-generated landslide that displaced marine sediments to depths of 1,000 m depth. Geomorphology dating using the fault-scarp diffusion hypothesis suggests that the 3200-2800 BP earthquake event could have triggered its configuration.

Keywords Submarine mass failures • High-resolution swath bathymetric data • Geomorphologic scarp dating • Tsunami • Seismic reflection • Manglares basin • Colombia

C.A. Vargas
Departamento de Geociencias, Universidad Nacional de Colombia,
Ed. Manuel Ancizar, Bogotá, Colombia
e-mail: cavargasj@unal.edu.co

P. Mann (✉)
Department of Earth and Atmospheric Sciences, University of Houston, Houston,
TX 77204-5007, USA
e-mail: pmann277@gmail.com

C. Gómez
Agencia Nacional de Hidrocarburos, Av. El Dorado, Edif. Cámara
Colombiana Infraestructura, Bogota, Colombia
e-mail: clemencia.gomez@anh.gov.co

Y. Yamada et al. (eds.), *Submarine Mass Movements and Their Consequences*,
Advances in Natural and Technological Hazards Research 31,
DOI 10.1007/978-94-007-2162-3_33,

33.1 Introduction

The North Ecuador–South Colombia (NESC) subduction margin includes two onshore basins, the Tumaco in Colombia and the Borbon in Ecuador, and the Manglares basin in the offshore area (Fig. 33.1). The Manglares basin has been interpreted as a single forearc basin that extends from the Jama-Quininde Fault in Ecuador to north of the Garrapatas Fault in Colombia (Marcaillou and Collot 2008). The region has been the site of large great-thrust earthquakes associated with subduction of the Nazca plate beneath the South American plate (Fig. 33.1). Because seamounts and other subducting asperities are actively subducting, the resulting earthquakes are large and destructive events commonly associated with large tsunamis (Kanamori and McNally 1982; Beck and Ruff 1984).

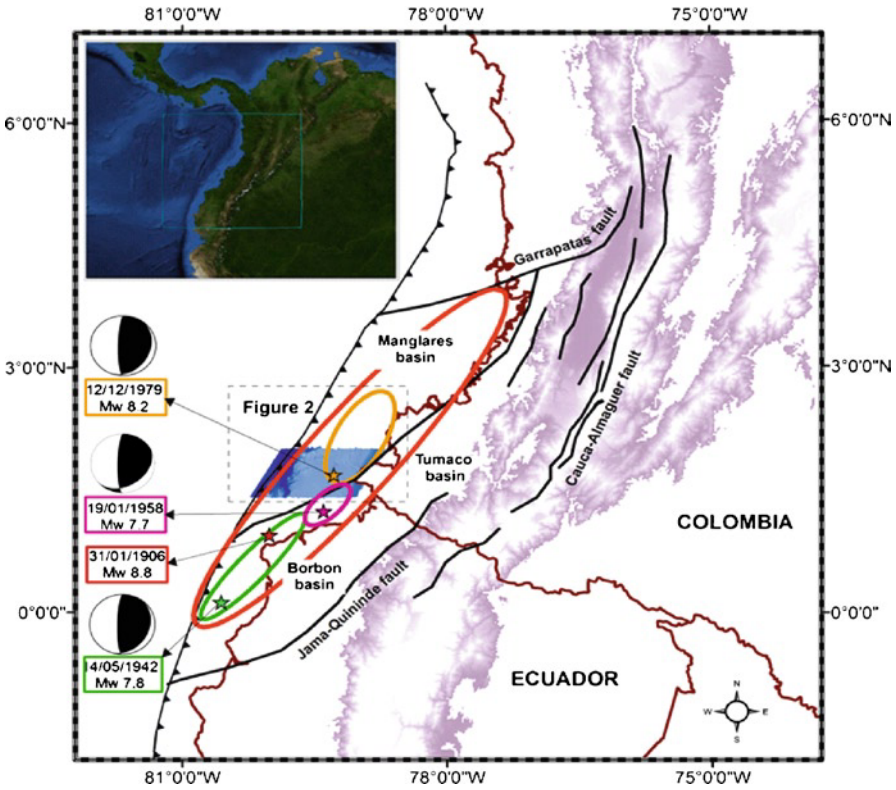

Fig. 33.1 Location of the Manglares offshore forearc basin along the North Ecuador-South Colombia (*NESC*) subduction margin showing the site of four (Mw >7) great-thrust earthquakes (*stars*). The rupture of the 1906 event (*red ellipse*) involves the area of the 1942, 1958 and 1979 events (*green, purple* and *yellow ellipses* respectively). *Dashed square* contains the area where high-resolution-bathymetric data was acquired by the ANH campaign in 2008

At least four large (Mw >7) earthquakes occurred along the Manglares basin: the 1906 event (Mw 8.8) ruptured a 500 km long segment of the trench (Fig. 33.1). Three smaller events in 1942 (Mw 7.8), 1958 (Mw 7.7) and 1979 (Mw 8.2) ruptured this same area. The 1906 triggering of three events occurred as a cluster while the sequence of 1942, 1958 and 1979 included hiatuses of about 20 years between major events (Kanamori and McNally 1982). Although the triggering and recurrence interval between these large thrust events remains a question for seismologists to address, there is no question that past and future tsunamis and submarine landslides will result from large earthquakes along this margin.

Hazards are significant for populated coastal areas. During the 1906 earthquake, the towns of Tumaco (Colombia) and Esmeraldas (Ecuador) were partially destroyed by a tsunami, and submarine cables were broken in numerous places between Buenaventura and Panama (Askew et al. 1985). Similarly, during the 1979 tsunami in Tumaco, waves swept houses landward into a lagoonal area where at least 220 people were killed (Herd et al. 1981).

While morphologic scars of submarine mass failures are probably associated with great-earthquakes generated along the NESC margin (Collot et al. 2004; Ratzov et al. 2007, 2010), there are significant uncertainties surrounding the age of these scars and their genetic relationship to local faults and historical great-earthquakes. In this work we present a new high-resolution-bathymetric image of the Manglares basin seafloor, acquired by the National Hydrocarbons Agency of Colombia (ANH) during 2008, and used this map to analyze scarp profiles that surround the breakaway areas of the large slides. These profiles provide relative morphologic dating of the submarine environment and are used to infer recent tectonic mechanisms for triggering submarine landslides and controlling the structure of the Manglares basin.

33.2 Tectonic Setting of the NESC Margin

The NESC margin is a region of strong crustal deformation related to the subduction of the oceanic Nazca plate beneath the South-American continental plate. Oceanic crust of the Nazca plate in this area is less than 26 Ma (Lonsdale 2005), and underlies the Carnegie Ridge, the Yaquina Graben, as well other seamounts. During its subduction beneath the NESC coast asperities on the downgoing Nazca plate produce lateral variations of seismicity, arc magmatism, vertical and horizontal deformation, and controls the modern sediment distribution along the margin (Gutscher et al. 1999).

The basement of the NESC margin consists of accreted terranes composed of oceanic plateau and island arc crust. An east–west compressive regime following accretion of the oceanic terranes has created a north–south-trending belt associated with deep, forearc sedimentary basins. The development of these fore-arc basins during the last 5 Ma is thought to have been controlled by the collision of the Panama-Baudo block and escape of the North Andean block to the northeast (Witt et al. 2006).

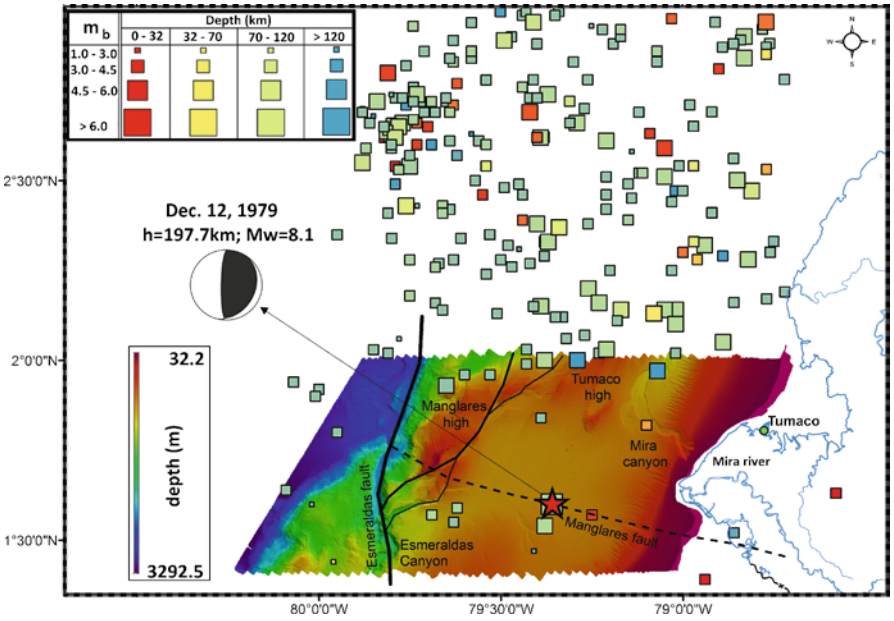

Fig. 33.2 Main morphologic features detected from high-resolution swath bathymetric data in the study area. It has been superposed seismicity reported by NEIC-USGS (1974–2011), as well the focal mechanism of the 1979 event

One of these basins, the Manglares, is segmented by the transverse Manglares and Esmeraldas faults (Marcaillou and Collot 2008) (Fig. 33.2). North of the Manglares fault, the Manglares basin reaches a water depth ~870 m, and becomes deeply incised by the Mira canyon. South of the Manglares fault, the Manglares basin reaches a bathymetric of—1,300 m and is almost flat-bottomed. Western areas of the Manglares basin shows bathymetric promontories including the Tumaco high (50 m in depth) and the Manglares high (~90 m in depth), as well as deep incisions like the Esmeralda canyon. The axis of the Esmeralda canyon is ~2.2 km deep and follows the north–northwest-striking Esmeraldas fault zone.

The morphology of the margin, the diversion of drainage networks and changes in areas of modern coastal accretion all support active subsidence of the margin (Dumont et al. 2006). Large earthquakes during the twentieth century in the Manglares basin testify to this pattern of permanent subsidence, e.g., after the 1979 earthquake (Fig. 33.2), a 200-km stretch of the coast tectonically subsided as much as 1.6 m (Herd et al. 1981). The earthquake effects on these areas of sedimented seafloor slopes are thought to be responsible of the great submarine mass movement along the Mira canyon (Ratzov et al. 2010).

33.3 Data and Methods

The bathymetric data presented in this paper were acquired by the R/V ARC-PROVIDENCIA in the frame of the joint research campaign leadership during a collaborative research study by the National Hydrocarbons Agency (ANH) and the Colombian Navy. Swath bathymetry and oceanographic data in an area of the Exclusive Economic Zone of the Colombian Pacific (1° 25′N–2°N; 78° 44′W–80° 14′W) were acquired simultaneously (Fig. 33.2). A swath-bathymetry-multibeam-echosounder of low frequency system "ATLAS HIDROSWEEP MD2" was used. The system worked with an array of 395 beams to obtain an angular look direction of 152°. The system has two transmitters and two receivers which operate at a frequency of 30 kHz at a depth range between 10 and 5,000 m.

Because the Mira canyon is one of the main features detected by the bathymetric survey and is associated with recent submarine mass failure, we performed a quantitative geomorphologic analysis of scarps in the canyon to constrain a range of ages for its formation. Dating of scarps might reveal whether the formation of the canyon accompanied or was modified by any of the great thrust earthquakes of the 20th century. This study followed Hanks (2000) by applying the diffusion equation under transport-limited conditions. Equation 33.1 is a linear, second-order differential equation that relates the change in elevation H to time t using the proportionality constant κ and landscape curvature x (distance along the profile):

$$\frac{\partial H}{\partial t} = \kappa \frac{\partial^2 H}{\partial x^2} \tag{33.1}$$

where diffusivity (κ) with dimensions $[L^2T^{-1}]$, varies with climate, scarp material, and scarp height. The slope aspect (Hanks et al. 1984) is considered constant over the timescales investigated. Hanks (2000) expresses Eq. 33.1 to reduce the scarp slope as follows:

$$\left.\frac{\partial u}{\partial x}\right|_{x=0} - b = \frac{a}{\sqrt{\pi \kappa t}} \equiv tan\theta_s - tan\theta_f \tag{33.2}$$

In this reduction, $\theta_s = tan^{-1}\left(\left.\frac{\partial u}{\partial x}\right|_{x=0}\right)$ represents the maximum slope-scarp angle, $\theta_f = tan^{-1}b$ is the fan slope angle, and α is the effective half-vertical displacement. Five bathymetric profiles at the head of the canyon submarine landslide were compared with theoretical profiles estimated by a numerical solutions of the diffusion equation expressed in (33.1). A least-square fit was performed by iterative adjustment of measurements of the effective displacement (2α) and the angles θ_s and θ_f. Constant κ and variable t were merged for estimating range of values that best fitting the data. This approach means that the resulting profiles are not exclusively dependent on κ or t, but rather on their product. For example, the same profile will result for $\kappa = 1$ m^2/year and $t = 10$ year or $\kappa = 10$ m^2/year and $t = 1$ year.

Finally, descriptive analyses of geomorphologic features in the entire area were done using the bathymetric data. Seismic lines collected during the program Pacific-1982 by ECOPETROL (Colombian Company of Petroleum) were used for interpreting active tectonic process in the area of the basin.

33.4 Results

33.4.1 Geomorphologic Scarp Analysis Along the Mira Canyon

The five bathymetric profiles presented in the Fig. 33.3 tested κt values ranging between 0.001 and 10,000 m^2. A unique value was not found; instead we identified a best fit collection of values that varied between 1,000 and 4,000 m^2. Table 33.1 presents the results for all profiles. Although this range of values has been seen in marine environments near the study area (Mitchell 1996), the complex tectonic setting allows different scenarios for the timing of deformation and its effects on the patterns of submarine sedimentation.

The drainage basins in the NESC margin are located within the humid tropics and are characterized by high but relatively constant temperature, high rainfall rates, and high humidity. Average rainfall in the entire Pacific basin ranges from 2,000 to 12,700 mm $year^{-1}$ (Restrepo and Lopez 2008). In addition to the high tectonic activity and progradation on a narrow shelf bordering a deep trench (Figs. 33.2 and 33.4), deltas along this margin are influenced differentially by fluvial discharge, wave energy and tides at its several distributary mouths. The nearby Mira, Patia and San Juan rivers have built some of the largest Pacific deltas of South America, and their sediment flux to the Pacific Ocean yield 1,025 $t\,km^{-2}\,year^{-1}$, 980 $t\,km^{-2}\,year^{-1}$ and 1,150 $t\,km^{-2}\,year^{-1}$, respectively. (Restrepo and Lopez 2008).

From global observations, the warm temperate region has the highest sediment yield of all climatic zones and accounts for nearly two-thirds of the global sediment delivery. Also, river basins draining high mountains (>3000 m) contribute ~60% of the global sediment flux to the coastal zone (Syvitski et al. 2005). The Andes, next to the NESC margin, has eroding mountains up to 4,000 m altitude. This combination of weather, high rates of fluvial discharge and sediment flux support fast erosion and sedimentation into the Manglares basin; these recent sediments may obscure scars associated with older submarine landslides. Nevertheless, because of the wide range of values for the diffusion constant κ, there is a large uncertainty in our age estimate for the creation of the Mira canyon.

33.4.2 Margin Erosion and Sediment Flux of the Manglares Basin

Sediments incorporated into the Manglares basin from the Patia and Mira rivers are responsible for smoothing the seabed to near-flat areas (Fig. 33.4a, b). Some portion

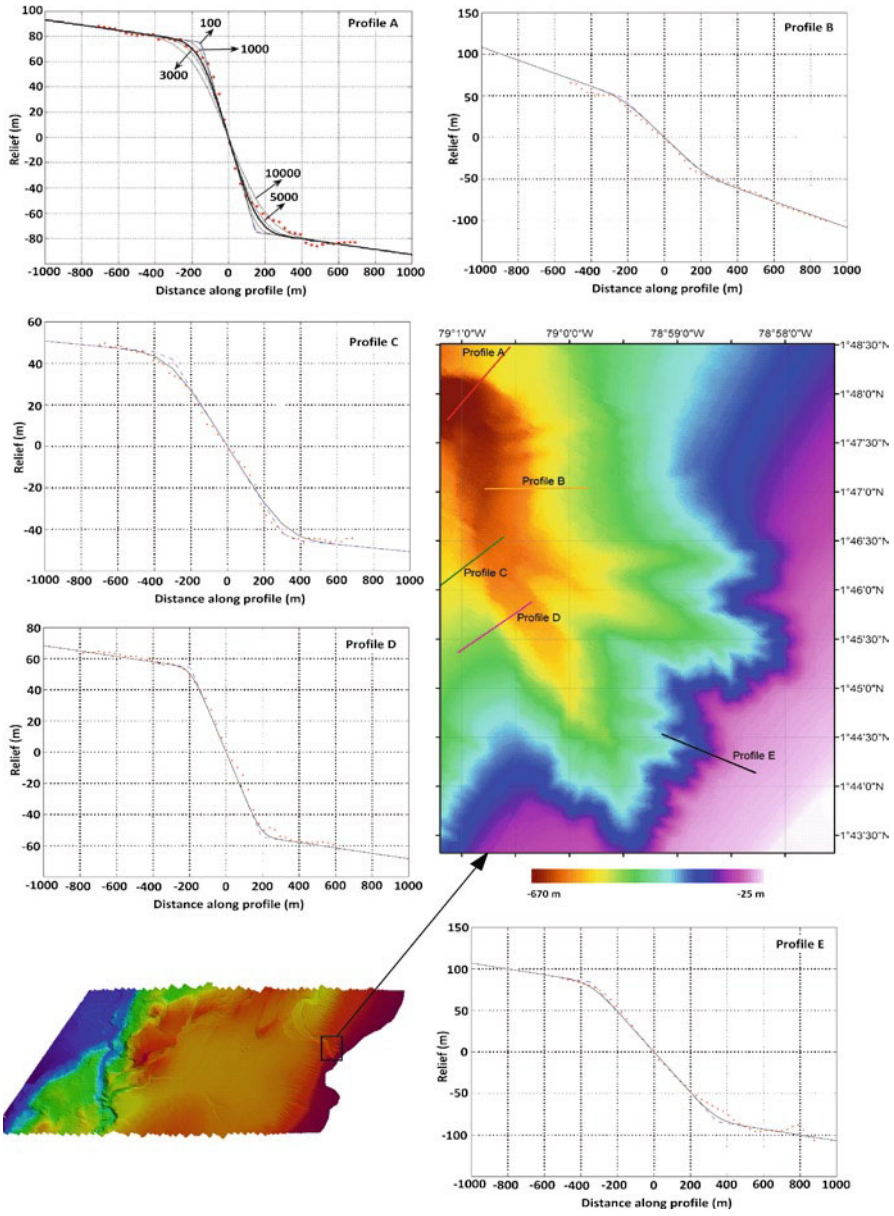

Fig. 33.3 Geomorphologic scarps analyses along the Mira canyon using the diffusion approximation. Five profiles located around the head of the landslide were used to estimate a range of relative ages for its formation (see location in the map and bathymetric surface). Although several test were done (e.g., see *profile A*), the best fit for all profiles corresponds to the time range $\kappa\, t = 1{,}000–4{,}000\ m^2$

Table 33.1 Results of the geomorphologic scarp-dating analyses in five bathymetric profiles located in the head of the submarine landslide of the Mira canyon (see Fig. 33.3)

	Effective vertical displacement (m) – 2α	Fan slope (°) – θ_f	Maximum slope – scarp (°) – θ_s	Range of relative age (m^2) – κt
Profile A	72	1.2	29	1,000–3,000
Profile B	30	4.4	12	1,000–4,000
Profile C	37	0.9	8	1,000–4,000
Profile D	51	1.0	16	1,000–3,000
Profile E	71	2.0	14	1,000–3,000

of these sediments travels to the trench via depressions like the Mira and Esmeraldas canyons (Fig. 33.4b, c). As a result of the high rate of sedimentation, active east–west and north–south faults that cross the Manglares basin are buried.

Segment A of the seismic line P-1982-1750S (Figs. 33.4a and 33.5a) shows how the high rate of sedimentation is responsible of covering the basin. An expression of this sedimentation rate are the active submarine channels, like the Mira canyon (Fig. 33.5a), which exhibits a thickness contrast between the channel bottom and surrounding deposits. Measurements suggest at least 100 m of sediments overlie the channel floor and the reference level in this part of the basin. Many faults reach the channel floor level (yellow area); other faults cut the most recent sedimentary layer, suggesting that active tectonics is interacting with the high sedimentation rate to control the geometry of the modern basin floor.

Along the continental slope, gullies are aligned with Vertical or near-vertical faults (e.g., Manglares fault in Fig. 33.4b). These gullies facilitate the development of submarine landslides, whose material is incorporated into the basin (see yellow arrows). Segment B of the seismic line P-1982-1750S (Fig. 33.5b) illustrates the nature of these slope gullies. Low resolution of seismic data does not allow imaging of presumed faults underlying gullies but we nevertheless propose that most gullies have formed along fault-controlled weaknesses. In addition, old channels and gullies formed are incorporated into the basin during fast sedimentation (see gray ellipses in Fig. 33.5b).

Because the diffusion constant for erosion of submarine environments is low (Mitchell 1996), we may expect that high rates of continental sedimentation will fill the Manglares basin. Earthquakes also would accelerate the incorporation of landslide material into the Manglares basin. In seismic line P-1982-1600S (Fig. 33.5c) it is possible to detect areas where chaotic reflectors suggest incorporation of submarine landslides into the fill of Manglares basin. The submarine landslide associated with the Mira canyon is 44 km, 3 km wide, and has an incision depth of 0.1 km. Because of the submarine landslide track in the flat areas (slopes < 2%) reaches ~30 km, it is possible that the volume of displaced sediments has taken place in several episodes.

Finally, although the NESC margin represents a region of intense crustal deformation, related to the subduction of the oceanic Nazca plate beneath the South-American continental plate, two families of faults are present: (1) The most evident and active NNE-striking thrust faults that, control the geometry of the accreted

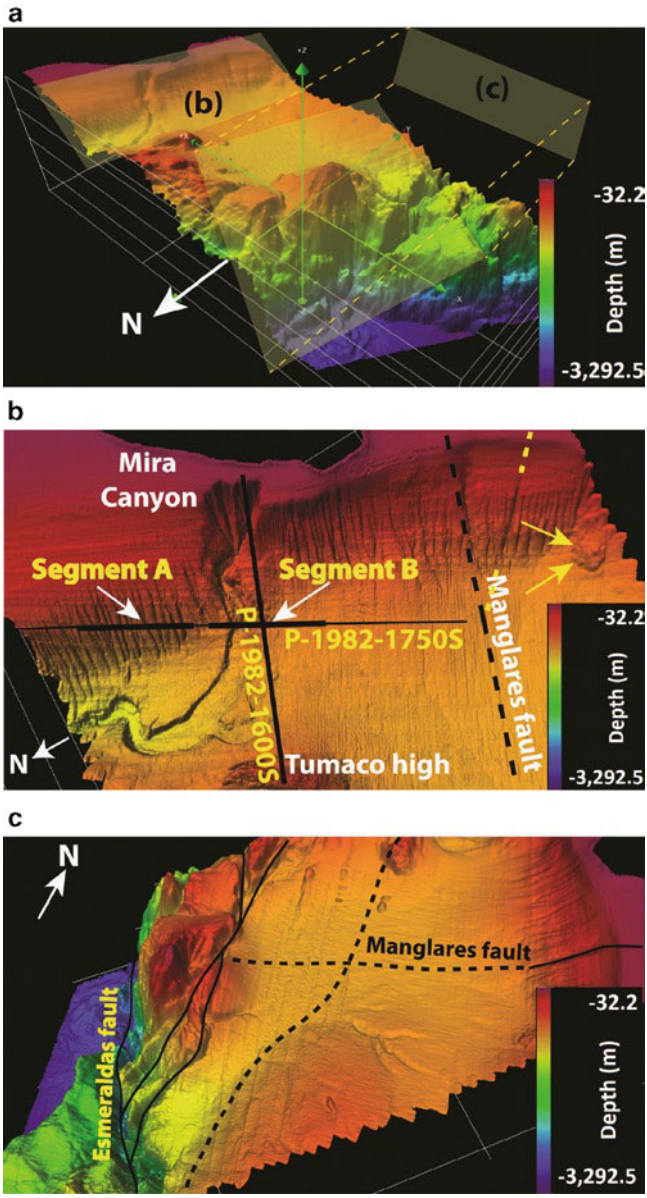

Fig. 33.4 (**a**) Bathymetric surface projecting two perspective panels (**b**) Perspective view toward the Mira Canyon. *Black bold lines* correspond to seismic lines analyzed in this work. *Dashed lines* are suggesting inferred faults. *Yellow arrows* are indicate a submarine landslide (**c**) Perspective view toward the Esmeraldas fault indicating a strong structural control near to the trench. Because of the high sedimentary charge from Mira and Patia rivers, the Manglares basin is hiding other faults (*dashed lines* show inferred faults)

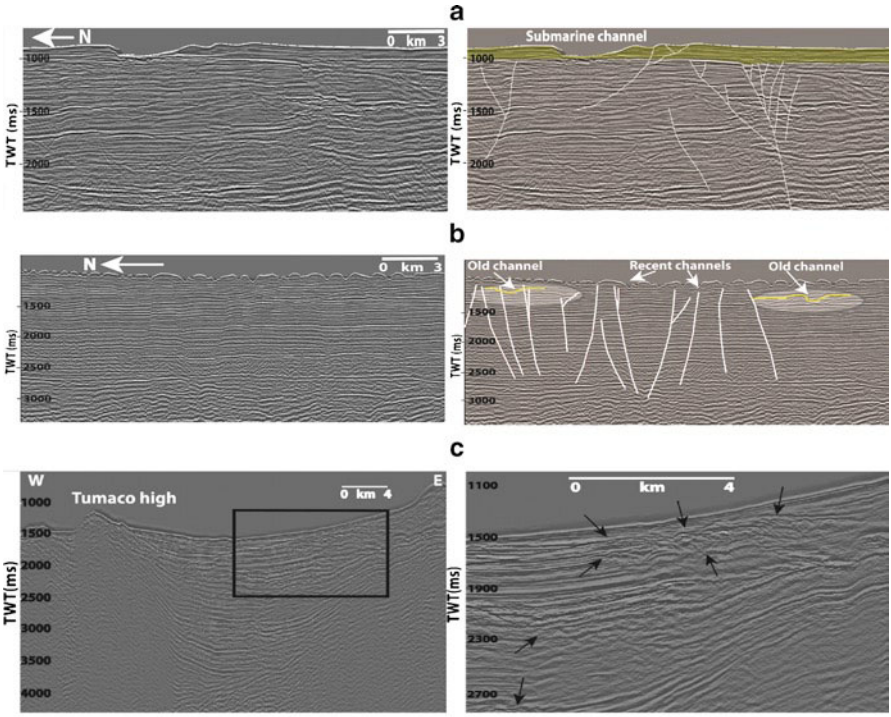

Fig. 33.5 Seismic images of the time-migrated lines P-1982-1750S (**a**) and (**b**), and P-1982-1600S (**c**) acquired by ECOPETROL (see Fig. 33.4b). *Left panels* are uninterpreted images and *right panels* correspond to their respective interpretations (**a**) **Segment A** indicating the submarine channel of the Mira canyon and recent sediments that covering the active tectonic in the Manglares basin (**b**) **Segment B** showing slope gullies controlled by faults that in turn act as planes of weakness that facilitate the generation of submarine slides. *Ellipses* highlight the presence of old channels (gullies?) that have been incorporated into the Manglares basin by rapid sedimentation and overlap of submarine landslides (**c**) Zoom that testifies the presence of an overlap of submarine landslides during the recent building of the Manglares basin. One of the last events is suggested by the *black arrows*

material in the western area (e.g., Tumaco high in Fig. 33.5c); and (2) the WNW faults, which control the slope gullies and subsequent submarine landslides that add material to the basin.

33.5 Discussion

Crustal splay faults related to accretion along the NESC margin have been proposed as a mechanism to rupture the crust in this subduction area (Collot et al. 2004). Geomorphologic expressions of this accretion process and detected by the bathymetric data of this work include the Esmeraldas fault, the Manglares high and the Tumaco high, whose areas are partly covered by an up-to 3.3-km-thick deep-sea

turbidite system in the Manglares basin (Fig. 33.4b, c). Collot et al. (2007) has suggested that the turbidite system feeds the Colombian trench via the Esmeraldas, Patia and Mira canyons and rivers. According to these authors, this region of thick sediment appears to be dominantly subducting beneath an erosional margin basement, thus forming a km-thick subduction channel that is modulated by the subduction of a buried, large horst and graben structure on the downgoing Nazca plate. This region of thick sediment and rough oceanic crust subduction coincides with the zone of hypocenters of subduction earthquakes, which occur beneath the subsiding Manglares fore-arc basin. As consequence of these large events, long-term subsidence of the Manglares basin has been well-documented (Herd et al. 1981). The accommodation of the oceanic crust and the respective co-seismic subsidence may have triggered the development of the Mira canyon. However uncertainty about age of this canyon is difficult to constrain. In addition to the large earthquakes of the twentieth century, Dumont et al. (2006) have reported evidence of a 3200-2800 BP earthquake event affecting the Esmeraldas-Tumaco area. Any of these events, or even contributions of each one, may be responsible for today's geometry of the Mira canyon. Nevertheless, constraining the timing of the Mira canyon in such a submarine environment constitutes a challenge for quantitative geomorphology dating. During our attempt in this paper we found that the main uncertainty is the definition of a plausible diffusion constant κ. We also found that a linear solution to the scarp-fault diffusion hypothesis may be far to an accurate solution. Moreover, recent observations of the 1959 Hebgen Lake, Montana, earthquake scarp and similar features worldwide confirm that scarps require a finite period of mass failure to reach the initial conditions for hillslope diffusion, so the age of features less than 1,000 year old cannot be accurately estimated with methods based only on the linear diffusion equation (Kogan and Bendick 2011).

Taking into account the high complexity of the problem, the submarine setting, the high rates of sediment flux and the lack of deep oceanographic conditions, we have tested three different scenarios in order to identify the triggering event that initiated the Mira canyon. Accepting ages like (a) 30 year for the 1979 event, due to its proximity to the canyon; (b) 112 year for the 1906 event, due to its large energy; and (c) ~3,000 year, due to large ground effects along the entire region (Dumont et al. 2006); the linear solution to the scarp-fault diffusion hypothesis is supporting κ values ranging between 33 and 133 for case (a); 8.9 and 35.7 for case (b); and 0.001 and 1.33 for case (c). The lower limit of the scenario (c) is near to the κ values reported by Mitchell (1996) for submarine conditions near the Galapagos spreading center in the Pacific Ocean. In that case, the most probable event that triggered the Mira canyon may correspond to the 3200-2800 BP earthquake event.

33.6 Conclusions

- The morphological features imaged in the study area with the high-resolution bathymetric survey include the Tumaco high, the Emerald canyon and the Mira canyon, limited on its western edge by the Manglares high. Geophysical studies

in the area suggests that these prominent highs correspond to fragments of basement raised pplifted during the accretion process and/or the presence of oceanic asperities being brought during the subduction.
- The Manglares basin is segmented by transverse faults, some of them are partly covered by a deep-sea turbidite system that feeds the Colombian trench via the Esmeraldas, Patia and Mira canyons and rivers.
- Along the continental slope, gullies are aligned with vertical to near-vertical faults. These gullies facilitate the development of submarine landslides, whose material is incorporated into the Manglares basin.
- Earthquakes may be responsible for accelerating the incorporation of submarine landslide materials into the Manglares basin.
- The Mira canyon is a prominent scar of the Manglares basin that is 44 km long, 3 km wide, and with a depth of incision of 0.1 km. The most probable earthquake event that triggered the Mira canyon as a slide scar could correspond to the 3200-2800 BP earthquake event.

Acknowledgments The authors would like to express their appreciation to National Hydrocarbons Agency of Colombia for permitting use of the seismic and bathymetric data. This work was conducted under the seismotectonic research of the Graduate Program of Geophysics of the Universidad Nacional de Colombia and the CBTH project of the University of Texas at Austin. We also thank the reviewers Drs. L. Moscardelli and V. Huerfano for critiquing and improving this manuscript. This study was partially supported by COLCIENCIAS throughout projects 1233-333-18664, 1233-487-25728, Contracts 201-2006 and 589-2009; CGL2005-04541-C03-02 and CGL2008-00869/BTE (UPC, MICCIN, FEDER). Seismic sections were done with SMT software.

References

Askew BL, Algermissen ST (eds) Proano E (1985) Catalog of earthquakes for South America, Vol. 6, Hypocenter and Intensity Data, CERESIS, Lima

Beck SL, Ruff LJ (1984) The rupture process of the great 1979 Colombia earthquake: evidence for the asperity model. J Geophys Res 89:9281–9291

Collot J-Y, Marcaillou B, Sage F, Michaud F, Agudelo W, Charvis P, Graindorge D, Gutscher MA, Spence GD (2004) Are rupture zone limits of great subduction earthquakes controlled by upper plate structures? Evidence from multichannel seismic reflection data acquired across the northern Ecuador – southwest Colombia margin. J Geophys Res 109:B11103. doi:10.1029/2004JB003060

Collot J-Y, Marcaillou B, Agudelo W, Ribodetti A, D'Acremont E (2007) The Mw 8.8, 1906 Colombia-Ecuador subduction earthquake: seismic structure and thermal regime of the plate boundary. Am Geophys Union, Spring Meeting 2007, abstract #T43A-04

Dumont JF, Santana E, Valdez F, Tihay JP, Usselmann P, Iturralde D, Navarette E (2006) Fan beheading and drainage diversion as evidence of a 3200-2800 BP earthquake event in the Esmeraldas-Tumaco seismic zone: a case study for the effects of great subduction earthquakes. Geomorphology 74:100–123

Gutscher MA, Malavieille J, Lallemand S, Collot JY (1999) Tectonic segmentation of the North Andean margin: impact of the Carnegie Ridge collision. Earth Planet Sci Lett 168:255–270

Hanks TC (2000) The age of scarplike landforms from diffusion-equation analysis. In: Nollet JS, Sowers JM, Lettis WR (eds) Quaternary geochronology: methods and applications. American Geophysical Union, Washington, DC

Hanks TC, Bucknam RC, Lajoie KR, Wallace RE (1984) Modification of wave-cut and faulting-controlled landforms. J Geophys Res 89:5771–5786

Herd DG, Leslie T, Meyer H, Arango JL, Person JW, Mendoza C (1981) The great Tumaco, Colombia earthquake of 12 December 1979. Science 211:441–445

Kanamori H, McNally KC (1982) Variable rupture mode of the subduction zone along the Ecuador-Colombia coast. Bull Seism Soc Am 72(4):1241–1253

Kogan L, Bendick R (2011) A mass failure model for the initial degradation of fault scarps, with application to the 1959 scarps at Hebgen Lake. Montana Bull Seism Soc Am 101(1):68–78. doi:10.1785/0120100107

Lonsdale P (2005) Creation of the Cocos and Nazca plates by fission of the Farallon plate. Tectonophysics 404:237–264

Marcaillou B, Collot JY (2008) Chronostratigraphy and tectonic deformation of the North Ecuadorian–South Colombian offshore Manglares forearc basin. Mar Geol 255:30–44

Mitchell NC (1996) Creep in pelagic sediments and potential for morphologic dating of marine fault scarps. Geophys Res Lett 23(5):483–486

Ratzov G, Collot J-Y, Sosson M, Migeon S (2010) Mass transport deposits in the northern Ecuador subduction trench: result from frontal erosion over multiple seismic cycles. Earth Planet Sci Lett 296:89–102

Ratzov G, Sosson M, Collot J.-Y, Migeon S, Michaud F, Lopez E, Le Gonidec Y (2007) Submarine landslides along the North Ecuador South Colombia convergent margin: possible tectonic control, in submarine mass movements and their consequences, pp. 47–55, In: Lykousis V, Sakellariou D, Locat J (eds) Springer, Dordrecht.

Restrepo JD, Lopez S (2008) Morphodynamics of the Pacific and Caribbean deltas of Colombia. S Am J Earth Sci 25:1–21

Syvitski JPM, Kettner AJ, Correggiari A, Nelson BW (2005) Distributary channels and their impact on sediment dispersal. Mar Geol 222–223:75–94

Witt C, Bourgois J, Michaud F, Ordonez M, Jimenez N, Sosson M (2006) Development of the Gulf of Guayaquil (Ecuador) during the Quaternary as an effect of the North Andean block tectonic escape. Tectonics 25:TC3017. doi:10.1029/2004TC001723

Chapter 34
Submarine Mass Wasting Off Southern Central Chile: Distribution and Possible Mechanisms of Slope Failure at an Active Continental Margin

David Völker, Jacob Geersen, Jan H. Behrmann, and Willhelm R. Weinrebe

Abstract Around 5–6% of the convergent continental margin of Southern Central Chile (33–42°S) is shaped by a variety of submarine mass wasting processes. We use swath bathymetric data covering >90% of the continental slope to map and investigate mass wasting-related seafloor features. In total, 62 submarine landslides are found that we separate into four categories (slides related to canyons, slides on open slopes, lower slope collapses and giant slope failures) with different failure mechanisms, preconditioning factors and time scales.

Keywords Submarine landslide • Mass-failure • Mass-transport • Slope failure Active continental margin

34.1 Introduction

With increasing coverage of submarine slopes by swath bathymetry echosounder data, the importance of downslope transport processes for shaping the seafloor becomes evident. Along with the increase in the number of described submarine slides, the knowledge of their variability in size, shape and internal deformation improves. The background relative to slope failure at convergent continental margins is fundamentally different from that of passive continental margins, because: (1) uplift and slope oversteepening are caused by frontal and basal sediment accretion, subduction erosion or seamount subduction; (2) megathrust earthquakes occur with a

D. Völker (✉) • J. Geersen • J.H. Behrmann • W.R. Weinrebe
SFB574, IFM-GEOMAR Leibniz Institute for Marine Sciences,
University of Kiel, Wischhofstr. 1-3, Kiel, Germany
e-mail: dvoelker@ifm-geomar.de

Y. Yamada et al. (eds.), *Submarine Mass Movements and Their Consequences*,
Advances in Natural and Technological Hazards Research 31,
DOI 10.1007/978-94-007-2162-3_34,

frequency in the range of centuries. In this study we present a dataset on mass-wasting related features affecting the continental slope of the Southern-Central Chile active margin (33–42°S, Fig. 34.1); the amount and detail of the data we analyze is comparable with that of datasets from passive margins (Hühnerbach and Masson 2004). The digital appendix to this article contains spreadsheet data on dimensions, properties and positions of these submarine landslides as well as mappable GIS data of detail features of the individual slides in the GRASS and ArcGIS format.

34.1.1 Geological Setting

The geological framework of the Southern Central Chilean continental margin is controlled by the subduction of the oceanic Nazca plate beneath South America at a present rate of 6.6 cm/year and an azimuth of about N78°W (Angermann et al. 1999). Until late Miocene, subduction erosion has controlled the marine forearc. Since then, sediment accretion resulted in the buildup of an accretionary prism between 33°S, where the Juan-Fernandez Ridge is subducting, and 46.5°S, where the Chile Triple Junction is located (e.g., Bangs and Cande 1997, Fig. 34.1). A common morphological feature of the study area is a lower continental slope with steep segments (up to 30°) alternating with trench-parallel belts of less steep and even landward verging seafloor. This morphology is caused by the continuous deformation of the accretionary prism (Contreras-Reyes et al. 2008). In contrast, the upper continental slope appears smoother and the seafloor here is only interrupted by ridges and escarpments that are surface expressions of faults (Geersen et al. 2011). Seismic studies (Contreras-Reyes et al. 2008) show that the transition coincides with a landward increase in seismic velocities. The rocks that underlie the upper slope are seen as part of a Mesozoic accretionary complex that serves as active backstop for the presently deforming prism (Bangs and Cande 1997). This general morphological pattern is interrupted offshore Arauco Peninsula (36.5–39°S). Here, uplift across transpressive upper plate faults, that are aligned oblique to the direction of plate motion controls the morphotectonic setting on the mainland (Melnick et al. 2009; Rehak et al. 2008) and likely also affects the marine forearc (Geersen et al. 2011).

Seven major submarine canyons incise the continental margin in the study area. From N to S these are San Antonio, Mataquito, Itata, BioBio, Paleo-Pellahuen, Imperial/Tolten and CalleCalle canyons (Fig. 34.1a). All major canyons are directly connected to river systems that drain the Andes and the Coastal Cordillera.

Plate convergence results in large subduction earthquakes ($Mw > 8.5$) by which the main seismogenic segments have been defined. The recurrence interval of megathrust earthquakes for the individual segments typically lies between 150 and 200 years (Lomnitz 1970). On 27 February 2010, the Central Chilean Maule Region between Constitución and Concepción was hit by such a megathrust earthquake of Mw 8.8. Strong earthquakes are considered potential triggers for slope failure and submarine landslides.

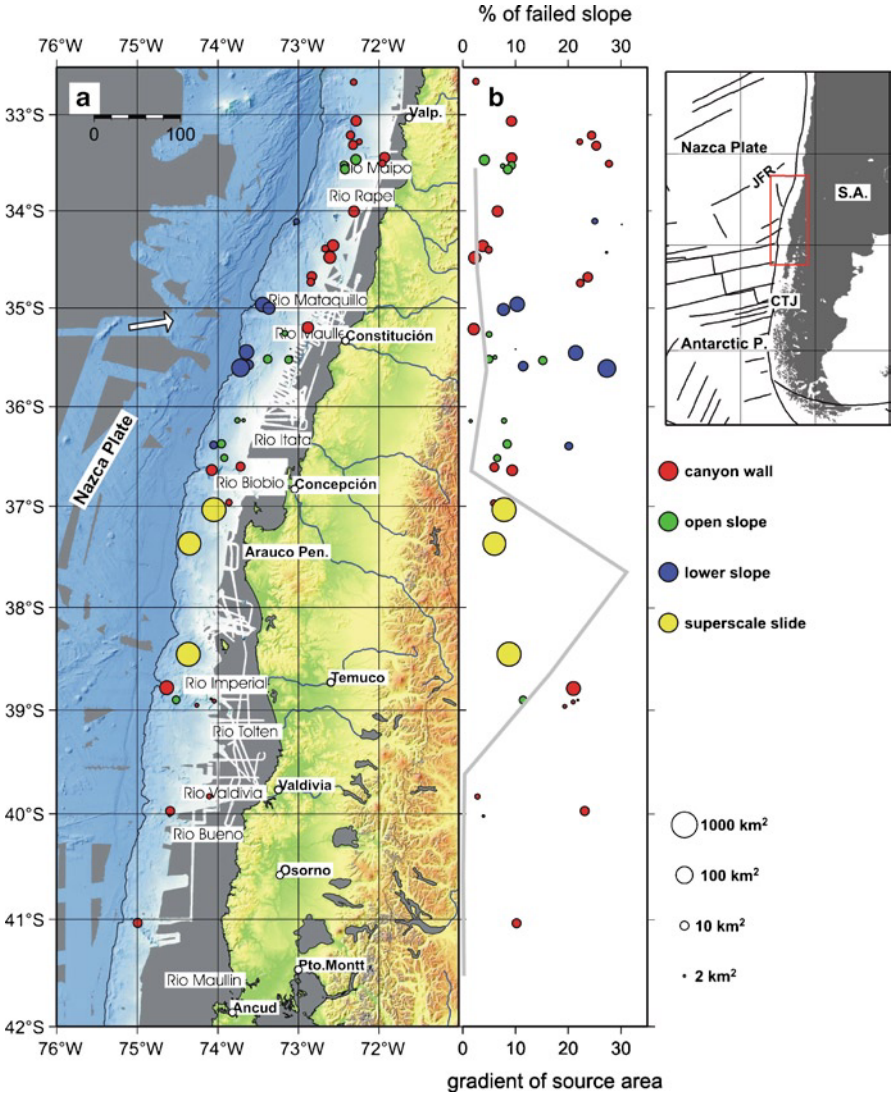

Fig. 34.1 (**a**) Bathymetric map of the working area, from a compilation of bathymetric cruises. The centers of submarine landslides are indicated as *points* (*red* = canyon wall collapses, *blue* = failures of lowermost slope, *green* = open slope failures, *yellow* = superscale failures) (**b**) Spatial distribution of submarine landslides along the continental slope of Central Chile and distribution with slope gradient. Size of symbols is log-scaled to the total affected area. The percentage of areas affected by slides in latitudinal segments of 1° is given as *curve*

34.1.2 Methods

Bathymetric datasets have been acquired during successive cruises on board RV SONNE, RV METEOR and RRS JAMES COOK using deep water echo sounders (SIMRAD EM-120 and 122); data cover ~90% of the continental slope off Central Chile. After post-processing, Digital Elevation Models (DEMs) were calculated to digitize details of the morphology and determine gradients and areal extent of related features. Bathymetric data acquired prior to and shortly after the 27 February 2010 Mw 8.8 Maule earthquake are available, allowing to image seafloor deformation related to the earthquake.

The volume of the material involved in the slides can be estimated from swath bathymetry data alone, if the resulting bathymetric features are well preserved and the background morphology is simple. In such cases, volumes are calculated by restoring a (hypothetical) original surface at either the slope scarp or at the place of redeposition and determining the volume difference between both. This is done with the numerical tool "the healer" (Völker 2009).

34.2 Results

In total, 62 submarine landslides were mapped with areal extent ranging between 1 and 1,285 km^2. Roughly, 5.7% of the continental slope between 33°S and 42°S is affected by mass wasting, but within certain slope sectors this value increases significantly; in particular, the zone off Arauco Peninsula (between 37°S and 38°S) stands out with 31% of failed slope (Fig. 34.1b). Based on their different morphology, size and area of occurrence, we distinguish four basic groups of sediment failure: (1) failure related to submarine canyons, (2) failure on open slopes, (3) failure affecting the lowermost continental margin and (4) failure at the scale of the entire slope. The latitudinal distribution, the size and the slope gradient for each of the slides herein documented is shown in Fig. 34.1b, together with the ratio of failed/unfailed slope area. The distinction coincides with fundamentally different failure mechanisms. In the following we present details for each of the four types of slides, providing the base for a discussion of preconditioning factors, possible triggers and frequency of slope failure.

34.2.1 Slides Related to Submarine Canyons

Half of the slope failures (33) are related to submarine canyons and all of the seven major canyons are bordered by slides. The slides are small in size (<30 km^2, with only three slides >30 and <90 km^2) and appear independent of the water depth (Fig. 34.1).

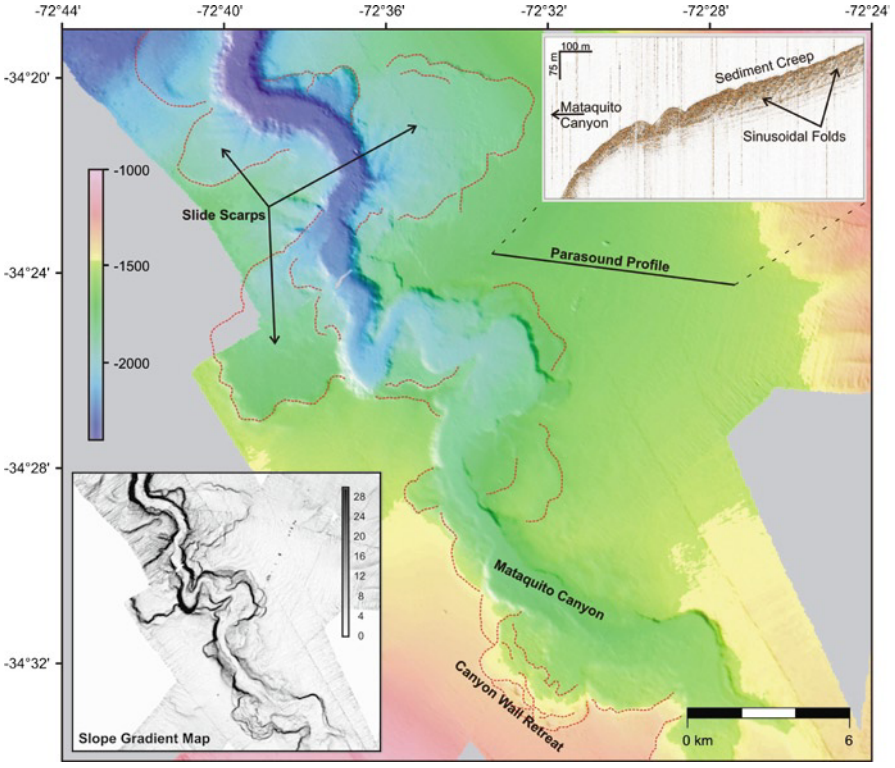

Fig. 34.2 Mass wasting at the sides of Mataquito Canyon. The map shows semicircular indentations of the canyon walls and multiple generations of flat-floored retrogressive failures that extend from the canyon wall collapses. The sediment echosounder profile shows creep deformation affecting sediment upslope of the failures

They are discernible as retreat of the canyon walls in the form of semicircular indentations that in places merge into elongate canyon wall collapses (Fig. 34.2). Often, there are secondary slides that extend from the canyon wall failures onto the open slope, forming pan-shaped depressions with steep walls (10–27°, Fig. 34.2) and a flat floor parallel to the undisturbed slope. The walls of secondary slides can be modified by further generations of semi-circular depressions. Upslope of some large failures, creep of sediment is obvious in the form of wavy deformations affecting otherwise parallel strata of hemipelagic sediment (Fig. 34.2).

In some cases, the collapsed material is still present as sagged and rotated sediment body within the canyons, but more often it is missing, likely because it is distributed within the canyons or transported into the trench. Within the BioBio Canyon, material of three consecutive failure events was found in a gravity core, whereas the San Antonio Canyon floor is devoid of unlithified sediments (Linke et al. 2011).

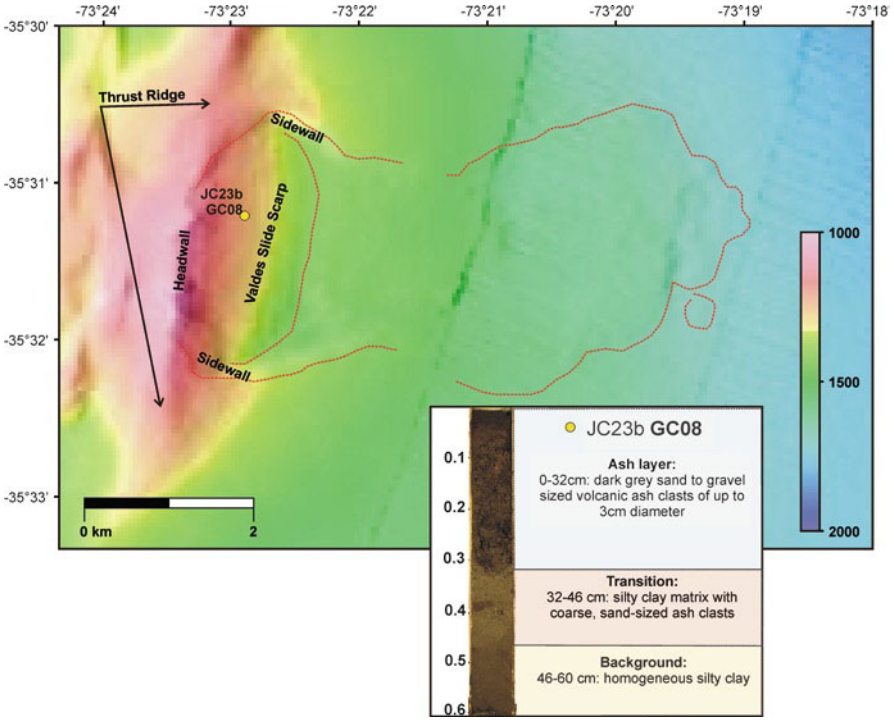

Fig. 34.3 Valdes Slide on the upper continental slope. This slide developed on the landward side of a prominent thrust ridge. Gravity core JC23b-GC08 from the exposed slide scar sampled a 30 cm thick ash clast layer

34.2.2 Slides on the Open Slope

Submarine slides on the open slopes have similar dimensions to those related to canyons (1–30 km^2). Seventeen slides of this category occur in water depths between 200 and 2,300 m where the slope gradient is less than 16° (Fig. 34.1b). The majority does not show any discernible relationship with the irregular topography and seems to have formed on gently inclined smooth slopes that are largely unfailed around them. The evacuation site typically has the form of isolated pan-shaped depressions with clearly defined lateral and head walls. In most cases, morphological features typical for displaced sediment are not clearly evidenced, perhaps being absent or buried.

Three slides fall out of this scheme as they are related to a trench-parallel thrust ridge on the middle slope which represents the surface expression of a deep-seated fault (Geersen et al. 2011) and produced differential uplift at the side of a slope basin (Contardo et al. 2008). Of those, the Valdes Slide formed at the landward side of this ridge and transported debris landward (Fig. 34.3). At the slide scar of Valdes Slide, a 30 cm thick volcanic ash clast layer was exposed (Anasetti et al. 2010).

34.2.3 Failure of the Lowermost Continental Slope

Steep (~30°) parts of the lowermost continental slope show a number of indentations, interrupting largely unfailed slopes between 34°S and 37°S (Fig. 34.1). Six slides of this kind are preserved in water depths between 2,100 and 5,000 m and two smaller slides lie on the flanks of sediment thrust ridges at the deformation front of the subduction zone. Lower slope collapses are significantly larger than slides related to canyons (15–217 km^2) and form irregular, steep, bowl-shaped depressions that end at the flat trench floor. In most cases, the displaced rock is either buried in the trench fill or absent.

Among this category, the Reloca Slide is the most noticeable because of its size and volume (217 km^2, 24 km^3, Völker et al. 2009) and because the displaced rocks are preserved as prominent features in the Chile Trench. The lower continental slope facing Reloca Slide is steep (20–30°) and with an arcuate shape reflecting the slide headscarp, which is characterized by a well-preserved crown at about 2,900–3,000 m water depth, thus forming a steep and straight ramp of 2,000 m elevation (Fig. 34.4).

The slide deposits consist of three blocks rising some 100 m and about 25 smaller blocks rising some 10 m above a cone of scattered debris (Fig. 34.4, outlines in yellow). The debris field has a run-out distance of 18 km and crosses (and partly buries) the 50–60 m deep axial channel of the Chile Trench. The larger blocks appear angular with steep flanks and lie directly at the foot of the continental slope. The blocks together make up roughly 90% of the material that is missing at the slope scar. The smaller blocks form clusters with a number of blocks aligned at the outer rim of the debris cone.

34.2.4 Giant Slope Failures

Offshore Arauco Peninsula (Fig. 34.1), three huge slope indentations ranging in areal extent 1,285, 924 and 1,145 km^2, respectively, shape the continental slope down to the abyssal plain and notably change the seismic reflection pattern of the sedimentary trench fill (Geersen et al. submitted, Fig. 34.5 insert). Two of these failures cause a landward retreat of the shelf break. The volume of material missing at the slope is in the order of 300–500 km^3 for each of the three slides.

The failure structures are discernible as elongate embayments with steep, up to 500 m high lateral and headwalls and chaotic seafloor morphology in the centers. The significant morphological differences between failed and unfailed slope suggests that huge rock volumes have been involved in the failure.

Seismic reflection profiles across the Chile Trench in front of these slope embayments show a chaotic interval embedded into well stratified undisturbed (turbiditic) sediments (Geersen et al. submitted). This is in marked contrast with the typical reflection pattern of the trench fill elsewhere, characterized by well-stratified sediment onlapping onto the subducting Nazca Plate (Fig. 34.5, inserts).

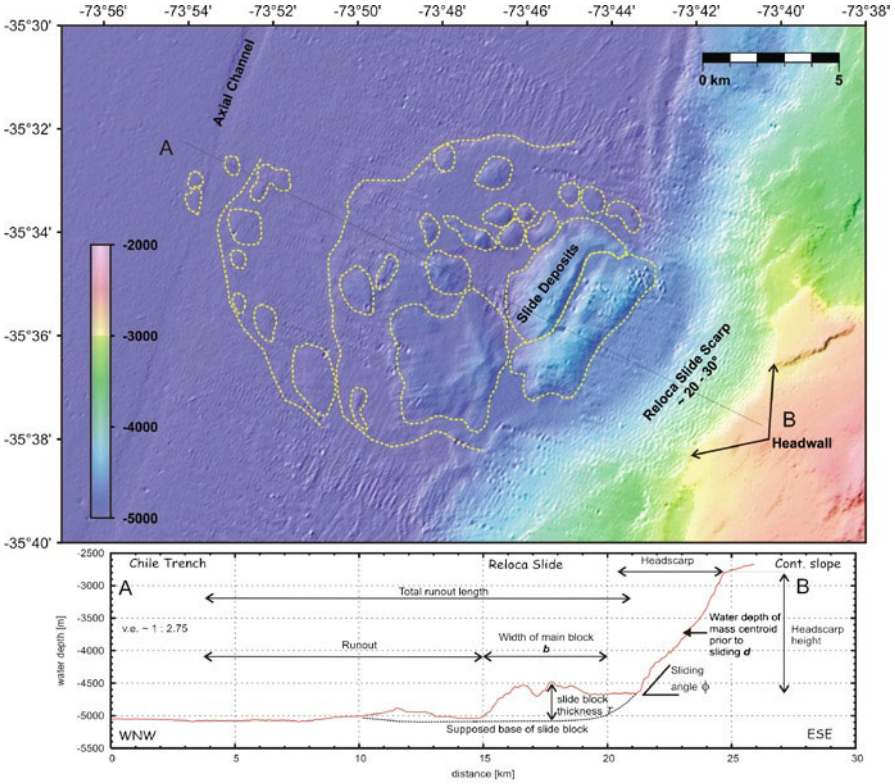

Fig. 34.4 Reloca Slide: Bathymetry and cross section along the slide complex. The depth profile runs from point *A* to *B*

34.3 Discussion and Conclusion

The flat slope-parallel floor of the evacuation areas of slides related to canyons and on open slopes suggests translational failure along lithologically defined weak layers some tens of meters below the seafloor. The most plausible cause for submarine canyon wall collapse is the destabilization by continuous or periodic canyon incision by sediment transport. The retrogression by secondary slides as well as the initiation of creep in slope sediments is a consequence of the removal of support with the initial collapse. As the canyons seem to have been more active during the last glacial (Völker et al. 2006), probably many of the features predate the Holocene. Retrogressions follow the initial wall collapses and often appear morphologically fresh. The youngest of a series of mass-wasting-related sediment units in the BioBio Canyon has a minimum age of 0.7–1 ka (Völker et al. submitted).

For slides on open slopes, failure mechanism is less evident. In the vicinity of tectonic features such as the thrust ridges where Valdes Slide is observed (Fig. 34.4), a

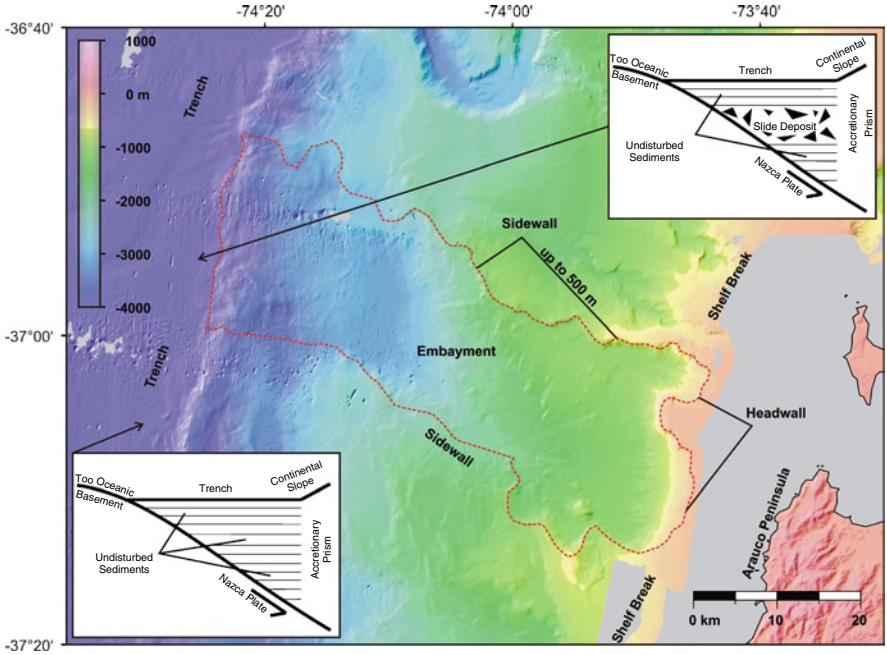

Fig. 34.5 Giant slide offshore Arauco Penisula. The slope indentation is bordered by steep walls, impinges on the course of the shelf break and reaches down to the sediment-filled Chile Trench. *Inserts* show simplified schemes of the seismic reflection pattern along the trench fill in front and south of the slope embayment

combination of continuous oversteepening and earthquake-induced vertical motion is possible. For a large number of slides, however, triggering and failure mechanisms are enigmatic, as the morphological conditions do not seem to differ from the surrounding unfailed slope. While Valdes Slide appears fresh in terms of morphology, Taza slide is covered by some 20 m of well-stratified sediment, as can be seen in sediment echosounder data.

The nature of the weak layers is unknown so far, but they seem to be present at discrete depth levels. Valdes slide appears to have failed along a thick, coarse layer of volcanic ash. Tephra layers of the Southern Volcanic Zone of Chile form huge sediment bodies on land and are found in cores offshore (Völker et al. 2006). They are considered potential weak layers because of their mechanical behaviour when subject to earthquake ground motion (Harders et al. 2010). However, neither new submarine landslides on the open slopes nor fresh failures of canyon or slide walls seem to have formed as a consequence of the Maule earthquake (Chadwell et al. 2010; Weinrebe et al. 2010; Völker et al. submitted).

Lower slope collapses and giant slope failures differ from the former groups by cutting deeper than 100 m into lithified rocks that lie beneath the slope sedimentary cover. At the lowermost slope this is material of the frontal prism that was accreted

over the last 6 Ma, while in water depths less than 2,000 m this can be material of a Mesozoic accretionary complex, of Permian-Oligocene forearc basins as well as of the Paleozoic continental framework (Contreras-Reyes et al. 2008). The displaced rock bodies are some 100 m thick and the failure planes are slightly curved, indicating detachment planes that are not lithologically defined. Also, both types appear only within given latitudes where the continental margin is affected by particular tectonic lineaments that determine local to regional uplift of the marine forearc (Geersen et al. 2011).

The area where large lower slope collapses are present is characterized by localized uplift due to focussed basal sediment accretion. Here, the lowermost slope is particularly steep and may have reached a critical angle. Reloca Slide postdates the incision of the central axial channel of the Chile Trench (Fig. 34.3). The channel is believed to have been carved out about 10–12 ka BP (Völker et al. 2006).

Super-scale failures are restricted to offshore Arauco Peninsula which has been described as an anomalous stretch of forearc in terms of morphostructural setting, uplift history and occurrence of continental faults (Rehak et al. 2008; Melnick and Echtler 2006; Melnick et al. 2009). Uplift of the marine forearc seems to be the main agent leading to slope over-steepening, finally preconditioning the observed slope instabilities (Geersen et al. 2011). The thickness of the sediment cover of the slide-related debris corresponds to a minimum age of 200 ka for the youngest of these events. To our knowledge, the described slope failures are among the largest landslide deposits at active margins known to date.

Dating of a large number of the described slides is required to investigate possible links to climatic cycles as well as for a geohazard analysis. Geotechnical experiments aiming to understand the nature of weak layers will be carried out for Reloca and Valdes slide.

References

Anasetti A, Krastel S, Weinrebe W, Klaucke I, Bialas J (2010) Detailed analysis of the Valdes slide: a landward facing slope failure off Chile. In: Abstract EGU2010-13497 presented at 2010 general assembly of the EGU, Vienna, 02–07 May 2010

Angermann D, Klotz J, Reigber C (1999) Space-geodetic estimation of the Nazca-South America Euler vector. Earth Planet Sci Lett 171(3):329–334

Bangs NL, Cande SC (1997) Episodic development of a convergent margin inferred from structures and processes along the southern Chilean margin. Tectonics 16:489–503

Chadwell CD, Lonsdale P, Kluesner JW, Sweeney AD, Weinrebe W, Behrmann JH, Diaz-Naveas JL, Contreras Reyes E (2010) An examination of "before" and "after" bathymetry for uplift of the sea floor following the Feb. 27, 2010 Maule, Chile Earthquake. Abstract G33A-0851 presented at 2010 fall meeting, AGU, San Francisco, 13–17 Dec 2010

Contardo X, Cembrano J, Jensen A, Díaz-Naveas J (2008) Tectono-sedimentary evolution of marine slope basins in the Chilean forearc (33°30′–36°50′S): insights into their link with the subduction process. Tectonophysics 459(1–4):206–218

Contreras-Reyes E, Grevemeyer I, Flueh ER, Reichert C (2008) Upper lithospheric structure of the subduction zone offshore of southern Arauco Peninsula, Chile, at ~38°S. J Geophys Res 113:B07303

Geersen J, Behrmann JH, Völker D, Krastel S, Ranero CR, Diaz-Naveas J, Weinrebe RW (2011) Active tectonics of the South Chilean marine forearc (35°S–40°S). Tectonics. doi:10.1029/2010TC002777

Geersen J, Völker D, Behrmann JH, Reichert C, Krastel S (submitted) Pleistocene giant slope failures offshore Arauco Peninsula, Southern Chile. J Geol Soc

Harders R, Kutterolf S, Hensen C, Moerz T, Brueckmann W (2010) Tephra layers: a controlling factor on submarine translational sliding? Geochem Geophys Geosyst 11(5):Q05S23

Hühnerbach V, Masson DG (2004) Landslides in the North Atlantic and its adjacent seas: an analysis of their morphology, setting and behaviour. Mar Geol 213(1–4):343–362

Linke, P. and scientific cruise participants (2011). FS SONNE Fahrtbericht/Cruise Report SO210 ChiFlux - Identification and investigation of fluid flux, mass wasting and sediments in the forearc of the central Chile subduction zone, Valparaíso-Valparaíso, 23.09.-01.11.2010. IFM-GEOMAR Reports, 44, 112 pp., doi: 10.3289/ifm560geomar_rep_44_2011

Lomnitz C (1970) Major earthquakes and tsunamis in Chile during the period 1535 to 1955. Int J Earth Sci 59(3):938–960. doi:10.1007/BF02042278

Melnick D, Echtler HP (2006) Inversion of forearc basins in south-central Chile caused by rapid glacial age trench fill. Geology 34(9):709–712

Melnick D, Bookhagen B, Strecker MR, Echtler HP (2009) Segmentation of megathrust rupture zones from fore-arc deformation patterns over hundreds to millions of years, Arauco peninsula, Chile. J Geophys Res 114:B01407. doi:10.1029/2008JB005788

Rehak K, Strecker MR, Echtler HP (2008) Morphotectonic segmentation of an active forearc, 37°–41°S, Chile. Geomorphology 94(1–2):98–116

Völker D (2009) A simple and efficient GIS tool for volume calculations of submarine landslides. Geo Mar Lett. doi:10.1007/s00367-009-0176-0

Völker D, Wiedicke M, Ladage S, Gaedicke C, Reichert C, Rauch K, Kramer W, Heubeck C (2006) Latitudinal variation in sedimentary processes in the Peru-Chile Trench off Central Chile. In: Oncken O et al (eds) The Andes – active subduction orogeny, Frontiers in earth sciences. Springer, Berlin/Heidelberg, pp 193–216

Völker D, Weinrebe W, Behrmann JH, Bialas J, Klaeschen D (2009) Mass wasting at the base of the south central Chilean continental margin: the Reloca Slide. Adv Geosci 22:155–167

Völker D, Scholz F, Geersen J (submitted) Recent submarine slide in the rupture area of the 27 February 2010 Maule earthquake offshore Chile. Mar Geo

Weinrebe W, Behrmann JH, Chadwell CD, Lonsdale P, Sweeney AD, Diaz-Naveas JL, Contreras Reyes E (2010) High-resolution seafloor bathymetry of the rupture area “before” and “after” the magnitude 8.8 Chilean earthquake of 2010. Abstract G33A-0852 presented at 2010 fall meeting, AGU, San Francisco, 13–17 Dec 2010

Chapter 35
An Overview of the Role of Long-Term Tectonics and Incoming Plate Structure on Segmentation of Submarine Mass Wasting Phenomena Along the Middle America Trench

Rieka Harders, César R. Ranero, and Wilhelm Weinrebe

Abstract We study mass wasting along the Middle America Trench (MAT), a subduction zone dominated by tectonic erosion, using a comprehensive data set of seafloor relief. We integrate previous studies of long-term tectonic processes to analyze how they influence the evolution of the slope structure and precondition the continental slope for mass wasting. We have used the distribution of an inventory of 147 slope failure structures along the MAT to discuss their relation to subduction erosion. We interpret that preconditioning of the slope by long-term tectonics, interacts in a shorter-term scale with features on the under-thrusting oceanic plate to modulate the abundance and types of mass wasting phenomena. The complex origin of the incoming oceanic plate has produced abrupt lateral changes in plate age, crustal thickness, relief, and response to bending deformation at the trench, leading to its partitioning into six segments. We found that the continental-slope failure style and abundance are partitioned into six segments that spatially match the ocean plate segments.

Keywords Submarine landslide • Convergent margin • Subduction erosion

35.1 Introduction

At convergent margins with accretionary prisms most landslides and slumps seem related to contractional tectonics and fluid seepage, and have shorter lengths than failures at Atlantic continental slopes (McAdoo et al. 2000). Studies of submarine

R. Harders (✉) • W. Weinrebe
SFB 574 and IFM-GEOMAR, Wischhofstrasse 1-3, Kiel 24148, Germany
e-mail: rharders@ifm-geomar.de

C.R. Ranero
ICREA at CSIC, Barcelona Center for Subsurface Imaging, Instituto de Ciencias del Mar, Pg. Marítim de la Barceloneta 37-49, Barcelona 08003, Spain

Y. Yamada et al. (eds.), *Submarine Mass Movements and Their Consequences*, Advances in Natural and Technological Hazards Research 31,
DOI 10.1007/978-94-007-2162-3_35,

mass wasting at convergent margins dominated by tectonic erosion are comparatively limited; however, this type of system is active in about 50% of the world subduction zones. Failures have been studied at slopes in Peru (von Huene et al. 1989), Costa Rica and Nicaragua (von Huene et al. 2004a; Hühnerbach et al. 2005) and New Zealand (Kukowski et al. 2011) but extensive studies have not been attempted. Harders et al. (2011) have constructed an inventory of 147 slope failure structures along ~1,300 km of the continental slope of the MAT. The data have been collected along the MAT from the Mexico–Guatemala border to southernmost Costa Rica. This region has been investigated by international programs during the last four decades and particularly during the last decade as focus area of the US-Margins and German SFB 574 programs. The goal of this contribution is to analyze how preconditioning of the continental slope by long-term tectonics and interacts with changes in the character of the currently subducting oceanic plate to modulate mass wasting phenomena.

35.1.1 Oceanic Plate Segmentation

The oceanic Cocos Plate subducts under the Caribbean Plate along the MAT at a rate of ~85 mm/year in the study region (DeMets 2001). The Cocos Plate is composed of lithosphere formed at the Cocos-Nazca and East Pacific Rise spreading centers, one of them affected by a hot spot (Fig. 35.1). The complex origin of the plate has produced abrupt lateral changes in plate character, including variation in plate age, crustal thickness, plate relief, and response to bending deformation at the trench (Barckhausen et al. 2001; Ranero et al. 2005). The section of the plate subducting under most of Costa Rica was formed at the Cocos-Nazca spreading center influenced by Galapagos hotspot. Changes in hotspot-ridge interaction formed distinct plate segments (Fig. 35.1).

The Cocos Ridge segment has 10–18-km-thick crust that creates a comparatively shallow swell with a relief festooned by elongated km-high ridges and few-hundred-meter high seamounts. To the NW is a seamount segment characterized by 7–8 km-thick crust with 2–3 km-high, 10–30 km wide seamounts, guyots and ridges. Offshore of the North Nicoya Peninsula the smoothest ocean seafloor of the entire region is subducted. The plate under-thrusting from offshore North Nicoya Peninsula to Guatemala was formed at the East Pacific rise (Fig. 35.1). The segment offshore Nicaragua has ~5.5 km-thick-crust, numerous ~0.5–1.0-km-high seamounts and is heavily faulted by bending of the plate before under-thrusting. Normal faults form a rugged terrain, with 200–500-m-high horst and graben relief striking parallel to the trench axis. Two other segments subducts under El Salvador and Guatemala. The Guatemala segment has the highest topography of up to 800-m-high ridges formed by bending-related faults that strike oblique to the trench axis (Ranero et al. 2005).

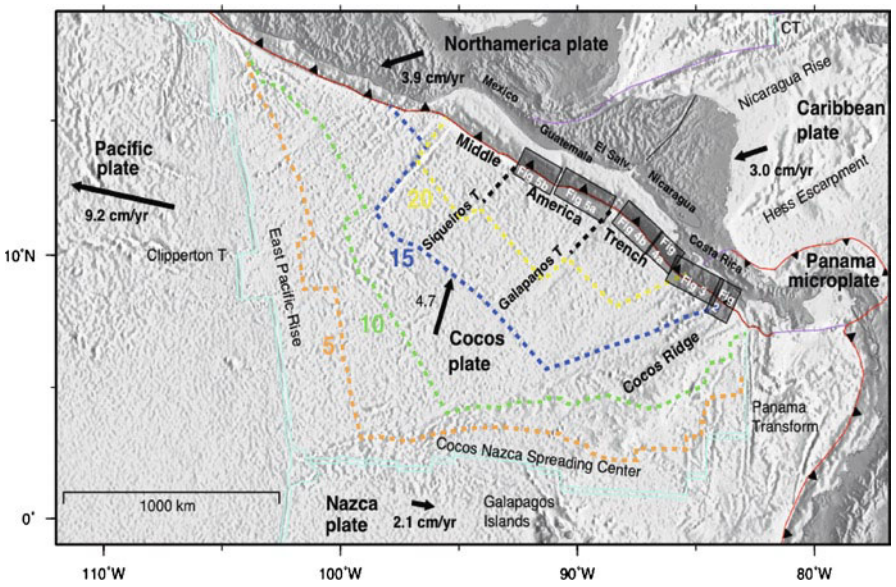

Fig. 35.1 Tectonic plates of the subduction system of Central America. The plate subducting along the Middle America Trench was formed at the Cocos-Nazca Spreading Center in the south-eastern and at the East Pacific Rise in the north. Isochrones are marked by *dashed-lines*, with age in million years. The *semi-transparent box* marks study region with segments discussed in the text

35.1.2 Tectonic Erosion Processes

The study region of the MAT is dominated by long-term tectonic erosion processes that have operated in the entire area for the last ~15–25 m.y. (Ranero et al. 2000). Tectonic erosion processes remove material from the base of the overriding plate and transfer it to the subduction channel to be transported to deeper levels. Thus, tectonic erosion implies the progressive migration of the plate boundary into shallower levels of the overriding plate. The upward movement of the plate boundary fault is probably assisted by over-pressured fluids at the fault zone, that hydrofracture the base of the overriding plate and migrate up, leading to the establishment of a new shallower decollement (von Huene et al. 2004b). Tectonic erosion causes large-scale fracturing and faulting, slope over-steepening, and subsidence that fundamentally influence the structural evolution of the geological units under, and the morphology of, the continental slope (Ranero et al. 2008). The intensity and location of tectonic erosion processes appear to be spatially constrained by the relative abundance of fluids at the plate boundary (Ranero et al. 2008). The intensity and location of tectonic erosion has been interpreted as the dominant process that determines the structural evolution of the continental slope (von Huene et al. 2004b; Ranero et al. 2008).

35.2 Relationships Between Ocean Plate Character, Tectonic Erosion and Mass Wasting

The six segments of the oceanic plate described in Sect. 35.1 are found to correspond to six segments of the continental slope. Each of the slope segments displays distinct tectonic styles, slope morphology, and differences in type, abundance and spatial occurrence of mass wasting structures.

35.2.1 Osa Peninsula – Cocos Ridge Segment

The thick crust of Cocos ridge forms a ~100 km broad swell of seafloor about 1.0–2.0 km shallower that the rest of the incoming plate segments. The buoyancy of the young plate (14 Ma) with thick crust has dramatic effects in subduction processes. The plate does not appreciably bend approaching the trench axis and collides with the overriding plate causing slope-wide deformation (Fig. 35.2). The young plate age is associated to high heat flow and sediment dehydration in the subduction channel occurs across a comparatively narrow, shallow area about 20 km wide (Ranero et al. 2008). This area is positioned under, and spatially matches the width of, the narrowest (15–20 km) and steepest (average of 10–15°) continental slope in the region, situated offshore Osa Peninsula (Fig. 35.2). We interpret that the slope width

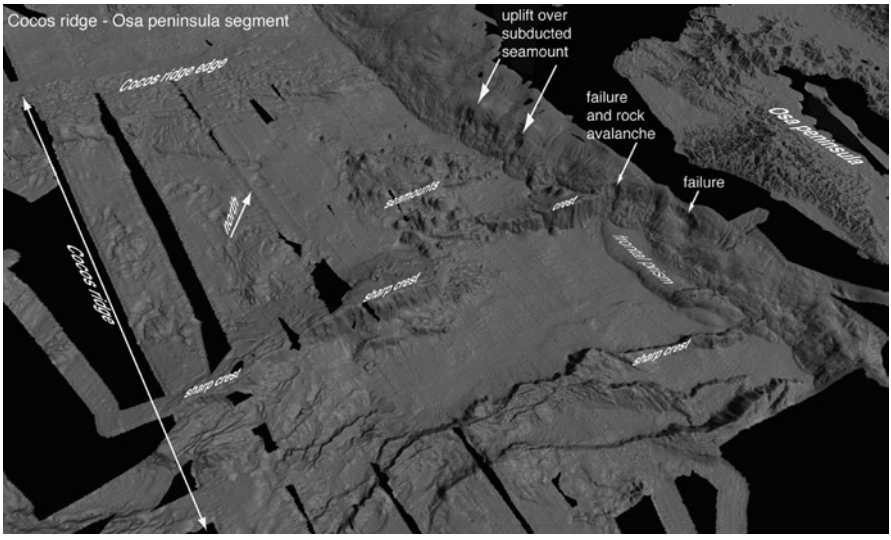

Fig. 35.2 Artificially illuminated, perspective view of Cocos Ridge, continental slope, and Osa Peninsula (3× vertical exaggeration [v.e.]). The image is 130 km wide along the trench axis. Ridge topography is elevated 1–2 km compared to the plate to the north. Trench axis depth is 1,950 m at SE edge of figure and 2,920 m at NW edge. The plate is ornamented with ridges up to ~1 km above surrounding seafloor and groups of small seamounts

is governed by the width of the underlying area of mineral dewatering, so that it is controlled by basal tectonic erosion of material of the overriding plate with concomitant subsidence.

The slope terrain is characterized by mass-failure morphology including concave scarps and rotational failures, and associated rock avalanches which deposit debris over the incoming plate seafloor (Fig. 35.2). Deformation of the slope appears so intense that canyon systems are poorly developed. In the SE, the slope is impinged by 0.5–1.0-km-high sharp crests of the Cocos Ridge that have created through time a rugged morphology across upper to lower slope. Landslides are ≤12 km long and ≤5 km wide. Their headwall are steep scarps up to 1 km high with angles ranging from 50° in the upper part to 30° in the lower part. Block deposits consist of large boulders up to 50 m high and 600 m long that extend 3–6 km into the smooth ocean plate seafloor. Deposits from some scarps are probably tectonically kneaded into the slope frontal units at the convergence rate of ~9 km per 100,000 year.

35.2.2 Central Costa Rica – Seamounts Segment

The central Costa Rica segment immediately north of the Cocos Ridge segment, is marked by an abrupt broadening of the slope from ~15–20 km to ~50–60 km width and a change in the average slope dip to less than 5° (Figs. 35.2 and 35.3). Here, the incoming oceanic plate is spotted with large conical seamounts, low ridges, and guyots created by the Galapagos Hotspot (Figs. 35.1 and 35.3). The prominent slope deformation caused by subduction of the features on the incoming plate for at least the last 300,000 years in this segment has attracted considerable scientific investigation, and major failures have been extensively studied (von Huene et al. 2004a, Harders et al. 2011).

Colliding seamounts remove sectors of the slope toe, causing a 10–20 km landward retreat of the deformation front. A frontal sediment prism is subsequently re-built by sediment kneading possibly coming from slope mass wasting. As collision progresses, seamounts under-thrust and uplift the slope as indicated by domes located above the seamounts (Ranero and von Huene 2000). Uplift causes widespread fracturing of the overriding plate extending further that the dome. Further movement of the seamounts causes rotational slumping in their wake. Slumps are >20 km long and wide and with rotational slide planes with steep headwalls up to 40° dip and 1 km high (Harders et al. 2011). This segment ends northwards where a fossil triple junction on the oceanic plate and associated low ridge under-thrust the continental plate (Barckhausen et al. 2001). The ridge causes a cohesive rotational slope failure (Harders et al. 2011).

Some slumps appear complex, and involve blocks with deep detachment planes that possibly cut the entire overriding plate of up to a 4–5 km thick in the lower or middle slope (Ranero and von Huene 2000). Evidence for deep-cutting headwalls comes from fluids rising from the plate boundary during subduction that have been measured at faults and headwalls at various places along the slope (Ranero et al.

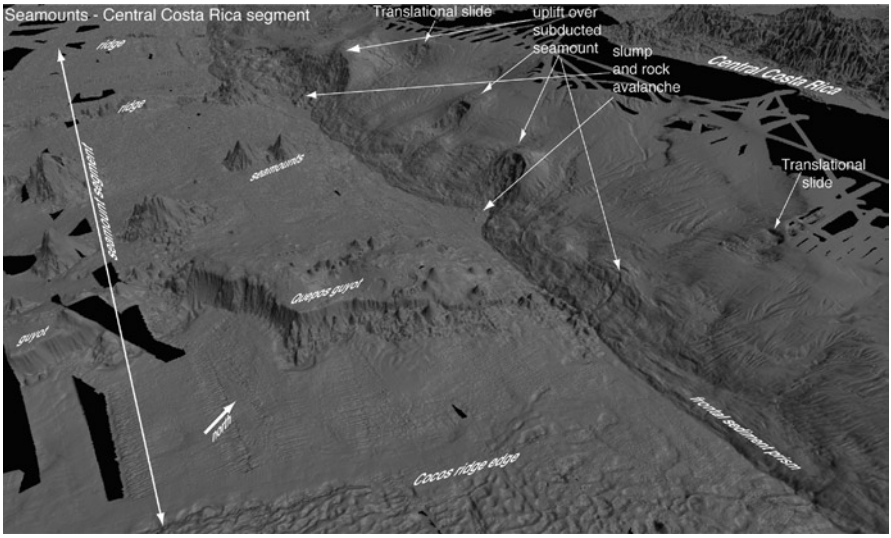

Fig. 35.3 Artificially illuminated, perspective view of the relief of the seamount segment and slope off Central Costa Rica (3× v.e.). The image is 270 km wide along the trench axis. Trench axis depth is 2,000 m at SE edge of figure and 4,200 m at NW edge. The ocean plate is festooned with 2–3 km tall seamounts and guyots and 0.5–1.0 km high ridges

2008). Collocated shallower detachment planes involve strata collapsing as rock avalanches along 20–30-km wide slope furrows marking seamounts progression (Fig. 35.3). Further seamount under-thrusting beneath the upper slope changes the style of failure. In the upper slope, the plate is 10–12 km thick and it seems to be too strong to be entirely fractured (von Huene et al. 2000). Local uplift is accompanied by moderate over-steepening to <10° dip causing translational sliding of sediment (Harders et al. 2011).

In spite of the intense deformation caused by subduction of numerous high-relief features in this segment, which are almost as extensive as structures ornamenting Cocos Ridge, canyon systems are better developed here. Canyons are largely absent or confined to the upper slope offshore along most of Osa Peninsula where the shallowest section of Cocos Ridge subducts (Fig. 35.2). However, canyon systems are more abundant, reaching the middle or lower slope across the wider slope of Central Costa Rica segment (Fig. 35.3). This observation indicates a different slope evolution and somewhat longer slope stability for sectors of this segment. The greater stability, shallower average slope dip angle, and broader slope may be related to changes in tectonic erosion processes along the plate boundary. This proposition is supported by a comparatively lower heat flux in this segment, leading to a wider region of early mineral dehydration along the plate boundary (Ranero et al. 2008), and thus a comparatively broader area where over-pressured fluids and associated hydrofracturing promote removal of overriding plate material and concurrent subsidence.

35.2.3 North Nicoya – Smooth Ocean Floor Segment

This segment displays a remarkable different morphology compared to the other segments. The incoming plate is similar in age to the Central Costa Rica-seamount segment (Barckhausen et al. 2001), and although the thermal structure is locally cooler, at segment scale the temperature at the plate boundary does not differ much to the seamount segment. The width of the slope is also similar, and average slope dips of 5–10° somewhat higher (Fig. 35.4). These observations indicate a comparable width of the area of tectonic erosion, and gradual subsidence. In spite of evidence of extensional normal faulting associated to tectonic erosion and slightly higher average slope dip angle, the segment lacks noticeable failures. Here, slope failures are limited to a few small translational slides (~3 km wide headwalls) within the middle slope (Harders et al. 2010). The different slope stability of this segment when compared the other segments is probably related to the absence of large topographic features on the subducting plate, as inferred from the featureless incoming plate of this segment.

35.2.4 Nicaragua – Oceanic Bend-Faulting Segment

Although the transition from the North Nicoya to the Nicaragua segment is not abrupt but gradual in both the continental slope and ocean plate morphology (Fig. 35.4), the change leads to a slope displaying the most fractured terrain and denser distribution of landslide scars in the study region. Similarly, the oceanic plate is cut by bending-related extensional faulting that gradually increases in offset and intensity paralleling the increase in overriding plate deformation.

The distribution of the continental slope morphology of this segment contrasts to that of other segments. The slope is divided in a gently sloping upper, steep middle and comparatively featureless lower slope. The relatively steep continental middle slope, with 10–15° average gradient, is cut by pervasive trench-axis parallel extensional faults and concentrates most slope failures that often seem to initiate at coalescent fault plates (Fig. 35.4). Landslide scars are generally smaller that in Central Costa Rica and Osa Peninsula segments, ranging in size from a few km to a maximum of 6 km width and 12 km length and with headwalls ≤260 m. In marked contrast to the central Costa Rica and Osa Peninsula segments, all landslides in the North Nicoya segment are translational (Harders et al. 2011). The distinct character of the continental slope morphology indicates a new change in the tectonic processes that govern its evolution.

The three sectors morphology of the continental slope is probably related to the effect that the ocean plate relief has on tectonic erosion processes along the plate boundary. The ocean-plate faults form half-grabens that create a terrain of long ridges with relief up to 0.5 km high at the trench axis. Subduction of those trench-axis-parallel ridges deforms the lower continental slope creating low ridges that strike parallel to, and morphologically mimic, the ocean plate ridges (Fig. 35.4).

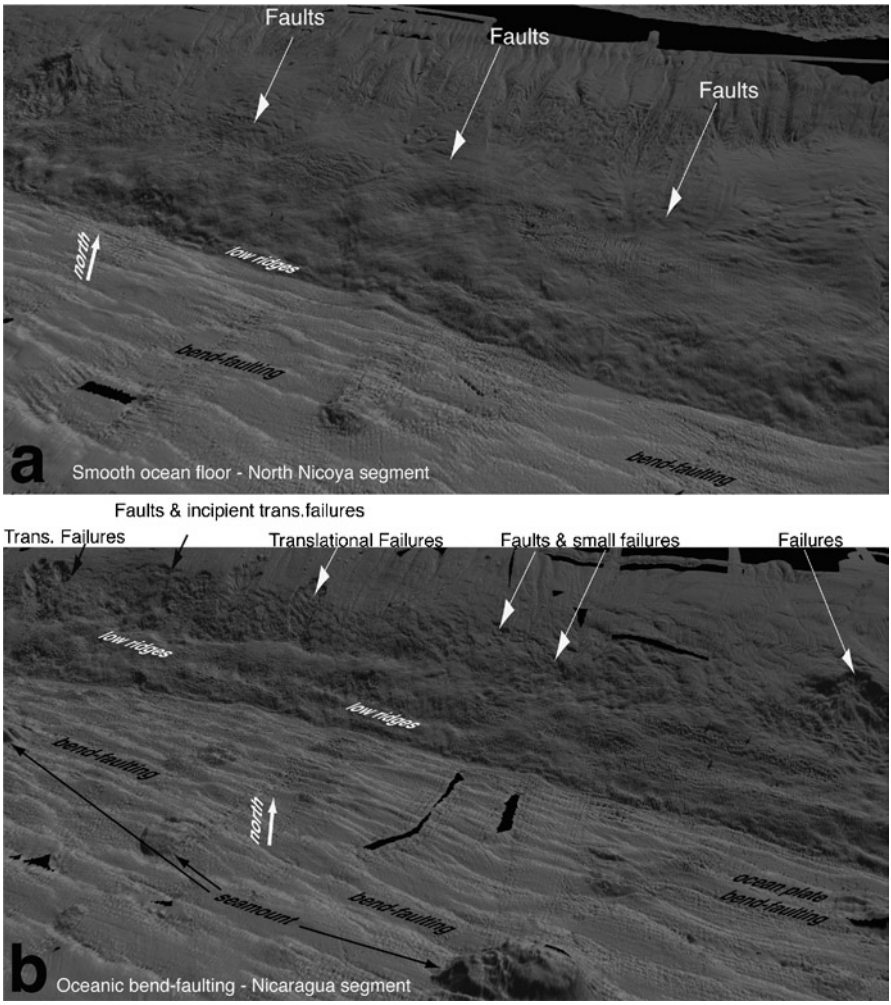

Fig. 35.4 Artificially illuminated, perspective view of the relief of the ocean plate and continental slope offshore North Nicoya Peninsula and Nicaragua (3× v.e.) (**a**) The comparatively smooth ocean plate and tectonically little-disturbed offshore North Nicoya Peninsula. The image is 120 km wide along the trench axis, depth along trench axis is 4,200 m at SE edge and 5,100 m at NW edge (**b**) The heavily faulted ocean plate with numerous seamounts. The image is 130 km wide along the trench axis. Trench axis depth is 5,000 m at SE edge and 5,400 m at NW edge. The middle continental slope is strongly fractured, cut by extensional faults and has many translational landslide scars

The continental plate is deformed and faulted as it rides over the subducted oceanic half grabens. The subducted grabens are possibly also an efficient mean for transportation of fractured upper plate material deeper into the subduction zone. Tectonic erosion by the subducting ridges is probably most efficient under the lower slope,

where increased material removal possibly causes over-steepening and extension of the middle slope, promoting faulting and landsliding that increase in intensity in parallel to the lateral increase in bending-related fault intensity in the oceanic plate from North Nicoya to Nicaragua (Fig. 35.4).

In addition, the oceanic plate contains abundant seamounts of dimensions smaller than in the Central Costa Rica segment, but which may have some localized effect in mass wasting processes along this segment. In particular, it is possibly that local uplift above seamounts imaged with seismic data (McIntosh et al. 2007) may have helped in the failure process of the largest slides. However, upper plate fracturing by seamounts is very limited – in comparison to Central Costa Rica- and all slides are translational.

35.2.5 El Salvador – Oblique Bend-Faulting Segment

The along strike transition from the Nicaragua to the El Salvador segment is abrupt and appears to be the consequence of two superimposed changes. A major modification is a change in the strike of the deep slab which is displayed at the surface as a change in trench axis strike of the (Fig. 35.1) (Ranero et al. 2005). This change causes bending-related faults in the oceanic plate to under-thrust at an oblique angle of ~40° to the trench strike (Fig. 35.5). The second change is that the ocean plate is separated from the Nicaragua segment by the fossil Galapagos Transform trace, which implies that the plate was created in a different segment of the spreading center (Fig. 35.1). A fundamental difference across the transform trace is that the ocean plate in the El Salvador segment contains few seamounts of much smaller dimensions (compare Figs. 35.4b and 35.5a).

In spite of the intense ocean plate faulting, the effect on the overriding plate on the El Salvador segment appears less pronounced than in the Nicaragua segment. The lower continental slope displays subdued ridges that parallel the ridges in the incoming plate, but basal erosion of the overriding plate appears to be less intense. The result is that the middle slope seems comparatively less faulted and slide scars are noticeably absent. The upper slope also displays some indication of longer tectonic stability because canyon systems, sculpted by small translational failures (≤5 by 3 km), seem better established. These failures do not appear directly related to tectonic processes.

35.2.6 Guatemala – Ocean Propagator Topography Segment

The transition from El Salvador to Guatemala segment is gradual and involves changes in the continental slope and ocean plate morphology that take place over a few tens of km. The style of deformation has produced a slope that at first sight may resemble similar to Nicaragua segment, but in Guatemala abundant failures are typically small and rotational, and large translational slides as those in Nicaragua are absent (Fig. 35.5b). Failure appears related to normal faulting across the slope that is of comparatively larger dimensions than at Nicaragua or El Salvador segments. In

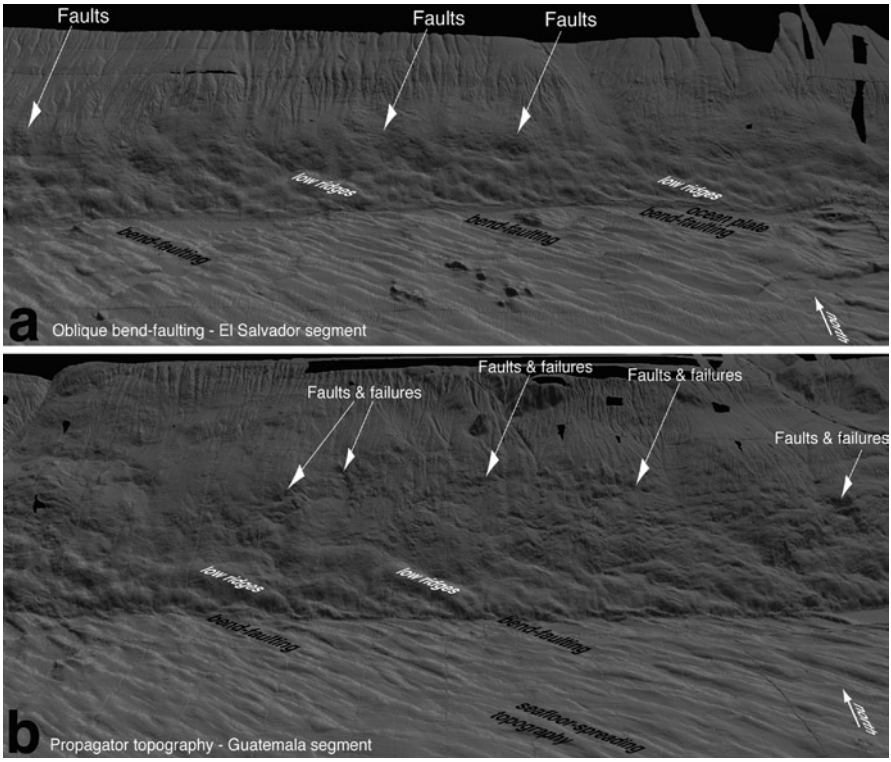

Fig. 35.5 Artificially illuminated, perspective view of the ocean plate and continental slope offshore El Salvador and Guatemala (3× v.e.) (**a**) Relief of the strongly faulted ocean plate and tectonically disturbed slope offshore El Salvador. The image is 200 km wide along the trench axis. Trench axis depth is 5,300 m at SE edge and 5,800 m at NW edge (**b**) Relief of the ocean plate and rugged slope offshore Guatemala. The image is 164 km wide along the trench axis. Trench axis depth is 6,100 m at SE edge and 6,500 m at NW edge

general, the slope is more tectonically deformed than in the neighbor El Salvador segment and displays a considerable more rugged morphology and shallower canyon systems in the upper slope. An exception are two large canyon near the tow edges of the segments that reach near the trench axis and are unique features along the study sector of the MAT.

The ocean plate of this segment displays the highest seafloor-spreading inherited topography, visible away from the trench axis in spite of ~300 m of hemipelagic sediment cover (Fig. 35.5b). This several-hundred-meter high topography formed by interaction of a palo-spreading center propagator and the Siqueiros transform (Fig. 35.1) mapped at the northern segment edge. This topography is exacerbated approaching the trench axis by bending-related faulting, creating the most prominent ocean-plate terrain in the study region. The upper-plate deformation caused by under-trusting this topography may relate to the comparatively increased faulting and associated slope failures of this segment.

35.3 Conclusions

Our analysis indicates that long-term subduction tectonics processes precondition the structure of the continental slope. Those processes are possibly controlled by factors like long term sediment supply to the trench, thickness and nature of subducting sediment, convergence rate, and plate age. Superimposed over that millions-of-year-long evolution, shorter term processes determined by the character on the currently subducting incoming oceanic plate appear to determine the type, dimensions and abundance of mass wasting events in an area. The main plate characteristics that seem to modulate landsliding phenomena include crust thickness, plate age and topographic features on the plate. Lateral changes in long-term tectonic interacting with variation of the character of the incoming oceanic plate along the MAT have led to a segmentation of mass wasting processes at the continental slope.

Acknowledgements This publication is contribution no. 210 of the Sonderforschungsbereich 574 "Volatiles and Fluids in Subduction Zones" at Kiel University funded by Deutsche Forschungsgemeinschaft (DFG). The data were collected during cruises of German R/V Sonne funded by the Ministry of Science and Education (BMBF) and R/V Meteor the Deutsche Forschungsgemeinschaft (DFG), and US R/V Ewing funded by NSF. We acknowledge the reviews of J. Chaytor and R. von Huene that helped improve the clarity of the paper.

References

Barckhausen GA, Ranero CR, von Huene R, Cande S, Roeser H (2001) Revised tectonic boundaries in the Cocos Plate off Costa Rica: implications for the segmentation of the convergent margin and for plate tectonic models. J Geophys Res 106:19207–19220

DeMets C (2001) A new estimate for present-day Cocos-Caribbean plate motion: implications for slip along the central American volcanic arc. Geophys Res Lett 28:4043–4046

Harders R, Kutterolf S, Hensen C, Moerz T, Brueckmann W (2010) Tephra layers: a controlling factor on submarine translational sliding? Geochem Geophys Geosyst 11:Q05S23. doi:10.1029/2009GC002844

Harders R, Ranero CR, Weinrebe, W, Behrmann, JH (2011) Submarine slope failure along the convergent continental margin of the Middle America Trench. Geochem Geophys Geochsyst 12: Q05S32, doi:10.1029/2010GC003401

Hühnerbach V, Masson DG, Bohrmann G, Bull JM, Weinrebe W (2005) Deformation and submarine landsliding caused by seamount subduction beneath the Costa Rica continental margin – new insights from high-resolution sidescan sonar data. In: Hodgons DM, Flint SS (eds) Submarine slope systems: processes and products, Geological Society Special Publications 244. The Geological Society, Bath, pp 195–205

Kukowski N, Greinert J, Henrys S (2010) Morphometric and critical taper analysis of the Rock Garden region, Hikurangi Margin, New Zealand: implications for slope stability and potential tsunami generation. Mar Geol 272:141–153. doi:10.1016/j.margeo.2009.06.004, 0025-3227

McAdoo BG, Pratson LF, Orange DL (2000) Submarine landslide geomorphology, US continental slope. Mar Geol 169:103–136

McIntosh KD, Silver EA, Ahmed I, Berhorst A, Ranero CR, Kelly RK, Flueh ER (2007) The Nicaragua convergent margin: seismic reflection imaging of the source of a tsunami earthquake, Rica. In: Dixon T, Moore JC (eds) The seismogenic zone of subduction thrust faults. Columbia University Press, New York, pp 257–287

Ranero, CR, von Huene R, Flueh E, Duarte M, Baca D, and McIntosh K (2000) A cross section of the convergent Pacific margin of Nicaragua. Tectonics 19 (2): 335–357. doi:10.1029/1999TC900045

Ranero CR, Villaseñor A, Phipps Morgan J, Weinrebe W, (2005) Relationship between bend-faulting at trenches and interslab seismicity. Geochem Geophys Geosyst 6: Q12002. doi:10.1029/2005GC000997

Ranero CR, Grevemeyer I, Sahling H, Barckhausen U, Hensen C, Wallmann K, Weinrebe W, Vannucchi P, von Huene R, McIntosh K (2008) The hydrogeological system of erosional convergent margins and its influence on tectonics and interplate seismogenesis. Geochem Geophys Geosyst 9:Q03S04. doi:10.1029/2007GC001679

von Huene R, Bourgois J, Miller J, Pautot G (1989) A large tsunamogenic landslide and debris flow along the Peru Trench. J Geophys Res 94:1703–1714

von Huene R, Ranero CR, Weinrebe W and Hinz K (2000) Quaternary convergent margin tectonics of Costa Rica, segmentation of the Cocos Plate, and Central American volcanism. Tectonics 19:314–334. doi:10.1029/1999TC001143

von Huene R, Ranero CR, Watts P (2004a) Tsunamigenic slope failure along the Middle America Trench in two tectonic settings. Mar Geol 203:303–317

von Huene R, Ranero CR, Vannucchi P (2004b) A model for subduction erosion. Geology 32:913. doi:10.1130/G20563.1

Part V
Post-Failure Dynamics

Chapter 36
Dynamics of Submarine Liquefied Sediment Flows: Theory, Experiments and Analysis of Field Behavior

Shinji Sassa and Hideo Sekiguchi

Abstract This paper describes an extension of the computational code LIQSEDFLOW. The salient features of the code lie in the capabilities to describe the multi-phased physics of subaqueous sediment gravity flows. Specifically, it combines Navier-Stokes/continuity equations and equations for advection and hindered settling of grains for a liquefied soil domain, with a consolidation equation for the underlying, progressively solidifying soil domain, via a transition layer that is characterized by zero effective stress and a small yet discernable stiffness. Evolutions of the flow and solidification surfaces are traced as part of solution by using a volume-of-fluid (VOF) technique. The predicted features of gravity flows of initially fluidized sediments with different concentrations conform to the observed performances in two-dimensional flume tests. The submarine flow slide that occurred in 1980 on the Klamath River delta, California is also discussed. The present results demonstrate the crucial role of two-phase physics, particularly solidification, in reproducing the concurrent processes of flow stratification, deceleration, and redeposition, as well as in the formation of scarps and terrace in submarine liquefied sediment flows.

Keywords Submarine landslide • Sediment gravity flow • Liquefaction • Solidification • Coastal oceans

S. Sassa (✉)
Port and Airport Research Institute, 3-1-1 Nagase, Yokosuka 239-0826, Japan
e-mail: sassa@ipc.pari.go.jp

H. Sekiguchi
Osaka City University, Osaka, Japan

Y. Yamada et al. (eds.), *Submarine Mass Movements and Their Consequences*,
Advances in Natural and Technological Hazards Research 31,
DOI 10.1007/978-94-007-2162-3_36,

36.1 Introduction

Subaqueous sediment gravity flows (SSGF) have become an increasingly important subject for research in relation to geomorphodynamics of sediment routing systems connecting river basins, estuaries and coastal oceans. Also, submarine landslides and flow slides have received considerable attention in view of their destructive power and associated consequences in nearshore and offshore facilities (Hampton et al. 1996; UNESCO 2009). Fluid-sediment interaction is a key process that features any SSGF (Fig. 36.1). However, current flow models are mostly depth-averaged and/or rheologically based (Nittrouer et al. 2007). Therefore, they cannot adequately describe the multi-phased nature of SSGF as pore fluid migration and associated solidification that accompanies the process of flowage leading to redeposition. The integration of fluid-dynamics and soil mechanics approaches is indispensable in advancing the physics of SSGF.

The authors have proposed a theoretical framework called "LIQSEDFLOW" (Sassa et al. 2003) to predict the flow dynamics of hyperconcentrated sediment-water mixtures that may result from liquefaction or fluidization under dynamic environmental loading. The emphasis of the analysis procedure is placed on considering the multi-phased nature of SSGF. Notably, it accounts for the occurrence of progressive solidification due to pore fluid migration in the flowing fluidized sediment.

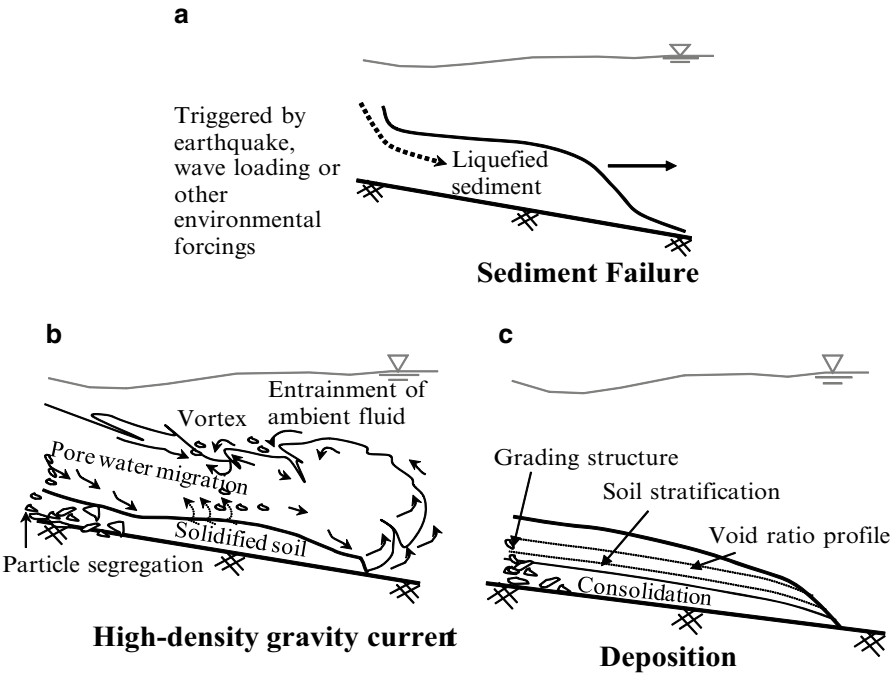

Fig. 36.1 Features of subaqueous sediment gravity flows

This paper describes an extension of LIQSEDFLOW, with due consideration of the effect of hindered settling and advection of grains during flowage. The predicted behaviour of SSGF is discussed in light of the characteristics of flow stratification, deceleration, and redeposition. Comparison is made between predictions and observations made in the flume experiments of Amiruddin et al. (2006). Furthermore, the flow dynamics and associated morphology of the 1980 Klamath River delta submarine slide (Field et al. 1982) are discussed in light of the analytical framework developed.

36.2 Flume Experiments on Submarine Liquefied Sediment Flows

Let us first describe some relevant characteristics of submarine liquefied sediment flows, on the basis of our recent observations in a two-dimensional flume as reported in Amiruddin et al. (2006). The deposits of fine-grained sands were liquefied by imposing upward seepage and were allowed to flow out over a horizontal floor of the channel. The observed flow configurations of initially fluidized sediment with $c = 38\%$ are shown in Fig. 36.2a. One can visually identify the temporal evolution of the gravity flow head as well as the solidification front (SF) and flow surface (FS) of the highly concentrated gravity flow. The fluidized sediment gravity flow consisted of three regions: $0 < z < SF$; $SF < z < FS$ and $FS < z$, as typified by the velocity profiles as shown in Fig. 36.2b. Specifically, the region between the base and solidification front ($0 < z < SF$) represents the internally formed solidified zone in which the sediment had zero velocities, reestablishing a grain-supported framework. In the region $SF < z < FS$, the highly concentrated sediment flew in non-turbulent regime. In contrast, the region above the flow surface ($FS < z$) was effected by turbulence and entrainment of ambient water, since this region contained only dilute sediment clouds in suspension (Fig. 36.2a).

The observed evolution of flow surface and solidification front at three different stations is shown in Fig. 36.2c. One can see that as soon as the head of the gravity flow went past a given station, solidification there started developing from the bottom of the flow, eventually reaching the flow surface. It is interesting to note that at the three stations in Fig. 36.2c, the solidification front reached the flow surface at essentially the same time, namely at t ~3 s. This suggests the "freezing" of the main body of the SSGF.

36.3 Theory for Submarine Liquefied Sediment Flows

36.3.1 Problem Definition

Consider a body of submerged granular soil that has just undergone liquefaction or fluidization under the action of storm waves, earthquakes or excessive seepage forces.

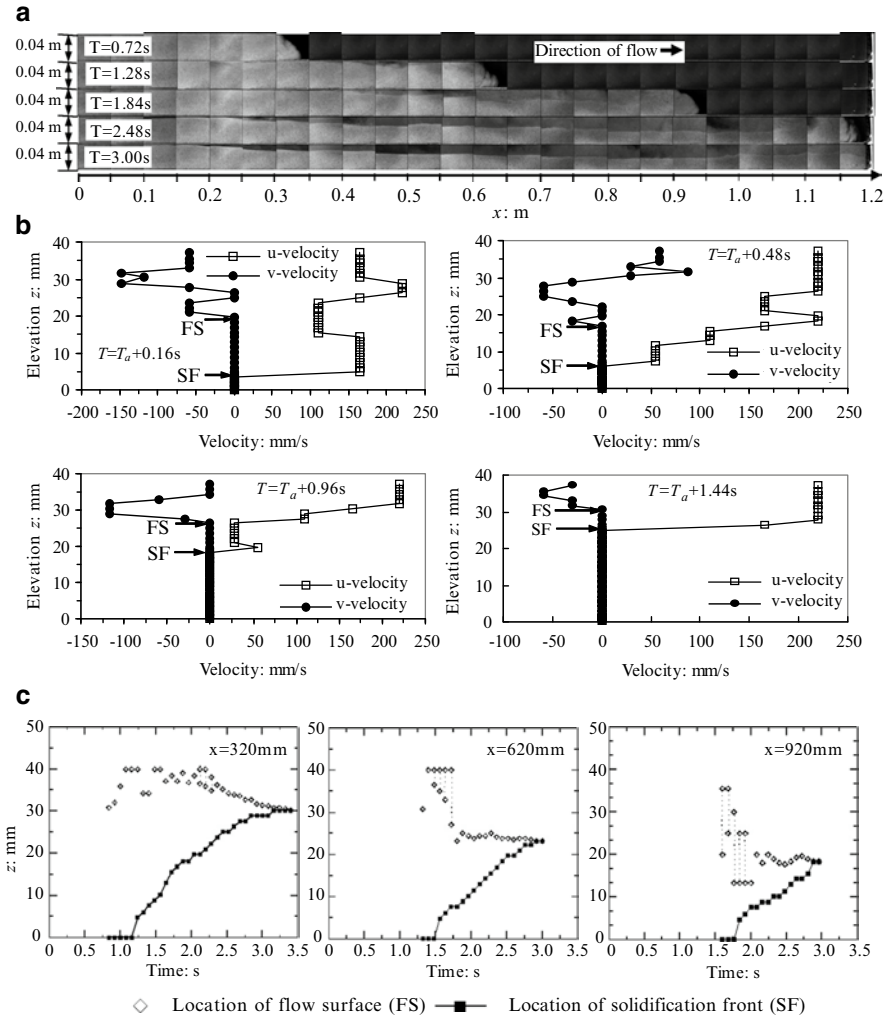

Fig. 36.2 Observed features of subaqueous liquefied sediment flow with c = 38%. (**a**) Flow configurations; (**b**) Profiles of flow velocities with elevation at a fixed station x = 0.62 m, T_a represents the time when the flow head reached the station concerned; (**c**) Evolutions of flow surface and solidification front at three different stations

The liquefied sediment, with a mass density ρ_2, will start collapsing under gravity into an ambient fluid with a mass density ρ_1 (Fig. 36.3). The depth of the ambient fluid h is assumed here to be constant during flowage. The liquefied flow will undergo hindered settling and advection of grains while undergoing progressive solidification. Progressive solidification is a sort of phase-change process that allows transitory fluid-like particulate sediment to reestablish a grain-supported framework during

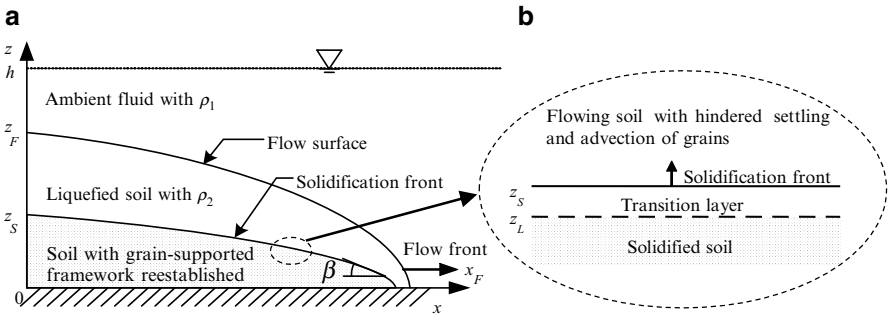

Fig. 36.3 (**a**) Definition for theory of subaqueous liquefied sediment flows undergoing progressive solidification; (**b**) a transition layer incorporated between flowing liquefied soil and solidified soil

continued disturbances and has been demonstrated theoretically as well as experimentally in gravity flows (Sassa et al. 2003; Amiruddin et al. (2006)) and under wave loading (Miyamoto et al. 2004; Sumer et al. 2004, 2006).

The pore fluid pressure p at a generic point in the sediment may be divided into two components. Namely,

$$p = p_e + p_s \tag{36.1}$$

Here p_s is the hydrostatic pressure expressed as $p_s = \rho_1 g (h - z)$ where g refers to earth's gravity, and p_e represents the excess pressure due to contractancy of the sediment.

36.3.2 Formulation for the Domain of Liquefied Flow

For the purpose of non-dimensional formulation, let us denote a reference length as a and a reference velocity as $U_r = \sqrt{ga}$. The non-dimensional time T may then be expressed as $U_r\ t/a$ and the non-dimensional excess pore pressure P_e may be expressed as $p_e/(\rho_2 - \rho_1)U_r^2$. It is important here to note that the boundary conditions on the flow surface (Fig. 36.3a) can be described by $P_e = 0$, with reference to Eq. 36.1.

The two-dimensional system of Navier-Stokes equations, considering the effect of the excess pore pressure P_e, for describing the dynamics of the subaqueous liquefied flows may then be expressed as (Sassa et al. 2003):

$$\frac{\partial U}{\partial X} + \frac{\partial V}{\partial Z} = 0 \tag{36.2}$$

$$\frac{\partial U}{\partial T} + U\frac{\partial U}{\partial X} + V\frac{\partial U}{\partial Z} = -\frac{\rho_2 - \rho_1}{\rho_2}\frac{\partial P_e}{\partial X} + \frac{1}{R_e}\left(\frac{\partial^2 U}{\partial X^2} + \frac{\partial^2 U}{\partial Z^2}\right) \tag{36.3}$$

$$\frac{\partial V}{\partial T}+U\frac{\partial V}{\partial X}+V\frac{\partial V}{\partial Z}=-\frac{\rho_2-\rho_1}{\rho_2}\frac{\partial P_e}{\partial Z}+\frac{1}{R_e}\left(\frac{\partial^2 V}{\partial X^2}+\frac{\partial^2 V}{\partial Z^2}\right)-\frac{\rho_2-\rho_1}{\rho_2} \tag{36.4}$$

Here $U=u/U_r$ is the non-dimensional velocity in the X-direction, $V=v/U_r$ is the non-dimensional velocity in the Z-direction and R_e is the Reynolds number as expressed by HU_r/ν where ν is the kinematic viscosity of the flowing liquefied soil.

The hindered settling and advection of grains during the course of liquefied flow may be effected by the following equation in terms of sediment concentration C:

$$-\frac{\partial\left(C\cdot U\right)}{\partial X}-\frac{\partial\left(C\cdot V\right)}{\partial Z}+\frac{\partial\left(C\cdot W_s\right)}{\partial Z}=\frac{\partial C}{\partial T} \tag{36.5}$$

where $W_s=w_s/U_r$ is the non-dimensional particles settling velocity. Note here that the above Eq. 36.5 does not involve any diffusion term, since we focus here on the highly concentrated gravity flow of liquefied sediment.

The particles settling velocity depends on C. Here, we adopt the following equation proposed by Richardson and Zaki (1954):

$$W_s=W_0\left(1-C\right)^n \; with \; n=4.65 \tag{36.6}$$

where $W_0=w_0/U_r$ stands for the non-dimensional terminal free settling velocity (Stokes settling velocity). The applicability of Eq. 36.6 to liquefied sediment has been verified experimentally (Sassa and Sekiguchi 2010).

36.3.3 Formulation for the Domain Undergoing Solidification

The process of solidification in the course of the liquefied flow may be described by the two-dimensional equation of consolidation. Let K_w be the Darcy permeability coefficient, which is non-dimensionalized by dividing by U_r. Let M be the constrained modulus of the soil skeleton, which is non-dimensionalized by dividing by $(\rho_2-\rho_1)U_r^2$. The consolidation equation then reads

$$\frac{\partial\left(\sigma_m-P_e\right)}{\partial T}=-\frac{\rho_2-\rho_1}{\rho_1}M\cdot K_w\left(\frac{\partial^2 P_e}{\partial X^2}+\frac{\partial^2 P_e}{\partial Z^2}\right) \tag{36.7}$$

where σ_m is the non-dimensional mean total stress of the solidifying sediment. Note here that the value of the constrained modulus M should increase with increasing effective confining pressure. With reference to Sassa et al. (2001), we adopt the following simple relationship:

$$M=(Z_s-Z)\cdot M_r \; for \; 0\le Z\le Z_s \tag{36.8}$$

where M_r is the reference value of M for the sediment having a non-dimensional thickness of unity.

36.3.4 Numerical Solution Procedures

The liquefied flow domain and the solidifying domain as formulated above are consistently coupled through a thin transition layer with zero effective stress yet having marginally discernable stiffness, as shown in Fig. 36.3. By introducing the transition layer, one can reproduce the phase change in which the transitory fluid-like particulate sediment reestablishes a grain-supported framework involving effective stress, thereby enabling the advance of the solidification front. The evolution of the flow and solidification surfaces are traced as part of solution by using a volume-of-fluid (VOF) technique (Hirt and Nichols 1981). Here the soil undergoing solidification has zero velocities and acts as being an obstacle to the flowing liquefied soil. The details of the related numerical scheme are summarized in Sassa and Sekiguchi (2010).

In a computational step, the solidification front may be judged to be an active one and moves upward if the effective stress increment in the transition layer becomes positive. This means that the transition layer becomes a part of solidified soil region, thereby giving rise to the shift of a transition layer to immediately above the solidified soil by definition. Also, in order to address the effect of hindered settling upon solidification, we make the solidification front active if the sediment concentration there exceeds by a certain amount, that was set at 1% here, the mass concentration of the initially fluidized sediment. Calculations were performed by turns for the flow region above updated solidification front and for the solidifying region under updated flow field. Accordingly, the interaction between flowing liquefied soil and solidifying soil was solved until targeted time was reached. The slope of the solidification surface, β, was monitored during each computational cycle, and if necessary corrected, so as not to exceed a critical angle β_{cr} in view of the frictional resistance of the soil.

36.4 Analysis of the Experimental Behaviour

A series of analyses of subaqueous liquefied sediment flows were performed using the LIQSEDFLOW described above. Here we targeted the two-dimensional flume tests of Amiruddin et al. (2006). The material parameters used are summarized in Table 36.1. The viscosity of the liquefied soil may vary depending on the states of liquefaction (Sumer and Fredsøe 2002). Here, we kept the Reynolds number of the fluidized sediments as equivalent with that of pure water so as to avoid any artificial viscosity, and thus to elucidate the role of two-phase physics with solidification.

The predicted changes in the configuration of the subaqueous liquefied flow at sediment concentration $C = 38\%$ are illustrated in Fig. 36.4 for three different times. Note that at $t = 0$, the solidification front coincides with the bottom of the liquefied sediment. It is seen that at $t = 0.2$ s the liquefied sediment has been collapsing and the solidification front has progressed upwards. The liquefied sediment then undergoes a significant flow deformation at $t = 0.8$ s. The solidified zone has developed

Table 36.1 Material parameters used in analyses of subaqueous liquefied sediment flows

C: %	R_e	k_w: mm/s	M_r	tan β_{cr}	w_o: mm/s
30, 34, 38, 42, 50*	100,000	0.15	400	0.35, 0.4, 0.5, 0.55, 0.6*	20

The asterisk denotes the values used in the field analysis

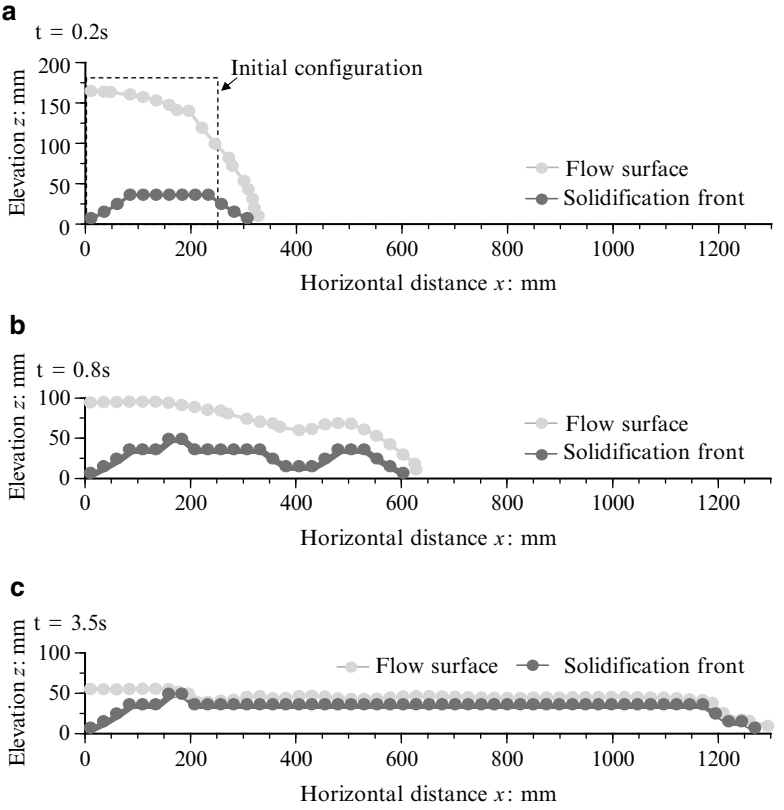

Fig. 36.4 Predicted flow stratifications leading to redeposition in subaqueous liquefied sediment flow (c = 38%)

further upwards and laterally in a wavy fashion. At this stage, a marked decelerating flow regime has taken place due to interactions between the flowing fluidized sediment and the accreting solidified soil with a grain-supported framework reestablished. The characteristics of flow deceleration will be described later. Eventually, the liquefied flow becomes markedly elongated at t = 3.5 s, and comes to stop since the solidification front reaches the flow surface at essentially the same instant of time. This indicates the occurrence of "freezing" of the main body of the sediment gravity flow.

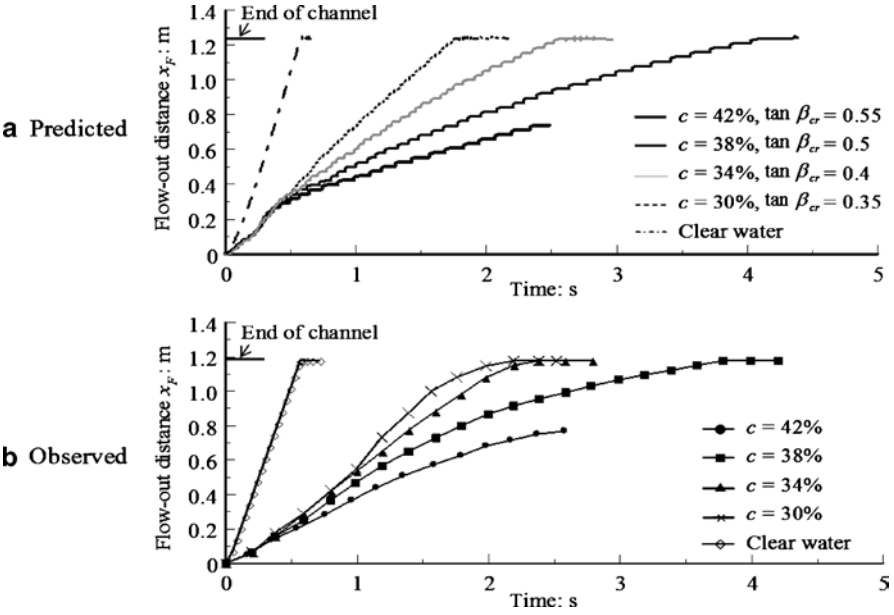

Fig. 36.5 Predicted (**a**) and observed (**b**) time histories of flow-out distance for clear water and four different sediment concentrations

The predicted features of flow stratification leading to redeposition are found to be well consistent with what has been observed in the flume experiments on SSGF as reported by Amiruddin et al. (2006).

In the course of the SSGF, the sediment concentration changes due to advection and hindered settling of grains as well as due to the occurrence of progressive solidification. However, our analyses have shown that the effect of the hindered settling upon flow deceleration appears only marginal, and the occurrence of progressive solidification is essentially responsible for the marked flow deceleration leading to redeposition (Sassa and Sekiguchi 2010).

Predicted and observed time histories of flow-out distance for four SSGF with different sediment concentrations together with that of a gravity flow of water exhibit a rapid rate of flowage (Fig. 36.5). Closer examination shows that all predicted sediment gravity flows exhibit decelerating flowage, except for the early stage of flow initiation. Indeed, the flow potential of subaqueous liquefied flows decreases markedly with increasing sediment concentrations, and increasing critical angle β_{cr}, due to frictional resistance of solidified soil. These predicted flow-out characteristics compare favorably with the observed flow-out characteristics.

In summary, all the results described above demonstrate the predictive capabilities of LIQSEDFLOW in realistically simulating the dynamics of SSGF. This also indicates that the marked flow deceleration leading to "freezing" of the flow is indeed predictable on the basis of the two-phase physics with solidification.

36.5 Analysis of the Field Behaviour

The above-described features concerning the dynamics of submarine liquefied flows are further explored with reference to a field event where a major earthquake with the magnitude of 7.2 on November 8, 1980 triggered extensive submarine flow slides, which ranged 20 km along and 1 km across shelf on a very gentle 0.25º slope on the Klamath River delta, California (Field et al. 1982). The seabed was of fine-grained sands, and the reported indicators of liquefaction included sand boils and collapse craters. The cross-shelf seafloor profiles before and after the earthquake on the basis of high-resolution seismic reflection records are shown in Fig. 36.6a, b respectively. The flow morphology involved the area of essentially flat terrace as well as multiple scarps with an aggregate relief of less than 2 m near the flow front. An analysis was performed using the LIQSEDFLOW by assuming that the 1 km-long surficial sediment in a loose state of packing underwent liquefaction in the maximum thickness of 5 m under a 0.25º slope due to the earthquake shaking (Field et al. 1982). The material parameters used in this field analysis are shown in Table 36.1.

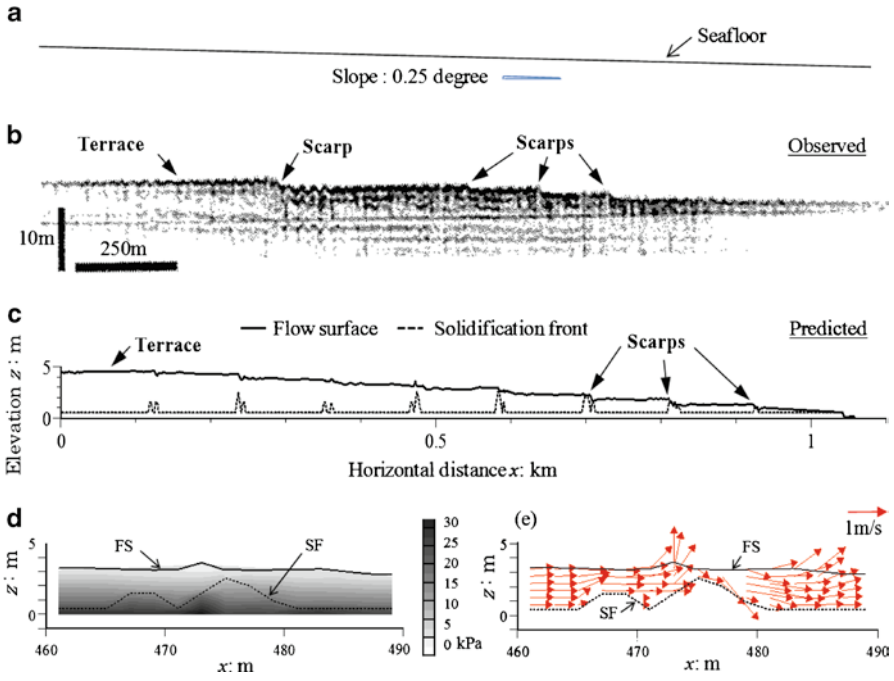

Fig. 36.6 The 1980 submarine slide: The cross-shelf seafloor profiles (**a**) before and (**b**) after the earthquake as reported by Field et al.(1982); (**c**) Predicted flow configurations with solidification front; (**d**) Predicted distributions of excess pore pressures and (**e**) velocity vectors at the vicinity of the solidification front

The predicted flow configurations with solidification front after 1 min following the occurrence of liquefaction are shown in Fig. 36.6c. The multiple scarps as well as the terrace were predicted to occur in the flow configurations. Notably, the area of the scarp formation corresponded to locations where the solidification front reached earlier the flow surface than other locations, giving rise to the intermittent flat area between each scarp formed. The predicted distributions of excess pore pressures and velocity vectors at the vicinity of the solidification front, at x = 460–490 m, are shown in Fig. 36.6d, e. Here, it is interesting to observe the occurrence of an ejection of liquefied sands as a result of the interaction between the flowing liquefied sediment and the solidification front.

In summary, the predicted flow dynamics and the associated morphology of the 1980 submarine slide are found to be consistent with the field evidence as reported by Field et al. (1982). The combined results of the analyses of the field and the experimental behaviour also demonstrate that the way in which the submarine liquefied flows ensue with the progress of solidification may depend on a number of factors such as slope, volume of liquefied sediment, location in the flow direction and material properties of the seabed. These important facets of the submarine flow slides are worth close investigation in future studies. Also, the paper has focused on the dynamics of liquefied flows, placing the flows of clay-rich materials beyond the scope of this study. As fluidized flows can originate through failure of sediments of varying clay content (Breien et al. 2010), the dynamics addressed here should be fundamental in such submarine flow slides.

36.6 Conclusions

The computational code LIQSEDFLOW proposed by the authors has been extended to incorporate the effect of hindered settling and advection of grains on the processes of SSGF. The principal findings and conclusions obtained in the present study are:

(a) LIQSEDFLOW has proven capable of consistently simulating the dynamics of subaqueous liquefied sediment flows leading to redeposition on the basis of two-phase physics. Highly concentrated fluidized flows decelerate and come to stop as a consequence of the solidification that occurs and develops inside the sediment gravity flow.
(b) The predicted features of flow stratification, deceleration and redeposition of SSGF following fluidization conform well to the experimentally observed features of the gravity flows as reported by Amiruddin et al. (2006).
(c) The flow-out potential of subaqueous gravity flows decrease considerably with increasing sediment concentration. Notably, we have shown that the effect of progressive solidification upon flowage at a given sediment concentration can be reasonably reproduced by introducing the concept of a concentration-dependent, critical angle of deposition in light of the frictional resistance of sediment with grain-supported framework reestablished.

(d) LIQSEDFLOW has reproduced the essential features of the submarine flow slide that occurred in 1980 on the Klamath River delta, California (Field et al. 1982). Indeed, the predicted formation of the multiple scarps and terrace are found to be closely associated with the flow dynamics that occurs at/around the vicinity of the solidification front.
(e) The present results emphasize the crucial role of the two-phase physics, particularly solidification, in reproducing the sequence of concurrent processes of submarine liquefied sediment flows, thereby warranting wider applications of LIQSEDFLOW to geohazard mitigation.

References

Amiruddin, Sekiguchi H, Sassa S (2006) Subaqueous sediment gravity flows undergoing progressive solidification. Nor J Geol 86:285–293

Breien H, Blasio FV, Elverhøi A, Nystuen JP, Harbitz CB (2010) Transport mechanisms of sand in deep-marine environments-Insights based on laboratory experiments. J Sediment Res 80:975–990

Field ME, Gardner JV, Jennings AE, Edwards ED (1982) Earthquake-induced sediment failures on a 0.25° slope, Klamath River delta, California. Geology 10:542–546

Hampton MA, Lee HJ, Locat J (1996) Submarine landslides. Rev Geophys 34:33–60

Hirt CW, Nichols BD (1981) Volume of fluid (VOF) method for the dynamics of free boundaries. J Comput Phys 39:201–225

Miyamoto J, Sassa S, Sekiguchi H (2004) Progressive solidification of a liquefied sand layer during continued wave loading. Géotechnique 54(10):617–629

Nittrouer CA, Austin JA, Field ME, Kravitz JH, Syvitski JPM, Wiberg PL (2007) Continental margin sedimentation: SP 37 International Association of Sedimentologists. Blackwell Publishing, Malden, 549 p

Richardson JF, Zaki WN (1954) Sedimentation and fluidization: part 1. Trans Inst Chem Eng 32:35–53

Sassa S, Sekiguchi H (2010) LIQSEDFLOW: Role of two-phase physics in subaqueous sediment gravity flows. Soils Found 50(4):495–504

Sassa S, Sekiguchi H, Miyamoto J (2001) Analysis of progressive liquefaction as a moving boundary problem. Géotechnique 51(10):847–857

Sassa S, Miyamoto J, Sekiguchi H (2003) The dynamics of liquefied sediment flow undergoing progressive solidification. In: Locat J, Mienert J (eds) Submarine mass movements and their consequences, Advances in natural technological hazards research 19. Springer, Dordrecht, pp 95–102

Sumer BM, Fredsøe J (2002) The mechanics of scour in the marine environment, vol 17, Advanced series on ocean engineering. World Scientific, Hackensack

Sumer BM, Hatipoglu F, Fredsøe J (2004) The cycle of soil behaviour during wave liquefaction. In: Proceedings of 29th international conference on coastal engineering, Lisbon, pp 19–24

Sumer BM, Hatipoglu F, Fredsøe J, Sumer SK (2006) The sequence of sediment behaviour during wave-induced liquefaction. Sedimentology 53(3):611–629

UNESCO (2009) IGCP-511, 585. http://www.igcp585.org/

Chapter 37
Undrained Sediment Loading Key to Long-Runout Submarine Mass Movements: Evidence from the Caribbean Volcanic Arc

Barry Voight, Anne Le Friant, Georges Boudon, Christine Deplus, Jean-Christophe Komorowski, Elodie Lebas, R. Stephen J. Sparks, Peter Talling, and Jess Trofimovs

Abstract Long undersea debris runout can be facilitated by a boundary layer formed by weak marine sediments under a moving slide mass. Undrained loading of such offshore sediment results in a profound drop of basal shear resistance, compared to subaerial shear resistance, enabling long undersea runout. Thus large long-runout submarine landslides are not truly enigmatic (Voight and Elsworth 1992, 1997), but are understandable in terms of conventional geotechnical principles. A corollary is that remoulded undrained strength, and *not* friction angle, should be used for basal resistance in numerical simulations. This hypothesis is testable via drilling and examining the structure at the soles of undersea debris avalanches for indications of incorporation of sheared marine sediments, by tests of soil properties, and by simulations. Such considerations of emplacement process are an aim of ongoing research in the Lesser Antilles (Caribbean Sea), where multiple offshore debris avalanche and dome-collapse debris deposits have been identified since 1999 on swath bathymetric surveys collected in five oceanographic cruises. This paper reviews the prehistoric and historic collapses that have occurred offshore of Antilles arc islands and summarizes ongoing research on emplacement processes.

B. Voight (✉)
Geosciences, Penn State University, University Park, PA 16802, USA
e-mail: voight@ems.psu.edu

A. Le Friant • G. Boudon • C. Deplus • J.-C. Komorowski • E. Lebas
Institut de Physique du Globe de Paris, 1 rue Jussieu, 75238, Paris Cedex 05, France

R.S.J. Sparks
Department of Earth Sciences, University of Bristol, Bristol BS8 1TH, UK

P. Talling • J. Trofimovs
National Oceanography Centre, European Way, Southampton SO14 3ZH, UK

Y. Yamada et al. (eds.), *Submarine Mass Movements and Their Consequences*,
Advances in Natural and Technological Hazards Research 31,
DOI 10.1007/978-94-007-2162-3_37, © Springer Science+Business Media B.V. 2012

Keywords Submarine landslide • Submarine mass movement • Mass-transport deposit • Geohazard • Lesser Antilles • Marine geophysical surveys • Undrained shear strength • Hydroplaning

37.1 Introduction

The Lesser Antilles volcanic arc along the eastern edge of the Caribbean Sea constitutes a unique setting where volcanic activity since the mid-Oligocene has resulted in the construction of numerous volcanic islands. In this region at least 52 flank collapses events have occurred and have generated submarine mass movements (SMM), 15 of which have occurred within the last 12,000 years (Fig. 37.1) (Boudon et al. 2007; Lebas et al. 2011; Samper et al. 2008). The aim of this paper is threefold: (1) to introduce readers to SMM and related deposits of the Caribbean arc as deduced largely from marine geophysical surveys since 1999; (2) to outline plans for future investigations of SMM and sediment deposits; and (3) to identify specific issues on emplacement mechanisms and mechanics related to mobility of SMM.

37.2 SMM of the Lesser Antilles Arc

Boudon et al. (2007) provide a comprehensive review. Early studies had identified horseshoe-shaped depressions on active volcanoes of Montserrat, Dominica, Martinique, St. Lucia, and St. Vincent, and proposed an origin from sector collapse (following the example of Mount St Helens, Voight et al. 1981; Voight 2000), but only rarely were the associated deposits recognized (Boudon et al. 1984, 1987). More recently a partial collapse of the crater wall on Montserrat was observed and studied (Voight et al. 2002), and large collapses of the active lava dome occurred (Mattioli et al. 2007; Le Friant et al. 2009, 2010). A major advance of understanding of SMM followed a series of geophysical surveys from Montserrat to St. Lucia during the AGUADOMAR cruise in 1999, and the CARAVAL cruise in 2002 to St Vincent (Fig. 37.1) (Deplus et al. 2001; Le Friant et al. 2002, 2004; Boudon et al. 2007). Additional high-resolution seismic data have been collected recently (JCR123; GWADASEIS cruise 2009–72 channels; JC45/46 cruise 2010–60 channels) to investigate in detail the environment of Montserrat. Overall the deposits display hummocky morphology on swath bathymetry, a speckled pattern on backscatter images, hyperbolic reflections on 3.5 kHz echo sounder data and diffracting units on seismic data. The new seismic data have vertical resolutions of ~3 to 4 m while the previous data were ~10 to ~20 m (Lebas et al. 2011). Such a vertical resolution has allowed us to distinguish superimposed SMM deposits at depth by highlighting well-bedded sedimentary units lying between SMM units, to accurately locate the boundaries of each SMM deposit and to estimate deposit thickness. The seismic surveys demonstrate that debris avalanche deposits and their basal contacts can be imaged successfully in the Lesser Antilles.

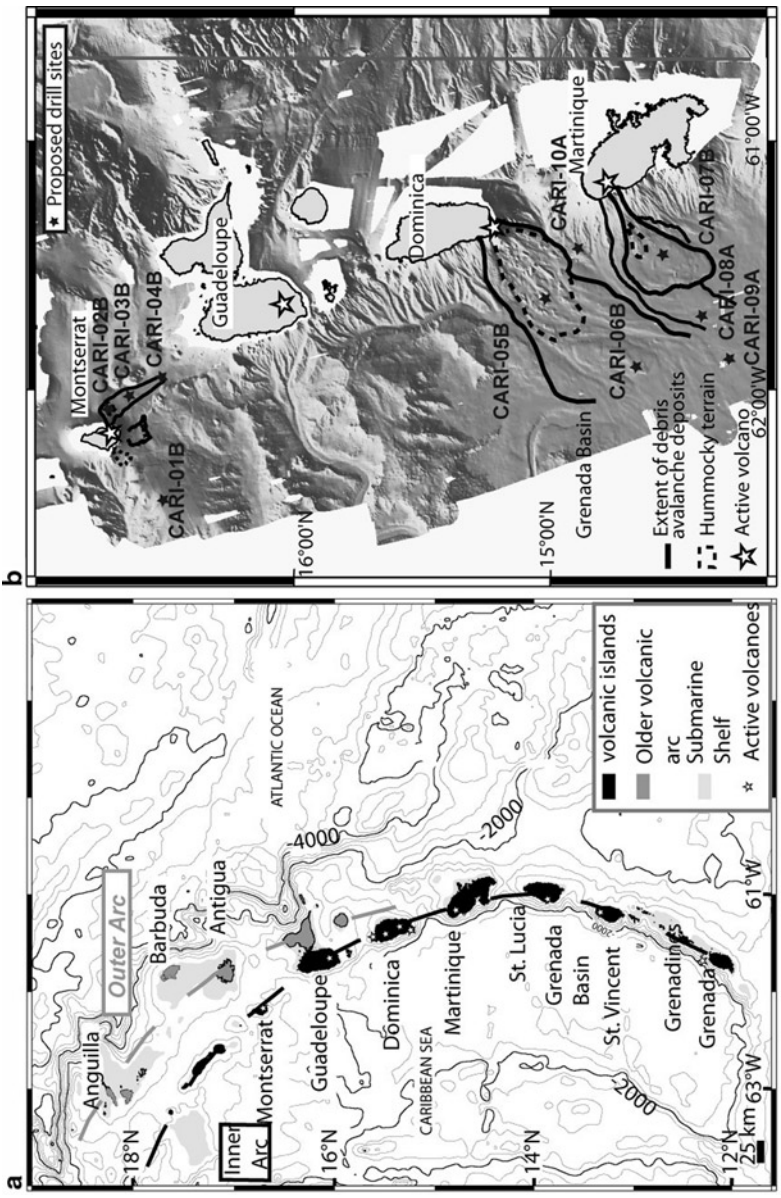

Fig. 37.1 (**a**) Lesser Antilles Arc (**b**) Main SMM deposits from Montserrat to Martinique, superposed on swath bathymetry (Modified from Boudon et al. 2007). Scheduled IODP drill sites are annotated

37.2.1 Montserrat

Volcanism started on Montserrat ~2.6 Ma at Silver Hills in the north, moved to Centre Hills between 0.5 and 1.0 Ma, with the youngest volcanism in Soufrière Hills in the south (~300 ka-present) (Harford et al. 2002). The ongoing eruption of the Soufrière Hills volcano started in 1995 (Druitt and Kokelaar 2002). Activity has included lava dome growth and collapse, explosive activity, flank collapse, redistribution of pyroclastic materials by debris flows on land and turbidity currents offshore, and minor tsunamis. Prehistoric flank collapses have been recognized on Soufrière Hills and Centre Hills volcanoes (Le Friant et al. 2004). The English's crater event occurred ~2,000 years ago (Boudon et al. 2007), producing deposit 1 (volume ~0.5 km^3) (Fig. 37.2). Debris avalanche deposit 2 (extent: 200 km^2, volume ~5 km^3) probably resulted from a combined submarine and subaerial flank collapse of the eastern flank of the volcano dated between 130 and 112 ka (Le Friant et al. 2004, 2008, Lebas et al. 2011). The combined Montserrat marine geophysical data set is now the most complete of any Lesser Antilles island (Lebas et al. 2011).

37.2.2 Martinique

Martinique consists of several volcanic centres, and evolution of the active Montagne Pelée volcano has been marked by three major flank collapses (~0.1 Ma, ~25,000 years, ~9,000 years ago), which systematically destroyed the western flank of the volcano (Le Friant et al. 2003a; Boudon et al. 2005, 2007). The collapse volumes vary from 2 to 25 km^3 and debris avalanches flowed down to the Grenada Basin (Fig. 37.3).

37.2.3 SMM Targets for Research Drilling

The range of features of Caribbean SMM deposits, their high frequency of occurrence in comparison with Hawaiian volcanoes (e.g., Hawaii: Moore et al. 1989), and the ability to collect detailed seismic data, are important reasons for studying Lesser Antilles SMM. Edifice collapses are of high concern on the small Caribbean islands as a large portion of the debris avalanches flowed into the sea, generating potentially destructive tsunamis (e.g., Heinrich et al. 1998; Mattioli et al. 2007). Le Friant et al. (2010) have shown that up to 70% by volume of erupted products in the arc are delivered to the surrounding marine environment.

The intent of IODP Expedition 340 (scheduled February-March 2012) is to document the evolution of three volcanic islands in the arc which represent the range of behaviours and eruptive styles: Montserrat in the north (where Soufrière Hills volcano has been erupting and creating serious hazards since 1995), Martinique, and Dominica. A main goal is to understand the timing and emplacement processes

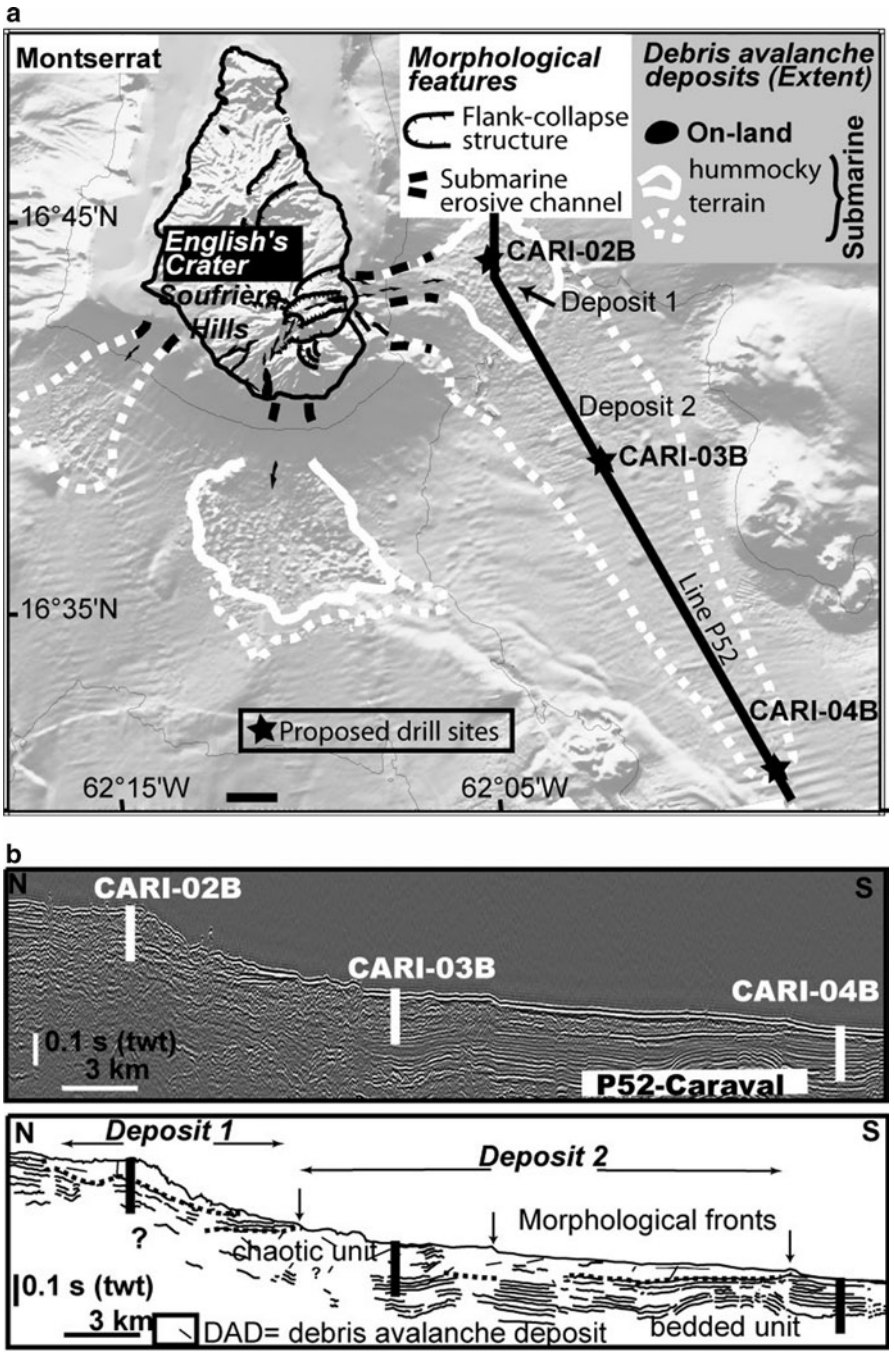

Fig. 37.2 (**a**) Montserrat. Debris avalanche deposits and drill sites (**b**) Debris avalanche deposits, Seismic line 52, Caraval cruise, 2002. Scheduled IODP drilling sites are annotated

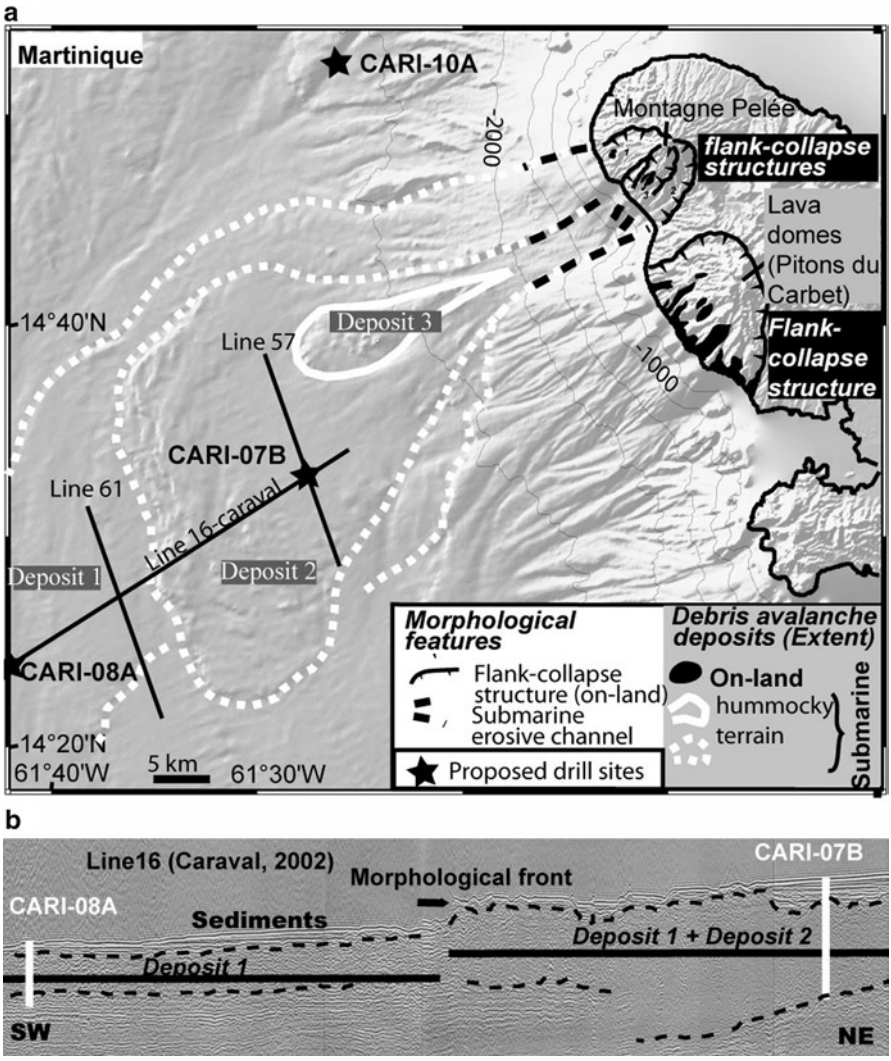

Fig. 37.3 (**a**) Martinique, shaded bathymetry. SMM deposits and drill sites (**b**) Transverse air gun profile, Line 16, Caraval cruise, 2002. Scheduled IODP drilling sites are annotated

of debris avalanches and SMM produced by flank collapse, with implications for tsunami hazards.

37.3 Emplacement Mechanisms and SMM Mobility

SMM runout can be facilitated by mobilization of undrained large-strain shear strength in subjacent fine grained marine sediments. These may be quantified in terms of stress changes where the stress tensor is decomposed into components that

represent the mean stress and deviatoric stress, with the Skempton (1954) coefficients B (~1 for fine grained sediments) and A_f. The overriding influence is an increase in pore pressure in the marine sediments that negates the total stress increase from the overriding slide mass. The remoulded undrained strength (S_{ur}) of the sediment is mobilized and not immediately augmented by the increase in confining pressure. The loading is thus undrained when SMM emplacement speed is high compared to seepage and pressure-dissipation rate in subjacent fine grained sediments of low permeability. For undrained loading – loading at constant volume and voids ratio – the strength is independent of any changes in total normal stress, and depends only on voids ratio or water content as influenced say by normal consolidation under a few meters of sedimentation load prior to slide emplacement, and remoulding. Thus undrained loading by moving landslides over soft fine-grained submarine sediments offshore of islands is likely to result in profound drop of basal landslide shear resistance (Voight and Elsworth 1992, 1997). On this basis Voight and Elsworth (1992) asserted that large long-runout submarine landslides such as those offshore Hawaii were not truly enigmatic; they appear to be completely understandable in terms of well-known geotechnical principles.

This hypothesis is testable via drilling by examining the structure at the soles of undersea debris avalanches for indications of incorporated sheared marine sediments, and perhaps (in some cases) by use of modern borehole technology to assess whether cored materials and existing pore pressure distributions in recently emplaced debris deposits are consistent with theory.

The submarine emplacement of the last flank collapse event (9,000 yBP) on Martinique, with volume 2.7 km^3, was simulated by finite difference numerical models in which parameters were estimated by trial and error, on the basis of runout distance and shape of deposits (Fig. 37.4) (Le Friant et al. 2003b). Two behaviors were considered, a fluid one with viscous law, and a solid one with friction law. For a viscous law, motion never ceases and a more realistic model was recognized as a visco-plastic fluid, citing Voight et al. (1983) and Norem et al. (1990), or a comparable bi-viscous approximation (Sousa and Voight 1991, 1995). For the solids case the modeling considered a simple Coulomb law (constant ratio of shear stress to normal stress at slide mass base), and also the Pouliquen (1999) empirical model in which friction is assumed a function of mean velocity and thickness of the granular layer. In the simulations, for a viscous-Coulomb friction model (a Bingham model was not used) best agreement was found with a viscosity of 7.5 m^2/s (similar to the Ontake debris avalanche, Voight and Sousa (1994)) and basal friction angle of 0.5°. A Coulomb model (base friction 7°) matched runout but not distribution of mass, with a steep deposit snout. The best overall fit was given by the Pouliquen model with two friction angles, 6° (corresponding to base friction) and 15°. Qualitatively the results are consistent with the average friction being low compared to static friction angles of volcanic rocks and sediments, and crudely comparable to the ratio of fall height to runout distance (H/L) (Pariseau and Voight 1979; Voight et al. 1985). However for water-saturated materials, the apparent friction angle (or coefficient) is a function of the actual friction angle and the pore fluid pressure (Voight 1978, pp. 154–155; Sassa 1988; Voight and Elsworth 1997, pp. 11–14). Similar simulations

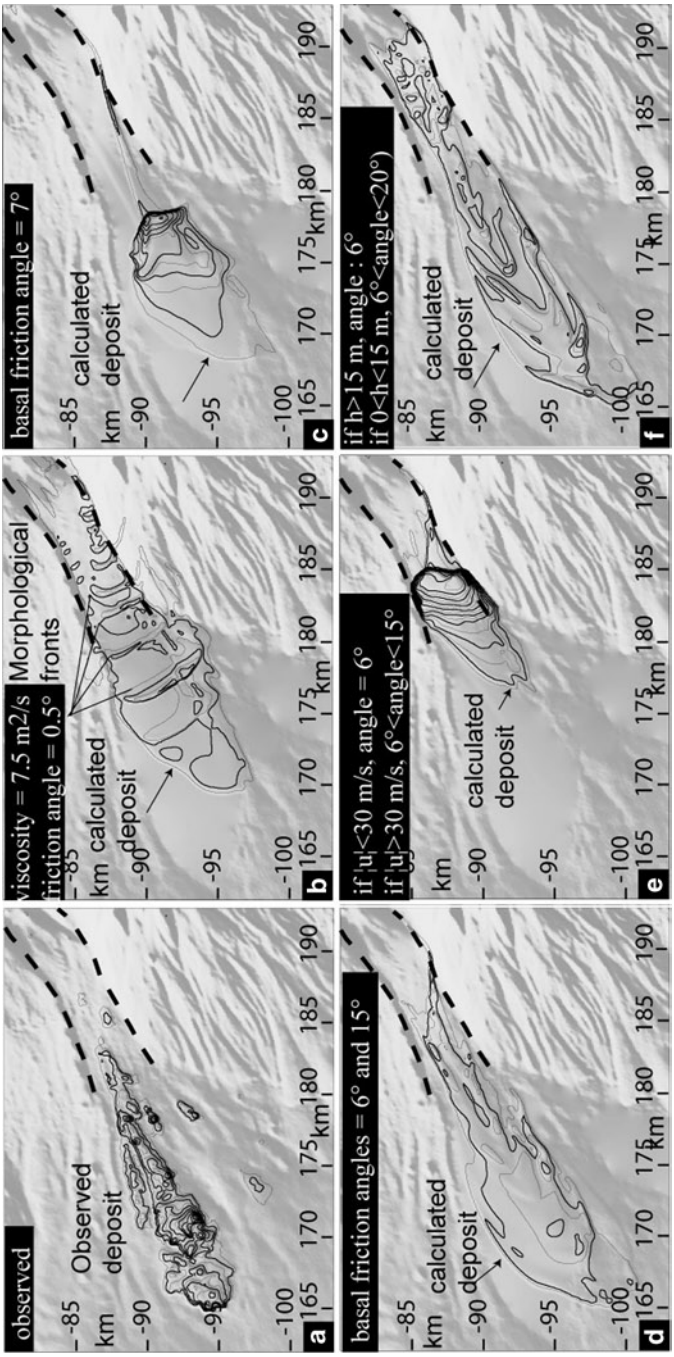

Fig. 37.4 (**a**) Observed deposit thickness, over shaded bathymetry (**b–f**) Calculated deposit thickness for (**b**) viscous-Coulomb model, (**c**) Coulomb-type friction law, (**d**) Pouliquen law, (**e**) Coulomb-type law with velocity-varying friction, (**f**) Coulomb-type law with thickness-varying friction (From Le Friant et al. 2003a, b)

were run for the well-studied 1997 Boxing Day debris avalanche (c.50 × 106 m^3) on Montserrat (Heinrich et al. 2001; Voight et al. 2002), which did not quite run to the sea but which exhibited low apparent friction angles (<15°). The difference between the Montserrat and Martinique avalanche dynamics (much lower apparent friction for Martinique) likely resides in the effects of a boundary layer of weak, undrained-loaded marine sediments in the latter case.

However the simulations to date emphasized a frictional basal layer, whereas in the Voight-Elsworth (1992) hypothesis the appropriate boundary-layer resistance is taken as the remoulded undrained strength (S_{ur}) – essentially a constant over the base of the moving avalanche and not a friction-based term influenced by local slide thickness during emplacement. This relation is consistent with Dade and Huppert (1998) who suggested from scaling relationships that a constant-stress resistance law applies to long-runout mass movements. The argument can be contested in some cases for subaerial slides (e.g., Voight et al. 2002) which formed the basis of their model, but is completely consistent for submarine slides incorporating a basal boundary layer with undrained strength S_{ur}. Thus we suggest that the use of remoulded undrained strength, and *not* friction angle, is appropriate generally for simulations of basal resistance of SMMs. The undrained strength is likely to vary along the runout track, due to variations in marine sediments, and typically may decrease due to finer distal material.

The values of S_{ur} can be estimated by standard geotechnical methods such as piezocone or vane in-situ and lab tests. Values will depend on province and nature of sediment (hemipelagic vs. turbidite facies, etc.) and deposit history, but typical offshore results suggest S_{ur} of a few to tens kPa for sediment depths of 1–10 m (e.g., Kowsmann et al. 2003). Such tests are needed within the Caribbean arc basins.

The phenomenon of hydroplaning has been noted as well (as in car tires losing contact with wet roadways), in particular for the head of debris flows (Mohrig et al. 1998), but also for debris avalanches (Sassa 1988; Voight and Sousa 1994). Hydroplaning can increase runout (Elverhoi et al. 2005). A hydroplane water film can reduce or eliminate shear coupling to the substrate and thus reduce entrainment or expansion of the boundary layer to include a deeper (and stronger) sediment section. With absence or depletion of a lubricating layer, shear coupling to subjacent sediments can occur to bulk the slide mass and affect basal resistance. Pore pressure enhancement can occur through shear friction (Voight and Faust 1992), but this requires shear coupling.

Finally, we note that not all SMM observed are of the long-runout variety, implying higher basal resistance. Reasons for this include: (1) the repetition of slide events with short time separations. The build-up of pelagic sedimentation is slow (a few cm in a 1,000 years) such that if collapse events occur within a "short" time span, a soft marine sediment layer may not exist to "lubricate" successive flows or to over-ride the roughness of previous SMM deposits. Some examples of repeated collapses are seen offshore Montserrat (Le Friant et al. 2010). (2) Deposits in topographic lows may be dominated by turbidity current deposition, and such deposits may be variable from place-to-place, stronger proximally, and stronger than hemipelagic sediments. (3) Some SMM are slump-like deposits not disposed to large displacement.

37.4 Conclusions

Accordingly, whether significant substrate erosion or bulk entrainment occurs to develop a weak sole layer is a crucial question for understanding the dynamics and mobility of SMM and for using realistic parameters in numerical simulations of flow processes. Is undrained loading of overridden (and incorporated) marine sediments as proposed by Voight and Elsworth the correct general explanation for long undersea SMM runouts? Deplus et al. (2001) proposed that submarine debris avalanches in the Lesser Antilles cut significantly into underlying sedimentary layers during emplacement, incorporate large amounts of marine sediment, and disturb underlying stratigraphy. Such erosion and sediment deformation is apparent in some seismic profiles, and the volume of deposits deduced from seismic data seems perhaps an order of magnitude larger than the estimated collapsed volume on-land (Le Friant et al. 2003a). We await the IODP results with considerable interest.

Acknowledgment We thank Prof. N. Oyagi and S. R. Young for reviews. The study was supported by NSF in the US and by IPGP, CNRS and IFREMER in France. We thank captains, crews and the participating scientists of the different cruises.

References

Boudon G, Semet MP, Vincent PM (1984) Flank failure – directed blast eruption at Soufriere, Guadaloupe, French West Indies: a 3000-yr-old Mt St Helens? Geology 12:350–353

Boudon G, Semet MP, Vincent PM (1987) Magma and hydrothermally driven sector collapses: the 3100 and 11,500 yBP eruptions of la Grande decouverte (La Soufriere) volcano, Guadaloupe, West Indies. J Volcanol Geotherm Res 33:317–323

Boudon G, Le Friant A, Villemant B, Viodé J-P (2005) Martinique. In: Volcanic atlas of the Lesser Antilles. University of the West Indies, Trinidad/Tobago

Boudon G, Le Friant A, Komorowski J-C, Deplus C, Semet MP (2007) Volcano flank instability in the Lesser Antilles Arc: diversity of scale, processes, and temporal recurrence. J Geophys Res 112:B08205. doi:10.1029/2006JB004674

Dade WB, Huppert HE (1998) Long runout rockfalls. Geology 26:803–806

Deplus C, Le Friant A, Boudon G et al (2001) Submarine evidence for large-scale debris avalanches in the Lesser Antilles arc. Earth Plan Sci Lett 192(2):145–157

Druitt TH, Kokelaar P (2002) The eruption of Soufriere Hills Volcano, Montserrat, from 1995 to 1999. Mem Geol Soc Lond 21:639

Elverhoi A, Issler D, De Biasio F et al (2005) Emerging insights into the dynamics of submarine debris flows. Nat Haz Earth Syst Sci 5:633–648

Harford CL, Pringle MS, Sparks RSJ, Young SR (2002) The volcanic evolution of Montserrat using $^{40}Ar/^{39}Ar$ geochronology. Mem Geol Soc Lond 21:93–113

Heinrich P, Mangeney A, Guibourg S, Roche R, Boudon G, Cheminée JL (1998) Simulation of water waves generated by a potential debris avalanche in Montserrat, Lesser Antilles. Geophys Res Lett 25(19):3697–3700

Heinrich P, Boudon G, Komorowski J-C, Sparks RSJ, Herd R, Voight B (2001) Numerical simulation of the December 1997 debris avalanche in Montserrat, Lesser Antilles. Geophys Res Lett 28:2529–2532

Kowsmann RO et al (2003) Shear-strength signatures of mass movements, continental slope of Campos Basin, Brazil. In: Locat J, Mienert J (eds) Submarine mass movements and their consequences. Kluwer, Dordrecht, pp 239–246

Le Friant A, Boudon G, Komorowski J-C, Deplus C (2002) L'île de la Dominique, à l'origine des avalanches de débris les plus volumineuses de l'arc des Petites Antilles. Comptes Rendus de l'Académie des Sciences 334:235–243

Le Friant A, Boudon G, Deplus C, Villemant B (2003a) Large scale flank collapse events during the activity of Montagne Pelée, Martinique, Lesser Antilles. J Geophys Res 108(B1):2055

Le Friant A, Heinrich P, Deplus C, Boudon G (2003b) Numerical simulation of the last flank collapse event of Montagne Pelée, Martinique, Lesser Antilles. Geophys Res Lett 30(2):1034

Le Friant A, Harford C, Deplus C, Boudon G, Sparks S, Herd R, Komorowski J-C (2004) Geomorphological evolution of Montserrat (West Indies): importance of flank collapse and erosional processes. J Geol Soc Lond 161:147–160

Le Friant A, Lock EJ, Hart MB, Leng MJ, Smart CW, Sparks RSJ, Boudon G, Deplus C, Komorowski J-C (2008) Late Pleistocene tephrochronology of marine sediments adjacent to Montserrat, Lesser Antilles volcanic arc. J Geol Soc Lond 165:279–289

Le Friant A, Deplus C, Boudon G, Sparks RSJ, Trofimovs J, Talling P (2009) Submarine deposition of volcaniclastic material from the 1995–2005 eruptions of Soufrière Hill Volcano, Montserrat, West Indies. J Geol Soc Lond 166:171–182

Le Friant A, Deplus C, Boudon G, Feuillet N, Trofimovs J et al (2010) Eruption of Soufriere Hills (1995–2009) from an offshore perspective: insights from repeated swath bathymetry surveys. Geophys Res Lett 37:L11307

Lebas E, Le Friant A, Boudon G et al (2011) Multiple widespread landslides during the long-term evolution of a volcanic island: insights from high-resolution seismic data, Montserrat, Lesser Antilles. Geochem Geophys Geosyst 12:Q07011

Mattioli GS, Voight B, Linde AT et al (2007) Unique and remarkable dilatometer measurements of pyroclastic flow–generated tsunamis. Geology 35:25–28

Mohrig D, Whipple K, Hondzo M, Ellis C, Parker G (1998) Hydroplaning of subaqueous flows. Geol Soc Amer Bull 110:387–394

Moore JG, Clague DA, Holcomb RT et al (1989) Prodigious submarine landslides on the Hawaiian ridge. J Geophys Res 94(B12):17465–17484

Norem H, Locat J, Schieldrop B (1990) An approach to the physics and modeling of submarine flowslides. Mar Geotechnol 9:93–111

Pariseau WG, Voight B (1979) Rockslides and avalanches: basic principles and perspectives in the realm of civil and mining operations. In: Voight B (ed) Rockslides and avalanches, 2: engineering sites. Elsevier, Amsterdam, pp 1–92

Pouliquen O (1999) Scaling laws in granular flows down rough inclined planes. Phys Fluids 11:542–548

Samper A, Quidelleur X, Boudon G et al (2008) Radiometric dating of three large volume flank-collapses in the Lesser Antilles Arc. J Volcanol Geotherm Res. doi:10.1016/j.jvolgeores.2008.04.018

Sassa K (1988) Geotechnical model for the motion of landslides. In: Proceedings of the 5th international symposium on landslides, Lausanne, Balkema, Rotterdam, pp 37–55

Skempton AW (1954) The pore pressure coefficients A and B. Geotechnique 4:143–147

Sousa J, Voight B (1991) Continuum simulation of flow failure. Geotechnique 41:515–538

Sousa J, Voight B (1995) Multiple-pulsed debris avalanche emplacement at Mount St Helens in 1980: evidence from numerical continuum flow simulation. J Volcanol Geotherm Res 66:227–250

Voight B (ed) (1978) Rockslides and avalanches, 1. Natural phenomena. Elsevier, Amsterdam, 833 pp

Voight B (2000) Structural stability of andesite volcanoes and lava domes. Phil Trans Roy Soc Lond A 358:1663–1703

Voight B, Elsworth D (1992) Resolution of mechanics problems for prodigious Hawaiian landslides: magmatic intrusions simultaneously increase driving forces and reduce driving resistance by fluid pressure enhancement. Eos Trans AGU 73(43):506

Voight B, Elsworth D (1997) Failure of volcano slopes. Geotechnique 47:1–31

Voight B, Faust C (1992) Frictional heat and strength loss in some rapid landslides: error correction and affirmation of mechanism for the Vaiont landslide. Geotechnique 42:641–643

Voight B, Sousa J (1994) Lessons from Ontake-san: a comparative analysis of debris avalanche dynamics. Eng Geol 38:261–297

Voight B, Glicken H, Janda RJ, Douglass PM (1981) Catastrophic rockslide-avalanche of May 18. Prof Paper US Geol Surv 1250:347–378

Voight B, Janda RJ, Glicken H, Douglass PM (1983) Nature and mechanics of the Mount St Helens rockslide-avalanche of 18 May 1980. Geotechnique 33:243–273

Voight B, Janda RJ, Glicken H, Douglass PM (1985) Nature and mechanics of the Mount St Helens rockslide-avalanche of 18 May 1980: reply. Geotechnique 35:357–368

Voight B, Komorowski J-C, Norton GE et al (2002) The 26 December (Boxing Day) sector collapse and debris avalanche at Soufriere Hills Volcano, Montserrat. Mem Geol Soc London 21:363–407

Chapter 38
Impact Drag Forces on Pipelines Caused by Submarine Glide Blocks or Out-Runner Blocks

Ken Chi, Arash Zakeri, and Bipul Hawlader

Abstract This paper discusses the forces resulting from the impact of an intact submarine landslide (the glide block or out-runner block region) on a suspended submarine pipeline. Eight physical experiments were conducted using the geotechnical centrifuge facility at C-CORE. In prototype scale, clay chunks equivalent to 12 m×6 m×4.5 m (l×w×h) were used to model the glide blocks or out-runner blocks. They had *su* ranging from 4 to 7 kPa, and impact velocities ranging from 0.1 to 1.3 m/s. The clay blocks impacted the suspended pipes at a direction normal to the pipe axis. The diameters of the pipes were 0.19 and 0.29 m. Based on these experimental results, a method to estimate the impact drag force on a pipeline caused by a submarine glide block or out-runner block was developed.

Keywords Centrifuge modelling • Design of submarine pipeline • Glide block • Soil and pipe interaction • Submarine landslide

K. Chi
C-CORE, Captain Robert A. Bartlett Building, Morrissey Road, St. John's, NL A1B 3X5, Canada

Faculty of Engineering and Applied Science, Memorial University of Newfoundland, St. John's, NL A1B 3X5, Canada
e-mail: kfchi@mun.ca

A. Zakeri (✉)
C-CORE, Captain Robert A. Bartlett Building, Morrissey Road, St. John's, NL A1B 3X5, Canada
e-mail: arash.zakeri@c-core.ca

B. Hawlader
Faculty of Engineering and Applied Science, Memorial University of Newfoundland, St. John's, NL A1B 3X5, Canada

Y. Yamada et al. (eds.), *Submarine Mass Movements and Their Consequences*, Advances in Natural and Technological Hazards Research 31,
DOI 10.1007/978-94-007-2162-3_38, © Springer Science+Business Media B.V. 2012

38.1 Introduction

A length of submarine pipeline system can range from hundreds of metres to kilometres. It is preferable to route pipelines away from geohazard areas, but this is not always practical. Due to hydroplaning (De Blasio et al. 2004; Elverhoi et al. 2005; Harbitz et al. 2003), submarine landslides and associated density flows can travel distances in the order of tens to hundreds of kilometres on gentle slopes (0.5°–3°) within hours to days (Nadim and Locat 2005), and damage downstream installations such as pipelines. Due to increasing deep-water petroleum fields, research to understand the mechanisms and the risks posed by submarine landslides has increased in the past decade (Kvalstad 2007). Estimating the magnitude of drag forces on pipelines caused by density flow impact is an important design consideration in offshore engineering (Zakeri 2009c). However, no research has been conducted for the drag force exerted by glide blocks or out-runner blocks on submarine pipelines.

This paper adopts a geotechnical approach and presents a quantitative study of the drag force exerted by an impacting submarine glide block or out-runner block on suspended pipelines at an angle normal to its axis. It is based on a series of physical tests carried out in the geotechnical centrifuge at C-CORE under submerged condition. A centrifugal force of 30 times the Earth's gravity was applied to simulate scenarios of a 12 m×6 m×4.5 m (l×w×h) intact block impacting a pipeline with diameters of 0.19 and 0.29 m at a speed ranging from 0.1 to 1.3 m/s.

38.2 Terminology and Definitions

In this paper, the term glide block refers to an intact hydroplaning block of cohesive sediment during early stages of failure that has not disintegrated. Out-runner block refers to an intact block of cohesive sediment that has departed from the parent landslide and continues to ride freely downstream as a result of hydroplaning. Both glide blocks and out-runner blocks have not been remoulded and still carry the strength properties of the parent landslide. Debris flow refers to a cohesive (clay-rich) flow with a minimum sediment concentration of 50% by volume that is fully remoulded and fluidized. It can be described by rheological models for non-Newtonian fluids (e.g., Bingham, Herschel-Bulkley models).

38.3 Background Information and Literature Review

To quantify the drag force of a submarine landslide on a pipeline, two approaches have been adopted: a geotechnical or fluid dynamic approach. The geotechnical approach relates the generated force to a linear or a power-law relationship to the

soil shear strength. The fluid dynamic approach relates the fluids dynamic and rheology principles of a non-Newtonian fluid flow (Zakeri 2009c).

In the geotechnical approach, the drag force per unit length of a pipeline, F_D, is estimated from the following general form of equation:

$$F_D = k \cdot s_u \cdot D \tag{38.1}$$

where, k is the model parameter (a constant or shear strain rate dependent), s_u is the undrained shear strength of the soil, and D is the pipe diameter. Demars (1978), Swanson and Jones (1982), Bea and Aurora (1983), Audibert and Nyman (1979), and Summers and Nyman (1985) all adopted the conventional geotechnical approach, where the parameter k is constant, to study drag forces on buried pipelines in unstable clay-rich slopes. Georgiadis (1991) investigated the strain-rate dependency of the drag force on a pipeline embedded in a moving clay-rich soil mass, and added a strain rate dependency to the equation (i.e. k is a function of strain rate).

In the fluid dynamics approach (e.g., De Blasio et al. 2004; Gauer et al. 2006; Imran et al. 2001), the drag force per unit length of a pipeline is estimated from the following equation:

$$F_D = \frac{1}{2} \cdot \rho \cdot C_D \cdot U_\infty^2 \cdot D \tag{38.2}$$

where, ρ is the density of the density flow, C_D is the drag coefficient and U_∞ is the free upstream velocity. Zakeri et al. (2008) adopted the fluid dynamics approach to estimate the drag forces on suspended (elevated one pipe diameter high) and laid-on-seafloor pipelines. In that work, a slurry mixture of kaolin clay, silica sand, water and black diamond coal slag (for visual purposes) was used to simulate the debris flow impact at attack angles ranging from 0° (longitudinal) to 90° (normal) (Zakeri 2009a, b, d; Zakeri et al. 2009). For debris flows, the following relationship has been proposed to estimate the drag force coefficient for drag forces normal to the pipe axis:

Suspended pipeline:

$$C_D = 1.4 + \frac{17.5}{Re_{non-Newtonian}^{1.25}} \tag{38.3}$$

Laid-on-seafloor pipeline:

$$C_D = 1.25 + \frac{11.0}{Re_{non-Newtonian}^{1.15}} \tag{38.4}$$

In the above equation, $\mathrm{Re}_{\text{non-Newtonian}}$ is defined by $\rho U_\infty^2 / \tau$ where, τ is the fluid shear stress at a certain shear rate (see Eq. 38.5) caused by pipe-debris flow interaction upon impact.

Table 38.1 General scaling factors adopted for centrifuge testing

Physical property	Unit	Model scale
Gravitational acceleration	LT^{-2}	N
Dimension – length and diameter	L	1/N
Stress	$ML^{-1}T^{-2}$	1
Force	MLT^{-2}	$1/N^2$
Force per length	MT^{-2}	1/N
Velocity	LT^{-1}	1
Strain	–	1
Shear strain rate	T^{-1}	N

38.4 Model Scaling Considerations

Geotechnical centrifuge is useful for modeling large-scale nonlinear problems for which gravity is a primary driving force. Procedures for geotechnical centrifuge modelling and appropriate scaling laws are given by Taylor (1995) and Garnier et al. (2007). See Table 38.1 for some general scaling laws. Geotechnical materials have nonlinear mechanical properties that depend on the effective stress and stress history. The centrifuge applies an increased "gravitational" acceleration to physical models in order to produce identical self-weight stresses in the model and prototype. The one to one scaling of stress enhances the similarity of geotechnical models and makes it possible to obtain accurate data to help solve complex problems such as soil-structure interaction. Centrifuge model testing provides data to improve our understanding of basic mechanisms of deformation and provides verification of numerical models.

For modeling of glide blocks or out-runner blocks, which are essentially intact sections of a failed slope of cohesive material, one needs to reproduce the correct stress level within the soil mass to ensure that s_u, which depends on the effective stress level, is similar to that of prototype situations. s_u of 4 to 20 kPa are typically observed within the upper 10 m of seabed profiles. s_u profiles similar to prototype situations can be reproduced in the centrifuge.

To model subaqueous conditions, the tests were carried out under submerged conditions. This is important as the entrapped water in the wake behind the pipe plays a role in the magnitude of the drag force.

The shear strain rates ($\dot{\gamma}$) in the model will be N times higher (30 times in this case) than that in the prototype. Randolph et al. (2005) demonstrated that the s_u of kaolin clay increases by 10–15% per log cycle increase in strain rate. Here, for the soil-pipe interaction the shear strain rate is defined by:

$$\dot{\gamma} = \frac{U_\infty}{D} \tag{38.5}$$

Where, U_∞ is the glide block or out-runner block impact velocity (used for the free upstream velocity in Eq. 38.2). The Reynolds number from interaction of the block with the ambient water is high.

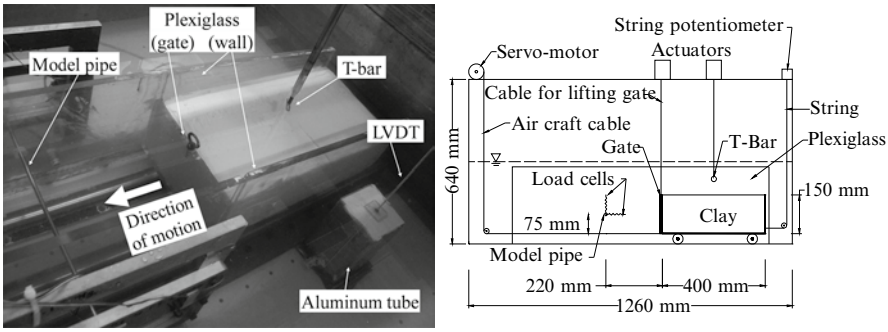

Fig. 38.1 Experiment setup

38.5 Centrifuge Modeling

Dimensions described below are in model terms. The experiments were conducted inside a 1,260 mm×1,020 mm×640 mm (l×w×h) strong box (Fig. 38.1). Inside the strong box, there are two 1,000 mm×11.3 mm×300 mm (l×w×h) Plexiglass walls 200 mm apart. Inside the flume (the gap between the Plexiglass), there is an "L" shaped aluminum cart in which the clay block is placed. The clay block is constrained by the cart, two Plexiglass walls and a Plexiglass gate at the front. Two linear precision shafts are used to guide the cart as it travels. The front of the cart is connected by a cable to a servo-motor which almost instantaneously accelerates the cart to impact velocities as high as 1.3 m/s. The influence of the plexiglass walls on the moving clay block is insignificant (i.e. slip-free boundary conditions) (Crowe et al. 2001). The back of the cart is connected by a string to a potentiometer to measure the traveled distance.

Two solid stainless steel rods, to model the pipeline, with outer diameter of 6.35 mm and 9.52 mm are used. The model pipe is placed in the flume with both ends extended through a 20 mm diameter hole in the Plexiglass. Both ends of the pipe are fitted into the pipe mounts, which are connected to two load cells by two 3 mm aluminum rods, in order to measure horizontal and vertical forces independently. Verification was done to ensure that the load cells do not significantly influence one another. Located outside the flume and near the cart is an aluminum rectangular tube, measuring 80 mm×80 mm×200 mm (l×w×h), which is filled with clay at the top portion and sand at the lower portion. It is used to monitor centrifuge consolidation by measuring the top surface displacement with a linear variable differential transformer (LVDT). Two actuators are employed to conduct a T-bar test and for lifting the Plexiglass gate. T-bar test is used in soft clay to determine the s_u (Stewart and Randolph 1994). The T-bar apparatus consists of a bar (7.5 mm in diameter and 30 mm long) connected perpendicular to the main shaft. The penetration rate used was 3 mm/s.

38.5.1 Sample Preparation and Centrifuge Testing Procedures

The clay blocks were made of 100% kaolin clay having a liquid limit (LL) = 60%, plastic limit (PL) = 32% and specific gravity (G_s) = 2.6. The slurry was consolidated in steps to the desired vertical effective stress (ranged from 40 to 80 kPa). The clay block was cut from the consolidated clay to around 400 mm long, 200 mm wide and 150 mm high and placed on the aluminum cart. A separate soil sample contained in the aluminum tube was prepared for monitoring centrifuge consolidation. The strong box is then filled with water to a height of around 340 mm. During the centrifuge test, the clay was allowed to consolidate under self weight for 2–3 h; resulting a minimum height of 140 mm. After consolidation, a T-bar test was conducted on the clay block to determine its intact and remoulded s_u profiles. Then the Plexiglass gate was raised and the servo-motor pulled the cart towards the model pipe, impacting the model pipe at the mid-height of the clay block. The data were recorded at 40 Hz for the T-bar test and 400–2,000 Hz for the impact test.

When the gate was lifted, a portion of the front face of the clay failed due to the locally increased shear stress. The failure pattern is similar to an undrained failure of a vertical cut with a slope of approximately 45°. The test setup was designed to allow the failed material to flow under the cart and have little influence on the steady state condition measured as the clay flowed around the model pipe.

38.6 Experiment Results, Analysis, and Discussion

A total of eight tests were conducted at different S_u, pipe diameters and impact velocities. Table 38.2 provides a summary of the test conditions and results. Model pipe diameter of 6.35 mm was used in test 1, 2, 3 and 8, and pipe diameter of 9.52 mm was used in tests 4–7. The moisture contents, taken from the undisturbed clay sample in the aluminum tube after test completion, were between 60% and 75%.

38.6.1 Undrained Shear Strength Profiles

The s_u assessed with the T-bar was calculated using the following equation:

$$s_u = \frac{P}{N_b \cdot d} \tag{38.6}$$

where P is force per unit length on the T-bar, d is the diameter of the T-bar, and N_b is a T-bar factor. In this study, N_b = 10.5 was used (Stewart and Randolph 1994). The T-bar results were corrected for the buoyancy effect of water. The remoulded s_u was assessed by cycling the T-bar up and down until the resistance reached a steady value. This typically occurred after five cycles. The remoulded s_u were around 35–50% of the initial s_u. Due to technical problems, the T-bar data for test numbers

Table 38.2 Summary of test conditions and results

Test no.	Velocity (m/s)	s_u[a] (kPa)	F_D (N/m)	$\dot{\gamma}$ (1/s)	k
1	0.2	4.3	327.5	24.5	12.0
2	0.2	4.7	333.2	32.8	11.2
3	0.1	4.3	297.2	16.5	10.8
4	0.1	4.1	385.4	10.8	9.9
5	0.2	4.1	383.0	21.3	9.8
6	1.3	4.3	609.0	136.6	14.7
7	0.8	6.0	728.5	81.4	12.8
8	0.3	6.7	483.7	47.8	11.3

[a]Intact s_u at pipe location

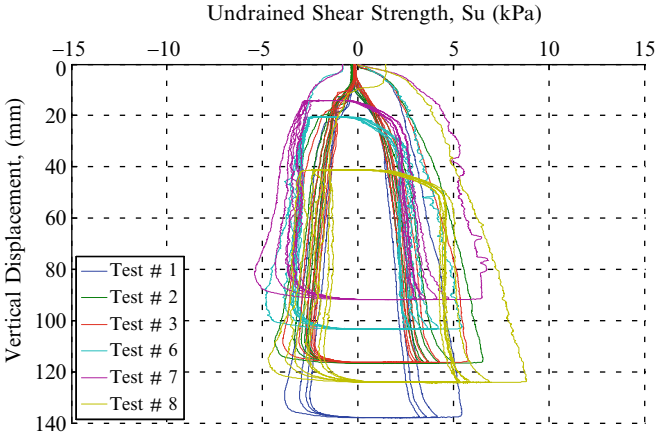

Fig. 38.2 Undrained shear strength profiles of the tests

4 and 5 were not recorded and were estimated from test number 1, which had the same final consolidation stress. T-bar voltage for test 8 shifted after the initial penetration and the remould strength was not used. Figure 38.2 illustrates the measured s_u profiles. The undrained shear strength (s_u) of the kaolin clay blocks used in this study ranged from 4 to 7 kPa.

38.6.2 Analysis of Drag Forces: Force-Displacement Relationship

Figure 38.3 shows the development of horizontal drag force per unit length with displacement. Oliveira et al. (2010) demonstrated through physical modeling, that when *h*/*D* (height/diameter) ratio is greater than 1, the vertical forces become virtually negligible. In the experiments with *h*/*D* ratios ranging from 6.8 to 12.8, the

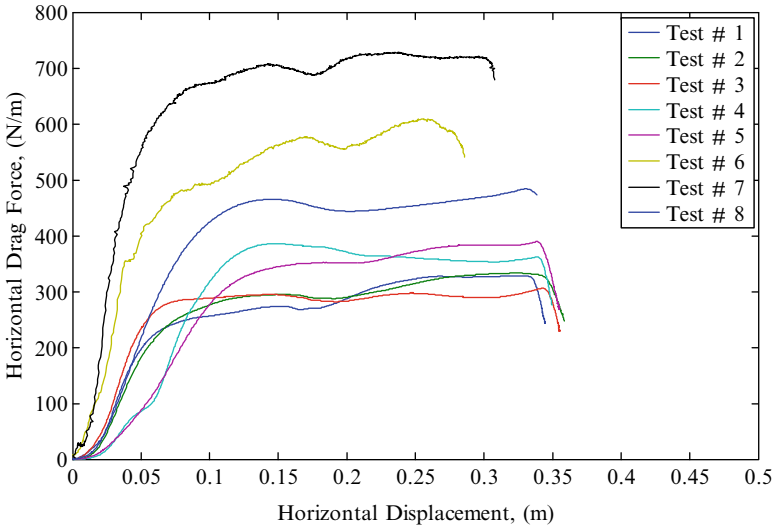

Fig. 38.3 Development of horizontal drag force in model terms

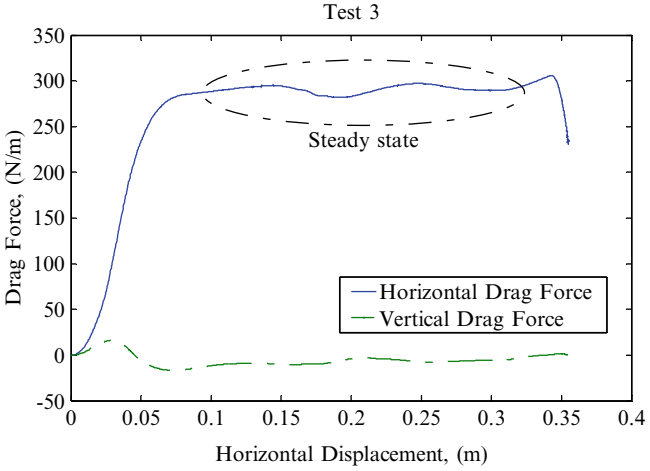

Fig. 38.4 Horizontal and vertical drag force generated in model term

magnitude of the upward vertical forces were insignificant compared to the horizontal forces. There was typically a small increase of vertical force at the beginning of each impact (Fig. 38.4), resulting from the failed portion of clay. Vertical force diminishes as penetration continues.

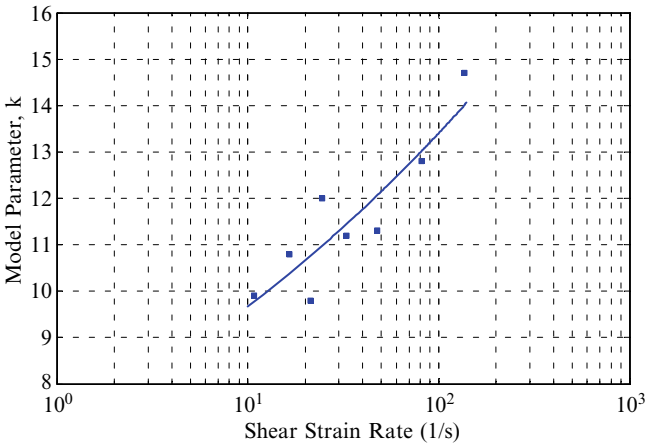

Fig. 38.5 Model parameter, k, versus shear strain rate for model terms

Figure 38.5 shows the variation of the model parameter k with shear strain rate. The parameter k has been calculated using Eq. 38.1 ($k = F_D/s_u D$), where F_D is maximum over the steady state condition as shown in Figs. 38.3 and 38.4.

The following power function could be used to represent the variation of k with shear strain rate. The k parameter is scaled one to one.

$$k = 6.97 \cdot \dot{\gamma}^{0.14} \tag{38.7}$$

The Eq. 38.7 can be directly applied to prototype situations. It should be noted that the shear strain rates (as defined by Eq. 38.5) in the model is N times larger than that in the prototype. As a result, it is possible to simulate a wide range of impact situations in the centrifuge. For example, a typical diameter of 0.3 m and impact velocity of 7.5 m/s in the field results in a shear rate of 25 s^{-1}, which is well within the range tested in the centrifuge.

38.7 Conclusions

The experiments presented in this paper investigate the impact of glide blocks or out-runner blocks on suspended submarine pipelines. The s_u of the clay (4–7 kPa) resulted in simulated shear strain rates between 10 and 137 s^{-1}. This covers a wide range of impact situations. A relationship for the k parameter was proposed based on experimental data. In the absence of more information, the recommended design equation for k (Eq. 38.7) could be used within the range of shear rates investigated in this study.

Acknowledgments The presented work was supported by C-CORE which is greatly acknowledged. We express our sincere gratitude to Bradley Elliott, Gerry Piercey, Derry Nicholl, Don Cameron and Karl Tuff of the C-CORE Geotechnical Group for their significant efforts, help and contribution to this research program. We greatly appreciate the efforts of Dr. Peter Gauer, whose comments have improved this paper and the help in the past with the previous works and Dr. Andy Take for his comments as well.

References

Audibert JME, Nyman KJ (1979) Soil restraint against horizontal motion of pipes. J Geotechnical Eng Div Am Soc Civil Eng (ASCE) 105(12):1555–1558

Bea RG, Aurora RP (1983) Design of pipelines in mudslide areas. Offshore Technology Conference (OTC), Huston, Texas: 1985–1995

Crowe CT, Elger DF, Roberson JA (2001) Engineering fluid mechanics. Wiely, New York

De Blasio FV, Elverhoi A, Issler D, Harbitz CB, Bryn P, Lien R (2004) Flow models of natural debris flows originating from overconsolidated clay materials. Mar Geol 213(1–4):439–455

Demars KR (1978) Design of marine pipelines for areas of unstable sediment. Transportation Eng J ASCE 104(1):109–112

Elverhoi A, Issler D, De Blasio FV, Ilstad T, Harbitz CB, Gauer P (2005) Emerging insights into the dynamics of submarine debris flows. Nat Hazards Earth Syst Sci 5(5):633–648

Garnier J, Gaudin C, Springman SM et al (2007) Catalogue of scaling laws and similitude questions in centrifuge modelling. Int J Phys Model Geotechnics 7(3):1–24

Gauer P, Elverhoi A, Issler D, De Blasio FV (2006) On numerical simulations of subaqueous slides: back-calculations of laboratory experiments of clay-rich slides. Norwegian J Geol 86(3):295–300

Georgiadis M (1991) Landslide drag forces on pipelines. Soils Found 31(1):156–161

Harbitz CB, Parker G, Elverhoi A, Marr JG, Mohrig D (2003) Hydroplaning of subaqueous debris flows and glide blocks: analytical solutions and discussion. J Geophys Res-Solid Earth 108(B7):2349

Imran J, Harff P, Parker G (2001) A numerical model of submarine debris flow with graphical user interface. Comput Geosci 27(6):717–729

Kvalstad TJ (2007) What is the current "Best Practice" in offshore geohazard investigations? A state-of-the-art review (OTC 18545). Offshore Technology Conference (OTC), Houston

Nadim F, Locat TJ (2005) Risk assessment for submarine slides. In: Hunger O, Fell R, Couture R, Eberhardt E (eds) Paper presented at the international conference for landslide risk management, 31 May–3 June 2005. A.A. Balkema, Vancouver, pp 321–334

Oliveira JRMS, Almeida RSS, Almeida MCF, Borges RG (2010) Physical modeling of lateral clay-pipe interaction. J Geotech Geoenviron Eng 136(7):950–956

Randolph M, Cassidy M, Gourvenec S (2005) The Challenges of Offshore Geotechnical Engineering (Keynote). In: Proceedings of 16th international symposium on soil mechanics and geotechnical engineering (ISSMGE), Balkema, Osaka, pp 123–176

Stewart DP, Randolph MF (1994) T-Bar penetration testing in soft clay. J Geotech Eng ASCE 120(12):6

Summers PB, Nyman DJ (1985) An approximate procedure for assessing the effects of mudslides on offshore pipelines. J Energy Resour Technol-Trans ASME 107(4):426–432

Swanson RC, Jones WT (1982) Mudslide effects on offshore pipelines. Transportation Eng J ASCE 108(6):585–600

Taylor RN (1995) Geotechnical centrifuge technology. Blackie Academic & Professional, London

Zakeri A (2009a) Corrigendum to submarine debris flow impact on pipelines – part II: numerical analysis. Coastal Eng 56(1):1

Zakeri A (2009b) Estimating drag forces on suspended and laid-on-seafloor pipelines caused by clay-rich submarine debris flow impact. In: Mosher D et al (eds) Paper presented at the submarine mass movements and their consequences, Nov 2009, Austin, vol 28. Springer, Dordrecht, pp 83–94

Zakeri A (2009c) Review of the state-of-the-art: drag forces on submarine pipelines and piles caused by landslide or debris flow impact. J Offshore Mech Arctic Eng, Am Soc Mech Eng (ASME) 131(1):014001–014008. doi:10.1115/1111.2957922

Zakeri A (2009d) Submarine debris flow impact on suspended (Free-Span) pipelines: normal and longitudinal drag forces. Ocean Eng 36:10

Zakeri A, Høeg D, Nadim F (2008) Submarine debris flow impact on pipelines – part I: experimental investigation. Coastal Eng 55:1209–1218

Zakeri A, Hoeg D, Nadim F (2009) Submarine debris flow impact on pipelines: numerical modeling of drag forces for mitigation and control measures. SPE Projects, Facilities and Construction, Mar 2009: 11

Chapter 39
A Surging Behaviour of Glacigenic Debris Flows

Jan Sverre Laberg, Runar Johansen, and Stefan Bünz

Abstract Based on industry 3-dimensional seismic data, covering an area of 2,190 km^2 of the continental slope offshore mid-Norway, the frontal part of glacigenic debris flow deposits have been studied. The debris flows are up to 6 km wide, 60 m thick and have a length of more than 40 km. Time-slices show that their frontal part is characterized by a zone of front-parallel lineations. The individual lineations are up to some tens of meters wide and they can be followed for several kilometers. In the seismic lines these lineations correspond to dipping reflections, probably formed by sediment compression and thrusting during the final stage of flow. Compression and thrusting implies a surging flow behavior, previously reported from experimental studies of hydroplaning. Thus a surging behavior of the studied flows is inferred to be related to the process of hydroplaning which may lead to surge due to acceleration and detachment of the frontal part from the rest of the flow. Hydroplaning also explains the long run-out of these flows.

Keywords Debris flows, Flow behavior, 3D seismic, Norwegian sea

39.1 Introduction

Trough-mouth fans (Vorren et al. 1989) and prograding wedges (Dahlgren et al. 2005) are large depocenters of glacigenic sediments on high-latitude continental slopes in front of shelf troughs, representing important archives of former glaciations (Vorren and Laberg 1997; Sejrup et al. 2005). Unlike low-latitude and river-fed fans the trough-mouth fans and prograding wedges are dominated by debris flow deposits. Individual deposits have a lobe-formed geometry, and lobes up to 24 km

J.S. Laberg (✉) • R. Johansen • S. Bünz
Department of Geology, University of Tromsø, N-9037 Tromsø, Norway
e-mail: jan.laberg@uit.no

Y. Yamada et al. (eds.), *Submarine Mass Movements and Their Consequences*,
Advances in Natural and Technological Hazards Research 31,
DOI 10.1007/978-94-007-2162-3_39,

wide and 50 m thick can be followed for up to ~200 km on slopes of very low gradient (<1°) (e.g., Laberg and Vorren 1995; Nygård et al. 2005). Stacked sets of lobes, separated by glacimarine and hemipelagic sediments, have been deposited during glacial maxima when the ice front reached the shelf break. These are short periods of very high input of glacigenic sediments from fast-flowing ice streams (Laberg and Vorren 1996; Dahlgren et al. 2002; Nygård et al. 2007).

As no trough-mouth fans and wedges are presently active, reconstructing the paleoenvironment during the release of these flows, their properties, flow mechanics and behavior can only be inferred from the depositional record, supported by laboratory experiments and modeling. Because of this, many aspects of the debris flows and their paleoenvironmental setting is still poorly known. Based on 3-dimensional seismic data, covering the frontal part of several debris flow deposits, our aim is to elucidate on the flow behavior during the final stage of flow. An improved understanding of the flow behavior and run-out of debris flows is a prerequisite for predictions of the potential impact on sea-floor infrastructure by future events.

39.2 Data Base

Our data base comprises two 3-dimensional seismic data sets (SH0402 and SH0701), covering an area of 2,190 km^2 of the continental slope offshore mid-Norway (Fig. 39.1). The data is industry seismic, acquired for hydrocarbon exploration by Norske Shell AS. The bin spacing is 6.25 m, and the dominant frequency at the base of the studied seismic unit is 85 Hz (SH0701) and 65 Hz (SH0402). The data was interpreted and visualized using the Petrel 2008.1 software from Schlumberger.

39.3 Late Cenozoic Evolution of the Mid-Norwegian Continental Margin

The Naust formation (Dalland et al. 1988) offshore mid-Norway comprises an 86,000 km^3 prograding wedge of late Pliocene and Pleistocene glacigenic sediments (Stuevold and Eldholm 1996; Evans et al. 2000; Rise et al. 2010). During its deposition the mid-Norwegian margin experienced a total progradation in the order of about 150 km (Henriksen and Vorren 1996). Detailed studies of the younger part of this prograding wedge, using high-resolution seismic data, showed that it is mainly composed of thick glacigenic debris flow packages interbedded with hemipelagic and contouritic sediments (Dahlgren et al. 2002; Hjelstuen et al. 2004). Most of these sediments are deposited during peak glacials, short periods when the Fennoscandian Ice Sheet reached the shelf break (Dahlgren and Vorren 2003; Hjelstuen et al. 2004; Laberg and Vorren 2004; Rise et al. 2010).

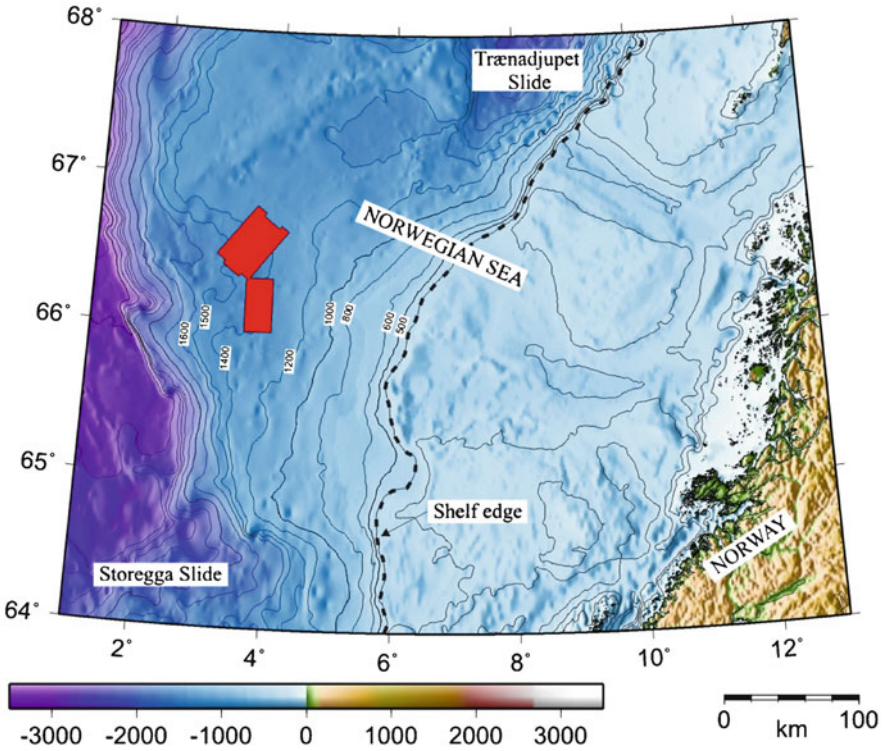

Fig. 39.1 Bathymetric map of the study area. The location of the two 3-dimensional seismic data sets, SH0402 and SH0701 (northern), is indicated

39.4 Results

Seismic Unit 1 is part of the distal Naust Formation and comprises mid – Pleistocene glacigenic sediments (Johansen 2010). The unit was identified within 3D block SH0402 and the southern part of SH0701. To the west (outside the study area) Unit 1 is remobilized by the Vigrid Slide (Johansen 2010), which by Rise et al. (2010) is considered to be part of the larger Sklinnadjupet Slide. Unit 1 has an elongated mounded geometry with the longest axis oriented NW-SE, and it reaches a thickness of up to ~135 m (using a P-wave velocity of 1,800 m/s) (Fig. 39.2).

Internally, the unit is characterized by an acoustically transparent matrix comprising medium to high amplitude reflections. Individual reflections are mainly subhorisontal or mounded, and can be followed for up to several kilometers. Sets of dipping reflections have also been found (see below). The subhorisontal reflections form the base of elongated, lobe-shaped deposits being up to 6 km wide, 60 m thick (Fig. 39.3) and with a length of 40 km. This is, however, a minimum length.

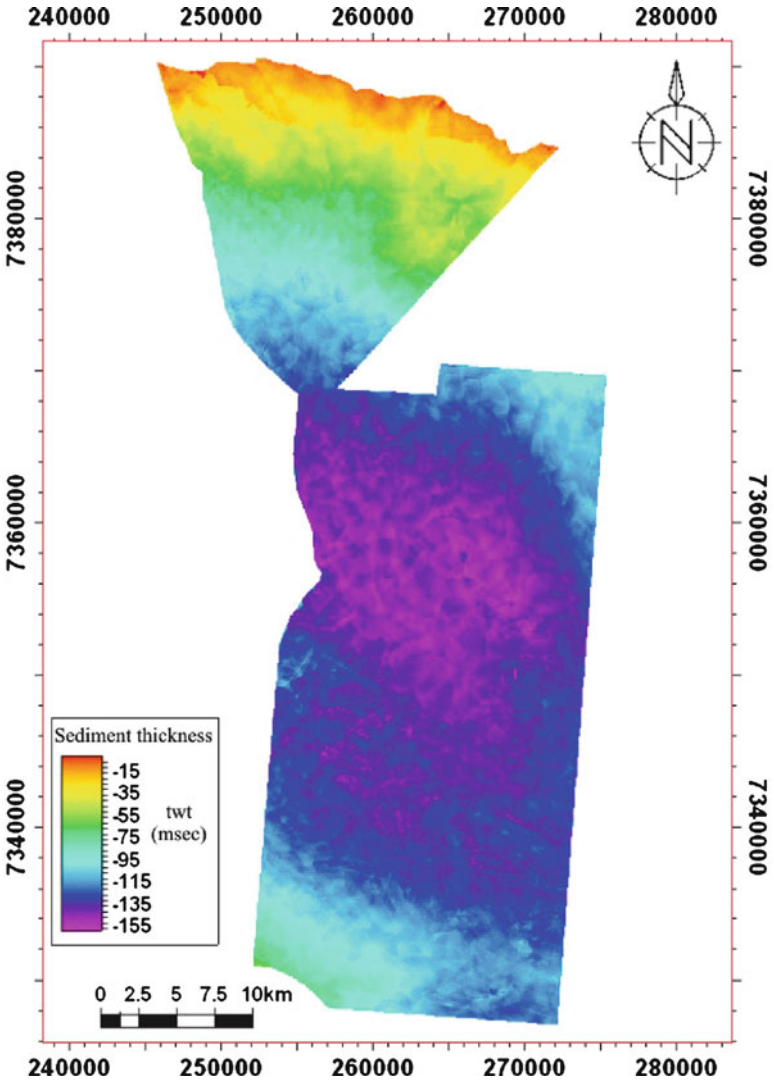

Fig. 39.2 Isopach map of seismic Unit 1 comprising mid Pleistocene glacigenic debris flows

Assuming that they originated near the shelf break, their run-out was probably ~100 km. The geometry of these deposits is very similar to muddy glacigenic debris flows previously studied Norwegian (see Vorren et al. 1998 for a review), and other, glaciated margins (e.g., Tripsanas and Piper 2008). Thus we infer that the lobes observed in the 3D seismic are muddy glacigenic debris flow deposits.

Within the study area, the frontal part of some ten debris flows, with about the same run-out, has been identified. Individual deposits are stacked on top of each other,

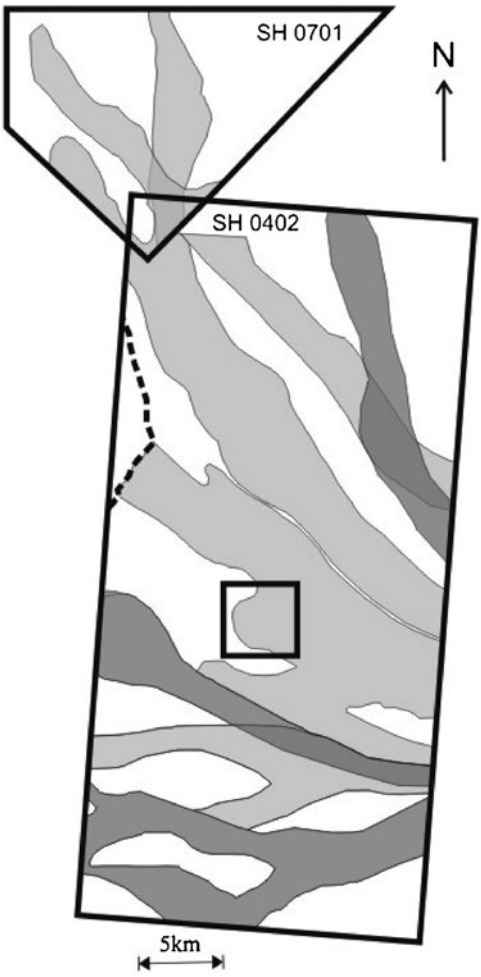

Fig. 39.3 Interpretive sketch of the outline of the elongated, lobe-shaped deposits of seismic Unit 1. Individual deposits are up to 6 km wide, 60 m thick and have a length of more than 40 km. Some of the younger lobes are indicated by darker gray. *Black box* outlines Fig. 39.4 and *stippled line* is the eastern limit of the area affected by the Vigrid Slide

younger flows being deposited in lows between older deposits (Fig. 39.3). This is a pattern characteristic for Trough Mouth Fans (Vorren et al. 1989; Laberg and Vorren 1996; Nygård et al. 2002) and prograding wedges (Dahlgren et al. 2005), but which is different from debris flow deposits on low latitude fans as the Mississippi fan (Schwab et al. 1996; Talling et al. 2010). Time-slices (Fig. 39.4) show that their frontal part is characterized by a zone of front-parallel lineations. This zone can be subdivided into sub-zones comprising lineations that are up to some tens of meters wide, and which can be followed for several kilometers. The subzones are bounded by a pronounced lineation which on seismic lines corresponds to a dipping reflection (Fig. 39.4).

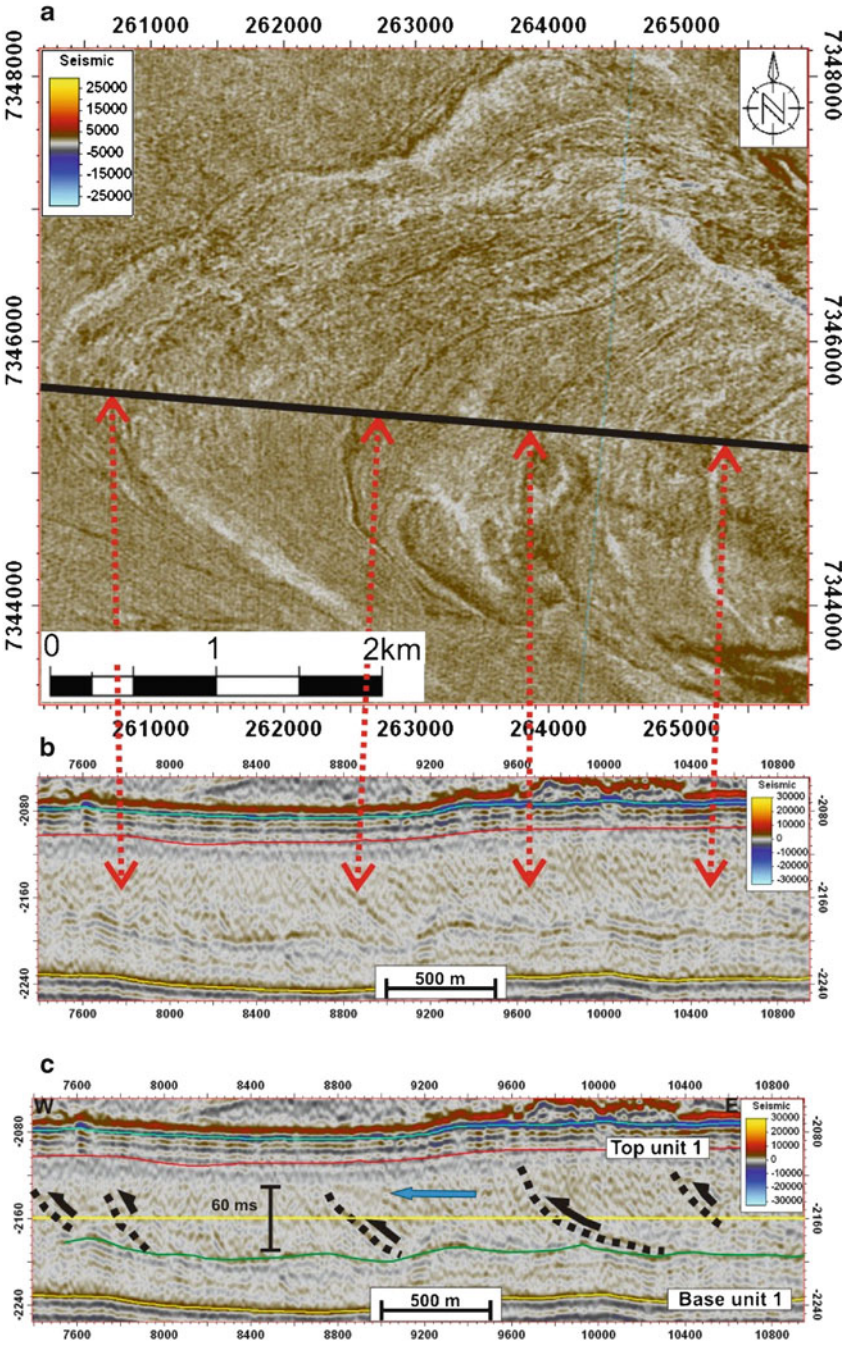
a
261000
262000
263000
264000
265000
7348000
7346000
7344000
Seismic
25000
15000
5000
-5000
-15000
-25000
N
0
1
2km
b
7600
8000
8400
8800
9200
9600
10000
10400
10800
-2080
-2160
-2240
Seismic
30000
20000
10000
0
-10000
-20000
-30000
500 m
c
W
E
Top unit 1
60 ms
500 m
Base unit 1

39.5 Discussion

Glacigenic debris flows have in a number of studies been shown to have originated from subglacial till transported to the shelf edge by ice streams during glacial maximums (Vorren et al. 1989; Aksu and Hiscott 1992; Laberg and Vorren 1995; King et al. 1996; Vorren and Laberg 1997). An enigmatic characteristic of these deposits is their long run-out which has been explained by the process of hydroplaning and/or progressive wetting of the shear layer based on results from laboratory experiments, leading to decoupling of the sediments from the bed (e.g., Mohrig et al. 1998; Elverhøi et al. 2005; Issler et al. 2005). For the glacigenic debris flows deposited on the Bear Island Trough Mouth Fan during the last glacial maximum, support of this interpretation is the fact that the flows seemingly moved across the lower part of the fan without affecting the underlying sediments (Laberg and Vorren 2000). Also in the area of this study we find that the debris flows have a very long run-out distance (~100 km) on a low-gradient slope which is difficult to explain without invoking hydroplaning and/or progressive wetting of the shear layer.

The frontal parts of the debris flows identified within 3D blocks SH0402 and SH0701 are characterized by a zone of front-parallel lineations which on seismic lines corresponds to dipping reflections (Fig. 39.4). We suggest that the dipping reflections are thrust-planes formed due to sediment compression and thrusting during the final stage of flow. Compression may imply a surging flow behavior as previously inferred for at least one of the large debris flows on the Bear Island TMF from which side-scan data, with the necessary level of resolution, was available (Laberg and Vorren 2000). If correct, the frontal part of the debris flows did not freeze "en masse" but was the result of the aggradation of several sediment pulses. According to this interpretation the acoustic contrasts forming the lineations was due to grain-size and/or physical properties variations between the individual flow pulses.

Experimental studies have shown that hydroplaning may lead to frontal detachment of submarine flows due to the induction of tensile stresses behind the front (Ilstad et al. 2004; De Blasio et al. 2006). We suggest that this process of frontal detachment results in a surging flow behavior as inferred for the studied debris flows. An alternative which cannot be ruled out is that individual sediment pulses originated from successive retrogressive failures in the source area. However, we find this interpretation less likely as this probably would result in deposition of a number

Fig. 39.4 (**a**) Time-slices of the frontal part of one of the elongated, lobe-shaped deposits of seismic Unit 1 (see Fig. 39.3 for location). The frontal part is characterized by a zone of front-parallel lineations which can be divided into sub-zones comprising lineations that are up to some tens of meters wide. The subzones are bounded by a pronounced lineation which on seismic lines corresponds to a dipping reflection (locations indicated by *red arrows*) (**b**) Seismic line along the frontal part showing that the upper Unit 1 is dominated by dipping reflections corresponding to lineations on the time-slice (**c**) Interpretation of seismic line in Fig. 39.4b, showing the location of some of the dipping reflections inferred to be thrust-planes formed due to sediment compression and thrusting during the final stage of flow. *Blue arrow* indicates the flow direction and yellow line shows the depth of the time slice of (a)

of individual deposits as seen in the upper Storegga Slide (Haflidason et al. 2004) rather than aggradation within one as shown here.

Studies of subaerial debris flows, including large-scale laboratory experiments (e.g., Major and Iverson 1999) and recent field observations (McArdell et al. 2007; McCoy et al. 2010), show that these flows had a non-uniform pore-fluid pressure distribution, affecting the resisting friction forces. This distribution allows the development of surge fronts. Surges with the highest excess pore fluid pressure have been found to have the longest run-out (McCoy et al. 2010). The natural flows studied by McCoy et al. (2010) also showed indications of sorting as coarse-grained fronts were followed by fine-grained tails. However, very little is presently known on the pore-fluid pressure within their submarine counterparts as this is difficult to measure in laboratory experiments (Elverhøi et al. 2005). Thus, if and how pore-fluid pressure may affect the flow behavior of submarine flows is presently not known.

39.6 Conclusions

1. Detailed studies of frontal parts of glacigenic debris flows show that they are characterized by front parallel lineations corresponding to dipping reflections on seismic profiles. The dipping reflections are thrust-planes formed due to sediment compression and thrusting during the final stage of flow, implying surging flow behaviour.
2. Surge has been described for subaerial flows. Laboratory experiments indicates that it may also affect submarine flows but for different reasons. In the former case it is inferred to be related to the non-uniform distribution pore-fluid pressure, in the latter case it is probably related to acceleration and detachment of the head due to hydroplaning. The influence of the pore-fluid pressure on the flow behavior of the submarine flows studied here is not known while hydroplaning also explains their long run-out. Based on this we suggest that the studied debris flows had a surging flow behavior due to hydroplaning causing their frontal part to accelerate away from the main body.

Acknowledgements This work is a contribution to the *Loslope* project and we acknowledge the Research Council of Norway for financial support and the reviewers D. Winkelmann and B. O. Hjelstuen. The bathymetry for Fig. 39.1 was displayed using the Generic Mapping Tools (GMT) software (Wessel and Smith 1998). The University of Tromsø acknowledges Schlumberger for seismic interpretation software and Norske Shell AS for providing the 3D seismic data base.

References

Aksu AE, Hiscott RN (1992) Shingled Quaternary debris flow lenses on the north-east Newfoundland slope. Sedimentology 39:193–206

Dahlgren KIT, Vorren TO (2003) Sedimentary environment and glacial history during the last 40 ka of the Vøring continental margin, mid-Norway. Mar Geol 193:93–127

Dahlgren KIT, Vorren TO, Laberg JS (2002) Late Quaternary glacial development of the mid-Norwegian margin −65 to 68° N. Mar Petrol Geol 19:1089–1113
Dahlgren KIT, Vorren TO, Stoker MS et al (2005) Late Cenozoic prograding wedges on the NW European continental margin: their formation and relationship to tectonics and climate. Mar Petrol Geol 22:1089–1110
Dalland A, Worsley D, Ofstad K (1988) A lithostratigraphic scheme for the Mesozoic and Cenozoic succession offshore mid- and northern Norway. Norwegian Petrol Dir Bull 4:65
De Blasio FV, Elverhøi A, Engvik LE et al (2006) Understanding the high mobility of subaqueous debris flows. Norwegian J Geol 86:275–284
Elverhøi A, Issler D, De Blasio FV et al (2005) Emerging insights into the dynamics of submarine debris flows. Nat Hazards Earth Syst Sci 5:633–648
Evans D, McGiveron S, McNeill AE et al (2000) Plio-Pleistocene deposits on the mid-Norway margin and their implications for late Cenozoic uplift of the Norwegian mainland. Glob Planet Change 24:233–237
Haflidason H, Sejrup HP, Nygård A et al (2004) The Storegga slide: architecture, geometry and slide development. Mar Geol 213:201–234
Henriksen S, Vorren TO (1996) Late Cenozoic sedimentation and uplift history on the mid-Norwegian continental shelf. Glob Planet Change 12:171–199
Hjelstuen BO, Sejrup HP, Haflidason H, Berg K, Bryn P (2004) Neogene and Quaternary depositional environments on the Norwegian continental margin, 62°N–68°N. Mar Geol 213: 257–276
Ilstad T, De Blasio FV, Elverhøi A et al (2004) On the frontal dynamics and morphology of submarine debris flows. Mar Geol 213:481–497
Issler D, De Blasio FV, Elverhøi A et al (2005) Scaling behaviour of clay-rich submarine debris flows. Mar Petrol Geol 22:187–194
Johansen R (2010) 3D seismisk analyse av begravde rasavsetninger på den SV delen av Vøringmarginen. Master thesis, University of Tromsø, pp 99 (in Norw)
King EL, Sejrup HP, Haflidason H et al (1996) Quaternary seismic stratigraphy of the North Sea Fan: glacially-fed gravity flow aprons, hemipelagic sediments, and large submarine slides. Mar Geol 130:293–315
Laberg JS, Vorren TO (1995) Late Weichselian submarine debris flow deposits on the Bear Island Trough Mouth Fan. Mar Geol 127:45–72
Laberg JS, Vorren TO (1996) The Middle and Late Pleistocene evolution of the Bear Island Trough Mouth Fan. Glob Planet Change 12:309–330
Laberg JS, Vorren TO (2000) Flow behaviour of the submarine glacigenic debris flows on the Bear Island Trough Mouth Fan, western Barents Sea. Sedimentology 47:1105–1117
Laberg JS, Vorren TO (2004) Weichselian and Holocene growth of the northern high-latitude Lofoten Contourite Drift on the continental slope of Norway. Sediment Geol 164:1–17
Major JJ, Iverson RM (1999) Debris-flow deposition: effects of pore-fluid pressure and friction concentrated at flow margins. Geol Soc Am Bull 110:1424–1434
McArdell BW, Bartelt P, Kowalski J (2007) Field observations of basal forces and fluid pore pressure in a debris flow. Geophys Res Lett 34:L07406. doi:10.1029/2006GL029183
McCoy SW, Kean JW, Coe JA et al (2010) Evolution of a natural debris flow: in situ measurements of flow dynamics, video imagery, and terrestrial laser scanning. Geology 38:735–738. doi:10.1130/G30928.1
Mohrig D, Whipple KX, Hondzo M et al (1998) Hydroplaning of subaqueous debris flows. Geol Soc Am Bull 110:387–394
Nygård A, Sejrup HP, Haflidason H, King EL (2002) Geometry and genesis of glacigenic debris flows on the North Sea Fan: TOBI imagery and deep-tow boomer evidence. Mar Geol 188:15–33
Nygård A, Sejrup HP, Haflidason H, Bryn P (2005) The glacial North Sea Fan, southern Norwegian Margin: architecture and evolution from the upper continental slope to the deep-sea basin. Mar Petrol Geol 22:71–84
Nygård A, Sejrup HP, Haflidason H et al (2007) Extreme sediment and ice discharge from marine based ice streams: new evidence from the North Sea. Geology 35:395–398

Rise L, Chand S, Hjelstuen BO et al (2010) Late Cenozoic geological development of the south Vøring margin, mid-Norway. Mar Petrol Geol 27:1789–1803
Schwab WC, Lee HJ, Twichell DC et al (1996) Sediment mass-flow processes on a depositional lobe, outer Mississippi Fan. J Sediment Res 66:916–927
Sejrup HP, Hjelstuen BO, Dahlgren KIT et al (2005) Pleistocene glacial history of the NW European continental margin. Mar Petrol Geol 22:1111–1129
Stuevold LM, Eldholm O (1996) Cenozoic uplift of Fennoscandia inferred from a study of the mid-Norwegian margin. Glob Planet Change 12:359–386
Talling PJ, Wynn RB, Schmmidt DN et al (2010) How did thin submarine debris flows carry boulder-sized intraclasts for remarkable distances across low gradients to the far reaches of the Mississippi Fan? J Sediment Res 80:829–851
Tripsanas EK, Piper DJW (2008) Glaciogenic debris-flow deposits of Orphan Basin, offshore eastern Canada: sedimentological and rheological properties, origin, and relationship to meltwater discharge. J Sediment Res 78:724–744
Vorren TO, Laberg JS (1997) Trough mouth fans – palaeoclimate and ice-sheet monitors. Quat Sci Rev 16:865–881
Vorren TO, Lebesbye E, Andreassen K et al (1989) Glacigenic sediments on a passive continental margin as exemplified by the Barents Sea. Mar Geol 85:251–272
Vorren TO, Laberg JS, Blaume F et al (1998) The Norwegian-Greenland Sea continental margins: morphology and late Quaternary sedimentary processes and environment. Quat Sci Rev 17:273–302
Wessel P, Smith WHF (1998) Improved version of the generic mapping tools released. EOS Trans AGU 79:579

Chapter 40
Failure Processes and Gravity-Flow Transformation Revealed by High-Resolution AUV Swath Bathymetry on the Nice Continental Slope (Ligurian Sea)

Sébastien Migeon, Antonio Cattaneo, Virginie Hassoun, Alexandre Dano, Aurélie Casedevant, and Etienne Ruellan

Abstract The continental slope offshore Nice is a natural laboratory to investigate submarine landslides and gravity-flow processes. Using EM300 bathymetry data (spatial resolution of 25 m), about 250 scars with volume less than 8×10^8 m^3 were identified. The AUV bathymetric data (spatial resolution of 2 m) revealed a greater number of scar-related failures with two main morphologies: some scars are affected by retrogressive processes of erosion, suggesting failures were triggered a long time ago, while other scars exhibit no evidence of post-failure erosion, suggesting they could have been triggered recently. Downslope from the scars, there are scattered blocks, on average 5-m high and 40-m wide, and well-developed asymmetrical waves, on average 2-m high and 20-m in wavelength. Such evolution could be evidence for the transformation of the remobilized deposits into cohesive flows then turbulent flows. Such transformation took place over a distance of less than 6–8 km.

Keywords Multibeam bathymetry • Submarine failures • Gravity flows • Scars • Bedforms

S. Migeon (✉) • V. Hassoun • A. Dano • E. Ruellan
UMR GéoAzur, UNS-UPMC-CNRS-IRD, Port de la Darse,
06235 Villefranche/Mer, France
e-mail: migeon@geoazur.obs-vlfr.fr

A. Cattaneo
Géoaciences Marines, IFREMER, BP70, F-29280 Plouzané Cédex, France

A. Casedevant
UMR EPOC, University Bordeaux 1, Avenue des Facultés, 33405 Talence, France

Y. Yamada et al. (eds.), *Submarine Mass Movements and Their Consequences*,
Advances in Natural and Technological Hazards Research 31,
DOI 10.1007/978-94-007-2162-3_40, © Springer Science+Business Media B.V. 2012

40.1 Introduction

Submarine failures have a strong impact on the shaping of continental slopes through time. Large-scale failures of volumes exceeding several hundreds of km^3 can drastically change the morphology of the slope instantaneously but are rare, with a return period of several thousands years or more (Haflidason et al. 2005; Garziglia et al. 2008). Small-scale failures with volume lesser than several hundreds of m^3 are more difficult to detect using conventional ship-based tools but are probably much more common, like on the canyon flanks where return periods of 5 years or less have been evaluated where repeated bathymetric surveys were conducted (Smith et al. 2007). Thus, small-scale features could also have a strong impact on the evolution of continental slopes over a short time periods, i.e. at human scale.

In submarine environments, reliable geohazard assessment requires the identification of the signatures of different types of slope instabilities, the evaluation of their age, and the discrimination between several pre-conditioning and triggering factors (Locat 2001). Identification of potential areas where slope movements could be triggered and precise understanding of processes of failures from the morphologies and internal architectures require data with spatial resolution of about a metre. To address these problems, the continental slope offshore Nice (Ligurian Sea) was mapped using an Autonomous Underwater Vehicle (AUV) operating an EM2000 swath mapping system.

Since the 1979 failure event that affected the shelf edge offshore the Nice airport, the continental slope offshore Nice became a natural laboratory to investigate problems of slope stability (Cochonat et al. 1993; Mulder et al. 1994; Leynaud and Sultan 2010; Sultan et al. 2010). Until now, most of the studies focused on the source area of the 1979 failure (Mulder et al. 1997; Dan et al. 2007) and only few contributions concentrated on the analysis of failure-related morphologies (Klaucke and Cochonat 1999) and their interpretation in term of failure processes, rather than in the potential downslope transformation of landslides into gravity flows as it happened for the 1979 failure (Mulder et al. 1997). The purpose of this paper is two-fold: (1) to investigate the distribution of submarine landslides on the Nice continental slope and to estimate frequency and causes of triggering based on the integration of hull-mounted EM300 and AUV bathymetric data; (2) to show the benefit of very-high resolution bathymetric AUV data in describing and understanding failure-related processes.

40.2 Methods

Seafloor and failure morphologies were investigated using multibeam bathymetry collected using a hull-mounted Simrad EM300 (MALISAR1 cruise, 2006) and an EM2000 mounted on an AUV (MALISAR4 (2009) and AUVNIS (2010) cruises). These bathymetric data allowed for the generation of DTM with a spatial resolution

of 25 m and 2 m respectively. As the failure scars were well defined in the resulting bathymetric maps, it was possible to calculate the volume of sediment missing in the scar areas by subtracting the reconstructed pre-landslide morphology from the post-landslide seafloor with the softwares Caraibes (Ifremer) and GMT (Wessel and Smith 1998). AUV data allowed a detailed analysis of the scars geometry and discrimination between different seafloor morphologies related to several gravity-flow processes.

40.3 Results

The slope offshore the city of Nice (Fig. 40.1) extends from the shelf break, at a depth of 20–50 m, to the confluence of the Var and Paillon canyons, at a depth of 1,600 m. This area receives sediment from the Var and Paillon rivers, with an annual

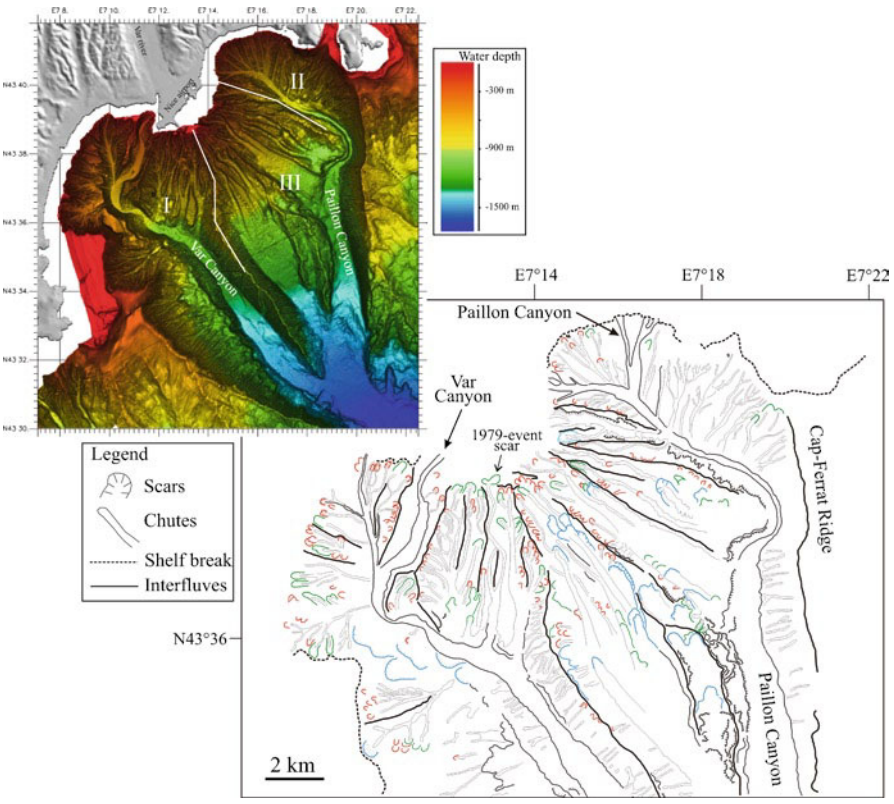

Fig. 40.1 Interpretative map of the continental slope offshore Nice illustrating the distribution of Groups 1 (*red*), 2 (*green*) and 3 (*blue*). The inset is the shaded bathymetric map of the area with the location of Zones I, II and III

Table 40.1 Four "Groups" of failure scars are classed by size (width and height of the scar) on the continental slope offshore Nice

Type of data	"Group" of scars by size	Width (m)		Height (m)		Average surface (m^2)
		Min	Max	Min	Max	
Hull-mounted EM300	Group 1 "Small scars"	80	150	20	30	$10–20 \times 10^3$
	Group 2 "Medium scars"	150	250	30	60	$40–80 \times 10^3$
	Group 3 "Large scars"	250	500	60	90	$100–150 \times 10^3$
AUV EM2000	Group 4 "Very small scars"	30	70	>2	10	$1–3 \times 10^3$

budget of about $1.6–3 \times 10^6$ t for the Var river (Mulder et al. 1996). Based on the new, higher-resolution data, we re-visited the identification and distribution of gravity processes previously proposed by Klaucke and Cochonat (1999) and Klaucke et al. (2000). By comparison with these works, a larger number of failure-related scars was identified and the features interpreted by these authors as canyon floors or valleys are now identified as erosional chutes related to slope failures or imbricated scars.

40.3.1 General Distribution of Scars from EM300 Bathymetric Data

The morphology of the seafloor is mainly moulded by failure-induced scars and chutes that represent 90–95% of the total surface of the studied area (Fig. 40.1). About 250 scars were identified on the upper continental slope (water depth: 20–1,000 m), where slope angles are between 10° and 15°. Between 1,000 and 1,600 m, the slope angle decreases to less than 6°, failure scars are less abundant. Based on scars analysis using EM300 data only (Fig. 40.1), three groups were discriminated (Table 40.1) within three Zones of the continental slope (Fig. 40.1). Zones I and II are located nearby the mouth of the Var and Paillon rivers respectively, while Zone III is located away from direct river supply.

In Zones I and II, failure scars exhibit similar size, distribution and morphology. About 80% of the scars are small scars, 15% are medium scars and only 5% are large scars. The 1979-event scar (Zone I) is a medium scar. Small-size failures are thus largely predominant. The study of spatial distribution of scars reveals that:

- small scars are mostly located at the shelf break and along the crest and on the flanks of the interfluves (Fig. 40.1), where the local slope angle varies between 30° and 15°;
- medium and large scars are mostly located at greater water depth on the continental slope, where the local slope angle varies between 10° and 6°.

In Zones I and II, volumes of missing sediment within the scars are, on average, less than 7×10^7 m^3. Whatever their location on the continental slope, the scars mainly exhibit a semi-circular morphology. Each scar is prolonged downslope by a

chute revealing the erosive power of the failed mass. Chutes are in their upstream part comparable in size with the scars, then enlarge to 200–400 m in width and to 40–80 m in depth downslope, suggesting an increasing erosion of the seafloor.

Zone III exhibits a change in the size and distribution of scars (Fig. 40.1). Twenty percent of the scars are small scars, 45% are medium scars and 35% are large scars. In this zone, medium – to large-scale failures are predominant. The analysis of the spatial distribution of scars reveals that:

- about 14% of the scars are located near the shelf break and belong to the small scars category;
- about 86% of the scars were triggered at water depth greater than 200 m and are medium to large scars.

In Zone III, volumes of missing sediment within the scars are, on average, less than 8×10^8 m^3. Morphologies of scars and chutes are similar to those from Zones I and II. Chutes gradually enlarge from about 100–500 m in width and to 70–100 m in depth downslope.

In the three zones, the scars are steep (about 15–30°) and the chutes have a smooth floor. These features still look "fresh" on the present-day seafloor, suggesting they could have been generated until recent time.

40.3.2 Detailed Description of Scars and Chutes from AUV Data

AUV bathymetric data were collected in an area comprised between the Var and Paillon Canyons (Zones I and III, Fig. 40.2). Due to their higher resolution, the AUV data reveal a higher number of scars detectable at the seafloor, and more detailed morphology of scars and chutes.

The number of scars revealed by the AUV data is five times greater than previously described from EM300 data in Zones I and III. In areas of higher slope angle, the number of scars revealed is as much as eight times greater than the number shown by the EM300 dataset. Such a strong increase is explained by the dramatic increase in resolution of bathymetric data and could affect the results of quantitative spatial analysis on landslide size distribution (Chaytor et al. 2009). The new scars identified on the AUV data result from small-scale failure events (Group 4, Table 40.1). Scar morphologies are 30–70 m in width and 10 m or less in height, and volume of evacuated sediment ranges from 20 to 200×10^3 m^3. These very small scars are mainly found associated with average local slope angle of 18–30°.

An additional strong difference comes from the AUV-based morphological analysis of scars and chutes, all apparently similar on the EM300 data. Two different scar morphologies (SM) can be discriminated on the AUV data. A first morphology, SM1, consists of simple, isolated semi-circular and steep (about 30–35°) scars (Fig. 40.3b). In contrast, SM2 exhibit a more complex plan-view pattern consisting in several imbricated or juxtaposed small-scale scars, less than 40-m wide and 10-m

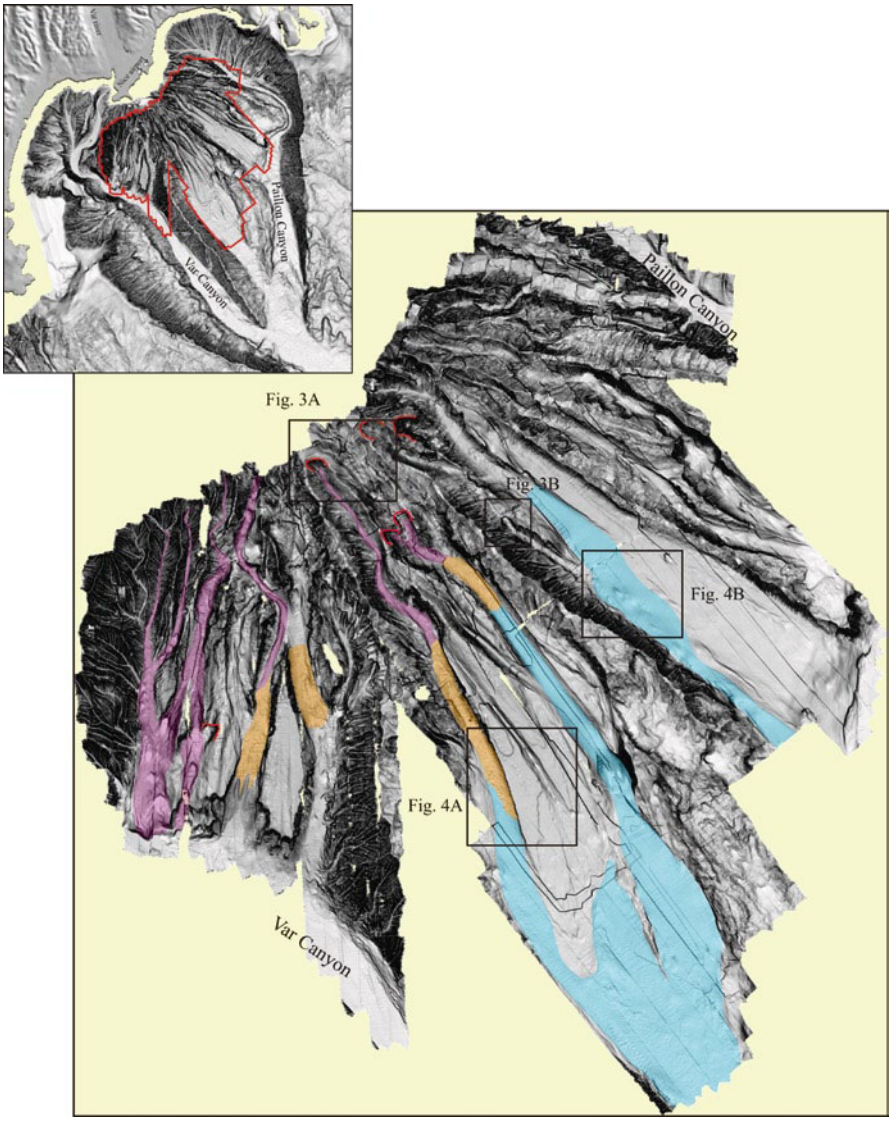

Fig. 40.2 Shaded bathymetric map (AUV data) illustrating the location of CM1 (*purple*), CM2 (*orange*) and CM3 (*blue*) on the continental slope. The inset shows the location of the AUV data on the continental slope. Location of Figs. 40.3 and 40.4 is also shown

deep (Fig. 40.3a). SM2 have a gentler slope angle (about 20°). Many scars interpreted as simple semi-circular morphologies on the EM300 data correspond to SM2 on the AUV data. Both SM1 and SM2 concern failures belonging to the four Groups defined in Table 40.1.

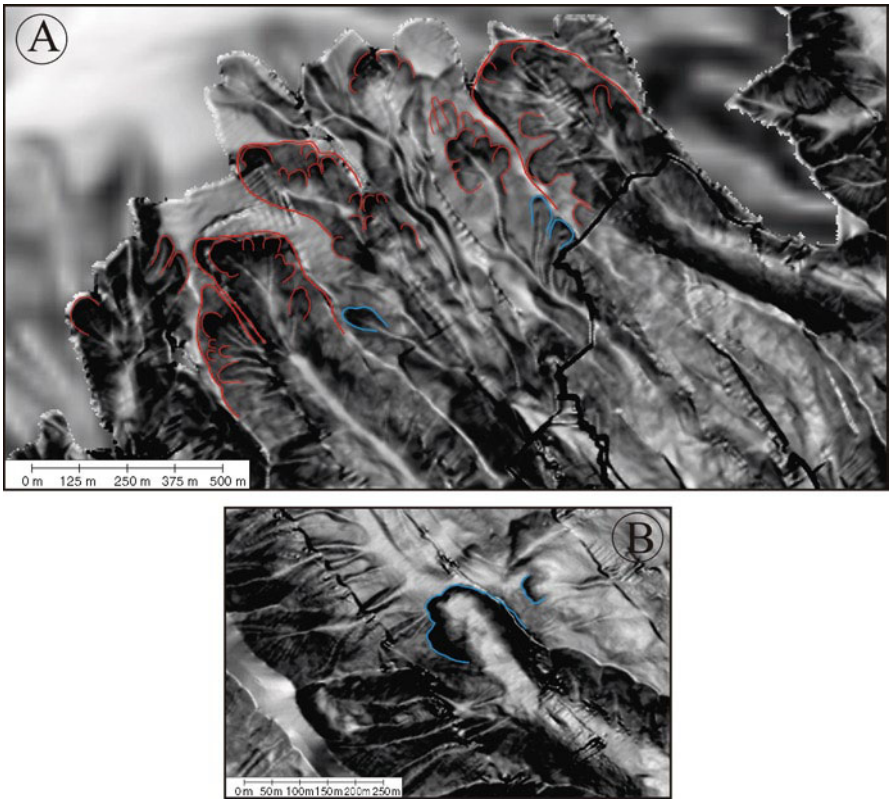

Fig. 40.3 Shaded bathymetric map (AUV data) illustrating scar morphologies SM1 (*blue*) and SM2 (*red*). Figure location shown in Fig. 40.2

The AUV dataset also shows that chute morphology is more diversified than previously identifiable using only EM300 data. Three chutes morphologies (CM) are distinguished. CM1 consist of a flat and smooth seafloor. Over-incisions are also observed at several places in CM1 (Fig. 40.4a), and correlate with local abrupt increase of the slope angle, as observed in the upper part of Zones I and III (Fig. 40.2). CM2 consist of a rough seafloor related to the presence of scattered blocks, 30–40 m in diameter and about 5-m high, and transverse ridge-like morphologies (Fig. 40.4a). This is observed at the base of Zone I and in Zone III (Fig. 40.2). CM3 consist of wavy structures oriented perpendicular to the chutes axis (Fig. 40.4a, b). The structures are about 20 m in wavelength and 2–5-m high, with crests that are slightly sinuous and 50–200-m long. Each wavy structure exhibits an asymmetrical cross-section, with a flatter and longer upstream flank and a steeper and shorter downstream flank (Fig. 40.4c). CM3 are only located at the base of Zone III (Fig. 40.2).

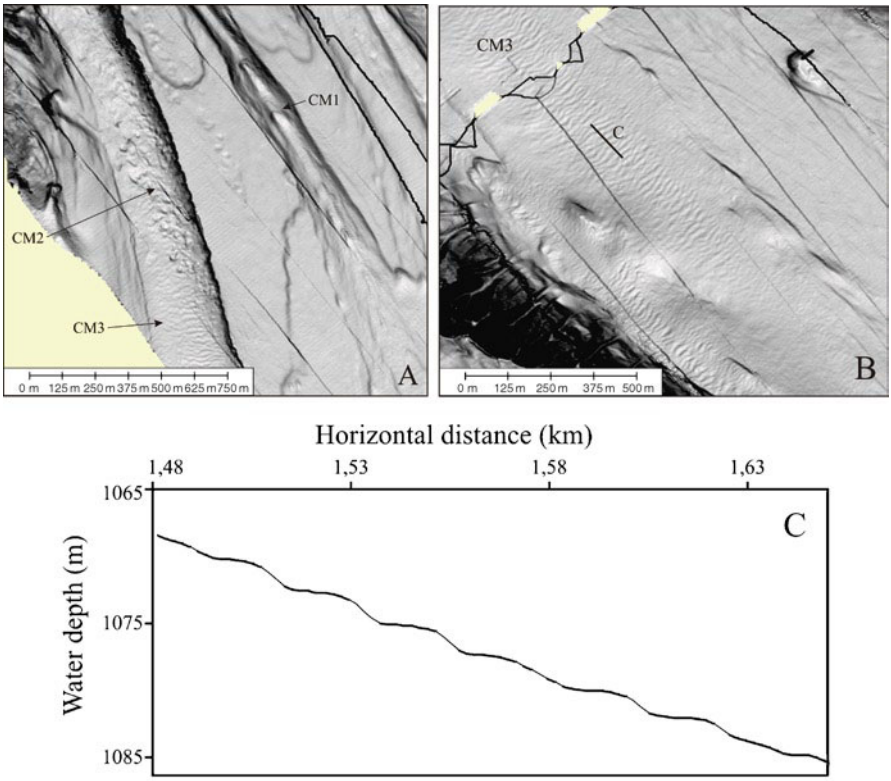

Fig. 40.4 (**a**) and (**b**) are shaded bathymetric map (AUV data) illustrating chute morphologies CM1, CM2 and CM3. (**c**) is a topographic profile illustrating the size and geometry of bedforms. Figure location shown in Fig. 40.2

40.4 Discussion

40.4.1 Processes of Continental-Slope Failure and Erosion

In Zones I, II and III, scar morphologies identified on EM300 data have undistinguishable features and single chutes relate to single scars, suggesting that single-phase failure events triggered on the continental slope. The two types of SM identified on the AUV data reveal that the scars could be the result of either a single phase (SM1) or multiple phases (SM2) of failure. Once a main scar is formed from an initial failure generated at the seafloor (SM1), the local oversteepening created along this scar, together with the sediment decompression affecting the surrounding deposits, promotes secondary small-scale failures directly on the main scar as it adjusts to an equilibrium profile and creates a new morphology (SM2). So SM1 and SM2 could highlight successive steps of scar evolution through time. When observed on the present-day seafloor, SM1 are thus though to characterise the latest failure

events leaving behind a steep, fresh scar, while SM2 could characterise older scars that are returning or have already returned to stable slope conditions through mechanism of retrogressive failures.

The downslope increasing size of the chutes can be interpreted as a result of the increase of both erosional power and volume of the mass flows. For the 1979 event, the comparison between the initial volume estimated from the scar area (3×10^6 m^3) and the volume of the whole chute (6×10^7 m^3) suggests the mass flow expanded to 20 times its volume over less than 6 km. In that case, basal erosion leading to an increasing flow volume is probably accentuated by the high slope angle.

As the 250 identified scars from Groups 1–3 only affect the Holocene drape (Klaucke and Cochonat 1999), a mean frequency of triggering could be one event every 50 years at the scale of the Holocene.

40.4.2 Potential Triggering Mechanisms

In Zones I and II, failure events are abundant but involved relatively small volumes of sediment. In these two zones, sediment deposition mainly results from hyperpycnal flows or decantation from surface plumes (Mulder et al. 1996; Klaucke et al. 2000). At the mouth of the Var river, hyperpycnal flows have return frequency of 2–5 year during the Late Holocene (Mulder et al. 1998). The areas affected by hyperpycnal flows are characterized by sedimentation rates as high as 1–2 m/100 year (Mulder et al. 2001). Geotechnical analyses described the deposits in these areas as underconsolidated (Cochonat et al. 1993). Conjunction between underconsolidation and slope angles of 15–30° on the upper continental slope suggests that gravity-driven failures could occur regularly. In addition, hyperpycnal flows could have a direct impact on the triggering of small-scale failures through mechanisms of sustained friction along the seabed, and erosion leading to local oversteepening.

In Zone III, failure events are less frequent than in Zones I and II but involve larger volumes of sediment. Here, superficial Holocene deposits consist of alternating coarser- and finer-grained beds (Klaucke et al. 2000) and are characterised as normally consolidated to slightly overconsolidated (Cochonat et al. 1993). With slope angles lower than 10° and in static conditions, failures should involve sediment thickness less than few meters (Cochonat et al. 1993), which does not fit with our observations. External factors must be invoked to explain the fact that failure plans developed at 30–90 m below the seafloor. The presence of fresh-water springs and free gas in the sediment was identified by Dan et al. (2007) and Sultan et al. (2010) at shallow water depth offshore the Nice airport but they are absent at greater depth on the continental slope. The recurrent seismic activity affecting the base of the continental slope and the Southern Alps could be a good candidate. Because the epicentres of earthquakes with Mw = 4.0–6.0 are located in the basin, horizontal accelerations on the Nice slope are probably not strong enough to trigger a failure but the repetitive action of earthquakes could lead to a gradual degradation of sediment properties, mainly the coarser layers that are prone to liquefaction, and to the development of weakness layers.

40.4.3 Some Insights into Gravity Flow Transformation

It is well-known that a continuum of transformation does exist between mass-wasting events, cohesive flows and turbulent flows (Mulder and Cochonat 1996, among others), but the changes of slope angle and distance necessary for these changes to occur are still poorly understood. The three CM styles identified on the AUV data help to understand these processes. CM1 are always located immediately downslope from the scars (Fig. 40.2). They should reflect the first phase of seafloor erosion related to flow acceleration, as described from flume experiments, before the velocity of the mass flow reaches a more or less constant value (Mohrig et al. 1999; Marr et al. 2001). When observed, CM2 are located downslope from CM1 (Fig. 40.2) and are thought to characterise debris-flow deposits. Finally, CM3 located downslope from CM2 (Fig. 40.2) are interpreted as fields of downslope-migrating bedforms build by turbulent flows. The presence of CM2 at some places at the base of Zone I suggests that remobilized deposits are mostly completely evacuated to the Var Canyon, the continental slope being a by-passing/erosion area. In Zone III, the succession of CM1/CM2/CM3 suggests a complete transformation of remobilized deposits into debris flows, and then later, turbulent flows. An initial stage of seafloor erosion by a moving mass flow usually occurs within the first 2–3 km downslope from scars, where the slope angle is about 10–15°. Then, as slope angle decreases to 6–8°, deposition by debris flows takes place over the next 0.5–2 km. The sharp contact between CM2 to CM3 highlights that debris flows stop abruptly when the slope angle decreases to less than 4–5°. The continuum of sea-bed structures between CM2 and CM3 suggests that turbulent flows probably already existed on top of debris flows and impacted the seafloor morphology as soon as debris flows froze. Complete transformation between debris flows and turbulent flows could thus have taken place over distances as short as 0.5–2 km. Then, turbulent flows develop over the next 8 km, to the Var Valley.

40.5 Conclusion

We presented a re-examination of the seafloor morphology of the continental slope offshore the city of Nice. The analysis of new multibeam data allowed us to identify morphologies of several types and sizes of failure scars and gravity flow deposits. Very-high-resolution AUV data allow for identification of a higher number of scars and a better characterisation of their morphological variability. Such results can be of interest in other regions with steep continental slopes in the assessment of landslide geohazards. The proposed quantifications of the traces presumably left by gravity flows could in turn provide input into numerical models describing flow transformation.

Acknowledgements We thank the captains and crew of the RV Le Suroît and l'Europe (Ifremer-Genavir) and all our colleagues who participated in the cruises. This work was funded by the French program (INSU-CNRS) "Action Marges". We are grateful to Silvia Ceramicola, Thierry Mulder and Jason Chaytor for their constructive comments and suggestions that improved the manuscript.

References

Chaytor JD, ten Brink US, Solow AR, Andrews BD (2009) Size distribution of submarine landslides along the U.S. Atlantic margin. Mar Geol 264:16–27

Cochonat P, Dodd L, Bourillet J-F, Savoye B (1993) Geotechnical characteristics and instability of submarine slope sediments, the Nice slope (N-W Mediterranean Sea). Mar Georesour Geotechnol 11:131–151

Dan G, Sultan N, Savoye B (2007) The 1979 Nice harbour catastrophe revisited: trigger mechanism inferred from geotechnical measurements and numerical modelling. Mar Geol 245:40–64

Garziglia S, Migeon S, Ducassou E, Loncke L, Mascle J (2008) Mass-transport deposits on the Rosetta province (NW Nile deep-sea turbidite system, Egyptian margin): characteristics, distribution, and potential causal processes. Mar Geol 250:180–198

Haflidason H, Lien R, Sejrup HP, Forsberg CF, Bryn P (2005) The dating and morphometry of the Storegga slide. Mar Petrol Geol 22:123–136

Klaucke I, Cochonat P (1999) Analysis of past seafloor failures on the continental slope off Nice (SE France). Geo-Mar Let 19:245–253

Klaucke I, Savoye B, Cochonat P (2000) Patterns and processes of sediment dispersal on the continental slope off Nice, SE France. Mar Geol 162:405–422

Leynaud D, Sultan N (2010) 3-D slope stability analysis: a probability approach applied to the Nice slope (SE France). Mar Geol 269:89–106

Locat J (2001) Instabilities along ocean margins: a geomorphological and geotechnical perspective. Mar Petrol Geol 18:503–512

Marr JG, Harff PA, Shanmugam G, Parker G (2001) Experiments on subaqueous sandy gravity flows: the role of clay and water content in flow dynamics and depositional structures. Geol Soc Am Bull 113:1377–1386

Mohrig D, Elverhoi A, Parker G (1999) Experiments on the relative mobility of muddy subaqueous and subaerial debris flows, and their capacity to remobilize antecedent deposits. Mar Geol 154:117–129

Mulder T, Cochonat P (1996) Classification of offshore mass movements. J Sediment Res 66:43–57

Mulder T, Tisot J-P, Cochonat P, Bourillet JF (1994) Regional assessment of mass failure events in the Baie des Anges, Mediterranean Sea. Mar Geol 122:29–45

Mulder T, Savoye B, Syvitski JPM, Parize O (1996) Des courants de turbidité hyperpycnaux dans la tête du canyon du Var ? Données hydrologiques et observations de terrain. Oceanologica Acta 20:607–626

Mulder T, Savoye B, Syvitski JPM (1997) Numerical modelling of a mid-sized gravity flow: the 1979 Nice turbidity current (dynamics, processes, sediment budget and seafloor impact). Sedimentology 44:305–326

Mulder T, Savoye B, Piper DJW, Syvitski JPM (1998) The Var submarine sedimentary system: understanding Holocene sediment delivery processes and their importance to the geological record. In: Stocker MS, Evans D, Cramp A (eds) Geological processes on continental margins: sedimentation, mass-wasting and stability, Geological society special publication. Geological Society, London, pp 146–166

Mulder T, Migeon S, Savoye B, Jouanneau J-M (2001) Twentieth century floods recorded in the deep Mediterranean sediments. Geology 29:1011–1014

Smith DP, Kvitek R, Iampietro PJ, Wong K (2007) Twenty-nine months of geomorphic change in upper Monterey Canyon (2002–2005). Mar Geol 236:79–94

Sultan N, Savoye B, Jouet G, Leynaud D, Cochonat P, Henry P, Stegmann S, Kopf A (2010) Investigation of a possible submarine landslide at the Var delta front (Nice continental slope, southeast France). Can Geotech J 47:486–496

Wessel P, Smith WHF (1998) New, improved version of the generic mapping tools released. EOS Trans 79:579

Chapter 41
Submarine Landslides, Gulf of Mexico Continental Slope: Insights into Transport Processes from Fabrics and Geotechnical Data

Jan H. Behrmann and Sandra Meissl

Abstract Ursa Basin on the Gulf of Mexico continental slope is a site of extremely fast sedimentation, building thick sequences of underconsolidated and overpressured muds and clays. Frequent sliding created mass transport deposits (MTD). In a study of strength, frictional behaviour, and fabrics of IODP Expedition 308 drillcores we find that mass transport is governed by very low friction coefficients and peak shear strengths of the sediments. The majority of the samples shows velocity weakening, enabling runaway instabilities in the sediment once deformation has started. While sediments at the bases of MTD seem to strengthen by the sliding, those below the bases remain weak, constraining a hazard for slide reactivation. Submarine sediment sliding leaves a strong and irreversible imprint, changing fabric geometries, and reducing the pore space. This is a transport phenomenon leading to expulsion of large amounts of pore fluids during sliding. MTD transport is probably as cohesive bodies, defining a considerable geohazard potential.

Keywords Landslide • Sediment • Strength • Fabric • Gulf of Mexico • Mass transport

41.1 Introduction

Continental slopes and rises around the world are marked with major landslide scars. Many are quite large, and submarine sliding is an important mechanism for transferring sedimentary material into the deep sea. When such poorly consolidated

J.H. Behrmann (✉) • S. Meissl
IFM-GEOMAR, Leibniz Institute for Marine Sciences, University of Kiel,
Wischhofstr. 1-3, 24148 Kiel, Germany
e-mail: jbehrmann@ifm-geomar.de

Y. Yamada et al. (eds.), *Submarine Mass Movements and Their Consequences*,
Advances in Natural and Technological Hazards Research 31,
DOI 10.1007/978-94-007-2162-3_41,

sediment masses move in the form of slumps, debris flows or mud flows, there are variable degrees of clay realignment by remoulding and shearing (e.g., Bohlke and Bennett 1980). Especially the clay fabric influences the geotechnical properties of the resulting deposits (e.g., Bennett et al. 1981). During mobilization sediments become fluidized through temporary fabric collapse, or by grains becoming buoyant during the ingress of externally derived fluids (Maltman and Bolton 2003). In fossil sediments weak preferred orientations of grains and thus a higher degree of consolidation can form during slumping, and the fabric is retained in the later diagenetic history (Paterson and Tobisch 1993). Thus, submarine mass transport is expected to leave a lasting imprint on the sediment fabrics, and will result in different geotechnical properties. Here we first assess the potential importance of velocity weakening (e.g., Scholz 1997) by analyzing the results of ring shear experiments. Second, we address the question whether slumped sediment has fabrics and structures different from sediment produced by fallout, and we attempt to quantify this difference. We build our study on the unique data set created during IODP Expedition 308 to the Ursa Basin (Flemings et al. 2006).

Along the northern margin of the Gulf of Mexico clastic sediments transported by the Mississippi river are the main input since the late Cenozoic. On the continental slope salt diapirism, associated faulting, and very rapid (cm per year; Flemings et al. 2006), mud-dominated sedimentation forms the hummocky bathymetry (Fig. 41.1a) with discrete basins and intervening ridges (Tripsanas et al. 2004; Sawyer et al. 2007), and leads to severe overpressure (Flemings et al. 2008).

To the west, Ursa Basin (Fig. 41.1b) is limited by Mars Ridge, a bathymetric high hosting the Mars Production Platform (Mars TLP; Fig. 41.1b), and to the east by a very large area of slope failure (McAdoo et al. 2000). In cross section (Fig. 41.1c) the basin fill is a wedge shaped sediment package, thickening to the West. There are four stratigraphic units; from old to young these are: the sandy/silty Blue Unit, the Ursa Canyon channel levee system, the Southwest Pass Canyon channel levee system, and a muddy hemipelagic cover unit (Sawyer et al. 2007). During IODP Expedition 308 (Flemings et al. 2006) three sites were drilled along the seismic profile shown in Fig. 41.1c. Sites U1324 and U1322 were cored continuously (Fig. 41.2). Upslope, Site U1324 shows lower overpressure (Flemings et al. 2008) and less MTD than Site U1322 (Fig. 41.2). Site U1322 has the thinnest sediment cover above the permeable Blue Unit. Over 50% of the section there are MTD, reflecting a history of intense and repetitive downslope mass transport by submarine sliding.

41.2 Geotechnical Data

We present and discuss three types of geotechnical data to assess the strength of the normally sedimented material, and that of material subsequently involved in submarine mass transport (the MTD).

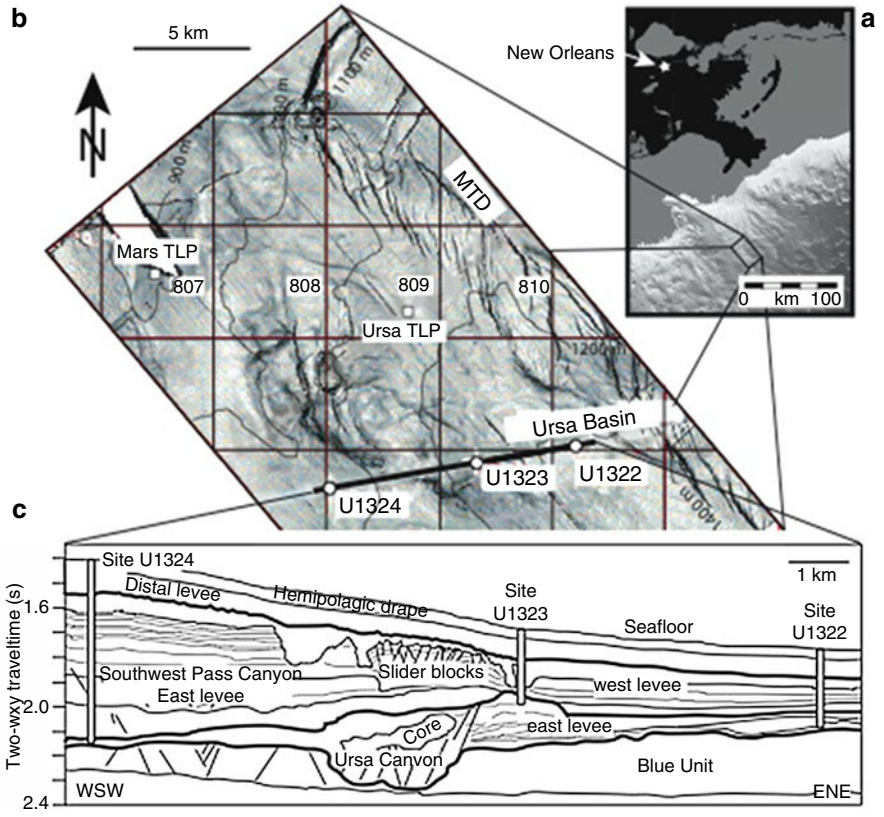

Fig. 41.1 (**a**) Bathymetric sketch map of the seafloor of the Northern Gulf of Mexico continental slope (**b**) Dip map of the seafloor at Ursa Basin (After Flemings et al. 2008) (**c**) WSW-ENE section along the Ursa Basin drilling transect interpreted from 3D reflection seismic data (After Flemings et al. 2008)

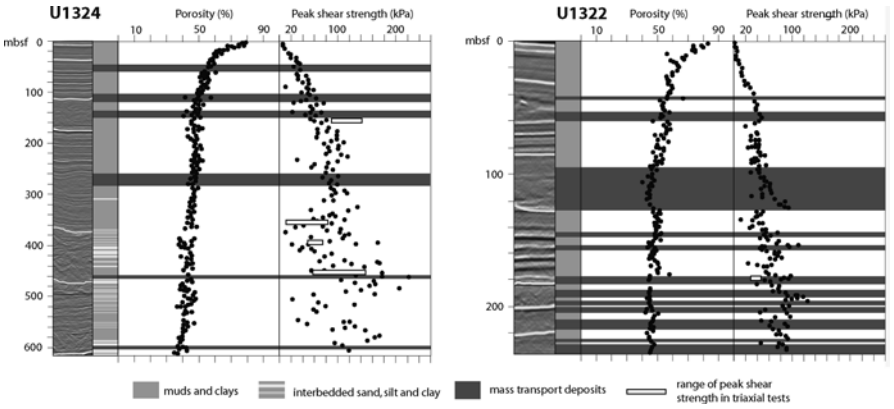

Fig. 41.2 Composite core log diagram of IODP Sites U1324 and U1322. From *left* to *right*: seismic strip chart, superposed sequence of normally sedimented muds, silts and sands (*light grey*) and sequences affected by submarine mass wasting (*dark grey*) (Data from: Flemings et al. (2006), Meissl et al. (2010)

The most comprehensive data set showing downhole variations in shear strength are the shipboard automated vane shear measurements (AVS; Flemings et al. 2006). The data are shown in Fig. 41.2, along with downhole porosity variations.

Obviously shear strength is a function of porosity, explaining the increase in shear strength with depth at Site U1324. At Site U1322 the bases of some MTD are markedly less porous and substantially stronger than the subjacent hemipelagics. This effect is most obvious at the base of the thick MTD near 130 mbsf, and suggests that important grain fabric and strength changes occurred in the sediment during the submarine slumping.

Five samples were subjected to consolidated-undrained (CU) triaxial tests with confining pressures ranging from 0.5 to 1.8 MPa. Results are documented in Meissl et al. (2010). Four samples come from Site U1324, and represent normally sedimented material from a variety of settings (Flemings et al. 2006). The samples were taken from depths between 154.4 and 406.7 mbsf. Peak shear stresses are very small (42–140 kPa), and corroborate the shipboard results (see logs in Fig. 41.2). An exception is the sample from 153.4 mbsf at Site U1324, which is the only one from a core catcher. Meissl et al. (2010) infer that additional consolidation may have been applied to the sample by the piston coring process. One sample comes from the base of a major mass transport deposit (MTD) at Site U1322. This material is weaker than the normally sedimented material from Site U1324, with peak stresses between 27 and 42 kPa.

Six samples were analyzed by ring shear testing (e.g., Lupini et al. 1981). Method description and data compilations for four of the samples are found in Meissl et al. (2010). Results from two additional samples were added for this paper. Ring shear testing is especially useful to simulate high-strain deformation during large movements on slump surfaces. Variation of shearing rates during the experiment allows the assessment of velocity effects (e.g., Scholz 1997). Velocity strengthening materials are considered as being capable of stable sliding, while velocity weakening allows unstable slip to develop, creating a mechanical runaway situation. Materials showing velocity weakening are especially prone to submarine sliding.

Measurements were performed with axial loads ranging from approximately 2 MPa to approximately 16 MPa at four rates of shear, starting with 0.014 or 0.005 mm/min, then accelerating to 0.18 mm/min, then to 1.8 mm/min, and finally slowing down to 0.005 mm/min (see also Meissl et al. 2010). The principal advantage of ring shear testing is the possibility to carry out isochoric simple shear to quasi-infinite strain. In nature this is the case along the failure plane of a landslide or in a fault zone. Shearing at different velocities can be used to determine the velocity dependence of friction, giving information about the weakening or strengthening capabilities of the tested material (e.g., Scholz 1997). The commonly used parameter to describe velocity weakening or strengthening in a sample is the difference (a-b) between the increase in the friction coefficient

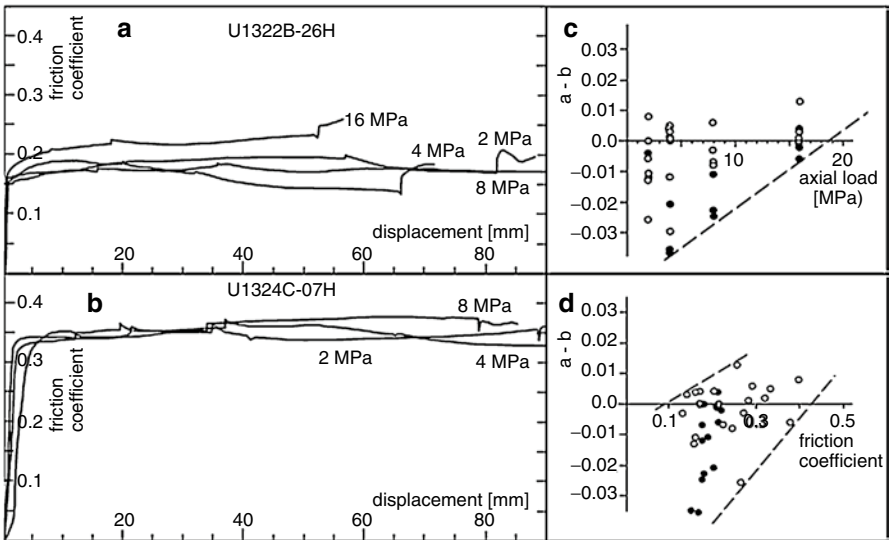

Fig. 41.3 Results of ring shear experiments. (**a**, **b**) friction coefficients plotted against displacement. (**a**) MTD, Site U1322, (**b**) Normally sedimented mud, Site U1324. (**c**) a-b plotted vs. axial load, all experiments. Negative a-b denotes velocity softening, positive values denote velocity hardening. (**d**) a-b plotted vs. friction coefficient

recorded when shearing is accelerated (spikes in Fig. 41.3a, b), and the following drop to a quasi-steady plateau value. If a-b is negative, then the material is said to show velocity weakening, if a-b is positive, the material shows velocity strengthening.

The two examples in Fig. 41.3a, b show the range of the friction coefficients (0.13–0.37) observed in the experiments. Sample U1322B-26H, a MTB, has low friction coefficients, and no systematic variations with varying axial load. Sample U1324C-07H, a normally sedimented mud, has the highest friction coefficients.

Values of a-b from all samples are given in Table 41.1. Almost all MTD have negative a-b values, suggesting dominant velocity weakening behaviour. Two of the normally sedimented muds show dominant velocity weakening, the other two are dominantly velocity hardening. When all a-b values are plotted against axial load (Fig. 41.3c) it is evident that the range of a-b decreases with increasing axial load, and absolute values are shifted towards the field of velocity hardening. If a-b values are plotted against friction coefficient (Fig. 41.3d), normally sedimented muds (open circles in Fig. 41.3c, d) have a wide range of friction coefficients, with the majority of high-friction materials showing velocity hardening. MTD materials (solid circles) almost all show low friction coefficients and velocity weakening. Implications of these observations will be discussed below.

Table 41.1 a–b Values and velocity effects in ring shear tests

Sample	Stress	a	b	a–b	Effect	a	b	a–b	Effect
1322B-026H	2 MPa	0.002	0.014	–0.012	Softening	0.004	0.011	–0.007	Softening
213.9 mbsf	4 MPa	0.002	0.038	–0.036	Softening	0.006	0.006	0.000	Constant
MTD	8 MPa	0.002	0.027	–0.025	Softening				
	16 MPa	0.007	0.009	–0.002	Softening	0.004	0.000	0.004	Hardening
1322D-003H	4 MPa	0.011	0.048	–0.037	Softening	0.009	0.030	–0.021	Softening
103 mbsf	8 MPa	0.007	0.030	–0.023	Softening	0.004	0.015	–0.011	Softening
MTD	16 MPa	0.005	0.011	–0.006	Softening	0.004	0.005	–0.001	Softening
1322B-017H-cc	2 MPa	0.009	0.001	0.008	Hardening	0.008	0.014	–0.006	Softening*
410.4 mbsf	4 MPa	0.009	0.004	0.005	Hardening	0.009	0.007	0.002	Hardening*
Fallout sediment	8 MPa	0.007	0.001	0.006	Hardening	0.006	0.009	–0.003	Softening
1324B-044H	2 MPa	0.003	0.014	–0.011	Softening				
353.7 mbsf	4 MPa	0.159	0.129	–0.030	Softening				
Fallout sediment	16 MPa	0.005	0.005	0.000	Constant				
1324B-050H	2 MPa	0.013	0.038	–0.025	Softening				
390 mbsf	4 MPa	0.004	0.016	–0.012	Softening	0.002	0.001	0.001	Hardening
Fallout sediment	8 MPa	0.003	0.010	–0.007	Softening	0.004	0.012	–0.008	Softening
	16 MPa	0.002	0.001	0.001	Hardening				
1324B-004H	2 MPa	0.013	0.026	–0.013	Softening	0.011	0.011	0.000	Constant
24 mbsf	4 MPa	0.015	0.012	0.003	Hardening	0.012	0.008	0.004	Hardening
Fallout sediment	16 MPa	0.013	0.000	0.013	Hardening	0.010	0.006	0.004	Hardening

Left: velocity change 0.18–1.8 mm/min, right: velocity change 0.014–0.18 or * 0.005–0.18 mm/min

41.3 Microstructures, Fabrics, and Strain

In the following we present pertinent observations regarding microstructures and fabrics. Normally sedimented muds in shallow cores show low degrees of shape preferred orientation (SPO) of clay minerals (Fig. 41.4a). Intensity of SPO increases with depth, and the example in Fig. 41.4b shows that not only clay SPO (cl in Fig. 41.4b) develops normal to the core axis with increasing porosity loss and compactional strain, but also preferred orientations of detrital minerals, mostly quartz (qz). Unique to MTD samples are microscopic slickensides (Fig. 41.4c).

Compactional strains can be computed from loss of porosity relative to initial porosity of the sediment, and from the intensity of the SPO fabric (see Kopf and Behrmann 1997). We have analyzed clay SPO by counting sheet silicate orientations within 10° sectors relative to the horizontal (i.e. bedding). Two examples are shown in Fig. 41.4d. Shortening normal to bedding is then computed using the March equations (Kopf and Behrmann 1997). Values up to 48% were measured in Site U1324 samples (Fig. 41.4e) and up to 56% in Site U1322 samples (Fig. 41.4f). Strain increases downhole. At Site U1322 strains in MTD (open squares in Fig. 41.4f) are up to 15% higher than those in the overlying normally sedimented muds (solid squares in Fig. 41.4e, f).

An independent method for estimation of uniaxial shortening is to refer measured porosity (Fig. 41.2) to an initial porosity (see Kopf and Behrmann 1997), which in our case was taken to be represented by average sediment porosity in the uppermost 10 m of core. Downhole strain curves computed from porosity using this

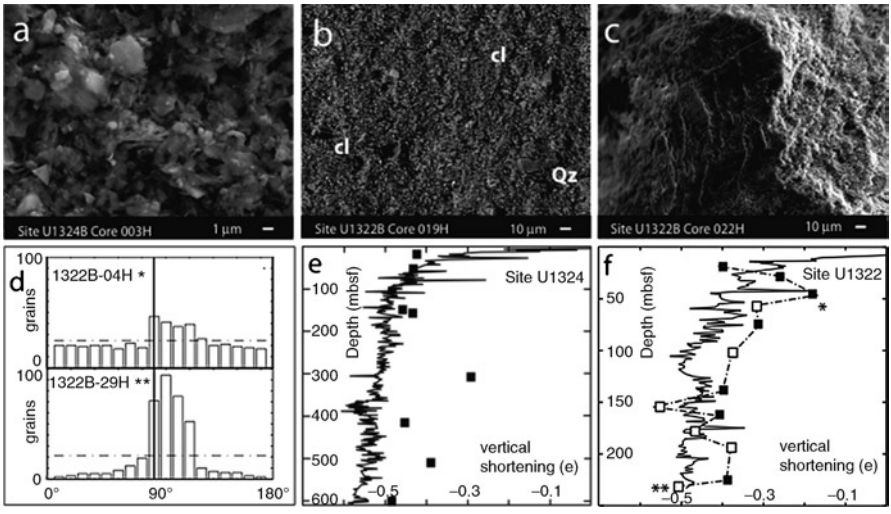

Fig. 41.4 Fabrics in Ursa Basin cores (**a**) clay fabric, (**b**) grain fabric (**a**) and (**b**) are backscattered electron SEM images (**c**) secondary electron image of micro-slickenside in MTD (**d**) data examples of clay SPO. Bedding orientation at 90° (**e**, **f**) downhole variations of vertical shortening. Asterisks: data examples shown in (**d**)

method are shown in Fig. 41.4e, f. Mostly, strains from SPO are somewhat lower than those calculated from porosity loss. We ascribe this to the fact that collapsing microfossil tests result in loss of porosity, but do not contribute to the attenuation of micropore space between clay aggregates when rotating into a sub-horizontal preferred orientation.

41.4 Discussion and Conclusion

We start the discussion by considering the downslope shear stresses acting on the sediments in the Ursa Basin. The basin floor along the profile (Fig. 41.1c) is inclined eastward by about 1.7°, resulting in a downhole increase of strata parallel traction for both drillsites as depicted in Fig. 41.5a, b. This is based on the mechanical model in Fig. 41.5c, discussed in similar form by Hampton et al. (1996). A plot of shear strength data from both Sites (uppermost 250 m) in Fig. 41.5a, b shows that in the upper 70 mbsf sediments can statically resist downslope movement to at least 3° inclination. Further downhole almost all Site U1324 data indicate slope stability up to 2° inclination. At Site U1322 the situation is different (Fig. 41.5b). Below 70 mbsf most deposits are strong enough to support slopes up to 5°, except for 5 week intervals with no samples that would resist downslope stresses from inclinations >3°. Stability against downslope sliding here is not given in samples left of the dotted line indicating the 1.7° downslope angle. The resulting "weak" intervals may be prone to slide reactivation even under current static conditions. While some MTD bases have experienced strengthening by sliding, the sediments below slide bases are weak (compare Figs. 41.2 and 41.5b). Slides are thus susceptible to reactivation,

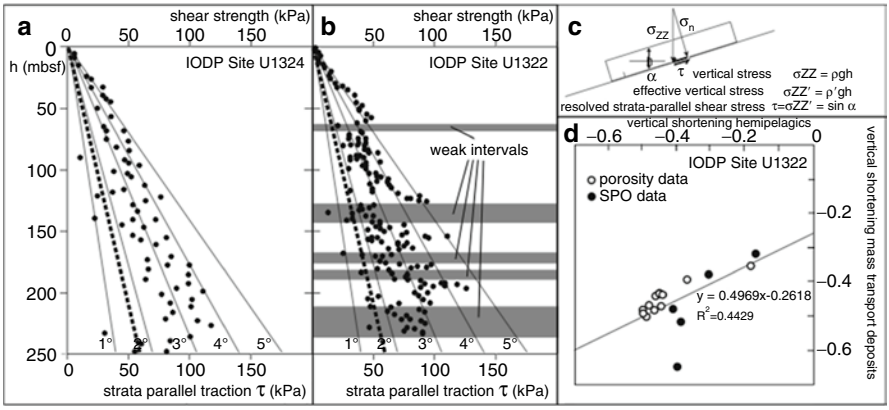

Fig. 41.5 (**a**, **b**) diagrams relating strata-parallel traction for slopes of different inclinations, and shear strength data. *Dotted line* is the average slope angle in the Ursa Basin (**c**) Stresses acting on a slice of thickness h on an infinite submarine slope. ρ = density, ρ' = immersed density, g = gravitational acceleration (**d**) strain in hemipelagic sediment plotted versus strain in subjacent mass transport deposits, Site U1322

including the possibility to form multi-stage, stacked deposits. As MTD materials react to stress build-up and accelerating deformation by velocity weakening, they may be critical for slide (re)activation.

Another interesting aspect is evident when average shortening from each MTD and the immediately overlying layer of hemipelagics for Site U1322 are compared (Fig. 41.5d). As neighboring units share a common post-slide compaction history, the slope of the correlation function depicts the contribution of additional shortening by the mass transport process. In the case of the uppermost pair of values this discrepancy is between 14% and 16%, indicating that the submarine sliding induces at least this amount of volume loss by additional compaction in the MTD. Downhole the discrepancy becomes smaller, an effect to be expected, as the hemipelagics and MTD couples are subjected to a common diagenetic history after deposition and – in the case of MTD – sliding. The additional strain in MTD is a transport phenomenon leading to expulsion of large amounts of pore fluids during sliding. This allows the conclusion that MTD transport is probably as a cohesive body akin to an avalanche of wet snow on land. In summary we state that the young sediments in the Ursa Basin are extremely weak. MTD materials and some of the normally sedimented muds are capable of unstable sliding and their geohazard potential is thus considerable. Sliding induces additional strain, leaving a strong and irreversible imprint on the sediment fabric

Acknowledgements Reviewed by A. Camerlenghi and Y. Yamamoto. This paper summarizes post-cruise research of IODP Expedition 308. We thank the Master, all personnel, and scientists aboard R/V JOIDES RESOLUTION, and especially Michael Stipp, for input and assistance. This work was funded by DFG Grant BE 1041/20 to JHB.

References

Bennett RH, Bryant WR, Keller GH (1981) Clay fabrics of selected submarine sediment: fundamental properties and models. J Sediment Petrol 51:217–232

Bohlke BM, Bennett RH (1980) Mississippi prodelta crusts: a clay fabric and geotechnical analysis. Mar Geotechnol 4:55–82

Flemings PB, Behrmann JH, John, CM, the Expedition 308 Scientists (2006) Proceedings of the IODP 308. Integrated Ocean Drilling Program Management International, Inc., College Station. doi: 10.2204/iodp.proc.308.101.2206

Flemings PB, Long H, Dugan B, Germaine J, John CM, Behrmann JH, Sawyer D (2008) Erratum to "Pore pressure penetrometers document high overpressure near the seafloor where multiple submarine landslides have occurred on the continental slope, offshore Louisiana, Gulf of Mexico". Earth Planet Sci Lett 274:269–283

Hampton MA, Lee HJ, Locat J (1996) Submarine landslides. Rev Geophys 34:33–59

Kopf A, Behrmann JH (1997) Fabric evolution and mechanisms of diagenesis in fine grained sediments from the Kita-Yamato trough, Japan Sea. J Sediment Res 67:604–614

Lupini JF, Skinner AE, Vaughan PR (1981) The drained residual strength of cohesive soils. Geotechnique 31:181–213

Maltman AJ, Bolton A (2003) How sediments become mobilized. In: van Rensbergen P, Hillis RR, Maltman AJ, Morley CK (eds) Subsurface sediment mobilization, Geological society special publications 216. The Geological Society, London, pp 9–20

McAdoo BG, Pratson LF, Orange DL (2000) Submarine landslide geomorphology, US continental slope. Mar Geol 169:103–106

Meissl S, Behrmann J, Behrmann JH (2010) Data report: preliminary assessment of Pleistocene sediment strength in the Ursa Basin (Gulf of Mexico continental slope) from triaxial and ring shear test data. In: Proceedings of the IODP, 308, IODP Management International, Inc., College Station. doi: 10.2204/iodp.proc.308.211.2010

Paterson SR, Tobisch OT (1993) Pre-lithification structures, deformation mechanisms, and fabric ellipsoids in slumped turbidites from the Pigeon Point Formation, California. Tectonophysics 222:135–149

Sawyer DE, Flemings PB, Shipp RC, Winker CD (2007) Seismic geomorphology, lithology, and evolution of the late Pleistocene Mars-Ursa turbidite region, Mississippi Canyon area, northern Gulf of Mexico. AAPG Bull 91:215–234

Scholz CH (1997) Earthquakes and friction laws. Nature 391:37–42

Tripsanas EK, Bryant WR, Doyle EH (2004) Slope-instability processes caused by salt movements in a complex deep-water environment, Bryant Canyon area, northwest Gulf of Mexico. AAPG Bull 88:801–823

Part VI
Landslide Generated Tsunamis

Chapter 42
Tsunamis Generated by Submarine Landslides

Kenji Satake

Abstract Submarine landslides can generate tsunamis and cause coastal hazard. Because the horizontal scale of submarine landslide is comparable to water depth and much smaller than the scale of earthquake fault area, the tsunami characteristics is very different from earthquake-generated tsunami which is usually approximated as a shallow-water wave. Several approaches have been proposed to model the tsunami generation by submarine landslides, and they can be grouped into: landslide as fluid motion, rigid-body motion, and initial or kinematic water surface profiles. Two examples of tsunamis from submarine landslides are described. The first one is the 1998 Papua New Guinea tsunami. While the tsunami records at far-field, around Japan, were basically reproduced by earthquake fault motion, locally large tsunami heights around Sissano Lagoon needed additional source such as submarine slumping. The 1741 Oshima-oshima tsunami in Japan Sea was modeled by a submarine landslide associated with sector collapse of the volcano. While the subaerial landslide size and volume were not enough to produce the tsunami that caused damage as far as Korean coast, tsunami simulation from the recently mapped submarine landslide could reproduce the observed tsunami heights.

Keywords Submarine landslide • Tsunami • Numerical modeling • 1998 Papua New Guinea tsunami • 1771 Oshima-oshima tsunami

K. Satake (✉)
Earthquake Research Institute, The University of Tokyo, 1-1-1 Yayoi,
Bunkyo-ku, Tokyo 113-0032, Japan
e-mail: satake@eri.u-tokyo.ac.jp

Y. Yamada et al. (eds.), *Submarine Mass Movements and Their Consequences*,
Advances in Natural and Technological Hazards Research 31,
DOI 10.1007/978-94-007-2162-3_42, © Springer Science+Business Media B.V. 2012

42.1 Introduction

Tsunamis are generated by various submarine processes such as earthquakes, volcanic eruptions or landslides, and can cause damage across the ocean. For example, the 2004 Indian Ocean tsunami, generated by the giant Sumatra-Andaman earthquake (M 9.2) caused more than 230,000 casualties in more than ten countries around the Indian Ocean. Tsunamis from the 1960 (M 9.5) and 2010 (M 8.8) Chilean earthquakes propagated across the Pacific Ocean and caused damage as far as in Japan, in addition to the nearby Chilean coast. The recent 2011 Tohoku earthquake (M 9.0) caused the worst tsunami disaster in Japanese history.

While most tsunamis are generated by great earthquakes, tsunamis and their damage from submarine landslides may be significant. In this paper, difference between the earthquake and landslide generated tsunamis are first described with basic hydrodynamics, and several methods to model landslide tsunami generation are reviewed. Then, two case studies are described: the 1998 Papua New Guinea tsunami and the 1741 Oshima-oshima tsunami.

42.2 Hydrodynamics of Tsunamis

The equation of motion for water waves can be given as (e.g., Johnson 1997; Pond and Pickard 1978):

$$\frac{\partial V}{\partial t} + V \cdot \nabla V = -g - \frac{1}{\rho} \nabla p \tag{42.1}$$

where $\boldsymbol{V}$ is the velocity vector, $\boldsymbol{g}$ is the gravitational acceleration, ρ and p are water density and pressure, respectively. The above equation of motion indicates that the water surface displacement and gravity are the acting forces. The phase velocity c of gravity waves is given as:

$$c = \left(\frac{g}{k} \tanh kd \right)^{\frac{1}{2}} = \left(\frac{g\lambda}{2\pi} \tanh \frac{2\pi d}{\lambda} \right)^{\frac{1}{2}} \tag{42.2}$$

where k is wave number, λ is wavelength and d is water depth. Equation 42.2 shows that the wavelength and water depth are the two important parameters that control the propagation.

When the horizontal scale of motion, or the wavelength, λ, is much larger than the water depth ($\lambda \gg d$), the vertical acceleration of water is negligible compared to the gravity. This means that the horizontal motion of water mass is almost uniform from the bottom to the surface. Such a wave is called a shallow-water wave or a long wave (Fig. 42.1b). In this case, (42.2) becomes $c = \sqrt{gd}$, i.e., the phase velocity is a function of water depth only. For tsunamis, typical ocean depth is about 4–5 km for the Pacific Ocean and a large earthquake has a source area of several

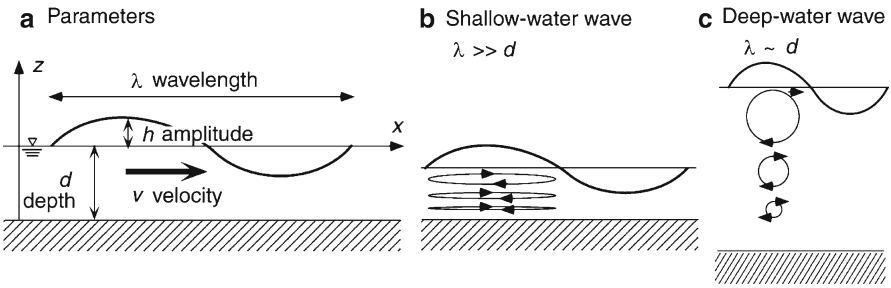

Fig. 42.1 (**a**) Parameters for the water waves (**b**) Shallow-water, or long-wave, approximation (**c**) Deep-water, or surface-wave, approximation

tens to hundreds of km. Hence the shallow-water approximation is appropriate for earthquake-generated tsunamis, even though the actual ocean depth is deep.

When, on the other hand, the wavelength is comparable to water depth, Eq. 42.2 becomes $c = \sqrt{\frac{g}{k}} = \sqrt{\frac{g\lambda}{2\pi}}$, i.e., the velocity depends on wavelength. Such a wave is called a deep-ocean wave or a short wave (Fig. 42.1c). The longer wavelength component of waves propagates faster than the shorter wavelength component, hence the wave shows dispersion, and cannot reach a long distance with the initial profile. In case of landslide-generated waves, the wavelength (typically a few km) could be comparable to the water depth, hence it may be approximated as deep-water waves.

It is important to note that "shallow" or "deep" water does not refer to actual water depth, but the relative depth compared with horizontal scale of the source. For the studies of tsunami sources, shallow-water waves are usually assumed. Once waves are dispersed, they do not carry initial information on the source, hence it is difficult to use them for the study of tsunami source.

42.3 Modeling Landslide-Generated Tsunamis

Tsunamis from submarine landslides have been actively studied since the 1990s and several special issues on observations or modeling have been published (Keating et al. 2000; Bardet et al. 2003; Yalçıner et al. 2003; Tappin 2004). For modeling tsunami generation by submarine landslides, various approaches, such as theoretical studies (e.g., Pelinovsky 2003) or physical experiments in tanks (e.g., Watts 2000) have been carried out. In this section, numerical methods to model landslide tsunami generation are briefly summarized.

Tsunami generation process by submarine landslide sources has been modeled in many ways. These can be grouped into four categories: viscous fluid model, rigid-body, or block, model, initial static water surface profile, and moving kinematic water surface profile (Fig. 42.2).

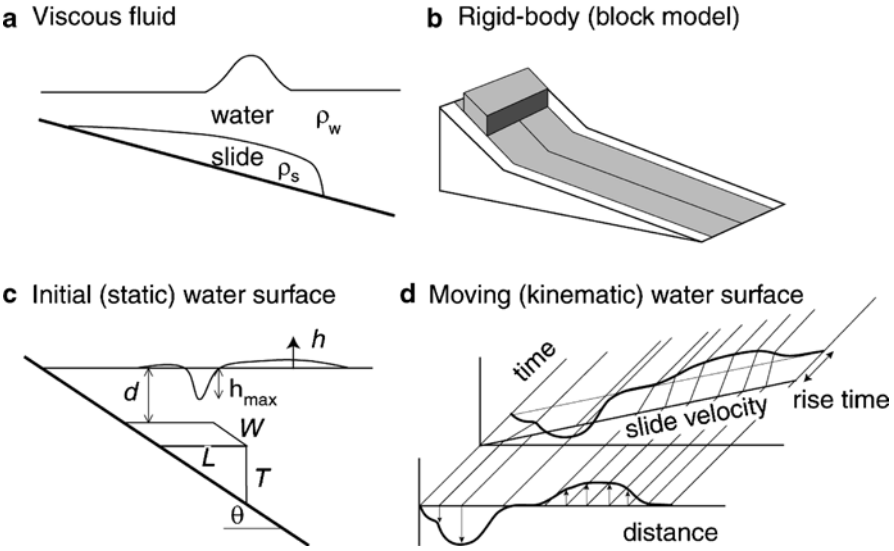

Fig. 42.2 Four different approaches for tsunami generation from submarine landslides

In the dynamic fluid flow approach (Fig. 42.2a), landslide is treated as fluid and its evolution is calculated simultaneously with tsunami generation. Jiang and LeBlond (1994) treated a landslide as incompressible viscous flow and sea water as inviscid flow, and formulated the multi-phase fluid dynamics. Rzadkiewicz et al. (1997) modeled landslide and water as viscoplastic fluid and dispersive ideal fluid, respectively, and compared the results with analytical solutions and physical experiments. Fine et al. (2003) modeled the subaerial and submarine slides as viscous flows, and compared the results with rigid-body model. They found that the viscous flow and rigid-body motion produce different largest waves for the submarine landslides. Heinrich et al. (2000), Titov and Gonzalez (2001) and Imamura and Hashi (2003) applied a similar method to the submarine landslide of the 1998 Papua New Guinea tsunami. Kawamata et al. (2005) modeled the submarine landslide of the 1741 Oshima-oshima tsunami by two layer model.

In the rigid-body approach (Fig. 42.2b), temporal change of water height due to progress of submarine landslide is prescribed and used to compute tsunami propagation. Harbitz (1992) assumed a box-shaped slide for the Storegga slide, Ward (2001) used a chain of rigid boxes to model the Storegga and other submarine slides. Tinti et al. (1997) introduced a block model of landslide and simulate the landslide motion, and Tinti et al. (2005) applied this method for the 2002 tsunami generated around Stromboli volcano.

In the static approach (Fig. 42.2c), an initial water surface profile due to submarine landslide is assumed. Grilli and Watts (2005), based on the results of physical and numerical experiments, introduced a parametric initial profile. Synolakis et al. (2002) and Satake and Tanioka (2003) used the same approach to model the 1998 Papua New Guinea tsunami. This approach, however, does not consider the landslide propagation and ignore the kinematic energy from the submarine landslide.

The last approach (Fig. 42.2d) assumes the moving water surface profile as the initial motion of tsunami propagation. Todorovska et al. (2003) introduced five kinematic models to represent submarine landslides and slumps. Satake et al. (2002) introduced a simple kinematic landslide model on the basis of bathymetry change and applied it to the Hawaiian landslides. These studies found that the slide velocity is one of the important parameters to control the tsunami amplitudes. The same procedure was also applied to the 1741 Oshima–oshima slide and shown in Sect 42.5.

42.4 The 1998 Papua New Guinea Tsunami

The 1998 Papua New Guinea tsunami occurred following an earthquake (M 7.1) on July 17. The tsunami heights were as large as 15 m around Sissano Lagoon on the northern coast of New Guinea Island near the epicenter, and the total casualties were reported to be more than 2,000. The large tsunami (>5 m), however, was limited to a small region (~40 km) along the coast (Kawata et al. 1999). The origin of this unusual tsunami has been studied by many researchers (Matsuyama et al. 1999; Geist 2000; Heinrich et al. 2000; Titov and Gonzalez 2001; Synolakis et al. 2002; Satake and Tanioka 2003).

The tsunami was also recorded at six tide gauges and two ocean-bottom pressure gauges around Japan. Their amplitudes are <10 cm. Satake and Tanioka (2003) modeled these tsunami waveforms and found that fault models (either low-angle fault expected from an interplate earthquake or high-angle fault suggesting an intraplate earthquake) with 40 km fault length, as expected from an M ~ 7 earthquake, can reproduce the amplitudes and waveforms observed around Japan.

However, they also found that local tsunami heights around Sissano Lagoon computed from low-angle or high-angle fault models were much smaller than the observed tsunami heights. In order to reproduce the large tsunami, small additional source such as splay fault or submarine landslide was needed. As an example, a slump model with a volume of ~1 km^3, in addition to the low-angle fault model could roughly reproduce the large tsunami and its local concentration around Sissano Lagoon (Fig. 42.3b). Synolakis et al. (2002) modeled the slump source with a volume of 4 km^3, 4.5 km long, 4 km wide, 600 m thick, and reproduced the coastal tsunami heights. Heinrich et al. (2000) also modeled a submarine slump of 4 km^3 volume and slide distance of 5 km. Titov and Gonzalez (2001) modeled a slump with larger area (10 km × 10 km) but smaller volume (<1 km^3). Imamura and Hashi (2003) concluded that a slump source with 4–8 km^3 can reproduce the coastal tsunami heights.

While many studies could "successfully" reproduce the coastal tsunami heights from submarine slump models, their locations and volumes are variable, due to lack of conclusive submarine evidence. There are several candidate features of submarine slumps, but the dates or volume were not constrained from the submarine geological surveys such as bathymetric/side-scan sonar mapping, seismic reflection surveys or dive surveys by using Remotely Operated Vehicle (Synolakis et al. 2002).

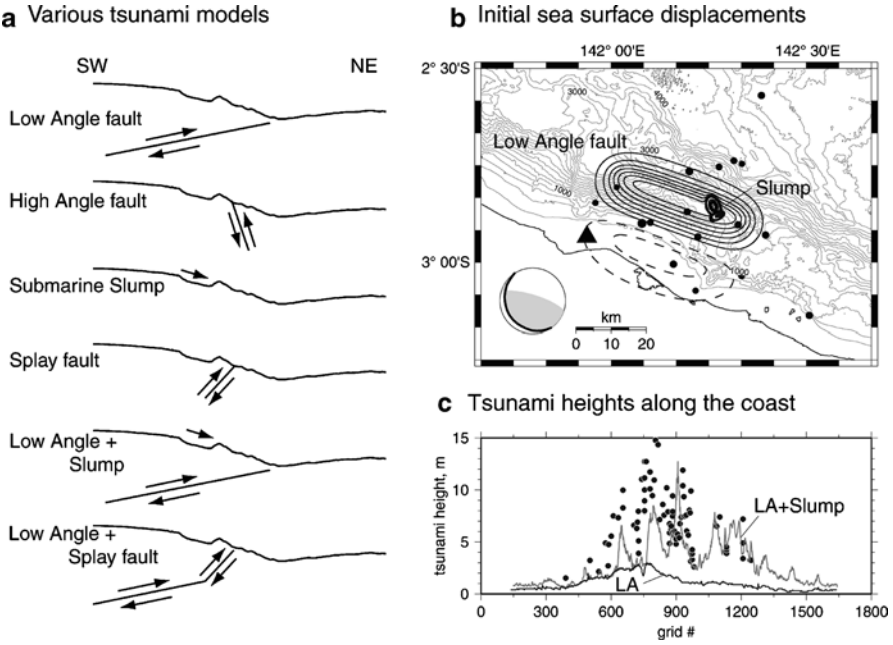

Fig. 42.3 (**a**) Various tsunami source models (**b**) Initial sea surface displacements in the source region of the 1998 Papua New Guinea earthquake. *Solid triangle* and *solid circles* indicate epicenters of the mainshock and aftershocks, respectively (**c**) Tsunami heights measured and computed along the coast shown in (**b**) Based on Satake and Tanioka (2003)

Okal and Synolakis (2004) fit the run-up height distribution $\zeta(y)$ along a beach (in the y direction) by the following function:

$$\zeta(y) = \frac{b}{\left[(y-c)/a\right]^2 + 1} \tag{42.3}$$

where parameters a, b, and c are estimated from the observed data. They show that $I_2 = b/a$, the aspect ratio of maximum run-up heights to extent of run-up along beach, can be used as a discriminant of the nature of tsunami source, either dislocation (earthquake fault) or landslide source. Seismic dislocation sources have I_2 smaller than 10^{-4} whereas a landslide source has a larger value.

42.5 The 1741 Oshima-Oshima Tsunami

In 1741, a very destructive tsunami was originated from around Oshima-oshima, a small volcanic island southwest off Hokkaido which became active in the same year, and caused significant damage on the coasts around Japan Sea including about

2,000 casualties (Satake 2007). On the Hokkaido coast, the maximum height was estimated as 13 m, although larger heights were estimated from less reliable legends. On the Tsugaru coast of northern Honshu, the tsunami heights were estimated as 4–6 m. The tsunami damage was also recorded in the western Japan and on the east coast of Korean Peninsula, from which the tsunami heights were estimated as 1–4 m (8 m based on legends).

The generation mechanism of the 1741 tsunami has been controversial. The tsunami source is located between the recent tsunamigenic earthquakes, but there is no historical records documenting earthquake ground motion. In contrast, the records indicate volcanic activity of Oshima-oshima including a large-scale sector collapse, although the volume change associated with the subaerial landslide, 0.4 km^3, was too small to explain the observed tsunami heights (Aida 1984).

Detailed swath bathymetry surveys have been conducted around Oshima-oshima and a high-resolution map shows two characteristic features of a volcano collapse landslide: an open sector collapse with steep lateral walls extending about 5 km from the summit crater, and an area of hummocky terrain on the lower slope of the island. Based on these data, Satake and Kato (2001) reconstructed the subaerial and submarine sector collapse and debris avalanche of the 1741 eruption. The total volume of the collapse is estimated as 2.4 km^3. The total volume of debris deposits, which extends as far as 16 km from the island, is 2.5 km^3 and roughly equals to the missing slide volume.

Satake (2007) applied the kinematic slide model to compute tsunami heights on the Hokkaido, Tsugaru and western Honshu and Korean coasts (Fig. 42.4c). He could reproduce the tsunami heights from a model with landslide velocity of 40 m/s and rise time of 2 min. The slide velocity is similar to the tsunami phase velocity in the source area, causing the coupling of tsunami and submarine landslide, and making large tsunami heights. Kawamata et al. (2005) could also reproduce the tsunami heights by adjusting landslide parameters of two-layer fluid model.

42.6 Conclusions

1. Tsunamis generated by submarine landslides are different from earthquake generated tsunamis, because the source length and water depth are typically similar. Such a wave may be treated a deep-water wave, which shows dispersive character and cannot propagate a long distance with the initial profile.
2. Generation process of submarine landslide has been modeled in various ways. They can be grouped into: viscous flows, rigid-body (or block model), initial static water profile, and moving kinetic water profiles.
3. The 1998 Papua New Guinea tsunami needs secondary source near the Sissano coast, in order to reproduce unusual tsunami heights and concentration. Tsunami modelings from submarine slumps have reproduced the coastal tsunami heights, but the location and volume of the slump are variable from model to model.

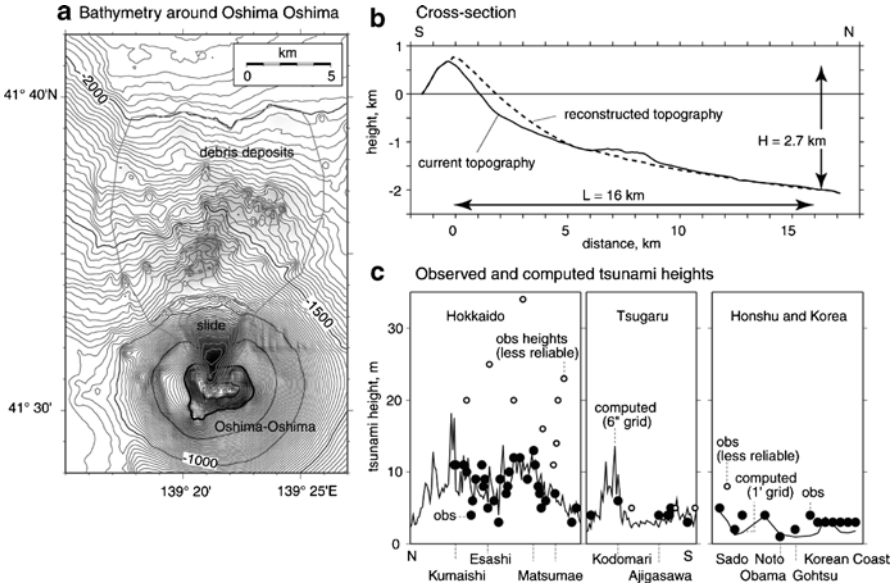

Fig. 42.4 (**a**) Bathymetry and its change around Oshima-oshima volcano (**b**) North-south cross section of the current and reconstructed bathymetry, from Satake and Kato (2001) (**c**) The tsunami heights on Hokkaido, Tsugaru, and Honshu and Korean coasts, compared with the simulation from submarine landslide (Satake 2007)

4. The 1741 Oshima–oshima tsunami in Japan Sea was generated by submarine landslide associated with the sector collapse of the volcano, which extended ~5 km from the volcano and debris were brought by ~15 km. Numerical models from this landslide could reproduce the tsunami heights around the Japan Sea.

Acknowledgments The author thanks to reviewers Drs. Stefano Tinti and Sasha Rabinovich, and Editor Dr. Yasuhiro Yamada for their careful reviews of the manuscript.

References

Aida I (1984) An estimation of tsunamis generated by volcanic eruptions – the 1741 eruption of Oshima-Ohshima, Hokkaido- (in Japanese with English abstract). Bull Earthq Res Inst Univ Tokyo 59:519–531

Bardet S-P, Synolakis CE, Davies HL, Imamura F, Okal EA (2003) Landslide tsunamis: recent findings and research directions. Pure Appl Geophys 160:1793–2221 (Special issue)

Fine IV, Rabinovich AB, Thomson RE, Kulikov EA (2003) Numerical modeling of tsunami generation by submarine and subaerial landslides. In: Yalçıner AC, Pelinovsky E, Okal E, Synolakis CE (eds) Submarine landslides and tsunamis. Kluwer, Dordrecht/Boston, pp 69–88

Geist E (2000) Origin of the 17 July 1998 Papua New Guinea tsunami: earthquake or landslide? Seism Res Lett 71:344–351

Grilli ST, Watts P (2005) Tsunami generation by submarine mass failure I: modeling, experimental validation, and sensitivity analyses. J Waterway Port Coast Ocean Eng 131:283–297
Harbitz CB (1992) Model simulations of tsunamis generated by the Storegga slides. Mar Geol 105:1–21
Heinrich P, Piatanesi A, Okal E, Hebert H (2000) Near-field modeling numerical modeling of the July 17, 1998 tsunami in Papua New Guinea. Geophys Res Lett 27:2027–2030
Imamura F, Hashi K (2003) Re-examination of the source mechanism of the 1998 Papua New Guinea earthquake and tsunami. Pure Appl Geophys 160:2071–2086
Jiang L, LeBlond P (1994) Three-dimensional modeling of tsunami generation due to a submarine mudslide. J Phys Ocean 24:559–572
Johnson RS (1997) A modern introduction to the mathematical theory of water waves. Cambridge University Press, Cambridge/New York, 447 pp
Kawamata K, Takaoka K, Ban K, Imamura F, Yamaki S, Kobayashi E (2005) Model of tsunami generation by collapse of volcanic eruption: the 1741 Oshima-Oshima tsunami. In: Satake K (ed) Tsunamis: case studies and recent developments. Springer, Dordrecht, pp 79–96
Kawata Y, Benson BC, Borrero JC, Borrero JL, Davies HL, Lange WPD, Imamura F, Letz H, Nott J, Synolakis CE (1999) Tsunami in Papua New Guinea was as intense as first thought. Eos Trans Am Geophys Union 80:101–105
Keating BH, Waythomas CF, Dawson AG (2000) Landslide and tsunamis. Pure Appl Geophys 157:871–1313 (Special issue)
Matsuyama M, Walsh JP, Yeh H (1999) The effect of bathymetry on tsunami characteristics at Sisano Lagoon, Papua New Guinea. Geophys Res Lett 26:3513–3516
Okal EA, Synolakis CE (2004) Source discriminants for near-field tsunamis. Geophys J Int 158:899–912
Pelinovsky E (2003) Analytical models of tsunami generation by submarine landslides. In: Yalçıner AC, Pelinovsky E, Okal E, Synolakis CE (eds) Submarine landslides and tsunamis. Kluwer, Dordrecht/Boston, pp 111–128
Pond S, Pickard GL (1978) Introductory dynamical oceanography. Pergamon, Oxford/New York, 329 pp
Rzadkiewicz SA, Mariotti C, Heinrich P (1997) Numerical simulation of submarine landslides and their hydraulic effects. J Waterway Port Coast Ocean Eng 123:149–157
Satake K (2007) Volcanic origin of the 1741 Oshima-Oshima tsunami in the Japan Sea. Earth Planet Space 59:381–390
Satake K, Kato Y (2001) The 1741 Oshima-Oshima eruption: extent and volume of submarine debris avalanche. Geophys Res Lett 28:427–430
Satake K, Tanioka Y (2003) The July 1998 Papua New Guinea earthquake: mechanism and quantification of unusual tsunami generation. Pure Appl Geophys 160:2087–2118
Satake K, Smith JR, Shinozaki K (2002) Three-dimensional reconstruction and tsunami model of the Nuuanu and Wailau landslides, Hawaii. In: Takahashi E, Lipman P, Garcia M, Naka J, Aramaki S (eds) Hawaiian volcanoes: deep underwater perspectives, vol 128. American Geophysical Union, Washington, DC, pp 333–346
Synolakis CE, Bardet JP, Borrero JC, Davies HL, Okal EA, Silver EA, Sweet S, Tappin DR (2002) The slump origin of the 1998 Papua New Guinea tsunami. Proc R Soc Lond Ser A 458:763–778
Tappin D (2004) Submarine-slump-generated tsunamis. Mar Geol 203:199–380 (Special issue)
Tinti S, Bortolucci E, Vannini C (1997) A block-based theoretical model suited to gravitational sliding. Nat Hazard 16:1–28
Tinti S, Maramai A, Armigliato A, Graziani L, Manucci A, Pagnoni G, Zaniboni F (2005) Observations of physical effects from tsunamis of December 30, 2002 at Stromboli volcano, southern Italy. Bull Volcanol 68:450–561
Titov VV, Gonzalez FI (2001) Numerical study of the source of the July 17, 1998 PNG tsunami. In: Hebensreit GT (ed) Tsunami research at the end of a critical decade. Kluwer, Dordrecht/Boston, pp 197–207

Todorovska MI, Hayir A, Trifunac MD (2003) Near-field amplitudes of tsunami from submarine slumps and slides. In: Yalçıner AC, Pelinovsky E, Okal E, Synolakis CE (eds) Submarine landslides and tsunamis. Kluwer, Dordrecht/Boston, pp 59–68

Ward SN (2001) Landslide tsunami. J Geophys Res 106:11201–11215

Watts P (2000) Tsunami features of solid block underwater landslides. J Waterway Port Coast Ocean Eng 126:144–152

Yalçıner AC, Pelinovsky E, Okal E, Synolakis CE (2003) Submarine landslides and tsunamis, vol 21, NATO science series IV. Kluwer, Dordrecht/Boston, 328 pp

Chapter 43
Micro-bathymetric Evidence for the Effect of Submarine Mass Movement on Tsunami Generation During the 2009 Suruga Bay Earthquake, Japan

Toshitaka Baba, Hiroyuki Matsumoto, Kazuhiko Kashiwase, Tadahiro Hyakudome, Yoshiyuki Kaneda, and Mamoru Sano

Abstract A moderate earthquake (Mw 6.4) caused a submarine mass movement in Suruga Bay, Japan on 11th August, 2009. The earthquake was also accompanied by a tsunami, which was observed at various observatories around Suruga Bay. A micro-bathymetric map was obtained from an autonomous underwater vehicle (AUV) survey of *Urashima* in the area where the submarine mass movement occurred. The *Urashima* cruised close to the seafloor and collected very high resolution bathymetric data as a raster graphic image with pixels arranged in a 1 m by 1 m square grid. The 3D seafloor image obtained clearly shows an escarpment (450 m wide and 10–15 m deep) approximately 5 km off the coast. Bedforms which were considered to have been formed due to earthquake-induced turbidity currents, spread wide in the survey area. The bedforms appear at about 20–30 m interval, and are lower than 1 m in height. A numerical simulation of the tsunami assuming that the fault motion and submarine mass movement occurred simultaneously provided a better match with the tsunami observation records at Yaizu tidal station and other stations than a simulation based on fault motion alone.

Keywords Submarine mass movement • Tsunami • AUV • Micro-bathymetry

T. Baba (✉) • H. Matsumoto • K. Kashiwase • Y. Kaneda
Earthquake and Tsunami Research Project for Disaster Prevention,
Japan Agency for Marine-Earth Science and Technology, 2-15 Natsushima-cho,
Yokosuka 237-0061, Japan
e-mail: babat@jamstec.go.jp

T. Hyakudome
Marine Technology Center, Japan Agency for Marine-Earth Science and Technology,
2-15 Natsushima-cho, Yokosuka 237-0061, Japan

M. Sano
Nippon Marine Enterprises, Ltd, Nissei Yokosuka Center Building (8th Floor),
14-1, Ogawa-cho, Yokosuka 238-0004, Japan

Y. Yamada et al. (eds.), *Submarine Mass Movements and Their Consequences*,
Advances in Natural and Technological Hazards Research 31,
DOI 10.1007/978-94-007-2162-3_43,

43.1 Introduction

A submarine earthquake of moment magnitude 6.4 occurred on 11th August 2009 under Suruga Bay, Japan, (hereafter, the 2009 Suruga Bay earthquake, Fig. 43.1). This area, where the Philippine Sea Plate subducts beneath the Eurasian Plate, had been highlighted as an area of specific earthquake threat as described in the law enacted in 1978. The hypocentral depth of the earthquake was estimated to be 23 km, originating in a right-lateral strike-slip fault with the compression axes oriented in a north–south direction (Japan Meteorological Agency 2009; Aoi et al. 2010). The earthquake was inferred to be an intraplate event within the Philippine Sea plate beneath the Eurasian plate. The earthquake was accompanied by a tsunami that was recorded at various stations around Suruga Bay; the instruments included tide gauges, ocean-bottom pressure gauges (Iwase et al. 2003), ultra-sonic wave meters of the Nationwide Ocean Wave Information Network for Ports and Harbors (NOWPHAS) (Nagai 2002), and a GPS tsunami meter (Kato et al. 2005). The maximum recorded positive tsunami amplitude was about 30 cm with about a 60 cm drawback at the Yaizu tidal gauge station (Japan Meteorological Agency 2009). Several fault models for the earthquake were developed from teleseismic data (Yamanaka 2009), strong-motion data (Aoi et al. 2010), and crustal deformation data (Geospatial Information

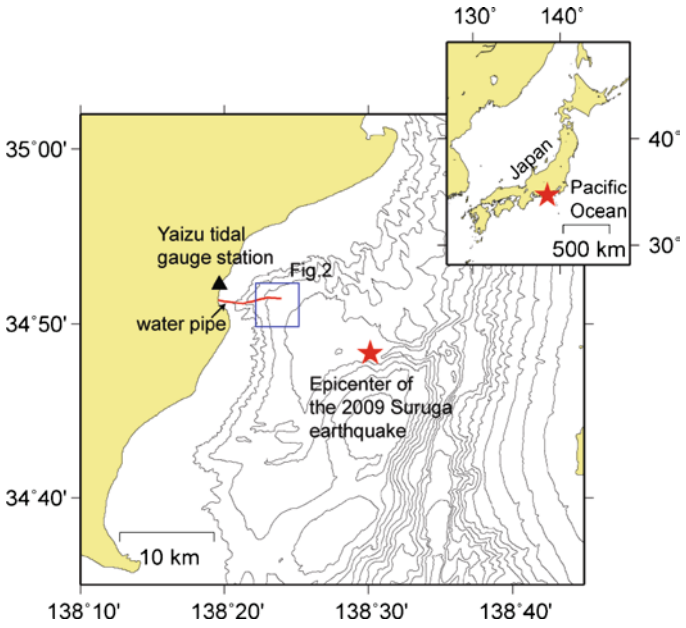

Fig. 43.1 Regional location and bathymetric map of the study area. Bathymetric contour interval is 200 m. The *red line* indicates the original position of the Suruga deep-sea water plant water pipe that was damaged and moved by the earthquake. Location of the high-resolution bathymetric map (Fig. 43.2) is also shown

Authority of Japan 2009) but none of these models could accurately simulate the tsunami waveform observed at the tidal gauge station in Yaizu. This implies that faulting movement alone could not have caused the 2009 Suruga Bay tsunami.

During the 2009 Suruga Bay earthquake, strong ground motions were recorded all around Suruga Bay. Maximum ground accelerations larger than 0.7 gal were reached at a strong-ground-motion station at the Japan Meteorological Agency (JMA). A JMA-scale seismic intensity of 6-lower was observed widely around the bay. The intense shaking was responsible for a landslide that momentarily suspended the traffic of the Tomei Expressway. During the earthquake structural damage to the Suruga deep-sea water plant near Yaizu occurred. The water plant pumps sea water from depths of 397 and 687 m on land through two intake pipes, of which the deepest one was damaged, and the supply of deep-sea water was suspended. Matsumoto et al. (2012) used a remotely operated vehicle to search for the missing 687-m-depth pipe, and found that it had been carried approximately 2 km down slope and was bent along a seafloor canyon axis. It was also discovered that a submarine slope failure had caused a strong mixed flow of water and surface sediments, and moved a shipwreck. The pipe had stopped muddy sediment on its southwestern side, while its steel-wire armor had been torn apart. These observations altogether suggest that the pipe had been damaged and carried down slope by turbidity currents caused by the earthquake.

Following the visual observations by Matsumoto et al. (2012), we used the remotely controlled autonomous underwater vehicle (AUV) *Urashima* (Aoki et al. 2008) owned by the Japan Agency for Marine-Earth Science and Technology (JAMSTEC) to acquire extremely high-resolution bathymetric data in the region of submarine mass movement. The 2009 Suruga Bay earthquake occurred within the source region of the anticipated great earthquake known as the Tokai earthquake. Evidence of earthquake-induced seafloor mass movements in this region would show that these need to be taken into account in tsunami generation during any future earthquakes. This paper presents the micro-bathymetry of this area and proofs the presence of a submarine mass movement triggered by the 2009 Suruga Bay earthquake. We then, discuss if this mass movement was large enough to cause the remarkable change in tsunami heights during the 2009 Suruga Bay earthquake.

43.2 Micro-Bathymetric Mapping

43.2.1 Bathymetric Data Acquisition and Analysis

AUV *Urashima* is the world's largest autonomous deep-sea exploration robot having been progressively developed by JAMSTEC since 1998 (Aoki et al. 2008). The near-cylindrical vehicle is 10.6 m long, 1.3 m wide and 1.5 m high and was designed to minimize hydrodynamic drag. The maximum water depth it can work at is 3,500 m. It is equipped with an inertial navigation system (INS) for independent

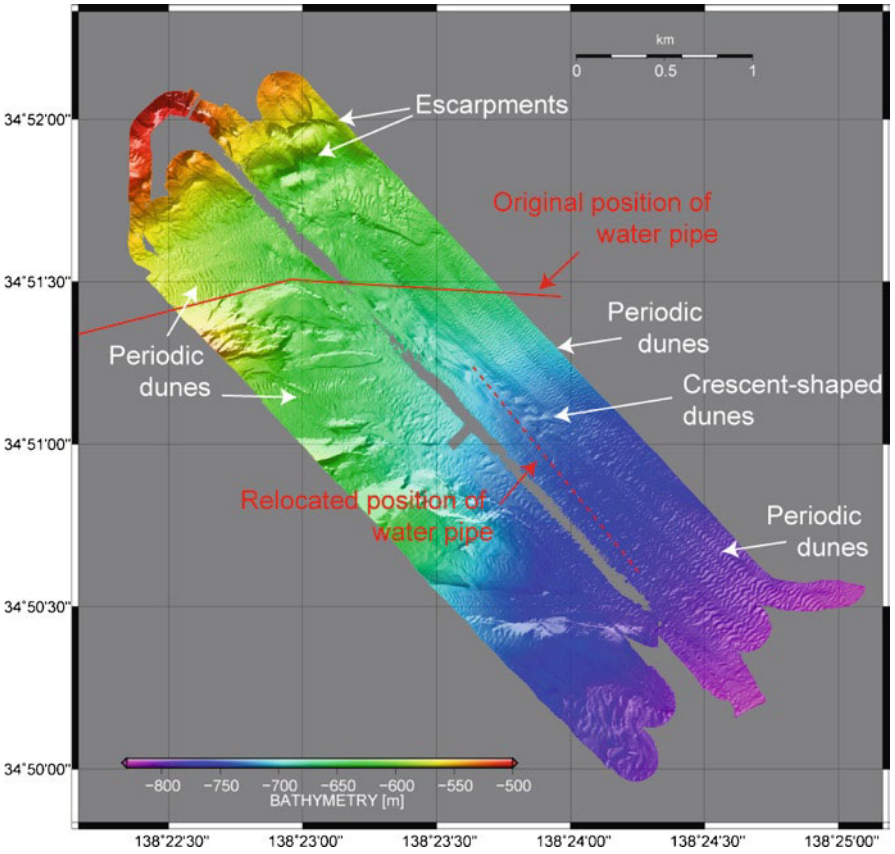

Fig. 43.2 Micro-bathymetric map obtained from data recorded by the AUV Urashima showing escarpments and bedforms. The water pipe was moved from its original site (*red line*) to a position about 2 km down slope (*red dashed line*) by the submarine mass movements. The bathymetric data were gridded at an interval of about 1 m

determination of its own location and can follow predefined courses configured in its onboard computer. The *Urashima* cruises close to the seafloor and uses a multi-beam echo sounder to acquire bathymetric data that can be gridded at about 1-m intervals. This is far superior to ship-borne surveys where the highest resolution bathymetric data is about 30 m.

Two dives were undertaken in Suruga Bay by *Urashima* on February 27 and March 1, 2010, a little over 6 months after the earthquake. In addition to self-tracking by the INS in the AUV, the course of the *Urashima* during these dives was tracked from the supporting research vessel *Yokosuka* using the super-short base-line (SSBL) method. The *Urashima* cruised at a constant height of approximately 80 m above the seafloor. Over the two dives, the vehicle cruised a total of about 45 km with a total area surveyed of ~5.85×10^6 m^2 (1.3 km × 4.5 km) including coverage of the area to which the water pipe was moved by the submarine mass movement (Fig. 43.2).

The raw bathymetric data was corrected for the local sound velocity depth profile. We used both the INS and SSBL data to determine the bathymetric data position. Tidal components were removed to improve the bathymetric image. Corrections were also made for disturbances due to roll and pitch of the vehicle. Spike-like noises on the data were manually removed. The vertical resolution of the bathymetric data is 0.5% of the height of the recording vehicle above the seafloor.

43.2.2 High-Resolution Bathymetric Map

The water depth in the mapped area ranges from 500 to 850 m and the average slope of the seafloor is 4°. In the area near latitude 34°52′N, longitude 138°23′E, about 1 km north of the original position of the water pipe, the *Urashima* data revealed two escarpments bounding a 450-m-wide area that is 10–15 m deeper than the surrounding seafloor level (Fig. 43.2), thus providing morphologic evidence of submarine slumping. The bathymetric map also depicts bedforms along a canyon that indicate seaward flow of sediments over a large portion of the survey area. The bathymetric map shows that the wavelength of bedforms varies between 20 and 30 m, and their height from 0.5 to 1 m, showing a relatively regular periodicity. On the middle slope of the canyon (around 34°51′10″N, 138°23′50″E), the periodic bedforms appear to have been replaced by isolated crescent-shaped bedforms resembling desert barchans.

43.3 Discussion

43.3.1 Bathymetric Evidence for Submarine Mass Movements

Immediately after the Suruga Bay earthquake, the temperature and the turbidity of deep-sea water at the Suruga deep-sea water plant increased, suggesting that the plant had been affected by the earthquake. Matsumoto et al. (2012) used a remotely operated vehicle (ROV) to investigate the facility and discovered that the 687-m water pipe had been dislodged and moved at least 2 km seaward from its operational position. These observations provide evidence that submarine mass movements had occurred during or immediately after the 2009 Suruga Bay earthquake. Furthermore, it is important that the overall picture of the mass movements is understood so that contribution from these mass movements to tsunami generation can be assessed.

The micro-bathymetric map compiled from *Urashima* data shows that the dislodged water pipe lays along a submarine canyon axis (Fig. 43.2), which indicates that the pipe was torn from its operational position by a turbidity current that flowed down along the canyon. Escarpments observed above the original position of the pipe suggest that the turbidity current was initiated by a submarine slump. Comparison of bathymetric survey data recorded from the sea surface by R/V

Natsushima in December 2009 (Matsumoto et al. 2012) with data recorded by the same vessel in 2004 and 2006 shows that after the 2009 earthquake the seafloor subsided by roughly 10 m in the region ~5 km off the coast near Yaizu. This location corresponds to that of the submarine slump indentified in the *Urashima* data. Thus, both the location and amount of subsidence revealed by the two *Natsushima* surveys are consistent with the location and scarp height (10–15 m) of the submarine slump imaged by the *Urashima* survey. It is highly likely that the submarine slump that occurred upslope from the water pipe was a result of strong shaking induced by the 2009 Suruga Bay earthquake. The failure generated a turbidity current that flowed at least 3–4 km down the submarine canyon.

The micro-bathymetric map also shows widely distributed bedforms that appear to continue beyond the survey region (Fig. 43.2). Seafloor bedforms are generally formed by either bottom currents or turbidity currents. According to Wynn and Stow (2002), the crest of bedforms formed by turbidity currents are normally slope-parallel, whereas the crests of bedforms formed by bottom currents are normally oblique to the regional slope. Turbidity current bedforms are typically more regular in shape than bottom current bedforms (e.g., Flood et al. 1993). The bathymetric map shows that the dune crests are aligned parallel to the slope contours, and they show regular periodicity. These observations suggest that the bedforms in the survey region were formed by turbidity currents rather than by bottom currents. As no large rivers flow into Suruga Bay near the study area, it is unlikely that the turbidity currents that created the bedforms were the result of a rapid increase in river discharge following heavy onshore rain. Furthermore, visual observations of the seafloor by ROV (Matsumoto et al. 2012) indicate that the seafloor in the area of the dislodged pipe is covered by marine mud rather than by sediments of terrestrial origin. The ROV observations also showed that part of the dislodged water pipe was covered by the crest of a dune, whereas another part lay uncovered in a dune valley, suggesting that movement of the water pipe and creation of the bedforms were simultaneous. Thus, we can infer that widespread turbidity currents were triggered by the 2009 Suruga Bay earthquake, in addition to the submarine slump about 1 km north of the original position of the water pipe.

43.3.2 Tsunami Simulation

Shortly after the 2009 Suruga Bay earthquake, we carried out numerical simulations of tsunami waves by using fault models estimated from the crustal deformation or seismic wave data, but they failed to reproduce the observed tsunami waveforms. We show here numerical simulations of the 2009 Suruga tsunami assuming the fault motion was accompanied by a submarine mass movement. As in previous studies (e.g., Satake 2001; Abe et al. 2008), we took into account the differences of bathymetry before and after the submarine mass movement. We assumed negative sea surface displacement above sediment evacuation areas and positive sea surface displacement above sediment deposition areas. We created a model of the vertical displacement at

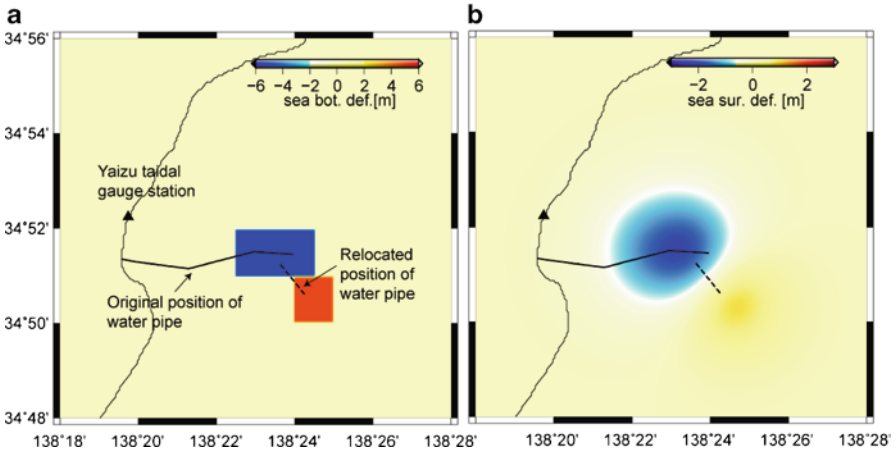

Fig. 43.3 (**a**) Modeled vertical deformation at the seafloor due to the submarine mass movement (**b**) The initial sea-surface deformation obtained by applying Kajiura's (1963) method to the modeled vertical deformation

the seafloor caused by the submarine mass movements on the basis of the results of the Urashima survey (Fig. 43.3a). The initial sea-surface deformation was finally calculated by applying Kajiura's (1963) method to the vertical displacement model (Fig. 43.3b). We assumed that the rise time for sea-surface deformation due to the submarine mass movement was 300 s. As migration velocities of the submarine slump and the turbidity currents are unknown, we did not include the effect of the horizontal movement of the submarine materials on tsunami generation. To simulate tsunami wave propagation, we solved linear long-wave equations in a finite difference scheme at 2 arc second intervals.

We compare the simulation of a tsunami caused by the combined effect of the fault motion and submarine mass movement (i.e., the "compound model"; Fig. 43.4a, c) with that for a tsunami caused by fault motion alone (the "fault-only model"; Fig. 43.4b, d). We also compare the simulated and observed tsunami waveforms at Yaizu (tide gauge), Shimizu, and Omaezaki (NOWPHAS) stations (Fig. 43.5). Figure 43.4a shows that the submarine mass movement near the coast created a short-wavelength tsunami. The first tsunami arrival at Yaizu for the compound model is a negative displacement, which agrees with the observed waveform, whereas that of the fault-only model is a positive displacement (Fig. 43.5). The amplitude of the compound model tsunami is larger than that of the fault-only model. The short-wavelength tsunami caused by the submarine mass movement propagated to the coast northeast and southwest of Yaizu, and it is independent of the tsunami generated by the fault-only model (Fig. 43.4c). Short-wavelength tsunami waveforms that we attributed to the submarine mass movement can be identified in data recorded at Shimizu and Omaezaki around 60 min. after the earthquake (Fig. 43.5). These waveforms are absent from the tsunami simulation based on the fault-only model (Figs. 43.4d and 43.5). Thus, the numerical simulation of the tsunami caused by

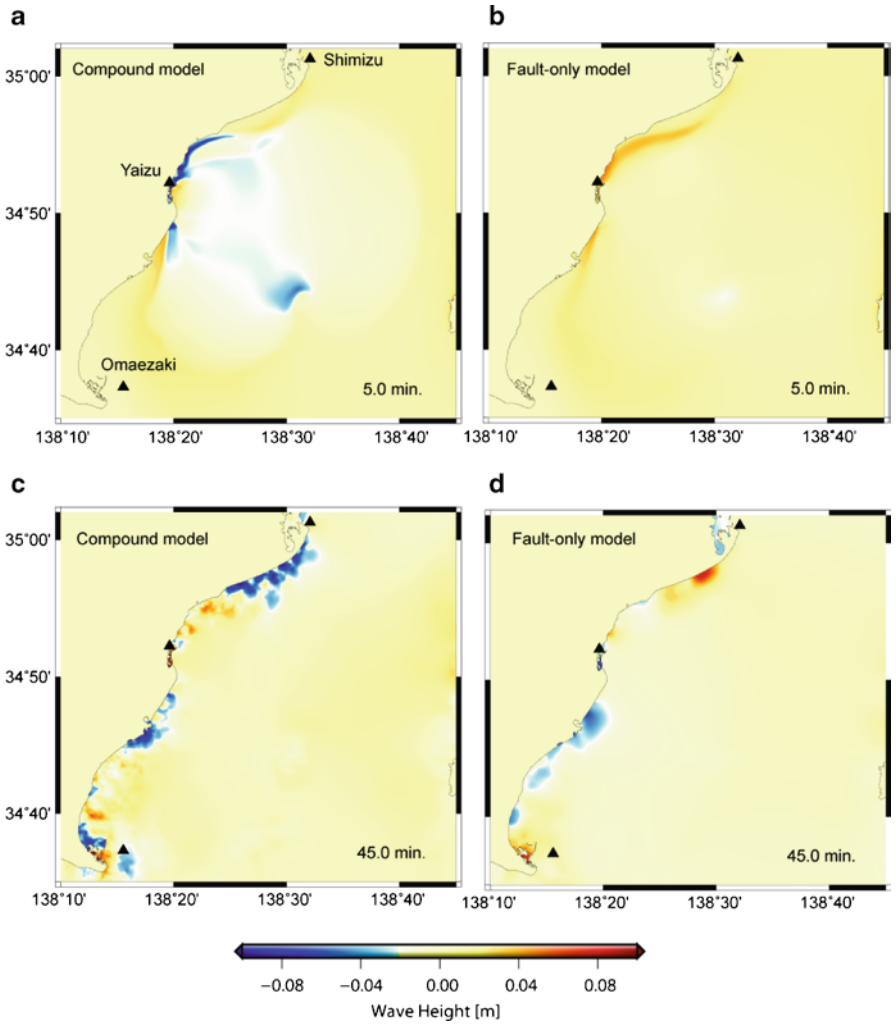

Fig. 43.4 Snapshots showing tsunami simulations 5 and 45 min after the 2009 Suruga Bay earthquake. *Panels* (**a**) and (**c**) Tsunami generated by simultaneous fault motion and submarine mass movement. *Panels* (**b**) and (**d**): Tsunami generated by fault motion alone

simultaneous fault motion and submarine mass movement provides a better match with the tsunami observation records. However, we should mention that further investigation on tsunami modeling is needed because, for example, the first large negative deflection of the tsunami waveform recorded at Yaizu has not yet been reproduced by our simulations. More accurate information about the submarine mass movement, such as the onset of movement, the sliding velocity, and volume of the mass movement is necessary for more detailed tsunami modeling.

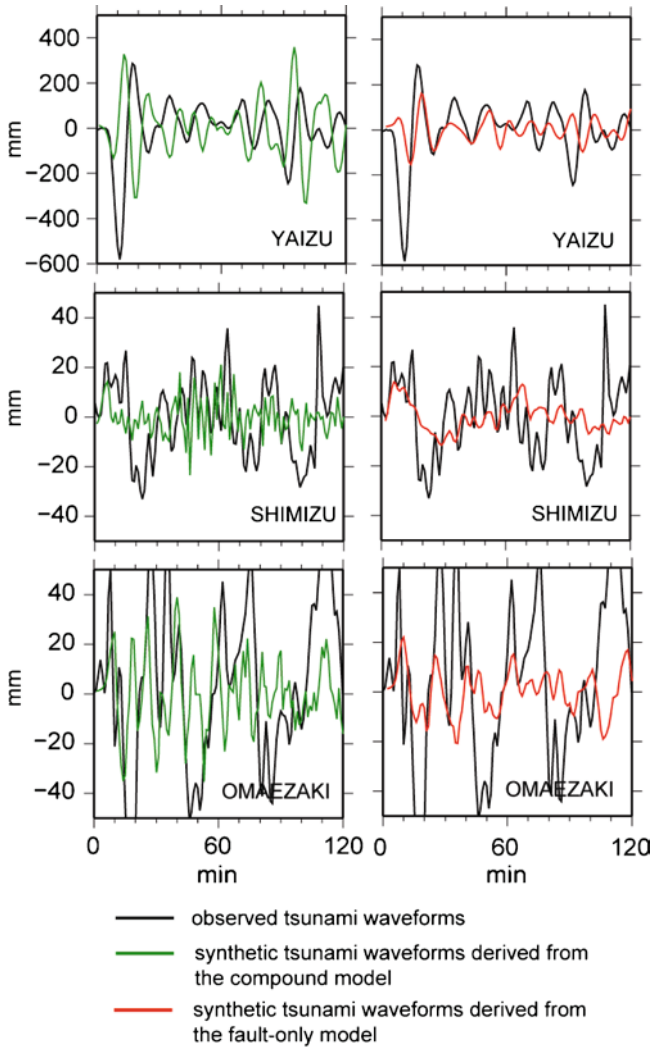

Fig. 43.5 Comparison of observed and synthetic tsunami waveforms at Yaizu tidal gauge station, and Shimizu and Omaezaki wave-meter stations. See Fig. 43.4a for the station locations. The synthetic waveforms in the *left-hand panels* were generated assuming simultaneous fault motion and submarine mass movement: those in the *right-hand panels* were generated assuming fault motion only

43.4 Conclusions

Data acquired by AUV *Urashima* approximately 5 km off the coast at Yaizu, provided a high-resolution 3D image of the seafloor that clearly showed two escarpments bounding a 450-m-wide area that is 10–15 m deeper than the surrounding seafloor. The data also resolved a system of bedforms of 20–30-m wavelength and less than

1 m height that are widely distributed over the survey region. The orientation and shape of the dunes system suggests that it was formed by earthquake-induced turbidity currents. Numerical simulations of the tsunami during the 2009 Suruga Bay earthquake, assuming that the tsunami resulted from the combined effect of a submarine mass movement and fault movement, matched the observed tsunami records better than those excluding the mass movement. We finally conclude that a submarine slump and large-scale turbidity currents were caused by the 2009 Suruga Bay earthquake and which contributed to the tsunami generation. However, further investigation is needed for understanding the relationship between earthquake shaking, submarine mass movements, and tsunami. It is still unclear how earthquake magnitude relates to the magnitude of submarine mass movements. Submarine mass movements have generated unexpected tsunamis (e.g., Tappin et al. 2008) or caused damage to seafloor installations such as telecommunication cables (e.g., Hsu et al. 2008) in the past.

Acknowledgments The authors thank the captain, marine technicians, and crews of JAMSTEC Research Vessel, Yokosuka, and the operations team of the AUV Urashima for their expert help. The tide gauge and NOWPHAS records were provided by the Japan Meteorological Agency and the Port and Airport Research Institute, respectively. We also thank the editor, Dr. Roger Urgeles, and the two reviewers, Drs. David Völker and Kazuo Konagai, for helpful comments.

References

Abe I, Goto K, Imamura F, Shimizu K (2008) Numerical simulation of the tsunami generated by the 2007 Noto Hanto earthquake and implications for unusual tidal surges observed in Toyama Bay. Earth Planet Space 60:133–138

Aoi S, Enescu B, Suzuki W, Asano Y, Obara K, Kunugi T, Shiomi K (2010) Stress transfer in the Tokai subduction zone from the 2009 Suruga Bay earthquake in Japan. Nat Geosci. doi:10.1038/NGEO885

Aoki T, Tsukioka S, Yoshida H, Hyakudome T, Ishibashi S, Sawa T, Ishikawa A, Tahara J, Yamamoto I, Ohkusu M (2008) Advanced technologies for cruising AUV Urashima. Int J Offshore Polar Eng 18:1–10

Flood RD, Shor AN, Manley PL (1993) Morphology of abyssal mud waves at Project MUDWAVES site in the Argentine Basin. Deep Sea Res II 40:859–888

Geospatial Information Authority of Japan (2009) Report of the earthquake in the Suruga Bay on 11 August, 2009 (Japanese only): http://www.gsi.go.jp/kohokocho/h21-8-11-sizuoka.html

Hsu SK, Kuo J, Lo CL, Tsai CH, Doo WB, Ku CY, Sibuet JC (2008) Turbidity currents, submarine landslide and the 2006 Pingtung earthquake off SW Taiwan. Terr Atmos Ocean Sci 19:767–772. doi:103319/TAO.2008.19.6.767(PT

Iwase R, Asakawa K, Mikada H, Goto T, Mitsuzawa K, Kawaguchi K, Hirata K, Kahio Y (2003) Off Hatsushima Island observatory in Sagami Bay: multidisciplinary long term observation at cold seepage site with underwater mateable connectors for future use. In: Proceedings of the 3rd international workshop on scientific use of submarine cables and related technologies, pp 31–34

Japan Meteorological Agency (2009) Monthly report on earthquake and volcanoes in Japan 2009, pp 42–67 (in Japanese)

Kajiura K (1963) The leading wave of a tsunami. Bull Earthq Res Inst Univ Tokyo 41:545–571

Kato T, Terada Y, Ito K, Hattori R, Abe T, Miyatake T, Koshimura S, Nagai T (2005) Tsunami due to the 2004 September 5th off the Kii peninsula earthquake, Japan, recorded by a new GPS buoy. Earth Planet Space 57:297–301

Matsumoto H, Baba T, Kashiwase K, Misu T, Kaneda Y (2012) Discovery of submarine landslide evidence due to the 2009 Suruga Bay earthquake. In: Yamada Y et al (eds) Submarine mass movements and their consequences, vol. 31, Advances in natural and technological hazards research. Springer, Dordrecht, pp 549–559

Nagai T (2002) Development and improvement of the nationwide coastal wave observation network. Techno-Ocean'2002: Paper-TI-1-2, p 4

Satake K (2001) Tsunami modeling from submarine landslides. Proc ITS 2001:665–674

Tappin DR, Watts P, Grill ST (2008) The Papua New Guinea tsunami of 17 July 1998: anatomy of a catastrophic event. Nat Hazards Earth Syst Sci 8:243–266

Wynn RB, Stow DAV (2002) Classification and characterisation of deep-water sediment waves. Mar Geol 192:7–22

Yamanaka Y (2009) Nagoya University seismological note, No. 20 (in Japanese). http://www.seis.nagoya-u.ac.jp/sanchu/Seismo_Note/2009/NGY20.html

Chapter 44
Re-evaluation of the 1771 Meiwa Tsunami Source Model, Southern Ryukyu Islands, Japan

Keitaro Miyazawa, Kazuhisa Goto, and Fumihiko Imamura

Abstract The 1771 Meiwa Tsunami, which was generated on 24 April 1771, struck the Miyako–Yaeyama Islands located in the southern part of the Ryukyu Islands, Japan. It was one of the most devastating tsunamis ever to hit Japan. Based on historical documents and recent field surveys, the run-up heights at some areas of the Miyako–Yaeyama Islands were estimated as up to 30 m at Ishigaki Island, although it is noteworthy that the extremely high run-up heights were only observed at the southeastern coast of the island and those in other areas were generally lower than 10–15 m. Based on these run-up heights, several tsunami source models have been proposed. However, the model remains controversial because the actual fault, the putative tsunami source, has not been identified. For this study, we conducted numerical calculations to test the tsunami source models. We used reliable observed run-up heights including newly available data around the Miyako Islands as well as the high-resolution bathymetric data with reef topography. By comparing estimated and calculated run-up heights, we tested the validity of the previously proposed models as well as that of our own. Results showed that the tsunami generated by the reverse dip–slip intraplate fault plus the subsequent occurrence of a submarine landslide offshore from southeastern Ishigaki Island is the preferred model because it reproduces the historically documented run-up heights well. In particular, this model explains unusually high run-up heights at the southeastern coast of Ishigaki Island

K. Miyazawa (✉) • F. Imamura
Disaster Control Research Center, Graduate School of Engineering, Tohoku University, Aoba 6-6-11-1104, Aramaki, Aoba-ku, Sendai, 980-8579, Japan
e-mail: miyazawa@tsunami2.civil.tohoku.ac.jp

K. Goto
Planetary Exploration Research Center, Chiba Institute of Technology, 2-17-1 Tsudanuma, Narashino, 275-0016, Chiba, Japan

Disaster Control Research Center, Graduate School of Engineering, Tohoku University, Aoba 6-6-11-1104, Aramaki, Aoba-ku, Sendai 980-8579, Japan

Y. Yamada et al. (eds.), *Submarine Mass Movements and Their Consequences*, Advances in Natural and Technological Hazards Research 31,
DOI 10.1007/978-94-007-2162-3_44, © Springer Science+Business Media B.V. 2012

as a result of the local effect of the submarine landslide. Possible evidence of some landslides has been found in this area, but a detailed submarine survey is necessary to confirm the source model and to find evidence of the submarine landslide generated by the 1771 earthquake.

Keywords 1771 Meiwa Tsunami • Miyako–Yaeyama Islands • Submarine landslide

44.1 Introduction

On 24 April 1771, a huge tsunami, called the 1771 Meiwa Tsunami, struck the Miyako–Yaeyama Islands in the southern part of the Ryukyu Islands group, Japan (Makino 1968). Maximum run-up heights of up to 30 m were estimated at Ishigaki Island. Tsunami casualties were estimated at about 12,000 (Makino 1968; Kawana 2000). There is a considerable amount of historical and geological evidence describing this tsunami (e.g., Goto et al. 2010). Consequently, this tsunami provides a good example for showing whether an historical tsunami source model can be determined accurately using an assortment of data. Nevertheless, the source model for this tsunami has long been enigmatic and highly controversial because a conventional fault model estimated from the empirical relation to the magnitude greatly underestimated the overall trend of tsunami run-up heights (e.g., Nakata and Kawana 1995).

Imamura et al. (2001) proposed a model by assuming a reverse dip–slip intraplate fault (Mw = 7.7) plus a submarine landslide at the southeastern offshore area of Ishigaki Island. Although this model reproduces the run-up heights at Ishigaki Island well, the fault dislocation is assumed to be 20 m, which is considered too large according to empirical data (Papazachos et al. 2004). Nakamura (2009) proposed the "tsunami earthquake (Mw = 8.0)" model along the Ryukyu subduction zone because of the absence of historical records describing strong ground tremors. However, the discovery of cracks on southeastern Ishigaki Island (Yamamoto 2008), which were probably formed by a strong ground tremor, contradict the tsunami earthquake model (Goto et al. 2010). In addition, a strong ground tremor at Miyako–Yaeyama Islands is reinforced by historical descriptions, which indicate that the aftershocks were sufficiently strong to generate liquefaction of the ground on Iriomote Island (T. Kawana, personal communication). This indicates that the main shock, which must have been stronger than any of the aftershocks, was stronger than previously thought. Moreover, these previous models do not incorporate the recent progress of historical and geological studies (e.g., Goto et al. 2010).

The Miyako–Yaeyama Islands are fringed by 1.5 km wide reefs which are less than 4 m deep. Therefore, a considerable amount of attenuation of the tsunami waves can be expected. Such reefs should be considered by any tsunami source model. However, earlier models failed to incorporate the effect of the reef because of the low resolution bathymetric data they used. Miyazawa et al. (2010) re-evaluated the model proposed by Imamura et al. (2001) using a high-resolution bathymetric dataset incorporating reef topography which was prepared for a hazard map of Okinawa Prefecture

(Yamashita et al. 2008). The results showed that tsunami run-up heights were more attenuated than previous results showed, illustrating the reef effect.

Fault models should therefore be revised to take into account these newly estimated run-up heights using the high-resolution bathymetric dataset. We re-evaluated the previous tsunami source models quantitatively and qualitatively following the model validation scheme proposed by Aida (1978). Additionally, we further conducted parameter studies of the fault model to seek a more reasonable source approximation.

44.2 Numerical Methods

44.2.1 Numerical Calculation for the Tsunami Inundation

We constructed a nested grid system across a wide area (regions 1 and 2) to the coast of each island (region 3) (Fig. 44.1). Spatial grid sizes of each region are, 300 m for region 1, 100 m for region 2 and 50 m for region 3. To simulate tsunami propagation in the open sea, we used a linear equation to describe a shallow-water wave on a spherical earth (Goto et al. 1997), with an allowance made for Coriolis force. Furthermore, to simulate tsunami propagation in the coastal zone and the inundation area, we used a nonlinear equation in a Cartesian coordinate system for a shallow-water wave, with allowance made for bottom friction. We used the staggered leap-frog method to solve equations of continuity (Eq. 44.1) and motion (Eqs. 44.2 and 44.3).

$$\frac{\partial \eta}{\partial t}+\frac{\partial M}{\partial x}+\frac{\partial N}{\partial y}=0 \tag{44.1}$$

$$\frac{\partial M}{\partial t}+\frac{\partial}{\partial x}\left(\frac{M^2}{D}\right)+\frac{\partial}{\partial y}\left(\frac{MN}{D}\right)+gD\frac{\partial \eta}{\partial x}+\frac{gn^2}{D^{\frac{7}{3}}}M\sqrt{M^2+N^2}=0 \tag{44.2}$$

$$\frac{\partial N}{\partial t}+\frac{\partial}{\partial y}\left(\frac{N^2}{D}\right)+\frac{\partial}{\partial x}\left(\frac{NM}{D}\right)+gD\frac{\partial \eta}{\partial y}+\frac{gn^2}{D^{\frac{7}{3}}}N\sqrt{N^2+M^2}=0 \tag{44.3}$$

In these equations, M and N denote discharge fluxes in the x- and y-directions respectively. D stands for the total water depth ($=h+\eta$), and n is the Manning's roughness (= 0.025). The calculation time is up to 3 h after tsunami generation.

44.2.2 Method for Quantitative Evaluation of the Model

We conducted numerical modeling of propagation and run-up of the tsunami to reassess the previous models presented by Imamura et al. (2001) (hereinafter IM model) and Nakamura (2009) (hereinafter, NK model). Furthermore, we revised the

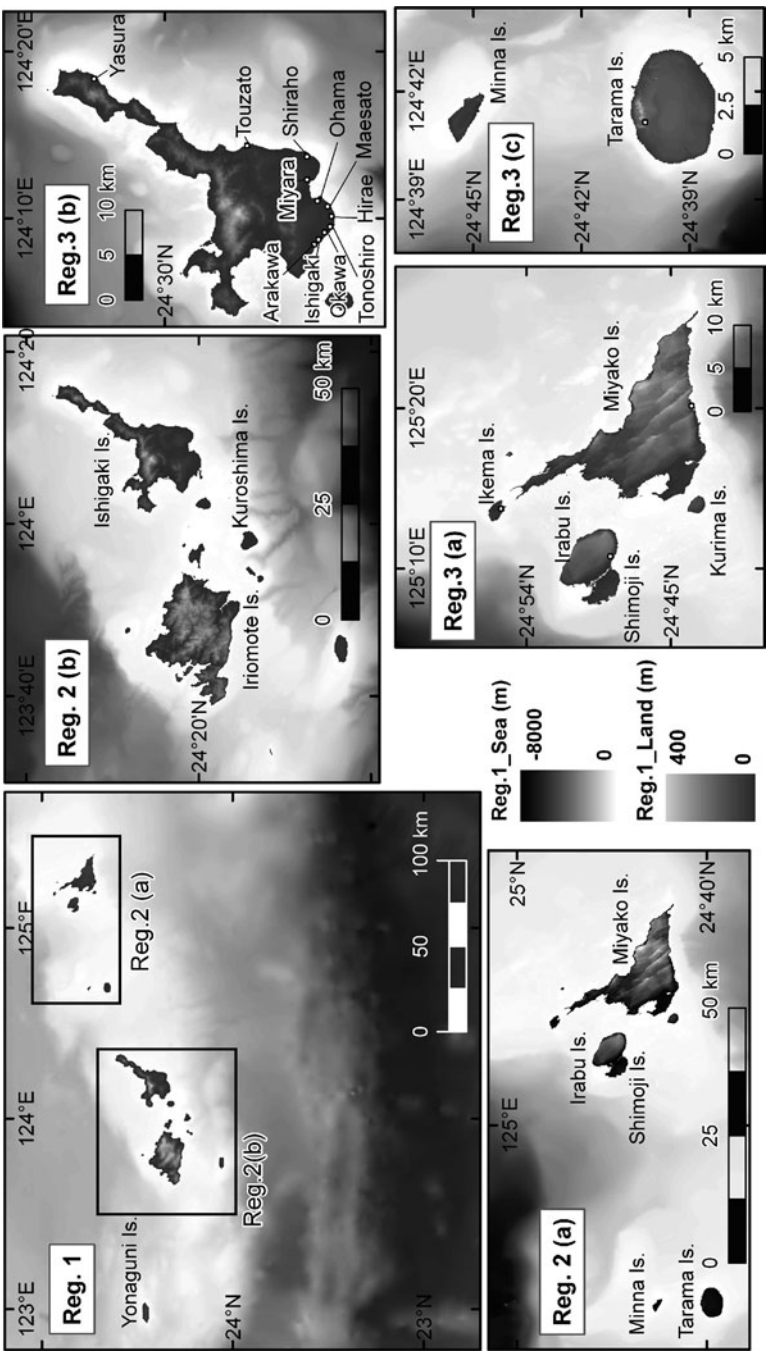

Fig. 44.1 Computational domains for this study from the *Region 1 (Reg. 1*), *Region 2 (Reg. 2(a)* (Miyako-Islands) and *2(b)* (Yaeyama Islands excluding the Yonaguni Island)), and the *Regions 3 (Reg. 3(a)–3(c))*

Table 44.1 Parameters of tsunami source models used for this study

	lat. (°)	long (°)	length (km)	width (km)	strike (°)	dip (°)	slip (°)	dislocation (m)	depth (km)
IM–model (Imamura et al. 2001) *Mw = 7.7*									
Fault	23.9870	124.5450	40	20	270	70	90	20	5
Submarine landslide	24.0780	124.5450	15	10	260	70	90	90	–
NK model (Nakamura 2009) Mw = 8.0									
Fault	23.1550	125.3560	150	30	255	12	90	16	5
MY model (this study) Mw = 8.2									
Fault 1	24.2805	125.3722	70	35	240	70	90	12	5
Fault 2	23.9100	124.8000	72	36	259	70	90	12	5
Submarine landslide	24.1348	124.2640	12	5	76	70	90	80	–

The magnitude (Mw) of each model is calculated based on the fault length and width

IM model and tested a new one (the MY model). To imitate the submarine landslide, we tentatively assumed a fault displacement along the slope following the procedure of Imamura et al. (2001). However, a submarine landslide model should be adopted for future work for accurate reproduction of the tsunami generated by the submarine landslide. Parameters of each source model are presented in Table 44.1. Initial water levels are shown in Fig. 44.2.

Detailed explanations of damage from the 1771 Meiwa Tsunami were recorded in "*Kyuyo*", the official history of the Dynasty of the Ryukyus, local histories, and legends (e.g., Makino 1968). Maximum run-up heights at each village can be estimated from these historical descriptions. Goto et al. (2010) recently re-evaluated the run-up heights at each village based upon such information, and also considered the uncertainties of the data. We used their results, as depicted in Fig. 44.3, to validate the model.

To quantitatively compare the calculated run-up heights with the observed values, we adopt the geometric mean K and the geometric standard deviation κ proposed by Aida (1978), the values for which are calculated from the following equations.

$$\log K = \frac{1}{n}\sum_{i=1}^{n} \log K_i \tag{44.4}$$

$$\log \kappa = \left[\frac{1}{n}\left(\sum_{i=1}^{n} (\log K_i)^2\right) - n(\log K_i)^2\right]^{1/2} \tag{44.5}$$

In Eqs. 44.4 and 44.5, n is the number of points, K_i is R_i/H_i (R_i is the observed run-up height at i point and H_i is a calculated run-up height at i point). The Japan Society of Civil Engineers (JSCE) (2002) recommended $0.95 < K < 1.05$ and $\kappa < 1.45$ as criteria for a good tsunami source model. These criteria are frequently used as an index to evaluate the reproducibility of the tsunami source models (e.g., Nakamura 2009).

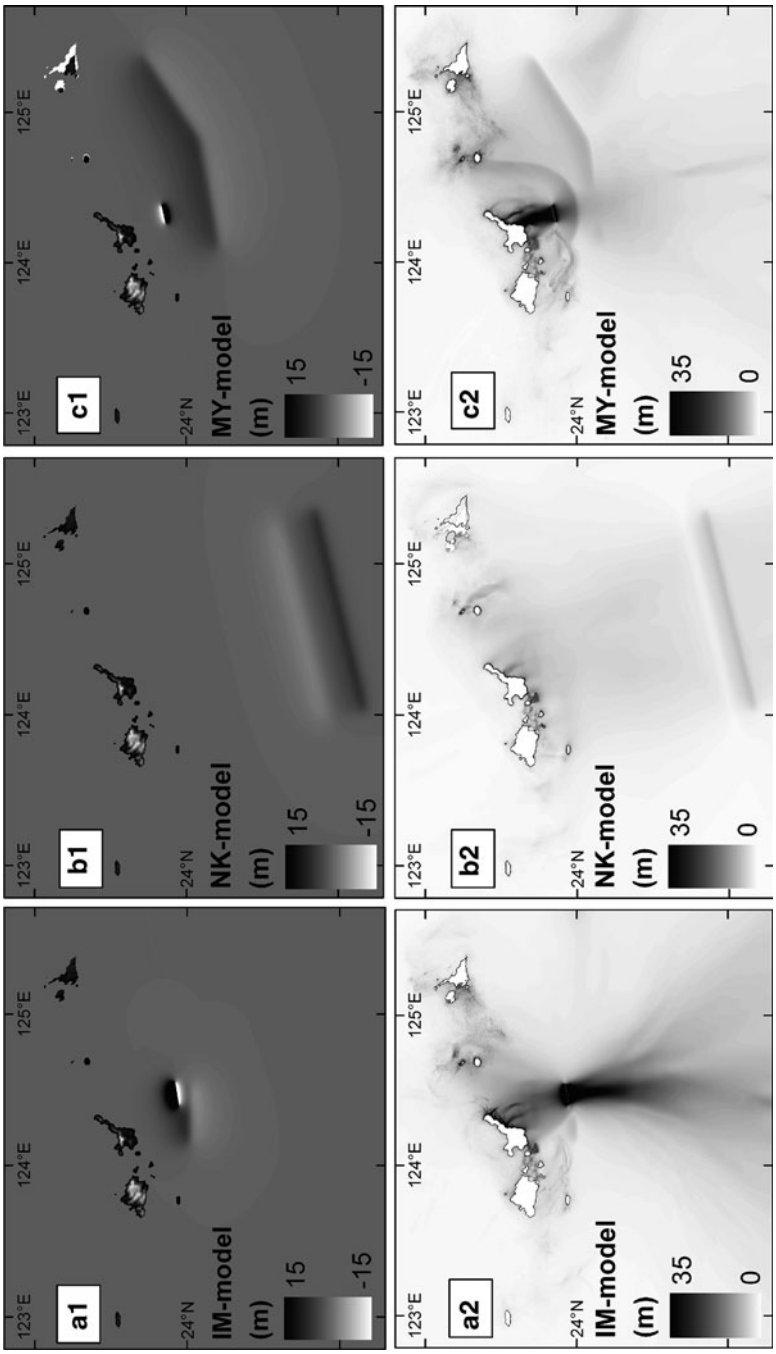

Fig. 44.2 Initial and maximum water levels of the IM–model (**a1** and **a2**), NK-model, (**b1** and **b2**), and MY–model (**c1** and **c2**)

44.3 Numerical Results

The IM model reproduced run-up heights over the whole area well, but the run-up heights of four points at the southeast to east coasts of Ishigaki Island (Maesato, Shiraho, Touzato and Yasura) are considerably overestimated (Fig. 44.3). The NK model underestimated the run-up height at most points of Ishigaki Island. Moreover, no run-up was observed at Ikema Island.

We tested 63 cases and reaffirmed that any fault model that follows the empirical relation between the magnitude and dislocation of the fault fails to explain the observed run-up heights on the Miyako–Yaeyama Islands. To explain the general trend of run-up heights in the general area, at least 12 m of dislocation must occur (Fig. 44.3). Moreover, to explain the unusually high run-up heights on southeastern Ishigaki Island, we must assume a small submarine landslide off the southeast of Ishigaki Island. Using these parameters, our model (MY model in Table 44.1) reproduces most of the distribution of run-up heights on each island, although it underestimates the observed heights at Miyako and Ikema islands.

The IM model satisfies K and κ values with the criteria of the JSCE (2002) (Table 44.2). On the other hand, the other two models (NK and MY models) are good for κ but not for K, although the K value of the MY model is very close to the criteria of the JSCE (2002).

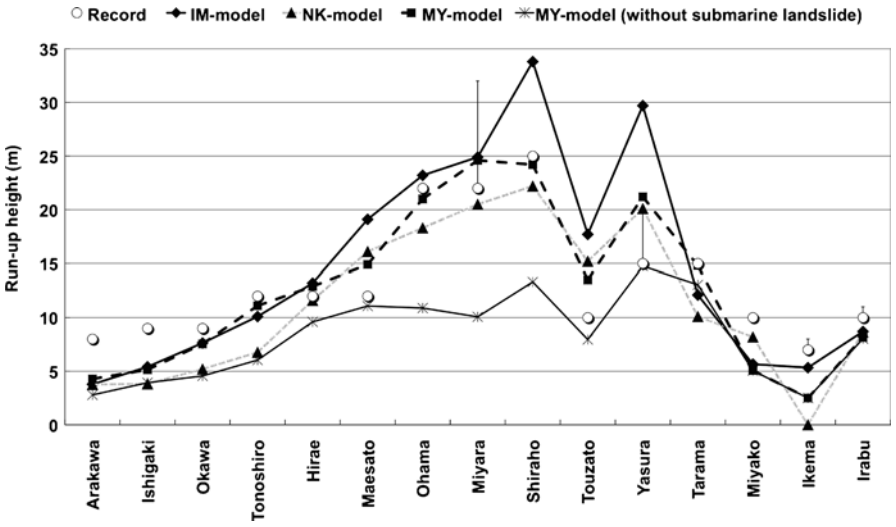

Fig. 44.3 Estimated and calculated run-up heights for each model. Vertical bars at Miyara, Yasura, Ikema and Irabu denote error ranges of estimated run-up heights

Table 44.2 K and κ values estimated in this study for each model

Tsunami source model	K ($0.95 < K < 1.05$)	κ ($\kappa < 1.45$)
IM model	0.97	1.04
NK model	0.75	1.21
MY model	0.92	1.04

44.4 Discussion

An important feature of the 1771 Meiwa Tsunami of relevance to the source model is that according to historical documents the first wave receded (at least at the southern end of Ishigaki Island) (e.g., Makino 1968). This feature is satisfied by the NK (thrust-type fault) and the MY (landslide generates the receding wave near the Ishigaki Island) models, although the IM model is not consistent with this feature because of the assumption made about landslide direction.

Our numerical analyses reveals that only the IM model satisfies the criteria of both K and κ values recommended by the JSCE (2002). This result differs significantly from that obtained by Nakamura (2009), who estimated $K = 1.2$ and $\kappa = 1.3$ for the IM-model, and $K \approx 1.0$ and $\kappa = 1.22$ for the NK model, and who suggested that the latter was the best fit. This difference depends largely on the model assumptions and bathymetric data. Nakamura (2009) used bathymetric data with a 225 m grid cell size and estimated K and κ values at 9 points. These assumptions contrast strikingly to those used in this study where we used high resolution bathymetric data (50 m grid cell size) and estimated K and κ values at 15 points based upon reliable historical descriptions. Moreover, Nakamura (2009) assumed a fictitious vertical wall along the 10 m isobath and calculated maximum wave heights at this depth and compared them with the run-up heights recorded in the historical documents. Consequently, the effect of the wide reef flat (Miyazawa et al. 2010), was neglected in his calculations.

Although the IM model yields good K and κ values, this model considerably overestimates the run-up heights at four important points on the southeast to east coasts of Ishigaki Island. These points show exceptionally high observed run-up heights and therefore characterize the unusual tsunami run-up pattern of the 1771 Meiwa Tsunami. In addition, the dislocation of this model (20 m) may be too large and is probably unrealistic. Consequently, we conclude that this model does not yield the best results.

The NK model satisfies only the range of κ values, whereas the K value is well outside the required range. The potential exists to yield better K and κ values for the NK model if the fault parameters are changed. However, the model must be compatible with recent archaeological and historical evidence, which suggests a stronger ground tremor at Ishigaki Island than previously thought (e.g., Yamamoto 2008). Moreover, no tsunami damage was recorded at Yonaguni Island in the western Miyako–Yaeyama Islands (Fig. 44.1) and Okinawa Islands, which suggests that a large, locally focused tsunami occurred close to Ishigaki Island in 1771 (Goto et al. 2010).

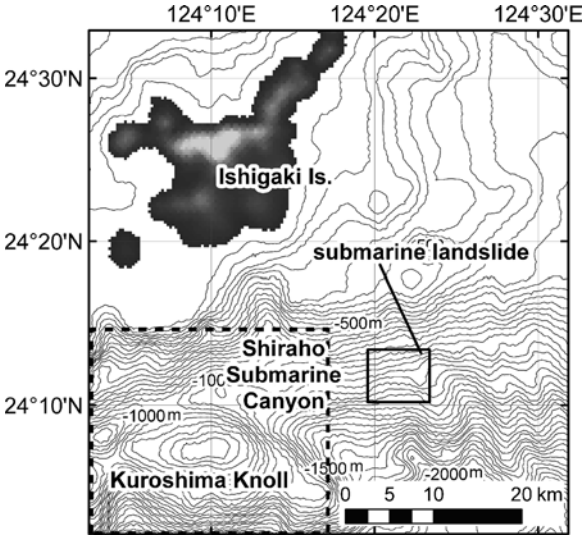

Fig. 44.4 Location of the submarine landslide assumed by this study (*solid square*). *The dotted square* denotes the survey area by Matsumoto et al. (2001)

The MY model explains the general trend well, including the unusual run-up heights on the southeastern coast of Ishigaki Island (Fig. 44.3). However, the model assumes a larger dislocation (12 m) than that estimated using the empirical data from the magnitude (6.7 m, Wells and Coppersmith 1994). Moreover, no actual fault has been found to date. Consequently, it is important to conduct a detailed survey in an attempt to trace the possible fault scarp in this area.

The MY model also assumes a submarine landslide offshore from the southeastern side of Ishigaki Island to explain the unusual (but local) run-up heights there. Although Matsumoto et al. (2001) discovered a possible submarine landslide near the Kuroshima Knoll (Fig. 44.4), our calculations revealed that the assumption of the landslide at this position did not explain well the tsunami run-up heights. On the other hand, our proposed area has not been studied in detail. For that reason, there is no evidence to verify whether a submarine landslide was induced by the 1771 earthquake in this area. Nevertheless, it is noteworthy that our proposed area is situated close to the upper slope of the Shiraho Canyon, which might be the area where submarine landslide(s) have been generated in the past. High-resolution bathymetric surveys, direct observation by a remotely operated vehicle (ROV) and sampling of sediment cores in this area are necessary to clarify the possible existence of a submarine landslide generated by the 1771 earthquake.

44.5 Conclusion

We re-evaluated previously proposed source models for the 1771 Meiwa Tsunami using high-resolution bathymetric data and updated run-up heights, neither of which had been used previously. All conventional fault models following the empirical relation

to the magnitude fail to explain the overall trend of the observed run-up heights, especially those reported on southeastern Ishigaki Island. Although we prefer the intraplate fault plus submarine landslide model rather than the 'tsunami earthquake' one, a large fault dislocation might have to be accepted to explain the overall trend coupled with a local submarine landslide(s) offshore from the southeastern coast of Ishigaki Island. Evidence for the fault and any submarine landslide remain elusive. Numerous surveys must be carried out to validate the proposed tsunami source model.

Acknowledgments We thank K. Ikehara, J. Goff, H. Machiyama, and T. Kawana for their valuable suggestions and comments. This research was supported by a Grant-in-Aid from JSPS (F. Imamura: no. 22241042).

References

Aida I (1978) Reliability of a tsunami source model derived from fault parameters. J Phys Earth 26:57–73

Goto C, Ogawa Y, Shuto N, Imamura F (1997) Numerical method of tsunami simulation with the leap-frog scheme. IUGG/IOC Time Project, IOC manuals and guides 35. UNESCO, Paris, 130 pp

Goto K, Kawana T, Imamura F (2010) Historical and geological evidence of boulders deposited by tsunamis, southern Ryukyu Islands, Japan. Earth-Sci Rev 102:77–99

Imamura F, Yoshida I, Moore A (2001) Numerical study of the 1771 Meiwa tsunami at Ishigaki Island, Okinawa and the movement of the tsunami stones. Proc Coastal Eng JSCE 48:346–350 (in Japanese)

Japan Society of Civil Engineers (The Tsunami Evaluation Subcommittee, The Nuclear Civil Engineering Committee) (2002) Tsunami assessment method for nuclear power plants in Japan. Japan Society of Civil Engineers, Tokyo, 321 p (in Japanese)

Kawana T (2000) Field guidebook for tsunami disaster prevention. Research association for Tokai, To-nankai and Nankai Earthquake Tsunamis, Osaka, 25 p (in Japanese)

Makino K (1968) The Meiwa tsunami at Yaeyama. Published by author, Ishigaki, 462 pp (in Japanese)

Matsumoto T, Kimura M, Nakamura M, Ono T (2001) Large-scale slope failure and active erosion occurring in the southwest Ryukyu fore-arc area. Nat Haz Earth Syst Sci 1:203–211

Miyazawa K, Goto K, Imamura F (2010) Effect of wide fringing reefs on the estimation of the tsunami source model: a case study for the 1771 Meiwa tsunami at Ishigaki Island, Japan. In: 3rd international tsunami field symposium, Sendai, April 2010, pp 209–210

Nakamura M (2009) Fault model of the 1771 Yaeyama earthquake along the Ryukyu Trench estimated from the devastating tsunami. Geophys Res Lett 36:L19307

Nakata T, Kawana T (1995) Historical and prehistorical large tsunamis in the southern Ryukyus, Japan. In: Tsuchiya Y, Shuto N (eds) Tsunami: progress in prediction, disaster prevention and warning. Kluwer Academic Publishers, Dordrecht/Boston, pp 211–222

Papazachos BC, Scordilis EM, Panagiotopoulos DG, Papazachos CB, Karakaisis GF (2004) Global relations between seismic fault parameters and moment magnitude of earthquakes. Bull Geol Soc Greece 36, 2004. In: Proceedings of the 10th international congress, Thessaloniki, April 2004, pp 1482–1489

Wells DL, Coppersmith KJ (1994) New empirical relationships among magnitude, rupture length, rupture width, rupture area, and surface displacement. Bull Seismol Soc Am 84:974–1002

Yamamoto M (2008) Trace of earthquake and tsunami in Ishigaki Island, Yaeyama Archipelago. Archaeol J Jpn 577:9–14 (in Japanese)

Yamashita T, Nakamura Y, Miyagi E, Oka H, Nishioka Y, Takeuchi H, Kyan T, Hoshi M (2008) Evaluation of inundation and damage caused by tsunamis and storm surges on the coast of Okinawa prefecture. Proc Coast Eng JSCE 55:306–310 (in Japanese)

Chapter 45
The 1978 Quick Clay Landslide at Rissa, Mid Norway: Subaqueous Morphology and Tsunami Simulations

Jean-Sebastien L'Heureux, Raymond S. Eilertsen, Sylfest Glimsdal, Dieter Issler, Inger-Lise Solberg, and Carl B. Harbitz

Abstract The 1978 landslide at Rissa is the largest to have struck Norway during the last century and is world-famous because it was filmed. Swath bathymetry data and seismic reflection profiles reveal detailed information about the subaqueous morphology of the mass-transport deposits (MTD). Results show that the landslide affected nearly 20% of the lake floor and that it exhibits a complex morphology including distinct lobes, transverse ridges, longitudinal ridges, flow structures and rafted blocks. The rafted blocks found at the outer-rim of the MTD travelled a distance of over 1,000 m in the early stage of the landslide on an almost flat basin floor. Simulation of sediment dynamics and tsunami modelling show that the rafted blocks most likely triggered the flood wave with a recorded maximum surface elevation of 6.8 m.

Keywords Rissa landslide • Quick clay • Coastal setting • Mass transport deposits • Mobility • Numerical simulations • Tsunami modelling

45.1 Introduction

Landslides are common in the sensitive marine clay deposits of Canada and Scandinavia. When occurring along fjords, lakes or rivers these landslides can generate destructive tsunamis. Although relatively rare, such events can cause much dam-

J.-S. L'Heureux (✉) • I.-L. Solberg
Geological Survey of Norway (NGU) & International Centre for Geohazards (ICG), Trondheim, Norway
e-mail: jean.lheureux@ngu.no

R.S. Eilertsen
Geological Survey of Norway (NGU), Tromsø, Norway

S. Glimsdal • D. Issler • C.B. Harbitz
Norwegian Geotechnical Institute (NGI) & ICG, Oslo, Norway

Y. Yamada et al. (eds.), *Submarine Mass Movements and Their Consequences*, Advances in Natural and Technological Hazards Research 31,
DOI 10.1007/978-94-007-2162-3_45, © Springer Science+Business Media B.V. 2012

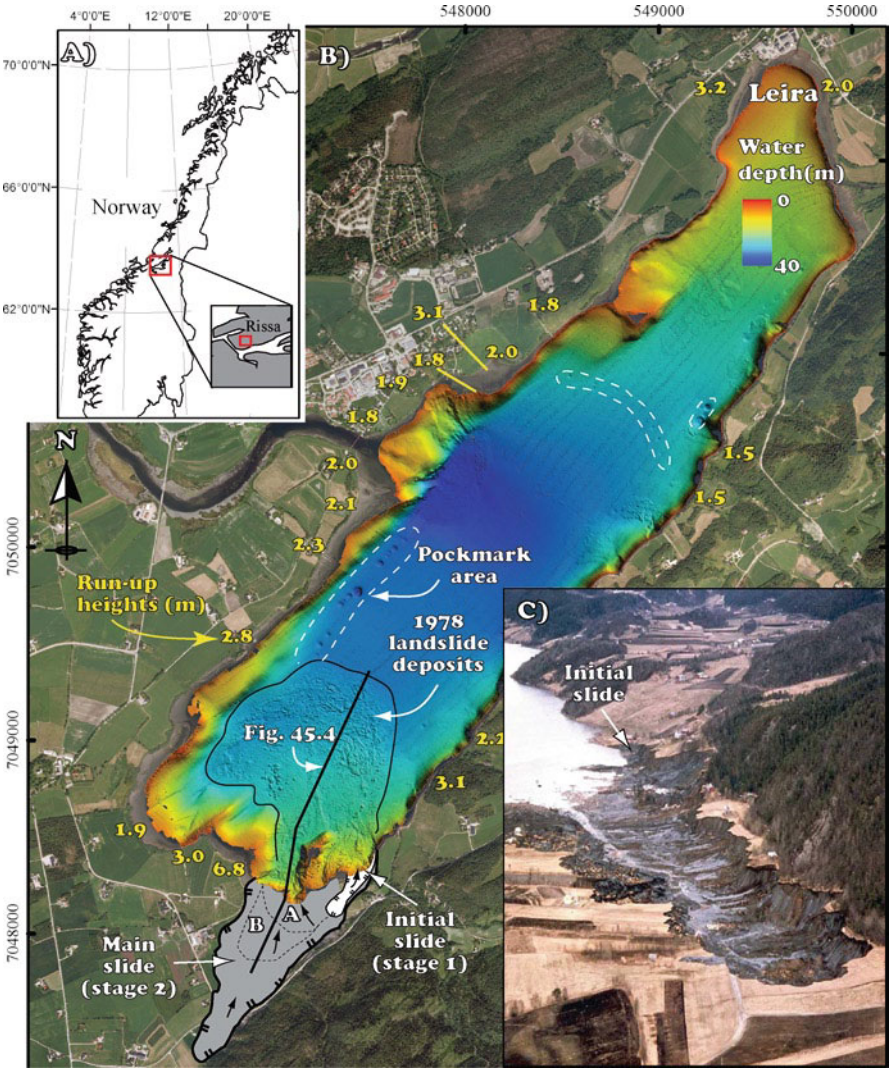

Fig. 45.1 (**a**) Location of Rissa in mid Norway and (**b**) shaded relief image of Lake Botnen. Registered run-up heights from the generated tsunami following the 1978 landslide are shown around Lake Botnen in *yellow* (Data from Larsen 1978). Also shown are the location of the initial slide and the flakes *A* and *B* that caused the tsunami. The *black arrows* indicate direction of movement (**c**) Picture of the Rissa landslide in 1978 (Photograph courtesy of Aftenposten)

age and loss of life. The increasing societal awareness for such natural hazards calls for a better understanding of the link between such landslides and their potential to generate tsunamis.

The famous 1978 quick-clay landslide at Rissa is the largest to have struck Norway in the last century. Of the 40 people caught in the landslide, one person died.

The water waves that were generated by the landslide as it entered Lake Botnen, caused flooding and much damage in the village at the other side of the lake. Run-up heights of up to 6.8 m were documented along the lakeshore (Fig. 45.1).

In this paper, we present an integrated and multi-disciplinary study focusing on the subaqueous morphology, mobility and tsunamigenic implication of the 1978 Rissa landslide. The aim is to better understand the failure and depositional processes of the Rissa landslide, and to discuss its implication on the generation of the tsunami waves. Additionally, the available detailed information on the Rissa landslide and tsunami (i.e. eye-witnesses and amateur videos) is used to constrain our tsunami simulations.

45.2 Setting and Review of the 1978 Landslide at Rissa

Lake Botnen at Rissa is a 1 km narrow and 5 km long inlet connected to the Trondheimsfjord by a shallow river. Following the last glacial period, the area was subject to intense glacio-isostatic rebound and a relative fall of sea level. The marine limit lies at 160 m above the present sea level (Reite 1987). The lowlands along the shores of Lake Botnen are relatively flat and are almost entirely covered by thick glacio-marine and marine deposits, locally overlain by littoral deposits (Reite 1987). During their emergence in the Holocene, marine deposits were exposed to fresh groundwater flow and leaching of salts from the pore water which resulted in the development of very sensitive clay, i.e. quick clays (Rosenquist 1953).

The 1978 landslide took place at the south-western corner of Lake Botnen (Fig. 45.1b). Gregersen (1981) described the landslide as a two-stage process. At first, an initial slide was triggered by excavation and stockpiling along the lakeshore. During this initial failure, 70–90 m of the shoreline slid out into the lake, including half of the recently placed earth-fill. The slide edges were 5–6 m high and extended 15–25 m inland. The landslide developed retrogressively in the south-western direction over the next 40 min. The sediments liquefied completely during the sliding and the debris literally poured into the lake. At this stage the landslide area took the shape of a long and narrow pit open towards the lake (Figs. 45.1 and 45.2). The initial landslide evacuation area covered a surface of 25–30,000 m^2 (i.e. 6–8% of the final slide area) (Gregersen 1981).

The main landslide started almost immediately after retrogressive sliding had reached the boundaries of stage 1 (Fig. 45.1b). At this point, large flakes of dry crust (150 m × 200 m) started moving towards the lake, not through the existing gate opening, but in the direction of the terrain slope onshore (see *arrows*; Fig. 45.1b).

The velocity was initially moderate (flake A; Fig. 45.1b), of the order of 10–20 km/h, and increased to 30–40 km/h (flake B; Fig. 45.1b). Houses and farms can be seen floating on the sliding masses on the amateur videos. A series of smaller and retrogressive slides followed over a short period of time. The sliding process propagated to the mountain side where it stopped. The main sliding stage lasted for approximately 5 min and covered 92–94% of the total slide area (0.33 km^2). The total volume of mobilized sediment has been estimated in the range of $5–6 \times 10^6$ m^3.

45.3 Data and Methods

Bathymetry data were acquired in 2010 using a 250 kHz interferometric sonar system (GeoAcoustics) mounted onboard of a 7 m long craft. Sound velocity in the water adjacent to the transmitters/receivers was measured with a Valport 650 Sound Velocity Profiler (SVP). These measurements were performed systematically to obtain optimal velocity profiles for calculation of water depths. Positioning was performed by means of differential GPS with an accuracy of ±1 m. The bathymetric data are presented with a grid spacing of 1 m. During this survey, a grid of seismic data was also collected using a 3.5 kHz parametric sub-bottom profiler. Two-way travel time was converted to water depth and sediment thickness using a constant sound velocity of 1,470 $m\,s^{-1}$.

45.4 Subaqueous Morphology

Bathymetry data from Lake Botnen reveal a gently dipping basin with steep shoreline slopes (up to 35°). The basin reaches a maximum water depth of 38 m in the central part of the lake. The 1978 mass-transport deposits (MTD) are clearly identified in the southern part of the basin and described below.

45.4.1 Initial Failure Area

Outside the area of the initial landslide, the bathymetry data reveals a 135 m long and 4 m high shore-parallel escarpment (Fig. 45.2). The escarpment extends for more than 100 m to the north in the basin and is draped by a thin veneer of sediments with scattered hummocks (up to 10 m wide). The source of this drape is ascribed to the sediment from the SW-NE oriented, narrow, landslide pit that developed in the first stage of the landslide (Fig. 45.1).

A morphological high is present to the west of the initial slide (Fig. 45.2). This high, interpreted as bedrock from seismic data, constrained the displacements in the initial stage and forced the main landslide event to open a new gate to the west (see main gate; Fig. 45.2). The bathymetry data also reveal a ridge and trough morphology between the morphological high and the initial slide escarpment (Fig. 45.2). These morphological features show a staircase pattern and could be indicative of lateral spreading off the lakeshore in the early stage of the landslide.

Pockmarks are identified at several locations on the lake floor (Figs. 45.1–45.3). These crater-like features, which are up to 60 m wide and 4 m deep, occur at the foot of the shoreline slopes and could testify to high pore-pressure gradients in the near-shore sediments. It is therefore likely that naturally driven excess pore pressures contributed to the onset of failure in 1978.

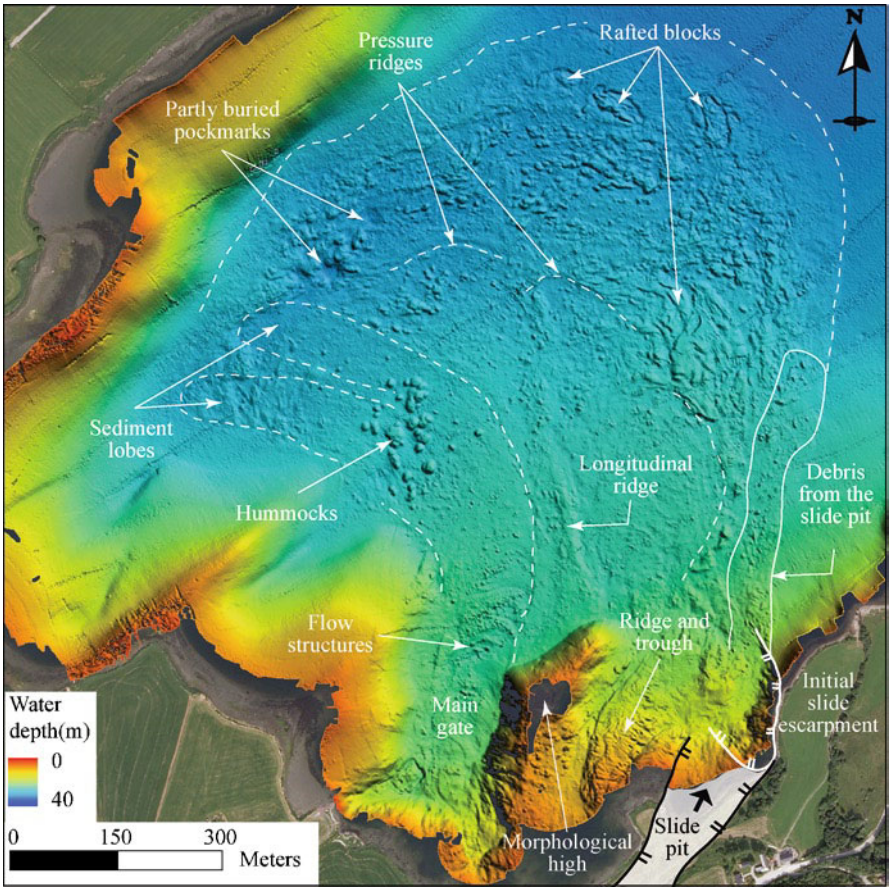

Fig. 45.2 Shaded relief image with morphological interpretation of the 1978 landslide deposits

45.4.2 Main Slide Body

Deposits from the main landslide cover a large portion of the basin floor (up to 20% of the lake). The total area covered by the landslide deposits is 0.76 km^2 and the maximum length of 1.2 km. Seismic data show an average thickness of 6–8 m and thus a total volume of 4.4–5.8×10^6 m^3 (Fig. 45.3). Two types of MTDs are identified on the shaded relief image (Fig. 45.2). The first type consists of well-constrained sediment lobes of fine grained sediments and containing randomly deposited small blocks/hummocks (less than 20 m in diameter). The lobes show many flow structures, whereas the blocks have a semicircular to triangular footprint. The distal portion of the lobes is characterized by arcuate pressure ridges up to 100–200 m long (Fig. 45.2). Such ridges are usually compressional and are mainly associated with flow deceleration combined with continued sediment flow piling up (Posamentier and Kolla 2003). A 400 m long and up to 1 m high longitudinal ridge also occurs on the basin floor in the vicinity of the lobes (Fig. 45.2).

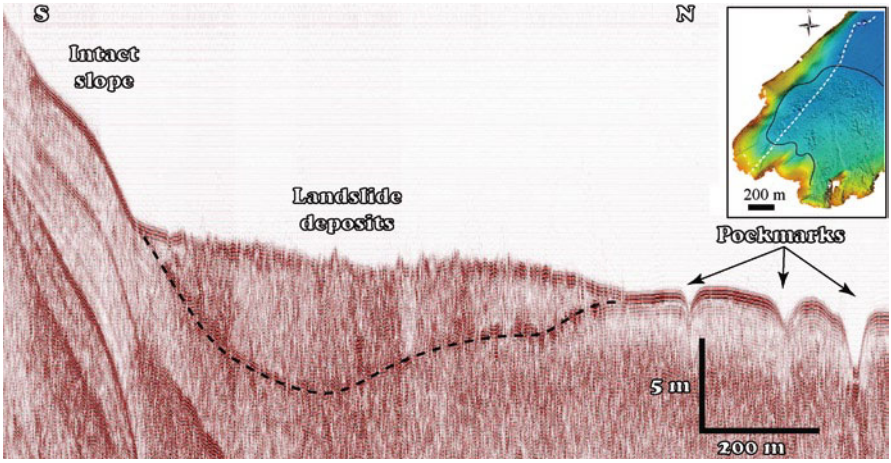

Fig. 45.3 Seismic reflection profile NGU-1008123 showing the thickness of the 1978 landslide deposits. Note also the pockmarks in front of the landslide deposits

Part of the sediment lobes can be traced back to the open gate west of the morphological high (Fig. 45.2). The character of the lobes suggests that they were deposited in the later stage of the landslide when the clay and debris completely liquefied. The longitudinal ridge may result from simultaneous flows of different velocity, combined with eddies generated to the north of the morphological high since large swirls were witnessed in the lake during the event. Additionally, some of the hummocks on the basin floor could represent houses which sank into the lake several days after the landslide event.

The second type of MTDs is found in the frontal part of the landslide deposits. Here, much larger blocks are found (Figs. 45.2 and 45.3). The blocks show rectangular and elongated forms and are typically 80–200 m long and 30–100 m wide. Some of these blocks have travelled up to 1,150 m from the shoreline. The blocks rise 1–2 m above the lake floor and are oriented transverse to the flow direction.

The grouping of the blocks at the outer rim of the deposit suggests that these features are related. Rafted blocks are frequently observed in translational landslides (Mulder and Cochonat 1996) and often go together with debris flows (Ilstad et al. 2004). As such the larger blocks appear to be remnants of the large flakes sediment that rafted towards the lake in the early stage of landsliding. Seismic data also shows that some of the blocks were covered by thin sediment plumes in the final stages of the landslide.

45.5 Post-failure Analysis of the Landslide

In order to create the input for comprehensive tsunami simulations, a dynamical back-calculation of the landslide evolution from the point where it enters the lake until it stops is needed. The eyewitness reports suggest that the main waves were generated

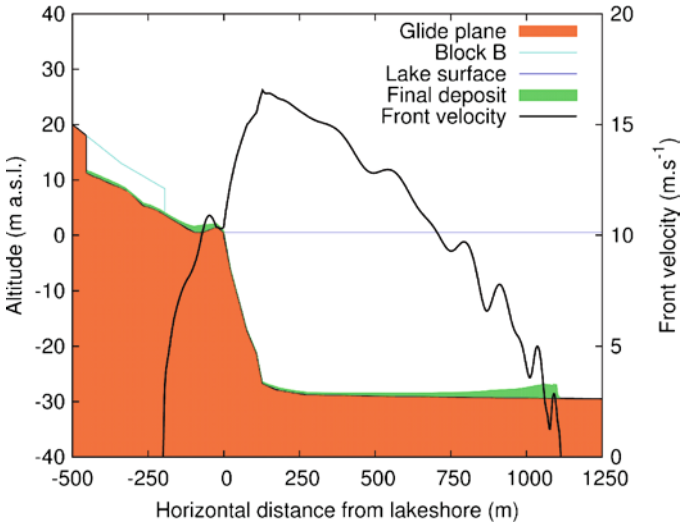

Fig. 45.4 Frontal flow velocity and final sediment deposit for block B using the BING model. See Fig. 45.1b for the location of block B

in the second stage of the landslide when the large flakes of dry crust entered the lake. The flakes were of similar size, but the first was only half as fast as the second due to obstructions in the path (i.e. during the opening of the main gate). Here we concentrate on the second flake (i.e. flake B; Fig. 45.1b). For this exploratory study, we opted for the numerical model BING (Imran et al. 2001), which simulates the flow of a Herschel–Bulkley fluid with a plug layer riding on top of the shear layer using 1D depth-averaged equations. The rheological exponent n was set to 0.5 to reflect the shear-thinning property of clay. Ideally, the yield strength τ_y and viscosity coefficient ν would be determined from laboratory tests of the slide material. However, remoulding and incorporation of ambient water or very soft seafloor sediments may drastically change the material properties in the shear layer (De Blasio et al. 2003). The values of τ_y and ν were adjusted to reproduce the observed run-out distance. In all simulations, values of τ_y between 0.1 and 0.3 kPa (depending on the value chosen for ν) were needed to attain the observed run-out. These values are well inside the range expected for the remoulded shear strength of quick clay (i.e. <0.5 kPa).

The pronounced curvature at several points along the slope profile shown in Fig. 45.4 required substantial artificial damping. Even then, the run-out distance proved to be highly sensitive to the input parameter values (e.g., reducing τ_y by as little as 1% can make the run-out distance increase by more than 20%). The deposit exhibits a thick head about as long as the block at release (Fig. 45.4). This is similar to the morphological observations presented above. In all simulations, the flow velocity increases sharply to 15–18 m/s on the 10–15° steep shoreline slope (Fig. 45.4).

45.6 Tsunami Modelling

In the numerical modelling, the slide (or block) is described as a flexible box. The box slide is slightly rounded to avoid numerical instability. The length and width of the block are described from eye-witness observations and they are set to 200 and 150 m, respectively. Simulations are made for a 7 m high block, using an analytical slide velocity progression formula as well as the velocity extracted from the BING simulations. For the analytical approach the initial and maximum velocity is set to the one observed on the video (i.e. 11 m/s) and decays smoothly following a sinusoidal velocity profile until the run-out distances are reached (~1,000 m). The velocity profile from the BING simulations follows much the same pattern, but has a maximum underwater velocity close to 18 m/s (Fig. 45.4). The approach for the analytical slide progression velocity follows closely the description by Løvholt et al. (2005). The generation phase is modelled by a tsunami model called GloBouss (Pedersen and Løvholt 2008). For the run-up heights and maximum water levels, the model called MOST is applied (Titov and Gonzalez 1997).

Results from the tsunami simulations are presented in Fig. 45.5 for both landslide velocity models. Compared to the observed run-up heights (Fig. 45.1), the

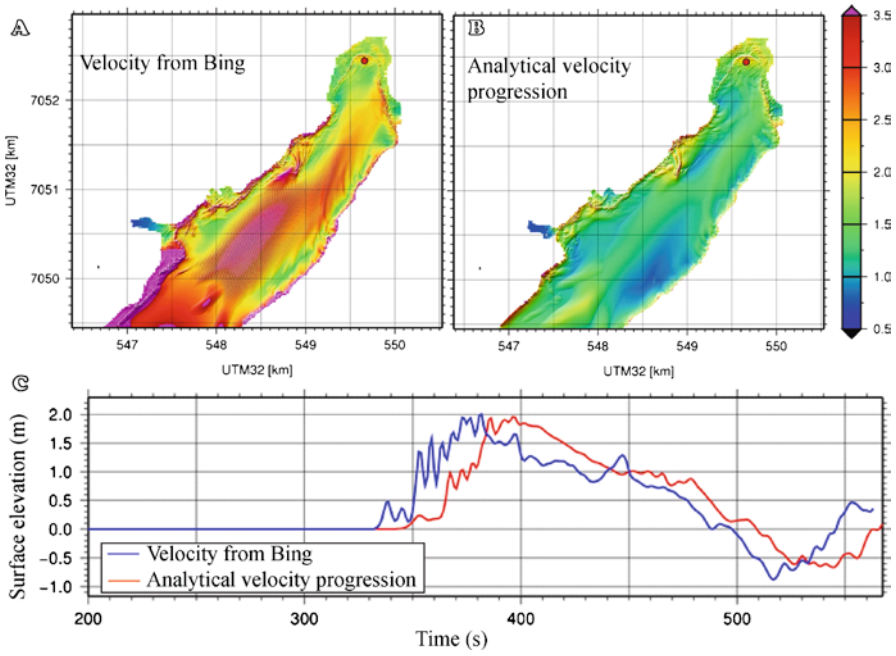

Fig. 45.5 Maximum surface elevation and run-up heights (m) from tsunami simulations when using velocity profiles from (**a**) the Bing model and (**b**) the analytical model (i.e. from video observations) (**c**) Time series from a synthetic gauge (marked with a *red bullet* in panels (**a**) and (**b**)) located in the northern part of Botnen near Leira and showing the surface elevation for both slide velocity progressions as explained in the text

results using the velocity model from BING shows a significant overestimation of the maximum water level in the southernmost part of Botnen (Fig. 45.5a). Better matching is found in the northern part due to the extensive wave breaking and wave height reduction in these shallower waters. Tsunami modelling gives a better match when the analytical slide velocity progression is used (Fig. 45.5b). Along the western shoreline of Botnen the run-up heights are overestimated by 0.5–1.5 m. Simulated heights are close to the observed ones in the northern part (at Leira) and along the eastern margin of the basin (±10–30%). The southernmost part of the lake is not evaluated here, since the run-up model cannot be initiated directly by a slide motion but must read input from the tsunami model along a boundary outside the slide area. In Fig. 45.5c we compare the surface elevation at a synthetic gauge at the northern side of the lake. As described above, the two different scenarios give similar results here, including wave breaking close to the shoreline, and the duration of the first (main) wave peak is 2–3 min. This is comparable to the real wave which was described as one large breaking wave.

45.7 Conclusions

The available detailed information on the 1978 landslide at Rissa in mid Norway offers a unique possibility to study the landslide development, the post-failure dynamics and the generation of a tsunami. In this study, the integrated data set indicates that the water waves in Lake Botnen were generated by movement of large flakes towards the lake. Shaded relief imagery and numerical simulations show that parts of these flakes, or blocks, remained relatively intact and travelled for more than 1,000 m on the basin floor at velocities up to 18 m/s. The transportation of large flakes of dry crust is frequently observed in quick clay landslides (Ter-Stepanian 2000). Therefore, in coastal areas where quick clays are found, it is important to assess the possibility for such flakes to develop prior to any tsunamigenic hazard assessments. Finally, comparison of modelled and registered tsunami run-up heights shows the importance of correctly estimating the landslide velocity profile when assessing the tsunami-generating capacity of coastal landslides.

Acknowledgments We thank O. Totland and J.A. Dahl for their help during the acquisition of the geophysical data and are grateful to G. Corner and M. Vanneste for their constructive reviews. This is contribution no. 357 of the International Centre for Geohazards.

References

De Blasio FV, Issler D, Elverhøi A, Harbitz CB, Ilstad T, Bryn P, Lien R, Løvholt F (2003) Dynamics, velocity and run-out of the giant Storegga slide. In: Locat J, Mienert J (eds) Submarine mass movements and their consequences. Kluwer, Dordrecht, pp 223–230

Gregersen O (1981) The quick clay landslide in Rissa, Norway. NGI Publ 135:1–6

Ilstad T, De Blasio FV, Elverhøi A, Harbitz CB, Engvik L, Longva O, Marr JG (2004) On the frontal dynamics and morphology of submarine debris flows. Mar Geol 213:481–497

Imran J, Harff P, Parker G (2001) A numerical model of submarine debris flows with graphical user interface. Comp Geosci 274:717–729

Larsen JO (1978) Leirskred, Rissa Kommune. Bølgedannelse I sjøen Botnen som følge av skredet (Clay landslide at Rissa – Wave formation in Lake Botnen following the landslide). NGI report 78028-5. Norwegian Geotechnical Institute, Oslo

Løvholt F, Harbitz CB, Haugen KB (2005) A parametric study of tsunamis generated by submarine slides in the Ormen Lange/Storegga area off western Norway. Mar Petrol Geol 22:219–223

Mulder T, Cochonat P (1996) Classification of offshore mass movements. J Sediment Res 66:43–57

Pedersen G, Løvholt F (2008) Documentation of a global Boussinesq solver. Dept of Mathematics, University of Oslo, Norway. http://urn.nb.no/URN:NBN:no-27775accessed 18/08/2011

Posamentier HW, Kolla V (2003) Seismic geomorphology and stratigraphy of depositional elements in deep-water settings. J Sediment Res 73:367–388

Reite AJ (1987) Rissa. Quaternary map – 1522 II – M 1:50 000. with description. Geological Survey of Norway

Rosenquist IT (1953) Considerations on the sensitivity of Norwegian quick-clays. Geotechnique 3:195–200

Ter-Stepanian G (2000) Quick clay landslides: their enigmatic features and mechanism. Bull Eng Geol Environ 59:47–57

Titov VV, Gonzalez FI (1997) Implementation and testing of the method of splitting tsunami (MOST) model. NOAA. Technical Memorandum ERL PMEL-112, 11 pp

Chapter 46
Geowave Validation with Case Studies: Accurate Geology Reproduces Observations

Philip Watts and David R. Tappin

Abstract Boussinesq wave models have been introduced in tsunami science with considerable success. Methodical simulations of case studies provide a critical form of validation for these models. In current simulation techniques, developed since the 1998 Papua New Guinea event, carefully derived tsunami sources are input into a fourth order Boussinesq water wave simulation code (Geowave) capable of capturing wave dissipation, wave breaking, wave dispersion, and nonlinear wave activity. When the tsunami source is known, almost all tsunami observations can be captured with a single, direct Boussinesq simulation. Here, we summarize case studies for the following events: 125 k BP, Alika 2, Hawaii, US, 1908 Messina Strait, Italy, 1946 Unimak, Alaska, US, 1998 Sissano, Papua New Guinea, among other tsunami events.

Keywords Boussinesq • Earthquake • Landslide • Volcano • Tsunami • Mass failure • Case studies • Validation • Runup • Edge wave • Breaking wave • Convergence • Grid size

46.1 Introduction

Rapid advances in marine geological mapping techniques, and the development of Boussinesq wave models have raised the bar on tsunami science. Better geological inputs required better wave models (Dalrymple et al. 2006). For mass failures, the

P. Watts (✉)
Applied Fluids Engineering, Inc, 6216 E. Pacific Coast Highway, #237,
Long Beach, CA 90803, USA
e-mail: phil.watts@appliedfluids.com

D.R. Tappin
British Geological Survey, Kingsley Dunham Centre, Keyworth, Nottingham NG12 5GG, UK

Y. Yamada et al. (eds.), *Submarine Mass Movements and Their Consequences*,
Advances in Natural and Technological Hazards Research 31,
DOI 10.1007/978-94-007-2162-3_46, © Springer Science+Business Media B.V. 2012

combination of multibeam echo sounder (MBES) and sub-bottom seismic data have improved the identification of and detailed events surrounding tsunami generation, especially for landslide tsunamis (e.g., Tappin et al. 2001). Geowave's treatment of water waves is sufficiently accurate to inform the marine geology of mass failure, and *vice versa*, a clear indication that geology and water waves possess data of similar quality and accuracy. This synergy is what enabled the work presented below and what makes the case studies so instructive.

Geowave arose out of the complex simulation demands of the 1998 Papua New Guinea tsunami. As a Boussinesq water wave model (see Wei et al. 1995; Wei and Kirby 1995), Geowave captures wave physics and tsunami runup with a level of detail often lacking in other models, notably wave dispersion and wave breaking from landslide tsunamis. However, it soon became apparent from other case studies that the model could provide valuable lessons regarding many different tsunami sources, in addition to landslide tsunamis. The purposes for creating Geowave back in 2001 were multiple: to expand the number and kind of tsunami sources available, to raise the bar on tsunami propagation and runup accuracy, to broaden the outputs available to describe tsunami impact, and to provide an open source tsunami community model.

46.2 Geowave Background

Geowave simulates tsunami generation, propagation, and inundation using a fourth order fully nonlinear, fully dispersive Boussinesq wave model with multiple wave dissipation mechanisms, wave breaking, and dry land overflow (Wei et al. 1999; Chen et al. 2000; Kennedy et al. 2000). Geowave provides a programming architecture to generate multiple tsunami sources with TOPICS and to insert those tsunami sources at the appropriate time into a simulation run in a modified version of FUNWAVE. Within Geowave, a call is made to TOPICS for each tsunami source, and a call is made to FUNWAVE to begin the simulation once all tsunami sources are specified. FUNWAVE constitutes the essential core of Geowave. FUNWAVE has been available as an open source community model under a GNU General Public License since before 1998. FUNWAVE has more than 1,400 registered users.

TOPICS produces 3D tsunami sources for tsunamis generated by earthquakes (using Okada 1985), subaerial landslides, subaerial rock slides, subaerial debris flows (using Walder et al. 2003), volcanic pyroclastic flows (using Waythomas et al. 2006), submarine slides, submarine slumps (using Grilli and Watts 2005; Watts et al. 2005), among other possible tsunami sources. A 3D tsunami source comprises a free surface shape as well as two horizontal water velocity fields. The tsunami source is input into FUNWAVE as three distinct grid files, one for the free surface and two for orthogonal velocity components, respectively. Each tsunami source has an associated time of occurrence, wave period, wavelength, and water depth that is tracked and known in Geowave. Tsunami sources can be used as initial conditions, or introduced in the middle of a tsunami simulation, at specified times of occurrence.

One of the lessons learned from case studies is the frequent need for a considerable number of tsunami sources. Multiple tsunami sources enable complex fault structures or slip distributions to be built up (e.g., Watts 2006), or propagation of fault rupture along extensive distances and multiple fault segments (e.g., Grilli et al. 2007), or combinations of various earthquakes with mass failures (e.g., Day et al. 2005). A "design wave train source" enables a Geowave user to input water waves, from any direction, with some specified wavelength and amplitude. This is a powerful tool for parametric studies of tsunami response of various structures (e.g., harbors or piers). A "separate tsunami source" gives the user the ability to input any arbitrary tsunami source whatsoever. For example, this option has been used to simulate the highly unusual 1883 Krakatau tsunami source, to restart Geowave simulations that have been halted mid course, and to input a sophisticated seismic inversion source of the recent Tohoku tsunami (see Watts, this volume).

46.3 Tsunami Community Models

There are several tsunami community models available, and each have their own merits. For example, COULWAVE is another well known Boussinesq model (e.g., Lynett 2006). Geowave has been distributed around the world to more than 40 research groups in more than 12 nations as an open source tsunami community model. Geowave is distributed online through the Center for Applied Coastal Research (CACR) web site at the University of Delaware:

http://chinacat.coastal.udel.edu/~kirby/programs/funwave/funwave.html

Geowave 1.0 has been in continuous use since 2002 by the authors (e.g., Watts et al. 2003). Geowave 1.1 was released in 2009. All studies using Geowave reported herein employed the same executable file made available to registered users of Geowave. The only known modifications of the source code have been to increase the size of the simulation domain in the array declarations, and to parallelize the code for use on modern clusters. For these reasons, Geowave can be seen to be a stable application with well known operational parameters and consistent behavior (see Kirby et al. 1998).

46.4 Widely Varied Tsunami Sources

Geowave has been used for historical case studies with one dominant tsunami source, and others that are complex combinations of geological events. Some of the studies of earthquake tsunamis involved large M = 9 events (Watts 2006; Grilli et al. 2007; Ioualalen et al. 2007), whereas others were from significantly smaller earthquakes (Day et al. 2005; Ioualalen et al. 2006). Geowave was applied to a number of submarine mass failures and landslide tsunamis (Watts et al. 2003; Fryer et al. 2004; Day et al. 2005; Greene et al. 2006; Rahiman et al. 2007; Tappin et al. 2008a).

We note the 1975 Kalapana event studied by Day et al. (2005) featured significant earthquake and landslide tsunamis, and therefore appears in the previous two categories simultaneously.

Geowave was applied to a number of volcanic tsunamis, which involve several different wave generation mechanisms, and so are subject to further distinctions and classification. Several tsunamis generated by pyroclastic flows (Waythomas and Watts 2003; Mattioli et al. 2007) were studied with Geowave. Historical case studies and predictive scenarios of tsunamis generated by subaerial debris flows down the flanks of volcanoes (Walder et al. 2006; Waythomas et al. 2006) have also been studied with Geowave. Finally, tsunamis generated by volcano flank collapse (Day et al. 2005; Waythomas et al. 2009) were examined with Geowave as a form of catastrophic mass failure.

46.4.1 Examples of Specific Case Studies

A Geowave simulation of the Dec. 24, 2004 Sumatra tsunami was carried out with five seismic sources, each one corresponding to a different morphology of the subduction zone, and each one having a different time of rupture, respectively (Grilli et al. 2007). The rupture timing was validated with satellite observations made over the Indian Ocean before the tsunami sources were independently used to reproduce runup along the coast of Thailand. Geowave achieved a remarkable 92% correlation with numerous (>50) runup observations, and explained 85% of observed runup variance, both measures of accuracy applying to the coast of Thailand (Ioualalen et al. 2007). In addition, the detailed character, sequence, and magnitude of tsunami attack was reproduced at Phi Phi Island and compared with first hand observations.

The 1908 Messina Strait tsunami is one of those events where the earthquake tsunami simply fails to capture the magnitude of tsunami runup (Tinti and Armigliato 2003; Tappin et al. 2008b). Shortly after the tsunami, runup measurements were made along the Sicilian and Calabrian coastlines at dozens of locations, revealing three distinct concentrations of tsunami runup between 5 and 10 m above sea level. Two out of the three regions of concentrated runup have known mass failures that reproduce the documented tsunami amplitudes and times of arrival with considerable accuracy. One of these mass failures consists of slumping along the underwater flank of Etna, estimated to be 8 km long by 8 km wide by 800 m deep along a 5° incline. The Etna slump produces >5 m maximum runup above sea level concentrated along 25 km of the Sicilian coastline from the towns of Riposto to Catania. Others have also used Geowave to model this event (e.g., Favalli et al. 2009).

The 1975 Kalapana, Hawaii tsunami is of particular interest because it involves volcano flank movement with at least two earthquake faults, the formation of a graben along the coast, and significant mass failure, all from the same volcanic structure and a single geological event (Day et al. 2005). When the mechanical model of flank movement is grasped, then it can be simulated with Geowave and no less than three tsunami sources: two seismic and one mass failure. Despite such mechanical

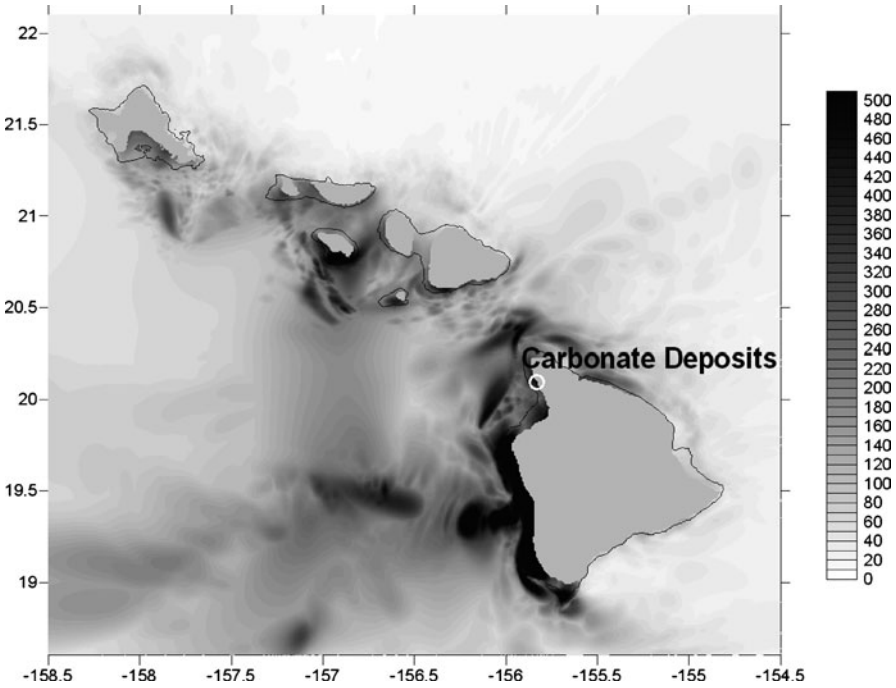

Fig. 46.1 Maximum elevation in meters above sea level for the Alika 2 volcanic mass failure, simulated on a uniform latitude and longitude grid supplied by John Smith

complexity, the tsunami simulation results capture almost all wave observations. More importantly, each one of the three tsunami sources on the island of Hawaii has a unique pattern of runup distribution in isolation. Taken individually, each one of these runup distributions fails to reproduce the runup observations. Taken together, the combined tsunami sources reproduce the runup observations quite well for all measurements.

The giant landslide that occurred 125 k years BP along the Kona coast of Hawaii is an example of volcano flank collapse (Lipman et al. 1988; Moore et al. 1989). The Alika 2 landslide generated a tsunami hundreds of meters in elevation above sea level that carried reef and shell deposits high up the hillsides of Hawaii (McMurtry et al. 2004a, b). Carbonate deposits on the flank of Kohala volcano were dated to around the time of the Alika 2 failure, at elevations of around 400 m above sea level, consistent with simulated runup values at that site (see Fig. 46.1).

46.5 Boussinesq Simulation Specifics

There are important and hazardous wave phenomena that a Boussinesq model readily captures. One telling example is shoaling of the highly nonlinear and relatively short wavelength landslide tsunami in the 1998 Papua New Guinea event.

Tappin et al. (2008a) show that three distinct NSWW models with three different discretization schemes fail to propagate the tsunami past the 20 m depth contour, effectively causing the tsunami to vanish roughly 2,000 m before it reaches the sand spit in front of Sissano Lagoon.

Another wave phenomenon that Boussinesq models capture well is edge waves propagating parallel to the coastline, often in sequences of elevation and depression waves traveling in opposite directions through each other. Geowave produces an abundance of large amplitude edge waves when tsunamis attack a rough coastline (e.g., Waythomas and Watts 2003; Day et al. 2005; Watts 2006; Mattioli et al. 2007; Rahiman et al. 2007). Edge waves often interact with shoreline features and with each other to produce the largest tsunami runup (e.g., Greene et al. 2006). That is, hazardous tsunami runup does not occur from tsunami attack perpendicular to the shoreline alone. Hazardous tsunami runup also happens when positive edge waves interact with each other, or when edge waves are trapped by some shoreline feature.

Tappin et al. (2008a) show the complicated wave breaking pattern for the 1998 Papua New Guinea tsunami, where a patchwork of strong wave breaking (presumably plunging breakers) reproduced specific eyewitness observations and specific wave records. Sometimes, wave breaking will occur just offshore; other times, wave breaking occurs onshore, for reasons both of nonlinear wave shoaling and of apparent hydraulic jumps. Therefore, the wave physics at play must be checked each and every time with some care.

Bathymetry grid size refinement tends to increase tsunami runup and inundation until maximum values are reached. This is a well known and well studied fact that all users of Geowave should check during each and every simulation (e.g., Ioualalen et al. 2007; Tappin et al. 2008a). The only way to know if a bathymetry grid is sufficiently refined to converge onto maximal runup is to keep refining the grid. For example, it is common to use 200–400 m uniform grids for earthquake tsunamis, and 50 m uniform grids for shorter wavelength landslide tsunamis.

46.6 Innovations with Geowave

The current version Geowave 1.1 uses uniform grids in the simulation domain, although nested grids have been used by Ioualalen et al. (2007). Geowave 1.1 is set up to stop a simulation and restart it on a finer grid, if such spatial refinement is needed. Geowave was intended to model local tsunami impact, as opposed to transoceanic tsunami propagation. A new computer model, called Spherical Boussinesq, was introduced that includes the Coriolis force (Kirby et al. 2009). In addition, a new beta version of FUNWAVE is being released at the web site provided above. These facts signal that the science of Boussinesq water wave models continues to advance. The same is true for 3D tsunami sources, which are being revised with the help of full Navier-Stokes models of landslide tsunami generation (e.g., Abadie et al. 2010).

46.7 Conclusions

Boussinesq wave models offer considerable benefits to tsunami science. Many historical tsunami case studies serve to validate tsunami community models such as Geowave. Geowave has sufficient accuracy to resolve wave features related to specific geological interpretations of sea floor rupture and mass failure. With careful marine geology interpretation, it is now common to capture almost all tsunami observations with a single, direct Boussinesq simulation. We summarize and reference case studies for many tsunami events.

Acknowledgement D. Tappin publishes with the permission of the Executive Director, British Geological Survey, NERC, United Kingdom.

References

Abadie S, Morichon D, Grilli ST, Glockner S (2010) A three-fluid model to simulate waves generated by subaerial landslides. Coast Eng 57:779–794

Chen Q, Kirby JT, Dalrymple RA, Kennedy AB, Chawla A (2000) Boussinesq modeling of wave transformation, breaking and runup. II: two horizontal dimensions. J Waterway Port Coast Ocean Eng 126:48–56

Dalrymple RA, Grilli ST, Kirby JT (2006) Tsunamis and challenges for accurate modeling. Oceanography 19(1):142–151

Day SJ, Watts P, Grilli ST, Kirby JT (2005) Mechanical models of the 1975 Kalapana, Hawaii earthquake and tsunami. Mar Geol 215(1–2):59–92

Favalli M, Boschi E, Mazzarini F, Pareschi MT (2009) Seismic and landslide source of the 1908 Straits of Messina tsunami (Sicily, Italy). Geophys Res Lett 36:L16304. doi:10.1029/2009GL039135

Fryer GL, Watts P, Pratson LF (2004) Source of the great tsunami of 1 April 1946: a landslide in the upper Aleutian forearc. Mar Geol 203:201–218

Greene HG, Murai LY, Watts P, Maher NA, Fisher MA, Paull CE, Eichhubl P (2006) Submarine landslides in the Santa Barbara Channel as potential tsunami sources. Nat Haz Earth Sci Syst EGU 6:63–88

Grilli ST, Watts P (2005) Tsunami generation by submarine mass failure part I: modeling, experimental validation, and sensitivity analysis. J Waterway Port Coast Ocean Eng ASCE 131(6):283–297

Grilli ST, Ioualalen M, Asavanant J, Shi F, Kirby JT, Watts P (2007) Source constraints and model simulation of the December 26, 2004 Indian Ocean tsunami. J Waterway Port Coast Ocean Eng ASCE 133(6):414–428

Ioualalen M, Pelletier B, Watts P, Regnier M (2006) Numerical modeling of the 26th November 1999 Vanuatu tsunami. J Geophys Res 111(C6). doi:10.1029/2005JC003249

Ioualalen M, Asavanant J, Kaewbanjak N, Grilli ST, Kirby JT, Watts P (2007) Modeling the 26 December 2004 Indian Ocean tsunami: case study of impact in Thailand. J Geophys Res 112. doi:10.1029/2006JC003850

Kennedy AB, Chen Q, Kirby JT, Dalrymple RA (2000) Boussinesq modeling of wave transformation, breaking and runup. I: one dimension. J Waterway Port Coast Ocean Eng 126:39–47

Kirby JT, Wei G, Chen Q, Kennedy AB, Dalrymple RA (1998) FUNWAVE 1.0. Fully nonlinear Boussinesq wave model. Documentation and user's manual. Report CACR-98-06, Center for Applied Coastal Research, Department of Civil and Environmental Engineering, University of Delaware, Newark

Kirby JT, Pophet N, Shi F, Grilli ST (2009) Basin scale tsunami propagation modeling using Boussinesq models: parallel implementation in spherical coordinates. In: Proceedings of the WCCE-ECCE-TCCE joint conference on earthquake and tsunami, Istanbul, 22–24 June, paper 100

Lipman PW, Normark WR, Moore JG, Wilson JB, Gutmacher C (1988) The giant submarine Alika debris slide, Mauna Loa, Hawaii. J Geophys Res 93:4279–4299

Lynett P (2006) Nearshore modeling using high-order Boussinesq equations. J Waterway Port Coast Ocean Eng ASCE 132(5):348–357

Mattioli GS, Voight B, Linde AT, Watts P, Widiwijayanti C, Young SR, Elsworth D, Malin PE, Shalev E, Van Boskirk E, Johnston W, Sparks RSJ, Neuberg J, Bass V, Dunkley P, Herd R, Syers T, Williams P, Williams D (2007) Unique and remarkable dilatometer measurements of pyroclastic flow–generated tsunamis. Geology 35(1):25–28

McMurtry GM, Watts P, Fryer GJ, Smith JR, Imamura F (2004a) Giant landslides, mega-tsunamis, and paleo-sea level in the Hawaiian islands. Mar Geol 203:219–233

McMurtry GM, Fryer GJ, Tappin DR, Wilkinson IP, Williams M, Fietzke J, Garbe-Schoenberg D, Watts P (2004b) Megatsunami deposits on Kohala volcano, Hawaii from flank collapse of Mauna Loa. Geology 32(9):741–744

Moore JG, Clague DA, Holcomb RT, Lipman PW, Normark WR, Torresan ME (1989) Prodigious submarine landslides on the Hawaiian ridge. J Geophys Res 94(B12):17465–17484

Okada S (1985) Surface displacement due to shear and tensile faults in a half-space. Bull Seismol Soc Am 75:1135–1154

Rahiman TIH, Pettinga JR, Watts P (2007) The source mechanism and numerical modelling of the 1953 Suva tsunami, Fiji. Mar Geol 237(2):55–70

Tappin DR, Watts P, McMurtry GM, Lafoy Y, Matsumoto T (2001) The Sissano, Papua New Guinea Tsunami of July 1998 – offshore evidence on the source mechanism. Mar Geol 175:1–23

Tappin DR, Watts P, Grilli ST (2008a) The Papua New Guinea tsunami of July 17, 1998: anatomy of a catastrophic event. Nat Haz Earth Syst Sci NHESS 8:243–266

Tappin DR, Watts P, Grilli ST, Dubosq S, Billi A, Pophet N, Marani MP (2008b) The 1908 Messina tsunami some comments on the source: earthquake, submarine landslide or a combination of both? Eos Trans AGU 89(53): Fall Meet. Suppl., Abstract S41D-07

Tinti S, Armigliato A (2003) The use of scenarios to evaluate the tsunami impact in southern Italy. Mar Geol 199(221)

Walder JS, Watts P, Sorensen OE, Janssen K (2003) Water waves generated by subaerial mass flows. J Geophys Res 108(B5):2236–2255

Walder JS, Watts P, Waythomas CF (2006) Mapping tsunami hazards associated with debris flow into a reservoir. J Hyd Eng ASCE 132(1):1–11

Watts P (2006) Case study of the 1755 Portugal tsunami. Private consulting report

Watts P, Grilli ST, Kirby JT, Fryer GJ, Tappin DR (2003) Landslide tsunami case studies using a Boussinesq model and a fully nonlinear tsunami generation model. Nat Haz Earth Sci Syst EGU 3(5):391–402

Watts P, Grilli ST, Tappin DR, Fryer GJ (2005) Tsunami generation by submarine mass failure part II: predictive equations and case studies. J Waterway Port Coast Ocean Eng ASCE 131(6):298–310

Waythomas CF, Watts P (2003) Numerical simulation of tsunami generation by pryoclastic flow at Aniakchak Volcano, Alaska. Geophys Res Lett 3014:1751–1755

Waythomas CF, Watts P, Walder JS (2006) Numerical simulation of tsunami generation by cold volcanic mass flows at Augustine volcano, Alaska. Nat Haz Earth Syst Sci NHESS 6:671–685

Waythomas CF, Watts P, Shi F, Kirby JT (2009) Pacific Basin tsunami hazards associated with submarine mass flows in the Aleutian Islands of Alaska. Quat Sci Rev 28:1006–1019

Wei G, Kirby JT (1995) A time-dependent numerical code for extended Boussinesq equations'. J Waterway Port Coast Ocean Eng 120:251–261

Wei G, Kirby JT, Grilli ST, Subramanya R (1995) A fully nonlinear Boussinesq model for surface waves. I. Highly nonlinear, unsteady waves. J Fluid Mech 294:71–92

Wei G, Kirby JT, Sinha A (1999) Generation of waves in Boussinesq models using a source function method. Coast Eng 36:271–299

Chapter 47
Tsunami Hazards for Nuclear Power Plants: Mass Failures, Uncertainty, and Warning

Philip Watts

Abstract The 2011 Tohoku tsunami portends the beginning of a new era in tsunami hazard assessment. A new level of detail will be demanded to secure every valve, pipe, pump or fuel tank at nuclear power plants (NPPs). Three issues stand out at the dawn of this new era: earthquake magnitudes, landslide tsunamis, and probabilistic tsunami hazard assessment (PTHA). The challenges of estimating a maximum earthquake magnitude along some margin continue to be studied. While any potential role of mass failures and landslide tsunamis in the Tohoku event is unknown now, factoring for these tsunami-sources is essential to hazard assessment, and their full impact needs to be found. Armed with a thorough set of tsunami hazards, a probabilistic framework is needed, one that can reach comfortably to 50,000 year events, and quite possibly to volcanic events with 100,000 year or longer recurrence intervals. Effectiveness will ultimately be measured by NPPs that withstand tsunami attack and resume operations shortly thereafter, exactly as planned and with no surprises.

Keywords Tsunamis • Case studies • Hazard assessment • Probability • Nuclear power plant • Aleatory uncertainty • Epistemic uncertainty • Tsunami warning

47.1 Introduction

A novel view of tsunami hazards has emerged out of ongoing research efforts and the 2011 Tohoku tsunami in Japan. This paper relates the novel view to nuclear power plants (NPPs). Tsunamis are known to be hazardous, but the conditions and

P. Watts (✉)
Applied Fluids Engineering, Inc, 6216 E. Pacific Coast Highway, #237,
Long Beach, CA 90803, USA
e-mail: phil.watts@appliedfluids.com

Y. Yamada et al. (eds.), *Submarine Mass Movements and Their Consequences*,
Advances in Natural and Technological Hazards Research 31,
DOI 10.1007/978-94-007-2162-3_47, © Springer Science+Business Media B.V. 2012

frequencies with which they are hazardous to NPPs remain elusive. The geology of tsunami generation is often complex (e.g., Day et al. 2005; Ioualalen et al. 2007; Tappin et al. 2008). Likewise, the wave physics of tsunami propagation and inundation are similarly complex (e.g., Dalrymple et al. 2006; Tappin et al. 2008). Despite an abundance of complexity, NPPs demand accurate tsunami hazard assessment.

Tsunamis are a relatively common natural hazard. That being said, most events are small in amplitude (Grilli et al. 2009) and many of those events presumably go unreported or undocumented (Tinti and Armigliato 2003). Tsunamis of modest amplitude happen from time to time and sometimes inflict damage or casualties to local industry or populations, respectively (e.g., Imamura et al. 1995; Ioualalen et al. 2006; Rahiman et al. 2007). Catastrophic tsunamis occur less often, and require careful analyses of their impact on sensitive sites such as NPPs. The scope of tsunami hazards in Table 47.1 is incredibly broad and encompasses catastrophic earthquake tsunamis, landslide tsunamis, and volcanic tsunamis.

Landslide tsunamis have distinct features that originate from the triggering and acceleration of mass failures from rest (e.g., Watts et al. 2003). Submarine mass failures are usually triggered by earthquakes (Wright and Rathje 2003), although artesian water pressure may also play an important role (Greene et al. 2006). A magnitude 5.5 earthquake is sufficiently strong to trigger mass failures on land (Wilson and Keefer 1985). Tappin et al. (2001) documented numerous mass failures from a magnitude 7.1 offshore earthquake, including rock slides, surficial slides, and deep seated slumps. Hazardous landslide tsunamis can be triggered by earthquakes below the threshold of M = 7 currently used to issue tsunami warnings. The amplitude of landslide tsunamis does not correlate with earthquake magnitude, so that larger earthquakes do not produce larger landslide tsunamis, and *vice versa* (Watts 2004). The theoretical maximum tsunami amplitude corresponds to the vertical center of mass displacement of the mass failure (Striem and Miloh 1976). Moreover, transoceanic landslide tsunamis are possible for the largest of submarine mass failures (Waythomas et al. 2009). Landslide tsunamis require a new kind of tsunami warning system (Watts 2001).

Table 47.1 describes watershed tsunami events. Other events are expected to happen any year. For example, the Cascadia subduction zone off Oregon and Washington states was found to have catastrophic earthquake tsunamis every 300–500 years (Satake et al. 1996; Goldfinger et al. 2003). There are tsunamis of this magnitude every few decades, and these events can strike in almost any ocean of the world. At the site of the Fukushima NPP, Fig. 47.1 shows tsunami runup greater than 10 m above sea level, and water velocities on the order of 2 m/s, consistent with other events in Table 47.1. The more important lesson is perhaps implicit. It is unlikely the events in Table 47.1 would have been understood as tsunami hazards at the time they happened. Now that these tsunami hazard lessons are known and understood and documented, these kinds of catastrophic events and their threat to NPPs can be studied and prepared for in detail.

Table 47.1 Partial list of tsunami events[a]

Year	Location	Runup (m)	Deaths	Reference
Large magnitude earthquake tsunamis:				
1700	Cascadia subduction	N/A	N/A	Satake et al. (1996)
1755	Azores triple junction	30	~60,000	Baptista et al. (2003)
1960	Chile subduction	25	1,223	Eaton et al. (1961)
1964	Alaska subduction	67	124	Plafker et al. (1969)
2004	Sumatra subduction	50	225,000	Ioualalen et al. (2007)
2011	Tohoku subduction	>13	>20,000	N/A
Various mass failure tsunamis:				
1908	Messina, Italy	13	~60,000	Favalli et al. (2009)
1929	Grand Banks, Canada	7	28	Heezen et al. (1954)
1946	Unimak Island, AK	35	164	Fryer et al. (2004)
1958	Lituya Bay, Alaska	525	5	Miller (1960)
1964	Prince William Sound	67	124	Plafker et al. (1969)
1992	Flores Island, Ind.	26	1,169	Imamura et al. (1995)
1998	Sissano Lagoon, PNG	15	2,205	Tappin et al. (2008)
Various volcanic tsunamis:				
250 k	Alika 2, Hawaii	1,100	N/A	McMurtry et al. (2004)
1883	Krakatau, Indonesia	35	~36,000	Carey et al. (2001)
1975	Kalapana, Hawaii	14	2	Day et al. (2005)
2003	Montserrat, East Indies	7	N/A	Mattioli et al. (2007)

[a]Runup and deaths from the NOAA web site: www.ngdc.noaa.gov/hazard/tsu.shtml
(Shaded quantities are not from NGDC database. Number of dead may include multiple causes)

47.2 Aleatory Uncertainty

Aleatory uncertainty can be simply described as the uncertainty inherent to complex natural phenomena. Probabilistic Tsunami Hazard Assessment (PTHA) provides one means to deal with aleatory uncertainty. There are at least three known models capable of carrying out PTHA (Syvitski and Hutton 2003; Watts 2004; Grilli et al. 2009). The US Nuclear Regulatory Commission (NRC) is considering developing PTHA capabilities (Kammerer et al. 2008). However, the NRC currently proposes a "screening analysis" that rules out tsunami hazards (Prasad et al. 2009). A debatable concept called the "probable maximum tsunami" is introduced that depends on local historical events, rather than global tsunami hazard lessons. In contrast, PTHA is an inclusive and impartial analysis that assigns probabilities to every possible tsunami, without screening out events, and without relying on judgment calls.

The application of a simple PTHA to the Fukushima NPP site is illustrative of the process, and of the results available. The margin is split into two seismic zones, 3° north and 3° south of the 38° parallel, where a bend in the subduction zone occurs. The NPP site is at 37.425° Latitude. The Gutenberg-Richter relationships for the two seismic zones are

$$\text{North}: \quad M_w = 5.5493 - 1.9461 * \text{Log}_{10} n$$
$$\text{South}: \quad M_w = 5.6232 - 1.3985 * \text{Log}_{10} n$$

where n is the frequency of exceedance. These relationships were applied over a magnitude range $M_{min} = 5.5$ and $M_{max} = 8$ that extends beyond the range of the original seismic data. The magnitudes of two characteristic earthquakes are chosen to be $M = 8.6$ and $M = 9.2$ so that events larger than the recent Tohoku tsunami are enabled. Given equal frequencies of both characteristic events, and assuming complete seismic coupling for now, the maximum possible rate of occurrence of these events is given in Table 47.2. During PTHA, the rate of occurrence will be reduced in proportion to a randomly generated seismic coupling coefficient, within the limits specified in Table 47.2. The hypocenter depths range from 25 to 60 km in the north, and 20–55 km in the south. Table 47.4 summarizes results of the PTHA at the Fukushima NPP site. Recent data from TEPCO suggests runup between 14 and 15 m above sea level at most places around the NPP (see the TEPCO web site). The runup height suggests events of this size or greater can be expected to occur every 1,200 years according to the current analysis, a result that is subject to refinement. The last regional event of similar tsunami amplitude occurred in 869 AD, and so there is an appearance of at least qualitative agreement.

47.3 Epistemic Uncertainty

Epistemic uncertainty can be simply described as the inevitable differences that exist between acknowledged experts. What makes epistemic uncertainty so interesting and relevant is that tsunami experts agree to disagree about many different scientific topics. While it will never go away, epistemic uncertainty has the desirable qualities that it can be readily examined, understood, and quantified.

Transoceanic tsunami propagation is not usually thought of as a dispersive water wave phenomenon. However, wave dispersion was found to be essential in tsunami propagation (Hammack 1973), a fact that has been recognized in textbooks on water waves (e.g., Mei 1983). As more and more accurate seismic inversion techniques begin combining seismic records with DART buoy records (e.g., Sladen et al. 2010), the real world discrepancies that arise from missing dispersion become more noticeable in simulations. To demonstrate the phenomenon in a relative manner, the Tohoku tsunami was simulated by Geowave with and without dispersion, for the same discretization scheme, on the same bathymetry grid, and with the same tsunami source (see Ioualalen et al. 2007; Tappin et al. 2008). The bathymetry is a uniform 1,500 m grid in UTM projection using ETOPO1 data. A grid node was situated on top of DART Station 21418 (148.694° Long., 38.711° Lat.), the closest DART buoy to the earthquake epicenter. The tsunami propagation distance from the trench is 390 km, over a mean ocean depth of around 5,400 m, with a long-wave celerity of 230 m/s. Figure 47.2 compares the numerical wave gauge records at the buoy

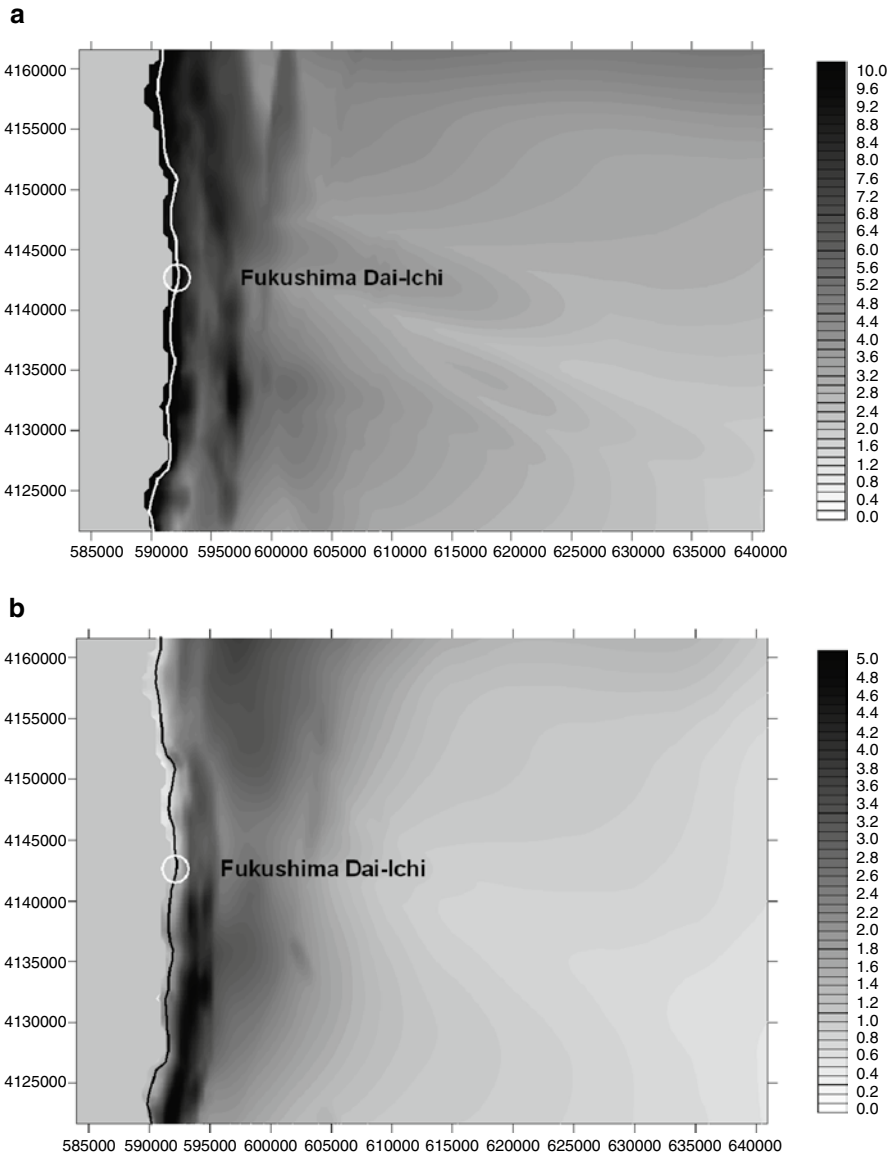

Fig. 47.1 Geowave simulation of the Tohoku tsunami using the Caltech tsunami source to provide (**a**) maximum tsunami elevation in meters above sea level over all time, and (**b**) maximum water velocity in meters per second over all time

Table 47.2 Seismic zone features for the PTHA analysis

Seismic zone	Convergence rate	Seis. coupling	Occurrence rate
North	8.0 cm/year	0.75–1.00	$\lambda_{char} = 0.00122$
South	7.5 cm/year	0.50–1.00	$\lambda_{char} = 0.00114$

Table 47.3 Tsunami results from 50,000 year synthetic records

Runup (m)	North #	South #	Total # >	Log n	Freq. (years)
9–10	21	12	163	−2.487	306
10–11	15	12	130	−2.585	385
11–12	16	11	103	−2.686	485
12–13	15	4	76	−2.818	658
13–14	10	5	57	−2.943	877
14–15	4	2	42	−3.076	1,190
15–16	9	0	36	−3.143	1,389
>16	22	5	27	−3.268	1,852

Table 47.4 Selected historical tsunamis along the Sanriku margin

Year	EQ magnitude	Runup (m)
1611	8.1	25
1677	8.1	6.0
1793	8.3	4.5
1843	8.4	4.5
1896	7.6	38
1933	8.4	29
1952	8.1	6.5
1968	8.2	6.0
2003	8.3	3.9

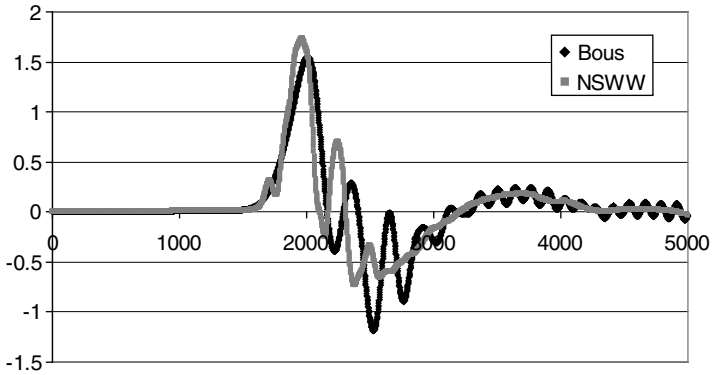

Fig. 47.2 Comparison of Geowave simulations run with *NSWW* and Boussinesq (*Bous*) wave equations of the Tohoku tsunami using the Caltech tsunami source at DART Station 21418

location for the two simulations. The peaks of the first elevation waves nearly coincide, although the NSWW simulation has a 1.734 m peak at 1964 s, whereas the Boussinesq simulation has a 1.549 m peak at 2007 s. The leading elevation waves are followed by widely varying wave trains, which is to be expected for a dispersive tsunami. The two wave gauge records end with matching low frequency oscillations, although the Boussinesq simulation has high frequency, low amplitude wave groups superposed on top.

47.4 Tsunami Hazard Maps

One of the benefits of modern tsunami simulations is that virtually any degree of accuracy is available from current computer models (typically Boussinesq or Navier-Stokes). When applied properly, the simulation results are limited only by the geology of the tsunami source. Walder et al. (2006) developed tsunami hazard maps for sediment transport modes, forces on structures, floating object displacements, boulder transport and emplacement, people and cars being swept away, etc. Grossi et al. (2008) produced a risk model to predict the cost of structural losses from tsunamis. In principle, every valve, pipe, pump, fuel tank, etc. at a NPP can be studied in either deterministic or probabilistic space (with a PTHA). Two hazard maps for the Fukushima NPP are shown in Fig. 47.3. The sediment transport map corresponds to suspended load transport. It was not safe to stand near the shoreline during the Tohoku tsunami at the NPP site. Other tsunami hazard maps are available, including car transport and structural forces imparted by a tsunami.

47.5 Tsunami Warning

Table 47.4 demonstrates the wide variety of tsunami runup for some of the great earthquakes and great tsunamis along the northeastern coast of the island of Honshu. In addition to the large intrinsic variability of earthquake tsunami runup, the events of 1611, 1896, and 1933 may include significant landslide tsunamis. Among these, the 1896 Sanriku tsunami stands out. The M = 7.6 earthquake magnitude of that event is almost certainly too small to generate runup of 38 m (Tappin et al. 2008). The recent Tohoku tsunami may also have had a landslide tsunami source contributing several meters of runup along the northern shore of Honshu at around 40° Latitude. In sum, there is a wide range in earthquake tsunami runup, and landslide tsunamis considerably increase both the complexity and range of tsunami runup. Watts (2001) proposed the proper context of tsunami warning is to identify the tsunami source. In general, there is a plethora of mature technologies for tsunami warning systems, water wave detection, earthquake detection, and landslide detection. These include ocean bottom seismographs, hydrophone arrays, hydrostatic pressure sensors, onshore GPS arrays, and water wave radars situated at the shoreline, among others. Each of these technologies has their merits, and working in tandem they would probably form a comprehensive and robust local tsunami warning system for NPPs. By identifying the tsunami source, detailed tsunami scenarios could be computed in advance, and specific response plans could be prepared in advance. By following the response plan, NPPs would resume operations shortly after the tsunami threat recedes.

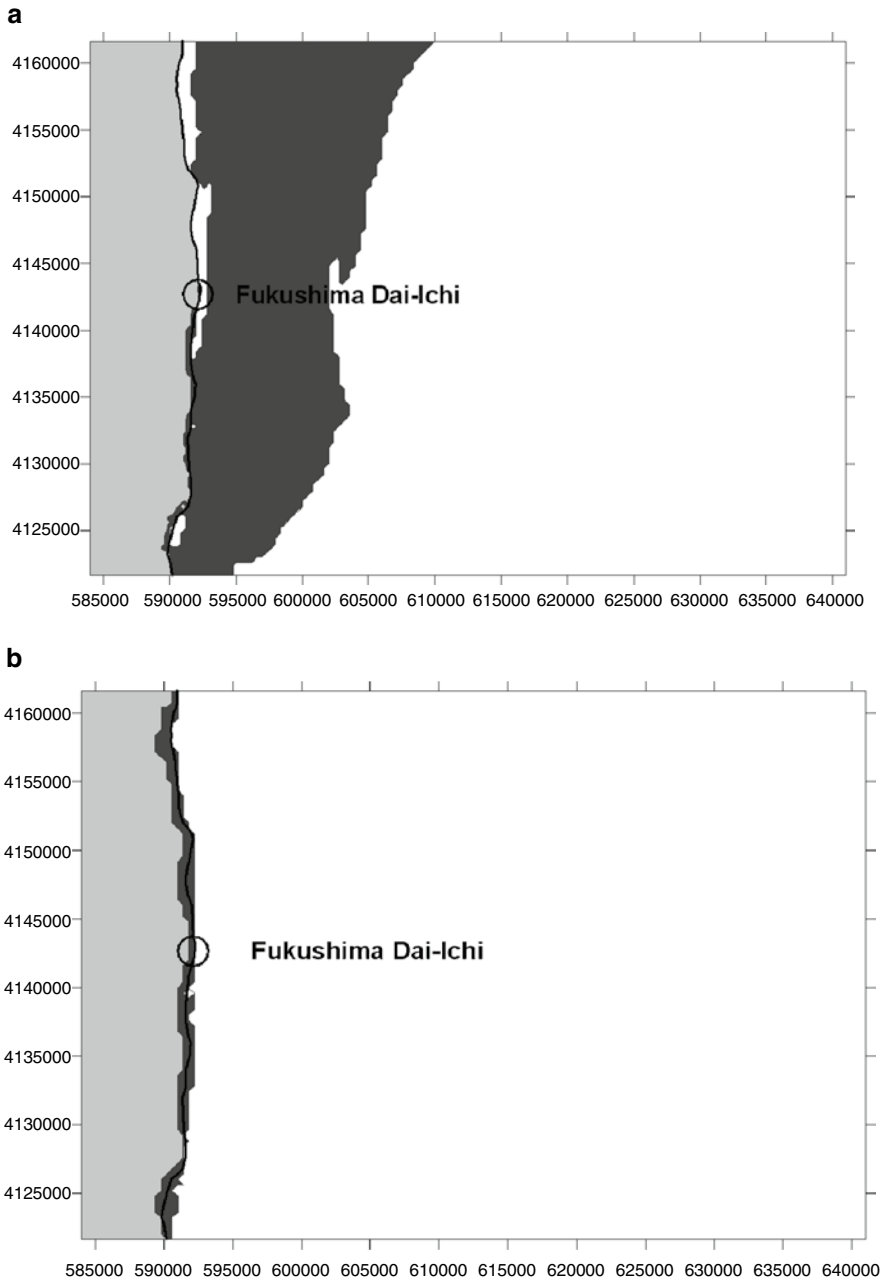

Fig. 47.3 Geowave simulation of the Tohoku tsunami using the Caltech tsunami source to provide (**a**) regions of fine sediment transport during tsunami attack, and (**b**) regions where people exposed to tsunami attack could not remain standing

47.6 Conclusions

It appears as if M = 9 or greater events deserve consideration for most tsunami hazard assessment studies. Landslide and volcanic tsunamis pose a similar hazard, and therefore deserve a place alongside the largest of earthquake tsunamis. A global perspective on tsunami hazards yields a list of some of the largest earthquake, mass failure, and volcanic events that should be considered as potential threats to NPPs. Tsunami hazard lessons yield defensible maximum threats. A probabilistic framework is provided by PTHA, which assigns probabilities to every possible tsunami. The advantage of PTHA is that it is an inclusive and impartial analysis that can reach comfortably to 50,000 year events and beyond. Careful comparisons should document variability among tsunami experts. Boussinesq and Navier-Stokes tsunami simulations enable much more sophisticated tsunami hazard maps. New designs for local tsunami warning systems are expected to provide direct knowledge of offshore tsunami sources. With these innovations in place, NPPs can expect to withstand tsunami attack and resume operations shortly thereafter.

Acknowledgments The author is grateful to Drs. Sladen and Simons for sharing the Caltech seismic source, to Ross Ridenoure for discussing the nuclear industry, to Rob Sewell for discussing uncertainty, and to Dr. David Mosher for handling the editorial process with grace and ease.

References

Baptista MA, Miranda JM, Chierici F, Zitellini N (2003) New study of the 1755 earthquake source based on multi-channel seismic survey data and tsunami modeling. Nat Haz Earth Syst Sci 3:333–340

Carey S, Morelli D, Sigurdsson H, Bronto S (2001) Tsunami deposits from major explosive eruptions: an example from the 1883 eruption of Krakatau. Geology 29:347–350

Dalrymple RA, Grilli ST, Kirby JT (2006) Tsunamis and challenges for accurate modeling. Oceanography 19(1):142–151

Day SJ, Watts P, Grilli ST, Kirby JT (2005) Mechanical models of the 1975 Kalapana, Hawaii earthquake and tsunami. Mar Geol 215(1–2):59–92

Eaton JP, Richter DH, Ault WU (1961) The tsunami of May 23, 1960, on the Island of Hawaii. Seismol Soc Am Bull 51(2):135–157

Favalli M, Boschi E, Mazzarini F, Pareschi MT (2009) Seismic and landslide source of the 1908 straits of Messina tsunami(Sicily, Italy). Geophys Res Lett 36:L16304. doi:10.1029/2009GL039135

Fryer GL, Watts P, Pratson LF (2004) Source of the great tsunami of 1 April 1946: a landslide in the upper Aleutian forearc. Mar Geol 203:201–218

Goldfinger C, Nelson CH, Johnson JE (2003) Deep-water turbidites as Holocene earthquake proxies: the Cascadia subduction zone and Northern San Andreas fault systems. Ann Geofisica 46:1169–1194

Greene HG, Murai LY, Watts P, Maher NA, Fisher MA, Paull CE, Eichhubl P (2006) Submarine landslides in the Santa Barbara channel as potential tsunami sources. Nat Haz Earth Sci Syst EGU 6:63–88

Grilli ST, Taylor O-DS, Baxter DP, Maretzki S (2009) Probabilistic approach for determining submarine landslide tsunami hazard along the upper East Coast of the United States. Mar Geol 264(1–2):74–97

Grossi P, Watts P, Boissonade A, Muir-Wood R (2008) Estimating losses from tsunami risk: focus on Southern California. In: Proceedings of the 14th world conference on earthquake engineering, Beijing

Hammack JL (1973) A note on tsunamis: their generation and propagation in an ocean of uniform depth. J Fluid Mech 60:769–799

Heezen BC, Ericsson DB, Ewing M (1954) Further evidence of a turbidity current following the 1929 Grand Banks earthquake. Deep Sea Res 1:193–202

Imamura F, Gica E, Takahashi T, Shuto N (1995) Numerical simulation of the 1992 Flores tsunami: interpretation of tsunami phenomena in northeastern Flores Island and damage at Babi Island. Pure Appl Geophys 144:555–568

Ioualalen M, Pelletier B, Watts P, Regnier M (2006) Numerical modeling of the 26th November 1999 Vanuatu tsunami. J Geophys Res 111(C6). doi:2005JC003249

Ioualalen M, Asavanant J, Kaewbanjak N, Grilli ST, Kirby JT, Watts P (2007) Modeling the 26 December 2004 Indian Ocean tsunami: case study of impact in Thailand. J Geophys Res 112:C07024. doi:2006JC003850

Kammerer AM, ten Brink US, Titov VV (2008) Overview of the U.S. Nuclear regulatory commission collaborative research program to assess tsunami hazard for nuclear power plants on the Atlantic and Gulf coasts. In: Proceedings of the 14th world conference on earthquake engineering, Beijing

Mattioli GS, Voight B, Linde AT, Watts P, Widiwijayanti C, Young SR, Elsworth D, Malin PE, Shalev E, Van Boskirk E, Johnston W, Sparks RSJ, Neuberg J, Bass V, Dunkley P, Herd R, Syers T, Williams P, Williams D (2007) Unique and remarkable dilatometer measurements of pyroclastic flow–generated tsunamis. Geology 35(1):25–28

McMurtry GM, Watts P, Fryer GJ, Smith JR, Imamura F (2004) Giant landslides, mega-tsunamis, and paleo-sea level in the Hawaiian Islands. Mar Geol 203:219–233

Mei CC (1983) The applied dynamics of ocean surface waves. World Scientific, Teaneck

Miller DJ (1960) Giant waves in Lituya Bay, Alaska. In: Professional paper 354-C, U.S. Geological survey. U.S., Department of Interior, Washington, DC

Plafker G, Kachadoorian R, Eckel EB, Mayo LR (1969) The Alaska earthquake March 27, 1964: various communities. U.S. Geological survey professional paper 542-G. U.S., Department of Interior, Washington, DC

Prasad, R, Cunningham E, Bagchi G (2009) Tsunami hazard assessment at nuclear power plant sites in the United States of America. Nuclear Regulatory Commission, NUREG/CR-6966, PNNL-17397

Rahiman TIH, Pettinga JR, Watts P (2007) The source mechanism and numerical modelling of the 1953 Suva tsunami, Fiji. Mar Geol 237(2):55–70

Satake K, Shimazaki K, Tsuji Y, Veda K (1996) Time and size of a giant earthquake in Cascadia inferred from Japanese tsunami record of January 1700. Nature 379:246–249

Sladen A, Tavera H, Simons M, Avouac JP, Konca AO, Perfettini H, Audin L, Fielding EJ, Ortega F, Cavagnoud R (2010) Source model of the 2007 *Mw* 8.0 Pisco, Peru earthquake: implications for seismogenic behavior of subduction megathrusts. J Geophys Res 115:B02405. doi:10.1029/2009JB006429

Striem HL, Miloh T (1976) Tsunamis induced by submarine slumpings off the coast of Israel. Int Hydrogr Rev 2:41–55

Syvitski JPM, Hutton EWH (2003) Failure of marine deposits and their redistribution by sediment gravity flows. Pure Appl Geophys PAGEOPH 160:2053–2069

Tappin DR, Watts P, McMurtry GM, Lafoy Y, Matsumoto T (2001) The Sissano, Papua New Guinea tsunami of July 1998 – offshore evidence on the source mechanism. Mar Geol 175:1–23

Tappin DR, Watts P, Grilli ST (2008) The Papua New Guinea tsunami of July 17, 1998: anatomy of a catastrophic event. Nat Haz Earth Syst Sci NHESS 8:243–266

Tinti S, Armigliato A (2003) The use of scenarios to evaluate the tsunami impact in southern Italy. Mar Geol 199:221–243

Walder JS, Watts P, Waythomas CF (2006) Mapping tsunami hazards associated with debris flow into a reservoir. J Hyd Eng ASCE 132(1):1–11

Watts P (2001) Some opportunities of the landslide tsunami hypothesis. Sci Tsunami Hazard 19(3):126–149

Watts P (2004) Probabilistic predictions of landslide tsunamis off Southern California. Mar Geol 203:281–301

Watts P, Grilli ST, Kirby JT, Fryer GJ, Tappin DR (2003) Landslide tsunami case studies using a Boussinesq model and a fully nonlinear tsunami generation model. Nat Haz Earth Sci Syst EGU 3(5):391–402

Waythomas CF, Watts P, Shi F, Kirby JT (2009) Pacific basin tsunami hazards associated with submarine mass flows in the Aleutian Islands of Alaska. Quat Sci Rev 28:1006–1019

Wilson RC, Keefer DK (1985) Predicting areal limits of earthquake-induced landsliding. In: Professional paper 1360, U.S. Geological survey. U.S., Department of Interior, Menlo Park

Wright SG, Rathje EM (2003) Triggering mechanisms of slope instability and their relationship to earthquakes and tsunamis. Pure Appl Geophys PAGEOPH 160:1865–1877

Part VII
Witnessing and Quasi-Witnessing of Slope Failures

Chapter 48
Submarine Slope Response to Earthquake Shaking Within Western Sagami Bay, Central Japan

Ken Ikehara, Juichiro Ashi, Hideaki Machiyama, and Masaaki Shirai

Abstract Earthquakes are a major trigger of submarine landslides. Strong ground shaking of the sea floor by an earthquake increases the sediment pore pressure and induces slope failure. As submarine landslides may generate tsunamis, it is important to understand the submarine slope response to earthquake ground shaking. Slope response may change spatially according to the strength of ground shaking and slope characteristics, such as submarine topography, gradient, sea bed materials, and sedimentation rate. For a better understanding of slope response, it is necessary to obtain data on changes to the sea floor following an earthquake. In 1997, 1998, and 2006, the JAMSTEC Hatsushima Deep-Sea Observatory recorded turbidity currents triggered by the Izu-toho-oki earthquake swarm (magnitude ~6) off Hatsushima Island in western Sagami Bay, Central Japan. In 2004, cores of undisturbed surface sediment were collected using a multiple corer at the foot of the submarine slope near the Observatory. No clear gravity-flow deposits (e.g., turbidites and debrites) were observed near the tops of the cores, indicating that earthquakes of magnitude ~6 have insufficient energy to generate clearly defined sandy

K. Ikehara (✉)
Geological Survey of Japan, AIST, Tsukuba Central 7, 1-1-1 Higashi,
Tsukuba, Ibaraki 305-8567, Japan
e-mail: k-ikehara@aist.go.jp

J. Ashi
Atmosphere and Ocean Research Institute, The University of Tokyo, 5-1-5 Kashiwanoha,
Kashiwa, Chiba 277-8564, Japan

H. Machiyama
Submarine Resources Research Project, JAMSTEC, 3173-25 Showa-machi, Kanazawa-ku,
Yokohama, 236-0001, Japan

M. Shirai
Tokyo Metropolitan University, 1-1 Minami-osawa, Hachioji, Tokyo 192-0397, Japan

Y. Yamada et al. (eds.), *Submarine Mass Movements and Their Consequences*,
Advances in Natural and Technological Hazards Research 31,
DOI 10.1007/978-94-007-2162-3_48, © Springer Science+Business Media B.V. 2012

turbidites on this slope. In contrast, several sandy turbidite layers are present in a piston core collected from a nearby site, suggesting that this site is affected by a larger magnitude of ground shaking than that produced by the Izu-toho-oki earthquakes. The most likely origin of this greater ground shaking is the Kanto earthquakes (magnitude ~8), the epicenter of which is located in the northwestern Sagami Trough.

Keywords Earthquake • Turbidity current • Slope failure • Turbidite

48.1 Introduction

Earthquakes are a major triggering mechanism of submarine slope failures. Strong ground motion of the sea floor caused by an earthquake results in increased pore pressure in sediments and reduced sediment strength, which lead in turn to slope failure. However, the degree of ground motion required to produce a slope failure is spatially variable, reflecting the influence of varying topographical and sedimentological characteristics such as slope angle, sediment grain size, and sediment thickness. It is necessary to understand how large earthquakes have the potential to produce large slope failures in a given location. Because a large submarine slope failure could produce a tsunami, knowledge of earthquake and slope-failure processes is important for the mitigation of natural hazards. Furthermore, such knowledge is important in deep-sea paleoseismology studies based on analyses of gravity flow deposits such as turbidites (e.g., Adams 1990; Goldfinger 2011). Therefore, it is crucial to examine the effects of recent earthquakes on the sea floor.

In this paper, we investigate the way in which large earthquakes produce sandy turbidite beds at the foot of a submarine slope in western Sagami Bay, Central Japan, where large plate-boundary-type Kanto earthquakes (magnitude (M_{JMA}) ~8) occur along with smaller Izu-toho-oki earthquake swarms (magnitude ~6). The data show that the swarms do not generate sandy turbidite deposits, although turbidity currents were observed.

48.2 Geological and Seismological Settings

The Sagami Trough (Fig. 48.1) marks the plate boundary between the Philippine and North American plates, beneath which the Pacific Plate is subducting. It has been inferred from tectonic geomorphology that large earthquakes have periodically occurred at this boundary (Sugimura and Naruse 1954, 1955; Matsuda et al. 1978; Nakata et al. 1980; Shishikura 1999, 2003; Shishikura et al. 2001), resulting in tsunamis and related sedimentary deposits at the Miura and Boso peninsulas (Fujiwara et al. 1997, 1999a, b). The most recent large earthquake along this boundary is the Taisho Kanto earthquake of magnitude 7.9, which occurred in 1923.

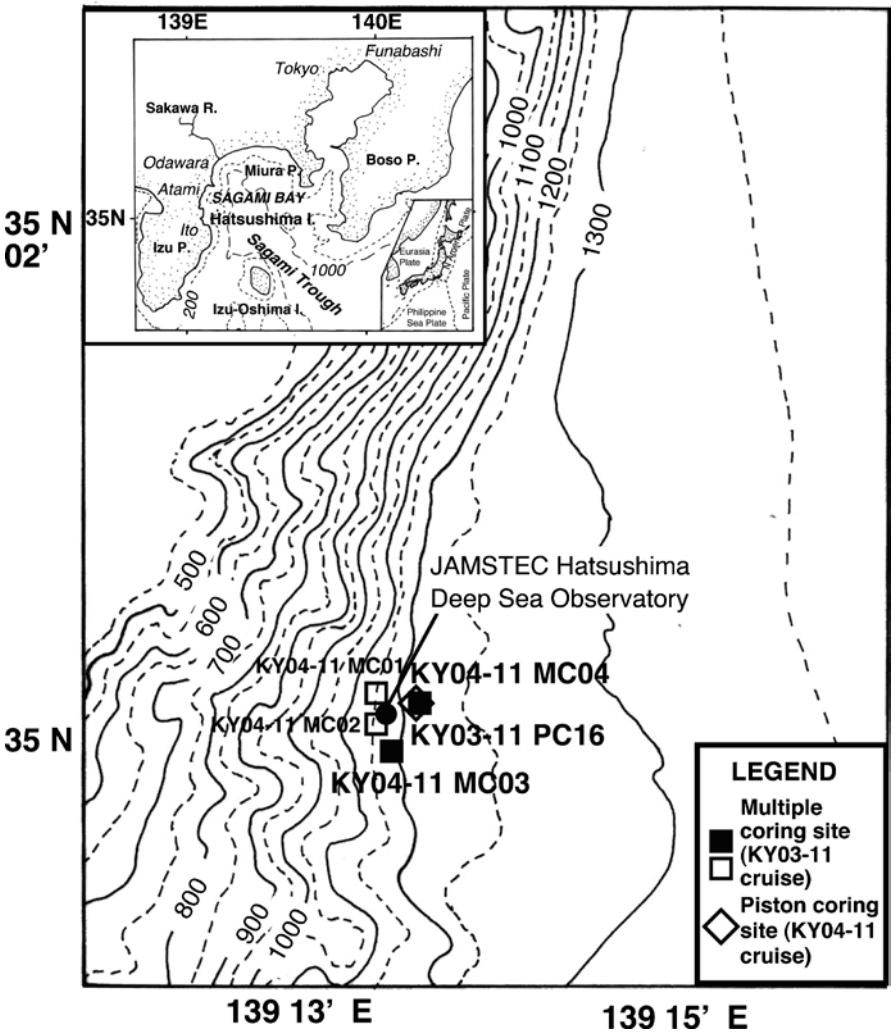

Fig. 48.1 Location and bathymetry of the study area

The Sagami Trough is a NW–SE-trending trough located in central Sagami Bay. The water depth in the trough deepens eastward. The trough becomes narrow south of the Boso Peninsula and changes to a submarine channel (the Boso submarine canyon) which reaches the triple junction of the three plates mentioned above. The Izu Peninsula, which represents the northernmost part of the Izu-Bonin arc, is located on the Philippine Plate and has collided with the Honshu arc.

The Sagami Bay region is characterized by a high level of tectonic activity. Active tectonism has created narrow shelves and steep submarine slopes around the bay. The basin contains thick deposits of Pliocene to early Pleistocene sediments,

and middle to late Pleistocene sediments of largely uniform thickness, except for some banks in the bay (Kimura 1976).

Submarine channels are developed on the northern and northeastern slopes of Sagami Bay, some of which are connected to major present-day rivers. However, there are no large rivers on the eastern Izu Peninsula, and no clear river-connected submarine channels and canyons on the western slope of the bay. The occurrence of small submarine fans near the exit of some of the submarine canyons (Kasaya et al. 2007) suggests gravitationally driven sediment supply through the canyons. Along the middle to upper slope of western Sagami Bay, acoustic basement is exposed, whereas the lower slope and basin floor are covered by the Quaternary Sagamiwan Group (Okamura et al. 1999).

Large interplate earthquakes, known as Kanto earthquakes, have occurred periodically along the Sagami Trough (e.g., Seno 1977). The epicenter of the 1923 Taisho Kanto earthquake was located in northwestern Sagami Bay. The magnitudes of the interplate earthquakes are ~8, which cause severe damage to the Tokyo metropolitan area. The other type of earthquake that occurs along the western slope of the bay is Izu-toho-oki earthquakes, which occur as swarms (magnitude ~6) that last for several months. Some earthquake swarms were accompanied by submarine volcanic activity, such as the 1989 and 1993 events.

Repeated turbidity currents triggered by earthquakes have been observed at the JAMSTEC Hatsushima Deep-Sea Observatory (JHDSO) (34°59.97′N, 139°13.69′E; water depth 1,177 m; Iwase et al. 1997, 1998; Kinoshita et al. 2006). In March 1997, April 1998, and April 2004, video footage recorded at JHDSO shows flows of turbid water with their velocities around 0.3 m/s following seismic events of the 1997, 1998, and 2004 Izu-toho-oki earthquake swarms (Iwase et al. 1997, 1998; Kinoshita et al. 2006). In addition, sudden changes in water temperature were recorded by a CTD mounted at JHDSO. These observations suggest that earthquakes triggered turbidity currents on the steep slope of western Sagami Bay. Fujioka et al. (1991) reported recent slope-failure deposits at the foot-of-slope near JHDSO caused by seismic and volcanic activity, including those associated with the Teishi Knoll submarine eruption in 1989.

48.3 Materials and Results

We collected two undisturbed surface-sediment samples (KY04-11 MC03: 35°00.09′N, 139°13.51′E, water depth 1,170 m; KY04-11 MC04: 35°00.17′N, 139°13.60′E, water depth 1,167 m) using a multiple corer during the KY04-11 cruise in 2004 near JHDSO (Fig.48.1). The MC03 and MC04 cores were 13.5 and 36.5 cm long, respectively, and were composed of homogeneous clayey silt without clearly defined sandy beds (Fig. 48.2).

Soft X-radiographs of the two cores show no clearly defined sandy layer and no erosional surface at the top of the cores (Fig. 48.2). The radiographs show a thin

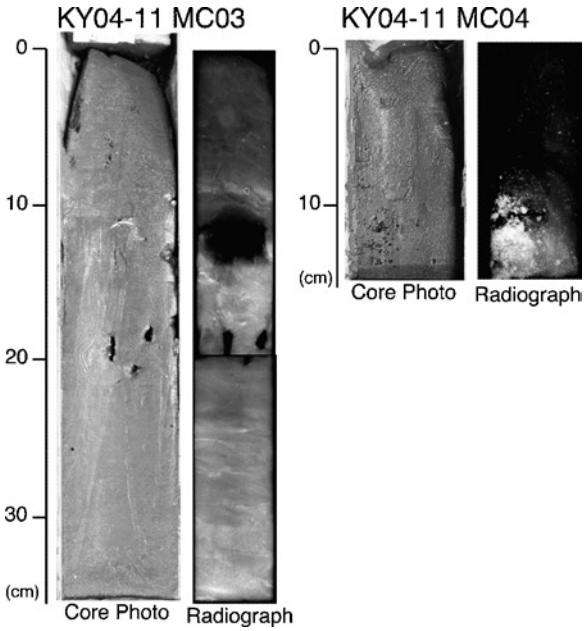

Fig. 48.2 Photographs and soft-X radiographs of the multiple corer samples

(0.5 cm thick) sand layer, including shell fragments, at 9 cm deep in MC03, and a coarse sand patch at 10–12 cm deep in MC04. Many sand grains are scattered throughout the muddy matrix of MC04. In contrast, layers of fine–medium sand with *Calyptogena* shell fragments (Fig. 48.3) occur in a piston core (KY03-11 PC16: 35°00.18′N, 139°13.58′E, water depth 1,201 m, total core length 340 cm) obtained from a site located close to MC04, slightly offshore (and offslope) from JHDSO. The base of sandy layers is clear and erosive (Fig. 48.3), and some of the sand layers contain upward-fining grading. These observations indicate that the sand layers are turbidites and that the sand grains may have been supplied from the submarine slope, which is the habitat for *Calyptogena*.

Radiocarbon age data for the KY03-11 PC16 core (2113 BC for the 159.5 cm deep horizon, 2590 BC for 198.5 cm deep horizon, 3717 BC for 297.5 cm deep horizon) indicate an average bulk sedimentation rate of 80–90 cm/ky, although the core-top sediments were not recovered during the piston coring. In contrast, the multiple corer is an excellent tool for collecting undisturbed surface sediments with an intact sediment–water interface (Barnett et al. 1984; Ikehara 1993). Thus, the MC03 (13.5 cm) and MC04 (36.5 cm) multiple cores preserved a sedimentary record dating back several hundred years from 2004. During the KY04-11 cruise, two additional, multiple core samples (KY04-11 MC01: 35°00.21′N, 139°13.47′E, water depth 1,171 m; KY04-11 MC02: 35°00.17′N, 139°13.47′E, water depth 1,173 m) were obtained near JHDSO. Although no detailed observations of these core samples were made, the surface samples (MC01, 10 cm long; MC02, 3.5 cm long) do not contain visually clear sand layers.

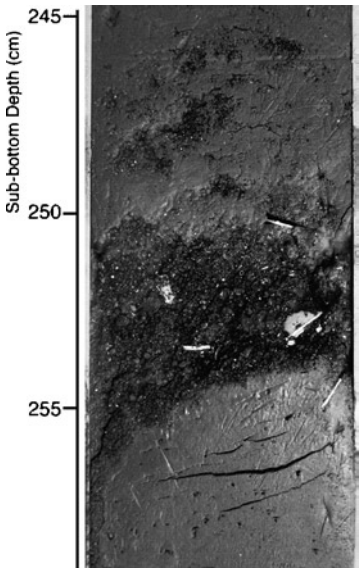

Fig. 48.3 Photograph of a sandy turbidite bed in core KY03-11 PC16. Note the erosional base of the sandy bed and the presence of Calyptogena shell fragments

48.4 Discussion

On the basis of the sedimentation rate (80–90 cm/ky) of hemipelagic mud at a nearby piston core KY03-11 PC16, the 1997 and 1998 earthquake swarms are inferred to have generated the sandy horizons near the top of the MC03 and MC04 cores. However, no sandy turbidites occur near the top of the cores, which may indicate that the turbidity currents of ~0.3 m/s (Iwase et al. 1997, 1998) created by the 1997 and 1998 Izu-toho-oki earthquake swarms did not have sufficient energy to produce sandy turbidite deposits. The lack of sand layers may also be explained by the destruction of thin sand layers by benthic activity after turbidite deposition. JHDSO is located at a site of cold-water seepage inhabited by benthic organisms such as *Calyptogena*. The high level of benthic activity at this site may disturb and deform the surface sediment. The MC03 and MC04 cores contain no sand patches and have low concentrations of sand grains near the core tops; sand grains remained in deeper sediments after bioturbation. Although coarse sand grains are found in MC04, the upward decrease in the concentration of sand grains, and the occurrence of a clear sand patch at 10–12 cm deep, suggests that sand grains were moved upwards from the sand patch horizon, which may originally have formed as a layer, but were not moved downward from the core top. Therefore, the effects of bioturbation cannot explain why sand layers from the 1997 to 1998 turbidity current events are missing in the MC03 and MC04 cores.

In contrast, clearly defined sandy turbidites are found in the piston core KY03-11 PC16 (Fig. 48.3). The site at which the piston core was recovered is located far from the fan delta slope of the Sakawa-gawa River (Fig. 48.1); thus, it is considered

unlikely that the sandy turbidites in the piston core originated from flood-related gravity flows. Given that core KY03-11 PC16 was collected from a site located farther offshore and downstream from JHDSO and from the MC03 and MC04 coring sites, the sandy turbidites in the piston core were probably formed by large turbidity currents that transported greater amounts of sand grains and *Calyptogena* shells than did the turbidity currents related to the Izu-toho-oki earthquake swarms (magnitude ~6).

Turbidite mud differs from hemipelagic mud in terms of grain size and composition, carbonate content, microfossil composition, grain fabric, sediment color, and X-ray attenuation (Rupke and Stanley 1974; O'Brien et al. 1980; Brunner and Ledbetter 1987; Krenmayr 1996). The absence of variations in grain size, sediment color (as observed by eye), and X-ray attenuation (Fig. 48.2) in the MC03 and MC04 cores suggests that no turbidite mud was deposited from the 1997 and 1998 seismic-related turbidity currents, or that very thin layers of turbidite mud were deposited but pervasively bioturbated. Thus, at this site, the preservation potential is low for turbidite deposits formed from muddy turbidity currents following slope failure induced by magnitude ~6 earthquakes. Considering the modern seismological setting of the western Sagami Bay, the sandy turbidites in core KY03-11 PC16 may have been triggered by the magnitude ~8 Kanto earthquakes.

48.5 Conclusion

We analyzed two undisturbed surface-sediment cores collected near JHDSO in western Sagami Bay, Central Japan. Sensors at JHDSO detected turbidity currents triggered by the Izu-toho-oki earthquake swarms. The JHDSO observations indicate that unconsolidated surface mud on a nearby slope would have slid and failed as a result of magnitude ~6 earthquakes. However, no sandy turbidites were observed at the top of multiple-corer cores, suggesting that turbidity currents of ~0.3 m/s (Iwase et al. 1997, 1998) created by the Izu-toho-oki earthquakes had insufficient energy to form sandy turbidites. Thus, the clearly defined sandy turbidite beds in a piston core collected from a site located farther from the slope may have formed in association with much larger earthquake events than the magnitude ~6 earthquakes, possibly magnitude ~8 Kanto earthquakes that occur in the northwestern region of Sagami Bay. Furthermore, the results indicate that not all of the turbidity currents triggered by seismic activity have been recorded in sediments as turbidite beds. To reconstruct the history of earthquake activity based on analyses of deep-sea turbidites, it is important to understand the details of how large earthquakes form turbidites in the specific area of interest.

Acknowledgments We express our thanks to chief scientists (Drs. Wonn Soh and Masataka Kinoshita of JAMSTEC), captains, crews and on-board scientists of KY03-11 and KY04-11 cruises. We also thank two reviewers, Drs. Yusuke Kubo and Osamu Fujiwara, for their constructive comments.

References

Adams J (1990) Paleoseismicity of the Cascade subduction zone: evidence from turbidites off the Oregon-Washington margin. Tectonics 9:569–583

Barnett PRO, Watson J, Connelly D (1984) A multiple corer for taking virtual undisturbed samples from shelf, bathyal and abyssal sediments. Oceanol Acta 7:399–408

Brunner CA, Ledbetter MT (1987) Sedimentological and micropaleontological detection of turbidite muds in hemipelagic sequences: an example from the late Pleistocene levee of Monterey Fan, central California continental margin. Mar Micropaleontol 12:223–239

Fujioka K, Gamo T, Kinoshita M, Koga K, Kaiho K, Yamano M, Tokuyama H (1991) Seismo-volcanic catastrophe happened in western Sagami Bay, central Japan –Results on R/V Tansei Maru KT89-11 cruise. J Phys Earth 39:267–297

Fujiwara O, Masuda F, Sakai T, Fuse K, Saito A (1997) Tsunami deposits in Holocene bay-floor muds and the uplift history of the Boso and Miura Peninsulas. Quat Res (Daiyonki-kenkyu) 36:73–86 (in Japanese with English abstract)

Fujiwara O, Masuda F, Sakai T, Irizuki T, Fuse K (1999a) Holocene tsunami deposits detected by drilling in drowned valleys of the Boso and Miura Peninsulas. Quat Res (Daiyonki-kenkyu) 38:41–58 (in Japanese with English abstract)

Fujiwara O, Masuda F, Sakai T, Irizuki T, Fuse K (1999b) Bay-floor deposits formed by great earthquakes during the past 10,000 yrs, near the Sagami Trough, Japan. Quat Res (Daiyonki-kenkyu) 38:489–501 (in Japanese with English abstract)

Goldfinger C (2011) Submarine paleoseismology based on turbidite records. Ann Rev Mar Sci 3:35–66

Ikehara K (1993) Multiple corer, a sampler for taking undisturbed surface sediments; for study on interaction between water and sediments. J Sediment Soc Jpn 39:85–89 (in Japanese)

Iwase R, Momma H, Kawaguchi K, Fujiwara N, Suzuki S, Mitsuzawa M (1997) Turbidity currents on the deep seafloor triggered by the earthquake swarm in the east off Izu Peninsula in March 1997 –observation by the long-term deep seafloor observatory off Hatsushima Island in Sagami Bay. JAMSTEC J Deep Sea Res 13:433–442 (in Japanese with English abstract)

Iwase R, Mitsuzawa M, Momma H (1998) Mudflow associated with the swarm earthquakes east off Izu Peninsula in April 1998, observed by the long-term deep sea floor observatory off Hatsushima Island in Sagami Bay. JAMSTEC J Deep Sea Res 14:301–317 (in Japanese with English abstract)

Kasaya T, Tukioka S, Yamamoto F, Hyakudome T, Sawa T, Yoshida H, Ishibashi S, Tahara J, Kinoshita M, Aoki T (2007) Acoustic images of submarine landslide in western Sagami Bay obtained by deep sea AUV "Urashima" in Sagami Bay. J Jpn Soc Mar Surv Tech 19:11–17 (in Japanese with English abstract)

Kimura M (1976) Submarine geological map of Sagami-nada Sea and its vicinity. Marine geology map series no. 3. Geological Survey of Japan, Tsukuba

Kinoshita M, Kasaya T, Goto T, Asakawa K, Iwase R, Mitsuzawa M (2006) Seafloor landslide off Hatsushima, western Sagami Bay induced by east off Izu Peninsula earthquake. J Jpn Landslide Soc 43:41–43 (in Japanese)

Krenmayr HG (1996) Hemipelagic and turbiditic mudstone facies associations in the Upper Cretaceous Gosau Group of the Northern Calcareous Alps (Austria). Sediment Geol 101:149–172

Matsuda T, Ota Y, Ando M, Yonekura N (1978) Fault mechanism and recurrence time of major earthquakes in southern Kanto district, Japan, as deduced from coastal terrace data. Geol Soc Am Bull 89:1610–1618

Nakata T, Koba M, Imaizumi T, Jo WR, Matsumoto H, Suganuma T (1980) Holocene marine terraces and seismic crustal movements in the southern part of Boso Peninsula, Kanto, Japan. Geogr Rev Jpn 53–1:29–44 (in Japanese with English abstract)

O'Brien NR, Nakazawa K, Tokuhashi S (1980) Use of clay fabric to distinguish turbiditic and hemipelagic siltstones and silts. Sedimentology 27:47–61

Okamura Y, Yuasa M, Kuramoto S (1999) Geological map of Suruga Bay. Marine geology map series no. 52. Geological Survey of Japan, Tsukuba

Rupke NA, Stanley DJ (1974) Distinctive properties of turbiditic and hemipelagic mud layers in the Algero-Balearic Basin, western Mediterranean Sea. Smithsonian Contrib Earth Sci 13:1–40

Seno T (1977) Recurrence time intervals of great earthquakes in the Sagami Trough region, Japan, as deduced from vertical crustal movement. Zishin 30:253–264 (in Japanese with English abstract)

Shishikura M (1999) Holocene marine terraces and seismic crustal movements in Hota Lowland in the southern part of Boso Peninsula, central Japan. Quat Res (Daiyonki-kenkyu) 38:17–28 (in Japanese with English abstract)

Shishikura M (2003) Cycle of interplate earthquake along the Sagami Trough, deduced from tectonic geomorphology. Bull Earthq Res Inst Univ Tokyo 78:245–254 (in Japanese with English abstract)

Shishikura M, Haraguchi T, Miyauchi T (2001) Timing and recurrence interval of the Taisho-type Kanto Earthquake, analyzing Holocene emerged shoreline topography in the Iwai Lowland, the southwestern Boso Peninsula, central Japan. Zishin 53:357–372 (in Japanese with English abstract)

Sugimura A, Naruse Y (1954) Changes in sea level, seismic upheavals, and coastal terraces in the southern Kanto region, Japan. (I). Jpn J Geol Geogr 24:101–113

Sugimura A, Naruse Y (1955) Changes in sea level, seismic upheavals, and coastal terraces in the southern Kanto region, Japan. (II). Jpn J Geol Geogr 26:165–176

Chapter 49
Discovery of Submarine Landslide Evidence Due to the 2009 Suruga Bay Earthquake

Hiroyuki Matsumoto, Toshitaka Baba, Kazuhiko Kashiwase, Toshiro Misu, and Yoshiyuki Kaneda

Abstract On August 11, 2009, at 05:07 JST, a moderate-to-large earthquake took place in the Suruga Bay of central Japan. It struck two deep-sea water pipes in the source area. Immediately after the event, both the temperature and the turbidity of the waters increased significantly. Surveys carried out in the source area revealed the level of damage to the water pipes. In this study, we report on the results of the visual survey performed by the remotely operated vehicle *Hyper-Dolphin* and the bathymetric data collected by the research vessel *Natsushima*. We found that one water pipe was moved at least 2 km downstream from its original location. The bathymetries obtained before and after the earthquake identified two types of geomorphologic features related to submarine landslide in the approximately 20 km^2 region. One of the features consists of extensive deepening and shallowing patterns newly created in the source area, suggesting mass slide traces processed during the earthquake. The other feature consists of a slide scar, slide blocks, and slope failures created locally in the upstream direction of the water pipe. This latter feature is evidence that mass slide took place and eventually moved the water pipe during the Suruga Bay earthquake.

Keywords Mass slide • Suruga Bay earthquake • Water pipe • Bathymetry

H. Matsumoto (✉) • T. Baba • K. Kashiwase • Y. Kaneda
Earthquake and Tsunami Research Project for Disaster Prevention, Japan Marine-Earth Science and Technology, 2-15, Natsushima, Yokosuka 237-0061, Japan
e-mail: hmatsumoto@jamstec.go.jp; babat@jamstec.go.jp

T. Misu
Shizuoka Prefecture, 9-6, Ohtemachi, Aoi-ku, Shizuoka 420-6801, Japan

Y. Yamada et al. (eds.), *Submarine Mass Movements and Their Consequences*, Advances in Natural and Technological Hazards Research 31,
DOI 10.1007/978-94-007-2162-3_49, © Springer Science+Business Media B.V. 2012

49.1 Introduction

On August 11, 2009 at 05:07 JST, a moderate-to-large earthquake took place in the Suruga Bay of central Japan. The moment magnitude of the earthquake was 6.4 and the hypocenter depth was 23 km. According to the preliminary report from the Japan Metrological Agency (JMA 2009), maximum seismic intensity reached VI-lower in several cities surrounding the Suruga Bay in Shizuoka Prefecture, including Izu, Yaizu, Makinohara, and Omaezaki. This earthquake will be referred to hereafter as the Suruga Bay earthquake. JMA issued the initial information on a possible large earthquake, namely the Tokai earthquake, immediately after the Suruga Bay earthquake. This report was prepared because it is generally believed that the Tokai segment of the plate boundary has not released its stress since the Tokai earthquake of 1854 (Ando 1975). The mechanism of the Suruga Bay earthquake was a thrust-fault type with a NNE-SSW lateral component (Fig. 49.1). It was a typical intraplate earthquake, with the hypocenter located in the subducting Philippine Sea plate. The hypocenters of the Suruga Bay earthquake sequences, i.e., the main shock and aftershock activities, imply that the fault plate extended 20 km × 20 km. As for the aftershocks' distribution after precise hypocenter relocation analysis, Aoi et al. (2010)

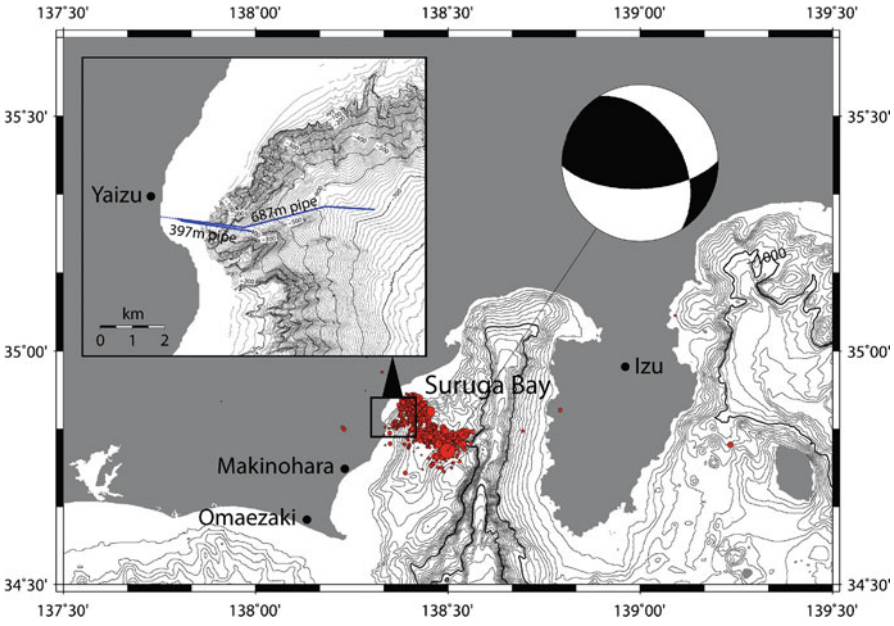

Fig. 49.1 Regional map of the Tokai area in Japan showing the epicenter and the focal mechanism of the earthquake that took place on August 11, 2009, as well as the distribution of the aftershocks that occurred over the following 24 h. The inset shows the location of two deep-sea water pipes in the Suruga Bay

suggested that there are two segments of aftershocks, indicating that the sequence occurred along two faults.

The Suruga Bay earthquake caused disastrous damage in the near-source area. The embankment of the Tomei highway collapsed in Makinohara city, side-floating occurred in the fishing port and harbor, and there was liquefaction at the Yaizu port due to the earthquake shaking (Shizuoka Prefecture 2009). A deep-sea water plant operated by Shizuoka Prefecture was located in the source area of the Suruga Bay earthquake. Abrupt changes in the quality of the deep-sea water were observed immediately after the earthquake. We postulated that something happened to the water pipes under the ocean. Four months after the earthquake, Japan Agency for Marine-Earth Science and Technology (JAMSTEC) launched a series of surveys in the near-source area of the Suruga Bay earthquake; three surveys were carried out by March 2010. The first survey was performed to observe the water pipes, the second was carried out to collect multibeam bathymetry data after the earthquake, and the final survey was performed to obtain a high-resolution bathymetric map using an autonomous underwater vehicle. The preliminary results of the first two surveys were reported by Matsumoto et al. (2010), and the results of the final survey were reported by Baba et al. (2012). This paper makes inferences based on the current water pipes' status and the multi-beam bathymetric data processing to provide additional interpretations of what happened under the ocean during the Suruga Bay earthquake.

49.2 Suruga Bay Deep-Sea Water Facility

Shizuoka prefecture has been operating a deep-sea water plant facility off Yaizu city since 2001 using two different layered deep-sea water pipes (Fig. 49.1). The shallow and deep water pipes are at depths of 397 and 687 m, respectively. Two water pipes have been deployed from Yaizu port parallel to the eastward direction. The shallow and deep water pipes are 3.3 and 7.3 km long, respectively. We call the 397 m pipe the short pipe and the 687 m pipe the long pipe. The water pipes are seamless and made with high-density polyethylene (HDPE) armored by steel wire. Although the diameters of the two pipes are slightly different, i.e., 240 and 270 mm, the tensile breaking strength is about 1,500 kN for the both pipes. A sluice gate attached by a 7.5-m-high truss scaffold is deployed at the end of both water pipes. The mouth of each water pipe is directed upward to enable clearer suction of the deep-sea water (See the next section).

The temperature and turbidity of the deep-sea water are measured instrumentally once a day at the water pipes' landing station. Figure 49.2 shows the time histories of the deep-sea water's temperature and turbidity in August 2009. Figure 49.2a displays the water temperatures, which are indicated as 9°C and 7°C for the 397 and 687 m waters, respectively, before the Suruga Bay earthquake. After the earthquake, however, the temperature obviously increased once by 7°C, and the high temperature

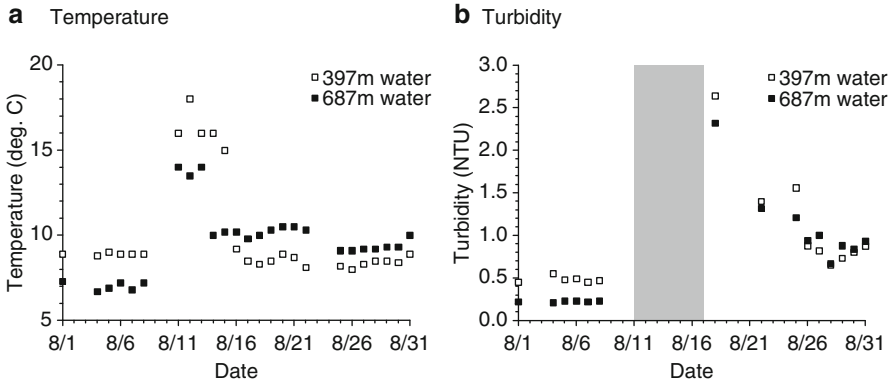

Fig. 49.2 Time histories of the deep-sea water in August 2009 with regard to (**a**) temperature and (**b**) turbidity. Note that turbidity data were saturated during the shaded period

was experienced for a few days. On 16 August, the temperature of the 397 m water returned to its original level, but that of the 687 m water was still 9°C. Although the temperature of the deep 687 m water must be lower than the shallow 397 m water, a thermal reverse occurred after the Suruga Bay earthquake.

On the other hand, the normal turbidities measured by the turbidity meter (2100P, HACH Co.) are 0.2 NTU (Nephelometric Turbidity Unit) and 0.5 NTU for 397 and 687 m water, respectively (Fig. 49.2b). However, after the Suruga Bay earthquake, the turbidities saturated the dynamic range for a week and then decreased gradually.

Furthermore, regional fishermen reported that fishnets were often captured by the bottom basement gap after the earthquake. The continuous increases in temperature and turbidity in the 687 m deep-sea water, as well as the fishermen's eyewitness accounts, imply that the long pipe was broken by the earthquake shaking or the crustal deformation.

49.3 Survey of the Earthquake Source Area

49.3.1 Overview

JAMSTEC carried out surveys in 2009 using the research vessel *Natsushima* to understand what occurred in the near-source area during the Suruga Bay earthquake. The first survey was designed to carry out a visual survey of two water pipes using the remotely operated vehicle (ROV) *Hyper-Dolphin*, and the following survey was performed to collect bathymetric data using the multibeam echo sounder system on the *Natsushima*.

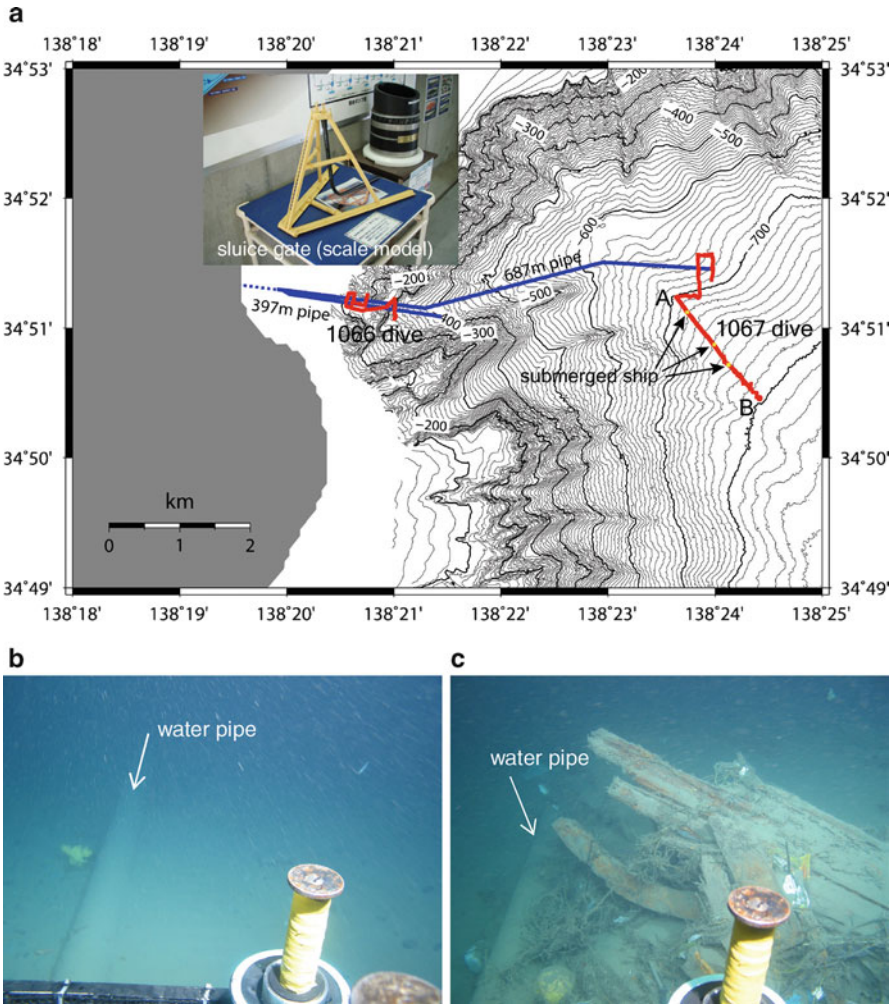

Fig. 49.3 (**a**) Two *Hyper-Dolphin* dive tracks and the location of the water pipes with a sluice gate scale model (**b**) Current status of the long pipe near location *A* (**c**) Submerged ship found at the long pipe. Both views are from upstream to downstream

49.3.2 Visual Survey by Hyper-Dolphin

Since we believed that the long pipe suffered severe damage, as mentioned in the previous section, two *Hyper-Dolphin* dives were carried out to reveal the location at which this damage occurred and the current status of the water pipes. We plotted the *Hyper Dolphin* tracks in Fig. 49.3a.

The first dive, i.e., the 1066 dive, was carried up to a depth of 200–300 m. This is because the temperature of the deep-sea water from the long pipe is still higher

than that from the short pipe after the Suruga Bay earthquake. We could find only one pipe at the bottom surface, suggesting the other pipe has been either moved away or been buried under the bottom.

The second dive, i.e., the 1067 dive, was carried out to find the sluice gate at the end of the long pipe (Fig. 49.3a). However, neither the water pipe nor the sluiced gate was found in the original location, but the long pipe was discovered at the location denoted by A in Fig. 49.3a, which was 500 m south of the original location. After discovering the long pipe, *Hyper-Dolphin* followed the long pipe toward the SE direction, i.e., downstream of the slope. Quite a thick layer of sediment was deposited on the SW side of the long pipe at the location where it was discovered by *Hyper-Dolphin* (Fig. 49.3b). On the way, we also found some wreckage of a submerged ship whose debris had covered the long pipe (Fig. 49.3c). As *Hyper-Dolphin* proceeded farther offshore, the long pipe was buried and exposed at water depth of about 750 m. Because the long pipe has been buried completely, we ultimately could not see it at a depth of 782 m, denoted by B in Fig. 49.3a. The section between A and B in Fig. 49.3a is the current long pipe location, but the NW end of the long pipe is still uninvestigated. After the visual survey by *Hyper-Dolphin*, we realized that the long pipe had been moved at least 2 km downstream from its original location due to the external massive force, i.e., the submarine landslide.

49.3.3 Bathymetric Survey by Natsushima

Bathymetry mapping is an efficient procedure for providing information on the occurrence and location of slope failures and scar heights. A bathymetric survey using the multibeam echo sounder system (SeaBat 8160, Reson Inc.) on the *Natsushima* was performed after the visual survey to locate and characterize submarine landslide.

The present multibeam bathymetric survey covers the source area of the Suruga Bay earthquake of approximately 400 km^2 (Fig. 49.4a). It was previously known that many small ridges (or gullies) formed at the western continental slope of Suruga Bay (Otsuka 1982). The water pipes have been laid along one of these gullies. Focusing on the original long pipe location, a slide scar with related slide blocks can be recognized in the area of 34°52′N in latitude and 138°23′E in longitude, approximately 1 km upstream from the original long pipe location. This scar is one of the submarine slide candidates displaced during the Suruga Bay earthquake because it is the nearest geomorphologic feature from the original long pipe location.

The multibeam echo sounder system of the *Natsushima* can simultaneously collect side-scan backscatter data (Fig. 49.4b). Strong intensity spots with diameters of a few tens of meters can be recognized along a submarine canyon in the northeastern part of the survey area, suggesting the presence of coarse-grained materials. It is likely that a large number of sand boils would be formed by liquefaction of underlying sand that was transported through the canyon and covered by surface mud. This

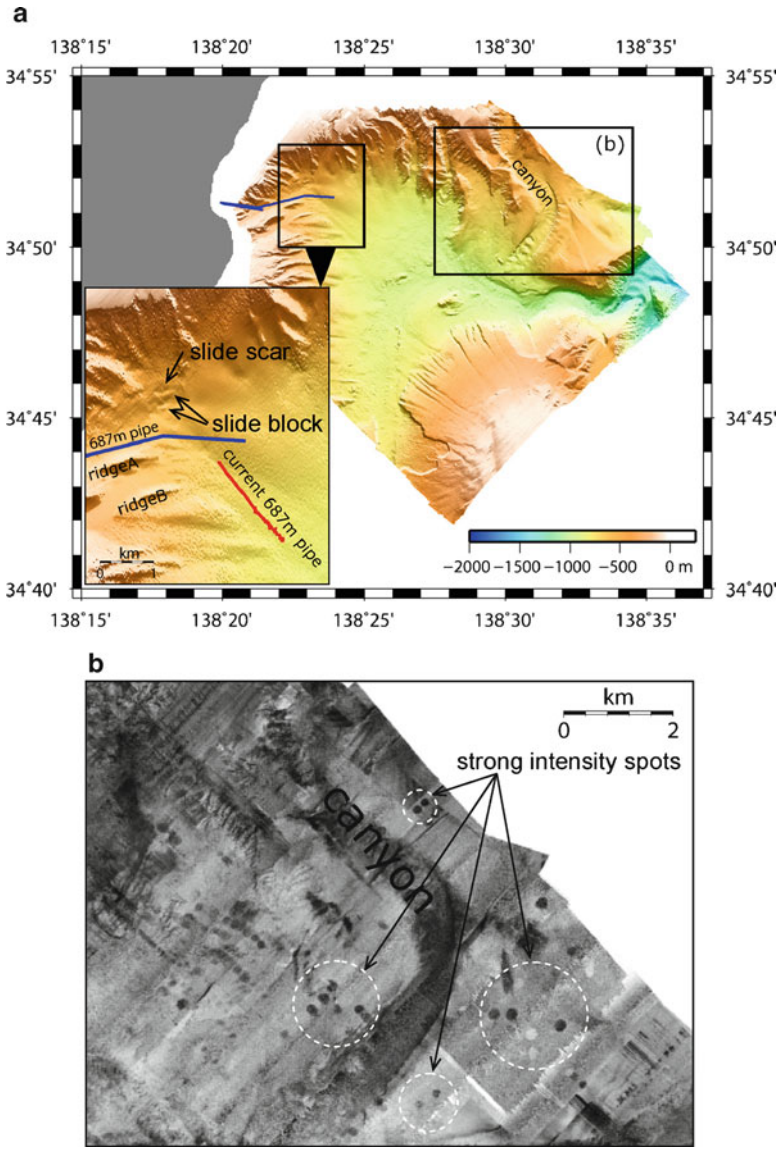

Fig. 49.4 (**a**) Multi-beam bathymetry obtained by *Natsushima* covering the earthquake source area in the Suruga Bay together with an enlarged view of the original and current water pipe locations superimposing the geomorphic features (**b**) Side-scan backscatter image clipped partly of the survey area

indicates that strong ground motion by the earthquake might result in liquefaction near the epicenter. Similar circular features were discovered at the river delta, 60 km northeast of the epicenter of the M7.0 earthquake that occurred in northern California in 1980; these were interpreted to be sand boils (Field et al. 1982).

49.4 Discussion and Implications

49.4.1 Submarine Landslide Source

The simplest way to understand where a submarine landslide occurs is to compare bathymetry data before and after the event. In 2004 and 2006, i.e., before the earthquake, *Natsushima* collected bathymetric data using the same equipment, which makes it possible for us to compare the bathymetries' data collected before and after the Suruga Bay earthquake. It should be noted that the bathymetry data collected before the earthquake do not have adequate resolution because the vessel's speed was relatively high. In addition, considerable co-seismic deformation due to seismic faulting had been created in the survey area. We neglect such factors in our data acquisition and processing. The difference between bathymetry data before and after the Suruga Bay earthquake has been calculated, and its focus on the visual survey area is shown in Fig. 49.5a, in which both the original and the current long pipe locations are displayed. This resulted in an extensive deepening pattern newly created in the survey area, which indicated that the continental slope has been reworked widely. On the other hand, a shallowing pattern was created downstream of the current water pipe location (Fig. 49.5a). In fact, the long pipe was buried periodically and ultimately fully buried by the sediment at the end of the visual survey. Both the translational and the depositional processes due to the mass slide occurred in the approximately 20 km^2 region. Although submarine landslide even on the 0.25° slope has been reported in the past (Field et al. 1982), in the Suruga Bay case, a mass slide took place on the 4° slope. Thus, we have revealed a full-scale scenario in which a mass slide has taken place and finally mixed the long pipe during the Suruga Bay earthquake.

Along the upstream direction of a gully on which the long pipe has been relocated, a large deepening spot can be recognized at the terrace of 34°52′N in latitude and 138°23′E in longitude, where the slide scar was discovered by the bathymetric survey. This distinct deepening spot is associated with the slide scar displaced during the Suruga Bay earthquake. Figure 49.5b, c show the depth profiles along the intersecting lines (b) and (c), respectively, in which bathymetries before and after the Suruga Bay earthquake are compared. A possible slide scar and related slide block are indicated in Fig. 49.5b, c, and its scale is 10 m high and 300 m wide at most. Another survey focusing on micro-bathymetry mapping by the autonomous underwater vehicle *Urashima* (Baba et al. 2012) also discovered the slide scar at the same location.

According to the visual survey results, quite a thick layer of the sediment has been deposited on the SW side of the long pipe (Fig. 49.3b). Because steep slopes on the small ridges, e.g., ridges A and B in Figs. 49.4a and 49.5a, have obviously resulted in deepening patterns after the earthquake, the slopes might collapse and involve gravity flow; and it might be ultimately banked up by the long pipe and deposited on the SW side of the long pipe relocated in advance.

Many factors have been suggested as probable or possible contributors to the initiation of submarine landslide (e.g., Masson et al. 2006). However, the present observation in the Suruga Bay indicated that several submarine slope failures

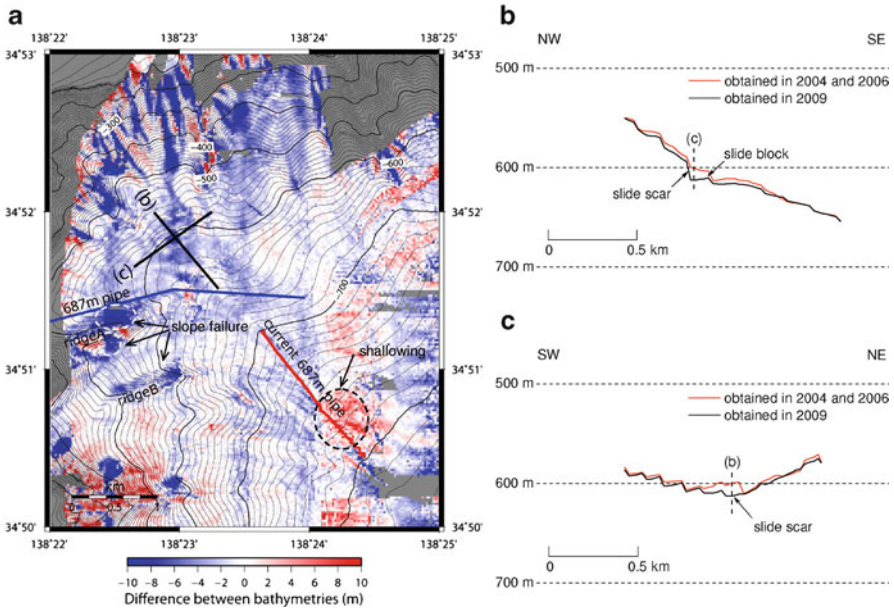

Fig. 49.5 (**a**) Difference between bathymetries obtained before and after the Suruga Bay earthquake with the current 687 m water pipe location mapped by *Hyper-Dolphin*. Two depth profiles obtained from the multibeam by *Natsushima* are compared (**b**) normal and (**c**) parallel to the slope, in which *red* and *black* lines represent before (2004 and 2006) and after (the present survey) the Suruga Bay earthquake, respectively. A possible slide scar is indicated in the profiles

occurred in the source area. Strong ground motion followed by subsurface liquefaction suggested by the presence of sand boils might significantly affect slope instability in the Suruga Bay.

49.4.2 Other Relevant Phenomena

It is worthwhile to note that the submarine cable deployed in the Suruga Trough, approximately 100 km south of the Suruga Bay earthquake source, was also damaged after 15 h and 52 min of the earthquake origin time. Similar phenomena have been reported during the recent 2006 Pingtung earthquake in Taiwan (Hsu et al. 2008). Gravity flow might reach there, and its averaged velocity was 1.8 m/s assuming the origin was immediately after the earthquake. This estimated speed is very low compared to the other turbidity current velocities experienced in the submarine cable breaks in the past. For example, Heezen and Ewing (1952) and Hsu et al. (2008) estimated the gravity flow's speed to be 6 m/s in the deep abyssal plain for the 1929 Grand Banks earthquake and 3.7 m/s even in the lower slope for the 2006 Pingtung earthquake, respectively. If the gravity flow actually reached 100 km south of the source, we should consider another possibility that might occur not immediately after the earthquake but some time afterward.

49.5 Conclusion

The Suruga Bay earthquake caused severe damage to the deep-sea water pipes deployed in the source area. For a deeper understanding of how the deep-sea water pipes were damaged, two surveys were carried out by the end of 2009. The present survey results are conclusively summarized as follows:

1. The long pipe was moved at least 2 km downstream due to mass slide from the original location during the Suruga Bay earthquake, and the downstream end of the current water pipe has been fully buried by the sediment.
2. Bathymetry data obtained in the present survey have revealed that a deepening pattern has appeared after the earthquake, while a slide scar has been locally created 1 km north of the original long pipe location. Slope collapse also might take place on the small ridges generating gravity flow and reach the current water pipe location with respect to the sediment deviation of the water pipe.
3. A large number of sand boils are identified along the submarine canyon near the epicenter, suggesting that liquefaction occurred due to the strong ground motion.

Thus, it has been shown that mass slide and gravity flow due to slope failures took place and finally mixed the long pipe during the Suruga Bay earthquake. However, the full extent of the damage to the deep-sea water pipes has not been revealed; in particular, the break position of the long pipe has not been identified. Further surveys and qualitative studies of the Suruga Bay case are necessary in the near-source area. The water pipe break that occurred as a result of the Suruga Bay earthquake shows the need to assess the massive slide with regard to other underwater infrastructures, such as submarine cables, pipe lines, submarine observatories, and so on.

Acknowledgments We would like to thank Hitoshi Hotta, executive director of JAMSTEC, for his help in carrying out this series of surveys. The fruitful discussion with Toshiya Kanamatsu was helpful in the present study. Ken Ikehara, Kohsaku Arai, and Oldrich Hungr kindly provided technical comments and scientific suggestions regarding submarine landslide to improve the manuscript. Some figures were prepared using GMT software (Wessel and Smith 1995).

References

Ando M (1975) Source mechanisms and tectonic significance of historical earthquakes along the Nankai trough, Japan. Techtonophysics 27:119–140

Aoi S, Enescu B, Suzuki W, Asano Y, Obara K, Kunugi T, Shiomi K (2010) Stress transfer in the Tokai subduction zone from the 2009 Suruga Bay earthquake in Japan. Nat Geosci 3:496–500

Baba T, Matsumoto H, Kashiwase K, Hyakudome T, Kaneda Y, Sano M (2012) Micro-bathymetric evidence for the effect of submarine mass movement on tsunami generation during the 2009 Suruga earthquake, Japan. In Yamada Y et al (eds) Submarine mass movements and their consequences, vol. 31, Advances in natural and technological hazards research. Springer, Dordrecht, pp 485–495

Field ME, Gardner JV, Jennings AE, Edwards BD (1982) Earthquake-induced sediment failures on a 0.25° slope, Klamath River delta, California. Geology 10:542–546

Heezen BC, Ewing M (1952) Turbidity currents and submarine slumps, and the 1929 Grand Banks earthquake. Am J Sci 250:849–873

Hsu SK, Kuo J, Lo CL, Tsai CH, Doo WB, Ku CY, Sibuet JC (2008) Turbidity currents, submarine landslide and the 2006 Pingtung earthquake off SW Taiwan. Terrest Atmos Ocean Sci 19:767–772. doi:103319/TAO.2008.19.6.767(PT)

Japan Meteorological Agency (2009) Earthquake in the Suruga Bay on August 11, 2009. In Japan Meteorological Agency Monthly report on earthquake and volcanoes in Japan, August 2009. Japan Meterological Agency, Tokyo, pp 42–67 (in Japanese)

Masson DG, Harbitz CB, Wynn RB, Pedersen G, Lovholt F (2006) Submarine landslides: process, triggers, and hazard prediction. Philos Trans R Soc A 364:2009–2039. doi:10.1098/rsta.2006.1810

Matsumoto H, Baba T, Kashiwase K, Kaneda Y, Misu T, Hori T (2010) Damage of deep water pipes due to the Suruga Bay earthquake on 11 August, 2009. J Jpn Soc Civ Eng Ser B2 (Coastal Eng) 66:1341–1345 (in Japanese)

Otsuka K (1982) Submarine sediment slide found on the west slope of the Senoumi-tai North Bank in western Suruga Bay, central Honshu, Japan. Geosci Rep Shizuoka Univ 7:87–95 (in Japanese)

Shizuoka Prefecture (2009) Report of the Suruga Bay earthquake No.4. Shizuoka Prefecture, Shizuoka, 7pp (in Japanese)

Wessel P, Smith WHF (1995) New version of the generic mapping tools released. EOS Trans AGU 76:329

Chapter 50
Settling of Earthquake-Induced Turbidity on the Accretionary Prism Slope of the Central Nankai Subduction Zone

Juichiro Ashi, Ken Ikehara, Masataka Kinoshita, and KY04-11 and KH-10-3 shipboard scientists

Abstract Studied of turbidite deposits can provide valuable paleoseismological information, such as earthquake recurrence intervals. However, there are few studies based on in situ observations of gravity flows during or soon after earthquakes. We used a remotely operated vehicle in dive surveys near the epicenters of the 2004 off the Kii Peninsula earthquakes (maximum magnitude 7.4) soon after and 6 years after the events. Video observations 20 days after the main shock revealed two turbid layers exhibiting different degrees of turbidity: a dilute suspension layer (DSL) and a bottom turbid layer (BTL). Pervasive distributions of DSL on the prism slope suggest that clouds of suspended sediments were induced by sliding, slumping, seafloor shaking, or sediment gravity flow at multiple locations during the earthquakes. BTL is a highly turbid layer of around 2.4 m thickness, the upper surface of which is sharply defined. That BTL was observed only in a slope basin implies that it was formed by a sediment gravity flow dumping muddy deposits in a depression. Our dive observations revealed that seafloor disturbance by seismic shaking plays a significant role in sediment redistribution in subduction zones.

Keywords Gravity flow • Suspension cloud • Slump • Sliding • Slope basin

J. Ashi (✉)
Atmosphere and Ocean Research Institute, The University of Tokyo, 5-1-5 Kashiwanoha, Kashiwa, Chiba 277-8564, Japan
e-mail: ashi@aori.u-tokyo.ac.jp

K. Ikehara
Geological Survey of Japan, AIST, Tsukuba Central 7, 1-1-1 Higashi, Tsukuba, Ibaraki 305-8567, Japan
e-mail: k-ikehara@aist.go.jp

M. Kinoshita
IFREE, JAMSTEC, 2-15 Natsushima, Yokosuka, Kanagawa 273-0061, Japan
e-mail: masa@jamstec.go.jp

Y. Yamada et al. (eds.), *Submarine Mass Movements and Their Consequences*, Advances in Natural and Technological Hazards Research 31,
DOI 10.1007/978-94-007-2162-3_50,

50.1 Introduction

Earthquake shaking is a major trigger of submarine slope failures and sediment gravity flows. The resultant submarine turbidite deposits can provide important paleoseismological information. Submarine slope failures induced by earthquakes have been investigated by seismic reflection surveys, swath bathymetry, sediment sampling, and dive surveys (e.g., Goldfinger 2011). However, few previous studies have included in situ observations during or soon after earthquakes. Among these, a report by Heezen et al. (1954) showed that sequential breaks of the undersea trans-Atlantic communication cables were the result of landslide-triggered turbidity currents during the 1929 Grand Banks earthquake. Thunell et al. (1999) reported increases of sediment suspension and sediment flux in the Cariaco basin from in situ monitoring of light scattering and sediment traps, and estimated considerable downslope displacement of sediments (10^5 tonnes) into the deep basin. The real-time deep seafloor observatory deployed by JAMSTEC in the Sagami Trough recorded video of mudflow events, and electromagnetic and other data, during the April 2006 earthquake there (Kasaya et al. 2009). Auto-brecciation of poorly consolidated surface sediment, as well as sliding or slumping, is evidence of seafloor deformation by earthquake shaking. Occurrences of auto-brecciation were observed by dives in the source areas of the 1993 earthquake off southwestern Hokkaido, Sea of Japan (Takeuchi et al. 1998), and in a surface core from the fault hanging wall in the Nankai accretionary prism off Kumano (Sakaguchi et al. 2009).

In this paper, we document occurrences of turbid seawater soon after the 2004 off the Kii Peninsula earthquakes (maximum magnitude 7.4) in the Nankai subduction zone. Observations were recorded with underwater video cameras. A revisit of the survey area 6 years after the earthquakes enabled us to examine the settling process and redistribution of the suspended mud cloud.

50.2 Geological and Geophysical Background

The Nankai Trough is a convergent margin at which the Philippine Sea plate is subducting to the northwest beneath the Eurasian plate at a rate of about 4 cm/year (Seno et al. 1993). The study area is in the central part of the Nankai subduction zone (Fig. 50.1) where extensive geological and geophysical surveys have been conducted to investigate potential sites for the IODP NanTroSEIZE drilling project (Kinoshita et al. 2009). This area is characterized by a well-developed forearc basin called the Kumano Trough and a NE–SW-trending continuous outer ridge. Multichannel seismic survey data demonstrate that mega-splay faults branch from the master décollement surface ~50 km landward of the prism toe to form an outer ridge (Park et al. 2002). Sequences of three or four large scarps on the prism slope provide the surface expression of these faults. A large number of small slope basins have developed at the bases of the fault scarps.

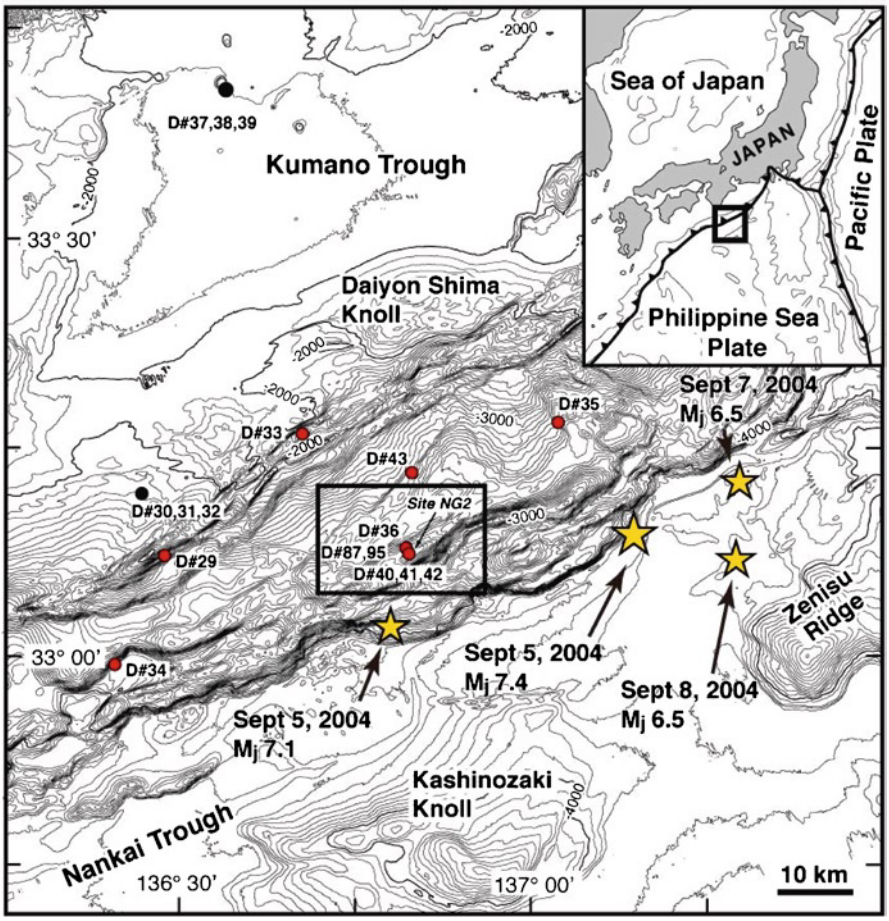

Fig. 50.1 Bathymetric map of the study area. *Stars* indicate epicenters of the 2004 off the Kii Peninsula earthquakes. Hypocenters and magnitudes were estimated by the Japan Meteorological Agency. *Red* and *black circles* show locations of dive sites with and without dilute suspension layer (DSL), respectively. *Rectangle* indicates the area covered by Fig. 50.3d

Great earthquakes have occurred repeatedly along the Nankai Trough. Historical records suggest that the rupture areas of these great earthquakes are segmented and that their recurrence interval is 100–150 years. Although few middle- to large-class earthquakes have been recorded during the period between the great earthquakes, a series of such earthquakes, the 2004 off the Kii Peninsula earthquakes, occurred near the axis of the Nankai Trough in September 2004. The main shock (Mj = 7.4, Mj: magnitude defined by the Japan Meteorological Agency) was southeast of the Daiyon Shima Knoll (Fig. 50.1). About 5 h before the main shock, a foreshock (Mj 7.1) occurred about 40 km to the southwest. These two earthquakes were accompanied by tsunamis. Major aftershocks (Mj 6.5) occurred 20 km east of the

main shock on 7 and 8 September. The aftershock distribution was determined in both the NW–SE and the ENE–WSW directions from ocean bottom seismometer observations (Sakai et al. 2005). The four shocks were intraplate earthquakes with hypocenters within the Philippine Sea plate. Tsunami waveform inversion results suggested that the fault strike of the main shock was perpendicular to the trough axis (Saito et al. 2010), although other fault models have also been proposed. However, most researchers agree that the foreshock was caused by dip slip on an ENE–WSW-striking fault (e.g., Saito et al. 2010).

50.3 Survey and Method

We carried out our seafloor observations from the Navigable Sampling System (NSS) of the Atmosphere and Ocean Research Institute of the University of Tokyo. The NSS is a remotely operated vehicle (ROV) designed to collect piston cores or to deploy heavy instruments on the seafloor with pinpoint accuracy. The NSS pilot vehicle has four thrusters, a payload hook, and two downward looking TV cameras. Seafloor observations are recorded by a color TV camera (CAM-A) hung from the pilot vehicle on an extension pipe, whereas payload surveillance is by means of a black-and-white TV camera (CAM-B) mounted on the pilot vehicle. The pilot vehicle is equipped with a pressure gauge to provide water-depth information and an acoustic altimeter to provide distance above the seafloor. Resolution of both instruments is 0.1 m.

The first cruise (KY04-11, 19–26 September 2004) in the area near the epicenters of the 2004 earthquakes was started from 2 weeks after the main shock by JAMSTEC's R/V *Kaiyo*. There were a total of 15 dives (dives 29–43; Fig. 50.1) during this cruise, 9 on the accretionary prism slopes northwest of the epicenters and 6 in the Kumano forearc basin (dives 30–32 and 37–39). The second cruise (KH-10-3; JAMSTEC R/V *Hakuho-maru*, 9–19 August 2010) was almost 6 years after the earthquakes and included two dives (87 and 95) to revisit the area around dives 36 and 40–42 of the previous cruise KY04-11.

50.4 Results

50.4.1 First Cruise (2004)

Dive 35 recorded only video observations at the prism slope 20 km northwest of the epicenter of the main shock (Fig. 50.1) because the dive site was too close to a commercial submarine cable to conduct piston core sampling. The transparency of the seawater decreased gradually with depth owing to increasing numbers of marine snow-like particles and then decreased rapidly from 200 m above the seafloor to the bottom (Fig. 50.2). Despite such a cloudy water column, seafloor conditions were not remarkable.

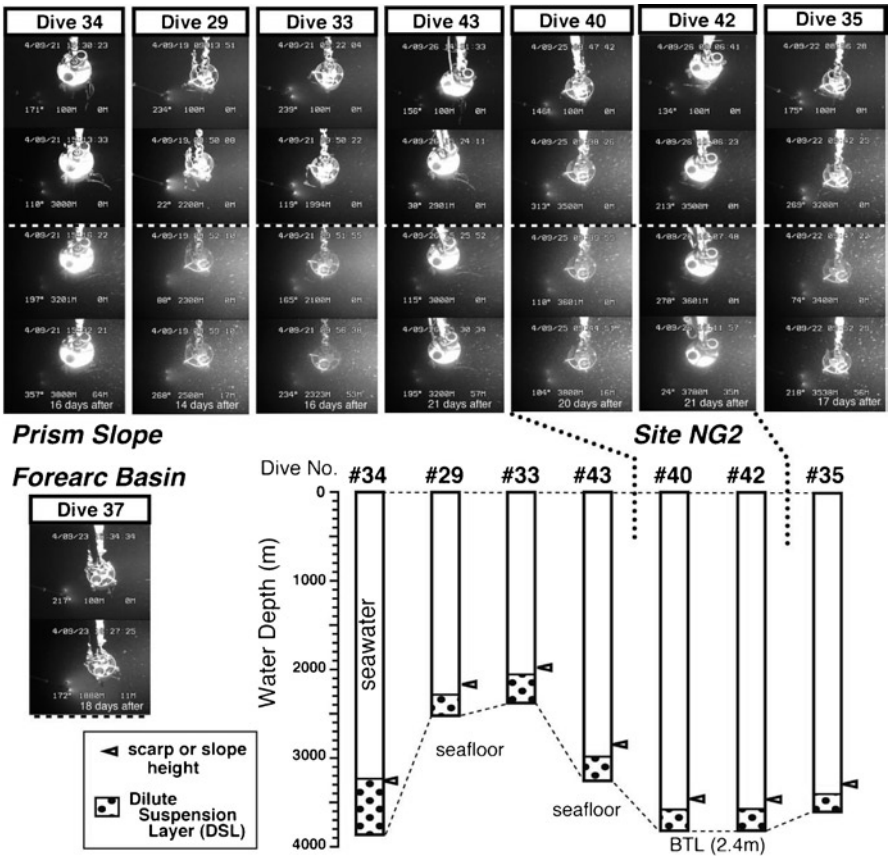

Fig. 50.2 Selected seafloor images and columns showing water depth and thickness of turbid layer. *Dashed lines* on images show the depths of sudden changes in turbidity. *Arrows* indicate the heights of scarps or steep slopes within 1 km upslope of dive site

Dive 36 was on the middle slope of the prism (Fig. 50.1). Turbid seawater was observed near the seafloor, although video images from CAM-B were not archived because of recording problems. CAM-A revealed ripple-like bedforms trending NE–SW and parallel to seafloor depth contours.

Dive 40 on 25 September 2004 (20 days after the main shock) was planned to take a piston-core sample from the slope basin near the foreshock epicenter (Fig. 50.1). This site (Site NG2 hereafter) also exhibited an increase of turbidity with water depth. Turbidity was so intense near the seafloor that it obscured the CAM-B video vision of the penetration of the piston-corer into the seafloor. Furthermore, an entire piston-corer system was lost when the main wire attaching it to the pilot vehicle broke during this dive. Thus, dive 41 was an attempted salvage operation on the same day. Despite 7 h of searching, we were unable to find the corer because of a layer of extremely high turbidity covering the seafloor. Our ROV observations, therefore, revealed two types of turbid layer: a dilute suspension layer

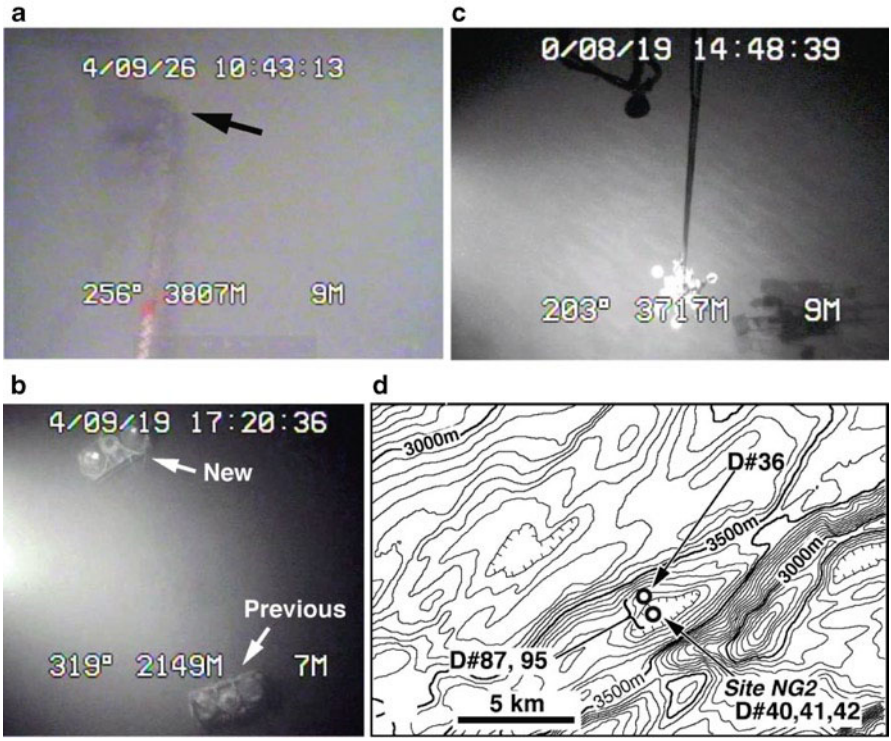

Fig. 50.3 Seafloor photographs and bathymetric map of the region around Site NG2. Notations on photographs show the date and time taken (*upper*); and heading, depth, and altitude of the ROV (*lower*, *left* to *right*) (**a**) CAM-A image of complete sinking of heat-flow probe system (marked by *arrow*) at Site NG2 during dive 42 (**b**) CAM-B image of heat-flow instruments during change over of systems during dive 30 (**c**) CAM-B image of ripple-like bedforms 640 m northwest of Site NG2 (**d**) Bathymetry around Site NG2 during dive 95 (location of map shown in Fig. 50.1)

(DSL) and a bottom turbid layer (BTL). The upper boundary of BTL was very clearly defined, forming a pseudo-seafloor.

To investigate the thickness of BTL at Site NG2, we used a pogo-type heat-flow probe system during dive 42 on 26 September. CAM-A revealed that the heat-flow probe system disappeared completely in BTL (Fig. 50.3a). Based on the height of the heat-flow instrument, BTL was more than 1.5 m thick at this location. BTL was observed only at Site NG2 during the 2004 cruise, and interestingly, it was not recognized at the dive 36 site, only 640 m northwest of Site NG2 (Fig. 50.3d).

DSL was found on the accretionary prism slope, but not in the forearc basin (Fig. 50.1). Seawater transparency was high at the southern margin of the forearc basin during dive 30, during which we replaced pop-up type heat-flow instruments used for long-term monitoring (Fig. 50.3b). The lack of BTL at this location was corroborated by a lack of sediment cover on the previously installed tool and no anomalous sinking of the original or replacement tools during the change over (Fig. 50.3b).

Because the pilot vehicle was not equipped with a turbidity meter, we approximated the thickness of DSL on the basis of whether or not the bottom frame of CAM-A was visible from CAM-B of the pilot vehicle; that is, we detected sudden changes of turbidity by entry into DSL (Fig. 50.2). The sites on the prism slope, except for dive 34, showed similar thicknesses of DSL (about 200–320 m) (Fig. 50.2) regardless of water depth and distance from the epicenters (Fig. 50.1). The site of dive 34 had an exceptionally thick DSL (about 630 m) (Fig. 50.2). The site of dive 33, in a depression landward of the outer ridge, lacked BTL, although DSL was relatively thick (320 m). Figure 50.2 also shows the height of scarps or slopes within 1 km upslope from each dive site.

50.4.2 Second Cruise (2010)

We revisited the study area during cruise KH-10-3 in 2010, about 6 years after the 2004 earthquakes. On 9 and 19 August we made two dives (87 and 95) at Site NG2 where BTL was observed during dives 40, 41, and 42 in 2004. However, we were unable to take piston-core samples in 2010 because of newly deployed commercial submarine cables near this site. The transparency of the seawater was high and there was no evidence of DSL and BTL during these dives. We observed many nest holes and some rubbish on the seafloor, which confirmed that the seafloor had returned to its normal condition. During dive 95 we also revisited the slope area 640 m northwest of Site NG2, where we again saw ripple-like bedforms (Fig. 50.3c) that had been recognized during dive 36 in 2004.

50.4.3 Differences of Water Depth in 2004 and 2010

The measured water depth (the sum of the values from the depth meter and altimeter) at Site NG2 during dives 40 and 42 in 2004 was 3816.0 ± 0.9 m (Fig. 50.4). During these dives, frequent altitude anomalies (zero values) were recorded, suggesting poor acoustic reflection from the seafloor. In 2010, the measured water depth during dive 87 at the same site was 3818.4 ± 1.0 m, with few altitude anomalies. The water depth difference between the two surveys was about 2.4 m. We believe that the shallower water depth detected in 2004 represented the upper boundary of BTL, which was detected by the sonic altimeter as a pseudo-seafloor.

50.5 Discussion

The measured water depth at Site NG2 6 years after the 2004 earthquakes was 2.4 m deeper than that about 20 days after the main shock (Fig. 50.4). We believe that the sonic altimeter detected the upper boundary of BTL, thus recording a pseudo-seafloor.

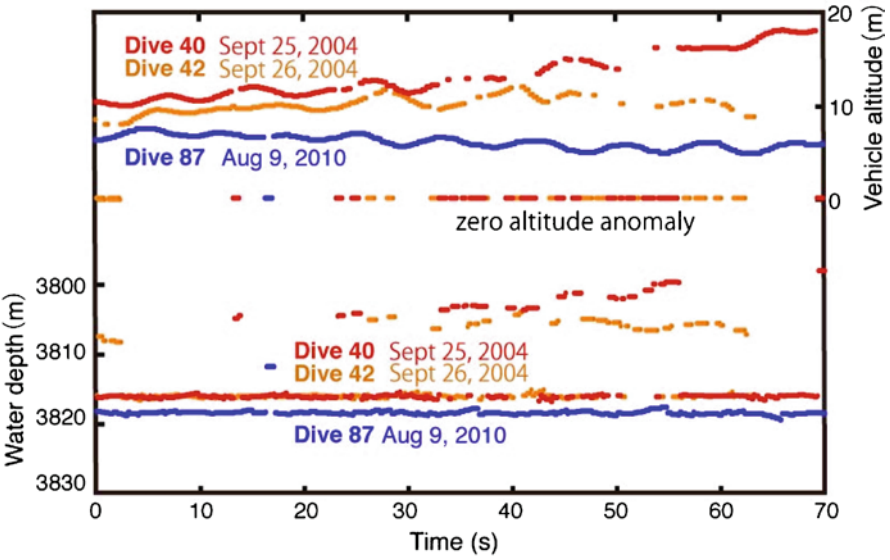

Fig. 50.4 Comparison of ROV altitudes (*upper*) and water depths (*lower*) during dives 40 and 42 (2004) with those of dive 87 (2010) at Site NG2

The zero-value anomalies of vehicle altitude recorded during dives 40 and 42 suggest that acoustic signals occasionally penetrated the upper boundary of BTL and that they were probably attenuated within it (Fig. 50.4). The combined precision of the ship's GPS and the ROV's acoustic positioning is thought to be about 20 m, based on past survey experience. However, water depth differences derived from positioning error would be small because Site NG2 is in an area of flat basin floor. The discrepancy between the surveys in 2004 and 2010, therefore, can be attributed to the presence or absence of BTL.

Water depths measured at the summit of a knoll in the forearc basin (lat 33°40.56′N, long 136°34.11′E) during dives in 2004, 2006, and 2010 fluctuated within 10 cm of 1,891 m, which suggests good precision in water depths determined by combining readings from the depth meter and the altimeter. We therefore conclude that the upper boundary of the BTL was approximately 2.4 m above the present seafloor (Figs. 50.4 and 50.5a). This thickness of BTL is consistent with our observation of the disappearance of the heat-flow probe system. It is likely that BTL was somewhat thicker than 2.4 m at the time of earthquake because some sediment settled from BTL and DSL on the former seafloor (Fig. 50.5a).

Video observations of the pseudo-seafloor show a sharp boundary between BTL and DSL. Similar boundaries (lutoclines) have been observed between heavily mud-laden bottom layers and clearer top layers in estuaries and muddy coastal environments (e.g., Wolanski et al. 1988). When suspended sediment concentrations in such bottom layers are higher than 10 gL^{-1}, the heavily mud-laden layer is defined as a fluid mud (Ross and Mehta 1989) and exhibits a decrease of settling velocity

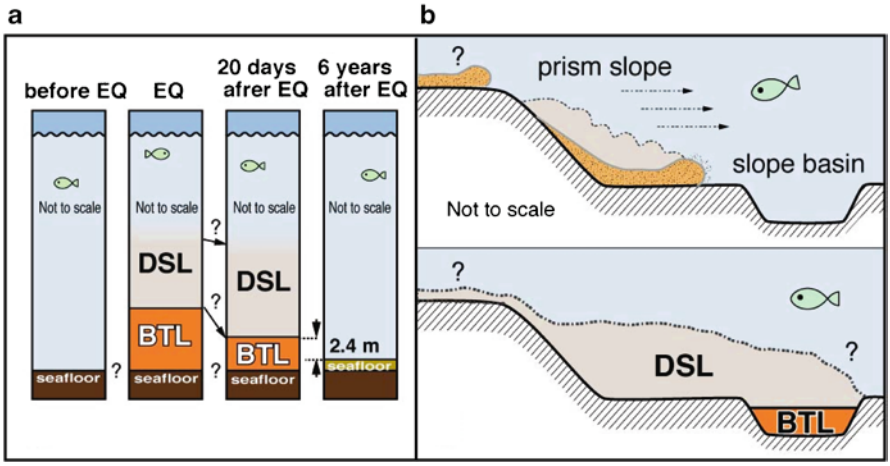

Fig. 50.5 Schematic illustration of (**a**) seafloor conditions before and after the 2004 earthquakes and (**b**) process of development of a dilute suspension layer (DSL) on a prism slope and a bottom turbid layer (BTL) in a slope basin

due to inter-particle hindrance. Although we have no data on suspended sediment concentrations in BTL, the sharp upper boundary of BTL that we observed suggests development of fluid mud at Site NG2.

The first dive at Site NG2 was conducted about 20 days after the earthquakes. It is possible that the upper boundary of BTL had descended somewhat before our dives (Fig. 50.5a); however, the depth changes of the upper boundary of BTL over a 1-day period during our 2004 cruise were not detectable (Fig. 50.4). Analyses of the particle size distribution and composition of sediments are needed to better understand the settling process after the earthquakes.

That BTL was observed only in the slope basin strongly indicates that it was formed by a sediment gravity flow dumping muddy deposits in a depression (Fig. 50.5b). We suggest that sediment gravity flows triggered by M 7 earthquakes probably contained unconsolidated hemipelagic mud from the prism slope and that these sediments flowed down to the slope basin. Downslope gravity flows are also suggested by the ripple-like bedforms observed during dives 35 and 95.

DSL was both widely distributed and very thick (~200–630 m) compared to BTL. The thickness of DSL corresponds well with the height of scarps or slopes within 1 km upslope (Figs. 50.1 and 50.2). For example, there is a large fault scarp less than 1 km upslope from the very thick DSL observed during dive 34 (Fig. 50.1). Moreover, the thickness of DSL at this site is greater than the height of the scarp (Fig. 50.2), suggesting that the clouds of suspended sediment came from further upslope, beyond the scarp (Fig. 50.5b).

The widespread distribution of DSL implies that clouds of suspended sediment were produced at multiple locations on the prism slope during the earthquakes by

sliding, slumping, seafloor shaking, or sediment gravity flow. The distribution extends to at least 40 km from the seismic source area (Fig. 50.1). Bottom currents flowing faster than 0.05 m/s encountered during previous submersible dives in this area (unpublished data) are likely to have contributed further to lateral dispersion of suspended sediment clouds (Fig. 50.5b).

50.6 Conclusion

Our ROV dive surveys near the epicenters of the 2004 off the Kii Peninsula earthquakes 20 days after and 6 years after the events revealed two kinds of turbid layers, DSL and BTL. These layers were present only soon after the earthquakes. The thickness of DSL coincided approximately with the height of scarps or slopes within 1 km in the upslope direction. The wide distribution of DSL suggested that sliding, slumping, seafloor shaking, and sediment gravity flows produced clouds of suspended sediment at multiple locations on the prism slope during the earthquakes. That BTL was observed only in the slope basin implies that dense muddy sediments in suspension were deposited in seafloor depressions. We concluded that the magnitude 7 earthquakes in 2004 caused widespread disturbance of the seafloor and redistributed surface sediments on the prism slope over an area extending at least 40 km from the seismic source area. Our in situ observations soon after the earthquakes confirmed that seafloor disturbance by seismic shaking plays a significant role in sediment redistribution in subduction zones.

Acknowledgements We thank the R/V *Kaiyo* and the R/V *Hakuho-maru* captains, crewmembers and technicians for their contributions of the success of the ROV surveys. Thanks are due to Atsushi Noda and Akira Takeuchi for critical reviews. Yasuhiro Yamada made constructive editorial comments for our manuscript. Various supports and suggestions for the studies by Hidekazu Tokuyama are highly appreciated. This work was supported by the Grant-in-Aid for Scientific Research on Innovative Areas (No. 21107003) from MEXT of Japan.

References

Goldfinger C (2011) Submarine paleoseismology based on turbidite records. Ann Rev Mar Sci 3:35–66

Heezen BC, Ericson DB, Ewing M (1954) Further evidence for a turbidity current following the 1929 Grand banks earthquake. Deep Sea Res 1(4):193–202. doi:10.1016/0146-6313(54)90001-5

Kasaya T, Mitsuzawa K, Goto T, Sayanagi K, Araki E, Asakawa K, Iwase R, Mikada H, Nagao T (2009) Trial of multidisciplinary observation at an expandable sub-marine cabled station "Off-Hatsushima Island Observatory" in Sagami Bay, Japan. Sensors 9:9241–9254. doi:10.3390/s91109241

Kinoshita M, Tobin H, Ashi J, Kimura G, Lallemant S, Screaton EJ, Curewitz D, Masago H, Moe KT, Expedition 314/315/316 Scientists (2009) In: Proceedings of the IODP, 314/315/316, Washington, DC. doi: 10.2204/iodp.proc.314315316.123

Park JO, Tsuru T, Kodaira S, Cummins PR, Kaneda Y (2002) Splay fault branching along the Nankai subduction zone. Science 297:1157–1160

Ross MA, Mehta AJ (1989) On the mechanics of lutoclines and fluid mud. J Coastal Res Spec Issue 5:51–61

Saito T, Satake K, Furumura T (2010) Tsunami waveform inversion including dispersive waves: the 2004 earthquake off Kii Peninsula, Japan. J Geophys Res 115:B06303. doi:10.1029/2009JB006884

Sakaguchi A, Kimura G, Strasser M, Murayama M, Curewitz D, Fergusson C, Milliken K, Nicholson U, Screaton L (2009) Episodic sediment disturbance on the mega-splay fault at Tonankai earthquake area, Nankai trough, Japan. In: American Geophysical Union, Fall Meeting 2008, abstract #T21F-07

Sakai S, Yamada T, Shinohara M, Hagiwara H, Kanazawa T, Obana K, Kodaira S, Kaneda Y (2005) Urgent aftershock observation of the 2004 off the Kii Peninsula earthquake using ocean bottom seismometers. Earth Planet Space 57:363–368

Seno T, Stein S, Grippe AE (1993) A model for the motion of the Philippine Sea plate consistent with NUVEL-1 and geological data. J Geophys Res 98:17941–17948

Takeuchi A, Shipboard Scientific Party of R/V *Yokosuka*, Japan Sea Cruise (1998) Bottom response to a tsunami earthquake: submersible observations in the epicenter area of the 1993 earthquake off southwestern Hokkaido, Sea of Japan. J Geophys Res 103(B10), 24:109–124, 125. doi: 10.1029/98JB00572

Thunell R, Tappa E, Varela R, Llano M, Astor Y, Muller-Karger F, Bohrer R (1999) Increased marine sediment suspension and fluxes following an earthquake. Nature 398:233–236

Wolanski E, Chappell J, Ridd P, Vertessy R (1988) Fluidization of mud in estuaries. J Geophys Res 93:2351–2361

Chapter 51
Study of Recent Small-Scale Landslides in Geologically Active Marine Areas Through Repeated Multibeam Surveys: Examples from the Southern Italy

Daniele Casalbore, Alessandro Bosman, and Francesco Latino Chiocci

Abstract Repeat multibeam surveys are used to investigate recent submarine landslides in three different areas on southern Italy, i.e. Stromboli, Southern Messina Strait and Punta Alice. High-resolution Digital Terrain Models (DTMs) depict the morphology of mass-wasting events, while residual maps of the difference between successive bathymetric surveys indicate failure volumes ranging from tens of thousands to millions of cubic meters. A tentative estimate of recurrence time for the slope failures was based on chronological constraints and historical reports, and gave values ranging from tens to hundreds of years. Characterizing mass-wasting events and their recurrence time is a necessary step for geo-hazard assessment of densely populated coastal areas.

Keywords Residual map • Bathymetry • Mass-wasting • Flash-flood • Tsunami

51.1 Introduction

The recognition of submarine landslides has exponentially increased in the last decades due to the development of remote-sensing techniques, among which multibeam bathymetric systems are the most effective means of improving our knowledge

D. Casalbore (✉) • A. Bosman
CNR, Istituto di Geologia Ambientale e Geoingegneria, Via Salaria km 29.300, Monterotondo Stazione (Roma), Roma 00016, Italy
e-mail: daniele.casalbore@unibo.it

F.L. Chiocci
Dip. Scienze della Terra, Sapienza. University of Roma, P.le Aldo Moro 5, Roma 00185, Italy

CNR, Istituto di Geologia Ambientale e Geoingegneria, Via Salaria km 29.300, Monterotondo Stazione (Roma), Roma 00016, Italy

Y. Yamada et al. (eds.), *Submarine Mass Movements and Their Consequences*, Advances in Natural and Technological Hazards Research 31,
DOI 10.1007/978-94-007-2162-3_51,

on morphological features related to these processes (i.e., McAdoo et al. 2000; Huhnerbach et al. 2004; Twichell et al. 2009; Chaytor et al. 2009). Submarine landslides are ubiquitous in different submarine settings and greatly range in size from tens of thousands of m^3 to thousands of km^3. Because of difficulties in mapping small features, most studies emphasized large failures (volume of km^3) and overlooked small landslide morphologies (e.g., McAdoo et al. 2000). Nevertheless, small mass-wasting events are extremely common in geologically active marine areas, playing a key role in transferring sediment from the coastal sector toward the basin (e.g., Lykousis et al. 2007 and references therein).

Moreover, in areas with a narrow continental shelf, submarine landslides often occur close to the coast and can represent a geo-hazard for coastal communities (Colantoni et al. 1992; Longva et al. 2003; Chiocci et al. 2008; Sultan et al. 2010). In such cases, repeat multibeam surveys offers a tool to define the characters and extent of the instability phenomena. By understanding the amount of material released in individual landslides, the distribution of landslides within a given geographic region, their recurrence time and the mechanisms responsible for the generation of the landslides, we may be able to determine the potential hazard of these events.

The aim of the study is to show examples of such studies on the flank of Stromboli Volcano and on two sites in geologically active areas, i.e. the Sicilian and Calabrian coasts, where the continental margin is steep and characterized by high-sedimentation rates.

51.1.1 Data and Methods

Data were collected by research vessels (*Universitatis, Thetis and Urania*) and small boats in shallow-water. Reson and Simrad multibeam systems operating at different frequencies (100, 240 and 455 kHz) were used to guarantee the maximum possible resolution for each bathymetric interval (Table 51.1).

All data were DGPS- or RTK-positioned (for shallow water) and processed with dedicated software, where all sensor data were merged and corrected for the effects of tide, attitude sensor (roll, pitch and yaw) and sound velocity variations. Manual editing and automated filters were used to "remove" erroneous soundings in order to obtain high-resolution DTMs with cell-size variable from 0.5 to 1 m in shallow water and 5–10 m at greater depths.

Residual maps were obtained as difference between successive multibeam surveys and they were generated mainly in shallow-water sectors (i.e., first 200 m bsl, apart from the Stromboli case) with a 3×3 m cell-size. The different dataset have been compared in each sector and used to detect reliable seafloor variations because (1) the surveys were acquired with a 100% bathymetric coverage sharing the same track-line orientation, (2) the high resolution of DTMs and the manual editing of raw soundings allowed us to distinguish real geological features from acoustic artifacts. Conversely, the uncertainties related to the use of DGPS corrections (accuracy of ± 2 m in plan-view) with respect RTK correction (accuracy of few centimeters) can lead to the shifting of morphologies and consequently affect the estimate of

Table 51.1 Multibeam surveys realized in the study areas; MBES: *R* Reson, *S* Simrad

Survey	Date	Min. depth	Max depth	Vessel	Position	MBES	Frequency kHz
The Stromboli 30 December 2002 eruption-generated landslide							
Vulcanit	24/02/02	−12 m	−1000 m	Thetis	DGPS	R 8111	100
CCE1	09/01/03	−1 m	−310 m	CP857	DGPS	R 8101–R 8125	240–455
The Southern Messina Strait 1st October 2009 flash-flood generated landslides							
Cala Andrè	01/06/07	−10 m	−120 m	Calafuria	DGPS	R 8125	455
BOB	25/11/09	−10 m	−1000 m	Urania	DGPS	S 710	50–70
The Punta Alice 12 December 2005 storm-generated landslide							
Cirò1	2/12/05	−40 m	−310 m	Alsea	RTK	R 8101	240
Cirò2	3/04/06	−10 m	−120 m	Akira	RTK	R 8125	455

seafloor variations and volume, as recently highlighted by Brothers et al. (2011). However, the errors associated to these uncertainties are significantly lower than the observed seafloor variations (tens of meters) and estimated volumes (tens of thousands up to some millions of m^3), so that their influence can be considered negligible in the estimation of the order of magnitude of these measurements.

51.2 Results

51.2.1 Case-Study 1: The Stromboli 30 December 2002 Eruption-Generated Landslide

The NW flank of Stromboli is characterized by a wide depression (Sciara del Fuoco, SdF in Fig. 51.1a), representing the last of four major collapses that affected the NW flank of the edifice in the last 13 ka (Romagnoli et al. 2009 and references therein). Presently, the SdF acts as the main conduit for the huge amount of volcaniclastic material produced by the persistent activity of Stromboli Volcano.

On 30 December 2002, a submarine landslide occurred along the NE portion of the SdF after 2 days of eruption; it generated tsunami waves that struck the Stromboli coastline with a run-up of 2–10 m, causing significant damage to houses and coastal facilities (Tinti et al. 2005). Multibeam bathymetry surveys collected 10 months before the slide and 10 days after the event allowed for the reconstruction of scar geometry and volume ($\approx 10 \times 10^6$ m^3) (Fig. 51.1b; see also Chiocci et al. 2008). The slide mainly affected the shallow (down 320 m bsl) and steeper (about 30°) part of the volcaniclastic apron. High slope gradients and the occurrence of very friable volcaniclastic rocks that may act as weak layers (Tommasi et al. 2008) were interpreted as the preconditioning factors for slope failures. Repetitive multibeam surveys were also used to monitor the healing of the submarine scar they revealed a very rapid infilling of the scar and return to the pre-slide morphology (Chiocci et al. 2008).

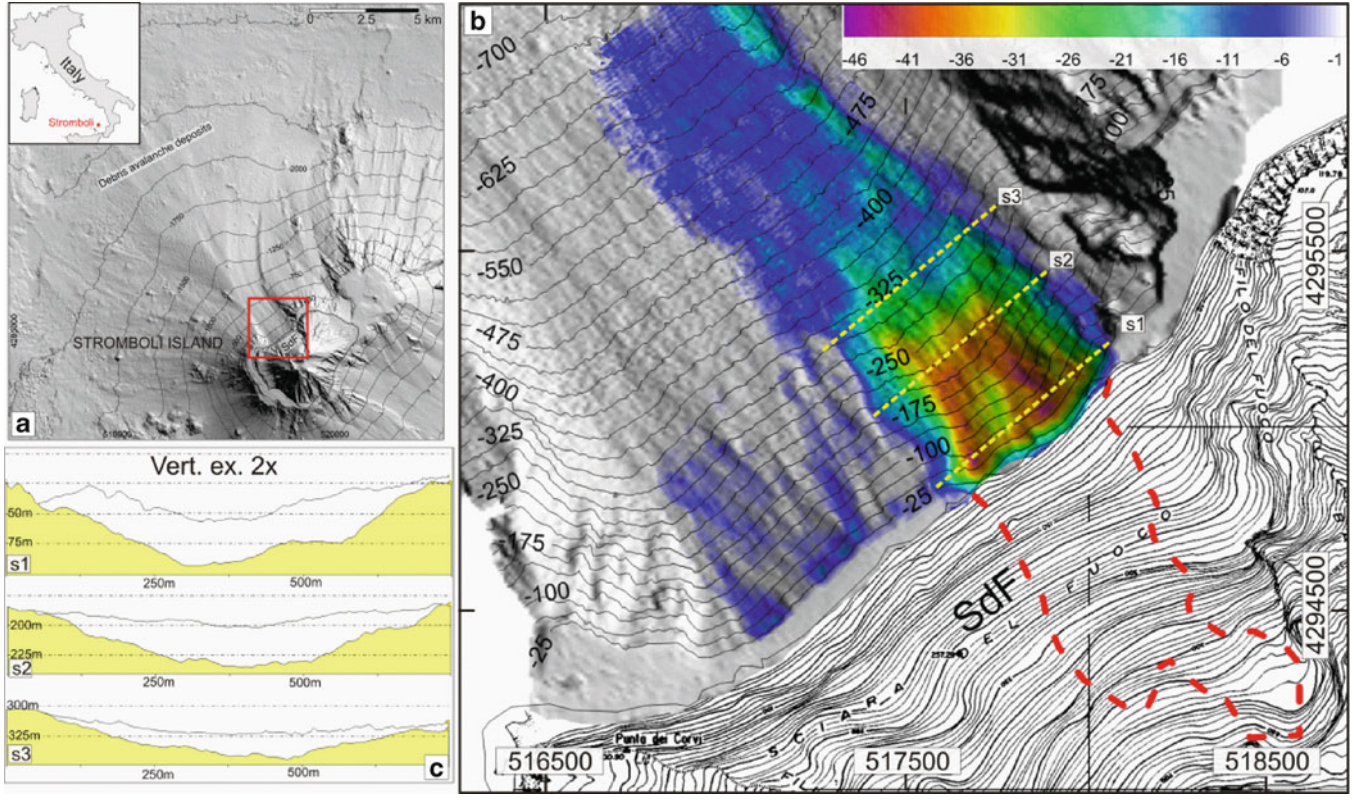

Fig. 51.1 (**a**) shaded relief map of the Stromboli volcano with the location of the study area (**b**) residual map (scale bar units are in meters) obtained as difference between pre- and post-"2002 Stromboli landslide" draped over the shaded relief of Sciara del Fuoco slope in the NW part of Stromboli volcano; the *red dashed line* indicates the subaerial landslides that occurred 7 min later with respect to the submarine landslide (**c**) three pre- and post-landslide cross-section of 2002 landslide scar are shown, for location see Fig. 51.1b

According to historical reports the Stromboli coast was struck by six tsunamis during the last century, most of them likely generated by local submarine landslides (Table 51.1 in Maramai et al. 2005). The rapid infilling of the landslide scar by volcaniclastic material produced at the summit crater supports a short recurrence interval for failures.

51.2.2 Case-Study 2: The Southern Messina Strait 1st October 2009 Flash-Flood Generated Landslides

The Messina Strait is characterized by mountains that are very close to the coast and carved by steep and short valleys, locally named Fiumara. These valleys are periodically affected by flash-floods (Guarnieri and Pirotta 2008).

On 1st October 2009, a small area between Scaletta Zanclea and Giampilieri villages (Fig. 51.2a) experienced very intense and concentrated rainfall that induced widespread small-scale mass-wasting in the catchment basins and flash-flood within the Fiumara. Such processes generated debris flows that caused 37 casualties and severe damage to the human settlements on the coast before entering the sea (Ortolani 2009).

The comparison of bathymetry collected 2 years before the 1st October 2009 flash-flood with a multibeam survey carried out 40 days after the event, allowed quantification of seafloor variations due to the debris flows. Residual maps, in fact, depict significant morphological changes only offshore the mouth of the two Fiumara (Fig. 51.2b, c), where a thick debris flow entered the sea. These variations may be thus considered as being produced by the 1st October flood. The mobilized volumes are estimated to be 20 and 65×10^3 m^3, respectively.

As mass-wasting features similar to those produced on 1st October 2009 have been also identified in other submarine canyons present along the neighboring coast (Fig. 51.2) located off of Fiumara mouths, a key role played by flood-generated hyperpycnal flows in their formation can be envisaged.

The frequency of submarine landslides in the area has been inferred by the density of major scars along a limited coastal zone (18 scars within 5.5 km^2). These major scars have been dismantling the 5 ka old submarine depositional terrace, made up of littoral sediment accumulated below wave-base level (Chiocci and Orlando 1996), so that a average frequency of occurrence of a major slide of 270 year can be estimated. Actually, each of major scars is made up by minor scars and their volume is of some 10^5 m^3, 5–10 times larger than the volume mobilized by the 1st October 2009 landslides. If we consider that 5–10 "1st October" events created each major scar, and that flash-floods recurrence time on the Fiumara ranges from tens to few hundred years (www.comune.messina.it), we may then estimate the occurrence of 100–200 landslides in the last 5 ka i.e. one landslide each 25–50 years.

It is also worth noting that high sedimentation rate and the frequent occurrence of medium and large earthquakes may contribute to the development of mass-wasting phenomena in the area, as witnessed by the fact that some submarine canyons are not directly related to Fiumara mouths (Fig. 51.2, see also Casalbore et al. 2011).

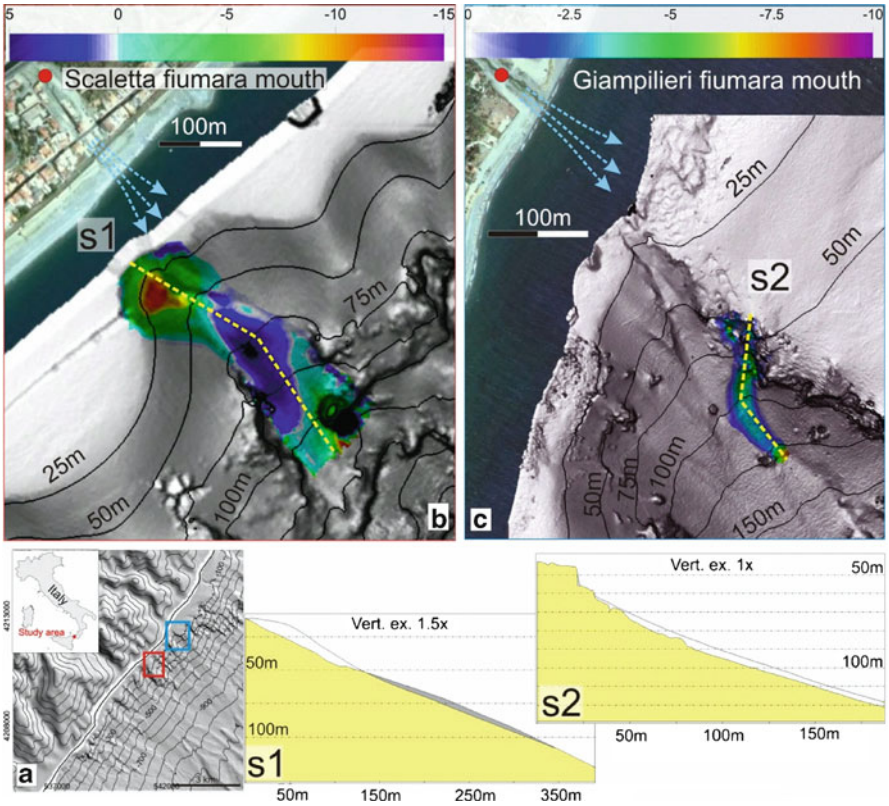

Fig. 51.2 Residual maps obtained as difference between pre- and post-"1st October Southern Messina Strait flash-flood" draped over shaded relief map of submarine sector offshore Scaletta (**2b**) and Giampilieri (**2c**) Fiumara mouths (location in Fig. 51.2a); the scale bar units are in meters. Below, two pre and post- flood bathymetric sections of the recognized landslides; the *grey* area in profile A–B depicts the landslide deposit related to the upslope failure

Even if no previous tsunamis or submarine cable breaks have been reported in this area, the proximity of the canyon headwalls at the coast (≈ 100 m), the fact that the 1st October 2009 landslide scar caused a strong retreat of the terrace edge of about 50 m landward (Fig. 51.2a) and the possibility that future failures could have headwall scarps intersecting the shoreline indicate the significance of these landslides as future geo-hazard for this densely inhabited coastal sector.

51.2.3 Case-Study 3: The Punta Alice 12 December 2005 Storm-Generated Landslide

Two multibeam surveys were collected in December 2005 and April 2006 in the coastal sector facing Punta Alice promontory in the Ionian Sea (Fig. 51.3a) to study the cause of a local and rapid subsidence (≈ 12 mm\year) affecting the coastal sector

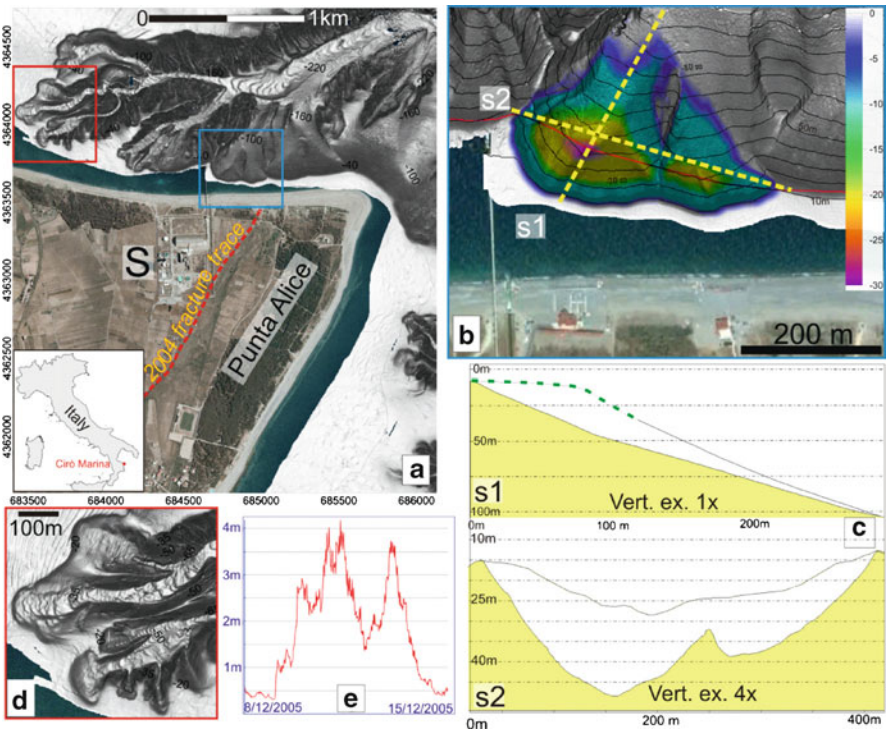

Fig. 51.3 (**a**) shaded relief of the sector offshore Punta Alice, where a canyon is present; the *red dashed lines* indicates the trace of a ground crack formed during July 2004 according to Sorriso Valvo 2008 (**b**) residual map obtained as difference between pre- and post-"12 December 2005 Punta Alice landslide" draped over the shaded relief of the sector offshore Punta Alice (location map is the blue box in Fig. 51.3a; the scale bar units are in meters) (**c**) two pre and post-slide bathymetric section (location in Fig. 51.3b); in section C–D, the *dashed green line* represents the reconstructed part of the landslide (see text for detail) (**d**) zoom of the canyon headwall showing the presence of several minor scars (location is the *red box* in Fig. 51.3a) (**e**) graph showing the significant wave height related to the storm that affected Punta Alice promontory on 12 December 2005

(Sorriso Valvo 2008). The first survey extends from 40 to 300 m, while the second covers the bathymetric range comprised between 10 and 120 m bsl so that an overlap zone is present between the two surveys. Although the goal of the survey was different, in the overlap zone the occurrence of a submarine landslide was revealed in the north-western part of Punta Alice (Fig. 51.3b). Because the 2005 survey only extended to −37 m, the pre-slide morphology was reconstructed using a pre-2006 aerial photo. This allowed us to map the edge of a shallow-water depositional terrace located about 10 m bsl (defined by a strong chromatic variation of the blue) and well-defined in the surrounding areas. The landslide caused a retreat of the terrace edge of about 60 m and this information constrained the reconstruction of the scar geometry (dashed green line in section s1 of Fig. 51.3c) and volume ($\approx 1 \times 10^6$ m^3).

Given the shallow depth of the landslide and the lack of significant earthquakes in that period, the most plausible triggering mechanism is the storm-wave cyclic

loading on the seafloor (Locat and Lee 2000 and reference therein), as a severe storm with wave height over 4 m struck this coastline on 12 December 2005 (Fig. 51.3e, www.idromare.it).

The frequency of "Punta Alice" slope failures is difficult to estimate. In fact, only two other scars similar to the "Punta Alice" one have been detected eastward of this scar. This figure would give 1–2 thousand years recurrence time for these slope failures using the high-stand submarine depositional terrace as a chronological marker. However, given the fact that the "Punta Alice" scar actually deepened a pre-existing overall concave morphology, this estimate can be significantly lower (i.e., in the order of some 100 years). In this regard, it should be considered that the morphology of similar scars in the surrounding areas may have been modified by successive smaller slope failures that have been largely recognized at the canyon headwall (Fig. 51.3d).

Finally, it is worth noting that the Punta Alice slide caused severe damage to a coastal chemical plant present in the area (S in Fig. 51.3a), highlighting its significance as geo-hazard for this coastal sector

51.3 Final Remarks

Recent small-scale submarine mass movements have been characterized by the use of repeated multibeam surveys in three marine areas of Southern Italy, each of them characterized by a different geological setting, preconditioning factors and trigger events (Table 51.2). The reconstruction of scar morphology has been, indeed, the

Table 51.2 Main characters of the recognized submarine landslides in this research

Landslide	Geological setting	Volume (m^3)	Preconditioning factor	Triggering factor	Recurrence time
Stromboli	Active volcano	$\approx 10 \times 10^6$	Slope oversteepening, high sedimentation rate volcaniclastic layers	Volcanic crisis	Tens up to one hundred of years
Southern Messina Strait	Canyon headwall	$\approx 50 \times 10^3$	Slope oversteepening, high sedimentation rate, undermining due to canyon retrogressive erosion	Flash-flood generated hyperpycnal flows	Tens of years
Punta Alice	Canyon headwall	$\approx 1 \times 10^6$	Local high subsidence, undermining due to canyon retrogressive erosion	Storm-wave loading	Hundreds of years

base for geological considerations that led us to the identification of the main preconditioning and triggering mechanisms of mass-wasting events; the latter are volcanic activity, flash-flood generated hyperpycnal flows and the cyclic loading of storm-wave for Stromboli, Southern Messina Strait and Punta Alice slides. The volume of the slope failures varies over three orders of magnitude (10^4–10^7 m^3) and their frequency has been roughly estimated in the order of one event each tens or some hundred years.

Of course, these estimates are tentative and the stability state of a submarine slope should rely on more detailed studies of single features with in situ measurements. However, the cost of detailed studies combined with the extremely high number of failures to examine make such hazard assessments prohibitively expensive. Therefore, we propose repeat multibeam surveys be used as a first-order tool in mass-wasting hazard assessments. Such surveys would resolve landslide size, distribution and aid in the characterization of their recurrence intervals, preconditioning mechanism and trigger events. Those factors are the base for a first-order geo-hazard assessment in populated coastal zones within geologically active areas, where submarine slope failures may occur a human timescale.

Acknowledgments Magic Project is gratefully acknowledged for the research fellowship funded to the first Author in order to study submarine instability processes on Italian continental margin. Jason Chaytor, David Twichell and Laura Brothers are acknowledged for useful suggestions that greatly improved the quality of the paper.

References

Brothers LL, Kelley JT, Belknap DF, Barnhardt WA, Andrews BA, Landon Maynard M (2011) Over a century of bathymetric observations and shallow sediment characterization in Belfast Bay, Maine USA: implications for pockmark field longevity. Geo-Mar Lett. doi:10.1007/s00367-011-0228-0

Casalbore D, Chiocci FL, Scarascia Mugnozza G, Tommasi P, Sposato A (2011) Flash-flood hyperpycnal flows generating shallow-water landslides at Fiumara mouths in Western Messina Strait (Italy). Mar Geophys Res. doi:10.1007/s11001-011-9128-y

Chaytor JD, Ten Brink US, Solow AR, Andrews BD (2009) Size distribution of submarine landslides along the U.S. Atlantic margin. Mar Geol 264:16–27

Chiocci FL, Orlando L (1996) Lowstand terraces on Tyrrhenian Sea steep continental slopes. Mar Geol 134:127–143

Chiocci FL, Romagnoli C, Bosman A (2008) Morphologic resilience and depositional processes due to the rapid evolution of the submerged Sciara del Fuoco (Stromboli Island) after the December 2002 submarine slide and tsunami. Geomorphology 100:356–365

Colantoni P, Gennesseaux M, Vanney JR, Ulzega A, Melegari G, Trombetta A (1992) Processi dinamici del canyon sottomarino di Gioia Tauro (Mare Tirreno). G di Geologia 3(54/2):199–213

Guarnieri P, Pirrotta C (2008) The response of drainage basins to the late Quaternary tectonics in the Sicilian side of the Messina Strait (NE Sicily). Geomorphology 95:260–273

Huhnerbach V, Masson DG, COSTA project partners (2004) Landslides in the north Atlantic and its adjacent seas: an analysis of their morphology, setting and behaviour. Mar Geol 213:343–362

Locat J, Lee H (2000) Submarine landslides: advances and challenges. Can Geotech J 39:193–212

Longva O, Janbu N, Blikra LH, Bøe R (2003) The 1996 Finneidfjord slide: seafloor failure and slide dynamics. In: Locat J, Mienert J (eds) Submarine mass movements and their consequences. Springer, Dordrecht, pp 531–538

Lykousis V, Sakellariou D, Rousakis G, Alexandri S, Kaberi H, Nomikou P, Georgiou P, Balas D (2007) Sediment failure processes in active grabens: the Western Gulf of Corinth (Greece). In: Lykousis V, Sakellariou D, Locat J (eds) Submarine mass movements and their consequences, 3rd International Symposium, pp 297–305

Maramai A, Graziani L, Tinti S (2005) Tsunamis in the Aeolian Islands (southern Italy): a review. Mar Geol 215:11–21

McAdoo BG, Pratson LF, Orange DL (2000) Submarine landslide geomorphology, US continental slope. Mar Geol 169:103–136

Ortolani (2009) Alluvione di Messina del 1° ottobre 2009. Le colate rapide di fango e detriti hanno devastato il territorio, le fiumare hanno retto. Geoitalia 29:31–36 www.geoitalia.org

Romagnoli C, Kokelaar P, Casalbore D, Chiocci FL (2009) Lateral collapses and active sedimentary processes on the northwestern flank of Stromboli volcano. Italy Mar Geol 265:101–119

Sorriso Valvo M (2008) Natural hazards and natural heritage – common origins and interference with cultural heritage. Geogr Fis Dinam Quat 31:231–237

Sultan N, Savoye B, Jouet G, Leynaud D, Cochonat P, Henry P, Stegmann S, Kopf A (2010) Investigation of a possible submarine landslide at the Var delta front (Nice continental slope, southeast France). Can Geotech J 47:486–496

Tinti S, Manucci A, Pagnoni G, Armigliato A, Zaniboni F (2005) The 30 December 2002 landslide induced tsunamis in Stromboli: sequence of events reconstructed from the eyewitness accounts. Nat Haz Earth Syst Sci 5:763–775

Tommasi P, Baldi P, Chiocci FL, Coltelli M, Marsella M, Romagnoli C (2008) Slope failures induced by the December 2002 eruption at Stromboli volcano. In: Calvari S, Inguaggiato S, Puglisi G, Ripepe M, Rosi M (eds) Learning from Stromboli. AGU Book, Washington, DC, pp 129–145

Twichell DC, Chaytor JD, Ten Brink US, Buczkowski B (2009) Morphology of late Quaternary submarine landslides along the U.S. Atlantic continental margin. Mar Geol 264:4–15

Part VIII
Architecture of Mass Transport Deposits/Complexes

Chapter 52
Sedimentary Mélanges and Fossil Mass-Transport Complexes: A Key for Better Understanding Submarine Mass Movements?

Gian Andrea Pini, Kei Ogata, Angelo Camerlenghi, Andrea Festa, Claudio Corrado Lucente, and Giulia Codegone

Abstract Mélanges originated from sedimentary processes (sedimentary mélanges) and olistostromes are frequently present in mountain chains worldwide. They are excellent fossil examples of mass-transport complexes (MTC), often cropping out in well-preserved and laterally continuous exposures. In this article we will show the results of the integrated study of fossil MTCs, including sedimentary mélanges/olistostromes, with a focus on the Apennines of Italy. Fossil MTCs, especially the basin-wide ones, are composite and multi-event units involving the entire spectra of mass-transport processes. The down-slope motion of these bodies is enabled by the relative movement of discrete masses, with progressive stratal disruption of rocks/sediment involved and flow transformation. Three kinds of MTC are here

G.A. Pini (✉)
Dipartimento di Scienze della Terra e Geologico-Ambientali, Università di Bologna,
via Zamboni, 67, I-40126 Bologna, Italy
e-mail: gianandrea.pini@unibo.it

K. Ogata
Department of Artic Geology, UNIS (University Centre in Svalbard),
Pb. 156, 9171 Longyearbyen, Norway
e-mail: kei.ogata@gmail.com

A. Camerlenghi
Departament d'Estratigrafia, P. i Geosciènces Marines, ICREA,
Istitució Catalana de Recerca I Estudis Advançats, c/o Universitat de Barcelona,
C/Martí i Franques, s/n, E-080028 Barcelona, Spain
e-mail: acamerlenghi@ub.edu

A. Festa • G. Codegone
Dipartimento di Scienze della Terra, Università degli Studi di Torino,
via Valperga Caluso, 35, I-10125 Torino, Italy
e-mail: andrea.festa@unito.it; giulia.codegone@unito.it

C.C. Lucente
Servizio Tecnico dei Bacini Conca e Marecchia, Regione Emilia-Romagna,
via Rosaspina, 7, I-47923 Rimini, Italy
e-mail: CLucente@regione.emilia-romagna.it

Y. Yamada et al. (eds.), *Submarine Mass Movements and Their Consequences*,
Advances in Natural and Technological Hazards Research 31,
DOI 10.1007/978-94-007-2162-3_52, © Springer Science+Business Media B.V. 2012

distinguished, in which the movements are enabled by (1) shear-dominated viscous flows within a muddy matrix, (2) mud-silt-sandy matrix sustained by fluid overpressure, (3) concentrated shear zones/surfaces with advection of grains and fluid (overpressured basal carpets). These MTC types may represent end-members of a continuum of products and correspond to different kinematics of transport and emplacement and to different relationship with the substratum. These observations should result in a better knowledge of mass-transport processes and bodies, in relation with the basin floor geometries.

Keywords Submarine landslides • Mass-transport complexes • Olistostromes • Mélanges

52.1 Introduction

The adjective chaotic has been often used to describe mass transport complexes (MTC, see Weimer and Shipp 2004) occurring on the seafloor and within the sedimentary record of continental margins, or exposed in mountain ranges world-wide. This definition takes into account the disruption and amalgamation of strata observed in the field or the chaotic appearance and the transparency using geophysical methods of investigation.

Chaotic rock units defined to as mélanges in the geologic literature crop out widely in orogenic belts. These units are characterized by block-in-matrix fabric and mixing of rocks with different degree of compaction, age, and provenance. Although an exclusive origin from tangential tectonic processes is commonly aprioristically assumed, mélanges can also originate from en-mass sedimentary processes (sedimentary mélanges) and mud/shale diapirism (Cowan 1985; Festa et al. 2010).

Olistostromes (Flores 1955) are sedimentary bodies showing highly disrupted strata up to block-in-matrix fabric and mixing of rocks of different ages and regional provenance. They fall, therefore, within the general definition of mélanges (Silver and Beutner 1980). Both terms have thus been widely used.

Sedimentary mélanges/olistostromes are MTCs usually showing comparable size with the largest modern, submarine landslides (Camerlenghi and Pini 2009). Surprisingly, they have been poorly studied from a sedimentological point of view. Studies in the literature aimed to distinguish these bodies from other mélanges, or to define more or less cyclic tectonic-stratigraphic events (Scherba 1987; Delteil et al. 2006).

This article illustrates the results of the integrated study of fossil MTCs, including sedimentary mélanges/olistostromes, with a focus on the Apennines of Italy. We will also address the main problems concerning the comparison between fossil (exposed on-land) and modern (in marine geophysical records) MTCs.

52.2 Types of MTC

Fossil MTCs, especially the large-scale and basin-wide ones, are complex units involving the entire spectrum of mass transport processes (Lucente and Pini 2003). Moreover, they often comprise discrete sub-units, defined on the base of composition, provenance, structures, and sense of movement. These sub-units can be either single mass transport events, pulses, or discrete masses moving differentially in the same event. Figures 52.1–52.5 represent the three different structural associations recognized.

Type 1 MTCs refer to mud-rich deposits characterized by the cohesive behavior of a viscous matrix. The distinctive fabric consist of centimeter- to meter-sized lithic blocks (limestones/marls, sandstones/siltstones or ophiolites) randomly dispersed in a matrix (Fig. 52.1a). The matrix is prevailingly of clays/shales and characterized by millimeter to sub-millimeter clasts of various composition, including indurate clays (brecciated or clastic matrix; Swarbick and Naylor 1980; Pini 1999) (Fig. 52.1b, e). This kind of fabric also acts as a binder, surrounding and sustaining bed packages of tens of meters up to kilometers in size (floaters, out-sized blocks)

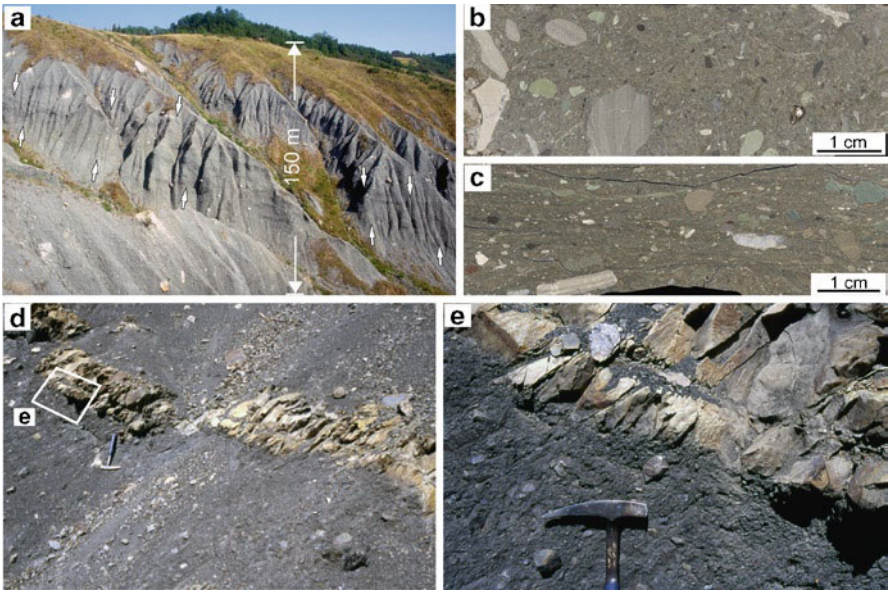

Fig. 52.1 Examples of Type 1 MTCs: (**a**) Olistostrome in the Oligocene-Miocene Epiligurian succession, Bologna area, northern Apennines. *Arrows* point out zones of matrix deformations (*shear zones*) (**b**) Brecciated matrix (**c**) Brecciated matrix deformed in shear zones (**d**) and (**e**) MTC passing upward to deposits by co-genetic turbulent flow. Segavecchia olistostrome, northern Apennines main divide

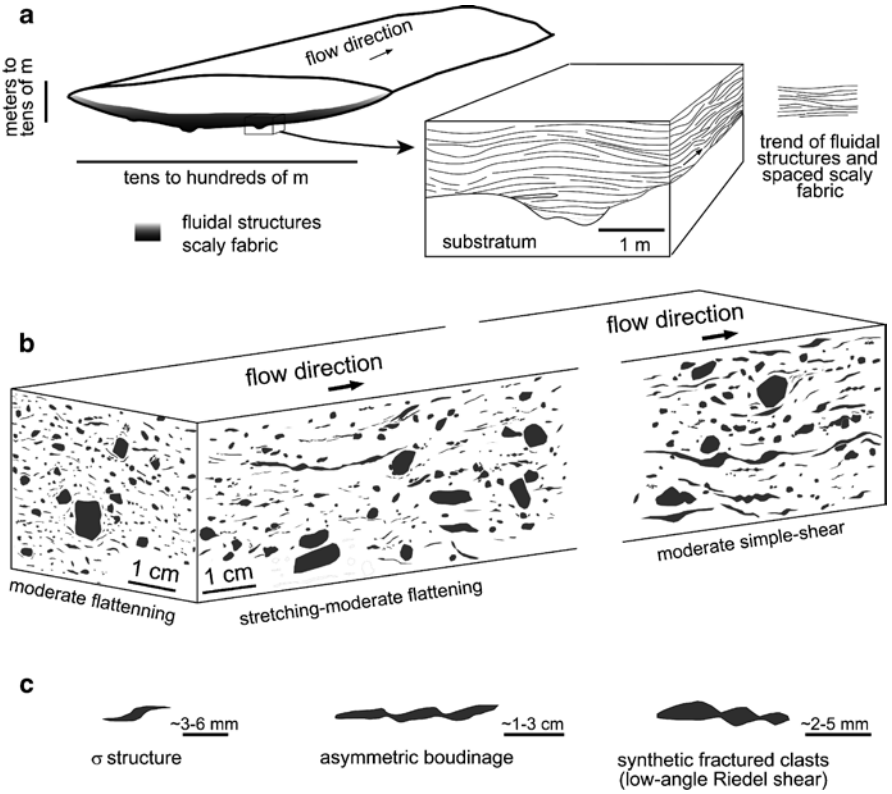

Fig. 52.2 Distribution, general attitude (**a**) and internal structures of the matrix (**b**) into the shear zones in Type 1 MTCs (**c**) deformation of clasts related to simple shear

(Marroni and Pandolfi 2001; Burg et al. 2008). Floaters surrounded by matrix can also predominate (Lucente and Pini 2003).

The block-in-matrix fabric derives from the further disruption and disaggregation of already deformed, mud-dominated, block-in-matrix units (broken formations/mélanges). The matrix derives from remolding of already mixed and deformed (scaly) clays. Floaters are the remnants of the protolith, which maintain the original fabric. Inverse grading of the largest blocks is observable for each individual flow. Meter to tens of meter-scale blocks, prevailingly composed of rocks from the substratum, are also concentrated at the base of MTCs in confined basins (Pini 1999).

The base of the bodies is characterized by spaced scaly fabric and by banding and fluidal structures of the matrix at meter to centimeter-scale at a low angle to the basal contact (Fig. 52.2a). Poorly consolidated clasts display extreme elongation in the direction of flow (Fig. 52.1c) together with a moderate flattening in other directions, and simple shear-related structures (Fig. 52.2b, c). These deformed zones accommodate the flow; simple shear may develop in reason of the increased coupling with the substratum.

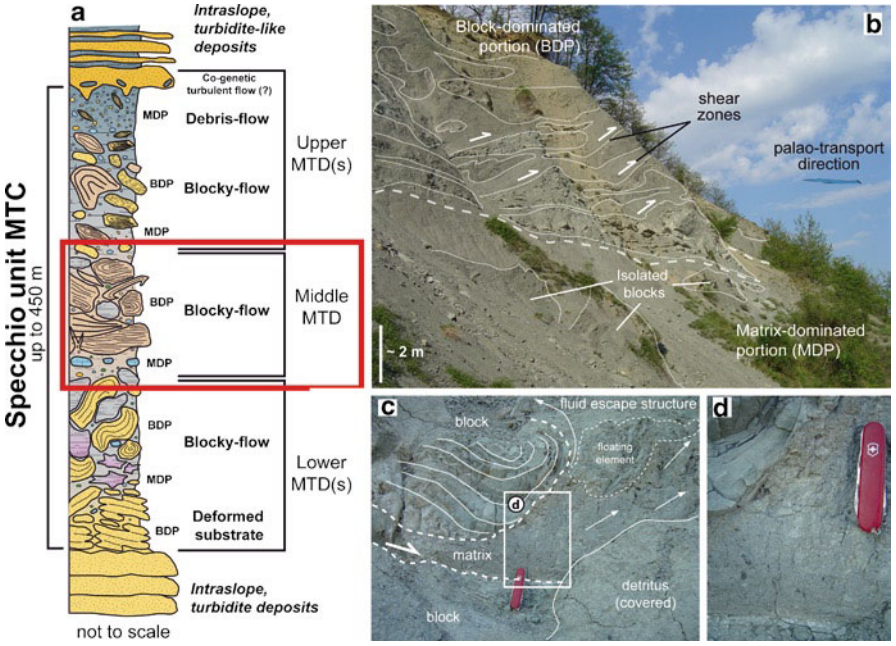

Fig. 52.3 Type 2 MTCs: (**a**) Conceptual stratigraphic log of the Specchio unit composed of at least three individual mass transport deposits (*MTDs*). Early Oligocene Epiligurian succession, northern Apennines. *MDP* = matrix-dominated portions, *BDP* = block-dominated portions (**b**) Outcrop appearance of the middle MTD (*red box* in *a*) (**c**) Picture of a *matrix-underlined* shear zone originating a fluid escape/injection structure. Note the soft sediment folding at the structure margin and the occurrence of hydro-plastically deformed clast floating in the matrix (**d**) Typical outcrop appearance of the liquefied (overpressured) matrix (location in *c*) (From Ogata 2010, adapted)

Such a kind of structure is also evident inside thick olistostromes, corresponding with zones of bock iso-orientation and matrix banding (Pini 1999; Burg et al. 2008) (Fig. 52.1a). These zones may represent the base of individual depositional events (Swarbick and Naylor 1980), or shear zones accommodating internal deformation in a single large-scale event (up to 400 m in thickness).

Type 2 MTCs are characterized by a clastic matrix represented by an unsorted, liquefied mixture of different grain-size populations dispersed within a fine-grained lithology (see Callot et al. 2008; Ogata 2010) (Fig. 52.3), resembling the typical characteristics of an hyper-concentrated suspension (sensu Mutti 1992). These types of MTC generate from a complex flow that is a debris-flow carrying out-size coherent blocks (meters to hundreds of meters across) usually arranged in isolated slump-like folds (blocky-flow deposits, Mutti et al. 2006) (Fig. 52.3b); generally speaking, their internal arrangement resembles a bipartite body, with a block-dominated portion overlying a matrix-dominated one (Ogata 2010) (Fig. 52.3a).

In outcrop, the usual appearance of this matrix is that of sandy/pebbly mudstone/siltstone (Fig. 52.3d) and it can be either diffused within the slide mass and/or concentrated in the basal portion and along the boundaries of discrete internal

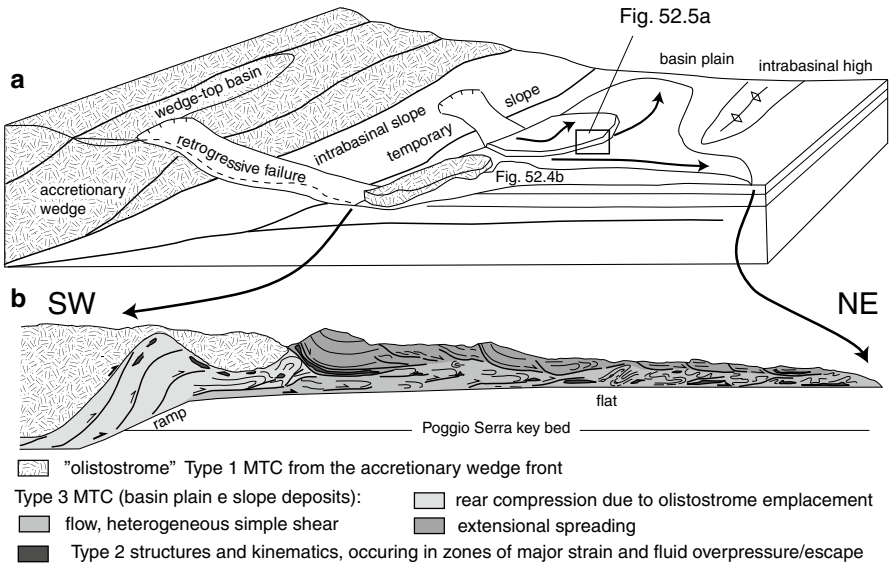

Fig. 52.4 Interpretative paleogeographic block diagram (**a**) and idealized section (**b**) of the Casaglia-Monte della Colonna MTC, Marnoso-arenacea Formation, middle Miocene foredeep of northern Apennines (*b* from Lucente and Pini 2003, modified, reprinted by permission of the American Journal of Science)

components (slide blocks). In particular, this matrix is commonly arranged within heterogeneous shear zones separating slide blocks, and it forms clastic injections (sedimentary dykes), which intrude discrete slide elements (Fig. 52.3c).

The matrix originates from the stratal disruption of poor- to un-lithified sediments, leading to a complete disaggregation and mixing of the involved lithologies, during the down-slope motion of the slide mass. Evidence of liquification (including fluidization, cyclic loading- and shear-related liquefaction; Allen 1982) highlights the occurrence of very rapid deformation acting in undrained conditions. The component sedimentary material primarily derives from the incorporation (erosion) of sediments covering the overridden seafloor and from the partial disaggregation of the blocks carried by the slide. The loose sediments of the uppermost part of the failed sedimentary succession may play a significant role as well.

Type 3 are slump/slide-like MTCs developed in sandy sediments (foredeep turbidites), in which the transport and emplacement is allowed by differential movement of individual bed-packages of different dimensions (Figs. 52.4b, 52.5a). The relative movement occurs along shear zones, represented by millimeters-thick surfaces characterized by "films" of silt and centimeters- to tens of centimeters-thick deformational bands in sandstones (Fig. 52.5c, d), associated to transport and rotation of clasts (occurring both independently and with grain breakage) and fluid elutriation (Dykstra 2005). Relatively wide (some m-thick) zones characterized by isoclinal folding, boudinage, liquification of sandy sediments and disaggregation of pelitic beds, develop less frequently (Lucente and Pini 2003), corresponding to localized Type 2 structures and behavior. The bed packages are characterized by folds, boudinage, extensional and contractional duplexes, and mesoscale thrusts.

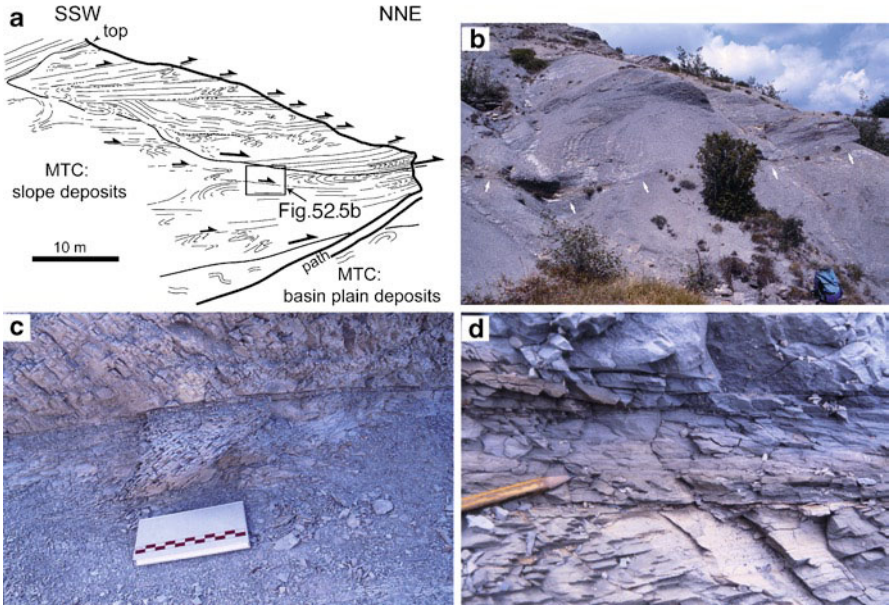

Fig. 52.5 Casaglia-Monte della Colonna Type 3 MTC (**a**) Sketch of the Campanara outcrop showing the main internal subdivisions (bed packages) and their reconstructed, relative movements. Location of the outcrop is in Fig. 52.4a (From Lucente and Pini 2003, modified, reprinted by permission of the American Journal of Science) (**b**), (**c**) and (**d**) Outcrop appearance of a belt of shear surfaces (highlighted by *white arrows* in *c*) at the base of a bed package

A decrease in dimensions of bed packages and an increase of stratal disruption is observable down-flow. The larger bed packages at the slide top imply a high competence to the flow, and/or to their preservation related to lower conditions of strain, giving rise to a hummocky upper surface (Trincardi and Normark 1989).

52.2.1 Mechanisms of Failure, Transport-Emplacement and Coupling with the Substratum

Basin-wide MTCs in the northern Apennines are commonly composed of an intrabasinal component, giving Type 2 or 3 sub-units, and an extrabasinal, "exotic" component resulting in Type 1 sub-units. The assemblage of Type 1 and 3 occurs in deep marine settings, in the foredeep (Lucente and Pini 2003), and is related to the retrogressive failure of the basin plain, the basin margin (slope), and the front of the accretionary wedge (Fig. 52.4a). Type 1 and 3 MTCs are associated with composite bodies originating in shallow marine to coastal setting in wedge-top basins (Ogata 2010; Ogata et al. 2012), where MTCs originated by retrogressive sliding of the basin margins. The "exotic" components with Type 1 behavior were supplied by intrabasinal highs confining the "mini-basins". Retrogressive sliding, cutting back the basin margins, is therefore a recurrent character of the studied MTCs.

As far as the transport-emplacement of the bodies is concerned, the three types should correspond to different velocities of movement, while the nature of the components (i.e. age, composition and lithification degree) should be related to the stratigraphic level of the rupture surface (i.e. shallow or deep seated, sedimentological/tectonic characters of the basin and margins).

Type 1 should represent slow moving bodies, being related to "viscous" shear zones in a clay-dominated matrix. With this kind of mechanics, thick olistostrome-like MTCs could not widely expand into the basins and should be proximal deposits, close to the failure areas. The elevated thickness of this kind of MTC may, however, represent the stack of more subsequent events, and, therefore, overcome these kinematic limits. When preserved, deposits from co-genetic turbulent flows evidence the stacking of single mass-transport events (Pini et al. 2004) (Fig. 52.1d, e).

These bodies can run relatively fast and for longer distances if sustained by a basal "carpet" comprising an overpressured mixture of water and loose sediment (hydroplaning, Mohrig et al. 1998). The shear zones at the base, and inside the bodies, can represent, in this case, zones of concentrated fluid overpressure. While related fluid-escape and injection-related structures commonly occur in Type 2 MTCs, no convincing evidence of such features have been observed so far, nor have dedicated studies been systematically carried on Type 1 MTCs.

Several lines of evidence from the Type 2 MTCs testify the high mobility of the matrix, suggesting fluid overpressure conditions as the main driving process. Such features imply a high velocity of the generating event (catastrophic).

In the Type 3 MTCs overall motion is partitioned in more masses, resulting in complex movement with simple shear at the base and extensional-spreading at the top (Lucente and Pini 2003) (Fig. 52.4a). This should imply a relative lower transport/emplacement velocity with respect to Type 2 MTCs.

The substratum seems to be extensively involved: rip-up clasts are evident in small Type 1 MTCs and the large blocks at the base of the largest bodies (Pini 1999) could be, at least in part, related to erosion of the substratum. The inclusion of substratum material (both coherent or completely loose) is typical of the Type 2 bodies, which are characterized by the major transport velocity. The bulk of coupling with the substratum (erosion in sedimentologic sense) should be related to the late evolutionary stages, when the slide mass momentum is, at least in part, transferred to the overridden seafloor (e.g., deceleration and freezing, changes in the slope gradients, impacting onto intrabasinal highs).

52.3 Conclusion

Through detailed field work, we approached sedimentary mélanges and olistostromes from both sedimentological and structural points of view, restoring the "dignity" of MTCs. The three types of bodies defined here show different mechanics of emplacement and transport, which can correspond to different velocity and mobility. The type is predetermined by MTC composition, which is in turn influenced by: (1) the

geometry and depositional style of pre-slide, basin margins and (2) the way the failures propagate (Fig. 52.4a). The final geometry of the MTCs and their internal features are also determined by the morphology of the depositional basin (Lucente and Pini 2003; Ogata 2010). Direct transition from a type to another is observable in some cases (Fig. 52.4b). In this framework, the three types may represent different stages of slide development, therefore defining end-members of a spectrum of processes.

Are these observations worthy for the understanding of modern MTCs and the definition and mitigation of the related hazards? The size paradox introduced by Woodcock (1979), pointing out that fossil MTCs were not comparable in size with modern ones, has been recovered through the recognition that huge chaotic units may be MTCs. From the increasing number of papers dedicated to the fossil MTCs, a substantial convergence is emerging among distribution, size and recurrence in time of modern and ancient MTCs in diverse geodynamic environments, progressively filling possible gaps (Camerlenghi and Pini 2009; Camerlenghi et al. 2010). Direct comparisons are tentatively possible when MTCs of comparable size are present in similar tectonic and sedimentological settings, such as the cases of Oligocene wedge-top basins of the northern Apennines (Ogata 2010; Ogata et al. 2012) and the Kumano basin in the Nankai forearc (Strasser et al. 2011).

Acknowledgments The authors are indebted with the Reviewer Mason Dykstra and Yuzuru Yamamoto and the Editor Ken Ikehara for their constructive reviews and the continuous support during the editorial process.

References

Allen JRL (1982) Sedimentary structures: their characters and physical basis. vol II, Developments in sedimentology 30B. Elsevier, Amsterdam

Burg J-P, Bernoulli D, Smit J et al (2008) A giant catastrophic mud-and-debris flow in the Miocene Makran. Terra Nova 20:188–193

Callot P, Sempere T, Odonne F, Robert E (2008) Giant submarine collapse of a carbonate platform at the Turonian-Coniacian transition: the Ayabacas formation, southern Peru. Basin Res 20:333–357

Camerlenghi A, Pini GA (2009) Mud volcanoes, olistostromes and Argille scagliose in the Mediterranean region. Sedimentology 56:319–365

Camerlenghi A, Urgeles R, Fantoni L (2010) A database on submarine landslides of the Mediterranean Sea. In: Mosher DC et al (eds) Submarine mass movements and their consequences, Advances in natural and technological hazards research, 28, Spinger, Dordrecht

Cowan DS (1985) Structural styles in Mesozoic and Cenozoic mélanges in the western Cordillera of North America. Geol Soc Am Bull 96:451–462

Delteil J, Mercier De Lepinay M et al (2006) Olistostromes marking tectonic events, East Coast, New Zealand. NZ J Geol Geophys 49:571–531

Dykstra M (2005) Dynamics of sediment mass-transport from the shelf to the deep seas. Unpublished Ph.D. Dissertation, University of California, Santa Barbara

Festa A, Pini GA, Dilek Y, Codegone G (2010) Mélanges and mélange-forming processes: a historical overview and new concepts. Int Geol Rev 52:1040–1105

Flores G (1955) Les résultats des études pour les recherches pétroliféres en Sicile: discussion. In: Proceedings of the 4th world petroleum congress, Rome. Carlo Colombo Editore, Rome

Lucente CC, Pini GA (2003) Anatomy and emplacement mechanism of a large sub-marine slide within the Miocene foredeep in the Northern Apennines, Italy: a field perspective. Am J Sci 303:565–602

Marroni M, Pandolfi L (2001) Debris flow and slide deposit at the top of the internal Liguride ophiolitic sequence, Northern Apennines, Italy: a record of frontal tectonic erosion in a fossil accretionary wedge. Island Arc 10:9–21

Mohrig D, Ellis C, Parker G et al (1998) Hydroplaning of subaqueous debris flows. Geol Soc Am Bull 110:387–394

Mutti E (1992) Turbidite sanstones. AGIP and Istituto di Geologia, Università di Parma, Parma

Mutti E, Carminatti M, Moreira JLP, Grassi AA (2006) Chaotic deposits: examples from the Brazilian offshore and from outcrop studies in the Spanish pyrenees and Northern apennines, Italy. American association of petroleum geologists annual meeting, Houston, 9–12 April

Ogata K (2010) Mass transport complexes in structurally-controlled basins: the Epiligurian Specchio Unit (Northern apennines, Italy). Unpublished Ph.D. thesis, University of Parma

Ogata K, Tinterri R, Pini GA, Mutti E (2012) The Specchio unit (northern Apennines, Italy): an ancient mass transport complex originated from near-coastal areas in an intra-slope setting. In: Yamada Y et al (eds) Submarine mass movements and their consequences, vol. 31, Advances in natural and technological hazards research. Springer, Dordrecht, pp 595–606

Pini GA (1999) Tectonosomes and olistostromes in the Argille Scagliose of the Northern Apennines, Italy. Geol Soc Am Spec Paper 73

Pini GA, Lucente CC, Cowan DS et al (2004) The role of olistostromes and argille scagliose in the structural evolution of the Nothern Apennines. In: Guerrieri L, Rischia I, Serva L (eds) Field trip guidebooks, 32nd IGC Florence. Mem Descr Carta Geol It 63: B13

Scherba IG (1987) Stage and phases of formation of Cenozoic olistostromes in the Alpine Fold Belt. In: Leonov G, Khain VE (eds) Global correlation of tectonic movements. Wiley, New York

Silver EA, Beutner EC (1980) Melanges. Geology 8:32–34

Strasser M, Moore G, Kimura G et al (2011) Slumping and mass-transport deposition in the Nankai forearc: evidence from IODP drilling and 3-D reflection seismic data. Geochem Geophys Geosyst 12:Q0AD13. doi:10.1029/2010GC003431

Swarbick RE, Naylor MA (1980) The Kathikas mélanges, SW Cyprus: late Cretaceous submarine debris flows. Sedimentology 27:63–78

Trincardi F, Normark WR (1989) Pleistocene Suvero slide, Paola basin, southern Italy. Mar Petrol Geol 6:324–335

Weimer P, Shipp C (2004) Mass transport complexes: musing on past uses and suggestions for future directions. Offshore technology conference, Paper 16752, Houston, 3–6 May 2004

Woodcock NH (1979) Size of submarine slides and their significance. J Struct Geol 1:137–142

Chapter 53
The Specchio Unit (Northern Apennines, Italy): An Ancient Mass Transport Complex Originated from Near-Coastal Areas in an Intra-Slope Setting

Kei Ogata, Roberto Tinterri, Gian Andrea Pini, and Emiliano Mutti

Abstract Within the Eocene-Oligocene syn-orogenic deposits of the Epiligurian succession (Northern Apennines of Italy), a field-based study of the Specchio Unit (lower Rupelian) reveals that this complex is made up of three distinct but amalgamated mass-transport deposits (MTDs), the largest of which reaches a maximum volume of ca. 150 km^3. These bodies were deposited inside the complex system of intraslope basin systems, developed atop the submerged Ligurian accretionary prism at the collision with the Adria continental plate. The MTDs originated from catastrophic retrogressive collapses starting from the upper slope and involving progressively shallow-water environments, from distal shelfal pro-delta and delta-front sediments up to proximal coastal fan-delta deposits. These recurrent and close in time, catastrophic slope failures were probably caused by tectonic and climatic triggers, such as the enhanced tectonic activity due to incipient Apenninic continental collision and the onset of harsh climatic conditions, as suggested by oxygen isotopic maxima (e.g., Oi-1a event). Although the wedge toe/foredeep systems are generally

K. Ogata (✉)
Department of Arctic Geology UNIS (University Centre in Svalbard),
Pb. 156, 9171 Longyearbyen, Norway
e-mail: kei.ogata@unis.no

R. Tinterri
Dipartimento di Scienze della Terra, Università degli Studi di Parma,
Viale G.P. Usberti 157/A, Campus, 43100 Parma, Italy

G.A. Pini
Dipartimento di Scienze della Terra e Geologico-Ambientali, Università di Bologna,
Via Zamboni, 67, 40127 Bologna, Italy
e-mail: gianandrea.pini@unibo.it

E. Mutti
Localita' Nociveglia, 24 - 43041 Bedonia (Parma), Italy

Y. Yamada et al. (eds.), *Submarine Mass Movements and Their Consequences*,
Advances in Natural and Technological Hazards Research 31,
DOI 10.1007/978-94-007-2162-3_53, © Springer Science+Business Media B.V. 2012

considered the principal *loci* of such, usually located in deep-water settings, here we stress the importance of catastrophic mass transport events also atop the wedge, in shallow-water depositional domains. Mass transport processes also have a fundamental role in reshaping the upper physiographic profile of an evolving accretionary wedge. The correct interpretation of such mass transport processes has also important implications for geohazard forecasting in modern active continental margins, for example in terms of tsunamigenic potential.

Keywords Ancient mass-transport deposits • Epiligurian succession • Ranzano Formation • Catastrophic process • Failure depth

53.1 Introduction

Geophysical surveys of modern continental margins have strongly enhanced our understanding of mass transport deposits (MTDs), better defining their geometry and shape, and highlighting their implications in term of geohazard (Mosher et al. 2009). On the other hand, studies on ancient MTDs exposed in orogenic belts provided detailed information on internal structures and their relationships with encasing sediments, allowing important considerations on triggering mechanisms and transport/depositional processes (Lucente and Pini 2003; Callot et al. 2008).

Importantly, the integration of geophysical and outcrop data reveals that modern convergent continental margins show little or no evidence of catastrophic, large-scale submarine landslides, compared to what inferred from exposed orogenic belts (Camerlenghi et al. 2009).

The tsunamigenic potential of submarine landslides, as defined by modern marine geology, could be extrapolated through some diagnostic features: (1) depth and location of failure, (2) process velocity, (3) volume and consolidation state of involved material, and (4) physiography of the depositional setting (Lykousis et al. 2007) and (5) run-out. These features can be directly and indirectly recognized through the sedimentologic and structural analysis of ancient, on-land-exposed MTDs, and their stratigraphic constrain within the sedimentary succession.

The analyzed Specchio unit is an ancient, basin-wide mass transport complex originated within wedge-top, lower Oligocene deposits of the Ranzano Formation of the Epiligurian succession, cropping out in the eastern side of the northern Apennines (Italy). This complex originated through multiple, retrogressive, catastrophic collapses involving shallow-water, proximal environments and was emplaced in the intra-slope domain. Three main depositional events have been triggered by these collapses, the largest of which shows an overall volume of dry sediment of ~150 km^3 (Ogata 2010).

This work highlights the importance of outcrop studies in the recognition of tsunamigenic diagnostic features of ancient MTDs, although basin margins are eroded away and direct evidence of related tsunami(s) are no longer recognizable.

53.2 The Northern Apennines and the Epiligurian Succession

The allochthonous Ligurian nappe (Ligurian units) is the remnant of a Late Cretaceous-Eocene accretionary prism thrust over a foreland fold-and-thrust belt during the Neogene tectonic evolution of the Apennines (Cerrina Feroni et al. 2004; Molli 2008; Argnani 2009). Late Eocene to Miocene syntectonic sequences, the Epiligurian succession (Ricci Lucchi 1986), were deposited in wedge-top basins transported atop the NE-ward advancing Ligurian nappe (piggy-back basins; Ori and Friend 1984).

The Eocene-Oligocene interval of the Epiligurian succession deposited within a complex basin system elongated in NW-SE direction (Fig. 53.1a), extending southeast of the Tertiary Piedmont Basin (TPB) (Cibin et al. 2001). Together with the TPB, this sedimentary interval represents a large episutural basin, developed after the mesoalpine event along the eastern margin of the Western Alps/paleo Apennines system (Mutti et al. 1995).

The Eocene-Oligocene Epiligurian succession comprises (Bettelli et al. 1989) pelagic and hemipelagic sediments (Monte Piano Fm., MMP), with mud-rich chaotic bodies at the base (Baiso "breccias", BAI), and coarse–grained, turbidite-like deposits (Ranzano Fm., see below). This succession has been deposited at lower- to upper-bathyal depths (Di Giulio et al. 2002).

The Ranzano Fm. is classically subdivided in three litostratigraphic members (Catanzariti et al. 1997; Martelli et al. 1998): (1) upper Priabonian Pizzo d'Oca Mb. (PZO), (2) lower Rupelian Val Pessola Mb. (R1), and (3) upper Rupelian Varano de' Melegari Mb. (R3) (Fig. 53.1b). These members roughly coincide with unconformity-bounded units (Mutti et al. 1995).

These are mainly turbiditic deposits supplied from HP/LT metamorphic, continental crust (PZO), ophiolites of the Ligurian units (R1) and calcareous flysch of the Ligurian units (R3) (Cibin et al. 2001).

Notably, close to the Villavernia-Varzi/Ottone-Levanto tectonic line (VVOL; Fig. 53.1a), R1 consists of fossiliferous shelfal deposits, while in the eastern TPB it consists of fan-delta conglomerates (Mutti et al. 1995).

The Specchio unit (R2) is intercalated between R1 and R3 successions, which represent the pre- and post-slide deposits, respectively (Fig. 53.1).

53.3 The Specchio Unit

53.3.1 General Fabric

The general fabric/texture is dominantly defined by a fine-grained, unsorted *matrix* which envelopes, injects and sustains discrete slide elements, ranging from hundred of m-scale slabs to mm-scale particles (*blocks* and *clasts*).

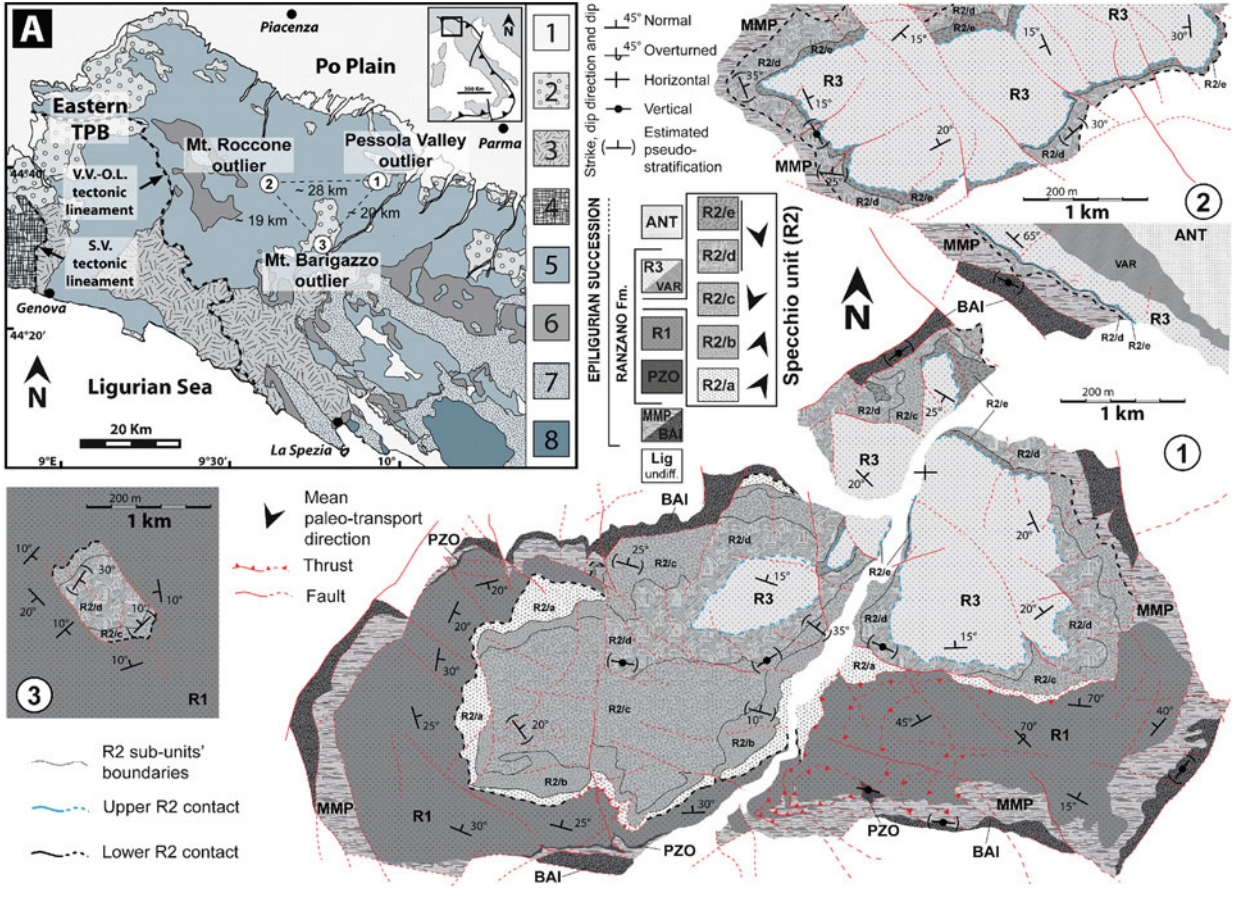

Fig. 53.1 (**a**) Simplified geological map of the northern Apennines: (1) Plio-Quaternary units, (2) Epiligurian and Tertiary Piedmont Basin units, (3) Internal Ligurian units, (4) Voltri Group (Alpine HP/LT metamorphic units), (5) External Ligurian units, (6) Subligurian units, (7) Tuscan units, (8) Apuane Alps (Tuscan low-grade metamorphic units) (**b**) Location and detailed geological maps (and explanation) of the analyzed Epiligurian outliers; *LIG*: Ligurian substratum undifferenciated; *VAR*: chaotic lithofacies embedded in R3; *ANT*: Lower Miocene Antognola Fm

Evidence of liquefaction-fluidization characterizes the matrix, which originated from fast remolding and mixing of unconsolidated to poorly consolidated sediment, either failed and/or eroded from the seafloor during the mass transport event (Ogata 2010).

Blocks are parts of beds or bed-packages (regularly bedded to stratally disrupted). Most of the blocks are usually arranged in detached (rootless) slump-like folds. These blocks can be embedded as floating isolated elements, or be clustered in contact, separated by thin matrix-underlined shear surfaces.

These blocks still contain primary signatures of the original depositional environment (i.e. sedimentary facies associations, ichnofacies, fossils, authigenic minerals, etc.), giving fundamental information on their provenances.

53.3.2 A Composite, Multi-event Complex

The Specchio unit has been subdivided in five mappable sub-units, R2/a, R2/b, R2/c, R2/d and R2/e from the base to the top, on the basis of composition, facies associations, textures/fabric and stratigraphic position (Figs. 53.1 and 53.2). These bodies also show different paleo-transport directions, obtained through structural analysis of planar (i.e. syn-sedimentary shear surfaces, folds axial planes) and linear features (i.e. fold axes plunge and trend, sheath folds long axes) (Strachan and Alsop 2006).

The two lower sub-units (R2/a and R2/b) represent local N-NE-directed MTDs, because of the ramp-flat geometry of the basal contact and the limited lateral extent. They might represent the denudation/degradation complex (Morley 2009) of syn-sedimentary, intrabasinal growing highs bounding the depocenter of the Pessola Valley outlier (thrust stacking, Fig. 53.1b).

R2/a is almost exclusively composed of depocentral R1 sediments, probably provided by the deep erosion of the seafloor (see Fig. 53.1b). R2/b originates from the same failure zone and shows the same transport direction. The significant addiction of material from the MMP, BAI and subordinately by Ligurian-derived shales may suggest a deepening of the original basal rupture surface down into the core of the structural highs, rooted in the chaotic complexes of the Ligurian substratum. Since their close association and vertical continuity, R2/a and R2/b may represent different pulses of the same event.

R2/c comprises R1, PZO and MMP blocks, and boulders/clasts from Ligurian carbonates, and shows S-directed palaeo-transport directions. It represents a relatively long run-out event, triggered by the collapse of a marginal high located in the northern sectors, and draped by deposits coeval with the depocentral R1 and PZO sediments. The emplacement of this MTD may have temporarily smoothed the topography favoring the wider extent of the following S-SE-directed mass transport events.

R2/d and R2/e represent two phases of the same generating event coming from NE sectors. Their occurrence in every analyzed outlier, testifies a basin-wide event, composed of material coming from proximal deposits of the PZO-R1 units, bearing

Fig. 53.2 Simplified logs of the Specchio unit for the analyzed outliers (location in Fig. 53.1) and photos of the internal elements (locations are labeled in the logs) (**a**) Oxidized lignite clast (**b**) carbonate cobble with lithodome burrows (**c**) fan-delta conglomerate block (**d**) bioclastic sandstone (mainly *nummulites*) composing shelfal blocks (**e**) *planolites*-type bioturbation in shelfal blocks (**f**) very thin bedded sandstones-mudstones couplets in pro-delta block (**g**) *zoophycos*-type bioturbation in pro-deltaic blocks (**h**) and (**i**) Ligurian (exotic) carbonate blocks (encircled knife and hammer for scale) (**j**) *ophiomorpha*-type bioturbation in delta-front block (**k**) Ligurian (exotic) angular carbonate clast with original encasing shales

evidence of shelfal, fan delta, delta-slope and pro-delta facies. Bioturbations, fossils and sparse glauconite nodules within bedded blocks, lithodome borings in pebbles and cobbles, and the overall upward increase of plant fragments (oxidized lignite), confirm a provenance from shallow-marine environments, close to the coastline (Fig. 53.2). This suggests the retrogressive collapse of the basin-margin sediments, roughly from the southeastern TPB, constraining the possible failure zone close to the VVOL, representing large-scale structural high during Early Oligocene, (Mutti et al. 1995).

53.3.3 Slide Kinematics

In each MTD, blocks predominate in the upper part while relatively continuous m- to ten of m-thick, matrix-dominated interval occurs in the lower part (Fig. 53.2), evidencing a bi-partite sliding process.

The abundant matrix acts as a lubricant medium, accommodating internal friction forces, and enhancing the slide mass mobility. In this framework, matrix-dominated portions act as overpressured horizons that "passively" transport the overlying block-dominated portions (Ogata 2010).

These evidences suggest blocky- and debris-flow process as driving mechanisms, thus representing catastrophic failures (high volume, fast-rated, episodic events) (Mutti et al. 2006; Mutti et al. 2009; Ogata 2010).

Notably, the paleo-transport directions of these events reveal their spreading along the inferred main axis of the depocenters (i.e. parallel to the regional strike and perpendicular to the growing direction of the accretionary prism), due to lateral confinement (Fig. 53.3).

53.3.4 Possible Regional Triggering Causes

Aside the local conditioning factors, regional triggers are required to justify the generalized collapse of different intrabasinal/marginal highs, and the large amount of failed material.

The Lower Rupelian represents a period of reorganization of the Alps/Apennines orogenic system (Molli 2008; Argnani 2009): tectonic activity during this time is confirmed by syn-sedimentary thrusts deforming MMP, PZO and R1 (Catanzariti et al. 1999) and the possible onset/closure of an early Apenninic foredeep (Aveto-Petrignacola Formation) (Catanzariti et al. 2003). Andesitic clasts in the latter and related detritus in the R3 testify coeval calcalkaline volcanism (Cibin et al. 1998).

In the same time span the Eocene-Oligocene climatic shift took place (Oi-1 event; Miller et al. 1991): the regional unconformity at the base of the R1 roughly correspond to the onset of this transition (Catanzariti et al. 1997). In this framework, the Specchio unit events perfectly coincide with an enhanced eustatic fall (Oi-1a phase; Miller et al. 2008) (Fig. 53.3).

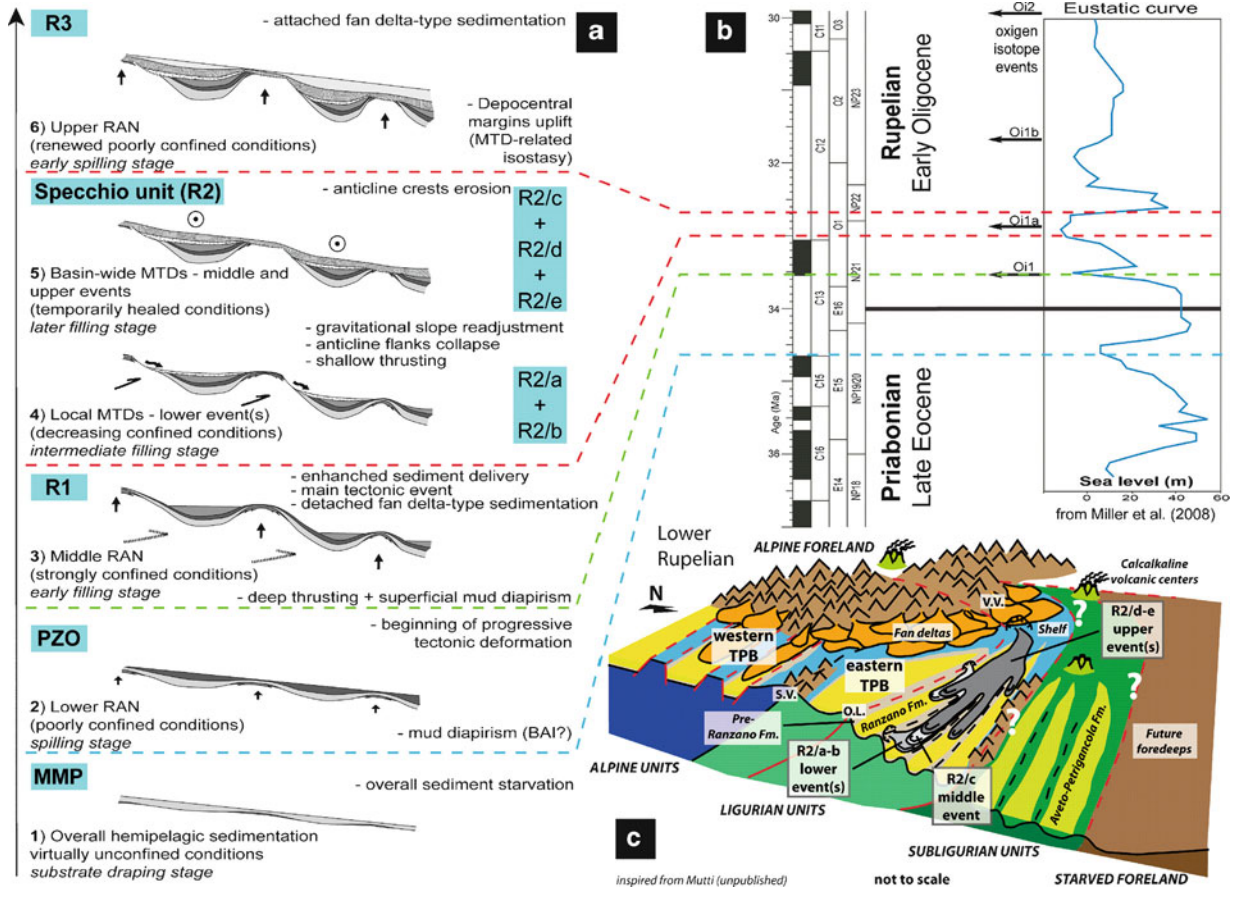

Fig. 53.3 (**a**) Schematic cartoon showing depositional stages of the Ranzano Fm. and Specchio unit and the evolution of the basinal system physiography; linked time constrain in B (**b**) Chronographic scheme for the Eocene-Oligocene transition with location of the oxygen isotopes events and related eustatic curve (From Miller et al. 2008) (**c**) Conceptual block diagram showing the inferred setting for the Specchio unit MTDs deposition

Aside the possible "auto-cyclic" character these MTDs emplacement (i.e. each event causes the following), the possible triggering mechanisms should be attributed to the combined effect of: (1) seismic-shocks, (2) sedimentary overloading (e.g., enhanced fluvial discharge), (3) progressive tectonic-induced slope oversteepening, and (4) severe climatic events (e.g., flood-related failures and/or storm-wave cyclic loading). Although a generalized and rapid sea-level fall may suggest that gas hydrates dissociation can be one of the main possible triggers, the shift toward a cold climate should increase their stability field, acting in some kind of negative feedback relationship (Grozic 2009).

53.4 Conclusions

The Specchio unit is a MTC contained within the Ranzano Fm. (Priabonian-Rupelian) of the Epiligurian succession (northern Apennine), and it is generated by the rapid accumulation of at least three MTDs: (1) the basal one(s) coming from the southern sectors, of mixed extra- and intrabasinal composition, originated from structural highs close to the depocentral areas, (2) the middle one coming from the northern sectors, of mainly intrabasinal composition, originated from structures located in a relatively distal position from the main depocenters, and (3) the upper one(s) coming from northern sectors, composed of shallow-water related sediments failed from the basin margins, in proximal position in respect to the inferred feeding areas (i.e. coastal areas). Thus, the inferred originating event(s) developed through an overall retrogressive process, cutting back from upper-slope/shelf-break settings to shelfal, shallow-water environments, up to the coastline.

The Specchio unit emplacement is thought to represent the rapid sedimentary response to the synergic effect of long-termed tectonic and climatic factors both acting during the Early Oligocene: active syn-sedimentary tectonism (controlled by the readjustment of proto-apenninic wedge) and eustatic sea-level fall (related to the Eocene-Oligocene climatic transition).

In summary, we stress the importance of field-based studies as an extremely useful tool to identify diagnostic tsunamigenic characteristic within the slide mass, even if related tsunami deposits are no longer recognizable in the sedimentary record.

Acknowledgments The authors thank the reviewers F. Odonne, Y. Ogawa and F. Gamberi for their constructive comments. Data presented in this paper are from the doctoral research of K. Ogata at the University of Parma.

References

Argnani A (2009) Plate tectonics and the boundary between Alps and Apennines. Ital J Geosci 128:317–330

Bettelli G, Bonazzi U, Fazzini P, Panini F (1989) Schema introduttivo alla geologia delle Epiliguri dell'Appennino Modenese e delle aree limitrofe. Mem Soc Geol Ital 39:215–244

Callot P, Sempere T, Odonne F, Robert E (2008) Giant submarine collapse of a carbonate platform at the Turonian-Coniacian transition: the Ayabacas formation, southern Peru. Basin Res 20:333–357

Camerlenghi A, Urgeles R, Fantoni L (2009) A database on submarine landslides of the Mediterranean Sea. In: Mosher DC, Shipp C, Moscardelli L, Chaytor J, Baxter C, Lee HJ, Urgeles R (eds) Submarine mass movements and their consequences, Advances in natural and technological hazard research 28. Springer, Dordrecht, pp 491–501

Catanzariti R, Rio D, Martelli L (1997) Late Eocene to Oligocene calcareous nannofossil biostratigraphy in Northern Apennines: the Ranzano Sandstone. Mem Sci Geol Ital 49:207–253

Catanzariti R, Cerrina Feroni A, Ottria G, Vescovi P (1999) Lower Oligocene thrust-system in the epi-Ligurian succession: evidence from the Enza Valley (northern Apennines, Italy). Geodinamica Acta 12(2):81–96

Catanzariti R, Cerrina Feroni A, Marroni M, Ottria G, Pandolfi L (2003) Ophiolites debris in the Aveto unit (Trebbia Valley, Northern Apennines, Italy): a record of the Early Oligocene apenninic foredeep? EGS – AGU – EUG joint assembly, Nice, 6–11 April.

Cerrina Feroni A, Ottria G, Ellero A (2004) The Northern Apennine, Italy: geological structure and transpressive evolution. In: Crescenti U, D'Offizi S, Merlino S, Sacchi L (eds) Geology of Italy. Special Volume of the Italian Geological Society for the IGC 32 Florence-2004, pp 14–32

Cibin U, Tateo F, Catanzariti R, Martelli L, Rio D (1998) Composizione, origine ed età del vulcanismo andesitico oligocenico inferiore dell'Appennino Settentrionale: le intercalazioni vulcano-derivate nella formazione di Ranzano. Boll Soc Geol Ital 117:569–581

Cibin U, Spadafora E, Zuffa GG, Castellarin A (2001) Continental collision history from arenites of episutural basins in the Northern Apennines, Italy. GSA Bull 113(1):4–19

Di Giulio A, Mancin N, Martelli L (2002) Geohistory of the Ligurian orogenic wedge: first inferences from Epiligurian sediments. Boll Soc Geol Ital Spec Vol 1:375–384

Grozic JLH (2009) Interplay between gas hydrates and submarine slope failure. In: Mosher DC, Shipp RC, Moscardelli L, Chaytor JD, Baxter CDP, Lee HJ, Urgeles R (eds) Submarine mass movements and their consequences, Advances in natural and technological hazards research 28., pp 11–30

Lucente CC, Pini GA (2003) Anatomy and emplacement mechanism of a large submarine slide within a Miocene foredeep in the Northern Appennines, Italy: a field perspective. Am J Sci 303:565–602

Lykousis V, Sakellariou D, Locat J (eds) (2007) Submarine mass movements and their consequences. Advances in natural and technological hazards research 27. Springer, Dordrecht

Martelli L, Cibin U, Di Giulio A, Catanzariti R (1998) Litostratigrafia della Formazione di Ranzano (Priaboniano sup.-Rupeliano, Appennino Settentrionale e Bacino Terziario Ligure Piemontese). Boll Soc Geol Ital 117:151–185

Miller KG, Wright JD, Fairbanks RG (1991) Unlocking the ice house: oligocene-miocene oxygen isotopes, eustasy and margin erosion. J Geophys Res 96:6829–6848

Miller KG, Browning JV, Aubry MP, Wade BS, Katz ME, Kulpecz AA, Wright JD (2008) Eocene-Oligocene global climate and sea-level changes: St. Stephens Quarry, Alabama. GSA Bull 120(1/2):34–53

Molli G (2008) Northern Apennine-Corsica orogenic system: an updated review. In: Siegesmund S, Fügenschuh B, Froitzheim N (eds) Tectonic aspects of the Alpine-Dinaride-Carpathian system. Geological Society of London, Spec Publ 298, pp 413–442

Morley CK (2009) Growth of folds in a deep-water setting. Geosphere 5(2):59–89

Mosher DC, Shipp RC, Moscardelli L, Chaytor JD, Baxter CDP, Lee HJ, Urgeles R (eds) (2009) Submarine mass movements and their consequences. Advances in natural and technological hazards research 28. Springer, Dordrecht

Mutti E, Papani L, Di Biase D, Davoli G, Mora S, Segadelli S, Tinterri R (1995) Il Bacino Terziario Epimesoalpino e le sue implicazioni sui rapporti tra Alpi ed Appennino. Mem Sci Geolo Padova 47:217–244

Mutti E, Carminatti M, Moreira JLP, Grassi AA (2006) Chaotic deposits: examples from the Brazilian offshore and from outcrop studies in the Spanish Pyrenees and Northern Apennines, Italy. A.A.P.G. Annual meeting, Houston, 9–12 April

Mutti E, Ogata K, Tinterri R, Carè D (2009) Fine-grained unsorted matrix as evidence of excess pore pressure in sedimentary chaotic units. 27th I.A.S. International meeting, Alghero (Sardinia), 20–23 Sept

Ogata K (2010) Mass transport complexes in structurally-controlled basins: the Epiligurian Specchio Unit (Northern Apennines, Italy). Unpublished PhD thesis, University of Parma

Ori GG, Friend PF (1984) Sedimentary basins formed and carried piggy-back on active thrust sheets. Geology 12:475–478

Ricci Lucchi F (1986) The foreland basin system of the Northern Apennines and related clastic wedges: a preliminary outline. Giornale di Geol 48(1):165–185

Strachan LJ, Alsop GI (2006) Slump folds as estimators of palaeoslope: a case study from the Fisherstreet Slump of County Clare, Ireland. Basin Res 18:451–470

Chapter 54
Internal Stress Fields of a Large-Scale Submarine Debris Flow

Hajime Naruse and Makoto Otsubo

Abstract Numerical experiments on subaqueous mass transport processes were conducted to understand the internal stress field associate with a natural example of a submarine debris flow, which was revealed by detailed analysis of a deposit exposed as a nearly 1.6 km continuous outcrop. Deposits of gravelly mudstone containing large deformed sedimentary blocks occur in the Upper Cretaceous to Paleogene Akkeshi Formation distributed in the Hokkaido Island, northern Japan. Application of the multiple inverse method to meso-scale faults observed in the blocks reveals possible internal paleostress fields that existed prior to deposition. This analysis suggested two different stress fields: (1) a uni-axial compressional stress field, where the maximum principal compression axis is normal to the bedding surface, and (2) a tri-axial compressional stress field, where the orientation of maximum principal compression axis is parallel to the paleocurrent direction. The results of numerical experiments imply that the first of these stress fields is generated by radial spreading of the flow during its downcurrent movement, while the second stress field results from compression during deposition on the basin plain. A horizontal compression paleo-stress field can be an indicator of the paleocurrent direction of the debris-flow. In addition, it is also suggested that existence of a horizontal compression paleo-stress field can provide a clue for the initial conditions of the submarine landslide.

Keywords Debris flow • Numerical experiment • Slump • Submarine landslide • Paleostress analysis

H. Naruse (✉)
Faculty of Science, Department of Earth Sciences, Chiba University,
1-33 Yayoicho, Inage-ku, Chiba 263-8522, Japan
e-mail: naruse@faculty.chiba-u.jp

M. Otsubo
Research Center for Deep Geological Environments, National Institute
of Advanced Industrial Science and Technology, Tsukuba Central 7, 1-1, Higashi 1-Chome,
Tsukuba-shi, Ibaraki-ken 305-8567 Japan
e-mail: otsubo-m@aist.go.jp

Y. Yamada et al. (eds.), *Submarine Mass Movements and Their Consequences*,
Advances in Natural and Technological Hazards Research 31,
DOI 10.1007/978-94-007-2162-3_54, © Springer Science+Business Media B.V. 2012

54.1 Introduction

Mass-transport deposits are major components of depositional systems in the deep-sea environment (e.g., Weimer 1991). These deposits usually are muddy chaotic deposits, and are expected to act as permeability seals over channel deposits. These mass-transport deposits appear as transparent layers on seismic data and chaotic intervals in cores. In spite of their common occurrence and distinctive geometry, the dynamics of subaqueous mass transport processes (debris flows) are not well known. This is because direct observation of a subaqueous debris flow is virtually impossible. In addition, seismic data are inadequate for detailed research of debris-flow processes because of the acoustically transparent nature of chaotic deposits (e.g., Mayall et al. 2006). Finally, cores are too small quantitatively to analyze large-scale structure in this kind of deposit.

Thus, geological surveys of large outcrops and flume or numerical experiments seem to be necessary to understand the dynamics of large mass-flows. Naruse and Otsubo (2011) documented quantitatively the internal structures of a mass-transport deposit. Apparently, a single flow deposit, composed of gravelly mudstone and sedimentary blocks up to 100 m in diameter, was exposed as a nearly 1.6 km-long continuous outcrop. Naruse and Otsubo revealed the heterogeneous characteristics of the internal structures of this submarine mass flow, as well as paleostress fields inferred to be present from measurements of meso-scale faults in this deposit.

This study aims to interpret the paleostress field reconstructed from the large-scale subaqueous debris-flow studied by Naruse and Otsubo (2011), and to apply this to understand debris flow processes in general. Numerical experiments were conducted for this purpose; they were found to provide reasonable explanations of paleostress fields of the outcrop. This result underlines the significance and usefulness of paleostress analysis in order to characterize and interpret debrites.

54.2 Geologic Setting

The mass-transport deposit studied by Naruse and Otsubo (2011) is in the Akkeshi Formation, from the middle part of the Cretaceous-Paleocene Nemuro Group (Fig. 54.1). The Campanian–Paleocene Nemuro Group, which has been interpreted to be part of the fore-arc basin deposition of the Kuril Arc (Kiminami 1983), occurs in the eastern portion of Hokkaido Island. The regional strata of this group mostly consist of sediment gravity-flow deposits and hemipelagic mudstones (Naruse 2003). The age of the Nemuro Group ranges from Maastrichtian to Paleocene (Naruse 2003). The bedding strikes 60–80° east of north and dips 10–20° to the south. Distinct tectonic folding is not present.

The 900–1,300 m-thick Akkeshi Formation consists of three lithofacies. These units are thinly bedded (<15 cm thick) or laminated fine sandstone and mudstone, thickly bedded or structureless poorly-sorted, coarse sandstone, and chaotic deposits

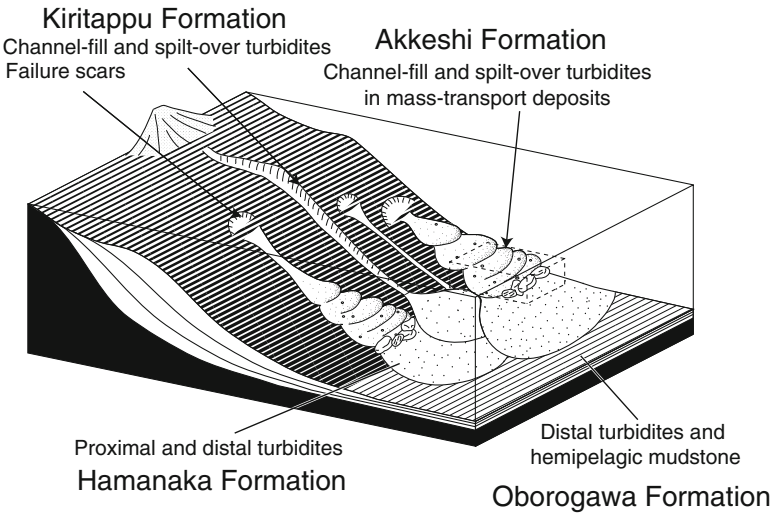

Fig. 54.1 Inferred depositional environments of the Nemuro Group (Modified from Naruse 2003)

(sensu Pickering et al. 1989). This depositional environment is interpreted as a submarine channel-levee complex and chaotic mass-transport deposits at the foot of a lower submarine slope (Naruse 2003). The Akkeshi Group is overlain by the Kiritappu and the Shiomi formations. The Shiomi Formation is a mud-prone deposit, and Naruse and Nifuku (2008) used the 3D morphology of ichnofossils to show that the Shiomi Formation was deposited in an upper-slope environment that was inclined southeastward at about 8°.

54.3 Reconstruction of Stress Field in Large-Scale Debris Flow from Geologic Record

A paleostress field of a large-scale subaqueous debris-flow was reconstructed from the deposit exposed in a 1.6-km continuous outcrop in the Akkeshi Formation. The methodology to reconstruct paleostress fields and results is outlined below (see Naruse and Otsubo 2011, for more details).

The debris-flow deposit in the Akkeshi Formation is composed of a gravelly mudstone, containing large deformed sedimentary blocks. The outcrop extends from northwest to southeast, which appears as parallel to strike of strata. Thus, the same bed is exposed along this outcrop. The outcrop is 5–30 m in height. Paleocurrent direction measured from turbidites outside of the mass-transport deposit suggests that the direction of sediment-transport oriented toward the southeast (Naruse 2003). Most of the deformed blocks in the outcrop reside in a gravelly mud matrix.

Abundant meso-scale faults occur in the sedimentary blocks within the debris-flow deposit. Discontinuities at the edges of blocks indicate that most meso-scale faults formed during block transport. A total of 22 striated meso-scale faults were measured for strike, dip, and direction of striations. A northwest-southeast orientation of strike measurements of faults dominates this dataset.

These data were analyzed using the multiple inverse method with k-means clustering (Otsubo et al. 2006). The multiple inverse method is a resampling technique that can separate stresses from relatively small numbers of heterogeneous fault-slip data (Yamaji 2000; Otsubo and Yamaji 2006). Multiple inverse methodology iteratively resamples data subsets from a set of fault-slip data, and determines optimal stress tensors for the subsets. Optimal solutions occur as reduced stress tensors. Significant stresses occur as clusters on stereograms that show principal stress orientations and stress ratios; clusters of these stresses are considered to be significant solutions. These clusters are automatically identified by the k-means clustering technique (Otsubo et al. 2006).

Two stress types existing in six potential paleostress clusters emerged from the results of the multiple inverse method. Type 1 stress fields are manifested as 1-axis compressional stress fields with vertical $\sigma 1$ axes, indicating a low stress ratio (approximately 0.1). Type 2 stress fields correspond to tri-axial compressional stress fields with $\sigma 1$ axes oriented northwest-southeast, i.e. parallel to the inferred paleocurrent direction (Naruse 2003). A uni-axial compressional stress field (Type 1), where $\sigma 1$ is normal to the bedding surface, suggests radial tension in all directions in the paleo-horizontal plane, because the estimated value of $\sigma 2$ is nearly equal to $\sigma 3$. A tri-axial compressional stress field (Type 2) implies a horizontal compression in a direction parallel to the paleocurrent. A Type 2 stress field can also be inferred from the preferred orientation of block folds (Naruse and Otsubo 2011). The extensional stress field could also result from compaction of the deposit after deposition; however, discontinuities at the edges of blocks indicate that most meso-scale faults measured in the outcrop formed during block transport, because the faults should also deform flow matrix if they were formed by post-depositional tectonic activity or compaction. The flow was estimated to be very thick (>30 m) so that the confining pressure could be large enough to produce the striated faults in blocks during its downslope movement (Naruse and Otsubo 2011). Therefore, these meso-scale faults at least partly record the internal stress fields of the flow.

54.4 Numerical Experiments

In total 64 numerical experiments were conducted to understand the internal paleostress fields identified by Naruse and Otsubo (2011). Although it is impossible to obtain realistic physical properties of the flows that are necessary to simulate subaqueous debris-flows precisely, numerical experiments enable investigation of the qualitative flow behavior and dependencies on governing variables.

54.4.1 Model Formulation

In the analysis presented here, a numerical model of debris flows based on the BING formulation (Imran et al. 2001) is employed. In the present implementation, the model assumes that the flow has a constant width normal to the flow direction and shows a Bingham rheology. This latter assumption may be justified because the debris-flow deposit exposed in the Akkeshi Formation is mostly composed of gravelly mud.

The numerical model BING uses following three equations to describe the basic dynamics of a muddy subaqueous debris flow (Lin and Leblond 1993; Pratson et al. 2000; Imran et al. 2001):

$$\frac{\partial h}{\partial t}+\frac{\partial}{\partial x}\left[U_p h_p+\frac{2}{3}U_p h_s\right]=0 \tag{54.1}$$

$$\begin{aligned}&\frac{2}{3}\frac{\partial}{\partial t}\left(U_p h_s\right)-U_p\frac{\partial h_s}{\partial t}+\frac{8}{15}\frac{\partial}{\partial x}\left(U_p{}^2 h_s\right)-\frac{2}{3}U_p\frac{\partial}{\partial x}U_p h_s\\&=h_s g\left(1-\frac{\rho}{\rho_m}\right)S-h_s g\left(1-\frac{\rho}{\rho_m}\right)\frac{\partial h}{\partial x}-2\frac{\mu_m}{\rho_m}\frac{U_p}{h_s}\end{aligned} \tag{54.2}$$

$$\begin{aligned}&\frac{\partial}{\partial t}\left(U_p h_p\right)-\frac{\partial}{\partial x}\left(U_p{}^2 h_p\right)+U_p\frac{\partial h_s}{\partial t}+\frac{2}{3}U_p\frac{\partial}{\partial x}U_p h_s\\&=h_p g\left(1-\frac{\rho}{\rho_m}\right)S-h_p g\left(1-\frac{\rho}{\rho_m}\right)\frac{\partial h}{\partial x}-\frac{\tau_m}{\rho_m}\end{aligned} \tag{54.3}$$

where ρ and ρ_m are density of the ambient fluid and the mudflow; ρ is slope; ρ is acceleration due to gravity; μ_m is dynamic viscosity; τ_m is yield strength of flow matrix; t and x denotes time and downslope location. h_p and h_s are thickness of plug and shear layers, and U_p is vertically averaged velocity of the plug layer. Equation 54.1 is the continuity equation expressing the mass conservation of sediment and fluid in the debris flow. Equations 54.2 and 54.3 are the momentum equations for the shear and plug layers, respectively, in a debris flow. Separate equations are necessary because of the different ways the two layers move, but the same forces govern the rate of change of momentum of both layers. This model (54.1–54.3) is solved numerically in a Lagrangian reference frame using a staggered-grid, finite-difference method. The details of the method are given in Imran et al. (2001).

The vertical strain rate in the debris flow was calculated as a proxy for stress fields experienced by sedimentary blocks contained in the flow. The vertical strain rate ε at location x is defined as:

$$\varepsilon(x)=\frac{1}{h(x)}\frac{\partial h(x)}{\partial t} \tag{54.4}$$

When this vertical strain rate is positive, the flow is being compressed horizontally. In contrast, a negative strain rate indicates horizontal expansion of the flow. Paleostress analysis reconstructs only the relative values of stress fields, and the model employed in this study considers only the dynamics of the flow matrix, not that of sedimentary blocks in the flow. Therefore, this study uses estimates of the vertical strain rate of the flow in order to infer qualitative characteristics of the internal stress fields of the debris flow in question.

54.4.2 Setting for Numerical Experiments

To evaluate the relative contributions of model parameters to flow strain processes, numerical experiments were conducted with variations in three model parameters: yield strength, dynamic viscosity of the flow matrix, and the maximum thickness of the initial geometry of the flow. The ranges of yield strength and dynamic viscosity that were studied were in the ranges 500–4,000 Pa and 0.13–1.08 Pa/s respectively. The maximum thickness of the initial flow geometry was varied from 25 to 200 m. In all experiments, a parabolic-shaped, initially static mound of debris with a length of 1 km long is released on a slope of 8° that extends for 5 km, and then suddenly drops to 0.3°, corresponding to a flat basin plain. A flow density of 1,500 kg/m^3 is used here.

54.5 Results

From viewpoint of the vertical strain rate of the flow, the result of the numerical experiments indicate that the muddy debris flow generally experiences two phases, i.e. extensional and compressional phases (Fig. 54.2). First, the flow significantly expands as it moves down the slope (Fig. 54.2a, b). Then, when it reaches the slope break, the debris-flow starts to decelerate with progressive horizontal compression of the flow body. Compressional ridges were often formed as the flow traversed the slope break (Fig. 54.2a). An extensional phase of the debris-flow was observed in all experimental runs, whereas it was not always possible to identify a clear compressional phase.

Physical properties of the flow matrix, especially dynamic viscosity, were found to strongly affect the behavior of simulated debris flows (Fig. 54.3). A low viscosity of the muddy matrix caused long run-out lengths of the debris flow onto the basin plain (Fig. 54.3a), and the flow compressional phase occasionally vanished at very low viscosity. In contrast, highly viscous flow tended to travel shorter lengths, and the compressional ridges developed strongly at the slope break (Fig. 54.3b, c).

The initial thickness of the debris-flow was also found to be an important factor in determining the run-out length of the flow (Fig. 54.4). Thick initial geometries resulted in fast and long-lived debris flows (Fig. 54.4c). However, the strain phases of the debris flow were found to be less strongly influenced by the initial geometry

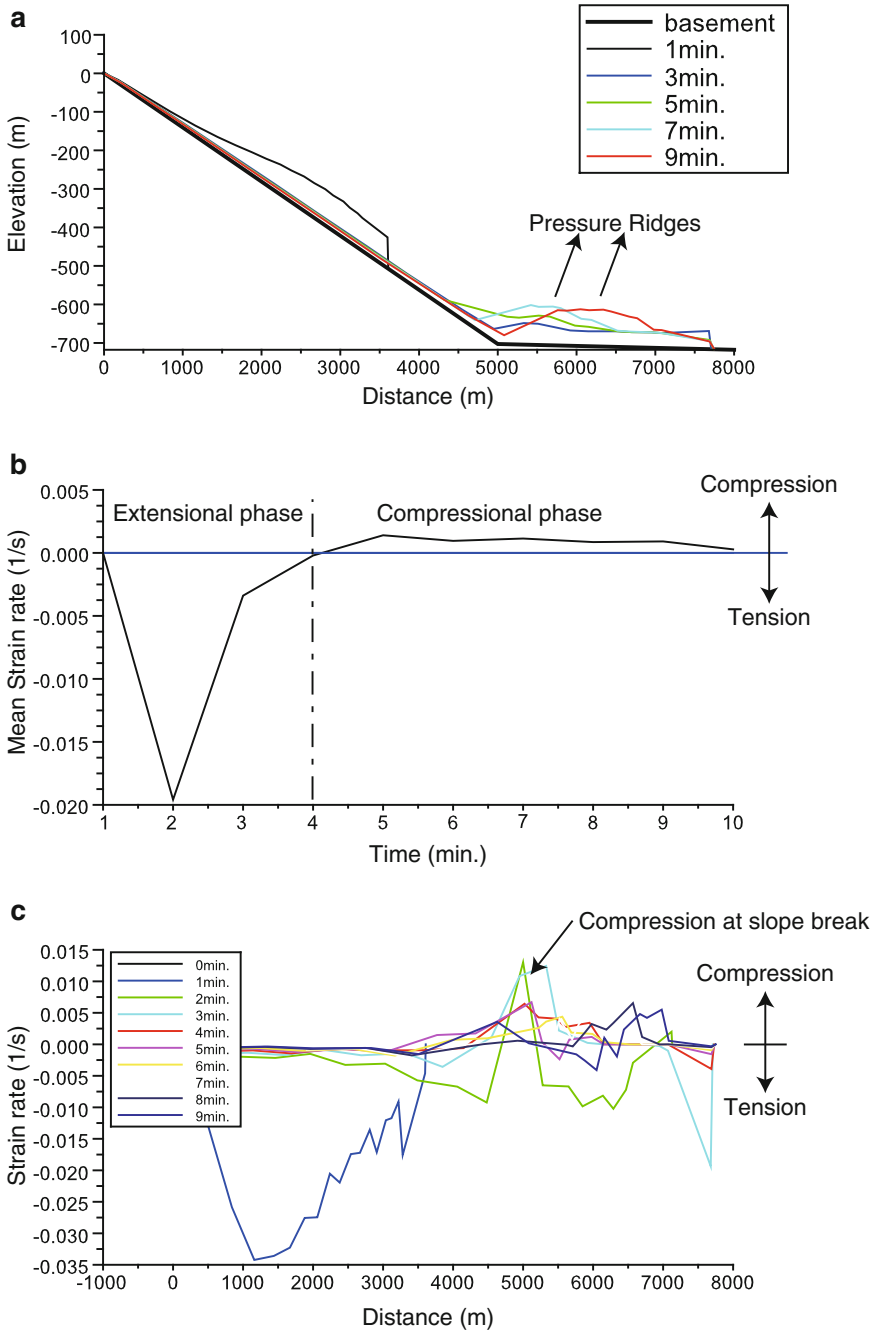

Fig. 54.2 A typical example of the result of a numerical experiment. Experimental conditions are: viscosity = 0.27 Pa/s; yield strength = 1,000 Pa; initial thickness of the flow = 25 m (**a**) Downslope movement of the simulated debris flow. Flow thickness has been exaggerated 10X. A pressure ridge was formed at the slope break (**b**) Time evolution of the averaged strain rate of the debris flow. Two distinct flow phases are recognized: the extensional and compressional phases (**c**) Spatial variations of the strain rate of the flow. Flow compression is prominent at the location of the slope break

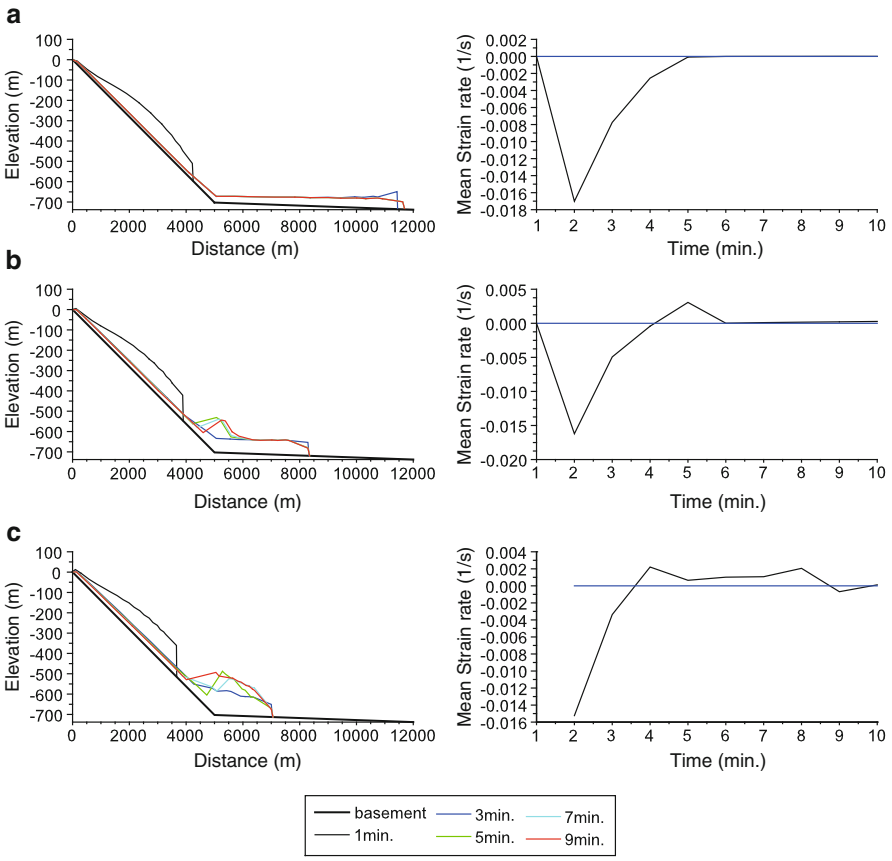

Fig. 54.3 (**a**) Flow thickness and the average strain rate of the simulated debris flow at viscosity 0.13 Pa/s (**b**) Flow thickness and the average strain rate of the simulated debris flow at viscosity 0.54 Pa/s (**c**) Flow thickness and the average strain rate of the simulated debris flow at viscosity 1.08 Pa/s. The yield strength and initial thickness of the flow are 4,000 Pa and 50 m, respectively, in these three experiments. Flow thickness has been exaggerated 10X

of flows. Both thick and thin flows experienced both extensional and compressional strain phases although the timing of the onset of the compressional phase varied depending on the initial geometry.

54.6 Discussion

The results of numerical experiments enabled interpretation of the multiple stress fields recorded in the mass transport deposit observed in outcrop. The paleostress analysis suggests that the flowing material exposed in the outcrop of the Akkeshi Formation experienced two different stress fields (Naruse and Otsubo 2011). Vertical

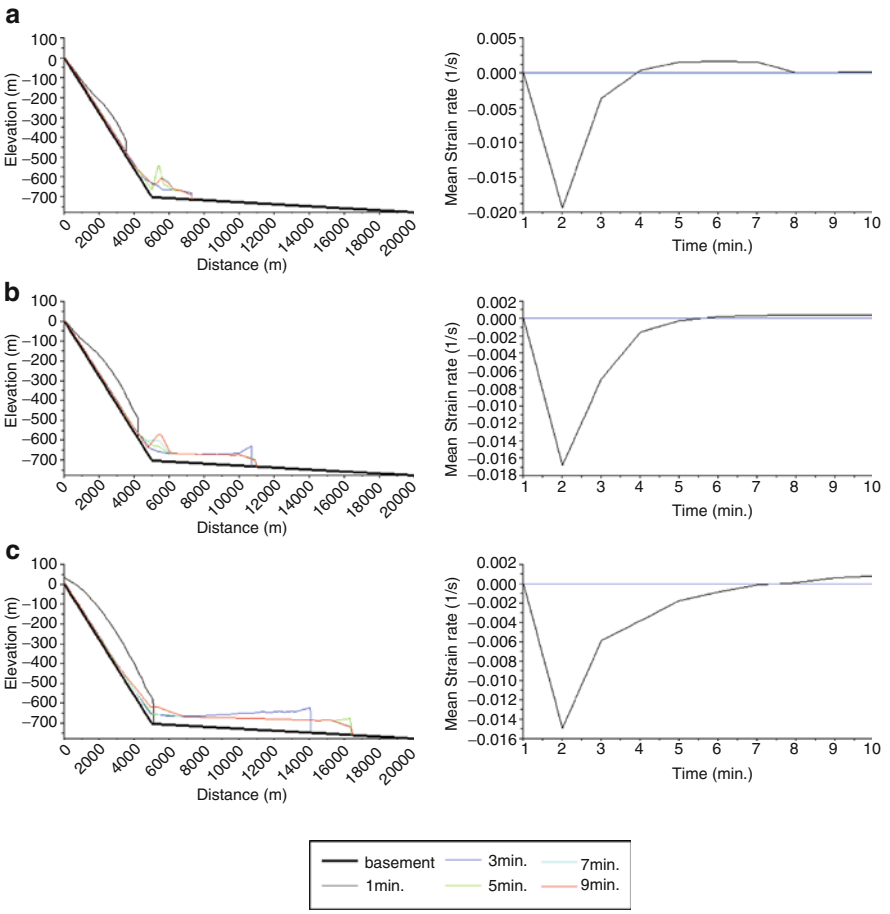

Fig. 54.4 (**a**) Flow thickness and average strain rate of a simulated debris flow with a 25-m initial thickness (**b**) Flow thickness and the average strain rate of a simulated debris flow with a 50-m in initial thickness (**c**) Flow thickness and the average strain rate of a simulated debris flow with a 100-m in initial thickness. The yield strength and dynamic viscosity of the flow are 2,000 Pa and 0.27 Pa/s, respectively, in these three experiments. Flow thickness has been exaggerated 10X

axial compression (Type 1) is indistinguishable from a uniform horizontal tensile stress field, so that it can be interpreted that this stress field corresponds to the extensional strain phase of debris flow that was recognized in the numerical experiments of this study. The experiments indicate that extension of the flow geometry is a common property of debris flows.

Tri-axial compressional stress fields (Type 2) with σ1 axes oriented parallel to paleocurrent direction were also detected by the paleostress analysis. On the basis of the results of the numerical experiments, this stress field can be attributed to the flow deceleration initiated by the slope break. The natural mass transport deposit commonly exhibits wrinkle-like structures on their top surfaces at the distal margin,

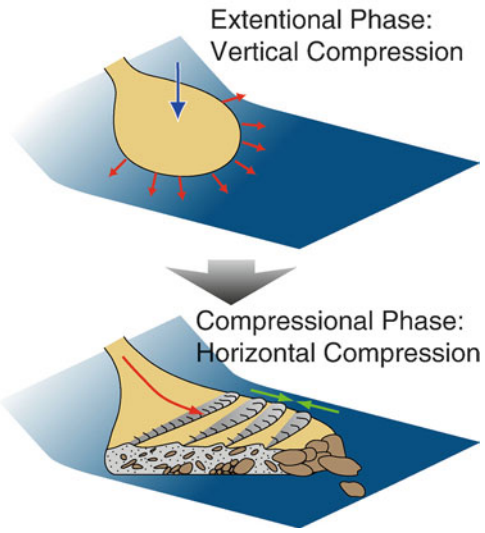

Fig. 54.5 Schematic diagram of transport and depositional processes of a mass flow, as inferred from both the outcrop itself and numerical experiments

which probably reflect pressure ridges (Prior et al. 1984). Thus, compressional stress during deposition can also be a common feature of natural mass flows (It should be recalled, however, that the compressional phase of the modeled flows was unclear in a few of the numerical experiments).

The interpretation of these two types of stress fields measured in the outcrop is currently tentative and verification such as cross-cutting relationships of faults and fault striae are necessary in future studies, but this study could provide some ground-truth evidences from the field that the compressional faults moved after the extensional faults (Fig. 54.5). The interpretation of paleostress field, especially the compressional phase, implies that stress analysis can be useful for the investigation of debris flow processes. Firstly, the analysis can deduce the paleocurrent direction of the submarine mass flow deposit. Estimation of paleocurrent direction and the entire geometry of mass flow deposits is generally difficult because of their chaotic appearance. This study suggests, however, that the current direction can be inferred if the horizontal compression stress field can be clearly detected in the outcrop data. Secondly, it is noteworthy that the compressional strain phase is not always recognized in experimental runs. Although currently difficult to predict quantitatively, the existence of a horizontal compressional stress field may imply a high viscosity of the flow matrix.

54.7 Conclusions

Numerical experiments on subaqueous mass transport processes were conducted to understand and interpret a field example of the internal stress field of the flow. Paleostress analysis of a large-scale mass-transport deposit revealed that the flow

experienced two different stress fields: (1) a uni-axial compressional stress field with the σ_1 axis oriented normal to the bedding surface and (2) a uni-axial compressional stress field with the σ_1 axis oriented parallel to paleocurrent direction. The result of numerical experiments implies that the first of these stress fields is created by a radial spreading of the flow during its downcurrent movement, while the second stress field results from compression during deposition on the basin plain.

Acknowledgments The authors thank the reviewers Drs. R.N. Hiscott and G. Parker for critiquing and improving this manuscript.

References

Imran J, Parker G, Locat J, Lee H (2001) 1D numerical model of muddy subaqueous and subaerial debris flow. J Hydraul Eng 127:959–968

Kiminami K (1983) Sedimentary petrography of the Nemuro Group. Chikyu Kagaku 33:152–162

Lin J, Leblond PH (1993) Numerical modeling of an underwater bingham plastic mudslide and the waves which it generates. J Geophys Res 98:10,303–10,317

Mayall M, Jones E, Casey M (2006) Turbidite channel reservoirs – key elements in facies prediction and effective development. Mar Petrol Geol 23:821–841

Naruse H (2003) Cretaceous to Paleocene depositional history of North-Pacific subduction zone; reconstruction from the Nemuro Group, eastern Hokkaido, northern Japan. Cretac Res 24:55–71

Naruse H, Nifuku K (2008) Three-dimensional morphology of the ichnofossil Phycosiphon incertum and its implication for paleoslope inclination. Palaios 23:270–279

Naruse H, Otsubo M (2011) Heterogeneity of Internal Structures in a Mass -transport Deposit, Upper Cretaceous to Paleocene Akkeshi Formation, Hokkaido Island, Northern Japan. In: Shipp RC, Weimer P, and Posamentier HW, (eds) Mass-Transport Deposits in Deepwater Settings. SEPM Special Publication No. 96, SEPM (Society for Sedimentary Geology), Tulsa, Oklahoma, pp 279–290

Otsubo M, Sato K, Yamaji A (2006) Computerized identification of stress tensors determined from heterogeneous fault-slip data by combining the multiple inverse method and k-means clustering. J Struct Geol 28:991–997

Otsubo M, Yamaji A (2006) Improved resolution of the multiple inverse method by eliminating erroneous solutions. Comput Geosci 32:1221–1227

Pickering KT, Hiscott RN, Hein FJ (1989) Deep marine environments: clastic sedimentation and tectonics. Unwin Hyman, London, 416 p

Pratson LF, Imran J, Parker G, Syvitski JPM, Hutton E (2000) Debris flow versus turbidity current: a modeling comparison of their dynamics and deposits. In: Bouma AH, Stone CG (eds) Fine grained turbidite systems, AAPG Memoir Vol 68/SEPM Special Publication No. 72, SEPM (Society for Sedimentary Geology), Tulsa, Oklahoma, pp 57–72

Prior DB, Bornhold BD, Johns MW (1984) Depositional characteristics of a submarine debris flow. J Geol 92:707–727

Weimer P (1991) Seismic facies, characteristics and variations in channel evolution, Mississippi Fan (Plio–Pleistocene), Gulf of Mexico. In: Weimer P, Link MH (eds) Seismic facies and sedimentary processes of submarine fans and turbidite systems. Springer, New York, pp 323–347

Yamaji A (2000) The multiple inverse method: a new technique to separate stresses from heterogeneous fault-slip data. J Struct Geol 22:441–452

Chapter 55
Distribution of Submarine Mass Movement Deposits: An Exhumed Basin Perspective

David M. Hodgson, Willem C. van der Merwe, and Stephen S. Flint

Abstract A wide range of mass movement deposits are preserved in the exhumed late Permian stratigraphy of the Karoo Basin, South Africa. An outcrop perspective permits their identification and analysis within a stratigraphic framework. The mass movement deposits identified vary in volume (m^3–10 km^3), palaeoenvironmental setting (distal basin-floor to delta clinothems), transport distance (*in situ* to 100's km) and process (founder, creep, slide, slump, debris-flow).

The analysed stratigraphic successions overall shallow upward from distal basin-floor, through proximal basin-floor and channelized submarine slope, to shelf-edge and shelf delta clinothems. The largest mass movement deposits are in the oldest stratigraphy, the Vischkuil Formation , which comprises distal basin-floor deposits intercalated with three regionally developed units (~10 km^3), and represent the initiation of a major sand delivery system. Mass movement deposits are rare in overlying sand-prone submarine fans and open slope stratigraphy (confined to margins of deep (50–150 m) composite erosion surfaces). In the stratigraphic transition from upper slope to shelf, soft-sediment deformation is widespread but detached deposits are only found basinward of the shelf-edge break. Open slope mass movement deposits are found where multiple basal stratigraphic units thin and change character abruptly, which indicates the presence of inherited intrabasinal topography that is healed. This geographic and stratigraphic distribution of mass movement deposits demonstrates the importance of steep unstable relief during that the initiation of long-term sediment supply triggers failure events, but also suggests a tectonically quiescent basin setting.

Keywords Karoo • Permian • Slide • Debris-flow • Stratigraphic distribution

D.M. Hodgson (✉) • W.C. van der Merwe • S.S. Flint
Stratigraphy Group, School of Environmental Sciences,
University of Liverpool, Liverpool, L15 3GP, UK
e-mail: hodgson@liv.ac.uk

Y. Yamada et al. (eds.), *Submarine Mass Movements and Their Consequences*,
Advances in Natural and Technological Hazards Research 31,
DOI 10.1007/978-94-007-2162-3_55, © Springer Science+Business Media B.V. 2012

55.1 Introduction

The spatial distribution of mass movement deposits can be viewed in imagery of the present seabed, and seismic reflection datasets can provide evidence of relative chronological distribution of chaotic seismic facies (e.g., Posamentier and Walker 2006). An outcrop perspective, however, allows process-based analysis within a stratigraphic framework, which permits the distribution of mass movement deposits to be placed in a palaeogeographic and sequence stratigraphic context. This paper is the first synthesis of the stratigraphic distribution of metres-scale mass movement deposits in two adjacent and contemporaneous well exposed distal basin-floor to shelf-edge successions of Permian age in the Karoo Basin, South Africa (Fig. 55.1). Commonly, deformation processes are linked to profile position and the links between these phenomena and their spatial and temporal development is explored.

55.2 Styles and Mechanisms of Sediment Remobilisation

Ancient soft-sediment deformation structures are classified into three main types: (1) *in situ* deformation structures related to water escaping and sediment loading with negligible downslope movement; (2) detached-deformation, such as slides, slumps, and debris flows, which involve deformation and transportation of sediment downslope, initially by laminar flow processes for long distances (tens of metres to kilometres); and (3) injection-related deformation, such as clastic dikes

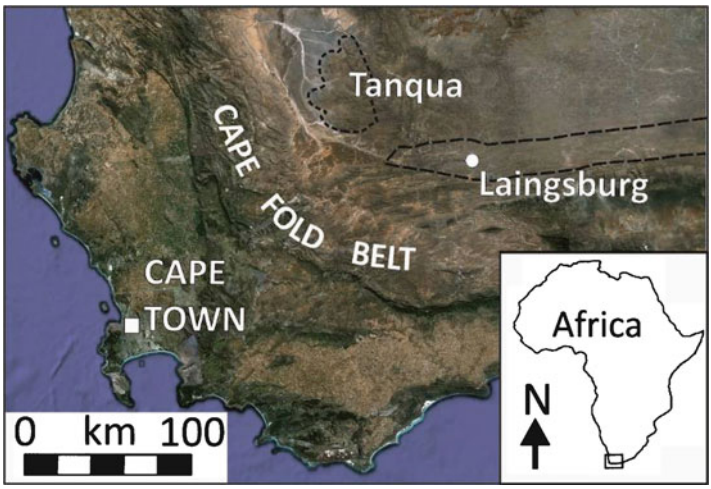

Fig. 55.1 Location map of the Tanqua and Laingsburg study areas in SW South Africa. The *dashed lines* indicate the approximate outcrop limit to the studied succession, and do not define the margins of depocentres

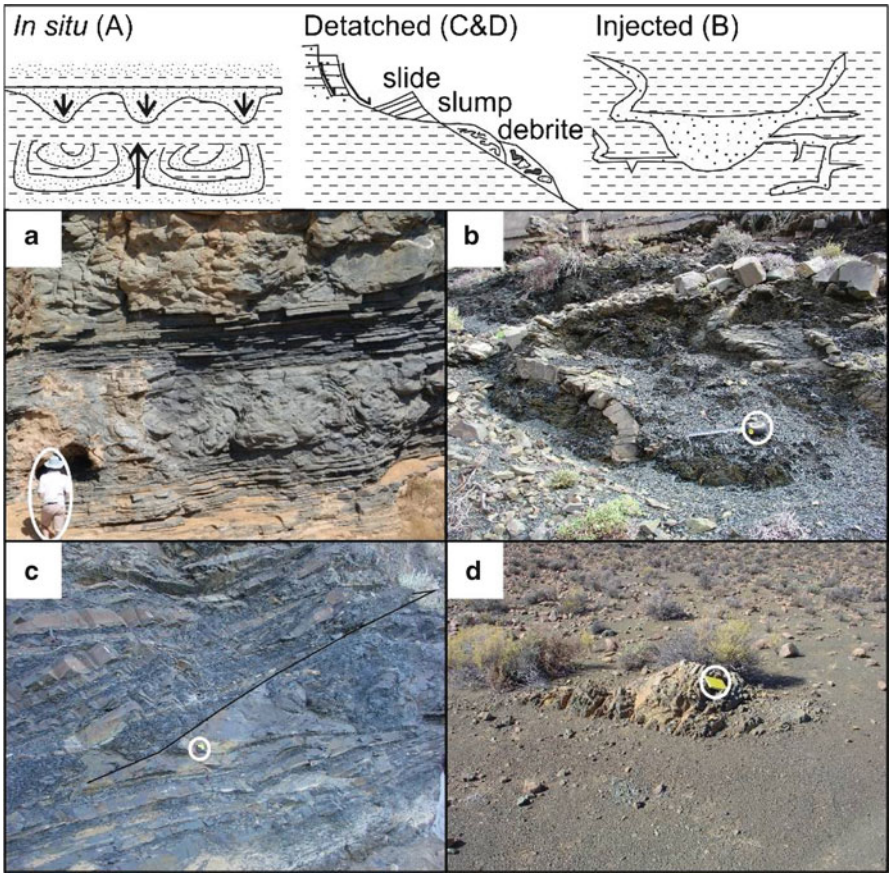

Fig. 55.2 Simple classification scheme of different soft-sediment deformation structures, with representative photographs (**a**) In situ deformation in Unit 5, Tanqua (geologist for scale) (**b**) Clastic dykes and sills beneath Unit E, Fort Brown Fm., Laingsburg (tape measure at 25 cm for scale) (**c**) thrust cutting verging fold in slide, Vischkuil Fm., Laingsburg (*compass clinometer circled* for scale) (**d**) Debrite with thin-bedded siltstone raft floating in fine-grained matrix, Unit D, Fort Brown Fm., Laingsburg (*notebook circled* for scale)

and sills that involve pressure- driven subsurface remobilization and forceful intrusion of sediment into surrounding strata (e.g., Maltman 1994; Oliveira et al. 2009) (Fig. 55.2).

Unconsolidated sediment in the shallow subsurface, i.e. typically <1 km burial depth, is prone to mobilisation as the porosity is high, cohesion and intergranular bonds are low, and fluid production rate by compaction is high (Maltman and Bolton 2003). Typically, soft-sediment deformation arises by interrupting the normally gradual process of pore-fluid expulsion. Additional loading is sustained by pore-fluid that is unable to dissipate adequately, the consequence of which is a loss of frictional strength and the onset of deformation through liquidization (Allen 1977).

Soft-sediment remobilisation, such as mass movement, may result from the deposition of sediments on a gradient and a downslope component of body force. Additionally, mass movement deposits commonly rest on discrete stratal surfaces (e.g., mudstones) permitting evaluation of the relationship between mass wasting and relative sea level change. Sediment creep is a semi-continuous process caused by load-induced stress whereas, slides, slumps, debris-flows and turbidity currents may occur with durations of minutes to hours. During any single down slope event these various processes may operate together or in a temporal sequence. For example, sediment creep may freeze/abate or alternatively, a critical threshold maybe reached causing failure and slumping which in turn, due to the entrainment of fluid may evolve into a debris flow and ultimately into a turbidity current.

55.3 Distribution of Deformation Facies Within the Karoo Succession

The Karoo Basin evolved from a retroarc basin with subsidence due to mantle flow (Permian) to a foreland basin (Triassic) (Tankard et al. 2009). In the Laingsburg depocentre (Fig. 55.1), a 1.8 km-thick stratigraphic succession that overall shallows upward from distal basin-floor (Vischkuil Fm.) through proximal basin-floor (Laingsburg Fm.) and channelized submarine slope (Fort Brown Fm.) to shelf and shelf-edge delta clinothems (Waterford Fm.) (Flint et al. 2011) (Fig. 55.3).

In the adjacent Tanqua depocentre (Fig. 55.1), c.500 m of mudstone and siltstone (Tierberg Formation) is followed by a c.400 m thick progradational succession of fine-grained, sand-rich submarine fans separated by claystone intervals (the Skoorsteenberg Formation; Hodgson et al. 2006), overlain by a c.300 m thick succession of submarine slope to shelf-edge and shelf edge delta depsoits (Kookfontein Formation; Wild et al. 2009) (Fig. 55.3).

Extensive previous work published on the Permian stratigraphy of the Karoo Basin permits the analysis of the spatial and temporal distribution of different mass movement processes and deposits within specific depositional environments (Fig. 55.4).

55.3.1 Distal (Mud-Prone) Basin-Floor

The Vischkuil Fm. (270 m of siltstone with thin sandstone turbidites; Fig. 55.3) represents an order of magnitude increase in siliciclastic input to the basin plain (Flint et al. 2011). The fine-grained nature of the succession, laterally extensive marker beds with intervening uniform thickness between markers, and the absence of channelization led Van der Merwe et al. (2009) to interpret the depositional environment for the Vischkuil Fm. as a low gradient basin plain setting. The upper Vischkuil Fm. comprises three depositional sequences, each bounded by a regionally developed mass movement deposits of a scale rarely observed at

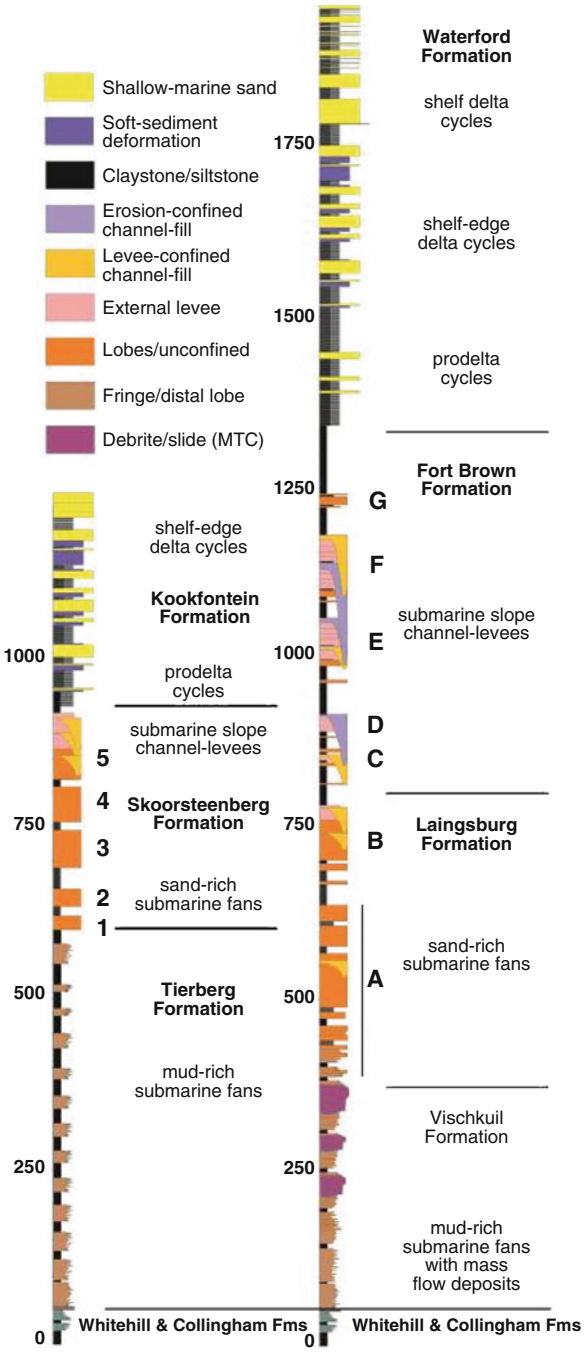

Fig. 55.3 Schematic stratigraphic logs of the lithostratigraphy in the Tanqua (*right*) and Laingsburg (*left*) areas

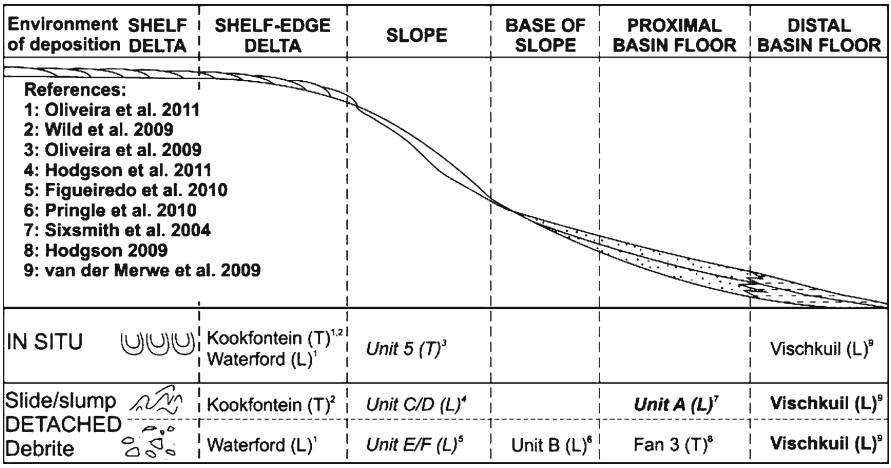

Fig. 55.4 Cartoon to indicate the stratigraphic distribution of mass movement deposits reported in the Karoo Basin. In bold are large volume examples, and in italics, deposits generated from erosional, depositional or inherited intrabasinal topography. Note the lack of large volume open slope examples identified

outcrop (van der Merwe et al. 2010) No equivalent large-scale mass movement deposits have been observed at the base of the Tanqua deep-water succession.

The mass movement deposits are composite bodies, with tightly folded and faulted basal slides (Fig. 55.2c) overlain by chaotic and more areally extensive debrites that can be physically correlated for 10's km in strike and dip sections. Van der Merwe et al. (2009, 2011) interpreted that the slides formed due to emplacement of the debrites because of (1) the abrupt contact between the slide and the debrite, (2) the similar thickness distributions of the two intervals, (3) the distribution of most intense folding and thrusting under thicker parts of the debrite (Fig. 55.2c), (4) the presence of the debrite under overturned folds, and (5) the slide is demonstrably local in its derivation as individual folded beds are mapped into undeformed strata outside the areas of deformation. The presence of laterally extensive marker beds directly above deformation intervals indicates minimal depositional topography was created and there was a return to a flat basin-floor after debrite emplacement.

55.3.2 Sand-Prone Submarine Fans

Mass movement deposits are rare in sand-prone submarine fan deposits in the Karoo Basin. Hybrid beds, which comprise turbidites with overlying linked debrites rich in mudstone and siltstone clasts, are common in the fringes of submarine lobes at the base of submarine fans in the Skoorsteenberg (Hodgson 2009) and Laingsburg Fms. (Fig. 55.3). Slides and slumps have been reported within and between basin-floor fans of Unit A, Laingsburg Fm., along the southern limb of the present-day

Heuningberg anticline (Sixsmith et al. 2004). Muddy slides (5–10 m-thick) are common in the mudstone between Unit A and Unit B in the same area, but are absent in the immediately overlying stratigraphy.

55.3.3 Base-of-Slope

Stratigraphic units interpreted to record base-of-slope settings, based on thick successions of juxtaposition of sand-prone channel-fills above submarine lobes (Unit B, Laingsburg Fm.; Unit 5, Skoorsteenberg Fm.) are largely unaffected by mass movement deposits. An extensive mudstone unit and channel-margin slides in Unit B are observed (Pringle et al. 2010). Meters-scale in situ deformation is also reported from thin-bedded units between submarine channel complexes in Unit 5. These features are attributed to creep and *in situ* dewatering processes above local steeper depositional gradients in overbank settings (Oliveira et al. 2009).

55.3.4 Erosional Submarine Slope

The Fort Brown Fm. in the Laingsburg depocentre is marked by several seismic-scale (kms wide, 100 + m thick) slope channel-levee systems separated by regional mudstone units (Figueiredo et al. 2010; Hodgson et al. 2011; Kane and Hodgson 2011). This led to the interpretation that the Fort Brown Fm. is an erosion-dominated submarine slope succession. Thick (5–40 m) mass movement deposits (slides and debrites) are identified to overlie deep (50–150 m) composite erosion surfaces in the channelized parts of channel-levee systems. Examples include Units C and D (Fig. 55.2d) (Hodgson et al. 2011) and Unit F (Figueiredo et al. 2010). These mass movement deposits are similar in lithology to older adjacent mudstone and levee successions and are interpreted to mark the collapse of oversteepened margins of the main erosional conduit rather than being sourced from farther upslope (Hodgson et al. 2011; Kane and Hodgson 2011).

The regional open slope mudstones between the channel-levee systems comprise claystones and very thin-bedded siltstones (mm-scale). This stratification indicates that these units are largely undeformed, and do not change thickness (apart from by overlying erosion). This suggests that mass movement deposits are rare on the open slope (Fig. 55.4). No slide scars or gravity-driven growth structures have been identified.

55.3.5 Shelf-Edge and Shelf Deltas

One of the most readily identifiable geomorphological points on the Earth's surface is the edge of the continental shelf where there is an increase in gradient that marks the geographic transition to the continental slope. This rollover is really an area

kilometers wide with changes in gradient of <3° making it difficult to constrain at outcrop. Following the criteria of Porębski and Steel (2003), Wild et al. (2009) and Oliveira et al. (2011) identified clinothem rollover positions in the Kookfontein and Waterford Fms. These criteria include a basinward thickening then thinning of packages of shelf- edge and shelf delta deposits, the presence of large-scale detached deformation facies, and an increase in the number of erosional features. Wild et al. (2009) and Oliveira et al. (2011) identified composite mass movement deposits (2–15 m thick), interpreted as slides or debrites depending on a qualitative assessment of the degree of internal disaggregation, basinward of the rollover.

Wild et al. (2009) proposed that a fall in relative sea level led to progradation and overextension of the delta onto the slope that led to the failure and detachment of gravitationally-unstable sediments and the emplacement of slides and debrites. The accretion of mass movement deposits to the slope facilitated shelf progradation.

In contrast, although soft sediment deformation structures are common in the shelf delta deposits, these are mainly small-scale (<2 m thick) and *in situ* features (Oliveira et al. 2011).

55.4 Discussion

55.4.1 Stratigraphic Control on Mass Movement Deposits

The stratigraphic distribution of the deformation facies investigated within this study indicates that different deformation assemblages occur in distinct palaeogeographical settings governed by a combination of profile position, depositional gradient and position within relative sea level cycles.

In the Tanqua area, the character and physiography of the Tanqua submarine slope changed over time, from a system defined by mixed bypass and depositional processes (Unit 5, Skoorsteenberg Fm.), to a largely accretionary system defined by shelf edge deltas and intraslope lobes (lower Kookfontein Fm.) (Wild et al. 2009). This change was accompanied by an overall reduction in slope angle and a change from a distinct shelf-slope-basin floor profile to a more ramp-like margin, and a systematic temporal and spatial change in deformation assemblages.

In the Laingsburg area, the volumetrically largest mass movement deposits in the 1.8 km-thick shallowing upward stratigraphy are in the basal and distal basin-floor Vischkuil Fm. It is significant that debrites large enough to deform the substrate in the Vischkuil Fm. occur prior to the establishment of a major sand delivery system (Laingsburg and Fort Brown Fms.). This suggests that they record the mass wasting of the submarine slope and shelf, which allowed the initiation of a major sediment supply system (Flint et al. 2011). The trigger of the mass movement deposits could be linked to increased tectonic activity, supported by the significant increase in sediment supply rates.

In comparison to other open slope successions (e.g., the Gull Island Fm., Carboniferous, Western Ireland, Martinsen 1989), there is a distinct lack of mass

movement deposits or slide scars in the Fort Brown Fm. The apparent stability of the slope may be due to the character of the mudstone, but also suggests a stabilised slope setting with lower gradients, and/or a tectonically quiescent setting. That the slope contains submarine conduits with >100 m of confinement (erosion and bounding levees) suggest a reasonable gradient to the slope. Therefore, the low amount of mass movement deposits on the slope support a setting with limited tectonic activity. The stratigraphic reoccurrence of detached deformation in shelf-edge delta successions is attributed to local oversteepening as the delta front merge with the slope.

55.4.2 Palaeogeographic Control on Mass Movement Deposits

There is also a palaeogeographic control on the distribution of mass movement deposits. In the Laingsburg area, there are multiple mass movement deposits comprising mudstone and siltstone along the southern limb of an anticline (Sixsmith et al. 2004). These are identified within Unit A, and between Unit A and Unit B, but not in the overlying slope stratigraphy. Their localised geographic presence is interpreted to be due to failure of thin-bedded turbidites, and the emplacement of slides and debrites from intrabasinal topography. This topography is likely inherited rather than from an incipient fold structure because the overlying stratigraphy is undeformed, and there is little evidence of strata thickness changes.

55.5 Conclusions

The extent of the outcrops in the Karoo Basin permits the stratigraphic distribution and variability of mass movement deposits to be considered at a scale comparable to many modern environments. Long-distance mass movement deposits are rare and found only in distal settings that mark the initiation of sediment supply and point to a combination of tectonics and relative sea-level control. The trigger mechanisms attributable to mass failure events are not clear when viewing an ancient deposit. However, local geographic concentrations can point to aseismic controls, such as static inherited intrabasinal relief.

References

Allen JRL (1977) The possible mechanics of convolute lamination in graded sand beds. J Geol Soc 134:19–31

Figueiredo J, Hodgson DM, Flint SS, Kavanagh JP (2010) Depositional environments and sequence stratigraphy of an exhumed permian mud-dominated submarine slope succession, Karoo Basin, South Africa. J Sediment Res 80:97–118. doi:10.2110/jsr.2010.002

Flint SS, Hodgson DM, Sprague AR, Brunt RL, Van der Merwe WC, Figueiredo J, Prélat A, Box D, Di Celma C, Kavanagh JP (2011) Depositional architecture and sequence stratigraphy of the Karoo basin floor to shelf edge succession, Laingsburg depocentre, South Africa. Mar Petrol Geol 28:658–674

Hodgson DM (2009) Origin and distribution of bipartite beds in sand-rich submarine fans: constraints from the Tanqua depocentre, Karoo Basin, South Africa. Mar Petrol Geol 26:1940–1956. doi:10.1016/j.marpetgeo.2009.02.011

Hodgson DM, Flint SS, Hodgetts D, Drinkwater NJ, Johannessen EP, Luthi SM (2006) Stratigraphic evolution of fine-grained submarine fan systems, Tanqua depocentre, Karoo Basin, South Africa. J Sediment Res 76:20–40

Hodgson DM, Di Celma C, Brunt RL, Flint SS (2011) Submarine slope degradation and aggradation and the stratigraphic evolution of channel-levee systems. J Geol Soc Lon 168:625–628

Kane I, Hodgson DM (2011) Submarine channel levees: nomenclature and criteria to differentiate subenvironments. Exhumed examples from the Rosario Fm. (Upper Cretaceous) of Baja California, Mexico, and the Laingsburg Fm. (Permian), Karoo Basin, S. Africa. Mar Petrol Geol 28:807–823

Maltman AJ (1994) Introduction and overview. In: Maltman AJ (ed) The geological deformation of sediments 1–35. Chapman and Hall, London

Maltman, AJ, Bolton, A (2003) How sediment become mobilized. In: Van Rensbergen P, Hillis, RR, Maltman AJ and Morley CK (eds) Subsurface sediment mobilization. Geol. Soc. London Spec. Publ. 216, pp 9–20

Martinsen, OJ (1989) Styles of soft-deformation on a Namurian (Carboniferous) delta slope, Western Irish Namurian Basin, Ireland. In: Whateley MKG, Pickering KT (eds) Deltas: sites and traps for fossil fuels. Geol. Soc. London Spec. Publ. 41, pp 167–177

Oliveira CMM, Hodgson DM, Flint SS (2009) Aseismic *in situ* soft-sediment deformation processes and products in submarine slope deposits of the Karoo Basin, South Africa. Sedimentology 56:1201–1225. doi:10.1111/j.1365-3091.2008.01029.x

Oliveira CMM, Hodgson DM, Flint SS (2011) Distribution of soft-sediment deformation structures in clinoform successions of the Permian Ecca Group, Karoo Basin, South Africa. Sediment Geol 235:314–330. doi:10.1016/j.sedgeo.2010.09.011

Porębski SJ, Steel RJ (2003) Shelf-margin deltas: their stratigraphic significance and relation to deepwater sands. Earth-Sci Rev 62:283–326

Posamentier HW, Walker RG (2006) Deep-water turbidites and submarine fans. In: Posamentier HW, Walker R (eds) Facies models revisited 399–520. Society for Sedimentary Geology, Tulsa

Pringle JK, Brunt RL, Hodgson DM, Flint SS (2010) Capturing stratigraphic and sedimentological complexity from submarine channel complexes outcrops to 3D digital models, Karoo Basin, South Africa. Petrol Geosci 16:307–330. doi:10.1144/1354-079309-028

Sixsmith PJ, Flint SS, Wickens HDeV, Johnson SD (2004) Anatomy and stratigraphic development of a basin floor turbidite system in the Laingsburg Formation, Main Karoo Basin, South Africa. J Sediment Res 74:239–254

Tankard AJ, Welsink H, Aukes P, Newton R, Stettler E (2009) Tectonic evolution of the Cape and Karoo basins of South Africa. Mar Petrol Geol 26:1379–1412

Van der Merwe WC, Hodgson DM, Flint SS (2009) Widespread syn-sedimentary deformation on a muddy deep-water basin-floor: the Vischkuil Formation (Permian), Karoo Basin, South Africa. Basin Res 21:389–406. doi:10.1111/j.1365-2117.2009.00396.x

Van der Merwe WC, Flint SS, Hodgson DM (2010) Sequence stratigraphy of an argillaceous, deepwater basin-plain succession: Vischkuil Formation (Permian), Karoo Basin, South Africa. Mar Petrol Geol 27:321–333. doi:10.1016/j.marpetgeo.2009.10.007

Van der Merwe WC, Hodgson DM, Flint SS (2011) Origin and terminal architecture of a submarine slide: a case study from the Permian Vischkuil Formation, Karoo Basin, South Africa. Online at *Sedimentology*. doi:10.1111/j.1365-3091.2011.01249.x

Wild R, Flint SS, Hodgson DM (2009) Stratigraphic evolution of the upper slope and shelf edge in the Karoo Basin, South Africa. Basin Res 21:502–527. doi:10.1111/j.1365-2117.2009.00409.x

Chapter 56
Seismic-Scale Rafted and Remnant Blocks over Salt Ridges in the Espírito Santo Basin, Brazil

Davide Gamboa, Tiago Alves, and Joe Cartwright

Abstract The Eocene-Oligocene stratigraphic succession of the Espírito Santo Basin, SE Brazil, comprises several Mass-Transport Deposits (MTDs), some of which contain individual blocks of strata. The blocks are classified as rafted blocks if transported over a glide plane, or remnant blocks if *in situ,* showing vertical stratigraphic continuity with underlying strata. A detailed 3D seismic analysis of a mass-transport deposit (MTD-A1) deposited at the base of an Eocene volcaniclastic complex (Abrolhos complex) reveals the presence of various blocks within the masses of failed strata. Blocks occur in the thickest areas of the MTD, along an alignment of salt diapirs and buried salt ridges. Block fragmentation is suggested to be associated to diapir-related faults, especially when these are closely aligned with *in-situ* blocks. The remnant blocks show low deformation, with sub-horizontal internal reflections, whereas rafted ones range from low to highly deformed blocks. Variations in the blocks' geometries suggest a lateral remobilisation in the order of 1,000 m, for a maximum of 4,000 m, for MTD-A1. The low remobilisation led to an unusual location of the MTD over the salt structures, contrasting with the typical remobilisation towards peripheral basins. The relation between MTD and salt-related structures can provide indicators to constrain the timing of halokinesis.

Keywords Mass-Transport Deposit • Remnant block • Rafted block • Salt ridge • Brazil

D. Gamboa (✉) • T. Alves • J. Cartwright
3D Seismic Lab, School of Earth and Ocean Sciences, Cardiff University,
Main Building, Park Place, CF10 3YE, Cardiff, UK
e-mail: GamboaDA1@cf.ac.uk

Y. Yamada et al. (eds.), *Submarine Mass Movements and Their Consequences*,
Advances in Natural and Technological Hazards Research 31,
DOI 10.1007/978-94-007-2162-3_56, © Springer Science+Business Media B.V. 2012

56.1 Introduction

The Cenozoic evolution of the southeast Brazilian margin is largely dominated by halokinesis. Deformation resulting from halokinesis is expressed by faulting, folding and localised subsidence of post-salt overburden units. These same processes are accompanied by widespread failure of strata flanking and above evolving salt structures (Fiduk et al. 2004). Thus, large blocks of remnant or rafted strata are common within MTDs in SE Brazil (Alves 2010; Alves and Cartwright 2009; Ashabranner et al. 2010; Jackson 2011). Remnant blocks are considered to be *in-situ* portions of strata that were not remobilised during slope failure. They commonly show stratigraphic continuity with strata underlying the MTD (Alves and Cartwright 2009). In contrast, rafted blocks comprise relatively undeformed strata transported downslope and usually resting on the basal gliding surface of the MTD. In some cases, blocks can also be seen 'floating' in the chaotic matrix of the failed material (e.g., Bull et al. 2009; Frey-Martinez et al. 2006; Lucente and Pini 2003).

This work focuses on a MTD located at the base of Eocene-Oligocene strata in the Espírito Santo Basin, SE Brazil (MTD-A1, Fig. 56.1). The aim is to investigate: (1) the internal deformation and distribution of failed blocks occurring above diapir ridges, (2) the relation between salt deformation and fragmentation of blocks, and (3) the use of MTD's as (temporal) markers for halokinesis.

56.2 Data and Methods

The 3D seismic dataset used covers an area of approximately 1,600 km^2 in the Espirito Santo basin (Fig. 56.1a). Data acquisition used a dual airgun array and six 5,700 m long streamers. The seismic signal was sampled at a 2 ms interval and zero-phase migrated with a 12.5 m grid line spacing. The analysis of MTD-A1 was based on the interpretation of vertical seismic profiles, being complemented with the use of TWT-thickness maps and seismic coherence slices (Fig. 56.1). Subsequent analyses of MTD-A1 consisted in the measurement of the block height, length and width.

56.3 Geological Setting

The Espírito Santo basin is located in the southeast Brazilian margin, being limited by the Abrolhos Plateau to the north and the Campos basin to the south (Fig. 56.1a). The post-rift evolution of the basin includes an Aptian transition phase characterised by the deposition of evaporitic units, followed by a Late Cretaceous drift phase. This drift phase is marked by a transgressive megasequence with deposition of carbonates and pelitic shales (Demercian et al. 1993; Fiduk et al. 2004; França et al. 2007). The top of the pelitic shales is marked by an Eocene unconformity on which

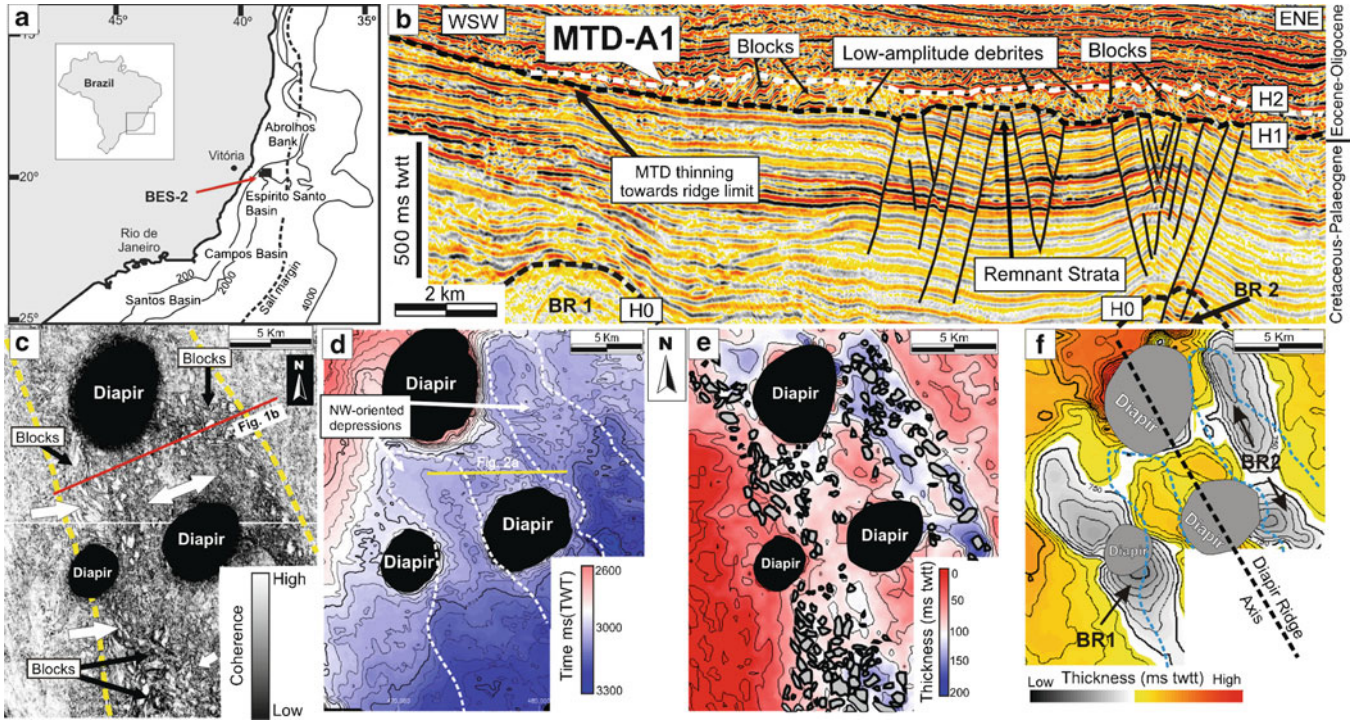

Fig. 56.1 (**a**) Regional map with the location of the Espírito Santo Basin and the study area (**b**) Seismic profile illustrating MTD-A1, which is bounded by horizons H1 and H2. Several salt-related Palaeocene faults are truncated at the base of the MTD (**c**) Coherence slice evidencing blocks in MTD-A1. *White arrows* indicate interpreted transport directions (**d**) Time map of H1, evidencing two northwest-oriented morphological depressions parallel to the diapir axis (**e**) Isochron map of MTD-A1 overlain with block occurrence (**f**) Thickness map between H0 and H1, evidencing two buried salt ridges (BR1 and BR2). *Blue dashed lines* outline the depressions shown in (**d**)

prograding sequences were deposited (Fiduk et al. 2004; França et al. 2007; Mohriak 2003). This same erosive surface coincides with the base of the studied MTD (Fig. 56.1b).

The Cenozoic evolution of the Espírito Santo basin was predominantly affected by thin-skinned tectonics above Aptian evaporites, with halokinesis leading to the development of southeast trending sediment fairways. Salt structures in the studied basin comprise diapirs and ridges with growth strata on the basin flanks limited to the Cretaceous. However, several diapirs and canopies have also developed significantly during the Cenozoic (Fiduk et al. 2004). In addition, the growth of salt structures has been associated with distinct faulting stages in Cenozoic strata (Alves et al. 2009; Baudon and Cartwright 2008). In the study area, an early episode of faulting affected Late Cretaceous to Eocene strata, with associated faults being truncated by the Mid-Eocene unconformity at the base of MTD-A1 (Fig. 56.1b). Post-Eocene faulting is less expressive being limited to the reactivation of Palaeogene faults over salt anticlines (Baudon and Cartwright 2008).

In this context, the paper focuses on a northwest oriented diapir ridge bounded by salt withdrawal basins. This diapiric region includes not only Cenozoic salt diapirs, but also two deeply buried salt ridges that follow the orientation of the main ridge axis (BR1 and BR2, Fig. 56.1).

56.4 Results

56.4.1 Internal Character of MTD-A1

The basal surface of MTD-A1 consists of an irregular hummocky horizon. The time-structure map of the basal surface shows two northwest trending depressions on the flanking regions of the diapir ridge (Fig. 56.1d). Strikingly, the thickness map in Fig. 56.1e shows the thickest accumulations of MTD-A1 occurring above the main diapir ridge, thinning towards the lateral salt-withdrawal basins, with thicknesses between 75 and 140 ms TWT.

MTD-A1 shows a varied seismic character. Features with moderate- to high-amplitude internal reflections correspond to failed blocks of poorly disturbed strata. Laterally, these contact with a debrite matrix of disaggregated remobilised strata represented by low-amplitude, chaotic reflections (Fig. 56.2). The blocks are better shown using coherence slices, which highlight them as geometric features (Fig. 56.1c). Blocks tend to be larger in the southern limit of the MTD.

Remnant blocks in seismic profiles show minor deformation and stratigraphic continuity with underlying strata (Fig. 56.2). Remnant blocks are often bounded by faults that propagated vertically within Late Cretaceous-Eocene strata. In addition, *in-situ* blocks can be partially faulted, showing concordant vertical displacement to the underlying strata (Fig. 56.2). In contrast, rafted blocks were variably remobilised and show different styles of deformation. Low deformation rafted blocks can be distinguished from remnant ones by their relation with underlying faults. Whereas

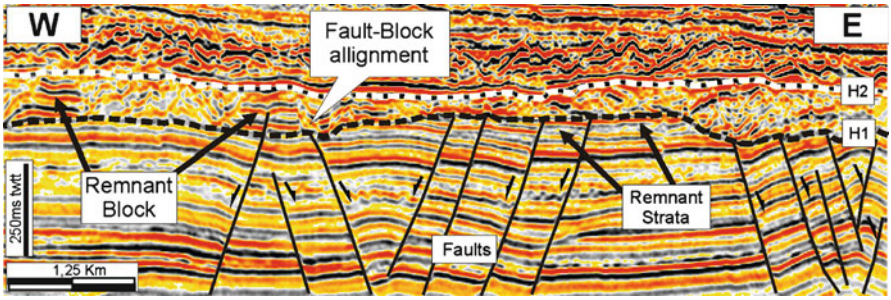

Fig. 56.2 Seismic profiles depicting the relation between faulting and the occurrence of remnant features. The flanks of the blocks are often aligned with underlying halokinesis-related crestal faults

the latter are often fault-bounded, rafted ones either do not show such relation or evidence lateral movement compromising the block-fault alignment.

Blocks occur only above the main diapir ridge, with no evidence of their presence towards the peripheral salt-withdrawal basins (Fig. 56.1). In addition, the blocks tend to form clusters towards the rims of MTD-A1, with scarcer blocks being observed over the axis of the diapiric ridge. Blocks are mainly observed in morphological depressions, which show thicker accumulations of failed strata (Fig. 56.1e). Also, the tallest blocks are observed in regions of greater MTD-A1 thickness.

56.4.2 Control of Underlying Fault Arrays on Block Geometry

The base of MTD-A1 coincides with an erosional surface truncating Late Cretaceous-Palaeogene faults (Fig. 56.1b). Only a minority of faults propagate vertically into younger units. Late Cretaceous-Palaeogene faults are associated to underlying salt anticlines. They propagated from the crest of buried salt ridges or developed as radial faults flanking buried salt structures (Fig. 56.1b and 56.3). Crestal faults tend to follow a northwest strike, parallel to the orientation of the salt anticlines. Other subsidiary fault sets tend to develop perpendicularly to the crestal faults. The analysis of seismic profiles and attribute maps suggest a genetic relation between faults and blocks. The blocks are predominantly oriented in a north or northwest direction, which is also the preferential direction of faults deforming the Late Cretaceous – Palaeocene units (Fig. 56.3).

Distinct styles of block deformation were observed in the studied MTD. Blocks exhibiting relatively minor deformation show sub-horizontal internal reflections, often sub-parallel to strata present below MTD-A1 (Fig. 56.4a). Moderately deformed blocks show folding of the internal strata, being this more predominant in larger blocks, or low dip caused by block rotation. Highly deformed blocks show strata dips exceeding 15°.

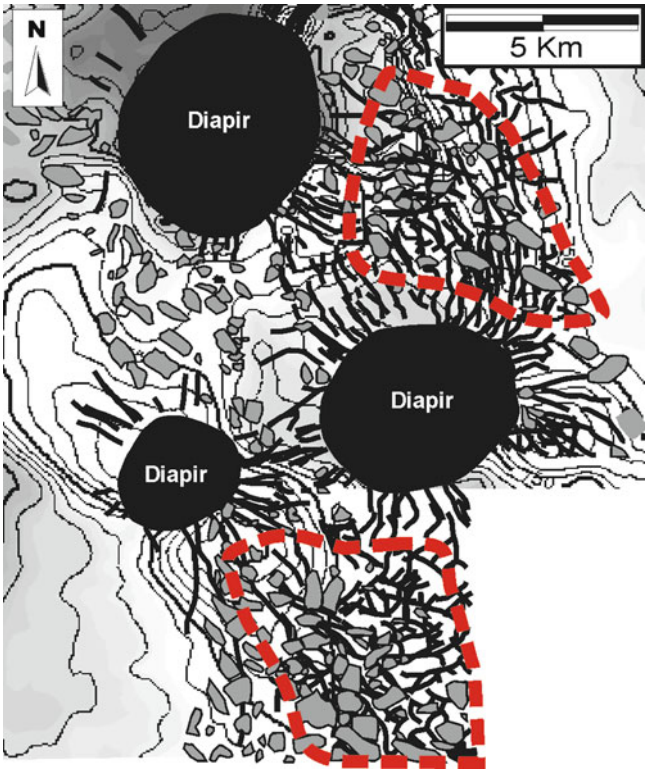

Fig. 56.3 Map of the morphology of H0 also showing the occurrence of crestal faults and blocks. Clusters with high block and fault density occurring above the buried salt ridges are evidenced by the *dashed red lines*

Considering the block distribution observed on seismic attribute maps (Fig. 56.1), and the spatial occurrence of the different deformation styles (Fig. 56.4b), transport in MTD-1 should not exceed 1,000 m in the central and southern locations. In contrast, higher remobilisation occurred along the western rim of MTD-1, where imbricated blocks predominate. Their geometry (Fig. 56.1b) indicates rotation and eastward movement of the blocks at the time of failure, implying a relative movement of these peripheral masses on the west in the order of 3–4 km. Nevertheless, there is no marked distinction between the variably deformed remnant or rafted blocks as these tend to show identical sizes (Fig. 56.4c, d).

56.5 Discussion and Conclusions

The MTD presented in this work shows an unusual relation between the failed strata and the presence of underlying salt structures. MTD-A1 is thicker above a diapiric ridge, where several remnant and rafted blocks are observed. This observation

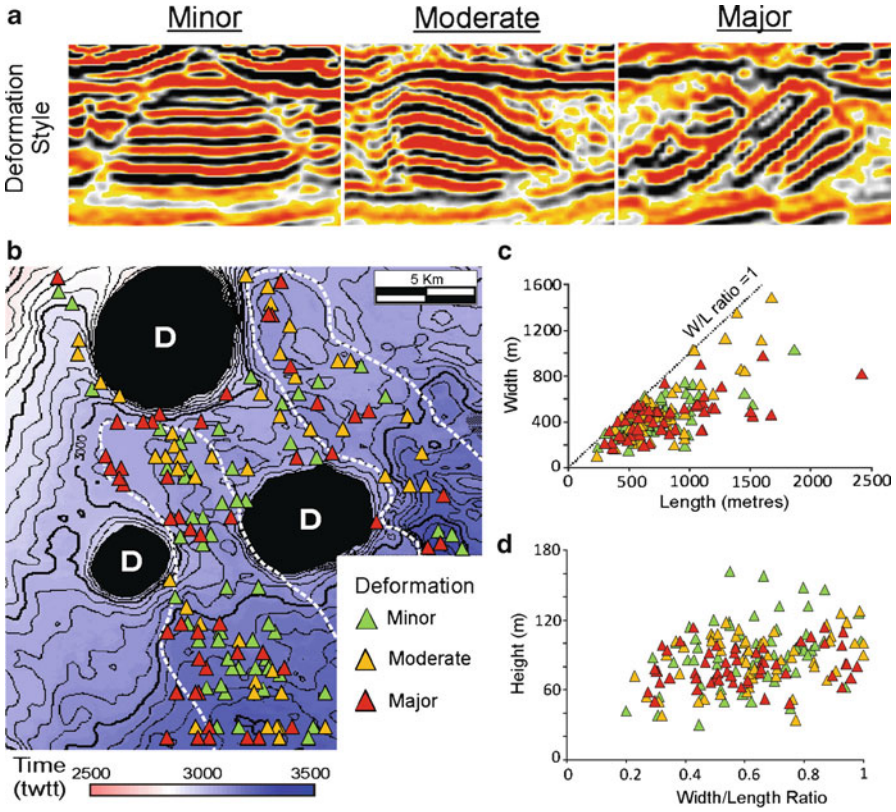

Fig. 56.4 (**a**) Three distinct styles of block deformation are observed in MTD-A1: Minor, Moderate and High (**b**) Distribution of the three styles of block deformation overlain on the time map of the MTD gliding surface (**c**) Graphic representation of width and length of the different deformation styles. The blocks show similar sizes, regardless of their deformation style (**d**) Plot of height and width/length ratio of the blocks

contrasts with the commonly observed pattern, in which thicker MTD accumulations occur towards the salt-withdrawal basins (McAdoo et al. 2000; Tripsanas et al. 2004). Our results suggest a common and localised source region for the remnant and rafted blocks. The hypothesis is sustained by relatively similar size of the blocks identified in MTD-A1, which can be used as an indicator of their proximity to the source regions (Bull et al. 2009). As shown in Fig. 56.4, the majority of blocks don't exceed widths, lengths and heights of 800, 1,000 and 120 m, respectively. In addition, high width-to-length ratios as the ones observed (Fig. 56.4c) tend to indicate a relative proximity to the block source regions (De Blasio et al. 2006). Furthermore, distinct block deformation also provides indications for the relative remobilisation of the MTD (Homza 2004). Increasing block deformation indicates larger travel distances and a zonation of deformation styles should be expected downslope. Nonetheless, in this study blocks showing the three distinct styles of deformation commonly occur alongside, particularly in the axial regions of the

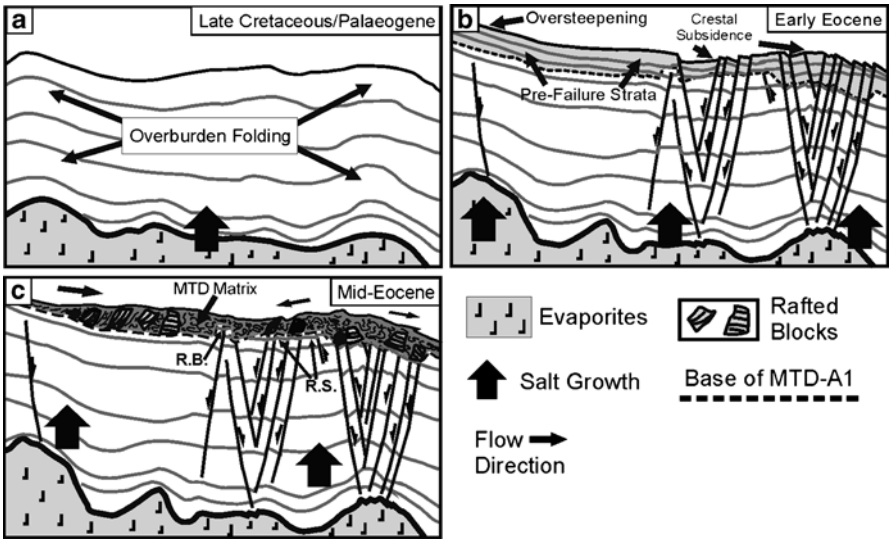

Fig. 56.5 Influence of salt growth on the genesis of MTD-A1 (**a**) Overburden deformation during Late Cretaceous/Early Palaeocene (**b**) Early Eocene faulting and ridge crest subsidence (**c**) Mid-Eocene collapse of strata overlying the diapir ridge. Deposition of MTD-A1 is limited to the area underlain by salt structures

diapiric ridge (Fig. 56.4b). Minor deformation is characteristic of either remnant or localised rafted blocks, thus suggesting short remobilisations in the clusters with variably deformed elements. As such, highly deformed blocks in these clusters were also shortly remobilised. This evidences that significant deformation heterogeneities can occur within localised, low remobilisation MTDs.

Salt growth played a key role in the formation of MTD-A1 as: (1) remnant blocks are bounded by crestal and radial faults, and (2) the highest frequencies of both block and faults are observed above buried salt anticlines (Fig. 56.3). The latter point evidences the main contrast of MTD-A1 with previous works which document the presence of remnant/rafted blocks on the salt-withdrawal basins bordering salt anticlines (e.g., Alves and Cartwright 2009; Tripsanas et al. 2004). By analysing the processes leading to the mass-failure we can estimate the timing of halokinesis. The early salt structures formed during Late Cretaceous and Palaeocene, mainly along limits of the modern diapiric ridge. The presence of thick strata of Late Palaeocene age over the buried salt ridges suggests these had a main growth phase limited to Early Palaeocene. This deformation may have formed a topographic high along the ridge area (Fig. 56.5a). Nevertheless, the arrays of crestal faults in Unit 1 evidence important salt-related overburden fracturation along the buried ridges during the Late Palaeocene (Figs. 56.3 and 56.5b). In later stages this deformation formed morphological depressions due to crestal subsidence along the ridges. As blocks are likely to represent lower Eocene strata, we can assume a similar time period for the overburden fracturation prior to failure.

Mid-Eocene halokinesis is interpreted to cause the mass-failure, as it is limited to the areas underlain by the diapiric ridge (Fig. 56.5c). In the axial regions remnant and less remobilised strata where conditioned by the pre-existing fractures resulting in the couple block-fault clustering. On the western rim of MTD-A1 faults are less evident (Fig. 56.3). As such, block genesis in here is interpreted to relate to steeper salt-induced gradients favouring collapse. Consequent rafted blocks were further transported towards the ridge axis.

The majority of Palaeocene faults are truncated at the base of MTD-A1 and do not show further growth in the overlying units (Figs. 56.1b and 56.2). This indicates a decline of halokinesis along the main diapiric ridge after the Mid-Eocene, with no further deformation occurring over the buried ridges. Instead, this was only focused in the growth of later diapirs. The relation between mass-wasting and salt-related deformation structures can provide additional indicators that allow a better constrain of salt growth phases.

The influence of halokinesis in MTD-A1 is also observed on its irregular gliding surface. This follows a laterally continuous uniform layer on the western regions of the MTD, but acquires an irregular profile on the regions with high fault density. Thus, salt-induced fracturation is interpreted to be, in the study area, the main control on the geometry of mass-failure gliding surfaces, and potentially over any evolving salt anticlines.

Acknowledgements The authors are grateful to CGG-Veritas for the permission conceded to publish this research paper. Jose Frey-Martínez and Mads Huuse are thanked for their comments on early versions of the manuscript. D. Gamboa thanks the Fundação para a Ciência e a Tecnologia (FCT) for the SFRH/BD/38819/2007 Ph.D. grant.

References

Alves TM (2010) 3D Seismic examples of differential compaction in mass-transport deposits and their effect on post-failure strata. Mar Geol 271:212–224

Alves TM, Cartwright JA (2009) Volume balance of a submarine landslide in the Espírito Santo Basin, offshore Brazil: quantifying seafloor erosion, sediment accumulation and depletion. Earth Planet Sci Lett 288:572–580

Alves TM, Cartwright J, Davies RJ (2009) Faulting of salt-withdrawal basins during early halokinesis: effects on the Paleogene Rio Doce Canyon system (Espírito Santo Basin, Brazil). Am Assoc Petrol Geol Bull 93:617–652

Ashabranner LB, Tripsanas EK, Shipp RC (2010) Multi-direction flow in a Mass-Transport Deposit, Santos Basin, offshore Brazil. In: Mosher DC, Shipp RC, Moscardelli L, Chaytor JD, Baxter CDP, Lee HJ, Urgeles R (eds) Submarine mass movements and their consequences. Springer, Dordrecht, pp 247–255

Baudon C, Cartwright J (2008) The kinematics of reactivation of normal faults using high resolution throw mapping. J Struct Geol 30:1072–1084

Bull S, Cartwright J, Huuse M (2009) A review of kinematic indicators from mass-transport complexes using 3D seismic data. Mar Petrol Geol 26:1132–1151

De Blasio FV, Engvik LE, Elverhøi A (2006) Sliding of outrunner blocks from submarine landslides. Geophys Res Lett 33. doi:10.1029/2005GL025165

Demercian S, Szatmari P, Cobbold PR (1993) Style and pattern of salt diapirs due to thin-skinned gravitational gliding, Campos and Santos basins, offshore Brazil. Tectonophysics 228:393–433

Fiduk JC, Brush ER, Anderson LE, Gibbs PB, Rowan MG (2004) Salt deformation, magmatism, and hydrocarbon prospectivity in the Espirito Santo Basin, offshore Brazil. In: Post PJ, Olson DL, Lyons KT, Palmes SL, Harison PF, Rosen NC (eds) Salt-sediment interactions and hydrocarbon prospectivity: concepts, applications, and case studies for the 21st century. GCSSEPM 24th Annual Research Conference, Houston, pp 370–392

França RL, Del Rey AC, Tagliari CV, Brandão JR, Fontanelli PR (2007) Bacia de Espírito Santo. Bol Geosci Petrobras 15:501–509

Frey-Martínez J, Cartwright J, James D (2006) Frontally confined versus frontally emergent submarine landslides: a 3D seismic characterisation. Mar Petrol Geol 23:585–604

Homza TX (2004) A structural interpretation of the Fish Creek Slide (Lower Cretaceous), northern Alaska. Am Assoc Petrol Geol Bull 88:265–278

Jackson CAL (2011) Three-dimensional seismic analysis of megaclast deformation within a mass transport deposit; implications for debris flow kinematics. Geology 39:203–206

Lucente CC, Pini GA (2003) Anatomy and emplacement mechanism of a large submarine slide within a Miocene foredeep in the northern Apennines, Italy: a field perspective. Am J Sci 303:565–602

McAdoo BG, Pratson LF, Orange DL (2000) Submarine landslide geomorphology, US continental slope. Mar Geol 169:103–136

Mohriak WU (2003) Bacias sedimentares da margem continental Brasileira. In: Bizzi LA, Schobbenhaus C, Vidotti RM, Gonçalves JH (eds) Geologia, Tectonica e Recursos Minerais do Brasil. CPRM, Manaus, pp 87–165

Tripsanas EK, Bryant WR, Phaneuf BA (2004) Slope-instability processes caused by salt movements in a complex deep-water environment, Bryant Canyon area, northwest Gulf of Mexico. Am Assoc Petrol Geol Bull 88:801–823

Chapter 57
Permian and Triassic Submarine Landslide Deposits in a Jurassic Accretionary Complex in Central Japan

Satoru Kojima and Hiroyoshi Sano

Abstract Rocks of the Mino terrane, central Japan, are composed mainly of Permian basalts capped by shallow-marine limestone, Lower Permian to Early Jurassic deep-sea radiolarian chert, and post-Early Jurassic terrigenous rocks. Mélanges incorporating blocks of these Permian to Jurassic rocks within a Middle to Upper Jurassic shale matrix are also major components of the terrane. The Mino terrane rocks are interpreted as Jurassic accretionary complexes on the basis of their lithology, age, and structure. The chert units contain two lines of evidence for submarine landslide episodes that occurred intermittently in mid-ocean regions during the Permian and Triassic. First, the upper Lower to middle Middle Permian chert unit incorporates resedimented carbonates, which were transported in submarine debris and turbidity flows from a shallow-marine buildup on the top of a seamount, down onto its lower flank, where the cherts were accumulating. Second, although most of the Mino terrane pelagic chert facies lack coarse land-derived clastic grains, the Middle to Upper Triassic chert contains thin beds and laminae of clastic debris. These grains are sand- to granule-sized and polymictic, consisting of chert, siliceous shale, basic or intermediate volcanic rocks, altered volcanic glass, polycrystalline quartz, and a glauconite-like mineral. These clastic sediments are interpreted as representing the distal facies of submarine landslide deposits, most likely derived from nearby oceanic islands. Comparable clastic sediment layers are also found in Middle Triassic deep-sea chert in a Jurassic accretionary complex in Far East Russia.

Keywords Submarine landslide • Permian • Triassic • Chert • Accretionary complex

S. Kojima (✉)
Department of Civil Engineering, Gifu University, Gifu 501-1193, Japan
e-mail: skojima@gifu-u.ac.jp

H. Sano
Department of Earth and Planetary Sciences, Kyushu University, Fukuoka 812-8581, Japan

Y. Yamada et al. (eds.), *Submarine Mass Movements and Their Consequences*,
Advances in Natural and Technological Hazards Research 31,
DOI 10.1007/978-94-007-2162-3_57, © Springer Science+Business Media B.V. 2012

57.1 Introduction

Recent marine geological research has revealed that submarine landslides are common events, not only along continental margins (e.g., Lee 2009; Mosher et al. 2009) but in mid-ocean regions (e.g., Masson 1996; Takahashi et al. 2002; Oehler et al. 2008). Submarine landslides are also expected to have occurred in the geologic past; however, it is often difficult to recognize ancient landslide deposits because of their low preservation potential.

To increase our understanding of ancient submarine landslide events, we examined pre-Jurassic submarine landslide deposits on land, and compared modern and ancient submarine landslides. Our study focuses on Permian and Triassic submarine landslide deposits within the deep-sea radiolarian cherts of the Mino terrane, central Japan.

57.2 Geologic Setting

The Mino terrane is a Jurassic subduction-related accretionary complex in Japan (Mizutani 1990). It comprises an oceanic assemblage including Permian basalts and limestone, Permian to Early Jurassic radiolarian chert, and a terrigenous assemblage of Middle to Late Jurassic sandstone, mudstone, and conglomerate. Another major component of the terrane is mélanges incorporating blocks of these Permian to Jurassic rocks within a Middle to Upper Jurassic shale matrix (Fig. 57.1; Matsuda and Isozaki 1991; Sano and Kojima 2000). Wakita (1988) subdivided the rocks of the Mino terrane into six tectonostratigraphic units, comprising two coherent units and four mélange units. These units are tectonically stacked to form an imbricate, downward-younging structure. The accretionary events occurred from the Middle Jurassic to the earliest Cretaceous (Fig. 57.2). The Mino terrane rocks are unconformably overlain by acidic volcanic rocks and are intruded by Late Cretaceous plutonic rocks (Fig. 57.1).

The Permian submarine landslide deposits, as examined here, occur within the Funafuseyama unit, a representative mélange unit comprising large slabs of Permian basalt, shallow-marine carbonates, and deep-sea chert and related siliceous rocks within a sparse matrix of Middle Jurassic mudstone (Fig. 57.1). Sano (1988) considered the Permian oceanic rocks to be sediments associated with a mid-oceanic seamount. The geochemical signatures of the basalts indicate their origin as an oceanic island formed by hot-spot volcanism near a mid-ocean ridge (Jones et al. 1993).

Triassic submarine landslide deposits are intercalated within the chert of the Kamiaso unit. A coherent succession is preserved, comprising Lower Triassic siliceous claystone, Middle Triassic to Early Jurassic chert, and Middle Jurassic turbiditic sandstone and mudstone, in ascending order. This succession represents the ocean-plate stratigraphy of deep-sea facies (Matsuda and Isozaki 1991). Paleomagnetic analyses of the Middle Triassic cherts indicate they were deposited in the equatorial regions of the Southern Hemisphere (Ando et al. 2001).

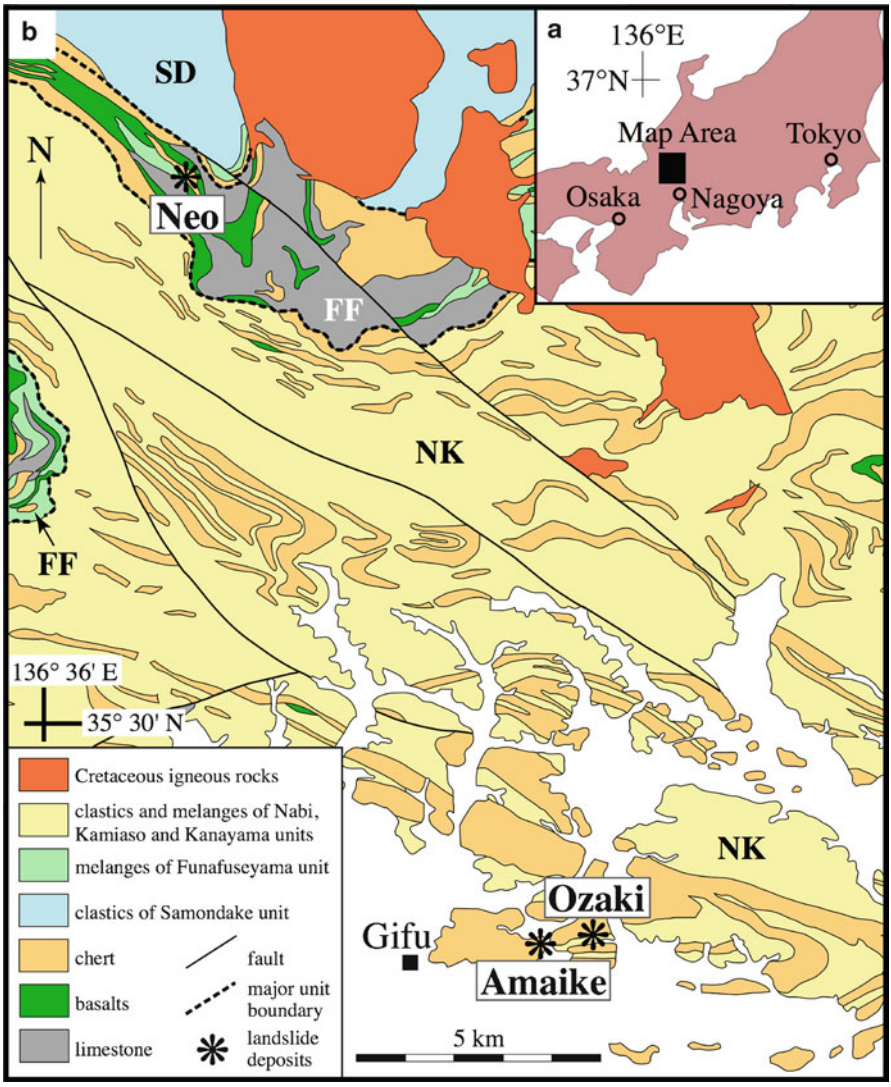

Fig. 57.1 Index map (**a**) and geological map (**b**) of the study area, modified from the Geological Survey of Japan (1992). *FF*: Funafuseyama unit, *NK*: Nabi, Kamiaso, and Kanayama units, *SD*: Samondake unit

57.3 Submarine Landslide Deposits in the Mino Terrane

We examine the Permian and Triassic submarine landslide deposits of the Mino terrane in the Neo area and in the Ozaki and Amaike areas, respectively (Fig. 57.1).

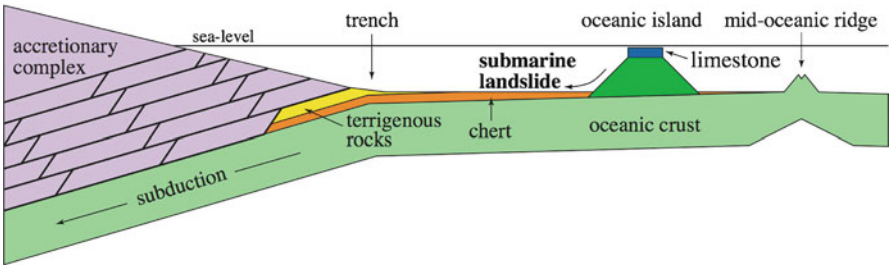

Fig. 57.2 Schematic cross-section showing the formative process of the accretionary complexes of the Mino terrane, and the site of submarine landslides that produced resedimented dolomite and volcaniclastic sandstone embedded within deep-sea radiolarian chert

57.3.1 Resedimented Carbonates in Permian Chert

Sano (1988) divided the Permian oceanic rocks of the Neo area into three nearly coeval formations: the Funabuseyama Formation (shallow-marine limestones), the Amanokawara Formation (limestone breccias), and the Hashikadani Formation (deep-sea cherts). These units are interpreted as sediments at the top, on the upper flank, and on the lower flank of a mid-oceanic seamount, respectively.

We identify several landslide-related, resedimented carbonate facies in the deep-sea cherts of the Hashikadani Formation (Fig. 57.3). The facies which is most representative of the landslide deposits is a massive dolomite in the Artinskian chert. Thin dolomite beds alternating with chert in the basal Artinskian, and dolomite and limestone lenses embedded in the Middle Permian chert, are interpreted as resedimented carbonates.

The massive dolomite unit (ca. 75 m thick) is composed almost entirely of light gray dolomite, with a small amount of limestone breccia in the lower part along with chert nodules. No distinct sedimentary structures are recognized. Thin dolomite beds alternating with the basal Artinskian chert contain crudely graded and parallel laminae. The dolomite and limestone lenses in the Middle Permian chert are less than 1 m thick, and are laterally discrete, with lithologically sharp outlines (Fig. 57.4a).

The dolomite of the Hashikadani Formation is better described as dolomitic sandstone, mainly comprising an aggregate of relatively well-sorted, discrete, anhedral to subhedral, sand- to silt-sized dolomite grains. Sporadic limestone and basalt fragments, and isolated crinoid and fusuline debris occur within the sparse matrix (Fig. 57.4b, e). The limestone breccia consists of granule- to cobble-sized, angular limestone and basalt clasts, chaotically set in a matrix of dolomitic sandstone. The graded dolomite comprises discrete, anhedral dolomite grains in a matrix of siliceous lime-mudstone, and grades upward into radiolarian lime-mudstone and chert (Fig. 57.4c, d).

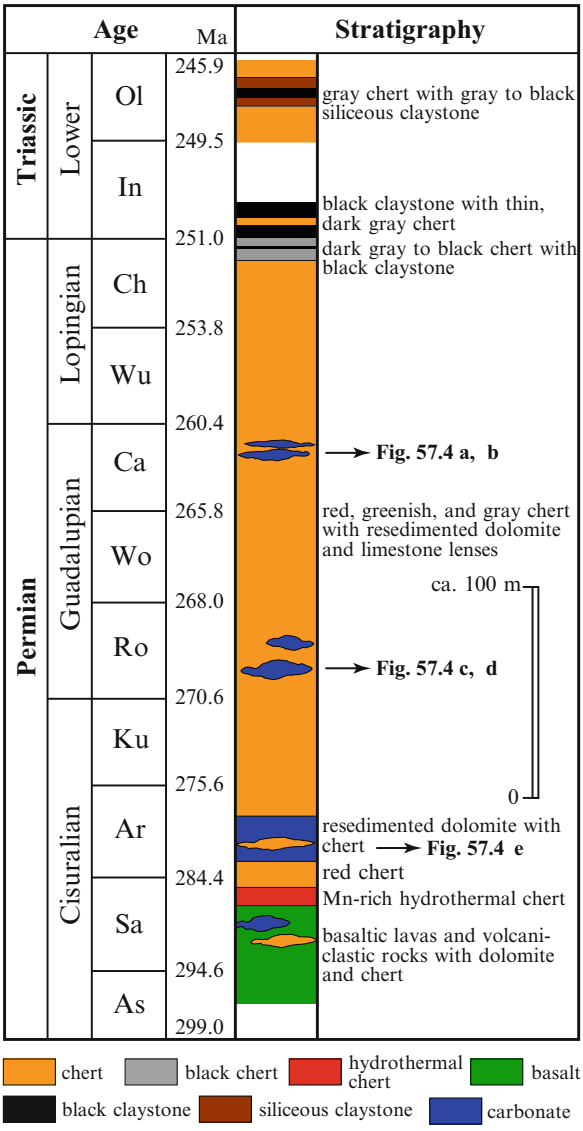

Fig. 57.3 Columnar section of the Permian Hashikadani Formation in the Neo area, modified from Sano et al. (2010). The location of the section is shown in Fig. 57.1. *As*: Asselian, *Sa*: Sakmarian, *Ar*: Artinskian, *Ku*: Kungurian, *Ro*: Roadian, *Wo*: Wordian, *Ca*: Capitanian, *Wu*: Wuchiapingian, *Ch*: Changhsingian, *In*: Induan, *Ol*: Olenekian. Radiometric ages are from Ogg et al. (2008)

All lines of evidence indicate that the dolomite and limestone breccia were originally shallow-marine carbonate deposits, which were displaced downslope into a deeper basin where the chert was accumulating (Fig. 57.5). We consider the shallow-marine carbonates to have been transported in sediment-gravity flows, including debris and turbidity flows, probably generated by submarine landslide events on the upper flank of the seamount.

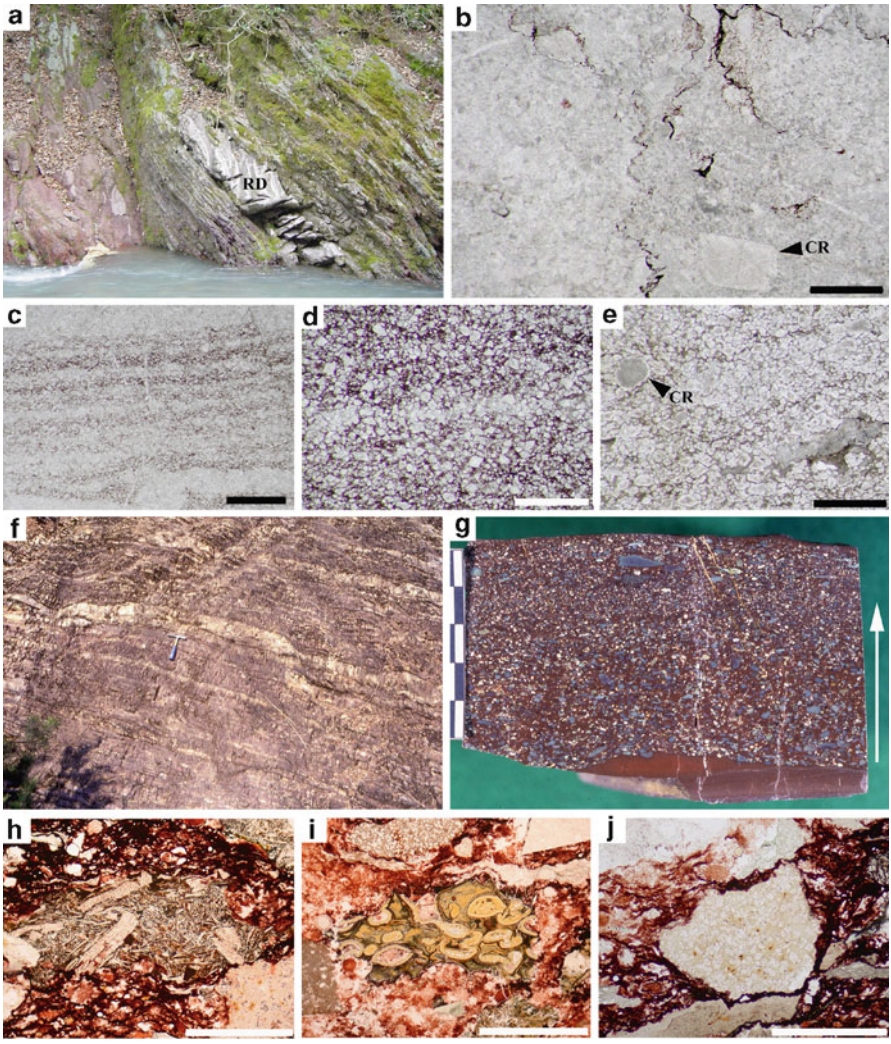

Fig. 57.4 Photographs showing Permian resedimented carbonate rocks in the Neo area (**a**–**e**) and Triassic resedimented sandstone in the Ozaki and Amaike areas (**f**–**j**) in the Mino terrane. (**a**) Resedimented dolomitic limestone pod (*RD*) embedded within Middle Permian red radiolarian chert. The pod is 50 cm thick and has a well-defined outline. (**b**–**e**) Thin-section photomicrographs of resedimented carbonate rocks. The stratigraphic horizons of the rocks are shown in Fig. 57.3. Plane polarized light. (**b**) Coarsely crystalline, dolomitic limestone containing sparse crinoid debris (*CR*), from about 1.2 m below the resedimented dolomitic limestone of Fig. 57.4a. Scale bar = 1 mm. (**c**) Laminae of predominantly sand-sized dolomite grains within a reddish siliceous mudstone associated with radiolarian chert. Scale bar = 2 mm. (**d**) Close-up view of Fig. 57.4c. The dolomite grains are discrete and mostly anhedral, with minor euhedral rhombs. Scale bar = 1 mm. (**e**) Dolomitic sandstone comprising densely packed, discrete, sand-sized dolomite grains with occasional lithic fragments of limestone (*lower right*) and crinoid debris (*CR*). Scale bar = 2 mm. (**f**) Resedimented volcaniclastic sandstone (about 6 cm thick) embedded within Late Triassic red radiolarian chert and white crystalline chert at Ozaki. The horizon of the sandstone formation is

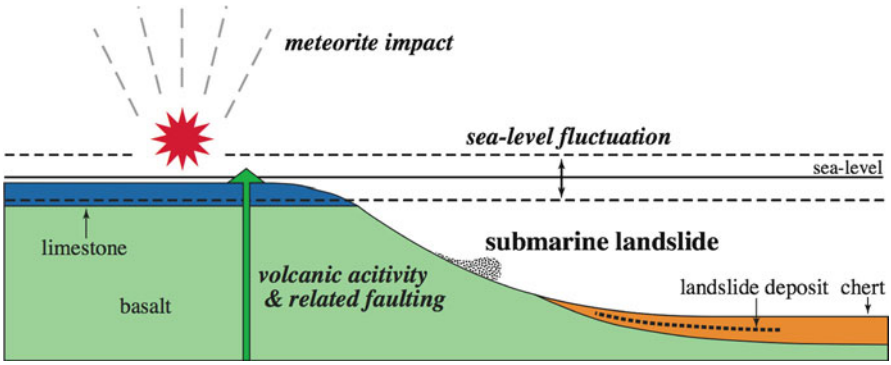

Fig. 57.5 Schematic diagram showing the possible causes of Permian and Triassic submarine landslides of the Mino terrane

57.3.2 Volcaniclastic Sandstone in Triassic Chert

Triassic landslide deposits are represented by volcaniclastic sandstone intercalated within the chert succession in the Ozaki and Amaike areas (Fig. 57.1; Kojima et al. 1999). We apply the term 'sandstone' to the volcaniclastic sediments described in this paper, because they are strongly dominated by sand-sized particles. The volcaniclastic sandstone is very rare rock in the chert formations, but is an important event-indicating sediment.

The chert is reddish brown, and rhythmically alternates with clayey partings and intermittent, more intensely crystallized white chert beds (Fig. 57.4f). Individual chert beds range in thickness from 5 to 10 cm.

The volcaniclastic sandstone occurs as thin beds, usually 3–7 cm thick, within the ribbon-bedded chert (Fig. 57.4g). The sandstone beds are parallel- and cross-laminated, and graded, with gently undulating erosional surfaces (Fig. 57.4g). Clasts are usually angular, and occur as a poorly sorted, polymictic association. Most dominant are chert clasts (Table 57.1), followed by basalts (Fig. 57.4h) and vesicular volcanic glass fragments (Fig. 57.4i). Subordinate amounts of polycrystalline quartz, apatite, and dolomite are also present. The dolomite fragments are composed of quartz or chlorite pseudomorphs after dolomite (Fig. 57.4j). Obviously reworked, isolated individuals of radiolarian and conodont fossils occur as reworked

Fig. 57.4 (continued) just at the hammer head for the scale. (**g**) Polished surface of the resedimented volcaniclastic sandstone at Ozaki. Note the lower graded interval (*arrow*) overlain by another (?) coarser layer. Scale: 5 cm, (**h**–**j**) Photomicrographs of characteristic clasts in the volcaniclastic sandstone at Ozaki. Plane polarized light. (**h**) Basaltic or andesitic volcanic rock fragment. Scale bar = 0.5 mm. (**i**) Altered vesicular volcanic glass fragment. Scale bar = 1 mm. (**j**) Clast composed mainly of quartz pseudomorphs after dolomite. Scale bar = 0.5 mm. *f*–*j* are modified from Kojima et al. (1999)

Table 57.1 Modal composition of sandstone in Triassic chert of the Mino terrane

	Ozaki-1	Ozaki-2	Amaike-1	Amaike-2
cht	28.4	19.6	48.4	10.4
ssh	5.6	3.6	4	1.8
vol	4.8	5.8	1.6	–
vgl	0.8	6	2	1.6
plq	0.8	0.6	0.6	0.2
apt	1	1.6	0.2	–
dlm	2.2	2.6	–	–
rad	7	5.8	3	19.6
mtx	48.2	53.8	39	65.8
oth	1.2	0.6	1.2	0.6
Total	100.00%	100.00%	100.00%	100.00%

cht chert, *ssh* siliceous shale, *vol* volcanic rock, *vgl* volcanic glass, *plq* polycrystalline quartz, *apt* apatite, *dlm* dolomite, *rad* radiolarian remains, *mtx* matrix, *oth* others (opaque minerals and unknown clasts)

clasts. The volcaniclastic sandstone matrix comprises reddish brown siliceous shale with abundant radiolarian remains. Lithologically comparable volcaniclastic sandstones also occur in the Hisuikyo area, about 35 km NE of the Ozaki-Amaike area (Kojima et al. 1999), and in the Samarka terrane of Far East Russia (Kojima et al. 1997), which is the northern extension of the Mino terrane (Kojima et al. 2000).

Radiolarian fossils obtained from the cherts located immediately below and above a volcaniclastic sandstone bed provide clues to the depositional age. Kojima et al. (1999) dated the volcaniclastic rocks as early Carnian in Ozaki, and middle Ladinian and early Carnian for the two separate sandstone beds in Amaike. The rocks in the Hisuikyo area are dated as late Anisian to early Ladinian, despite Permian to Early Triassic radiolarians and conodonts also occur as reworked clastic fragments (Kojima et al. 1999). The volcaniclastic sandstone in the Samarka terrane is Ladinian in age (Kojima et al. 1997).

57.4 Comparison with Landslide Deposits in the Modern Ocean

The Permian and Triassic landslide events recorded in the deep-sea chert of the Mino terrane occurred in or around volcanic islands located in mid-ocean basins. Similar submarine landslides have been described in the modern Pacific, Indian and Atlantic oceans. For example, Whitman et al. (1986) described reworked sediments, including shallow-water carbonates, at DSDP Site 585 in the East Mariana Basin, at a water depth of about 6,100 m. The sediments recovered from this site are subdivided into six units, the lowermost unit of which (590–893 m sub-bottom depth) is middle

Albian to upper Aptian in age and composed of volcaniclastic turbidites. The clast types include altered volcanic glass, volcanic lithic and crystalline fragments, celadonite, and zeolites. Some of the turbidites contain large amounts of shallow-marine carbonate debris, including ooids, benthic foraminifera, algae, bryozoans, and rudist fragments. Although Whitman et al. (1986) attributed the cause of the turbidity flows to volcanic activity, submarine landslides must have played an important role in transporting the shallow-water carbonates into the deep sea.

Naka et al. (1993, 2002) described several volcaniclastic sand and silt layers embedded within the pelagic sediments around the Hawaiian Islands. Two piston cores were recovered from the Hawaiian Deep and the Hawaiian Arch, about 120 and 250 km southeast of Hawaii Island, respectively (Naka et al. 2002). The volcaniclastic layers in these cores contain sedimentary structures characteristic of turbidites, such as graded bedding and sharp erosional contacts with the underlying pelagic sediments, and yield older fossils than the underlying and overlying pelagic sediments. The clastic fragments include basaltic glass, volcanic rock, plagioclase, olivine, pyroxene, opaque minerals, and minor amounts of evolved micropumice. Naka et al. (1993, 2002) interpreted these volcaniclastic turbidites as the products of submarine landslides along the southeastern flank of Hawaii Island.

The characteristics of the submarine-landslide deposits in modern deep-sea basins, as described above, are similar to those of the Permian resedimented carbonate and Triassic volcaniclastic sandstone of the Mino terrane. The similarities strongly indicate that the Permian and Triassic deposits are the products of submarine landslides. Although the triggers for the landslide activity remain uncertain, they may have included volcanic activity, sea-level fluctuations, meteorite impact, and tsunami (Fig. 57.5).

57.5 Conclusions

Permian and Triassic pelagic chert of the Mino terrane, central Japan, contains two lines of evidence for the occurrence of submarine landslide events in mid-ocean regions. First, the upper Lower to middle Middle Permian chert unit incorporates resedimented carbonates that were transported downslope in submarine debris and turbidity flows from a shallow-marine deposit on the top of a seamount. Second, the Middle to Upper Triassic chert contains thin beds and laminae of resedimented clastic debris; the clasts are sand- to granule-grained and consist of chert, siliceous shale, basic and intermediate volcanic rocks, altered volcanic glass, polycrystalline quartz, and a glauconite-like mineral. By comparison with similar deposits in modern ocean basins, these reworked sediments are interpreted as submarine landslide deposits, probably derived from nearby oceanic islands.

Acknowledgments The authors would like to express their appreciation to T. Onoue, K. Kashiwagi, and Y. Yamada for their review of manuscript.

References

Ando A, Kodama K, Kojima S (2001) Low-latitude and Southern hemisphere origin of Anisian (Triassic) bedded chert in the Inuyama area, Mino terrane, central Japan. J Geophys Res 106:1973–1986

Geological Survey of Japan (1992) 1:200,000 geologic sheet map Gifu. Geol Surv Japan, Tukuba

Jones G, Valsami-Jones E, Sano H (1993) Nature and tectonic setting of accreted basalts from the Mino terrane, central Japan. J Geol Soc Lon 150:1167–1181

Kojima S, Sugiyama K, Kemkin IV, Khanchuk AI, Mizutani S (1997) Clastic rocks in Triassic bedded chert of the Mino terrane, central Japan and the Samarka terrane, Sikhote-Alin, Russia. In: Wang N, Remane J (eds) Proceedings of 30th international geological congress, Utrecht. VSP 11, pp 181–188

Kojima S, Ando H, Kida M, Mizutani S, Sakata Y, Sugiyama K, Tsukada H (1999) Clastic rocks in Triassic bedded chert in the Mino terrane, central Japan: their petrographic properties and radiolarian ages. J Geol Soc Jpn 105:421–434 (JE)

Kojima S, Kemkin IV, Kametaka M, Ando A (2000) A correlation of accretionary complexes between southern Sikhote-Alin of Russia and inner zone of Southwest Japan. Geosci J 4:175–185

Lee HJ (2009) Timing of occurrence of large submarine landslides on the Atlantic Ocean margin. Mar Geol 264:53–64

Masson DG (1996) Catastrophic collapse of the volcanic island of Hierro 15 ka ago and the history of landslides in the Canary Islands. Geology 24:231–234

Matsuda T, Isozaki Y (1991) Well-documented travel history of Mesozoic pelagic chert in Japan: from remote ocean to subduction zone. Tectonics 10:475–499

Mizutani S (1990) Mino Terrane. In: Ichikawa K, Mizutani S, Hara I, Hada S, Yao A, (eds) Pre-cretaceous Terranes of Japan. Osaka, Publ IGCP Proj No.224, pp 121–135

Mosher DC, Shipp RC, Moscardelli L, Chaytor JD, Baxter CDP, Lee HJ, Urgeles R (2009) Submarine mass movements and their consequences. Advances in natural and technological hazards research 28. Springer, Dordrecht

Naka J, Tsugaru R, Danhara T, Tanaka T, Fujioka K (1993) Sedimentary processes of volcaniclastic sediments, Leg 136. In: Wilkens RH, Firth J, Bender J, et al (eds) Proceedings of ODP, College Station. Sci Results 136, pp 85–95

Naka J, Kanamatsu T, Lipman PW, Sisson TW, Tsuboyama N, Morgan JK, Smith JR, Ui T (2002) Deep-sea volcaniclastic sedimentation around the southern flank of Hawaii. In: Takahashi E, Lipman PW, Garcia MO, Naka J, Aramaki S (eds) Hawaiian volcanoes: deep underwater perspectives. Geophys Monog 128. American Geophysical Union, Washington, DC, pp 29–50

Oehler JF, Lenat JF, Labazuy P (2008) Growth and collapse of the Reunion Island volcanoes. Bull Volcanol 70:717–742

Ogg JG, Ogg G, Gradstein FM (2008) The concise geologic time scale. Cambridge University Press, Cambridge/New York

Sano H (1988) Permian oceanic-rocks of Mino terrane, central Japan. Part I. Chert facies. J Geol Soc Jpn 94:697–709

Sano H, Kojima S (2000) Carboniferous to Jurassic oceanic rocks of Mino-Tamba-Ashio terrane, southwest Japan. Mem Geol Soc Jpn 55:123–144 (JE)

Sano H, Kuwahara K, Yao A, Agematsu S (2010) Panthalassan seamount-associated Permian-Triassic boundary siliceous rocks, Mino terrane, central Japan. Paleont Res 14:293–314

Takahashi E, Lipman PW, Garcia MO, Naka J, Aramaki S (2002) Hawaiian volcanoes, deep underwater perspectives. Geophysical Monograph 128. AGU, Washington, DC

Wakita K (1988) Origin of chaotically mixed rock bodies in the Early Jurassic to Early Cretaceous sedimentary complex of the Mino terrane, central Japan. Bull Geol Surv Jpn 39:675–757

Whitman JM, Baltuck M, Haggerty JA (1986) Turbidite sedimentology and history of the East Mariana Basin. Init Rep DSDP 89:365–388

JE: in Japanese with English abstract

Chapter 58
Systematic Spatial Variations in the Fabric and Physical Properties of Mass-Transport Deposits in the Ursa Region, Northern Gulf of Mexico

Yuzuru Yamamoto and Derek E. Sawyer

Abstract We clarified the interrelations between deformation and spatial variations in the physical properties and fabric of mass-transport deposits (MTDs) within the Ursa Basin in the Gulf of Mexico, based on measurements of the anisotropy of magnetic susceptibility (AMS) and porosity, and observations of the rock fabric. Drillholes sunk as part of the Integrated Ocean Drilling Program (IODP) Expedition 308 (Sites U1322, U1323, and U1324) penetrated clay-rich MTDs in the Ursa Region within the uppermost 600 m below the seafloor. The soft-sediment deformation within the Ursa MTDs is characterized by contorted sediments and a homogenized appearance. Site U1322 shows evidence of major mechanical and strain decoupling at the base of the MTDs; i.e., the intensity of the magnetic lineation, porosity, and shear strength show gradual changes in the upper parts of the MTDs, with a sharp offset in these parameters at the contact with the underlying unit. At the grain scale, these MTDs are characterized by strong shearing-induced textures (S–C structures) and bedding-oblique foliations. However, at Site U1324, MTDs show only minor variations in fabric and physical properties despite being correlatives of those at Site U1322. Site U1324 is located near the headwall areas of MTDs, whereas Site U1322 lies near the toe areas. Therefore, at Site U1324 the MTDs are close to their pre-failure condition, whereas the sediments at Site U1322 record high strain and long-distance transport. The obtained values of differential porosity and magnetic lineation (indicative of grain alignment) show a systematic relation between the sites, indicating that the physical properties of sediments in MTDs are controlled by the fabric.

Keywords Mass-Transport Deposits (MTDs) • AMS • Ursa • Gulf of Mexico

Y. Yamamoto (✉)
IFREE, JAMSTEC, Yokohama 236-0001, Japan
e-mail: yuzuru-y@jamstec.go.jp

D.E. Sawyer
ExxonMobil Exploration, 222 Benmar Dr, Houston, TX 77060, USA

Y. Yamada et al. (eds.), *Submarine Mass Movements and Their Consequences*,
Advances in Natural and Technological Hazards Research 31,
DOI 10.1007/978-94-007-2162-3_58, © Springer Science+Business Media B.V. 2012

58.1 Introduction

Mass-transport deposits (MTDs) are the products of significant mass-wasting processes, such as slides, slumps, and debris flows (e.g., Stow 1986; Lucente and Pini 2008). MTDs occur when the downslope component of shear stress exceeds the resisting strength. This can be accomplished through, for example, earthquakes, overpressure, and over-steepening. Submarine mass movements are an important geohazard to human life because they can generate large tsunamis (e.g., Bondevik et al. 2005; Talling et al. 2007). They also pose hazards to offshore infrastructure including telecommunication cables (e.g., Heezen and Ewing 1952) and oil–gas platforms (e.g., Bea et al. 1983).

Studies of ancient MTDs (e.g., Lucente and Pini 2008; Yamamoto et al. 2007, 2009) and modern MTDs (e.g., Flemings et al. 2006, 2008; Sawyer et al. 2009) have revealed the meso-scale internal structures and spatial variations in lithofacies/physical properties, respectively. However, the link between grain-scale fabric, bulk physical properties, and large-scale deformation features within MTDs are not well understood. These relations are important in assessing the risk of MTDs reactivation as a geohazard, because they result in mechanical and fluid-flow heterogeneity in the sedimentary mass.

Integrated Ocean Drilling Program (IODP) Expedition 308 penetrated several MTDs in the Ursa Region in the northern Gulf of Mexico (Flemings et al. 2006, 2008). The expedition also cored and logged the entire sequences of MTDs and coherent intervals, and found densification phenomena of clay-rich MTDs (Flemings et al. 2008; Sawyer et al. 2009).

The present paper focuses on spatial variations in fabric development and related variations in physical properties within MTDs of the Ursa Region, based on analyses of the preferred orientation of magnetic grains, as derived from the anisotropy of magnetic susceptibility (AMS), and based on observations by scanning-electron microscope (SEM). AMS is a useful method to infer the strain distribution in MTDs because the AMS ellipsoid is commonly coaxial with the strain ellipsoid, and the Kmin (the minimum susceptibility) axis is generally oriented parallel to the axis of maximum shortening strain (e.g., Borradaile 1988, 1991). To extract the fabric characteristics from MTDs, we performed AMS and SEM analyses for entire sequences of MTDs and coherent units recovered by IODP Expedition 308.

58.2 Geologic Setting

The Ursa Basin is located 210 km (~125 miles) southeast of New Orleans, Louisiana (USA), on the upper Mississippi Fan in water depths ranging from 800 to 1,500 m (Fig. 58.1). Late Pleistocene deposits in the Ursa Basin are associated with a much larger system in the north-central Gulf of Mexico: the Eastern Depositional Complex (e.g., Coleman and Roberts 1988; McFarlan and LeRoy 1988). Very high sedimentation rates (3–10 mm/year) during the Late Pleistocene in this area contributed to

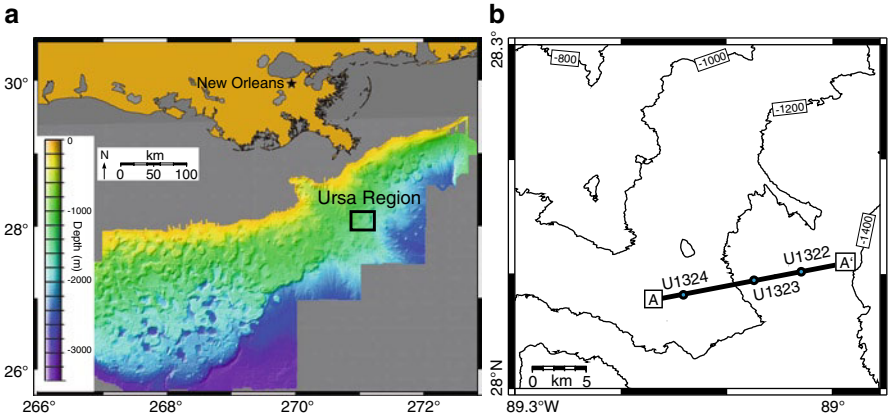

Fig. 58.1 Index map of the Ursa Region (Gulf of Mexico), located on the eastern levee of the Mississippi-canyon channel levee system (**a**, **b**). (**b**) Enlarged bathymetric map indicating drilling sites. Position is indicated by rectangle in (**a**)

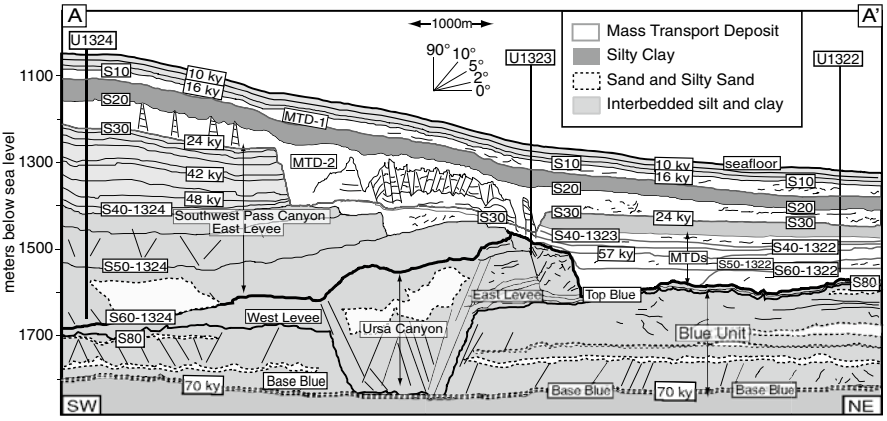

Fig. 58.2 Cross-section along A–A' in Fig. 58.1, which intersects the drillholes sunk during IODP 308 (After Sawyer et al. 2009). Mass-transport deposits (*MTDs*) occur primarily within the thick, silty clay levee deposits. No coring was conducted at Site U1323

the development of overpressure and slope failure (Flemings et al. 2006, 2008; Dugan and Germaine 2008).

The shallow stratigraphy at Ursa (upper 1,000 m below the sea floor) comprises the Blue Unit basin-floor fan, two channel-levee systems, and numerous MTDs (Fig. 58.2). The Blue Unit (~300 m below the seafloor) is a ponded sand-prone basin-floor fan noted for causing shallow-water flow problems in this area (Ostermeier et al. 2002). The Blue Unit is overlain and incised by two channel-levee systems with thick mud-prone levees (Sawyer et al. 2007). The levees contain numerous mud-prone MTDs and can be mapped from seismic reflection data

as a semi-transparent and chaotic seismic facies (Fig. 58.2) (Sawyer et al. 2009). In core and log data, the MTDs are characterized by low porosity (high bulk density) and high resistivity compared with non-MTD units (Dugan et al. 2007; Sawyer et al. 2009).

58.3 MTD Deformation: Seismic and Physical Properties

Clay-rich MTDs in the Ursa Region are identified as a chaotic facies or discontinuous stratified facies, both characterized by low-amplitude MTD zones and high-amplitude basal reflections (Sawyer et al. 2009; Fig. 58.2). Contorted layers and homogenized sediments have been identified in the MTDs from Sites U1322B and U1324B. The contorted layers tend to occur in the upper parts of MTDs, whereas the homogenized sediments tend to occur in the basal parts. NW-SE-trending grooves are identified from the basal surfaces of MTDs (Sawyer et al. 2009; Fig. 58.3) that indicate the movement direction of the deposits.

Resistivity profiles show a gradual increase in the upper parts of MTDs, and a sharp drop between the lowermost parts of MTDs and the underlying coherent sedimentary units (Fig. 58.4). Porosity profiles show a gradual decrease from the top to the bottom of MTDs, with a sharp recovery in the underlying coherent sedimentary units. These data indicate that the MTDs are denser than the coherent intervals and that densification is greatest at the base of each MTD, resulting in a strong basal reflection.

58.4 Fabric in the MTDs

58.4.1 Sampling and Laboratory Procedures

Samples for AMS measurements were collected from clay and mud parts of the MTDs, rather than from sandy parts. The most common method of sampling soft sediment is to insert plastic cubes (~10 cm^3) into the sediment, although this may damage the fabric due to shear against the wall of the cube. To minimize disturbance to the fabric, the samples were collected as follows. The samples were taken from split core using 10 cm^3 plastic tubes (inner diameter, ~30 mm). The outer rim, top, and bottom of each tube sample were cut and removed using a wire saw, and cubic-shaped specimens (18–20 mm on each side) were prepared. The specimens were then placed in plastic cubes and sent for AMS measurements using a KLY-4 Kappabridge instrument at AIST (National Institute of Advanced Industrial Science and Technology), Japan.

The AMS specimens were then observed by SEM. Because the samples are mainly poorly consolidated clay-rich sediments, the t-butyl alcohol freeze-drying method (Takizawa et al. 1995) was adopted to minimize any disturbance of the original microstructures due to surface tension effects.

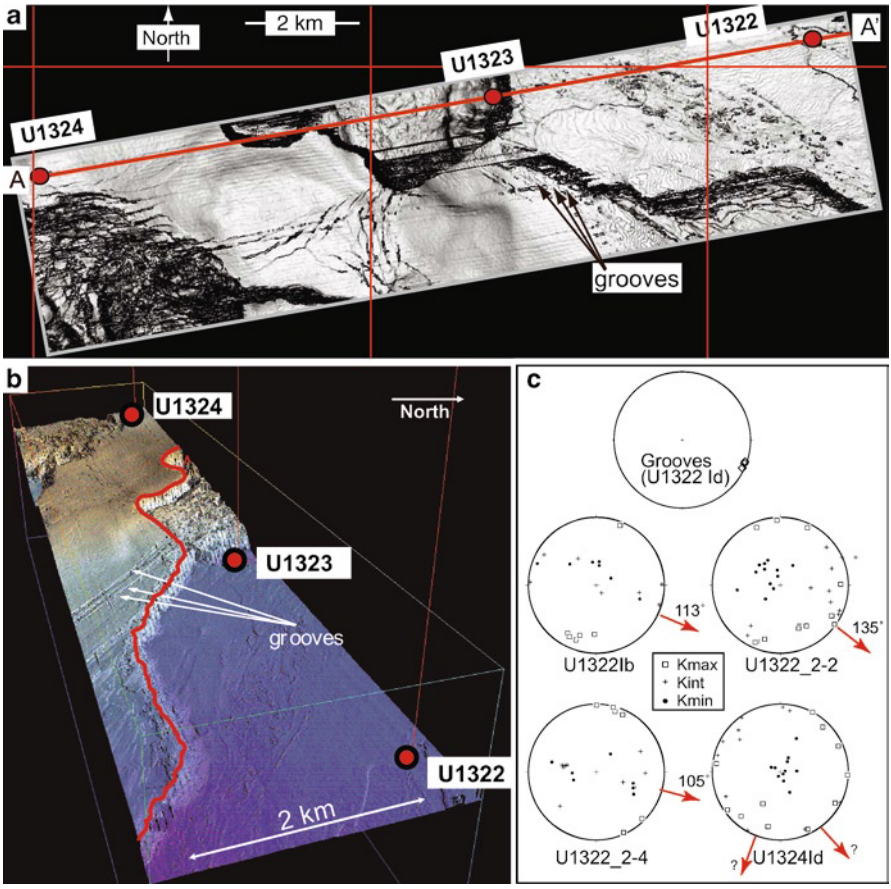

Fig. 58.3 (**a**) Dip map of the base of MTD-2, seismic reflection S30 (see Fig. 58.2), showing steep side scarps and linear groove traces (Sawyer et al. 2009) (**b**) Whale-view diagram showing linear groove traces and steep side scarps (**c**) Stereoplots (lower-hemisphere equal-area projections) showing the orientations of groove traces and magnetic susceptibility ellipsoids measured from mass-transport deposits (*MTDs*) in the Ursa Region. *Red arrows* indicate the slip direction of MTDs inferred from the attitudes of magnetic susceptibility ellipsoids. Note that the estimated slip direction is consistent with the orientations of grooves

58.4.2 Results

The specimens yielded magnetic susceptibilities of 9.78×10^{-5} to 1.23×10^{-3} SI units. The bulk magnetic susceptibilities tend to increase with increasing burial depth, because the amount of magnetic grains in the specimens increases with decreasing porosity. However, the susceptibilities poorly reflect the structural and lithological variations. Franke et al. (2009) identified detrital iron oxide minerals as the main magnetic carrier in these rocks.

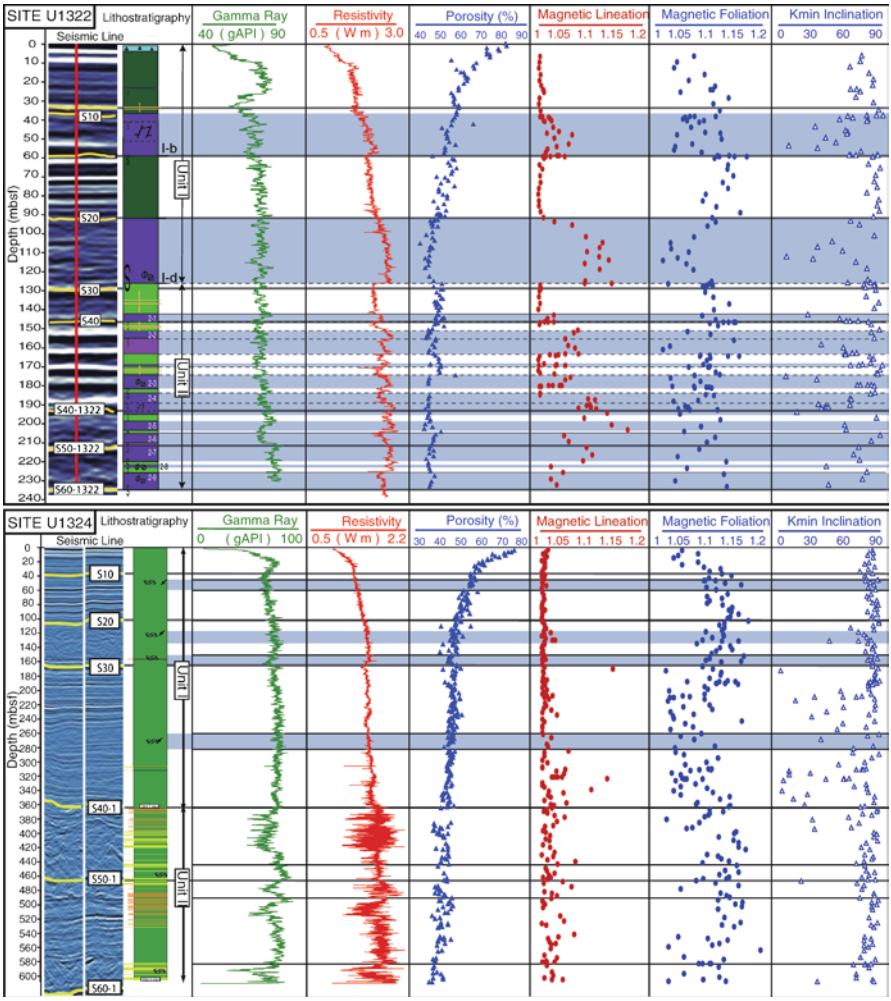

Fig. 58.4 Logging data and AMS profile for Sites U1322B (*upper*) and U1324B (*lower*). Logging data (*gamma ray* and resistivity) and porosity data are from IODP Expedition 308 (Flemings et al. 2006). *Blue-colored* background in the profile corresponds to intervals of mass-transport deposits (*MTDs*)

The coherent sedimentary units show a small value (close to 1) of magnetic lineation (Kmax/Kint: maximum/intermediate susceptibility), indicating a random Kmax orientation (Fig. 58.4). Within several tens of meters of the seafloor, the magnetic foliation shows a progressive increase with decreasing porosity. In coherent units, the inclination of Kmin (the minimum susceptibility) is close to 90°. These data indicate that the fabric in the coherent intervals was controlled by compaction related to gravity. The MTD intervals are characterized by strong magnetic

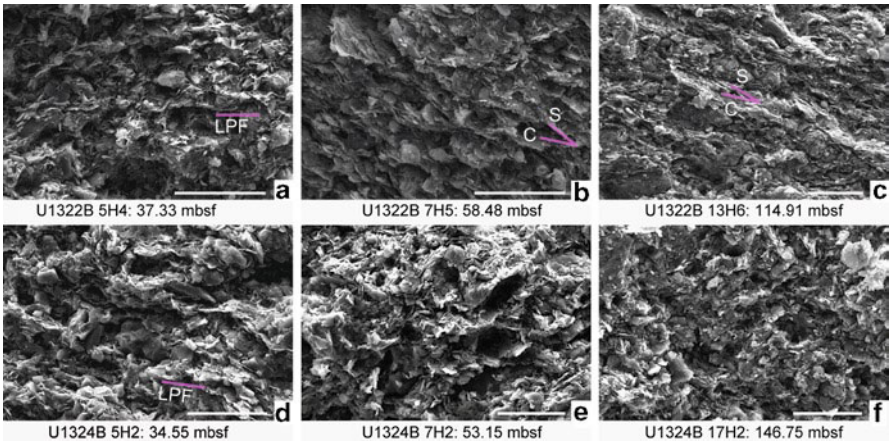

Fig. 58.5 SEM images taken from normal (coherent) sediments (**a**, **d**) and from mass-transport deposits (*MTDs*; **b**, **c**, **e**, **f**). Images (**a**–**c**) Site U1322B (**d**–**f**) Site U1324B. Scale bars are 20 μm. The normal sediments are characterized by layer-parallel compaction fabrics, whereas the MTDs are characterized by composite S–C shear fabrics. *LPF*: Layer-parallel foliation

lineation and weak magnetic foliation, and the inclination of Kmin is disturbed compared with coherent sedimentary units. At Site U1322B, the intensity of the magnetic lineation shows a gradual increase in the upper parts of MTDs, whereas a sharp downward drop is seen between the lowermost parts of MTDs and the underlying coherent units. Although some of the MTDs at Site U1324B can be lithologically and seismically correlated to MTDs at Site U1322B, they show only minor variations in the magnetic ellipsoids, as also observed for variations in porosity, gamma ray, and resistivity.

The orientations of the AMS axes were restored to geological coordinates using onboard paleomagnetic data (Flemings et al. 2006). Kmax axes tend to trend NNE–SSW or NE–SW, or show a NE–SW girdle distribution (Fig. 58.3c). Both of these patterns of Kmax orientation are accompanied by a girdle distribution of Kmin and Kint along WNW–ESE or NW–SE.

SEM observations reveal that clay in the sediments consists of planar clay particles and silt grains (Fig. 58.5). The SEM observations revealed no difference between coherent layers and MTDs in terms of the grain size distribution and clay mineral content. These findings are consistent with previous grain-size analyses of these rocks (Sawyer et al. 2008). The fabric in coherent intervals is characterized by a bedding-parallel foliation that may represent a compaction fabric (Fig. 58.5a, d). The MTD intervals at Site U1322B are characterized by intensively developed layer-parallel and oblique foliations (Fig. 58.5b, c). In most cases, the layer-parallel foliation cuts and displaces the oblique foliation, indicating that these foliations represent the two components of an S–C shear structure. Faint shear-induced fabric is developed in MTDs at Site U1324B (Fig. 58.5e, f).

58.5 Discussions

Magnetic ellipsoids obtained for the coherent interval are characterized by a relatively weak magnetic lineation (close to 1), a relatively strong magnetic foliation, and a Kmin oriented perpendicular to bedding planes (Fig. 58.4). These findings are indicative of the compaction of clay-rich sediments, as also indicated by the occurrence of a bedding-parallel foliation (Fig. 58.5a). In contrast, compare with the coherent intervals, the MTD intervals show a remarkable increment in the magnetic lineation, decrement in the magnetic foliation, and shallowing of the Kmin inclination. The profiles of these parameters are consistent with those of gamma ray, resistivity, and porosity (Fig. 58.4), indicating that vertical variations in the physical properties of the rock mass are associated with grain rotation within the MTDs.

The measured variations in magnetic lineation are especially sensitive to variations in the above parameters. The MTDs at Site U1322 contain an intense shear-induced S–C structure, accompanied by a strong magnetic lineation, whereas the MTDs at Site U1324 contain a weak shear structure and a relatively weaker magnetic lineation (cf. Fig. 58.5b, c with Fig. 58.5 e, f). Site U1324 is located near the headwall areas of the MTDs, whereas Site U1322 is located near the toe areas. Therefore, the MTD sediments at Site U1324 are close to their pre-failure condition, whereas those at Site U1322 record high strain and long-distance transport.

Kmax axes tend to trend NNE–SSW or NE–SW, or define a NE–SW girdle distribution (Fig. 58.3c). Kmin and Kint tend to define WNW–ESE or NE–SE girdle distributions. Based on the results of a previous experimental study that examined the relation between the AMS distribution and the flow direction of turbidites (Taira 1989), the MTDs of the present study are inferred to have moved to the ESE or SE, which is consistent with the orientations of grooves on the basal surfaces of the MTDs (Fig. 58.3c).

Grain rotation is inferred to have occurred during movement of the MTDs, resulting in spatial variations in the physical properties of the sediment. Grain rotation during soft-sediment deformation results in the collapse of large pore spaces (Yamamoto 2006), resulting in turn in compaction of the sediments and a decrease in permeability.

The occurrence of gradual changes in the intensity of magnetic lineation within the upper part of MTDs indicates that the shear zones within the MTDs show an upward increase in thickness. The sharp drop in the intensity of magnetic lineation and in porosity between the lowermost parts of MTDs and the underlying coherent sedimentary units indicates that major mechanical decoupling has developed in the lowermost parts of the MTDs. Because there is no difference in lithology between areas within and below MTDs, the decoupling may have occurred due to fluid pressure.

The occurrence of grain rotation during movement of the MTDs resulted in reduced porosity and the formation of impermeable layers. Given that permeability was controlled by shear-induced grain rotation and compaction, fluid pressure was probably elevated in areas immediately below the impermeable MTDs, resulting in

instability of the MTDs, the development of mechanical decoupling, and possibly subsequent reactivation of MTDs. Such a feedback process may have resulted in thickening of the shear zone or the development of large MTDs.

Acknowledgments The samples analyzed in this study were provided by the Integrated Ocean Drilling Program (IODP). We thank the scientists and technical staff of IODP Expedition 308 for their assistance. Andrea Festa and Yujin Kitamura are appreciated for their detailed and constructive reviews, which improved the manuscript.

References

Bea RG, Sircar P, Niedoroda AW (1983) Wave-induced slides in South Pass Block 70, Mississippi Delta. J Geotech Eng 109:619–644

Bondevik S, Løvholt F, Harbitz CB et al (2005) The Storegga slide tsunami – comparing field observations with numerical simulations. Mar Petrol Geol 22:195–208

Borradaile GJ (1988) Magnetic susceptibility, petrofabrics and strain. Tectonophysics 156:1–20

Borradaile GJ (1991) Correlation of strain with anisotropy of magnetic susceptibility (AMS). Pure Appl Geophys 135:15–29

Coleman JM, Roberts HH (1988) Late Quaternary depositional framework of the Louisiana continental shelf and upper continental slope. Trans GCAGS 38:407–419

Dugan B, Flemings PB, Urgeles R et al (2007) Physical properties of mass transport complexes in the Ursa Region, northern Gulf of Mexico (IODP Expedition 308) determined from log, core, and seismic data, OTC 18704. Offshore technology conference, Houston, pp 1–13

Dugan B, Germaine JT (2008) Near-seafloor overpressure in the deepwater Mississippi Canyon, northern Gulf of Mexico. Geophys Res Lett 35:L02304. doi:10.1029/2007GL032275

Flemings PB, Behrmann JH, John CM, Exp 308 Scientists (2006) Gulf of Mexico hydrogeology. In: Flemings PB, Behrmann JH, John CM (eds) Proceedings of the integrated ocean drilling program 308, College Station (Integrated Ocean Drilling Program Management International, Inc), TX

Flemings PB, Long H, Dugan B et al (2008) Pore pressure penetrometers document high overpressure near the seafloor where multiple submarine landslides have occurred on the continental slope, offshore Louisiana, Gulf of Mexico. Earth Planet Sci Lett 269:309–324. doi:310.1016/j.epsl.2008.1006.1027

Franke C, Fu Y, Heslop D, von Dobeneck T (2009) Data report: natural remanent magnetization of IODP Holes U1319A, U1320A, U1322B, and U1324B and magnetic carrier identification by scanning electron microscopy. In: Flemings PB, Behrmann JH, John CM, Expedition 308 Scientists (eds) Proceedings of the IODP 308, College Station (Integrated Ocean Drilling Program Management International, Inc), TX

Heezen BC, Ewing M (1952) Turbidity currents and submarine slumps and the 1929 Grand Banks earthquake. Am J Sci 250:849–873

Lucente CC, Pini GA (2008) Basin-widemass-wasting complexes as markers of the Oligo–Miocene foredeep-accretionary wedge evolution in the Northern Apennines, Italy. Basin Res 20:49–71

McFarlan E, LeRoy DO (1988) Subsurface geology of the Late Tertiary and Quaternary deposits, coastal Louisiana, and the adjacent continental shelf. Trans Gulf Coast Assoc Geol Soc 38:421–433

Ostermeier RM, Pelletier JH, Winker CD, Nicholson JW, Cowan CK (2002) Dealing with shallow-water flow in the deepwater Gulf of Mexico. Lead Edge 21:660–668

Sawyer DE, Flemings PB, Shipp RC, Winker CD (2007) Seismic geomorphology, lithology, and evolution of the late-Pleistocene Mars-Ursa turbidite region, Mississippi Canyon area, northern Gulf of Mexico. AAPG Bull 91:215–234. doi:10.1306/08290605190

Sawyer DE, Jacoby R, Flemings PB Germaine JT (2008) Data report: particle size analysis of sediments in the Ursa Basin, IODP Expedition 308 Sites U1324 and U1322, northern Gulf of Mexico. In: Flemings PB, Behrmann JH, John CM, Expedition 308 Scientists (eds) Proceedings of the IODP 308, College Station (Integrated Ocean Drilling Program Management International, Inc), TX

Sawyer DE, Flemings PB, Dugan B, Germaine JT (2009) Retrogressive failures recorded in mass transport deposits in the Ursa Basin, Northern Gulf of Mexico. J Geophys Res 114:B10102. doi:10.1029/2008JB006159

Stow DAA (1986) Deep clastic seas. In: Reading HG (ed) Sedimentary environments and facies. Blackwell, Oxford, pp 399–444

Taira A (1989) Magnetic fabrics and depositional processes. In: Taira A, Masuda F (eds) Sedimentary facies in the active plate margin. TERRAPUB, Tokyo, pp 619–630

Takizawa S, Kawata T, Ohno Y (1995) A method of fixation and freeze drying of soft sediments containing water. J Geol Soc Jpn 101:941–944

Talling PJ, Wynn RB, Masson DG et al (2007) Onset of submarine debris flow deposition far from original giant landslide. Nature 450:541–544

Yamamoto Y (2006) Systematic variation of shear-induced physical properties and fabrics in the Miura–Boso accretionary prism: the earliest processes during off scraping. Earth Planet Sci Lett 244:270–284. doi:10.1016/j.epsl.2006.01.049

Yamamoto Y, Ogawa Y, Uchino T, Muraoka S, Chiba T (2007) Large-scale chaotically mixed sedimentary body within the Late Pliocene to Pleistocene Chikura Group, Central Japan. Island Arc 16:505–507

Yamamoto Y, Nidaira M, Ohta Y, Ogawa Y (2009) Formation of chaotic rock-units during primary accretion processes: examples from the Miura–Boso accretionary complex, Central Japan. Island Arc 18:496–512

Chapter 59
Records of Submarine Landslides in Subduction Input Recovered by IODP Expedition 322, Nankai Trough, Japan

Yujin Kitamura and Yuzuru Yamamoto

Abstract Submarine landslides in the active continental margin are the earliest tectonically-driven deformation for sediments underthrusting to the plate boundary. Asymmetric bathymetry across trenches results in the common occurrence of the large scarps related to the mass transport on the steeper accretionary prism surface. Gently tilted oceanic plates off trenches are, however, also sufficient for sliding. Within the framework of the Nankai Trough Seismogenic Zone Experiment (NanTroSEIZE) of the Integrated Ocean Drilling Program (IODP), we drilled two sites (Sites C0011 and C0012) in the subduction input sediments and recovered samples with a specific feature of sliding in a very shallow depth. This feature is composed of fine-grained gouge-like material accompanied by sheared planar fabric. It is typically crosscut by bioturbation, which indicates its formation in a quite shallow depth. In the middle part of Hole C0012A, the bedding tilts significantly compared to the bedding in the hole above and below. This localized inclination indicates block sliding of the sediments. These observations suggest that the surface of the incoming oceanic plate into the Nankai Trough is quite active, as represented by sub-seafloor slidings in different scale. Our observation shows that the input sediments are already deformed before reaching the trench. The fact of the earlier deformation prior to subduction is important for understanding further deformation processes along plate boundaries in subduction zones.

Keywords D/V Chikyu • NanTroSEIZE • Submarine landslide • Subduction input

Y. Kitamura (✉)
Japan Agency for Marine-Earth Science and Technology, Institute for Research on Earth Evolution, 2-15 Natsushima-cho, Yokosuka, Kanagawa 237-0061, Japan
e-mail: ykitamura@jamstec.go.jp

Y. Yamamoto
Japan Agency for Marine-Earth Science and Technology, Institute for Research on Earth Evolution, 3173-25 Showa-machi, Kanazawa-ku, Yokohama, Kanagawa 236-0001, Japan
e-mail: yuzuru-y@jamstec.go.jp

Y. Yamada et al. (eds.), *Submarine Mass Movements and Their Consequences*,
Advances in Natural and Technological Hazards Research 31,
DOI 10.1007/978-94-007-2162-3_59, © Springer Science+Business Media B.V. 2012

59.1 Introduction

Landslides can occur anywhere on the earth surface, even in the deep sea. Understanding the process is very important because of the negative impact of landslides on human society, such as defects in ocean floor cables, the release of methane hydrates or tsunamis. Sediments on an unstable slope can be triggered to slide by excess gravitational forces against resisting forces or by the shaking of earthquakes. Even when an earthquake does not occur, a submarine large mass transport can generate a hazardous tsunami (e.g., the 1979 Nice airport submarine landslide; Gennesseaux et al. 1980).

Subduction zones act as incubators of submarine landslides because of the variety of topography and repeating shock of earthquakes. A subduction zone fulfills the conditions for submarine landslides because of its environment (open continental slope) and assisting features of the convergent margin (earthquake shaking and tectonic steepening) (Hampton et al. 1996). The ocean-continent subduction zone intrinsically forms asymmetric bathymetry across the trench, i.e., the steeper slope on the landside. Submarine landslides in active margins tend to be smaller than those in passive margins (e.g., Yamada et al. 2010), which may result from active triggering by earthquakes that induce much more frequent slope failure. There are many scarps in the trench slope of the studied Nankai Trough as in other subduction zones. Subduction of seamounts also induces large submarine landslides. Yamazaki and Okamura (1989) reported a great embayment along the Nankai Trough off Shikoku Island, Japan, and concluded that it was formed by a seamount subduction with supporting data of aeromagnetic anomaly.

The angle of slopes is a critical factor, but does not have to be large. Initiation of slope failure is determined by the balance of the generally used Mohr-Coulomb failure criterion and the shear stress acting downslope, which yields equal angles of the slope and the internal friction of the sediments (see Hampton et al. 1996 for the mathematical details). The very shallow part of the deposited sediments is under hydrostatic pressure and there is almost no cohesion inside. With such non-resistant sediments, a very slight tilt can cause sliding; for example, 0.01° of Mississippi River delta slides (Prior and Coleman 1978). And once sediment flow begins, the sediment can travel several hundreds kilometers unless deposition is triggered by a remarkably small but abrupt decrease in slope angle (from 0.05° to 0.01°, example from Agadir basin off Morocco, Talling et al. 2007). Thus, the seaward abyssal plane beyond a trench at the convergent margin is not an exception for the submarine landslide. An observation of onland chaotic rock outcrops suggests slumping prior to accretion (Yamamoto et al. 2009). Here we show a line of evidence for two types of submarine landslides of different scales observed in the drilled cores from the subduction input recovered during the Integrated Ocean Drilling Program (IODP) Expedition 322.

59.2 Results of IODP Exp. 322

IODP Expedition 322 is a part of a multi-stage and multi-expedition drilling program of the Nankai Trough Seismogenic Zone Experiment (NanTroSEIZE) in the framework of the IODP (Tobin and Kinoshita 2006). The final goal of the NanTroSEIZE is to recover material from the seismogenic zone at a depth of about 7 km below the seafloor and to install observatories in the boreholes for long-term monitoring of the seismogenic plate boundary. The Nankai Trough region of southwest Japan is among the most extensively studied subduction zones in the world, and has a well documented 1,300 year history of great earthquakes and associated tsunamis (Ando 1975). The Philippine Sea plate is subducting beneath the Eurasian plate at the Nankai Trough with the convergent direction approximately orthogonal to the trough axis. Sediments of the Shikoku Basin are actively accreting at the deformation front (Kimura et al. 2007).

During Expedition 322, cores were collected from two drill sites in the seaward Nankai Trough (Sites C0011 and C0012, Fig. 59.1) to examine the characteristics of incoming sedimentary strata and igneous basement prior to their arrival at the subduction front (Saito et al. 2010). The drill sites are located in the Shikoku Basin, which formed during the early and middle Miocene epochs by the seafloor spreading along the back-arc side of the Izu-Bonin volcanic chain (Okino et al. 1994; Kobayashi 1995): one site is at the crest of a bathymetric high (Kashinosaki Knoll) and the other along the northwest flank of the knoll. Coring was actually conducted at Holes C0011B (340–881 m drilling depth below seafloor [DSF]) and C0012A (60–561 m DSF).

Onboard examination identified seven and four lithologic units at Sites C0012 and C0011, respectively (Fig. 59.1). Unit I is the so-called upper Shikoku Basin, which has been recognized in the Nankai Trough region in combination with the underlying lower Shikoku Basin corresponding to Units III and IV in these sites. The upper Shikoku Basin is characterized by silty clay with thin interbeds of volcanic ash, while the lower Shikoku Basin consists of dominant bioturbated hemipelagic silty claystone in Unit III and muddy turbidites in Unit IV. The abundant tuffaceous and volcaniclastic turbidites observed in Unit II have no equivalent at any other previous Ocean Drilling Program (ODP) or IODP site in the Nankai Trough (Saito et al. 2010). Unit II is tentatively interpreted as the distal parts of a submarine fan that was sourced from the Izu-Bonin arc (Saito et al. 2010). Units V and VI are composed of volcaniclastic-rich deposits and pelagic red-colored claystone, respectively. In Unit VII, 38.2 m of basalts were recovered at the bottom of Hole C0012A. The age determined by microfossils and paleomagnetic polarity corresponds well between the two sites. The time span of each unit is roughly as follows: Units I, <7 Ma; Unit II, 7–10 Ma; Unit III, 10–12 Ma; Unit IV, 12–14 Ma; Unit V, 14–20 Ma.

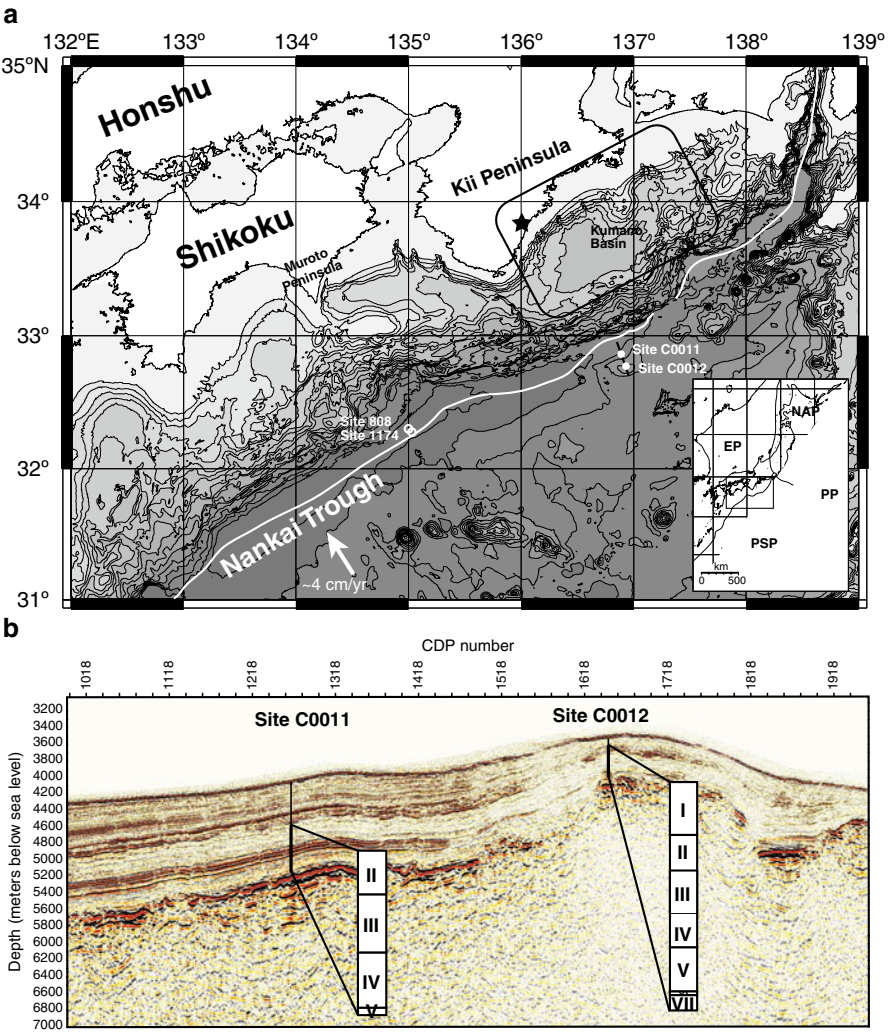

Fig. 59.1 (**a**) Bathymetrical map of the studied Nankai Trough. (**b**) Seismic profile along the black line in Fig. 59.1a. Litholigic units for cored interval at Sites C0011 and C0012 are shown (modified after Saito et al. 2010)

59.3 Bedding Inclination Anomaly in Sites C0011 and C0012

No significant structural variation is usually expected in sediments on the oceanic plate before subduction (e.g., Sites 1173 and 1177, reference sites for the Nankai accretionary prism off Cape Muroto and Cape Ashizuri, respectively); however, the dip angles of the bedding planes at Sites C0011 and C0012 show a considerable difference from those observed in the previous drill sites.

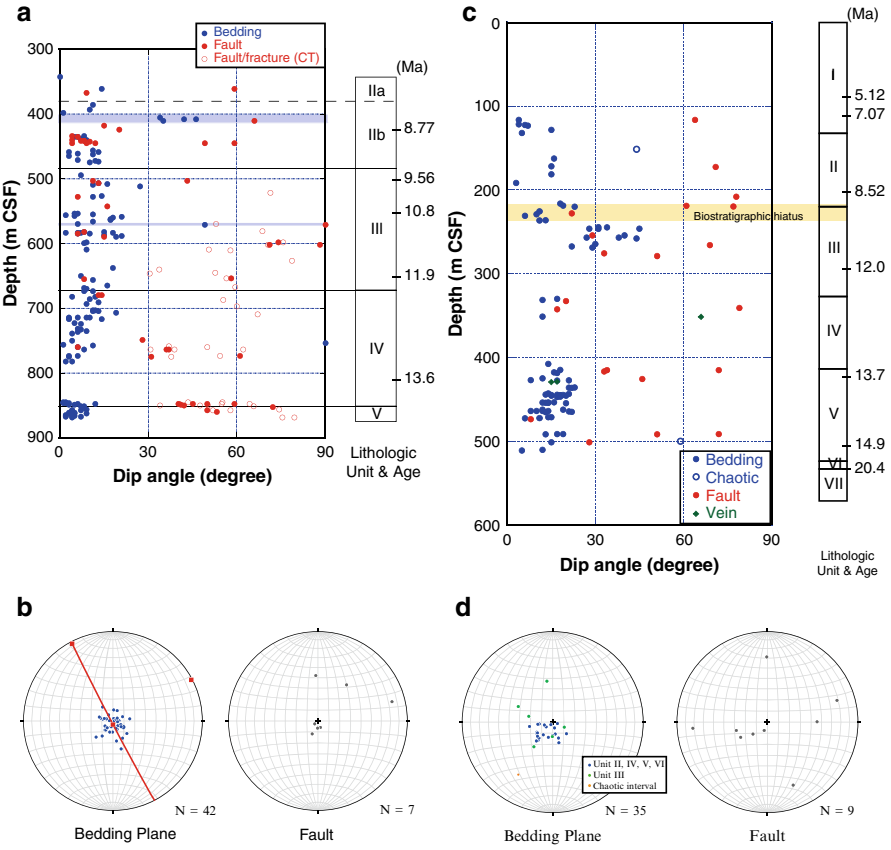

Fig. 59.2 (**a**) Dip angle variation of bedding and fault planes plotted against depth at Site C0011. Blue highlights correspond to chaotic deposits in core. CT = computed tomography. (**b**) Stereo plots (*lower hemisphere*) of bedding planes and faults at Site C0011 after paleomagnetic correction. (**c**) Dip angle variation of bedding and fault planes plotted against depth at Site C0012. *Yellow* highlight = possible biostratigraphic hiatus (Saito et al. 2010). (**d**) Stereo plots (*lower hemisphere*) of bedding planes and faults at Site C0012 after paleomagnetic correction

Although highly bioturbated hemipelagic sediments often prevented actual surface measurement, bedding is generally recognizable at Site C0011. The distribution of planar structures and lithologic units with depth are shown in Fig. 59.2a. The main structural features found in Hole C0011B were sub-horizontal bedding attitudes and fault distribution, such that layer-parallel faults were found at shallow depths, while high-angle faults were found at greater depths. The bedding planes at Site C0011 generally dip almost horizontal or 10–20°, and faults that are parallel to the bedding planes characterize the structure in this site. Bedding in lithologic Unit III is scattered between 0° and 30°, whereas the bedding dips in Units II, IV, and V

are concentrated below 20°. High-angle bedding planes are distributed only in the interval corresponding to the chaotic deposits in Core 322-C0011B-8R (403.00–412.50 m core depth below seafloor [CSF], Unit II) and Section 28R-2 (569.46–569.99 m CSF, Unit III) (Fig. 59.2a). The poles of the bedding and faults at Site C0011 cluster around the subhorizontal inclination (Fig. 59.2b). The cylindrical best fit of the bedding poles indicates a weak distribution along the north-northwest–south-southeast, perpendicular to the trench axis. These attitudes of the bedding planes correspond reasonably well with the data deduced from Logging-While-Drilling image analysis (Saito et al. 2010, Figure F22). These data indicate the bedding inclination was controlled by trenchward dipping of the bathymetric slopes on the seaward side of the trench.

The bedding planes in Site C0012 generally dip <25° in lithologic Units I, II, IV, and V. On the other hand, from Cores 322-C0012A-22R through 24R (244.20–272.70 m CSF) in the upper part of Unit III, the bedding shows anomalously steep inclination with a maximum dip of 45°. Although no bedding could be measured in Cores 322-C0012A-25R through 29R (272.70–313.82 m CSF) because of bioturbation, core surface lineaments, such as Zoophycos burrows, which tend to be parallel to the bedding plane, are apparently steep (Fig. 59.3a). Thus, Unit III is apparently characterized throughout by steep-dipping bedding planes. The bottom of the steep-bedding interval is expected to be between Sections 322-C0012A-29R-4 and 31R-1 (313.26–330.16 m CSF) (the bedding could not be recognized in Section 29R-CC and there was no recovery for Core 30R). The bedding-dip in Unit III at Site C0011 also presents a larger variability compared to Units II, IV and V, though the variation is faint. Small-scale chaotic deposits are observed in Sections 322-C0012A-12R-CC (151.02–159.00 m CSF) and 49R-1 (499.50–499.93 m CSF) (Fig. 59.2c).

Figure 59.2d shows the reoriented plot of the planar structures to the geographic coordinate system using paleomagnetic data (Saito et al. 2010). The dominant bedding planes concentrate around the subhorizontal inclination dipping northward. Data from a steeply inclined interval in Unit III show girdle distribution trending north-northwest–south-southeast (Fig. 59.2d). From these data, we inferred that although the bedding planes at this site are tilted to the north, the bedding planes in Unit III show large block rotation, possibly because of northward sliding.

59.4 Structures Observed in Core

The major deformation structures observed in Sites C0011 and C0012 are layer-parallel faults (Fig. 59.3b), high-angle faults (Fig. 59.3d) and bioturbated dark-colored deformation bands (Fig. 59.3c). Most faults in lithologic Units II and III are characterized by healed faults with layer parallel attitudes in Site C0011. These faults are characterized by higher bulk density under X-ray Computed Tomography (CT) image observation (Saito et al. 2010), which is indicative of shear-induced compaction. Poor recovery and highly bioturbated hemipelagic sediments resulted in a fewer number of similar faults at Site C0012, but the overall impression of

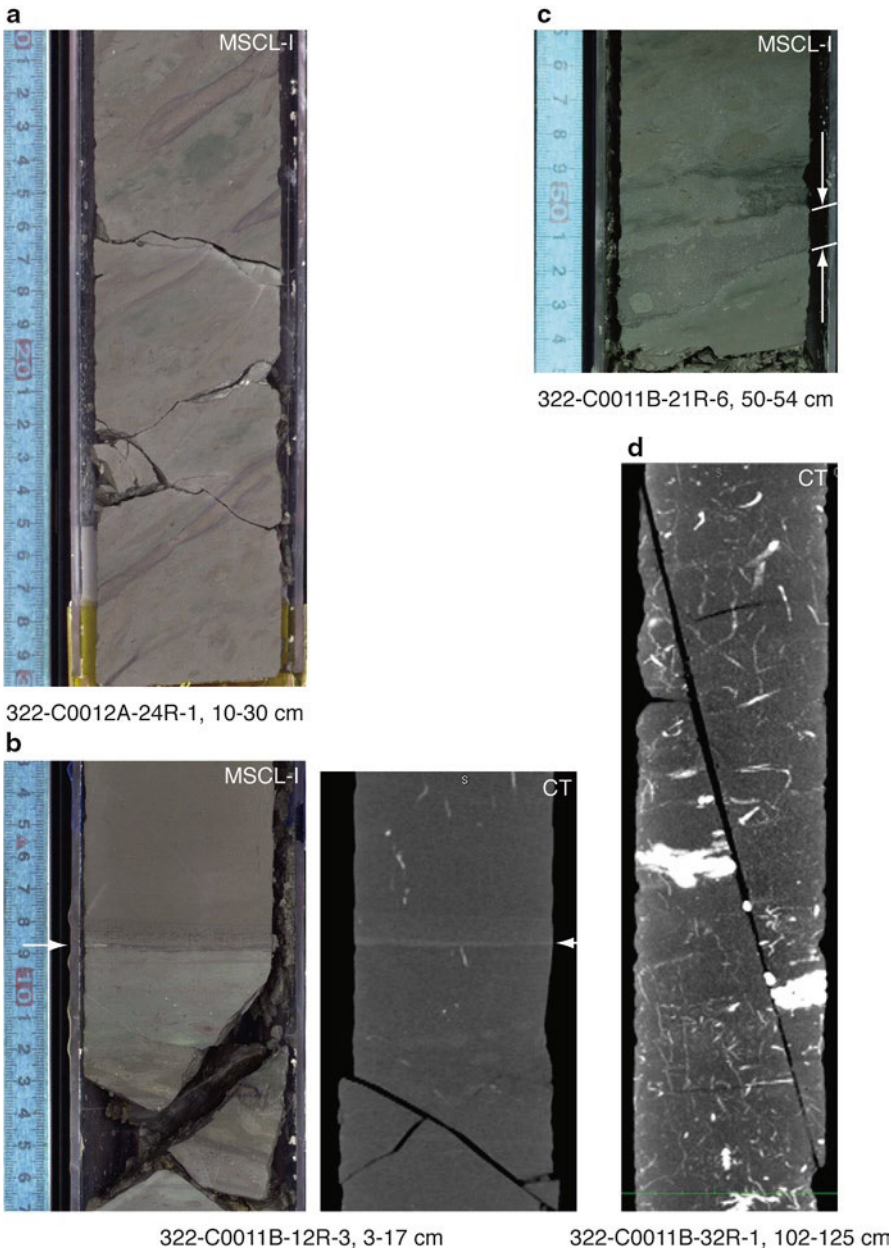

Fig. 59.3 Typical structures observed in cores. (**a**) steeply inclined sediments in Unit III at Site C0012. (**b**) Example of layer-parallel fault (*arrows*). (**c**) Bioturbated dark-colored deformation band (**d**) High-angle fault displaces a bright layer (possibly a burrow). MSCL-I = photo image logger, CT = X-ray computed tomography image

shipboard observation in the two sites are equivalent. Although layer-parallel faults were not reported at Sites 1173 and 1177, they are well identified in the late Miocene-Pliocene accretionary complex and Pliocene-Pleistocene cover sediments in the Miura Peninsula, central Japan (e.g., Yamamoto et al. 2005). Similar structures are also reported from the toe of the Nankai accretionary complex, off Muroto, at Sites 808 and 1174 (Maltman et al. 1993; Ujiie et al. 2004). These analogous examples suggest that layer-parallel faults have formed soon after sedimentation.

High angle faults generally develop in both Sites C0011 and C0012 (Figs. 59.2a, c) and dip over 45°. They exhibit brittle deformation features without gouging or CT value variation (Saito et al. 2010).

Another layer-parallel structure which was clearly distinguished from above mentioned faults was observed in these sites. Although layer-parallel faults commonly accompany very thin deformation bands (~1–2 mm), some of them have thick (>1 cm), dark-colored deformation bands (Fig. 59.3c). These deformation bands are filled with well-sorted, fine, dark material and have some rounded clasts of silty claystone. These apparent clasts are burrows, which connect to the upper adjacent layer in X-ray CT images. These bioturbated claystones were also reported at Site 1173 during ODP Leg 190 (Moore et al. 2001). The band that occurs at interval 322-C0011B-31R-3, 100–117 cm (589.40–589.57 m CSF, Fig. 59.3), accompanies a much darker, thin layer at its bottom, which indicates shear flow. The dark matrix has a slightly less dense CT signature than the host rock. These deformation structures indicate submarine soft-sediment sliding or creep in a shallow enough subsurface to be bioturbated. The bands occur from Units II to V at Site C0012, whereas we only observed them in Unit III at Site C0011.

59.5 Discussion

59.5.1 Large Mass Block Sliding

The anomalous bedding inclination in Unit III may have been formed by a large block sliding on the northward-tilted seafloor. An apparent change in bedding dip distribution was also reported at Site 1173 off Muroto Peninsula (Moore et al. 2001). The bedding inclination in Unit III at Site 1173 varies from 0° to 30°, where the upper units show almost completely horizontal bedding. In our study, the bedding data fluctuates in a range of 20–30° in all units. The reason for such an uncertainty is unclear; however, the anomalous bedding in Site C0012 ranges from 22° to 45°. This distinctive shift in the bedding inclination of the continuous interval suggests block rotation. The upper boundary of this inclined block was not recognized in the cores, but is expected to be between Sections 322-C0012A-21R-CC and 22R-1 (238.09–245.54 m CSF). A possible hiatus in the interval 322-C0012A-19R-1, 32 cm, through 21R-3, 7 cm (216.02–235.76 m CSF) was reported (Saito et al. 2010), which does not overlap with the slide-induced unconformity. This slight incompatibility in the possible unconformity can be explained by a single event, which we propose as follows. As shown in Fig. 59.4, a relatively large submarine

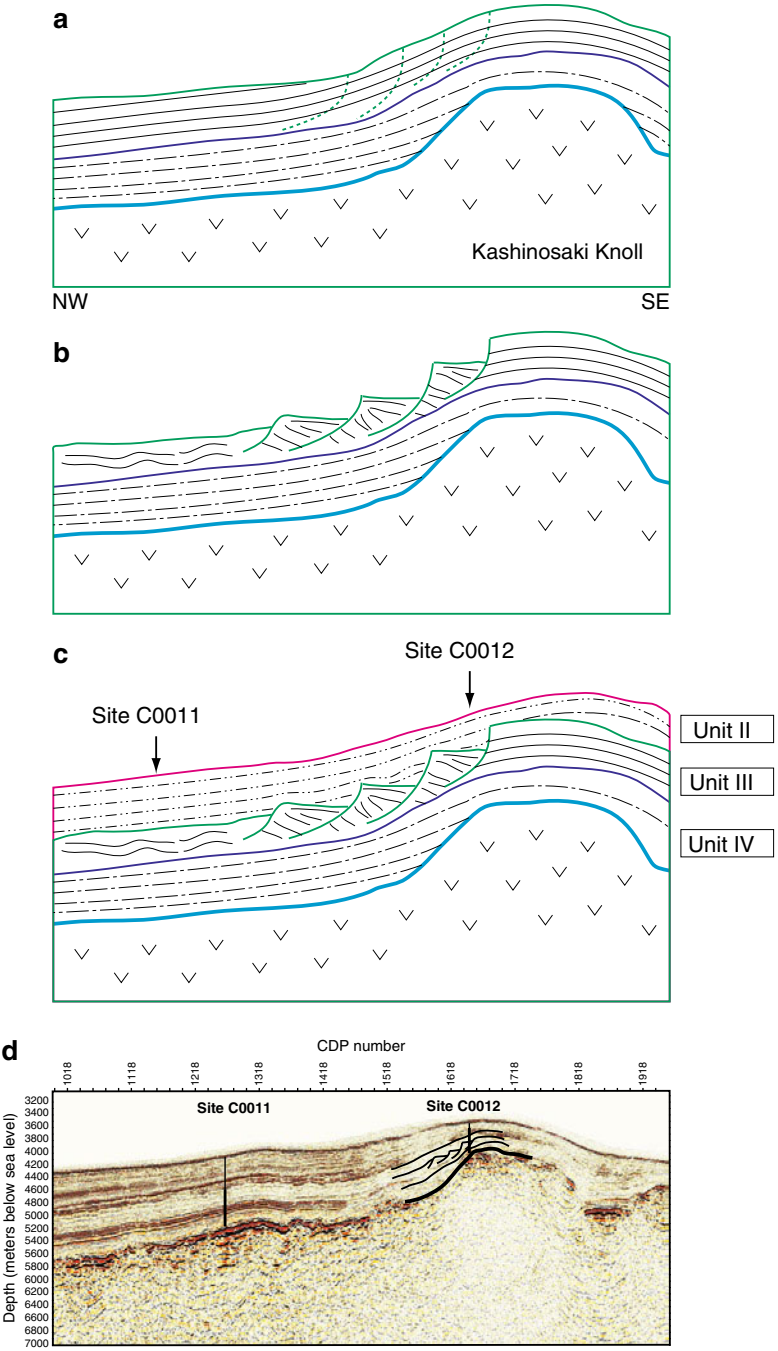

Fig. 59.4 Schematiccartoon showing a submarine landslide event that could create the steeply inclined interval in Unit III at Site C0012. (**a**) Initial deposition of the Unit III horizon. (**b**) Submarine landslide induces block rotation in the flank of the Kashinosaki knoll. Note that redeposition at the surface of the rotated blocks would cause the discrepancy between the biostratigraphic hiatus and the inclined bedding. (**c**) Unit II sedimentation. Base of the rotated blocks and the boundary between Units III and IV are not well considered here because of poor core recovery and intense drilling disturbance. (**d**) Imaginary setting of block rotation projected over the seismic profile used in Fig. 59.1b

landslide occurred in the northern slope of the Kashinosaki Knoll in middle Miocene at the time when the lower Shikoku basin was formed. Large block rotation occurred near the headwall of the landslide around Site C0012 and mass transports laterally with less rotation at the foot of the Knoll around Site C0011, which resulted in the steep bedding interval in Site C0012 while faint variation in Site C0011. During block rotation by submarine sliding, the surface sediments may have been soft enough to be suspended and redeposited, followed by sedimentation of fine-grained materials to attempt to smooth any residual seafloor topography (Fig. 59.4). In this case, the hiatus apparently shifted upward. In addition, Unit III consists almost entirely of hemipelagic claystone, which makes structural features hard to detect from the seismic profile. The lower boundary or sliding surface is expected to be between Sections 322-C0012A-29R-4 and 31R-1 (313.26–330.16 m CSF), which is above the top of Unit IV (Section 31R-4, 74 cm; 331.81 m CSF). Because of poor core recovery, bioturbation and the originally clayey composition, it is difficult to identify any sign of redeposition in the core. The Preliminary Report of Expedition 333, which recovered the upper missing part of Sites C0011 and C0012, briefly reports the similar interval of continuous bedding inclination anomaly in the shallow part of the sites (Expedition 333 Scientists 2011). Further investigation of these cores may support our interpretation.

High-angle faults/fractures at Site C0012 strike north-northwest– south-southeast, and the poles show girdle distribution trending east-northeast to west-southwest (Fig. 59.2d). Because most of the slickenlines on the fault surfaces exhibit dip-slip movement, the intermediate principal stress ($\sigma 2$) apparently trends north-northwest–south-southeast, perpendicular to the trench, which is similar to the stress trend at Site C0011.

59.5.2 Possible Surface Sliding

The presence of the bioturbated dark-colored deformation bands mentioned in Sect. 59.4 suggests something interesting. Bioturbation is usually promoted in a very shallow depth. Mixed sediments formed by benthic bioactivity in the present ocean floor are generally less than 5 cm thick (Teal et al., 2008). The formation depth of the bioturbated dark-colored deformation bands seems to be slightly deeper, because we clearly recognized burrows in them, indicating that the bioactivity is not very high. A formation depth of about 10 cm is possible. Consequently, we assume that these bioturbated dark-colored deformation bands were originally a surface mass sliding of very soft sediments whose basal deformation zone suffered from bioturbation afterwards. The difference in the distribution of the bands between the two sites may result from the ease of sliding according to their slope angle, where steeper Site C0012 has a broader occurrence of the bands. Such a surface mass movement before subduction is inferred from onland outcrops in an accretionary complex in the Miura Peninsula, central Japan (Yamamoto et al. 2009).

59.6 Conclusion

The structures observed at Sites C0011 and C0012 confirm that, as expected from the criterion of landslide initiation and from outcrops of chaotic deposit on land (Yamamoto et al. 2009), the sediments on the pre-subducting oceanic plate are capable of submarine landslide. The major difference between the two drilled sites is the inclination of the seafloor, i.e., the ordinary trenchward gentle tilt at Site C0011 and the steeper surface on a topographic high at Site C0012, which may result in the distribution of structures such as large block sliding only at Site C0012 and surface creeping at both sites. Generally, a large submarine landslide accompanying block rotation takes place on the steeper surface of accretionary prism landward trenches, but when there are knolls or seamounts on the oceanic plate, submarine landslides can also occur. This fact is very important when we consider sediment deformation in the subduction zone, because some deformation structures are formed before reaching the deformation front.

Acknowledgments We are grateful to the Expedition 322 Scientists and onboard laboratory technicians from Marine Works Japan Co. Ltd. for their hard work and discussions with us during the expedition. We would especially like to thank the co-chiefs, Mike Underwood and Sanny Saito and the Expedition Project Manager, Yusuke Kubo, for their dedication to the success of the expedition and Hajime Naruse for his onboard discussions and suggestions. The shipboard paleomagnetists, Hirokuni Oda, Xixi Zhao and Tomohiro Yamamoto, kindly provided paleomagnetic data for structural reconstruction. This research used samples and data provided by the Integrated Ocean Drilling Program (IODP). This work was partially supported by KAKENHI 19GS0211 and 21107001. We thank Gaku Kimura, Yoshitaka Hashimoto and the guest editor Yasuhiro Yamada for their thoughtful and careful reviews which have led to an improved version of this manuscript.

References

Ando M (1975) Source mechanisms and tectonic significance of historical earthquakes along Nankai Trough, Japan. Tectonophysics 27:119–140

Expedition 333 Scientists (2011) NanTroSEIZE Stage 2: subduction inputs 2 and heat flow. IODP Preliminary Report 333, doi:10.2204/iodp.pr.333.2011

Gennesseaux M, Mauffret A, Pautot G (1980) Submarine landslides on the continental-slope near Nice and the breaking of submarine cables in the Ligurian Sea (western Mediterranean). Comptes Rendus Hebdomadaires Des Seances De L'Academie Des Sciences Serie D 290:959–962

Hampton MA, Lee HJ, Locat J (1996) Submarine landslides. Rev Geophys 34:33–59

Kimura G, Kitamura Y, Hashimoto Y, Yamaguchi A, Shibata T, Ujiie K, Okamoto S (2007) Transition of accretionary wedge structures around the up-dip limit of the seismogenic subduction zone. Earth and Planet Sci Lett 255:471–484

Kobayashi K (1995) Role of subducted lithospheric slab in uplift and subsidence of the northwestern Pacific margins. Mar Geol 127:119–144

Maltman AJ, Byrne T, Karig DE, Lallemant S, Knipe R, Prior D (1993) In: Hill IA, Taira, A., Firth, J.V., et al. (eds) Proceeding of the ODP, Scientific Results (Ocean Drilling Program), College Station p. 123–133

Moore GF, Taira A, Klaus A, et al. (2001) Proceeding of the ODP, initial reports (Ocean Drilling Program), College Station

Okino K, Shimakawa Y, Nagaoka S (1994) Evolution of the Shikoku basin. J Geomagn Geoelectr 46:463–479

Prior DB, Coleman JM (1978) Disintegrating retrogressive landslides on very-low-angle subaqueous slopes, Mississippi Delta. Mar Geotechnol 3:37–60

Saito S, Underwood MB, Kubo Y, Expedition 333 Scientists (2010) Proceeding of the IODP, Integrated Ocean Drilling Program management international, Tokyo

Talling PJ, Wynn RB, Masson DG, Frenz M, Cronin BT, Schiebel R, Akhmetzhanov AM, Dallmeier-Tiessen S, Benetti S, Weaver PPE, Georgiopoulou A, Zuhlsdorff C, Amy LA (2007) Onset of submarine debris flow deposition far from original giant landslide. Nature. doi:10.1038/nature06313

Teal LR, Bulling MT, Parker ER, Solan M (2008) Global patterns of bioturbation intensity and mixed depth of marine soft sediments. Aquatic Biology 2:207–218

Tobin HJ, Kinoshita M (2006) Investigations of seismogenesis at the Nankai Trough, Japan. IODP Scientific Prospectus, NanTroSEIZE Stage 1:doi:10.2204/iodp.sp.nantroseize1.2006

Ujiie K, Maltman AJ, Sanchez-Gomez M (2004) Origin of deformation bands in argillaceous sediments at the toe of the Nankai accretionary prism, southwest Japan. J Struct Geol 26:221–231

Yamada Y, Yamashita Y, Yamamoto Y (2010) Submarine landslides at subduction margins: insights from physical models. Tectonophysics. doi:10.1016/j.tecto.2009.09.007

Yamamoto Y, Mukoyoshi H, Ogawa Y (2005) Structural characteristics of an on land shallowly buried accretionary prism: rapidly uplifted Neogene accreted sediments on the Miura-Boso Peninsula, central Japan. Tectonics. doi:1029/2005TC001823

Yamamoto Y, Nidaira M, Ohta Y, Ogawa Y (2009) Formation of chaotic rock units during primary accretion processes: examples from the Miura-Boso accretionary complex, central Japan. Island Arc. doi:10.1111/j.1440-1738.2009.00676.x

Yamazaki T, Okamura Y (1989) Subducting seamounts and deformation of overriding forearc wedges around Japan. Tectonophysics 160:207–229

Chapter 60
Scientific Drilling of Mass-Transport Deposits in the Nankai Accretionary Wedge: First Results from IODP Expedition 333

Michael Strasser, Pierre Henry, Toshiya Kanamatsu, Moe K. Thu, Gregory F. Moore, and IODP Expedition 333 Scientists

Abstract Integrated Ocean Drilling Program (IODP) Expedition 333 drilled and cored a Pleistocene-to-Holocene succession of a slope-basin in the Nankai accretionary wedge, offshore southwest Japan. The slope-basin represents the depocentre for downslope sediment transport and comprises several mass-transport deposits (MTDs), including an up to 180 m thick MTD. The recovered section (0–315 m below seafloor) records ~1 Million years of submarine landsliding history in this active tectonic setting. We present D/V *Chikyu* shipboard results from Site C0018,

M. Strasser (✉)
Geological Institue, ETH Zurich, Switzerland
e-mail: strasser@erdw.ethz.ch

P. Henry
CEREGE - College de France, Aix en Provence, France

T. Kanamatsu
IFREE-JAMSTEC, Yokohama, Japan
e-mail: toshiyak@jamstec.go.jp

M.K. Thu
CDEX-JAMSTEC, Yokohama, Japan

G.F. Moore
University of Hawaii, Honolulu, USA

IODP Expedition 333 Scientists
Alves T (UnivCardiff, UK); Bauersachs T (UnivKiel, Germany); Chiyonobu S (RITE-Kyoto, Jp); Daigle H (RiceUniv, USA); Ekinci K (UnivMissouri, USA); Gao S (UnivNanjing, China); Garcon M (CEREGE, France); Kawamura K (Fukada GeolInst, Jp), Kitamura Y (JAMSTEC, Jp); Laberg JS (UnivTromsø, Norway); Lee G (PukyongUniv, Korea); Lee Y (Korea InstGeosci); Lu Y (UnivAlabama, USA); Marcaillou B (UnivAntilles&Guayne, France); Matsubayashi O (AIST Tsukuba, Jp); Nagahashi Y (FukushimaUniv, Jp); Novak B (W.WashingtonUniv, USA); Saito Y (DoshishaUniv, Jp); Satoguchi Y (LakeBiwaMuseum, Jp); Screaton E (Univ.Florida, USA); Scudder R (BostonUniv, USA); Yamaguchi A (Univ.Tokyo, Jp)

Y. Yamada et al. (eds.), *Submarine Mass Movements and Their Consequences*,
Advances in Natural and Technological Hazards Research 31,
DOI 10.1007/978-94-007-2162-3_60, © Springer Science+Business Media B.V. 2012

including litho- bio- magneto- and tephra-stratigraphy and physical properties data. Six MTDs of thickness ranging from 0.5 to 61 m were identified from visual core description and X-ray CT-scans. The thickest MTD is also the oldest (emplaced between 0.85 and 1.05 Ma) and it coincides with a lithological transition between a sandy turbidite sequence below, and ash-bearing hemipelagites comprising several MTDs above. The deformation style within the MTD is heterogeneous: intervals of disturbed sediments are interbedded within intervals inferred to retain original, coherent bedding. In three occurrences the base of the MTD is defined by a shear zone within fine-grained sediments. These observations suggest that slumping and mass-transport is dominated by localized plastic deformation. Furthermore, mass movements are an active process that is shaping the present-day seafloor, as evidenced by numerous surficial slump scars and the occurrence of a shallowly buried, presumably Holocene MTD at Site C0018.

Keywords Submarine landslides • Scientific Ocean Drilling • C0018 • Mass-transport deposits • Integrated Ocean Drilling program (IODP) • Nankai Trough

60.1 Introduction

With increasing awareness of oceanic geohazards, submarine slides are gaining wide attention not only because of their catastrophic impacts (e.g., slide-induced tsunamis), but also because they can be triggered by processes such as earthquakes, rapid sedimentation, gas release, or clathrate dissociation, many of which represent geohazards themselves (Morgan et al. 2008 and references therein). Ocean drilling is critical to understanding such geohazards, given that the submarine geological record preserves structures and deposits of past occurrences. In 2005, IODP Expedition 308 in the Gulf of Mexico illuminated the relationships between sedimentation, consolidation, and fluid-flow vs. slope-failure initiation and mass-transport processes on passive margins (e.g., Sawyer et al. 2009; Stigall and Dugan 2010). However, we lack comparable comprehensive datasets on active margins where tectonic processes and earthquakes are additional agents in controlling occurrence, nature and evolution of slope failures.

Here, we present new results from Site C0018, which was drilled and cored during IODP Expedition 333 (Dec 2010 – Jan 2011) to recover a Pleistocene-to-Holocene succession of MTDs within a slope-basin in the outer forearc of the Nankai subduction zone, off the coast of SW Japan (Fig. 60.1). Overall, drilling at Site C0018 aimed at (i) establishing a well-dated Quaternary submarine landslide history as it may relate to the tectonic evolution of the accretionary prism and (ii) reconstructing sliding and transport dynamics of submarine landslides as it may relate to the tsunamigenic potential of such event (Henry et al. 2010). In this paper we present initial shipboard results with a special focus on the identification and character of MTDs.

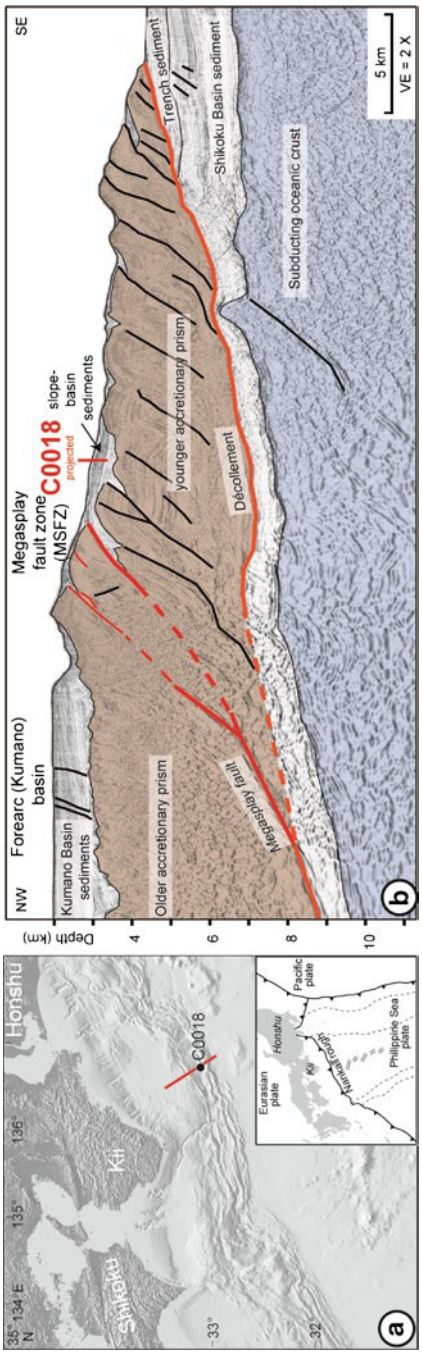

Fig. 60.1 Map (**a**) and interpreted seismic line (**b**) showing geological setting of the Nankai accretionary wedge and location of site C0018. Figure modified from Moore et al. (2009)

60.2 Geologic Setting

The Nankai accretionary complex is formed by subduction of the Philippine Sea plate beneath the Eurasian plate along the Nankai Trough (Fig. 60.1a). Accretion of trench-fill turbidites and Shikoku Basin hemipelagic sediments results in ridge-basin topography with filled slope-basins that generally increase in depth and sedimentary thickness landwards from southeast-to-northwest (Fig. 60.1b). Beneath the upper slope and Kumano Basin, a regional splay fault system, termed "megasplay" (Tobin and Kinoshita 2006), discontinuously cuts across the older part of the prism and overrides younger slope basin sediments (Moore et al. 2009).

Interpretation of 3D reflection seismic data and geological information from nearby IODP drill Sites C0004 and C0008 document a complex temporal and spatial evolution of the shallow megasplay fault zone (MSFZ) and anticline-structures in the underlying accretionary prism, characterized by alternating periods of high and low structural activity on individual structural segments (Strasser et al. 2009; Kimura et al. 2011). Seabed topography thus shows significant variations perpendicular to, and along strike of, the regional slope (Fig. 60.2a): The surface slope of the MSFZ's hanging wall portion in the eastern domain is much gentler than in the western domain, where it is characterized by steep and rough topography indicating slumping and erosion into the upthrust accretionary prism. The eastern domain, however, shows several shallow-seated (50–100 m) slump scars within the slope-apron sedimentary cover along the seaward side of growing anticline structures seaward of the MSFZ (Fig. 60.2). These features are in contrast to the western domain, where the lower slope gradually dips SE and has a rather smooth surface.

Site C0018 is located ~3 km seaward from the splay-fault tip in a slope-basin that (1) represents the depocenter for downslope mass transport from the MSFZ-area, (2) is characterized by several MTDs (Fig. 60.2b, Strasser et al. 2011), and (3) includes an exceptionally large, as thick as 180 m, MTD. At the drill Site, the sedimentary succession is divided into two Seismic Units (hereafter termed SU1a and SU1b; Strasser et al. 2011): SU1b is distinct from SU1a by its acoustic character showing several parallel high-amplitude horizons within the middle part of the slope basin. In contrast, SU1a is characterized by a low-amplitude reflection pattern that contains laterally-confined, acoustically transparent-to-chaotic MTDs (Fig. 60.2b). The thickest MTD occurs at the transition between these two units. Drilling at Site C0018, which is located where the MTD bodies wedge out and where basal erosion is minimal, allowed for ground-truthing and dating of the seismic-stratigraphic interpretation and sampling the MTDs across the most complete and longest stratigraphic succession.

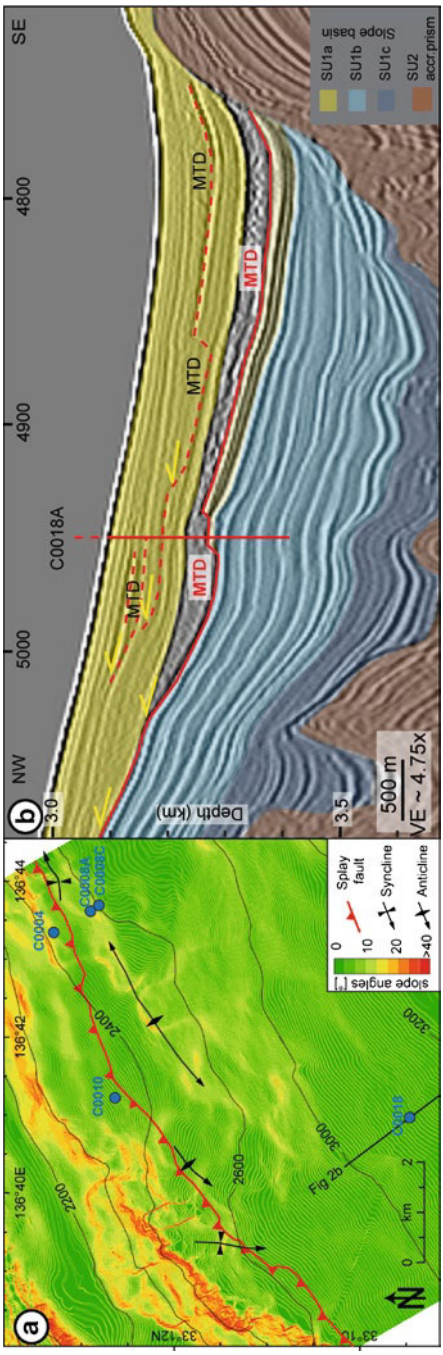

Fig. 60.2 Slope angle map with geologic structures showing location of the buried splay fault tip, and anticline/syncline structures in the underlying accretionary after Kimura et al. (2011). (**b**) Interpreted seismic profile crossing the drill site, modified after Strasser et al. (2011) (see text for detailed description)

60.3 Results

60.3.1 General Overview of Drilling Results

Sediments cored at Site C0018 are subdivided into two Lithologic Subunits (Fig. 60.3), which correlate with SU1a and SU1b:

Lithologic Subunit 1a (U1a) is primarily composed of bioturbated hemipelagic mud intercalated with thin, few-cm thick, subhorizontal and SE-dipping layers of varying coarse and fine volcanic ash and MTDs. A thick ash layer, which correlates to the onland tephra "Pink" dated 0.99–1.05 Ma (Hayashida et al. 1996) occurs close to the base of U1a at 190.6 m core depth below seafloor (mCSF). This age is supported by magnetostratigraphic constraints correlating the base of a short normal polarity interval immediately below the subunit boundary to the base of the Jaramillo subchron (1.07 Ma), and is also consistent with the maximum age for this boundary estimated from calcareous nannofossils (<1.24 Ma). U1a, thus spans from 0 to ~1 Ma and the averaged sedimentation rates is ~19 cm/ka. Minor normal faults with moderate to high dip angles (50–80°) are developed in the lower part of U1a and reflect vertical maximum principal stress likely in response to the sedimentation and burial processes within the slope basin. Progressive burial and consolidation is indicated by the general downward increase and decrease of undrained shear strength and porosity, respectively (Fig. 60.3).

Lithologic Subunit 1b (U1b) comprises a sequence of sandy turbidites interbedded with silty clay. Subhorizontally dipping, 4–20 cm-thick sand layers typically show a sharp and erosional base and normal grading. Bed spacing is 20–30 cm in average, but muddy intervals up to 4 m thick comprising no intercalated turbidites occasionally occur. Turbidite sands have mixed composition with quartz, plagioclase, and abundant lithic fragments of both metamorphic and volcanic origin, indicating a siliciclastic source.

The base of U1b, as inferred from core-seismic correlation (Fig. 60.2), was not cored at Site C0018. Strasser et al. (2011) estimate an age for the SU1c-to-SU1b transition of ~1.55 Ma, which is consistent with new C0018-biostratigraphic age constraints indicating a depositional age of the oldest sediments cored to be younger than 1.67 Ma. Averaged sedimentation rate within U1b is ~40 cm/ka, and thus significantly higher than in U1a. Porosity and undrained shear strength (measured in muddy intervals) are generally constant throughout U1b and show values slightly higher and lower, respectively, than what would be expected from downward extrapolating the general trends from U1a. The drop in shear strength below the subunit boundary may be related to the change of coring system at this depth. If real, however, this observation may be interpreted to reflect a general state of slight underconsolidation, potentially resulting from the high sedimentation rates within this interval and the deposition of the thick MTD immediately above.

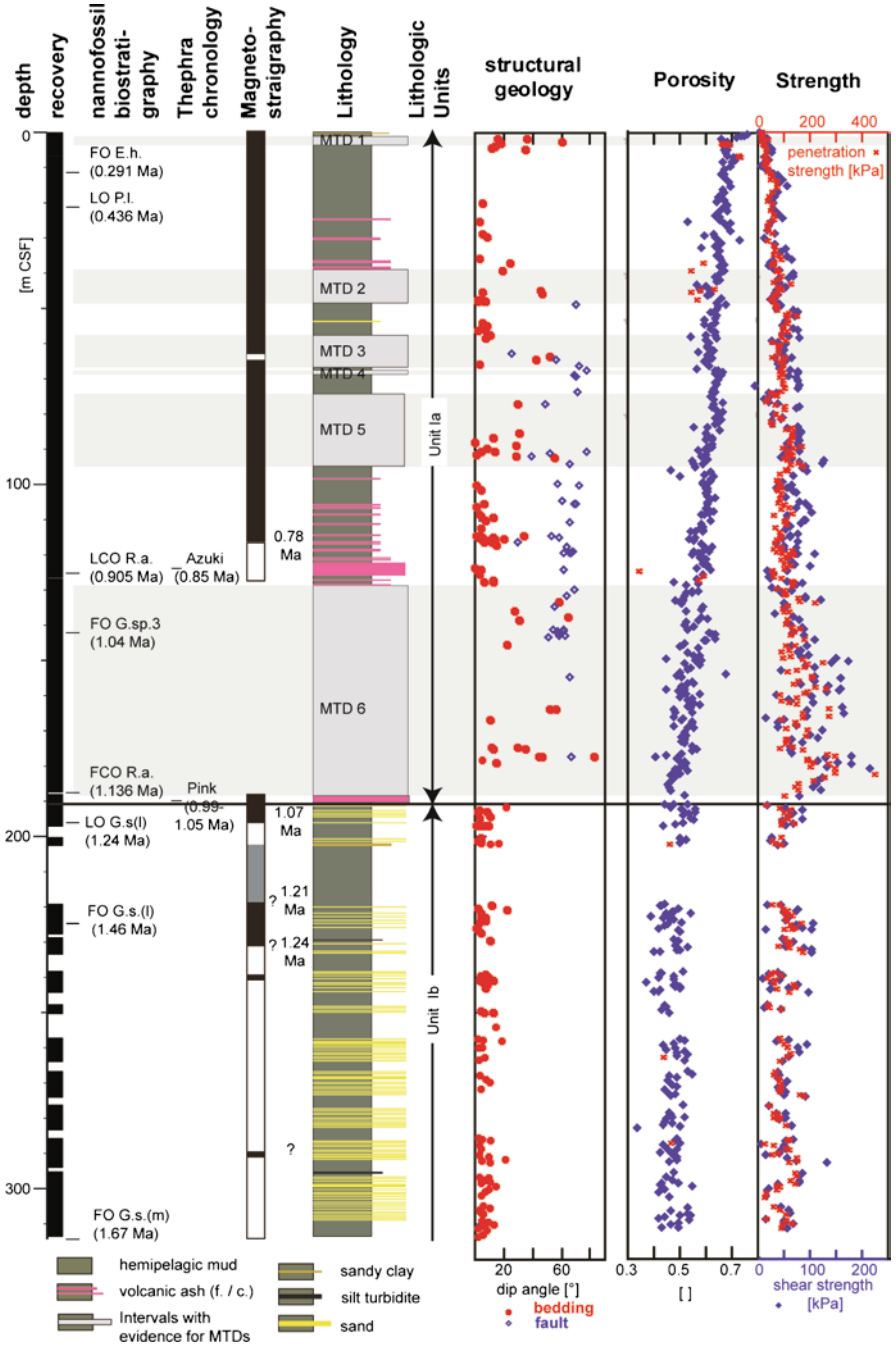

Fig. 60.3 Summary diagram of IODP Expedition 333 Site C0018 shipboard results. Abbreviations for nannofossil datums are: *F(C)O* first (consistent) occurrence, *L(C)O* last (consistent) occurrence, *E.h.* Emiliania Huxley, *P.l.* Pseudoemiliania lacunosa, *R.a.* Reticulofenestra asanoi, *G.sp.(l, m)* Gephyrocapsa species (large, medium)

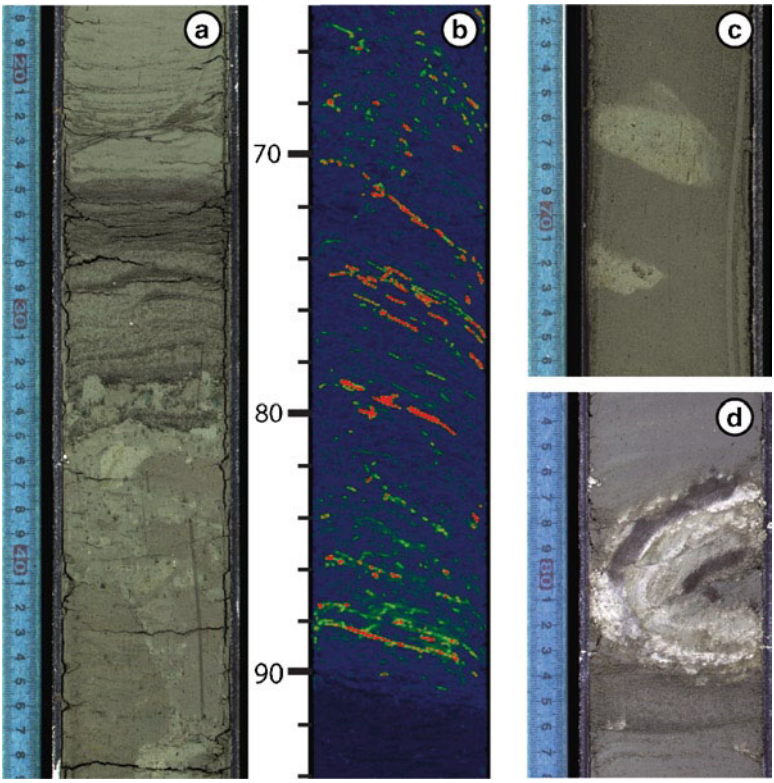

Fig. 60.4 Evidence for MTDs as observed in cores and X-CT scans: (**a**) visible light image of core C0018A-5 H-5, showing turbidite overlying top of MTD 2. (**b**) Semi-transparent rendering of X-CT-image C0018A-6 H-2, showing organization of pyrite mineralizations as lineations, and low angle planar discontinuities with associated increase in CT values indicating shearing at the base of MTD2. (**c**) visible light image of core C0018A-1 H-4, showing mud clasts in sandy silty-clay matrix within MTD1. (**d**) visible light image of core C0018A-5 H-6, showing slump fold within MTD 2

60.3.2 MTDs at Site C0018

Six intervals with evidence for MTDs are observed within U1a and numbered from top to bottom (Fig. 60.3). Below, we first describe general aspects of these MTDs and then describe details of observed features of each individual MTD.

MTDs at Site C0018 range in thickness from 0.5 to 61 m and have a cumulative thickness of 98 m, thus accounting for half of the total thickness of U1a. The upper boundary/contact is well defined for MTDs 1, 2, 6, and is marked by an MTD-overlying turbidite for two of them (MTDs 2 and 6; Fig. 60.4a). Identification of the lower boundary/contact often is more difficult: Conceptually, it may either appear as a potentially erosional contact or shear zone between fluidized and/or sheared sediments, respectively, above, and flat lying, undisturbed sediments

below. However, deformation could also occur in the underlying sediments, as a consequence of shear during flow and/or post-depositional loading (e.g., Frey-Martinez et al. 2006). X-CT images turned out to be very useful for identification of the base of MTDs. We infer that shear zones define the base of MTD 2, 3 and 5, by interpreting the organization of pyrite mineralizations as lineations, and low angle planar discontinuities with associated increase in CT values as evidence for shearing (Fig. 60.4b). Additionally, physical properties data (Fig. 60.3) show that MTD intervals display an increased compaction gradient compared with the average porosity-depth trend, and slight reversals (porosity increasing with depth) are observed near the base of MTDs 2, 3, 5 and 6.

MTD1 occurs at 1.4 mCSF, thus indicating a relatively young, potentially Holocene age (assuming constant averaged sedimentation rate for the whole U1a of 19 cm/ka). This youngest MTD extends over 2.9 m of mudclast-bearing chaotic sediment (Fig. 60.4c) and convolute beddings.

MTD2 is older than 0.4 Ma but younger than 0.8 Ma, as indicated by bio- and magneto-stratigraphic datums, respectively (Fig. 60.3) A cylindrically folded white ash occurs within the upper part of this 7.3 m-thick MTD (Fig. 60.4d). Structural analysis reveals a nearly horizontal fold axis striking E-W with a subhorizontal axial plane, implying plastic deformation in a cohesive flow of N-S direction. This inferred flow direction is consistent with observed slump scars north of the drilled site, as evidenced in bathymetric data (Fig. 60.2). In its lower part, MTD2 comprises several intervals of coherent bedding bounded by shear zones, as identified by X-CT image analysis. The lowermost one defines the MTD base (Fig. 60.4c).

The top of MTD3 comprises an interval with visual evidence of mixed sediments. Examination of CT-scan and structural data reveal the thickness of this MTD to be 7.7 m, with a 2 mm-thick clay layer as potential shear zone at its inferred base.

MTD4 is a thin interval (50 cm) associated with a fluidized ash layer, which likely is the primary structure, but deformation due to coring disturbance and gas-expansion upon core retrieval cannot fully be excluded.

MTD5 is a 18.5 m-thick interval, which extends over cores that were also disturbed by the coring process. Evidence for remobilization include mixed sediment, mud clasts, convolute bedding and tilted strata. A shear zone with a sharp lower boundary on CT-scan images defines the base.

MTD6 is a 61.4-m interval between 127.6 and 188.6 mCSF and corresponds to the main MTD body identified in the seismic data. A turbidite deposit immediately overlies its upper boundary. Chaotic and convolute beddings, and mixing of ash with hemipelagic deposits are observed in the cores, but other intervals remain coherently bedded. Several internal shear zones are identified from CT-scans in the lower part of MTD 6, but none could be positively identified as the basal surface. The base of the thick MTD was thus defined at the top of the Pink Ash layer. A graded volcanic marker bed, correlated to the Azuki tephra, which is dated on land to 0.85–0.9 Ma (Hayashida et al 1996), occurs within less than a meter above the top of MTD 6, and provides a minimum age for the emplacement of the thick MTD in the study area.

No older MTDs have so far been identified from cores within U1b. Core recovery was very low in some intervals (Fig. 60.3). Hence, in contrast to nearly complete core recovery to the base of U1a, MTDs in thickness up to 9.5 m could have been missed within U1b. Also, core quality generally was lower as the coring system formed fractured biscuits of 2–3 cm thickness. Hence, detailed structural analysis of the up to 4 m-thick muddy intervals within U1b was hampered by drilling disturbance and further analysis are needed to identify potential evidence for MTDs within these intervals.

60.4 Discussion and Outlook

Results from Site C0018 document a remarkable lithological transition between a sandy turbidite sequence below and ash-bearing hemipelagites that contain MTDs above. Turbidite deposition ceased ~1 Ma, which documents a change in sediment delivery and routing pattern. At other sites drilled in the slope basin (C0008) and on the splay-fault hangingwall (C0004) this transition is not as sharp, but there are fewer sand/silt turbidites over the last 1–1.3 Ma than in underlying deposits (Strasser et al. 2011). During the same time period, a northward shift in the sediment depocentre is observed within the Kumano forearc basin following ~300 kyr of extensive landward tilting of the outer Kumano basin sediments, which has been interpreted to represent an episode of motion along the megasplay that formed the modern fault geometry (Gulick et al. 2010). Hence, one possible explanation for the shift is that the uplift of the outer arc high confined most of the turbidity currents to the Kumano Basin and thus progressively shut off sand input to the slope-basin seaward of the MSFZ. Alternatively, the observed evolution could correspond to a local change of slope and depositional environment from a perched basin trapping sand transported by turbidity currents to a slope environment. MTD 6 is correlative with this lithological transition and thus potentially may be related to the overall structural evolution of the MSFZ area and/or the change in sedimentation regime. However, all younger MTDs observed in C0018 postdate the main structural phase of slip on the MSFZ and may be rather associated with shallow-seated slope failure processes within the post-1 Ma sedimentary cover overlying the MSFZ and anticline structure.

The most important findings for these younger MTDs are: (i) The heterogeneous nature of deformation and relative distribution of chaotic, pebbly, or mixed sediment intervals vs. intervals of coherent bedding and localized shear zones, suggests that plastic deformation is predominant and that slumping only partly evolved into mud flows; (ii) Slumping is an active process, suggested by numerous surficial slump scars and the occurrence of the young presumably Holocene MTD; (iii) The spacing between individual MTDs suggests submarine slope destabilization does not occur systematically during subduction earthquakes that have a recurrence rate on the order of 100–200 years (Ando 1975). Hence, yet-to-be-further-investigated preconditioning factors may exert the first-order control on destabilization

processes and MTD formation over the last 1 Ma and in the future. They will be the focus of upcoming studies integrating higher-resolution age constraints, more detailed sedimentological and structural investigations of MTDs, 3D-seismic interpretation and seismic attribute analysis, geotechnical laboratory analysis, as well as data and results from nearby IODP drill sites on the past and current stress state, activity and structural evolution of MSFZ area and Nankai accretionary wedge.

Acknowledgments This research used samples and data provided by the Integrated Ocean Drilling Program (IODP). The authors acknowledge constructive comments by reviewers Derek Sawyer and Arito Sakaguchi.

References

Ando M (1975) Source mechanisms and tectonic significance of historical earthquakes along the Nankai trough, Japan. Tectonophysics 27:119–140

Frey-Martinez J et al (2006) Frontally confined versus frontally emergent submarine landslides: A 3D seismic characterisation. Mar Petrol Geol 23:585–604

Gulick SPS et al (2010) Rapid forearc basin uplift and megasplay fault development from 3D seismic images of Nankai margin off Kii Peninsula, Japan. Earth Planet Sci Lett 300:55–62

Hayashida A et al (1996) Correlation of widespread tephra deposits based on paleomagnetic directions: link between a volcanic field and sedimentary sequences in Japan. Quatern Int 105:332–340

Henry P et al (2010) NanTroSEIZE stage 2: subduction inputs 2 and heat flow. IODP Sci Prosp 333. doi:10.2204/iodp.sp. 333.2010

Kimura G et al (2011) Spatial and temporal evolution of the megasplay fault in the Nankai Trough. Geochem Geophy Geosy 12:Q0A008. doi:10.1029/2010GC003335

Moore GF et al (2009) Structural and seismic stratigraphic framework of the NanTroSEIZE stage 1 transect. In: Kinoshita M et al (ed) Proceeding IODP, 314/315/316: Washington. doi:10.2204/iodp.proc.314315316.102.2009

Morgan JK et al (2008) Addressing geohazards through ocean drilling. Sci Drill 7:15–30

Sawyer DE et al (2009) Retrogressive failures recorded in mass transport deposits in the Ursa Basin, Northern Gulf of Mexico. J Geophy Res 114:B10102

Stigall J, Dugan B (2010) Overpressure and earthquake initiated slope failure in the Ursa region, northern Gulf of Mexico. J Geophy Res 115:B04101

Strasser M et al (2009) Origin and evolution of a splay fault in the Nankai accretionary wedge. Nat Geosci 2:648–652. doi:10.1038/ngeo609

Strasser M et al (2011) Slumping and mass transport deposition in the Nankai fore arc: evidence from IODP drilling and 3-D reflection seismic data. Geochem Geophy Geosy 12:Q0AD13. doi:10.1029/2010GC003431

Tobin HJ, Kinoshita M (2006) NanTroSEIZE: the IDOP Nankai Trough seismogenic zone experiment. Sci Drill 2:23–27

Chapter 61
Rock-Magnetostratigraphy of Hawaiian Archipelagic Sediments: Timing of Giant Submarine Landslides of the Hawaiian Ridge

Toshiya Kanamatsu and Duane Champion

Abstract Volcaniclastic layers deposited on an abyssal plain to the south of Oahu Island, by distal turbidity currents from Hawaiian giant submarine landslides are studied by the means of paleomagnetic and rock-magnetic stratigraphy. The established stratigraphy reveals intervals of high magnetite mineral concentration in the volcaniclastic layers due to these submarine landslides. Two major time intervals of the volcaniclastic layers are recognized in the upper Brunhes Chron (0–250 ka). The correlation between magnetic susceptibility and the global benthic $\delta^{18}O$ stack record indicates that two time intervals of volcaniclastic layers are about 91–114 ka, and 216–245 ka in age. The Alika and South Kona landslides in the submarine west flank of Hawaii Island are the most likely candidate events for the source of these volcaniclastic layers which traveled long distances from the source area.

Keywords Submarine landslide • Hawaiian volcanism • Paleomagnetism • Rock-magnetic property

61.1 Introduction

Topographic surveys of the Hawaiian deep-sea floor uncovered a wide distribution of scarred volcanic flanks caused by giant submarine landslides (Moore et al. 1989; Smith et al. 2002; Eakins et al. 2003; Holcomb and Robinson 2004). It has been

T. Kanamatsu (✉)
Institute for Research on Earth Evolution, Japan Agency for Marine-Earth Science and Technology (JAMSTEC), 2-15 Natsushima-cho, 237-0061, Yokosuka, Japan
e-mail: toshiyak@jamstec.go.jp

D. Champion
Volcano Science Center, U.S. Geological Survey, MS-910, 345 Middlefield Rd, Menlo Park, CA 94025, USA

Y. Yamada et al. (eds.), *Submarine Mass Movements and Their Consequences*, Advances in Natural and Technological Hazards Research 31,
DOI 10.1007/978-94-007-2162-3_61,

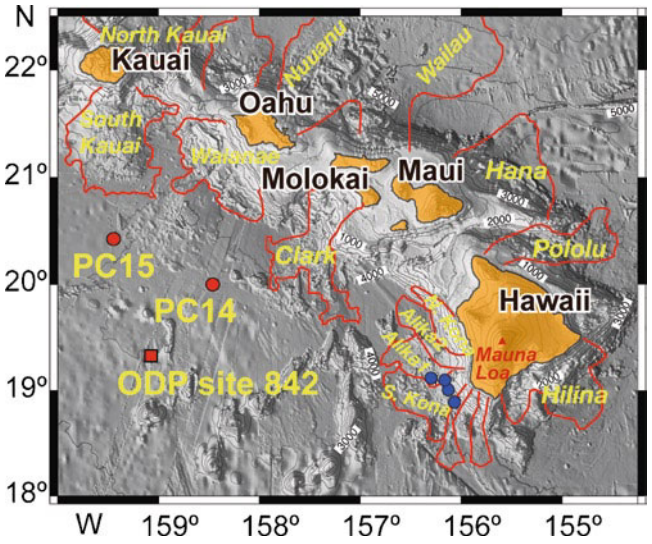

Fig. 61.1 Distribution of Hawaiian submarine landslides. *Red circle*: locations of piston-cores PC14 and PC15 obtained during KR01-12 cruise. *Red square*: location of Ocean Drilling Program Site 842, Leg 136. *Blue circle*: locations of rock sample recovered by the submersible "Shinkai 6500" during YK02-04 & 05 cruises for SIRM/k measurement

suggested that the collapse of the flanks is a principle process accompanying Hawaiian volcano growth. However, the style and timing of the collapses is not always obvious from their morphology. For instance, several landslides are intermingled on the ocean floor of the western side of Hawaii Island (Fig. 61.1), and the sequence of formation and source areas of the landslides are still under debate (Lipman et al. 2003; Morgan and Clague 2003; Hammer et al. 2006; Lipman and Coombs 2006).

Understanding the mechanisms and timing of these giant submarine landslides is important for hazard mitigation because the slides would be closely associated with earthquakes, coastline submergence, and the generation of tsunamis. Giant Hawaiian submarine landslides are believed to produce large tsunami simultaneous with their collapse (e.g., Moore and Moore 1988). The currently active Hilina Fault, developing along the south flank of Kilauea, is expected to fail catastrophically one day and produce a huge tsunami. A precipitous collapse could cause a tsunami to strike the coastal area of western South America, and the area of Oceania (Ward 2002).

Landslides from the Hawaiian volcanoes will transport volcaniclastic material to the nearby deep-sea floor. Long-distance transport of volcaniclastic sediment, generated by Hawaiian submarine landslides, has been suggested by several previous studies (e.g., Garcia and Hull 1994). Cores sampled by the Ocean Drilling Program (ODP) at ODP site 842, located 265 km south of the islands on the outer side of the Hawaiian Arch, contain turbidites with volcanic glass fragments that indicate origin

from the Hawaiian Islands (Garcia and Hull 1994). Therefore, if stratigraphy of distal volcaniclastic sediments in the pelagic deep-sea sediment can be resolved, then the timing and the origins of giant submarine landslides could be determined. Two piston cores containing volcaniclastic layers taken from south of the Hawaiian Ridge were studied in order to understand the timing and emplacement processes of these volcaniclastic sediments as distal records of Hawaiian submarine landslides (Fig. 61.1).

61.2 Paleomagnetism of the Piston Cores

KR01-12 cruise was carried out in 2001 by R/V Kairei of Japan Agency for Marine-Earth Science and Technology as part of a series of Japan-USA collaborative survey in the underwater flank of the Hawaiian volcanoes (e.g., Coombs et al. 2006). Cores PC14 (963.7 cm) and PC15 (943 cm) were recovered 150 km south-southwest, and 180 km southwest of Oahu Island, respectively during KR01-12 (Fig. 61.1). Lithologies of the cores correlate well with one another. In particular, both cores contain several thin volcaniclastic sand layers in their upper 300 cm (Fig. 61.2), which underlain by more than 600 cm of massive brown clay. Much thicker volcaniclastic layers of PC14 than those of PC15 suggest that source areas of volcanicastic sand are located east to the location of PC14.

The chronology of the sediment cores was studied utilizing both paleomagnetic and rock-magnetic techniques. Natural remanent magnetization (NRM), and remanent magnetizations after alternating-field demagnetizations (AFD) were routinely measured in order to evaluate stability of NRM. Saturation isothermal remanent magnetization (SIRM) experiments were performed to identify the magnetic properties of the samples. In addition, low-field magnetic susceptibility (k) measurements were made to estimate the concentration of magnetic minerals.

61.3 Results

61.3.1 Magnetostratigraphy

Most samples exhibit stable remanent magnetizations (Fig. 61.3a). Characteristic remanent magnetization (ChRM) components were calculated by the principal component analysis (PCA) method (Kirschvink 1980), as applied to the 10–50 mT AFD interval. Polarity changes found in cores PC14 and PC15 were interpreted in relation to the time scale of Lourens et al. (2004), assuming a relatively constant sedimentation rate (Fig. 61.2).

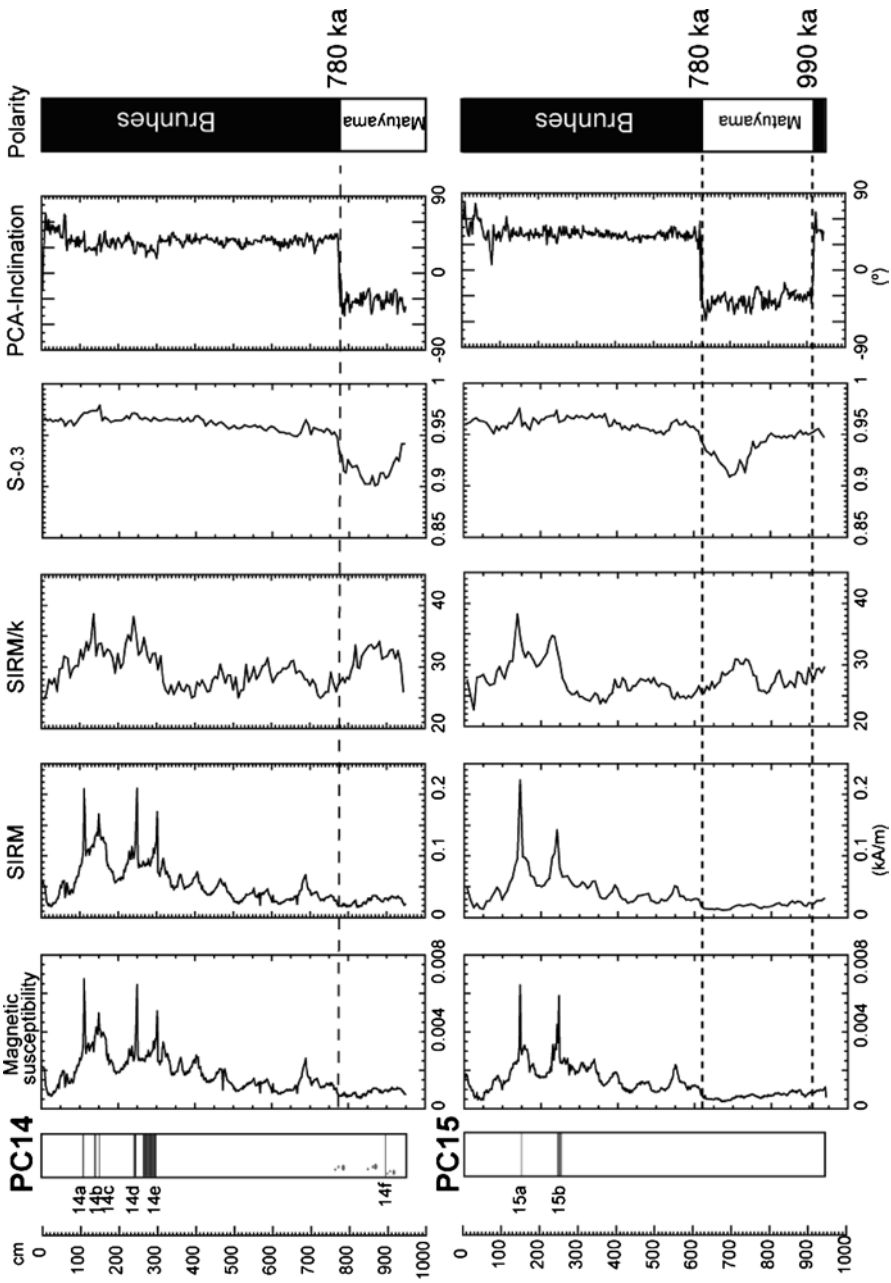

Fig. 61.2 *Left panels*: simplified lithology of sediment cores PC14 and PC15. Number beside each lithologic column identifies the discrete volcaniclastic layer. Profiles of magnetic parameters and paleomagnetic inclination variation and their magnetic polarity interpretation for PC14 and PC15

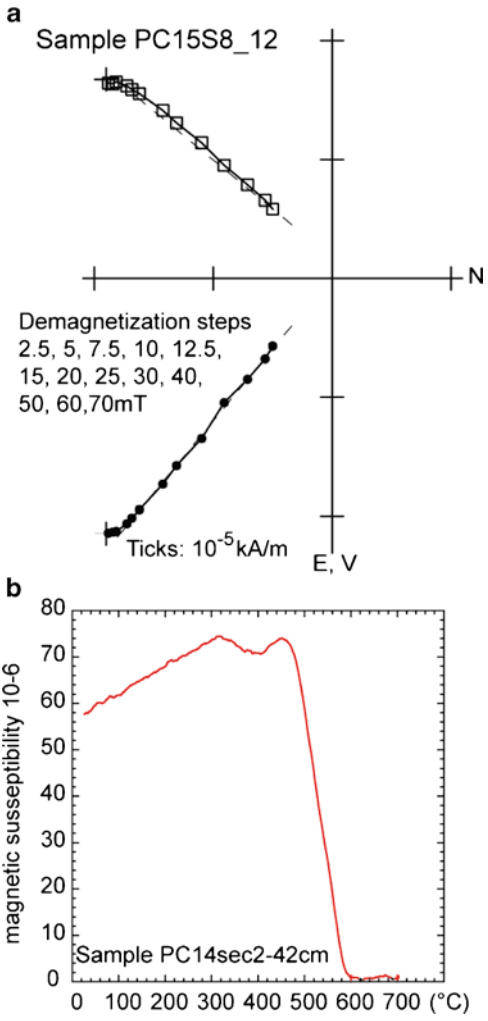

Fig. 61.3 (**a**): Representative orthogonal projections of alternating field demagnetization experiments. *Open* and *closed symbols* indicate the vertical and horizontal planes, respectively. (**b**): Example of magnetic susceptibility curve with temperature change. Magnetic susceptibility drop around 580°C indicates presence of magnetite in the sample

61.3.2 Rock-Magnetic Properties

SIRM and *k* principally reveal the amount of ferrimagnetic minerals present in a sample. Their variations between the cores are correlated well. Higher values appear during the Brunhes Chron in the profiles of *k* and SIRM in cores PC14 and PC15, and most volcaniclastic layers are corresponding to the horizons of high magnetic mineral content (Fig. 61.2).

The $S_{-0.3}$ value as defined by Bloemendal et al. (1992) during the Brunhes Chron are high (> ca. 0.95), indicating the dominant presence of ferrimagnetic minerals such as magnetite (Fig. 61.2). The presence of magnetite is actually demonstrated by the measurement of magnetic susceptibility while heating. A sudden decrease of magnetic susceptibility at temperatures above 580–590°C (Fig. 61.3b) indicates

the magnetite presence. Conversely, $S_{-0.3}$ on samples taken from just below the Brunhes-Matuyama boundary are remarkably low indicating that some presence of antiferrimagnetic minerals (e.g., hematite). SIRM/*k* ratio, as a proxy of magnetic grain size (Thompson 1986), varies inversely with magnetic grain size, if magnetite is a dominant magnetic mineral in the samples. SIRM/*k* in the time interval of the Brunhes Chron, magnetite dominant interval ($S_{-0.3} > 0.95$), shows a distinction between upper and lower Brunhes time in both cores. Much finer-grained magnetite is revealed in the upper Brunhes Chron, and the coarser grains in the lower Brunhes Chron.

61.3.3 Age Models for PC14 and PC15

The variation in *k* with depth of PC14 and PC15 involves a cyclic fluctuation (ca 100ky cycle), accompanied by sharp peaks (see Fig. 61.2). The sediment recovered from the southern Hawaiian ridge includes pelagic clay and siliceous biogenic tests, in addition to volcaniclastic material. Our interpretation is that the cyclic fluctuation resulted from changes in the abundance of materials, primarily controlled by the glacial and interglacial cycles. Based on this assumption, the global benthic $\delta^{18}O$ stack record: LR04 (Lisiecki and Raymo 2005) was correlated to the magnetic susceptibility patterns of PC14 and PC15 using the polarity boundaries as anchor points. The correlations are fairly straightforward during the timeframe of marine isotope stages MIS 1- MIS 7 (linear correlations are 0.611 for PC14 and 0.511 for PC15) (Fig. 61.5). In contrast, the amplitude of *k* variation, which might be correlated during MIS 9-MIS 19, is smaller (linear correlations are 0.522 for PC14 and 0.421 for PC15). Probably the smooth and low amplitudes of *k* patterns arise from sediment mixing processes by bioturbations in a post-depositional phase. It may cause some unknown error in age estimation, although we suppose that horizons of peaks in k profiles are not shifted, and no critical error is involved in this correlation. Age models for both PC14 and PC15 established based on the correlations between LR04 and *k* patterns reveal that the sedimentation rate changed to 1.1–1.3 cm/ky, from a lower rate of 0.6–0.9 cm/ky at about 250 ka. The thickness of the volcaniclastic sand/silt layers was removed from the depth estimates for the linear interpolation between tie points. Then specific age estimations of the distinct volcaniclastic layers as visually identified, are performed using the age models.

61.4 Discussion

The result of age estimations for the volcaniclastic layers shows that the ages are concentrated in periods of 99–129 ka, and 218–230 ka (Fig. 61.4a). McMurtry et al. (1999) summarizes that the ages of the Alika 2 event range from 112 ± 15 to 127 ± 24 ka, and South Kona or Alika 1 from 200 to 250 ka; both are distributed in

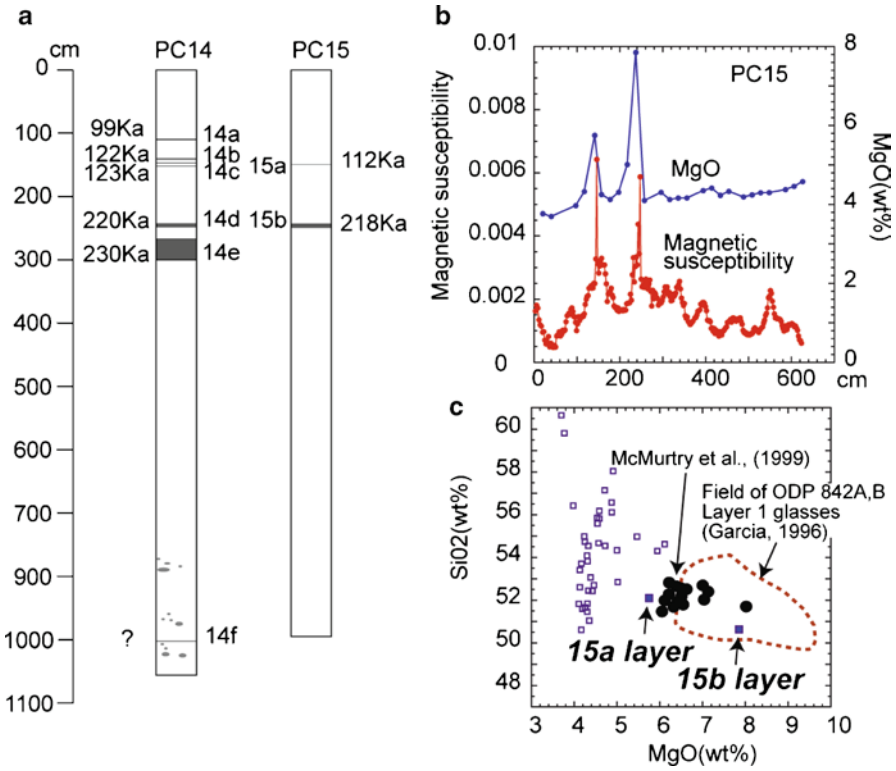

Fig. 61.4 (**a**): Estimated age of volcaniclastic layers derived from the correlations. (**b**): Downcore variations of MgO (wt%) of bulk sediment and magnetic susceptibility for PC15. (**c**): MgO vs. SiO2 for samples of PC15 sediments. *Open squares*: mud sediment. *Closed squares*: volcaniclastic layers. *Broken lines* and *closed circles* show the ranges of volcaniclastic glass, which can have regarded to have originated from Mauna Loa volcano (McMurtry et al. 1999)

the submarine west flank of Hawaii Island. Morgan et al. (2007) also revealed that the age of South Kona ladslide is around ~280 ka. The ages of volcaniclastic layers of PC14 and PC15 show simultaneous time frames to those of the Alika 2 and South Kona/Alika 1 landslides. Garcia (1996) suggests that a volcanic sand layer in the upper Brunhes at site ODP Site 842, which is located near our study area, is derived from Mauna Loa volcano, Hawaii Island (Fig. 61.1). Downcore chemical variations in the bulk sediments from XRF of PC15 also suggest that the volcaniclastic layers originate from Mauna Loa volcano. High MgO (ca. 6–8 wt.%) contents are found in the peaks of magnetic susceptibility arising from volcaniclastic layers at 112 ka and 218 ka (Fig. 61.4b). A plot of MgO vs. SiO2 shows that samples from both layers exhibit the chemical end member composition of Mauna Loa type lava (Fig. 61.4c). Thus, the sediment chemical composition data suggest that the volcaniclastic material was transported from Mauna Loa volcano to south of Oahu Island over long-distances (200–300 km). Taking into account, the age estimations, the Alika 2 and

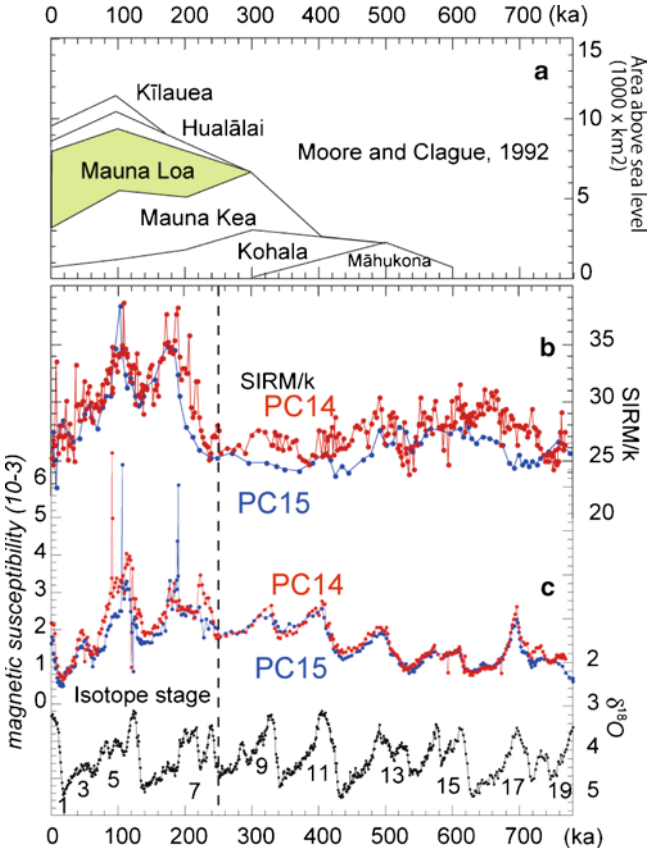

Fig. 61.5 (**a**): Volcano growth of Hawaii Island (Moore and Clague 1992), and magnetic properties changes in PC14 and PC15. (**b**): SIRM/k profile of PC14 and PC15. (**c**): magnetic susceptibility profile of PC14 and PC15, and LR04 stack of globally distributed benthic $\delta^{18}O$ records (Lisiecki and Raymo 2005)

South Kona/Alika 1 landslides are the most likely candidate events for the sources of these volcaniclastic layers.

Higher amplitudes in the *k* profiles since 250 ka is suggestive of increasing volcaniclastic material in the sediments. The SIRM/k ratio especially indicates the start of fining magnetite grain size since 250 ka (Fig. 61.5). A mean value of SIRM/k produced from ten volcanic rocks sampled from the source area of Alika and South Kona Slide, that is the west flank of Hawaii Island (Fig. 61.1), is 37. Whereas SIRM/k values of the sediment older than 250 ka are less than 30 (Fig. 61.5). So it appears that the volcanic material from the Alika and South Kona Slides plausibly enhanced the SIRM/k of the sediment of PC14 and PC15. The higher SIRM/*k* value of sediments, then accordingly, can be interpreted to reflect the addition of volcanic material to the abyssal sediments. The increase in sedimentation rate after 250 ka

indicating increasing sediment flux to the core sites is consistent with this statement. Hawaii Island is thought to have started growing ca. 800 ka. The largest volcano on Hawaii, Mauna Loa volcano, is believed to have emerged above sea level at about 300–400 ka (Moore and Clague 1992). Thus, the observed changes in magnetic properties possibly represents the onset of input of Mauna Loa's volcaniclastic material to the abyssal plain.

It is noteworthy that the magnetic susceptibility and the oxygen isotope curves are well synchronized, and the horizons of obvious volcaniclastic layers (positive spikes in k) generally occur during the higher peaks of the oxygen isotope curve (Fig. 61.5). This association suggests that giant submarine landslides in Hawaiian Island occurred during these interglacial periods. Each isotope stage is known as a period of warm temperature and a high-stand of sea level. Some discussion has already been published on the timing for Hawaiian Giant submarine slides, exploring whether they are associated with glacial or interglacial stages. McMurtry et al. (1999, 2004) proposed that the trigger for giant landslides may relate to climate change and wetter periods, which would increase the possibility of groundwater intrusion, and consequent phreatic eruptions of shallow magma chambers. They pointed out that this mechanism is different from the case of continental margins where giant submarine landslides occur frequently during glacial stages due to the exposure of the unstable slope flank in the low-stand of sea level. Although more case studies are needed to confirm their model (McMurtry et al. 2009), the contemporaneity between the volcaniclastic layers and sea-level high-stands, suggests that volcaniclastic layers may serve as a proxy for the giant submarine landslide and climate change, at least for the last 250 ky. This result should be an important key to understanding the triggers for these recurrent Hawaiian submarine landslides.

61.5 Conclusion

On the south side of the Hawaiian Ridge, the established paleomagnetic and rock-magnetic stratigraphy reveals that two major time intervals of the volcaniclastic layers are recognized in the upper Brunhes Chron, between 0 and 250 ka. The correlation between magnetic susceptibility and the global benthic $\delta^{18}O$ stack record reveals that the upper interval involves separate volcaniclastic layers that are about 91–114 ka, and 216–245 ka. The Alika 2 and South Kona/Alika 1 landslides in Hawaii Island are the most likely candidate events for the origin of these volcaniclastic layers. It suggests that the volcaniclastic material were supplied as turbidites traveling long distances.

Acknowledgments We thank Kazue Tsuchida and Hiroshi Takei for their laboratory support work at JAMSTEC, and Drs. Jiro Naka and Hisayoshi Yokose for the fruitful discussions. We greatly thank the reviewers Drs. Julia Morgan and Gary McMurtry for significantly improving this manuscript.

References

Bloemendal J, King JW, Hall FR, Doh S-J (1992) Rock magnetism of Late Neogene and Pleistocene deep-sea sediments: relationship to sediment source, diagenetic processes, and sediment lithology. J Geophys Res 97:4361–4375

Coombs M, Eakins B, Cervell P (2006) Growth and collapse of Hawaiian volcanoes. J Volcanol Geotherm Res 151:vii–viii

Eakins B, Robinson J, Kanamatsu T, Naka J, Smith J, Takahashi E, Clague D (2003) Hawaii's volcanoes revealed, U.S. Geological Survey, Geologic Investigations Series Map I-2809

Garcia M (1996) Turbidite from slope failure on Hawaii volcanoes. In: McGuire W, Jones A, Neuberg J (eds) Volcano instability on the earth and other planets, vol 110. Geological Soceity Special Publication, London, pp 281–294

Garcia M, Hull D (1994) Turbidite from giant Hawaiian landslides: results from ocean drilling program site 842. Geology 22:159–162

Hammer J, Coombs M, Shamberger P, Kimura J (2006) Submarine sliver in North Kona: a window into the early magmatic and growth history of Hualalai Volcano, Hawaii. J Volcanol Geotherm Res 151:157–188

Holcomb R, Robinson J (2004) Maps of Hawaiian islands exclusive economic zone interpreted from GLORIA Sidescan-Sonar imagery, U.S. Geological Survey, Geologic Investigations Series Map I-2824

Kirschvink J (1980) The least-square line and plane and the analysis of paleomagnetic data. Geophys J R Astron Soc 62:699–718

Lipman P, Coombs M (2006) North Kona slump: submarine flank failure during the early(?) tholeiitic shield stage of Hualalai Volcano. J Volcanol Geotherm Res 151:189–216

Lipman P, Eakins B, Yokose H (2003) Ups and downs on spreading flanks of ocean-island volcanoes: evidence from Mauna Loa Kīlauea. Geology 31:841–844

Lisiecki L, Raymo M (2005) A Pliocene-Pleistocene stack of 57 globally distributed benthic δ18O records. Paleoceanography 20:PA1003. doi:10.1029/2004PA001071

Lourens L, Hilgen F, Shackleton N, Laskar J, Wilson D (2004) The Neogene period. In: Gradstein F, Ogg J, Smith A (eds) A geological time scale 2004. Cambridge, Cambridge University Press, pp 409–440

McMurtry G, Herrero-Bervera E, Cremer M, Smith L, Resig J, Sherman C, Torresan M (1999) Stratigraphic constraints on the timing and emplacement of the Alika 2 giant Hawaiian submarine landslide. J Volcanol Geotherm Res 94:35–58

McMurtry G, Watts P, Fryer G, Smith J, Imamura F (2004) Giant landslides, mega-tsunamis, and paleo-sea level in the Hawaiian islands. Mar Geol 203:219–233

McMurtry G, Fryer G, Tappin D, Fietzke J (2009) Massive volcanic flank failure and megatsunami generation evolve in response to quaternary climate change. Eos Trans AGU 90(52), Fall Meet Suppl, Abstract NH53B-07

Moore J, Clague D (1992) Volcano growth and evolution of the island of Hawaii. Geol Soc Am Bull 104(11):1471–1484

Moore G, Moore J (1988) Large-scale bedforms in boulder gravel produced by giant waves in Hawaii. Geol Soc Am Spec Pap 229:1–10

Moore J, Clague D, Holcomb R, Lipman P, Normark W, Torresan M (1989) Progressive submarine landslides on the Hawaiian Ridge. J Geophys Res 94:17465–17484

Morgan J, Clague D (2003) Volcanic spreading on Mauna Loa Volcano, HI: evidence from accretion, alternation, and exhumation of volcaniclastic sediments. Geology 30:411–414

Morgan J, Clague D, Borchers D, Davis A, Milliken K (2007) Mauna Loa's submarine western flank: landsliding, deep volcanic spreading, and hydrothermal alteration. Geochem Geophys Geosyst 8:Q05002. doi:10.1029/2006GC001420

Smith J, Satake K, Suyehiro K (2002) Deepwater multibeam sonar surveys along the southeastern Hawaii Ridge: guide to the CD-ROM. In: Takahashi E, Lipman P, Garcia M, Naka J, Aramaki S (eds) The evolution of Hawaiian volcanoes, resent progress in deep underwater research, AGU monograph 128, pp 3–9

Thompson R (1986) Modeling magnetization data using SIMPLEX. Phys Earth Planet Inter 42:113–127

Ward S (2002) Slip-sliding away. Nature 415:973–974

Chapter 62
Gravity Flow Deposits in the Deep Rockall Trough, Northeast Atlantic

Aggeliki Georgiopoulou, Sara Benetti, Patrick M. Shannon, Peter D.W. Haughton, and Stephen McCarron

Abstract The north-western margin of the Irish Rockall Trough in the Northeast Atlantic is dominated by the scarps of the Rockall Bank Mass Flow (RBMF) which extends towards the centre of the Rockall Trough, whereas the eastern margin is incised by numerous canyons that have no obvious associated fans at the foot of the slope. Terminal lobes associated with the glaciogenic Donegal-Barra Fan extend into the Rockall Trough from the northeast, whereas in the southwest the seafloor is dominated by the Feni Drift, a giant contourite drift formed by ocean bottom currents which was truncated by the sidewalls and depositional lobes of the RBMF. In June 2010 the RV Celtic Explorer cruise CE10008 collected the first comprehensive set of piston cores from the Irish sector of the deep Rockall Trough. Here we report on a sub-set of those cores recovered from across and beyond the bathymetric expression of the RBMF eastern outer limit in order to determine whether gravity flows were released during this event and whether they have traversed across the basin. The cores, taken in water depths of nearly 3,000 m, reveal that significant coarse sediment (up to coarse sand) was emplaced on the deep basin floor by both turbidity currents and bottom currents. We identify several discrete turbidite sand and silt deposits with geochemical signatures that point to different source areas. The youngest two appear to have been generated from the area occupied by the RBMF to the west during the Holocene. The remaining turbidite beds came from an

A. Georgiopoulou (✉) • P.M. Shannon • P.D.W. Haughton
UCD School of Geological Sciences, University College Dublin, Belfield, Dublin 4, Ireland
e-mail: aggie.georg@ucd.ie

S. Benetti
School of Environmental Sciences, University of Ulster, Cromore Road, Coleraine, BT52 1SA, Northern Ireland, UK

S. McCarron
Department of Geography, National University of Ireland, Maynooth, Co Kildare, Ireland

Y. Yamada et al. (eds.), *Submarine Mass Movements and Their Consequences*,
Advances in Natural and Technological Hazards Research 31,
DOI 10.1007/978-94-007-2162-3_62, © Springer Science+Business Media B.V. 2012

easterly or northeasterly source and tie back to the Donegal-Barra Fan and are probably glacially related. Between the two periods we find a thick (>1.5 m) contouritic sand, possibly formed by bottom current reworking of the Feni Drift.

Keywords Rockall Bank Mass Flow • Donegal-Barra Fan • Turbidite • Contourite • Provenance

62.1 Introduction

A multibeam swath bathymetric survey of the Irish territorial seabed below the 200 m isobath was carried out by the Irish National Seabed Survey (INSS) in 2000–2001, a joint project between the Geological Survey of Ireland and the Marine Institute (Ireland). Studies of the seabed morphology and sediment transport processes following acquisition of this dataset demonstrated the complicated and interacting oceanographic processes that have been taking place offshore western Ireland (Elliot et al. 2006, 2010), with slope failure scarps and gravity-driven sediment transport to the deep basin evident on the margins and the floor of the Rockall Trough.

In June 2010, RV Celtic Explorer cruise CE10008 collected the first comprehensive set of piston cores from the Irish sector of the deep Rockall Trough (ca 3,000 m water depth). The objective of the cruise was to sample the deepest area of the northern Rockall basin where interpretation of seismic data suggests optimal ponding of gravity flow deposits (Elliott et al. 2010). Therefore, debris flows and/or turbidity currents that were generated on the margins are expected to deposit preferentially in this area. In this paper we present the first results from a sub-set of these cores. The purpose of this study is to characterise the gravity flow deposits and identify the signature of different sources that contribute coarse sediment in the deep Rockall Trough.

62.2 Study Area and Regional Setting

The study area is located in the centre of the deep northern Rockall Trough (Fig. 62.1). The Rockall Trough is an elongate, steep-sided, NE-SW trending intracontinental basin on the continental shelf west of Ireland and the UK. It is between 200 and 250 km wide and nearly 3,000 m deep in the northern part. It is part of a highly topographically irregular margin that reflects a long history of Mesozoic-Cenozoic rifting and plate reorganisation processes across the NE Atlantic margin that led to the opening of the NE Atlantic Ocean in the Early Eocene (Naylor and Shannon 2011).

Deep ocean circulation was established in Late Eocene time leading to sediment being distributed by both alongslope and downslope processes (Stoker et al. 2005;

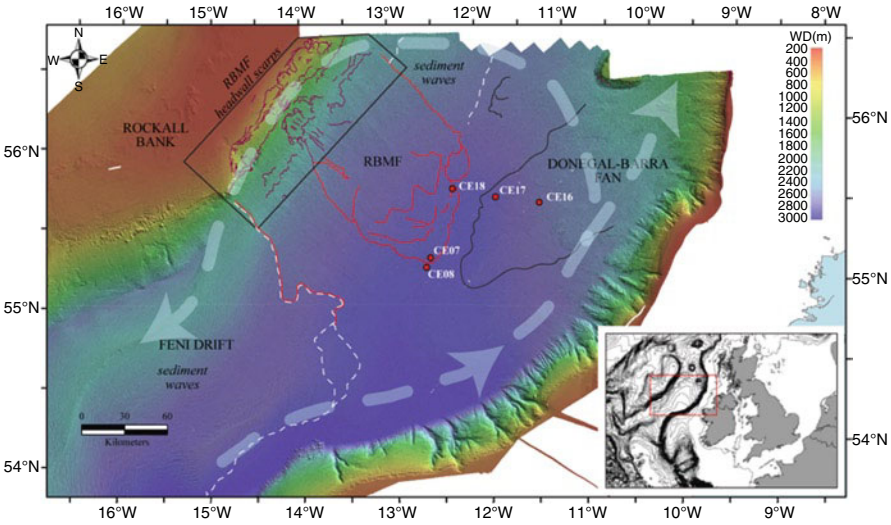

Fig. 62.1 Shaded multibeam bathymetry of the study area with location of cores and setting of the Rockall Bank Mass Flow (RBMF) (*red lines*), the Feni Drift and associated fields of sediment waves, the Donegal-Barra Fan (DBF) and the canyons on the eastern margin. The *black lines* indicate the extent of the DBF lobes, the *white dashed lines* the outline of the Feni Dift and the purple lines scarps on the Rockall Bank associated with the RBMF (after Sacchetti et al. 2011).The counter-clockwise bottom current circulation is also indicated (*light blue arrows*)

Elliott et al. 2006). The dominant bottom current oceanographic regime circulates in a counter-clockwise manner and involves generally northward flow along the eastern margin, and southward flow along the western margin (Fig. 62.1) (New and Smythe-Wright 2001). Bottom current circulation is manifested by a giant contourite drift the Feni Drift, whose crest impinges against the Rockall Bank (Stoker et al. 2005).

The Rockall Bank Mass Flow (RBMF) (Fig. 62.1), a large submarine landslide that has affected a total of 24,000 km^2, lies on the Rockall Bank margin, (Unnithan et al. 2001; Elliott et al. 2010). Multiple failure scarps up to 22 km long and 150 m high and overlapping depositional lobes were described by Elliott et al. (2010). The short term triggering mechanism is not known, but the long-term instability control was suggested to be differential sedimentation and erosion on the slope associated with development of the Feni Drift (Elliott et al. 2010). The RBMF complex has been postulated to have taken place at different stages during the last glacial and early post-glacial periods (10.2–21.7 ka) (Flood et al. 1979; Faugères et al. 1981; Øvrebø et al. 2005; Elliott et al. 2010).

The eastern margin of the Rockall Trough is considered to straddle the southern limit of the glaciated North Atlantic margin and is dominated by canyons and associated slope failure features (Fig. 62.1). These slope features first developed in mid-Cenozoic times and were locally re-utilised by glaciomarine discharge from Pleistocene ice sheets (Elliott et al. 2006; O'Reilly et al. 2007). The Donegal/Barra

Fan (DBF) (Fig. 62.1) is a morphologically and sedimentologically distinct feature of the northeastern margin of the Rockall Trough. It is a trough-mouth fan that drained the British Irish Ice Sheet (BIIS) and was formed by sediment that was carried to the shelf-edge break by the ice sheet (Vorren and Laberg 2001; Armishaw et al. 1998; Dunlop et al. 2010).

62.3 Data and Methods

A 6-m long Modular Piston Coring System (Geo-Marine Survey Systems), with 10 cm diameter core liners, was used during CE10008. The longest core retrieval was 4 m. The cores used in this study were collected from the edges of the distal lobes of the RBMF and form a transect from the top of the terminal lobe across the edge onto the seafloor seemingly unaffected by the slide complex (Fig. 62.1).

Core processing analyses include detailed lithological and internal structure descriptions, photography and physical properties (p-wave velocity, gamma-ray density and magnetic susceptibility) acquired with the use of a Multi-Sensor Core Logger (MSCL) at the National University of Ireland Maynooth (Fig. 62.2). Two of these cores, CE10008_08 (abbreviated CE08) and CE10008_16 (abbreviated CE16), were also logged for chemical elemental composition on an ITRAX scanner at the UCD School of Geography, Planning and Environmental Policy of the University College Dublin (Fig. 62.2).

62.4 Results and Discussion

62.4.1 Sedimentary Facies and Core Correlation

The cores generally comprise stiff, hemipelagic grey mud and lighter beige to brown mud punctuated by coarser-grained layers of beige and grey to dark grey sandy and silty, sometimes laminated, beds. Three main facies are identified by their grain size, colour, degree of bioturbation and internal structures (Fig. 62.3).

The cores were then visually correlated (Fig. 62.4) based on sediment colour, relative position of the strata down-core and the physical properties derived from the MSCL measurements. At least nine correlatable coarse-grained beds were identified across the cores, whose physical properties are characterised by peaks of higher values relative to the bounding pelagic beds. Here we present the sedimentary facies that were found in the deep Rockall Trough and discuss their origins.

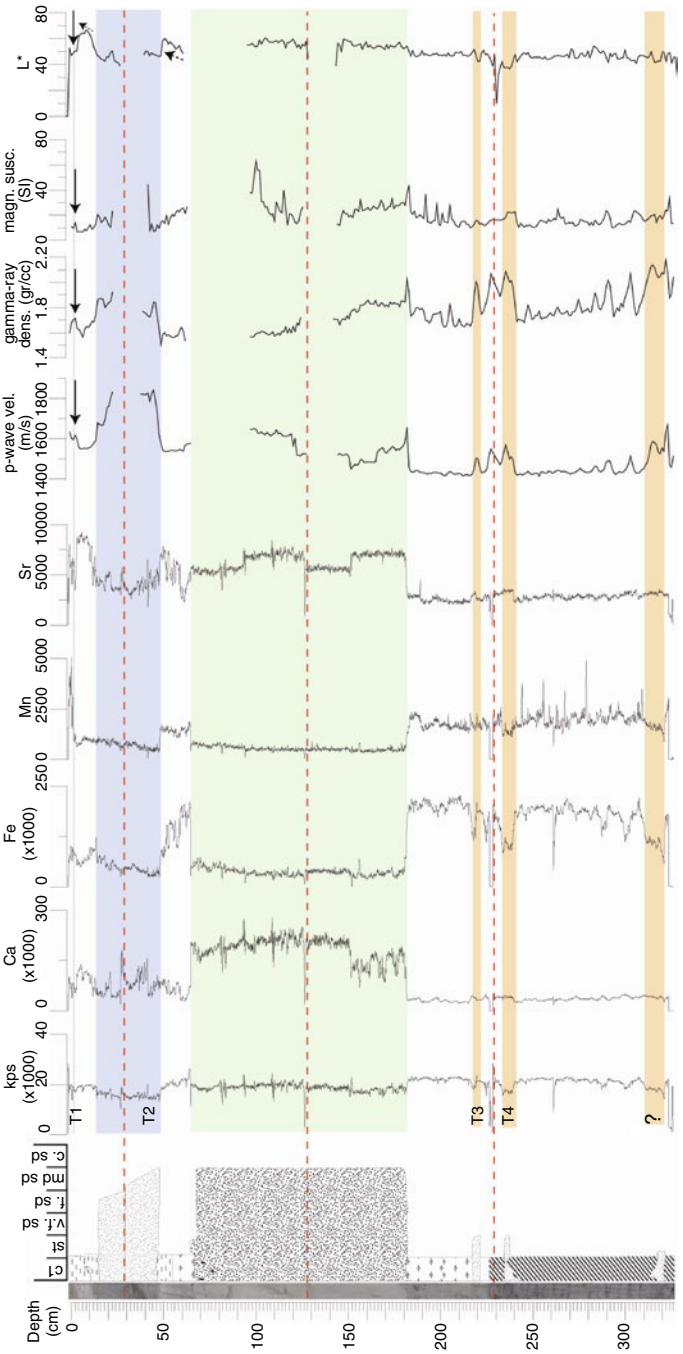

Fig. 62.2 Core CE08 showing the analytical techniques performed for the cores. From *left to right*: Photograph, lithological (facies) interpretation (see text for details), geochemical curves generated by the ITRAX in counts per second (kps) and physical properties and lightness (L*) measured on the MSCL. The *red dashed lines* indicate the section breaks; *spikes* in the data at those boundaries are spurious. Note the spikes in the physical properties signalled by the very thin in this core turbidite T1 (indicated with *black arrows*). The increase of lightness from 60 cm bsf upwards (*dashed arrows*) is characteristic of Holocene sediments in the North Atlantic (Chapman and Shackleton 2000). The colour coding is *green* for the foraminiferal sand, *blue* for the events that post-date it and *orange* for the events that precede it. For location of core see Fig. 62.1

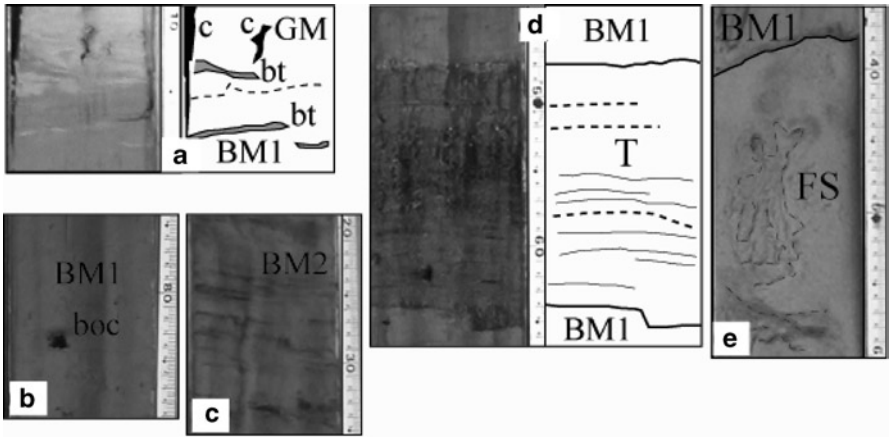

Fig. 62.3 Sedimentary facies identified in the cores. (**a**) *Grey* mud and its contact with *brown* mud facies BM1 (b). (**b**) and (**c**) are the two *brown* mud facies, note the *black* staining in BM2, (**d**) *laminated* sand and silt (note the *sharp* base and *top* boundaries with BM1), and (**e**) the water-saturated foraminiferal sand with *sharp top* boundary to facies BM1 (note the features created by the liquid nature of the sand when split). *c* = crack, *bt* = bioturbation, *boc* = black organic clast

62.4.1.1 Fine-Grained Muds

The cores are dominated by fine-grained muds, almost clayey in grain-size except for the presence of occasional foraminifera. We subdivided them based on their colour and degree of bioturbation;

- Light brown (e.g., Munsell 10YR 7/1, 2.5Y 6/2 and 2.5Y 6/3) moderately bioturbated by worm burrows with low p-wave velocity, low gamma-ray density and low magnetic susceptibility (facies GM);
- Dark grey/brown (e.g., Munsell 5Y 4/1 and 2.5Y 4/2) lightly bioturbated of similar physical properties to GM (facies BM1) (Figs. 62.2 and 62.3). Black rounded and almost spherical floating pebbles and gravels were sometimes found in this facies;
- A third facies (BM2) is similar to BM1 but appeared banded with black staining upon splitting (Fig. 62.3). The black staining subsequently disappeared, replaced by a very subtle orange hue around scattered coarse sand grains.

The group of mud facies is interpreted as the hemipelagic "background" sediments of the deep Rockall Trough, where the colour variability, degree of bioturbation and foraminifera content are determined by the glacial-interglacial cycle. Facies GM is interpreted to represent interglacial periods whereas facies BM1 and BM2, containing pebbles of drop-stones and ice rafted debris, represent glacial periods.

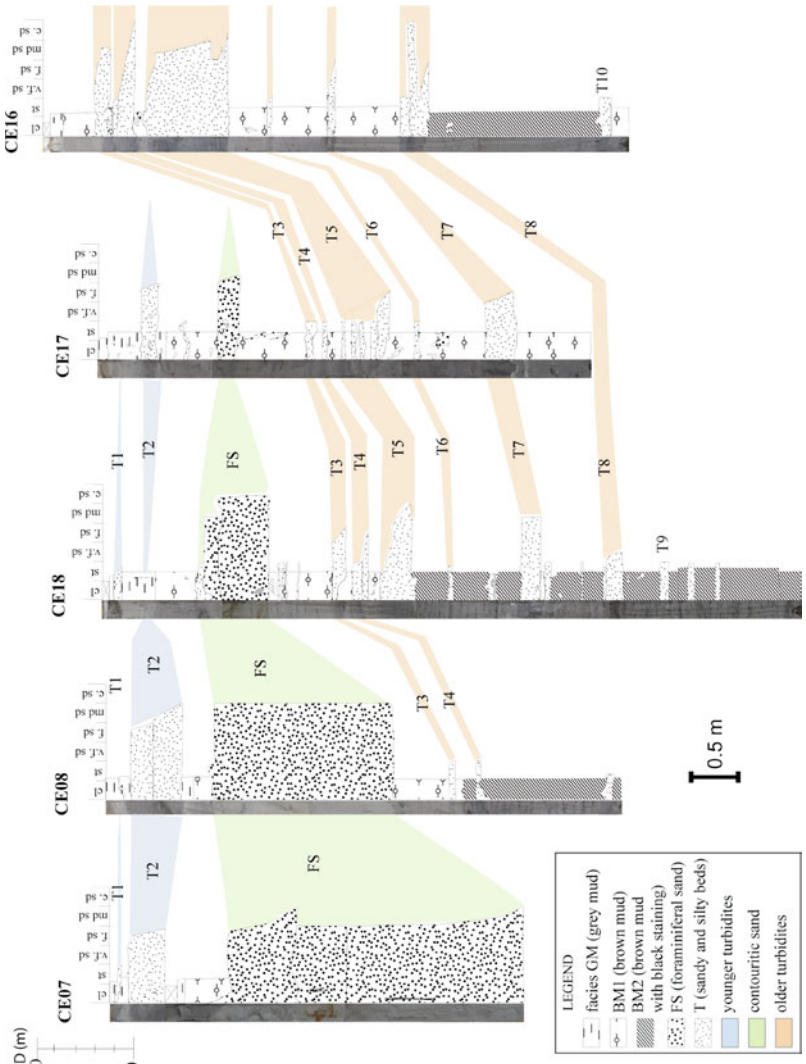

Fig. 62.4 Correlation of coarse-grained beds in the five cores. Eight correlatable turbidites have been identified and one contouritic sand. Note how the youngest turbidites and the contouritic sand are absent in the northeasternmost and shallowest of the five cores. The *colour coding* for the younger and older turbidites and the foraminiferal sand is the same as in Figs. 62.2 and 62.5. For core locations see Fig. 62.1

62.4.1.2 Graded Sands and Silts (Facies T)

The beds belonging to this group are dark grey in colour, show erosional sharp basal boundaries, are normally graded and most times are parallel- but also cross-laminated (Fig. 62.3d). They have sharp top contacts with an abrupt transition to the pelagic facies described above (Fig. 62.3d). When the cores were split they appeared water saturated but most of the water escaped at that stage, in some cases disturbing primary laminations. Water retention was most likely due to the sharp basal and top boundaries that created a strong contrast between the low-porosity hemipelagic layers that enclosed the porous sand layers, buffering water transmission towards the seafloor.

The physical properties signal of facies T is clearly distinguishable on the MSCL curves due to sharp positive spikes in p-wave velocity, gamma-ray density and magnetic susceptibility compared to the hemipelagic facies (Fig. 62.2). Due to their graded and laminated character these beds are interpreted as turbidites. The characteristic fingerprint of the turbidites in the physical properties was used to identify very thin turbidite beds as even a few grains left by the current are enough to generate a response in the physical properties (indicated in Fig. 62.2 with black arrows). Eight of the nine correlated coarse-grained beds (T1–T8) belong to this group. However, otsher beds with similar characteristics were identified in the cores (e.g., T9 and T10) but they appear localised and we were unable to correlate them through the core suite.

The turbidites lack mud caps and have sharp upper contacts, which sometimes appear erosional truncating the top laminae of the turbidite (Fig. 62.3d). These contacts are interpreted as evidence of ocean bottom current activity that influenced the depositional record of the turbidity current in the deepest part of the basin. Bottom currents either captured the fine-grained cloud of the turbidity currents before it settled or eroded and removed the mud cap after deposition. The sharp upper boundary of the turbidites demonstrates erosional processes but it cannot be determined if the erosion occur during deposition or post-deposition of the turbidite. However, it is also likely that some of the sharp upper contacts indicate bypassing of the finer cloud to the deeper basin.

62.4.1.3 Foraminiferal Water-Saturated Sand (FS)

A thick bed, more than 1.5 m in some cores, of generally ungraded and very poorly sorted, water-saturated foraminiferal medium sand was found in four of the five cores (Figs. 62.2 and 62.4). It mostly appears structureless, especially where it is thickest, but in places some faint lamination is seen. The grain assemblage consists to the larger proportion of planktic formanifera and the rest is made up mostly of quartz, mica and glauconite. This bed is found nearly 0.5 m below the seabed and with high mobility when split due to its high water content. In some cases it is found flushed along the edges of the plastic liner and even settling above the seafloor sediments as they are also identified in the trigger weight core.

The structureless character of this bed may be a result of core disturbance, but some original structure would be expected to be preserved in some parts of the bed as we observed in graded sands that were disturbed. In core CE18 some laminations are preserved near the base even though it appears highly disturbed towards the top. Therefore we believe that where the sand is structureless it reflects original depositional character.

The characteristics of this facies are very similar to a sandy contourite described further north in the Faroe-Shetland Channel (Masson et al. 2010). Due to the presence of glauconite, which forms in water depths down to 500 m (Tucker 1991), we believe this sand has a continental shelf origin. The only core lacking the sandy contourite is CE16 which was retrieved from a location more than 300 m shallower than the cores with the thickest expression of facies FS (CE07and CE08) (Figs. 62.1 and 62.4). Therefore the position of the cores that contain the sand can be considered as a depth marker for the bottom current circulation, i.e. the current circulates below 2,800 m water depth. This has been reported to be the water depth range of the Antarctic Bottom Water up to 56°N (New and Smyth-Wright 2001).

62.4.2 Turbidite Provenance

Figure 62.4 shows the relative stratigraphic position and correlation of the turbidite and sandy contourite beds within and between the cores. It is evident that even though the location of the cores is at a water depth of 3,000 m and at a distance of more than 200 km from terrestrial sediment sources, there is still a large contribution of coarse siliciclastic sediments (silt to medium/coarse sand). The turbidites have been termed T1–T10. In this section we assess the source areas of the sediment flows.

The northern Rockall Trough is bound by steep-sided margins that show evidence of significant sediment remobilisation. To the east lies the canyon system that incises the slope offshore western Ireland (Elliott et al. 2006; Sacchetti et al. 2011), to the northeast there are the depositional lobes of the DBF that reach far enough southwest to be within the study area (O'Reilly et al. 2007; Sacchetti et al. 2011), and to the west there are the scarps on the Rockall Bank associated with the RBMF (Fig. 62.1) (Øvrebø et al. 2005; Elliott et al. 2010).

The elemental concentrations for the coarse-grained beds were cross-plotted in order to identify geochemical differences and distinguish source areas. Three distinct areas are evident in the plots of Fig. 62.5. High Ca and Sr relative to Fe, Mn, and Si characterise the foraminiferal sand. The turbidites form two groups on the plots, with high Fe, high Mn, low Ca and low Sr for the older turbidites in the lower parts of the core, and high Sr but low Ca and Fe for the younger turbidites. Both turbidites have relatively high Si content as would be expected for non-biogenic sediments.

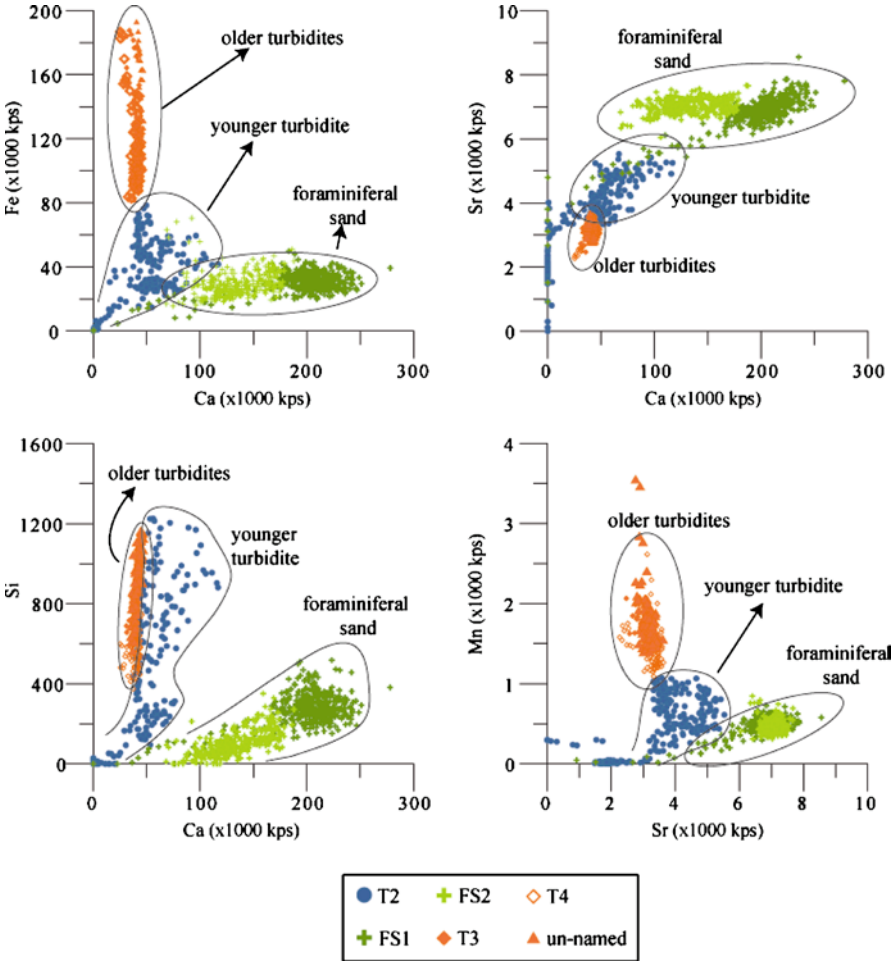

Fig. 62.5 Cross-plots of ITRAX- generated Ca, Fe, Sr, Si and Mn concentrations (counts per second) in the coarse beds of core CE08. Note the distinct grouping of the older turbidites relative to the younger turbidite and the foraminiferal sand (*colour coding* follows that of Figs. 62.2 and 62.4)

62.4.2.1 Eastern Margin Canyons

There are no obvious depositional lobes on the floor of the basin associated with the canyons on the eastern margin as the bathymetric dataset demonstrates (Sacchetti et al. 2011). Physiographically, it is not possible that these canyons could be sources as turbidity currents would have to flow counter to the seabed gradient to deposit in the area of the cores. Consequently we believe that none of the turbidites in the cores were generated from this part of the margin.

62.4.2.2 Donegal-Barra Fan

Thickness and grain-size trends of turbidites T3–T10 suggest they were introduced from a northeasterly source, i.e. the beds thin and fine from the northeastern cores towards the west and southwest (Fig. 62.4). Cores CE16, CE17 and CE18 that contain these beds were retrieved from the terminal reaches of the DBF lobes, while core CE08, which contains only thin T3 and T4, is retrieved from further southwest suggesting that this location only received the finer tail of those turbidity currents (Fig. 62.1). Therefore, we believe that these turbidites were generated in a location upslope of the DBF.

62.4.2.3 Rockall Bank Scarps

The geographical distribution of the thickness and grain-size of turbidites T1 and T2 suggests that they originated from a westerly source, i.e. the Rockall Bank area and thatthey may even be associated with the scarps linked to the RBMF. T1 and T2 are the youngest turbidites, and we believe may have occurred within the Holocene as they are found within the GM interglacial facies where the colour lightness of the sediments measured on the MSCL has an increasing trend (Fig. 62.2) which has been reported to be a characteristic of Holocene sediments in the North Atlantic (Chapman and Shackleton 2000). It is likely that these turbidites were deposited by turbidity currents generated through water entrainment and flow transformation during the RBMF events, but further chronological analyses will be conducted in order to establish the relationship of these turbidites with the RBMF.

62.5 Conclusions

The new deep-water core dataset from the Rockall Trough shows that there has been significant input of coarse-grained sediment by gravity flows and turbidity currents. Two sources of turbidites have been identified that are distinctly different in elemental composition and clearly separated in time. It appears that regular input of turbidity currents initially reached the deepest part of the northern Rockall Trough basin from a northeasterly direction, where the Donegal-Barra Fan is located. We tentatively suggest that these were generated during the last glacial period when the British Irish Ice Sheet cap extended offshore. Following this period, a contourite sand was deposited and possibly buried rapidly, preserving a high water content. In more recent times turbidites originating from the area occupied by the RBMF were deposited. It is likely that these turbidites are linked to transformation of the RBMF events and may offer further insight into the sequence of events that created the extensive scarps on the Rockall Bank slope and the overlapping lobes on the seabed. Evidence of bottom current activity exists throughout the record with sharp, erosional top boundaries for almost all the turbidite beds.

Acknowledgements AG and SB would like to thank the Captain and Crew, of RV Celtic Explorer, cruise participants and Mr Áodhan Fitzgerald of the Marine Institute, for their invaluable assistance during cruise CE10008. This research survey was carried out under the *Sea Change* strategy with the support of the Marine Institute and the Marine Research Sub-programme of the National Development Plan 2007–2013. The UCD authors acknowledge funding from a Griffith Geoscience Research Award of the Department of Communications, Energy and Natural Resources under the National Geoscience Programme 2007–2013 (Ireland). Bathymetric data from the INSS project are downloadable from https://jetstream.gsi.ie/iwdds/index.html. We are also grateful to the reviewers Dr David Hodgson and Dr John Howe and the editor Dr Jason Chaytor for their constructive comments.

References

Armishaw JE, Holmes RW, Stow DAV (1998) Morphology and sedimentation on the Hebrides slope and Barra Fan, NW UK continental margin. In: Stoker MS, Evans D, Cramp A (eds) Geological processes on continental margins: sedimentation, mass-wasting and stability, Geological Soceity, London, Special Publication 129, pp 81–104

Chapman MR, Shackleton NJ (2000) Evidence of 550-year and 1000-year cyclicities in North Atlantic circulation patterns during the Holocene. The Holocene 10:287–291

Dunlop P, Shannon R, Quinn R, McCabe AM, Doyle E (2010) Marine geophysical evidence for ice sheet extension on the Malin Shelf: new evidence for the western limits of the British Irish Ice Sheet. Mar Geol 276:86–99

Elliott GM, Shannon PM, Haughton PDW, Praeg D, O'Reilly B (2006) Mid- to late Cenozoic canyon development on the eastern margin of the Rockall Trough, offshore Ireland. Mar Geol 229:113–132

Elliott GM, Shannon PM, Haughton PDW, Øvrebø LK (2010) The Rockall Bank mass flow: collapse of a moated contourite drift onlapping the eastern flank of the Rockall Bank, west of Ireland. Mar Petrol Geol 27:92–107

Faugères J-C, Gonthier E, Grousset F, Poutiers J (1981) The Feni Drift: the importance and meaning of slump deposits on the eastern slope of the Rockall Bank. Mar Geol 40:49–57

Flood RD, Hollister CD, Lonsdale P (1979) Disruption of the Feni sediment drift by debris flows from Rockall Bank. Mar Geol 32:311–334

Masson DG, Plets RMK, Huvenne VAI, Wynn RB, Bett BJ (2010) Sedimentology and depositional history of Holocene sandy contourites on the lower slope of the Faroe-Shetland channel, northwest of the UK. Mar Geol 268:85–96

Naylor D, Shannon PM (2011) Petroleum geology of Ireland. Dunedin Academic Press, Edinburgh, 262 pp

New AL, Smythe-Wright D (2001) Aspects of the circulation in the Rockall Trough. Cont Shelf Res 21:777–810

O'Reilly BM, Shannon PM, Readman PW (2007) Shelf to slope sedimentation processes and the impact of Plio-Pleistocene glaciations in the northeast Atlantic, west of Ireland. Mar Geol 238:21–44

Øvrebø LK, Haughton PDW, Shannon PM (2005) Temporal and spatial variations in late quaternary slope sedimentation along the undersupplied margins of the Rockall Trough, offshore west Ireland. Norw J Geol 85:279–294

Sacchetti F, Benetti S, Georgiopoulou A, Dunlop P, Quinn R (2011) Geomorphology of the Irish Rockall Trough, North Atlantic Ocean, mapped from multibeam bathymetric and backscatter data. J Maps 2011:60–81

Stoker MS, Praeg D, Hjelstuen BO, Laberg JS, Nielsen T, Shannon PM (2005) Neogene stratigraphy and the sedimentary and oceanographic development of the NW European Atlantic margin. Mar Petrol Geol 22:977–1005

Tucker ME (1991) Sedimentary petrology: an introduction to the origin of sedimentary rocks, 2nd edn. Blackwell Science Ltd., London, p 260

Unnithan V, Shannon PM, McGrane K, Readman PDW, Jacob AWB, Keary R, Kenyon NH (2001) Slope stability and sediment redistribution in the Rockall Trough: constraints from GLORIA. In: Shannon PM, Haughton PDW, Corcoran DV (eds) The petroleum exploration of Ireland's offshore basins, vol 188. Geological Soceity, London, Special Publication, pp 439–454

Vorren TO, Laberg JS (2001) Late quaternary sedimentary processes and environment on the Norwegian-Greenland Sea continental margins. In: Martinsen OJ, Dreyer T (eds) Sedimentary environments offshore Norway-palaeozoic to recent. Elsevier, Amsterdam, pp 451–456

Part IX
Relevance of Natural Climate Change in Triggering Slope Failures

Chapter 63
Submarine Mass Wasting in Isfjorden, Spitsbergen

Matthias Forwick and Tore O. Vorren

Abstract The fjords of the Isfjorden system, Spitsbergen, have been exposed to recurrent submarine mass wasting during the past c. 14,100 years. Slides, slumps, debris-flows and turbidites are mainly deposited in front of tidewater glaciers and river deltas, but also in areas without the influence of such major sediment sources. Slope failures are most often related to high sediment supply and earthquakes. Mass-transport activity in the Isfjorden area shows several similarities to sub-polar and temperate fjord settings with regard to submarine landform assemblages, run-out distances and the amount of reworked sediments. However, a striking difference to other glaciated fjords is the absence of turbidites distal to terminal moraines deposited during the late Holocene.

Keywords Fjords • Submarine mass movements • Trigger mechanisms • Chronology

63.1 Introduction

The slopes of fjords are frequently exposed to failures occasionally affecting human lives and infrastructure (e.g., Longva et al. 2003). Typically, the largest and most frequent slope failures occur shortly after the retreat of grounded ice, and up to 50% or more of the sediments may be reworked in some fjords (e.g., Holtedahl 1975; Aarseth et al. 1989). Several factors can lead to slope failures in fjords, including sediment loading (over longer time or rapidly), earthquakes, sea-level fluctuations

M. Forwick (✉) • T.O. Vorren
Department of Geology, University of Tromsø, N-9037 Tromsø, Norway
e-mail: Matthias.Forwick@uit.no; Tore.Vorren@uit.no

Y. Yamada et al. (eds.), *Submarine Mass Movements and Their Consequences*,
Advances in Natural and Technological Hazards Research 31,
DOI 10.1007/978-94-007-2162-3_63, © Springer Science+Business Media B.V. 2012

(isostatic rebound, tsunamis, tides), long-lasting heavy rain, as well as human activities (e.g., Syvitski et al. 1987).

In this paper, we integrate published results with new data providing evidence of submarine mass-transport activity in the Isfjorden area. We discuss the chronology and trigger mechanisms for the slope failures and compare the results with other glaciated and non-glaciated fjord systems.

63.2 Physiography

The Isfjorden system is the largest fjord system on Spitsbergen, Svalbard, encompassing the trunk fjord Isfjorden and 13 tributary fjords and bays (Fig. 63.1c). It is approx. 100 km long and up to 425 m deep.

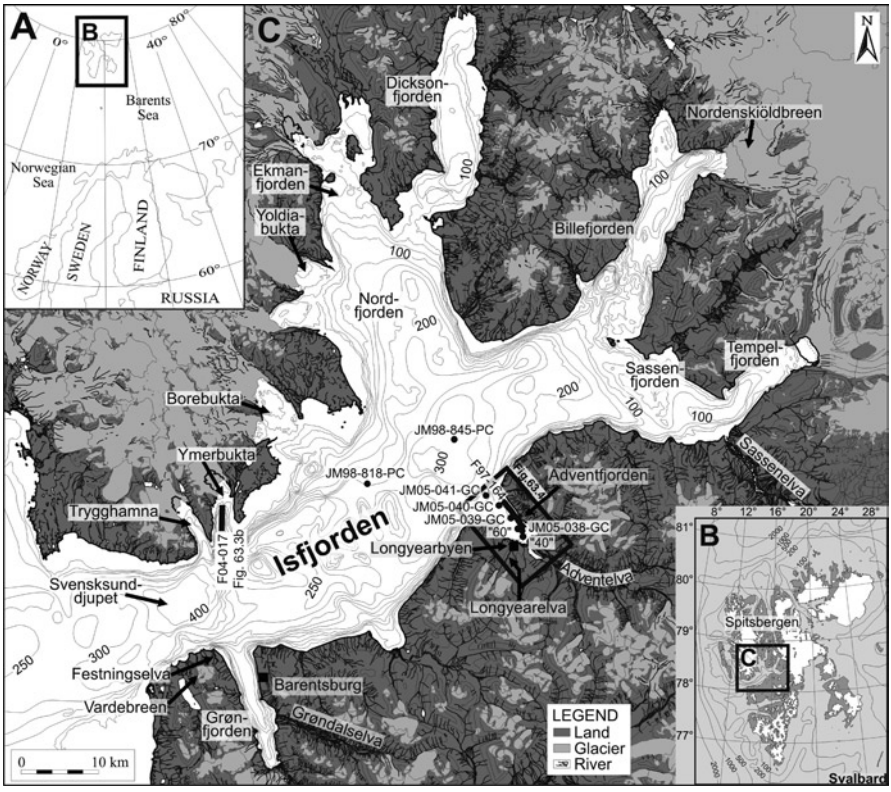

Fig. 63.1 Overview maps. (**a**) Map of Scandinavia. (**b**) Map of Svalbard. (**c**) Map of the study area. Place names mentioned in the text, core locations and the locations of seismic profiles are indicated. For positions of the cores see Table 63.1

Nine tidewater glaciers are present at the heads of some fjords and bays (Fig. 63.1c). Fluvial runoff occurs either from single rivers or from large, braided river systems. Most of the rivers are glacially fed and their runoff season is usually from June to September, with peak runoff in July (Killingtveit et al. 2003).

63.3 Material and Methods

This paper integrates published and unpublished data. Results presented in the figures were selected from data collected with R/V *Jan Mayen* in 1997, 1998, 2002–2006 and 2008. Swath-bathymetry data were acquired with a Kongsberg Maritime EM 300 multibeam echo sounder and the high-resolution seismic data were collected with a 10 kW hull-mounted 3.5 kHz penetration echo sounder. Sediment cores were retrieved with a 6-m long gravity corer.

63.4 Results

Three types of mass-transport deposits (MTDs) are distinguished: (1) *glacigenic MTDs*, related to slope failure and sediment reworking in front of and/or beneath tidewater glaciers and/or ice streams; (2) *fluvial MTDs* off river mouths, and (3) *other MTDs* that are related neither to glaciers nor rivers.

63.4.1 Glacigenic MTDs

Debris-flow lobes were deposited in front of or beneath glaciers during the last glacial (late Weichselian/earliest Holocene) and the late Holocene (for an overview see Forwick and Vorren 2011). Lobes deposited during the last glacial are up to 4.5 km long, 1.7 km wide and 25 m thick; lobes of late Holocene age are up to about 3 km long, approx. 2.5 km wide and 25 m thick. Several down-slope oriented flow structures and blocks, a few meters wide, occur within late Holocene lobes in Ekmanfjorden and Borebukta (for locations see Fig. 63.1c; Boulton et al. 1996; Plassen et al. 2004; Ottesen and Dowdeswell 2006), as well as in Trygghamna, Ymerbukta (Fig. 63.2), Billefjorden and Tempelfjorden.

The late Holocene lobes in Yoldiabukta and Tempelfjorden (for locations see Fig. 63.1c) are composed of massive, clayey silt with varying amounts of clasts (Plassen et al. 2004). Slight deformation occurs in the uppermost centimetres of the lobe in Tempelfjorden. The uppermost approx. 1.2 m of the lobe in Billefjorden contain several lithological units (mostly mud and sand with varying amounts of clasts) that are partly intensely deformed (Baeten 2007).

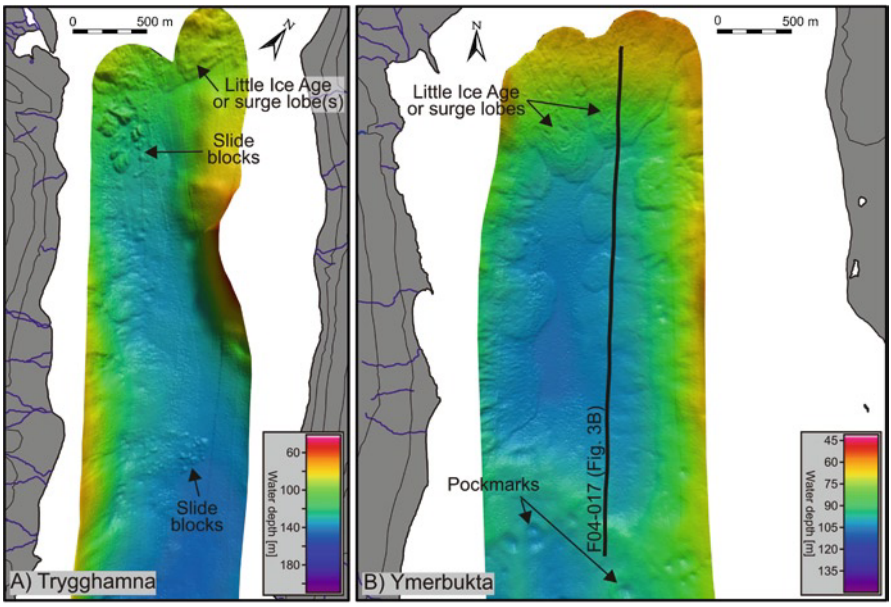

Fig. 63.2 Swath-bathymetry data from Trygghamna (**a**) and Ymerbukta (**b**), showing glacigenic and other MTDs. The pockmarks in Ymerbukta were described by Forwick et al. (2009). For location see Fig. 63.1

Approximately 140 and 100 sandy MTDs were identified within stratified glacimarine sequences of Late Weichselian age in the cores JM98-818-PC and JM98-845-PC from central Isfjorden (for locations see Fig. 63.1c, Table 63.1; Forwick and Vorren 2009). They are up to 2.5 cm thick, but generally thinner than 5 mm. Their decreasing number upcore was interpreted to reflect the change from glacier proximal to glacier distal environments during the last deglaciation (Forwick and Vorren 2009).

63.4.2 Fluvial MTDs

Chutes and gullies on the slopes of the prograding rivers Adventelva and Longyearelva in Adventfjorden provide evidence of sediment reworking (for locations see Fig. 63.1c; Prior et al. 1981). This was later confirmed by *in-situ* measurements of turbidity flows (Zajączkowski and Włodarska-Kowalczuk 2007).

A downfjord thinning sequence of acoustically stratified sediments in Adventfjorden indicates that the main source is Adventelva delta (Fig. 63.3a). Four gravity cores, retrieved adjacent to the seismic profile (Fig. 63.4, Table 63.1), are generally composed of muddy sediments, with intercalations of sandy intervals and clasts. The sandy strata have generally sharp and often erosive lower boundaries. They are up to 12 cm thick in the core closest to the fjord head (JM05-038-GC) and

Table 63.1 Locations of cores mentioned in the text

Core	Latitude [N]	Longitude [E]	Water depth [m]	Reference
JM05-038-GC	78°14.27′	015°41.01′	42	This study
JM05-039-GC	78°15.17′	015°37.22′	70	This study
JM05-040-GC	78°16.04′	015°33.17′	87	This study
JM05-041-GC	78°16.74′	015°28.78′	120	This study
JM98-818-PC	78°17.57′	014°48.17′	239	Forwick and Vorren (2009)
JM98-845-PC	78°20.64′	015°18.11′	257	Forwick and Vorren (2009)
”40”	78°13.87′	015°41.22′	–	Zajączkowski and Włodarska-Kowalczuk (2007)
”60”	78°14.41′	015°39.53′	–	Zajączkowski and Włodarska-Kowalczuk (2007)

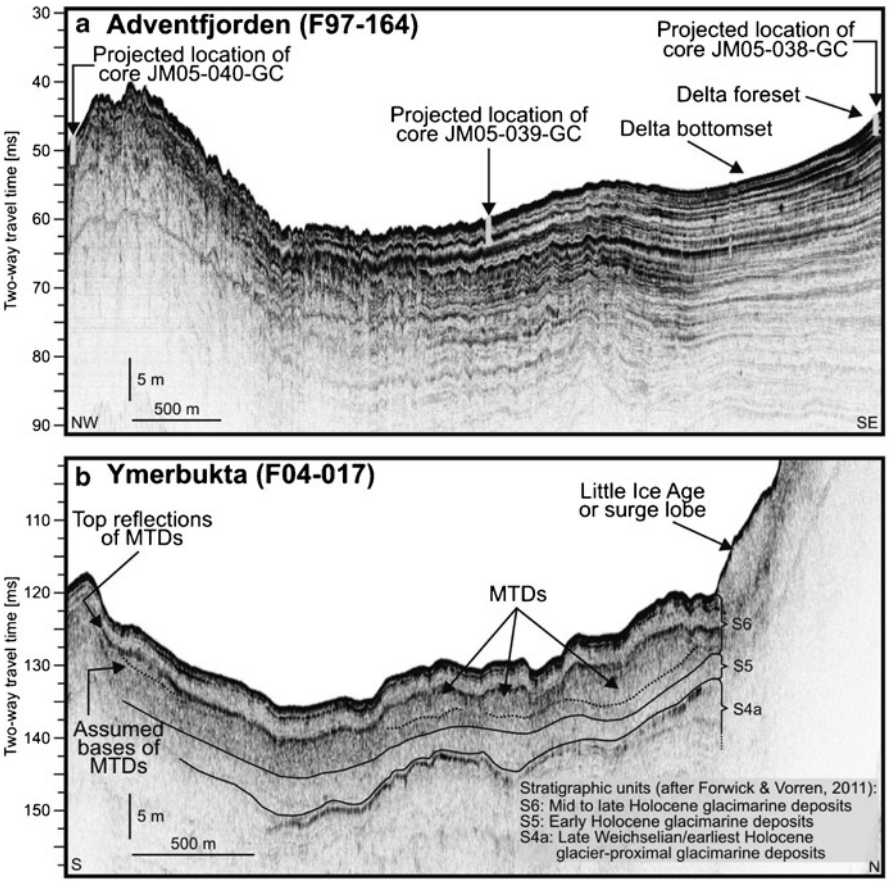

Fig. 63.3 High-resolution seismic profiles from Adventfjorden (**a**) and Ymerbukta (**b**). The length of the vertical bars (*in meters*) is based on an assumed p-wave velocity of 1,600 m/s (after Forwick and Vorren 2011 and references therein). *Grey vertical bars* in (*a*) indicate core lengths. For locations of the profiles see Figs. 63.1c and 63.4

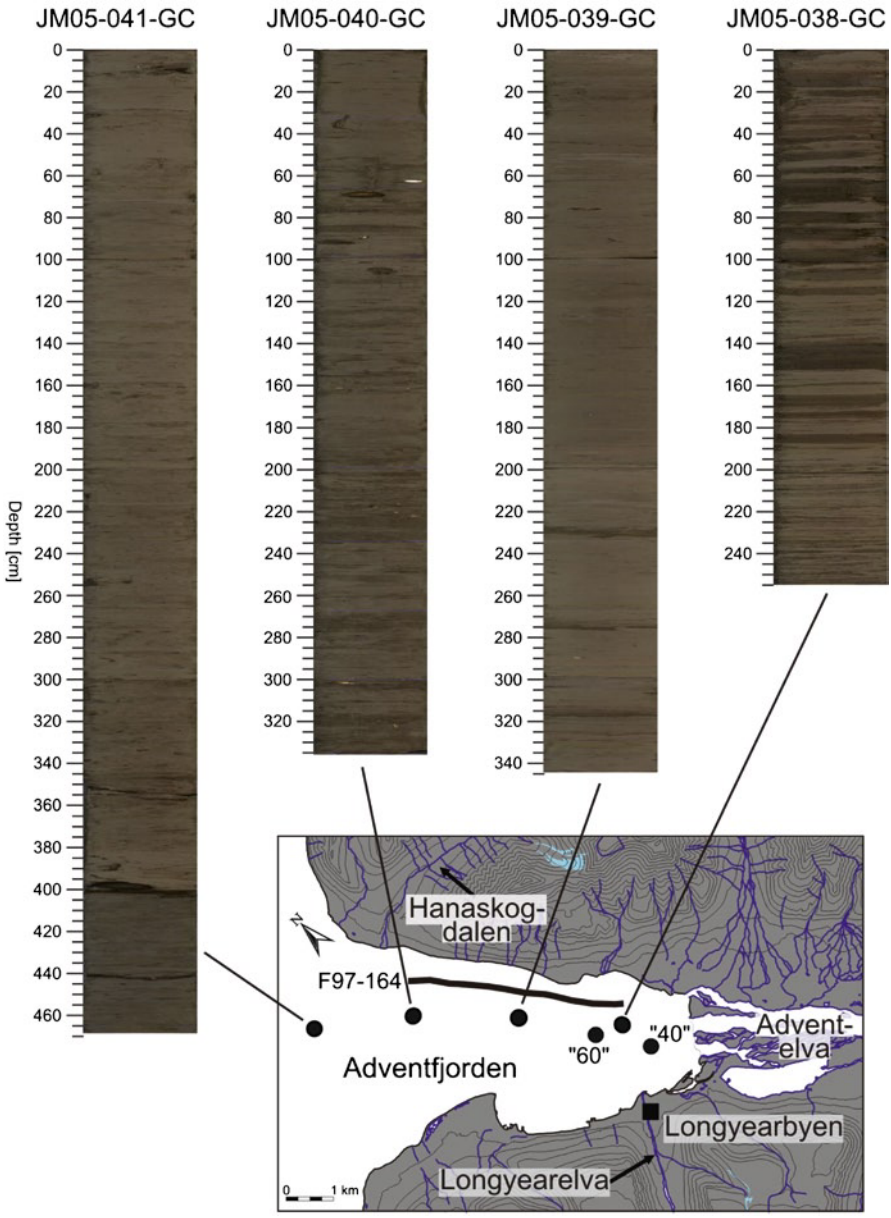

Fig. 63.4 Colour images of sediment cores from Adventfjorden. Turbidites are reflected by darker intervals. The *solid black line* on the map indicates the location of the 3.5 kHz penetration echo sounder profile F97-164 shown on Fig. 63.3a. The numbers 40 and 60 show the locations of cores described by Zajączkowski and Włodarska-Kowalczuk 2007. For location of the inset map see Fig. 63.1c

usually thinner than 5 cm in the other cores. They are interpreted as turbidites mainly derived from slope failures on the delta of Adventelva.

The cores JM05-040-GC and JM05-041-GC contain turbidites indicating that sediment reworking also takes place in the outer parts of the fjord. This is most probably related to sediment supply from the river draining through Hanaskogdalen (Fig. 63.4).

Variable lithological compositions of the cores JM05-038-GC and JM05-039-GC, as well as the cores 40 and 60 of Zajączkowski and Włodarska-Kowalczuk 2007 (for locations see Fig. 63.4; Table 63.1) indicate marked horizontal and vertical variations in sedimentation in the inner parts of Adventfjorden.

Recurrent mass wasting beyond river mouths was also reported from Svensksunddjupet, Billefjorden, Sassenfjorden and Tempelfjorden (for locations see Fig. 63.1c; Baeten 2007; Forwick and Vorren 2007; Forwick et al. 2010; Szczuciński and Zajączkowski in press). Acoustically stratified sediments in Grønfjorden most probably reflect lithological variations related to mass wasting on the river delta of Grøndalselva (for locations see Fig. 63.1c; compare with Elverhøi et al. 1983).

63.4.3 Other MTDs

The slopes not directly supplied with sediments from glaciers and rivers are also occasionally affected by mass wasting (e.g., Elverhøi et al. 1983). Fourteen, partly erosive MTDs of maximum 6 m thickness and lateral extents of about 4,750 × 4,000 m^2 were described from Svensksunddjupet (Forwick and Vorren 2007).

Numerous sediment lobes, up to 500 m long, 500 m wide and less than 5 m thick enter Ymerbukta from the fjord sides (Fig. 63.2b). These can be debris-flow deposits or slumps. Stacked deposits on the eastern side seem to originate from the same source. High-resolution seismics (Fig. 63.3b) reveal that several lobes on the eastern side of the fjord were deposited synchronously and that they are presently covered with approx. 3 m of sediment. In Trygghamna, sediment lobes are generally less well outlined on the seafloor compared to Ymerbukta (Fig. 63.2). However, two areas with several slide blocks occur close to the western slope. Whereas the largest block close to the fjord mouth is approx. 80 m wide, 40 m long and 2 m high, the blocks from the slide in the inner parts of the fjord are maximum 150 m wide, about 100 m long and up to 8 m high.

63.5 Chronology

Numerous sandy MTDs and sediment wedges were deposited during the deglaciation of the study area between 14,100 and 11,200 cal. years BP (Forwick and Vorren 2009, 2011). Regional and local mass wasting occurred in Svensksunddjupet and Sassenfjorden/Tempelfjorden occasionally during the early and mid Holocene (for locations see Fig. 63.1c; Forwick and Vorren 2007; Forwick et al. 2010).

The stratigraphic locations of the MTDs in Ymerbukta suggest that these are of late Holocene age (Fig. 63.3b). 'Fresh' looking and partly superposing MTDs, e.g., along the fjord sides in inner Ymerbukta (Fig. 63.2b), Billefjorden (Baeten 2007) and Tempelfjorden (Forwick et al. 2010) indicate relatively recent mass wasting beyond river mouths. Sediment lobes were deposited proximal to all tidewater glaciers during the Little Ice Age (Elverhøi et al. 1995; Boulton et al. 1996; Plassen et al. 2004; Ottesen and Dowdeswell 2006; Forwick and Vorren 2011). Modern sediment reworking was suggested and observed beyond river mouths in Adventfjorden and Billefjorden (Prior et al. 1981; Zajączkowski and Włodarska-Kowalczuk 2007; Szczuciński and Zajączkowski in press).

63.6 Discussion

63.6.1 Pre-conditions and Trigger Mechanisms

Pre-conditions and trigger mechanisms for slope failures in the study area include (1) seismic activity due to rapid postglacial isostatic rebound; (2) rapid progradation and deposition and/or increased sediment supply; (3) cyclic loading induced by surface waves and/or low tides; (4) increased pore pressure as consequence of relative sea-level fall and/or presence of gas (e.g., Prior et al. 1981; Baeten 2007; Forwick and Vorren 2007, 2009, 2011; Zajączkowski and Włodarska-Kowalczuk 2007; Forwick et al. 2010; Szczuciński and Zajączkowski in press).

Because the largest numbers of MTDs was identified in front of rivers and glaciers, rapid sedimentation, locally supported by tidal variations, is the most likely contributing factor. Earthquakes can trigger submarine landslides at present times, because old fault zones are occasionally still active (Pirli et al. 2010). However, their frequency is probably significantly reduced compared to shortly after the deglaciation when the isostatic uplift was much more rapid than at present (e.g., Stewart et al. 2000; Forman et al. 2004).

63.6.2 Comparison to Other Fjords

63.6.2.1 Size and Composition

The relatively large sizes and volumes of glacigenic MTDs, in comparison to fluvial MTDs, as well as various degrees of sorting might be explained in the way that advancing glacier fronts remobilise and mix significant amounts of sediments that are subsequently deposited during a single event and/or as a continuously failing, mobile push moraine during the readvance (e.g., Plassen et al. 2004; Kristensen et al. 2009). The more continuous supply of sediments to river deltas, on the other hand, lead to more frequent, smaller and better sorted MTDs.

63.6.2.2 Run-Out Distance

The large-scale bathymetry in the study area limits the maximum run-out distance of MTDs to approx. 25 km, but no available data provides evidence of such long travel distances. The MTDs that probably travelled the longest distances are the glacigenic turbidites in central Isfjorden (in core JM98-845-PC; for location see Fig. 63.1; Table 63.1; Forwick and Vorren 2009). Assuming that their source area was either located at the mouth of Adventfjorden or to the northeast of the core site, they have travelled maximum about 11 km. This is in the same order as for fluvial turbidites in Kangerdluk (Disko Fjord) on west Greenland (e.g., Gilbert et al. 2002). However, it is significantly shorter than in Bute Inlet (British Columbia) where distances of up to 50 km were observed (Prior et al. 1987).

63.6.2.3 Turbidity-Flow Activity

Chutes and levees are usually characteristic features for increased turbidity-flow activity in many fjord regimes, and recurrent turbidity-flow activity was reported beyond the fronts of tidewater glaciers in temperate and sub-polar regimes (e.g., Gilbert 1983 and references therein; Mackiewicz et al. 1984). Acoustic and lithological data from the deltas off Adventelva, Festningselva and Sassenelva (Prior et al. 1981; Forwick and Vorren 2007; Forwick et al. 2010; this study) show that chutes frequently act as pathways for (partly erosive) turbidity flows also in the Isfjorden area (for location see Fig. 63.1c).

The tidewater glaciers in the study area reached their maximum late Holocene extents during the Little Ice Age and/or at the termination of surges. Several sediment cores from Billefjorden, Tempelfjorden, Yoldiabukta and Borebukta penetrate the top of glacigenic debris lobes or other sediments that were deposited during or after these maximum Holocene extents (Plassen et al. 2004; Baeten 2007; Forwick et al. 2010). Even though increased meltwater runoff during surges and increased sediment supply should be expected (compare with Gilbert et al. 2002), no signs of increased turbidity-flow activity are found in the study area (see e.g., Forwick et al. 2010). This might indicate that the glacier fronts retreated quickly from their maximum extents and that turbidity-flow deposition occurred on the backslopes of the terminal moraines, or that flows originating from the grounding lines were trapped proximal to the terminal moraine.

63.6.2.4 Enhanced Mass Wasting Shortly After the Ice Retreat

The deposits of recurrent slope failures shortly after the deglaciation were observed several fjords (e.g., Forwick and Vorren 2002; Hjelstuen et al. 2009). Glacigenic debris lobes of Late Weichselian age in the study area might have been deposited shortly after the ice retreat (Forwick and Vorren 2011). Additionally, a single event around 9,650 cal. years BP, leading to simultaneous failures on several slopes of Svensksunddjupet (for locations see Fig. 63.1c), was ascribed to seismic activity

related to enhanced postglacial isostatic uplift (Forwick and Vorren 2007). However, the limited lateral distribution of such events indicates that mass wasting shortly after the deglaciation was not very pronounced, as e.g., on mainland Norway (e.g., Hjelstuen et al. 2009). Explanations for this difference might be (1) different sizes of the catchment areas and, hence different amounts of sediments available; (2) colder basal regimes beneath a thinner ice cover on Svalbard, compared to more temperate regimes beneath thicker glaciers in Norway (Siegert and Dowdeswell 2002) and hence reduced erosion and sediment supply; (3) reduced seismic activity due to less and/or slower isostatic rebound (compare Forman et al. 2004 with Vorren et al. 2008); (4) too rapid deglaciation preventing the deposition of sufficient amounts of sediments to cause instabilities.

63.6.2.5 Amount of Reworked Sediments

The amount of reworked sediments can vary between >50% and not more than 5% in fjords in Norway and east Greenland (Holtedahl 1975; Syvitski et al. 1996; Hjelstuen et al. 2009). In the Isfjorden area, the amount of reworked material may exceed 50% in the vicinity of large braided river systems (e.g., core JM05-038-GC). However, the available data indicates that – apart from local exceptions – mass wasting plays a minor role for the sediment accumulation in the Isfjorden area.

63.7 Conclusions

- The Isfjorden area has been exposed to recurrent submarine mass wasting since the deglaciation of the mouth of Isfjorden, approx. 14,100 years ago.
- Mass wasting is particularly pronounced on slopes in front of tidewater glaciers and river deltas.
- Mass-transport deposits include slides, slumps, debris-flow deposits and turbidites.
- The most frequent pre-conditioning factors and trigger mechanisms are probably high sediment supply and earthquakes.
- Several similarities between the study area and other fjord settings exist with regard to landform assemblages, run-out distances and the amount of reworked sediments. A striking difference is, however, the absence of turbidites distal to terminal moraines deposited during the late Holocene.

Acknowledgements The new data presented in this study was collected during the strategic university programmes *Sedimentary Processes and Palaeoenvironment in Northern Fjords* (SPINOF; 1997–2001) and *Sedimentary Processes and Palaeoenvironment on Northern Continental Margins* (SPONCOM; 2002–2006) at the Department of Geology, University of Tromsø. Both programmes were financed by the Research Council of Norway. We thank the masters and crews of R/V *Jan Mayen* for their assistance at sea. Steinar Iversen and Jan P. Holm are acknowledged for their invaluable support during and after the data collection. Det norske oljeselskap asa is acknowledged for the financial support of MF during writing of the manuscript. Finally, we thank editor Yujiro Ogawa and Maarten Vanneste for their constructive reviews of the manuscript.

References

Aarseth I, Lønne Ø, Giskeødegaard O (1989) Submarine slides in glaciomarine sediments form some western Norwegian fjords. Mar Geol 88:1–21

Baeten N (2007) Late Weichselian and Holocene sedimentary processes and environments in Billefjorden, Svalbard. M.Sc. Thesis, University of Tromsø

Boulton GS, van der Meer JJM, Hart J, Beets D, Ruegg GHJ, van der Wateren FM, Jarvis J (1996) Till and moraine emplacement in a deforming bed surge - an example from a marine environment. Quat Sci Rev 15:961–987

Elverhøi A, Lønne Ø, Seland R (1983) Glaciomarine sedimentation in a modern fjord environment, Spitsbergen. Polar Res 1:127–149

Elverhøi A, Svendsen JI, Solheim A, Andersen ES, Milliman J, Mangerud J, Hooke RL (1995) Late quaternary sediment yield from the High Arctic Svalbard Area. J Geol 103:1–17

Forman SL, Lubinski DJ, Ingólfsson Ó, Zeegerg JJ, Snyder JA, Siegert MJ, Matishov GG (2004) A review of postglacial emergence on Svalbard, Franz Josef Land and Novaya Zemlya, northern Eurasia. Quat Sci Rev 23:1391–1434

Forwick M, Vorren TO (2002) Deglaciation history and post-glacial mass movements in Balsfjorden, northern Norway. Polar Res 21:259–266

Forwick M, Vorren TO (2007) Holocene mass-transport activity in and climate outer Isfjorden, Spitsbergen: marine and subsurface evidence. Holocene 17:707–716

Forwick M, Vorren TO (2009) Late Weichselian and Holocene sedimentary environments and ice rafting in Isfjorden, Spitsbergen. Palaeogeogr Palaeocl 280:258–274

Forwick M, Vorren TO (2011) Stratigraphy and deglaciation of the Isfjorden area, Spitsbergen. Nor J Geol 90:163–179

Forwick M, Baeten NJ, Vorren TO (2009) Pockmarks in Spitsbergen fjords. Nor J Geol 89:65–77

Forwick M, Vorren TO, Hald M, Korsun S, Roh Y, Vogt C, Yoo K-C (2010) Spatial and temporal influence of glaciers and rivers on the sedimentary environment in Sassenfjorden and Tempelfjorden, Spitsbergen. In: Howe JA, Austin WEN, Forwick M, Paetzel M (eds) Fjord systems and archives, vol 344. Geological Soceity Special Publications, London, pp 163–193

Gilbert R (1983) Sedimentary processes of Canadian Arctic fjords. Sediment Geol 36:147–175

Gilbert R, Nielsen N, Möller H, Desloges JR, Rasch M (2002) Glacimarine sedimentation in Kangerdluk (Disko Fjord), West Greenland, in response to a surging glacier. Mar Geol 191:1–18

Hjelstuen BO, Haflidason H, Sejrup HP, Lysså A (2009) Sedimentary processes and depositional environments in glaciated fjord systems – Evidence from Nordfjord, Norway. Mar Geol 258:88–99

Holtedahl H (1975) The geology of the Hardangerfjord, West Norway. Norg Geol Unders 323:1–87

Killingtveit Å, Petterson L-E, Sand K (2003) Water balance investigations in Svalbard. Polar Res 22:61–174

Kristensen L, Benn DI, Hormes A, Ottesen D (2009) Mud aprons in front of Svalbard surge moraines: evidence of subglacial deforming layers or proglacial tectonites? Geomorphology 111:206–221

Longva O, Janbu N, Blikra LH, Bøe R (2003) The 1996 Finneidfjord slide; seafloor failure and slide dynamics. In: Locat J, Mienert J (eds) Submarine mass movements and their consequences. Kluwer, Dordrecht, pp 531–538

Mackiewicz NE, Powell RD, Carlson PR, Molnia BF (1984) Interlaminated ice-proximal glaciomarine sediments in Muir Inlet, Alaska. Mar Geol 57:113–147

Ottesen D, Dowdeswell JA (2006) Assemblages of submarine landforms produced by tidewater glaciers in Svalbard. J Geophys Res 111. doi:10.1029/2005/JF000330

Pirli M, Schweitzer J, Ottemöller L, Raeesi M, Mjelde R, Atakan K, Guterch A, Gibbons SJ, Paulsen B, Dębski W, Wiejacz P, Kværna T (2010) Preliminary analysis of the 21 February 2008 Svalbard (Norway) seismic sequence. Seismol Res Lett. doi:10.1785/gssrl.81.1.63

Plassen L, Vorren TO, Forwick M (2004) Integrated acoustic and coring investigations of glacigenic deposits in Spitsbergen fjords. Polar Res 23:89–110

Prior DB, Wiseman JWJ, Bryant WR (1981) Submarine chutes on the slopes of fjord deltas. Nature 290:326–328

Prior DB, Bronhold BD, Wiseman JWJ, Lowe DL (1987) Turbidity current activity in a British Columbia fjord. Science 237:1330–1333

Siegert MJ, Dowdeswell JA (2002) Late Weichselian iceberg, surface-melt and sediment production from the Eurasian ice sheet: results from numerical ice-sheet modelling. Mar Geol 188:109–227

Stewart IS, Sauber J, Rose J (2000) Glacio-seismotectonics: ice sheets, crustal deformation and seismicity. Quat Sci Rev 19:1367–1389

Syvitski JPM, Burrell DC, Skei JM (1987) Fjords – processes and products. Springer, New York

Syvitski JPM, Andrews JT, Dowdeswell JA (1996) Sediment deposition in an iceberg-dominated glacimarine environment, East Greenland: basin fill implications. Glob Planet Change 12:251–270

Szczuciński W, Zajączkowski M (in press) Factors controlling downward fluxes of particulate matter in glacier-contact and on-glacier contact settings in a subpolar fjord (Billefjorden, Svalbard). In: Li M, Sherwood C, Hill P (eds) Sediments, morphology and sedimentary processes on continental shelves. IAS Special Publication, Wiley-Blackwell Publishing 44

Vorren TO, Mangerud J, Blikra LH, Nesje A, Sveian H (2008) The emergence of modern Norway. In: Ramberg I, Brynhi I, Nøttvedt A, Rangnes K (eds) The making of a land – geology of Norway. Geological Society of Norway, Trondheim, pp 534–559

Zajączkowski M, Włodarska-Kowalczuk M (2007) Dynamic sedimentary environments of an Arctic glacier-fed river estuary (Adventfjorden, Svalbard): I. flux, deposition, and sediment dynamics. Estuar Coast Shelf S 74:285–296

Chapter 64
Comparison of Quaternary Glaciogenic Debris Flows with Blocky Mass-Transport Deposits in Orphan Basin, Offshore Eastern Canada

Gang Li, D. Calvin Campbell, David Mosher, and David J.W. Piper

Abstract Quaternary deposits in southern Orphan Basin include complex mass transport deposits (MTD) comprising both glaciogenic debris flows (GDF) and blocky MTD. 3D seismic reflection data were used to highlight the difference between the two types of MTD. The main MTD in southern Orphan Basin were sourced from the slope off Trinity Trough in the west of the basin. On the Trinity Trough-mouth Fan, a succession of GDF was deposited above horizon B5, interpreted to date from Marine Isotope Stage (MIS) 12. Beyond the direct influence of Trinity Trough, MTD unit 2 below horizon B5 is confined within pre-existing channels, which are in approximately the same location as the modern Bonanza Channel and Sheridan Channel. Blocky MTD are characterized by linear and divergent basal grooves and chaotic internal facies. Dispersed blocks, less than 1 km^2 in area, are commonly present within the blocky MTD on the southern Orphan slope. The tongue of the main Sheridan MTD is sharp-edged, with a series of closely spaced pressure ridges. 3D seismic data of GDFs show few features diagnostic of blocky MTD. Both stacked GDF lobes and channelized GDF are observed on Trinity Trough-mouth Fan.

Keywords 3D seismic volume • Horizon B5 • Failure corridor • Trough-mouth fan

G. Li (✉)
Department of Coastal Ocean Science, Nanjing University, Nanjing 210093, China
e-mail: gangli1@hotmail.com

D.C. Campbell • D. Mosher • D.J.W. Piper
Geological Survey of Canada (Atlantic), Bedford Institute of Oceanography, 1006, Darmouth, NS, B2Y 4A2 Canada

Y. Yamada et al. (eds.), *Submarine Mass Movements and Their Consequences*,
Advances in Natural and Technological Hazards Research 31,
DOI 10.1007/978-94-007-2162-3_64, © Springer Science+Business Media B.V. 2012

64.1 Introduction

Orphan Basin is a large submarine embayment located offshore eastern Canada (Fig. 64.1). Two-dimensional (2D) high-resolution seismic reflection profiles and piston cores acquired over the slope and basin floor display a complex history of mass transport deposition, with variations in depositional geometry and acoustic facies throughout the Quaternary (e.g., Hiscott and Aksu 1996; Campbell 2005; Deptuck et al. 2007; Tripsanas and Piper 2008). A major change in mass transport deposit (MTD) acoustic facies occurred around 500 ka (Campbell 2005). Prior to this, MTDs consist of slumps and slides and show acoustically-chaotic facies. Beginning around MIS 12 (~500 ka), MTD are predominantly glaciogenic debris flows (GDFs) sourced from a major transverse trough on the shelf-Trinity Trough (Fig. 64.1). These GDFs are acoustically transparent, forming stacked lenticular lobes, and appear less erosional.

In this paper, new results from three-dimensional (3D) industrial seismic reflection data are presented that illustrate the changes in MTD seismic geomorphology

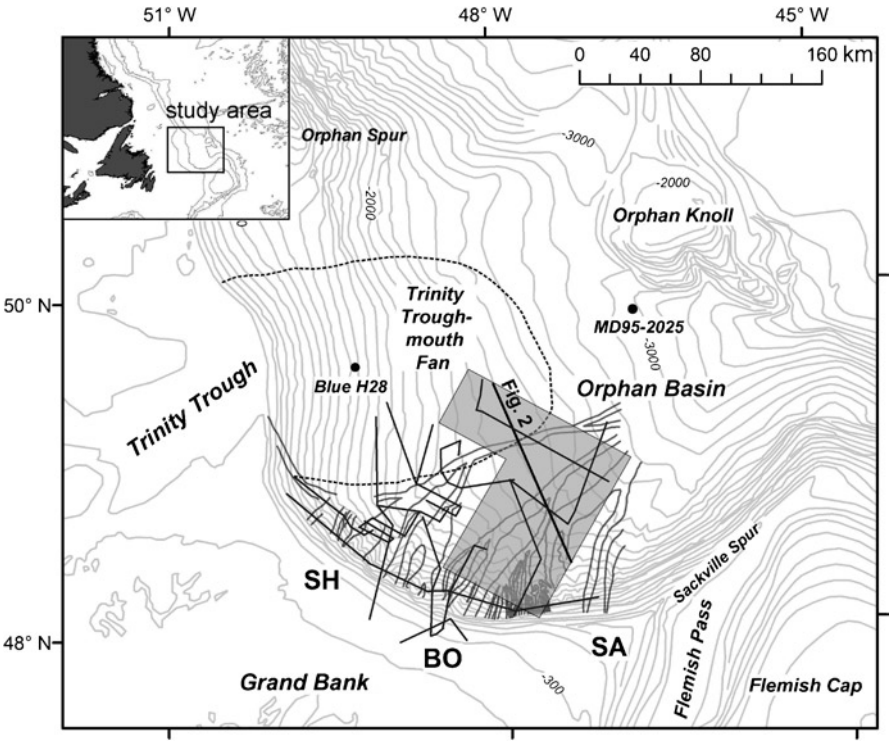

Fig. 64.1 Map of southern Orphan Basin showing regional bathymetry in meters, 3D seismic seismic survey (*grey boxes*), 2D seismic reflection profiles (*black lines*), location of Fig. 64.2, the Blue H28 well and MD95-2025. Modern canyon systems are redrawn from Tripsanas et al. (2008). *SH*: Sheridan Canyon, *BO*: Bonanza Canyon, *SA*: Sackville Canyon

in Orphan Basin. The 3D seismic geomorphology of GDFs has rarely been described in the literature, therefore the purpose of this paper is to characterize features that are likely unique to GDFs and highlight differences between these deposits and the underlying MTD.

64.2 Regional Geology

Orphan Basin formed through rifting of the North Atlantic in the late Mesozoic, followed by the deposition of a thick sedimentary succession north and northeast of Grand Bank of Newfoundland (Hogg and Enachescu 2007). The modern slope morphology is greatly influenced by Quaternary glaciation. The central slope is smooth and has a low gradient of 1–2°. A trough-mouth fan fed by glacial sediments is located seaward off Trinity Trough. This wedge consists of stacked MTD and acoustically stratified units (Hiscott and Aksu 1996). The south slope, between Trinity Trough-mouth Fan and Sackville Spur, has a much steeper gradient (4–6°) and is incised by numerous canyons. Three channel systems are informally designated the Sheridan Canyon, Bonanza Canyon and Sackville Canyon (Fig. 64.1) (Tripsanas and Piper 2008).

64.3 Methods

The 3D seismic reflection survey covers an area of 10,770 km^2 along the lower slope and deep basin in water depths from 1,600 to 2,600 m (Fig. 64.1). The spatial resolution of this 3D seismic survey grid is 25 m. The maximum vertical resolution of 3D seismic survey is 6 m with a frequency of 75 Hz. The upper 0.5 s (twtt) of seismic data were available for this study. A reprocessed high resolution subset of the 3D data provides a maximum vertical resolution of ~2 m (at 200 Hz). Previously acquired 2D high-resolution seismic reflection profiles by the Geological Survey of Canada (GSC) collected between 1999 and 2005 aided seismic correlation in areas not covered by the 3D survey. The single-channel 2D seismic reflection profiles have a vertical resolution of ~1 m and image ~1 s (twtt) of the subsurface. The workflow for interpreting the 3D seismic volume is followed as Posamentier et al. (2007). Stratal slicing or proportional slicing is adopted in which the slice is made by proportionally sampling of seismic traces between two seismic horizons.

64.4 Results

64.4.1 Seismic Stratigraphy

This study focuses on Quaternary MTD in southern Orphan Basin. Five horizons bounding the main MTD units were traced in the 3D seismic volume (Fig. 64.2 and

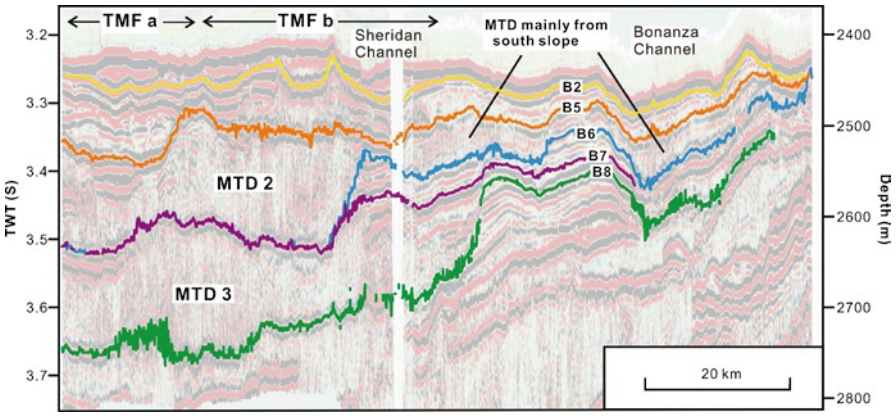

Fig. 64.2 3D seismic section in the southern Orphan Basin defining the main interpreted horizons and mass-transport-deposit units. The spatial scale of *TMF a* and *TMF b* can be found on Fig. 64.4a. The 3D seismic data were acquired by Chevron, ExxonMobil, imperial Oil and Shell

Table 64.1 Seismic stratigraphy used in this study

Key horizons (Campbell 2005)	Interpreted horizons (this study)	Main MTD units		Estimated chronology
Blue	B2	MTD 1	Mainly GDF	MIS 2
Yellow	B5	MTD 2	Non-glaciogenic MTD	MIS 12
	B6			Early–Middle Pleistocene
	B7	MTD 3	Non-glaciogenic MTD	
	B8			
Purple		Regional unconformity		Early Pleistocene

Table 64.1). Constrained by piston cores and high resolution Huntec profiles (Tripsanas and Piper 2008), horizon B2 corresponds to the base of GDF deposits in MIS 2 from Trinity Trough. Horizon B5 corresponds to the reflector Yellow defined by Hiscott and Aksu (1996) and Campbell (2005), marking the base of the GDF succession on the central Trinity Trough-mouth Fan. The age of horizon B5 was estimated as ~500 ka (MIS 12) from correlation with core MD95-2025 (Tripsanas et al. 2007). Below horizon B5, MTD have a much larger volume, with a thickness over 75 m and a width over 20 km. Three more horizons, termed B6, B7 and B8, bound two pre-MIS 12 MTD sequences (Fig. 64.2). The three horizons are located above a regional Early Pleistocene (1.8 Ma) seismic marker (Campbell 2005) (Table 64.1) correlated from the Blue H-28 well. B6, B7 and B8 are estimated to be younger than 1 Ma based on average sedimentation rates in some sites where only thin MTD are present (Campbell 2005) (Table 64.1).

64.4.2 Pre-MIS 12 Blocky Mass Transport Deposits (MTDs 2 and 3)

Figure 64.3 presents the detailed internal structure of the non-glaciogenic mass transport deposits in MTD unit 2. The MTD are characterized by chaotic and disrupted seismic facies which are easily discriminated from the undisturbed sediments. Blocks with undisturbed internal structure are dispersed in the MTD bodies. Most bocks are less than 1 km^2 except for some unusual blocks which are larger than 5 km^2. Floating and in-situ blocks are observed in cross sections. The in-situ blocks are rooted in the strata below and are likely erosional remnants, whereas the floating blocks overlie MTD and some floating blocks are deformed. In the toe domain of the main Sheridan MTD (MTD a), arcuate pressure ridges (C in Fig. 64.3) are observed. The toe domain is approximately 15 km long and 10 km wide and covered an area of approximately 120 km^2.

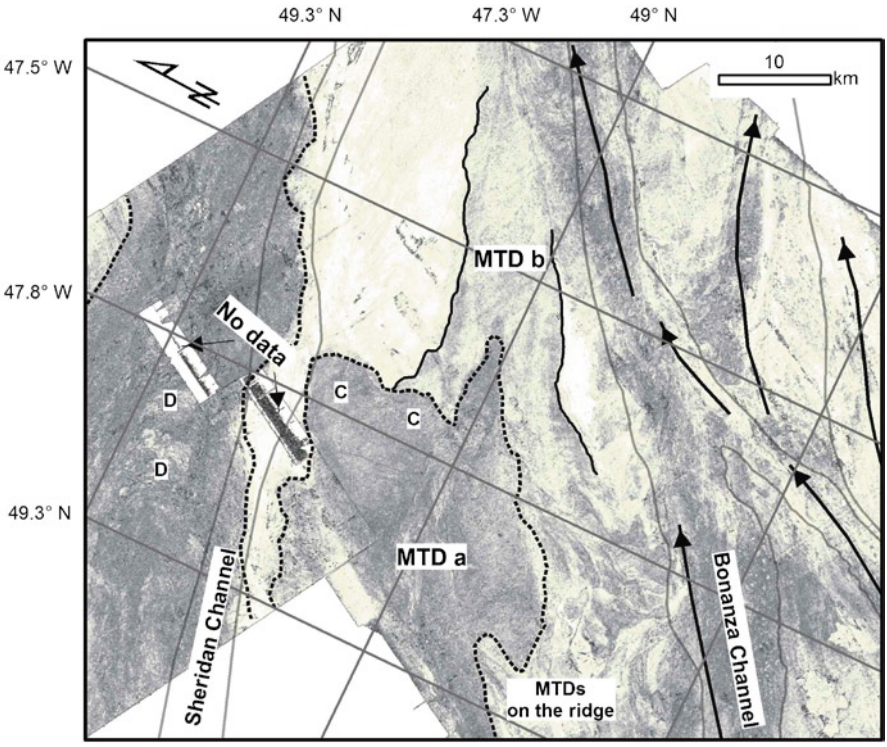

Fig. 64.3 Coherency map of the stratal slice through MTD unit 2 (1/3 thickness above B6). *Arrows* show the direction of movement inferred from the pattern of basal grooves. *D*: blocks; *C*: arcuate pressure ridges; Two part of the Sheridan MTD were divided: *MTD a* (highly deformed blocky MTD) and *MTD b* (less deformed MTD). The location of Fig. 64.3 is labeled on Fig. 64.4b. The 3D seismic data were acquired by Chevron, ExxonMobil, imperial Oil and Shell

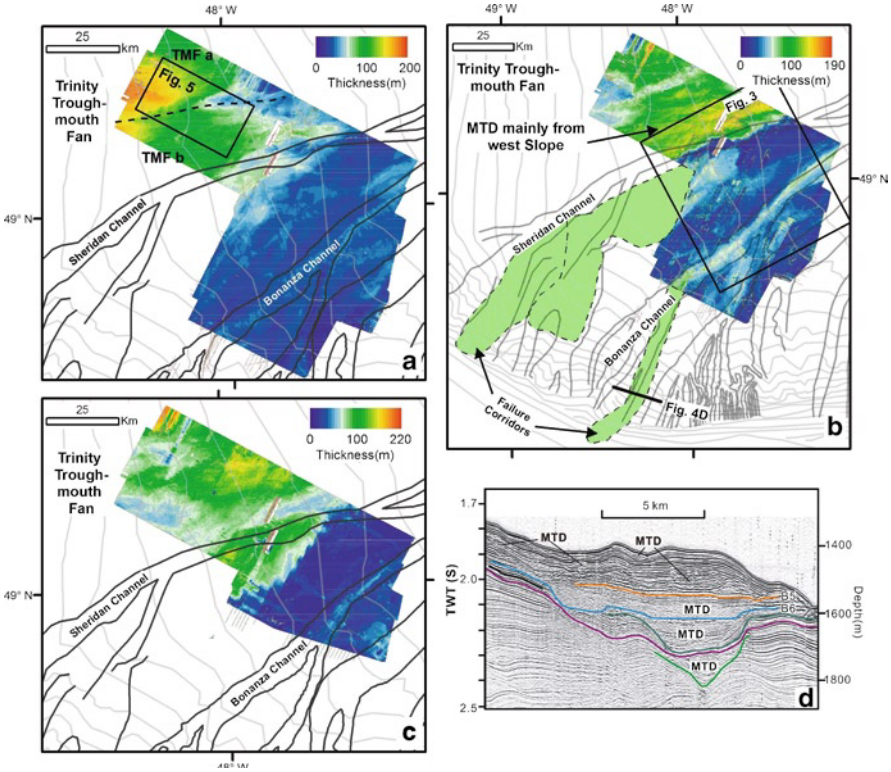

Fig. 64.4 *Thickness* map showing the spatial distribution of MTD: (**a**) Sediment thickness between B5 and the sea floor (MTD unit 1); (**b**) Thickness map of MTD unit 2. The approximate route of MTD unit 2 on the slope was determined from 2D seismic profiles (partly from Campbell 2005); (**c**) Thickness map of MTD unit 3; (**d**) 2D seismic profile on the middle slope showing stacked MTD constrained by the old Bonanza Canyon. The 3D seismic data were acquired by Chevron, ExxonMobil, imperial Oil and Shell

Thickness maps of horizons B6–B5 and B8–B7 define the distribution of MTD units 2 and 3 (Figs. 64.2 and 64.4b, c). MTD units 3 and 2 are thickest (> 150 m) north of Bonanza Channel (Fig. 64.4). The coherency map of the stratal slice within MTD 3 exhibits secondary slide along the MTD margin, likely triggered by the main mass movement. The lateral silde is 10–15 km wide and consists of parallel to subparallel blocks. Most blocks are hundreds of meters wide and are truncated by high-angle faults. The spatial alignment of these blocks suggests that they are locally derived from undisturbed sediments in the deep basin, not from the upper slope. The prevailing strike of the linear blocks is at a ~ 20–30° angle with the undisturbed edge. The total volume of the lateral slide is over 50 km^3.

The thickness map of MTD unit 2 shows three separate sources. The northernmost MTD with maximum thickness over 150 m was likely sourced from the western

slope of Orphan Basin (Fig. 64.4b). In southern Orphan Basin, two channelized MTD bodies are in approximately the same location as the overlying Bonanza Channel and Sheridan Channel. 2D seismic profiles were used to determine the source of channelized MTDs on the slope (Fig. 64.4b). In both cases, multiple stacked MTD fill failure corridors on the slope and MTD distribution suggests the source area along the southern slope of Orphan Basin (Fig. 64.4d). The Sheridan Channel failure corridor is over 13 km wide while the Bonanza Channel failure corridor is about 6 km wide. (Fig. 64.4b). 2D seismic reflection data seaward of the 3D seismic datasets show that both channelized MTDs eventually coalesce. On the ridges between the Bonanza MTD and the Sheridan MTD, complex chaotic patches (Fig. 64.3) indicate secondary mass movement features/events confined to the channels. Downslope from the highly deformed Sheridan MTD (MTD a in Fig. 64.3), a less-chaotic deposit (MTD b in Fig. 64.3) with fewer deformation structures has run out from the main MTD.

64.4.3 Post-MIS 12 GDF Mass Transport Deposits (MTD 1)

Above horizon B5, the GDFs have transparent acoustic character (Fig. 64.2; also illustrated by Tripsanas and Piper 2008). Two types of GDF are shown: stacked GDF lobes and channelized GDFs (Fig. 64.5a). In the stacked GDF zone, the centers of individual GDF lobes are homogeneous, whereas the chaotic rims in seismic similarity delineate the boundaries of individual lobes in planview that result in an anastamosing pattern (Fig. 64.5a). The seafloor coherency map (Fig. 64.5b) depicts the small gullies distributed on the flank of the uppermost GDF lobes. Similarly, the chaotic-rim structure within the buried GDF strata may indicate small gullies at the margins and in between GDF lobes. These elongate lobes are 3–5 km wide. The plan view geometry apparent in the 3D seismic volume is consistent with published examples of multibeam bathymetry of GDFs (e.g., Laberg et al. 2010). Some GDFs constrained within submarine channels are shown in Fig. 64.5a. The base of these channels is flat and the width/depth ratio is between 300 and 500. Tripsanas and Piper (2008) showed that these underlying channels were produced by melt-water erosion during earlier deglaciation. In cross-section, the two GDF types have transparent acoustic character, but distinct flow lines in the internal and top surface of the channelized GDF differentiate it from the stacked GDF (Fig. 64.5a).

The seismic geomorphology of the horizons above B5 appears to show that the northern Trinity Trough-mouth Fan (TMF a in Fig. 64.4a) completely consists of a GDF succession and in the southern Trinity Trough-mouth Fan (TMF b in Fig. 64.4a) the upper MTD are the GDF deposits. On the southern Trinity Trough-mouth Fan (TMF b), the lower MTD were interpreted as blocky non-glaciogenic MTD, with chaotic acoustic character similar to the underlying MTD units, and long, curvilinear basal grooves.

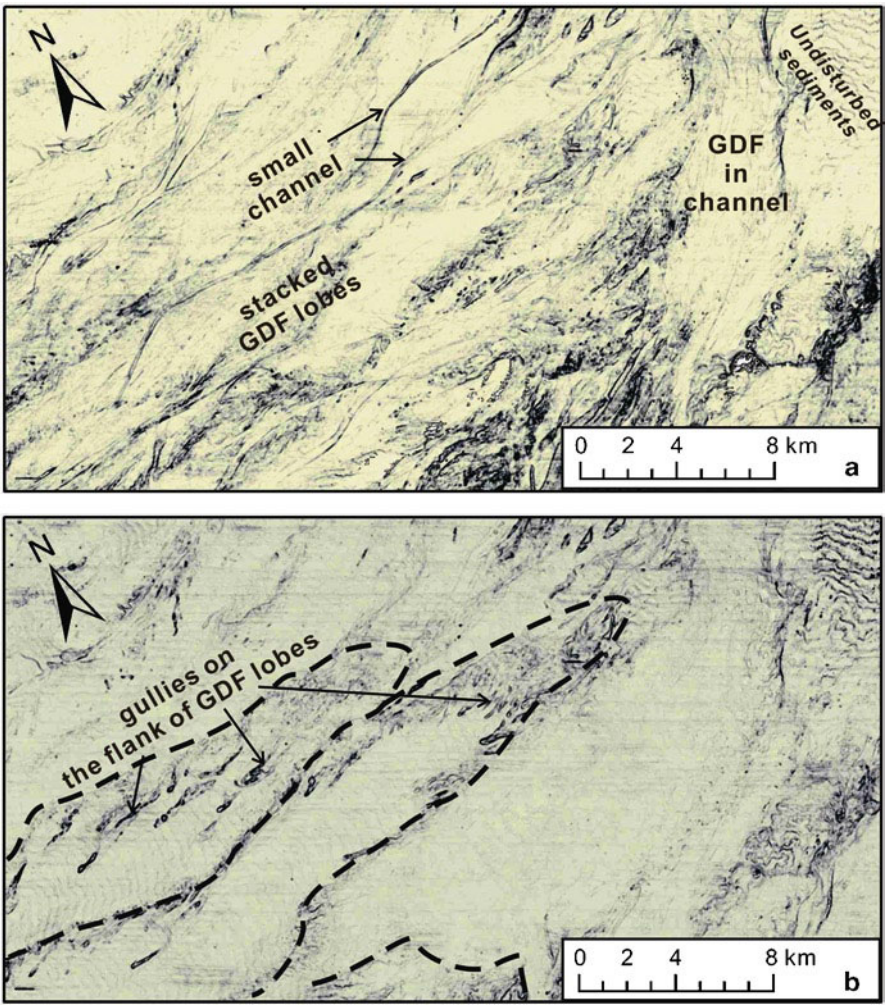

Fig. 64.5 Seismic geomorphology of the uppermost GDF deposits. (**a**) Coherency map of the stratal slice through GDF deposits (1/2 thickness above B2). Typical GDF lobes and GDF-fill channel are shown. Several narrow but long channels are labeled. (**b**) Sea-floor coherency map depicts the uppermost GDF lobes. Small gullies around GDF lobes are well-defined. Dash lines outline the uppermost lobes. The location of Fig. 64.5 is labeled on Fig. 64.4a. The 3D seismic data were acquired by Chevron, ExxonMobil, imperial Oil and Shell

64.5 Discussion

Hiscott and Aksu (1996) presented an industry multichannel seismic line on Trinity Trough-mouth Fan showing the sedimentary sequence and transparent wedges within this glacial sedimentary sequence. The sedimentary sequence of

Trinity Trough-mouth Fan is similar to the Lancaster Trough-mouth Fan in Baffin Bay, consisting of a lower aggradational sequence and an upper aggradation-progradational sequence (Li et al. 2011). In the case of Trinity Trough-mouth Fan, the lower aggradational sequence of Hiscott and Aksu (1996) contains three mounded wedges. The lower limit of these wedges is consistent with a lithological change in the Blue H-28 well presumably dated at 1.8 Ma, with the upper 550 mbsf consisting of unconsolidated sandy and gravelly sediment, consistent with their interpretation of glacial origin (Hiscott and Aksu 1996). The transition to the aggradation-progradational sequence in Orphan Basin coincides with the onset of deposition of distinct, acoustically transparent GDFs above horizon B5. By using the average sedimentation rate from the Blue H-28 well, this transition is estimated to occur at 0. 5 Ma (Campbell 2005).

Prior to the onset of GDF deposition, the thickness maps of MTD units 2 and 3 show the thickest MTD in the southern Orphan Basin were still sourced from Trinity Trough area (Figs. 64.4B and 64.4C). This suggests that Trinity Trough was the main outlet of an ice stream in the early–middle Pleistocene. However, mainly proglacial and glaciomarine sediments were deposited on the upper and middle slope during this time, causing the slope steepening. Eventually, these deposits were transported downslope by large-volume and low-frequency mass transport events, perhaps triggered by periodic earthquakes, the oversteepening of the upper slope, and ice loading, as inferred for blocky MTD on the Labrador margin by Deptuck et al. (2007). A nearly identical glacial margin evolution was recognized in the North Sea Fan, in a similar trough-mouth fan setting (King et al. 1996). The 3D seismic data indicate that these earlier thick MTD were blocky MTD, caused deformation of surrounding sediments, and likely incorporated local sediments as they moved down slope. Our data suggest that below the southern slope of Orphan Basin, outside the direct influence of Trinity Trough, MTD were confined within pre-existing channels and mass transport processes influenced the location of channels later in the Quaternary. For example, below MTD unit 2 (Fig. 64.2), there are indications that some channels formed before the overlying MTD. The 3D seismic data also show that several slides and slumps covering an area of 150 km^2 eventually became confined in channels. There is also evidence of both frontal confinement and emergence (Frey-Martinez et al. 2006), with compression structures at the toe of the Sheridan MTD and debris flows further basinward (Fig. 64.3).

In contrast, MTD unit 1 corresponds to higher-frequency, shelf-crossing glaciations in the middle–late Pleistocene. Glacial sediments transported by ice streams through Trinity Trough constructed the trough mouth fan and formed numerous stacked GDFs (Fig. 64.2). GDFs generally have long run-out distances and can flow on a low-gradient slope (Elverhøi et al. 1997). Where GDFs have been sampled (Tripsanas and Piper 2008) the internal structure commonly shows a high level of homogeneity both in the sedimentology and physical properties. The monotonous nature of the density and acoustic velocity of GDFs explains the high level of acoustic transparency of these deposits in seismic profiles. Our data show that many of the features diagnostic of MTD in seismic data (e.g., Posamentier and Kolla 2003; Bull et al. 2009) are absent in GDFs. For example, there is no evidence of translated or

"rafted" blocks, basal scour has not been observed, compressional features are absent, as well as chaotic internal reflectivity. Overall, there is little evidence of erosion associated with GDFs. They form low relief, shingled depositional lobes, filling inter-lobe depression and occasionally occupying ancestral channels. Their mounded and lobate appearance is likely enhanced by minor erosion of their margins by subsequent turbidity currents.

64.6 Conclusions

In southern Orphan Basin Quaternary MTD were mainly sourced from Trinity Trough. As previously shown, horizon B5 (approximately MIS 12) marks a change in style of MTDs. GDF are mainly present above B5 but MTD unit 1 (above B5) still contains some non-glaciogenic MTD on the southern part of Trinity Trough-mouth Fan. Below horizon B5, the deposits are dominated by blocky MTD.

On the southern slope, two failure corridors filled with multiple stacked MTDs were discovered by the integration of 3D seismic volume and 2D high-resolution seismic reflection profiles. The two failure corridors are in approximately the same location as the overlying Bonanza Channel and Sheridan Channel.

GDF and blocky MTD show distinctly different seismic geomorphologic features. Many of the features diagnostic of blocky MTD in 3D seismic data are absent in GDFs, with no internal deformation structures and no basal grooves. The basal feature of the GDF shows the less-erosional character. Subsequent remobilization on GDF lobes are indicated by many small gullies around the GDF lobes. Blocky MTD clearly show basal erosion, lateral shear, and both frontally confined and emergent terminations.

Acknowledgements Work supported by the Geoscience for East Coast Offshore Development project of the Geological Survey of Canada and by the Program for Energy R&D (PERD). Gang Li is supported by the China Scholarship Foundation. Our best thanks to Chevron, ExxonMobil, imperial Oil and Shell for provision of the upper part of their 3-D cube and permission to publish interpretations. We also thank the reviewers Lorena Moscardelli, Kimberly Jenner, Ned King and Francky Saint-Ange for improving this manuscript.

References

Bull S, Cartwright J, Huuse M (2009) A review of kinematic indicators from mass-transport complexes using 3D seismic data. Mar Petrol Geol 26:1132–1151

Campbell DC (2005) Major quaternary mass-transport deposits in southern Orphan Basin, offshore Newfoundland and Labrador. Geological survey of Canada. Curr Res 2005–D3

Deptuck ME, Mosher DC, Campbell DC, Hughes-Clarke JE, Noseworthy D (2007) Along slope variations in mass failures and relationships to major Plio-Pleistocene morphological elements, SW Labrador Sea. In: Lykousis V, Sakellariou D, Locat J (eds) Submarine mass movements and their consequences. Springer, Dordrecht, pp 299–306

Elverhøi A, Norem H, Andersen ES, Dowdeswell JA, Fossen I, Haflidason H, Kenyon NH, Laberg JS, King EL, Sejrup HP, Solheim A, Vorren T (1997) On the origin and flow behavior of submarine slides on deep-sea fans along the Norwegian–Barents Sea continental margin. Geo-Mar Lett 17:119–125

Frey-Martínez J, Cartwright J, James D (2006) Frontally confined versus frontally emergent submarine landslides: a 3D seismic characterization. Mar Petrol Geol 23:585–604

Hiscott RN, Aksu AE (1996) Quaternary sedimentary processes and budgets in Orphan Basin, southwestern Labrador Sea. Quat Res 45:160–175

Hogg JR, Enachescu ME (2007) Exploration potential of the deepwater petroleum systems of Newfoundland and Labrador Margins. In: Offshore technology conference, Houston

King EL, Sejrup HP, Haflidason H, Elverhøi A, Aarseth I (1996) Quaternary seismic stratigraphy of the North Sea Fan: glacially-fed gravity flow aprons, hemipelagic sediments, and large submarine slides. Mar Geol 130:293–315

Laberg JS, Andreassen K, Knies J, Vorren TO, Winsborrow M (2010) Late Pliocene–Pleistocene development of the Barents sea ice sheet. Geology 38:107–110

Li G, Piper DJW, Campbell DC (2011) The Quaternary lancaster sound trough-mouth fan, NW Baffin Bay. J Quat Sci 26:511–522

Posamentier HW, Kolla V (2003) Seismic geomorphology and stratigraphy of depositional elements in deep-water settings. J Sediment Res 73:367–388

Posamentier HW, Davies RJ, Cartwright JA, Wood L (2007) Seismic geomorphology - an overview. In: Davies RJ, Posamentier HW, Wood L, Cartwright JA (eds) Seismic geomorphology: applications to hydrocarbon exploration and production, vol 277. Geological Society, London, pp 1–14, Special Publications

Tripsanas EK, Piper DJW (2008) Glaciogenic debris-flow deposits of Orphan Basin, offshore eastern Canada: sedimentological and rheological properties, origin, and relationship to meltwater discharge. J Sediment Res 78:724–744

Tripsanas EK, Piper DJW, Jarrett KA (2007) Logs of piston cores and interpreted ultra-high-resolution seismic profiles, Orphan Basin. Geological Survey of Canada Open File 5299

Tripsanas EK, Piper DJW, Campbell DC (2008) Evolution and depositional structure of earthquake-induced mass movements and gravity flows: Southwest Orphan Basin, Labrador Sea. Mar Petrol Geol 25:645–662

Chapter 65
Recent Submarine Landslides on the Continental Slope of Storfjorden and Kveithola Trough-Mouth Fans (North West Barents Sea)

Renata G. Lucchi, Maria T. Pedrosa, Angelo Camerlenghi, Roger Urgeles, Ben De Mol, and Michele Rebesco

Abstract Up to 12 submarine landslides retain a morphological evidence as concave amphitheater-like depressions of various sizes on the middle and upper slope of the Storfjorden and Kveithola Trough-Mouth Fans (TMFs), NW Barents Sea. The largest of them show lateral scarps 35–40 m high that reach the continental shelf edge and cover an area of at least 1,120 km^2. Submarine landslides are translational, with headwall and laterals scarps clearly cut into Last Glacial Maximum debris flows deposits. The largest landslides seem to be rooted at the base of a terrigenous/hemipelagic sedimentary unit inferred to be of Middle Weichselian age

R.G. Lucchi (✉)
Departament d'Estratigrafia Paleontologia y Geociències Marines, Facultat de Geología, Universitat de Barcelona, Barcelona, Spain

Istituto Nazionale di Oceanografia e di Geofisica Sperimentale (OGS), Trieste, Italy
e-mail: rglucchi@inogs.it

M.T. Pedrosa
Departament d'Estratigrafia Paleontologia y Geociències Marines, Facultat de Geología, Universitat de Barcelona, Barcelona, Spain

A. Camerlenghi
Departament d'Estratigrafia Paleontologia y Geociències Marines, Facultat de Geología, Universitat de Barcelona, Barcelona, Spain

ICREA, Istitució Catalana de Recerca i Estudis Avançats, Barcelona, Spain

R. Urgeles
Departament de Geologia Marina, Institut de Ciències del Mar (CSIC), Barcelona, Spain

B. De Mol
Institut de Ciències del Mar (CSIC), Passeig Marítim de la Barceloneta, 37-49, 08003 Barcelona, Catalonia, Spain

M. Rebesco
Dept. Estratigrafia, Paleontologia i Geociències Marines, Facultat de Geologia, Universitat de Barcelona, c/ Martí i Franquès s/n 08028, Barcelona, Catalonia, Spain

Parc Científic de Barcelona, c/ Adolf Florensa 8 08028, Barcelona, Catalonia, Spain

Y. Yamada et al. (eds.), *Submarine Mass Movements and Their Consequences*,
Advances in Natural and Technological Hazards Research 31,
DOI 10.1007/978-94-007-2162-3_65, © Springer Science+Business Media B.V. 2012

(Marine Isotopic Stage 3). Stratigraphic, lithological and geotechnical observations suggest that the rapid deposition of a thick sequence of fine-grained, high water content interlaminate plumites is the most important controlling factors in the generation of submarine landslides on the southern Storfjorden and Kveithola TMFs.

Keywords Barents Sea • Storfjorden • Kveithola • Trough-mouth fans • Ice stream • Submarine landslide • Debris flow

65.1 Introduction

High-latitude, glacially-influenced continental margins are prone to gravitational failure and generation of submarine landslides as result of highly variable sedimentation style and geological processes both spatially and temporally, which are closely related to the glacial-interglacial cyclicity (Lee 2009). Sedimentation on these margins is controlled by drastic increases in accumulation rate during short periods of glacial maxima (Dimakis et al. 2000; Elverhøi et al. 2002) when ice streams deliver dense sub-glacial sediments at the continental shelf edge. However, also deglaciation periods are characterized by rapid accumulation of sediments from subglacial melt-water discharge (Vorren et al. 1998; Lekens et al. 2005), whereas periods of lesser continental ice extent and interglacials are characterized by either slow hemipelagic sedimentation or deposition of contourites (Bryn et al. 2005; Laberg and Camerlenghi 2008).

The purpose of this article is to present novel evidence of recent widespread mass wasting of the southern sector of the Storfjorden and the Kveithola Trough-Mouth Fans (TMFs) in the NW Barents Sea (Fig. 65.1). These sectors of the margin contrast with adjacent northern Storfjorden continental slope lacking evidence of mass wasting. The stratigraphic information available in this area suggests onset of glacially influenced sedimentation in the Late Pliocene, when the Barents Sea Ice Sheet begun to reach the continental shelf edge episodically (Hjelstuen et al. 2007; Knies et al. 2009), with alternated deposition of glacigenic debris flows and interglacial sediments (Laberg and Vorren 1996). Compared to the larger Bjørnøya (Bear Island) TMF to the south, the Storfjorden TMF is steeper with a smaller size of the debris flows.

While detailed geotechnical investigations are in progress, we summarize physical properties, lithology and depositional processes of the uppermost sedimentary sequence. These are thought to contain important information for slope stability in the region.

65.2 Methods

The data presented in this article were collected during *BIO Hespérides* IPY cruise SVAIS (2007) and R/V *OGS-Explora* IPY Cruise EGLACOM (2008, Fig. 65.1). The two surveys resulted in a multibeam bathymetric coverage of about 15,340 km^2,

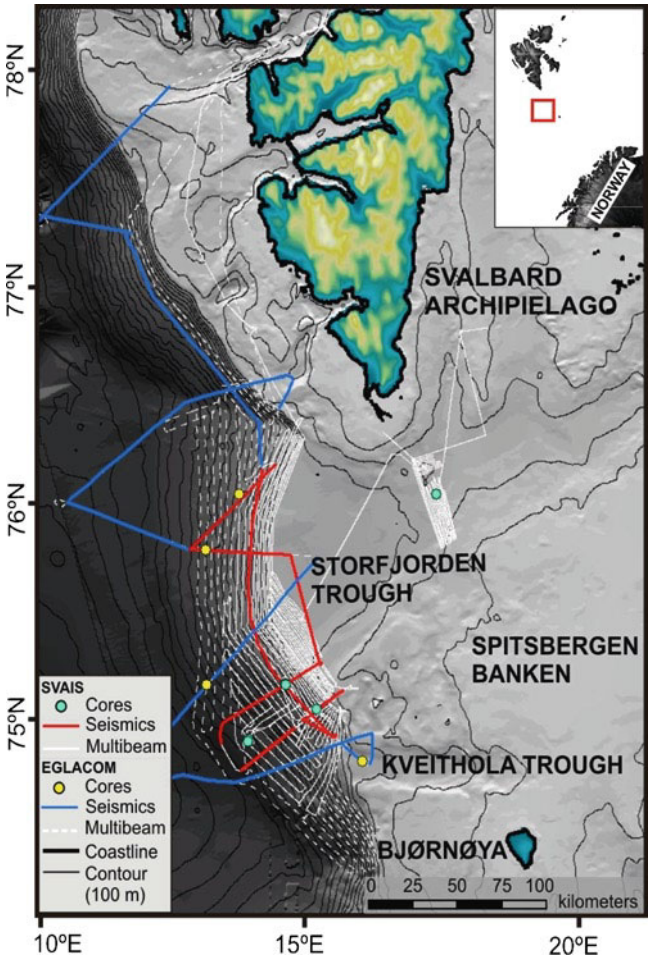

Fig. 65.1 Study area on the NW Barents Sea with multibeam and seismic records and location of the sediment cores collected within the SVAIS and EGLACOM projects

with a total length of acquired digital sub-bottom (TOPAS and Chirp) profiler data nearly 9,500 km. A total of ten piston and gravity cores were recovered on the continental slope and shelf of both TMFs systems. Preliminary data from the cruises are available in Colmenero-Hidalgo et al. (2009), Rebesco et al. (2011, 2012), and Pedrosa et al. (2011).

Sediment cores were analysed through an X-ray CT-scan, visually logged, photographed and scanned with a GEOTEK multi-sensor core logger (MSCL). Undrained shear strength was performed every 10 cm on clay/silty-clay intervals using both a British fall cone (Leroueil and Le Bihan 1996) and a motorized vane shear strength instrument (following BS-1377 (1990)). Sub-samples where collected

every 10–5 cm for water content, grain size analysis, biostratigraphic investigation and AMS^{14}C dating on foraminiferal tests (*N. pachyderma* monospecies and/or mixed benthic and planktonic).

65.3 Morphology

The central and northern sectors of Storfjorden TMF present a rather uniform seafloor morphology (Fig. 65.2). The continental shelf edge located approximately along the 420 m isobath is followed downslope by a 2–3 km wide band of relatively steep seafloor gradient locally exceeding 3°. Further downslope, the gradient settles uniformly between 0.5° and 1.5°. This relief is interrupted by a set of nearly straight gullies about 1 km wide, cutting 10 m below the local seafloor (bsf). Gullies are typically 5–10 km long and gradually disappear downslope at 900–1,200 m water

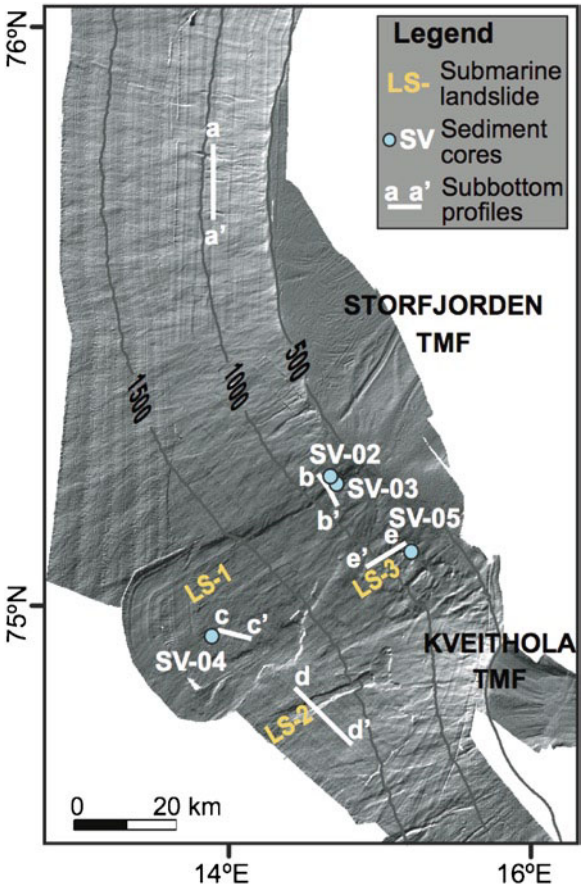

Fig. 65.2 Swath bathymetry map of the study area with indication of submarine landslides, sediment cores, and location of chirp profiles

depth (Pedrosa et al. 2011). There, the continental slope sediment surface is made of an alternation of subdued mounds consisting of depositional lobes of glacigenic debris flows (Laberg and Vorren 1996).

The southern sector of Storfjorden TMF and the northern sector of Kveithola TMF present, instead, a more articulated seafloor morphology with an uppermost steeper (up to 5°) and in places wider (10 km) slope. Gullies are narrower (200–500 m), more deeply incised (down to 15 mbsf), and longer (up to 50 km). Here the most significant morphological feature is the presence of several shallow submarine landslides whose headwall scarps are commonly located between 600 and 800 m water depth cutting 15–40 m into the sedimentary column. Only the two coalescent scars of landslide LS-2 are in deeper water (1,200–1,300 m) on the Kveithola TMF (Fig. 65.2). Sidewall scarps are morphologically evident down to about 1,800 m water depth. The largest landslide scar LS-1 appears to be composed of several coalescent scars, some of which are located in deep water. The seafloor enclosed by the headwall and lateral scarps is slightly stream-lined and is likely to represent the surface of the translational zone. From the bathymetric data there is no clear evidence of where deposition of the failed-sediment took place.

65.4 Shallow Sediment Structure

In the sub-bottom profiler records all submarine landslides cut the uppermost three seismic units identified on this margin (Fig. 65.3a):

- Unit A is the uppermost depositional unit, which drapes the entire margin and has a thickness ranging from 3.75 m on the central and northern Storfjorden TMF (Fig. 65.3a), to 15 m in the southern area where submarine landslides occur (Fig. 65.3b, c, depth calculated using a reference Vp of 1,500 $m\,s^{-1}$). This unit is composed by an uppermost acoustically transparent interval (A1) and a basal acoustically laminated part (A2) both with variable thickness.
- Unit B occurs as a seismically transparent unit (Fig. 65.3b, c) or with internal hummocky reflector configuration (Fig. 65.3a) having an irregular upper boundary and often a basal erosive surface. This unit is up to 45 m thick and continuous throughout the central and northern sectors of Storfjorden TMF (Fig. 65.3a), whereas in the southern area, Unit B is occasionally missing or reduced to individual lenses up to 20 m thick (Fig. 65.3b, c).
- Unit C displays high amplitude, parallel to sub-parallel reflectors with a high lateral continuity and a rather homogeneous thickness of about 20 m. In places it is incised by paleo-gullies filled by the overlying sediments of Unit B.

The basal detachment surface of the landslides is located at the boundary between Unit C and the underlying Unit D, which is similar to Unit B and represents in most cases the acoustic basement (Fig. 65.4a). Unit D is widespread on the entire Storfjorden and Kveithola TMFs having a consistent thickness of about 30 m (Fig. 65.3).

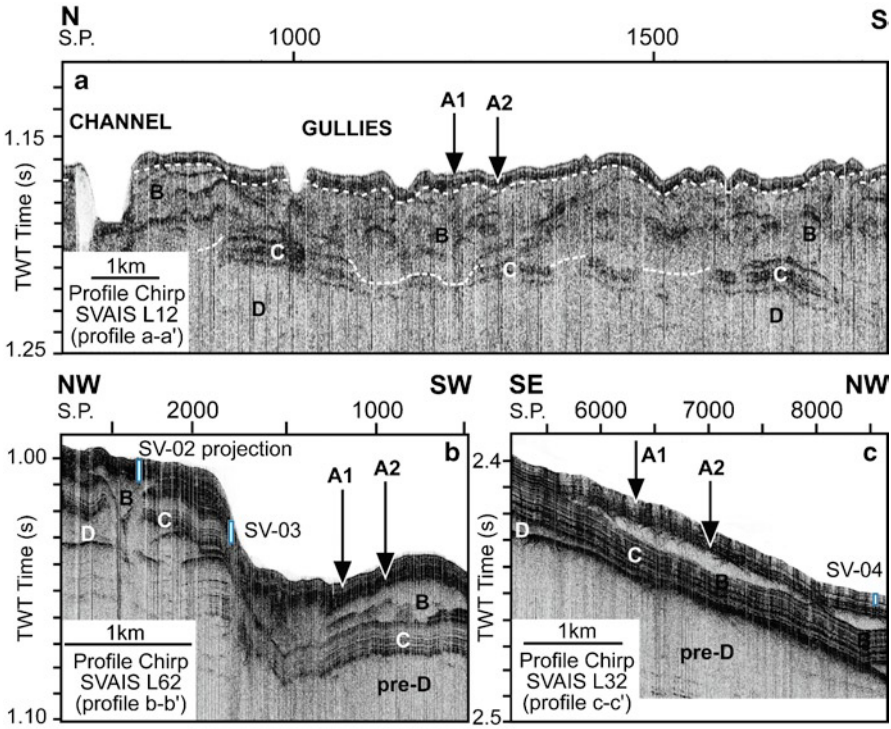

Fig. 65.3 (**a**) Chirp profiles across the upper slope of the northern Storfjorden TMF. (**b**) Chirp profile on the upper slope of the NW sidewall of landslide LS-01 and location of cores SV-02, -03. (**c**) Chirp profile across the mid slope of landslide LS-01 and location of core SV-04

65.5 Lithofacies and Physical Properties

The sediments composing seismic Units A and B have been sampled in cores SV-02 and -04 (Fig. 65.5). The uppermost acoustically transparent Unit A1 consists on heavily bioturbated and crudely layered mud recovered in the mid slope cores (SV-04), and structureless IRD-rich silt recovered in the upper slope (SV-02). Dating indicates Holocene sediments (interglacial stage). Below this interval the acoustically stratified Unit A2 is composed by finely laminated mud interbedded with sandy layers. These deposits are thinner in the mid slope (0.15 m in core SV-04) compared to the upper slope (3.3 m in core SV-02 and over 4.5 m in SV-03, Fig. 65.3b). At the base of Unit A2 is a thin (less than 1 m) deposit of structureless medium/coarse-grained silt with sparse ice rafted debris (IRD). Sediment dating indicates Late Weichselian (deglaciation phase).

Further down-core is either a highly consolidated diamicton (LGM glacial debris flow deposit of seismic Unit B; i.e. base of core SV-02), or a water-rich

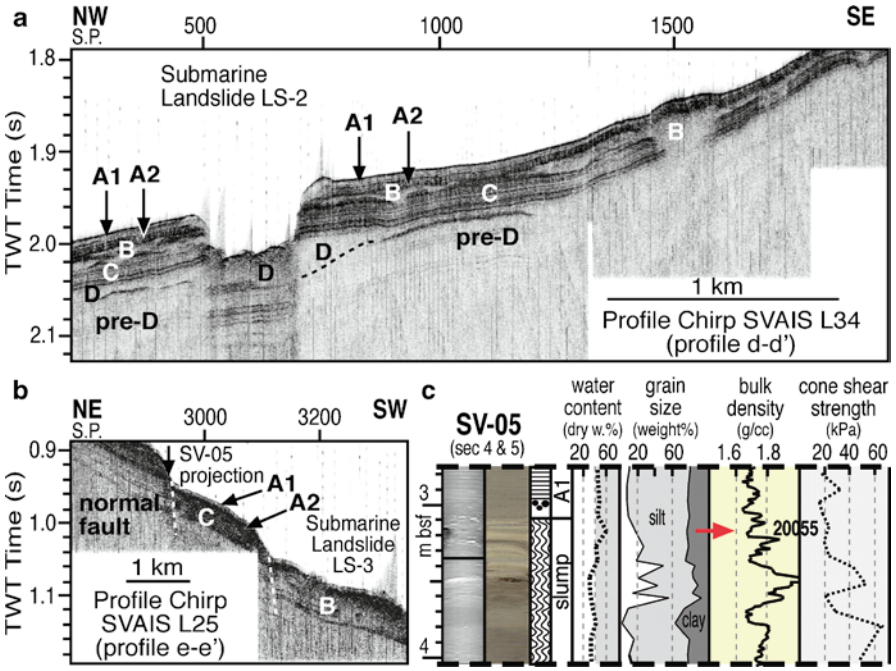

Fig. 65.4 Seismic and geological evidences of landslides and slumps**.** (**a**) Chirp profile across landslide *LS-2* displaying the uppermost seismic Units *A, B*, and *C*. (**b**) Location of core SV-05 on the chirp profile along landslide LS-3; (**c**) slump deposit below the interlaminated facies in core SV-05. Dating indicates pre-LGM sediments. Core log legend as in Fig. 65.5

debris flow/slump deposit, probably representing the upper part of the sediments remoulded by submarine landslides (i.e. base of core SV-04 and -05; Figs. 65.4, 65.5).

Seismic Units C and D have not been sampled. However, due to the acoustic analogy with the laminated part of Unit A, Unit C is thought to be made of interlaminated sediments that likely deposited in the Middle Weichselian (approximately between 60 and 23 ka). Unit D is, therefore, a deeper interval of glacigenic debris flows correlated to the Middle Weichselian glacial maximum between 65 and 60 ka (Mangerud et al. 1998; Pedrosa et al. 2011).

The lithofacies described in Unit A and B differ for physical properties (Fig. 65.5). The highest water content (Wc =129–150%) and lowest shear strength (Su =2–12 kPa) were measured in the uppermost bioturbated and crudely laminated mud (Unit A1, SV-04) that largely contrast with the underlying IRD-rich and interlaminated sediments. On the upper slope the Wc decreases progressively in the interlaminated sediments down to 41–50% (sandy layers and laminated mud respectively) and 45% in the underlying IRD-rich silts. Accordingly, the sediment bulk density and Su increase down-core within Unit A2.

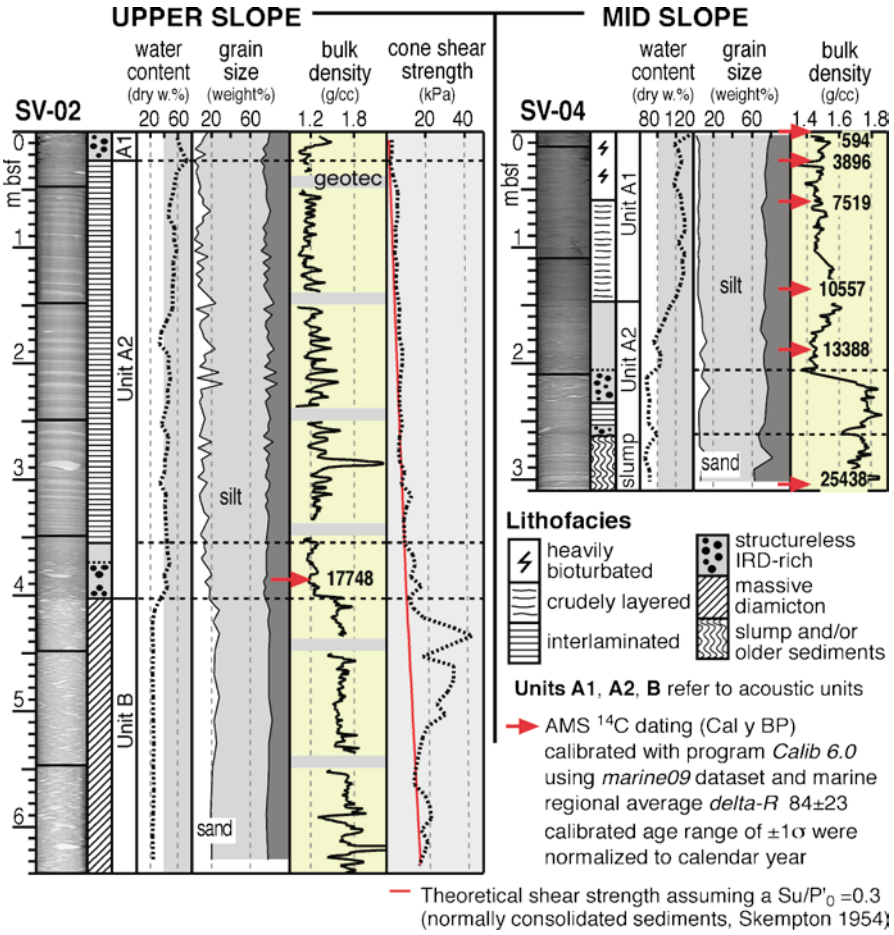

Fig. 65.5 Lithology and physical properties of cores SV-02 and –04. Whole-round samples for geotechnical purposes were collected after X-rays analysis but prior to MSCL scan

A sharp lithological/physical property change occurs at the boundary between the structureless IRD-rich silts at the base of Unit A2 and the glacigenic diamicton of Unit B (SV-02). Wc drops from 45% to 23% while the bulk density increases from 1.8 to 2.2 g cc^{-1} and Su increases from 20 to 44 kPa (Fig. 65.5). A comparison between down core trends of the measured Su and the theoretical Su profile for equivalent normally consolidated sediments suggest over consolidation of the glacigenic diamicton (Fig. 65.5).

The high shear strength measured in the older slumped sediments recovered at the base of core SV-05 is associated to the presence of a sandy interval (Fig. 65.4c).

65.6 Discussion

65.6.1 Lithofacies and Stratigraphy

Landslide LS-2, at least in its lower part, appears to be the youngest event studied in the area as the translational zone imaged in Fig. 65.4a is apparently not draped by the postglacial sediments of Unit A, leaving Unit D exposed at the sea surface. For this drape not to be resolved in the sub-bottom profiler data, its thickness, if any, must not exceed a few decimetres. According to the stratigraphy/age of the studied core a drape of a few decimetres would correspond to a few thousands years or, in any case, not older than Holocene time. Conversely, in the large composite landslide LS-1 the translational area contains at least the last three undisturbed seismic Units A, B, and C (Fig. 65.3b). Therefore, such landslides must have occurred prior to, or at the beginning of the Middle Weichselian (before deposition of Unit C, approximately around 70 ka). The morphology of the composite scars of LS-1 suggests that later failures might have happened in the lower slope.

The detachment surface of the observed landslides occurs at the boundary between the interlaminated sediments deposited during periods of deglaciation (plumites, Unit C), and the underlying glacigenic debris flows deposited during the preceding glacial maximum (Units D). Both sediment types represent episodes of rapid accumulation in which the resulting deposits, however, largely differ in water content and shear strength characteristics.

The interlaminated lithofacies is deposited preferentially on the upper continental slope as a consequence of the initial subglacial meltwater outbursts when the ice stream is grounded at or near the continental shelf edge. Plumites deposition occurs proximal to the source and the depocentre is thought to migrate landwards on the continental shelf as the grounding line retreats. Dating of the interlaminated facies from the upper slope of the southern Storfjorden TMF suggests deposition might have occurred in a few hundreds years with a sedimentation rate as high as 3.2 cm yr^{-1} (Lucchi et al. 2010).

The underlying diamicton represents the frontal/basal glacial moraine deposited massively over the shelf edge during glacial maxima that may last a few thousands years, so that 45 m of deposit would results in an average of sediment accumulation rate in the order of 1 cm yr^{-1}. In contrast to the interlaminated facies, the resulting deposit is overconsolidated with low water content and high shear strength.

65.6.2 Sedimentary Processes Relevant to Slope Stability

The Late Quaternary sedimentary record in southern Storfjorden and Kveithola TMFs, characterized by recurrent failure of the continental slope (see also Rebesco et al. 2012), differs from the northern stable part of Storfjorden TMF.

The southern sector of the TMF contains a thicker Middle and Upper Weichselian interlaminated sequence (Units C and A respectively) that can reach 45–50 m in thickness (Figs. 65.3 and 65.4). Such sequence is discontinuously interbedded with the LGM diamicton (Unit B) that attains up to 20 m in thickness in individual lenses. According to Lucchi et al. (2010) the proximity of the southern Storfjorden TMF to the Spitsbergen Banken, determined a longer persistence of the ice stream close to the shelf edge during the Middle and Late Weichselian, so that the upper continental slope received a prolonged input from subglacial meltwater plumes causing the deposition of an expanded plumite sequence.

We suggest that the most important sedimentological process preconditioning the generation of submarine landslides in this part of the Storfjorden TMF is the rapid deposition of a thick sequence of fine-grained, high water content plumites leading to low shear strength relatively to the underlying sediments. Within plumites (Unit C), the excess pore water pressure induced by the rapid emplacement of the high-density, low-permeability glacial diamicton (Unit B) cannot be dissipated, generating a decrease in the effective stress that determines the failure. Our seismic profiles suggest the detachment occurs at the base of the interlaminated sequence (between Units C and D).

Conversely, in the central and northern part of Storfjorden TMF, the dominance of the thick, continuous, low water content and high shear strength diamicton determines an overall stability of the slope.

65.7 Conclusions

Two types of mass wasting deposits are identified on Storfjorden and Kveithola TMF slopes: (1) low water content, high shear strength, overconsolidated glacigenic diamicton directly related to short periods of ice streams grounded at the continental shelf edge during glacial maxima; (2) slump deposits and debrites occurring within landslide scars.

Submarine landslides are confined to the southern part of the Storfjorden and on the Kveithola TMFs. Analysis of the sediment lithofacies distribution with respect to the extent in time and space of submarine landslides suggests that an important factor in determining slope instability is the thickness of the fine-grained interlaminated lithofacies (plumites). According to our data, failure occurs preferentially along the boundary between plumites and the underlying diamicton. Rapid loading of plumites by younger glacial diamicton is thought to result in excess pore water pressure leading to reduce effective stress that determines conditions favourable to failure.

Acknowledgements This study is supported by Spanish IPY projects SVAIS (POL2006-07390/CGL) and IPY-NICE STREAMS (CTM2009-06370-E/ANT), the Spanish project DEGLABAR (CTM2010-17386) and by OGS IPY Project EGLACOM. We acknowledge Solheim A. and Winkermann D. for revision and improvement of the manuscript. We thank ENI E&P Division for the analysis with X-ray CT scan.

References

Bryn P, Berg K, Forsberg CF, Solheim A, Kvalstad TJ (2005) Explaining the Storegga Slide. Mar Petrol Geol 22:11–19

BS-1377 (1990) British standard methods for soils for engineering purposes, Part 7, Shear strength tests (total stress). British Standards Institution, p 46

Colmenero-Hidalgo E, Rigual Hernández AS, Lucchi RG, Bárcena MA, Sierro FJ, Flores J-A, de Vernal A, Camerlenghi A (2009) Analysis of a new micropalaeontological record from the southern margin of the Svalbard Archipelago (Arctic Ocean): preliminary results and palaeoceanographic implications. Geogaceta 46:91–94

Dimakis P, Elverhøi A, Høeg K, Solheim A, Harbitz C, Laberg JS, Vorren TO, Marr J (2000) Submarine slope stability on high-latitude glaciated Svalbard–Barents Sea margin. Mar Geol 162:303–316

Elverhoi A, De Blasio FV, Butt FA, Issler D, Harbitz C, Engvik L, Solheim A, Marr J (2002) Submarine mass-wasting on glacially-influenced continental slopes: processes and dynamics. In: Dowdeswell JA, O-Cofaigh C (eds) Glacier-influenced sedimentation on high-latitude continental margins, Journal of Geological Soceity, London, Special Publication 203, pp 73–87

Hjelstuen BO, Eldholm O, Faleide JI (2007) Recurrent Pleistocene mega-failures on the SW Barrents Sea margin. Earth Planet Sci Lett 258:605–618

Knies J, Matthiessen J, Vogt C, Laberg JS, Hjelstuem BO, Smelror M, Larsen E, Andreassen K, Eidvin T, Vorrem TO (2009) The Plio-Pleistocene glaciations of the Barents Sea-Svalbard region: a new model based on revised chronostratigraphy. Quat Sci Rev 28:812–829

Laberg JS, Camerlenghi A (2008) Significance of contourites for submarine slope stability. In: Rebesco M, Camerlenghi A (eds) contourites, vol 60, Development in Sedimentology Series. Elsevier, Amsterdam, pp 537–556

Laberg JS, Vorren TO (1996) The glacier-fed fan at the mouth of Storfjorden trough, western Barren Sea: a comparative study. Geol Rundsch 85:338–349

Lee HJ (2009) Timing of occurrence of large submarine landslides on the Atlantic Ocean margin. Mar Geol 264:53–64

Lekens WAH, Sejrup HP, Haflidason H, Petersen GØ, Hjelstuen B, Knorr G (2005) Laminated sediments preceding Heinrich event 1 in the Northern North Sea and Southern Norwegian Sea: Origin, processes and regional linkage. Mar Geol 216:27–50

Leroueil S, Le Bihan JP (1996) Liquid limits and fall cones. Can Geotech J 33:793–798

Lucchi RG, Camerlenghi A, Colmenero-Hidalgo E, Sierro FJ, Bárcena MA, Flores JA, Urgeles R, Macri P, Sagnotti L, Caburlotto A (2010) Sedimentary processes on the Storfjorden trough-mouth fan during last deglaciation phase: the role of subglacial meltwater plumes on continental margin sedimentation. Geophys Res Abstr 12: EGU2010-5753-2

Mangerud J, Dokken T, Hebbeln D, Heggen B, Ingólfsson Ó, Landvik JY, Mejdahl V, Svendsen JI, Vorren TO (1998) Fluctuations of the Svalbard-Barents sea ice sheet during the last 150,000 years. Quat Sci Rev 17:11–42

Pedrosa MT, Camerlenghi A, De Mol B, Urgeles R, Rebesco M, Lucchi RG, SVAIS, EGLACOM cruises shipboard parties (2011) Seabed morphology and shallow sedimentary structure of the Storfjorden and Kveithola Trough-Mouth Fans (north west Barents Sea). Mar Geol 286:65–81

Rebesco M, Liu Y, Camerlenghi A, Winsborrow M, Laberg JS, Caburlotto A, Diviacco P, Accettella D, Sauli C, Wardell N, Tomini I (2011) Deglaciation of the Barents Sea ice sheet - a swath bathymetric and sub-bottom seismic study from the Kveithola Trough. Mar Geol 279:141–147

Rebesco M, Pedrosa MT, Camerlenghi A, Lucchi RG, Sauli C, Dem Mol B, Madrussani G, Urgeles R, Rossi G, Böhm G (2012) One Million Years of Climatic Generated Landslide Events on the Northwestern Barents Sea Continental Margin. In: Yamada Y et al (eds) Submarine mass movements and their consequences, vol. 31, Advances in natural and technological hazards research. Springer, Dordrecht, pp 747–756

Skempton AW (1954) Discussion of the structure of inorganic soils. J Soil Mech Found Div 80:263–264

Vorren TO, Laberg JS, Blaume F, Dowdeswell JA, Kenyon NH, Mienert J, Rumohr J, Werner F (1998) The Norwegian-Greenland sea continental margins: morphology and late quaternary sedimentary processes and environment. Quat Sci Rev 17:273–302

Chapter 66
One Million Years of Climatic Generated Landslide Events on the Northwestern Barents Sea Continental Margin

Michele Rebesco, Maria T. Pedrosa, Angelo Camerlenghi, Renata G. Lucchi, Chiara Sauli, Ben De Mol, Gianni Madrussani, Roger Urgeles, Giuliana Rossi, and Gualtiero Böhm

Abstract Relatively recent, shallow landslides are imaged both on swath bathymetry, sub-bottom and multichannel seismic reflection (MCS) data from the upper-middle continental slope on the Storfjorden and Kveithola Trough Mouth Fans, NW Barents Sea margin. Giant paleo-landslide deposits, detected only by MCS profiles, are characterized by chaotic acoustic units up to about 250 m thick on the lower continental slope. The thickest, oldest landslide, dated between 1 and 0.8 Ma,

M. Rebesco (✉) • C. Sauli • G. Madrussani • G. Rossi • G. Böhm
Istituto Nazionale di Oceanografia e di Geofisica Sperimentale - OGS, Borgo Grotta Gigante 42/C 34010, Sgonico (TS), Italy
e-mail: mrebesco@ogs.trieste.it

M.T. Pedrosa
Departament d'Estratigrafia Paleontologia i Geociències Marines, Facultat de Geologia, Universitat de Barcelona, C/ Martí i Franquès, s/n, E-08028 Barcelona, Spain

A. Camerlenghi
Departament d'Estratigrafia Paleontologia i Geociències Marines, Facultat de Geologia, Universitat de Barcelona, C/ Martí i Franquès, s/n, E-08028 Barcelona, Spain

ICREA, Istitució Catalana de Recerca i Estudis Avançats, Barcelona, Spain

R.G. Lucchi
Istituto Nazionale di Oceanografia e di Geofisica Sperimentale - OGS, Borgo Grotta Gigante 42/C 34010, Sgonico (TS), Italy

Departament d'Estratigrafia Paleontologia i Geociències Marines, Facultat de Geologia, Universitat de Barcelona, C/ Martí i Franquès, s/n, E-08028 Barcelona, Spain

B. De Mol
Dept. Estratigrafia, Paleontologia i Geociències Marines, Facultat de Geologia, Universitat de Barcelona, c/ Martí i Franquès s/n 08028, Barcelona, Catalonia, Spain

Parc Científic de Barcelona, c/ Adolf Florensa 8 08028, Barcelona, Catalonia, Spain

R. Urgeles
Institut de Ciències del Mar (CSIC), Passeig Marítim de la Barceloneta, 37-49, 08003 Barcelona, Catalonia, Spain

Y. Yamada et al. (eds.), *Submarine Mass Movements and Their Consequences*, Advances in Natural and Technological Hazards Research 31,
DOI 10.1007/978-94-007-2162-3_66, © Springer Science+Business Media B.V. 2012

took place just after the large-scale intensification of glaciation in the Barents Sea. The apparent spatial coincidence of landslides and channels with the boundary between the two fan systems, that are generated due to huge quantities of sediments transported to the continental slope by paleo-ice streams, suggests a common controlling climatic process for their development. Most probably the slides are related to the abundance of basal meltwater beneath the ice sheet, which in addition to determining ice stream motion and lubrication also influences the behavior of mass wasting processes.

Keywords Submarine landslide • Continental slope • Seismic reflection • Seafloor morphology • NW Barents Sea margin

66.1 Introduction

Sedimentation on the Storfjorden and Kveithola Trough Mouth Fans (TMFs) on the NW Barents Sea continental margin (Fig. 66.1) has been influenced by the presence of ice during the late Cenozoic. Beside the common sedimentary processes operating at low latitudes (as transport and deposition by contour currents and mass-wasting), high latitudes are affected by glacial processes, which characterizes the nature and rates of all sedimentary processes (Dowdeswell et al. 2002). Major periods of margin progradation are associated with relatively short time intervals of ice terminating at the shelf break during glacial maxima. Fleets of icebergs and associated Ice Rafted Debris (IRD), cascades of meltwater and large quantities of suspended sediments (plumes), and unsorted debris, concentrate at the mouths of fast-flowing ice streams occupying cross-shelf troughs (Solheim et al. 1998). These sediments are efficiently reworked and delivered into the basins by Glacigenic Debris Flows (GDFs). Contrary to low-latitude fans that are fed by rivers through a channel levee complex, glacier-fed TMFs, receive their main sedimentary input from a glacier margin at the shelf break. As a result, high-latitude depocenters are mostly elongated across the upper slope, whereas low-latitude deep-sea fans lie on the middle slope (Laberg and Vorren 1996).

New seismic and morphobathymetric data from the NW Barents Sea are used in this paper to examine a sequence of landslides and to shed light on the importance of the sedimentological control for continental slope instability at high latitude continental margins.

66.1.1 Regional Geology

A landslide off Kveithola Trough (Fig. 66.1) was firstly recognized, along with the adjacent INBIS channel, in GLORIA long-range side-scan sonar and 3.5 kHz data acquired in summer 1994 (Vorren et al. 1998). However, the data did not sufficiently resolve this area of instability and lacked the sedimentological calibration to

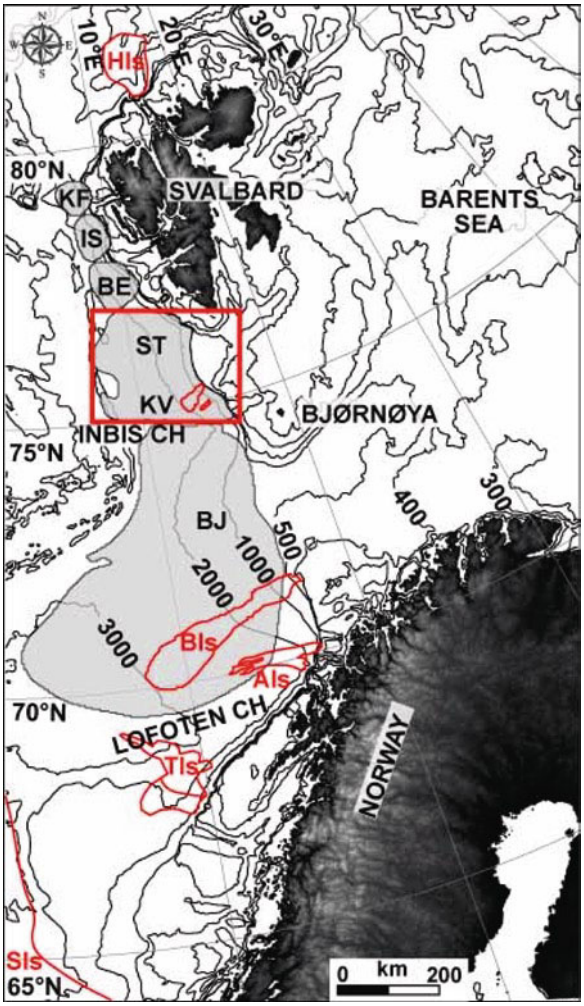

Fig. 66.1 Location map of study area (*red square*). Major TMF (*KF* = Kongsfjorden, *IS* = Isfjorden, *BE* = Bellsund, *ST* = Storfjorden, *KV* = Kveithola, *BJ* = Bjørnøya), landslides (*Hls* = Hinlopen, *Kls* = Kveithola, *Bls* = Bjørnøyrenna, *Als* = Andøya, *Tls* = Trænadjupet, *Sls* = Storegga) and channels (INBIS and Lofoten) are shown

characterize the channel system. Nevertheless, the continental slope off Kveithola Trough is one of the major areas of instability of the Norwegian-Barents Sea-Svalbard margin along with Hinlopen, Bjørnøya, Andøya, Trænadjupet and Storegga landslides (Fig. 66.1).

Channel systems are extremely unusual along this >2,000 km long continental margin and are confined to the INBIS and Lofoten channels (Fig. 66.1). The Lofoten Channel has been directly fed by subglacial-debris, in addition to turbid subglacial meltwater plumes. Canyon preservation and continued development can be attributed

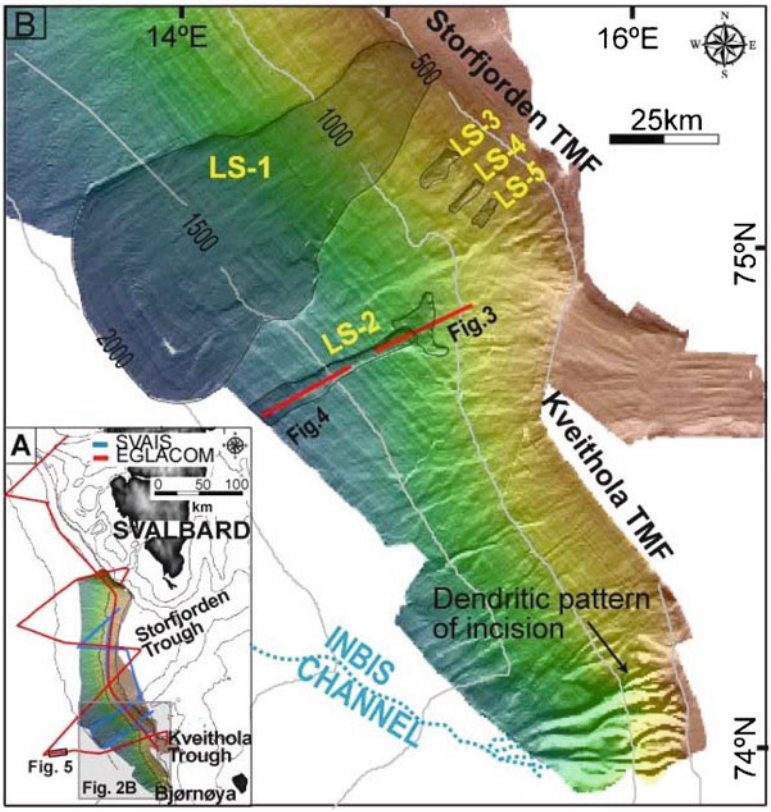

Fig. 66.2 Swath bathymetry data. (**a**) Position of the *seismic lines* (*red* = multi-channel, *blue* = single channel) superposed on the whole multi-beam data. Location of Figs. 66.2b and 66.5 is also shown. (**b**) close up of multi-beam data showing the major landslides (LS-1, LS-2, LS-3, LS-4 and LS-5). Location of Figs. 66.3 and 66.4 is also shown

directly to the comparatively low sedimentation rates during glacial-maxima conditions, as ice streams produced regional depocentres away (to the north and south) from this area of relatively slow-flowing ice (Taylor et al. 2002). The INBIS Channel is located in a similar setting (Figs. 66.1 and 66.2), in the inter-TMF area between the regional depocentres of the Bear Island and, the much smaller, Kveithola TMFs (Vorren et al. 1998).

The TMFs along this margin (Fig. 66.1) are (from north to south): the Kongsfjorden, Isfjorden, Bellsund Storfjorden, Kveithola and Bjørnøya Fans (Fig. 66.1). These fans contain an archive of past ice sheet expansion and recession. The main element of these fans is a series of GDFs. However, considerable areas of TMFs are also dominated by plumites and/or contourites, which are significant for fan development either during periods of reduced GDF deposition or during glacial maxima, concurrently with (but elsewhere from) GDF (Taylor et al. 2002).

In contrary, in areas between ice streams, where slower ice reached the shelf break and TMF are not present, the continental slope is characterized by large-scale sediment landslides and canyon systems (Vorren et al. 1998; Dowdeswell et al. 2002; Taylor et al. 2002).

66.1.2 Data and Methods

The data presented in this paper were acquired during two research cruises carried out within the International Polar Year (IPY). The Spanish SVAIS cruise (*BIO Hespérides,* summer 2007) and the Italian EGLACOM cruise (*R/V OGS-Explora,* summer 2008), both contributed to IPY Activity 367 NICE-STREAMS, aiming at understanding erosion and depositional systems associated with ice streams. Data acquisition focused on the Storfjorden and Kveithola TMFs (Fig. 66.2a) and included collection of multi- and single-channel seismic profiles, swath bathymetry and sub-bottom profiler data.

For deep and shallow water multi-beam echo-sounding respectively, the *BIO Hespérides* employed a Simrad EM120 (mean frequency of 12 kHz) and a EM1002S (mean frequency of 95 kHz), while the *R/V OGS-Explora* employed a Reson MB8150 (mean frequency of 12 kHz) and a MB8111 (operating at a mean frequency of 100 kHz). The joint multi-beam bathymetric survey area covered by both cruises is about 15,340 km^2. For sub-bottom profiling, the Kongsberg TOPAS PS 18 hull-mounted parametric sub-bottom profiler was used on the *BIO Hespérides*, while the hull-mounted Benthos CAP-6600 sub-bottom chirp profiler was used on the *R/V OGS-Explora.* The total length of acquired sub-bottom profiler data is nearly 9,500 km.

The acquisition of the MCS data was performed on board *R/V OGS-Explora* with a 1,200 m long digital streamer with 96 channels (spaced 12.5 m) and a 160 cubic inches array of sleeve guns. Fold coverage was 24, shot interval 25 m and sampling rate 1 ms. Finally, an integrated interpretation of all data has been performed using the Kingdom Suite software provided by Seismic Micro-Technology. The total length of acquired MCS profiles is 1,071 km.

The acquisition of the single-channel seismic data was performed on board the *BIO Hespérides* with a 10-m ministreamer with 10 hydrophones and a 3,44 1G.I. gun. Shot interval was 6 s (15.5 m at 5 kt), sampling rate 0.5 ms and record length 5 s. The total length of acquired single-channels seismic profiles is 518 km.

66.2 Results

Both surface and buried landslides identified on the basis of our multi-beam and seismic reflection data lie in a restricted part of the continental slope (about 50 km wide) between the southern part of the Storfjorden TMF and the Kveithola TMF. The previous described Kveithola landslide observed in the GLORIA data would

correspond to one of these landslides. Only relatively minor landslides are identified in the multi-beam data from the northern Storfjorden TMF, and in the seismic data that crosses the Isfjorden and Bellsund TMFs (Figs. 66.1, 66.2a) further north. At the southern flank of the Bear Island TMF, immediately south of Kveithola TMFs, the seabed is characterized by a dendritic pattern of deep, V-shaped incisions (Fig. 66.2b), similar to those on non-glacial continental margins. It is most likely that these incisions converge, outside our bathymetric coverage, into a major channel on the lower continental slope, which ultimately merges with the previously reported INBIS channel system (Vorren et al. 1998).

Numerous shallow, relatively recent landslides detected on the swath bathymetry, and giant buried paleo-landslides identified on seismic data almost coincide in space. This series of sediment instabilities includes composite head walls (recognizable in the modern morphology) that are indicative of a multi-phase origin.

Landslide 1 (LS-1, Fig. 66.2b), the largest shallow landslide is fan-shaped and is bounded by 35–40 m high side- and head-walls which are sloping 5–7° (and locally up to over 10°). Minor scars complicate the morphology of the sidewalls. The translational domain of the landslide (between the main head wall and the landward edge of the depositional area) covers an area of about 1,100 km^2 in our data. However, it is clear that the landslide continues further downslope, with the depositional domain not imaged by our data. The minimum volume of sediments removed by this landslide (the part within our surveys) is approximately 33 km^3, assuming that the slope between the side- and headwalls was continuous before failure. The slope gradient, both within the landslide and in the surrounding continental slope, ranges between 1° and 2°.

Southeast of LS-1, other bowl-shaped depressions (landslides LS-2, LS-3, LS-4, LS-5 and minor others not labeled in Fig. 66.2b) have been identified on the upper continental slope (Pedrosa et al. 2011). The depression of Landslide 2 (LS-2) is narrow and elongated, only slightly widening downslope and with a moderately broader headwall area at c. 1,300 m water depth (Figs. 66.2b and 66.3). The depression is about 20 km long and about 2 km wide, hence enclosing an area of nearly 50 km^2. The side- and head walls are nearly 30 m high and hence the volume of sediments removed is < 2 km^3.

A more modest but larger secondary head wall is present about 4 km landward of the main head wall of the landslide, and is apparently generated by a series of successive and adjacent, minor landslides. The translational domain of LS-2 is about 15 km long, hence with the deposition initiating already within the terminal part of the imaged depressed area. The depositional domain of LS-2 is about 15 km long (Fig. 66.4), hence indicating a total run-out of nearly 30 km for this landslide.

Beneath, and for a distance of up to 13 km landward of the main head wall of LS-2, a paleo-landslide (PLS-2) is observed in the MCS data (Figs. 66.4 and 66.5). The slide debrite is about 200 ms (twt) thick. The glide plane of this slide is stepvise shallowing up-slope indicating a backstepping nature of this slide event. This paleo-landslide is interpreted as a multi-phase predecessor of LS-2. The glide-plane of PLS-2 corresponds with Reflector R1 (Fig. 66.3) in the stratigraphic framework as established by Faleide et al. (1996). Reflector R1 has an age of about 0.2 Ma (Butt et al. 2000) and provides the maximum age of this landslide. The seismic data indicate a run-out of at least 100 km for this slide event.

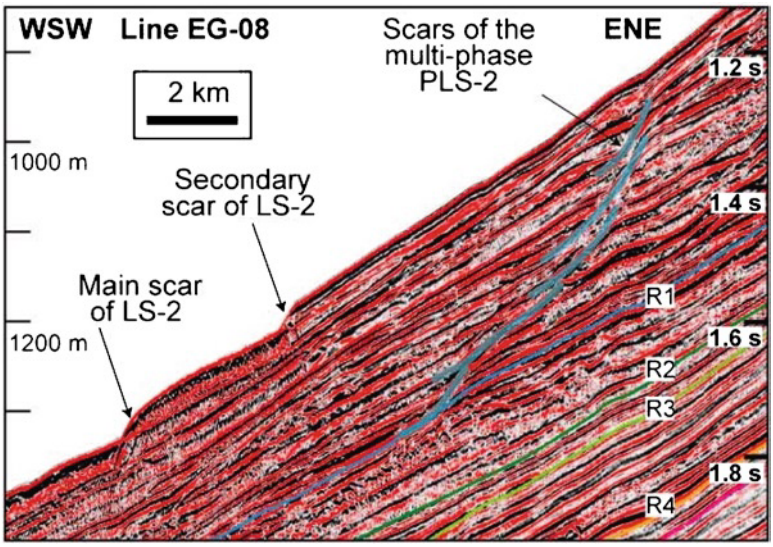

Fig. 66.3 Multi-channel seismic profile EG-08 showing the head wall of LS-2 and PLS-2

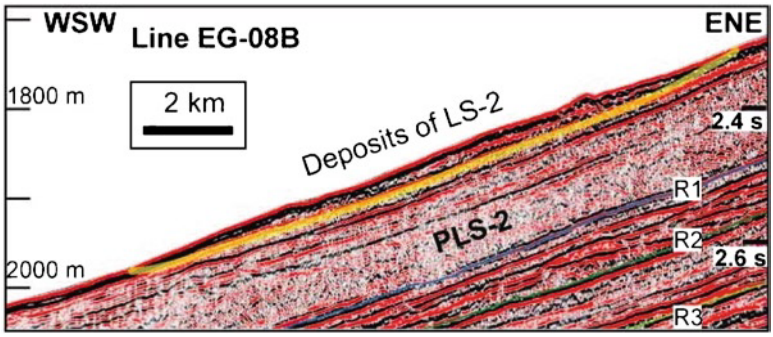

Fig. 66.4 Multi-channel seismic profile EG-08B showing the deposits of LS-2 and PLS-2

An older slide debrite (PLS-1, Fig. 66.5) is more than 250 ms (twt) thick (about 250 m using the nearly 2,000 ms^{-1} stack velocity). The glide plan of this slide event corresponds to Reflector R4 (Faleide et al. 1996), which has an age of about 1 Ma (Butt et al. 2000). Thus, this is the maximum age for this landslide. The minimum age is provided by Reflector R3 (Faleide et al. 1996), that has an approximate age of 0.8 Ma (Butt et al. 2000). PLS-1 likely moved downslope, hence not along profile EG-08B, as suggested by the abrupt eastward termination of PLS-1 (Fig. 66.5). Moreover, it is located in correspondence of the downslope prolongation of the SL-1, at a distance of about 100 km from its head wall. We hence infer that this giant paleo landslide is likely a predecessor of SL-1, and that its head wall (not crossed by our seismic profiles that are oblique to the slope) is likely located on the upper

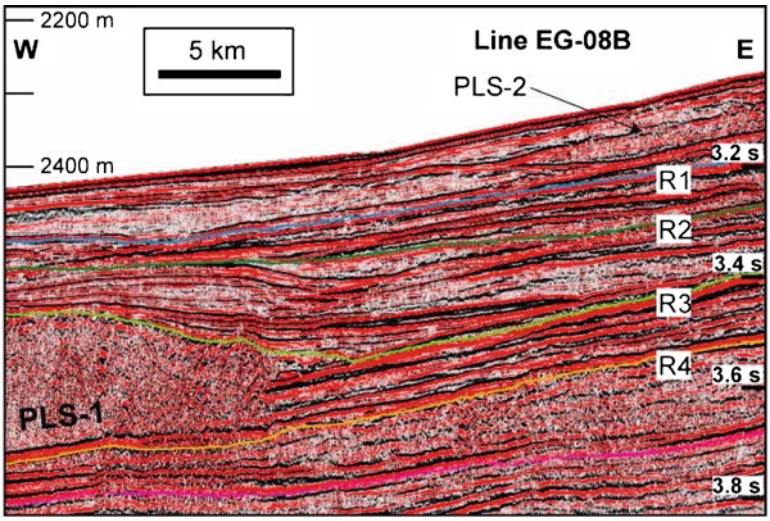

Fig. 66.5 MCS profile EG-08B showing the deposits of PLS-1 and-2 and other smaller ones in between

slope. If our inferences are correct, the minimum run-out of PLS-1 is at least 100 km, comparable with that of PLS-2.

66.3 Discussion and Conclusions

The location on the Storfjorden and Kveithola TMFs and the presence of GDF deposits interbedded with high water-content, low shear strength plumites (Lucchi et al. 2012), suggest a glacial (climatic) control on the landslides occurrence and frequency. Similarly to the scenario developed for the Storegga landslide (Haflidason et al. 2005), it is the climatically-controlled cyclic deposition of different sediment types that determines in situ conditions on the continental slope, which favor slope instability (Lucchi et al. 2012). The analysis of sub-bottom profiles suggests that the base of the surface landslides is the base of laminated sediments interpreted as plumites deposited from meltwater flows produced during the pen-ultimate deglaciation (MIS 3; Pedrosa et al. 2011; Lucchi et al. 2012). Such plumites constitute a laterally extensive homogenous layer of high clay and water content sediments with low shear strength that may develop excess pore pressure and subsequent reduced effective stress in response to rapid loading by GDF during some glacial periods (Haflidason et al. 2005).

The landslides described in this paper lie in a restricted part of the continental slope at the boundary between the adjacent Storfjorden and Kveithola TMFs, whereas the INBIS Channel lies in the inter-TMF area between the Kveithola and Bjørnøya TMFs. The location of the INBIS Channel is consistent with the model of

Dowdeswell et al. (2002), which suggests that TMF progradation occurs mainly by GDF stacking in front of ice streams, whereas canyon systems occur at the margin areas between ice streams where slower moving ice reached the shelf break and the delivery of sediments is significantly lower. That model suggested also that large-scale sediment landslides occur in areas of intermediate rates of ice-sheet delivery of sediment, at the periphery of TMFs. This may also be the case of the landslides that we described, but in addition we suggest that water-rich, clayey sediments with low shear strength deposited by meltwater during deglaciation (plumites) play as well an essential role. The landslides in fact occur just in front of the Kveithola Trough, which is an area of recognized production of meltwater plumes (Fohrmann et al. 1998; Sarnthein et al. 2003). In the area of the landslides, the thickness of the GDF deposits (and possibly hence the rate of glacial sediment delivery) is lower than in the northern part of the Storfjorden TMF, but the thickness of the plumites is larger (Lucchi et al. 2012). The first fact may hence be consistent with the model of Dowdeswell et al. (2002), but the second fact seems to us a more significant controlling factor.

The stratigraphic position of the major paleo-landslides identified suggests a climatic control on their origin. The presence of some discontinuous reflectors with chaotic features above R7 (2.3 Ma) in the Storfjorden TMF (Hjelstuen et al. 1996) and complex reflection pattern with large imbricated blocks above R5 (1.4 Ma) in the Bjørnøya TMF (Fiedler and Faleide 1996) were already interpreted to represent mass movements resulting from increasing sediment transport to the margin, associated respectively to the onset and intensification of glaciations. The giant paleo landslide that we indentified (PLS-1), dated between 1 and 0.8 Ma, took place just after the large-scale intensification of glaciation in the Barents Sea, with expansion of the ice sheet beyond the shelf edge, which occurred at about 1.0 Ma (Knies et al. 2009). The exceptional thickness of this landslide and the absence of comparable landslides in the underlying sedimentary succession (Fig. 66.5) suggest to us that this slope failure was produced by the first major expansion of the ice sheet in the Barents Sea and consequent sudden increase of the sediment delivery to the margin. The relatively small dimension of the subsequent failures (between R3 and R1) would be due to the relatively minor amount of clastic sediments at disposal on the continental shelf after the first major expansion of the ice sheet and consequent sediment delivery to the continental slope. Conversely, the reoccurrence of a very large paleo landslide above the 0.2 Ma R1 reflector (PLS-2) may be related to the increased expansion of the water-rich, clayey sediments with low shear strength deposited by melt water plumes and contour currents, more effective in the last 0.2 Ma (Hjelstuen et al. 1996).

Acknowledgments This work was conducted within the International Polar Year (IPY) Activity 367 (Neogene ice streams and sedimentary processes on high-latitude continental margins — NICE STREAMS). Support for this study has been provided by the Italian EGLACOM and MELTSTORM projects, Spanish project SVAIS (POL2006-07390/CGL), DEGLABAR (CTM2010-17386) and NICE STREAMS-Spain (CTM2009-06370-E). We also thank the reviewers Associate Prof. B. Hjelstuen and Dr. C. Escutia Dotti for critical suggestions and improvements to this manuscript.

References

Butt FA, Elverhøi A, Solheim A, Forsberg CF (2000) Deciphering late Cenozoic evolution of the western Svalbard margin based of ODP Site 986 results. Mar Geo 169:373–390

Dowdeswell JA, Ó Cofaigh C, Taylor J, Kenyon NH, Mienert J, Wilken M (2002) On the architecture of highlatitude continental margins: the influence of ice-sheet and sea-ice processes in the Polar North Atlantic. In: Dowdeswell JA, Ó Cofaigh C (eds) Glacier-influenced sedimentation on high-latitude continental margins. Geological Soceity, London, Special Publication 203, pp 33–54

Faleide JI, Solheim A, Fiedler A, Hjelstuen BO, Andersen ES, Vanneste K (1996) Late Cenozoic evolution of the western Barents Sea-Svalbard continental margin. Glob Planet Change 12:53–74

Fiedler A, Faleide JI (1996) Cenozoic sedimentation along the southwestern Barents Sea margin in relation to uplift and erosion of the shelf. Glob Planet Change 12:75–93

Fohrmann H, Backhaus JO, Blaume F, Rumohr J (1998) Sediments in bottom-arrested gravity plumes: numerical case studies. J Phys Oceanogr 28:2250–2274

Haflidason H, Lien R, Sejrup HP, Forsberg CF, Bryn P (2005) The dating and morphometry of the Storegga Slide. Mar Petrol Geol 22:123–136

Hjelstuen BO, Elverhøi A, Faleide JI (1996) Cenozoic erosion and sediment yield in the drainage area of the Storfjorden Fan. Glob Planet Change 12:95–117

Knies J, Matthiessen J, Vogt C, Laberg JS, Hjelstuem BO, Smelror M, Larsen E, Andreassen K, Eidvin T, Vorren TO (2009) The Plio-Pleistocene glaciations of the Barents Sea-Svalbard region: a new model based on revised chronostratigraphy. Quat Sci Rev 28:812–829

Laberg JS, Vorren TO (1996) The glacier-fed fan at the mouth of Storfjorden Trough, western Barents Sea: a comparative study. Geol Rundsch 85:338–349

Lucchi RG, Pedrosa MT, Camerlenghi A, Urgeles R, De Mol B, Rebesco M (2012) Recent submarine landslides on the continental slope of Storfjorden and Kveitehola Trough-Mouth Fans (north west Barents Sea). In: Yamada Y et al (eds) Submarine mass movements and their consequences, vol. 31, Advances in natural and technological hazards research. Springer, Dordrecht pp 735–745

Pedrosa MT, Camerlenghi A, De Mol B, Urgeles R, Rebesco M, Lucchi RG, SVAIS, EGLACOM Cruises shipboard parties (2011) Seabed morphology and shallow sedimentary structure of the Storfjorden and Kveitehola Trough-Mouth Fans (north west Barents Sea). Mar Geol 286:65–81

Sarnthein M, van Kreveld S, Erlenkeuser H, Grootes PM, Kucera M, Pflaumann U, Schulz M (2003) Centennial-to-millennial-scale periodicities of Holocene climate and sediment injections off the western Barents shelf, 75°N. Boreas 32:447–461

Solheim A, Faleide JI, Andersen ES, Elverhøi A, Forsberg CF, Vanneste K, Uenzelmann-Neben G, Channell JET (1998) Late Cenozoic seismic stratigraphy and glacial geological development of the East Greenland and Svalbard-Barents Sea continental margins. Quat Sci Rev 17:155–184

Taylor J, Dowdeswell JA, Kenyon NH, O´ Cofaigh C (2002) Late Quaternary compositional architecture of trough mouth fans: debris flows and suspended sediments on the Norwegian Sea margin. In: Dowdeswell JA, O´ Cofaigh C (eds) Glacier-influenced sedimentation on high-latitude continental margins. Geological Society, London, Special Publication 203, pp 55–71

Vorren TO, Laberg JS, Blaumme F, Dowdeswell JA, Kenyon NH, Mienert J, Rumohr J, Werner F (1998) The Norwegian-Greenland Sea continental margins: morphology and late quaternary sedimentary processes and environment. Quat Sci Rev 17:273–302

Author Index

Y. Yamada et al. (eds.), *Submarine Mass Movements and Their Consequences*,
Advances in Natural and Technological Hazards Research 31,
DOI 10.1007/978-94-007-2162-3, © Springer Science+Business Media B.V. 2012

Subject Index

Y. Yamada et al. (eds.), *Submarine Mass Movements and Their Consequences*, Advances in Natural and Technological Hazards Research 31,
DOI 10.1007/978-94-007-2162-3, © Springer Science+Business Media B.V. 2012